On the Redox Tuning of 3*d* and 5*f* Metal Complexes with Lewis Acids

By
Amit Kumar
M.Sc., Institute of Chemical Technology, Mumbai, India 2015
B.Sc., St. Xavier's College, Mumbai, India 2013

Submitted to the graduate degree program in Chemistry and the Graduate Faculty of the University of Kansas in partial fulfillment of the requirements for the degree Doctor of Philosophy.

Chair: Prof. James D. Blakemore

Prof. Mikhail V. Barybin

Prof. Timothy A. Jackson

Prof. Jon A. Tunge

Prof. Alan M. Allgeier

Date Defended: 02 June 2021

The dissertation committee for Amit Kumar certifies that this is the approved version of the following dissertation:

On the Redox Tuning of 3*d* and 5*f* Metal Complexes with Lewis Acids

_____

Chair: Prof. James D. Blakemore

Date Approved: 14 June 2021

Abstract

The behavior of Lewis acidic metal ions in multimetallic systems has become a subject of intense interest in recent years. Investigations in this area are inspired by the functioning of Nature's oxygen-evolving complex (OEC) in Photosystem II, which features a redox-inactive Ca^{2+} ion involved in reduction potential modulation. In Part I of this dissertation, synthetic, structural, spectroscopic, and electrochemical findings are described for the elucidation, parametrization, and effective leveraging of Lewis acid effects in heterobimetallic complexes of a *d*-block element, nickel, and an *f*-block element, uranium. Incorporation of Lewis acidic metal ions into heterobimetallic complexes for chemical and electrochemical tuning has typically focused on *d*-block elements, but here, this strategy was applied to uranium for the first time. In particular, the redox properties of the uranyl ion (UO_2^{2+}) have been optimized through formation of heterobimetallic complexes, an outcome needed for development of next-generation nuclear fuel reprocessing technologies. To accomplish this goal, nickel and uranyl complexes were divergently prepared with macrocyclic Reinhoudt-type ligands featuring pendant crown-ether-like sites that readily bind a wide range of redox-inactive metal cations (M = Cs^+, Rb^+, K^+, Na^+, Li^+, Ca^{2+}, Nd^{3+}, and Y^{3+}). This divergent strategy, enabled by deliberate preparation of appropriate monometallic precursor complexes, affords unique access to complexes with highly Lewis-acidic trivalent cations, a class of compounds that have previously been inaccessible. Through electrochemical determination of thermodynamic reduction potentials, heterogeneous electron transfer rate constants, and reorganization energy values associated with the U^{VI}/U^{V} redox manifold, quantitative trends were measured and used to formulate a mechanistic framework for optimized uranyl redox cycling and design rules for supramolecular structures that promote efficient electrode-driven actinide chemistry. In Part II of this dissertation, the development of tunable heterobimetallic catalysts for ethylene polymerization and preparation of heterobimetallic complexes with diimine-dioxime-type ligands are discussed. Such chemistries can be understood in the context of the general strategy of incorporating Lewis acidic redox-inactive metals, in that multiple metals are found to operate synergistically in all the systems described here. Taken together, the findings described in this dissertation show that interactions with Lewis acids can be used for the rational tuning of the properties of elements across the periodic table.

Acknowledgements

First and foremost, I would like to thank my advisor and mentor, Prof. James Blakemore, for his constant support and advice throughout my graduate school career, both in my professional and personal life. When I was applying for graduate school, I sent applications to a plethora of universities across the United States to pursue a Ph.D. in Organic Chemistry. However, as soon as I met James, I was so impressed with his multidisciplinary research areas that I could not resist joining his group and switch my research interest to Inorganic Chemistry. He was also the first person to give me a ray of hope when I was contacting various faculty mentors for the possibility of joining their research groups, and that probably drove me towards pursuing higher studies in Inorganic Chemistry. I can now confidently say that my first choice was the best choice. James is a fantastic advisor and has been tremendously supportive of me in the past five years. I never imagined that I would have a boss who is always available to interact and discuss new ideas and possibilities in science every time I approached him. Furthermore, he never hesitated to send me to domestic and international conferences and motivated me to network with people in the scientific community. In addition, he diligently read all my manuscripts and edited them in front of me to help me understand various intricacies associated with scientific writing. Overall, he has been a tremendous mentor and a teacher, and I believe it will be quite difficult for me to find someone like him.

I am thankful to my committee members, Professor Misha Barybin and Professor Timothy Jackson, who have served in my comprehensive exam and dissertation defense. Their helpful advice in my research throughout my graduate school and the teaching of fundamental and advanced inorganic chemistry concepts have shaped me into a better

chemist. It would be unwise not to mention Prof. Barybin's immense contribution in teaching me NMR Spectroscopy and Prof. Jackson's easy-to-digest teaching methodologies in making me learn concepts in inorganic spectroscopy. I would also like to thank members of my committee, Prof. Alan Allgeier, for his guidance in my research projects and his wisdom in career options in the industry and academia, and Prof. Jon Tunge for teaching me concepts in physical organic chemistry like never before. I would also like to mention Prof. Tunge's responsible role as an Associate Chair of Graduate Studies in the Department of Chemistry. He has shown great care for graduate students in this role and never failed to provide the one and only love of graduate students, food, during graduate appreciation week.

I would be remiss not to mention Prof. Davide Lionetti's contributions to my success thus far. My first project at KU was the brainchild of Davide, and his mentoring and guidance helped me publish my first paper in a matter of eight months. His love for chemistry is closely comparable with his penchant towards coffee, ducks, and Inter Milan Football Club. The colossal amount of synthetic chemistry knowledge residing in his brain has taught me to independently make and characterize new inorganic metal complexes, train me to handle compounds in an inert atmosphere, and understand the way chemistry operates in nature. He has played a significant role in my professional career, and this dissertation would have been incomplete without his support.

Another person without whom I wouldn't have published 25 crystal structures is our very own and eccentric crystallographer, Dr. Victor Day. I have never met a person who is critical when it comes to crystallography and, at the same time, has a great sense of humor. He sat with me in front of the computer for several hours, teaching me concepts in chemical crystallography. I never saw him getting annoyed with me if I couldn't understand anything.

It has been an absolute pleasure working with Victor, and I will miss him, his love for sambuca, and his homemade Indian Chicken Curry (which actually never tasted like Indian), of course not to mention all the celebration parties he hosted in his humungous palace.

Next, thanks are due to my seniors David Sconyers and Yun Peng, who helped me understand electrochemistry and synthetic inorganic chemistry right from scratch and for treating me like a baby when I joined Blakemore Group. Special shoutout to my favorite lab members Julie Hopkins and Wade Henke, for being with my ups and downs since the beginning of my graduate school career. Julie became my first real American friend and taught me the pronunciation of some of the English words in an American accent, and I reciprocated by making fun of her for her articulation of 'Breafkast.' On the other hand, Wade was always available to help me fix my car, in addition to helping me with chemistry concepts, and especially removing the burden from my back by literally doing the heavy lifting in the lab. I will also miss dancing with him on top of the table in a bar and being a karaoke partner. Next, thanks to Joe Karnes for being a great human being and for annoying me with his senseless although humorous comments. Although his joy for hot sauce was at a different level, I will miss the glow on his face when he successfully manages to annoy me with his banters. Thanks are also due to my batchmates Shrikant Londhe, Galina Bulgakova, and Yuri Lee, without whom I wouldn't have survived the cultural shock-prone year of my graduate school. Galina for always taking time out to barge into my office and being available to get a cup of coffee with me. Yuri, for joining me in the brave step of changing fields from organic to inorganic. Special mention to my ex-roommate and ex-college mate from my Master's, Shrikant, for providing his shoulders to cry every time I missed my family.

I am also very thankful for my mentee (in the lab) and mentor (in the gym), Shaun Kelsey, for motivating me to work out with him at 7 am in the morning and helping me lose more than 10 pounds in three months. My biceps and triceps have some shape because of this gem, and I genuinely cherish his friendship. To Emily Mikeska and Christian Nilles, though I did not get to spend a lot of fun time with you due to the pandemic, I have been blessed with the amount of life knowledge you have provided me in the past two years. Emily, for teaching me how to play Munchkin, lending me books and showing me how a farmer's market looks like. Christian for being a great rival partner in soccer (although Everton will never be as good as Liverpool) and for bringing delicious food to the office. I still do not understand how he gets time to do gardening, baking, pickling, cooking, along with presenting ten plus slides at group meetings.

I have also had the chance to work with several undergraduates and post-baccalaureate researchers who are now carrying the legacy of Blakemore lab in different universities. I would especially like to thank Keaton Prather, Will Moore, and Tyler Kerr in particular. Keaton's availability after 6 pm every day to play ping pong with me in the office and relieve my stress, for his remarkable sense of humor, and for teaching me how to live, will always be cherished. I was touched when Keatong came all the way from Notre Dame to surprise me with a bottle of wine after I defended my dissertation. I will dearly miss Will Moore's storytelling skills that always ended with a lame joke, his evergreen smiling face whenever I gave a presentation, and his love for the hawk. Tyler Kerr for teaching me many techniques in the lab and sending me beautiful cards every year in collaboration with his girlfriend and my friend & batchmate Angelika Trujilo.

Thanks are due to my collaborators from Chevron Phillips Chemical Company, Dr. Carlos Cruz and Jared Barr, for showing me how my work can be helpful in the real world. Their industrial experiences and insights have helped me gain the skills necessary for the industry. Because of our collaboration, I entered the facility and research center of one of the biggest polyethylene-making companies. Most of the work described in chapters six and seven was performed in collaboration with Carlos and Jared, and it was after working with them, I realized that my work could be useful in future someday to make consumer products.

Lastly, this acknowledgment section would not be complete without mentioning my support pillars in Lawrence. To my family-like friends Riddhi Golwankar, Ankit Verma, Ankita Katiyar, Prasenjit Srivastava, Priya Singh, Sayantani Basu, Juhi Kidwai, and Aparna Chakravarti, I cannot imagine the last three years of my graduate school without their friendship, and I am blessed to have met them. Without them, this journey might never have seen the light of the day. To Aparna for letting me tease her for her Hindi language speaking skills and for bringing gifts and flowers during festivals and after my dissertation defense. To Priya for making us laugh with her naiveness and for being an excellent Roti maker. To Sayantani for her lively nature and for providing philosophical sympathy whenever I felt low. To Juhi for her bold and funny comments and for making delicious food, especially during Ramzan. To Prasenjit for making alcoholic drinks for me and then taking care of me when I stopped being sober. To Ankit for being a fantastic roommate, and for being an amazing cooking partner and an excellent FIFA partner. To Ankita, for tying me Rakhi and spoiling me by giving me presents, making me an adult by teaching me how to live, and for being available anytime for some gossip. Finally, to Riddhi for being my favorite roommate labmate and for her emotional support and letting me play with her pet tortoise, Poppy.

Dedication

I wholeheartedly dedicate this dissertation to my parents. Without their parenting and pampering, I wouldn't have been a better person and thus a better chemist. Their unconditional love and encouragement were the most valuable pillars of support for my success as a graduate student. To my Mummy Dharmsheela and Papa Triloki Nath, you have created a good human being, and I owe my whole life to you. To my brother Deepak, for being a role model, for answering my silly and smart questions, and for helping me financially whenever I was deprived of money. I couldn't have asked for a better sibling, even if we never were engaged in a brawl.

Table of Contents

Appendices for Chapters in Part II

List of Figures and Tables

जब हम बाधाओं से निपटते हैं, तो हम साहस और लचीलापन के छिपे हुए भंडार पाते हैं जो हमें नहीं पता था कि हमारे पास है। और यह केवल तब होता है जब हम असफलता का सामना करते हैं, हमें पता चलता है कि ये संसाधन हमेशा हमारे भीतर थे। हमें केवल उन्हें खोजने और अपने जीवन के साथ आगे बढ़ने की आवश्यकता है।

When we tackle obstacles, we find hidden reserves of courage and resilience we did not know we had. And it is only when we are faced with failure, do we realize that these resources were always there within us. We only need to find them and move on with our lives.

-- Dr. A. P. J. Abdul Kalam

(11th President of India)

Chapter 1

Introduction to Lewis Acid Effects in Heterobimetallic Complexes of *d*- and *f*-block Elements

1.1 Introduction

"Two are better than one if two act as one"- Mike Krzyzewski

This quote from the famous American basketball player and coach Mike Krzyzewski is quite applicable to the vast field of inorganic chemistry. Metals can exhibit unique characteristics and cooperativity when placed in close proximity using appropriately designed ligands, engendering reactivities that cannot be achieved when the constituent metal species are used separately.[1,2] Nature takes advantage of these multimetallic effects in enzymes that utilize multiple metals to carry out small molecule transformations. As a central example, the oxygen-evolving complex (OEC) of Photosystem II (PSII) contains an assembly of four manganese centers and a Ca^{2+} center connected by oxido bridges.[3] PSII utilizes the redox properties of the redox-active Mn centers to facilitate the biological production of O_2 from H_2O in algae, cyanobacteria, and green plants. But, even after decades of research into the mechanism by which PSII converts water to dioxygen, questions persist regarding the precise role(s) of Ca^{2+} ion in the "cubane" ($[Mn_3O_4Ca]$) subsite of OEC. Calcium(II) is redox-inactive at biologically-relevant potentials,[4] and thus cannot provide redox flexibility, in contrast to the Mn centers present in the cluster. However, the Ca^{2+} ion is an essential cofactor, and its presence in the OEC is necessary for performing water oxidation; substitution of Ca^{2+} with any other metal ion results in lowered efficiencies for catalysis. On the other hand, Sr^{2+} is notable as it can substitute for Ca^{2+}, but the resulting Sr-substituted OEC can turnover with only 40% activity when compared with the naturally preferred Ca-containing OEC.[5,6]

In light of these results, one hypothesis in the field is that the similar Lewis acidities of Ca^{2+} and Sr^{2+} could be responsible for the observation that the complexes containing these

ions are the only ones active for water oxidation. The Lewis acidity values for Ca^{2+} and Sr^{2+} ions, quantified in the form of the pK_a value(s) of bound water ligands in metal-aqua complexes of the corresponding Lewis acidic ions, are 12.6 and 13.2, respectively.[7] Such discussions of Lewis acidity have often centered on the possible role of Ca^{2+} (or Sr^{2+}) ions as active substrate (water) binding sites.[8,9,10,11] In this regard, results from X-ray diffraction studies of the OEC have shown that water molecules are indeed bound to Ca^{2+} in the resting state of the cluster. On the other hand, direct studies of the OEC are challenging, and thus numerous research efforts have been focused on developing systems which mimic the cubane structure of the OEC and contain redox-inactive metals in order to understand the exact role of Ca^{2+} ion in OEC and the relevance of so-called Lewis acid effects.[8] Key to these efforts is the assembly of biomimetic multimetallic systems, an endeavor bursting with possibilities but often plagued by synthetic challenges with their origin in the difficulty of bringing multiple metals into close proximity with each other. Often, heterometallic species are in equilibrium with free redox-inactive ions in solution, and a large excess of Lewis acidic metal additive is often used.[12,13] The presence of such equilibria complicates interpretation of results and typically hinders conclusive determinations of the effects of redox-inactive metals on redox processes in these systems.

An alternative approach to mapping Lewis acid effects is preparation of bioinspired heterobimetallic complexes that avoid the speciation concerns of biomimetic systems. In most of the work described in this dissertation, we have followed this path and utilized heteroditopic ligands that feature orthogonal sites for binding a redox-active metal and a single redox-inactive metal in close proximity.[14,15] This strategy allowed us to systematically tune the redox properties of redox-active metals by placing different redox-inactive metals

in a nearby site that span a broad range of Lewis acidity values. This modulation of the redox properties of the redox-active metals using Lewis acid effects affords new insights into the role(s) of these redox-inactive metals in multimetallic systems. Chapter 2 describes our initial wayfinding study that utilized this strategy for installation of a broad range of redox-inactive Lewis acids, including the useful Ca^{2+} ion as well as the important and highly acidic trivalent cations Nd^{3+} and Y^{3+}, in close proximity to a redox-active Ni^{2+} center. The results from this work could be well-parametrized in the context of Lewis-acidity-driven trends, and enabled rational tuning of the redox properties of nickel.

The use of Lewis acidic redox-inactive metal ions to modulate redox processes involving transition metal complexes is a popular strategy in the field.[8,15,16] Indeed, the incorporation of secondary metal ions into complexes containing a redox-active metal has emerged as a viable and widely utilized strategy for systematic tuning of redox chemistry.[15,17] However, analogous effects in complexes of redox-active *f*-block elements, especially actinides, have been underexplored, and only a few examples of systematic investigations have appeared in the literature.[18,19] On the other hand, the available literature suggested to us that use of Lewis acidic metal ions would be quite effective for modulation of the chemistry of the redox-active UO_2^{2+} ion. Keeping in mind the powerful quantitative aspect of such a strategy, the influence of redox-inactive metals on the redox chemistry of the UO_2^{2+} ion has received less attention than it deserves. In particular, the sort of quantitative electrochemical work upon which findings in this area would be based has been unavailable until now.

Uranium is a radioactive element and is the heaviest element which occurs naturally on earth in significant quantities. From the chemist's perspective, a crucial feature of uranium chemistry lies in its unique coordination requirements; these coordination requirements can

be conceptualized to result from the large size of uranium atoms, which contain many electrons, as well as the involvement of exotic 5*f* and 6*d* orbitals in covalent bonding. Uranium is an abundant element, despite its location at the extreme of the periodic table, and has been used actively since 1951 as a fuel for virtually carbon-free production of electricity via nuclear fission. Due to the high energy density of uranium-based fuel, nuclear power is a very low-carbon energy source, even lower than solar or wind power when considering total lifetime-of-technology emissions and manufacturing costs.[20,21] Moreover, nuclear power is continuously available and quite reliable, unlike solar or wind energy which are themselves intermittent. From this perspective, nuclear fission represents an important component of the world's supply of low-carbon energy. Of course, on the other hand, continued use of nuclear fission for power production is tainted by serious concerns about the ultimate disposition of used nuclear fuels and related materials. Thus, new approaches to handling, reprocessing, and recycling nuclear fuels are crucial for the long-term viability of this energy source.[22]

After usage, the fuel rods from nuclear reactors are stored in specially designed water pools or dry-cask storage systems. This stored spent nuclear fuel still contains more than 90% of its potential energy[23] and can, in principle, be reprocessed and chemically purified to provide fresh and useful uranium-containing fuels. However, it is very difficult to reprocess spent nuclear fuels because harsh conditions are needed, lowering energy efficiency. Conventional reprocessing also markedly increases the net carbon emissions associated with this otherwise low-carbon energy source, through use of harsh reagents like Cl_2 gas (as oxidants), Ca^0 or Li^0 (as reductants), and extreme conditions and temperatures that can be as high as 750^{o}C.[24]

In aerobic environments and in the presence of water, uranium typically exists in the form of the highly water-soluble and stable UO_2^{2+} species.[25] Due to the strength and highly covalent nature of the U–O bonds, processing of UO_2^{2+} and other oxidic forms of uranium into nuclear fuels is energetically demanding and logistically difficult.[26] Cleavage of U–O bonds is a necessary step in fuel processing and recycling, however, making it a crucial one for optimization. There are few rational approaches available for modulating the reactivity of UO_2^{2+}, making the design of suitable chemical reagents difficult.[27,28] However, one clue about how to design such reagents is that the reduction of UO_2^{2+} to a more reduced state can accelerate separation and make functionalization and/or breaking of the U–O bonds much easier.[29]

In this light, breaking U–O bonds is an important problem, one that ultimately requires reduction chemistry. Seminal work by Arnold and co-workers shows that the binding of redox-inactive metals to certain complexes containing the uranyl ion (UO_2^{2+}) provides a stabilizing environment for reduced form(s) of U derived from U^{VI} starting materials, i.e., U^{V} and/or other lower-valent states.[29,19] This stabilization afforded by redox-inactive Lewis acidic metals allowed Arnold and co-workers to isolate U^{V} species. However, in Arnold's systems, the Lewis acid interacts directly with an oxygen atom of the UO_2^{2+} moiety, a situation hindering further functionalization of the oxygen atoms upon reduction. Similarly, Hayton and co-workers have measured positive shifts in the reduction potentials of U centers using silyl groups for oxo functionalization.[30] In Hayton's systems, the silyl groups interact directly with the oxygen atoms of the UO_2^{2+} moiety, similar to Arnold's case. We anticipated that a platform like our own developed for heterobimetallic Ni^{2+} chemistry could be useful in enabling tuning of the electronic properties of the uranium center while avoiding these

direct uranyl oxo-to-electrophile/metal interactions. Further, we anticipated that redox modulation of uranium could serve as a strategy for tuning the activation of the strong U–O bonds in UO_2^{2+} and perhaps contribute fundamental knowledge toward the development of next-generation strategies for nuclear waste remediation.

In this dissertation, we show that use of Lewis acids and macrocyclic ligands can indeed modulate the reduction potentials required for uranium redox cycling, and that this strategy offers a quantitative method for gaining insights into the speciation chemistry of uranium with Lewis acids. Chapters 3 and 4 discuss the design of tailored supramolecular systems that hold uranium near secondary Lewis acidic and redox-inactive metals, a situation that we show can activate the U–O bonds for functionalization. Cyclic voltammetry experiments enabled examination of the redox properties of the UO_2^{2+} ion in the presence of the various secondary metals placed in close proximity. Our findings from the work with uranium suggest that both supramolecular structural effects and Lewis acidity considerations will be involved in successfully controlling and, ultimately, optimizing the binding of secondary metal ions, ligand reorganization energies, and electron transfer rates to uranium. These parameters are important, since they influence the thermodynamic stability of the various uranium oxidation states and the kinetics of their interconversion.

Our studies of Lewis acidic ion-modulated chemistry, like most in the field, are carried out in acetonitrile (CH_3CN), which is a polar organic solvent. The pK_a-based Lewis acidity descriptor measured in water is often used to parametrize behavior in such polar organic solvents, a situation attributable to the general usefulness of the pK_a-based scale measured in water as well as the challenges associated with development of alternative quantification schemes. Use of an acidity scale developed in water for parametrization of chemical effects

measured in other solvents is a significant concern, however, since solvent effects are known to strongly influence the outcomes of chemical reactivity.[15,31] Chapter 5 of this dissertation describes detailed studies aimed at understanding and parametrizing the behavior of Lewis acidic ions in non-aqueous conditions, namely in the organic solvents CH_3CN and dichloromethane (CH_2Cl_2). Since, most of the polar organic solvents do not release free H^+ ions in solution (a condition needed for measurement of pK_a) when they interact with Lewis acidic metal ions, there has historically been a lack of direct measures of the Lewis acidity of metal ions in polar organic solvents. Our new work in this area, however, shows that triphenylphosphine oxide (TPPO) can be used as a ^{31}P nuclear magnetic resonance (NMR) probe to quantify both the Lewis acidity of redox-inactive metal ions as well as their tendency to bind TPPO, which is moderately Lewis basic owing to the presence of the electron-rich oxygen atom. In our work, we compared results for a library of thirteen metal triflate salts using the Gutmann-Beckett method.[32,33] Notably, plots comparing the pK_a values of the corresponding metal-aqua species $[\mathbf{M}(H_2O)_m]^{n+}$ measured in H_2O with the newly measured ^{31}P NMR shifts of TPPO in the presence of these metals in deuterated acetonitrile (d_3-MeCN) and deuterated dichloromethane (CD_2Cl_2) display tightly co-linear relationships, suggesting similar behavior for these ions in water, d_3-MeCN, and CD_2Cl_2. This collinearity provides an insight into the usefulness of the pK_a descriptor in wide-ranging applications beyond those in aqueous media. However, our work also shows that the aqueous pK_a values and other single-measurement descriptors, while useful, provide only a snapshot of the influence of Lewis acidity on multimetallic chemical systems.

Thus, the chapters in Part I of this dissertation detail our work to understand and effectively leverage Lewis acid effects for tuning of the redox properties of heterobimetallic

complexes containing redox-active *d*-block (nickel) and *f*-block (uranium) elements held in macrocyclic ligand frameworks. Ideally, the fundamental lessons gleaned from this work could contribute to development of next-generation nuclear fuel reprocessing technologies and actinide handling systems.

In Part II of this dissertation, the focus shifts toward the realm of Lewis acid effects in molecular catalysis research. As inspiration for this work, we mention here that redox-inactive metal ions have been found to affect the catalytic behavior of heterogeneous mixed-metal oxides in transformations such as water oxidation and dioxygen reduction.[34,35] These observations have generated interest in molecular systems designed to investigate these heterometallic effects, aiming to develop general schemes for exploiting them in relevant catalytic reactions. Indeed, in the field of polymerization catalysis, many "single-site" homogenous catalysts feature two metal centers in close proximity that are bridged by ligands such as halides, hydrides, and even methylene groups.[36,37,38] These heterobimetallic systems include catalysts containing metal combinations such as titanium-chromium[39] and titanium-aluminum[40] that selectively produce polyethylene materials with properties of interest such as high molecular weight or narrow molecular weight distribution. For example, a catalyst studied by Marks & co-workers, containing both titanium and chromium, selectively produces *n*-butyl branched polyethylene.[39] In these Ti complexes, Cr and Al centers act as Lewis acids and play important roles in the enhancement of the polymerization activity. Heterobimetallic catalysts with late transition metals such as Ni and Pd in the presence of alkali metals as Lewis acids have also been studied for polymerization by Do & co-workers.[41,42] These catalysts similarly display a significant increase in the polymerization activity in comparison to their monometallic analogues. Thus, the cooperative effects

engendered by the heterobimetallic nature of these catalysts play a significant role in promoting greater polymerization activities and selectivity. Seeing this, we have noted the key role of Al(III) centers in driving polymerization activity, a situation attributable to the high Lewis acidity of this ion (pK_a of $[Al(H_2O)_m]^{3+}$ = 5.0).[7]

Chapters 6 and 7 detail our chemical and electrochemical studies of three different heterobimetallic Ti^{III}-Al^{III} complexes with varying alkyl groups that serve as polymerization catalyst precursors. The research described in these two chapters was completed with collaborators from Chevron Phillips Chemical, who recently developed the complexes investigated in our work, which are Natta-like titanium-aluminum half-sandwich complexes supported by indenyl and phosphinimide ligands. In our collaborative work, we have outlined the redox chemistry by which one-electron reduction of Ti(IV) centers in these complexes takes place and how the reduced form, Ti(III), is stabilized by the nearby Lewis acidic Al(III) center. Perhaps unsurprisingly, this redox reactivity impacts the properties of the polyethylene produced by the catalysts.

Complementing this work in polymerization chemistry, Chapter 8 describes the chemical, electrochemical, and catalytic properties of a final distinctive family of heterobimetallic complexes. Taking inspiration from the usefulness of half-sandwich complexes in the vast field of polymerization as well as from some of our lab's work in half-sandwich rhodium complexes,[43] we show that organometallic half-sandwich [Cp*M] (M = Rh, Ir) fragments (where Cp* is η^5-pentamethylcyclopentadienyl) can be installed into the workhorse diimine-dioxime ligand system. The new heterobimetallic compounds could be prepared by *in situ* protonolysis reactivity of precursor Ni(II) or Co(III) monometallic complexes with suitable [Cp*M] species. The findings from preliminary catalytic studies carried out with the [Co,Rh]

variant show that the bimetallic system catalyzes hydrogenation of an aldehyde to alcohol more cleanly than the individual monometallic precursor complexes. This suggests that our new family of complexes could be useful in future studies of multimetallic chemistry, especially in light of the starring role of other [Cp*M] complexes in diverse catalytic systems.

In summary, this dissertation in two parts represents a series of vignettes that showcase the use of Lewis acids to modulate the properties of diverse chemical systems, especially heterobimetallic complexes. Since several of the systems developed and investigated here do useful things, it reconfirms that heteromultimetallic chemistry and Lewis acid-driven tuning is an attractive strategy for enabling new reactivity. With this outlook, tuning of metal complexes with Lewis acids certainly deserves further attention and development in the future.

1.2 References

(1) Cooper, B. G.; Napoline, J. W.; Thomas, C. M. Catalytic Applications of Early/Late Heterobimetallic Complexes. *Catal. Rev.* **2012,** *54*, 1-40.

(2) Buchwalter, P.; Rosé, J.; Braunstein, P. Multimetallic catalysis based on heterometallic complexes and clusters. *Chem. Rev.* **2015**, *115*, 28–126.

(3) (a) McEvoy, J. P.; G. W. Brudvig, G. W. Water-splitting chemistry of photosystem II. *Chem. Rev.* **2006**, *106*, 4455–4483. (b) Yano, J.; Yachandra, V. Mn_4Ca Cluster in Photosynthesis: Where and How Water is Oxidized to Dioxygen. *Chem. Rev.* **2014**, *114*, 4175–4205

(4) Bard, A. J.; Parsons, R.; Jordan, J. *Standard Potentials in Aqueous Solution*. M. Dekker: New York, 1985.

(5) Boussac, A.; Rutherford, A. W. *Biochemistry* **1988**, *27*, 3476.

(6) Brudvig, G. W. *Phil. Trans. R. Soc. B* **2008**, *363*, 1211.

(7) Perrin, D. D. *Ionisation Constants of Inorganic Acids and Bases in Aqueous Solution*. Pergamon, 1982.

(8) a) Kanady, J. S.; Tsui, E. Y.; Day, M. W.; Agapie, T. A synthetic model of the Mn_3Ca subsite of the oxygen-evolving complex in photosystem II. *Science* **2011**, *333*, 733 –736; b) Tsui, E. Y.; Kanady, J. S.; Agapie, T. Synthetic cluster models of biological and heterogeneous manganese catalysts for O_2 evolution. *Inorg. Chem.* **2013**, *52*, 13833 – 13848.

(9) Lee, C. I.; Lakshmi, K.; Brudvig, G. W. Probing the functional role of Ca^{2+} in the oxygen-evolving complex of photosystem II by metal ion inhibition. *Biochemistry* **2007,** *46*, 3211-3223.

(10) Yachandra, V. K.; Yano, J. Calcium in the oxygen-evolving complex: Structural and mechanistic role determined by X-ray spectroscopy. *J. Photochem. Photobiol. B* **2011,** *104*, 51-59.

(11) Pecoraro, V. L.; Baldwin, M. J.; Caudle, M. T.; Hsieh, W. Y.; Law, N. A. A proposal for water oxidation in photosystem II. *Pure Appl. Chem.* **1998,** *70*, 925-929.

(12) Swart, M. A change in the oxidation state of iron: scandium is not innocent. *Chem. Commun.* **2013**, *49*, 6650-6652.

(13) Prakash, J.; Rohde, G. T.; Meier, K. K.; Jasniewski, A. J.; Van Heuvelen, K. M.; Munck, E.; Que, L. Spectroscopic Identification of an Fe^{III} Center, not Fe^{IV}, in the Crystalline Sc-O-Fe Adduct Derived from $[Fe^{IV}(O)(TMC)]^{2+}$. *J. Am. Chem. Soc.* **2015**, *137*, 3478-3481.

(14) Vanstaveren, C. J.; Vaneerden, J.; Vanveggel, F. C. J. M.; Harkema, S.; Reinhoudt, D. N. Cocomplexation of Neutral Guests and Electrophilic Metal-Cations in Synthetic Macrocyclic Hosts. *J. Am. Chem. Soc.* **1988**, *110*, 4994-5008.

(15) Reath, A. H.; Ziller, J. W.; Tsay, C.; Ryan, A. J.; Yang, J. Y. Redox Potential and Electronic Structure Effects of Proximal Nonredox Active Cations in Cobalt Schiff Base Complexes. *Inorg. Chem.* **2017**, *56*, 3713-3718.

(16) (a) Tsui, E. Y.; Tran, R.; Yano, J.; Agapie, T. Redox-inactive metals modulate the reduction potential in heterometallic manganese–oxido clusters. *Nat. Chem.* **2013**, *5*, 293. (b) Yiu, S.-M.; Man, W.-L.; Lau, T.-C. Efficient Catalytic Oxidation of Alkanes by Lewis Acid/$[Os^{VI}(N)Cl_4]^-$ Using Peroxides as Terminal Oxidants. Evidence for a Metal-Based Active Intermediate. *J. Am. Chem. Soc.* **2008**, *130*, 10821-10827. (c) Du, H.; Lo, P.-K.; Hu, Z.; Liang, H.; Lau, K.-C.; Wang, Y.-N.; Lam, W. W. Y.; Lau, T.-C. Lewis acid-activated oxidation of alcohols by permanganate. *Chem. Commun.* **2011**, *47*, 7143-7145. (d) Fukuzumi, S.; Morimoto, Y.; Kotani, H.; Naumov, P.; Lee, Y.-M.; Nam, W. Crystal structure of a metal ion-bound oxoiron(IV) complex and implications for biological electron transfer. *Nat. Chem.* **2010**, *2*, 756. (e) Bang, S.; Lee, Y.-M.; Hong, S.; Cho, K.-B.; Nishida, Y.; Seo, M. S.; Sarangi, R.; Fukuzumi, S.; Nam, W. Redox-inactive

metal ions modulate the reactivity and oxygen release of mononuclear non-haem iron(III)–peroxo complexes. *Nat. Chem.* **2014**, *6*, 934. (f) Park, Y. J.; Ziller, J. W.; Borovik, A. S. The Effects of Redox-Inactive Metal Ions on the Activation of Dioxygen: Isolation and Characterization of a Heterobimetallic Complex Containing a Mn^{III}-(μ-OH)-Ca^{II} Core. *J. Am. Chem. Soc.* **2011**, *133*, 9258-61. (g) Lacy, D. C.; Park, Y. J.; Ziller, J. W.; Yano, J.; Borovik, A. S. Assembly and Properties of Heterobimetallic $Co^{II/III}$/Ca^{II} Complexes with Aquo and Hydroxo Ligands. *J. Am. Chem. Soc.* **2012**, *134*, 17526-35. (h) Horwitz, C. P.; Ciringh, Y. Synthesis and electrochemical properties of oxo-bridged manganese dimers incorporating alkali and alkaline-earth cations. *Inorg. Chim. Acta* **1994**, *225*, 191-200.

(17) (a) Fukuzumi, S., Electron-transfer properties of high-valent metal-oxo complexes. *Coord. Chem. Rev.* **2013**, *257*, 1564-1575. (b) Nam, W.; Lee, Y. M.; Fukuzumi, S., Tuning Reactivity and Mechanism in Oxidation Reactions by Mononuclear Nonheme Iron(IV)-Oxo Complexes. *Acc. Chem. Res.* **2014**, *47*, 1146-1154. (c) Fukuzumi, S.; Ohkubo, K.; Lee, Y. M.; Nam, W., Lewis Acid Coupled Electron Transfer of Metal-Oxygen Intermediates. *Chem. Eur. J.* **2015**, *21*, 17548-17559. (d) Park, J.; Morimoto, Y.; Lee, Y. M.; Nam, W.; Fukuzumi, S., Unified View of Oxidative C-H Bond Cleavage and Sulfoxidation by a Nonheme Iron(IV)-Oxo Complex via Lewis Acid-Promoted Electron Transfer. *Inorg. Chem.* **2014**, *53*, 3618-3628.

(18) (a) Robinson, J. R.; Carroll, P. J.; Walsh, P. J.; Schelter, E. J. The Impact of Ligand Reorganization on Cerium(III) Oxidation Chemistry. *Angew. Chem. Int. Ed.* **2012**, *51*, 10159-10163. (b) Robinson, J. R.; Gordon, Z.; Booth, C. H.; Carroll, P. J.; Walsh, P. J.; Schelter, E. J. Tuning Reactivity and Electronic Properties through Ligand Reorganization within a Cerium Heterobimetallic Framework. *J. Am. Chem. Soc.* **2013**, *135*, 19016-19024.

(19) (a) Arnold, P. L.; Patel, D.; Wilson, C.; Love, J. B. Reduction and selective oxo group silylation of the uranyl dication. *Nature* **2008**, *451*, 315-317. (b) Arnold, P. L.; Pecharman, A. F.; Hollis, E.; Yahia, A.; Maron, L.; Parsons, S.; Love, J. B. Uranyl oxo

activation and functionalization by metal cation coordination. *Nat. Chem.* **2010**, *2*, 1056-1061. (c) Zegke, M.; Nichol, G. S.; Arnold, P. L.; Love, J. B., Catalytic one-electron reduction of uranyl(VI) to Group 1 uranyl(V) complexes via Al(III) coordination. *Chem. Commun.* **2015**, *51*, 5876-5879.

(20) Morgan, M. G.; Abdulla, A.; Ford, M. J.; Rath, M. US nuclear power: The vanishing low-carbon wedge. *Proc. Nat. Acad. Sci.* **2018,** *115*, 7184-7189.

(21) Westinghouse Electric Company LLC. https://www.westinghousenuclear.com/tomorrows-energy (accessed May 26, 2021).

(22) Lumetta, G. J.; *Separations for the nuclear fuel cycle in the 21st century.* American Chemical Society: Washington, DC, 2006.

(23) Office of Nuclear Energy. *5 Fast Facts about Spent Nuclear Fuel.* https://www.energy.gov/ne/articles/5-fast-facts-about-spent-nuclear-fuel (accessed May 26, 2021).

(24) D. L.; Jarvinen, G. Pyrochemical Salt Processing. *Actinide Res. Quarterly* **2008**, 10-13.

(25) Meinrath, G. Coordination of uranyl(VI) carbonate species in aqueous solutions. *J. Radioanal. Nucl. Chem.* **1996,** *211*, 349-362.

(26) Meinrath, G. Coordination of uranyl(VI) carbonate species in aqueous solutions. *J. Radioanal. Nucl. Chem.* **1996,** *211*, 349-362.

(27) Wang, K.-X.; Chen, J.-S. Extended Structures and Physicochemical Properties of Uranyl-Organic Compounds. *Acc. Chem. Res.* **2011,** *44*, 531-540.

(28) Ephritikhine, M. The vitality of uranium molecular chemistry at the dawn of the XXIst century. *Dalton Trans.* **2006,** 2501-2516.

(29) Arnold, P. L.; Patel, D.; Wilson, C.; Love, J. B. Reduction and selective oxo group silylation of the uranyl dication. *Nature* **2008**, *451*, 315-317.

(30) Schnaars, D. D.; Wu, G.; Hayton, T. W. Silylation of the Uranyl Ion Using B(C6F5)3-Activated Et_3SiH. *Inorg. Chem.* **2011,** *50*, 9642-9649.

(31) Lionetti, D.; Suseno, S.; Tsui, E. Y.; Lu, L.; Stich, T. A.; Carsch, K. M.; Nielsen, R. J.; Goddard, W. A.; Britt, R. D.; Agapie, T. Effects of Lewis Acidic Metal Ions (M) on Oxygen-Atom Transfer Reactivity of Heterometallic Mn_3MO_4 Cubane and $Fe_3MO(OH)$ and $Mn_3MO(OH)$ Clusters. *Inorg. Chem.* **2019,** *58,* 2336-2345.

(32) Mayer, U.; Gutmann, V.; Gerger, W. The acceptor number — A quantitative empirical parameter for the electrophilic properties of solvents. *Monatsh. Chem.* **1975,** *106*, 1235-1257.

(33) Beckett, M. A.; Strickland, G. C.; Holland, J. R.; Sukumar Varma, K. A convenient n.m.r. method for the measurement of Lewis acidity at boron centres: correlation of reaction rates of Lewis acid initiated epoxide polymerizations with Lewis acidity. *Polymer* **1996,** *37*, 4629-4631.

(34) Suntivich, J.; Gasteiger, H. A.; Yabuuchi, N.; Nakanishi, H.; Goodenough, J. B.; Shao-Horn, Y. Design principles for oxygen-reduction activity on perovskite oxide catalysts for fuel cells and metal-air batteries. *Nat. Chem.* **2011**, *3*, 546-550.

(35) Zaharieva, I.; Najafpour, M. M.; Wiechen, M.; Haumann, M.; Kurz, P.; Dau, H. Synthetic manganese-calcium oxides mimic the water-oxidizing complex of photosynthesis functionally and structurally. *Energy Environ. Sci.* **2011**, *4*, 2400-2408.

(36) Delferro, M.; Marks, T. J. Multinuclear Olefin Polymerization Catalysts. *Chem. Rev.* **2011,** *111*, 2450-2485.

(37) Krusic, P. J.; Tebbe, F. N. ESR study of a paramagnetic titanium methylene complex and of its reactions with olefins. *Inorg. Chem.* **1982,** *21*, 2900-2902.

(38) Thompson, R.; Nakamaru-Ogiso, E.; Chen, C.-H.; Pink, M.; Mindiola, D. J. Structural Elucidation of the Illustrious Tebbe Reagent. *Organometallics* **2014,** *33*, 429-432.

(39) Liu, S.; Motta, A.; Delferro, M.; Marks, T. J. Synthesis, Characterization, and Heterobimetallic Cooperation in a Titanium–Chromium Catalyst for Highly Branched Polyethylenes. *J. Am. Chem. Soc.* **2013,** *135*, 8830-8833.

(40) Natta, G.; Pino, P.; Mazzanti, G.; Giannini, U. A Crystallizable Organometallic Complex Containing Titanium and Aluminum. *J. Am. Chem. Soc.* **1957,** *79*, 2975-2976

(41) Cai, Z.; Xiao, D.; Do, L. H. Fine-Tuning Nickel Phenoxyimine Olefin Polymerization Catalysts: Performance Boosting by Alkali Cations. *J. Am. Chem. Soc.* **2015,** *137*, 15501-15510.

(42) Cai, Z.; Do, L. H. Thermally Robust Heterobimetallic Palladium–Alkali Catalysts for Ethylene and Alkyl Acrylate Copolymerization. *Organometallics* **2018,** *37*, 3874-3882.

(43) Boyd, E. A.; Lionetti, D.; Henke, W. C.; Day, V. W.; Blakemore, J. D. Preparation, Characterization, and Electrochemical Activation of a Model [Cp*Rh] Hydride. *Inorg. Chem.* **2019**, *58*, 3606-3615. (b) Hopkins, J. A.; Lionetti, D.; Day, V. W.; Blakemore, J. D. Chemical and Electrochemical Properties of [Cp*Rh] Complexes Supported by a Hybrid Phosphine-Imine Ligand. *Organometallics* **2019,** *38*, 1300-1310. (c) Hopkins, J. A.; Lionetti, D.; Day, V. W.; Blakemore, J. D. Synthesis and reactivity studies of a [Cp*Rh] complex supported by a methylene-bridged hybrid phosphine-imine ligand. *J. Organomet. Chem.* **2020**, *921*, 121294.

Part I

Chapter 2

Trivalent Lewis Acidic Cations Govern the Electronic Properties and Stability of Heterobimetallic Complexes of Nickel

This chapter is adapted from a published manuscript:

Kumar, A.; Lionetti, D.; Day, V. W.; Blakemore, J. D. Trivalent Lewis Acidic Cations Govern the Electronic Properties and Stability of Heterobimetallic Complexes of Nickel. *Chem. Eur. J.* **2018**, *24*, 141-149.

2.1 Introduction

Heterometallic sites that have two or more metals in close proximity (< 5 Å) often show unique behavior that is inaccessible with simpler homometallic analogues.[1,2] The presence of multiple metal centers can give rise to synergistic properties, including improved substrate binding,[3] enhanced rates of catalysis, and unique stability.[4] These features contribute to the high activity of multimetallic active sites in enzymes that catalyze complex reactions, for example N_2 fixation by nitrogenase[5] or O_2 reduction by cytochrome *c* oxidase.[6]

Redox-inactive metals can also modulate the properties of multimetallic active sites. For example, the oxygen-evolving complex (OEC), a tetramanganese oxo-bridged cluster in the enzyme Photosystem II contains a crucial Ca^{2+} ion that assists in oxidation of water to generate oxygen gas.[7] The Lewis acidity of this ion, which is redox-inactive at biologically-relevant potentials, is postulated to be important in this role; Sr^{2+}-substituted PSII is also active for O_2 evolution, but while some other cations (including dications such as Cd^{2+}) do bind in the OEC, these analogues do not display O_2 evolution activity. This highlights that charge is not the sole feature that regulates oxygen evolution, and suggests that Lewis acidity may be implicated as a descriptor of binding and activity.[8,9]

In part inspired by these observations from natural systems, synthetic efforts to understand and exploit the interactions of transition metals and Lewis acidic redox-inactive cations is an active research area. For example, model compounds for the OEC in PSII that contain [Mn] and [Ca] have been assembled.[10,11,12,13] Some compounds rely on multitopic ligands that can coordinate the metals and hold them near to each other. More broadly, a number of groups have studied novel reactivity patterns obtained with systems including Lewis acidic cations. Seminal work from Lau and co-workers has demonstrated significant

rate accelerations in metal-catalyzed oxidations of organic substrates in the presence of Lewis acids.[14] Collins also observed enhanced O-atom transfer by binding of secondary cations to a high-valent metal oxo complex.[15] Early electrochemical work from Horwitz examined interactions between oxo-bridged manganese complexes and added Lewis acids.[16] More recently, Borovik has investigated the effects of redox-inactive metal ions on the properties of manganese and iron complexes. [17,18]

In several interesting cases, the highly Lewis-acidic metals Sc^{3+} and Y^{3+} promote peroxide O–O bond cleavage in Fe^{III}–O_2–M^{3+} species, leading to generation of reactive [Fe^{IV}=O] intermediates.[19,20,21] In this chemistry, and in some of the cases discussed above, the heterobimetallic complexes are often not isolated, but formed *in situ* by combination of multiple metal-containing precursors. This straightforward approach is especially useful for catalytic applications, where multiple additives can be mixed to assemble an active catalyst. Notably, the Lewis acidities of Y^{3+} and other trivalent ions are significantly greater than other ions such as Ca^{2+} or Sr^{2+}; consequently, there is a privileged position for Y^{3+} and Sc^{3+} in modulating the reactivity of the iron complexes described above.[19]

However, despite the relevance of these heterometallic effects to possible applications in catalysis[2] and energy science,[22] chemical preparation of compounds that contain trivalent Lewis-acidic ions with a transition metal has received less attention than it deserves. Tsui et al. and Herbert et al. have quantified Lewis acidity effects in multimetallic manganese[23] and iron[24] oxo-bridged clusters, respectively. They find a distinctive shift in reduction potential of their clusters as a function of the Lewis acidity of a bound redox-inactive metal, including the trivalent rare-earth cations Y^{3+} and Nd^{3+}.

One possible strategy for preparation of heterobimetallic complexes involves synthesis of ditopic frameworks with binding motifs that display distinct ligand properties and that can therefore facilitate orthogonal metallations.[1] With this approach, the precise tuning of the properties and reactivity of heterobimetallic complexes can be understood by comparison of the monometallic and the isolated heterobimetallic species. Several ligands of this variety are known in the literature.[25] Reinhoudt and co-workers introduced a ditopic ligand[26] based on a metal salophen core with a nearby crown-ether-like moiety[27] for binding a second metal (see Scheme 2.1). Related macrocyclic salen or salophen type complexes have been extensively used in the fields of coordination[28.29] and supramolecular[30.31] chemistry; several studies have examined complexes of this general type incorporating multiple metals.[16.32.33] Along this line, Yang and co-workers recently reported heterobimetallic complexes of Co^{2+} with Na^{+}, K^{+}, Ca^{2+}, and Sr^{2+}; the $Co^{II/I}$ reduction potentials and spectroscopic properties of these compounds were found to vary as a function of the Lewis acidity of the redox-inactive cation.[34] This study demonstrates the usefulness of ditopic ligands in assembling well-defined heterobimetallic compounds, as the compounds are quite stable and amenable to solution studies.

We have recently been investigating multidentate, polyphenoxide ligand scaffolds that support trivalent cations,[35] and our interest was piqued by the possibility of introducing analogous fragments into a ditopic framework to access heterobimetallic species. In particular, we were interested in testing how trivalent cations (specifically, Y^{3+} and Nd^{3+}) would modulate the structure, electronic properties, and reduction potentials of a nearby nickel center. We anticipated that such studies would provide important structural and spectroscopic insights into the use of highly Lewis acidic metals in catalytic contexts.[19]

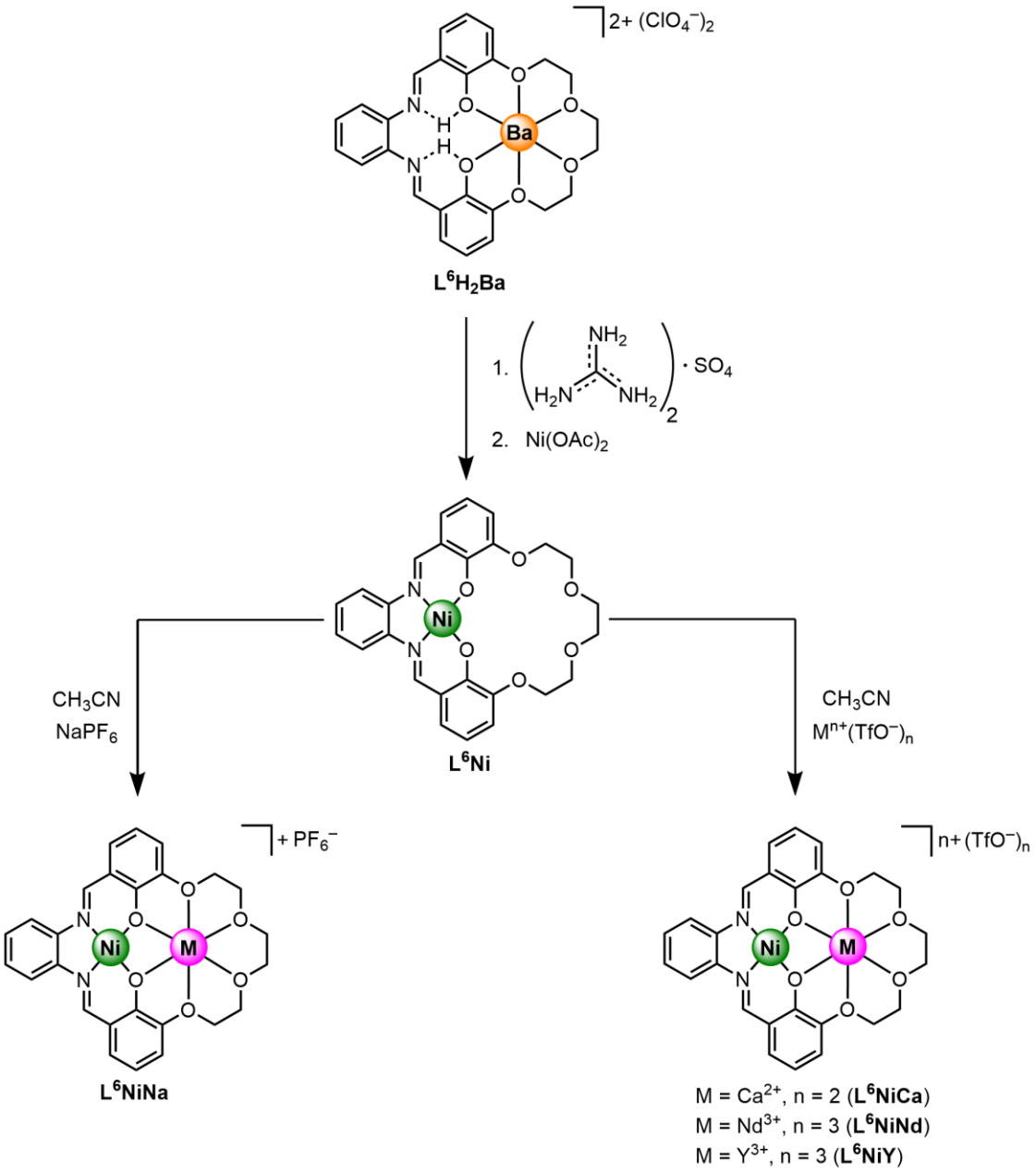

Scheme 2.1. Divergent synthetic strategy for preparation of heterobimetallic nickel complexes.

Along this line, we now report a divergent synthetic strategy for generation of stable heterobimetallic complexes based on metallation of the macrocyclic, ditopic platform **L^{6}Ni** (see Scheme 2.1)[26] with a variety of redox-inactive metals (Na^+, Ca^{2+}, Nd^{3+}, Y^{3+}). The Nd^{3+} and Y^{3+} complexes are the first examples of stable heterobimetallic complexes of these

elements with a first-row transition metal in a macrocyclic ligand environment. They complement unsupported analogues that feature bridging ligands but without a stabilizing macrocyclic environment.[36,37] Our macrocyclic complexes are stable in acetonitrile solution and amenable to study by solution spectroscopic methods and electrochemistry. However, electrochemical experiments reveal that the complexes of Nd^{3+} and Y^{3+} are unstable in dimethylformamide (DMF); conversely, they can survive for hours in acetonitrile (MeCN), similar to the complexes of Na^{+} and Ca^{2+}. We conclude that the high Lewis acidity of these elements drives association with DMF, and thus we propose that future studies relying on these elements could usefully include studies of solvent-dependent behavior.

2.2 Results

In this work, we have employed a divergent synthetic strategy, in which preparation of a common nickel-containing material (**L^6Ni**; see Scheme 2.1) precedes metallation by suitable reagents of redox-inactive metal cations. This approach has the advantage that once a supply of the monometallic precursor complex is prepared, a variety of heterobimetallic complexes can be readily accessed. Our strategy relies on the ditopic ligand platform that was originally developed by Reinhoudt and co-workers.[26] In this chemistry, 2,3-dihydroxybenzaldehyde and tetraethylene glycol ditosylate are reacted together to provide a linear dialdehyde precursor. This dialdehyde undergoes Ba^{2+}-templated macrocyclization with *o*-phenylenediamine to yield complex **L^6H_2Ba** (Scheme 2.1) in reasonable yields. Treatment of the barium complex with guanidinium sulfate in a biphasic mixture of chloroform ($CHCl_3$) and water results in precipitation of $BaSO_4$; subsequent addition of nickel(II) acetate in methanol (MeOH) generates clean **L^6Ni**. From this point, **L^6Ni** is a suitable synthon for preparation of heterobimetallic complexes.

Although **L^{6}Ni** and related analogues have been deployed in a variety of contexts, no solid-state structure of **L^{6}Ni** has been available. For comparison to our heterobimetallic structures (*vide infra*), single crystals of **L^{6}Ni** suitable for X-ray diffraction (XRD) studies were grown by slow cooling of a concentrated solution of **L^{6}Ni** in MeCN. As predicted from nuclear magnetic resonance (NMR) experiments, the nickel center in **L^{6}Ni** is formally in the +2 oxidation state, and is coordinated to the square-planar Schiff base cavity of the macrocyclic ligand framework (Figure 2.1). This cavity provides an L_2X_2-type environment by coordination of two imine nitrogens and two phenolate oxygens to the nickel(II) center. The complex is overall neutral, with co-crystallized MeCN as the only other component found in the crystal data (see Appendix A for details).

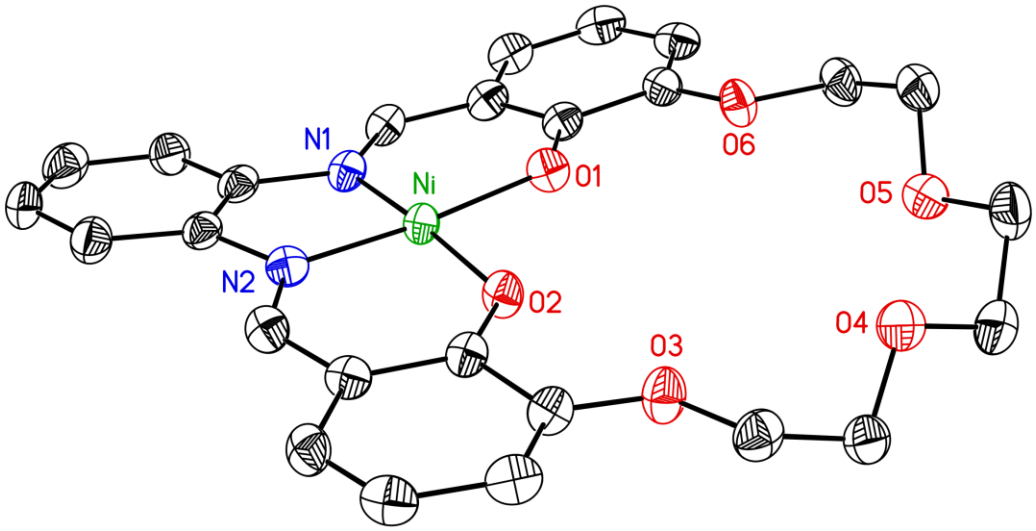

Figure 2.1. Solid-state structure (XRD) of **L^{6}Ni**. Hydrogen atoms and two molecules of co-crystallized MeCN solvent are omitted for clarity. Displacement ellipsoids are shown at the 50% probability level.

With **L^{6}Ni** in hand, we targeted incorporation of a range of Lewis acidic cations for comparisons of structural, spectroscopic, and electrochemical properties across the range of heterobimetallic compounds. In these studies we elected to use the pK_a of the redox-inactive

metal–aqua complex as a measure of Lewis acidity,[38] an approach that has successfully been employed in several literature reports.[23,24] Specifically, we chose sodium (pK_a = 14.7), calcium (12.7), neodymium (8.4), and yttrium (8.3) as redox-inactive metals for the present work. Yttrium and neodymium are especially attractive, as they are relevant to enhancements in oxidative reactivity with iron compounds (*vide supra*).[19,20,21] Notably, structurally characterized heterobimetallic nickel compounds of Nd^{3+} or Y^{3+} in macrocyclic ligands have not been available in prior synthetic and spectroscopic work.[36,37] Furthermore, the broad range of Lewis acidities displayed by the chosen redox-inactive metals facilitates interpretation of any observed trends in structural or spectroscopic features.

Treatment of **L^{6}Ni** with sodium hexafluorophosphate or calcium trifluoromethanesulfonate (triflate, $^-$OTf) in MeCN results in generation of heterobimetallic complexes in which sodium and calcium, respectively, are bound in the crown ether-like cavity of **L^{6}Ni** (see Experimental Section for details on synthetic procedures). Single crystals of **L^{6}NiNa** and **L^{6}NiCa** were grown by vapor diffusion of Et_2O into concentrated solutions of the complexes in MeCN and MeOH, respectively. The solid-state structure of **L^{6}NiNa** reveals incorporation of the sodium ion in the crown-like cavity with a coordination number (CN) of seven (Figure 2.2, left). As expected, an outer-sphere hexafluorophosphate ion is present, but does not interact covalently with the heterobimetallic fragment. Conversely, the solid-state structure of **L^{6}NiCa** reveals that the calcium ion incorporated into the crown cavity has a CN of eight, with coordination of the six macrocyclic O-atoms, plus two triflate anions bound in the κ^1 mode (Figure 2.2, right). The higher CN for Ca^{2+} is not unexpected, due to the higher charge and the presence of the more coordinating triflate counteranion.

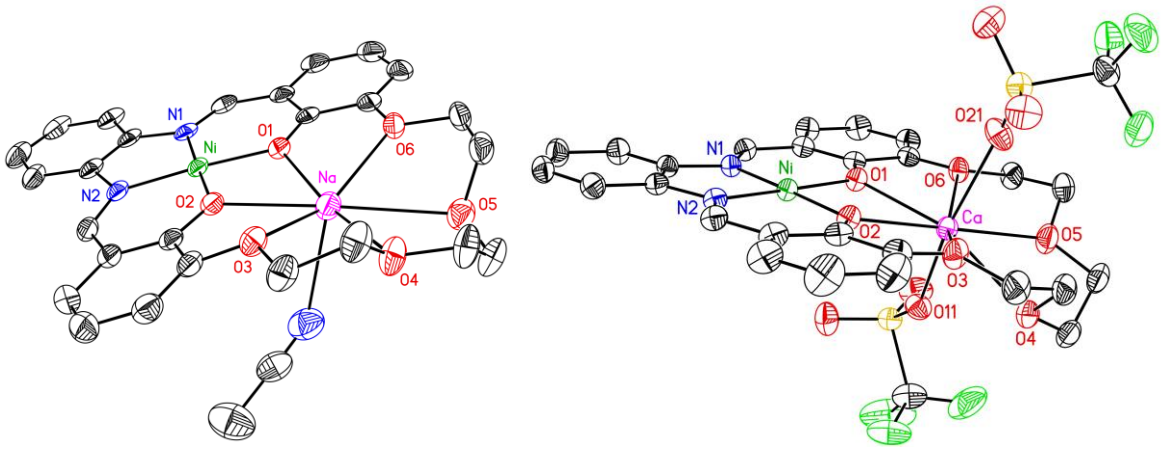

Figure 2.2. Solid-state structures (XRD) of **L^{6}NiNa** (left) and **L^{6}NiCa** (right). Displacement ellipsoids are shown at the 50% probability level. Hydrogen atoms and one hexafluorophosphate counteranion in the structure of **L^{6}NiNa** are omitted for clarity.

To our delight, treatment of **L^{6}Ni** with neodymium triflate or yttrium triflate results in a distinctive color change from deep red to yellow. Spectroscopic evidence (*vide infra*) is consistent with coordination of the trivalent ions into the crown-like cavity. Single-crystal XRD confirms the successful preparation of both **L^{6}NiNd** and **L^{6}NiY** (Figure 2.3). **L^{6}NiNd** features the Nd^{3+} ion fully coordinated by the six crown-like O-atoms, plus three triflate anions bound in the κ^1 mode, giving a CN of 9 (Figure 2.3, left). In accord with the similar Lewis acidities of Nd^{3+} and Y^{3+},[38] the yttrium center in **L^{6}NiY** is also 9-coordinate with three κ^1 triflates (Figure 2.3, right). In **L^{6}NiY**, one triflate serves as a bridging ligand between the Ni and Y centers; intriguingly, there is a weak interaction (*ca.* 2.79 Å) between the Ni metal center and an O-atom (O12) of a Y-bound triflate counterion.

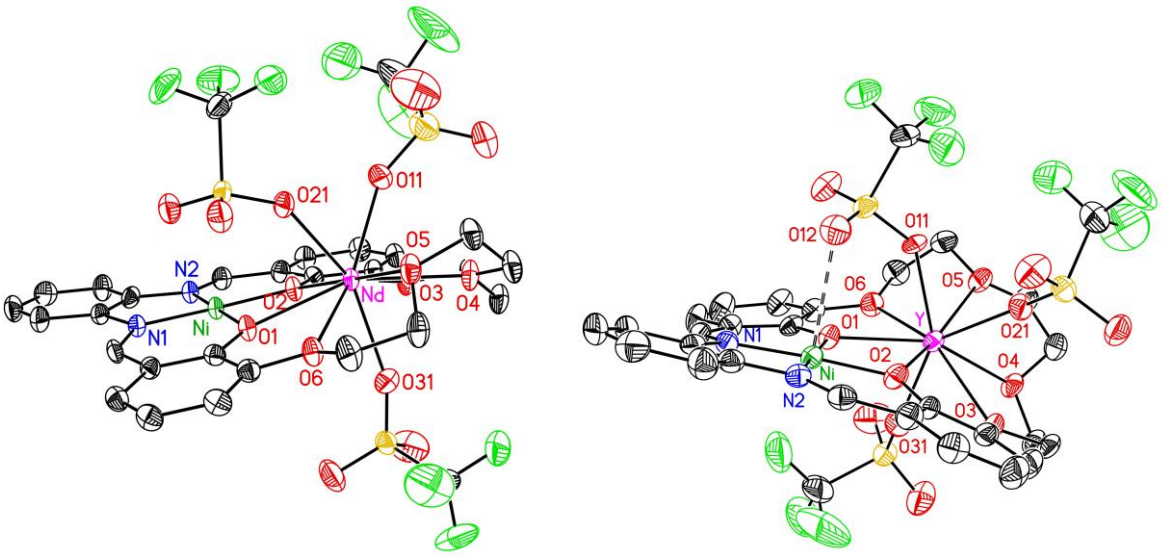

Figure 2.3. Solid-state structures (XRD) of **L^{6}NiNd** (left) and **L^{6}NiY** (right). Displacement ellipsoids are shown at the 50% probability level. Hydrogen atoms are omitted for clarity.

Inspection of this series of analogous structures reveals no discernible trends in bond distances around the Ni metal center as a function of the Lewis acidity of the redox-inactive cation M. Likewise, we observe no significant trend in distances between the redox inactive ion and the bridging O-atoms of the phenoxide ligands (See Table 2.1 for select bond metrics). However, we do observe that the structure of **L^{6}NiY** displays a significantly shorter intermetallic Ni–M distance (by nearly 0.1 Å) than all the other structures. This is in accord with the shortest M–$O_{phenoxide}$ distance of the series, and is likely due to the presence of the unique bridging triflate ligand (*vide supra*). Interestingly, this bridging triflate motif was only observed for yttrium, the most Lewis acidic metal in our study. We note that the average Ni-N_{imine} distance in **L^{6}NiY** is also the shortest of our series, in accord with pronounced changes in the electronic structure of this compound due to the close proximity of the trivalent cation (*vide infra*). Comparing the distances between the redox-inactive M and the triflate O-atoms, the only distance of note is the rather long Y–O11 distance of 2.350(4) Å.

This is significantly longer than Y–O21 (2.291(5) Å) and Y–O31 (2.306(5) Å), due to the unique bridging nature of the triflate anion containing O11 in **L^{6}NiY**. On average, the Nd–$O_{triflate}$ distances are significantly longer (2.428 Å), while the Ca–$O_{triflate}$ distances are similar on average (2.331 Å).

Table 2.1. Selected distances (Å) computed from the solid-state (XRD) structures of the heterobimetallic complexes.

Complex	pK_a of $[M(H_2O)_m]^{n+}$	Ni–M[a] (Å)	Ni–N (avg)[b] (Å)	Ni–O (avg)[c] (Å)	M–O (avg)[d] (Å)
L^{6}Ni	-	-	1.854	1.854	-
L^{6}NiNa	14.8	3.504(1)	1.858	1.844	2.466
L^{6}NiCa	12.7	3.475(1)	1.859	1.857	2.433
L^{6}NiNd	8.4	3.505(1)	1.854	1.858	2.458
L^{6}NiY	8.3	3.398(1)	1.847	1.844	2.348

[a] M is the redox-inactive metal in the crown-ether-like pocket. [b] Average of the distances between Ni and N1 and N2 of the imine groups. [c] Average of the distances between Ni and O1 and O2 of the phenoxide ligands. [d] Average of the distances between M and O1 and O2 of the bridging phenoxide ligands.

With these results in hand, we next moved to interrogate the electronic structure of the heterobimetallic compounds by spectroscopy (data summarized in Table 2.2). Electronic absorption spectra collected for the parent monometallic complex **L^{6}Ni** reveal a response typical of Schiff base nickel(II) complexes: a lowest energy band with λ_{max} at 486 nm with molar absorptivity of 6800 M^{-1} cm^{-1} (Figure 2.4). Based on its position and intensity, and in agreement with prior literature, this transition can be assigned to a metal-to-ligand charge transfer.[39]

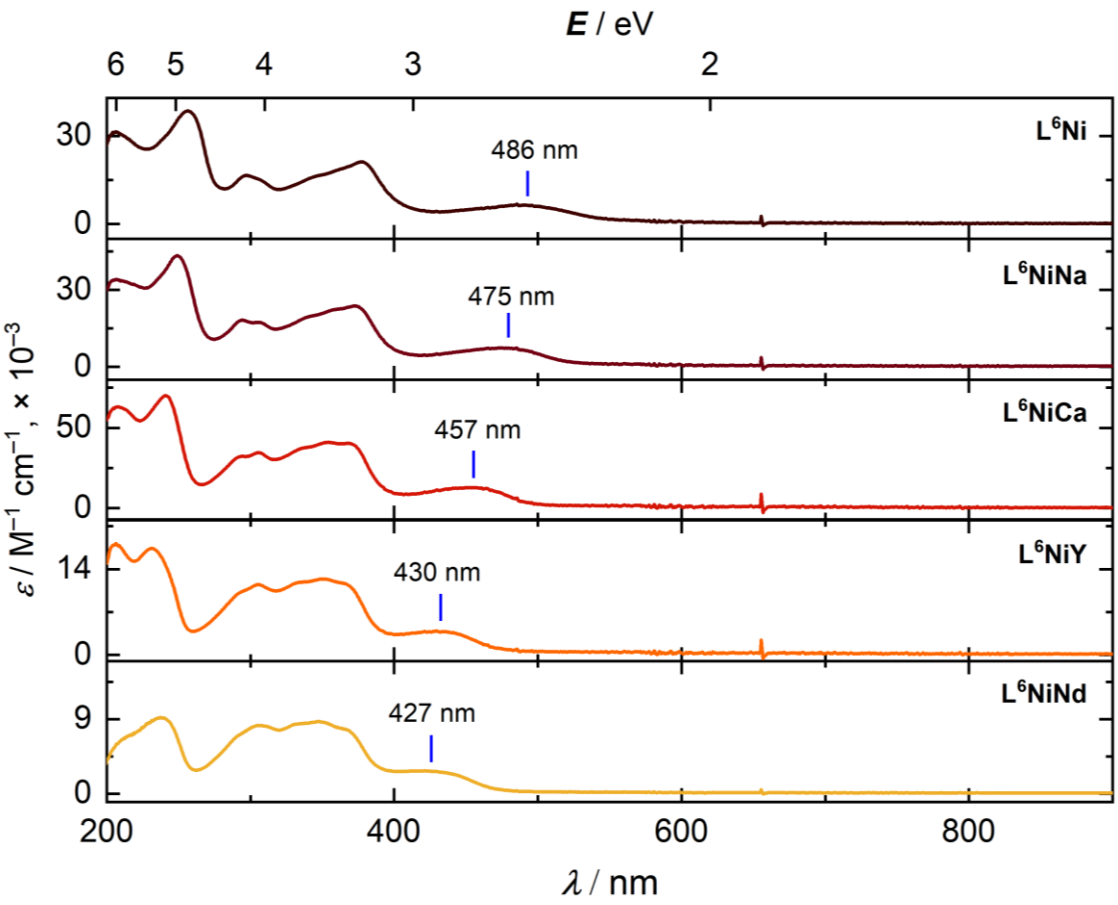

Figure 2.4. Stacked electronic absorption (EA) spectra of the Ni complexes in CH_3CN.

Upon installation of the redox-inactive cations in the crown-ether-like cavity, this MLCT band shifts to higher energy (Figure 2.4). This is consistent with a shift in the position of the metal-centered HOMO of these compounds to lower energies by interaction of the ligand with the redox-inactive cations via the phenoxide groups. Specifically, attenuated donation from the phenoxide groups to the nickel center should lower the HOMO, resulting in widening of the HOMO-LUMO gap. According to this model, the effect of the redox-inactive cations on the ligand π-system (LUMO) must be minor in comparison to the effect on the nickel center. Plotting the energy of the MLCT band (in eV) versus the pK_a of the corresponding metal–aqua ion reveals a uniform, linear trend in

the shift in the HOMO-LUMO gap of 44 meV per pK_a unit (Figure 2.5). While the electronic structure of the metal complexes is most strongly perturbed by the trivalent cations, the effects engendered by these metals are in line with those observed for divalent or monovalent ions. This is in agreement with work examining the effect of redox-inactive cations on the reduction potentials of manganese[23] or iron[24] oxo clusters.

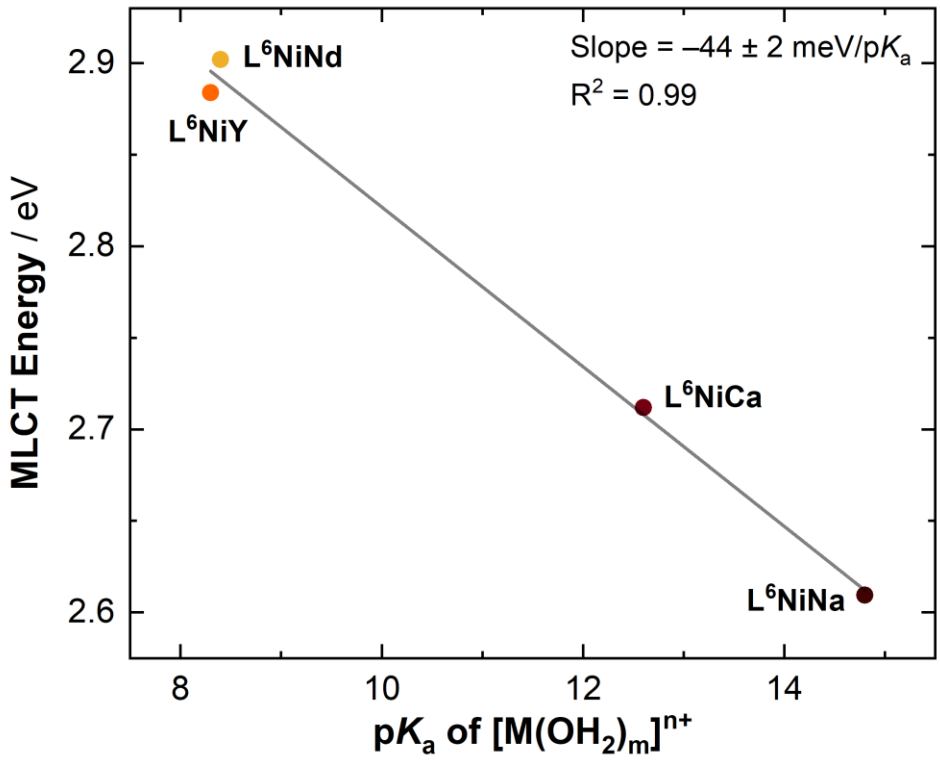

Figure 2.5. Dependence of the lowest-energy absorption band (MLCT energy) of the **L^{6}NiM** complexes on the Lewis acidity (pK_a) of the corresponding **M**-aqua complexes.

The chemical shift for the signal corresponding to the imine proton in the ^{1}H NMR spectra for the bimetallic complexes provides a useful readout of the effects of incorporation of Lewis acids (see Appendix A, Figure A12). A minimal shift in the position of the imine proton resonance from 8.6 for **L^{6}NiNa** to 8.7 ppm for **L^{6}NiCa**. However, this resonance is shifted to 16.5 ppm in **L^{6}NiNd**, and to 19.0 ppm for **L^{6}NiY**. These results

indicate a marked acidification of the imine protons upon coordination of the trivalent ions, which results in the observed deshielding effect. This observation may form the basis for an important design rule for future work, in that acidification of vulnerable moieties on organic ligands may activate decomposition mechanisms that are normally not accessible without the action of strongly Lewis acidic metal ions.

Table 2.2. Selected spectroscopic features of the Ni complexes in acetonitrile solvent.

Complex	pK_a of $[M(H_2O)_m]^{n+}$	λ_{max} (nm)[a] [ε (M^{-1} cm^{-1})]	$\delta(H_{imine})$[b] (ppm)	ν_{imine}[c] (cm^{-1})
L^6Ni	-	486 [6800]	-	1610
L^6NiNa	14.7	475 [7400]	8.6	1613
L^6NiCa	12.7	457 [12900]	8.7	1616
L^6NiNd	8.4	427 [2800]	16.5	1659
L^6NiY	8.3	430 [3900]	19.0	1664

[a] UV-vis spectra shown in Figure 2.4. [b] NMR spectra shown in Appendix A. Solvent: CD_3CN. [c] Infrared spectra shown in Appendix A.

Consistent with this observation of acidification of the imine protons by ^{1}H NMR, we also observe a shift of the imine C=N stretch to higher energies in infrared spectra (see Appendix A, Figure A25 for spectra) upon coordination of the Lewis acidic cations. This can be assigned to arise from strengthening of the C–N interaction as the Lewis acidity of the associated ion increases. Presumably, this bond strengthens due to decreased back donation into the imine group upon coordination of the Lewis acidic cations. As observed in the ^{1}H NMR resonances of the imine protons, the largest shift in the imine stretch was

encountered for **L^{6}NiNd** and **L^{6}NiY** (see Appendix A, Figure A12). As in the case of the MLCT energy, the imine stretch was found to vary linearly over the range of Lewis acidities investigated here, with a shift of 8.3 cm^{-1} per pK_a unit (see Appendix A, Figure A26 for plot). This uniform trend is consistent with a similar mode of interaction between the imine moieties and the Lewis acidic cations in the compounds; the cations are tightly bound in their macrocyclic host ligand environment, even in coordinating acetonitrile solvent.

Considering the high stability exhibited by all of our heterobimetallic complexes in acetonitrile, we were encouraged to interrogate their electrochemical properties. Electrochemical data has not been available for heterobimetallic nickel complexes with similar Schiff-base ligands in the past; this may be due in part to poor stability of non-macrocyclic ligand environments. Here, we began by examining the electrochemical properties of the compounds in dimethylformamide (DMF) solution. (**L^{6}NiCa** is only sparingly soluble in MeCN, making experiments more challenging.) Details regarding the electrochemical studies are given in the Experimental Section.

Cyclic voltammograms collected for the compounds in dimethylformamide reveal a single, irreversible reduction (see Appendix A, Figure A37 for voltammograms; electrochemical data summarized in Table 2.3). An analogous reduction has been observed previously for monometallic nickel derivatives with unsubstituted salophen ligands.[40] **L^{6}Ni** is reduced near –2 V vs. the ferrocenium/ ferrocene couple (denoted hereafter as Fc$^{+/0}$) ($E_{p,c}$ = –1.89 V where $E_{p,c}$ denotes the cathodic peak current of the irreversible process). The potentials required for reduction of **L^{6}NiNa** and **L^{6}NiCa**, $E_{p,c}$ = –1.73 V and –1.53 V, respectively, are consistent with coordination of the Lewis acidic ion resulting in a shift of

the reduction potentials to less negative values. The reductive electrochemistry can be assigned to undergo an EC-type mechanism,[41] as the initial electrochemical reduction is followed by a chemical reaction. At least one product of this chemical reaction is susceptible to re-oxidation at potentials shifted positive of $E_{p,c}$.

Table 2.3. Reduction potentials of the Ni complexes in DMF and acetonitrile.

Complex	$E_{p,c}$ in DMF (V)[a]	$E_{p,c}$ in MeCN (V)[b]
L^{6}Ni	–1.89	–1.84
L^{6}NiNa	–1.73	–1.65
L^{6}NiCa	–1.53	–1.42
L^{6}NiNd	N/A [c]	–1.18
L^{6}NiY	N/A [c]	–1.22

[a] Reported versus the ferrocenium/ferrocene couple ($Fc^{+/0}$). Conditions: 0.1 M $[^nBu_4N]^+[PF_6]^-$ in DMF; 100 mV/s. [b] Reported versus $Fc^{+/0}$. Conditions: 0.1 M $[^nBu_4N]^+[PF_6]^-$ in MeCN; 100 mV/s. [c] Compound not stable as gauged from electronic absorption data and electrochemical measurements.

To confirm that the redox events observed by cyclic voltammetry (CV) indeed correspond to electron transfer processes involving the desired compounds, we titrated a sample of **L^{6}Ni** (in the electrochemical cell) with increasing quantities of $Ca(OTf)_2$. Addition of 0.5 equiv. of Ca^{2+} results in appearance of a new reduction wave, $E_{p,c}$, at –1.51 V. The original reduction wave for **L^{6}Ni** (at –1.89 V) is diminished upon Ca^{2+} addition, confirming conversion of **L^{6}Ni** to **L^{6}NiCa** by rapid metalation of the crown-ether-like cavity of the macrocyclic ligand (see Figure 2.6). A second, minor reduction process is

observed with $E_{p,c} \approx -1.75$ V, perhaps consistent with interaction of the Ca^{2+} ion with multiple Ni centers.

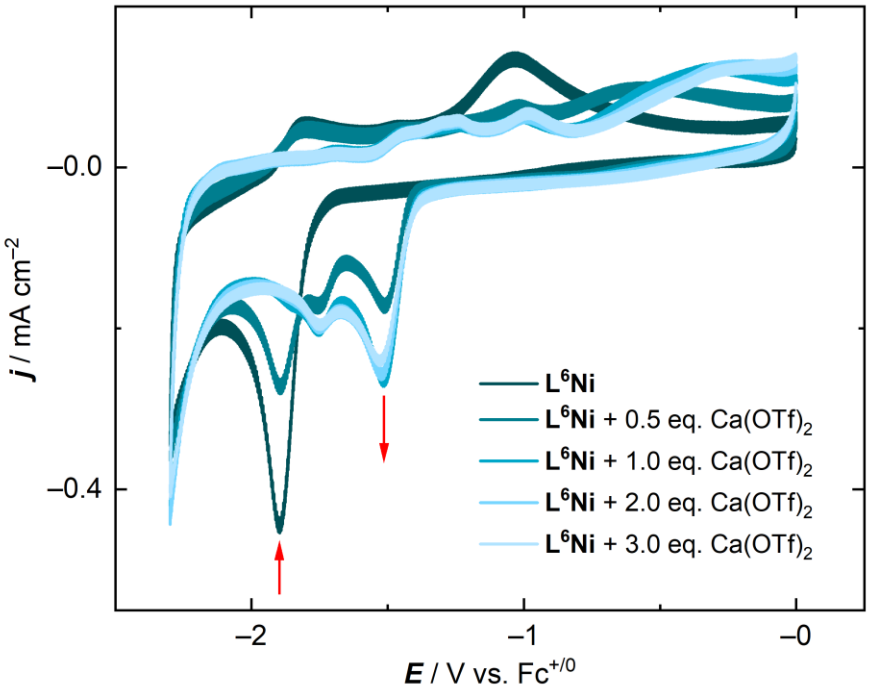

Figure 2.6. Electrochemical response of **L^{6}Ni** in DMF upon addition of various amounts of $Ca(OTf)_2$. Growth of the reduction process with $E_{p,c} = -1.51$ V indicates coordination of Ca^{2+} to **L^{6}Ni**, giving *in-situ* generation of **L^{6}NiCa**.

We were surprised, however, to observe that voltammograms of **L^{6}NiNd** and **L^{6}NiY** did not show similar clearly resolved reduction processes in DMF. The reduction potential measured in both of these latter cases was near –1.8 V (see Appendix A for voltammograms). This value of –1.8 V does not fit with the trend set by the other compounds; significantly, the peak potential measured for **L^{6}NiNd** and **L^{6}NiY** (near –1.8 V) is very similar to **L^{6}Ni**, which is reduced at –1.89 V. This suggested to us that the highly Lewis acidic Nd^{3+} and Y^{3+} ions might be lost from the macrocyclic ligand in the presence of highly coordinating DMF solvent.

The electrochemical response of the heterobimetallic complexes in MeCN is much simpler (see Figure 2.7). The single, irreversible reduction event observed with **L^{6}Ni** in DMF solvent is retained in MeCN albeit with a minor shift ($E_{p,c}$ = –1.84 V in MeCN vs. –1.89 V in DMF). The heterobimetallic complexes show similar irreversible reduction processes (again consistent with EC behavior) that shift to less negative potentials as a function of the Lewis acidity of the paired cation.

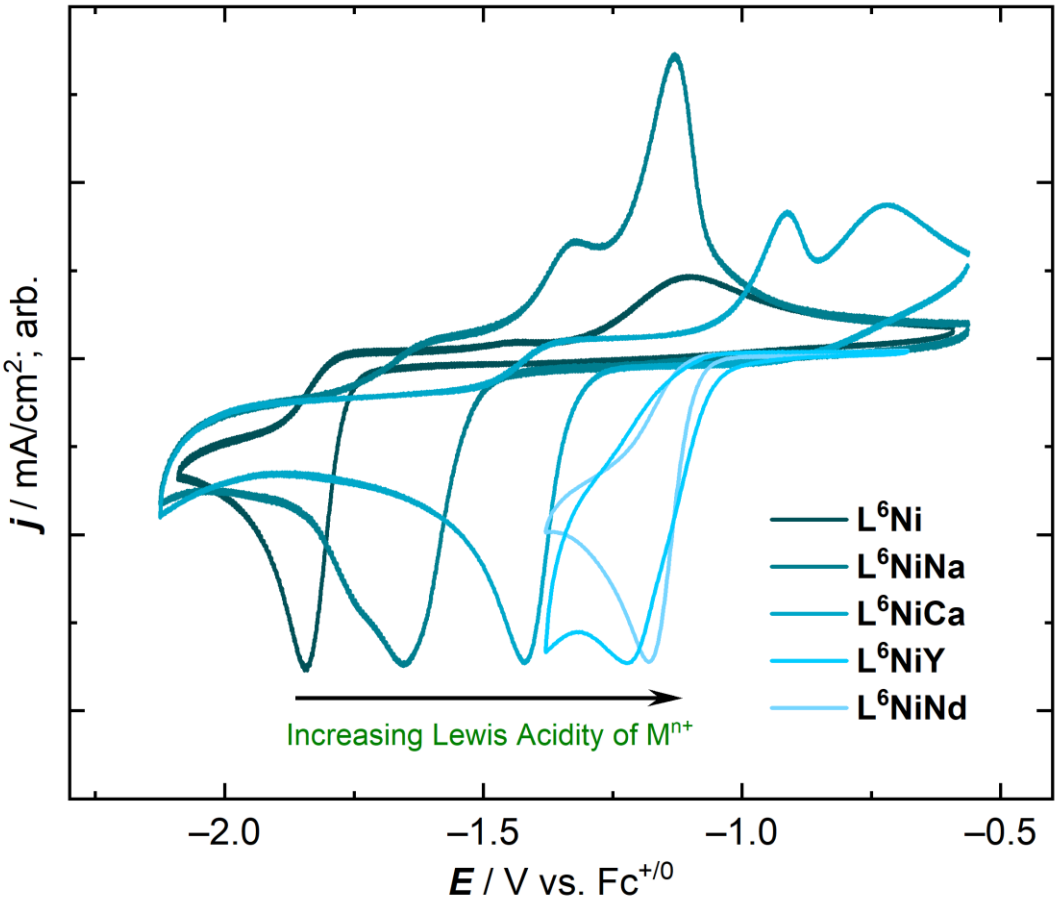

Figure 2.7. Overlay of CV data for **L^{6}Ni** and **L^{6}NiM** complexes in MeCN (0.1 M $[nBu_4N]^+[PF_6]^-$, 100 mV/s).

Specifically, examination of $E_{p,c}$ as a function of the Lewis acidity of the added cation gives an average shift in the reduction potential of the resulting heterobimetallic complex

of 67 mV per pK_a unit (Figure 2.8). As in the spectroscopic data (*vide supra*), the trivalent and highly Lewis acidic cations resulted in the most pronounced shift of $E_{p,c}$. Although the Lewis acidity of yttrium is greater than that of neodymium (pK_a = 8.3 vs. 8.4), the reduction peak potential measured for **L^{6}NiNd** is more positive than that of **L^{6}NiY**. This can be ascribed to uncertainties in the electrochemical data, as interpretations regarding peak potentials for irreversible processes can be complicated by secondary effects. Similar uncertainty was encountered by Agapie and co-workers,[23,24] and we have quantified our error here as 67 ± 9 mV/pK_a which corresponds to ±17% error. Thus, there is a clear and uniform trend of modulated reduction potential upon coordination of Lewis acidic metals to **L^{6}Ni**, even for the unusual trivalent analogues that are the focus of this study.

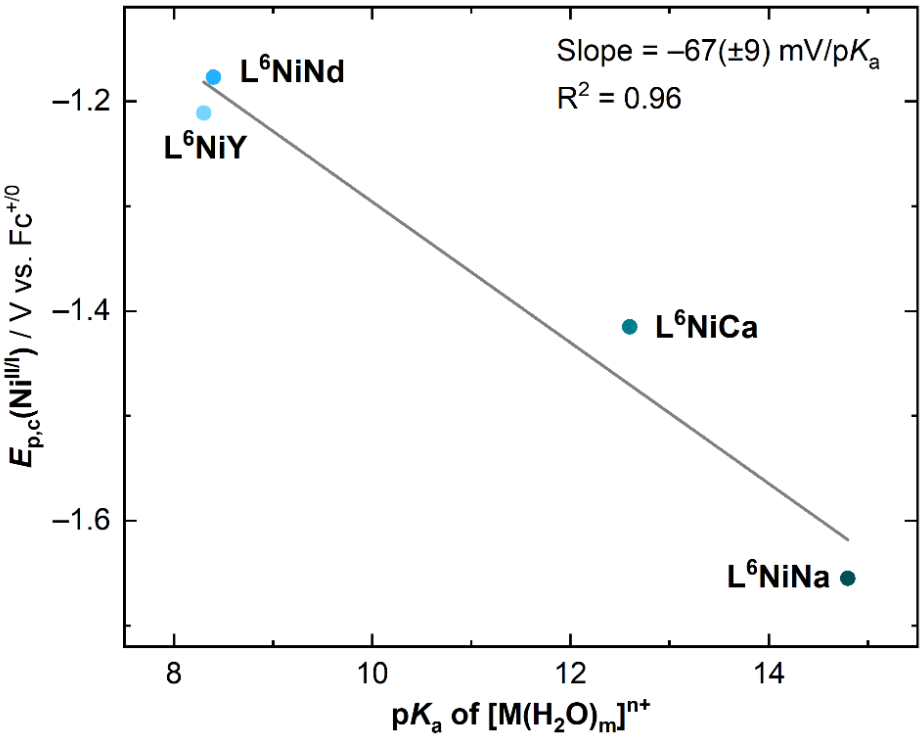

Figure 2.8. Plot of $E_{p,c}(Ni^{II/I})$ vs. pK_a of $[M(H_2O)_m]^{n+}$.

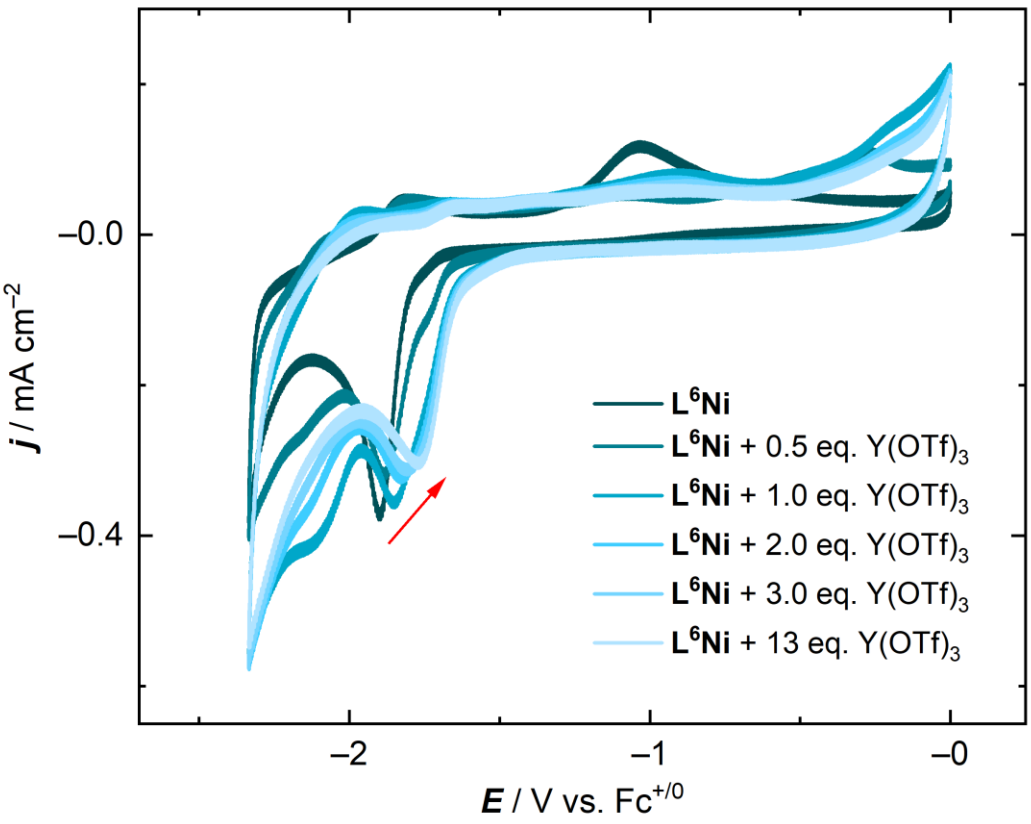

Figure 2.9. Electrochemical response of **L^{6}Ni** in DMF upon addition of various amounts of $Y(OTf)_3$. The initial reduction of **L^{6}Ni** occurs near –1.8 V, and this signal undergoes only minor changes as Y^{3+} is added.

A second set of electronic absorption spectra confirms DMF-driven loss of Nd^{3+} and Y^{3+} from our macrocyclic ligand environment (see Appendix A, Figure A24 for stacked spectra). There are only minor differences in the spectra of **L^{6}NiNd** and **L^{6}NiY** versus **L^{6}Ni** in DMF, consistent with virtually complete loss of the trivalent ion from the isolated compounds. Consistent with this assignment, there were only minor changes in cyclic voltammograms of **L^{6}Ni** upon titration with up to 13 equiv. of $Y(OTf)_3$. Rather than appearance of a new, unique reduction wave corresponding to the heterobimetallic compound, we observe only a single, broad reduction that gradually shifts to less negative

potentials as a function of added yttrium (see Figure 2.9). In this experiment, $E_{p,c}$ shifts over a narrow potential range from –1.88 to –1.77 V. The original, reasonably sharp peak for reduction of **L^{6}Ni** is located at –1.89 V, and thus addition of even 13 equiv. of Y^{3+} does not result in a significant shift in the reduction potential. This is consistent with an equilibrium exchange process that results in only minor occupation of the macrocyclic ligand environment by Y^{3+}.[16a] The broadened peak position in the titration experiment is further suggestive of a rapid equilibrium—the various forms of the metal complex present in solution are rapidly interconverting under these conditions and thus are not stable on the timescale of the CV experiment.

2.3 Discussion

Tsui et al. recently demonstrated that heterometallic manganese–oxido clusters containing a redox-inactive cation show a reduction potential shift of 100 mV per pK_a unit.[23] In these clusters, the redox-active component of the system, a nearby manganese center, is closely associated with the redox-inactive metal, giving rise to the distinctive shifts in reduction potential. Similar results have been demonstrated for iron analogues of these compounds, with a measured dependence on the Lewis acidity of the redox-active metal center of 70 mV per pK_a unit.[24] The attenuated coupling in these two cases can be ascribed to differences between iron and manganese, although exact comparisons are difficult.

In our new work, the coupling between the nickel center and the redox-inactive metal is apparently not significantly different from these cases. We have determined an average reduction potential shift of 67 ± 9 mV per pK_a unit in our heterobimetallic compounds. This is consistent with coupling driven by the bridging phenolate groups in our compounds. Appealingly, our results here span the same Lewis-acidity range (from Na^+ (14.7) to Y^{3+}

(8.3)) used in the manganese and iron cluster work, allowing this comparison of coupling to be made under reasonable conditions. Additionally, our results align well with those from a narrower Lewis acidity range studied by Yang and co-workers in heterobimetallic complexes of cobalt.[34]

Our compounds and electrochemical studies extend the range of available data on the modulation of reduction potentials by trivalent redox-inactive metals like Y^{3+}. First, in terms of useful trends, we find a linear relationship between most spectroscopic properties and Lewis acidity. Second, we find that the heterobimetallic compounds containing trivalent Lewis acidic cations may be especially prone to speciation or decomposition in coordinating solvents like DMF. We were able to clearly assign loss of both Y^{3+} and Nd^{3+} from our ligand framework; the loss occurs despite the use of a hexadentate and macrocyclic ligand that we expected would impart stability to the heterobimetallic compounds.[26] Conversely, **L^{6}Ni**, **L^{6}NiNa**, and **L^{6}NiCa** are stable in both DMF and MeCN, allowing their reduction peak potentials ($E_{p,c}$) to be measured in both solvents. The potentials are not significantly different, suggesting that DMF and MeCN do not significantly perturb the coordination environment around Ni or M in these compounds.

As noted in the introduction, addition of the highly Lewis acidic Y^{3+} and Sc^{3+} ions results in enhanced reactivity of certain iron peroxo complexes.[20,21] The enhanced activity is readily achieved by addition of multiple equivalents of M^{3+} to the reaction mixture of interest. Our electrochemical studies show that (even in a macrocyclic environment designed to favor retention of a heterobimetallic structure) redox-inactive cations like Y^{3+} can engage in rapid equilibrium processes. Thus, speciation processes under catalytic or electrochemical conditions could contribute to reactivity, or even afford a range of structures that differ from

the starting materials. In the current work, we encountered loss of defined structure in the presence of DMF. Although the stability of cation-crown complexes has been of interest for some years,[27] more data on the stability of trivalent cations in crown-ether-like cavities is needed in this area.[42,43] We suggest that future work on multimetallic complexes could usefully include such related stability studies, as the information gained on the speciation of catalysts could lead to improvements in their activity by rational design.[44]

2.4 Conclusions

We have synthesized and characterized a small family of heterobimetallic complexes in a macrocyclic, ditopic ligand framework. These complexes pair a nickel salophen moiety with a variety of redox-inactive Lewis acidic cations (Na^+, Ca^{2+}, Nd^{3+}, and Y^{3+}) bound in a crown ether-like environment. We find that the energy of the MLCT band, the acidity of the imine protons, and the imine stretching frequency are all correlated linearly with the Lewis acidity of the redox-inactive metal as judged by the pK_a of the corresponding $[M(H_2O)_m]^{n+}$ species. At the extreme end of the pK_a scale, for the ions Y^{3+} and Nd^{3+}, the heterobimetallic complexes are unstable in DMF. Exposure of our compounds to DMF results in demetallation of the crown ether-like cavity of the ligand framework, as judged by both electronic absorption spectra and electrochemical studies. However, the macrocyclic framework successfully imparts sufficient stability to the heterobimetallic compounds in MeCN to enable a full electrochemical study in this solvent. The results, taken together, demonstrate that heterobimetallic complexes of nickel and trivalent redox-inactive cations are highly Lewis acidic and could find future applications, if conditions are carefully selected to maintain their unique structures.

2.5 Experimental Details

2.5.1 General Considerations

All manipulations were carried out in dry N_2-filled gloveboxes (Vacuum Atmospheres Co., Hawthorne, CA) or under N_2 atmosphere using standard Schlenk techniques unless otherwise noted. All solvents were of commercial grade and dried over activated alumina using a PPT Glass Contour (Nashua, NH) solvent purification system prior to use, and were stored over molecular sieves. All chemicals were from major commercial suppliers and used after extensive drying. 2,3-dihydroxybenzaldehyde was sublimed in vacuo. Deuterated NMR solvents were purchased from Cambridge Isotope Laboratories; CD_3CN was dried over molecular sieves. ^{1}H, ^{13}C, ^{19}F, and ^{31}P NMR spectra were collected on 400 and 500 MHz Bruker spectrometers and referenced to the residual protio-solvent signal in the case of ^{1}H and ^{13}C, and to the deuterium lock signal in the case of ^{19}F and ^{31}P unless otherwise noted. Chemical shifts (δ) are reported in units of ppm, and coupling constants (J) are reported in Hz. NMR spectra are given in Appendix A (Figures A1 to A12). Elemental analyses were performed by Midwest Microlab, Inc. (Indianapolis, IN).

2.5.2 Synthesis

Synthesis of 3,3´-(3,6-Dioxaoctane-1,8-diyldioxy)bis(2-hydroxybenzaldehyde) (1)

Under inert atmosphere of nitrogen, a dry Schlenk flask was loaded with 2,3-dihydroxybenzaldehyde (1.39 g, 10.0 mmol) dissolved in 5 mL of dry THF. This solution was cannula transferred to a suspension of NaH (0.528 g, 22.0 mmol) in 5 mL of dry THF under N_2 over a period of 30 minutes. The temperature was kept below 25^{o}C. After 1 hour of stirring, triethylene glycol ditosylate (2.30 g, 5.00 mmol) dissolved in 5 mL of THF was

added in one go by cannula transfer. The mixture was stirred for 24 hours under N_2 atmosphere. Addition of 60 mL of water resulted in a dark brown solution which was extracted twice with 60 mL portions of $CHCl_3$. The aqueous layer was treated with 6 M HCl until the pH of the mixture was 1. This mixture was then extracted with three 10 mL portions of $CHCl_3$. The combined organic layers were washed with 1 M HCl and dried over anhydrous $MgSO_4$. Evaporation of solvent yielded a yellow viscous oil which was purified by column chromatography to give a pale yellow solid. Yield: 34% (341 mg). Spectroscopic characterizations were in agreement with reported literature.[1]

Synthesis of L^6H_2Ba

To a dry three-necked flask under inert atmosphere, $Ba(ClO_4)_2$ (172 mg, 0.512 mmol) was dissolved in 50 mL of dry, degassed MeOH (0.01 M) and 1 equiv. of dialdehyde **1** (200 mg, 0.512 mmol) in 5 mL THF (0.1 M) was added slowly under reflux. 1 equiv. of 1,2-phenylenediamine (55.4 mg, 0.512 mmol) in 5 mL MeOH (0.1 M) was added dropwise over a period of 1 hour. The reaction mixture was refluxed for 30 minutes. After cooling down to room temperature, the resulting orange barium complex was filtered and washed twice with cold MeOH. Yield: 50% (209 mg). Spectroscopic characterizations were in agreement with reported literature.[1]

Synthesis of L^6Ni

Guanidium sulfate (116 mg, 0.54 mmol) in 25 mL water was added to a suspension of **L^6H_2Ba** (208 mg, 0.26 mmol) in 25 mL $CHCl_3$ under stirring until the organic layer was clear. The organic layer was separated, concentrated and diluted with 15 mL MeOH. To this orange solution, 1 equiv. of $Ni(OAc)_2$ in 5 mL MeOH was added and the mixture was stirred

for 30 minutes. The red precipitate was filtered and washed with cold $CHCl_3$. Yield: 89% (120 mg). Spectroscopic characterizations were in agreement with reported literature.[26] Crystals suitable for X-ray diffraction were obtained by slow cooling a solution of **L^{6}Ni** in MeCN.

General procedure for preparation of L^{6}NiM.

Under inert atmosphere, a heterogenous solution of **L^{6}Ni** in MeCN was added to 1 equiv. of corresponding metal salt solution in MeCN and stirred for 30 minutes. The color changed from red to yellow, orange or deep red. The solvent was removed in vacuo to give the desired product in good yield. Yields were in the range of 85-95%. Additional details are given in Appendix A.

Mass spectrometry data collected on solutions containing the heterobimetallic compounds revealed only the presence of **L^{6}Ni** with an associated potassium cation in each case. Therefore, we conclude that the compounds are not stable to the conditions present in our electrospray ionization (ESI) mass spectrometer. For **L^{6}Ni**: ESI-MS (positive) m/z: 557.1 (100%) (**L^{6}Ni** + K^+), 558.1 (31%), 559.1 (54%).

L^{6}NiNa. Yield: 85%. ^{1}H NMR (400 MHz, CD_3CN) δ 8.45 (s, 2H), 7.85 (dd, $^3J_{H,H}$ = 6.3 Hz, $^3J_{H,H}$ = 3.3 Hz, 2H), 7.29 (dd, $^3J_{H,H}$ = 6.3 Hz, $^3J_{H,H}$ = 3.3 Hz, 2H), 7.15 (dd, $^3J_{H,H}$ = 8.3 Hz, $^3J_{H,H}$ = 1.5 Hz, 2H), 6.93 (dd, $^3J_{H,H}$ = 7.7 Hz, $^3J_{H,H}$ = 1.5 Hz, 2H), 6.69 (dd, J = 8.1, 7.7 Hz, 2H), 4.12 – 4.05 (m, 4H), 3.89 – 3.82 (m, 4H), 3.74 (s, 4H). $^{13}C\{^1H\}$ NMR (126 Hz, CD_3CN) δ 157.27, 155.16, 149.48, 143.18, 128.78, 126.38, 120.63, 116.42, 115.13, 69.49, 68.04, 67.62. ^{19}F NMR (376 Hz, CD_3CN) δ –72.02, –73.90. ^{31}P NMR (162 Hz, CD_3CN) δ –131.55, –135.91, –140.27, –144.64, –149.00, –153.36, –157.72. Anal. Calcd. for

$C_{28}H_{27}N_3NiNaO_6PF_6$ (**L^{6}NiNa**): C 46.18, H 3.74, N 5.77; Found: C 46.24, H 3.79, N 5.77. Electronic absorption spectrum (MeCN): 249 (43000), 294 (18200), 305 (17400), 373 (23700), 475 nm (7400 M^{-1} cm^{-1}).

L^{6}NiCa. Yield: 93%. ^{1}H NMR (500 MHz, CD_3OD) δ 10.47 (bs, 2H), 8.13 (dd, $^3J_{H,H}$ = 6.0 Hz, $^3J_{H,H}$ = 2.8 Hz, 2H), 7.49 (dd, $^3J_{H,H}$ = 5.9 Hz, $^3J_{H,H}$ = 2.8 Hz, 2H), 7.43 (dd, $^3J_{H,H}$ = 8.0 Hz, $^3J_{H,H}$ = 1.7 Hz, 2H), 7.35 (dd, $^3J_{H,H}$ = 8.0 Hz, $^3J_{H,H}$ = 2.2 Hz, 2H), 6.93 (dd, *J* = 7.9, 2.3 Hz, 2H), 4.41-4.35 (m, 4H), 3.89-3.82 (m, 4H), 4.02 (s, 4H). $^{13}C\{^1H\}$ NMR (126 Hz, CD_3OD) δ 158.13, 150.91, 150.28, 141.11, 129.22, 127.03, 121.01, 117.51, 116.69, 116.26, 69.05, 67.73, 66.83. ^{19}F NMR (376 Hz, CD_3OD) δ –80.11. Electronic absorption spectrum (MeCN): 241 (70100), 295 (32300), 306 (34600), 354 (41000), 367 (40400), 457 nm (12900 M^{-1} cm^{-1}). Anal. Calcd. for $C_{28}H_{24}N_2NiCaO_{12}F_6S_2$ (**L^{6}NiCa**): C 39.22, H 2.82, N 3.27; Found: C 39.15, H 2.86, N 3.26.

L^{6}NiNd. Yield: 89%. ^{1}H NMR (400 MHz, CD_3CN) δ 16.48, 11.00, 9.51, 8.62, 6.92, 3.67, 5.29, 2.40, 1.84. ^{19}F NMR (376 Hz, CD_3OD) δ –80.11. Electronic absorption spectrum (MeCN): 238 (9200), 307 (8200), 332 (8400), 347 (8700), 422 nm (2800 M^{-1} cm^{-1}). Anal. Calcd. for $C_{29}H_{24}N_2NiNdO_{15}F_9S_3$ (**L^{6}NiNd**): C 31.36, H 2.18, N 2.52; Found: C 27.44, H 2.08, N 2.65. Satisfactory analysis (±0.4%) could not be obtained for **L^{6}NiNd**; this is likely due to high sensitivity of the compound to water.

L^{6}NiY. Yield: 88%. ^{1}H NMR (400 MHz, CD_3CN) δ 18.8-19.2 (bs, 2H), 7.96-8.04 (m, 2H), 7.74-7.79 (m, 4H), 7.56 (d, $^3J_{H,H}$ = 7.9 Hz, 2H), 7.07 (t, $^3J_{H,H}$ = 8.0 Hz, 2H), 6.69 (dd, *J* = 8.1, 7.7 Hz, 2H), 4.64 (t, $^3J_{H,H}$ = 5.0 Hz, 4H), 4.39 (t, $^3J_{H,H}$ = 5.0 Hz, 4H), 4.30 (s, 4H). ^{19}F NMR (376 Hz, CD_3CN) δ –79.24. Electronic absorption spectrum (MeCN): 231 (17400),

305 (11500), 341 (12000), 351 (12400), 429 nm (3900 M^{-1} cm^{-1}). Anal. Calcd. for $C_{29}H_{24}N_2NiYO_{15}F_9S_3$ (**L^6NiY**): C 33.01, H 2.29, N 2.65; Found: C 33.16, H 2.44, N 2.66.

2.5.3 X-ray crystallography

Single crystals of the complex **L^6Ni** were obtained by slow cooling of a concentrated solution of the species in MeCN. Single crystals of the complexes **L^6NiNa**, **L^6NiNd**, **L^6NiY** were obtained by vapor diffusion of Et_2O in a concentrated solution of each species in MeCN. Single crystals of the complex **L^6NiCa** were obtained by vapor diffusion of Et_2O in a concentrated solution of the species in MeOH. For additional details for collection and refining of data see Appendix A.

2.5.4 Electrochemistry

Electrochemical experiments were carried out in a N_2-filled glovebox in dry, degassed MeCN or DMF. 0.10 M tetra(n-butylammonium) hexafluorophosphate ($[nBu_4N]^+[PF_6]^-$); Sigma-Aldrich, electrochemical grade) served as the supporting electrolyte. Measurements were made with a Gamry Reference 600+ Potentiostat/Galvanostat using a standard three-electrode configuration. The working electrode was the basal plane of highly oriented pyrolytic graphite (HOPG) (GraphiteStore.com, Buffalo Grove, Ill.; surface area: 0.09 cm^2), the counter electrode was a platinum wire (Kurt J. Lesker, Jefferson Hills, PA; 99.99%, 0.5 mm diameter), and a silver wire immersed in electrolyte served as a pseudo-reference electrode (CH Instruments). The reference was separated from the working solution by a Vycor frit (Bioanalytical Systems, Inc.). Ferrocene (Sigma Aldrich; twice-sublimed) was added to electrolyte solution prior to the beginning of each experiment; the midpoint potential of the ferrocenium/ferrocene couple (denoted as $Fc^{+/0}$) served as an external

standard for comparison of the recorded potentials. Concentrations of analyte for CV were ca. 10^{-2} to 10^{-3} mM unless otherwise noted.

2.5.5 Spectroscopy

Infrared spectra were recorded on a PerkinElmer Spectrum 100 FTIR spectrometer at room temperature; solution samples were prepared inside a dry N_2-atmosphere glovebox and sealed in 0.1 mm NaCl cells. All measurements were collected in acetonitrile (MeCN) solution in order to access the spectral regions of interest. Electronic absorption spectra were collected with an Ocean Optics Flame spectrometer, in a 1-cm path length quartz cuvette.

2.6 Acknowledgements

The authors thank David Sconyers for assistance with electrochemistry, and Dr. Justin Douglas and Sarah Neuenswander for assistance with NMR spectroscopy. The work in this chapter was supported by the University of Kansas, and by the US National Science Foundation through award CBET-1605524.

2.7 References

(1) Gavrilova, A. L.; Bosnich, B. Principles of mononucleating and binucleating ligand design. *Chem. Rev.* **2004**, *104*, 349-384.

(2) Buchwalter, P.; Rosé, J.; Braunstein, P. Multimetallic catalysis based on heterometallic complexes and clusters. *Chem. Rev.* **2015**, *115*, 28-126.

(3) Ogo, S.; Kabe, R.; Uehara, K.; Kure, B.; Nishimura, T.; Menon, S. C.; Harada, R.; Fukuzumi, S.; Higuchi, Y.; Ohhara, T.; Tamada, T; Kuroki, R. A dinuclear Ni (μ-H) Ru complex derived from H_2. *Science* **2007**, *316*, 585-587.

(4) Kure, B. Sano, M.; Nakajima, T.; Tanase, T. Systematic Heterodinuclear Complexes with MM′(μ-meppp) Centers That Tune the Properties of a Nesting Hydride (M = Ni, Pd, Pt; M′ = Rh, Ir; H_2meppp = *meso*-1,3 Bis[(mercaptoethyl)phenylphosphino]propane). *Organometallics* **2014**, *33*, 3950-3965.

(5) Howard, J. B.; Rees, D. C. How many metals does it take to fix N2? A mechanistic overview of biological nitrogen fixation. *Proc. Natl. Acad. Sci. U.S.A.* **2006**, *103*, 17088-17093.

(6) Schultz, B. E.; Chan, S. I. Structures and proton-pumping strategies of mitochondrial respiratory enzymes. *Annu. Rev. Biophys. Biomol. Struct.* **2001**, *30*, 23-65.

(7) McEvoy, J. P.; Brudvig, G. W. Water-splitting chemistry of photosystem II. *Chem. Rev.* **2006**, *106*, 4455-4483. b) Yano, J.; Yachandra, V. Mn_4Ca Cluster in Photosynthesis: Where and How Water is Oxidized to Dioxygen. *Chem. Rev.* **2014**, *114*, 4175-4205.

(8) Hendry, G.; Wydrzynski, T. ^{18}O Isotope Exchange Measurements Reveal that Calcium Is Involved in the Binding of One Substrate-Water Molecule to the Oxygen-Evolving Complex in Photosystem II. *Biochemistry* **2003**, *42*, 6209-6217.

(9) Vrettos, J. S.; Stone, D. A.; Brudvig, G. W. Quantifying the Ion Selectivity of the Ca^{2+} Site in Photosystem II: Evidence for Direct Involvement of Ca^{2+} in O_2 Formation. *Biochemistry* **2001**, *40*, 7937-7945.

(10) Limburg, J.; Vrettos, J. S.; Liable-Sands, L. M.; Rheingold, A. L.; Crabtree, R. H.; Brudvig, G. W. A functional model for OO bond formation by the O_2-evolving complex in photosystem II. *Science* **1999**, *283*, 1524-1527.

(11) a) Kanady, J. S.; Tsui, E. Y.; Day, M. W.; Agapie, T. A synthetic model of the Mn_3Ca subsite of the oxygen-evolving complex in photosystem II. *Science* **2011**, *333*, 733-736. b) Tsui, E. Y.; Kanady, J. S.; Agapie, T. Synthetic Cluster Models of Biological and Heterogeneous Manganese Catalysts for O_2 Evolution. *Inorg. Chem.* **2013**, *52*, 13833-13848.

(12) Mukherjee, S. Stull, J. A. Yano, J. Stamatatos, T. C. Pringouri, K. Stich, T. A. Abboud, K. A. Britt, R. D. Yachandra, V. K. Christou, G. Synthetic model of the asymmetric $[Mn_3CaO_4]$ cubane core of the oxygen-evolving complex of photosystem II. *Proc. Nat. Acad. Sci. U.S.A.* **2012**, *109*, 2257-2262.

(13) Zhang, C. Chen, C. Dong, H. Shen, J. R. Dau, H. Zhao, J. A synthetic Mn_4Ca-cluster mimicking the oxygen-evolving center of photosynthesis. *Science* **2015**, *348*, 690.

(14) a) Lau, T. C.; Mak, C. K. Oxidation of alkanes by barium ruthenate in acetic acid: catalysis by Lewis acids. *J. Chem. Soc. Chem. Commun.* **1993**, 766-767. b) Lau, T. C.; Wu, Z. B.; Bai, Z. L.; Mak, C. K. Lewis-acid catalysed oxidation of alkanes by chromate and permanganate. *J. Chem. Soc. Dalton Trans.* **1995**, 695. c) Ho, C. M.; Lau, T. C., Lewis acid activated oxidation of alkanes by barium ferrate. *New J. Chem.* **2000**, *24*, 587-590. d) Yiu, S. M.; Wu, Z. B.; Mak, C. K.; Lau, T. C. $FeCl_3$-Activated oxidation of alkanes by $[Os(N)O_3]^-$. *J. Am. Chem. Soc.* **2004**, *126*, 14921-14929. e) Du, H.; Lo, P. K.; Hu, Z.; Liang, H.; Lau, K. C.; Wang, Y. N.; Lam, W. W.; Lau, T. C., Lewis acid-activated oxidation of alcohols by permanganate. *Chem. Commun.* **2011**, *47*, 7143-7145.

(15) 1. Miller, C. G.; Gordon-Wylie, S. W.; Horwitz, C. P.; Strazisar, S. A.; Peraino, D. K.; Clark, G. R.; Weintraub, S. T.; Collins, T. J. A method for driving O-atom transfer: secondary ion binding to a tetraamide macrocyclic ligand. *J. Am. Chem. Soc.* **1998**, *120*, 11540-11541.

(16) a) Horwitz, C. P.; Ciringh, Y. Synthesis and electrochemical properties of oxo-bridged manganese dimers incorporating alkali and alkaline earth cations. *Inorg. Chim. Acta* **1994**, *225*, 191-200. b) Horwitz, C. P.; Ciringh, Y.; Weintraub, S. T. Formation pathway of a Mn (IV), Mn (IV) bis (μ-oxo) dimer that incorporates alkali and alkaline earth cations and electron transfer properties of the dimer. *Inorg. Chim. Acta* **1999**, *294*, 133-139.

(17) Park, Y. J.; Ziller, J. W.; Borovik, A. The effects of redox-inactive metal ions on the activation of dioxygen: isolation and characterization of a heterobimetallic complex containing a Mn^{III}–(μ-OH)–Ca^{II} core. *J. Am. Chem. Soc.* **2011**, *133*, 9258-9261.

(18) a) Park, Y. J.; Cook, S. A.; Sickerman, N. S.; Sano, Y.; Ziller, J. W.; Borovik, A., Heterobimetallic complexes with M^{III}-(μ-OH)-M^{II} cores (M^{III} = Fe, Mn, Ga; M^{II} = Ca, Sr, and Ba): structural, kinetic, and redox properties. *Chem. Sci.* **2013**, *4*, 717-726. b) Sano, Y.; Weitz, A. C.; Ziller, J. W.; Hendrich, M. P.; Borovik, A. Unsymmetrical bimetallic complexes with M^{II}–(μ-OH)–M^{III} cores ($M^{II}M^{III}$ = $Fe^{II}Fe^{III}$, $Mn^{II}Fe^{III}$, $Mn^{II}Mn^{III}$): structural, magnetic, and redox properties. *Inorg. Chem.* **2013**, *52*, 10229-10231.

(19) a) Nam, W. Synthetic mononuclear nonheme iron–oxygen intermediates. *Acc. Chem. Res.* **2015**, *48*, 2415-2423. b) Fukuzumi, S.; Ohkubo, K.; Lee, Y. M.; Nam, W. Lewis acid coupled electron transfer of metal–oxygen intermediates. *Chem. Eur. J.* **2015**, *21*, 17548-17559.

(20) Li, F.; Van Heuvelen, K. M.; Meier, K. K.; Münck, E.; Que Jr, L. Sc^{3+}-triggered oxoiron (IV) formation from O_2 and its non-heme iron (II) precursor via a Sc^{3+}–peroxo–Fe^{3+} intermediate. *J. Am. Chem. Soc.* **2013**, *135*, 10198-10201.

(21) Lee, Y.-M.; Bang, S.; Kim, Y. M.; Cho, J.; Hong, S.; Nomura, T.; Ogura, T.; Troeppner, O.; Ivanović-Burmazović, I.; Sarangi, R. A mononuclear nonheme iron (III)–peroxo complex binding redox-inactive metal ions. *Chem. Sci.* **2013**, *4*, 3917-3923.

(22) 1. Wiechen, M.; Zaharieva, I.; Dau, H.; Kurz, P. Layered manganese oxides for water-oxidation: alkaline earth cations influence catalytic activity in a photosystem II-like fashion. *Chem. Sci.* **2012**, *3*, 2330-2339.

(23) a) Tsui, E. Y.; Tran, R.; Yano, J.; Agapie, T. Redox-inactive metals modulate the reduction potential in heterometallic manganese–oxido clusters. *Nat. Chem.* **2013**, *5*, 293-299. b) Tsui, E. Y.; Agapie, T. Reduction potentials of heterometallic manganese–oxido cubane complexes modulated by redox-inactive metals. *Proc. Nat. Acad. Sci. U.S.A.* **2013**, *110*, 10084-10088. c) Lin, P.-H.; Takase, M. K.; Agapie, T. Investigations of the Effect of the Non-Manganese Metal in Heterometallic-Oxido Cluster Models of the Oxygen Evolving Complex of Photosystem II: Lanthanides as Substitutes for Calcium. *Inorg. Chem.* **2015**, *54*, 59-64.

(24) Herbert, D. E.; Lionetti, D.; Rittle, J.; Agapie, T. Heterometallic Triiron-Oxo/Hydroxo Clusters: Effect of Redox-Inactive Metals. *J. Am. Chem. Soc.* **2013**, *135*, 19075-19078.

(25) 1. Dam, H. H.; Reinhoudt, D. N.; Verboom, W. Multicoordinate ligands for actinide/lanthanide separations. *Chem. Soc. Rev.* **2007**, *36*, 367-377.

(26) Van Staveren, C. J.; Van Eerden, J.; Van Veggel, F. C. J. M.; Harkema, S.; Reinhoudt, D. N. Cocomplexation of neutral guests and electrophilic metal cations in synthetic macrocyclic hosts. *J. Am. Chem. Soc.* **1988**, *110*, 4994-5008.

(27) a) Gokel, G. W.; Leevy, W. M.; Weber, M. E. Crown ethers: sensors for ions and molecular scaffolds for materials and biological models. *Chem. Rev.* **2004**, *104*, 2723-2750. b) Bradshaw, J. S.; Izatt, R. M. Crown ethers: the search for selective ion ligating agents. *Acc. Chem. Res.* **1997**, *30*, 338-345.

(28) Vigato, P. A.; Tamburini, S. The challenge of cyclic and acyclic schiff bases and related derivatives. *Coord. Chem. Rev.* **2004**, *248*, 1717-2128.

(29) Akine, S.; Utsuno, F.; Piao, S.; Orita, H.; Tsuzuki, S.; Nabeshima, T. Synthesis, ion recognition ability, and metal-assisted aggregation behavior of dinuclear metallohosts having a bis (saloph) macrocyclic ligand. *Inorg. Chem.* **2016**, *55*, 810-821.

(30) Nabeshima, T.; Yamamura, M., Cooperative formation and functions of multimetal supramolecular systems. *Pure Appl. Chem.* **2013**, *85*, 763-776.

(31) Kremer, C.; Lützen, A. Artificial allosteric receptors. *Chem. Eur. J.* **2013**, *19*, 6162-6196.

(32) Tamburini, S.; Vigato, P. A.; Gatos, M.; Bertolo, L.; Casellato, U. Molecular movements inside [1+1] asymmetric compartmental macrocycles: Formation of positional mononuclear and hetero-dinuclear lanthanide(III) isomers and related homo-dinuclear complexes. *Inorg. Chim. Acta* **2006**, *359*, 183-196.

(33) Tamburini, S.; Sitran, S.; Peruzzo, V.; Vigato, P. A. The Role of Functionalisation, Asymmetry and Shape of a New Macrocyclic Compartmental Ligand in the Formation of Mononuclear, Homo- and Heterodinuclear Lanthanide(III) Complexes. *Eur. J. Inorg. Chem.* **2009**, *2009*, 155-167.

(34) 1Reath, A. H.; Ziller, J. W.; Tsay, C.; Ryan, A. J.; Yang, J. Y. Redox Potential and Electronic Structure Effects of Proximal Nonredox Active Cations in Cobalt Schiff Base Complexes. *Inorg. Chem.*, **2017**, *56*, 3713-3718.

(35) Lionetti, D.; Day, V. W.; Blakemore, J. D. Noncovalent immobilization and surface characterization of lanthanide complexes on carbon electrodes. *Dalton Trans.* **2017,** *46*, 11779-11789.

(36) a) Gleizes, A.; Julve, M.; Kuzmina, N.; Alikhanyan, A.; Lloret, F.; Malkerova, I.; Sanz, J. L.; Senocq, F. Heterobimetallic *d—f* Metal Complexes as Potential Single-Source Precursors for MOCVD: Structure and Thermodynamic Study of the Sublimation of [Ni(salen)Ln(hfa)$_3$], Ln= Y, Gd. *Eur. J. Inorg. Chem.* **1998**, *1998*, 1169-1174. b) Sutter, J. P.; Dhers, S.; Costes, J. P.; Duhayon, C. Dissimilar supramolecular organization for the heterotrimetallic assemblage {LNiLn{W(CN)$_8$}] with Ln = Y and La (L = Schiff-base derivative). *C. R. Chim.* **2008**, *11*, 1200-1206. c) Maurice, R.; Vendier, L.; Costes, J. P. Magnetic anisotropy in Ni^{II}–Y^{III} binuclear complexes: on the importance of both the first coordination sphere of the Ni^{II} ion and the Y^{III} ion belonging to the second coordination sphere. *Inorg. Chem.* **2011**, *50*, 11075-11081. d) Colacio, E.; Ruiz, J.; Mota, A. J.; Palacios, M. A.; Cremades, E.; Ruiz, E.; White, F. J.; Brechin, E. K. Family of Carboxylate-and Nitrate-diphenoxo Triply Bridged Dinuclear $Ni^{II}Ln^{III}$ Complexes (Ln =

Eu, Gd, Tb, Ho, Er, Y): Synthesis, Experimental and Theoretical Magneto-Structural Studies, and Single-Molecule Magnet Behavior. *Inorg. Chem.* **2012**, *51*, 5857-5868. e) Cosquer, G.; Pointillart, F.; Le Guennic, B.; Le Gal, Y.; Golhen, S.; Cador, O.; Ouahab, L. 3d4f heterobimetallic dinuclear and tetranuclear complexes involving tetrathiafulvalene as ligands: X-ray structures and magnetic and photophysical investigations. *Inorg. Chem.* **2012**, *51*, 8488-8501.

(37) a) Koner, R.; Lin, H. H.; Wei, H. H.; Mohanta, S. Syntheses, Structures, and Magnetic Properties of Diphenoxo-Bridged $M^{II}Ln^{III}$ Complexes Derived from N, N‘-Ethylenebis (3-ethoxysalicylaldiimine) (M = Cu or Ni; Ln = Ce−Yb): Observation of Surprisingly Strong Exchange Interactions. *Inorg. Chem.* **2005**, *44*, 3524-3536. b) T. D. Pasatoiu, J.-P. Sutter, A. M. Madalan, F. Z. C. Fellah, C. Duhayon, M. Andruh, *Inorg. Chem.* **2011**, *50*, 5890-5898. c) Ding, L.; Jin, W.; Chu, Z.; Chen, L.; Lü, X.; Yuan, G.; Song, J.; Fan, D. Bao, F. Bulk solvent-free melt ring-opening polymerization (ROP) of L-lactide catalyzed by Ni(II) and Ni(II)–Ln(III) complexes based on the acyclic Salen-type Schiff-base ligand**.** *Inorg. Chem. Commun.* **2011**, *14*, 1274-1278. d) 1Cristóvão, B.; Kłak, J.; Miroslaw, B. Synthesis, crystal structures and magnetic behavior of Ni^{II}–4f–Ni^{II} compounds. *Polyhedron* **2012,** *43*, 47-54. e) Im, H. J.; Lee, S. W. Compartment compounds as secondary building units for the preparation of 3d–4f coordination polymers: Preparation, structures, and properties of [NiLn(L)$(NO_3)_2$(4-pyp)(EtOH)] (Ln = Nd, Eu; H_2L = 1,3-bis((3-methoxysalicylidene)amino)propane; 4-Hpyp = 4-pyridinepropionic acid). *Polyhedron* **2015**, *101*, 48-55. f) S. Y. Im, S. J. Park, H. J. Im, S. W. Lee, *Polyhedron* **2016**, *117*, 231-243.

(38) Perrin, D. D. *Ionisation Constants of Inorganic Acids and Bases in Aqueous Solution* (Pergamon, 1982).

(39) a) Crawford, S. M. The ultra-violet and visible spectra of some transition metal chelates with N,N'-bis-(*o*-hydroxybenzylidene)ethylenediamine and N,N'-bis-(*o*-hydroxybenzylidene)-*o*-phenylenediamine and related compounds. *Spectrochim. Acta* **1963**, *19*, 255-270. b) Di Bella, S.; Fragalà, I.; Ledoux, I.; Diaz-Garcia, M. A.; Marks, T.

J. Synthesis, characterization, optical spectroscopic, electronic structure, and second-order nonlinear optical (NLO) properties of a novel class of donor−acceptor bis (salicylaldiminato)nickel(II) Schiff base NLO chromophores. *J. Am. Chem. Soc.* **1997**, *119*, 9550-9557.

(40) Isse, A. A.; Gennaro, A.; Vianello, E. A study of the electrochemical reduction mechanism of Ni (salophen) in DMF. *Electrochim. Acta* **1992**, *37*, 113-118.

(41) J.-M. Saveant, *Elements of Molecular and Biomolecular Electrochemistry*, Wiley, Hoboken, NJ, 2006.

(42) a) Rounaghi, G.; Mohajeri, M.; Soruri, F.; Kakhki, R. M. Solvent influence upon complex formation between dibenzo-18-crown-6 with the Y^{3+} metal cation in pure and binary mixed organic solvents. *J. Chem. Eng. Data* **2011**, *56*, 2836-2840. b) Bünzli, J.-C. G.; Klein, B.; Wessner, D.; Schenk, K. J.; Chapuis, G.; Bombieri, G.; De Paoli, G. *Inorg. Chim. Acta* **1981**, *54*, L43-L46.

(43) a) Rogers, R. D.; Kurihara, L. K.; Voss, E. J., The f-element/crown ether complexes. 5. Structural changes in complexes of lanthanide chloride hydrates with 18-crown-6 accompanying decreases in Ln^{3+} ionic radii: synthesis and structures of $[M(OH_2)_7(OHMe)][MCl(OH_2)_2(18\text{-crown-6})]_2Cl_7 \bullet 2H_2O$ (M = yttrium, dysprosium). *Inorg. Chem.* **1987**, *26*, 2360-2365. b) Willey, G. R.; Lakin, M. T.; Alcock, N. W. Crown ether complexation of scandium(III), yttrium(III) and lanthanum(III) halides. Synthesis and spectroscopic characterisation of anhydrous cationic metal-oxacrown species and crystal structure of a scandium benzocrown. *J. Chem. Soc., Dalton Trans.* **1993**, 3407-3411.

(44) Sconyers, D. J.; Blakemore, J. D. Distinguishing between homogeneous and heterogeneous hydrogen-evolution catalysis with molecular cobalt complexes. *Chem. Commun.* **2017**, *53*, 7286-7289.

Chapter 3

Redox-Inactive Metal Cations Modulate the Reduction Potential of the Uranyl Ion in Macrocyclic Complexes

This chapter is adapted from a published manuscript:

Kumar, A.; Lionetti, D.; Day, V. W.; Blakemore, J. D. Redox-Inactive Metal Cations Modulate the Reduction Potential of the Uranyl Ion in Macrocyclic Complexes. *J. Am. Chem. Soc.* **2020**, *142*, 3032-3041.

3.1 Introduction

Nuclear fission of uranium is attractive for meeting current and future energy needs, in that this technology does not release significant amounts of carbon dioxide during routine use. However, separation and reprocessing of used nuclear fuels, aspects that are critical to the long-term viability of this technology, remain challenging due in part to difficulties associated with chemical transformation of various forms of uranium. Specifically, (re)processing of uranium requires cleavage of strong and chemically robust U–O bonds.[1,2,3] The U–O bonds in the water-soluble uranyl dication (UO_2^{2+}) are known to be especially strong ($\Delta H_{U=O,gas}$ = 148 kcal mol^{-1}), contributing to this species' persistence in the environment and its importance in model studies of U–O bond activation.[4]

In the field of UO_2^{2+} chemistry,[5] scattered reports suggest that Lewis acids can become involved in U–O activation. Arnold, Love, and co-workers, in the context of studying silylation of UO_2^{2+} by trimethylsilylamide in the presence of a strong reductant,[6] found that the desired U^V products were stabilized by a Lewis acid (Fe^{2+} or Zn^{2+}) present in a nearby binding site. Notably, U^V complexes could not be isolated without the addition of Fe^{2+} or Zn^{2+}, suggesting a key role for these metal cations. Complementary work from Hayton and co-workers and Arnold, Love, and co-workers have shown significant positive shifts in $E(U^{VI}/U^V)$ caused by functionalization of the oxo moieties with Lewis acidic electrophilic groups (e.g., SiR_3, $B(C_6F_5)_3$).[7,8,9,10] Mazzanti and co-workers have also measured a positive shift in $E(U^{VI}/U^V)$ upon association of UO_2^{2+} complexes with Fe^{2+}.[11] However, no quantitative studies of reduction potential tuning of $E(U^{VI}/U^V)$ for UO_2^{2+} or other redox processes in 5*f* species by Lewis acidic metal cations are available.

From the field of first-row transition metal chemistry, an effective strategy for rationally tuning the properties and reactivity of redox-active complexes involves placement of redox-inactive Lewis acidic metal cations in close proximity to the redox-active metals. This approach is inspired by the presence of an essential redox-inactive Ca^{2+} ion in the Oxygen-Evolving Complex (OEC) of Photosystem II, the enzyme responsible for biological O_2 evolution.[12,13] Agapie and co-workers' studies of related multimetallic clusters incorporating redox-inactive metals have revealed that the cluster reduction potentials vary linearly with the Lewis acidity of the incorporated redox-inactive ions across a broad range.[14,15] Thus, the requirement for the Ca^{2+} ion can at least in part be ascribed to tuning of the reduction potential(s) of the nearby redox-active manganese ions present in the OEC.

Related tuning effects have been obtained in artificial transition metal catalysts by the interaction of metal oxo moieties with Lewis acidic metal cations (e.g., Sc^{3+}).[16,17] These effects are broadly useful as shown by Nam and Fukuzumi[18,19] as well as Borovik.[20,21] Alternatively, heteroditopic ligand frameworks with well-defined sites for binding of both redox-active and redox-inactive metals can be used to study heterometallic effects.[22] Yang has used a convergent synthetic approach with such a strategy to assemble Co and Fe compounds.[23,24] This approach is reminiscent of work from Matsunaga and Shibasaki, in which they prepared diverse families of dinuclear Schiff base compounds for use as catalysts.[25] On the other hand, our group has used a divergent approach with a related scaffold to afford rapid access to various heterobimetallic complexes of Ni, including species featuring important trivalent Lewis acids.[26] Considering the lack of quantitative data on redox tuning of UO_2^{2+} by redox-inactive Lewis acids, we anticipated that the modularity of

our synthetic approach might enable preparation of new UO_2^{2+} complexes with a range of Lewis acids for new studies of redox tuning.

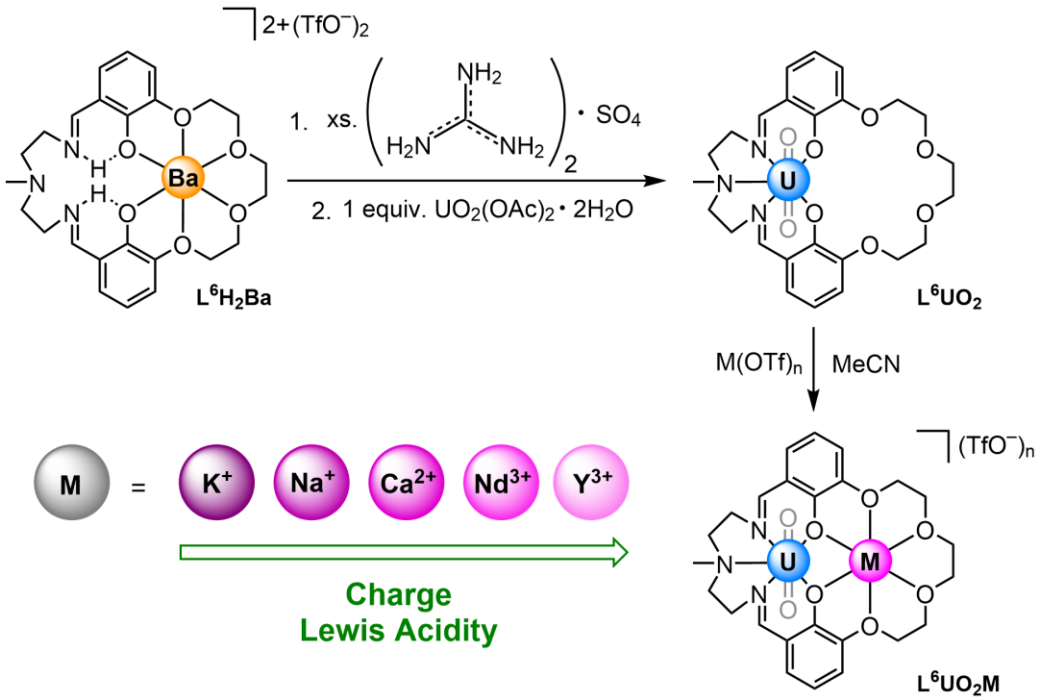

Scheme 3.1. Synthesis of heterobimetallic complexes of UO_2^{2+}.

Here, we report the divergent synthesis and study of macrocyclic heterobimetallic complexes of UO_2^{2+} with a range of redox-inactive Lewis acidic metal cations (namely, K^+, Na^+, Ca^{2+}, Nd^{3+}, and Y^{3+}). These redox-inactive metals span a wide range of Lewis acidity, as judged by the pK_a values of their corresponding metal aqua cations (pK_a = 16.0 for K^+, 8.3 for Y^{3+}).[27] Notably, the synthesized compounds (Scheme 3.1) are the first examples of structurally characterized heterobimetallic macrocyclic UO_2^{2+} complexes, and thus they complement analogous structures that feature bridging ligands but lack a stabilizing macrocyclic environment.[28,29,30] Spectroscopic and structural characterization in concert with electrochemical studies reveal that the compounds are stable in solution and that, as a result, the U^{VI}/U^{V} reduction potential can be rationally tuned in the complexes. This tuning

effect is engendered by the proximity of the UO_2^{2+} ion to the Lewis acids within the macrocyclic frameworks.

3.2 Results

3.2.1 Synthesis and characterization of the heterobimetallic species

Our heterobimetallic complexes are based upon a family of ditopic macrocycles developed by Reinhoudt[31,32] and elaborated upon by Vigato[33,34,35,36] that feature a Schiff-base binding site for UO_2^{2+} that is appended with a second crown-ether-like site for binding of redox-inactive metal cations. Our synthetic strategy (Scheme 3.1) centers on preparation of a common uranyl-containing macrocyclic compound **L^6UO_2** that can undergo divergent metalation with suitable reagents to install the redox-inactive metal cations. **L^6UO_2** was prepared from **L^6H_2Ba**, a previously known compound lacking prior structural characterization.[35] Single crystals of **L^6H_2Ba** suitable for X-ray diffraction (XRD) analysis were grown, confirming the presence of a pentadentate pocket (featuring one trialkylamine, two imine moieties, and two phenol groups) that is poised to bind UO_2^{2+} (Figure 3.1).

Indeed, the UO_2^{2+} complex **L^6UO_2** can be synthesized by stirring 1 equiv. of **L^6H_2Ba** with 10 equiv. of guanidinium sulfate in a biphasic water/chloroform system. Subsequent treatment of the organic layer with $UO_2(OAc)_2 \cdot 2H_2O$ affords **L^6UO_2** as a red solid.[35] As predicted from nuclear magnetic resonance (NMR) experiments (see Appendix B, Figure B5), single-crystal XRD analysis confirms the coordination of UO_2^{2+} in **L^6UO_2** to the pentadentate Schiff-base cavity of **L^6H_2** (Figure 3.1). The pentadentate site provides the desired L_3,X_2-type coordination environment, with the result that no further ligands are bound to the formally U^{VI} center beyond the two oxo groups and the macrocycle. This

situation leaves the adjacent crown ether-like cavity open and poised to bind Lewis acidic metals.

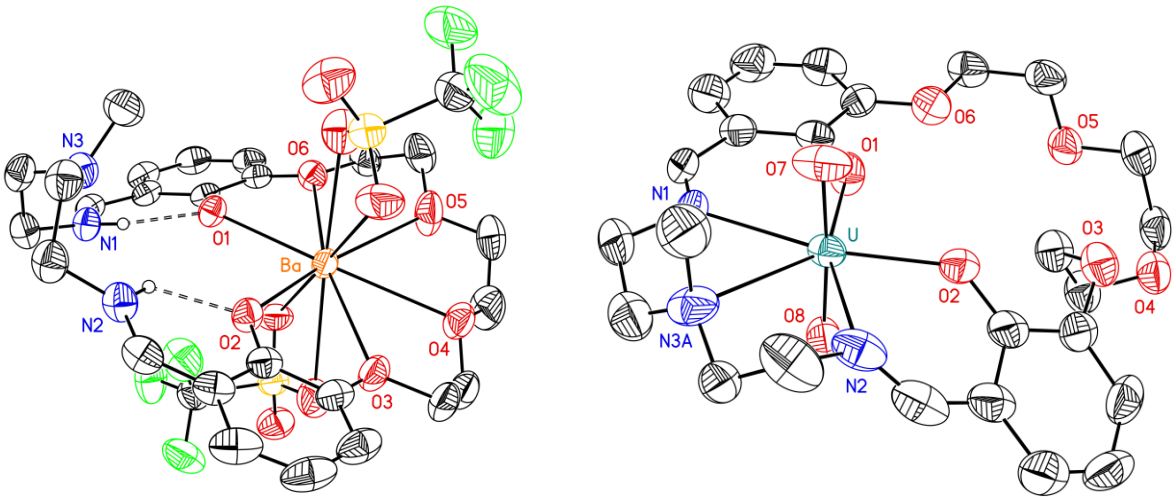

Figure 3.1. Solid-state structures (from XRD) of $\mathbf{L^6H_2Ba}$ (left) and $\mathbf{L^6UO_2}$ (right). Outer-sphere triflate counteranions and H-atoms, except those covalently bonded to N1 and N2, are omitted for clarity. Displacement ellipsoids are shown at the 50% probability level.

The heterobimetallic complexes of the form $\mathbf{L^6UO_2M}$ can be prepared by reaction of $\mathbf{L^6UO_2}$ with the corresponding metal triflate salts.[26] Specifically, treatment of $\mathbf{L^6UO_2}$ with triflate salts of K^+, Na^+, Ca^{2+}, Nd^{3+}, and Y^{3+} results in the generation of 1:1 heterobimetallic compounds with virtually quantitative yield in each case. ^{1}H NMR spectra (see Appendix B, Figures B6, B8, B10, B12, and B14) indicate that the redox-inactive metal ions are bound in the crown ether-like site of $\mathbf{L^6UO_2}$ and that the complexes are stable in CH_3CN solution (see Experimental Section for detailed synthetic procedures and full characterization). Notably, no evidence of scrambling of the metal ions between the two binding sites was observed, confirming the utility of the $\mathbf{L^6H_2}$ scaffold in divergent synthetic schemes relying on orthogonal metalation.

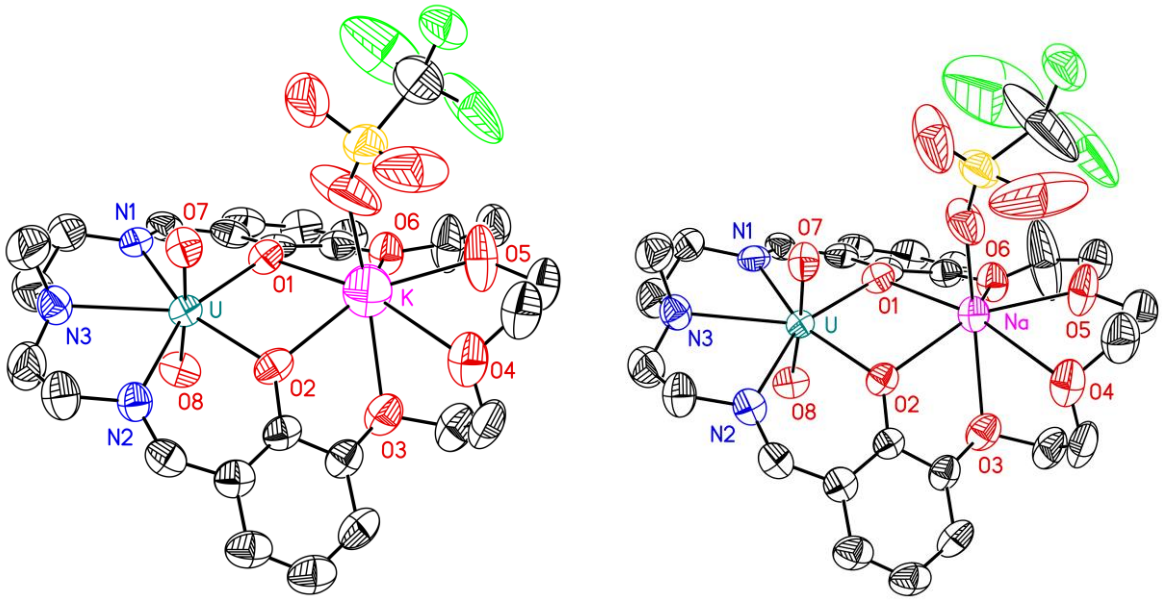

Figure 3.2. Solid-state structures (from XRD) of **L^{6}UO$_2$K** (left) and **L^{6}UO$_2$Na** (right). Outer-sphere triflate counteranions and all H-atoms are omitted for clarity. Displacement ellipsoids are shown at the 50% probability level.

3.2.2 X-ray diffraction studies

XRD analysis of single crystals of the heterobimetallic complexes containing K^+, Na^+, Ca^{2+}, and Y^{3+} confirms assembly of the desired $U^{VI}(\mu\text{-}O_{Ar})_2M^{n+}$ cores. The UO_2^{2+} moiety remains structurally intact in all the compounds, with $U–O_{oxo}$ distances in a tight range from 1.771(6) to 1.795(4) Å (see Table 3.1 for structural parameters). **L^{6}UO$_2$Na** and **L^{6}UO$_2$K** crystallize with isomorphous structures, confirming incorporation of the redox-inactive ions in the crown-ether cavity with coordination numbers (CN) of seven (Figure 3.2). XRD analysis of **L^{6}UO$_2$Ca** and **L^{6}UO$_2$Y** reveals a higher CN of nine for the redox-inactive ions in these compounds, consistent with the larger size of Ca^{2+} and Y^{3+} (Figure 3.3). In **L^{6}UO$_2$Ca**, the Ca^{2+} ion is ligated by six macrocyclic O-atoms, two MeOH ligands, and one κ^1 triflate. In **L^{6}UO$_2$Y**, Y^{3+} is ligated by six macrocyclic O-atoms, one bound CH_3CN ligand, and two κ^1 triflates. Thus, for both **L^{6}UO$_2$Ca** and **L^{6}UO$_2$Y**, one triflate counter-anion is

outer-sphere. This finding contrasts with our prior work (mentioned in Chapter 2) on analogous [Ni,Ca] and [Ni,Y] complexes, in which two and three triflate counter-anions, respectively, are coordinated to the redox-inactive metal rather than being found in the outer sphere.[26]

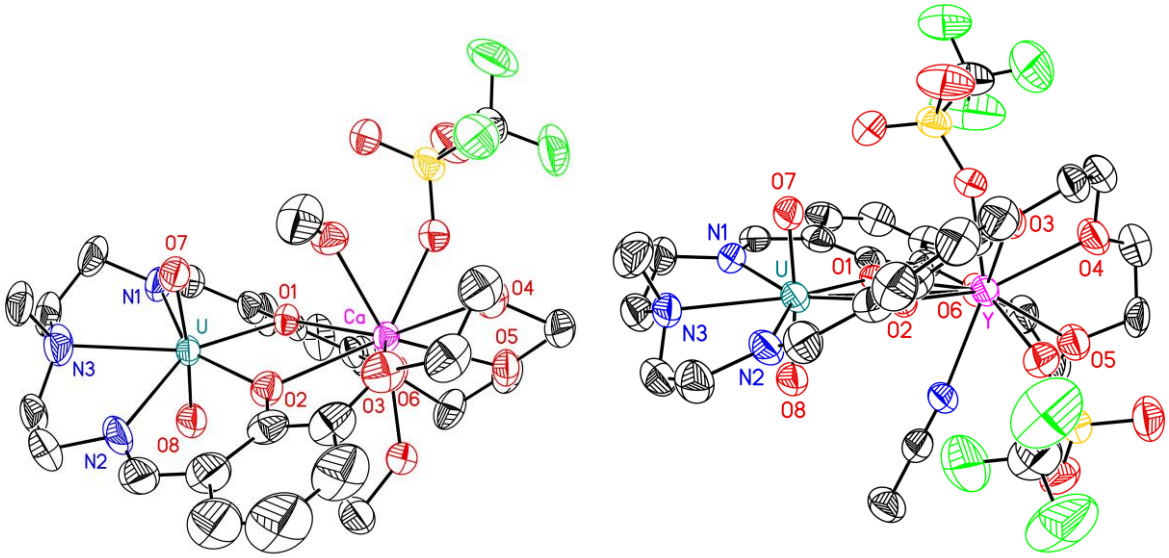

Figure 3.3. Solid-state structures (from XRD) of **L^{6}UO$_2$Ca** (left) and **L^{6}UO$_2$Y** (right). Outer-sphere triflate counteranions and all H-atoms are omitted for clarity. Displacement ellipsoids are shown at the 50% probability level.

The XRD data reveal that the macrocyclic structure is significantly deformed upon coordination of the Lewis acidic metals. Deformation of the crown-ether-like site across the family of compounds was quantified by comparing the root mean square deviation of the six macrocyclic O-atoms from the mean plane defined from the positions of those atoms (defined as ω_{crown}; see Appendix B and Table 3.1 for details). For the heterobimetallic compounds, ω_{crown} varies from 0.609 to 0.717 Å, a significant increase from the value of 0.358 measured for **L^{6}UO$_2$**. In part, the distortion in the bimetallic compounds may be ascribable to steric clash induced by the spatially demanding pentadentate site containing

the UO_2^{2+} moiety; this situation is reflected in low values for the related ω_{salben} parameter in all the uranyl-containing compounds. Consistent with this model, the ω_{crown} value for **L^6H_2Ba** (0.233) is significantly lower than that for **L^6UO_2** (Figure 3.1). Furthermore, the O1•••O2 distance is significantly compressed as the Lewis acidity of **M** increases, corresponding to a drawing together of these macrocyclic atoms upon coordination of the redox-inactive metals.

Table 3.1. Comparison of $[\mathbf{M}(H_2O)_m]^{n+}$ complex pK_a values, selected bond lengths, interatomic distances, and root mean square deviations (ω).

Complex	**L^6H_2Ba**	**L^6UO_2**	**L^6UO_2K**	**L^6UO_2Na**	**L^6UO_2Ca**	**L^6UO_2Y**
pK_a of $[M(H_2O)_m]^{n+}$	13.4	-	16.0	14.8	12.6	8.3
U–O7	-	1.783(8)	1.773(7)	1.782(5)	1.795(4)	1.771(6)
U–O8	-	1.792(7)	1.781(7)	1.780(5)	1.783(4)	1.788(7)
O1•••O2	3.641	3.137	2.994	2.973	2.948	2.778
U•••M	-	-	3.681(5)	3.668(3)	3.923(1)	3.884(1)
ω_{crown}[a]	0.233	0.358	0.715	0.717	0.609	0.671
ω_{salben}[b]	0.607	0.049	0.155	0.157	0.203	0.169
$\omega_{iminophenoxide}$[c]	0.021, 0.055	0.012, 0.050	0.047, 0.129	0.043, 0.126	0.085, 0.083	0.076, 0.121

(a) Defined as root mean square deviation (rmsd) of the following atoms from the mean plane of their positions: O1, O2, O3, O4, O5, and O6. (b) RMSD of O1, O2, N1, N2, and N3. (c) RMSD of N1, O6, C1, C2, C3, C4, C5, C6 and C7; N2, O3, C14, C15, C16, C17, C18, C19 and C20. Atom labels are consistent with those given in the raw crystallographic data (see Appendix B).

3.2.3 Electronic absorption spectroscopy

With these results in hand, we moved to interrogate the influence of redox-inactive metals on the electronic properties of the heterobimetallic complexes.

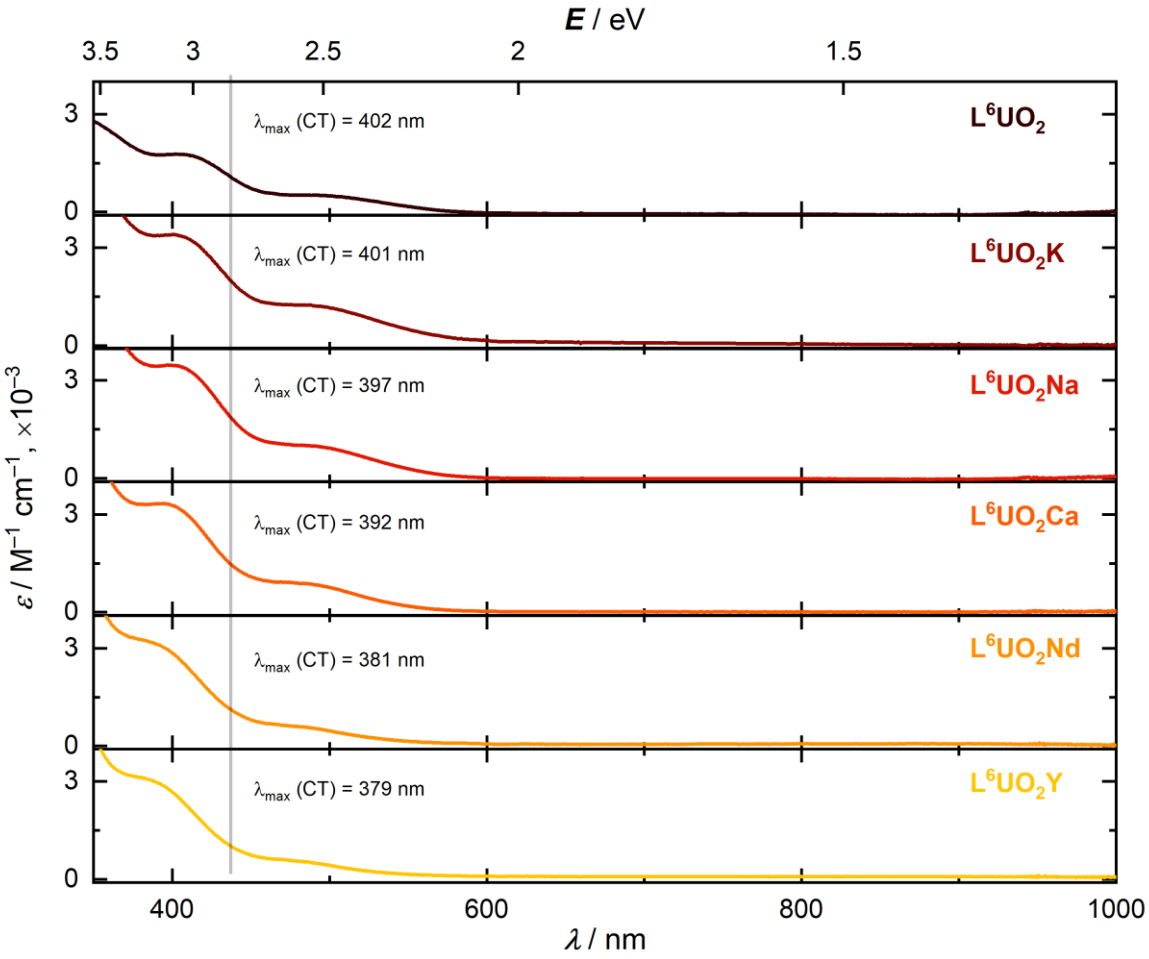

Figure 3.4. Stacked electronic absorption spectra of the **L^{6}UO$_2$** and **L^{6}UO$_2$M** complexes.

The electronic absorption spectrum of the parent **L^{6}UO$_2$** complex displays three charge-transfer (CT) bands that appear to involve the UO_2^{2+} moiety, on the basis of their molar absorptivities ($\varepsilon \approx 10^3$ M^{-1} cm^{-1}; see Figure 3.4). Two higher energy and higher absorptivity ($\varepsilon \approx 10^4$ M^{-1} cm^{-1}) bands are also present at $\lambda < 350$ nm; these are attributable to intraligand

π-to-π* transitions (see Appendix B, Figure B16). Upon Lewis acid binding and formation of the heterobimetallic complexes, the π-to-π* transitions undergo significant shifts (see Appendix B, Figure B23), consistent with direct interaction between the Lewis acids and the macrocyclic ligand framework.

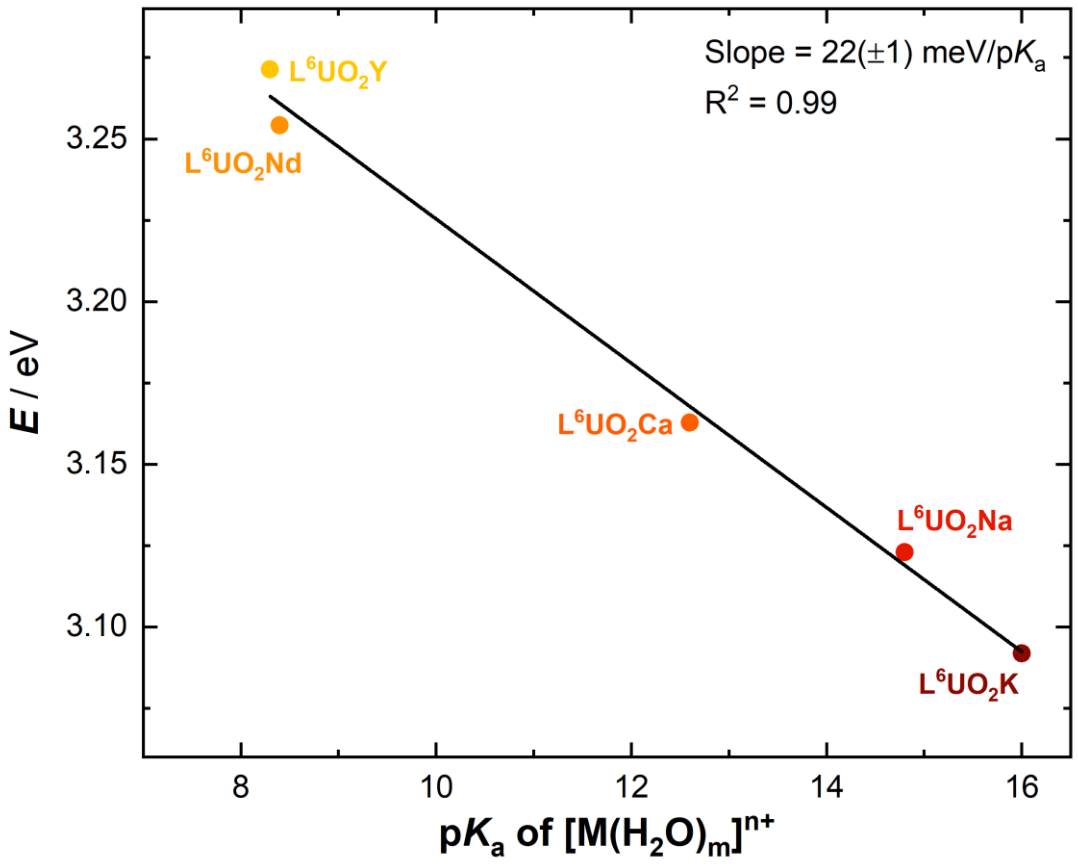

Figure 3.5. Dependence of the lowest-energy absorption band (CT energy) of the **L^6UO_2M** complexes on the Lewis acidity (pK_a) of the corresponding **M** aqua complexes.

Closer examination of the energy of the CT bands for the heterobimetallic compounds with λ_{max} near 400 nm (Figure 3.4; deconvoluted with Gaussian fitting, see Appendix B, Figure B18) as a function of the pK_a value of the incorporated Lewis acids reveals a linear trend with a slope of 22±1 meV/pK_a (Figure 3.5). Thus, Lewis acids appear to reliably tune the electronic properties of UO_2^{2+} complexes, a phenomenon not previously explored.

Trivalent redox-inactive cations engender the strongest perturbations while mono- and divalent cations offer more modest shifts. Notably, the distinctive dependence of the absorption maximum near 400 nm for the **L^{6}UO$_2$M** complexes on pK_a is reminiscent of a similar relationship measured for our series of heterobimetallic complexes of nickel.[26] In those compounds, we found a corresponding slope of 44±2 meV/pK_a (see Chapter 2) for a similar CT band assigned in those cases as ligand-to-metal in character. Interestingly, the changes in the electronic absorption spectra as a function of Lewis acidity appear more modest (by a factor of ca. 2) for the case of UO_2^{2+} versus Ni.

3.2.4 Electrochemistry

Having observed the apparent high stability of the heterobimetallic complexes in acetonitrile solutions, we were encouraged to investigate their electrochemical properties with cyclic voltammetry (CV) (Figure 3.6). Notably, electrochemical data has not been previously available for UO_2^{2+} held in close proximity to redox-inactive Lewis acids; this may be attributable to the poor stability of non-macrocyclic complexes of UO_2^{2+} containing other metals. To begin, CV data for **L^{6}UO$_2$** reveal a chemically reversible reduction at $E_{1/2}$ = –1.54 V vs. ferrocenium/ferrocene (denoted hereafter as $Fc^{+/0}$; see Appendix B and Figure B24 for further details). The measured peak-to-peak separation, ΔE_p, of 76 mV at a scan rate of 100 mV/s is consistent with reasonably fast electron transfer. According to the criteria elaborated by Zanello and Connelly,[37] including the findings that the ratio of anodic and cathodic peak currents is near unity ($i_{p,a}/i_{p,c} \approx 1$), the value of $E_{1/2}$ is independent of scan rate, and ΔE_p is relatively near to the ideal 57 mV (see Figure B26), this process can be considered electrochemically reversible. Furthermore, on the basis of studies of similar non-macrocyclic monometallic UO_2^{2+} complexes, this process can be reliably assigned to $U^{VI/V}$ redox

cycling.[38] As both the cathodic and anodic waves are linearly proportional to scan rate (see Appendix B, Figure B25), both the U^{VI} and U^{V} forms of **L^6UO_2** are confirmed as freely diffusing.[39]

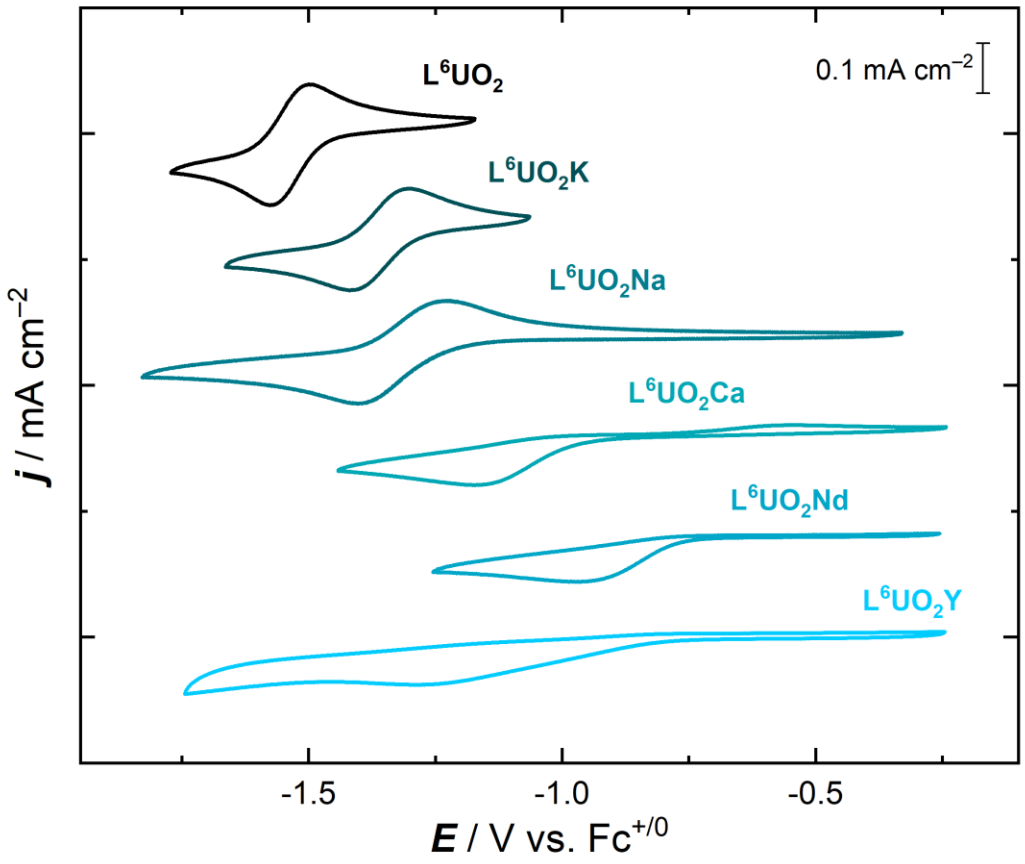

Figure 3.6. Cyclic voltammetry data for **L^6UO_2** and **L^6UO_2M** complexes (Conditions: 0.1 M $[^nBu_4N]^+[PF_6]^-$ in CH_3CN; scan rate: 100 mV/s; [U] = 1 mM).

The potentials required for the reduction of **L^6UO_2K** and **L^6UO_2Na**, –1.36 and –1.32 V vs. $Fc^{+/0,}$ respectively, are consistent with retention of the coordinated Lewis acids resulting in shift of the U^{VI}/U^{V} reduction potentials to more positive values. Scan rate-dependent studies reveal that both **L^6UO_2K** and **L^6UO_2Na** in both the U^{VI} and U^{V} states are freely diffusing (see Appendix B, Figures B28 and B30). However, the measured ΔE_p values at 100 mV/s are greater at 89 mV and 181 mV, respectively, indicating diminished

electrochemical reversibility and lower rates of electron transfer than that observed for **L^{6}UO$_2$**.[37] Finally, we note that greater stability during redox cycling is encountered for **L^{6}UO$_2$K** than **L^{6}UO$_2$Na** (see Appendix B, Figure B31). In particular, multiple cycling experiments (see Appendix B, Figures B31 and B32) suggest that electrode fouling occurs upon reduction of **L^{6}UO$_2$Na**, presumably attributable to chemical reactivity that follows the initial reduction; this theory is confirmed by experiments with polished or new electrodes (Figure B33). We anticipate the greater stability of the reduced form of **L^{6}UO$_2$K** is due to the better size match between 18-crown-6 moieties and K^+ (vs. Na^+).[40,41]

The noted trends continue for **L^{6}UO$_2$Ca**, which undergoes reduction with a peak cathodic potential ($E_{p,c}$) shifted to a more positive value of –1.18 V vs. $Fc^{+/0}$. The calcium complex behaves with yet poorer apparent electrochemical reversibility, displaying a quite large ΔE_p of 641 mV (see Appendix B, Figure B34). CV data for **L^{6}UO$_2$Nd** reveal fully irreversible behavior, with only a single reduction observed with $E_{p,c}$ = –0.98 V that is consistent with a freely diffusing compound retaining the coordinated Nd^{3+} ion (see Appendix B, Figure B37). Finally, freely diffusing **L^{6}UO$_2$Y** undergoes reduction at a more negative value of $E_{p,c}$ = –1.29 V (see Appendix B, Figure B39). The voltammetric response for this compound, however, is quite broad and thus consistent with markedly slowed electron transfer which complicates direct comparison of $E_{p,c}$ values with the other compounds in the series.

For the cases of **L^{6}UO$_2$** and **L^{6}UO$_2$K**, one-electron reduction of the starting compounds to form [U^V] species was confirmed through spectroelectrochemistry with UV-visible detection (see Appendix B, Figures B44–B47 for data). Spectral changes in the range of 400 nm were observed upon reduction of both compounds, consistent with results from prior studies38 showing generation of [U^V] species. For **L^{6}UO$_2$**, isosbestic points corresponding

to generation of a single [U^V] species were measured over 5 minutes at 357 and 413 nm. Similarly, spectra of **L^6UO_2K** revealed isosbestic points at 355 and 415 nm. However, a unique new feature was also observed at 650 nm upon reduction of **L^6UO_2K** suggesting influence of K^+ on the nascent [U^V] product. Additional minor spectral changes were observed with **L^6UO_2K** over ca. 30 min, suggesting additional speciation occurs at longer times in this system. This is consistent with a role for the Lewis acid in promoting new reactivity, and thus future efforts will include efforts to isolate and characterize the products of (electro)chemical reduction of the heterobimetallic compounds described here.

Regarding general trends in the binding strengths of Lewis acidic metal ions **M** with the 18-crown-6-like cavity of **L^6H_2**, we find that the more Lewis acidic ion Y^{3+} can displace both K^+ and Ca^{2+} (see Appendix B, Figures B41 and B42). Thus, although K^+ may be anticipated from supramolecular chemistry to have an ideal size match with the 18-crown-6 cavity, the greater Lewis acidity of Y^{3+} or Ca^{2+} (see Appendix B, Figure B43) prevents K^+ from displacing these ions from the crown. However, NMR studies do confirm that K^+ displaces Na^+ in 1:1 competition experiments, in line with the better size match between 18-crown-6 and K^+. This is also consistent with the similar Lewis acidities of K^+ and Na^+ (pK_a = 16 vs. 14.8, respectively).27

3.3 Discussion

In our previous work with heterobimetallic [Ni,M] complexes (see Chapter 2), we tabulated cathodic peak reduction potentials in order to quantify the influence of redox-inactive Lewis acids on Ni^{II}/Ni^{I} reduction processes.[26] Taking the same strategy here for the **L^6UO_2M** series, plotting $E_{p,c}$ for the U^{VI}/U^V reduction events versus the Lewis acid pK_a values reveals a slope of 61(±9) mV/pK_a (Figure 3.7). Data for Y^{3+} has been excluded from

this analysis due to the obvious slow electron transfer encountered with **L^{6}UO$_2$Y**, a phenomenon complicating understanding of the thermodynamic influence of Lewis acids on these systems. The trend for $E_{p,c}$ reveals that there is a clear and uniform trend of modulated reduction potential upon incorporation of Lewis acidic metals into macrocyclic UO_2^{2+} complexes. Similar to transition metal systems, trivalent Lewis acids result in the most pronounced shift in $E_{p,c}$.

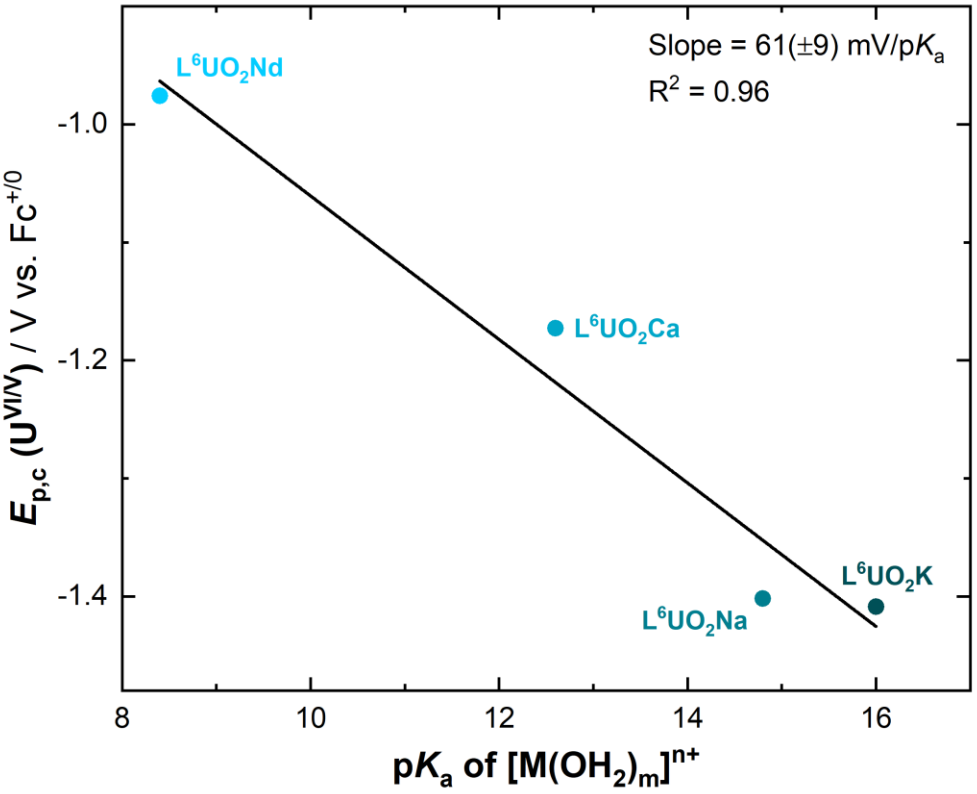

Figure 3.7. Plot of $E_{p,c}(U^{VI/V})$ vs. pK_a of $[\mathbf{M}(H_2O)_m]^{n+}$.

The shift of $E_{p,c}$ for the series of **L^{6}UO$_2$M** complexes is comparable to that measured for our prior [Ni,M] complexes (see Chapter 2) of 67(±9) mV/pK_a both in magnitude and estimated variance (15% vs. 17%, respectively). This suggests that the mechanism underlying tuning of actinyl ions' properties by Lewis acids may bear significant similarities

to that operating with first-row transition metals. However, both our series of heterobimetallic compounds rely on phenolates that bridge between the redox-active U and Ni and the redox-inactive metals **M**. Thus, one contributor to the observed similar trends in redox behavior may be the common Lewis acid-driven tuning of the bridging ligands. On the other hand, 3*d* and 5*f* metals can be expected to experience different degrees of covalency in their coordination chemistry, suggesting that further investigation of these effects could be an appealing new strategy for study of metal-ligand covalency in the challenging 5*f* elements. In any case, studies of these new effects could shed light on both the mechanism of Lewis acid tuning and changes that result in terms of structure and bonding (e.g., U–O bond order).

In addition to the uniform trend in $E_{p,c}$ observed for these heterobimetallic compounds, it is notable that the more Lewis acidic metals engender greater irreversibility to the reductive electrochemistry of the U^{VI}/U^{V} process. To investigate this phenomenon further, the heterogeneous electron-transfer rate constants were calculated for the heterobimetallic compounds that display both anodic and cathodic waves associated with the U^{VI}/U^{V} redox system, namely **L^6UO_2K**, **L^6UO_2Na**, **and L^6UO_2Ca**. This was accomplished through the use of a standard working curve that allows conversion of the measured ΔE_p values to k^0.[42,43] Carrying out this calculation reveals that the k^0 values are 2.3, 0.7, and 0.029 x 10^{-3} cm s^{-1}, respectively. The wide span of values is intriguing, considering the compounds share the common supporting macrocyclic ligand **L^6H_2**. Even more intriguing, a plot of log k^0 vs. pK_a of $[\mathbf{M}(H_2O)_m]^{n+}$ reveals an essentially linear relationship (Figure 3.8). Consequently, we conclude that Lewis acidity governs not only the thermodynamics ($E_{1/2}$ value) of uranyl

reduction in macrocyclic bimetallic complexes, but also strongly influences the kinetics (k^0) of uranyl reduction.

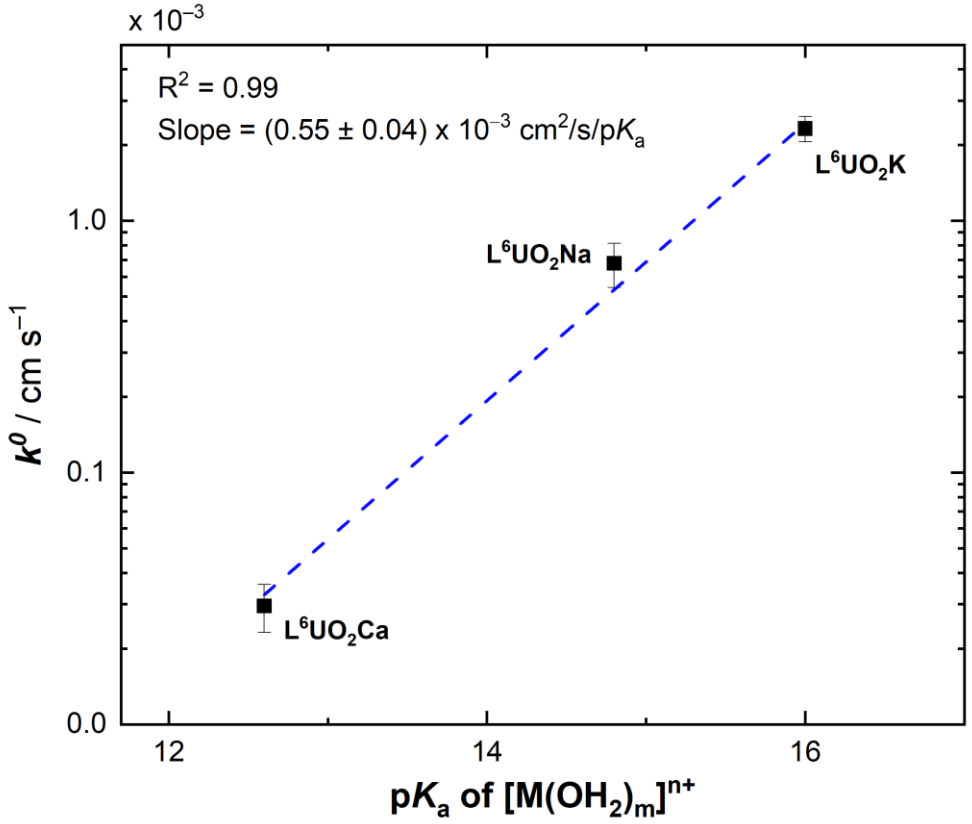

Figure 3.8. Plot of k^0 vs. pK_a of [**M**$(H_2O)_m]^{n+}$. R^2 for the linear fit is 0.99.

At this stage, we hypothesize that increasingly significant structural changes occur upon reduction of the adducts containing more Lewis acidic ions, resulting in greater reorganization upon reduction and thus the more irreversible behavior and attenuated values of k^0. Considering minor oxidative waves appear at rather positive potentials for each of the M = Ca^{2+}, Nd^{3+}, Y^{3+} adducts following reduction (see Appendix B, Figures B35, B37, and B39), these more robust Lewis acids appear to promote new chemical reactivity. As the subsequent re-oxidation features for Ca^{2+}, Nd^{3+}, and Y^{3+} adducts appear at similar potentials, the products of this new chemical reactivity may undergo dissociation of the redox-inactive

metals to yield similar compounds. More generally, the data could imply that there is a common intermediate generated by the follow-up chemical reactivity. In any case, heterobimetallic complexes of UO_2^{2+} appear to offer a new platform for studying redox processes with this challenging ion, including reductive routes relevant to nuclear waste remediation. Chemical and electrochemical studies aimed at leveraging such a strategy are presently underway.

3.4 Conclusions

Redox-inactive Lewis acidic metals have been shown to be effective in uniformly tuning the electronic properties and reduction potential of the UO_2^{2+} ion in macrocyclic complexes. These findings have been enabled by synthesis of the first series of structurally characterized, macrocyclic, heterobimetallic actinide compounds. Similar to the case of model transition metal compounds, we find a shift in reduction potential of 61(±9) mV/pK_a for heterobimetallic compounds that feature redox-inactive metals that span a range in Lewis acidity from 16.0 (K^+) to 8.3 (Y^{3+}). Incorporation of the strongly Lewis acidic trivalent ion Nd^{3+} (pK_a = 8.4) results in a significant shift of $E_{p,c}(U^{VI}/U^{V})$ to a potential that is 560 mV more positive than the corresponding monometallic precursor. These wide-ranging shifts differ from comparisons of electronic spectroscopic data, which indicate an attenuated influence of the Lewis acids in the case of the UO_2^{2+} compounds studied here. Electrochemical studies also suggest diminished electron transfer rates and thus implicate greater chemical reorganization upon reduction in systems featuring the more acidic di- and trivalent redox-inactive ions. Taken together, these findings reveal the scope of tuning possible with actinides by redox-inactive metals for the first time.

3.5 Experimental Details

3.5.1 General Considerations

All manipulations were carried out in dry N_2-filled gloveboxes (Vacuum Atmospheres Co., Hawthorne, CA) or under N_2 atmosphere using standard Schlenk techniques unless otherwise noted. All solvents were of commercial grade and dried over activated alumina using a PPT Glass Contour (Nashua, NH) solvent purification system prior to use, and were stored over molecular sieves. All chemicals were from major commercial suppliers and used as received or after extensive drying. 2,3-dihydroxybenzaldehyde was sublimed in vacuo before use. CD_3CN was purchased from Cambridge Isotope Laboratories and dried over 3 Å molecular sieves. ^1H, ^{13}C, and ^{19}F NMR spectra were collected on 400 and 500 MHz Bruker spectrometers and referenced to the residual protio-solvent signal[44] in the case of ^1H and ^{13}C. ^{19}F NMR spectra were referenced and reported relative to CCl_3F as an external standard following the recommended scale based on ratios of absolute frequencies (Ξ).[45,46] Chemical shifts (δ) are reported in units of ppm and coupling constants (J) are reported in Hz. NMR spectra are given in Appendix B (Figures B1 to B15). Electronic absorption spectra were collected with an Ocean Optics Flame spectrometer, in a 1-cm path length quartz cuvette.

Regarding special safety precautions needed for this work, depleted uranium is a weak alpha-particle emitter; all manipulations of U-containing materials should be carried out in a laboratory equipped with appropriate radiation safety protocols.

3.5.2 Electrochemical Methods

Electrochemical experiments were carried out in a N_2-filled glovebox in dry, degassed CH_3CN. 0.10 M tetra(n-butylammonium) hexafluorophosphate ($[^nBu_4N]^+[PF_6]^-$); Sigma-Aldrich, electrochemical grade) served as the supporting electrolyte. Measurements were made with a Gamry Reference 600+ Potentiostat/Galvanostat using a standard three-electrode configuration. The working electrode was the basal plane of highly oriented pyrolytic graphite (HOPG) (GraphiteStore.com, Buffalo Grove, Ill.; surface area: 0.09 cm^2), the counter electrode was a platinum wire (Kurt J. Lesker, Jefferson Hills, PA; 99.99%, 0.5 mm diameter), and a silver wire immersed in electrolyte served as a pseudoreference electrode (CH Instruments). The reference was separated from the working solution by a Vycor frit (Bioanalytical Systems, Inc.). Ferrocene (Sigma Aldrich; twice-sublimed) was added to the electrolyte solution prior to the beginning of each experiment; the midpoint potential of the ferrocenium/ferrocene couple (denoted as $Fc^{+/0}$) served as an external standard for comparison of the recorded potentials. The average peak-to-peak potential (ΔE_p) for $Fc^{+/0}$ across the experiments reported in this work was 91(±19) mV. Concentrations of analyte for cyclic voltammetry were ca. 0.1 to 1 mM unless otherwise noted.

Spectroelectrochemisty was carried out in the same glovebox as described above (N_2 atmosphere), with 0.10 M $[^nBu_4N]^+[PF_6]^-$ in CH_3CN electrolyte for $\mathbf{L^6UO_2K}$ and 0.10 M $[^nBu_4N]^+[PF_6]^-$ in DMF electrolyte for $\mathbf{L^6UO_2}$. A thin layer quartz cell was used with a Teflon cap for housing the electrodes (ALS Co., Ltd., path length: 1.0 mm). The working electrode was a platinum mesh/flag electrode covered with a PTFE shrink tube up to the flag, and the counter and reference electrodes were both platinum wires (ALS Co., Ltd.).

3.5.3 Synthesis and characterization

Synthesis of 3,3'-(3,6-Dioxaoctane-1,8-diyldioxy)bis(2-hydroxybenzaldehyde). Under an inert atmosphere of nitrogen, a dry Schlenk flask was loaded with 2,3-dihydroxybenzaldehyde (3.0 g, 21.7 mmol) dissolved in 10 mL of dry THF. This solution was transferred using a syringe to a suspension of NaH (1.15 g, 47.8 mmol) in 10 mL of dry THF under N_2 over a period of 2 hours. The temperature was kept below 25°C. The color change to bright yellow indicates the formation of the disodium salt of 2,3-dihydroxybenzaldehyde. The ice bath was removed after addition and the mixture was stirred for 1 hour at room temperature. Under a positive flow of N_2, triethylene glycol ditosylate (5.0 g, 10.9 mmol) dissolved in 30 mL of dry THF was added to the yellow mixture in a single aliquot using a syringe. The resulting mixture was then stirred for 60 hours under a static N_2 atmosphere. Addition of 100 mL of water resulted in a dark brown solution that was extracted twice with $CHCl_3$. The aqueous layer was treated with 6 M HCl until the pH of the mixture was 1. This mixture was then extracted with three portions of $CHCl_3$. The combined organic layers were washed with 1 M HCl and dried over anhydrous $MgSO_4$. Evaporation of the solvent yielded a pale-yellow solid, which was used without any further purification. Yield: 93% (4.0 g). Spectroscopic characterization by ^{1}H NMR (see Appendix B, Figure B1) confirms the expected structure in agreement with a prior literature report.[32]

Synthesis of L^6H_2Ba. To a three-necked flask, $Ba(OTf)_2$ (4.46 g, 10.2 mmol) dissolved in 1 L of CH_3OH (0.01 M) and 1 equiv. of 3,3'-(3,6-Dioxaoctane-1,8-diyldioxy)bis(2-hydroxybenzaldehyde) (4.0 g, 10.2 mmol) in 100 mL THF (0.1 M) were added slowly under reflux. 1 equiv. of N-Methyl-2,2'-diaminodiethylamine (1.2 g, 10.2 mmol) in 100 mL CH_3OH (0.1 M) was added dropwise over a period of 6 hours. The reaction mixture was

refluxed for 30 minutes. After cooling down to room temperature, the resulting yellow-colored solution was evaporated on the rotary evaporator and Schlenk line and washed with diethyl ether to give a yellow crystalline solid. Crystals suitable for X-ray diffraction were obtained by vapor diffusion of diethyl ether into a solution of **L^6H_2Ba** in CH_3CN.

L^6H_2Ba. Yield: 95%. ^{1}H NMR (400 MHz, CD_3CN) δ (ppm): 13.60 (bs, 2H), 8.30 (s, 1H), 8.27 (s, 1H), 6.96 – 6.89 (m, 4H), 6.46 (t, $^3J_{H,H}$ = 7.9 Hz), 4.20 – 4.16 (m, 4H), 3.98 – 4.02 (m, 4H), 3.84 (s, 4H), 3.69 – 3.63 (m, 4H), 2.78 – 2.73 (m, 4H), 2.37 (s, 3H). ^{19}F NMR (376 Hz, CD_3CN) δ –80.12. $^{13}C\{^1H\}$ NMR (126 MHz, CD_3CN) δ (ppm): 168.34, 151.96, 127.02, 123.16, 120.61, 116.12, 114.64, 113.65, 70.95, 70.13, 67.53, 59.09, 51.21, 44.56.

Elemental analysis for **L^6H_2Ba** was performed by Midwest Microlab, Inc. (Indianapolis, IN). Anal. Calcd. for $C_{27}H_{33}N_3O_{12}F_6S_2Ba$ (**L^6H_2Ba**): C 35.75, H 3.67, N 4.63; Found: C 35.81, H 3.74, N 4.39.

Synthesis of L^6UO_2. An excess of guanidinium sulfate (1.76 g, 8.16 mmol) dissolved in water was added to a suspension of **L^6H_2Ba** (370 mg, 0.41 mmol) in $CHCl_3$ under stirring until the organic layer was clear. The organic layer was separated, concentrated, and diluted using MeOH. To this yellow solution, 1 equiv. of $UO_2(OAc)_2$•$2H_2O$ dissolved in MeOH was added, and the mixture was stirred overnight. The resulting red precipitate was filtered and washed with cold MeOH. Crystals suitable for X-ray diffraction were obtained by vapor diffusion of diethyl ether into a DMF solution of **L^6UO_2**. Spectroscopic characterization by ^{1}H NMR confirmed the expected structure in agreement with a prior literature report.[35]

L^6UO_2. Yield: 50%. ^{1}H NMR (500 MHz, CD_3CN) δ (ppm): 9.56 (s, 2H), 7.30 (d, $^3J_{H,H}$ = 7.8 Hz, 2H), 7.24 (d, $^3J_{H,H}$ = 7.8 Hz, 2H), 6.71 (t, $^3J_{H,H}$ = 7.9 Hz, 2H), 5.02 (t, $^3J_{H,H}$ = 14.0

Hz, 2H), 4.62 – 4.58 (m, 2H), 4.41 (t, $^{3}J_{H,H}$ = 4.1 Hz, 4H), 4.11 – 3.97 (m, 4H), 3.95 – 3.87 (m, 2H), 3.84 (s, 4H), 3.65 – 3.57 (m, 2H), 3.22 (s, 3H). Anal. Calcd. for $C_{25}H_{31}N_3O_8U$ (**L^6UO_2**): C 40.60, H 4.23, N 5.68; Found: C 35.17, H 3.32, N 3.81. Cyclic Voltammetry (0.1 M $[^nBu_4N]^+[PF_6]^-$ in CH_3CN): $E_{1/2}$ = –1.54 V vs. $Fc^{+/0}$. Electronic absorption spectrum in CH_3CN (M^{-1} cm^{-1}): 243 (11500), 272 (7300), 337 (3000), 402 (1800), 482 (514) nm.

Synthesis of L^6UO_2M complexes. Under an inert atmosphere, a heterogeneous solution of **L^6UO_2** in CH_3CN was added to 1 equiv. of corresponding metal salt solution in CH_3CN and stirred overnight. The color change depends on the identity of the metal triflate salt used; the product color ranges from pale red to orange to yellow as a function of increasing Lewis acidity. The solvent was removed in vacuo to give the desired product. Yields were typically in the range of 85-95%. Crystals suitable for X-ray diffraction were obtained by vapor diffusion of diethyl ether into a CH_3CN solution of the **L^6UO_2M** complexes for **L^6UO_2K,** **L^6UO_2Na,** and **L^6UO_2Y**. Crystals of **L^6UO_2Ca** suitable for X-ray diffraction were obtained by vapor diffusion of diethyl ether into a CH_3OH solution stored outside the glovebox.

Elemental analyses for **L^6UO_2** and the **L^6UO_2M** complexes were performed by the UC Berkeley Microanalytical Facility (Berkeley, CA). Due to limitations in sample handling procedures for these acutely moisture-sensitive compounds, satisfactory analysis (±0.4%) could not be obtained for four of the five new heterobimetallic compounds reported here and **L^6UO_2**. Satisfactory analysis was obtained for **L^6UO_2Nd.**

L^6UO_2K. Yield: 94%. ^{1}H NMR (500 MHz, CD_3CN) δ (ppm): 9.60 (s, 2H), 7.54 (d, $^{3}J_{H,H}$ = 8.0 Hz, 2H), 7.49 (d, $^{3}J_{H,H}$ = 8.0 Hz, 2H), 7.11 (t, $^{3}J_{H,H}$ = 8.0 Hz, 2H), 5.17 – 5.07 (m, 2H), 4.86 – 4.74 (m, 6H), 4.42 (t, $^{3}J_{H,H}$ = 4.5 Hz, 4H), 4.35 (s, 4H), 4.10 – 4.01 (m, 2H), 3.96 – 3.86 (m, 2H), 3.40 (s, 3H). ^{19}F NMR (376 Hz, CD_3CN) δ –79.28. Anal. Calcd. for

$C_{26}H_{31}F_3KN_3O_{11}SU$ (**L^6UO_2K**): C 33.66, H 3.37, N 4.53; Found: C 29.02, H 3.60, N 2.97. Cyclic Voltammetry (0.1 M $[^nBu_4N]^+[PF_6]^-$ in CH_3CN): $E_{1/2}$ = –1.36 V vs. $Fc^{+/0}$. Electronic absorption spectrum in CH_3CN (M^{-1} cm^{-1}): 246 (13900), 272 (12100), 329 (6200), 401 (1800), 478 (1200) nm.

L^6UO_2Na. Yield: 89%. ^{1}H NMR (500 MHz, CD_3CN) δ (ppm): 9.53 (s, 2H), 7.40 (d, $^3J_{H,H}$ = 7.8 Hz, 2H), 7.30 (d, $^3J_{H,H}$ = 7.8 Hz, 2H), 6.95 (t, $^3J_{H,H}$ = 7.8 Hz, 2H), 5.10 – 5.00 (m, 2H), 4.66 – 4.58 (m, 2H), 4.43 – 4.38 (m, 4H), 3.95 – 3.91 (m, 4H), 3.84 – 3.80 (m, 6H), 3.72 – 3.69 (m, 2H), 3.27 (s, 3H). ^{19}F NMR (376 Hz, CD_3CN) δ –80.19. Anal. Calcd. for $C_{26}H_{31}F_3NaN_3O_{11}SU$ (**L^6UO_2Na**): C 34.26, H 3.43, N 4.61; Found: C 35.95, H 3.54, N 4.74. Cyclic Voltammetry (0.1 M $[^nBu_4N]^+[PF_6]^-$ in CH_3CN): $E_{1/2}$ = –1.32 V vs. $Fc^{+/0}$. Electronic absorption spectrum in CH_3CN (M^{-1} cm^{-1}): 247 (12700), 272 (13100), 329 (6900), 397 (3500), 483 (1000) nm.

L^6UO_2Ca. Yield: 90%. ^{1}H NMR (500 MHz, CD_3CN) δ (ppm): 9.56 (s, 2H), 7.47 (d, $^3J_{H,H}$ = 7.8 Hz, 2H), 7.40 (d, $^3J_{H,H}$ = 7.8 Hz, 2H), 6.81 (t, $^3J_{H,H}$ = 7.8 Hz, 2H), 5.13 – 5.04 (m, 2H), 4.75 – 4.66 (m, 2H), 4.53 (t, $^3J_{H,H}$ = 4.4 Hz, 4H), 4.12 (t, $^3J_{H,H}$ = 4.4 Hz, 4H), 4.03 – 3.95 (m, 6H), 3.82 – 3.76 (m, 2H), 3.33 (s, 3H). ^{19}F NMR (376 Hz, CD_3CN) δ –80.16. Anal. Calcd. for $C_{27}H_{31}CaF_6N_3O_{14}S_2U$ (**L^6UO_2Ca**): C 30.09, H 2.90, N 3.90; Found: C 26.81, H 2.09, N 2.36. Cyclic Voltammetry (0.1 M $[^nBu_4N]^+[PF_6]^-$ in CH_3CN): $E_{p,c}$ = –1.17 V vs. $Fc^{+/0}$. Electronic absorption spectrum in CH_3CN (M^{-1} cm^{-1}): 243 (13300), 272 (12800), 314 (8400), 392 (3300), 473 (900) nm.

L^6UO_2Y. Yield: 87%. ^{1}H NMR (500 MHz, CD_3CN) δ (ppm): 9.56 (t, 2H), 7.38 – 7.34 (dd, $^3J_{H,H}$ = 8.0 Hz, $^4J_{H,H}$ = 1.3 Hz, 2H), 7.28 – 7.24 (dd, $^3J_{H,H}$ = 8.0 Hz, $^4J_{H,H}$ = 1.3 Hz, 2H), 6.78 (t, $^3J_{H,H}$ = 7.9 Hz, 2H), 5.06 – 4.98 (m, 2H), 4.64 – 4.57 (m, 2H), 4.40 – 4.32 (m, 4H),

3.98 (t, $^{3}J_{H,H}$ = 4.3 Hz, 4H), 3.92 – 3.85 (m, 2H), 3.84 (s, 4H), 3.69 – 3.64 (m, 2H), 3.22 (s, 3H). ^{19}F NMR (376 Hz, CD_3CN) δ –79.40. Anal. Calcd. for $C_{30}H_{34}F_9N_4O_{17}S_3UY$ (**L^6UO_2Y** + CH_3CN): C 27.37, H 2.60, N 4.26; Found: C 24.89, H 2.07, N 2.88. Cyclic Voltammetry (0.1 M $[^nBu_4N]^+[PF_6]^-$ in CH_3CN): $E_{p,c}$ = –1.29 V vs. $Fc^{+/0}$. Electronic absorption spectrum in CH_3CN (M^{-1} cm^{-1}): 240 (11500), 272 (12100), 322 (6700), 379 (3100), 470 (600) nm.

L^6UO_2Nd. Yield: 91%. ^{1}H NMR (500 MHz, CD_3CN) δ (ppm): 11.01, 10.29, 9.39, 8.30, 7.86, 5.87, 5.55, 4.74, 4.45, 3.95, 3.42, 2.45. ^{19}F NMR (376 Hz, CD_3CN) δ –79.80. Anal. Calcd. for $C_{28}H_{31}F_9N_3NdO_{17}S_3U$ (**L^6UO_2Nd**): C 25.27, H 2.35, N 3.16; Found: C 25.17, H 2.21, N 3.05. Cyclic Voltammetry (0.1 M $[^nBu_4N]^+[PF_6]^-$ in CH_3CN): $E_{p,c}$ = –0.98 V vs. $Fc^{+/0}$. Electronic absorption spectrum in CH_3CN (M^{-1} cm^{-1}): 242 (11700), 272 (12400), 322 (7200), 381 (3300), 477 (600) nm.

3.6 Acknowledgements

The authors thank Dr. Justin Douglas and Sarah Neuenswander for assistance with NMR spectroscopy, and Michael Lemon and Alice Dale for assistance with radiation safety protocols. The work in this chapter was supported by the US Department of Energy, Office of Science, Office of Basic Energy Sciences through the Early Career Research Program (DE-SC0019169). The authors also acknowledge the US National Institutes of Health for support of the NMR instrumentation (S10OD016360 and S10RR024664) used in this study.

3.7 References

(1) Marçalo, J.; Gibson, J. K. Gas-Phase Energetics of Actinide Oxides: An Assessment of Neutral and Cationic Monoxides and Dioxides from Thorium to Curium. *J. Phys. Chem. A* **2009**, *113*, 12599-12606.

(2) Neidig, M. L.; Clark, D. L.; Martin, R. L. Covalency in *f*-element complexes. *Coord. Chem. Rev.* **2013**, *257*, 394-406.

(3) Kaltsoyannis, N.; Scott, P. *The f elements*. Oxford University Press Inc.: New York, 1999; p. 36.

(4) Meinrath, G. Coordination of uranyl(VI) carbonate species in aqueous solutions. *J. Radioanal and Nuclear Chem.* **1996**, *211*, 349-362.

(5) Cowie, B. E.; Purkis, J. M.; Austin, J.; Love, J. B.; Arnold, P. L. Thermal and Photochemical Reduction and Functionalization Chemistry of the Uranyl Dication, $[U^{VI}O_2]^{2+}$. *Chem. Rev.* **2019**, *119*, 10595-10637.

(6) Arnold, P. L.; Patel, D.; Wilson, C.; Love, J. B. Reduction and selective oxo group silylation of the uranyl dication. *Nature* **2008**, *451*, 315.

(7) Schnaars, D. D.; Wu, G.; Hayton, T. W. Silylation of the Uranyl Ion Using B(C6F5)3-Activated Et3SiH. *Inorg. Chem.* **2011**, *50*, 9642-9649.

(8) Bell, N. L.; Shaw, B.; Arnold, P. L.; Love, J. B. Uranyl to Uranium(IV) Conversion through Manipulation of Axial and Equatorial Ligands. *J. Am. Chem. Soc.* **2018**, *140*, 3378-3384.

(9) Arnold, P. L.; Pécharman, A.-F.; Hollis, E.; Yahia, A.; Maron, L.; Parsons, S.; Love, J. B. Uranyl oxo activation and functionalization by metal cation coordination. *Nat. Chem.* **2010**, *2*, 1056.

(10) Zegke, M.; Nichol, G. S.; Arnold, P. L.; Love, J. B. Catalytic one-electron reduction of uranyl(VI) to Group 1 uranyl(V) complexes *via* Al(III) coordination. *Chem. Commun.* **2015**, *51*, 5876-5879.

(11) Faizova, R.; White, S.; Scopelliti, R.; Mazzanti, M. The effect of iron binding on uranyl(V) stability. *Chem. Sci.* **2018**, *9*, 7520-7527.

(12) McEvoy, J. P.; Brudvig, G. W. Water-Splitting Chemistry of Photosystem II. *Chem. Rev.* **2006**, *106*, 4455-4483.

(13) Yano, J.; Yachandra, V. Mn_4Ca Cluster in Photosynthesis: Where and How Water is Oxidized to Dioxygen. *Chem. Rev.* **2014**, *114*, 4175-4205.

(14) Kanady, J. S.; Tsui, E. Y.; Day, M. W.; Agapie, T. A Synthetic Model of the Mn3Ca Subsite of the Oxygen-Evolving Complex in Photosystem II. *Science* **2011**, *333*, 733-736.

(15) Tsui, E. Y.; Tran, R.; Yano, J.; Agapie, T. Redox-inactive metals modulate the reduction potential in heterometallic manganese–oxido clusters. *Nat. Chem.* **2013**, *5*, 293.

(16) Yiu, S.-M.; Man, W.-L.; Lau, T.-C. Efficient Catalytic Oxidation of Alkanes by Lewis Acid/$[Os^{VI}(N)Cl_4]^-$ Using Peroxides as Terminal Oxidants. Evidence for a Metal-Based Active Intermediate. *J. Am. Chem. Soc.* **2008**, *130*, 10821-10827.

(17) Du, H.; Lo, P.-K.; Hu, Z.; Liang, H.; Lau, K.-C.; Wang, Y.-N.; Lam, W. W. Y.; Lau, T.-C. Lewis acid-activated oxidation of alcohols by permanganate. *Chem. Commun.* **2011**, *47*, 7143-7145.

(18) Fukuzumi, S.; Morimoto, Y.; Kotani, H.; Naumov, P.; Lee, Y.-M.; Nam, W. Crystal structure of a metal ion-bound oxoiron(IV) complex and implications for biological electron transfer. *Nat. Chem.* **2010**, *2*, 756.

(19) Bang, S.; Lee, Y.-M.; Hong, S.; Cho, K.-B.; Nishida, Y.; Seo, M. S.; Sarangi, R.; Fukuzumi, S.; Nam, W. Redox-inactive metal ions modulate the reactivity and oxygen release of mononuclear non-haem iron(III)–peroxo complexes. *Nat. Chem.* **2014**, *6*, 934.

(20) Park, Y. J.; Ziller, J. W.; Borovik, A. S. The Effects of Redox-Inactive Metal Ions on the Activation of Dioxygen: Isolation and Characterization of a Heterobimetallic Complex Containing a Mn^{III}-(μ-OH)-Ca^{II} Core. *J. Am. Chem. Soc.* **2011**, *133*, 9258-61.

(21) Lacy, D. C.; Park, Y. J.; Ziller, J. W.; Yano, J.; Borovik, A. S. Assembly and Properties of Heterobimetallic $Co^{II/III}$/Ca^{II} Complexes with Aquo and Hydroxo Ligands. *J. Am. Chem. Soc.* **2012**, *134*, 17526-35.

(22) Horwitz, C. P.; Ciringh, Y. Synthesis and electrochemical properties of oxo-bridged manganese dimers incorporating alkali and alkaline-earth cations. *Inorg. Chim. Acta* **1994**, *225*, 191-200.

(23) Reath, A. H.; Ziller, J. W.; Tsay, C.; Ryan, A. J.; Yang, J. Y. Redox Potential and Electronic Structure Effects of Proximal Nonredox Active Cations in Cobalt Schiff Base Complexes. *Inorg. Chem.* **2017**, *56*, 3713-3718.

(24) Chantarojsiri, T.; Ziller, J. W.; Yang, J. Y. Incorporation of redox-inactive cations promotes iron catalyzed aerobic C–H oxidation at mild potentials. *Chem. Sci.* **2018**, *9*, 2567-2574.

(25) Matsunaga, S.; Shibasaki, M., Multimetallic Schiff base complexes as cooperative asymmetric catalysts. *Synthesis* **2013,** *45*, 421-437.

(26) Kumar, A.; Lionetti, D.; Day, V. W.; Blakemore, J. D. Trivalent Lewis Acidic Cations Govern the Electronic Properties and Stability of Heterobimetallic Complexes of Nickel. *Chem. Eur. J.* **2018**, *24*, 141-149.

(27) Perrin, D. D. *Ionisation Constants of Inorganic Acids and Bases in Aqueous Solution*. Pergamon, 1982.

(28) Solari, E.; Corazza, F.; Floriani, C.; Chiesi-Villa, A.; Guastini, C., Polydentate ligand exchange via formation of a dimetallic complex. Crystal structures of [(thf)Fe(acen)MCl2](M = Fe or Zn), [ClFe(salphen)FeCl$(thf)_2$], [Ti(acen)$(thf)_2$][$CoCl_3$(thf)], and [Ti(acen)$(thf)_2]_2$[$Fe_3Cl_8(thf)_2$][acen =N,N′-

ethylenebis(acetylacetoneiminate), salphen =N,N′-o-phenylenebis(salicylideneiminate), and thf = tetrahydrofuran]. *J. Chem. Soc., Dalton Trans.* **1990,** 1345-1355.

(29) Guerriero, P.; Tamburini, S.; Vigato, P. A.; Russo, U.; Benelli, C., Mössbauer and magnetic properties of mononuclear, homo- and hetero-dinuclear complexes. *Inorg. Chim. Acta* **1993,** *213*, 279-287.

(30) Matsunaga, S.; Shibasaki, M., Recent advances in cooperative bimetallic asymmetric catalysis: dinuclear Schiff base complexes. *Chem. Commun.* **2014,** *50*, 1044-1057.

(31) Van Staveren, C. J.; Fenton, D. E.; Reinhoudt, D. N.; Van Eerden, J.; Harkema, S. Co-complexation of urea and UO_2^{2+} in a Schiff base macrocycle: a mimic of an enzyme binding site. *J. Am. Chem. Soc.* **1987**, *109*, 3456-3458.

(32) Van Staveren, C. J.; Van Eerden, J.; Van Veggel, F. C. J. M.; Harkema, S.; Reinhoudt, D. N. Cocomplexation of neutral guests and electrophilic metal cations in synthetic macrocyclic hosts. *J. Am. Chem. Soc.* **1988**, *110*, 4994-5008.

(33) Zanello, P.; Cinquantini, A.; Guerriero, P.; Tamburini, S.; Vigato, P. A. Electrochemical behaviour of acyclic and macrocyclic complexes of nickel(II), copper(II) and uranyl(VI). *Inorg. Chim. Acta* **1986**, *117*, 91-96.

(34) Casellato, U.; Tamburini, S.; Tomasin, P.; Vigato, P. A.; Aime, S.; Botta, M. Synthesis, X-ray Structure, and Solution NMR Studies of Ln(III) Complexes with a Macrocyclic Asymmetric Compartmental Schiff Base. Preference of the Ln(III) Ions for a Crown-Like Coordination Site. *Inorg. Chem.* **1999**, *38*, 2906-2916.

(35) Brianese, N.; Casellato, U.; Tamburini, S.; Tomasin, P.; Vigato, P. A., Asymmetric compartmental macrocyclic ligands and related mononuclear and hetero-dinuclear complexes with d- and/or f-metal ions. *Inorg. Chim. Acta* **1999,** *293*, 178-194.

(36) Casellato, U.; Tamburini, S.; Tomasin, P.; Vigato, P. A. Uranyl(VI) complexes with [1+1] asymmetric compartmental ligands containing a Schiff base and a crown ether-like chamber. *Inorg. Chim. Acta* **2002**, *341*, 118-126

(37) Zanello, P.; Connelly, N. G., *Inorganic Electrochemistry: Theory, Practice and Application*. Royal Society of Chemistry: Cambridge, 2003, pp. 55-58.

(38) Mizuoka, K.; Kim, S.-Y.; Hasegawa, M.; Hoshi, T.; Uchiyama, G.; Ikeda, Y. Electrochemical and Spectroelectrochemical Studies on UO_2(saloph)L (saloph = *N,N'*-Disalicylidene-*o*-phenylenediaminate, L = Dimethyl Sulfoxide or *N,N*-Dimethylformamide). *Inorg. Chem.* **2003**, *42*, 1031-1038.

(39) Savéant, J.-M., *Elements of Molecular and Biomolecular Electrochemistry*. Wiley: Hoboken, NJ, 2006.

(40) Pedersen, C. J. Cyclic polyethers and their complexes with metal salts. *J. Am. Chem. Soc.* **1967**, *89*, 7017-7036.

(41) Blakemore, J. D.; Chitta, R.; D'Souza, F. Synthesis and study of crown ether-appended boron dipyrrin chemosensors for cation detection. *Tet. Lett.* **2007**, *48*, 1977-1982.

(42) Nicholson, R. S., Theory and application of cyclic voltammetry for measurement of electrode reaction kinetics. *Anal. Chem.* **1965,** *37*, 1351-1355.

(43) Bard, A. J.; Faulkner, L. R., *Electrochemical Methods: Fundamentals and Applications*. 2nd ed.; Wiley: Hoboken, NJ, 2001.

(44) Fulmer, G. R.; Miller, A. J. M.; Sherden, N. H.; Gottlieb, H. E.; Nudelman, A.; Stoltz, B. M.; Bercaw, J. E.; Goldberg, K. I. NMR Chemical Shifts of Trace Impurities: Common Laboratory Solvents, Organics, and Gases in Deuterated Solvents Relevant to the Organometallic Chemist. *Organometallics* **2010**, *29*, 2176-2179.

(45) Harris, R.K.; Becker, E.D.; Cabral de Menezes, S.M.; Goodfellow, R.; Granger, P. NMR nomenclature. Nuclear spin properties and conventions for chemical shifts (IUPAC Recommendations 2001)**.** *Pure Appl. Chem.* **2001**, *73*, 1795-1818.

(46) Harris, R.K.; Becker, E.D.; Cabral de Menezes, S.M.; Granger, P.; Hoffman, R.E.; Zilm, K.W. Further conventions for NMR shielding and chemical shifts (IUPAC Recommendations 2008)**.** *Pure Appl. Chem.* **2008**, *80*, 59-84.

Chapter 4

Supramolecular Optimization of Electron Transfer to High-Valent Uranium in Heterobimetallic Complexes

4.1 Introduction

Despite being the heaviest naturally occurring element on the Earth in significant quantities, uranium is quite abundant—more prevalent in the crust than commonly encountered elements like platinum or silver. Generation of low-carbon power by nuclear fission is enabled by this ample global supply of uranium, which is scattered widely across the globe with significant deposits in the United States and elsewhere. In line with this situation, significant quantities of high-valent uranium, in the form of the highly stable and water-soluble uranyl ion (UO_2^{2+}) are found in seawater and some groundwaters.[1]

The chemical properties of uranium vary widely across its multiple accessible oxidation states, dominated under standard conditions by U^{VI} (in the uranyl dioxo species) as well as U^{III}. Important work has shown that the reduction of uranium leads to diminished aqueous solubility, making redox-driven approaches to sequestration of this element and related transuranic elements an attractive strategy for environmental remediation.[2,3] And, in the context of the nuclear fuel cycle, reduction of uranium to lower valent forms is a key requirement for both fuel preparation via enrichment as well as recycling from spent fuels.

One focus in the field of heavy element chemistry is elucidation of the involvement of the 5*f*- and 6*d*-orbitals in the chemistry of uranium, an effort that could provide the electronic considerations needed to rationally design ligand environments and reagents for funneling of uranium through improved chemical pathways.[4] As the involvement of these orbitals has been shown to depend both on oxidation state and ligand structure, important challenges remain in the field.[5] In this context, development of selective and efficient electrode-driven processes for uranium (and other actinide elements) handling offers a strategy for management of oxidation state. However, despite the centrality of redox chemistry to the

processing, handling, and safe disposal of uranium, gaining control over electron transfer to uranium has received less attention than it deserves. This is attributable to the challenge of experimentally determining needed fundamental quantities like reorganization energy with uranium-containing samples that must be handled carefully to avoid undesired speciation and/or radiation exposure.[6]

Recently, we have been investigating the role of Lewis acidic and redox-inactive metal ions in tuning the redox chemistry of uranium.[7] Secondary metal ions have been shown to modulate the reaction chemistry of uranium in several classes of compounds, with particular importance on oxo-bridged interactions that may arise in $U^{V}O_2$ complexes. Arnold, Hayton, Mazzanti, and others have mapped such systems in detail, cutting a path to understanding U–O activation coupled to reduction.[8] Our interest in this area was originally piqued when considering the role of redox-inactive metals in tuning the electron transfer behaviors of biological active sites and bioinspired model complexes, and we wondered if secondary metals might be used to rationally tune actinide redox chemistry in a similar fashion.[9] In recent work (described in Chapter 3), we showed that these effects are indeed as viable for tuning uranium as they are for the more commonly investigated 3*d* transition elements.[7,10]

However, interpreting the origin and scope of the tunability afforded by secondary redox-inactive metal ions in redox-active systems remains an area of significant inquiry. Ions' behaviors in heterobimetallic complexes have been interpreted, variously, as driven by Lewis acidity,[11] electrostatic interactions,[12] or structural effects.[13] In the case of tunable uranium chemistry, design rules for tailored control over both the thermodynamics and kinetics of heterogeneous electron transfer are not available, in part due to few studies wherein modular ligand frame works have been available with which to quantify and

elucidate these various effects. However, based on our recent studies regarding quantification of Lewis acidity in nonaqueous media,[14] we anticipated that consideration of supramolecular preferences in binding of secondary metal ions could provide a suitable framework for mapping involvement of the metals in uranium-centered redox chemistry.[15]

Here, we report a comparison of the U^{VI}/U^{V} electron-transfer chemistry of two related families of heterobimetallic complexes (**L^5UO_2M** and **L^6UO_2M**) that incorporate secondary redox-inactive metal ions M (where M is Cs^+, Rb^+, K^+, Na^+, Li^+, or Ca^{2+}, see Chart 4.1). The consequences of binding the secondary metal ions have been mapped, in order to reveal the influences of Lewis acidity, supramolecular ligand basicity/denticity, and association constants on both the thermodynamics and kinetics of uranium-centered reduction. The coordination properties of the secondary metal ion binding site (penta- vs. hexadentate) are demonstrated to govern the extent of acidity-driven potential tuning, in that the pentadentate framework which presents a more modest ligand basicity, displays a greater tuning range of reduction potentials. Electron transfer, on the other hand, can only be optimized by balancing the elucidated influences on the systems, giving rise to "volcano plots" for U^{VI}/U^{V} reduction that demonstrate design rules elaborated here for control of uranium redox cycling. Together, our results provide a mechanistic framework for development of future electrode-driven chemistries for actinide processing, effectively bridging from the field of heavy element chemistry to draw on bioinspired insights into electron transfer.

Chart 4.1. Two families of heterobimetallic complexes of uranium, with different pendant crown ether sites, studied in this report.

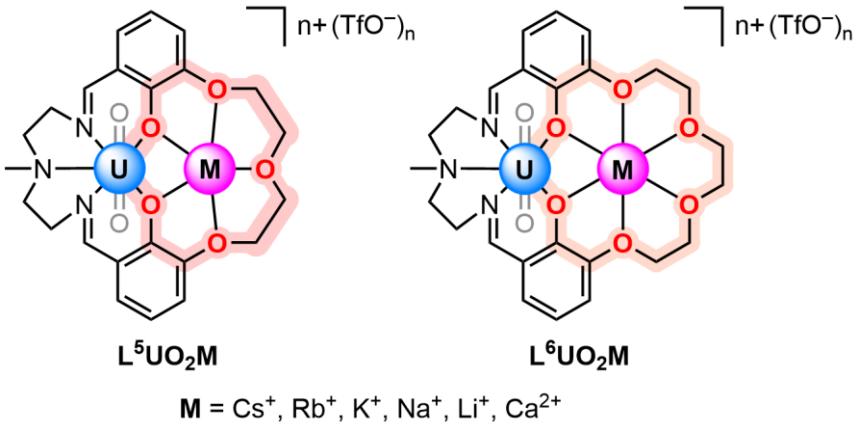

4.2 Results and Discussion

4.2.1 *In situ* Synthesis and Characterization of the Heterobimetallic Complexes

The two families of heterobimetallic complexes described here are based upon ligand framework design concepts which were introduced by Reinhoudt in the late 1980s,[16] but elaborated upon to a significant degree by Vigato and co-workers in subsequent work.[17] The ligands (denoted as $\mathbf{L^5H_2}$ and $\mathbf{L^6H_2}$) are heteroditopic in nature, presenting two different coordination sites for binding of two metal centers; a common Schiff-base site for UO_2^{2+} binding is found in both $\mathbf{L^5H_2}$ and $\mathbf{L^6H_2}$. The second binding site in each ligand (for secondary redox-inactive metal binding) is based upon an appended polyether chain, offering a 15-crown-5-like pentadentate site (as in $\mathbf{L^5H_2}$) or an 18-crown-6-like hexadentate site (as in $\mathbf{L^6H_2}$). These polyether sites are located adjacent to the uranyl-binding cavity such that the secondary metals can interact with uranium via bridging phenoxides. We previously utilized $\mathbf{L^6H_2}$ for divergent preparation of heterobimetallic uranyl complexes with mono-, di-, and tri-valent redox-inactive cations (Chapter 3), and were thus encouraged to prepare the related $\mathbf{L^5H_2}$ for our supramolecular studies here.[7]

To prepare $\mathbf{L^5H_2}$ and $\mathbf{L^6H_2}$, precursor complexes **BaPenta** and **BaHexa** were prepared according to literature procedures, and as in our prior work described in Chapter 3.[7,17] For the preparation of **BaPenta**, a linear dialdehyde precursor with three ether oxygens derived from diethylene glycol ditosylate was used in place of the corresponding triethylene glycol ditosylate with four ether oxygens used for the preparation of **BaHexa**. We find that Ba^{2+}-templated macrocyclization is effective for the preparation of both ligands, which can be isolated cleanly as their triflate salts. (See Experimental Section for details.) Notably, Vigato and co-workers previously isolated the perchlorate salt of **BaPenta**, but only limited characterization data of the complex was available at the time.[17]

Single crystals of BaPenta suitable for X-ray diffraction (XRD) analysis were grown by vapor diffusion of diethyl ether into a methanol solution of the complex. The data reveal that the complex crystallizes as 2:1 $\mathbf{L^5H_2}$:Ba adduct, wherein the Ba^{2+} center is sandwiched between the crown-ether-like sites of two $\mathbf{L^5H_2}$ units (Figure 4.1). In the structure, Ba^{2+} is coordinated to a total of 10 macrocyclic O atoms (five each from two $\mathbf{L^5H_2}$ ligands) and has a coordination number (CN) of 10. However, two Ba^{2+} centers are displayed in the asymmetric unit of the crystal obtained; this is because the Ba^{2+} ions sit on a crystallographic C_2 axis, and each has a full occupancy of 0.50 (see Appendix C, Figure C85). Two outer-sphere triflates are observable in the data, and have full occupancy values of 1.00, giving rise to the expected Ba^{2+}:OTf^- stoichiometry of 1:2. The formulation of the ligands as $\mathbf{L^5H_2}$ units (rather than as deprotonated forms) was confirmed by successful location and free refinement of the four phenol-derived H atoms (labeled as H1A, H2A, H1C, H2C in Figure 4.1). However, consistent with acidification of the phenols upon Ba^{2+} coordination, the nearby imine N-atoms assist in the formation of strong O–H•••N hydrogen bonds (O•••N

distances of ca. 2.61–2.64 Å). The presence of the H atoms was also confirmed by ^{1}H NMR spectroscopy (see Appendix C, Figure C1).

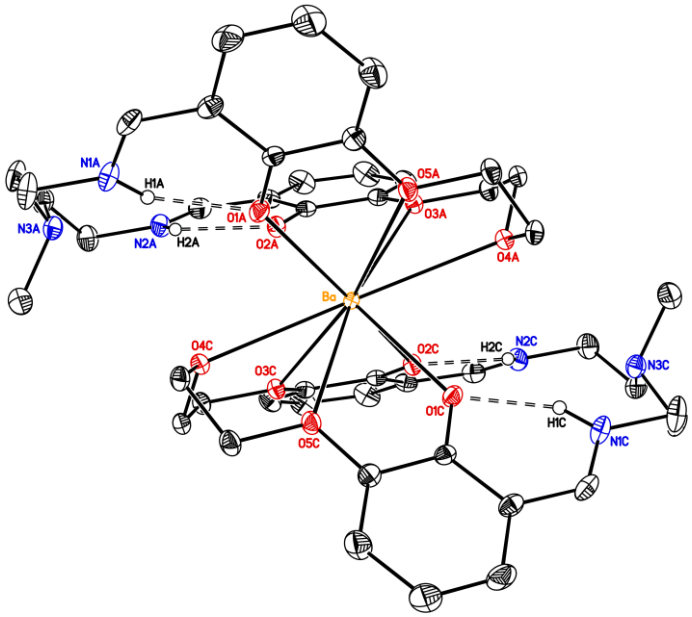

Figure 4.1. Solid-state structure (from XRD) of **BaPenta**. H atoms, except the ones hydrogen-bonded to O1, O2, O1A, O2A, O1C, O2C, and outersphere triflate counteranions are omitted for clarity. Displacement ellipsoids are shown at the 20% probability level.

Contrasting with the structure of **BaPenta**, prior data for **BaHexa** revealed a 1:1 $L^{6}H_2$:Ba adduct (Figure 4.2). The Ba^{2+} ion in the structure of **BaHexa** is coordinated to 6 macrocyclic O atoms (from $L^{6}H_2$ ligand), and its CN of 10 is satisfied by two κ^2-triflate inner-sphere counteranions, suggesting the preference of Ba^{2+} to coordinate to 10 atoms in our systems. Both the Ba complexes feature an empty pentadentate pocket with two phenol, two imine, and one trialkylamine groups. However, the Ba^{2+} ion is significantly displaced from the crown ether cavity in **BaPenta,** and this displacement was quantified by ψ parameter defined as the distance between Ba atom and the centroid of the plane defined by O1, O2, O3, O4, O5, and O6 (see Table 4.1). The ψ value for **BaPenta** is approximately five times greater than that of **BaHexa**. This displacement of Ba^{2+} from the plane is attributable to the

sandwiching nature of **BaPenta,** resulting in the Ba^{2+} sitting between two $\mathbf{L^5H_2}$ ligands rather than the 15-crown-5-like cavity. However, the 18-crown-6-like cavity in $\mathbf{L^6H_2}$ being larger in size allows for the Ba^{2+} to sit in the cavity resulting in a significantly smaller ψ value. Another useful parameter is ω_{salben} which is defined as the root mean square deviation of the three N atoms and the two phenoxide O atoms from the mean plane defined from the positions of those atoms. The value of ω_{salben} is larger for **BaHexa (**1.597 – 1.599 Å), possibly due to the Ba atom buried in the 18-crown-6-like cavity resulting in strain and subsequent distortion of the nearby pentadentate site. However, in **BaHexa** complex, this strain is released by the Ba^{2+} displaced away from the cavity, and therefore, the ω_{salben} significantly smaller (0.320 Å) as compared to **BaPenta**. Additionally, the separation between two phenoxide O atoms, denoted by O1•••O2, is smaller for **BaPenta** by 0.2 – 0.4 Å consistent with the displacement of the Ba atom from the 15-crown-5-like cavity relieving the strain in the cavity.

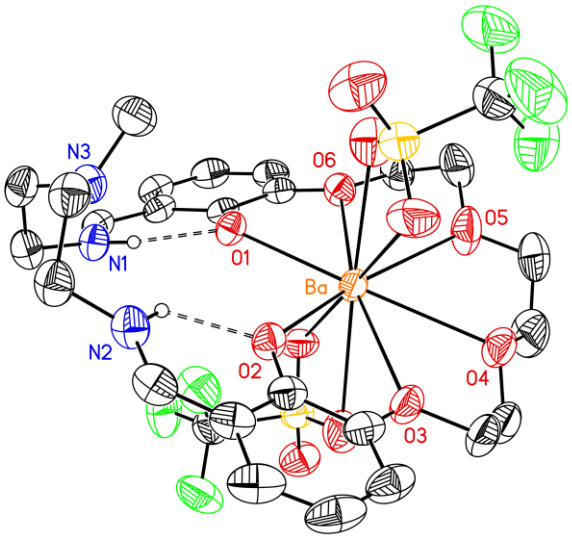

Figure 4.2. Solid-state structure (from XRD) of **BaHexa**. H atoms, except the ones hydrogen-bonded to O1 and O2 are omitted for clarity. Displacement ellipsoids are shown at the 20% probability level.

Table 4.1. Comparison of selected bond lengths, interatomic distances, root mean square deviations (ω), and displacement of select metal atoms from the plane (ψ) in Ba complexes.

Compound	**BaPenta**	**BaHexa[a]**
pK_a of $[M(H_2O)_m]^{n+}$	13.4	13.4
O1•••O2 (Å)	3.426(4), 3.230(4)	3.641(3)
M–$O_{phenoxo}$ (Å)	2.699(3), 2.742(3), 2.730(3), 2.689(3)	2.696(2), 2.693(2)
ω_{crown}[b]	0.286, 0.284	0.233
ω_{salben}[c]	0.203, 0.444	0.607
ψ_M[d] (Å)	1.599, 1.597	0.320

(a) Structural data taken from references 7 and 18 (CCDC 1960625). (b) Defined as the root mean square deviation (r.m.s.d.) of the following atoms from the mean plane of their positions: O1, O2, O3, O4, O5, and O6. (c) r.m.s.d. of O1, O2, N1, N2, and N3. (d) Distance between M atom and the centroid of the plane defined by O1, O2, O3, O4, O5, and O6. Atom labels are consistent with those given in the raw crystallographic data (see Appendix C).

Having observed the different coordination environments for **BaPenta** and **BaHexa**, we moved to prepare the desired uranyl complexes with both the ligands with appropriate stoichiometric amounts of UO_2^{2+} containing reagent. When the barium complexes are treated with guanidinium sulfate in a biphasic chloroform/water mixture, Ba^{2+} precipitates out as $BaSO_4$ in both cases, leaving behind the ligand framework in the chloroform layer. Subsequent treatment of the chloroform layer with 2 equiv. of $UO_2(OAc)_2{\cdot}2H_2O$ in **BaPenta** case and 1 equiv. of $UO_2(OAc)_2{\cdot}2H_2O$ in **BaHExa** case affords uranyl complexes, **L^5UO_2** and **L^6UO_2** respectively, as deep red solids (Scheme 4.1).[17d] The incorporation of UO_2^{2+} ion in the pentadentate site is achieved by the deprotonation of the phenolic protons by acetate ($^-$OAc) ions from $UO_2(OAc)_2{\cdot}2H_2O$, releasing acetic acid in the reaction mixture. This was

confirmed by disappearance of the peaks corresponding to the H atoms of the phenolic groups in the ^{1}H NMR of the **L^{5}UO$_2$** complex (see Appendix C, Figure C3).

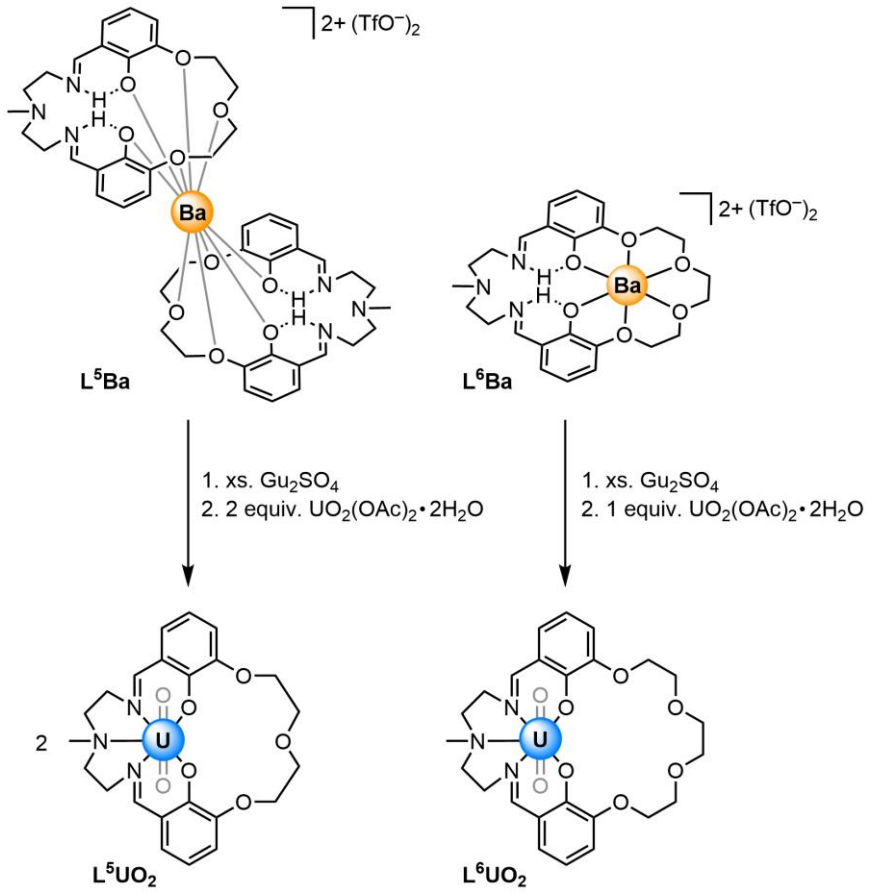

Scheme 4.1. Synthesis of monometallic uranyl complexes with 15-crown-6- and 18-crown-6-like appended moieties.

In our prior work from Chapter 3, we presented a complete structural and solution characterizations for the monometallic UO_2^{2+} complex **L^{6}UO$_2$**.[7] In addition, Vigato & co-workers published the solid-state XRD structure for the **L^{5}UO$_2$** with a co-crystallized water molecule.[17d] In this work, we were able to grow single crystals of **L^{5}UO$_2$** in an inert atmosphere with a co-crystallized CH_3CN molecule (see Appendix C, Figure C86). Both the complexes **L^{5}UO$_2$** and **L^{6}UO$_2$** display a pentadentate coordination environment for the UO_2^{2+} dication and an adjacent open crown ether-like cavity poised to bind redox-inactive

Lewis acidic metal ions. The planarity of the pentadentate site housing UO_2^{2+} was quantified by the ω_{salben} parameter (see Table 4.2). For both the monometallic UO_2^{2+} complexes, this ω_{salben} parameter is close to zero (0.082 and 0.049, respectively), suggesting negligible distortion of the planar pentadentate site. However, in the absence of UO_2^{2+} ion, the pentadentate site is significantly deformed with the value of ω_{salben} equal to 0.203 and 0.444 in **BaPenta** and 0.607 in **BaHexa**. This situation is reflected in the increased O1•••O2 separation by 0.1-0.5 Å in the monometallic UO_2^{2+} complexes as compared to the Ba complexes suggesting pulling apart of the phenoxide O atoms in the presence of larger and spatially demanding pentadentate site containing the UO_2^{2+} moiety. The ω_{crown} parameter, on the other hand, is distinctively different for both the UO_2^{2+} complexes with the values 0.060 for $\mathbf{L^5UO_2}$ and 0.358 for $\mathbf{L^6UO_2}$. This could be attributable to the larger size of the 18-crown-6-like site resulting in more flexibility of the crown in $\mathbf{L^6UO_2}$.

Table 4.2. Comparison of selected bond lengths, interatomic distances, root mean square deviations (ω), and displacement of select metal atoms from the plane (ψ) in monometallic UO_2^{2+} complexes.

Compound	$\mathbf{L^5UO_2}$	$\mathbf{L^6UO_2}$[a]
O1•••O2 (Å)	3.137(5)	3.137(10)
U–O$_{oxo}$ (Å)	1.779(4), 1.771(4)	1.783(8), 1.792(7)
U–O$_{oxo}$ (avg., Å)[b]	1.775(6)	1.788(11)
U–O$_{phenoxo}$ (Å)	2.230(4), 2.250(4)	2.250(7), 2.207(8)
ω_{crown}[c]	0.060	0.358
ω_{salben}[d]	0.082	0.049

(a) Structural data taken from references 7 and 19 (CCDC 1960626). (b) Average of the U–O7 and U–O8 bond distances. (c) Defined as the root mean square deviation (r.m.s.d.) of the following atoms from the mean plane of their positions: O1, O2, O3, O4, O5, and O6. (d) r.m.s.d. of O1, O2, N1, N2, and N3. Atom labels are consistent with those given in the raw crystallographic data (see Appendix C).

With the monometallic UO_2^{2+} complexes in hand, we turned to the *in situ* preparation of a family of heterobimetallic complexes. For this synthesis, we chose a series of monovalent ions (Cs^+, Rb^+, K^+, Na^+, Li^+) and a divalent ion (Ca^{2+}), with varying Lewis acidity values and ionic radii (see Table 4.3). Treatment of $\mathbf{L^5UO_2}$ or $\mathbf{L^6UO_2}$ with 1 equiv. of corresponding metal triflate salts of the ions (*vide infra*) in CD_3CN, results in a color change of the solution ranging from red to yellow with the increase in Lewis acidity. As expected from our prior studies with Ni^{2+}, $Zn^{2+,}$ and UO_2^{2+} complexes, ^{1}H NMR spectra for all the solutions discussed above display uniform shifts in the peaks, suggesting interaction of metal ions with the oxygen atoms of the crown ether-like cavity (see Appendix C, Figures C16, C17, C25, and C26).[7,10,20] The NMR studies also confirm the persistence and stability of the proposed heterobimetallic complexes of the form $\mathbf{L^5UO_2M}$ and $\mathbf{L^6UO_2M}$ (where M = Cs^+, Rb^+, K^+, Na^+, Li^+, and Ca^{2+}, see Chart 4.1) in CD_3CN.

Table 4.3. Lewis acidity, ionic radius and Z^2/r ratio of the redox-inactive metal ions

Ion	pK_a of $[M(H_2O)_m]^{n+}$	r for C.N. = 8 / Å	Z^2/r
Cs^+	16.34[a]	1.74[c]	0.0055[d]
Rb^+	16.29[a]	1.61	-
K^+	16.06[a]	1.51	0.0066
Na^+	14.8[b]	1.18	0.0088
Li^+	13.8[b]	0.92	0.0111
Ca^{2+}	12.6[b]	1.12	0.0351

[a]Taken from reference 14. [b]Taken from reference 21. [c]Taken from reference 22. [d]Taken from reference 23.

We attempted to grow crystals for **L^{5}UO$_2$M** complexes in our series by vapor diffusion technique. Our efforts to grow crystals for complexes containing Rb^+ and Cs^+ ions for both the families of ligands in this study, were unsuccessful possibly due to the larger size of these ions (see Table 4.3), resulting in inefficient crystal packing. Moreover, the smaller ionic radii for Li^+ ion for the 18-crown-6-like cavity hindered our ability to grow crystals of the **L^{6}UO$_2$Li** complex, possibly due to the significant deformation of the macrocyclic structure upon coordination of smaller Li^+ ion. However, we were able to grow crystals of the remaining **L^{5}UO$_2$M** complexes containing relatively smaller ions (K^+, Na^+, Li^+) by vapor diffusion of diethyl ether into a concentrated CH_3CN solution of these complexes (see Figure 4.3). For comparison, we included the data for the XRD analysis of single crystals for **L^{6}UO$_2$M** complexes (where M = K^+, Na^+, Li^+, and Ca^{2+}) in Table 4.4 that have also been discussed in detail in our prior work as described in Chapter 3.[7]

XRD analysis of the solid-state structures of **L^{5}UO$_2$M** (M = K^+, Na^+, Li^+) confirm assembly of the desired [U(μ-O$_{Ar}$)$_2$M^{n+}] cores. As expected from our previous study (see Chapter 3), these **M** ions are incorporated in the crown-ether-like cavity and ligated by five O atoms from the 15-crown-5-like cavity. Although all the three **M** ions have different ionic radii, they exhibit coordination numbers (C.N.) of six with the counteranion triflates bound to the metal ion in a κ^1 fashion. This observation is in line with analogous structures for **L^{6}UO$_2$K** and **L^{6}UO$_2$Na** complexes where the six O atoms of the crown-ether-like cavity and one κ^1-triflate show a C.N. of seven in each case. As was observed in our published **L^{6}UO$_2$M** (M = K^+, Na^+, Li^+, and Ca^{2+}) structures, the UO_2^{2+} moiety in **L^{5}UO$_2$M** (M = K^+, Na^+, Li^+) remains structurally intact, leading to a planar geometry of the pentadentate site. The U–O$_{oxo}$ distances in all three complexes range from 1.778(2) to 1.794(6) Å (see Table 4.4 for

structural parameters), complementing a similar range of values observed for U–O_{oxo} distances in the **L^{6}UO$_2$M** complexes and in the monometallic UO_2^{2+} complexes (see Table 4.2).

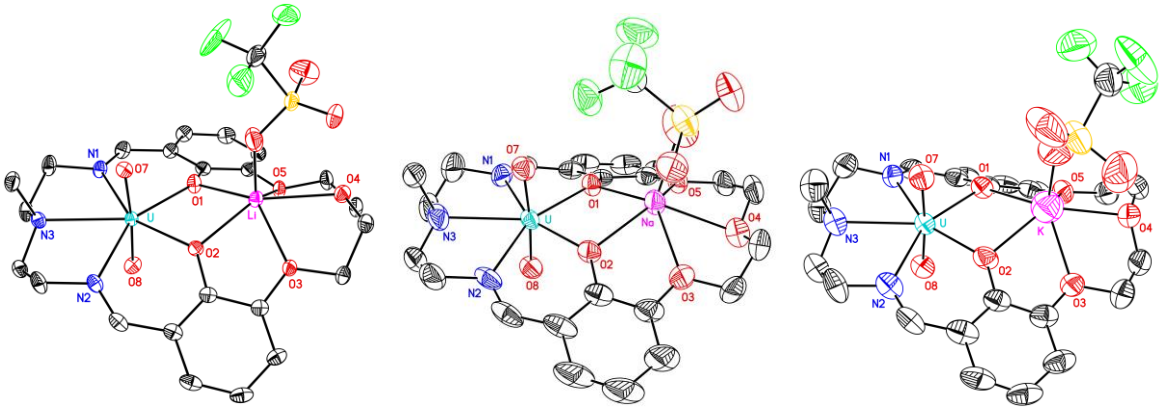

Figure 4.3. Solid-state structure (from XRD) of **L^{5}UO$_2$Li**, **L^{5}UO$_2$Na**, and **L^{5}UO$_2$K**. All H atoms and disordered triflates are omitted for clarity. Displacement ellipsoids are shown at the 50% probability level.

However, the features of crown-ether-like cavity vary significantly across the series of heterobimetallic complexes listed in Table 4.4. The XRD data for all the heterobimetallic complexes (**L^{5}UO$_2$Li**, **L^{5}UO$_2$Na**, **L^{5}UO$_2$K**, **L^{6}UO$_2$Na**, **L^{6}UO$_2$K**) reveal that the pentadentate pocket is slightly deformed (ω_{salben}: 0.049 – 0.082 for monometallic UO_2^{2+} complexes vs. 0.108 – 0.157 for bimetallic UO_2^{2+} complexes) upon **M** coordination while the crown-ether-like cavity undergoes a significant amount of distortion with the binding of the Lewis acid. The larger values of ω_{crown} for four heterobimetallic complexes, **L^{5}UO$_2$Li**, **L^{5}UO$_2$K**, **L^{6}UO$_2$Na**, **L^{6}UO$_2$K**, as compared to their respective monometallic analogues (by approximately 0.3 Å) may be ascribable to the steric clash incurred by the spatially demanding pentadentate cavity housing the relatively larger UO_2^{2+} moiety. Because of this situation, the ω_{salben} parameter in all the uranyl-containing compounds has lower values.

However, a surprising result was obtained for the **L^5UO_2Na** complex in that the value of ω_{crown} is the lowest at 0.028. We hypothesized that the Na^+ is a good fit for the 15-crown-5-like cavity, and therefore, the O atoms of the crown-ether-like cavity only slightly deviate from the plane defined by those atoms.

Table 4.4. Comparison of $[\mathbf{M}(H_2O)_m]^{n+}$ complex pK_a values, selected bond lengths, interatomic distances, root mean square deviations (ω), and displacement of select metal atoms from the plane (ψ) in heterobimetallic UO_2^{2+} complexes.

Compound	**L^5UO_2Li**	**L^5UO_2Na**	**L^6UO_2Na[a]**	**L^5UO_2K**	**L^6UO_2K[a]**
pK_a of $[M(H_2O)_m]^{n+}$	13.8	14.8	14.8	16.06	16.06
U•••M (Å)	3.488(4)	3.584(2)	3.668(3)	3.600(3)	3.681(5)
O1•••O2 (Å)	2.840(2)	2.991(6)	2.973(7)	2.931(8)	2.994(11)
U–O_{oxo} (avg., Å)[b]	1.781(3)	1.780(7)	1.781(7)	1.791(8)	1.777(10)
U–$O_{phenoxo}$ (Å)	2.260(2), 2.267(2)	2.281(4), 2.276(4)	2.247(6), 2.262(6)	2.267(5), 2.254(6)	2.244(8), 2.276(8)
M–$O_{phenoxo}$ (Å)	2.216(4), 2.289(4)	2.412(5), 2.412(5)	2.584(7), 2.435(8)	2.437(6), 2.389(7)	2.604(9), 2.454(11)
ω_{crown}[e]	0.400	0.028	0.717	0.365	0.715
ω_{salben}[f]	0.108	0.110	0.157	0.119	0.155
ψ_M[g]	0.594	0.805	0.669	0.831	0.684
pK_a of $[M(H_2O)_m]^{n+}$	13.8	14.8	14.8	16.06	16.06

(a) Structural data taken from references 7, 24 (CCDC 1960629) and 25 (CCDC 1960628). (b) Average of the U–O7 and U–O8 bond distances. Errors on the average bond lengths and bond angles were derived by propagation of error from the individual values and estimated standard deviations (e.s.d.'s). (e) Defined as the root mean square deviation (r.m.s.d.) of the following atoms from the mean plane of their positions: O1, O2, O3, O4, O5, and O6. (f) r.m.s.d. of O1, O2, N1, N2, and N3. (g) Distance between the atom **M** and the centroid of the plane defined by O1, O2, O3, O4, O5, and O6. Atom labels are consistent with those given in the raw crystallographic data (see Appendix C).

In our previous work mentioned in Chapter 3, we hypothesized that the O1•••O2 distance in the heterobimetallic complexes is significantly compressed as the Lewis acidity of **M** increases (as compared to the monometallic $\mathbf{L^5UO_2}$ and $\mathbf{L^6UO_2}$ complexes), corresponding to a drawing together of these macrocyclic atoms upon coordination of the redox-inactive metals.[7] However, this is not the case with the $\mathbf{L^5UO_2Na}$ complex, which has a larger value of O1•••O2 separation than its K^+ analogue $\mathbf{L^5UO_2Na}$ by 0.06 Å, considering the fact that the Lewis acidity of Na^+ is larger than K^+ (14.8 vs. 16.1, respectively). This finding could be attributable to a good size match between Na^+ and the 15-crown-5-like cavity resulting in drawing away of the O1 and O2 atoms from each other, causing a larger O1•••O2 separation. Furthermore, the Lewis acidity of the **M** has a significant effect on the $M–O_{phenoxo}$ bond distances. These distances are the smallest in the $\mathbf{L^5UO_2Li}$ complex, consistent with the lowest pK_a value of the Li-aqua species. This situation is also reflected in the lowest value of the U•••M distance in the Li^+ complex.

With the observation of the apparent stability of the heterobimetallic UO_2^{2+} complexes, as judged from the ^{1}H NMR, we moved to investigate the influence of the ligand structure and Lewis acidity on the electrochemical properties of these complexes. Notably, to the best of our knowledge, systematic electrochemical studies on the macrocyclic heterobimetallic uranyl complexes with the monovalent ions in close proximity to the UO_2^{2+} ion have not been previously studied. This could be attributable to the challenges in working with radioactive U and to the poor stability of complexes containing highly Lewis acidic UO_2^{2+} ion. Here, we will study and compare the Lewis acid effects through *in situ* cyclic voltammetry (CV) experiments on two different families of complexes (Figure 4.4). This was achieved by adding one equivalent of the corresponding metal triflate salts to a solution

of monometallic uranyl complex (either **L^5UO_2** or **L^6UO_2)** dissolved in the electrolyte (0.1 M $TBAPF_6$ in CH_3CN) solution and subsequently recording the CV data.

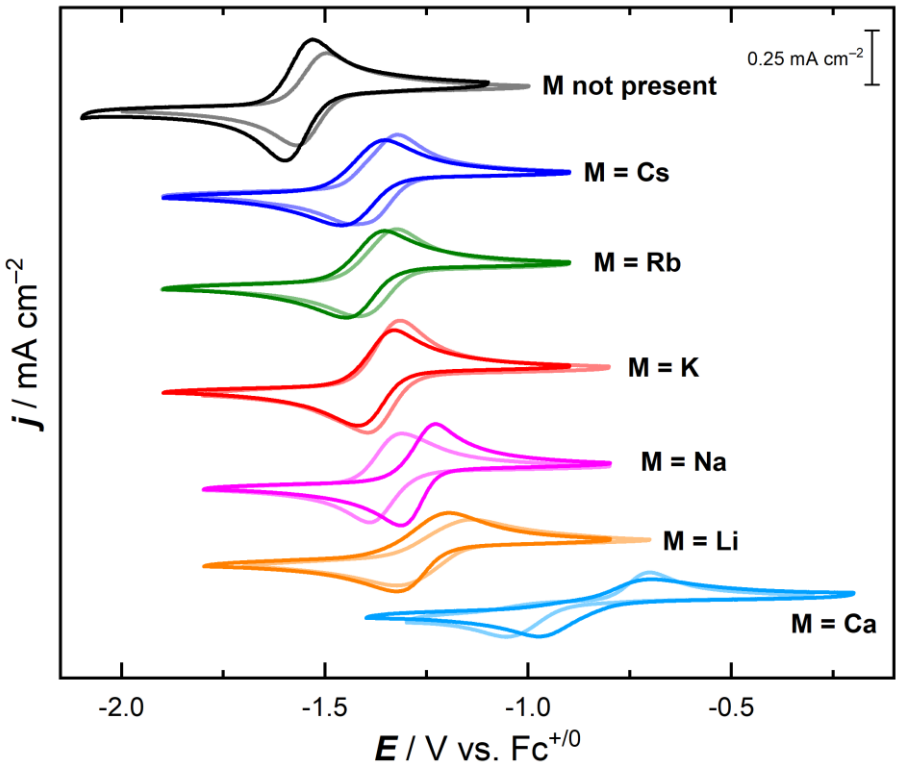

Figure 4.4. *In situ* cyclic voltammetry experiments for uranium complexes used in this study. **L^5UO_2** and **L^5UO_2M** complexes are represented by solid colors; **L^6UO_2** and **L^6UO_2M** complexes are represented by faded colors. Electrolyte: 0.1 M $TBAPF_6$ in MeCN, scan rate: 100 mV/s, electrode: highly oriented pyrolytic graphite.

To begin, CV data for **L^5UO_2** and **L^6UO_2** complexes display a chemically reversible reduction at $E_{1/2}$ = –1.60 V and –1.53 V vs. ferrocenium/ferrocene (denoted hereafter as $Fc^{+/0}$), respectively (see figure 4.4). The peak-to-peak separation measured at 100 mV/s scan rate for both the complexes (ΔE_p = 77 mV and 73 mV, respectively) is consistent with reasonably fast electron transfer. The more positive $E_{1/2}$ value for the **L^6UO_2** as compared to the **L^5UO_2** could be attributable to a stronger inductive effect provided by the extra O atom in the 18-crown-6-like cavity in the **L^6UO_2** complex and to the availability of more

flexible 18-crown-6-like pendant ether moiety upon reduction. On the basis of studies of analogous $\mathbf{L^6UO_2}$ complexes in our prior work as described in Chapter 3, this process can be reliably assigned to $U^{VI/V}$ couple and to an electrochemically reversible process. Since the anodic and cathodic waves are linearly proportional to the square root of scan rate, both the U^{VI} and U^{V} forms of $\mathbf{L^5UO_2}$ as well as $\mathbf{L^6UO_2}$ are confirmed as freely diffusing.[26]

Table 4.5. Electrochemical Characteristics of the $\mathbf{L^5UO_2}$ and $\mathbf{L^5UO_2M}$ complexes.

$\mathbf{M^{n+}}$	p$\boldsymbol{K}_\mathbf{a}$ of $\mathbf{[M(H_2O)_m]^{n+}}$	$\boldsymbol{E}_{1/2}$ / mV vs. $\mathbf{Fc^{+/0}}$	$\Delta\boldsymbol{E}_\mathbf{p}$ / mV	$\boldsymbol{k}^0$ / cm $\mathbf{s^{-1}}$ (X $\mathbf{10^{-3}}$)	λ
No M^{n+}	-	–1.60	77	9.54 ± 3.99	0.26 ± 0.05
Cs^+	16.34[a]	–1.46	108	3.43 ± 0.96	0.43 ± 0.04
Rb^+	16.29[a]	–1.45	100	4.92 ± 1.14	0.32 ± 0.02
K^+	16.06[a]	–1.42	91	5.24 ± 1.78	0.29 ± 0.03
Na^+	14.8[b]	–1.32	86	7.39 ± 1.26	0.19 ± 0.02
Li^+	13.8[b]	–1.26	130	2.01 ± 0.28	0.36 ± 0.02
Ca^{2+}	12.6[b]	–0.83	293	0.25 ± 0.05	0.55 ± 0.09

[a]Taken from reference 14. [b] Taken from reference 21.

When one equivalent redox-inactive Lewis acids are added in the electrochemical experiment, the CV data retains the chemically reversible process in all cases and shows a systematic shift in the $E_{1/2}$ values to more positive potentials in going from Cs^+ to Ca^{2+} (see Figure 4.4 and Tables 4.5 and 4.6). This shift of the U^{VI}/U^{V} reduction potentials to more positive values suggests retention of the coordinated Lewis acids in the crow-ether-like site. The $E_{1/2}$ values with the only divalent ion in our series, Ca^{2+}, shift significantly to positive potentials (more than 600 mV with respect to the monometallic UO_2^{2+} complexes) as

compared to the other analogous complexes. We attribute this behavior to the higher charge and Lewis acidity of the Ca^{2+} ion. Furthermore, scan rate-dependent studies reveal that both the families of heterobimetallic complexes, $\mathbf{L^5UO_2}$ and $\mathbf{L^6UO_2M}$, in both the U^{VI} and U^{V} states are freely diffusing.

Table 4.6. Electrochemical Characteristics of the $\mathbf{L^6UO_2}$ and $\mathbf{L^6UO_2M}$ complexes.

M^{n+}	pK_a of $[M(H_2O)_m]^{n+}$	$E_{1/2}$ / mV vs. $Fc^{+/0}$	ΔE_p / mV	k^0 / cm s^{-1} (X 10^{-3})	λ
No M^{n+}	-	–1.53	74	14.6 ± 2.46	0.21 ± 0.01
Cs^+	16.34[a]	–1.38	113	5.72 ± 1.89	0.48 ± 0.06
Rb^+	16.29[a]	–1.37	89	6.89 ± 1.38	0.35 ± 0.03
K^+	16.06[a]	–1.36	83	14.3 ± 1.52	0.25 ± 0.02
Na^+	14.8[b]	–1.35	79	13.5 ± 2.07	0.23 ± 0.01
Li^+	13.8[b]	–1.23	185	0.87 ± 0.13	0.69 ± 0.02
Ca^{2+}	12.6[b]	–0.88	348	0.19 ± 0.03	0.45 ± 0.05

[a]Taken from reference 14. [b] Taken from reference 21.

The noted positive shifts in the reduction potential have been observed for other heterobimetallic systems, including some of ours, containing one redox-active and one redox-inactive metal in close proximity.[10,20,12] In our previous work with [Ni,M] (refer Chapter 2), and [Zn,M] complexes, we plotted cathodic peak reduction potentials, $E_{p,c}$, for irreversible processes against the pK_a values of the corresponding redox-inactive metal aqua complexes. The plots revealed a clear dependence, and the least-squares fitting of the data to the linear correlation gave absolute values of 61 ± 9 mV/pK_a and 41 ± 3 mV/pK_a, respectively. However, since all of our heterobimetallic UO_2^{2+} complexes studied here

display reversible behavior, we chose their $E_{1/2}$ values and plotted them against respective pK_a values taking the same strategy. We omitted the data for the CV experiment with **L^{5}UO$_2$Ca** and **L^{6}UO$_2$Ca** in our plots due to the broad voltammetric response for both of these compounds, consistent with obvious slow electron transfer that can complicate our understanding of the thermodynamic influence of Lewis acids on these systems.

The data with monovalent ions revealed a clear and uniform trend in both sets of our bimetallic complexes, **L^{5}UO$_2$M** and **L^{6}UO$_2$M** (with a sensitivity of 63 ± 10 mV/pK_a and 49 ± 14 mV/pK_a, respectively), suggesting dependence of Lewis acidity on the thermodynamic potentials of these complexes (Figure 4.5). The sensitivity for **L^{5}UO$_2$M** complexes is slightly larger than that for the **L^{6}UO$_2$M** complexes. We attributed this to the higher Lewis acidity of the redox-inactive Lewis acids in 15-crown-5-like cavity, containing one less Lewis basic oxygen atom, as compared to the 18-crown-6-like cavity.

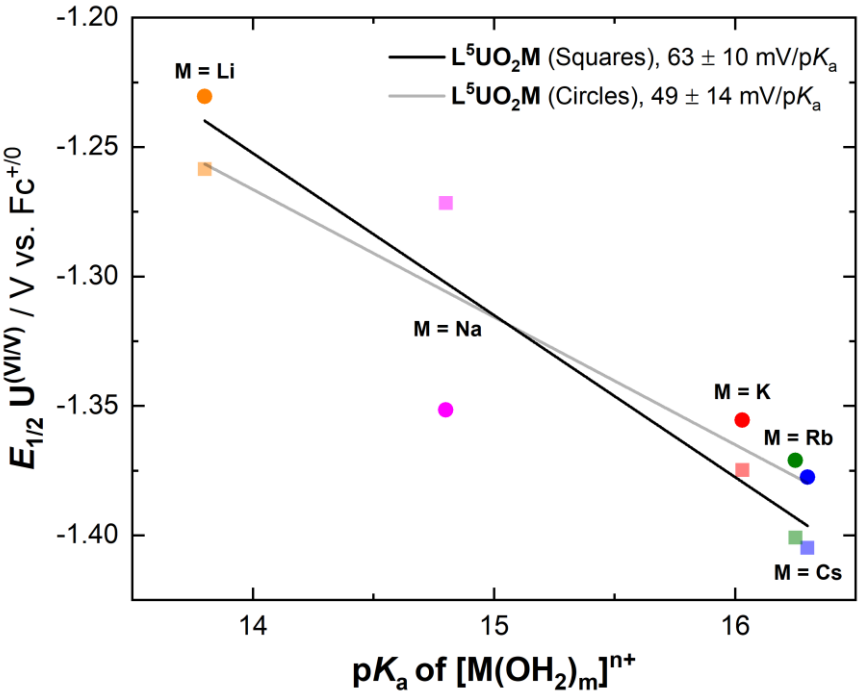

Figure 4.5. Plot of $E_{1/2}$(U$^{VI/V}$) vs. pK_a of [**M**(H$_2$O)$_m$]$^{n+}$.

To provide support for this theory, we carried out a simple *in situ* test wherein we mixed the monometallic UO_2^{2+} complex (**L^5UO_2** or **L^6UO_2**) with one equivalent of NaOTf and one equivalent of a strong ligand triphenylphosphine oxide (PPh_3O), as a ^{31}P NMR probe. We chose PPh_3O since in our previous work (as described in Chapter 5), we have shown that PPh_3O can be used as a ^{31}P NMR probe to quantify the Lewis acidity of redox-inactive metal ions in polar organic solvents, especially in deuterated acetonitrile (d_3-MeCN).[14] Our assumption is that the reaction of NaOTf and **L^5UO_2** or **L^6UO_2** complexes is quick and is possibly forming **L^5UO_2Na** and **L^6UO_2Na**, respectively. We can say this confidently since 1:1 experiment in our *in situ* NMR and *in situ* CV experiments showed shifts in the peaks as soon as the Lewis acidic triflate salts were added to the solution. Our PPh_3O study in d_3-MeCN showed that the peak in the $^{31}P\{^1H\}$ NMR for **L^5UO_2** case (25.39 ppm) is more deshielded in comparison to the peak observed for the **L^6UO_2** case (25.28 ppm) by 0.11 ppm (see Appendix C, Figure C81). This suggests that Na^+ ion is more Lewis acidic in the less Lewis basic 15-crown-5-like site. As a control, we performed an NMR experiment with only PPh_3O and NaOTf present in the d_3-MeCN solution. The $^{31}P\{^1H\}$ NMR, in this case, is significantly more deshielded to a value of 25.83 ppm attributable to the lack of a macrocyclic stabilization environment by Lewis basic crown-ether-like sites. We also monitored $^{19}F\{^1H\}$ NMR in these experiments (see Appendix C, Figure C82). The position of the single peak observed for **L^5UO_2**, and **L^6UO_2** case in the ^{19}F NMR differ only by 0.01 ppm, suggesting that the triflate counteranion is not bound to the Na^+ ion when it is in the crown-ether-like cavity and that the triflate is replaced by a strongly donating PPh_3O ligand. A similar trend was observed when the *in situ* NMR experiment was performed by mixing

monometallic UO_2^{2+} complex (**L^5UO_2** or **L^6UO_2**) with one equivalent of KOTf and one equivalent of PPh_3O (see Appendix C, Figures C83 and C84).

In addition to the uniform trend in $E_{1/2}$ observed for the heterobimetallic UO_2^{2+} complexes, the more Lewis acidic metal ions also affect the shape of the voltammograms. The voltammogram appears to become rather broad systematically as the Lewis acidity of the redox-inactive metal ions increases. This broadness can be quantified by measuring ΔE_p values (see Tables 4.5 and 4.6) at 100 mV/s from the CV data for the UO_2^{2+} complexes. As expected, the ΔE_p values increase with increasing Lewis acidity of the redox-inactive metal ions indicating diminished electrochemical reversibility, lower rates of heterogeneous electron transfer rates (k^0), and greater reorganization energy (λ). The ΔE_p values, especially for complexes containing Ca^{2+} are four times larger than their corresponding monometallic analogues suggesting significantly lower k^0 values and therefore larger λ values (a factor governing the kinetics of electron transfer to the UO_2^{2+} complexes), associated with higher charge and larger ionic radii of Ca^{2+} ion.

This qualitative explanation of k^0 and λ can be further elaborated by quantitative calculation of these parameters from the CV data. The k^0 values are determined by using the method of Nicholson[27] while the λ values are based upon methods developed by Savéant and Costentin (see Appendix C).[28] In general, the faster electron transfer (larger k^0 value) is associated with higher reorganization energy (larger λ value). The parameter λ includes two components: (i) an inner-sphere component corresponding to reorganization of the complex undergoing reduction (ii) an outer-sphere component representing reorientation of the solvent/environment around the complex upon reduction. However, although reorganization energy values can be readily calculated using the noted literature methods, the relationship

of the obtained values to more traditional reorganization energies obtained from studies of electron transfer in homogeneous solution may not be straightforward. We have calculated and included the reorganization energy values in this Dissertation for completeness, but rigorous interpretation of this aspect of the work deserves further attention.

An interesting feature that we observed in the CV data, particularly for the **L^5UO_2Na** and **L^6UO_2Na** complexes, was the difference in the shape of the voltammogram between the two complexes. We wondered if our calculations of k^0 and λ will give some insights into this phenomenon. To achieve this, we tabulated (Tables 4.5 and 4.6) and separately plotted a graph of k^0 vs. pK_a and λ vs. pK_a for both the families of our bimetallic complexes (Figure 4.6). To our delight, the k^0 value for the **L^5UO_2Na** complex is significantly higher as compared to the other complexes in the **L^5UO_2M** series, producing a "volcano" like plot (Figure 4.6). This non-monotonic trend surprises us and suggests that Na^+ is a good fit for the 15-crown-5-like cavity in our series of complexes studied here, complementing the smallest value of ω_{crown} for the **L^5UO_2Na** complex from the XRD data. As we go higher in Lewis acidity than Na^+, the k^0 values decreases for **L^5UO_2Li** and **L^5UO_2Ca**, with the k^0 for **L^5UO_2Ca** being the smallest among the series of **L^5UO_2M** complexes. We attribute this behavior observed for the series of **L^5UO_2Na, L^5UO_2Li,** and **L^5UO_2Ca** to a Lewis acid effect in that the highest Lewis acidic metal ion (see Table 4.3) in the heterobimetallic species is associated with the slowest heterogeneous electron transfer rate. Furthermore, as we go lower in Lewis acidity than Na^+, the k^0 values decreases again for **L^5UO_2K, L^5UO_2Rb,** and **L^5UO_2Cs,** with the k^0 for **L^5UO_2Cs** being the smallest among the series. We attribute this behavior observed for the series of **L^5UO_2Na, L^5UO_2K, L^5UO_2Rb,** and **L^5UO_2Cs** to a supramolecular effect in that the Lewis acidic metal ion with the larger ionic radii (see Table

4.3) in the heterobimetallic species is associated with the slowest heterogeneous electron transfer rate.

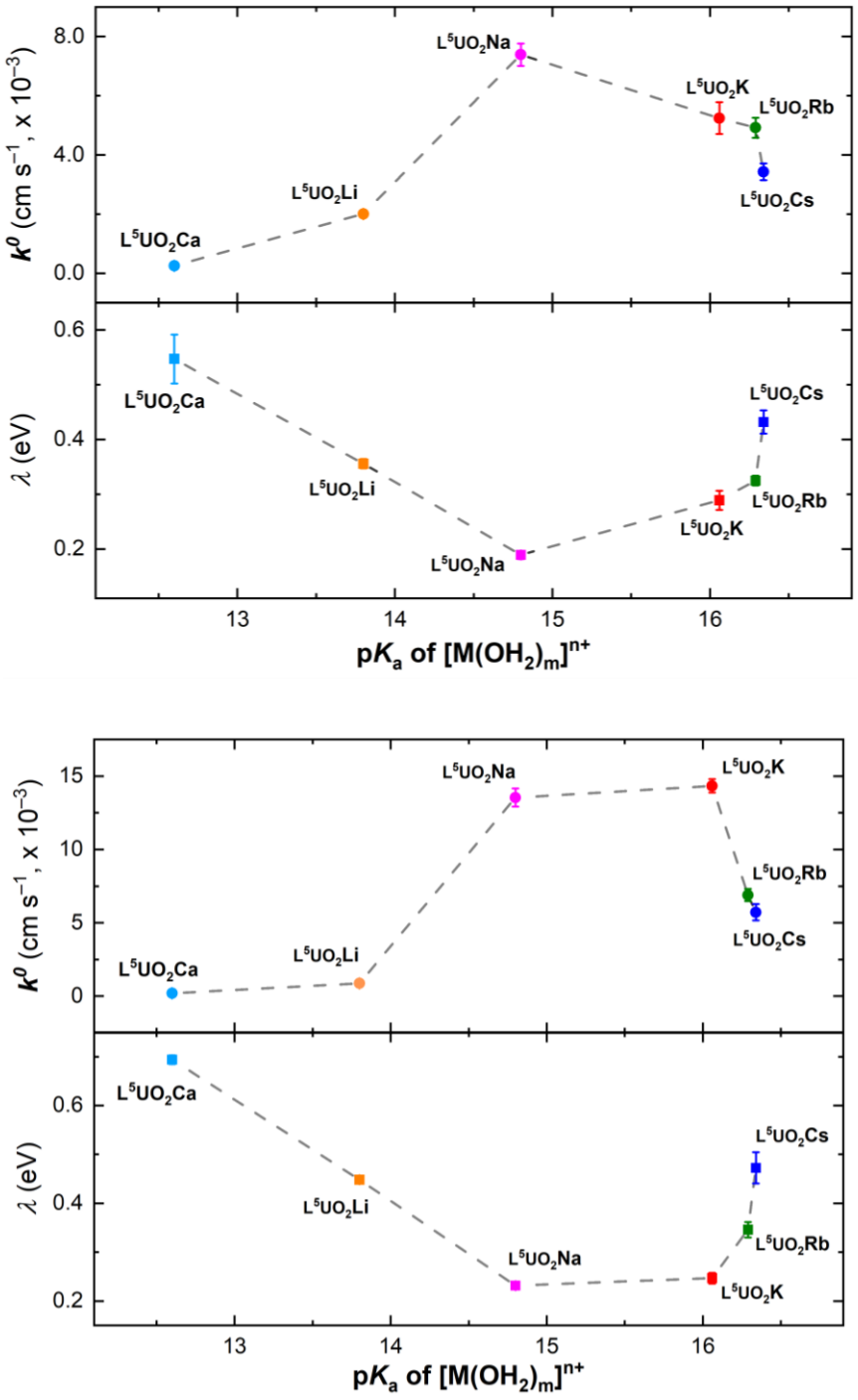

Figure 4.6. Plots of k_0 and λ vs. pK_a of [**M**$(H_2O)_m]^{n+}$ for the (i) **L^{5}UO$_2$** and **L^{5}UO$_2$M** complexes (top); (ii) **L^{6}UO$_2$** and **L^{6}UO$_2$M** complexes (bottom).

A similar trend was seen in the λ values for the **L^5UO_2M** complexes with the **L^5UO_2** **L^5UO_2Na** experiencing the smallest reorganization energy. We hypothesize that the diminished reorganization energy associated with the bimetallic species incorporating Na^+, is associated with macrocyclic rigidification, wherein the structures of the oxidized and reduced forms of the complexes differ less when there is a good size match between the guest (Na^+) and the host (**L^5UO_2**) species. Again, we feel at this stage that this viewpoint on the data is appropriate but further work to understand how our values of λ correspond to more established systems would seem to be called for.

We next moved on to study similar effects in complexes containing appended 18-crown-6-like cavity, i.e., **L^6UO_2** and **L^6UO_2M** complexes. Our assumption was that the k_0 value would be the largest for the **L^6UO_2** in the presence of one equivalent of KOTf. This assumption was based on the literature precedence of the good size match between K^+ and 18-crown-6 crown ether.[29] However, contrary to our assumption, determination of k_0 and λ values and plotting those parameters vs. the Lewis acid pK_a values reveal a good size match for both Na^+ and K^+ ions with the **L^6UO_2** complex (as judged by their higher k^0 and lower λ values in the series). All this suggests that Na^+ ion binds tightly to the 15-crown-5-like site in the **L^5UO_2** complex while both Na^+ and K^+ ions bind strongly to the 18-crown-6-like site in the **L^6UO_2** complex.

With these results in hand, we turned to the quantitative determination of the binding of the monovalent ions in both the monometallic UO_2^{2+} complexes. In particular, we imagined that titration studies of 1 equivalent of either **L^5UO_2** or **L^6UO_2** complex with increasing concentrations of the metal triflate salts of interest could reveal binding/association constants of the metal ions in the crown-ether-like cavities of these monometallic UO_2^{2+} complexes.

Thus, we carried out titration studies in d_3-MeCN, beginning with the triflate salts of the monovalent ions (Cs^+, Rb^+, K^+, Na^+, and Li^+). The δ^1H, corresponding to the protons of the N–CH_3, was measured for one equiv. of **L^5UO_2** or **L^6UO_2** in the presence of increasing concentrations of the individual metal salts (see Appendix C, Figures C41 – C80 for raw ^{1}H NMR data). As anticipated, the $\Delta\delta^1$H values shift, initially undergoing greater changes but eventually leveling off at higher titrant ion equivalencies, as the concentration of metal salt is increased (Figure 4.7). Inspection of the raw ^{1}H NMR data (see Appendix C, Figures S9-S13) also reveals that the more Lewis acidic ions (based on prior pK_a data) result in the largest absolute shifts in $\Delta\delta^1$H.

The titration data shown in Figure 4.7 strongly suggest that the monovalent ions in this study interact with **L^5UO_2** or **L^6UO_2** in a 1:1 stoichiometry, even in the presence of large excesses (>5 equiv.) of the individual metal ions. The values of association constant (K_a) and maximum achievable chemical shift difference ($\Delta\delta_{max}{}^1$H) can be extracted (see Tables 4.7 and 4.8) by the fitting of the collected data to a 1:1 binding isotherm,[30] as was discussed in our previous work (refer Chapter 5).[14] The K_a values quantify the tendency of each monovalent ion to associate with the monometallic UO_2^{2+} complexes in d_3-MeCN, while the $\Delta\delta_{max}{}^1$H values describe the maximum possible deshielding of the ^{1}H center in **L^5UO_2** or **L^6UO_2**, specifically at the condition where the metal ion of interest is maximally occupying its binding site. As expected, the K_a values for the experiments performed with **L^5UO_2** as 'host' species and Cs^+, Rb^+, or K^+ ions as 'guest' species increases with the decrease in the ionic radii suggesting a tighter association of the K^+ ion as compared to Cs^+ and Rb^+ in the 15-crown-5-like site of the **L^5UO_2**. The fitting of the titration data for the Li^+ and Na^+ ions with **L^5UO_2**, however, did not converge and returned poor-fitting results in both cases. This

could be attributed to the much tighter association of the smaller Li^+ and Na^+ ions with 15-crown-5-like cavity of the **L^{5}UO$_2$** complex, as judged by the leveling off of the $\Delta\delta_{max}$^{1}H values at or near 1:1 equivalence in the titration data.

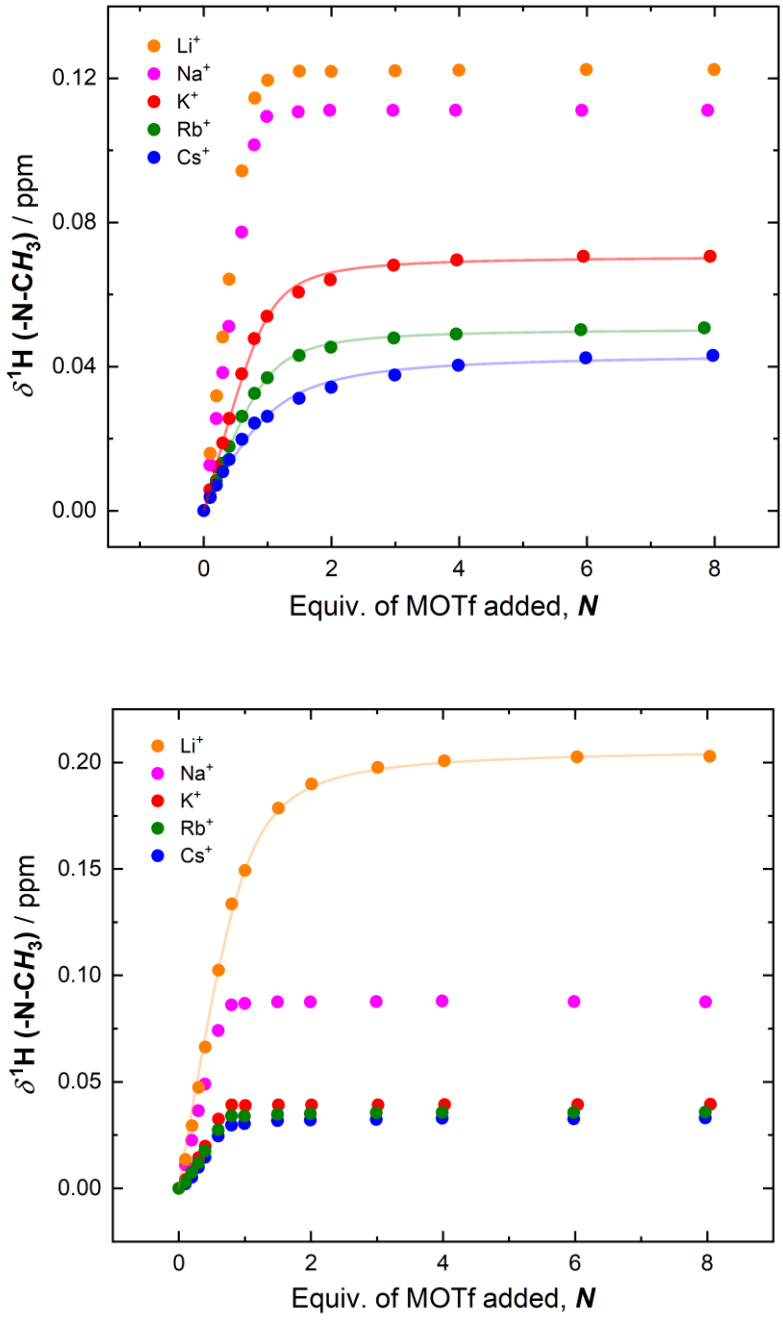

Figure 4.7. Titration studies showing 1:1 binding of monovalent metal ions and (i) **L^{5}UO$_2$** and (ii) **L^{6}UO$_2$**. Solvent: d_3-MeCN.

Table 4.7. Metal-aqua complex pK_a values and fitted parameters from 1:1 binding of **L^5UO_2** to the monovalent metal ions in this study.

Ion	pK_a of $[M(H_2O)_m]^{n+}$	$\Delta\delta_{max}$ ^{1}H / ppm	K_a / M^{-1}
Cs^+	16.34[a]	0.04	547 ± 78
Rb^+	16.29[a]	0.05	1365 ± 125
K^+	16.06[a]	0.07	1836 ± 258
Na^+	14.8[b]	0.11	$>10^5$
Li^+	13.8[b]	0.12	$>10^5$

[a]Taken from reference 14. [b]Taken from reference 21.

Table 4.8. Metal-aqua complex pK_a values and fitted parameters from 1:1 binding of **L^6UO_2** to the monovalent metal ions in this study.

Ion	pK_a of $[M(H_2O)_m]^{n+}$	$\Delta\delta_{max}$ ^{1}H / ppm	K_a / M^{-1}
Cs^+	16.34[a]	0.03	$>10^5$
Rb^+	16.29	0.04	$>10^5$
K^+	16.06[a]	0.04	$>10^5$
Na^+	14.8[b]	0.09	$>10^5$
Li^+	13.8[b]	0.21	1367 ± 184

[a]Taken from reference 14. [b]Taken from reference 21.

Similar tight associations were observed from the titration experiments of **L^6UO_2** complex with relatively larger ions (Na^+, K^+, Rb^+, Cs^+), and therefore, accurate values of the association constant for these four series of ions could not be obtained (Table 4.8). Notably, these tighter binding effects ($>10^5$ M^{-1}) are prevalent in the world of supramolecular chemistry, and the determination of association constant for such data is a limitation of the

simple NMR titration methods. Therefore, ongoing work in our laboratories is focused on obtaining further information on the association constants for ions that bind strongly to the crown-ether-like sites in our systems by using complex NMR methods such as competition experiments.

4.3 Conclusions

In conclusion, we have shown that the redox-inactive Lewis acids and ligand structure can uniformly and effectively tune the redox properties of U^{VI}/U^{V} chemistry in both the families of our macrocyclic UO_2^{2+} complexes. Furthermore, electrochemical and NMR titration studies suggest that the best combination of the "host-guest" system, as judged by optimized and rapid reduction as well as highest association constant, is formed when $\mathbf{L^5UO_2}$ interacts with 1 equivalent of Na^+. Through these findings, we were able to determine thermodynamic reduction potentials, heterogeneous electron transfer rate constants, and reorganization energy values associated with the U^{VI}/U^{V} redox manifold, which are useful parameters for uranium redox cycling. Taken together, these studies reveal the scope of optimization possible with uranium redox cycling and provide design rules for supramolecular structures to promote efficient electrode-driven actinide chemistry.

4.4 Experimental Details

4.4.1 General Considerations

All manipulations were carried out in dry NL6-filled gloveboxes (Vacuum Atmospheres Co., Hawthorne, CA) or under N_2 atmosphere using standard Schlenk techniques unless otherwise noted. All solvents were of commercial grade and dried over activated alumina using a PPT Glass Contour (Nashua, NH) solvent purification system prior to use, and were

stored over molecular sieves. All chemicals were from major commercial suppliers and used as received or after extensive drying. Deuterated NMR solvents were purchased from Cambridge Isotope Laboratories (Tewksbury, MA, USA). ^{1}H and ^{19}F NMR spectra were collected on a 400 MHz Bruker spectrometer (Bruker, Billerica, MA, USA) and referenced to the residual protio-solvent signal[31] in the case of ^{1}H. ^{19}F NMR spectra were referenced and reported relative to CCl_3F as external standards following the recommended scale based on ratios of absolute frequencies (Ξ).[32,33] Chemical shifts (δ) are reported in units of ppm and coupling constants (*J*) are reported in Hz. All experiments were conducted at room temperature (298 K).

Regarding special safety precautions needed for this work, depleted uranium is a weak alpha-particle emitter; all manipulations of U-containing materials should be carried out in a laboratory equipped with appropriate radiation safety protocols.

4.4.2 Electrochemical Methods

Electrochemical experiments were carried out in a NL6-filled glovebox in dry, degassed CH_3CN. 0.10 M tetra(*n*-butylammonium) hexafluorophosphate ($[^{n}Bu_4N]^{+}[PF_6]^{-}$); Sigma-Aldrich, electrochemical grade) served as the solvent and supporting electrolyte. Measurements were carried out with a Gamry Reference 600+ Potentiostat/Galvanostat (Gamry Instruments, Warminster, PA, USA), using a standard three-electrode configuration. The working electrode was the basal plane of highly oriented pyrolytic graphite (HOPG) (GraphiteStore.com, Buffalo Grove, Ill.; surface area: 0.09 cm^2), the counter electrode was a platinum wire (Kurt J. Lesker, Jefferson Hills, PA; 99.99%, 0.5 mm diameter), and a silver wire immersed in electrolyte served as a pseudoreference electrode (CH Instruments). The reference was separated from the working solution by a Vycor frit (Bioanalytical Systems,

Inc., West Lafayette, IN, USA). Ferrocene (Sigma Aldrich, St. Louis, MO, USA; twice-sublimed) was added to the electrolyte solution prior to the beginning of each experiment; the midpoint potential of the ferrocenium/ferrocene couple (denoted as $Fc^{+/0}$) served as an external standard for comparison of the recorded potentials. Concentrations of analytes for cyclic voltammetry were typically 1 mM unless otherwise noted. Experiments were conducted by first scanning cathodically, then anodically on the return sweep.

4.4.3 Synthesis and characterization

Complexes **BaHexa** and $\mathbf{L^6UO_2}$ were prepared according to literature procedures. Complexes **BaPenta** and $\mathbf{L^5UO_2}$ were prepared following literature procedures used for the preparation of **BaHexa** and $\mathbf{L^6UO_2}$, respectively. Spectroscopic characterizations of **BaPenta** and $\mathbf{L^5UO_2}$ by NMR (see Appendix C, Figures C1 – C3) confirmed preparation of the desired compounds. Crystals suitable for X-ray diffraction were obtained by vapor diffusion of diethyl ether into a CH_3CN solution of $\mathbf{L^5UO_2}$ and by vapor diffusion of diethyl ether into a CH_3OH solution of **BaPenta**. **BaPenta,** when dissolved in CD_3CN, contains complex peaks in the ^1H NMR suggesting different conformers of the complex in CD_3CN. This is also evident from the sandwiching nature of the **BaPenta** (*vide infra*) in solid-state (see Appendix C, Figure C85).

BaPenta. ^1H ^1H NMR (400 MHz, CD_3CN) δ 13.59 (bs, 3H), 8.28 (d, J = 13.3 Hz, 2H), 8.16 (d, J = 12.9 Hz, 1H), 6.97 – 6.73 (m, 6H), 6.44 (t, J = 7.9 Hz, 2H), 6.36 (t, J = 7.9 Hz, 1H), 4.22 (t, J = 4.7 Hz, 6H), 4.12 – 3.90 (m, 7H), 3.88 – 3.72 (m, 7H), 3.63 (dd, J = 6.4, 5.3 Hz, 2H), 2.79 – 2.66 (m, 6H), 2.47 (d, J = 11.7 Hz, 2H), 2.32 (s, 3H), 2.15 (s, 1H). $^{19}F\{^1H\}$ NMR (400 MHz, CD_3CN): δ –80.10.

L^5UO_2. ^{1}H NMR (400 MHz, CD_3CN) δ 9.50 (dd, $^4J_{H,H}$ = 2.1 Hz, $^4J_{H,H}$ = 1.1 Hz, 2H), 7.19 (dd, $^3J_{H,H}$ = 7.8 Hz, $^4J_{H,H}$ = 1.6 Hz, 2H), 7.15 (dd, $^3J_{H,H}$ = 7.9 Hz, $^4J_{H,H}$ = 1.6 Hz, 2H), 6.66 (t, $^3J_{H,H}$ = 7.8 Hz, 2H), 5.13 – 5.01 (m, 2H), 4.59 – 4.51 (m, 2H), 4.22 – 4.17 (m, 4H), 4.09 – 4.04 (m, 4H), 3.90 (td, $^3J_{H,H}$ = 13.2, $^4J_{H,H}$ = 4.6 Hz, 2H), 3.62 – 3.56 (m, 2H), 3.23 (s, 3H). Cyclic Voltammetry (0.1 M $[^nBu_4N]^+[PF_6]^-$ in CH_3CN): $E_{1/2}$ = –1.60 V vs. $Fc^{+/0}$.

***In situ* NMR scale preparation of L^5UO_2M complexes**. In a J-young NMR tube under an inert atmosphere, a solution of **L^5UO_2** in CD_3CN was added to 1 equiv. of corresponding metal salt solution in CD_3CN. The contents in the tube were mixed by vigorously shaking the tube, and the solution was left to equilibrate for 5 min before recording the ^{1}H and ^{19}F NMR (see Appendix C, Figures C4 – C15). Crystals suitable for X-ray diffraction were obtained by vapor diffusion of diethyl ether into a CH_3CN solution of the **L^5UO_2M** (M = K, Na, Li) complexes (see Chapter 4).

L^5UO_2Cs. ^{1}H NMR (400 MHz, CD_3CN): δ 9.52 (dd, $^4J_{H,H}$ = 2.1 Hz, $^4J_{H,H}$ = 1.0 Hz, 2H), 7.23 (dd, $^3J_{H,H}$ = 7.9 Hz, $^4J_{H,H}$ = 1.6 Hz, 2H), 7.20 (dd, $^3J_{H,H}$ =7.9 Hz, $^4J_{H,H}$ = 1.6 Hz, 2H), 6.72 (t, $^3J_{H,H}$ = 7.9 Hz, 2H), 5.14 – 5.03 (m, 2H), 4.62 – 4.52 (m, 2H), 4.23 – 4.15 (m, 4H), 4.04 – 3.96 (m, 4H), 3.89 (td, $^3J_{H,H}$ = 13.2 Hz, $^4J_{H,H}$ = 4.5 Hz, 2H), 3.68 – 3.60 (m, 2H), 3.26 (s, 3H). $^{19}F\{^1H\}$ NMR (400 MHz, CD_3CN): δ –80.22. Cyclic Voltammetry (0.1 M $[^nBu_4N]^+[PF_6]^-$ in CH_3CN): $E_{1/2}$ = –1.46 V vs. $Fc^{+/0}$.

L^5UO_2Rb. ^{1}H NMR (400 MHz, CD_3CN): δ 9.52 (dd, $^4J_{H,H}$ = 2.1 Hz, $^4J_{H,H}$ = 1.1 Hz, 2H), 7.28 (dd, $^3J_{H,H}$ = 7.9 Hz, $^4J_{H,H}$ = 1.5 Hz, 2H), 7.22 (dd, $^3J_{H,H}$ = 7.9 Hz, $^4J_{H,H}$ = 1.6 Hz, 2H), 6.74 (t, $^3J_{H,H}$ = 7.9 Hz, 2H), 5.16 – 5.05 (m, 2H), 4.62 – 4.53 (m, 2H), 4.31 – 4.19 (m, 4H), 4.08 – 4.01 (m, 4H), 3.90 (td, $^3J_{H,H}$ = 13.2 Hz, $^4J_{H,H}$ = 4.5 Hz, 2H), 3.70 – 3.61 (m, 2H), 3.27

(s, 3H). $^{19}F\{^{1}H\}$ NMR (400 MHz, CD_3CN): δ –80.22. Cyclic Voltammetry (0.1 M $[^{n}Bu_4N]^{+}[PF_6]^{-}$ in CH_3CN): $E_{1/2}$ = –1.45 V vs. $Fc^{+/0}$.

L^5UO_2K. ^{1}H NMR (400 MHz, CD_3CN) δ 9.52 (dd, $^{4}J_{H,H}$ = 2.1 Hz, $^{4}J_{H,H}$ = 1.1 Hz, 2H), 7.31 (dd, $^{3}J_{H,H}$ = 7.9, $^{4}J_{H,H}$ = 1.6 Hz, 2H), 7.23 (dd, $^{3}J_{H,H}$ = 7.9, $^{4}J_{H,H}$ = 1.6 Hz, 2H), 6.76 (t, $^{3}J_{H,H}$ = 7.9 Hz, 2H), 5.17 – 5.05 (m, 2H), 4.64 – 4.54 (m, 2H), 4.36 – 4.24 (m, 4H), 4.12 – 4.02 (m, 4H), 3.91 (td, $^{3}J_{H,H}$ = 13.2 Hz, $^{4}J_{H,H}$ = 4.6 Hz, 2H), 3.70 – 3.62 (m, 2H), 3.28 (s, 3H). $^{19}F\{^{1}H\}$ NMR (400 MHz, CD_3CN): δ –80.22. Cyclic Voltammetry (0.1 M $[^{n}Bu_4N]^{+}[PF_6]^{-}$ in CH_3CN): $E_{1/2}$ = –1.42 V vs. $Fc^{+/0}$.

L^5UO_2Na. ^{1}H NMR (400 MHz, CD_3CN) δ 9.52 (dd, $^{4}J_{H,H}$ = 2.1 Hz, $^{4}J_{H,H}$ = 1.1 Hz, 2H), 7.36 (dd, $^{3}J_{H,H}$ = 7.9 Hz, $^{4}J_{H,H}$ = 1.6 Hz, 2H), 7.28 (dd, $^{3}J_{H,H}$ = 7.9 Hz, $^{4}J_{H,H}$ = 1.5 Hz, 2H), 6.82 (t, $^{3}J_{H,H}$ = 7.9 Hz, 2H), 5.21 – 5.10 (m, 2H), 4.66 – 4.57 (m, 2H), 4.39 – 4.34 (m, 4H), 4.15 – 4.10 (m, 4H), 3.96 (td, $^{3}J_{H,H}$ = 13.3 Hz, $^{4}J_{H,H}$ = 4.5 Hz, 2H), 3.75 – 3.69 (m, 2H), 3.34 (s, 3H). $^{19}F\{^{1}H\}$ NMR (400 MHz, CD_3CN): δ –80.21. Cyclic Voltammetry (0.1 M $[^{n}Bu_4N]^{+}[PF_6]^{-}$ in CH_3CN): $E_{1/2}$ = –1.32 V vs. $Fc^{+/0}$.

L^5UO_2Li. ^{1}H NMR (400 MHz, CD_3CN) δ 9.50 (dd, $^{4}J_{H,H}$ = 2.0 Hz, $^{4}J_{H,H}$ = 1.0 Hz, 2H), 7.34 (dd, $^{3}J_{H,H}$ = 7.9 Hz, $^{4}J_{H,H}$ = 1.6 Hz, 2H), 7.27 (dd, $^{3}J_{H,H}$ = 8.0 Hz, $^{4}J_{H,H}$ = 1.5 Hz, 2H), 6.82 (t, $^{3}J_{H,H}$ = 7.9 Hz, 2H), 5.16 (m, 2H), 4.66 – 4.58 (m, 2H), 4.40 – 4.31 (m, 4H), 4.17 – 4.05 (m, 4H), 3.96 (td, $^{3}J_{H,H}$ = 13.2 Hz, $^{4}J_{H,H}$ = 4.5 Hz, 2H), 3.77 – 3.69 (m, 2H), 3.35 (s, 3H). $^{19}F\{^{1}H\}$ NMR (400 MHz, CD_3CN): δ –80.22. Cyclic Voltammetry (0.1 M $[^{n}Bu_4N]^{+}[PF_6]^{-}$ in CH_3CN): $E_{1/2}$ = –1.26 V vs. $Fc^{+/0}$.

L^5UO_2Ca. ^{1}H NMR (500 MHz, CD_3CN) δ 9.56 (s, 2H), 7.52 (d, $^{3}J_{H,H}$ = 8.0 Hz, 2H), 7.42 (d, $^{3}J_{H,H}$ = 7.9 Hz, 2H), 6.97 (t, $^{3}J_{H,H}$ = 8.0 Hz, 2H), 5.23 – 5.13 (m, 2H), 4.77 – 4.68 (m,

2H), 4.61 – 4.49 (m, 4H), 4.30 – 4.18 (m, 4H), 4.01 (td, $^{3}J_{H,H}$ = 13.2 Hz, $^{4}J_{H,H}$ = 4.7 Hz, 2H), 3.78 (dd, $^{3}J_{H,H}$ = 12.8 Hz, $^{4}J_{H,H}$ = 4.0 Hz, 2H), 3.38 (s, 3H). $^{19}F\{^{1}H\}$ NMR (500 MHz, CD_3CN): δ –80.18. Cyclic Voltammetry (0.1 M $[^{n}Bu_4N]^+[PF_6]^-$ in CH_3CN): $E_{1/2}$ = –0.83 V vs. $Fc^{+/0}$.

***In situ* NMR scale preparation of L^6UO_2M complexes**. In a J-young NMR tube under an inert atmosphere, a solution of **L^5UO_2** in CD_3CN was added to 1 equiv. of corresponding metal salt solution in CD_3CN. The contents in the tube were mixed by vigorously shaking the tube, and the solution was left to equilibrate for 5 min before recording the ^{1}H NMR (see Appendix C, Figures C18 – C24). All the **L^6UO_2M** complexes, when dissolved in CD_3CN, contains two conformers in 3:1 ratio, as determined by the integration of peaks in the ^{1}H NMR.

L^6UO_2Cs. ^{1}H NMR (400 MHz, CD_3CN) δ 9.56 (t, *J* = 1.5 Hz, 2H), 9.42 – 9.32 (s, 0.7H), 7.33 (dd, *J* = 8.0, 1.6 Hz, 2H), 7.24 (dd, *J* = 7.9, 1.6 Hz, 2H), 7.18 (dt, *J* = 7.9, 1.8 Hz, 0.7H), 6.97 (d, *J* = 7.6 Hz, 0.5H), 6.76 (t, *J* = 7.9 Hz, 2H), 6.64 (td, *J* = 7.8, 4.1 Hz, 0.7H), 5.08 – 4.88 (m, 3H), 4.64 – 4.30 (m, 7H), 4.07 – 3.46 (m, 18H), 3.21 (s, 3H), 3.16 (s, 1H). Cyclic Voltammetry (0.1 M $[^{n}Bu_4N]^+[PF_6]^-$ in CH_3CN): $E_{1/2}$ = –1.38 V vs. $Fc^{+/0}$.

L^6UO_2K. ^{1}H NMR (400 MHz, CD_3CN) δ 9.56 (t, *J* = 1.5 Hz, 2H), 9.47 – 9.43 (m, 0.7H), 7.35 (dd, *J* = 8.0, 1.6 Hz, 2H), 7.28 - 7.15 (m, 3.5H), 6.78 (t, *J* = 7.9 Hz, 2H), 6.62 (t, *J* = 7.8 Hz, 0.7H), 5.07 – 4.93 (m, 3H), 4.65 – 4.48 (m, 3H), 4.46 – 4.29 (m, 6H), 4.03 – 3.54 (m, 18H), 3.02 (s, 3H), 3.19 – 3.12 (m, 1H). Cyclic Voltammetry (0.1 M $[^{n}Bu_4N]^+[PF_6]^-$ in CH_3CN): $E_{1/2}$ = –1.36 V vs. $Fc^{+/0}$.

L^6UO_2Na. ^{1}H NMR (400 MHz, CD_3CN) δ 9.53 (t, *J* = 1.5 Hz, 2H), 9.50 (s, 0.7H), 7.40 (dd, *J* = 7.9, 1.6 Hz, 2H), 7.32 – 7.20 (m, 3.5H), 6.80 (t, *J* = 7.9 Hz, 2H), 6.72 (t, *J* = 7.9 Hz, 0.7H), 5.12 – 4.98 (m, 3H), 4.67 – 4.52 (m, 3H), 4.48 – 4.34 (m, 6H), 3.99 – 3.59 (m, 18H), 3.27 (s, 3H), 3.24 – 3.21 (m, 1H). Cyclic Voltammetry (0.1 M $[^nBu_4N]^+[PF_6]^-$ in CH_3CN): $E_{1/2}$ = –1.35 V vs. $Fc^{+/0}$.

L^6UO_2Li. ^{1}H NMR (400 MHz, CD_3CN) δ 9.51 (dd, *J* = 2.0, 1.0 Hz, 2H), 9.47 (s, 0.7H), 7.43 (dd, *J* = 7.9, 1.6 Hz, 2H), 7.33 (dd, *J* = 7.9, 1.6 Hz, 3H), 7.26 (dd, *J* = 7.9, 1.6 Hz, 0.7H), 6.81 (t, *J* = 7.9 Hz, 2H), 6.73 (t, *J* = 7.8 Hz, 0.7H), 5.21 – 5.02 (m, 3H), 4.67 – 4.45 (m, 8H), 4.02 – 3.63 (m, 17H), 3.33 (s, 3H), 3.29 – 3.22 (m, 1H). Cyclic Voltammetry (0.1 M $[^nBu_4N]^+[PF_6]^-$ in CH_3CN): $E_{1/2}$ = –1.23 V vs. $Fc^{+/0}$.

4.5 Acknowledgements

The authors thank Dr. Justin Douglas and Sarah Neuenswander for assistance with NMR spectroscopy, and Michael Lemon and Alice Dale for assistance with radiation safety protocols. This work was supported by the US Department of Energy, Office of Science, Office of Basic Energy Sciences through the Early Career Research Program (DE-SC0019169). The authors also acknowledge the US National Institutes of Health for support of the NMR instrumentation (S10OD016360 and S10RR024664) used in this study.

4.6 References

(1) Meinrath, G. Coordination of uranyl(VI) carbonate species in aqueous solutions. *J. Radioanal. Nucl. Chem.* **1996,** *211*, 349−362.

(2) Hixon, A. E.; Powell, B. A. Plutonium environmental chemistry: mechanisms for the surface-mediated reduction of Pu (V/VI). *Environ. Sci.: Process. Impacts* **2018,** *20*, 1306-1322.

(3) Hixon, A. E.; Powell, B. A. Observed changes in the mechanism and rates of Pu (V) reduction on hematite as a function of total plutonium concentration. *Environ. Sci. Technol.* **2014,** *48*, 9255-9262.

(4) Su, J.; Batista, E. R.; Boland, K. S.; Bone, S. E.; Bradley, J. A.; Cary, S. K.; Clark, D. L.; Conradson, S. D.; Ditter, A. S.; Kaltsoyannis, N.; Keith, J. M.; Kerridge, A.; Kozimor, S. A.; Löble, M. W.; Martin, R. L.; Minasian, S. G.; Mocko, V.; La Pierre, H. S.; Seidler, G. T.; Shuh, D. K.; Wilkerson, M. P.; Wolfsberg, L. E.; Yang, P. Energy-Degeneracy-Driven Covalency in Actinide Bonding. *J. Am. Chem. Soc.* **2018,** *140*, 17977-17984.

(5) Kelley, M. P.; Popov, I. A.; Jung, J.; Batista, E. R.; Yang, P. *Nat. Commun.* **2020**, *11*, 1-10.

(6) Marcus, R. A.; Sutin, N. Electron transfers in chemistry and biology. *Biochim. Biophys Acta. – Rev. Bioenerg.* **1985,** *811*, 265-322; b) B. S. Brunschwig, J. Logan, M. D. Newton and N. Sutin, *J. Am. Chem. Soc.* **1980**, *102*, 5798-5809.

(7) Kumar, A.; Lionetti, D.; Day, V. W.; Blakemore, J. D. Redox-Inactive Metal Cations Modulate the Reduction Potential of the Uranyl Ion in Macrocyclic Complexes. *J. Am. Chem. Soc.* **2020**, *142*, 3032-3041.

(8) (a) Arnold, P. L.; Patel, D.; Wilson, C.; Love, J. B. Reduction and selective oxo group silylation of the uranyl dication. *Nature* **2008**, *451*, 315. (b) Schnaars, D. D.; Wu, G.; Hayton, T. W. Silylation of the Uranyl Ion Using $B(C_6F_5)_3$-Activated Et_3SiH. *Inorg.*

Chem. **2011**, *50*, 9642−9649. (c) Arnold, P. L.; Pécharman, A.-F.; Hollis, E.; Yahia, A.; Maron, L.; Parsons, S.; Love, J. B. Uranyl oxo activation and functionalization by metal cation coordination. *Nat. Chem.* **2010**, *2*, 1056. (d) Faizova, R.; White, S.; Scopelliti, R.; Mazzanti, M. The effect of iron binding on uranyl(V) stability. *Chem. Sci.* **2018**, *9*, 7520−7527.

(9) (a) Fukuzumi, S., Electron-transfer properties of high-valent metal-oxo complexes. *Coord. Chem. Rev.* **2013**, *257*, 1564-1575. (b) Nam, W.; Lee, Y. M.; Fukuzumi, S., Tuning Reactivity and Mechanism in Oxidation Reactions by Mononuclear Nonheme Iron(IV)-Oxo Complexes. *Acc. Chem. Res.* **2014**, *47*, 1146-1154. (c) Fukuzumi, S.; Ohkubo, K.; Lee, Y. M.; Nam, W., Lewis Acid Coupled Electron Transfer of Metal-Oxygen Intermediates. *Chem. Eur. J.* **2015**, *21*, 17548-17559. (d) Park, J.; Morimoto, Y.; Lee, Y. M.; Nam, W.; Fukuzumi, S., Unified View of Oxidative C-H Bond Cleavage and Sulfoxidation by a Nonheme Iron(IV)-Oxo Complex via Lewis Acid-Promoted Electron Transfer. *Inorg. Chem.* **2014**, *53*, 3618-3628.

(10) Kumar, A.; Lionetti, D.; Day, V. W.; Blakemore, J. D. Trivalent Lewis Acidic Cations Govern the Electronic Properties and Stability of Heterobimetallic Complexes of Nickel. *Chem. Eur. J.* **2018**, *24*, 141-149.

(11) (a) Kanady, J. S.; Tsui, E. Y.; Day, M. W.; Agapie, T. A synthetic model of the Mn_3Ca subsite of the oxygen-evolving complex in photosystem II. *Science* **2011**, *333*, 733 –736; b) Tsui, E. Y.; Kanady, J. S.; Agapie, T. Synthetic cluster models of biological and heterogeneous manganese catalysts for O_2 evolution. *Inorg. Chem.* **2013**, *52*, 13833 – 13848. (c) Tsui, E. Y.; Tran, R.; Yano, J.; Agapie, T. Redox-inactive metals modulate the reduction potential in heterometallic manganese–oxido clusters. *Nat. Chem.* **2013**, *5*, 293. (d) Lionetti, D.; Suseno, S.; Tsui, E. Y.; Lu, L.; Stich, T. A.; Carsch, K. M.; Nielsen, R. J.; Goddard, W. A.; Britt, R. D.; Agapie, T. Effects of Lewis Acidic Metal Ions (M) on Oxygen-Atom Transfer Reactivity of Heterometallic Mn_3MO_4 Cubane and $Fe_3MO(OH)$ and $Mn_3MO(OH)$ Clusters. *Inorg. Chem.* **2019,** *58*, 2336-2345.

(12) Reath, A. H.; Ziller, J. W.; Tsay, C.; Ryan, A. J.; Yang, J. Y. Redox Potential and Electronic Structure Effects of Proximal Nonredox Active Cations in Cobalt Schiff Base Complexes. *Inorg. Chem.* **2017,** *56,* 3713-3718.

(13) (a) Robinson, J. R.; Carroll, P. J.; Walsh, P. J.; Schelter, E. J. The Impact of Ligand Reorganization on Cerium(III) Oxidation Chemistry. *Angew. Chem. Int. Ed.* **2012**, *51*, 10159-10163. (b) Robinson, J. R.; Gordon, Z.; Booth, C. H.; Carroll, P. J.; Walsh, P. J.; Schelter, E. J. Tuning Reactivity and Electronic Properties through Ligand Reorganization within a Cerium Heterobimetallic Framework. *J. Am. Chem. Soc.* **2013**, *135*, 19016-19024. (c) Rice, N. T.; Su, J.; Gompa, T. P.; Russo, D. R.; Telser, J.; Palatinus, L.; Bacsa, J.; Yang, P.; Batista, E. R.; La Pierre, H. S. Homoleptic Imidophosphorane Stabilization of Tetravalent Cerium. *Inorg. Chem.* **2019,** *58,* 5289-5304.

(14) Kumar, A.; Blakemore, J. D. On the Use of Aqueous Metal-Aqua pK_a Values as a Descriptor of Lewis Acidity. *Inorg. Chem.* **2021,** *60,* 1107-1115.

(15) (a) Milburn, G. H. W.; Truter, M. R.; Vickery, B. L. The crystal structure of a sodium complex, sodium perchlorate–bis-[NN′-ethylenebis(salicylideneiminato)copper(II)]. *Chem. Commun.* **1968**, *19*, 1188 (b) Truter, M. R. *Alkali Metal Complexes with Organic Ligands* (Berlin, Heidelberg) **1973**, pp. 71-111. (c) Floriani, C.; Calderazzo, F.; Randaccio, L. Crystal and molecular structure of a cationic sodium complex: the sodium tetraphenylborate adduct of NN′-ethylenebis(salicylideneiminato)cobalt(II). Cobalt(II), nickel(II), and copper(II) complexes of quadridentate Schiff bases as complexing agents for lithium, sodium, and ammonium cations. *J. Chem. Soc., Chem. Commun.* **1973**, *12*, 384-385.

(16) (a) Van Staveren, C. J.; Fenton, D. E.; Reinhoudt, D. N.; Van Eerden, J.; Harkema, S. Co-complexation of urea and UO_2^{2+} in a Schiff base macrocycle: a mimic of an enzyme binding site. *J. Am. Chem. Soc.* **1987**, *109*, 3456-3458. (b) Van Staveren, C. J.; Van Eerden, J.; Van Veggel, F. C. J. M.; Harkema, S.; Reinhoudt, D. N. Cocomplexation of

neutral guests and electrophilic metal cations in synthetic macrocyclic hosts. *J. Am. Chem. Soc.* **1988**, *110*, 4994-5008.

(17) (a) Zanello, P.; Cinquantini, A.; Guerriero, P.; Tamburini, S.; Vigato, P. A. Electrochemical behaviour of acyclic and macrocyclic complexes of nickel(II), copper(II) and uranyl(VI). *Inorg. Chim. Acta* **1986**, *117*, 91-96. (b) Casellato, U.; Tamburini, S.; Tomasin, P.; Vigato, P. A.; Aime, S.; Botta, M. Synthesis, X-ray Structure, and Solution NMR Studies of Ln(III) Complexes with a Macrocyclic Asymmetric Compartmental Schiff Base. Preference of the Ln(III) Ions for a Crown-Like Coordination Site. *Inorg. Chem.* **1999**, *38*, 2906-2916. (c) Brianese, N.; Casellato, U.; Tamburini, S.; Tomasin, P.; Vigato, P. A., Asymmetric compartmental macrocyclic ligands and related mononuclear and hetero-dinuclear complexes with d- and/or f-metal ions. *Inorg. Chim. Acta* **1999,** *293*, 178-194. (d) Casellato, U.; Tamburini, S.; Tomasin, P.; Vigato, P. A. Uranyl(VI) complexes with [1+1] asymmetric compartmental ligands containing a Schiff base and a crown ether-like chamber. *Inorg. Chim. Acta* **2002**, *341*, 118-126.

(18) Kumar, A.; Lionetti, D.; Day, V. W.; Blakemore, J. D. CCDC 1960625: Experimental Crystal Structure Determination, **2020**, DOI: 10.5517/ccdc.csd.cc23t5z3.

(19) Kumar, A.; Lionetti, D.; Day, V. W.; Blakemore, J. D. CCDC 1960626: Experimental Crystal Structure Determination, **2020**, DOI: 10.5517/ccdc.csd.cc23t605

(20) Kelsey, S.; Kumar, A.; Oliver, A. G.; Day, V. W.; Blakemore, J. D. Promotion and Tuning of the Electrochemical Reduction of Hetero- and Homobimetallic Zinc Complexes. *ChemElectroChem* **2021**, *Advance Article*, doi: 10.1002/celc.202100358.

(21) Perrin, D. D. *Ionisation Constants of Inorganic Acids and Bases in Aqueous Solution*. Pergamon, 1982.

(22) (a) Shannon, R. D.; Prewitt, C. T. Effective ionic radii in oxides and fluorides. *Acta Cryst. B* **1969,** *25*, 925-946. (b) Shannon, R. D.; Prewitt, C. T. Revised values of effective ionic radii. *Acta Cryst. B* **1970,** *26*, 1046-1048. (c) Shannon, R. D. Revised effective ionic

radii and systematic studies of interatomic distances in halides and chalcogenides. *Acta cryst.* A **1976,** *32*, 751-767.

(23) Wulfsberg, G. *Principles of Descriptive Inorganic Chemistry*. University Science Books: 1991.

(24) Kumar, A.; Lionetti, D.; Day, V. W.; Blakemore, J. D. CCDC 1960629: Experimental Crystal Structure Determination, 2020, DOI: 10.5517/ccdc.csd.cc23t638.

(25) Kumar, A.; Lionetti, D.; Day, V. W.; Blakemore, J. D. CCDC 1960628: Experimental Crystal Structure Determination, 2020, DOI: 10.5517/ccdc.csd.cc23t627.

(26) Savéant, J.-M. *Elements of Molecular and Biomolecular Electrochemistry*. Wiley: Hoboken, NJ, 2006.

(27) Nicholson, R. S. Theory and application of cyclic voltammetry for measurement of electrode reaction kinetics. *Anal. Chem.* **1965,** *37*, 1351-1355.

(28) Saveant, J. M.; Costentin, C. *Elements of Molecular and Biomolecular Electrochemistry*, *An Electrochemical Approach to Electron Transfer Chemistry*, Wiley, Hoboken, NJ, **2019**.

(29) Pedersen, C. J. Cyclic polyethers and their complexes with metal salts. *J. Am. Chem. Soc.* **1967**, *89*, 7017-7036.

(30) Thordarson, P. Determining association constants from titration experiments in supramolecular chemistry. *Chem. Soc. Rev.* **2011,** *40*, 1305-1323.

(31) Fulmer, G. R.; Miller, A. J. M.; Sherden, N. H.; Gottlieb, H. E.; Nudelman, A.; Stoltz, B. M.; Bercaw, J. E.; Goldberg, K. I. NMR Chemical Shifts of Trace Impurities: Common Laboratory Solvents, Organics, and Gases in Deuterated Solvents Relevant to the Organometallic Chemist. *Organometallics* **2010**, *29*, 2176-2179.

(32) Harris, R.K.; Becker, E.D.; Cabral de Menezes, S.M.; Goodfellow, R.; Granger, P. NMR nomenclature. Nuclear spin properties and conventions for chemical shifts (IUPAC Recommendations 2001)**.** *Pure Appl. Chem.* **2001**, *73*, 1795-1818.

(33) Harris, R.K.; Becker, E.D.; Cabral de Menezes, S.M.; Granger, P.; Hoffman, R.E.; Zilm, K.W. Further conventions for NMR shielding and chemical shifts (IUPAC Recommendations 2008)**.** *Pure Appl. Chem.* **2008**, *80*, 59-84.

Chapter 5

On the Use of Aqueous Metal-Aqua pK_a Values as a Descriptor of Lewis Acidity

This chapter is adapted from a published manuscript:

Kumar, A; Blakemore, J. D. On the Use of Aqueous Metal-Aqua pK_a Values as a Descriptor of Lewis Acidity. *Inorg. Chem.* **2021**, *60*, 1107 – 1115.

5.1 Introduction

Promotion of small-molecule activation processes by Lewis acids has emerged as an effective strategy for achieving otherwise difficult transformations. For example, the rate of CO_2 reduction by reduced metal complexes can be profoundly accelerated by incorporation of Lewis acids that promote C–O bond cleavage.[1] Similarly, the strong U–O bonds of the uranyl ion (UO_2^{2+}) can often only be activated through the concerted action of both Lewis acids and strong chemical reductants.[2,3] As the interactions between redox-active metals and the Lewis acid play a crucial role in determining reaction outcomes, significant effort remains devoted to development of ligand frameworks designed to bring Lewis acids into close proximity of metal centers, substrates, or reactive moieties of interest.[4,5,6,7]

Inspired by the presence of an essential Ca^{2+} ion in the Oxygen-Evolving Complex (OEC) of Photosystem II,[8,9] numerous research groups have turned to redox-inactive metal ions as a useful class of Lewis acids for modulating redox reactivity.[10,11] Common metal ions used for these purposes span a significant range of sizes/coordination numbers, and are often chosen from among mono-, di-, and tri-valent ions such as K^+, Na^+, Ca^{2+}, Y^{3+}, and Lu^{3+}. Strongly Lewis acidic trivalent cations such as Sc^{3+} attract especially significant attention, as the effects they promote are typically more pronounced than those engendered by weaker acids.[12,13,14,15] Indeed, understanding the relative effect(s) of Lewis acids is of particular interest from the standpoint of tunability and rational catalyst design.

Quantification of Lewis acidities remains an area of significant work despite efforts that have spanned decades.[16] Perhaps the most common Lewis acidity scale is based upon the pK_a value(s) of bound water ligands in metal-aqua complexes of the corresponding Lewis acidic ions. These values were compiled nearly 40 years ago in Perrin's highly cited

volume,[17] and although some ions are associated with only a few measurements, pK_a values are available for most mono-, di-, and tri-valent ions, giving this scale significant power. It has been successfully deployed in many studies in recent years, including those aimed at understanding the modulation of reduction potentials in important bioinorganic model compounds and diverse redox-active species.[18,19]

Most studies of Lewis acidic ion-modulated chemistry are carried out in acetonitrile (MeCN), dichloromethane (CH_2Cl_2), and other polar organic solvents; consequently, the pK_a-based Lewis acidity descriptor measured in water is often used to parametrize behavior in these other solvents, a situation of significant concern since solvent effects are known to strongly influence the outcomes of chemical reactivity. In our view, the abundance of Lewis acid effects that can be successfully interpreted with this scale is surprising. Fukuzumi and co-workers have attempted to bridge the gap, however, by developing an alternative scale based upon parameters derived from Lewis acid-modulated electron paramagnetic resonance spectra collected on *in situ*-generated superoxide species.[20,21] However, this scale is less intuitive and requires specialized equipment for further development, likely impeding its wider adoption. And, more recently, specialized luminescent probe molecules have been studied for quantification of Lewis acidity; in these approaches, the tailored probes and a fluorescence spectrometer are required.[22]

On the other hand, we were surprised to find that the Gutmann-Beckett method, in which Lewis acidity is interrogated by ^{31}P nuclear magnetic resonance (NMR) spectroscopy with a suitable phosphorus-containing probe molecule, typically a phosphine oxide, has not been employed for systematic quantification of the Lewis acidity of redox-inactive metal ions.[23,24] As this method has been found to be effective for alkaline earth metal complexes and some

transition metal compounds,[25,26] we anticipated that studies of the wider family of redox-inactive metal ions by this method might enable direct comparisons with the common aqueous pK_a scale as well as provide insights for new studies of Lewis acid-modulated chemistry.

Here, we report the first uniform measurements of the Lewis acidities of mono-, di-, and tri-valent redox-inactive metals (in the form of their triflate salts) with a modified form of the Gutmann-Beckett method. The chemical shift (δ^{31}P) values of triphenylphosphine oxide (TPPO, our chosen probe molecule) in the presence of various ions display clear trends in both d_3-MeCN and CD_2Cl_2, confirming the usefulness of this method in assaying the Lewis acidity of these metal ions. Titration studies reveal that TPPO binds to monovalent ions (Li^+, Na^+, K^+, Rb^+, and Cs^+) with 1:1 stoichiometry, whereas it can bind multiple divalent ions (Ba^{2+}, Sr^{2+}, and Ca^{2+}) cooperatively as shown by Hill analysis. Together with related findings for the trivalent ions, these studies highlight that association constants and concentration-dependent speciation should be considered carefully in studies of Lewis acid-modulated chemistry.

5.2 Results

In order to carry out this study, we selected the triflate (OTf^-) salts of common monovalent (Li^+, Na^+, K^+, Rb^+, Cs^+), divalent (Ba^{2+}, Sr^{2+}, Ca^{2+}, Zn^{2+}) and trivalent (La^{3+}, Y^{3+}, Lu^{3+}, Sc^{3+}) redox-inactive metals. These salts are attractive in that most are commercially available, all are soluble in common polar organic solvents (MeCN, CH_2Cl_2), and they all feature the weakly coordinating triflate counterion that should not interfere with binding of other ligands (like phosphine oxides) to the metal centers under our conditions. In the case of the commercially available LiOTf, NaOTf, KOTf, $Ba(OTf)_2$, $Ca(OTf)_2$,

$Zn(OTf)_2$, $La(OTf)_3$, $Y(OTf)_3$, $Lu(OTf)_3$, and $Sc(OTf)_3$, we confirmed the purity of the salts after extensive drying (180°C, 24 h; see Experimental Section and Appendix D) by infrared (IR) and ^1H and ^{19}F NMR spectroscopies, encountering no unusual features. RbOTf, CsOTf, and $Sr(OTf)_2$, which are not commercially available, were prepared by addition of triflic acid (HOTf) to aqueous suspensions of Rb_2CO_3, Cs_2CO_3, and $SrCO_3$ followed by extraction with MeCN. Characterization by NMR and powder X-ray diffraction (XRD) analysis (see Experimental Section and Appendix D) confirmed clean generation of the desired salts, which were also dried thoroughly before use.

In Gutmann's pioneering work,[23] triethylphosphine oxide (TEPO) was used as a Lewis base to determine the Lewis acidity of weakly coordinating solvents by observing changes in the ^{31}P chemical shift value ($\delta^{31}P$) when dissolved in the various solvents of interest. Beckett later extended this method, using TEPO to study the Lewis acidity of boron-based Lewis acids.[24] In our work, we selected the more commonly available triphenylphosphine oxide (TPPO) as a Lewis basic probe molecule; TPPO has the simultaneous advantages of high chemical stability and low cost (less than $1 per gram) in comparison to TEPO (ca. $70 per gram). And, appealingly, the predicted steric profiles of TPPO and TEPO are similar, based on geometric considerations from other related compounds.[27] In accord with these considerations, our findings do not suggest any unusual steric influences here.

In order to provide a direct comparison of the Lewis acidities of each of the metal cations in this study, we prepared 1:1 mixtures of each corresponding metal salt and TPPO in both d_3-MeCN and CD_2Cl_2 and interrogated the samples by $^{31}P\{^1H\}$ NMR. In all cases, the $\delta^{31}P$ of TPPO was shifted downfield, indicating association between the Lewis acidic ions and the TPPO probe molecule. In d_3-MeCN, all of the samples (except Lu^{3+} and Sc^{3+}) revealed

a single ^{31}P NMR resonance; very small $\Delta\delta^{31}$P values were observed for the monovalent metal ions, while greater downfield shifts were measured for the di- and tri-valent metal ions (see Figure 5.1). In CD_2Cl_2, similar phenomena were observed, except the addition of Y^{3+} and Lu^{3+} resulted in the appearance of multiple resonances (see Appendix D, Figures D7 and D8 for all spectra). Reasonable trends were observed in the data; for example, a fairly large $\Delta\delta^{31}$P (12.5 ppm) was measured for $Zn(OTf)_2$ in d_3-MeCN in comparison with the value for $Ca(OTf)_2$ (7.0 ppm), consistent with the similar charge but smaller size of Zn^{2+}.[28,29,30]

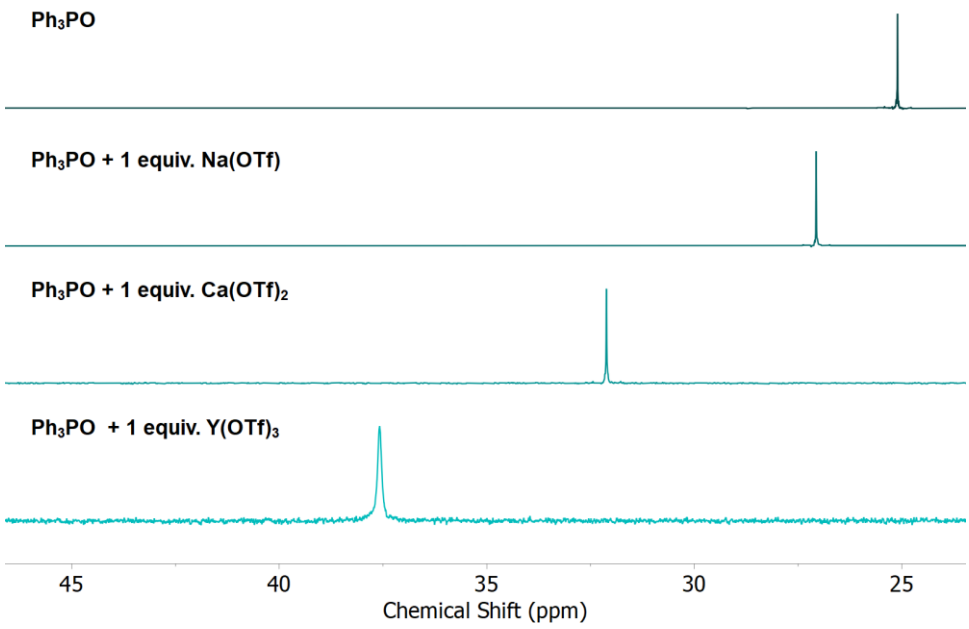

Figure 5.1. ^{31}P{^{1}H} NMR spectra of selected metal ions in the presence of 1 equiv. of TPPO showing the downfield shift with the increase in the Lewis acidity of the ions.

The plotting of the tabulated $\Delta\delta^{31}$P values (see Tables D2 and D3 Appendix D) for each Lewis acid in each solvent as a function of the pK_a values of the corresponding aqueous metal-aqua complexes[17] reveals clear and uniform trends in both cases (see Figure 5.2). In both solvent systems, the pK_a and $\Delta\delta^{31}$P values are tightly co-linear, suggesting similar Lewis acid behavior of the ions in water, acetonitrile, and dichloromethane.

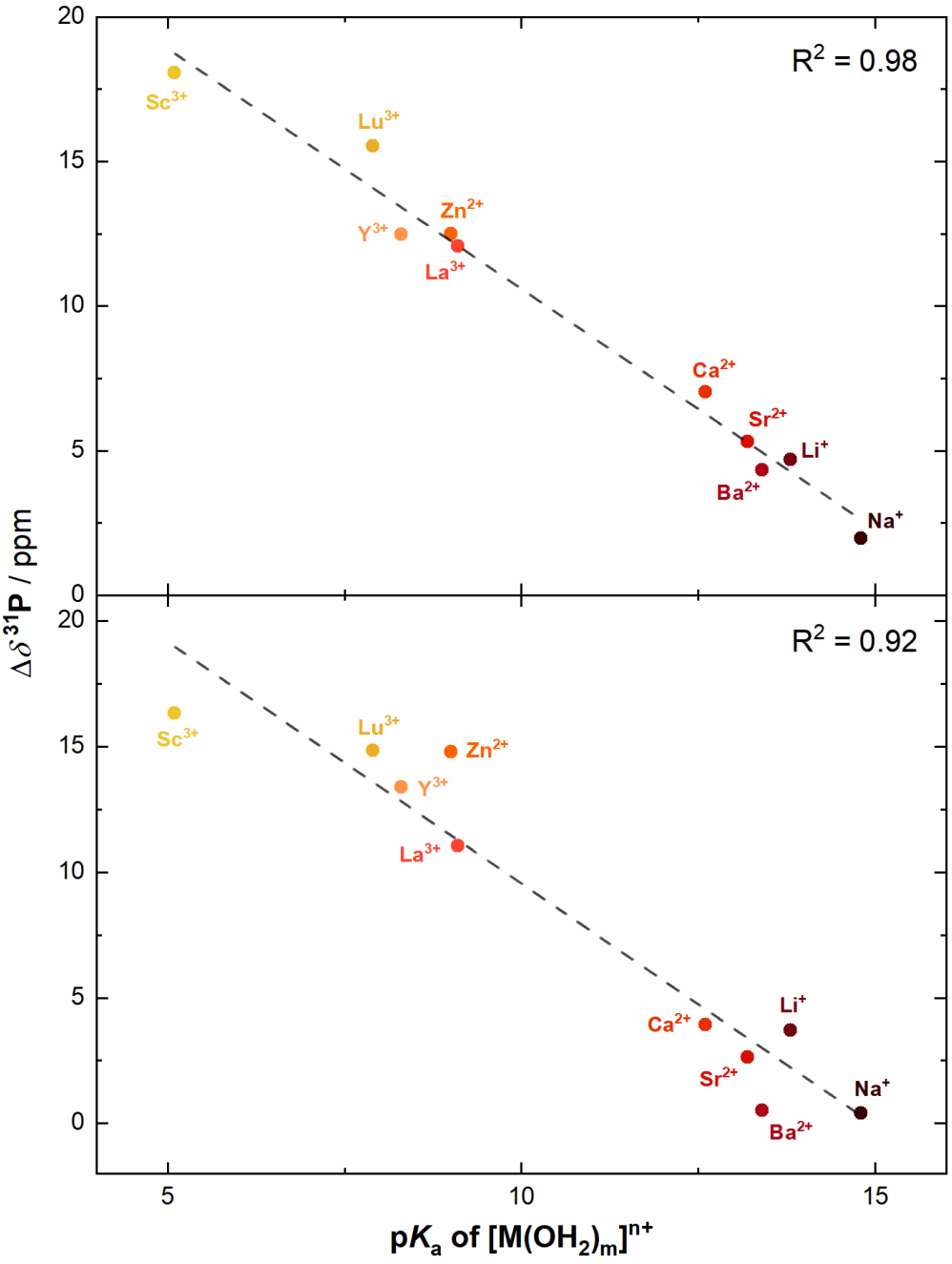

Figure 5.2. Relationship between the $\Delta\delta^{31}$P values for TPPO in the presence of various metal ions in (a) d_3-MeCN (upper panel) and (b) CD_2Cl_2 (lower panel) and the corresponding metal-aqua complex pK_a values. Metal-aqua pK_a values were taken from ref 17.

The co-linearity of the data spans the full series of valencies studied here, indicating that the Gutmann-Beckett-like descriptor of $\Delta\delta^{31}$P accommodates charge and ionic radius effects

in a similar manner to that of the pK_a scale in water. This is perhaps not surprising, however, since deshielding of ^{31}P in TPPO by Lewis acids is not unlike the withdrawal of electron density from bound water molecules in metal-aqua complexes. Changes in Lewis acidity are, indeed, commonly invoked as a cause of metal redox-induced protonation/deprotonation events in systems that display proton-coupled electron transfer behavior.[31] A comparison of the d_3-MeCN and CD_2Cl_2 solvent systems reveals greater scatter in the dichloromethane data, as judged by both goodness-of-fit (0.92 for CD_2Cl_2 versus 0.99 for d_3-MeCN) and error on the slope of the linear fit (10% and 4%, respectively); this may be due to the lesser coordinating nature of dichloromethane, which could make data collected in this solvent more sensitive to trace coordinating impurities (e.g., H_2O, Et_2O, tetrahydrofuran) that could be present under our otherwise air- and moisture-free conditions.

As mentioned above, a shortcoming of the aqueous metal-aqua pK_a values tabulated by Perrin[17] is the lack of data for certain challenging and/or uncommon ions. For example, no pK_a values are available for the less acidic Cs^+ and Rb^+ ions, and only a single imprecise value is available for K^+ (16.0-16.5), attesting to the experimental challenge of working at extreme pH values in water. However, with the relationships mapped in Figure 5.2, the pK_a values for Cs^+, Rb^+, and K^+ in water can be estimated by straightforward measurement of the δ^{31}P values for TPPO in the presence of 1 equivalent of the corresponding triflate salts. As expected, based on their increasing atomic radii, the estimated pK_a values determined in this way for K^+, Rb^+, and Cs^+ decrease across the series (16.06, 16.29, and 16.34; see Table 5.1). Notably, our value for K^+ is within error of a value (16.25) determined by ionization studies not included in Perrin's tabulation.[32] Estimations carried out with data collected in CD_2Cl_2 provide similar results within error (see Table D4 Appendix D).

Table 5.1. Data regarding select monovalent ions from this study.

M^{n+}	δ^{31}P / ppm	$\Delta\delta^{31}$P / ppm	Estimated pK_a[#]
K^+	25.68	0.57	16.06 ± 0.79[†]
Rb^+	25.34	0.20	16.29 ± 0.79[†]
Cs^+	25.25	0.12	16.34 ± 0.78[†]

[#]pK_a values for Cs^+, Rb^+, and K^+ in water were estimated by measuring δ^{31}P values for TPPO in the presence of 1 equivalent of the corresponding triflate salts. [†]Errors on the estimated pK_a values were derived from the uncertainty on the linear fit of the relationship between pK_a and $\Delta\delta^{31}$P as shown in Figure 5.2a.

With our modified form of the Gutmann-Beckett method in hand, more detailed studies are also possible, allowing movement beyond simple measurements on 1:1 solutions of metal triflate salts and TPPO. This is important, in part, due to the closeness of the estimated pK_a values for the monovalent ions given above. In particular, we imagined that titration studies of 1 equiv. of TPPO with increasing concentrations of individual metal salts could reveal association constants and speciation information of interest in interpreting Lewis acid-induced effects in diverse systems.[33]

Thus, beginning with the triflate salts of the monovalent ions (Li^+, Na^+, K^+, Rb^+, and Cs^+), we carried out titration studies (Figure 5.3) in d_3-MeCN wherein the δ^{31}P was measured for 1 equiv. of TPPO in the presence of increasing concentrations of the individual metal salts. As anticipated, the $\Delta\delta^{31}$P values shift as the concentration of metal salt is increased, initially undergoing greater changes but eventually leveling off at higher titrant ion equivalencies. Inspection of the raw ^{31}P NMR data (see Appendix D, Figures D9-D13) also reveals that the more Lewis acidic ions (based on prior pK_a data) result in the largest absolute shifts in $\Delta\delta^{31}$P.

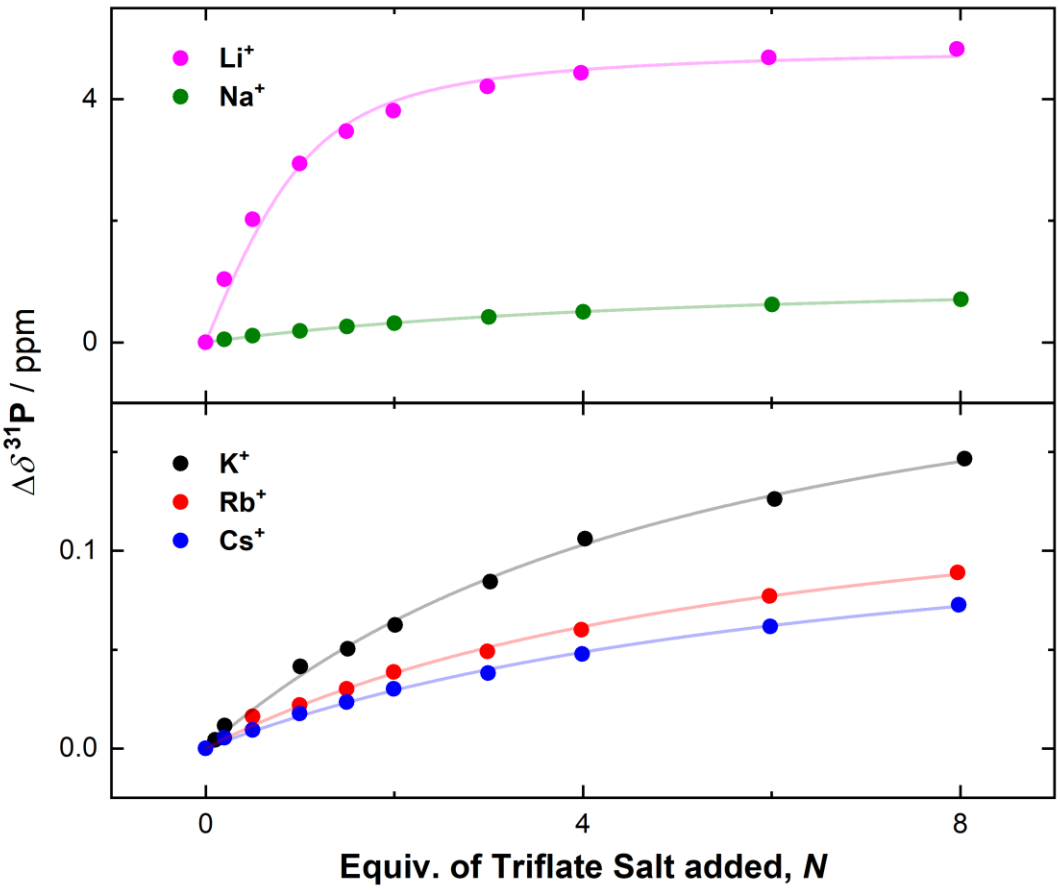

Figure 5.3. Titration studies showing 1:1 binding of monovalent metal ions and TPPO. Solvent: d_3-MeCN. $[TPPO]_0$ = 3.59 mM.

The titration data shown in Figure 5.3 strongly suggest that the monovalent ions in this study interact with TPPO in a 1:1 stoichiometry, even in the presence of large excesses (>5 equiv.) of the individual metal ions. This is borne out by fitting of the collected data to a 1:1 binding isotherm,[34] from which both the association constant (K_a) and maximum chemical shift ($\Delta\delta_{max}{}^{31}P$) can be extracted (see Table 5.2) using the following equation (Equation 1):

$$\frac{\Delta\delta}{\Delta\delta_{\max}} = \frac{1}{2}\left[\left(1 + N + \frac{1}{K_a[H_0]}\right) - \sqrt{\left(1 + N + \frac{1}{K_a[H_0]}\right)^2 - 4N}\right]$$

In this expression, $\Delta\delta_{max}$ is the maximum achievable chemical shift difference; K_a is the association constant. N is the number of equivalents of the given metal ion per TPPO and is equal to the ratio of total concentration of metal ion and TPPO "host" species, $[M^{n+}]/[H_0]$. The K_a values quantify the tendency of each monovalent ion to associate with TPPO in d_3-MeCN, while the $\Delta\delta_{max}{}^{31}P$ values describe the maximum possible deshielding of the ^{31}P center in TPPO, specifically at the condition where the metal ion of interest is maximally occupying its binding site on TPPO. From the data, an obvious trend emerges in the K_a values: the more strongly Lewis acidic ions associate more strongly with TPPO, as shown in the larger K_a values for the smaller ions (see Table 5.2 and Figure D25). The K_a value for Li^+ is the largest by far in this series, perhaps consistent with its quite large charge-to-radius ratio. Similarly, Li^+ serves to most strongly deshield the ^{31}P center in TPPO when it is maximally bound. Na^+ also induces a large $\Delta\delta_{max}{}^{31}P$ value, while the values for K^+, Rb^+, and Cs^+ are all similar. Thus, these more detailed findings measured in d_3-MeCN reinforce that the larger monovalent ions K^+, Rb^+, and Cs^+ all display similar properties in this solvent.

A plot of $\log(\Delta\delta_{max}{}^{31}P)$ vs. pK_a for the data given in Table 5.2 reveals a tightly colinear relationship between these quantities (Figure 5.4). Thus, we conclude that both $\Delta\delta_{max}{}^{31}P$, measured for bound TPPO in d_3-MeCN, and pK_a values, measured for aqua ligands in water, similarly report on the ability of the monovalent ions to modulate the electron density on bound ligands. In the measurements of metal-aqua complex pK_a values, an implicit assumption underpinning the measurements is that the water molecule (aqua ligand) undergoing deprotonation/protonation at a given pH value is resident on the given metal ion. Stated another way, the water molecule which is serving as the probe of Lewis acidity must be closely associated with the metal complex and thus maximally able to readout the Lewis

acidity of the metal center. Accordingly, the $\Delta\delta_{max}{}^{31}P$ values in Table 5.2 are especially tightly correlated with the aqueous pK_a values, because the $\Delta\delta_{max}{}^{31}P$ values represent a direct quantitation of the maximal deshielding effect that a single monovalent Lewis acid can induce on our TPPO probe molecule. In line with this picture, the error on the slope of the relationship in Figure 5.4 (3.5% error: –0.601 ± 0.021 ppm/pK_a; $R^2 = 0.996$) is significantly smaller than that for the $\Delta\delta^{31}P$ data at the arbitrary 1:1 ratio (4.0% error: –1.635 ± 0.065 ppm/pK_a; $R^2 = 0.987$) shown in the upper panel of Figure 5.2.

Table 5.2. Metal-aqua complex pK_a values and fitted parameters from 1:1 binding of TPPO to the monovalent metal ions in this study.

M^{n+}	pK_a of $[M(H_2O)_m]^{n+}$	r / Å for C.N. = 8[c]	K_a / M^{-1}	$\Delta\delta_{max}{}^{31}P$ / ppm
Li^+	13.8[a]	0.92	1009 ± 228[d]	4.89 ± 0.15[d]
Na^+	14.8 [a]	1.18	66.3 ± 4.7	1.10 ± 0.02
K^+	16.06[b]	1.51	61.2 ± 6.0	0.23 ± 0.01
Rb^+	16.29[b]	1.61	55.4 ± 6.7	0.15 ± 0.01
Cs^+	16.34[b]	1.74	45.1 ± 4.4	0.13 ± 0.01

[a]Taken from ref 17. [b]pK_a values for Cs^+, Rb^+, and K^+ in water were estimated by measuring $\delta^{31}P$ values for TPPO in the presence of 1 equivalent of the corresponding triflate salts. [c]From ref 30. [d]Errors were calculated from the direct nonlinear fit of Equation 1, and are given as ±1σ.

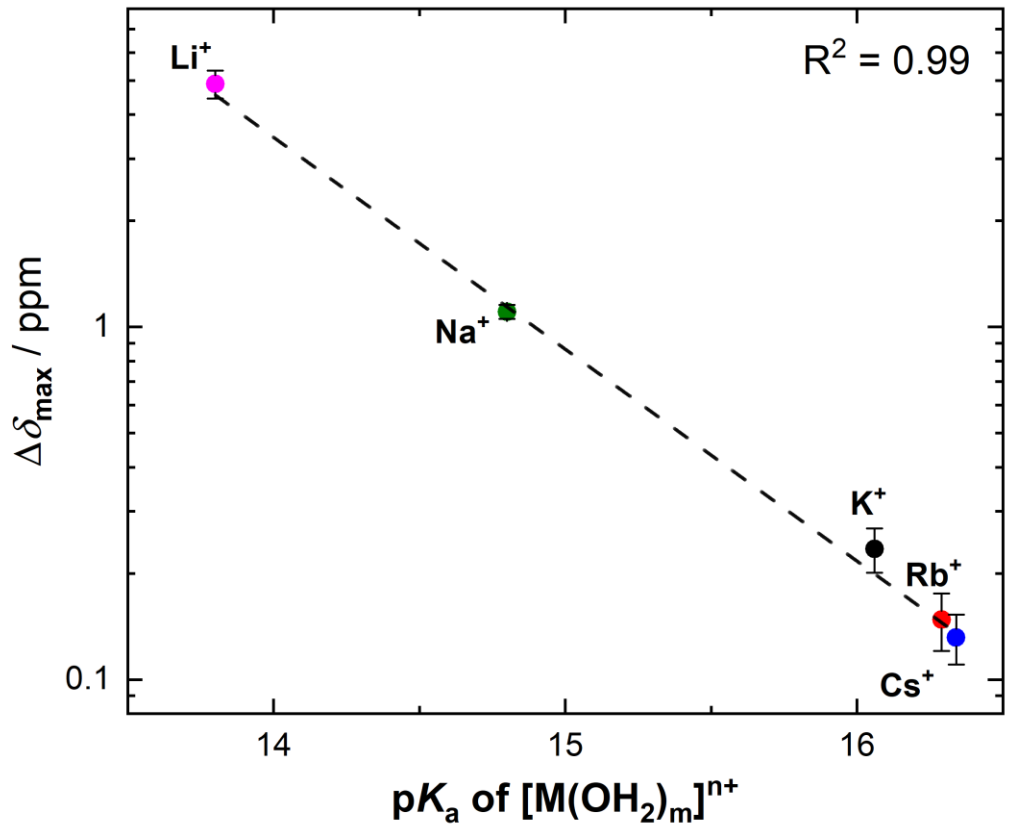

Figure 5.4. Plot of $\Delta\delta_{max}{}^{31}$P for TPPO binding in d_3-MeCN to monovalent metal ions versus the corresponding aqueous metal-aqua pK_a values. Errors on individual $\Delta\delta_{max}{}^{31}$P values were calculated from the direct nonlinear fit of Equation 1, and are given as ±3σ.

Titration studies were also extended to the cases of the divalent ions Ba^{2+}, Sr^{2+}, and Ca^{2+} (see Figure 5.5, upper panel). As we found with the monovalent ions, the $\Delta\delta^{31}$P value for TPPO shifts as the concentration of the given divalent metal salt is increased (see Appendix D, Figures D14-D16 for titration data). However, the large initial changes in $\Delta\delta^{31}$P were all measured at low equivalencies; at or near 1:1 equivalence, the $\Delta\delta^{31}$P value levels off near its apparent maximal value in the cases of all three divalent ions. This indicates that each of the ions tightly associates with TPPO. However, unlike the cases of the monovalent ions, fitting to a 1:1 binding isotherm[34] returns obviously poor results in each case, indicating that multiple binding events are involved in this chemistry and that 1:1 models for the behavior

of these systems are inappropriate. Thus, we conclude that multiple TPPO probe molecules can interact with a single divalent metal ion in d_3-MeCN.

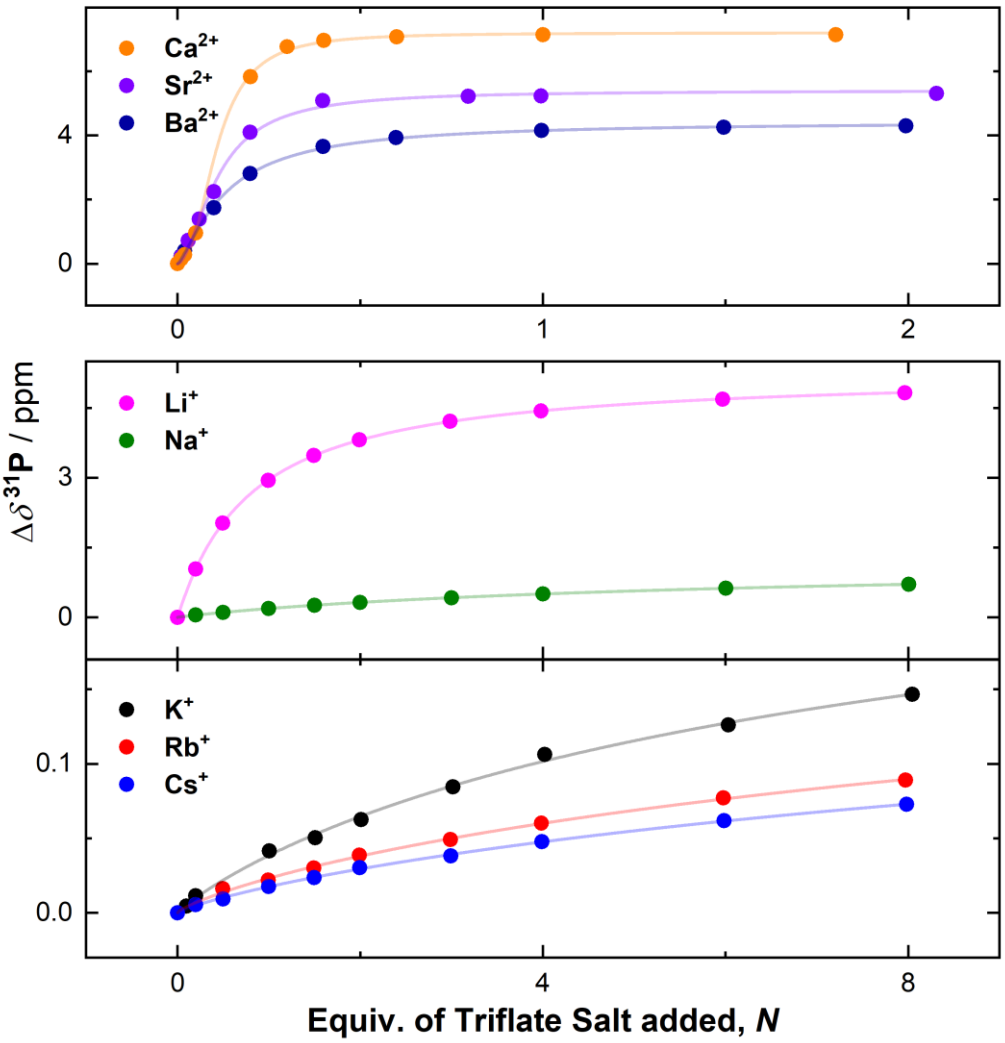

Figure 5.5. Titration data showing fit to the Hill-Langmuir equation given in the main text.

Significant work across several fields has been devoted to the problem of determining association constants for systems behaving with stoichiometries other than 1:1. From the perspective of supramolecular chemistry, the metal ion is the "guest" in our system and the TPPO is the "host"; TPPO can bind either one or two metal ions and could serve as both a terminal ligand or bridging ligand between two metal centers. As structural work is limited

on complexes of the redox-inactive metals with phosphine oxide ligands,[35] little prior work can guide interpretation of our results on the divalent metals. Thordarson,[34] Connors,[36] and others have considered the significant pitfalls in extracting equilibrium binding constants for even the 1:2 and 2:1 situations in host/guest chemistry; in these situations, contrasting with the relatively simple case of 1:1 binding, the needed binding isotherm equations are cubic and feature multiple unknown parameters that are challenging to extract.

On the other hand, the two regimes in our titration data for the divalent ions (with a nearly linear regime at low metal ion concentration and plateauing region at moderate to high concentrations) resemble behavior common in enzymology that can be described by the Hill-Langmuir Equation.[37,38,39] Indeed, we find that our titration data can be described by a form of the Hill-Langmuir equation; this enables quantitation of the influence of divalent metal ion concentration on the deshielding of the ^{31}P center in TPPO according to the following equation (Equation 2):

$$\Delta\delta = \frac{\Delta\delta'_{\max}(N)^{\alpha}}{\left(K_{1/2}\right)^{\alpha} + (N)^{\alpha}}$$

In this equation, $\Delta\delta'_{\max}$ is the maximum achievable chemical shift difference determined with this relationship, α is the Hill coefficient, and $K_{1/2}$ is the half-maximal concentration constant. *N*, as in Equation 1, is the number of equivalents of the given metal ion per TPPO at a given condition. Notably, Eq. 2 can be rearranged to give its linearized form known as the Hill equation (Equation 3) as follows:

$$\log\left[\frac{\Delta\delta}{\Delta\delta'_{\max} - \Delta\delta}\right] = \alpha \log N - \alpha \log K_{1/2}$$

In both of these expressions, the Hill coefficient, α, provides a measure of the cooperativity of binding of the "guest" ion M to the TPPO "host," while $K_{1/2}$ provides a measure of the affinity between the metal ion and TPPO by reporting the equivalents of M required to achieve half the value of $\Delta\delta'_{max}$ ^{31}P.

Our titration data obey the Hill-Langmuir Equation for both the challenging divalent ions as well as for the monovalent ions (see Table 5.3). In the case of the monovalent ions, the $K_{1/2}$ values match the trend found for the K_a values from the nonlinear fitting to the 1:1 binding isotherm; the stronger Lewis acids with larger K_a values also have smaller $K_{1/2}$ values, meaning the half-maximum chemical shift difference is achieved at lower concentrations than in the case of weaker Lewis acids. Furthermore, the value of α is near unity for most of the monovalent ions (Li^+, Na^+, and K^+), consistent with strictly 1:1 binding that does not involve interaction of multiple ions with a single TPPO unit (see Figure D23 and Table 5.3).

On the other hand, the value of α is less than unity for Rb^+ and Cs^+, suggesting slightly negative cooperativity, perhaps due to the possibility of binding of multiple TPPO molecules to these large ions at low metal ion concentrations (see Table 5.3). This may be reflective of the larger radii of these ions, which are known to give rise to a variety of structural effects in binding to ligands like crown ethers in supramolecular systems. At higher metal ion concentrations, the data saturate at a maximum value, suggesting 1:1 binding of the metal ion to TPPO. The negative cooperativity measured here is consistent with these findings and suggests that the Lewis acidity of a single Rb^+ or Cs^+ is diminished upon binding of a single TPPO, resulting in a smaller K_a value for the second binding event than the first.[40] However, as the values of α are only slightly less than unity, such binding of multiple TPPO molecules

does not play a major role in the chemistry under these conditions. Similarly, a titration of TPPO with Na^+ conducted at more deeply substoichiometric loadings (see Appendix D, Figures D30 and D31) suggests that multiple TPPO molecules can be favored to bind to even this ion when the conditions are right. Overall, though, we anticipate that TPPO can be reliably concluded on the basis of the direct fits to the Hill-Langmuir expression to interact with essentially only a single monovalent ion in these systems in d_3-MeCN.

Table 5.3. Fitted parameters from modeling of titration data with the Hill-Langmuir Equation.

M^{n+}	pK_a of $[M(H_2O)_m]^{n+}$	$\Delta\delta'_{max}$ ^{31}P / ppm [c]	$K_{1/2}$ / equiv. [c]	α [c]
Ca^{2+}	12.6[a]	7.20 ± 0.06	0.11 ± 0.01	2.42 ± 0.10
Sr^{2+}	13.2[a]	5.41 ± 0.11	0.11 ± 0.01	1.76 ± 0.15
Ba^{2+}	13.4[a]	4.45 ± 0.05	0.13 ± 0.01	1.31 ± 0.05
Li^+	13.8[a]	5.28 ± 0.01	0.79 ± 0.01	1.03 ± 0.01
Na^+	14.8[a]	1.26 ± 0.03	6.24 ± 0.30	0.96 ± 0.01
K^+	16.06[b]	0.30 ± 0.05	8.27 ± 3.19	0.90 ± 0.08
Rb^+	16.29[b]	0.26 ± 0.07	17.9 ± 10.2	0.81 ± 0.06
Cs^+	16.34[b]	0.23 ± 0.04	19.9 ± 7.4	0.83 ± 0.04

[a]From ref 17. [b]pK_a values for Cs^+, Rb^+, and K^+ in water were estimated by measuring δ^{31}P values for TPPO in the presence of 1 equivalent of the corresponding triflate salts. [c]Errors were calculated from the direct nonlinear fit of Equation 2 and are given as ±1σ.

Conversely, the fitted parameters extracted for the cases of the divalent ions reveal significant positive cooperativity in their binding with TPPO (α values significantly larger

than unity). Cooperativity of this type also implies a scenario in which the metal ion can bind effectively with multiple TPPO probe molecules. However, this situation differs due to the ions' high Lewis acidity from the cases of the larger monovalent ions, in that (i) multiple TPPO molecules can likely bind to each acidic divalent metal ion (for example, at small ion/TPPO ratios) and (ii) multiple divalent metals could bind to a single TPPO unit (for example, at large ion/TPPO ratios). In line with this theory, the few relevant results available from single-crystal X-ray diffraction (XRD) studies reported in the Cambridge Structural Database[41] reveal that phosphine oxides can serve as bridging ligands between redox-inactive metal ions like Na^+ and Co^{2+}.[35,42] Thus, it is reasonable to imagine that the positive cooperativity measured for the divalent ions is associated with, in part, the formation of multimetallic complexes bridged by TPPO ligands. The formation of such structures could presumably help satisfy the demanding coordination requirements of the voraciously Lewis acidic divalent ions.

The quantified parameters described above are consistent with those that can be derived from plotting the measured data with the linearized form of the Hill-Langmuir expression to produce a so-called Hill Plot (Figure 5.6). The apparent linearity of the data for K^+, Na^+, and Li^+ confirms the 1:1 binding stoichiometry and thus non-cooperative nature of the binding to TPPO. On the other hand, there are significant and obvious deviations from linearity in the data for the divalent ions, Ba^{2+} and Ca^{2+} in particular (see Appendix D, Figure D22 for other Hill plots). Indeed, the S-shaped response for Ca^{2+} and Ba^{2+} is consistent with the positive cooperativity indicated by the α values that are greater than unity (see Appendix D, Figures D21-D23). Extrapolation of tangents from the extremes of the data in Figures 5.6 and D22 for the divalent ions can be used to estimate an interaction energy describing the

difference in free energy change (ΔΔG) associated with the first and last metal ion associations with TPPO in these systems displaying cooperative behavior that arises from the greater than 1:1 binding stoichiometry (see Appendix D, Figure D28 and Table D5).[40] The interaction energies for Ca^{2+}, Sr^{2+}, and Ba^{2+} are 3.13, 1.50, and 0.82 kcal/mol, respectively. Perhaps unsurprisingly, these values trend in accord with the Lewis acidity of these ions as judged by the aqueous pK_a values as well as their ionic radii (see Appendix D, Figures D26 and D27). This can be attributed to size-driven variations in their coordination environments, which promote formation of dimeric or multimeric units under these conditions, contrasting with the behavior demonstrated by the monovalent ions.

With these results in hand for titrations of the mono- and di-valent ions, we were excited to pursue similar work with trivalent ions. In particular, we have been interested in the trivalent ions since these highly Lewis acidic species can be reliably used to induce large changes in the chemistry of multimetallic systems.[7,14] However, we find that titration of TPPO with La^{3+}, Y^{3+}, Lu^{3+}, and Sc^{3+} indicates complex speciation in all four cases, as evidenced by the observation of multiple species by $^{31}P\{^{1}H\}$ NMR (see Appendix D, Figures D17-D20). Moreover, the spectra do not uniformly or gradually shift but rather display abrupt transitions, indicating formation and disappearance of multiple species that cannot be readily identified. Although unsatisfactory for titration analysis, these results are consistent with the highly Lewis acidic nature of the trivalent ions and their tendency to display higher coordination numbers that could promote the speciation behavior observed here. However, the maximum shifts in $\delta^{31}P$ are the greatest for the trivalent ions among all those in our study, confirming the usefulness of the behavior at 1:1 stoichiometry (Figure 5.2) as a descriptor of the Lewis acidity of these challenging ions.

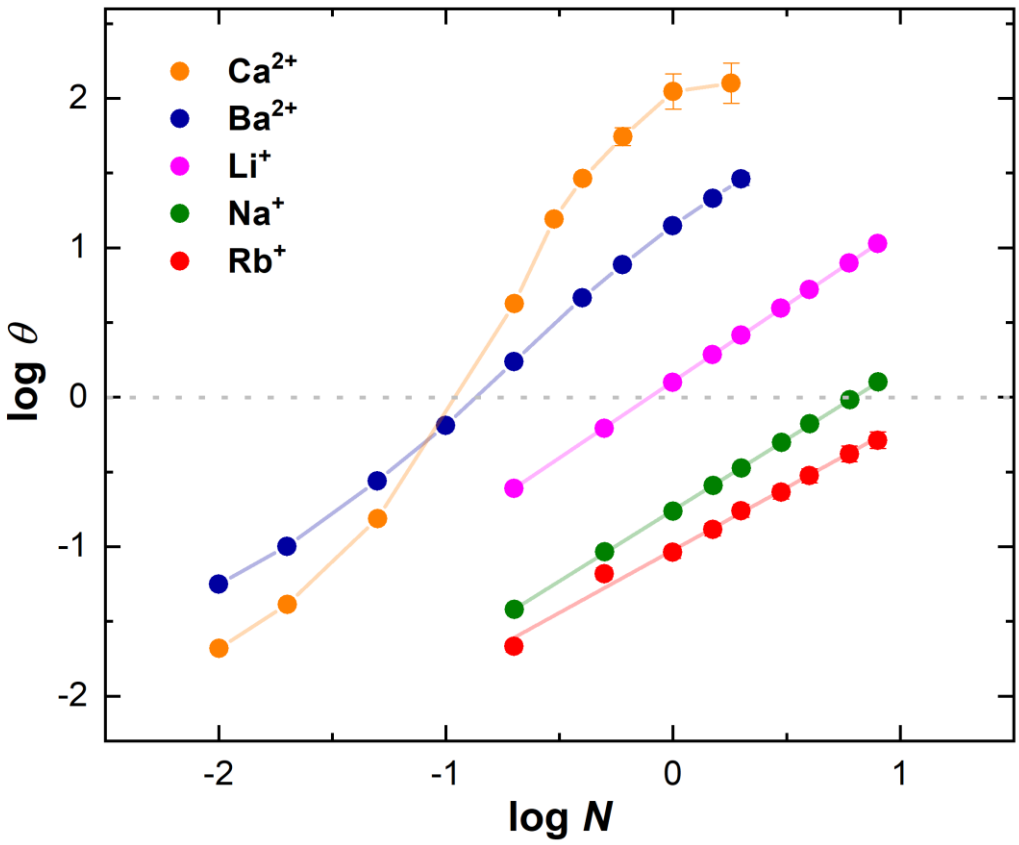

Figure 5.6. Hill plots for selected metal ions in this study. The y-axis is plotted from the relationship $\theta = [\Delta\delta/(\Delta\delta'_{max} - \Delta\delta)]$ representing normalization of the individual ^{31}P NMR shifts ($\Delta\delta$ values) for respective ions from their maximum shift ($\Delta\delta'_{max}$) determined from the direct nonlinear fit of the data to Equation 2. Errors on θ are small and provided in Figure D68 of Appendix D.

5.3 Discussion

We were inspired to carry out this study because of the widespread and successful utilization of metal-aqua pK_a values as descriptors for Lewis acidity. In our own work, we have measured linear free-energy relationships for various properties of heterobimetallic complexes of Ni and UO_2^{2+} (see Chapters 2, 3, and 4) with ranges of redox-inactive metal ions using this scale, despite making the measurements for our compounds in MeCN rather than H_2O.[7,14] The measurements and trends described in the work reported here help to

explain the usefulness of the metal-aqua pK_a descriptor, however, since we have found that the change in $\Delta\delta^{31}$P for TPPO in the presence of various mono-, di-, and tri-valent metal ions in d_3-MeCN and CD_2Cl_2 are co-linear with the pK_a values of the corresponding metal-aqua complexes. The measurements of $\Delta\delta^{31}$P represent a direct interrogation of the Lewis acidity of the metal ions themselves, as they induce deshielding of the ^{31}P center in TPPO when bound. As the $\Delta\delta^{31}$P (d_3-MeCN or CD_2Cl_2) and pK_a (H_2O) values are tightly correlated, we plan to continue using the intuitive aqueous pK_a scale, even for work in polar organic solvents. In our ongoing effort to interrogate changes in the chemical and electrochemical properties of tailored heterobimetallic complexes, we anticipate the pK_a-based descriptor will continue to be useful for both the conceptualization of trends and the plotting of linear free-energy relationships.

On the other hand, this study also highlights that there is significant further work needed in order to better understand and quantify the chemistry of the di- and tri-valent metal ions. In particular, experimental work to reveal details of the speciation chemistry of these ions in both aqueous and organic media would be helpful to better understand the roles that the di- and tri-valent Lewis acids can take in modulating the chemistry of other species. In our titrations with TPPO with the strongly Lewis acidic trivalent ions, we directly observed the formation of various species by ^{31}P NMR under conditions where only TPPO, OTf^-, and d_3-MeCN were available as ligands. These conditions are not unlike those often used for modulation of molecular catalysts in which exogenous Lewis acids are added to solutions containing reactive metal complexes that do not necessarily feature obvious binding sites for secondary metal ions. For example, the nature of interactions between Sc^{3+} and metal-oxo intermediates remains an area of vigorous investigation.[13,15] Consequently, we anticipate that

significant opportunities lie in the continued development of heterotopic ligand frameworks that can rationally direct binding of Lewis acids to redox-active metal complexes and catalysts. In such constructs, the speciation challenges of the trivalent ions may be overcome, unlocking their full potential to engender new, useful chemical reactivity modes.

5.4 Conclusions

We have used triphenylphosphine oxide (TPPO) as a ^{31}P NMR probe to quantify the Lewis acidity of redox-inactive metal ions in polar organic solvents, namely, deuterated acetonitrile (d^3-MeCN) and deuterated dichloromethane (CD_2Cl_2). A plot of the pK_a values of the corresponding metal-aqua species, $[M(H_2O)_m]^{n+}$, measured in H_2O, vs. the ^{31}P NMR shifts of TPPO in the presence of these metals reveals a tightly co-linear relationship, reinforcing the utility of the common approach of using the aqueous pK_a values as a descriptor of Lewis acidity, regardless of solvent. Our results show that concentration-dependent speciation and formation of multiple metal ion/ligand adducts are possible, especially for the more Lewis acidic di- and tri-valent metals. Taken together, these studies provide new insights into the behavior of the Lewis acidic metal cations in polar organic media and provide a new, uniform measure of Lewis acidity that may be useful in a variety of applications, especially the expanding field of small-molecule activation.

5.5 Experimental Details

5.5.1 General Considerations

All manipulations were carried out in dry N_2-filled gloveboxes (Vacuum Atmospheres Co., Hawthorne, CA) or under a N_2 atmosphere using standard Schlenk techniques unless otherwise noted. All solvents were of commercial grade that were dried over activated

alumina, using a PPT Glass Contour (Nashua, NH) solvent purification system prior to use, and were stored over molecular sieves. All chemicals were from major commercial suppliers and used as received or after extensive drying. CD_3CN and CD_2Cl_2 were purchased from Cambridge Isotope Laboratories (Tewksbury, MA, USA) and dried over 3 Å molecular sieves.

^{1}H, ^{13}C, ^{31}P, and ^{19}F NMR spectra were collected on a 400 MHz Bruker spectrometer (Bruker, Billerica, MA, USA) and referenced to the residual protio-solvent signal[43] in the case of ^{1}H and ^{13}C. ^{31}P and ^{19}F NMR spectra were referenced and reported relative to H_3PO_4 and CCl_3F, respectively, as external standards following the recommended scale based on ratios of absolute frequencies (Ξ).[44,45] Chemical shifts (δ) are reported in units of ppm and coupling constants (*J*) are reported in Hz. All experiments were conducted at room temperature (298 K). Individual error values in this report are based upon numerical fits to multipoint data sets unless otherwise noted.

Infrared (IR) spectra were collected under an inert atmosphere in a dry N_2-filled glovebox (Vacuum Atmospheres Co., Hawthorne, CA). Spectra were collected with a Shimadzu IRSpirit FTIR spectrometer equipped with a QATR-S single-reflection attenuated total reflectance (ATR) accessory and diamond prism plate. Solid samples of the dried triflate salts were interrogated (see Appendix D).

Following the general concept of Gutmann-Beckett method, where triethylphosphine oxide (TEPO) is commonly used as a probe molecule,[23,24] we implemented a modification by using triphenylphosphine oxide (TPPO) in place of TEPO for our experiments. The selection of TPPO as probe molecule was based on its wide availability and low cost. Here, dilute solutions of thoroughly dried triflate salts (Appendix D, Figures D32-D67) were

prepared in d_3-MeCN or CD_2Cl_2 dried over molecular sieves. Under an inert atmosphere in a glovebox, a weighing balance (with 0.1 mg precision) was used to prepare samples containing TPPO and the desired triflate salt. To estimate the error on the mass values, replicate mass readings were taken over 3 h (Appendix D, Table D6) on a representative sample of triflate salt (ca. 5 mg); the average value and estimated standard deviation were 5.5 ± 0.1 mg, representing a tolerable 1.8% error. For NMR measurements, dilute solutions of the triflate salts were prepared in d_3-MeCN; subsequently, varying volumes (ranging from 10 to 1000 μL) of these standard triflate salt solutions were then added to a TPPO solution via Hamilton microsyringe. The $^{31}P\{^1H\}$ NMR shifts for the TPPO probe molecule were then recorded; the chemical shifts are reported here with an accuracy of 0.01 ppm. Our group has found that this level of accuracy is appropriate, based on external referencing studies.

5.5.2 Synthesis and Characterization

Synthesis of $Sr(OTf)_2$. $Sr(OTf)_2$ was synthesized by following a modified literature procedure.[46] A three-necked flask was loaded with strontium carbonate ($SrCO_3$, 2.59 g, 17.5 mmol) and CH_3CN, forming a suspension. Under an inert atmosphere of N_2, triflic acid (CF_3SO_3H, 5.0 g, 33 mmol) was added dropwise to the suspension. After the addition was complete, the reaction mixture was refluxed for 3-4 h. The resulting clear solution was filtered to remove unreacted $SrCO_3$; the filtrate was evaporated and dried in vacuo at 180°C for 24 h to obtain a white solid, which was used without further purification. Yield: 99% (4.13 g).

Synthesis of RbOTf. RbOTf was synthesized by following a modified literature procedure.[47] A three-necked flask was loaded with rubidium carbonate (Rb_2CO_3, 4.05 g, 17.5 mmol) and water, forming a turbid solution. Under an inert atmosphere of N_2, triflic

acid (CF_3SO_3H, 5.0 g, 33 mmol) was added dropwise to the solution. After the addition was complete, the reaction mixture was stirred at room temperature for 1 h and then refluxed for 4 h. Water was evaporated, and the resulting solid was extracted with CH_3CN to remove unreacted Rb_2CO_3. The filtrate was evaporated and dried in vacuo at 180°C for 24 h to obtain a white solid, which was used without further purification. Yield: 86% (6.72 g).

Synthesis of CsOTf. CsOTf was synthesized by following a modified literature procedure.[48] A three-necked flask was loaded with cesium carbonate (Cs_2CO_3, 5.71 g, 17.5 mmol) and water, forming a turbid solution. Under an inert atmosphere of N_2, triflic acid (CF_3SO_3H, 5.0 g, 33 mmol) was added dropwise to the solution. After the addition was complete, the reaction mixture was stirred at room temperature for 1 h and then refluxed for 4 h. Water was evaporated, and the resulting solid was extracted with CH_3CN to remove unreacted Cs_2CO_3. The filtrate was evaporated and dried in vacuo at 180°C for 24 h to obtain a white solid, which was used without further purification. Yield: 93% (8.70 g).

5.5.3 Spectroscopic characterization.

The purities of these triflate salts were confirmed by IR and ^{19}F NMR spectroscopies and powder X-ray diffraction (PXRD; Appendix D, Figures D1-D6).

5.6 Acknowledgements

The authors thank Dr. Justin Douglas and Sarah Neuenswander for assistance with NMR spectroscopy. This work was supported by the US Department of Energy, Office of Science, Office of Basic Energy Sciences through the Early Career Research Program (DE-SC0019169).

5.7 References

(1) (a) Buss, J. A.; VanderVelde, D. G.; Agapie, T. Lewis Acid Enhancement of Proton Induced CO_2 Cleavage: Bond Weakening and Ligand Residence Time Effects. *J. Am. Chem. Soc.* **2018,** *140*, 10121-10125. (b) Sampson, M. D.; Kubiak, C. P. Manganese Electrocatalysts with Bulky Bipyridine Ligands: Utilizing Lewis Acids To Promote Carbon Dioxide Reduction at Low Overpotentials. *J. Am. Chem. Soc.* **2016,** *138*, 1386-1393.

(2) Fortier, S.; Hayton, T. W. Oxo ligand functionalization in the uranyl ion (UO22+). *Coord. Chem. Rev.* **2010,** *254*, 197-214.

(3) (a) Arnold, P. L.; Patel, D.; Wilson, C.; Love, J. B. Reduction and selective oxo group silylation of the uranyl dication. *Nature* **2008**, *451*, 315. (b) Schnaars, D. D.; Wu, G.; Hayton, T. W. Silylation of the Uranyl Ion Using $B(C_6F_5)_3$-Activated Et_3SiH. *Inorg. Chem.* **2011,** *50*, 9642-9649.

(4) Krogman, J. P.; Foxman, B. M.; Thomas, C. M. Activation of CO2 by a Heterobimetallic Zr/Co Complex. *J. Am. Chem. Soc.* **2011,** *133*, 14582-14585.

(5) Mankad, N. P. Diverse bimetallic mechanisms emerging from transition metal Lewis acid/base pairs: development of co-catalysis with metal carbenes and metal carbonyl anions. *Chem. Commun.* **2018,** *54*, 1291-1302.

(6) Brewster, T. P.; Nguyen, T. H.; Li, Z.; Eckenhoff, W. T.; Schley, N. D.; DeYonker, N. J. Synthesis and Characterization of Heterobimetallic Iridium–Aluminum and Rhodium–Aluminum Complexes. *Inorg. Chem.* **2018,** *57*, 1148-1157.

(7) Kumar, A.; Lionetti, D.; Day, V. W.; Blakemore, J. D. Redox-Inactive Metal Cations Modulate the Reduction Potential of the Uranyl Ion in Macrocyclic Complexes. *J. Am. Chem. Soc.* **2020,** *142*, 3032-3041.

(8) McEvoy, J. P.; Brudvig, G. W. Water-Splitting Chemistry of Photosystem II. *Chem. Rev.* **2006**, *106*, 4455-4483.

(9) Yano, J.; Yachandra, V. Mn4Ca Cluster in Photosynthesis: Where and How Water is Oxidized to Dioxygen. *Chem. Rev.* **2014**, *114*, 4175-4205.

(10) Kanady, J. S.; Tsui, E. Y.; Day, M. W.; Agapie, T. A Synthetic Model of the Mn3Ca Subsite of the Oxygen-Evolving Complex in Photosystem II. *Science* **2011**, *333*, 733-736.

(11) Tsui, E. Y.; Tran, R.; Yano, J.; Agapie, T. Redox-inactive metals modulate the reduction potential in heterometallic manganese–oxido clusters. *Nat. Chem.* **2013**, *5*, 293.

(12) Yiu, S.-M.; Man, W.-L.; Lau, T.-C. Efficient Catalytic Oxidation of Alkanes by Lewis Acid/$[Os^{VI}(N)Cl_4]$– Using Peroxides as Terminal Oxidants. Evidence for a Metal-Based Active Intermediate. *J. Am. Chem. Soc.* **2008**, *130*, 10821-10827.

(13) Fukuzumi, S.; Ohkubo, K.; Lee, Y.-M.; Nam, W. Lewis Acid Coupled Electron Transfer of Metal–Oxygen Intermediates. *Chem. Eur. J.* **2015,** *21*, 17548-17559.

(14) Kumar, A.; Lionetti, D.; Day, V. W.; Blakemore, J. D. Trivalent Lewis Acidic Cations Govern the Electronic Properties and Stability of Heterobimetallic Complexes of Nickel. *Chem. Eur. J.* **2018**, *24*, 141-149.

(15) Rice, D. B.; Grotemeyer, E. N.; Donovan, A. M.; Jackson, T. A. Effect of Lewis Acids on the Structure and Reactivity of a Mononuclear Hydroxomanganese(III) Complex. *Inorg. Chem.* **2020,** *59*, 2689-2700.

(16) (a) Jensen, W. B. The Lewis acid-base definitions: a status report. *Chem. Rev.* **1978,** *78*, 1-22. (b) Greb, L. Lewis superacids: classifications, candidates, and applications. *Chem. Eur. J.* **2018,** *24*, 17881-17896.

(17) Perrin, D. D. *Ionisation Constants of Inorganic Acids and Bases in Aqueous Solution*. Pergamon, 1982.

(18) Lionetti, D.; Suseno, S.; Tsui, E. Y.; Lu, L.; Stich, T. A.; Carsch, K. M.; Nielsen, R. J.; Goddard, W. A.; Britt, R. D.; Agapie, T. Effects of Lewis Acidic Metal Ions (M) on

Oxygen-Atom Transfer Reactivity of Heterometallic Mn_3MO_4 Cubane and $Fe_3MO(OH)$ and $Mn_3MO(OH)$ Clusters. *Inorg. Chem.* **2019,** *58,* 2336-2345.

(19) Reath, A. H.; Ziller, J. W.; Tsay, C.; Ryan, A. J.; Yang, J. Y. Redox Potential and Electronic Structure Effects of Proximal Nonredox Active Cations in Cobalt Schiff Base Complexes. *Inorg. Chem.* **2017,** *56,* 3713-3718.

(20) Fukuzumi, S.; Ohkubo, K. Quantitative evaluation of Lewis acidity of metal ions derived from the g values of ESR spectra of superoxide: metal ion complexes in relation to the promoting effects in electron transfer reactions. *Chem. Eur. J.* **2000,** *6*, 4532-4535.

(21) Ohkubo, K.; Suenobu, T.; Imahori, H.; Orita, A.; Otera, J.; Fukuzumi, S. Quantitative evaluation of Lewis acidity of organotin compounds and the catalytic reactivity in electron transfer. *Chem. Lett.* **2001,** *30*, 978-979.

(22) (a) Fukuzumi, S.; Ohkubo, K., Fluorescence maxima of 10-methylacridone− metal ion salt complexes: A convenient and quantitative measure of lewis acidity of metal ion salts. *J. Am. Chem. Soc.* **2002,** *124*, 10270-10271. (b) Hirano, T.; Sekiguchi, T.; Hashizume, D.; Ikeda, H.; Maki, S.; Niwa, H. Colorimetric and fluorometric sensing of the Lewis acidity of a metal ion by metal-ion complexation of imidazo[1,2-a]pyrazin-3(7H)-ones. *Tetrahedron* **2010,** *66,* 3842-3848. (c) Gaffen, J. R.; Bentley, J. N.; Torres, L. C.; Chu, C.; Baumgartner, T.; Caputo, C. B. A simple and effective method of determining Lewis acidity by using fluorescence. *Chem* **2019,** *5*, 1567-1583. (d) Bentley, J. N.; Elgadi, S. A.; Gaffen, J. R.; Demay-Drouhard, P.; Baumgartner, T.; Caputo, C. B. Fluorescent Lewis Adducts: A Practical Guide to Relative Lewis Acidity. *Organometallics* **2020**, *39,* 3645-3655.

(23) Mayer, U.; Gutmann, V.; Gerger, W. The acceptor number — A quantitative empirical parameter for the electrophilic properties of solvents. *Montash. Chem.* **1975,** *106,* 1235-1257.

(24) Beckett, M. A.; Strickland, G. C.; Holland, J. R.; Sukumar Varma, K. A convenient n.m.r. method for the measurement of Lewis acidity at boron centres: correlation of

reaction rates of Lewis acid initiated epoxide polymerizations with Lewis acidity. *Polymer* **1996,** *37*, 4629-4631.

(25) Jennings, J. J.; Wigman, B. W.; Armstrong, B. M.; Franz, A. K. NMR Quantification of the Effects of Ligands and Counterions on Lewis Acid Catalysis. *J. Org. Chem.* **2019,** *84*, 15845-15853.

(26) (a) Brand, S.; Pahl, J.; Elsen, H.; Harder, S. Frustrated Lewis Pair Chemistry with Magnesium Lewis Acids. *Eur. J. Inorg. Chem.* **2017,** *2017*, 4187-4195. (b) Pahl, J.; Brand, S.; Elsen, H.; Harder, S. Highly Lewis acidic cationic alkaline earth metal complexes. *Chem. Commun.* **2018,** *54*, 8685-8688. (c) Fischer, M.; Wolff, M. C.; del Horno, E.; Schmidtmann, M.; Beckhaus, R. Synthesis, Reactivity, and Insights into the Lewis Acidity of Mononuclear Titanocene Imido Complexes Bearing Sterically Demanding Terphenyl Moieties. *Organometallics* **2020,** *39*, 3232-3239.

(27) (a) Tolman, C. A. Phosphorus ligand exchange equilibriums on zerovalent nickel. Dominant role for steric effects. *J. Am. Chem. Soc.* **1970**, *92*, 2956-2965. (b) Boiadjiev, S. E.; Lightner, D. A. Steric Size in Conformational Analysis. Steric Compression Analyzed by Circular Dichroism Spectroscopy. *J. Am. Chem. Soc.* **2000,** *122*, 11328-11339.

(28) Shannon, R. D.; Prewitt, C. T. Effective ionic radii in oxides and fluorides. *Acta Cryst. B* **1969,** *25*, 925-946.

(29) Shannon, R. D.; Prewitt, C. T. Revised values of effective ionic radii. *Acta Cryst. B* **1970,** *26*, 1046-1048.

(30) Shannon, R. D. Revised effective ionic radii and systematic studies of interatomic distances in halides and chalcogenides. *Acta cryst.* A **1976,** *32*, 751-767.

(31) (a) Moyer, B. A.; Meyer, T. J. Properties of the oxo/aqua system $(bpy)_2(py)RuO^{2+}/(bpy)_2(py)Ru(OH_2)^{2+}$. *Inorg. Chem.* **1981,** *20*, 436-444. (b) Krishtalik,

L. I. Energetics of multielectron reactions. Photosynthetic oxygen evolution. *Biochim. Biophys. Acta, Bioenerg.* **1986,** *849*, 162-71.

(32) Harned, H. S.; Geary, C. G. The Ionic Activity Coefficient Product and Ionization of Water in Barium Chloride Solutions from 0 to 50°. *J. Am. Chem. Soc.* **1937,** *59*, 2032-2035.

(33) Labattut, A.; Tremblay, P.-L.; Moutounet, O.; Legault, C. Y. Experimental and Theoretical Quantification of the Lewis Acidity of Iodine (III) Species. *J. Org. Chem.* **2017,** *82*, 11891-11896.

(34) Thordarson, P. Determining association constants from titration experiments in supramolecular chemistry. *Chem. Soc. Rev.* **2011,** *40*, 1305-1323.

(35) (a) Cotton, F.; Mandal, S. Oxohalo complexes of W(V) and W(IV). The synthesis and crystal structures of $[WOCl(dppe)_2][BPh_4]$, $[PHMe_2Ph][WOBr_4(OPMe_2Ph)]$ and $[Li(OPMe_2Ph)(THF)]_2\,[WOBr_4(OPMe_2Ph)]_2$. *Eur. J. Solid State Inorg. Chem.* **1991,** *28*, 775-797. (b) Fenske, D.; Fischer, A. New Selenolato-Bridged Clusters of Iron and Nickel; the Structures of $[Fe_{12}\,(SePh)_{24}]$ and $[Na_2(POPh_3)_6][Ni_{20}Se_{12}(SeMe)_{10}]$. *Angew. Chem. Int. Ed.* **1995,** *34*, 307-309. (c) Hashem, E.; McCabe, T.; Schulzke, C.; Baker, R. J. Synthesis, structure and photophysical properties of $[UO_2X_2(O{=}PPh_3)_2]$ (X= Cl, Br, I). *Dalton Trans.* **2014,** *43*, 1125-1131. (d) Hanft, A.; Lichtenberg, C. Aminotroponiminates: ligand-centred, reversible redox events under oxidative conditions in sodium and bismuth complexes. *Dalton Trans.* **2018,** *47*, 10578-10589.

(36) Connors, K. A. *Binding Constants*, Wiley & Sons, New York, 1987.

(37) Hill, A. V. The possible effects of the aggregation of the molecules of haemoglobin on its dissociation curves. *J. Physiol.* **1910,** *40*, 4-7.

(38) Langmuir, I. The adsorption of gases on plane surfaces of glass, mica and platinum. *J. Am. Chem. Soc.* **1918,** *40*, 1361-1403.

(39) Weiss, J. N. The Hill equation revisited: uses and misuses. *FASEB J.* **1997,** *11*, 835-841.

(40) Dahlquist, F. The meaning of Scatchard and Hill plots. In *Methods in enzymology*, Elsevier: 1978; Vol. 48, 270-299.

(41) Groom, C. R.; Bruno, I. J.; Lightfoot, M. P.; Ward, S. C. The Cambridge Structural Database. *Acta Cryst.* **2016,** *B72*, 171-179.

(42) Cook, B. J.; Chen, C. H.; Caulton, K. G. A Multifunctional Pincer Ligand for Cobalt-Promoted Oxidation by N2O. *Chem. Eur. J.* **2018,** *24*, 5962-5966.

(43) Fulmer, G. R.; Miller, A. J. M.; Sherden, N. H.; Gottlieb, H. E.; Nudelman, A.; Stoltz, B. M.; Bercaw, J. E.; Goldberg, K. I. NMR Chemical Shifts of Trace Impurities: Common Laboratory Solvents, Organics, and Gases in Deuterated Solvents Relevant to the Organometallic Chemist. *Organometallics* **2010**, *29*, 2176-2179.

(44) Harris, R.K.; Becker, E.D.; Cabral de Menezes, S.M.; Goodfellow, R.; Granger, P. NMR nomenclature. Nuclear spin properties and conventions for chemical shifts (IUPAC Recommendations 2001)**.** *Pure Appl. Chem.* **2001**, *73*, 1795-1818.

(45) Harris, R.K.; Becker, E.D.; Cabral de Menezes, S.M.; Granger, P.; Hoffman, R.E.; Zilm, K.W. Further conventions for NMR shielding and chemical shifts (IUPAC Recommendations 2008)**.** *Pure Appl. Chem.* **2008**, *80*, 59-84.

(46) Benetollo, F.; Bombieri, G.; Samaria, K. M.; Vallarino, L. M.; Williams, J. W. Isomerism in calcium and strontium complexes of six-nitrogen-donor macrocyclic ligands with peripheral methyl substituents, and crystal structure of $[Sr(CF_3SO_3)_2(C_{24}H_{30}N_6)]$. *Polyhedron* **2001,** *20*, 3143-3148.

(47) Hildebrandt, L.; Dinnebier, R.; Jansen, M. Crystal structure and ionic conductivity of three polymorphic phases of rubidium trifluoromethyl sulfonate, $RbSO_3CF_3$. *Inorg. Chem.* **2006,** *45*, 3217-3223.

(48) Hildebrandt, L.; Dinnebier, R.; Jansen, M. Crystal structure and ionic conductivity of cesium trifluoromethyl sulfonate, $CsSO_3CF_3$. *Z. Anorg. Allg. Chem.* **2005,** *631*, 1660-1666.

Part II

Chapter 6

Understanding the Roles of Triethylaluminum in Phosphinimide-Supported Titanium Catalyst Systems for Ethylene Polymerization

This chapter is adapted from a published manuscript:

Barr, J. L.; Kumar, A.; Lionetti, D.; Cruz, C. A.; Blakemore, J. D. Understanding the Roles of Triethylaluminum in Phosphinimide-Supported Titanium Catalyst Systems for Ethylene Polymerization. *Organometallics,* **2019**, *39,* 2150-2155.

6.1 Introduction

Despite several decades of research into homogeneous catalysis of ethylene polymerization, industrial production of polyethylene (PE) remains dominated by heterogenous chromium systems, such as the Phillips Catalyst, titanium-based Ziegler catalysts, and to a much lesser extent, single-site catalysts.[1,2,3] In terms of both their applicability and adoption into the field, single-site catalysts are a 'frontier' technology for development of new applications of PE-based materials. The discovery of constrained geometry catalysts by Bercaw[4] and half-sandwich titanium phosphinimide catalyst systems by Stephan[5] are two rare examples of successful homogeneous systems that overcame the barriers to entry into this mature and highly demanding area of catalysis.[6] These catalysts have proven industrially useful for production of linear low-density polyethylene (LLDPE) film resins.

Along this line, Phillips Petroleum's (now Chevron Phillips Chemical) discovery and development of solid superacid materials capable of serving to both activate homogenous complexes for ethylene polymerization and act as a solid carrier for catalysts and polymer particles[7,8,9] prompted us to explore their behavior with other homogeneous ethylene polymerization catalysts that could be industrially relevant.

Here, we report the use of a half-sandwich titanium phosphinimide catalyst, [(Ind)(*t*Bu$_3$P=N)TiCl$_2$] (**1**; Ind = indenyl) with solid superacid materials (Chart 6.1). Our work shows that this compound is an effective ethylene polymerization catalyst. Furthermore, polymerization results prompted us to probe the nature of the active catalyst species with chemical and electrochemical studies, including synthetic efforts that have enabled isolation of a new heterobimetallic complex **2-Et** (Chart 6.1). With **1** and **2-Et**

available for study, structural and spectroscopic investigations have been used to reveal the multiple influences on this system, including its polymerization behavior, which arise from use of the strong Lewis acid triethylaluminum ($AlEt_3$).

Chart 6.1. Half-Sandwich Ti Complexes Supported by Phosphinimide Ligands

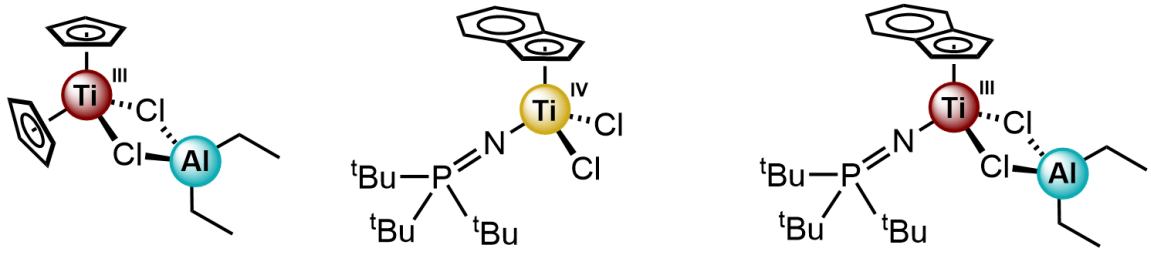

N
Natta 1957

1
This Work

2-Et
This Work

6.2 Results and Discussion

The reaction of **1**, prepared according to the literature,[10] with two to five equivalents of triethylaluminum in benzene or pentane at room temperature yields a deep emerald green solution after ca. 30 minutes of reaction time. ^{1}H and ^{31}P NMR studies carried out in C_6D_6 after 30 minutes reveal neither discernable peaks corresponding to the starting material, nor new peaks corresponding to indenyl or phosphinimide fragments that could be present in new diamagnetic compounds (see Appendix E, Figures E5 and E6 for example spectra). Removal of the solvent from the reaction vessel, followed by addition of pentane, filtration, and evaporation of volatiles *in vacuo* yields an emerald green crystalline solid (**2-Et**) in 83% isolated yield (see Experimental Section). Notably, these reaction conditions do not yield any detectable titanium alkyl species, which are often required for ethylene polymerization activity.[11]

Allowing a saturated pentane solution containing **2-Et** to stand at –35°C yielded dark green crystals suitable for single-crystal X-ray diffraction (XRD) studies. Additionally, XRD results for **1** have not previously been available, and thus crystals of this precursor complex were also grown by layering a toluene solution of **1** with hexane at –30°C. The data reveal that **2-Et** (see Figure 6.1, left structure) is a diethylaluminum adduct of **1** (see Figure 6.1, right structure) with two bridging chloride ligands, formulated as [(Ind)(tBu_3P=N)Ti(μ_2-Cl)$_2$AlEt$_2$]. The first coordination sphere around the titanium metal center retains the [η^5-Ind] and phosphinimide ligands of **1**, but with a shorter intraligand P=N distance of 1.589(4) Å in **2-Et** in comparison with 1.622(5) Å in **1**. The average Ti–Cl distance elongates to 2.527 Å in **2-Et** from 2.299 Å in **1**, as expected upon formation of the bridging interaction with the [AlEt$_2$] fragment. Formation of the diamond core motif, however, significantly constrains the Cl–Ti–Cl angle from 103.6(1)° in **1** to 81.5(1)° in **2-Et**. Notably, the P–N–Ti angle in **2-Et** is 175.9(2)°, denoting double-bond character in the N–Ti interaction, similar to the angle of 172.5(3)° in **1**.

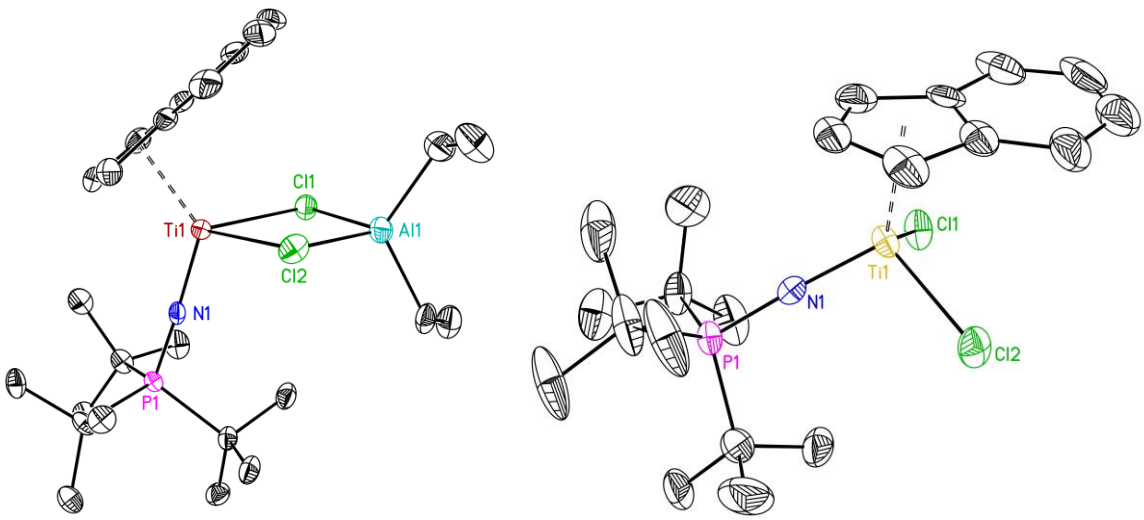

Figure 6.1. Solid-state structures (from XRD) of **2-Et** (left) and **1** (right). All H-atoms are omitted for clarity. Displacement ellipsoids are shown at the 50% probability level.

Precedent for generation of Ti(III) phosphinimide complexes is limited, and includes the reaction of dimethyl titanium phosphinimide compounds with excess trimethylaluminum to yield $CpTi(\mu^2\text{-}NPR_3)(\mu^4\text{-}C)(AlMe_2)_3$ and $[CpTi(\mu^2\text{-}Me)(\mu^2\text{-}NPR_3)(\mu^5\text{-}C)(AlMe_2)_3\cdot(AlMe_3)]$ (where Cp is cyclopentadienyl).[12,13,14] Notably, the behavior of dialkyl titanium phosphinimide catalysts with alkyl aluminum reagents appears quite different than the formation of the reduction product **2-Et** reported here. This observation supports the notion that divergent reactivity occurs between the case of **1** and $[(Ind)(t\text{Bu}_3\text{P=N})TiMe_2]$ during catalyst activation, leading to divergent PE materials in each case.

Complex **2-Et** is strikingly similar to Natta's $Cp_2Ti(\mu_2\text{-}Cl)_2AlEt_2$ (**N**) (Chart 6.1), first reported in 1957.[15] **N** can be readily prepared by reaction of titanocene dichloride with one equivalent of triethylaluminum, yielding the blue heterobimetallic **N**. Comparison of XRD data for **2-Et** and **N** reveal similar average distances for the Ti–Cl and Al–Cl interactions (2.5 Å), and similar distorted tetrahedral Ti and Al geometries.[16] The likeness between **2-Et** and **N** is perhaps not surprising, however, given the extrapolated steric similarity between phosphinimide and cyclopentadienyl-type ligands.[17]

To further characterize **2-Et**, we performed electron paramagnetic resonance (EPR) spectroscopy. Before reduction, **1** is diamagnetic and EPR silent, with a Ti(IV) center having a d^0 configuration and $S = 0$. On the other hand, the reduced species **2-Et** has a formally Ti(III) center with a d^1 configuration. As expected, treatment of **1** with $AlEt_3$ results in a new spectrum (Figure 6.2), attributable to **2-Et**, that displays axial symmetry and characteristic features at g = 1.98 and 1.94 in toluene at 55 K. These observations are consistent with formulation of **2-Et** as having the expected Ti(III) d^1 system with $S = 1/2$.[18] As no hyperfine coupling to the ^{14}N ($I = 1$) or ^{31}P ($I = ½$) atoms contained in the phosphinimide ligand is

visible, the radical appears mostly localized on the titanium(III) center. Notably, only a single species is apparent by EPR under our conditions in a variety of nonpolar organic solvents and the spectrum in toluene can be readily modeled as a single Ti^{III} species. (See Appendix E, Figure E20 for other EPR spectra and Figure E21 for modeling results.) Thus, we conclude that reduction of **1** to form **2-Et** proceeds cleanly, as judged by both NMR and EPR.

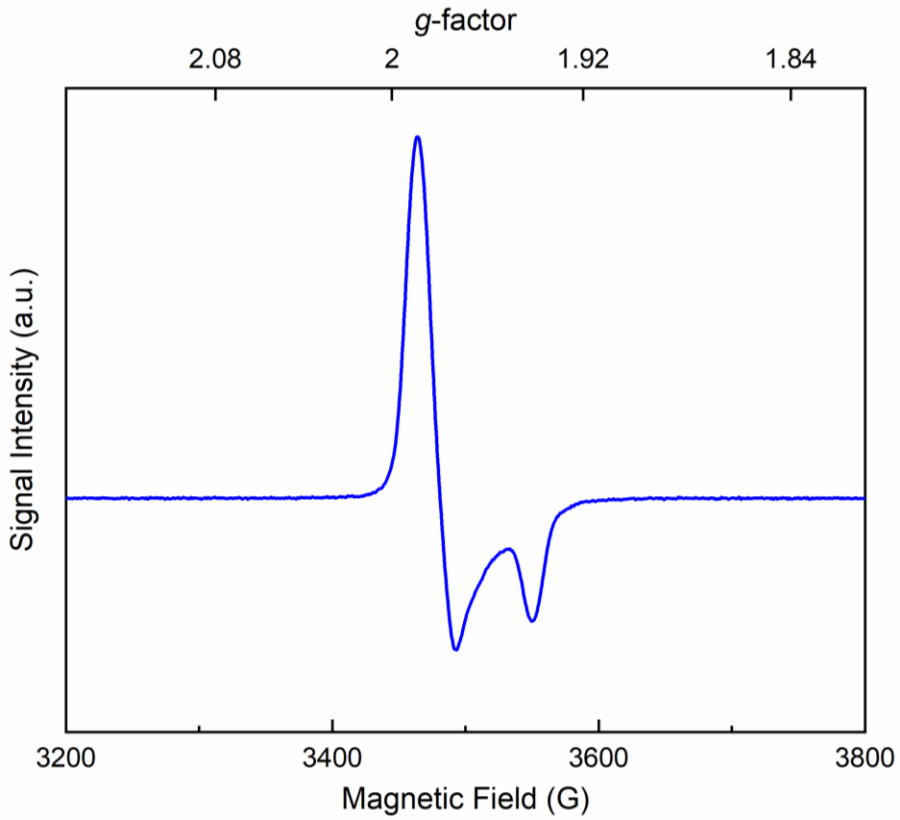

Figure 6.2. X-band continuous-wave EPR spectrum of **2-Et** in toluene. Conditions: T = 55 K; modulation amplitude = 4.0 G; time constant = 5 ms.

These results compare well with prior spectra collected for Natta's heterobimetallic complex **N**,[19] which are centered at g = 1.94 and display minimal hyperfine coupling. Notably, other reaction products[20] that can be generated from the reaction of Cp_2TiCl_2 with triethylaluminum and other aluminum alkyls display significantly different spectra,

including larger hyperfine couplings in some cases.[19,21] In all cases, however, treatment of the titanium(IV) starting material with aluminum alkyls leads to reduction of the metal center concomitant with gas evolution.[15,19] Consistent with these prior findings, gas chromatography results examining chemical reduction of **1** with $AlEt_3$ show production of ca. 1 equiv. of C_2H_6 per Ti center (see Appendix E, Figure E18). Production of C_2H_6 suggests cleavage of Ti–C bonds following alkylation results in generation of transient C_2H_5 radicals, which could scavenge H-atoms from the excess $AlEt_3$ present or solvent. Based on these observations for **2-Et** and **N**, aluminum alkyls can be viewed as reliably serving as both reducing agents and sources of $[AlR_2]$ equivalents in these systems.

Testing for ethylene polymerization activity with **1** and **2-Et** was conducted in an automated, semi-batch reactor under slurry conditions with isobutane diluent.[22] (see Experimental Section for details.) Experiments were carried out for 20 minutes (excluding charging time) using industrially relevant reaction temperature, ethylene, hydrogen, and 1-hexene concentrations.[23] In addition, 150 ppm of $AlEt_3$ in the isobutane diluent was added to the reactor with these other gases during operation, where it serves as an alkylating agent as well as a scavenger of catalyst poisons. The polymerization reactions were halted via fast evaporation (flashing) of the isobutane diluent, and product was collected as free-flowing small particles. For this work, titanium catalyst was introduced into the reactor in the form of a toluene solution containing **1** (as-synthesized, in the Ti(IV) state) or a freshly prepared benzene solution containing the heterobimetallic complex **2-Et**, formed by treatment of **1** with $AlEt_3$ *in situ* to yield the usual emerald-green colored solution.

Gratifyingly, the results confirm that both **1** and **2-Et** are precatalysts for ethylene polymerization, with significant turnover and yield of polyethylene (PE) in each case (see

Table 6.1 for details). As the activity on a [Ti] basis is not significantly different between the two catalyst preparations, we conclude that "pre-reduction" of **1** to form **2-Et** does not significantly decrease the number of [Ti] sites available for catalysis. However, the two catalysts systems differ slightly in the molecular weight distribution (MWD, M_w/M_n) of the product PE produced by the reactor in each case. Specifically, the use of **2-Et** (formed by pre-reduction of **1**) results in a narrower MWD (3.05) material in comparison to **1** (3.29), as determined by gel permeation chromatography (see Figure 6.3 and Table 6.1). In these experiments, the polymer produced with **2-Et** also exhibited a higher molecular weight than that produced with **1**, with M_w values increasing from 132 to 262 kg mol^{-1}, despite the use of identical reactor conditions. These results suggest that pre-reduction of **1** to form **2-Et**: (1) alters the nature of the catalytically active species, (2) does not significantly change the total number of active sites, and (3) the selection between **1** or **2-Et** as catalyst results in product PE with usefully different properties.

Table 6.1. Comparison of Select Ethylene Polymerization Conditions* and Polymer Properties.

Pre-reduced	Ti:Al Ratio	Polymer Yield (g)	[Ti] Activity (g PE/g Cat./hr)	M_n/1000 (g/mol)	M_w/1000 (g/mol)[#]	M_p/1000 (g/mol)	M_w/M_n[#]
No	1:100	93	279,000	40.11	132.09	86.53	3.29
Yes	1:100	85	255,000	85.83	261.95	210.40	3.05

*Conditions: Polymerization experiments were carried out using 0.001 g of Ti catalyst, 0.1 g of solid superacid, 150 ppm of additional $AlEt_3$ species added to the reactor relative to the isobutane diluent, 125 ppm of H_2, T = 80°C and t = 20 min. See experimental section for full experiment details. [&] M_n is number average molecular weight; M_w is weight average molecular weight; M_p is peak molecular weight. [#]Experimental error: M_w ±2%; M_w/M_n ±7%.

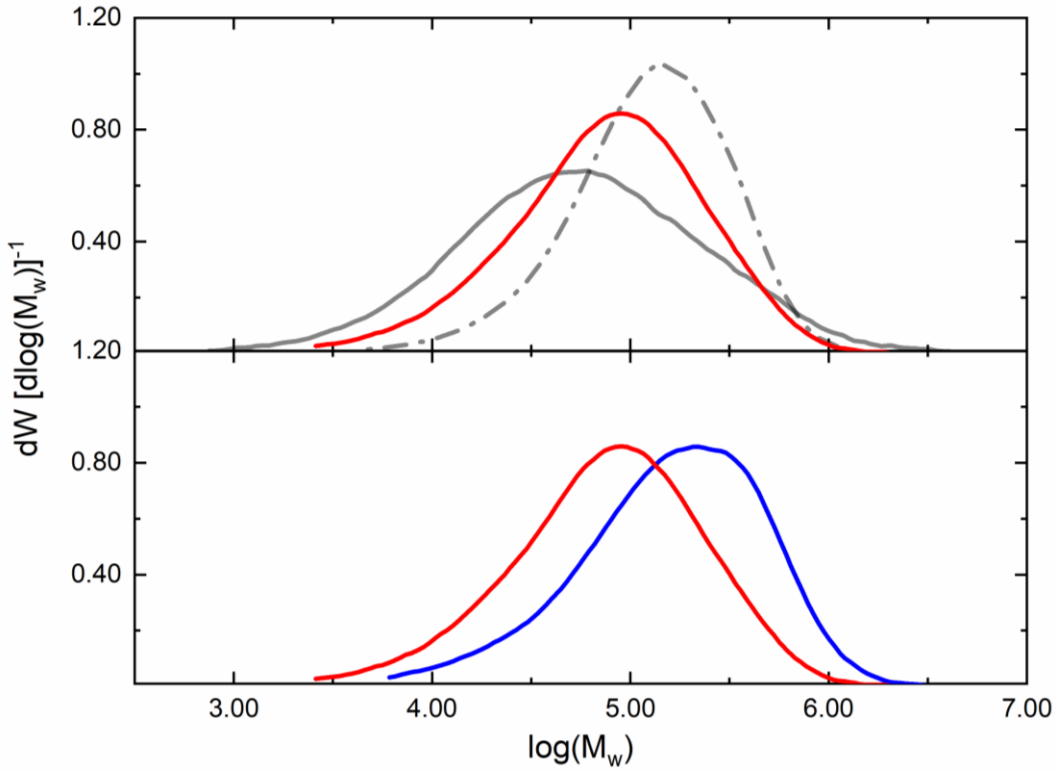

Figure 6.3. Gel permeation chromatograms for comparison of PE produced under a variety of conditions. Upper panel: PE produced with **1** (red line), Cr on silica catalyst (solid gray line), and a metallocene (dash-dot gray line). Lower panel: PE produced with **1** (red line) and "prereduced" **1** treated with triethylaluminum prior to introduction into the polymerization reactor (blue line).

For comparison, use of a single-site catalyst (such as a metallocene) yields significantly narrow MWD values of 2.3 – 2.8 under similar polymerization conditions.[24] These findings contrast with our work, indicating that there are likely multiple types of active polymerization sites, each producing polyethylene chains of different molecular weights and thus contributing to our wider MWD of 3.29 with **1** as catalyst (Figure 6.3). Such a situation is reminiscent of heterogeneous polymerization catalysis, in which a system like the Phillips Cr/silica catalyst produces broader MWD via multiple types of active sites. As Stephan's work with other phosphinimide catalysts suggests that these systems behave

homogeneously, yielding monodisperse polyethylene materials with narrow MWDs between 1.5 – 3 in virtually all cases, the results were especially intriguing.[25,26]

A notable difference between our work with **1** and findings from the literature lies in the nature of the phosphinimide pre-catalyst used in the polymerization experiments. Published work has largely utilized dialkylated phosphinimide precatalysts activated by MAO, borate salts or boranes for ethylene polymerization screening, whereas our work has focused on the dichloride precursor.[5,17,25] In our system, **1** and/or **2-Et** are presumably alkylated by $AlEt_3$ in the polymerization reactor in the presence of the solid superacid. This suggests that the difference in MWD may be a result of divergent pre-catalyst initiation chemistry. Stated another way, formation of active catalyst(s) by alkylation in the presence of superacid is a step that could occur for both **1** and **2-Et**. However, the observed propensity of **1** to undergo one-electron reduction by $AlEt_3$ suggests that partial reduction of precatalyst **1** could occur in the reactor, during the initiation phase of ethylene polymerization reactions. Thus, the amount of **2-Et** can be increased by carrying out the pre-reduction step before any titanium is introduced into the reactor. If both **1** and **2-Et** can undergo alkylation to produce different catalysts, a more broadly speciated polymerization system containing both Ti(IV) and Ti(III) species that are active for catalysis would be expected from direct use of **1** as precatalyst (i.e., carrying out catalysis without [Ti] pre-reduction). Consistent with this model, polymerization carried out with **2-Et** results in a narrower MWD in comparison to that with **1**.

The facile one-electron reduction of **1** by $AlEt_3$ in the synthetic work prompted us to carry out electrochemical investigations aimed at learning more about the properties of this system with regard to electron transfer. We elected to carry out the electrochemical work with **1**

rather than **2-Et**; **2-Et** is often an inconvenient, sticky solid when isolated, while **1** can be reliably isolated as a free-flowing powder. Cyclic voltammetry, carried out on a solution of **1** in THF solvent containing 0.1 M NBu_4PF_6 as supporting electrolyte, shows a single observable reduction event at $E_{p,c} = -2.12$ V vs. the ferrocenium/ferrocene couple (denoted hereafter as $Fc^{+/0}$; Figure 6.4, upper panel) within the limits of our experimental conditions. As the peak currents corresponding to reduction of **1** and those for oxidation/reduction of an equimolar amount of Cp_2Co are quite similar, we assign the observed reduction of **1** as a one-electron process (see Appendix E, Figure E12 for data). This reduction wave appears totally irreversible at slower scan rates, indicating that the titanium(III) species resulting from reduction of **1** is unstable under the electrochemical cell conditions and thus undergoes further reactivity. Notably, however, increased reversibility can be obtained at faster scan rates, suggesting that $[(Ind)(t\text{Bu}_3P{=}N)Ti^{III}Cl_2]^-$ is transiently produced and undergoes re-oxidation at $E_{p,a} \approx -1.9$ V vs. $Fc^{+/0}$ measured at 300 mV/s scan rate (see Appendix E, Figure E14). This overall profile is consistent with an EC-type mechanism, in which electrochemical reduction is followed by a rapid chemical reaction that depletes the population of the reduced compound near the electrode.[27] In addition, on the basis of the reductive peak currents measured as a function of scan rate, **1** is confirmed as a freely diffusing species in homogeneous solution under these conditions (see Appendix E, Figures E14 and E15 for data).

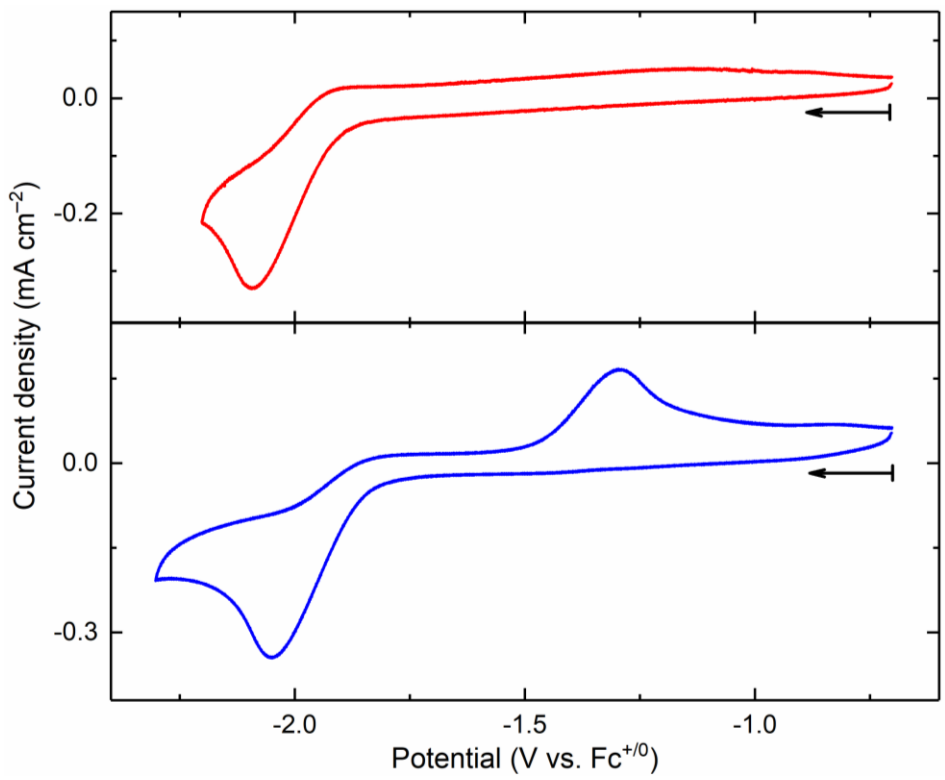

Figure 6.4. Cyclic Voltammetry data of **1** (red, upper panel), **1** in the presence of 6 eq. of $AlEt_3$ (blue, lower panel). Conditions: electrolyte, 0.1 M $[nBu_4N][PF_6]$ in THF; scan rate: 100 mV/s.

Two analogous complexes, Cp(*t*Bu_3P=N)$TiCl_2$ (**4**) and Cp*(*t*Bu_3P=N)$TiCl_2$ (**5**) were also interrogated by cyclic voltammetry under our conditions in THF electrolyte. These compounds each undergo a single, one-electron reduction in an EC-type process at quite negative potentials, measured at $E_{p,c}$ = –2.18 V vs. $Fc^{+/0}$ for **4** and $E_{p,c}$ = –2.36 V vs. $Fc^{+/0}$ for **5** (see Appendix E, Figures E10 and E11).[28] Notably, comparison of the $E_{p,c}$ values for three titanium(IV) complexes reveals the expected trend with cyclopentadienyl donor power, in which the [Cp*] compound undergoes the most negative reduction (–2.38 V vs. $Fc^{+/0}$) and the [Cp] and [Ind] compounds undergo reduction at more positive potentials (–2.19 and –2.10 V vs. $Fc^{+/0}$, respectively). Notably, the reduction of **1**, **4**, and **5** to the titanium(II) state was not apparent in any case under our conditions.

Cyclic voltammograms collected on solutions containing **1** and 6 equiv. of $AlEt_3$ reveal the appearance of a new oxidative feature at $E_{p,a}$ = –1.32 V vs. $Fc^{+/0}$ that is assigned to oxidation of **2-Et** (see Figure 6.4, lower panel). On the reductive side, the cathodic feature measured for **1** alone is retained with a very similar profile in the presence of $AlEt_3$, indicating that $AlEt_3$ does not interact significantly with **1** when titanium is in the +4 oxidation state. However, upon one-electron reduction, a fast reaction occurs with $AlEt_3$, leading to a new compound (**2-Et**; see Appendix E, Figure E22) in the reaction-diffusion layer near the electrode which undergoes oxidation at –1.32 V vs. $Fc^{+/0}$. On the basis of scan-rate dependent voltammetry, **2-Et** is freely diffusing in homogeneous solution (see Appendix E, Figures E14 and E15). Moreover, the cathodic wave corresponding to reduction of **1** does not display a return oxidation at any accessible scan rates in the presence of $AlEt_3$, confirming rapid reaction of one-electron reduced **1** with $AlEt_3$ (see Appendix E, Figure E14).

The anodic oxidation of **2-Et** occurs at $E_{p,a}$ = –1.32 V at 100 mV/s; this potential is well positive of the anodic oxidation of $[(Ind)(t\text{Bu}_3\text{P=N})\text{Ti}^{III}\text{Cl}_2]^-$ observed at $E_{p,a} \approx$ –1.9 V at faster scan rates (see Appendix E, Figure E14). Thus, we conclude that the $[AlEt_2]$ fragment behaves as an effective Lewis acid to the titanium center in **2-Et**. In general, Al^{3+} can be considered to be a potent Lewis acid; we note here the rather low pK_a value associated with its metal aqua ion (p$K_a \approx 5$ in H_2O).[29] The specific role of $[AlEt_2]$ as a Lewis acidic moiety is supported by the ca. 580 mV positive shift in $E_{p,a}$ between the two cases measured here. The finding of a positively-shifted reduction potential for **2-Et** vs. **1** is also in accord with recent studies from our laboratory aimed at quantifying the effects of trivalent redox-inactive Lewis acids on reduction potentials in heterobimetallic compounds.[30] Specifically, we have

measured a positive shift of ca. 67 mV/pK_a across a family of heterobimetallic nickel complexes with various Lewis acids.

The proposed electrochemical reaction sequence is in accord with the observed slower reaction of **1** with $AlEt_3$ under purely chemical conditions, as the reaction to produce the emerald-green solution of **2-Et** occurs on the minutes timescale at room temperature, apparently limited by sluggish kinetics of Al–C bond cleavage under the chosen conditions. This cleavage, however, leads to formation of transient radicals that drive reduction of **1** and formation of **2-Et**. Notably, in the electrochemical work, the electrode serves as an accelerating source of single reducing equivalents, allowing formation of **2-Et** near the electrode to proceed more quickly. Consistent with this model, bulk electrolysis of **1** in the presence of $AlEt_3$ at –2.4 V vs. $Fc^{+/0}$ generates ca. 1 equiv. of C_2H_6 per Ti center, similar to the case of the chemical work with $AlEt_3$ alone (see Appendix E, Figure E19). Furthermore, as only a single anodic wave ($E_{p,a}$ = –1.32 V vs. $Fc^{+/0}$) is observed in voltammetry under these conditions, we conclude that electrochemical reduction of **1** in the presence of $AlEt_3$ leads to clean generation of **2-Et**, similar to the purely chemical reaction with $AlEt_3$.

To confirm that **2-Et** is the product of electrochemical reduction of **1** in the presence of $AlEt_3$, we turned to spectroelectrochemistry. For comparison, **1** is yellow, and displays a lowest energy absorption band, attributable to ligand-to-metal charge transfer, at 390 nm (ε = 1049 M^{-1} cm^{-1}) in pentane (see Appendix E, Figure E7). Consistent with its emerald-green color, **2-Et** (when prepared chemically) displays a lowest-energy absorption band, attributable to a *d-d* transition in the d^1 system, at 636 nm (ε = 215 M^{-1} cm^{-1}) in pentane and 709 nm (ε = 390 M^{-1} cm^{-1}) in THF. Consistent with these observations, electrolysis of a solution containing **1** and $AlEt_3$ at –2.4 V vs. $Fc^{+/0}$ with simultaneous UV-visible monitoring

results in growth of a new absorption band centered at 709 nm (see Figure 6.5). The new band is virtually identical to that measured for chemically prepared **2-Et** in THF (see Appendix E, Figure E8), confirming that **2-Et** is indeed produced under electrochemical conditions. Isosbestic behavior is observed near 535 nm in these spectra, supporting clean interconversion of **1** to **2-Et**. Switching the electrolysis potential to –0.8 V vs. $Fc^{+/0}$ (positive of the anodic wave measured for **2-Et**, Figure 6.4) results in loss of the absorption band at 709 nm, consistent with assignment of the anodic wave at –1.31 V vs. $Fc^{+/0}$ as oxidation of **2-Et** and consequent regeneration of **1**.

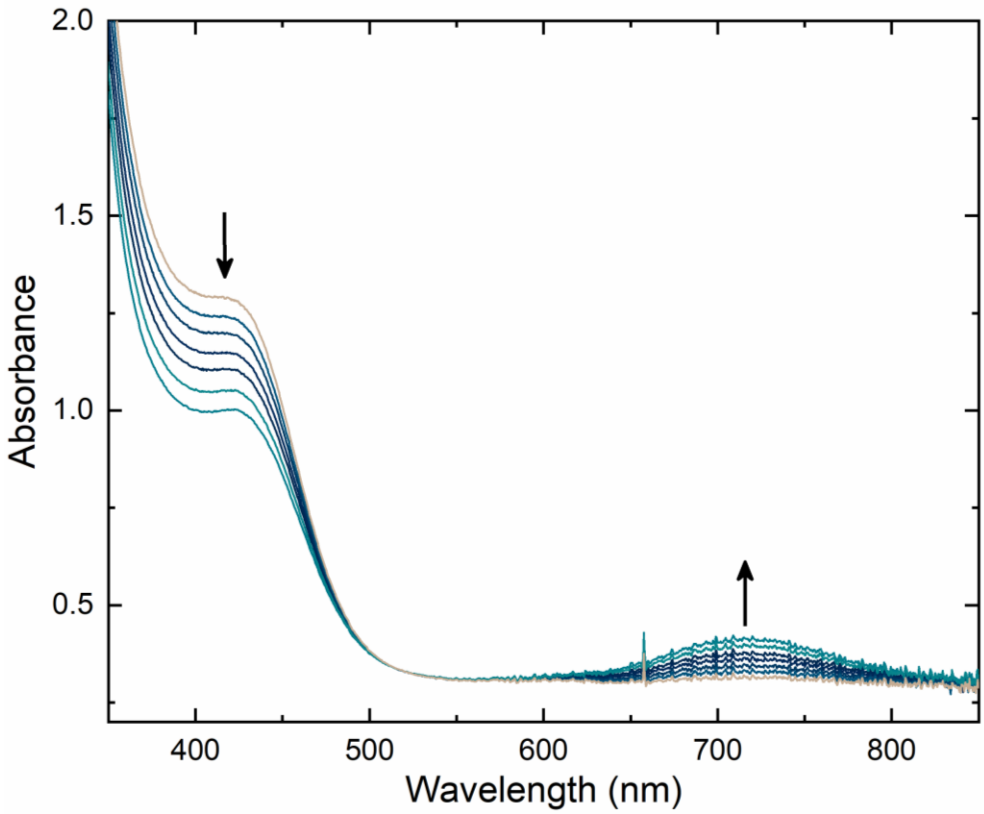

Figure 6.5. Spectroelectrochemical data for electrolysis of **1** in the presence of 2 eq. of $AlEt_3$. Initial potential for the experiment was –0.8 V vs. $Fc^{+/0}$ and step potential for generation of **2-Et** (characteristic feature at 709 nm) was –2.4 V vs. $Fc^{+/0}$. Conditions: 0.1 M $[nBu_4N][PF_6]$ in THF.

6.3 Conclusions

In conclusion, **1** undergoes reduction in the presence of $AlEt_3$ to form the heterobimetallic [$Ti^{III}Al^{III}$] compound **2-Et**. Both of these compounds function as precatalysts for ethylene polymerization, suggesting that catalyst activation/alkylation and chain termination is affected by the propensity of **1** to undergo one-electron reduction with $AlEt_3$. Chemical and electrochemical studies reveal that one-electron reduction of **1** in the presence of $AlEt_3$ leads to generation of **2-Et** with concomitant evolution of C_2H_6. These results also reveal that the Lewis acidic [$AlEt_2$] fragment effectively stabilizes **2-Et**, likely contributing to the narrower molecular weight distribution of PE produced with this compound as precatalyst in place of **1.** Ongoing work in our laboratories is focused on obtaining further understanding of the role(s) of Lewis acids in modulating the reduction potential and catalytic properties of these useful compounds.

6.4 Experimental Details

6.4.1 General Considerations

All manipulations were carried out in dry N_2-filled gloveboxes (Vacuum Atmospheres Co., Hawthorne, CA) or under N_2 atmosphere using standard Schlenk techniques unless otherwise noted. Ethylene was obtained from Airgas and was further purified through columns of 13X molecular sieves. 1-Hexene was obtained from Chevron Phillips Chemical Company LP and dried over A-201 type activated alumina. All solvents were of commercial grade and dried over activated alumina using a Pure Process Technology (PPT; Nashua, NH) solvent purification system prior to use, and were stored over molecular sieves or anhydrous solvents were purchased from Sigma-Aldrich and purified and stored over 13X molecular

sieves. Benzene-d_6 was purchased from Cambridge Isotope Labs, dried and stored over 13X molecular sieves. ^{1}H and ^{31}P NMR spectra were collected on 400 and 500 MHz Bruker spectrometers and referenced to the residual protio-solvent signal in the case of ^{1}H and to the deuterium lock signal in the case of ^{31}P unless otherwise noted. Triethylaluminum (1 M solution in hexane or 0.6 M solution in heptane), *t*Bu_3P and trimethylsilylazide were purchased from Sigma-Aldrich or Acros Organics and used as received. [(Ind)$TiCl_3$] was purchased from Strem Chemicals and used as received. **1** and the solid super acid activator were prepared according to literature methods.[31,32,33] All chemicals were from major commercial suppliers and used after extensive drying.

Electrochemical experiments were carried out in a N_2-filled glovebox in dry, degassed THF. 0.10 M tetra(n-butylammonium) hexafluorophosphate ($[nBu_4N]^+[PF_6]^-$); Sigma-Aldrich, electrochemical grade) served as the supporting electrolyte. Measurements were made with a Gamry Reference 600+ Potentiostat/Galvanostat using a standard three-electrode configuration. The working electrode was the basal plane of highly oriented pyrolytic graphite (HOPG) (GraphiteStore.com, Buffalo Grove, Ill.; surface area: 0.09 cm^2), the counter electrode was a platinum wire (Kurt J. Lesker, Jefferson Hills, PA; 99.99%, 0.5 mm diameter), and a silver wire immersed in electrolyte served as a pseudoreference electrode (CH Instruments). The reference was separated from the working solution by a Vycor frit (Bioanalytical Systems, Inc.). Ferrocene (Sigma Aldrich; twice-sublimed) was added to the solution after each experiment; the midpoint potential of the ferrocenium/ferrocene couple (denoted as $Fc^{+/0}$) served as an internal standard for comparison of the recorded potentials. Concentrations of analyte for cyclic voltammetry were ca. 1 to 2 mM unless otherwise noted.

Electronic absorption spectra were collected with an Ocean Optics Flame spectrometer, in a 1-cm path length quartz cuvette.

Spectroelectrochemisty was carried out in the same glovebox as described above (N_2 atmosphere), with 0.10 M $[nBu_4N]^+[PF_6]^-$ in THF as electrolyte. A thin layer quartz cell was used with a Teflon cap for housing the electrodes (ALS Co., Ltd., path length: 1.0 mm). The working electrode was a platinum mesh/flag electrode covered with a PTFE shrink tube up to the flag, and the counter and reference electrodes were both platinum wires (ALS Co., Ltd.).

Gas analysis for determination of gas evolution was performed with a Shimadzu GC-2014 Custom-GC gas chromatograph with a thermal conductivity detector and dual flame-ionization detectors. A custom set of eight columns and timed valves enable quantitative analysis of hydrogen, nitrogen, oxygen, carbon dioxide, carbon monoxide, methane, ethane, ethylene, and ethyne. Argon serves as the carrier gas. The instrument was calibrated with a standard checkout gas mixture (Agilent 5190-0519) prior to experimental runs to obtain quantitative data for ethylene.

Bulk electrolysis experiments were performed in a custom two-chamber electrochemical cell equipped with connections to achieve gas-tight operation. The working electrode was a HOPG plate (Graphitestore.com, Buffalo Grove, Ill.; surface area: 10 cm^2).

6.4.2 Bench Polymerization Experiments

Polymerizations were performed on a 2.2 L stainless steel reactor equipped with a marine stirrer rotating at 500 rpm. The reactor was surrounded by a stainless-steel jacket through which a stream of hot water was circulated, which permitted precise temperature control to

within half a degree centigrade. Prior to polymerization, the reactor was purged at 110–120^{o}C with nitrogen for at least 30 minutes. The reactor was then cooled and charged with 0.1 g of solid superacid, 0.5 mL of triethylaluminum (1 M in hexane, 0.5 mmol), and 0.001 g of **1** as a 1 mg/mL solution of catalyst in toluene, and filled with 1.2 L of isobutane liquid, in that order, under a stream of isobutane vapors at 45^{o}C. Finally, ethylene was added to the reactor to equal the desired pressure, which was maintained during the experiment. 1-hexene (10 g) was pumped directly into the reactor from a weighed storage vessel upon initiation of the polymerization experiment. Hydrogen was metered into the reactor along with the ethylene to a prescribed 125 ppm level. After the allotted reaction time, the ethylene flow was stopped, and the reactor was slowly depressurized and opened to recover the granular polymer powder. The reactor was clean with no indication of any wall scale, coating or other forms of fouling. The polymer powder was then removed and weighed, and the activity was determined from this weight and the measured time based on the amount of catalyst charged.

6.4.3 Melt Index Determination

Approximately 7 g of polymer was loaded into the barrel of a Tinius Olsen EP600 extrusion plastometer melt flow apparatus that was preheated to 190^{o}C. After a 6-minute melting time, a 2.16 kg weight (melt index) was automatically loaded onto the plunger to force the molten polyethylene through a circular die. The distance travelled by the weight and time are measured and used to calculate melt index in dg min^{-1}. Following melt flow determination, additional weights to produce a total of 21.6 kg (high load melt index) was automatically loaded onto the plunger to force the molten polyethylene through the circular die. The distance travelled by the weight and time are measured and used to calculate a high load melt index in dg min^{-1}.

6.4.4 SEC Measurements

Molecular weights and molecular weight distributions were obtained using a Polymer Labs (now an Agilent company) PL-220 gel permeation chromatograph with 1,2,4-trichlorobenzene as the solvent at a flow rate of 1 mL/min and at 145ºC. 2,6-di-*tert*-butyl-4-methylphenol (BHT) at a concentration of 0.5 g/L was used as a stabilizer in the solvent. An injection volume of 400 μL was used with a nominal polymer concentration of 1 g/L. Dissolution of the stabilized sample was carried out by heating at 150ºC for 5 h with occasional agitation. Three Waters HT-6E columns (7.8 x 300 mm) were used and calibrated with a broad linear polyethylene standard (Phillips Marlex® BHB 5003) whose molecular weight had previously been determined.

6.4.5 Synthesis and Characterization

Synthesis of 1

1 was prepared according to Stephan and co-workers.[31] ^{1}H NMR spectra collected for the synthesized material were in accord with prior results. Elemental analysis confirmed preparation of the desired material. Anal. Calc'd for $C_{21}H_{34}Cl_2NPTi$: C, 56.02; H, 7.61, N, 3.11. Found: C, 55.85; H, 7.42, N, 3.23.

Synthesis of 2-Et

In the glovebox under an inert atmosphere of nitrogen, a 20 mL scintillation vial was loaded with **1** (100 mg, 0.222 mmol) and suspended in 10 mL pentane or benzene. Using a syringe, 2 equiv. of 0.6 M solution of triethylaluminum ($AlEt_3$) in heptane (0.7 mL, 0.444 mmol) was added dropwise to this yellowish-green color suspension or solution, respectively, over a period of 15 minutes. The color of the solution changed from yellowish

green to emerald green within half an hour of addition. The resultant homogenous solution was stirred for another hour and concentrated. This viscous liquid was then refrigerated at –35°C to give deep emerald green crystals of **2-Et**. Satisfactory elemental analysis results for **2-Et** were not obtained despite several attempts, likely due to the acute sensitivity of this compound to air and moisture.

6.5 Acknowledgements

The authors thank Justin Douglas and Sarah Neuenswander for assistance with NMR and EPR spectroscopy, and Milan Gembicky and Curtis Moore for assistance with X-ray crystallographic characterization. The work in this chapter was supported by Chevron Phillips Chemical.

6.6 References

(1) McDaniel, M. P.; DesLauriers, P. J. *Ethylene Polymers, HDPE, Kirk-Othmer Encyclopedia of Chemical Technology* **2015**.

(2) Nexant Supplement I, Bimodal HDPE, PolyOlefins Planning Service Report, **2009**

(3) Nexant Supplement II, Global Metallocene LLDPE Review, PolyOlefins Planning Service Report, **2011**

(4) Shapiro, P. J.; Bunel, E.; Schaefer, W. P.; Bercaw, J. E., Scandium complex [{(η^5-C_5Me_4)Me_2Si(η^1-$NCMe_3$)}(PMe_3)ScH]$_2$: a unique example of a single-component -olefin polymerization catalyst. *Organometallics* **1990,** *9*, 867-869.

(5) Stephan, D. W.; Stewart, J. C.; Guérin, F.; Spence, R. E. v. H.; Xu, W.; Harrison, D. G., Phosphinimides as a Steric Equivalent to Cyclopentadienyl: An Approach to Ethylene Polymerization Catalyst Design. *Organometallics* **1999,** *18* , 1116-1118.

(6) Bell, S. IHS Chemical, LLDPE Process Summary, Process Economics Program Review, **2015**.

(7) McDaniel, M. P.; Collins, K. S.; Johnson, M. M.; Smith, J. L.; Benham, E. A.; Hawley, G. R.; Wittner, C. E.; Jensen, M. D. *Compositions that can produce polymers,* US6107230A, **2000**.

(8) McDaniel, M. P.; Collins, K. S.; Johnson, M. M.; Smith, J. L.; Benham, E. A.; Halwey, G. R.; Wittner, C. E.; Jensen, M. D. *Process for producing polymers using a composition comprising an organometal compound, a treated solid oxide compound, and an organoaluminum,* US6316553B1, **2001**.

(9) McDaniel, M.P.; Jensen, J. D.; Jayaratne, K.; Collins, K. S.; Benham, E. A.; McDaniel, N. D.; Das, P. K.; Martin, J. L.; Yang, Q.; Thorn, M. G.; Masino, A. P., *Metallocene Activation by Solid Acids*, Tailor-Made Polymers, Ed. Severn, J. R. and Chadwick, J .C., Wiley-VCH Verlag GmbH & Co., Weinheim, Germany, 2008.

(10) Guerin, F.; Beddie, C. L.; Stephan, D. W.; Spence, R. E. V. H.; Wurz, R., eta1- and eta5-indenyl and cyclopentadienyl tri-tert-butylphosphoraneiminatotitanium complexes. *Organometallics* **2001,** *20* , 3466 - 3471.

(11) (a) Cossee, P., Ziegler-Natta catalysis. I. Mechanism of polymerization of α-olefins with Ziegler-Natta catalysts. *J. Catal.* **1964,** *3*, 80-88. (b) Arlman, E. J.; Cossee, P., Ziegler-Natta catalysis. III. Stereospecific polymerization of propene with the catalyst system $TiCl_3$-$AlEt_3$. *J. Catal.* **1964,** *3*, 99-104.

(12) Kickham, J. E.; Guérin, F.; Stewart, J. C.; Urbanska, E.; Stephan, D. W., Multiple C−H Bond Activation: Reactions of Titanium−Phosphinimide Complexes with Trimethylaluminum. *Organometallics* **2001,** *20*, 1175-1182.

(13) Kickham, J. E.; Guérin, F.; Stephan, D. W., Divergent Pathways of C−H Bond Activation: Reactions of $(t\text{-}Bu_3PN)_2TiMe_2$ with Trimethylaluminum. *J. Am. Chem. Soc.* **2002,** *124*, 11486-11494.

(14) Graham, T. W.; Kickham, J.; Courtenay, S.; Wei, P.; Stephan, D. W., Reduction of Titanium(IV)-Phosphinimide Complexes: Routes to Ti(III) Dimers, Ti(IV)-Metallacycles, and Ti(II) Species. *Organometallics* **2004,** *23* , 3309 - 3318.

(15) Natta, G.; Pino, P.; Mazzanti, G.; Giannini, U., A Crystallizable Organometallic Complex Containing Titanium and Aluminum. *J. Am. Chem. Soc.* **1957,** *79* , 2975-2976.

(16) Natta, G.; Corradini, P.; Bassi, I. W., Crystal Structure of yhe Complex $(C_5H_5)_2TiCl_2Al(C_2H_5)_2$. *J. Am. Chem. Soc.* **1958,** *80*, 755-756.

(17) Stephan, D. W., The Road to Early-Transition-Metal Phosphinimide Olefin Polymerization Catalysts. *Organometallics* **2005,** *24*, 2548-2560.

(18) Sattler, A.; Aluthge, D. C.; Winkler, J. R.; Labinger, J. A.; Bercaw, J. E. Enhanced Productivity of a Supported Olefin Trimerization Catalyst. *ACS Catalysis* **2016,** *6*, 19-22.

(19) Allen, P. E. M.; Brown, J. K.; Obaid, R. M. S., Electron spin resonance (E.S.R.) studies of some complexes derived from dicyclopentadienyltitanium dichloride and trialkyl aluminum. *Trans. Faraday Soc.* **1963,** *59*, 1808-1814.

(20) (a) Obaid and co-workers found that the identity of the reaction products depend on the starting ratio of Ti:Al, most of the products were unstable in the presence of excess amounts of aluminum alkyls, and that use of triisobutylaluminum yielded distinctive results in comparison to other aluminum alkyls. (b) Egger, K. W., Kinetics of the intramolecular four-center elimination of isobutylene from triisobutylaluminum in the gas phase. *J. Am. Chem. Soc.* **1969,** *91*, 2867-2871. (c) Bent, B. E.; Nuzzo, R. G.; Dubois, L. H., Surface organometallic chemistry in the chemical vapor deposition of aluminum films using triisobutylaluminum: beta-hydride and beta-alkyl elimination reactions of surface alkyl intermediates. *J. Am. Chem. Soc.* **1989,** *111*, 1634-1644.

(21) (a) Mach, K.; Antropiusova, H.; Polacek, J., The structure of bis(dihaloalane-di-μ-halo)(η-arene)titanium(II) complexes containing different halogen atoms. *Transition Met. Chem.* **1979,** *4* , 312-315. (b) Mach, K.; Antropiusova, H.; Polacek, J., Ethyl-substituted (η^5-cyclopentadienyl)bis(dihaloalanedi-μ-halo)titanium(III) and (η^6-benzene)bis(dihaloalanedi-μ-halo)titanium(II) chloro and bromo complexes. *J. Organomet. Chem.* **1980,** *194* , 285-295. (c) Bulychev, B. M.; Kostenko, A. L.; Yakovleva, N. y. A.; Soloveichik, G. L., Interactions in Cp_2Ti_X-$AlH_{3-n}X_n$-$Et_2O(NEt_3)$ systems. *Transition Met. Chem.* **1981,** *6* , 32-36. (d) Tyrlik, S. K.; Korda, A.; Poppe, L.; Rockenbauer, A.; Gyoer, M., EPR spectra of products of the reaction of di-η^5-cyclopentadienyl(diethylalanedi-μ-chloro)titanium(III) with C_1 compounds. *J. Organomet. Chem.* **1987,** *336*, 343-348. (e) Mach, K.; Varga, V., Methyl-substituted cyclopentadienyl ligands: influence on the properties of titanocene chloro(ethyl)aluminates. *J. Organomet. Chem.* **1988,** *347*, 85-92.

(22) McDaniel, M. P., Influence of porosity on polyethylene molecular weight from the Phillips Cr/silica catalyst. *J. Catal.* **2009,** *261*, 34-49.

(23) (a) Buck, R. M.; Yang, Q.; Masino, A. P.; Wittner, C. E. *Catalyst systems containing a bridged metallocene,* US9040642B2, **2015**. (b) Yang, Q.; Jensen, M. D.; McDaniel, M. P., Alternative View of Long Chain Branch Formation by Metallocene Catalysts. *Macromolecules* **2010,** *43*, 8836-8852.

(24) Yang, Q.; Hlavinka, M. L. *Process for synthesizing bridged cyclopentadienyl-indenyl metallocenes* US8309747B2, **2012**.

(25) Stephan, D. W.; Guérin, F.; Spence, R. E. v. H.; Koch, L.; Gao, X.; Brown, S. J.; Swabey, J. W.; Wang, Q.; Xu, W.; Zoricak, P.; Harrison, D. G., Remarkably Active Non-Metallocene Ethylene Polymerization Catalysts. *Organometallics* **1999,** *18*, 2046-2048.

(26) Stephan, D. W.; Stewart, J. C.; Guérin, F.; Courtenay, S.; Kickham, J.; Hollink, E.; Beddie, C.; Hoskin, A.; Graham, T.; Wei, P.; Spence, R. E. v. H.; Xu, W.; Koch, L.; Gao, X.; Harrison, D. G., An Approach to Catalyst Design: Cyclopentadienyl-Titanium Phosphinimide Complexes in Ethylene Polymerization. *Organometallics* **2003,** *22*, 1937-1947.

(27) J.-M. Saveant, *Elements of Molecular and Biomolecular Electrochemistry*, Wiley, Hoboken, NJ, 2006.

(28) Risberg, E. D.; Mink, J.; Abbasi, A.; Skripkin, M. Y.; Hajba, L.; Lindqvist-Reis, P.; Bencze, E.; Sandstroem, M., Ambidentate coordination in hydrogen bonded dimethyl sulfoxide, $(CH_3)_2SO\cdots H_3O^+$, and in dichlorobis(dimethyl sulfoxide) palladium(II) and platinum(II) solid solvates, by vibrational and sulfur K-edge X-ray absorption spectroscopy. *Dalton Trans.* **2009**, 1328-1338.

(29) Perrin, D. D., *Ionisation Constants of Inorganic Acids and Bases in Aqueous Solution*, Pergamon, Oxford, **1982**.

(30) Kumar, A.; Lionetti, D.; Day, V. W.; Blakemore, J. D., Trivalent Lewis Acidic Cations Govern the Electronic Properties and Stability of Heterobimetallic Complexes of Nickel. *Chem. – A Eur. J.* **2018,** *24*, 141-149.

(31) (a) Stephan, D. W.; Stewart, J. C.; Guérin, F.; Spence, R. E. v. H.; Xu, W.; Harrison, D. G. *Organometallics* **1999**, *18*, 1116. (b) Guerin, F.; Beddie, C. L.; Stephan, D. W.; Spence, R. E. V. H.; Wurz, R., η1- and η5-indenyl and cyclopentadienyl tri-tert-butylphosphoraneiminato titanium complexes. *Organometallics* **2001,** *20,* 3466-3471.

(32) McDaniel, M. P.; Collins, K. S.; Johnson, M. M.; Smith, J. L.; Benham, E. A.; Hawley, G. R.; Wittner, C. E.; Jensen, M. D. US6107230A, **2000.**

(33) McDaniel, M. P.; Collins, K. S.; Johnson, M. M.; Smith, J. L.; Benham, E. A.; Halwey, G. R.;. Wittner, C. E.; Jensen, M. D. US6316553B1, **2001**.

Chapter 7

Heterobimetallic [Ti,Al] Complexes: Divergent Synthesis, Redox Properties, and Ethylene Polymerization Catalysis

This chapter is adapted from a submitted manuscript:

Kumar, A.; Barr, J. L.; Cruz, C. A.; Blakemore, J. D. Heterobimetallic [Ti,Al] Complexes: Divergent Synthesis, Redox Properties, and Ethylene Polymerization Catalysis. *Organometallics*, **2021**, *in press*.

7.1 Introduction

Aluminum alkyls of the form AlR_3 are prevalent in the polymerization industry and are known to perform numerous functions in the formation of polymers, like polyethylene.[1] In conjunction with famous catalysts such as the Ziegler-Natta catalyst,[2] the Phillips catalyst,[3] and some metallocenes,[4] these aluminum alkyls modulate polymer properties and enhance polymerization activity. They are also used as scavengers to remove poisons such as residual moisture and oxygen from catalytic reaction mixtures. Furthermore, methylaluminoxane (MAO), the product of treating trimethylaluminum ($AlMe_3$) with water, has been commonly used as a catalyst activator (or co-catalyst) for olefin polymerization by molecular systems since its accidental discovery in 1976 by Kaminsky.[5] These aluminum reagents are Lewis acids that can generate cationic metal centers from precatalysts and thereby form active catalysts capable of polymerizing ethylene.[6]

In studies of 'single-site' polymerization catalysis, molecular organometallic complexes have attracted significant attention; these systems have been known as especially useful catalysts for the production of linear low-density polyethylene (LLDPE) since the late 1950s.[7] Group IV transition metal complexes, in particular, emerged out of initially niche applications in the industry.[8]

Some of these 'single-site' homogenous catalysts include systems that are heterobimetallic in nature.[9,10] For instance, Marks & coworkers have reported a [Ti,Cr] olefin polymerization catalyst that selectively produces high molecular weight (M_w) *n*-butyl branched polyethylene (PE) at Cr sites in the catalyst with branch densities that are ca. 3 times greater than those achieved by analogous tandem systems.[11] This approach, wherein two transition metal centers are present in close proximity, can thus elicit pronounced

cooperative effects engendering greater polymerization activities and high molecular weight polymers.[9] Polymerization catalysts in which redox-active metals like titanium or zirconium are paired with highly Lewis acidic metals like aluminum have attracted significant interest.[12,13,14] Along this line, Do & coworkers have prepared two families of heterobimetallic Ni[15] and Pd[16] complexes featuring pendant polyethylene glycol that house Li^+, Na^+, and K^+ as Lewis acids. Their polymerization data display a significant increase in the polymerization activity, molecular weight, and branching frequency in contrast to their monometallic counterparts.

These newer systems are complemented by earlier examples of heterobimetallic structures that were discovered in the early days of polymerization chemistry. In particular, Natta and Tebbe provided notable examples in this area (complexes **N** and **T**, see Chart 7.1).[17,18,19] Their pioneering work showcased the rich coordination chemistry of titanium supported by two cyclopentadienyl (η^5-Cp) ligands and linked to an aluminum center by bridging chloride (**N**) and/or methylene (**T**) groups. Such metallocene-type systems remain popular in the field to this day,[4,20] as there continues to be significant developments around use of these structures for polymerization chemistry.[21,22] Structural diversity is readily accessible in these compounds through substitution of the simple Cp ligand with related analogues like indenyl (Ind) or pentamethylcyclopentadiene (Cp*).

The phosphinimide-type ligands developed by Stephan and coworkers are conceptually related to these traditional cyclopentadienyl-type ligands, and can be readily incorporated into structures suitable for polymerization chemistry.[23,24] In particular, phosphinimide ligands resemble Cp ligands in that they are anionic donors that present significant steric bulk; despite their rather distinctive structural connectivity, phosphinimides are sterically

similar to Cp. Complexes supported by phosphinimide ligands demonstrate high activities for olefin polymerization, comparable to or even better than traditional metallocenes.[25] This high activity may be attributable in part to the rather geometrically accessible nature of the Ti center in these compounds (Ti•••P distance of ca. 3.0 Å vs. Ti–$Cp_{centroid}$ distance of ca. 2.2 Å).[26]

Chart 7.1. Heterobimetallic [Ti,Al] complexes supported by phosphinimide ligands

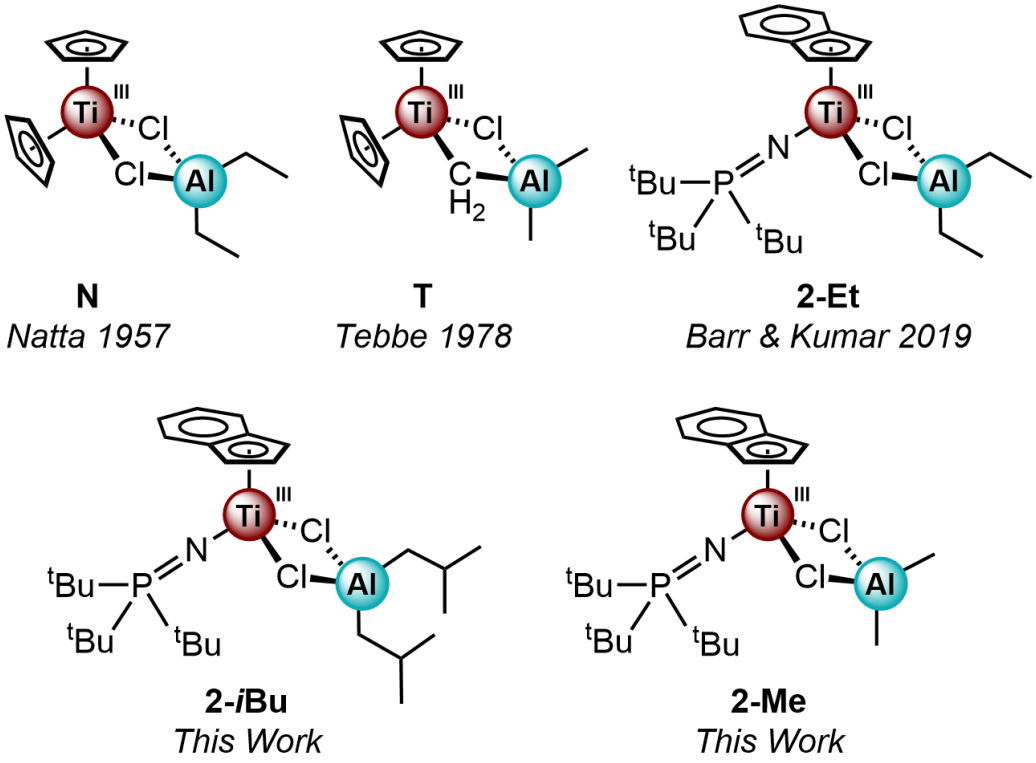

Building on this prior work with metallocene and phosphinimide ligands, we have recently studied the chemistry of a heterobimetallic [Ti,Al] species supported by indenyl and a phosphinimide ligand (**2-Et**, see Chart 7.1).[27] As **2-Et** is the first example of a heterobimetallic complex of titanium supported by a phosphinimide ligand, we have been particularly interested in the influence of the Lewis acidic Al(III) center on the properties of this compound.[28] Our work to date (Chapter 6) has shown that Al(III) stabilizes the formally

Ti(III) center in **2-Et**, and suggested that formation of this species impacts the outcomes of polymerization catalysis.[29,30] However, considering the promising catalytic activity of **2-Et** toward ethylene polymerization, we wondered if a broader family of complexes could be accessed and if these species could serve as tunable catalysts.

Here, we report the formation of two new heterobimetallic complexes of titanium [(Ind)(*t*Bu$_3$P=N)Ti(μ$_2$-Cl)$_2$Al*i*Bu$_2$] (**2-*i*Bu**) and [(Ind)(*t*Bu$_3$P=N)Ti(μ$_2$-Cl)$_2$AlMe$_2$] (**2-Me**; see Chart 7.1) and findings regarding the influence of the remote alkyl groups in the [AlR$_2$] fragment on the properties of the [Ti,Al] species. Synthetic work and complementary cyclic voltammetry (CV) experiments reveal similar chemical reactivity (on short time scales of seconds to minutes) upon reduction of **1** with Al*i*Bu$_3$ or AlMe$_3$, in comparison with the prior case of AlEt$_3$.[27] However, the heterobimetallic compounds display varying stabilities over longer timescales, and behave quite differently when employed as ethylene polymerization catalysts, particularly with respect to activity and the molecular weight distribution of product PE. Taken together, the spectroscopic, electrochemical, and catalytic results obtained here implicate roles for the alkyl groups in stabilizing the heterobimetallic species and tuning their involvement in polymerization catalysis. The selection of starting AlR$_3$ reagent used to generate the precatalyst affords a useful route to modified polymer properties.

7.2 Results

The procedure to synthesize complexes **2-*i*Bu** and **2-Me** was adapted from our previous report[27] using Stephan's useful precursor complex (Ind)(*t*Bu$_3$P=N)TiCl$_2$ (**1**).[31] The reaction of **1** with 2–5 equivalents of Al*i*Bu$_3$ or AlMe$_3$ in pentane at room temperature yields an emerald green or yellowish-green solution, respectively, after ca. 30 minutes of stirring (see

Experimental Section). Interrogation of the reaction mixtures using ^{1}H and ^{31}P NMR in C_6D_6 reveals neither discernable peaks corresponding to the starting material nor new peaks corresponding to indenyl or phosphinimide fragments (see Appendix F, Figures F1-F4 for spectra), suggesting paramagnetic species are formed in each case. These results are similar to what was observed in the case of $AlEt_3$, in that the exposure of **1** to $AlEt_3$ results in an emerald green solution that, following by workup, yields the isolable heterobimetallic species **2-Et**. Based on these observations, we were encouraged to attempt isolation of the anticipated new products **2-*i*Bu** and **2-Me**.

The emerald green solution resulting from the reaction of **1** with Al*i*Bu$_3$ for 30 min was subsequently concentrated *in vacuo* and stored at –35°C. The crystals obtained were emerald green in color and correspond to the structure of **2-*i*Bu** (*vide infra*) as predicted based on the solution coloration and similarity to results for **2-Et**. The structure of **2-*i*Bu** obtained from single-crystal X-ray diffraction analysis is quite similar to that of **2-Et** (see Figure 7.1) and reveals the expected diamond core motif containing two Ti centers and two bridging chloride ligands. The first coordination sphere around the titanium metal center retains the expected η^5-Ind and *t*Bu$_3$P=N ligands from **1**, while the terminal chloride ligands provided by **1** each adopt a μ_2-bridging mode between the formally Ti(III) and Al(III) centers in **2-*i*Bu**.

Generally speaking, the bond distances and angles in **2-Et** and **2-*i*Bu** are very similar (see Tables 7.1 and 7.2). For example, the average Ti–Cl distances are 2.526 Å and 2.527 Å, respectively. Notably, these values are significantly longer than the average Ti–Cl distance of 2.299 Å in the monometallic precursor **1**; this change is attributable to both the bridging nature of the chlorides in the bimetallic compounds as well as the formal reduction of Ti(IV) in **1** to Ti(III) in **2-Et** and **2-*i*Bu**. The titanium and aluminum centers in **2-Et** and **2-*i*Bu** adopt

similarly distorted geometries in both cases, accommodating acute Cl1–Ti–Cl2 (81.5(1)º and 80.8(1)º) and Cl1–Al–Cl2 (93.8(1)º and 92.6(1)º), respectively. Further, the intraligand P=N distance in **2-*i*Bu** (1.590(2) Å) is essentially indistinguishable from the value in **2-Et** (1.589(4) Å). Thus, we conclude that the substitution of *i*Bu for Et exerts only a minor influence over the electronic properties of the Ti center, consistent with the disposition of the alkyl groups on the aluminum at a significant distance from the titanium center.

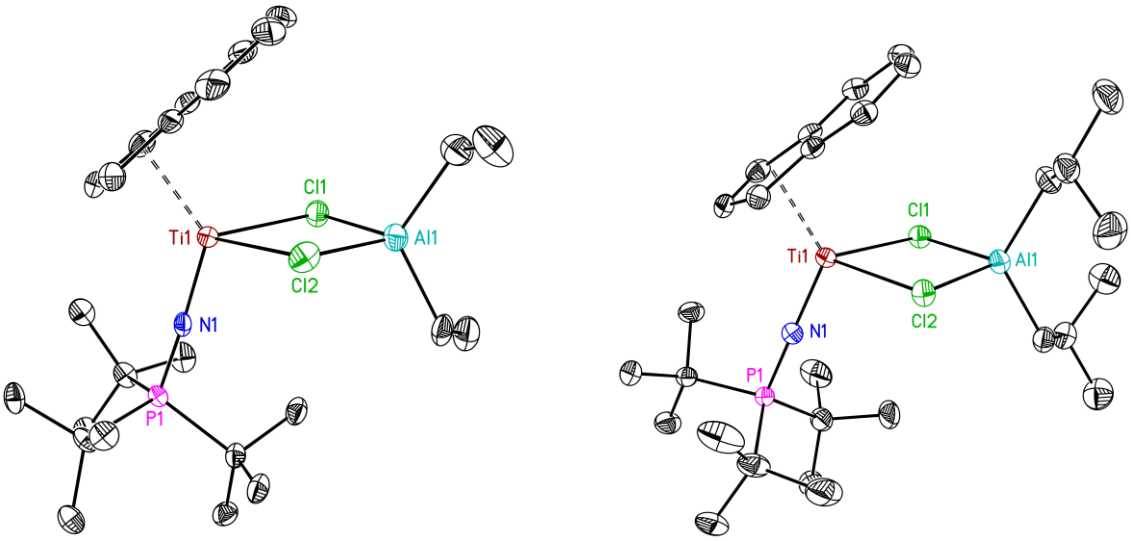

Figure 7.1. Solid-state structures (from XRD) of **2-Et** (left structure) and **2-*i*Bu** (right structure). All H-atoms are omitted for clarity. Displacement ellipsoids are shown at the 50% probability level.

On the other hand, there is a small but significant elongation of the Ti•••Al distance in **2-*i*Bu** (3.484 Å) vs. that in **2-Et** (3.455 Å). Presumably, this change is caused by steric strain induced by interaction of the more geometrically demanding isobutyl groups present on the Al center in **2-*i*Bu**. Further evidence for structural change prompted by this enhanced bulk comes from a measure of deformation of the diamond core; this was quantified with the $\omega_{diamond}$ parameter, signifying the root mean square deviation of the four atoms in the diamond core from the mean plane defined by the position of those atoms (Table 7.2).

Previously, we have used this parameter to measure macrocycle deplanarization.[28b] Here, the steric clash from the bulky isobutyl groups is indeed reflected in a higher value of $\omega_{diamond}$ value in **2-*i*Bu** (0.041) as compared to **2-Et** (0.028). This distortion apparently drives minor elongation of the Al–Cl distances as well as noticeable narrowing of the Cl1–Ti–Cl2 and Cl1–Al–Cl2 angles.

Table 7.1. Comparison of select bond lengths (Å).

Bonds	**1**	**2-Et**	**2-*i*Bu**	**3**
Ti–N	1.729(5)	1.797(4)	1.799(2)	1.972(5) – 1.997(6)
Ti–Cl$_{avg}$	2.299	2.526	2.527	2.294, 2.296
P=N	1.622(5)	1.589(4)	1.590(2)	1.621(4), 1.637(4)
Ti–Ind$_{centroid}$	2.113	2.077	2.081	-
Al–Cl$_{avg}$	-	2.259	2.264	-
Ti•••Al	-	3.455	3.484	-

Table 7.2. Comparison of select bond angles (°).

Angles	**1**	**2-Et**	**2-*i*Bu**	**3**
P–N–Ti	172.5(3)	175.9(2)	176.6(1)	139.1(4) – 141.5(4)
Cl–Ti–Cl	103.6(1)	81.5(1)	80.8(1)	112.6(1), 123.7(1)
Cl–Ti–N$_{avg}$	102.6	104.4	104.6	108.2, 111.2
Cl–Al–Cl	-	93.8(1)	92.6(1)	-
Al–Cl–Ti$_{avg}$	-	92.3	93.1	-
$\omega_{diamond}$[#]	-	0.028	0.041	0.054

#Defined as root mean square deviation (rmsd) of the following atoms from the mean plane defined by their positions: Ti1, Cl1, Cl2, and Al1.

In addition to the emerald green crystals of **2-*i*Bu**, very few orange-colored crystals were also visible when magnified. The diffraction pattern of those crystals identified the species as a homobimetallic titanium compound **3** (see Appendix F, Figure F26) which has undergone loss of the indenyl ligand as well as dimerization during the reduction. The diamond core in this species, formulated as $[(TiCl_2)_2(\mu_2\text{-}t\text{Bu}_3P{=}N)_2]$, contains two titanium(III) centers bound to two bridging chloride ligands each, which in turn is further bridged by two phosphinimide ligand interactions. However, unlike in the structure of **2-*i*Bu**, **3** does not contain an aluminum center. The structure of **3** is highly symmetrical, with similar Ti–Cl, Ti–N, and Ti–N–Ti bond lengths and angles for the two titanium atoms (see Tables 7.1 and 7.2). In comparison with **1**, **2-Et**, and **2-*i*Bu**, the P–N–Ti geometry in **3** is less linear, with an angle of 139.1(4) – 141.5(4)^o, attributable to the bridging role of the nitrogen atoms. The P=N distances in the homobimetallic species **3** is very similar to the P=N distance in **1**, a situation attributable to the presence of two phosphinimide ligands per Ti(III) center. Since this speciation product **3** was not encountered in the case of preparations of **2-Et**, we conclude that the presence of isobutyl groups on the aluminum center contributes to reduced stability of the heterobimetallic [Ti,Al] species and/or the preference for its formation. To the best of our knowledge, **3** is also the first structurally characterized species containing a Ti_2,N_2 diamond core.

2-*i*Bu could also be generated by reaction of **1** with a related aluminum reagent, diisobutylaluminum hydride (Al*i*Bu$_2$H), producing a teal-colored solution within 15 minutes. In this reaction, we were only able to identify crystals of **2-*i*Bu** (see Appendix F, Figure F25), after removing all the volatiles from the solution and storing the vial at –35^{o}C. No other crystals (of **3** or any other compounds) were visible under those conditions, which

may be due to the greater stability and lower reactivity of Al*i*Bu$_2$H. On the other hand, the formation of multiple species may be occurring despite not being able to collect crystals of **3**. This assumption is in accordance with gas chromatography-mass spectrometric (GC-MS) data (*vide infra*) that reveals the formation of biindene and isobutane when the reaction mixture obtained from the reduction of **1** with Al*i*Bu$_2$H (or Al*i*Bu$_3$) in benzene is quenched.[32] Surprisingly, reactions of **1** with AlEt$_3$, Al*i*Bu$_3$ or Al*i*Bu$_2$H do not yield any identifiable titanium alkyl species, a reaction commonly believed to be a prerequisite for achieving ethylene polymerization activity.[33,34]

Following the success of collecting significant quantities of crystalline **2-*i*Bu**, we attempted to isolate **2-Me**. However, attempts to obtain crystals suitable for X-ray diffraction were not successful. Often, such attempts led only to formation of solutions with a dark yellow coloration instead of the expected vibrant green color, suggesting speciation or decomposition. However, we do believe that a compound formulated as **2-Me** is forming on the basis of (i) the distinctive yellowish-green coloration at the early stage of the reaction and (ii) complementary cyclic voltammetry data implicating electro-promoted formation of the species (*vide infra*).

The striking structural similarity between **2-Et** and **2-*i*Bu** and apparently diminished stability of **2-Me** prompted us to carry out *in situ* electrochemical studies related to generation of these complexes and compare their profiles by cyclic voltammetry (CV).[35] *C*yclic voltammograms collected on a solution containing **1** and 5–6 equiv. of Al*i*Bu$_3$ in THF display a cathodic peak (Figure 7.2, blue trace) at $E_{p,c}$ = –2.08 V vs. the ferrocenium/ferrocene couple (denoted hereafter as $Fc^{+/0}$). When the scan is reversed, a return oxidation peak is observed at a more positive potential at $E_{p,a}$ = –1.32 V vs. $Fc^{+/0}$. The

CV profile of **1** in the presence of Al*i*Bu$_3$ is analogous to the voltammogram observed when AlEt$_3$ was employed (Figure 7.2, black trace), suggesting similar reactivity occurring on the time scale of the cyclic voltammetry. Like in the AlEt$_3$ case ($E_{p,c}$ = –2.06 V vs. $Fc^{+/0}$), we can reliably assign the cathodic process as a one-electron reduction leading to the initial formation of a monometallic Ti^{III} species **1′** from the starting Ti^{IV} species **1** (Figure 7.3).

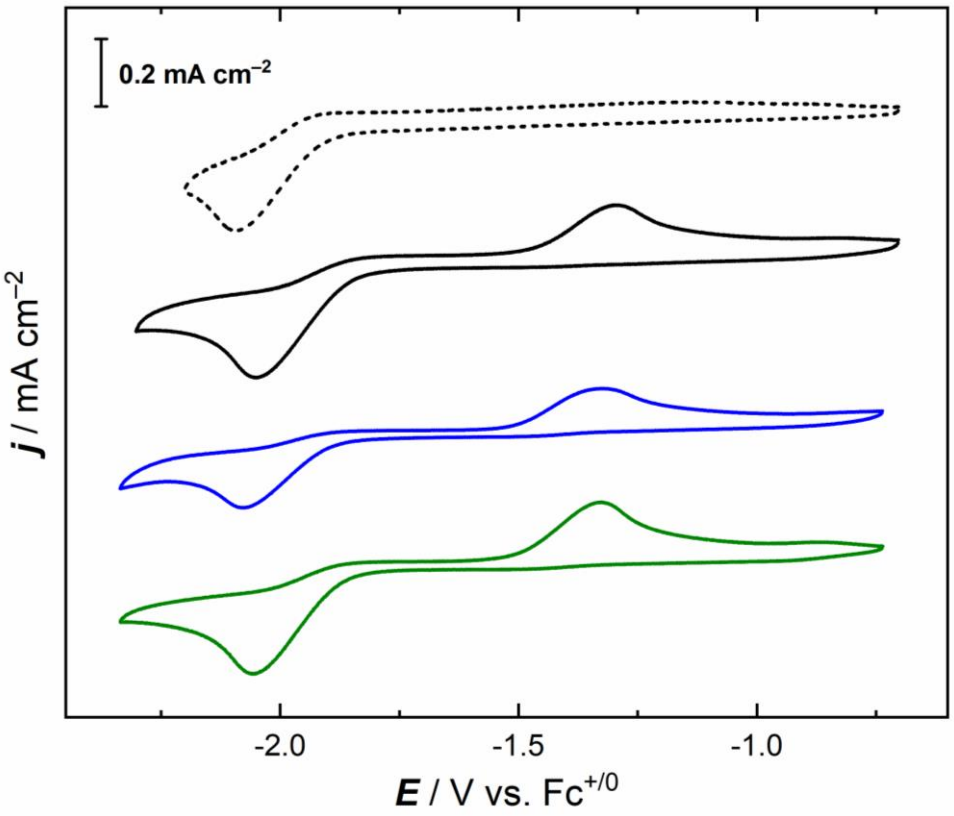

Figure 7.2. Cyclic voltammetry data for **1** (dotted black) and **1** in the presence of six equiv. of AlEt$_3$ (black), six equiv. of Al*i*Bu$_3$ (blue), and six equiv. of AlMe$_3$ (green). Conditions: 0.1 M $[^nBu_4N]^+[PF_6]^-$ in THF; scan rate: 100 mV/s.

Previously, we showed that the cyclic voltammogram of **1** in the absence of aluminum reagent displays an irreversible reduction at $E_{p,c}$ = –2.12 V at slower scan rates.[27] However, at a faster scan rate of 300 mV/s, a coupled return oxidation wave could be observed at $E_{p,a}$ ≈ –1.9 V vs. $Fc^{+/0}$, implicating formation of the transient Ti^{III} species **1′** (see Appendix F,

Figure F13). Appealingly, a similar redox feature was recently observed by Gansäuer and coworkers when they conducted voltammetry on Cp_2TiCl_2.[36] On the basis of this profile, we assign the reduction of **1** as an EC-type event,[37] wherein initial reduction of **1** to **1′** involves a follow-up chemical reaction leading to formation of redox-inactive products and, effectively, decomposition of the Ti complex, when a trialkylaluminum reagent is not available to react with the nascent **1′**.

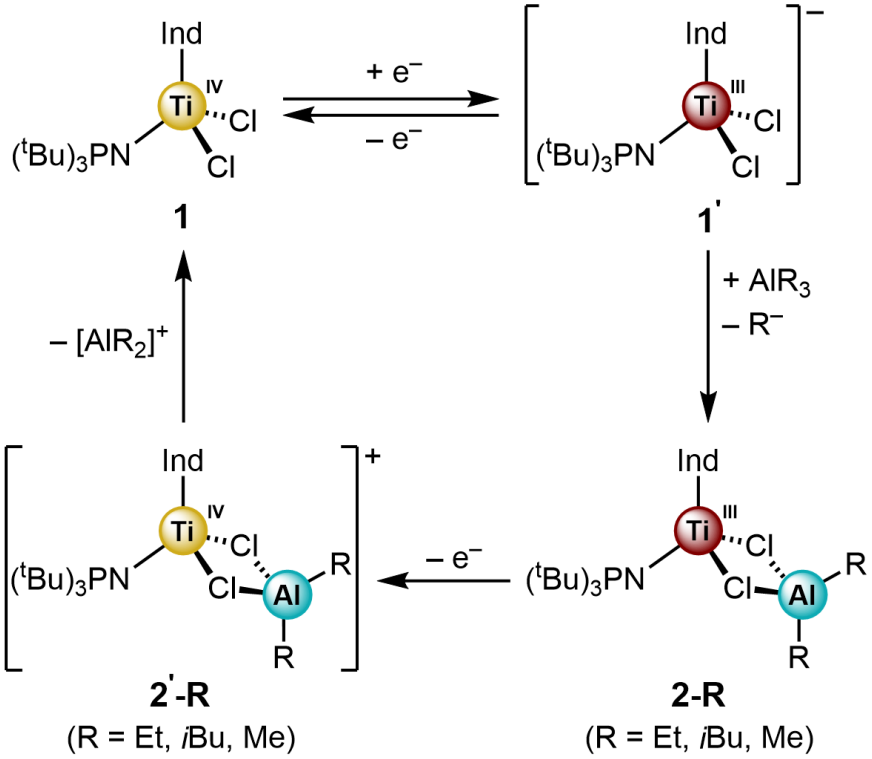

Figure 7.3. Electrochemical pathway for the formation of **2-R** from **1**.

When Al*i*Bu$_3$ is present in the electrochemical cell, the transiently generated Ti^{III} species **1′** can react with Al*i*Bu$_3$, generating the heterobimetallic complex **2-*i*Bu** in the reaction-diffusion layer near the electrode (see Figure 7.3). This one-electron reduction followed by a chemical reaction leading to the formation of **2-*i*Bu** from **1′** can be concluded to be relatively rapid because the redox wave remains irreversible even at high scan rates (see

Appendix F, Figures F9 and F10). Stated another way, the lack of observation of a return anodic wave indicates rapid consumption of **1′**, produced at the electrode surface, by reaction with the aluminum reagent. The related control experiments carried out in the absence of aluminum reagent do show limited reversibility at the higher scan rates,[27] confirming the production and intermediacy of **1′** in this process.

On the basis of the voltammetric data, species **2-*i*Bu** can undergo re-oxidation from the Ti^{III} form to a Ti^{IV} form at a modestly more positive potential ($E_{p,a}$ = –1.32 V vs. $Fc^{+/0}$) to generate another unstable transient species **2′-*i*Bu**, which presumably releases $[Al{i}Bu_2]^+$ cation to return the monometallic species **1**. The anodic wave for this process closely resembles the re-oxidation process observed for **2-Et** at $E_{p,a}$ = –1.32 V vs. $Fc^{+/0}$ (Figure 7.3). Consistent with these identical peak potentials, **2-Et** and **2-*i*Bu** are geometrically similar as judged by XRD studies, implicating similar environments for the Ti centers in both cases and thus supporting the tight similarity of their redox properties. Considering all of this, we conclude that the presence of ethyl versus isobutyl groups on the $[AlR_2]$ fragment does not significantly change the reduction potentials associated with the interconversion of Ti^{IV} to Ti^{III}. Furthermore, as no new processes or discernible side reactions are visible in the case of **2-*i*Bu**, we conclude that the electrochemical generation of **2-*i*Bu** is clean, as we have found for **2-Et** in prior work (Chapter 6).[27] This contrasts with the diminished stability of **2-*i*Bu** over the minutes-to-hours timescale as judged by the formation of the side product **3**.

Having observed the apparent similarity between the electrochemical profile of **2-*i*Bu** and **2-Et**, we next endeavored to investigate the electrochemistry of **1** in the presence of $AlMe_3$. Indeed, the CV profile of **1** in the presence of 6 equiv. of $AlMe_3$ in THF, displays a single cathodic reduction at $E_{p,c}$ = –2.06 V vs. $Fc^{+/0}$, similar to the case of $AlEt_3$ and $Al{i}Bu_3$, (Figure

7.3, green trace). As in the other cases, this cathodic process remains irreversible at higher scan rates (see Appendix F, Figures F11, and F12). However, similar to what we observed in the presence of $AlEt_3$[27] and Al*i*Bu_3, a peak is observed on the oxidative sweep at a more positive potential ($E_{p,a}$ = –1.33 V vs. $Fc^{+/0}$), consistent with re-oxidation of Ti^{III} to Ti^{IV}. Thus, we conclude that the full family of [Ti,Al] heterobimetallic complexes, including the apparently less stable complex **2-Me** can be generated at short times under electrochemical conditions, as judged by their similar redox chemistry on the timescale of cyclic voltammetry.

In all cases, the more positive potential of the anodic peak corresponding to oxidation of the complexes **2-R** (when compared to the apparent reduction potential of **1**) is attributable to the influence of the Lewis acidity of the corresponding [AlR_2] fragment. This shift in potential is in accord with work being carried out by some of us in the area of quantification of Lewis acid effects in redox chemistry.[28] Specifically, we have measured a positive shift of ca. 61(±9) mV/pK_a and 67(±9) mV/pK_a in two families of heterobimetallic uranyl and nickel complexes, respectively. In the case of the complexes explored here, the measured redox potentials are not greatly affected by the various alkyl groups present, consistent with the assignment of titanium-centered redox events in all cases.

With these results in hand, we moved to further investigate the influence of the alkyl groups present in the heterobimetallic complexes **2-R** with *in situ* UV/visible spectroscopy. As manifested in the synthetic work, complexes **2-Et** and **2-*i*Bu** are emerald green in color and display lowest-energy absorption bands at 709 nm (ε = 390 M^{-1} cm^{-1}) and 715 nm (ε = 202 M^{-1} cm^{-1}) in THF, respectively (see Appendix F, Figure F5). These bands are attributable to a *d-d* transition in the Ti(III) d^1 systems present in both complexes. In the less

polar solvent pentane, these bands are slightly blue-shifted to 617 nm (ε = 194 M^{-1} cm^{-1}) and 638 nm (ε = 136 M^{-1} cm^{-1}), respectively (see Appendix F, Figure F6). However, attempts at *in situ* preparation of **2-Me** do not show an analogous *d-d* band in either solvent system, suggesting decomposition or sluggish chemical reactivity at minutes to hours' time scale (see Appendix F, Figures F5 and F6).

In the context of understanding ligand influences on the properties of titanocene-type complexes, we previously investigated the electrochemical properties of two analogues of **1**, namely Cp(*t*Bu_3P=N)$TiCl_2$ (**4**) and Cp*(*t*Bu_3P=N)$TiCl_2$ (**5**) with cyclic voltammetry.[27] In this work, measured $E_{p,c}$ values for similar $Ti^{IV/III}$ reductions of **1**, **4**, and **5** confirm the expected ordering of donor strength (Ind < Cp < Cp*). Similar behavior was observed for dimethyl titanocene complexes which give a 100-mV anodic shift in the $Ti^{IV/III}$ reduction potential upon swapping Ind for Cp.[38]

However, as our polymerization studies included tests with Cp and Cp* ligands (*vide infra*), we added to our work with these compounds here by probing the electronic properties of **4** and **5** using UV/visible spectroscopy. In **4** and **5**, Ti is in the +4 oxidation state (d^0 system), and the lowest-energy absorption bands can be attributed to ligand-to-metal charge transfers (LMCT) which appear at 401 nm (ε = 840 M^{-1} cm^{-1}) and 367 nm (ε = 2320 M^{-1} cm^{-1}), respectively (see Appendix F, Figure F7).[39,40,41] Notably, **1** displays a corresponding LMCT band at 414 nm (ε = 1670 M^{-1} cm^{-1}). With these data plus the corresponding $E_{p,c}$ values mentioned above in hand, we plotted them together to reveal a tight linear correlation (Figure 7.4). This linear relationship confirms that the identity of the ligand (Ind vs. Cp vs. Cp*) influences the electronics of our phosphinimide-ligated system. A similar relationship for Group IV bent metallocenes was reported by Loukova & coworkers.[40,42] Such differences

in electronics could contribute to variation in olefin polymerization behavior when **1**, **4**, and **5** are employed as catalysts (see Appendix F, Figure F8).

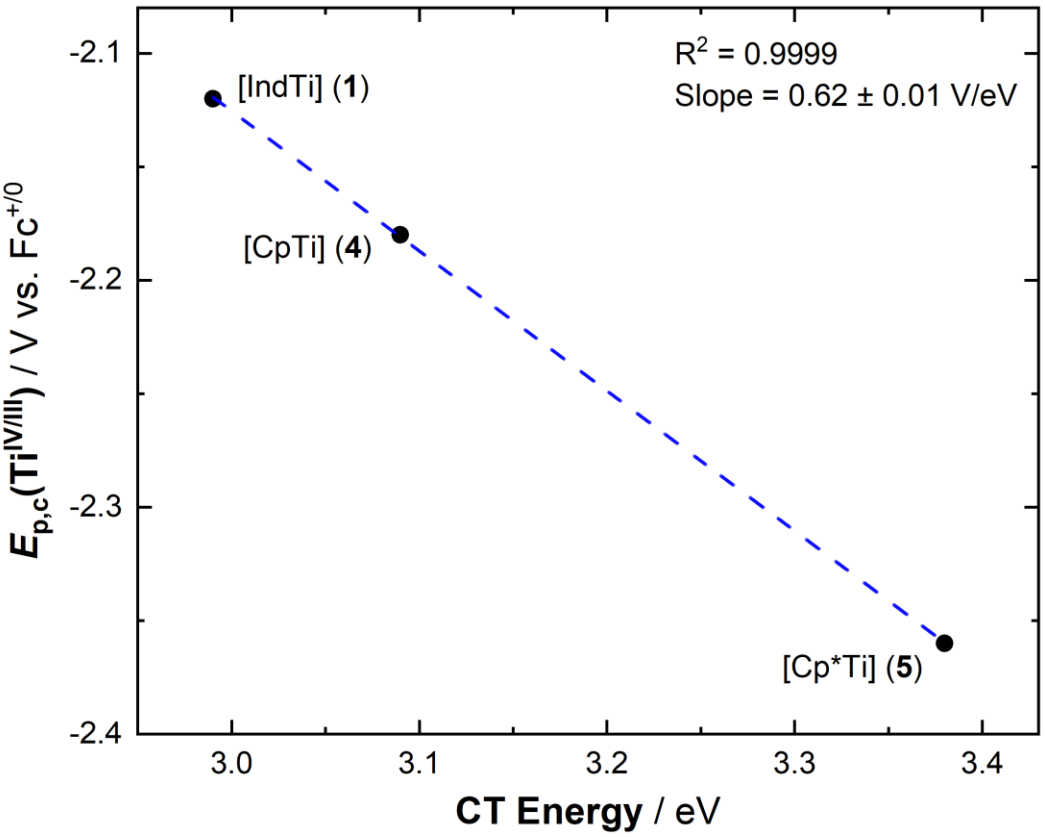

Figure 7.4. Dependence of the $E_{p,c}(Ti^{IV/III})$ of titanium complexes **1** ([IndTi]), **4** ([CpTi]), and **5** ([Cp*Ti]) on ligand-to-metal charge transfer (LMCT) band.

With all this information in hand from our synthetic and electrochemical studies, we next turned to electron paramagnetic resonance (EPR) spectroscopy to confirm the presence of Ti(III) centers in the isolated compounds, as well as compare isolated samples of **2-*i*Bu** and **2-Et** with *in situ* generated samples of **1** mixed with AlR_3. We anticipated such an effort would be fruitful, even for the recalcitrant **2-Me** system, because the cyclic voltammetry data suggest reasonable stability of all the bimetallic complexes on short timescales. Based on the similar signals observed with EPR for cases of all three complexes (see Figure 7.5),

we indeed conclude that analogous bimetallic species are formed at short times in all three cases.

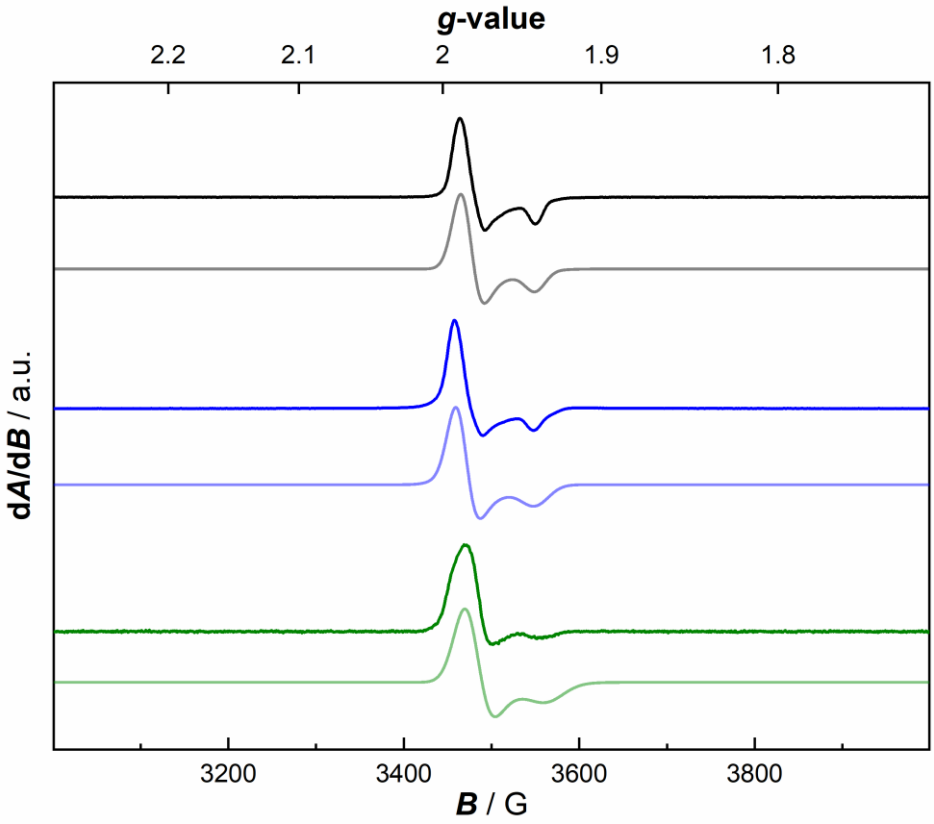

Figure 7.5. X-band continuous-wave EPR spectra of isolated **2-Et** (black; simulated spectrum in grey), isolated **2-*i*Bu** (blue; simulated spectrum in light blue) and *in situ* generated **2-Me** (green; simulated spectrum in light green) in frozen toluene.

EPR spectra (perpendicular mode) of isolated **2-*i*Bu** in frozen toluene display axial symmetry and characteristic features at g = 1.986 and 1.939 at 10 K (Figure 7.5, black trace). These features are very similar to those found in the spectrum of isolated **2-Et** (g = 1.984, 1.940; Figure 7.5, dark blue trace). These findings agree with the spectrum of isolated **2-Et** measured in our prior work (see Chapter 6),[27] and in both cases, are consistent with the expected formally Ti(III) centers having d^1 configurations with S = ½. Due to the lack of resolved hyperfine coupling to the Ti nucleus (I = ½) or superhyperfine coupling to the

nearby ^{14}N (I = 1) and ^{31}P (I = ½) atoms in the phosphinimide ligands, we assign the reduced metal species as S = ½ Ti(III) systems with the unpaired electron localized on the titanium centers in both cases. This assignment of metal-based radicals is consistent with the significant g anisotropy in the spectra.

The experimental EPR spectrum of **2-*i*Bu** could be successfully modeled using the EasySpin software. The axial spectral profile was well-reproduced using a single S = ½ system and g values consistent with a single Ti^{III} species (see Appendix F, Figure F20). Thus, we conclude that the reduction of **1** to form **2-*i*Bu** proceeds cleanly at a shorter time scale of approximately 1-2 hours, as judged by CV and EPR studies.

To compare with these clean results, however, we prepared a reaction mixture containing **1** and 5–6 equiv. of Al*i*Bu$_3$ and allowed it to stir for a longer period of 24 hours at room temperature, contrasting with the 30 min used for preparation of **2-*i*Bu** (*vide supra*). In the case of the longer reaction time, a distinct magenta-colored solution was observed. Interrogation of this solution's EPR spectrum produced a unique spectrum with more complex features than those evident in the cleanly isolated **2-*i*Bu** (see Appendix F, Figure F20) as well as *in situ* generated **2-*i*Bu** interrogated at shorter time scales (see Appendix F, Figure F22). Considering the observed formation of homobimetallic titanium species **3** under similar reaction conditions by XRD, we conclude that the more complex EPR spectra are consistent with formation of one or more additional products beyond **2-*i*Bu**. A parallel-mode spectrum for the magenta-clored solution was also collected, but revealed no additional signals consistent with integer-spin complexes (see Appendix F, Figure F23).

These results compare well with observation of multiple products in the study conducted by Obaid & coworkers when Cp_2TiCl_2 was reduced with the increasing amounts of Al*i*Bu$_3$.[43]

When stoichiometric amounts of titanium and aluminum reagents were used, a green color solution was obtained, which was assigned to the heterobimetallic complex of the form $Cp_2Ti(\mu_2\text{-}Cl)_2Al\textit{i}Bu_2$. The EPR spectra of this postulated species revealed an isotropic signal at g = 1.976. However, increasing the amount of added $Al\textit{i}Bu_3$ and allowing the reaction mixture to stir for 1-2 days resulted in a solution color change from green to violet-red; this color change is reminiscent of that in our case when we employed $Al\textit{i}Bu_3$ as a reagent. Obaid & coworkers attributed this change in color to the presence of excess amounts of $Al\textit{i}Bu_3$, leading to decomposition products. Limited characterization of this violet-red solution from Obaid's work suggested that it consisted of a single Ti^{III} species wherein the Ti center experiences a weak interaction with a single proton. The source of the proton was hypothesized by other researchers to be minor amounts of $Al\textit{i}Bu_2H$ present in $Al\textit{i}Bu_3$ reagent, which have been reported to form via slow decomposition over time.[32,44] However, in our case, the reaction of **1** with $Al\textit{i}Bu_2H$ yielded crystals exclusively of **2-*i*Bu** (*vide supra*), suggesting unlikeliness of the formation of dimer **3** from the presence of hydride impurities. Notably, a wide variety of spectral profiles have been obtained by other researchers from the reaction of Cp_2TiCl_2 with aluminum alkyl reagents, attesting the complexity of these systems and their sensitivity to precise details of the conditions used from study to study.[45,46,47,48,49] Nonetheless, based on the similarity of the obtained spectral profiles for **2-Et** and **2-*i*Bu**, our work here confirms that a key product of initial mixing of **1** and AlR_3 is **2-R**.

To complete our comparative study, we further recorded the EPR spectrum of a frozen solution of toluene containing a mixture of **1** and two equiv. of $AlMe_3$. This sample was prepared by layering of **1** and the aluminum reagent in the EPR tube under inert atmosphere followed by freezing in liquid nitrogen; the sample was then allowed to melt and mix only

briefly before immediate re-freezing and collection of EPR data. This method was used to avoid degradation of the postulated **2-Me** species over longer timescales. As anticipated on the basis of our other results, the EPR spectrum of the prepared mixture reveals an axial signal (g = 1.980, 1.932) very similar to those obtained for isolated **2-Et** and **2-*i*Bu** (see also Appendix F, Figure F21). Thus, we assign the spectral features as being associated with *in-situ*-generated **2-Me**. The spectral intensity was lower for this sample compared to the others, however, suggesting that a lower total concentration of **2-Me** was present in the sample, likely due to both the limited reaction time used as well as the modest stability of the complex.

In the proposed mechanism for electro-promoted generation of the complexes **2-R** (*vide supra*), we postulate the formation of a transient Ti^{III} monometallic species. We implicated this species as existing because of the observation of a reduction with $E_{p,c}$ = –2.30 V vs. $Fc^{+/0}$ in cyclic voltammetry, both with and without the presence of an aluminum reagent. And, because the reduction could be measured in the absence of aluminum, we anticipated that a chemical reduction experiment could be performed to characterize the implied transient titanium(III) species **1′** (see Figure 7.3) with EPR spectroscopy. Our layering technique was performed again here, by slowly thawing layers of **1** and a substoichiometric (0.9 equiv.) amount of ketyl radical (Na^+[benzophenone]$^-$, $E_{1/2}$ = –2.30 V vs. $Fc^{+/0}$ in THF)[50] in THF and allowing them to mix only immediately before collecting EPR data. Before reduction, **1** is a Ti(IV) complex with a d^0 configuration and S = 0 making it EPR silent. However, the EPR spectrum of the mixed solution (see Appendix F, Figure F17) revealed a new signal near g = 2 consistent with *in-situ* generation of the predicted reduced species **1′**.

This spectral data for **1′** could be modeled using the EasySpin software, revealing that the sample was a two-component mixture containing a species which could be satisfactorily modeled as the nascent but transient Ti(III) species **1′**. Notably, the appearance of the second radical signal is not consistent with ketyl radical, which displays a relatively narrower signal centered at $g \approx 2$ (see Appendix F, Figure F18). The distinctiveness of the spectral data for the mixture of **1′** as compared to the spectrum of ketyl radical itself provides good support for the formation of **1′**. Moreover, the spectrum obtained here for our mixture is dissimilar to the EPR signature previously reported by Stephan & coworkers for a Ti^{III}-Ti^{III} dimer containing phosphinimide ligands.[51] Intriguingly, this Ti^{III}-Ti^{III} dimer was also synthesized by reducing **1**, highlighting the modularity of this starting material for organometallic Ti chemistry.

In our previous work with **2-Et** (see Chapter 6),[27] we showed reduction of **1** by triethylaluminum results in generation of **2-Et** as well evolution of ethane gas.[17,43] This result suggested to us that alkylation of Ti^{IV} centers could be followed by cleavage of Ti–C bonds, resulting in release of transient C_2H_5 radicals, which could abstract H-atoms from the solvent or excess aluminum reagent present under the reaction conditions. With this motivation, we conducted an analogous gas chromatographic analysis for the reaction of **1** with Al*i*Bu_3 as a reductant. To our surprise, headspace analysis of the emerald green colored reaction mixture containing **1** plus 2 equiv. of Al*i*Bu_3 generated small amounts of methane gas after 1 hour of stirring (see Appendix F, Figure F14). This emerald green color solution could be quenched by quick exposure to air and mixing in a closed container to avoid loss of volatiles, resulting in a clear color change to yellow/orange; product analysis by GC-MS showed the formation isobutane as well as of biindene, implying that radical chemistry consumes **1** (as well as the

alkylating reagent) and gives rise to carbon-containing small molecules. Similar to the **2-Et** case, the formation of **2-*i*Bu** under purely chemical conditions could begin with alkylation of **1** followed by cleavage of Ti–C bonds. This reactivity pathway would generate isobutyl radicals and, following H-atom abstraction, yield the detected isobutane. The formation of biindene is attributable to the loss of the indenyl ligand from Ti, albeit in modest yield as confirmed in the synthetic work which yielded **3** in small amounts; **3** thus represents the Ti-containing product of indenyl radical loss from **1**.

When **1** and Al*i*Bu$_3$ were allowed to be stirred for a longer period of 24 hours, an increase in the concentration of methane gas was observed in GC. Moreover, a new gas, ethylene, was also observed (see Appendix F, Figure F15). These results agree with the color change of the solution to magenta as discussed above, in that longer reaction times promote radical reactions that could generate multiple products and more generally promote speciation of the system. On the other hand, the use of AlMe$_3$ as a reductant generated only methane (see Appendix F, Figure F16). This suggests that the cleavage of Ti–C bonds following methylation results in the generation of transient CH_3 radicals, which could scavenge H-atoms from reaction media. However, the corresponding GC-MS data do not show signals corresponding to biindene or isobutane. The lack of biindene as a product suggests that the speciation chemistry of the **2-Me** system is fundamentally different than that of the **2-*i*Bu** system, as well.

The synthesized [Ti,Al] complexes **2-R** were, finally, tested for catalytic ethylene polymerization activity. The experiments were conducted in an automated, semi-batch reactor under slurry conditions with isobutane diluent[52] (see Experimental Section for details) similar to those in our prior report.[27] Experiments were carried out for 20 min

(excluding charging time) using industrially-relevant reaction temperature and ethylene, hydrogen, and 1-hexene concentrations.[53,54] The catalyst material, along with these other gases, was charged in the reactor in two different ways. In the "non-prereduced" case, the titanium catalyst was introduced into the reactor in the form of a toluene solution containing **1**. In addition, 150 ppm of aluminum reagent (AlR_3) of interest in the isobutane diluent was added to the reactor, where it could serve as an alkylating agent as well as a scavenger of catalyst poisons. Alternatively, in the "prereduced" case, a freshly prepared benzene solution containing the heterobimetallic complex **2-R**, formed by the treatment of **1** with an appropriate aluminum reagent *in situ*, was introduced into the reactor. The polymerization reactions in all cases were halted via fast evaporation (flashing) of the isobutane diluent, and the product PE was collected as free-flowing small particles.

The polymerization results confirm that use of all the complexes and conditions studied here result in formation of competent precatalysts for ethylene polymerization, with production of significant yields of polyethylene and high turnovers on a titanium basis in each case (see Table 7.3 for details). In the cases of prereduction, where **1** and analogues bearing Cp or Cp* in place of Ind were treated with AlR_3 outside the reactor, decreased [Ti] activity were measured in all cases except that of **1** + $AlMe_3$, where a 5% enhancement in [Ti] activity was measured.

Table 7.3. Comparison of Select Ethylene Polymerization Conditions* and Polymer Properties.

Exp.	Pre-reduced	L-type	AlR_3 Type	Polymer Yield (g)	[Ti] Activity (g PE/g Cat./hr)	M_n/1000 (g/mol)#	M_w/1000 (g/mol)#	M_w/M_n#
1	No	Ind	$AlEt_3$	93	279,000	40.11	132.09	3.29
2	Yes	Ind	$AlEt_3$	85	255,000	85.83	261.95	3.05
3	No	Ind	$AlMe_3$	59	177,000	19.78	104.90	5.30
4	Yes	Ind	$AlMe_3$	62	186,000	25.37	140.17	5.53
5	No	Ind	Al*i*Bu_3	122	366,000	20.70	181.92	8.79
6	Yes	Ind	Al*i*Bu_3	116	348,000	43.12	461.93	10.71
7	No	Cp	$AlEt_3$	26	78,000	84.06	389.28	4.63
8	Yes	Cp	$AlEt_3$	24	72,000	139.35	657.11	4.72
9	No	Cp*	$AlEt_3$	126	378,000	22.59	103.10	4.56
10	Yes	Cp*	$AlEt_3$	118	354,000	18.86	86.15	4.57
11$	No	Ind	Al*i*Bu_3	102	201,000	57.25	700.19	12.23
12$	Yes	Ind	Al*i*Bu_3	64	192,000	20.50	175.80	8.58

*Conditions: All polymerization experiments were carried out using 0.001 g of Ti catalyst, 0.1 g of solid superacid, 150 ppm of additional $AlEt_3$ species added to the reactor relative to the isobutane diluent, 125 ppm of H_2, T = 80°C and t = 20 min. $Note that these experiments do not use a solid super acid, but instead use tris(pentafluorophenyl)borane as an activator. See the experimental section for full experiment details. #M_n is number-average molecular weight; M_w is weight-average molecular weight. Experimental error: M_w ±2%; M_w/M_n ±7%.

However, prereduction represents a valuable strategy, as it resulted in different molecular weight distributions (MWD, M_w/M_n) in each case (Figure 7.6). These shifts in MWD could

be attributable to differences in the initiation and/or speciation chemistry of the precatalysts. With regard to [Ti] activity, the observation of higher turnovers in the non-prereduced method is likely a consequence of the greater water and/or oxygen sensitivity of the reduced Ti^{III} forms. Furthermore, as the activity on a [Ti] basis does not differ significantly between the methods, the compounds likely undergo reduction *in situ* during the initiation phase of the polymerization process with AlR_3 added to the reactor with the other inputs.

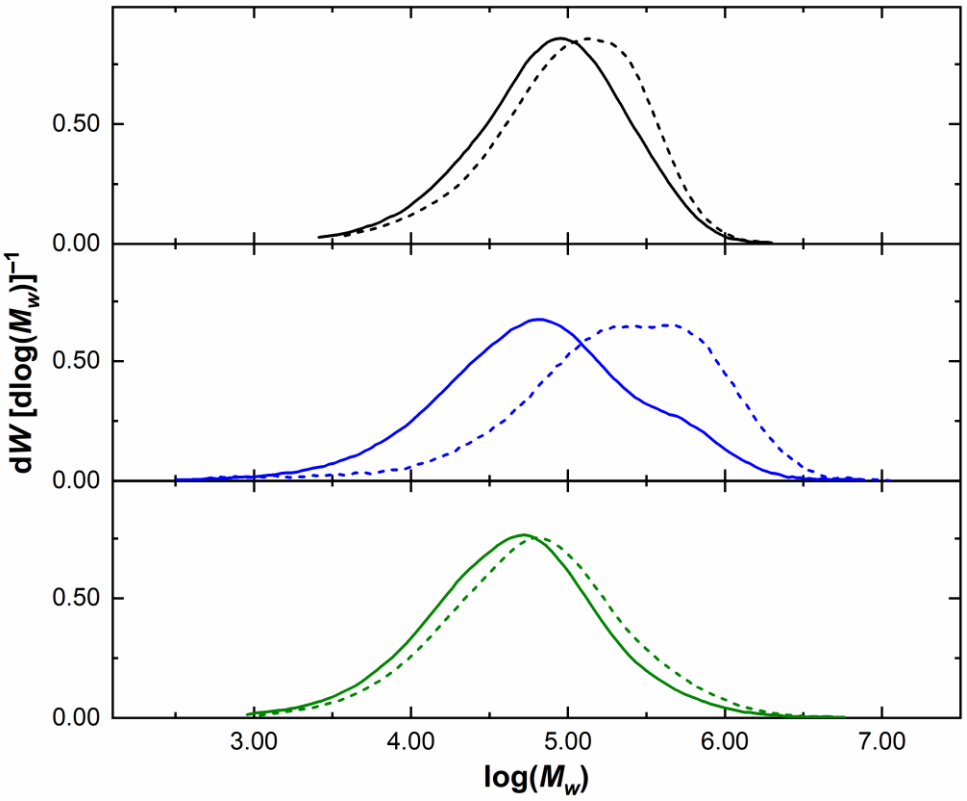

Figure 7.6. Gel permeation chromatograms for comparison of PE produced under a variety of conditions. Upper panel: PE produced with **1** and $AlEt_3$; not prereduced (black line) and prereduced (dotted black line). Middle panel: PE produced with **1** and Al*i*Bu_3; not prereduced (blue line) and prereduced (dotted blue line). Lower panel: PE produced with **1** and $AlMe_3$; not prereduced (green line) and prereduced (dotted green line).

Indeed, both the prereduced and non-prereduced methods can be considered useful for the generation of PE with a broader MWDs of 10.71 and 8.79, respectively (see Table 7.3,

entries 5 and 6). For comparison to these entries based on AliBu3, bridged cyclopentadienyl/indenyl metallocene catalysts generate polymers with narrow MWDs between 2.3 – 2.8 under similar polymerization conditions.[55] And, Stephan's work comparing metallocene- and phosphinimide-based catalysts yielded monodisperse polyethylene materials with significantly narrower MWDs (1.5 – 3).[25,26] Thus, our results with the **1** + Al*i*Bu$_3$ system represent a notable counterpoint to prior work in the field.

At the start of this work, we had questioned whether Ind would be essential for catalysis, and therefore, we looked specifically at the more stable **2-Et** system with Cp and Cp* ligands in place of Ind (Table 7.3, entries 7-10). And, as the complexes supported by Cp (**4**) and Cp* (**5**) ligands pre-date the Ind/Phosphinimide systems that we have been developing, we were intrigued to use them as precatalysts. Both **4** and **5**, supported by Cp, gives usefully broad MWD values that are larger than those accessible with **1**. However, the activity on a [Ti] basis with **4** is significantly lower than that accessible with most of our other tested systems (Table 7.3, entries 7 and 8). On the other hand, **5** appears to be more stable during catalysis with the highest [Ti] activity. This good activity, however, comes at the cost of among the narrowest MWD values in our study, regardless of the stage where AlR_3 is added to the Ti(IV) precursor (Table 7.3, entries 9 and 10).

Tris(pentafluorophenyl)borane (BCF) was also tested as an activator for ethylene polymerization in place of the solid superacid, using **1** as the catalyst with Al*i*Bu$_3$ as added aluminum reagent. **1** gave polymerization activity in both cases, but the MWD is different in both cases, which a nicely broad MWD of 12.23 in the case of the non-prereduced conditions. On the other hand, if prereduced, the [Ti] total polymer yield is lower, giving only ca. 55% of the output PE of the non-prereduced conditions. These findings suggest that

use of BCF as a further modification to the catalytic conditions is compatible with our catalyst systems based upon **1**.

7.3 Discussion

PE materials with broad MWDs are especially useful in processes such as extrusion blow molding, where the extruded polymer must be self-supporting before solidifying. In such a case, a material requires enough melt strength to prevent collapse. A broad MWD is advantageous in such a scenario, because the polymer viscosity will be low in the high-shear portions of the process. High molecular weight PE also tends to exhibit greater toughness and chemical resistance. Broad MWD polymers thus permit easier processing when employed as a raw material for generating useful end products.[56] As shown in Figure 7.5, MWD for the **2-*i*Bu** system (**1** prereduced with Al*i*Bu$_3$) is quite broad and significantly different (Table 7.3, entry 6) from all of both the prereduced and non-prereduced catalysts studied here. In particular, **2-*i*Bu** system outperforms the **2-Et** system that we previously reported (Table 7.3, entry 2).[27] This finding is in contrast to the work by Kojoh & coworkers, which showed an enhancement of activity with AlEt$_3$ over Al*i*Bu$_3$ (when incorporated as cocatalysts) for polymerization of propylene at temperatures of 50–100°C.[57]

The results from the chemical and electrochemical studies described earlier in this report are reflected in the polymerization results, including some notable trends. First, regarding the appealing tunable MWD values, the Al*i*Bu$_3$ based system is the champion, giving the largest MWD of any of the standard conditions tested. On the basis of our chemical and electrochemical studies, we anticipate that this may be attributable to formation of multiple active sites under the catalytic conditions. The stability of this system is reasonable, as supported by the successful isolation of **2-*i*Bu**. But, the system is prone to speciation as

shown by the time-dependent changes in EPR spectra as well as solution coloration. Such speciation may occur under catalytic conditions as well. Second, the polymer yield and [Ti] activity appear to vary with the steric bulk of the [AlR_2] unit; **2-Me** gives poor yields and activities regardless of the activation approach, whereas the analogous values for **2-*i*Bu** are excellent and the values for **2-Et** lie in between. These observations support the findings that **2-Me** is stable only at short timescales and, on the basis of the GC-MS results, undergoes speciation pathways that differ significantly from **2-*i*Bu**. Third and finally, our findings from the electrochemical work show that the redox properties of all three heterobimetallic species are similar; consequently, the observation of PE production from all cases may not be surprising. Similar redox processes are accessible at short times with all AlR_3 reagents explored here, while on the other hand, the R groups play a significant role in governing the polymer yield and MWD distributions, as described above.

7.4 Conclusions

In conclusion, **2-*i*Bu** and **2-Me** can serve, like **2-Et**, as precatalysts for ethylene polymerization. In comparison to the behavior previously reported for **2-Et**, our results show that, at 80°C, the polymerization activity is enhanced with **2-*i*Bu** both in terms of broader MWDs and polymer yields. Cyclic voltammograms of the precursor complex **1** in the presence of AlR_3 reagents (where R = Me, Et, and *i*Bu) display EC-type cathodic behavior and show that interaction with aluminum reagents stabilizes the [Ti^{III}] oxidation state. EPR spectra confirm that the reduction of **1** is metal-centered and also confirm the presence of similar Ti(III) centers in **2-Me**, **2-Et**, and **2-*i*Bu**. However, results from chemical and electrochemical studies show that the **2-Me** and **2-*i*Bu** complexes are less stable than **2-Et**, a finding also supported by the results of the polymerization studies. Taken together, the

findings reported here show that **1** represents a quite useful polymerization catalyst precursor, especially in light of the ability to tune the product PE characteristics using various AlR_3 activators.

7.5 Experimental Details

7.5.1 General Considerations

All manipulations were carried out in dry N_2-filled gloveboxes (Vacuum Atmospheres Co., Hawthorne, CA) or under N_2 atmosphere using standard Schlenk techniques unless otherwise noted. Ethylene was obtained from Airgas and was further purified through columns of 13X molecular sieves. 1-Hexene was obtained from Chevron Phillips Chemical Company LP and dried over A-201 type activated alumina. All solvents were of commercial grade and dried over activated alumina using a Pure Process Technology (PPT; Nashua, NH) solvent purification system prior to using, and were stored over molecular sieves or anhydrous solvents were purchased from Sigma-Aldrich and purified and stored over 13X molecular sieves. Benzene-d_6 was purchased from Cambridge Isotope Labs, dried, and stored over 13X molecular sieves. ^1H and ^{31}P NMR spectra were collected on 400 and 500 MHz Bruker spectrometers and referenced to the residual protio-solvent signal in the case of ^1H and to the deuterium lock signal in the case of ^{31}P unless otherwise noted. Triethylaluminum (1 M solution in hexane or 0.6 M solution in heptane), triisobutylaluminum (1.1 M solution in toluene), trimethylaluminum (1 M solution in heptane), *t*Bu_3P, [(Ind)$TiCl_3$] and trimethylsilylazide were purchased from major suppliers and used as received. **1**, **2-Et** and the solid super acid activator were prepared according to literature methods.[58,59] All chemicals were from major commercial suppliers and used after extensive drying.

Electrochemical experiments were carried out in an N_2-filled glovebox in dry, degassed THF. 0.10 M tetra(n-butylammonium) hexafluorophosphate ($[^nBu_4N]^+[PF_6]^-$); Sigma-Aldrich, electrochemical grade) served as the supporting electrolyte. Measurements were made with a Gamry Reference 600+ Potentiostat/Galvanostat using a standard three-electrode configuration. The working electrode was the basal plane of highly oriented pyrolytic graphite (HOPG) (GraphiteStore.com, Buffalo Grove, Ill.; surface area: 0.09 cm^2), the counter electrode was a platinum wire (Kurt J. Lesker, Jefferson Hills, PA; 99.99%, 0.5 mm diameter), and a silver wire immersed in electrolyte served as a pseudoreference electrode (CH Instruments). The reference was separated from the working solution by a Vycor frit (Bioanalytical Systems, Inc.). Ferrocene (Sigma Aldrich; twice-sublimed) was added to the solution after each experiment; the midpoint potential of the ferrocenium/ferrocene couple (denoted as $Fc^{+/0}$) served as an internal standard for comparison of the recorded potentials. Concentrations of analyte for cyclic voltammetry were ca. 1 to 2 mM unless otherwise noted.

Electronic absorption spectra were collected with an Ocean Optics Flame spectrometer in a 1-cm path length quartz cuvette.

Gas analysis for determination of gas evolution was performed with a Shimadzu GC-2014 Custom-GC gas chromatograph with a thermal conductivity detector and dual flame-ionization detectors. A custom set of eight columns and timed valves enables quantitative analysis of hydrogen, nitrogen, oxygen, carbon dioxide, carbon monoxide, methane, ethane, ethylene, and ethyne. Argon serves as the carrier gas. The instrument was calibrated with a standard checkout gas mixture (Agilent 5190-0519) prior to experimental runs to obtain quantitative data for methane, ethane, and ethylene.

Bench Polymerization Experiments

Polymerizations were performed on a 2.2 L stainless steel reactor equipped with a marine stirrer rotating at 500 rpm. The reactor was surrounded by a stainless-steel jacket through which a stream of hot water was circulated, which permitted precise temperature control to within half a degree centigrade. Before polymerization, the reactor was purged at 110–120^{o}C with nitrogen for at least 30 minutes. The reactor was then cooled and charged with 0.1 g of solid superacid, 0.5 mL of the appropriate alkyl aluminum (1 M in hexane, 0.5 mmol), and 0.001 g of **1** as a 1 mg/mL solution of the catalyst in toluene, and filled with 1.2 L of isobutane liquid, in that order, under a stream of isobutane vapors at 45^{o}C. Finally, ethylene was added to the reactor to equal the desired pressure, which was maintained during the experiment. 1-hexene (10 g) was pumped directly into the reactor from a weighed storage vessel upon initiation of the polymerization experiment. Hydrogen was metered into the reactor along with the ethylene to a prescribed 125 ppm-level. After the allotted reaction time, the ethylene flow was stopped, and the reactor was slowly depressurized and opened to recover the granular polymer powder. The reactor was clean with no indication of any wall scale, coating or other forms of fouling. The polymer powder was then removed and weighed, and the activity was determined from this weight and the measured time based on the amount of catalyst charged.

Melt Index Determination

Approximately 7 g of polymer was loaded into the barrel of a Tinius Olsen EP600 extrusion plastometer melt flow apparatus that was preheated to 190^{o}C. After a 6-minute melting time, a 2.16 kg weight (melt index) was automatically loaded onto the plunger to force the molten polyethylene through a circular die. The distance traveled by the weight

and time is measured and used to calculate the melt index in dg min^{-1}. Following melt flow determination, additional weights to produce a total of 21.6 kg (high load melt index) was automatically loaded onto the plunger to force the molten polyethylene through the circular die. The distance traveled by the weight and time is measured and used to calculate a high load melt index in dg min^{-1}.

SEC Measurements

Molecular weights and molecular weight distributions were obtained using a Polymer Labs (now an Agilent company) PL-220 gel permeation chromatograph with 1,2,4-trichlorobenzene as the solvent at a flow rate of 1 mL/min and at 145°C. 2,6-di-*tert*-butyl-4-methylphenol (BHT) at a concentration of 0.5 g/L was used as a stabilizer in the solvent. An injection volume of 400 μL was used with a nominal polymer concentration of 1 g/L. Dissolution of the stabilized sample was carried out by heating at 150°C for 5 h with occasional agitation. Three Waters HT-6E columns (7.8 x 300 mm) were used and calibrated with a broad linear polyethylene standard (Phillips Marlex® BHB 5003) whose molecular weight had previously been determined.

Synthesis of 2-*i*Bu and 3

In the glovebox under an inert atmosphere of nitrogen, a 20 mL scintillation vial was loaded with **1** (100 mg, 0.222 mmol) and suspended in 10 mL pentane. Using a syringe, 2 equiv. of 1.1 M solution of triisobutylaluminum (Al*i*Bu_3) in toluene (0.44 mL, 0.444 mmol) was added dropwise to this yellowish-green color suspension over a period of 15 minutes. The color of the solution changed from yellowish green to emerald green within half an hour of addition. The resultant homogenous solution was stirred for another hour and

concentrated. This viscous liquid was then refrigerated at –35°C to give a mixture of two kinds of crystals. Deep emerald green crystals were identified as **2-*i*Bu** and comprised the bulk of the product. On the other hand, orange crystals were identified as **3** and were only visually detected under a microscope prior to X-ray data collection. Satisfactory elemental analysis results for **2-*i*Bu** and **3** were not obtained despite several attempts, likely due to the acute sensitivity of this compound to air and moisture.

Synthesis of 2-Me

In the glovebox under an inert atmosphere of nitrogen, a 20 mL scintillation vial was loaded with **1** (50 mg, 0.111 mmol) and suspended in 10 mL pentane. Using a syringe, 2 equiv. of 1 M solution of trimethylaluminum ($AlMe_3$) in heptane (0.22 mL, 0.222 mmol) was added dropwise to this yellowish-green color suspension over a period of 15 minutes. The color of the suspension changed from yellowish-green to a homogenous light green solution within half an hour of addition. The resultant solution was stirred for another 3-4 hours and concentrated. This viscous liquid was then stored at –35°C and used as it is for spectroscopic analysis. Satisfactory elemental analysis results for **2-Me** were not obtained despite several attempts, likely due to the acute sensitivity of this compound to air and moisture.

7.6 Acknowledgements

The authors thank Justin Douglas and Sarah Neuenswander for assistance with NMR and EPR spectroscopy, Milan Gembicky and Curtis Moore for assistance with X-ray crystallography, and Sandy Kilpatrick (University of Leicester) for helpful discussions. The work in this chapter was supported by Chevron Phillips Chemical.

7.7 References

(1) Liu, B.; Tian, Z.; Jin, Y.; Zhao, N.; Liu, B. Effect of Alkyl Aluminums on Ethylene Polymerization Reactions with a Cr-V Bimetallic Catalyst. *Macromol. React. Eng.* **2018,** *12*, 1700059.

(2) Fisch, A. G. Ziegler-Natta Catalysts. *Kirk-Othmer Encyclopedia of Chemical Technology*, 2019.

(3) McDaniel, M. P. Chapter 3 - A Review of the Phillips Supported Chromium Catalyst and Its Commercial Use for Ethylene Polymerization. *Adv. Catal*. **2010**, *53*, 123-606.

(4) Alt, H. G.; Köppl, A. Effect of the Nature of Metallocene Complexes of Group IV Metals on Their Performance in Catalytic Ethylene and Propylene Polymerization. *Chem. Rev.* **2000,** *100*, 1205-1222.

(5) Kaminsky, W. Discovery of Methylaluminoxane as Cocatalyst for Olefin Polymerization. *Macromolecules* **2012,** *45*, 3289-3297.

(6) Bochmann, M. The Chemistry of Catalyst Activation: The Case of Group 4 Polymerization Catalysts. *Organometallics* **2010,** *29*, 4711-4740.

(7) Chum, P. S.; Swogger, K. W. Olefin polymer technologies—History and recent progress at The Dow Chemical Company. *Prog. Polym. Sci.* **2008,** *33*, 797-819.

(8) Klosin, J.; Fontaine, P. P.; Figueroa, R. Development of Group IV Molecular Catalysts for High Temperature Ethylene-α-Olefin Copolymerization Reactions. *Acc. Chem. Res.* **2015,** *48*, 2004-2016.

(9) Delferro, M.; Marks, T. J. Multinuclear Olefin Polymerization Catalysts. *Chem. Rev.* **2011,** *111*, 2450-2485.

(10) McInnis, J. P.; Delferro, M.; Marks, T. J. Multinuclear Group 4 Catalysis: Olefin Polymerization Pathways Modified by Strong Metal–Metal Cooperative Effects. *Acc. Chem. Res.* **2014,** *47*, 2545-2557.

(11) Liu, S.; Motta, A.; Delferro, M.; Marks, T. J., Synthesis, Characterization, and Heterobimetallic Cooperation in a Titanium–Chromium Catalyst for Highly Branched Polyethylenes. *J. Am. Chem. Soc.* **2013,** *135*, 8830-8833.

(12) Cai, Z.; Xiao, D.; Do, L. H. Cooperative Heterobimetallic Catalysts in Coordination Insertion Polymerization. *Comments Inorg. Chem.* **2019,** *39*, 27-50.

(13) Velthoen, M. E. Z.; Boereboom, J. M.; Bulo, R. E.; Weckhuysen, B. M. Insights into the activation of silica-supported metallocene olefin polymerization catalysts by methylaluminoxane. *Catal. Today* **2019,** *334*, 223-230.

(14) Coevoet, D.; Cramail, H.; Deffieux, A. U.V./visible spectroscopic study of the rac-Et(Ind)2ZrCl2/MAO olefin polymerization catalytic system, 1. Investigation in toluene. *Macromol. Chem. Phys.* **1998,** *199*, 1451-1457.

(15) Cai, Z.; Xiao, D.; Do, L. H. Fine-Tuning Nickel Phenoxyimine Olefin Polymerization Catalysts: Performance Boosting by Alkali Cations. *J. Am. Chem. Soc.* **2015,** *137*, 15501-15510.

(16) Cai, Z.; Do, L. H. Thermally Robust Heterobimetallic Palladium–Alkali Catalysts for Ethylene and Alkyl Acrylate Copolymerization. *Organometallics* **2018,** *37*, 3874-3882.

(17) Natta, G.; Pino, P.; Mazzanti, G.; Giannini, U. A Crystallizable Organometallic Complex Containing Titanium and Aluminum. *J. Am. Chem. Soc.* **1957,** *79*, 2975-2976

(18) Natta, G.; Corradini, P.; Bassi, I. W. Crystal Structure of the Complex $(C_5H_5)_2TiCl_2Al(C_2H_5)_2$. *J. Am. Chem. Soc.* **1958,** *80*, 755-756.

(19) Tebbe, F. N.; Parshall, G. W.; Reddy, G. S. Olefin homologation with titanium methylene compounds. *J. Am. Chem. Soc.* **1978,** *100*, 3611-3613.

(20) Alt, H. G., Metallocene complexes as catalysts for olefin polymerization. *Coord. Chem. Rev.* **2006,** *250*, 1-272.

(21) Chirik, P. J. Group 4 Transition Metal Sandwich Complexes: Still Fresh after Almost 60 Years. *Organometallics* **2010,** *29*, 1500-1517.

(22) Nishiura, M.; Guo, F.; Hou, Z. Half-Sandwich Rare-Earth-Catalyzed Olefin Polymerization, Carbometalation, and Hydroarylation. *Acc. Chem. Res.* **2015,** *48*, 2209-2220.

(23) Stephan, D. W.; Stewart, J. C.; Guérin, F.; Spence, R. E. v. H.; Xu, W.; Harrison, D. G. Phosphinimides as a Steric Equivalent to Cyclopentadienyl: An Approach to Ethylene Polymerization Catalyst Design. *Organometallics* **1999,** *18*, 1116-1118.

(24) Stephan, D. W. The Road to Early-Transition-Metal Phosphinimide Olefin Polymerization Catalysts. *Organometallics* **2005,** *24*, 2548-2560.

(25) Stephan, D. W.; Guérin, F.; Spence, R. E. v. H.; Koch, L.; Gao, X.; Brown, S. J.; Swabey, J. W.; Wang, Q.; Xu, W.; Zoricak, P.; Harrison, D. G. Remarkably Active Non-Metallocene Ethylene Polymerization Catalysts. *Organometallics* **1999,** *18*, 2046-2048.

(26) Stephan, D. W.; Stewart, J. C.; Guérin, F.; Courtenay, S.; Kickham, J.; Hollink, E.; Beddie, C.; Hoskin, A.; Graham, T.; Wei, P.; Spence, R. E. v. H.; Xu, W.; Koch, L.; Gao, X.; Harrison, D. G. An Approach to Catalyst Design: Cyclopentadienyl-Titanium Phosphinimide Complexes in Ethylene Polymerization. *Organometallics* **2003,** *22*, 1937-1947.

(27) Barr, J. L.; Kumar, A.; Lionetti, D.; Cruz, C. A.; Blakemore, J. D. Understanding the Roles of Triethylaluminum in Phosphinimide-Supported Titanium Catalyst Systems for Ethylene Polymerization. *Organometallics* **2019,** *38*, 2150-2155.

(28) (a) Kumar, A.; Lionetti, D.; Day, V. W.; Blakemore, J. D., Trivalent Lewis Acidic Cations Govern the Electronic Properties and Stability of Heterobimetallic Complexes of Nickel. *Chem. – Eur. J.* **2018,** *24*, 141-149. (b) Kumar, A.; Lionetti, D.; Day, V. W.;

Blakemore, J. D., Redox-Inactive Metal Cations Modulate the Reduction Potential of the Uranyl Ion in Macrocyclic Complexes. *J. Am. Chem. Soc.* **2020,** *142*, 3032-3041.

(29) Cruz, C. A.; Barr, J. L. *Catalyst systems containing low valent titanium-aluminum complexes and polymers produced therefrom*. US10000595B1, **2018**.

(30) Cruz, C. A.; Barr, J. L. *Methods for controlling molecular weight and molecular weight distribution of polyolefin during polymerization using combination of catalysts*. US10005865B1, **2018**.

(31) Guerin, F.; Beddie, C. L.; Stephan, D. W.; Spence, R. E. V. H.; Wurz, R. η1- and η5-indenyl and cyclopentadienyl tri-tert-butylphosphoraneiminatotitanium complexes. *Organometallics* **2001,** *20*, 3466 - 3471.

(32) Egger, K. W. Kinetics of the intramolecular four-center elimination of isobutylene from triisobutylaluminum in the gas phase. *J. Am. Chem. Soc.* **1969,** *91*, 2867-2871.

(33) Cossee, P., Ziegler-Natta catalysis I. Mechanism of polymerization of α-olefins with Ziegler-Natta catalysts. *J. Catal.* **1964,** *3*, 80-88.

(34) Arlman, E. J.; Cossee, P., Ziegler-Natta catalysis III. Stereospecific polymerization of propene with the catalyst system $TiCl_3$-$AlEt_3$. *J. Catal.* **1964,** *3*, 99-104.

(35) Schwemlein, H.; Tritschler, W.; Kiesele, H.; Brintzinger, H. H., ansa-Metallocene derivatives: IX. Electrochemical reactions of tetramethylethylene-bridged titanocene dichloride and dicarbonyl derivatives. *J. Organomet. Chem.* **1985,** *293*, 353-364.

(36) Liedtke, T.; Spannring, P.; Riccardi, L.; Gansäuer, A. Mechanism-Based Condition Screening for Sustainable Catalysis in Single-Electron Steps by Cyclic Voltammetry. *Angew. Chem. Int. Ed.* **2018,** *57*, 5006-5010.

(37) Savéant, J. M.; Costentin, C., *Elements of Molecular and Biomolecular Electrochemistry, An Electrochemical Approach to Electron Transfer Chemistry*. 2nd ed.; Wiley: Hoboken, NJ, 2019; pp. 616.

(38) Samuel, E.; Hénique, J. Phosphine complexes of Ti(III) and Zr(III): detection in solution by EPR/electrochemical methods. *J. Organomet. Chem.* **1996,** *512,* 183-187.

(39) Nguyen, K. T.; Lane, E. E.; McMillen, C. D.; Pienkos, J. A.; Wagenknecht, P. S., Is Indenyl a Stronger or Weaker Electron Donor Ligand than Cyclopentadienyl? Opposing Effects of Indenyl Electron Density and Ring Slipping on Electrochemical Potentials. *Organometallics* **2020,** *39,* 670-678.

(40) Loukova, G. V. The first experimental approach to probing frontier orbitals and HOMO–LUMO gap in bent metallocenes. *Chem. Phys. Lett.* **2002**, *353,* 244-252.

(41) Loukova, G. V.; Strelets, V. V. Electrochemical potentials, optical transitions, and frontier orbitals of non-bridged and bridged bent sandwich zirconocene complexes. *Russ. Chem. Bull.* **2000,** *49* (6), 1037-1039.

(42) Loukova, G. V.; Strelets, V. V. Electrochemical versus optical insight in frontier orbitals of Ti(IV), Zr(IV), and Hf(IV) bent metallocenes. *J. Organomet. Chem.* **2000,** *606,* 203-206.

(43) Allen, P. E. M.; Brown, J. K.; Obaid, R. M. S. Electron spin resonance studies of some complexes derived from dicyclopentadienyl-titanium dichloride and tri-alkyl aluminiums. *Trans. Faraday Soc.* **1963,** *59,* 1808-1814.

(44) Bent, B. E.; Nuzzo, R. G.; Dubois, L. H. Surface organometallic chemistry in the chemical vapor deposition of aluminum films using triisobutylaluminum: β-hydride and β-alkyl elimination reactions of surface alkyl intermediates. *J. Am. Chem. Soc.* **1989,** *111,* 1634-1644.

(45) Mach, K.; Antropiusova, H.; Polacek, J. The structure of bis(dihaloalane-di-μ-halo)(η-arene)titanium(II) complexes containing different halogen atoms. *Transition Met. Chem.* **1979,** *4*, 312-315.

(46) Mach, K.; Antropiusova, H.; Polacek, J. Ethyl-substituted (η^5-cyclopentadienyl)bis(dihaloalanedi-μ-halo)titanium(III) and (η^6-

benzene)bis(dihaloalanedi-μ-halo)titanium(II) chloro and bromo complexes. *J. Organomet. Chem.* **1980,** *194*, 285-295.

(47) Bulychev, B. M.; Kostenko, A. L.; Yakovleva, N. y. A.; Soloveichik, G. L. Interactions in Cp_2TiX-$AlH_{3-n}X_n$-$Et_2O(NEt_3)$ systems. *Transition Met. Chem.* **1981,** *6*, 32-36.

(48) Tyrlik, S. K.; Korda, A.; Poppe, L.; Rockenbauer, A.; Gyoer, M., EPR spectra of products of the reaction of di-η^5-cyclopentadienyl(diethylalanedi-μ-chloro)titanium(III) with C1 compounds. *J. Organomet. Chem.* **1987,** *336*, 343-348.

(49) Mach, K.; Varga, V., Methyl-substituted cyclopentadienyl ligands: influence on the properties of titanocene chloro(ethyl)aluminates. *J. Organomet. Chem.* **1988,** *347*, 85-92.

(50) Connelly, N. G.; Geiger, W. E. Chemical Redox Agents for Organometallic Chemistry. *Chem. Rev.* **1996,** *96*, 877-910.

(51) Sung, R. C. W.; Courtenay, S.; McGarvey, B. R.; Stephan, D. W. Synthesis, Structure, and Single-Crystal EPR Study of $[Cp(t\text{-}Bu_3PN)Ti(\mu\text{-}Cl)]_2$. *Inorg. Chem.* **2000,** *39*, 2542-2546.

(52) McDaniel, M. P. Influence of porosity on PE molecular weight from the Phillips Cr/silica catalyst. *J. Catal.* **2009,** *261*, 34-49.

(53) Buck, R. M.; Yang, Q.; Masino, A. P.; Wittner, C. E. *Catalyst systems containing a bridged metallocene.* US9040642B2, **2015**.

(54) Yang, Q.; Jensen, M. D.; McDaniel, M. P. Alternative View of Long Chain Branch Formation by Metallocene Catalysts. *Macromolecules* **2010**, *43*, 8836−8852.

(55) Yang, Q.; Hlavinka, M. L. *Process for synthesizing bridged cyclopentadienyl-indenyl metallocenes.* US8309747B2, **2012**.

(56) Rosato, D.; Rosato, D. *Overview. In Plastics Engineered Product Design*; Rosato, D., Rosato, D., Eds.; Elsevier Science: Amsterdam, 2003; pp 1-45.

(57) Kojoh, S.-i.; Kioka, M.; Kashiwa, N. The influences of cocatalyst on propylene polymerization at high temperature with a $MgCl_2$-supported $TiCl_4$ catalyst system. *Eur. Polym. J.* **1999**, *35*, 751-755.

(58) (a) Stephan, D. W.; Stewart, J. C.; Guérin, F.; Spence, R. E. v. H.; Xu, W.; Harrison, D. G. *Organometallics* **1999**, *18*, 1116. (b) Guerin, F.; Beddie, C. L.; Stephan, D. W.; Spence, R. E. V. H.; Wurz, R., η1- and η5-indenyl and cyclopentadienyl tri-*tert*-butylphosphoraneiminato titanium complexes. *Organometallics* **2001,** *20*, 3466-3471. (c) Barr, J. L.; Kumar, A.; Lionetti, D.; Cruz, C. A.; Blakemore, J. D. Understanding the Roles of Triethylaluminum in Phosphinimide-Supported Titanium Catalyst Systems for Ethylene Polymerization. *Organometallics* **2019,** *38*, 2150-2155.

(59) (a) McDaniel, M. P.; Collins, K. S.; Johnson, M. M.; Smith, J. L.; Benham, E. A.; Hawley, G. R.; Wittner, C. E.; Jensen, M. D. US6107230A, **2000**. (b) McDaniel, M. P.; Collins, K. S.; Johnson, M. M.; Smith, J. L.; Benham, E. A.; Halwey, G. R.; Wittner, C. E.; Jensen, M. D. US6316553B1, **2001**.

Chapter 8

Incorporation of [Cp*Rh] and [Cp*Ir] Species into Heterobimetallic Complexes via Protonolysis Reactivity and Dioximato Chelation

This chapter is adapted from a published preprint:

Kumar, A.; King, D. S.; Day, V. W.; Blakemore, J. D. Incorporation of [Cp*Rh] and [Cp*Ir] Species into Heterobimetallic Complexes via Protonolysis Reactivity and Dioximato Chelation. *submitted*, **2021**. Available online as a preprint from ChemRxiv (doi: 10.26434/chemrxiv.14529315.v1)

8.1 Introduction

Bringing two different metal centers into close proximity attracts considerable interest across a number of research areas. This is in part due to the unique properties and cooperativity that can be engendered in such compounds in comparison to their monometallic analogues.[1,2] Bimetallic complexes incorporating redox-active centers are especially notable for their redox flexibility and, often, improved substrate-binding capabilities. Indeed, nature takes advantage of multimetallic systems in many metalloenzymes capable of small-molecule activation. The oxygen-evolving complex (OEC) of Photosystem II utilizes four Mn centers and a conserved redox-inactive Ca^{2+} ion to catalyze the oxidation of water to oxygen.[3] Other multimetallic active sites perform reduction reactions such as conversion of O_2 by [Cu,Fe] cytochrome *c* oxidase,[4] fixation of N_2 by Fe- and Mo-containing nitrogenase,[5] and reduction of protons to dihydrogen by NiFe hydrogenase.[6] Inspired by these systems, many researchers have endeavored to design artificial metal complexes that engender synergistic involvement of multiple metals.[7] One especially vigorous area of investigation centers on use of secondary redox-inactive metals to tune the chemical properties of primary redox-active metal centers,[8,9,10] an approach of particular interest to us considering its versatility.[11,12,13] However, a unifying theme of all this work is the bringing together of two metals selectively, enabling studies of their individual roles in observed reactivity.

Tetraazamacrocyclic complexes containing the earth-abundant metals nickel and cobalt are perhaps best known as catalysts for electrochemical hydrogen generation.[14,15] A subset of these complexes can be derivatized by placement of a cationic [BF_2] bridging moiety in place of a bridging proton (H^+).[16,17] Such reactivity is conceptually related to the early work

of Busch and co-workers regarding glyoxime-type ligands and their macrocyclic metal complexes.[18] However, metal complexes supported by proton-bridged macrocyclic diimine-monooxime-monooximato-type ligand frameworks have also been attractive as synthons for construction of bimetallic complexes. Chaudhuri, Wieghardt, and co-workers were perhaps the first to realize potential in this space, and showed that a variety of first-row transition metals (Cr, Mn, Fe, Co, Ni, Cu) could be installed divergently in the dioximato site (see Chart 8.1).[19] Peters & co-workers leveraged the binucleating nature of these ligands to install Mg and Zn in close proximity to Co and Ni metal centers.[20] And, more recently, Cossairt and co-workers extended this approach further to incorporation of 4*d* metals, isolating [Co,Ru] and [Co,Cd] complexes.[21] A general feature uniting all this work is the net removal of a proton from the dioximato site and installation of a cationic metal fragment in its place.

Chart 8.1. Heterobimetallic complexes based upon diimine-monooxime-monooximato ligands.

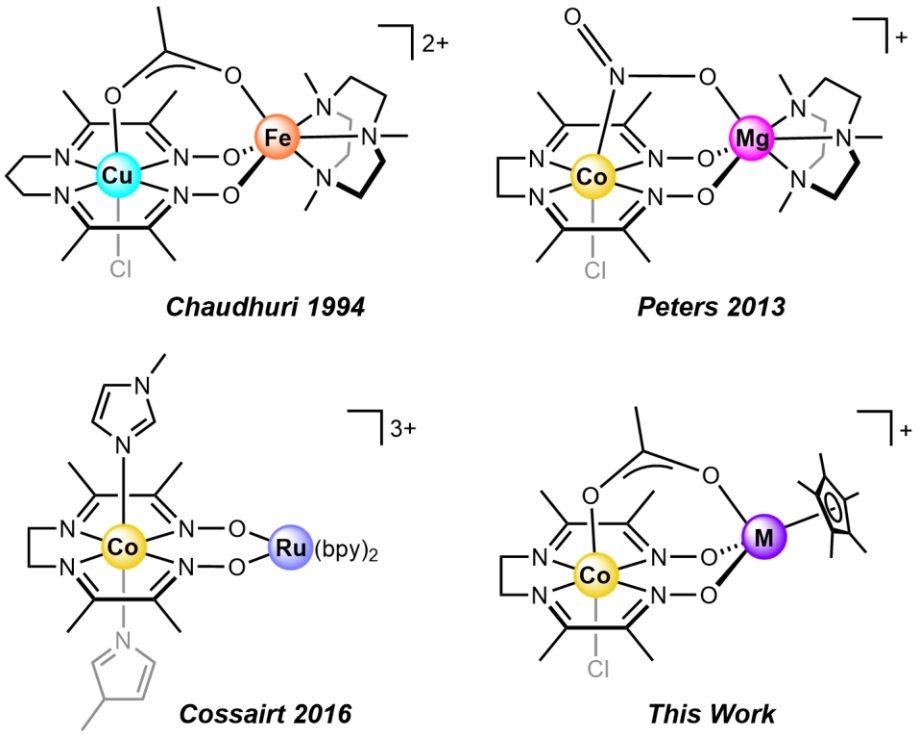

Half-sandwich Group 9 metal complexes supported by Cp* ligands (where Cp* is η^5-pentamethylcyclopentadienyl) represent a useful and synthetically versatile class of organometallic species.[22] Structures containing [Cp*M] fragments tend to be quite stable, due to the steric bulk and strong donor properties of Cp*,[23] but can also serve as catalysts for a variety of transformations.[24] In our own work, we have relied on the synthetic versatility of [Cp*Rh] complexes in particular, for preparation of new metal complexes useful for studies of proton management during catalysis.[25] Others have also leveraged this versatility to prepare attractive new types of heterobimetallic complexes and catalysts.[26,27,28] In the context of this work, we examined the literature and were surprised to find no prior synthetic work aimed at incorporating organometallic fragments like the [Cp*Rh] or [Cp*Ir] cores into metal complexes bearing dioximato sites. However, considering the successful prior work on bimetallic coordination compounds supported by diimine-dioximato ligands, we anticipated that the modularity of this chemistry might enable preparation of new heterobimetallic compounds containing organometallic [Cp*M] sites.

Here, we report two general procedures for synthesis of heterobimetallic complexes based upon diimine-dioximato ligands that incorporate half-sandwich [Cp*M] fragments (where M is Rh or Ir). The first procedure relies on Cp*M(OAc)$_2$ precursor complexes, denoted as **M-OAc** hereafter, which contain acetate ligands that can undergo protonolysis by the bridging protons present in monometallic Ni(II) and Co(III) diimine-monoxime-monooximato precursor complexes. The second procedure utilizes more common [Cp*MCl$_2$]$_2$ precursors in concert with exogeneous NaOAc, and is a useful route for generation of chloride-containing heterobimetallic complexes of Ni(II). Using these protonolysis-driven procedures, we have prepared and fully characterized six new

heterobimetallic complexes containing [Cp*Rh] or [Cp*Ir] fragments contained within diimine-dioximato chelating frameworks. In these systems, the tetraazamacrocylic core functions as a heteroditopic ligand, hosting either Ni(II) or Co(III) in its central tetradentate site and either Rh(III) or Ir(III) in its peripheral bidentate site. These complexes are the first examples of structurally characterized oxime-bridged heterobimetallics containing [Cp*Rh] and [Cp*Ir] moieties paired with 3*d* metals.[29] Solid-state X-ray diffraction studies along with spectroscopic and electrochemical investigations have been used to study the properties of the new heterobimetallic complexes. On the basis of the findings, we conclude that these complexes could be useful for studies of heterobimetallic chemistry involving organometallic species.

8.2 Results

8.2.1 Synthesis and Characterization

In order to prepare the target heterobimetallic complexes, we first synthesized precursor monometallic complexes supported by tetradentate diimine-dioxime-type ligands. We turned to the known ligands commonly abbreviated as $(DOH)_2$pn and $(DOH)_2$en for preparation of Ni(II) and Co(III) complexes, respectively.[30] $(DOH)_2$pn represents the diimine-dioxime-type ligand bridged by 1,3-propanediamine, while $(DOH)_2$en is bridged by ethylenediamine (see Scheme 8.1). Both ligands were prepared from diacetylmonoxime using literature procedures,[31] and no unusual features were encountered in either case. We selected these two different ligands for this work, because, in our hands, the $(DOH)_2$pn ligand could be used to generate clean nickel complexes, but was not suitable for generation of isolable cobalt complexes.

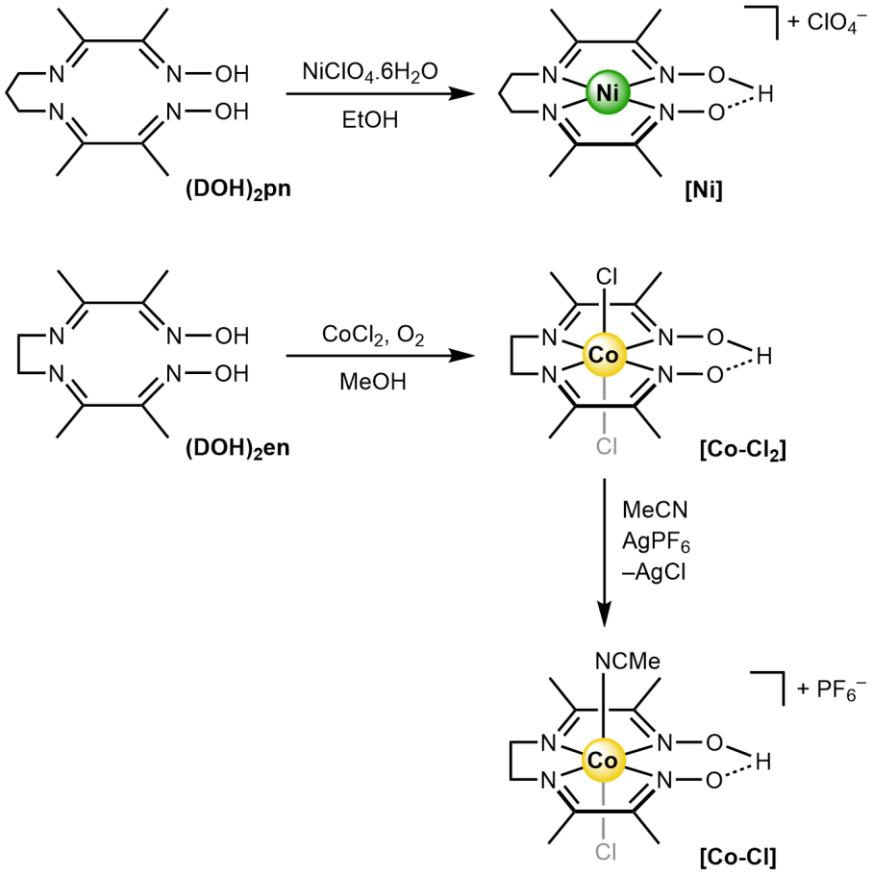

Scheme 8.1. Synthesis of nickel(II) and cobalt(III) monometallic complexes.

We synthesized the monometallic Ni(II) and Co(III) precursor complexes using literature procedures involving reaction of nickel perchlorate hexahydrate and cobalt dichloride with 1 equivalent of $(DOH)_2pn$ or $(DOH)_2en$, respectively.[30,31] The desired monometallic complexes, $[Ni(DO)(DOH)pn]ClO_4$ and $CoCl_2(DO)(DOH)en$, referred to hereafter as **Ni** and **Co-Cl2**, respectively (see Scheme 8.1), contain the key proton-bridged macrocyclic structures that enable preparation of heterobimetallic species. **Ni** was first prepared by Uhlig and Friedrich while **Co-Cl2** was first prepared by Marzilli.[30,32] In order to assemble the desired heterobimetallic complexes containing cobalt, however, we further prepared a new form of the complex, **Co-Cl**, by salt metathesis of **Co-Cl2** with $AgPF_6$, to generate the desired monochloride species (*vide infra)*. The **Co-Cl** complex could be isolated and was

characterized by ^{1}H NMR (see Experimental Section), but was used here only for preparation of the target heterobimetallics. Based on ^{1}H NMR, **Co-Cl** is associated with a single loosely bound acetonitrile solvent molecule, confirming the effectiveness of the desired salt metathesis reactivity (see Appendix G, Figure G10).

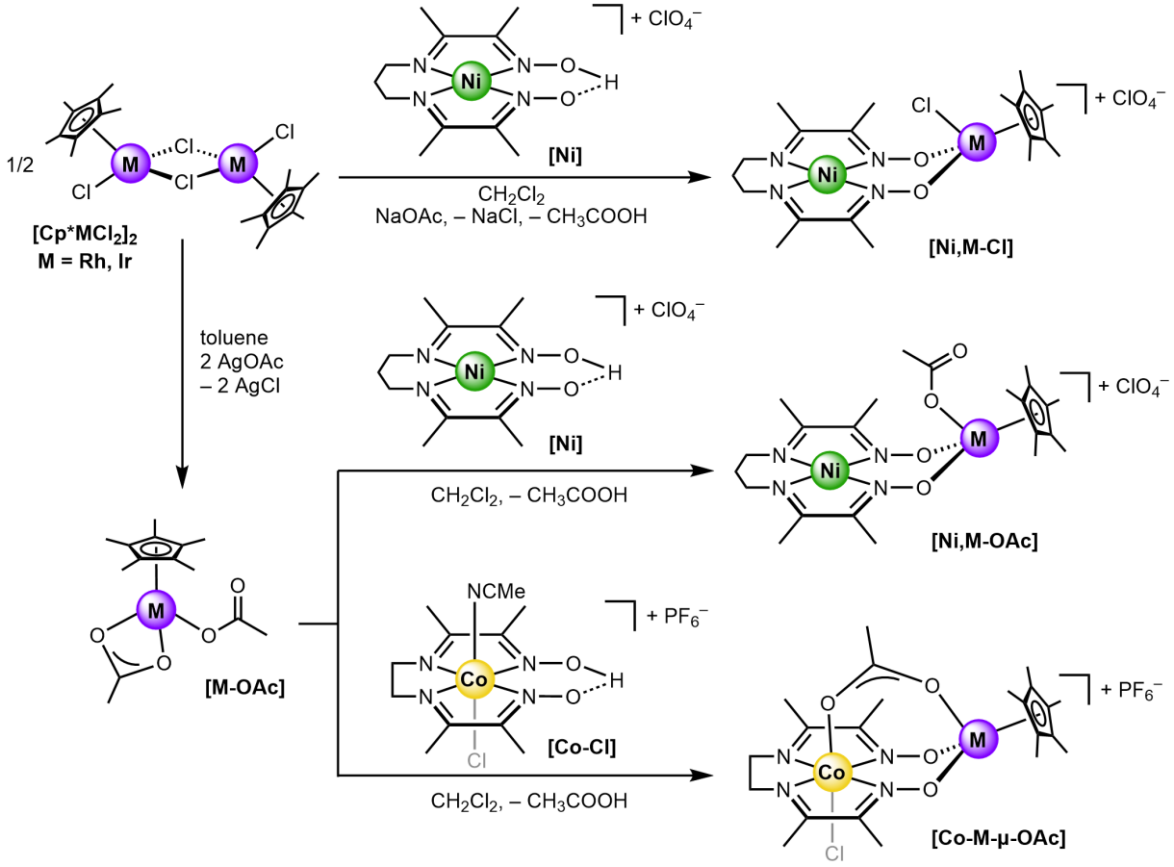

Scheme 8.2. Synthesis of heterobimetallic complexes of nickel(II) and cobalt(III) with rhodium(III) and iridium(III) secondary metals.

With both **Ni** and **Co-Cl** in hand, heterobimetallic complexes pairing the Ni(II) and Co(III) metal centers with [Cp*Rh] or [Cp*Ir] centers bearing acetate ions could be prepared by stirring with 1 equiv. of the appropriate Cp*M(OAc)$_2$ precursors (abbreviated as **M-OAc**) in dichloromethane, respectively. The desired heterobimetallic complexes were obtained following workup in good to excellent yields (>85%) in all cases (see Experimental Section).

In the reactions, the distinct smell of acetic acid could be identified in the environment of the reaction vial, confirming the desired protonolysis reactivity that affords the desired **Ni,Rh-OAc**, **Ni,Ir-OAc**, **Co,Rh-μ-OAc**, and **Co,Ir-μ-OAc** (see Scheme 8.2). Additionally, $[Cp^*RhCl_2]_2$ and $[Cp^*IrCl_2]_2$ could be used directly for generation of chloride-bound analogues of the nickel complexes.[33] This alternative procedure provided heterobimetallic complexes of the form **Ni,Rh-Cl** and **Ni,Ir-Cl** (see Scheme 8.2). Yields of these reactions were also good to excellent. Considering the clean protonolysis reactivity that we observed, we note that Peters[20] and Cossairt[21] utilized nitrogen-containing organic bases for installation of divalent metal ions in dioximato sites (see Chart 8.1). Our synthetic procedure is distinctive from these cases, since our byproducts of protonolysis and salt metathesis (acetic acid and sodium chloride, respectively) can be conveniently separated by filtration and removal of all volatiles *in vacuo*. Appealingly, all of the six new heterobimetallic complexes described here are diamagnetic; ^{1}H NMR resonances corresponding to the methyl groups on the diimine-dioximato metallomacrocycle appear as two singlets in CD_3CN, consistent with a C_s-symmetric appearance of the bimetallic complexes in solution (see Appendix G for all NMR spectra). A single, intense resonance corresponding to the five equivalent methyl groups of the η^5-Cp* ligand was also observed, confirming free rotation in solution. ^{1}H, ^{31}P, and ^{19}F NMR studies as well as elemental analysis of all the isolated materials were successfully obtained, confirming generation and clean isolation of the desired compounds (see Appendix G and Experimental section for details).

8.2.2 X-ray Diffraction Studies

Single crystals suitable for X-ray diffraction (XRD) analysis were obtained for all of the heterobimetallic complexes reported here. Crystals of five of the six compounds were grown

by vapor diffusion of diethyl ether into concentrated acetonitrile solutions of the desired complexes, while one exception was **Ni,Ir-Cl** which required diffusion of diethyl ether into a concentrated methanol solution of the complex. XRD analysis revealed the geometries around the Ni(II) centers to be square-planar in all cases, and around the Co(III) centers to be octahedral in all cases. Additionally, the geometries around the Rh and Ir centers were found to be *pseudo*-octahedral in all cases.

Solid-state structures of the Ni(II) complexes **Ni,M-Cl** and **Ni,M-OAc** (M = Rh or Ir) (Figures 8.1 and 8.2) reveal a preference for highly planar environments around the nickel centers. The planarity of the tetradentate sites containing nickel could be quantified in our diffraction data through the ω_{N4} parameter, which was defined here as the root-mean-square deviation of the four nitrogen donor atoms from the mean plane defined by the positions of those atoms. Inspection of the data (see Table 8.1) reveals that the value of the ω_{N4} parameter is very small for the monometallic precursor **Ni** at 0.006, and increases only slightly for each of the heterobimetallic complexes. On the other hand, the Ni(II) metal centers situated in the tetradentate sites are modestly displaced from the rather planar macrocyclic structures, as quantified with the $\psi_{M'}$ values given in Table 8.1. In particular, the Ni(II) centers are displaced only by ≥ 0.06 Å in all the relevant heterobimetallic complexes. On the other hand, the secondary metals M (Rh or Ir) are not located in the plane containing the macrocyclic N and O atoms in any case; this displacement was quantified by the ϕ angle, representing the angle between the plane defined by N1, N2, N3, N4, O1, O2 and the plane defined by O1, O2, and Rh/Ir. The ϕ angle increases slightly for **Ni,Ir-OAc** in comparison to the other derivatives, perhaps consistent with the larger size of Ir and steric demand of acetate versus

chloride. Overall, however, all the nickel complexes closely resemble each other on the basis of all the structural metrics (see Table 8.1).

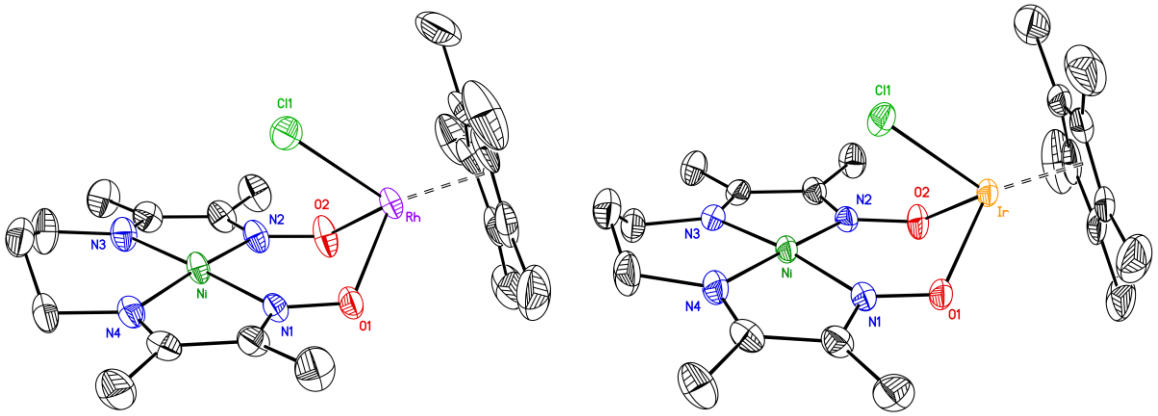

Figure 8.1. Solid-state structures from XRD of **Ni,Rh-Cl** (left) and **Ni,Ir-Cl** (right). All H-atoms, the outer-sphere perchlorate counteranion and co-crystallized CH_3CN solvent molecule are omitted for clarity. Displacement ellipsoids are shown at the 50% probability level.

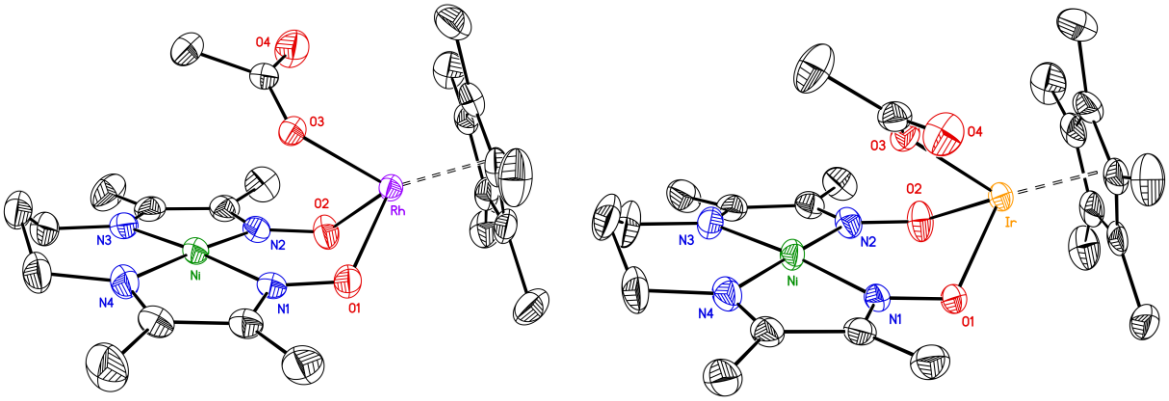

Figure 8.2. Solid-state structures from XRD of **Ni,Rh-OAc (**left) and **Ni,Ir-OAc** (right). All H-atoms, the outer-sphere perchlorate counteranion and co-crystallized CH_3CN solvent molecule are omitted for clarity. Displacement ellipsoids are shown at the 50% probability level.

Table 8.1. Comparison of structural parameters from X-ray diffraction studies for the Ni(II) and Co(III) complexes.

Compound	Ni[a]	Ni,Rh-Cl	Ni,Ir-Cl	Ni,Rh-OAc	Ni,Ir-OAc	Co-Cl_2[b]	Co,Rh-μ-OAc[c]	Co,Ir-μ-OAc[c]
M′•••M (Å)[d]	-	3.649(1)	3.677(1)	3.663(1)	3.725(1)	-	3.606(1)	3.643(1)
M–Cp*$_{cent}$ (Å)[e]	-	1.746	1.757	1.750	1.749	-	1.742	1.745
M–O_{avg} (Å)[f]	-	2.091(4)	2.099(4)	2.101(1)	2.102(4)	-	2.104(3)	2.100(4)
N–O_{avg} (Å)	1.336(3)	1.323(6)	1.336(6)	1.317(3)	1.325(6)	1.333(1)	1.319(4)	1.320(6)
M′–N_{avg} (Å)	1.882(3)	1.901(6)	1.898(6)	1.903(4)	1.902(8)	1.863(1)	1.880(5)	1.878(6)
O1•••O2 (Å)	2.420(2)	2.785(4)	2.771(4)	2.781(2)	2.770(4)	2.697(1)	3.062(3)	3.039(4)
∠ NOM$_{avg}$ (º)	-	118.0(3)	118.9(3)	118.5(2)	120.1(3)	-	117.7(2)	119.2(3)
∠ XMC$_{cent}$ (º) (X = Cl or O)	-	126.3	126.6	132.8	133.2	-	121.3	122.7
ϕ (º)[g]	-	124.9	125.6	125.1	128.3	-	135.2	137.3
ω_{N4}[h]	0.006	0.038	0.029	0.002	0.020	0.030	0.029	0.024
$\psi_{M'}$[i] (Å)	0.014	0.064	0.086	0.065	0.060	0.085	0.115	0.114

(a) Structural data taken from references 14 and 34 (CCDC 738487). (b) Structural data taken from references 31 and 35 (CCDC 646793). (c) **Co,Rh-μ-OAc** and **Co,Ir-μ-OAc** crystallize with isomorphous structures. (d) Here **M′** denotes Ni or Co and **M** denotes Rh or Ir. (e) Distance between centroid of the pentamethylcyclopentadienyl (Cp*) ring and Rh/Ir metal. (f) Errors on the average bond lengths and bond angles were derived by propagation of error from the individual values and estimated standard deviations (e.s.d.'s). (g) The angle between the plane defined by N1, N2, N3, N4, O1, O2 and the plane defined by Rh/Ir, O1, O2. (h) Defined as the root mean square deviation (r.m.s.d.) of the following atoms from the mean plane of their positions: N1, N2, N3, and N4. (i) Defined as distance between the Ni/Co and the centroid of the plane defined by N1, N2, N3, and N4. All atom labels are consistent with those given in the crystallographic data (see Appendix G).

The first coordination spheres of the Rh and Ir centers contain the η^5-Cp* ligand, the κ^2-[O_2]-diimine-dioximato site, as well a single chloride ion in the **Ni,M-Cl** cases or a κ^1-acetate group in the **Ni,M-OAc** cases. The geometry around M is *pseudo*-octahedral in each case,

and the value of ∠XMC$_{cent}$ (the angle defined by the positions of the X atom (chloride or O of acetate), the metal center M (Rh or Ir), and the centroid of the η^5-Cp* ligand) spans a tight range of 126.3º to 133.2º. These values are similar to the values of corresponding angles measured in previously published crystallographic data for water-bound **Rh-OAc** and dimethylsulfoxide-bound **Ir-OAc** complexes averaging to 127.0º and 129.9º, respectively.[36,37] Considering the similarity of these values, we conclude that the acetate ligands in the **[Ni,M-OAc]** complexes do not interact strongly with the pendant nickel(II) site contained in the macrocyclic ligand.

The Ni•••M distances are slightly smaller for Rh (3.649(1) Å and 3.663(1) Å) versus Ir (3.677(1) Å and 3.725(1) Å), consistent with the larger ionic radius of Ir(III) (0.68 Å) vs. Rh(III) (0.66 Å).[38] This finding implies that Rh could serve as a stronger Lewis acid to modulate the properties of the nickel center in comparison to iridium. This is in agreement with the tabulated pK_a values of the corresponding aqua ions of Rh(III) and Ir(III), which show that Rh(III) is more Lewis acidic (pK_a = 3.4) than Ir(III) (pK_a = 4.4) in H_2O.[39] The average N–O bond distances in the bimetallic complexes of nickel range from 1.317(3) Å to 1.336(6) Å, either indistinguishable from or slightly smaller than the value of 1.336(3) Å found in the monometallic precursor **Ni**. This suggests modest π-bonding interactions occur from O to M, consistent with the electronic nature of Rh and Ir as 4*d* and 5*d* transition metals. Such π-bonding effects have been considered previously for the related bimetallic [Ni,Zn] complexes studied by Peters and co-workers.[20a]

Data from XRD analysis of the Co(III) complexes are generally similar to the data collected with the Ni(II) complexes. However, an interesting counterpoint in the data for the **Co-M-μ-OAc** complexes (Figure 8.3) is the observation of bridging acetate ligands that span

the two different metal centers in the isomorphous structures. We were inspired to attempt installation of the bridging acetate ligands by the observation of such ligands in the work of Chaudhuri and co-workers.[19] Here, we anticipated that we could favor installation of bridging acetate ligands via generation of the synthon **Co-Cl**, which features a coordination site on Co(III) occupied in the monometallic precursor by presumably loosely bound CH_3CN; see Figure G10 in Appendix G). On the basis of the observed structures, this bound CH_3CN could indeed be readily displaced by acetate associated with the incoming [Cp*M] fragment, generating the desired acetate bridges between Co(III) and M(III). Supporting this viewpoint, the structures of the **Ni,M-OAc** complexes lack these bridging acetates; this is attributable to the general preference of Ni(II) to retain its square-planar geometry in the heterobimetallic complexes.

As in the Ni(II) complexes, the Co(III) ion is situated in the tetradentate macrocyclic site in all cases. Indeed, the ω_{N4} values for the **Co-Cl$_2$** precursor as well as all the bimetallic cobalt complexes span a narrow range from 0.024–0.030, consistent with relative rigidity of the diimine-dioximato framework. On the other hand, inspection of the $\psi_{M'}$ values for the heterobimetallic complexes reveals a significant displacement of the Co(III) centers by 0.114–0.115 Å from the plane of the diimine-dioximato ligand. This displacement is readily attributable to coordination of the bridging acetate ligand, which appears to pull the cobalt ion out of the plane due to strain induced by two-point binding of the acetate ligand. Such a structural deformation of the M′ site may contribute to the electrochemical behavior of these complexes (*vide infra*).

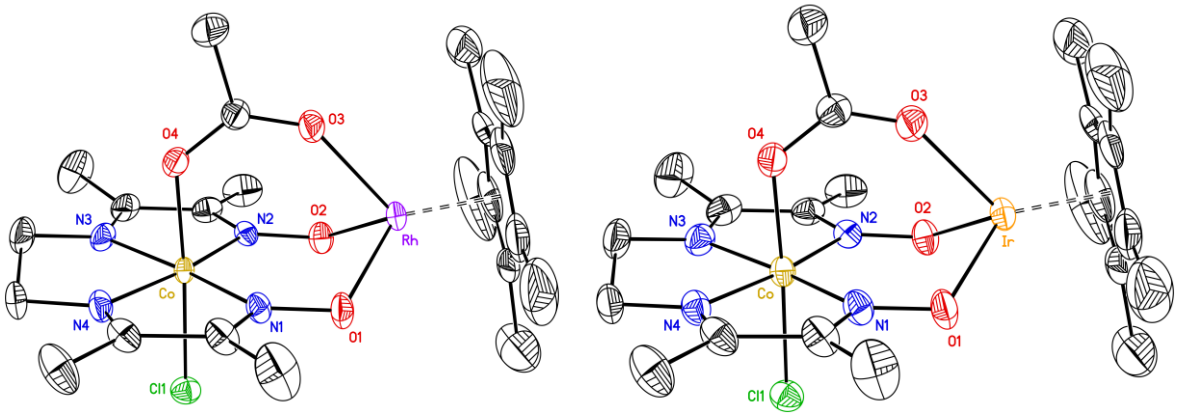

Figure 8.3. Solid-state structures from XRD of **Co,Rh-μ-OAc** (left) and **Co,Ir-μ-OAc** (right). All H-atoms and the outer-sphere hexafluorophosphate counteranion are omitted for clarity. Displacement ellipsoids are shown at the 50% probability level.

Surveying the complete family of structural results for the heterobimetallic complexes, a noticeable increase in the O1•••O2 interatomic distance (across the dioximato site) is apparent in comparison to the corresponding values for the monometallic complexes **Ni** and **Co-Cl$_2$**. O1 and O2 play the crucial role of ligating M, and consistent with the large sizes of Rh and Ir, the O1•••O2 distance increases in all cases by 0.342-0.365 Å (see Table 8.1). This increased separation is attributable to the large size of the Rh and Ir centers in comparison to H^+ found in the monometallic complexes, although such comparisons are difficult to quantify directly. Considering the monometallic complexes alone, the O1•••O2 separation in **Co-Cl$_2$** is 0.28 Å greater than in **Ni** (2.697(1) vs. 2.420(2) Å, respectively), a situation attributable to the more sterically demanding propyl backbone present in **Ni**, which likely 'pushes' the macrocyclic oximato moieties together and assists in formation of a strong O–H•••O hydrogen bond. Consistent with this theory, the analogue of **Ni** prepared with an ethyl backbone has an O1•••O2 separation of 2.616(1) Å, significantly greater (nearly 0.2 Å) than the value for **Ni** with a propyl bridge.[20a] This is consistent with a pulling apart of the two 'sides' of the ligand away from the oxygens, and opening up of the H-bonded O1•••O2 site.

Within this family of analogous structures, there are noticeable trends in the Ni•••M and Co•••M distances. For the nickel complexes, the Ni•••M distances are very similar for the pairs containing the same metals; **Ni,Rh-Cl** and **Ni,Rh-OAc** have distances of 3.649(1) and 3.663(1) Å, respectively, while **Ni,Ir-Cl** and **Ni,Ir-OAc** have slightly longer distances of 3.677(1) and 3.725(1) Å, respectively. This high degree of similarity attests to the lack of strong interactions between the chloride and κ^1-acetate ligands bound to Rh/Ir with nickel, while the slightly larger values for the acetate complexes do indicate a role for steric bulk in 'opening' of the concave face of the heterobimetallic structures. Moreover, the slightly longer distances between Ni and Ir are consistent with the larger size of Ir in comparison to Rh. For the pair of isomorphous cobalt complexes bridged by acetate ligands that interact with both metal centers, we note a significantly longer Co•••Ir distance of 3.643(1) Å versus a Co•••Rh distance of 3.606(1) Å. We anticipate that this and the 1.5° increase in the folding along the O1•••O2 vector are again attributable to the greater size of Ir in comparison to Rh and the fixed length of the acetate bridge. Finally, we note the M′•••M distances (where M′ is Ni or Co) are significantly larger for the nickel acetate complexes (3.663(1) and 3.725(1) Å, respectively) in comparison to the corresponding values for the cobalt acetate complexes (3.606(1) and 3.643(1) Å, respectively). These distances are consistent with the bridging role of the acetate ligand in the cobalt complexes, which draws the two metal centers together via two-point binding in the cobalt complexes.[40]

8.2.3 Electronic Absorption Spectroscopy

Dissolution of the isolated heterobimetallic complexes in CH_3CN results in orange to deep red solutions. To investigate the electronic properties of the compounds and compare them to the monometallic precursors, we turned to electronic absorption (EA) spectroscopy.

The EA spectrum of **Co-Cl$_2$** displays a lowest energy absorption band in the near-UV region with a maximum absorption wavelength (λ_{max}) at 350 nm with a molar absorptivity (ε) of ca. 3600 M^{-1} cm^{-1} (Figure 8.4). Based on its intensity, we assign this feature as a charge transfer (CT) band. Upon replacement of the proton bridge with the [Cp*M] organometallic fragments in **Co,Rh-μ-OAc** and **Co,Ir-μ-OAc**, the compounds absorb more strongly in the visible region and display red-shifted lowest energy absorption bands (λ_{max} = 411 nm; ε = 4500 M^{-1} cm^{-1} and λ_{max} = 431 nm; ε = 4000 M^{-1} cm^{-1}, respectively) complexes (Figure 8.4). The shifts in the lowest energy absorption maxima to longer wavelengths suggest a particular influence of the second metal on the electronic properties of the heterobimetallic complexes. Similar behavior was observed by Peters & co-workers in a related nitrito-bridged bimetallic complex of the form [Co^{III}-μ-NO_2-Mg], which displayed a lowest energy absorption maximum at 418 nm.[20b] Considering the similarity of the results for this [Co,Mg] heterobimetallic complex to our own, we hypothesize that coordination of Lewis acidic metals to the dioximato ligand framework drives the shift in absorption to lower energies. Both of the heterobimetallic cobalt complexes studied here as well as **Co-Cl$_2$** exhibit additional bands at higher energies; these are attributable to intraligand π-to-π* transitions with molar absorptivity values greater than 20,000 M^{-1} cm^{-1} in all cases. Consistent with the distal placement of the Rh/Ir centers with respect to the conjugated ligand backbone around the Co(III) center, these higher energy bands are relatively unperturbed by coordination of the secondary metals.

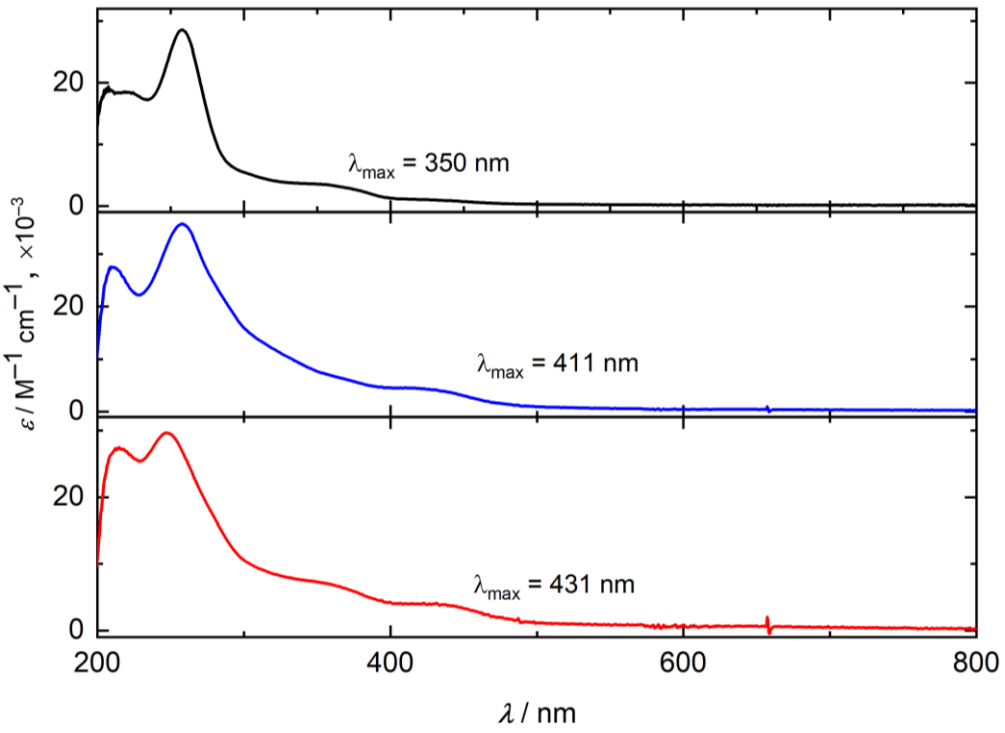

Figure 8.4. Stacked electronic absorption spectra for **Co-Cl$_2$** (black), **Co,Rh-μ-OAc** (blue), and **Co,Ir-μ-OAc** (red) in CH_3CN.

Similar to the heterobimetallic cobalt complexes, the heterobimetallic nickel complexes feature intraligand π-to-π* transitions in the UV region between 200 – 300 nm (ε > 15000 M^{-1} cm^{-1}) that strongly resemble bands present in the monometallic precursor **Ni** (see Appendix G, Figure G28 for all spectra). Along with these intense features, the heterobimetallic complexes display intense CT bands around 400 nm in all cases. The CT bands are strikingly similar in their absorption maxima for the rhodium complexes **Ni,Rh-Cl** (λ_{max} = 397 nm; ε = 5200 M^{-1} cm^{-1}) and **Ni,Rh-OAc** (λ_{max} = 395 nm; ε = 10800 M^{-1} cm^{-1}) and also the iridium complexes **Ni,Ir-Cl** (λ_{max} = 385 nm; ε = 6700 M^{-1} cm^{-1}) and **Ni,Ir-OAc** (λ_{max} = 388 nm; ε = 9600 M^{-1} cm^{-1}). Notably, the λ_{max} values are slightly blue-shifted for the Ir complexes in comparison to the analogous Rh complexes, a finding that diverges from the results obtained with the cobalt complexes (*vide supra*). On the other hand,

the acetate complexes have molar absorptivities that are much larger than for the analogous chloride complexes. Considered together with the ^{1}H NMR data (see Appendix G), the electronic absorption spectra confirm that the heterobimetallic complexes are persistent in solution, resulting in the unique spectra obtained in each case. Thus, we next turned to electrochemical studies to understand how the multiple metals impact the redox properties of the heterobimetallic compounds.

8.2.4 Electrochemistry

A primary goal of our study is to understand the influence of the [Cp*Rh] and [Cp*Ir] moieties on the electrochemical properties of the redox-active Ni- or Co-containing diimine-dioximato cores. Since these cores are redox-active and frequently used in catalysis, we were particularly curious to see how the presence of heavy metals (Rh and Ir) might affect the redox properties of these metal-containing ligands. In order to understand any intrinsic reduction processes for Rh^{III} and Ir^{III} centers in our systems, however, we first performed control cyclic voltammetry (CV) experiments on the **M-OAc** precursors. In our studies, we observed single chemically irreversible cathodic waves at quite negative reduction potentials for both **Rh-OAc** ($E_{p,c}$ = –1.57 V vs $Fc^{+/0}$) and **Ir-OAc** ($E_{p,c}$ = –2.04 V vs $Fc^{+/0;}$ see Appendix G, Figures G34 and G36). As the redox processes observed with the monometallic nickel and cobalt complexes as well as the heterobimetallics occur at significantly more positive potentials, we have tentatively considered the [Cp*M] fragments as redox-inactive at potentials positive of these potentials in the new compounds. However, bringing the Rh and Ir metal centers into proximity of the nickel and cobalt centers is not without consequence, as described below.

CV experiments have been previously performed on the parent monometallic complex **Ni** and the dibromide analogue of **Co-Cl$_2$** by Fontecave and co-workers.[14] Here, we re-confirmed the electrochemical properties of **Ni** and also collected fresh data for **Co-Cl$_2$** and **Co-Cl** (see Appendix G, Figures G29, G31 and G33). The electrochemical data for **Ni** (see Appendix G, Figure G29) revealed a chemically reversible reduction process at $E_{1/2}$ = –1.22 V vs the ferrocenium/ferrocene couple (denoted hereafter as $Fc^{+/0}$). This feature has been observed previously[14,20a] and has been assigned as a $Ni^{II/I}$ couple. Scan rate-dependent studies (see Appendix G, Figure G30) revealed a linear dependence of both the cathodic and anodic peak currents on the square root of scan rate confirming freely diffusing nature of both isolated **Ni** as well as its reduced form. A second chemically reversible wave was also observed at a more negative potential ($E_{1/2}$ = –1.80 V vs $Fc^{+/0}$). Notably, this redox process was not mentioned in the prior work from Fontecave and co-workers, although a similar feature was measured by Peters and co-workers.[20] Based on the quite negative reduction potential, we anticipate that this feature may correspond to a ligand-centered reduction, but we did not pursue a rigorous assignment here.

Compared to the relatively clean voltammograms obtained with monometallic **Ni** (see Appendix G, Figure G29), a more complex profile was obtained when electrochemical studies were performed on the heterobimetallic complexes containing nickel. Qualitatively, voltammograms of all four isolated [Ni,M] complexes are similar and display a single, chemically irreversible cathodic wave near $E_{p,c}$ = –1.48 V vs $Fc^{+/0}$ (see Appendix G, Figures G39–G42 for all the individual voltammograms). On the basis of the prior assignment of the first reduction of **Ni** as metal-centered from the work of Fontecave and co-workers, we assign this reduction as a Ni^{II}/Ni^{I} process. The reduced forms of the complexes are unstable,

however, as judged by CV, as in all cases the voltammograms lack a coupled re-oxidation wave, confirming speciation of the complexes into one or more different forms upon reduction. Multiple irreversible reduction features occur when scanning to more negative potentials (see Appendix G, Figures G39–G42), suggesting chemical speciation and the involvement of irreversible processes upon reduction of the [Ni,M] heterobimetallics. Considering the potentials involved, we anticipate that Rh- and/or Ir-centered reductions could be involved in this quite negative-potential redox chemistry. We have previously encountered chemically irreversible redox properties for half-sandwich rhodium complexes bearing select bidentate ligands, particularly in cases where the bidentate ligands are lost from the Rh metal center, promoting formation of dimeric and/or oligomeric complexes.[41] Considering the likely generation of an anionic Ni-containing fragment upon Ni-centered reduction, we anticipate such processes may be involved here.

On the other hand, the electrochemical properties of the heterobimetallic cobalt complexes displayed significantly more well-resolved electrochemical behavior. For comparison, the cyclic voltammogram of the monometallic **Co-Cl$_2$** complex (see Figure 8.5, black trace) displays a profile that can be assigned on the basis of prior work[14] as involving two separate 1e$^-$ redox processes which are overlapping with each other; the more positive process can be assigned as $Co^{III/II}$ ($E_{1/2}$ = ca. –0.75 V) and the more negative to $Co^{II/I}$ ($E_{1/2}$ = –0.98 V vs. $Fc^{+/0}$). Appealingly, all three accessible oxidation states of cobalt mentioned above are freely diffusing as judged by scan rate-dependent studies (see Appendix G, Figure G32). The appearance of the CV data for the **Co-Cl$_2$** differs from that of the dibromide analogue measured by Fontecave and co-workers, in that the reduction potentials display a greater separation of 540 mV in comparison to the much more modest 220 mV or so

measured here for **Co-Cl$_2$**. On the other hand, halide ligands are often lost upon reduction of Co^{III} to Co^{II}, a feature that could drive the small difference between the the $Co^{II/I}$ couple measured here for **Co-Cl$_2$** ($E_{1/2}$ = –0.98 V vs. $Fc^{+/0}$) and that of the dibromide analogue ($E_{1/2}$ = –1.11 V vs. $Fc^{+/0}$).[17] Furthermore, similar to the **Ni** case, the CV data of **Co-Cl$_2$** (see Appendix G, Figure G31) display a further, even more negative reduction process at $E_{1/2}$ = –2.03 V vs. $Fc^{+/0}$. Strikingly similar, although more complicated, features were generally observed in the electrochemical data of the monochloride species **Co-Cl** (see Appendix G, Figure G33), possibly due to flexible coordination number of the Co center, leading to the presence of multiple species in solution that can undergo reduction.

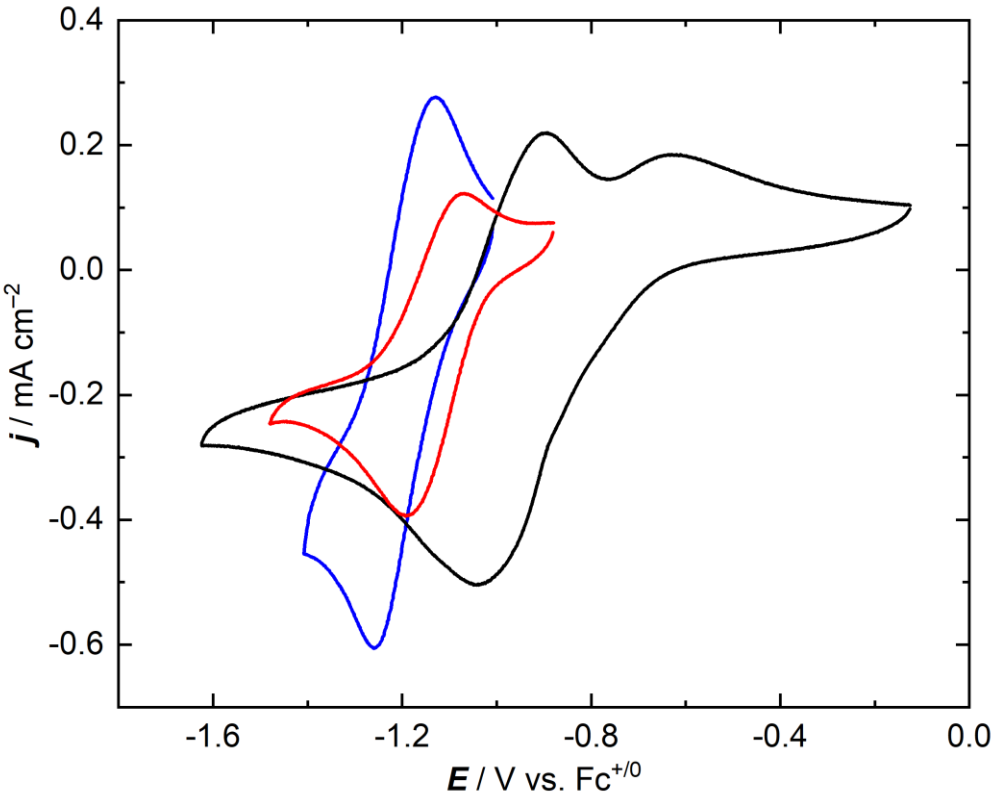

Figure 8.5. Cyclic voltammetry data for **Co-Cl$_2$** (black trace), **Co,Rh-μ-OAc** (blue trace), and **Co,Ir-μ-OAc** (red trace). Conditions: 0.1 M $[nBu_4N]^+[PF_6]^-$ in CH_3CN; scan rate: 100 mV/s; concentrations of all complexes were 2 mM.

To our delight, the CV profiles of the heterobimetallic complexes containing cobalt display a chemically reversible process at $E_{1/2}$ = –1.19 V vs $Fc^{+/0}$ for **Co,Rh-μ-OAc** and $E_{1/2}$ = –1.13 V vs $Fc^{+/0}$ for **Co,Ir-μ-OAc**. The voltammograms of both complexes display a return oxidation wave when the potential is switched after the first reduction process (Figure 8.5). We attribute this single electrochemically quasi-reversible and chemically reversible redox event to a $Co^{II/I}$ couple on the basis of its similarity to the $Co^{II/I}$ couple measured for **Co-Cl$_2$** as well as other cobalt complexes.[17] In addition, no further reductions were measured in the nearby potential range, suggesting shift of the corresponding $Co^{III/II}$ reduction to more positive potentials. However, similar to the [Ni,M] case, multiple irreversible reduction features occur in the cobalt heterobimetallic complexes when scanning more negative than –1.6 V or so (see Appendix G, Figures G47 and G48), suggesting chemical speciation and instability of the reduced forms of the complexes at more negative potentials. Scan rate-dependent studies on the **Co,M-μ-OAc** (see Appendix G, Figures G44 and G46) revealed a linear dependence of both the cathodic and anodic peak currents on the square root of scan rate, confirming freely diffusing nature of Co^{II} and Co^{I} forms of the complexes.

Inspection of the $E_{1/2}$ values from the CV data of the [Co,M] complexes reveals that the values for the $Co^{II/I}$ reduction are shifted by ca. 150 – 200 mV) to more negative values in comparison to value for **Co-Cl$_2$** (Figure 8.5). This potential shift is attributable the substitution of the macrocyclic bridging proton with the Rh^{III} or Ir^{III} metal centers. These large metals engage in covalent bonding with the dioximato ligand framework and could afford inductive effects via π-interactions that give rise to the noted potential shifts. In accord with this theory, the average N–O distances of the oximato moieties in the bimetallic complexes are shorter by a modest 0.015 Å as compared to their values in the monometallic

analogue. In this context, the effect of secondary metal coordination on the electrochemistry of nickel has been discussed previously by Peters & co-workers in reference to their [Ni,Zn] systems.[20a]

However, in comparison to the **Co,Ir-μ-OAc** complex, the $E_{1/2}$ value of the **Co,Rh-μ-OAc** complex is shifted 60 mV more negative. This shift is in opposition to the predicted trend on the basis of the Lewis acidity of Rh vs. Ir (*vide supra*) as well as the anticipated superior ability of Ir vs. Rh to engage in covalent bonding via more significant orbital overlap. However, these Lewis acidity and electronic arguments may be superceded by a structural effect, in that the Co•••M distances from the XRD data show that the Rh center is closer to Co by 0.037 Å as compared to the Ir center. This closeness, implying a possible tighter association of the acetate anion with cobalt in solution, would give rise to the more negative $E_{1/2}$ value. Schelter and co-workers have observed similar discrepancies between Lewis acidity and structural effects in their notable work with heteromultimetallic complexes of redox-active cerium.[42]

Considering the noted shifts in redox chemistry and electronic properties, we carried out a preliminary investigation of possible influences of the assembled metals on a model catalytic reaction. For this preliminary investigation, we utilized the heterobimetallic [Co,Rh] complex in a test for catalysis of hydrogenation (see Appendix G for details). For this study, we chose trifluoromethylbenzaldehyde (**A**) as a substrate, due to the general inertness of the aryl ring and trifluoromethyl group towards hydrogenation under our conditions and the ease of monitoring the reactions using ^{19}F NMR. The test was carried out at 50^{o}C for 24 hours in CD_3CN with 1 atm of H_2 gas and a catalytic amount of triethylamine. With 7 mol% loading of **Co,Rh-μ-OAc**, an 80% conversion of **A** to its hydrogenated

product, trifluoromethylbenzyl alcohol (**B**) was recorded (see Appendix G, Figures G49 and G51). Notably, no conversion of **A** to **B** was observed when the hydrogenation experiment was performed in the presence of 10 mol% of the parent complex **Co-Cl$_2$** or in the absence of any metal complex (see Appendix G, Figures G49 and G50). Low conversion (13%) was observed when 10 mol% of **Rh-OAc** was tested for catalysis (see Appendix G, Figures G49 and G52). When the hydrogenation was performed with a 1:1 mixture of the individual monometallic precursor complexes (**Co-Cl$_2$** + **Rh-OAc**), significant conversion (40%) of **A** to **B** was observed, but concomitantly with observation of multiple other products, suggesting unselective reactivity (see Appendix G, Figures G49 and G53). Thus, this preliminary study highlights an apparent advantage of [Co,Rh] toward hydrogenation, suggesting that our series of heterobimetallic complexes could be used in future studies of multimetallic chemistry.

8.3 Discussion

This work shows that the dioximato moiety present in both **Ni** and **Co-Cl$_2$** is suitable for chelation of [Cp*Rh] and [Cp*Ir] species, building on the elegant prior work of Chaudhuri, Peters, and Cossairt.[19,20,21] Notably, Rh and Ir are heavier elements than the various metals previously installed into the dioximato-type sites, expanding the versatility of this ligand environment. All of this synthetic chemistry suggests, however, that the dioximato moiety is a relatively flexible coordination site, capable of stably holding both redox-inactive and redox-active metals at moderate distances from the primary metal of 3.6–3.7 Å.

The new heterobimetallic complexes described here are stable in solution, much like the macrocyclic [Ni,M] and [UO_2,M] complexes that we have studied in our prior work (see Chapters 2 and 3, respectively), but nonetheless lack macrocyclic stabilization.[11,12] On the

other hand, the spectroscopic and electrochemical studies reveal only subtle influences of the secondary metals (Rh and Ir) on the properties of the first metal (Ni or Co). This situation of subtle tuning is attributable to the general similarity of Rh^{III} and Ir^{III}, however, considering their positions in the periodic table, sizes, and Lewis acidities.[39] In the current work, we anticipate that the small shifts in reduction potentials induced by the secondary metals can be concluded to be driven by structural factors promoted by the two-point acetate ligand binding and resultant electrostatic considerations.

Generally speaking, the utilization of *in situ* protonolysis reactivity with $Cp^*M(OAc)_2$ to generate the new heterobimetallic complexes described here is reminiscent of other ligation reactions of [Cp*M] complexes.[43] For example, 2-phenylpyridine does not present intrinsically acidic C–H bonds but can readily undergo cyclometallation at Ir(III) upon inclusion of weak bases like acetate due to pre-coordination of the pyridine moiety that leads to acidification of an *ortho*-phenyl C–H bond. This reactivity resembles the *in situ* deprotonation of **Ni** and **Co-Cl$_2$** utilized here, leading to the clean and generally high-yielding synthesis of the new heterobimetallic complexes. Considering the presence of significant electron density on the O-atoms of the proton-bridged macrocyclic precursor complexes, we anticipate that the flexible coordination environment of the $Cp^*M(OAc)_2$ and $[Cp^*MCl_2]_2$ complexes could enable a similar pre-coordination of these complexes to an oxime oxygen, resulting in acidification of the macrocyclic bridging proton. Such a reaction sequence highlights the general utility of these synthons for generation of other heterobimetallic complexes on these platforms in the future, particularly via routes involving protonolysis reactivity of suitable precursors.

8.4 Conclusions

We have synthesized and characterized a family of heterobimetallic complexes by pairing diimine-monoxime-monooximato macrocyclic ligands containing nickel and cobalt centers and organometallic half-sandwich [Cp*M] (M = Rh, Ir) fragments with a protonolysis strategy. In the solid-state structures of the six new heterobimetallic complexes, the Ni(II) centers prefer square-planar geometry while the Co(III) centers favor octahedral geometry, promoting bridging interactions of acetate across Co and Rh/Ir. Installation of Rh or Ir in place of the bridging proton in the dioximato site results in significant changes in the electrochemical profiles in all cases, demonstrating the utility of the second metal in changing the properties of these complexes. Preliminary hydrogenation studies with **Co,Rh-μ-OAc** revealed clean catalytic conversion of a substituted benzaldehyde to benzyl alcohol and suggest a key role of the multiple metal sites in the reactivity. Taken together, these findings illustrate that heterobimetallic complexes of the type described here could find future applications in the exciting area of multimetallic chemistry and catalysis.

8.5 Experimental Details

8.5.1 General Considerations

All manipulations were carried out in dry N_2-filled gloveboxes (Vacuum Atmospheres Co., Hawthorne, CA) or under N_2 atmosphere using standard Schlenk techniques unless otherwise noted. All solvents were of commercial grade and dried over activated alumina using a PPT Glass Contour (Nashua, NH) solvent purification system prior to use, and were stored over molecular sieves. All chemicals were from major commercial suppliers and used as received or after extensive drying.

Ligands $(DOH)_2$en and $(DOH)_2$pn were prepared according to literature procedures.[30,31] $[Cp^*RhCl_2]_2$ was synthesized according to the modified procedure reported by Sanford & co-workers, but the original procedure by Maitlis & co-workers was used in the synthesis of $[Cp^*IrCl_2]_2$.[33] **M-OAc** complexes were synthesized using methods described by Medola.[44] **Ni** complex was prepared using a literature procedure described by Uhlig and Friedrich.[30] Spectroscopic characterizations of all of the above compounds by ^{1}H NMR (see Appendix G, Figures G2 – G8) are in agreement with the prior literature reports.

Deuterated NMR solvents were purchased from Cambridge Isotope Laboratories (Tewksbury, MA, USA). ^{1}H, ^{31}P, and ^{19}F NMR spectra were collected on a 400 MHz Bruker spectrometer (Bruker, Billerica, MA, USA) and referenced to the residual protio-solvent signal[45] in the case of ^{1}H. ^{31}P and ^{19}F NMR spectra were referenced and reported relative to H_3PO_4 and CCl_3F, respectively, as external standards following the recommended scale based on ratios of absolute frequencies (Ξ).[46,47] Chemical shifts (δ) are reported in units of ppm and coupling constants (*J*) are reported in Hz. All experiments were conducted at room temperature (298 K). NMR spectra are given in Appendix G (Figures G2 to G28). Electronic absorption spectra were collected with an Ocean Optics Flame spectrometer equipped with DH-Mini light source, in a 1 cm path length quartz cuvette. Elemental analyses were performed by Midwest Microlab, Inc. (Indianapolis, IN, USA).

8.5.2 Electrochemical Methods

Electrochemical experiments were carried out in a N_2-filled glovebox in dry, degassed CH_3CN. 0.10 M tetra(*n*-butylammonium) hexafluorophosphate ($[^nBu_4N]^+[PF_6]^-$); Sigma-Aldrich, electrochemical grade) served as the solvent and supporting electrolyte. Measurements were carried out with a Gamry Reference 600+ Potentiostat/Galvanostat

(Gamry Instruments, Warminster, PA, USA), using a standard three-electrode configuration. The working electrode was the basal plane of highly oriented pyrolytic graphite (HOPG) (GraphiteStore.com, Buffalo Grove, Ill.; surface area: 0.09 cm^2), the counter electrode was a platinum wire (Kurt J. Lesker, Jefferson Hills, PA; 99.99%, 0.5 mm diameter), and a silver wire immersed in electrolyte served as a pseudoreference electrode (CH Instruments). The reference was separated from the working solution by a Vycor frit (Bioanalytical Systems, Inc., West Lafayette, IN, USA). Ferrocene (Sigma Aldrich, St. Louis, MO, USA; twice-sublimed) was added to the electrolyte solution prior to the beginning of each experiment; the midpoint potential of the ferrocenium/ferrocene couple (denoted as $Fc^{+/0}$) served as an external standard for comparison of the recorded potentials. Concentrations of analytes for cyclic voltammetry were typically 2 mM unless otherwise noted. Experiments were conducted by first scanning cathodically, then anodically on the return sweep.

8.5.3 Synthesis and characterization of monometallic cobalt complexes and heterobimetallic complexes

Synthesis of **Co-Cl$_2$**. The monometallic Co complex was synthesized by modification of a literature procedure.[31] A solution of anhydrous $CoCl_2$ (86 mg, 0.66 mmol) in dry methanol was added dropwise to a methanolic solution of $(DOH)_2$en (150 mg, 0.66 mmol) in air. A dark red solution was obtained, which was stirred for 3-4 hours in air until the observation of brown-colored precipitate. The brown precipitate was filtered on a frit and washed with 5 mL of cold methanol. This procedure is slightly different from the reported synthesis, in that the authors filtered the dark red solution after 20 minutes of stirring and allowed the filtrate to evaporate slowly in air. Yield = 60% (140 mg). Spectroscopic characterization by ^{1}H NMR (see Appendix G, Figure G9) confirmed preparation of the desired compound,

formulated as $CoCl_2(DOH)(DO)en$. ^1H NMR (400 MHz, CD_3CN): δ 13.85 (bs, 1H, *H4*), 4.66 (s, 4H, *H3*), 2.55 (t, $^5J_{H\text{-}H}$ = 1.4 Hz, 6H, *H1*), 2.43 (s, 6H, *H2*) ppm.

Synthesis of **Co-Cl**. In an inert atmosphere glovebox and in the dark, a solution of $AgPF_6$ (110 mg, 0.42 mmol) in acetonitrile was added dropwise to a solution of **Co-Cl$_2$** (160 mg, 0.45 mmol) in acetonitrile. The mixture was stirred overnight, and the resulting AgCl precipitate was filtered on a frit. The filtrate was evaporated *in vacuo* to give a dark yellow solid. Yield = 94% (190 mg). Spectroscopic characterization by ^1H, ^{19}F, and ^{31}P NMR (see Appendix G, Figures G10 – G12) confirmed isolation of the desired synthon, formulated as $[CoCl(NCCH_3)(DOH)(DO)en]PF_6$. ^1H NMR (400 MHz, CD_3CN): δ 9.77 (bs, 1H, *H4*), 4.68 (s, 4H, *H3*), 2.59 (s, 6H, *H1*), 2.46 (s, 6H, *H2*), 1.96 (s, 3H, *H5*) ppm. ^{19}F NMR (376 MHz, CD_3CN) δ −73.70 (d, $^1J_{F,P}$ = 706 Hz) ppm. ^{31}P NMR (162 MHz, CD_3CN) δ −145.48 (q, $^1J_{P,F}$ = 706 Hz) ppm

Synthesis of **Ni,M-Cl**. A solution of $NaOAc{\bullet}3H_2O$ (70 mg, 0.50 mmol) in dichloromethane was added dropwise to a mixture of **Ni** (200 mg, 0.50 mmol) and $[Cp^*MCl_2]_2$ (**M** = **Rh**: 155 mg, 0.25 mmol; **M** = **Ir**: 200 mg, 0.25 mmol) in dichloromethane The mixture was stirred overnight, and the resulting NaCl precipitate was filtered over a celite plug. The filtrate was evaporated *in vacuo*. The resulting solid was washed with 5 mL portions of toluene 3 to 4 times to remove unreacted $[Cp^*MCl_2]_2$ and with $CHCl_3$ to remove unreacted **Ni**. The resultant reddish-brown solid in each case was dried to not more than 50^{o}C to give the pure product. Vapor diffusion of Et_2O into a concentrated CH_3CN solution of **Ni,Rh-Cl** yielded single crystals suitable for X-ray diffraction studies. Vapor diffusion of Et_2O into a concentrated CH_3OH solution of **Ni,Ir-Cl** yielded single crystals suitable for X-ray diffraction studies. Spectroscopic characterizations by ^1H NMR (see Appendix G,

Figures G13 and G14) confirmed preparation of the desired compounds, formulated as [Ni(DOH)(DO)pnCp*RhCl]ClO_4 and [Ni(DOH)(DO)pnCp*IrCl]ClO_4, respectively. **Ni,Rh-Cl**: Yield = 88% (298 mg). ^{1}H NMR (400 MHz, CD_3CN) δ 3.26 – 3.17 (m, 2H, *H4*), 3.02 – 2.91 (m, 2H, *H4*), 2.09 (t, $^5J_{H\text{-}H}$ = 1.5 Hz, 6H, *H2*), 1.99 (s, 6H, *H3*), 1.64 (s, 15H, *H1*) ppm. Anal. Calcd for $C_{21}H_{33}Cl_2N_4NiO_6Rh$: C 37.65, H 4.96, N 8.36; Found: C 35.51, H 4.40, N 7.72. Calcd for $C_{21}H_{33}Cl_2N_4NiO_6Rh$ + CH_2Cl_2 + 0.5 CH_3CN: C 35.62, H 4.74, N 8.13. This analysis is consistent with the observation of tightly associated CH_2Cl_2 and CH_3CN in ^{1}H NMR (despite extensive drying) as well as consistent with the presence of co-crystallized CH_3CN in the XRD data for **Ni,Rh-Cl** (see Appendix G). **Ni,Ir-Cl**: Yield = 94% (360 mg). ^{1}H NMR (400 MHz, CD_3CN) δ 3.26 – 3.16 (m, 2H, *H4*), 3.06 – 2.96 (m, 2H, *H4*), 2.10 (t, $^5J_{H\text{-}H}$ = 1.5 Hz, 6H, *H2*), 1.97 (s, 6H, *H3*), 1.60 (s, 15H, *H1*) ppm. Anal. Calcd for $C_{21}H_{33}Cl_2N_4NiO_6Ir$: C 33.22, H 4.38, N 7.38; Found: C 33.50, H 4.23, N 7.36.

Syntheses of **Ni,M-OAc**. Under nitrogen, a solution of **M-OAc** (**M** = **Rh**: 150 mg, 0.42 mmol; **M** = **Ir**: 185 mg, 0.42 mmol) in dry dichloromethane was added dropwise to a solution of **Ni** (165 mg, 0.42 mmol) in dry dichloromethane. The dark red solution was stirred for 1-2 h, and the volatiles were evaporated *in vacuo* to give a reddish-brown solid in each case. At this stage, further work-up procedures were performed under ambient conditions without the use of an inert atmosphere. The solid was washed with 20 to 30 mL of diethyl ether to remove leftover acetic acid and then dried to not more than 50^{o}C to give the pure product. In both cases, vapor diffusion of Et_2O into a concentrated CH_3CN solution was employed to obtain single crystals suitable for X-ray diffraction. Spectroscopic characterizations by ^{1}H NMR (see Appendix G, Figures G15 and G16) confirmed preparation of the desired compounds, formulated as [Ni(DOH)(DO)pnCp*Rh($OCOCH_3$)]ClO_4 and

[Ni(DOH)(DO)pnCp*Ir($OCOCH_3$)]ClO_4, respectively. **Ni,Rh-OAc**: Yield = 94% (270 mg). ^{1}H NMR (400 MHz, CD_3CN) δ 3.57 (d, J = 15.8 Hz, 2H, *H4*), 3.13 (t, J = 13.7 Hz, 2H, *H4*), 2.30 (s, 3H, *H6*), 2.11 (s, 6H, *H2*), 2.00 (s, 6H, *H3*), 1.61 (s, 15H, *H1*) ppm. Anal. Calcd for $C_{23}H_{36}ClN_4NiO_8Rh$: C 39.83, H 5.23, N 8.08; Found: C 39.51, H 4.97, N 7.86. **Ni,Ir-OAc**: Yield = 91% (296 mg). ^{1}H NMR (400 MHz, CD_3CN) δ 3.29 – 3.21 (m, 2H, *H4*), 3.06 – 2.94 (m, 2H, *H4*), 2.39 (s, 3H, *H6*), 2.13 (s, 6H, *H2*), 2.00 (s, 6H, *H3*), 1.57 (s, 15H, *H1*) ppm. Anal. Calcd for $C_{23}H_{36}ClN_4NiO_8Ir$: C 35.28, H 4.63, N 7.16; Found: C 34.23, H 4.85, N 6.96. Calcd for $C_{23}H_{36}ClN_4NiO_8Ir + H_2O$: C 34.49, H 4.78, N 7.00. This analysis is consistent with the presence of tightly associated H_2O in the isolated compound, despite careful handling, and is consistent with the observation of H_2O in the isolated material by ^{1}H NMR (see Appendix G).

Syntheses of **Co,M-μ-OAc**. Under nitrogen, a solution of **M-OAc** (**M** = **Rh**: 160 mg, 0.45 mmol; **M** = **Ir**: 200 mg, 0.45 mmol) in dry dichloromethane was added dropwise to a solution of **Co-Cl** (190 mg, 0.41 mmol) in dry dichloromethane. The dark red solution was stirred for 1-2 h, and the volatiles were removed *in vacuo* to give a yellowish-brown solid in each case. At this stage, further work up procedures were performed under ambient conditions without the use of inert atmosphere. The solid was washed with 20 to 30 mL toluene and the washings were filtered through celite to remove acetic acid and excess **M-OAc** as filtrate. The residue left on the celite bed was washed with 10 to 20 mL of diethyl ether to remove toluene as filtrate. The combined filtrate from the above two steps were discarded. The residue left on the celite bed was then flushed with dichloromethane, and the collected filtrate was evaporated to give pure product which was then dried to not more than 50^{o}C. In both cases, vapor diffusion of Et_2O into a concentrated CH_3CN solution was

employed to obtain single crystals suitable for X-ray diffraction. Spectroscopic characterizations by ^{1}H NMR (see Appendix G, Figures G17 – G22) confirmed preparation of the desired compounds, formulated as [CoCl(DOH)(DO)pnCp*Rh(μ-OCOCH$_3$)]PF$_6$ and [CoCl(DOH)(DO)pnCp*Ir(μ-OCOCH$_3$)]PF$_6$, respectively. **Co,Rh-μ-OAc**: Yield = 90% (280 mg). ^{1}H NMR (400 MHz, CD$_3$CN) δ 4.41 (m, 4H, *H4*), 2.50 (s, 3H, *H2*), 2.41 (s, 6H, *H3*), 1.68 (s, 6H, *H5*), 1.65 (s, 15H, *H1*) ppm. ^{19}F NMR (376 MHz, CD$_3$CN) δ −73.80 (d, $^{1}J_{F,P}$ = 706 Hz) ppm. ^{31}P NMR (162 MHz, CD$_3$CN) δ −145.50 (q, $^{1}J_{P,F}$ = 706 Hz) ppm. Anal. Calcd for $C_{22}H_{34}ClCoF_6N_4O_4PRh$: C 34.73, H 4.50, N 7.36; Found: C 35.10, H 4.53, N 7.21. **[Co,Ir-μ-OAc]**: Yield = 85% (295 mg). ^{1}H NMR (400 MHz, CD$_3$CN) δ 4.43 (m, 4H, *H4*), 2.47 (s, 3H, *H2*), 2.41 (s, 6H, *H3*), 1.70 (s, 6H, *H5*), 1.58 (s, 15H, *H1*) ppm. ^{19}F NMR (376 MHz, CD$_3$CN) δ −73.70 (d, $^{1}J_{F,P}$ = 708 Hz) ppm. ^{31}P NMR (162 MHz, CD$_3$CN) δ −145.49 (q, $^{1}J_{P,F}$ = 708 Hz) ppm. Anal. Calcd for $C_{22}H_{34}ClCoF_6N_4O_4PIr$: C 31.08, H 4.03, N 6.59; Found: C 29.31, H 3.65, N 5.76. Calcd for $C_{22}H_{34}ClCoF_6N_4O_4PIr + CH_2Cl_2$: C 29.54, H 3.88, N 5.99. This analysis is consistent with the observation of tightly associated CH_2Cl_2 in isolated samples of **[Co,Ir-μ-OAc]** by ^{1}H NMR (see Appendix G).

8.5.4 Synthesis and characterization of other monometallic complexes

In the course of these studies, monometallic complexes of [Cp*M] bearing bidentate dimethylglyoxime and diphenylglyoxime ligands were also prepared and fully characterized. These complexes are [Cp*Ir(dmg)Cl]Cl, [Cp*Rh(dpg)Cl]PF$_6$, and [Cp*Ir(dpg)Cl]Cl where dmg is κ^2-dimethylglyoxime and dpg is κ^2-diphenylglyoxime. Notably, in course of completing the work described here, Kuwata and co-workers reported the synthesis and characterization of [Cp*Ir(dmg)Cl]Cl.[48] Analogous structure with Rh, formulated as

[Cp*Rh(dmg)Cl]Cl, has been previously synthesized and structurally characterized by Kölle et al.[49]

Synthesis of **dmgIr-Cl**. A solution of $[Cp^*IrCl_2]_2$ (100 mg, 0.12 mmol) in dichloromethane was added dropwise to a solution of dimethylglyoxime (29 mg, 0.25 mmol) in MeOH. The mixture was stirred for 12 h, and volatiles were removed *in vacuo* to give an orange solid. Vapor diffusion of Et_2O into a concentrated CH_3OH solution of **dmgIr-Cl** was employed to obtain single crystals suitable for X-ray diffraction studies. Spectroscopic characterization by ^1H NMR (see Appendix G, Figure G23) is in agreement with the prior literature report.[48] Yield = 90% (115 mg). ^1H NMR (400 MHz, CD_3OD) δ 2.41 (s, 6H, *H3*), 1.77 (s, 15H, *H1*) ppm. Anal. Calcd for $C_{14}H_{23}Cl_2N_2O_2Ir$: C 32.69, H 4.51, N 5.45; Found: C 32.53, H 4.11, N 5.37.

Synthesis of **dpgRh-Cl**. A solution of $[Cp^*RhCl_2]_2$ (180 mg, 0.29 mmol) in dichloromethane was added dropwise to a mixture of diphenylglyoxime (150 mg, 0.62 mmol) and $AgPF_6$ (158 mg, 0.62 mmol) in methanol. The mixture was stirred for 12 h, and the volatiles were removed *in vacuo* to give a yellow solid. Vapor diffusion of Et_2O into a concentrated CH_2Cl_2 solution of **dpgRh-Cl** was employed to obtain single crystals suitable for X-ray diffraction studies. Spectroscopic characterizations by ^1H, ^{19}F, and ^{31}P NMR (see Appendix G, Figures G24 – G26) confirmed preparation of the desired compound, formulated as $[Cp^*Rh(dpg)Cl]PF_6$. Yield = 90% (370 mg). ^1H NMR (400 MHz, CD_3OD): δ 7.34 – 7.21 (m, 6H, *H3*), 7.14 – 7.09 (m, 4H, *H3*), 1.82 (s, 15H, *H1*) ppm. ^{19}F NMR (376 MHz, CD_3OD) δ −75.34 (d, $^1J_{F,P}$ = 709 Hz) ppm. ^{31}P NMR (162 MHz, CD_3OD) δ −145.37 (q, $^1J_{P,F}$ = 709 Hz) ppm. Anal. Calcd for $C_{24}H_{27}ClF_6N_2O_2PRh$: C 43.76, H 4.13, N 4.25; Found: C 43.51, H 4.31, N 4.22.

Synthesis of **dpgIr-Cl**. A solution of $[Cp^*IrCl_2]_2$ (230 mg, 0.30 mmol) in dichloromethane was added dropwise to a solution of diphenylglyoxime (150 mg, 0.62 mmol) in methanol. The mixture was stirred for 24 h, and the volatiles were removed *in vacuo* to give a reddish-brown solid. Vapor diffusion of Et_2O into a concentrated CH_3CN solution of **dpgIr-Cl** was employed to obtain single crystals suitable for X-ray diffraction studies. Spectroscopic characterization by ^1H NMR (see Appendix G, Figure G27) confirmed preparation of the desired compound, formulated as [Cp*Ir(dpg)Cl]Cl. Yield = 92% (365 mg). ^1H NMR (400 MHz, CD_3OD): δ 7.40 – 7.29 (m, 6H, *H3*), 7.19 – 7.12 (m, 4H, *H3*), 1.88 (s, 15H, *H1*) ppm. Anal. Calcd for $C_{24}H_{27}Cl_2N_3O_2Ir$: C 45.14, H 4.26, N 4.39; Found: C 45.30, H 4.42, N 3.86. Calcd for $C_{24}H_{27}Cl_2N_3O_2Ir$ + 0.6 CH_3OH: C 44.92, H 4.50, N 4.26. This analysis is consistent with association of CH_3OH with isolated **dpgIr-Cl**, consistent with observation of this solvent impurity by ^1H NMR (see Appendix G).

8.6 Acknowledgements

The authors thank Dr. Justin Douglas and Sarah Neuenswander for their assistance with NMR spectroscopy and Prof. Davide Lionetti for assistance with the preliminary refinement of solid-state XRD data. The work in this chapter was supported by the US National Science Foundation through award OIA-1833087. Preliminary synthetic work was supported by the US National Science Foundation through the NSF REU Program in Chemistry at the University of Kansas (CHE-1560279). The authors also acknowledge the US National Institutes of Health for support of the NMR instrumentation used in this study (S10OD016360 and S10RR024664).

8.7 References

(1) Cooper, B. G.; Napoline, J. W.; Thomas, C. M. Catalytic Applications of Early/Late Heterobimetallic Complexes. *Catal. Rev.* **2012,** *54*, 1-40.

(2) Buchwalter, P.; Rosé, J.; Braunstein, P. Multimetallic catalysis based on heterometallic complexes and clusters. *Chem. Rev.* **2015**, *115*, 28–126.

(3) (a) McEvoy, J. P.; G. W. Brudvig, G. W. Water-splitting chemistry of photosystem II. *Chem. Rev.* **2006**, *106*, 4455–4483. (b) Yano, J.; Yachandra, V. Mn_4Ca Cluster in Photosynthesis: Where and How Water is Oxidized to Dioxygen. *Chem. Rev.* **2014**, *114*, 4175–4205.

(4) Tsukihara, T.; Shimokata, K.; Katayama, Y.; Shimada, H.; Muramoto, K.; Aoyoma, H.; Mochizuki, M.; Shinzawa-Itoh, K.; Yamashita, E.; Yao, M.; Ishimura, Y.; Yoshikawa, S. The low-spin heme of cytochrome *c* oxidase as the driving element of the proton-pumping process. *Proc. Natl. Acad. Sci. USA* **2003**, *100*, 15304.

(5) Spatzal, T.; Aksoyoglu, M.; Zhang, L. M.; Andrade, S. L. A.; Schleicher, E.; Weber, S.; Rees, D. C.; Einsle, O. Evidence for interstitial carbon in nitrogenase FeMo cofactor. *Science* **2011**, *334*, 940.

(6) (a) Volbeda, A.; Martin, L.; Cavazza, C.; Matho, M.; Faber, B. W.; Roseboom, W.; Albracht, S. P. J.; Garcin, E.; Rousset, M.; Fontecilla-Camps, J. C. Structural differences between the ready and unready oxidized states of [NiFe] hydrogenases. *J. Biol. Inorg. Chem.* **2005**, *10*, 239. (b) Bachmeier, A.; Armstrong, F. Solar-driven proton and carbon dioxide reduction to fuels - lessons from metalloenzymes. *Curr. Op. Chem. Biol.* **2015,** *25*, 141-151.

(7) Appel, A. M.; Bercaw, J. E.; Bocarsly, A. B.; Dobbek, H.; DuBois, D. L.; Dupuis, M.; Ferry, J. G.; Fujita, E.; Hille, R.; Kenis, P. J. A.; Kerfeld, C. A.; Morris, R. H.; Peden, C. H. F.; Portis, A. R.; Ragsdale, S. W.; Rauchfuss, T. B.; Reek, J. N. H.; Seefeldt, L. C.;

Thauer, R. K.; Waldrop, G. L. Frontiers, opportunities, and challenges in biochemical and chemical catalysis of CO_2 fixation. *Chem. Rev.* 2013, *113*, 6621.

(8) Tsui, E. Y.; Tran, R.; Yano, J.; Agapie, T. Redox-inactive metals modulate the reduction potential in heterometallic manganese-oxido clusters. *Nat. Chem.* **2013**, *5*, 293.

(9) Lee, Y.-M.; Bang, S.; Kim, Y. M.; Cho, J.; Hong, S.; Nomura, T.; Ogura, T.; Troeppner, O.; Ivanović-Burmazović, I.; Sarangi, R.; Fukuzumi, S.; Nam, W. A mononuclear nonheme iron(III)–peroxo complex binding redox-inactive metal ions. *Chem. Sci.* **2013**, *4*, 3917.

(10) Li, F.; Van Heuvelen, K. M.; Meier, K. K.; Münck, E.; Que, L. Sc^{3+}-Triggered Oxoiron(IV) Formation from O_2 and its Non-Heme Iron(II) Precursor via a Sc^{3+}–Peroxo–Fe^{3+} Intermediate. *J. Am. Chem. Soc.* **2013**, *135*, 10198-10201.

(11) Kumar, A.; Lionetti, D.; Day, V. W.; Blakemore, J. D. Trivalent Lewis Acidic Cations Govern the Electronic Properties and Stability of Heterobimetallic Complexes of Nickel. *Chem. Eur. J.* **2018,** *24*, 141-149.

(12) Kumar, A.; Lionetti, D.; Day, V. W.; Blakemore, J. D. Redox-Inactive Metal Cations Modulate the Reduction Potential of the Uranyl Ion in Macrocyclic Complexes. *J. Am. Chem. Soc.* **2020,** *142*, 3032-3041.

(13) Kelsey, S.; Kumar, A.; Oliver, A. G.; Day, V. W.; Blakemore, J. D. Promotion and Tuning of the Electrochemical Reduction of Hetero- and Homobimetallic Zinc Complexes. *ChemElectroChem* **2021**, *Advance Article*, doi: 10.1002/celc.202100358.

(14) Jacques, P.-A.; Artero, V.; Pécaut, J.; Fontecave, M. Cobalt and nickel diimine-dioxime complexes as molecular electrocatalysts for hydrogen evolution with low overvoltages. *Proc. Natl. Acad. Sci. U.S.A* **2009,** *106*, 20627-20632.

(15) McCrory, C. C.; Uyeda, C.; Peters, J. C. Electrocatalytic hydrogen evolution in acidic water with molecular cobalt tetraazamacrocycles. *J. Am. Chem. Soc.* **2012,** *134*, 3164-3170.

(16) (a) Schrauzer, G. N. Organocobalt chemistry of vitamin B12 model compounds (cobaloximes). *Acc. Chem. Res.* **1968,** *1*, 97-103 (b) Connolly, P.; Espenson, J. H. Cobalt-catalyzed evolution of molecular hydrogen. *Inorg. Chem.* **1986,** *25*, 2684-2688 (c) Dempsey, J. L.; Winkler, J. R.; Gray, H. B. Mechanism of H_2 Evolution from a Photogenerated Hydridocobaloxime. *J. Am. Chem. Soc.* **2010,** *132*, 16774-16776.

(17) Laga, S. M.; Blakemore, J. D.; Henling, L. M.; Brunschwig, B. S.; Gray, H. B. Catalysis of Proton Reduction by a [BO4]-Bridged Dicobalt Glyoxime. *Inorg. Chem.* **2014,** *53*, 12668-12670.

(18) Lance, K. A.; Goldsby, K. A.; Busch, D. H. Effective new cobalt(II) dioxygen carriers derived from dimethylglyoxime by the replacement of the linking protons with difluoroboron(1+). *Inorg. Chem.* **1990,** *29*, 4537-4544.

(19) Birkelbach, F.; Winter, M.; Floerke, U.; Haupt, H.-J.; Butzlaff, C.; Lengen, M.; Bill, E.; Trautwein, A. X.; Wieghardt, K.; Chaudhuri, P., Exchange Coupling in Homo-and Heterodinuclear Complexes $Cu^{II}M$ [M= Cr (III), Mn (III), Mn (II), Fe (III), Co (III), Co (II), Ni (II), Cu (II), Zn (II)]. Synthesis, Structures, and Spectroscopic Properties. *Inorganic Chemistry* **1994,** *33*, 3990-4001.

(20) (a) Uyeda, C.; Peters, J. C. Access to formally Ni (I) states in a heterobimetallic NiZn system. *Chem. Sci.* **2013,** *4*, 157-163. (b) Uyeda, C.; Peters, J. C. Selective nitrite reduction at heterobimetallic CoMg complexes. *J. Am. Chem. Soc.* **2013,** *135*, 12023-12031.

(21) Henckel, D. A.; Lin, Y. F.; McCormick, T. M.; Kaminsky, W.; Cossairt, B. M. A doubly deprotonated diimine dioximate metalloligand as a synthon for multimetallic complex assembly. *Dalton Trans.* **2016,** *45*, 10068-10075.

(22) Maitlis, P. M. (Pentamethylcyclopentadienyl)rhodium and -iridium complexes: approaches to new types of homogeneous catalysts. *Acc. Chem. Res.* **1978,** *11*, 301-307.

(23) (a) Brintzinger, H.; Bercaw, J. E. Bis(pentamethylcyclopentadienyl)titanium(II). Isolation and reactions with hydrogen, nitrogen, and carbon monoxide. *J. Am. Chem. Soc.*

1971, *93*, 2045-2046. (b) Manriquez, J. M.; Bercaw, J. E. Preparation of a dinitrogen complex of bis(pentamethylcyclopentadienyl)zirconium(II). Isolation and protonation leading to stoichiometric reduction of dinitrogen to hydrazine. *J. Am. Chem. Soc.* **1974**, *96*, 6229-6230.

(24) (a) Kölle, U.; Grätzel, M. Organometallic Rhodium(III) Complexes as Catalysts for the Photoreduction of Protons to Hydrogen on Colloidal TiO_2. *Angew. Chem. Int. Ed. Engl.* **1987,** *26*, 567-570. (b) Blakemore, J. D.; Schley, N. D.; Balcells, D.; Hull, J. F.; Olack, G. W.; Incarvito, C. D.; Eisenstein, O.; Brudvig, G. W.; Crabtree, R. H. Half-Sandwich Iridium Complexes for Homogeneous Water-Oxidation Catalysis. *J. Am. Chem. Soc.* **2010,** *132*, 16017-16029.

(25) (a) Boyd, E. A.; Lionetti, D.; Henke, W. C.; Day, V. W.; Blakemore, J. D. Preparation, Characterization, and Electrochemical Activation of a Model [Cp*Rh] Hydride. *Inorg. Chem.* **2019**, *58*, 3606-3615. (b) Hopkins, J. A.; Lionetti, D.; Day, V. W.; Blakemore, J. D. Chemical and Electrochemical Properties of [Cp*Rh] Complexes Supported by a Hybrid Phosphine-Imine Ligand. *Organometallics* **2019,** *38*, 1300-1310. (c) Hopkins, J. A.; Lionetti, D.; Day, V. W.; Blakemore, J. D. Synthesis and reactivity studies of a [Cp*Rh] complex supported by a methylene-bridged hybrid phosphine-imine ligand. *J. Organomet. Chem.* **2020**, *921*, 121294.

(26) Brewster, T. P.; Nguyen, T. H.; Li, Z.; Eckenhoff, W. T.; Schley, N. D.; DeYonker, N. J. Synthesis and Characterization of Heterobimetallic Iridium–Aluminum and Rhodium–Aluminum Complexes. *Inorg. Chem.* **2018,** *57*, 1148-1157

(27) (a) Oishi, M.; Kino, M.; Saso, M.; Oshima, M.; Suzuki, H. Early–Late Heterobimetallic Complexes with a Ta–Ir Multiple Bond: Bimetallic Oxidative Additions of C–H, N–H, and O–H Bonds. *Organometallics* **2012,** *31*, 4658-4661. (b) Lassalle, S.; Jabbour, R.; Schiltz, P.; Berruyer, P.; Todorova, T. K.; Veyre, L.; Gajan, D.; Lesage, A.; Thieuleux, C.; Camp, C. Metal–Metal Synergy in Well-Defined Surface Tantalum–Iridium Heterobimetallic Catalysts for H/D Exchange Reactions. *J. Am. Chem. Soc.* **2019,** *141*, 19321-19335

(28) Hostetler, M. J.; Bergman, R. G. Synthesis and reactivity of $Cp_2Ta(CH_2)_2Ir(CO)_2$: an early-late heterobimetallic complex that catalytically hydrogenates, isomerizes and hydrosilates alkenes. *J. Am. Chem. Soc.* **1990,** *112*, 8621-8623

(29) Groom, C. R.; Bruno, I. J.; Lightfoot, M. P.; Ward, S. C. The Cambridge Structural Database. *Acta Cryst. B.* **2016,** *72*, 171-179.

(30) Uhlig, E.; Friedrich, M. Untersuchungen an Oximkomplexen. III. Nickelchelate des Bis-(diacetylmonoxim-imino)-propans-1,3 und des Bis-(diacetylmonoxim-imino)-äthans-1,2. *Z. Anorg. Allg. Chem.* **1966**, *343*, 299-307.

(31) Roy, A. S.; Weyhermüller, T.; Ghosh, P. A new cobalodioxime and its three levels of H-bondings to 1D helical strand, 2D helices and 3D framework. *Inorg. Chem. Commun.* **2008**, *11*, 167-170.

(32) Seeber, R.; Parker Jr, W. O.; Marzilli, P. A.; Marzilli, L. G. Electrochemical synthesis of Costa-type cobalt complexes. *Organometallics* **1989,** *8*, 2377-2381.

(33) (a) White, C.; Yates, A.; Maitlis, P. M.; Heinekey, D. M., (η^5-Pentamethylcyclopentadienyl)Rhodium and -Iridium Compounds. *Inorg. Synth.* **1992**, *29*, 228-234. (b) Mantell, M. A.; Kampf, J. W.; Sanford, M. Improved Synthesis of $[Cp^RRhCl_2]_2$ Complexes. *Organometallics* **2018,** *37*, 3240-3242.

(34) Jacques, P.-A.; Artero, V.; Pecaut, J.; Fontecave, M. CCDC 738487: Experimental Crystal Structure Determination, **2010**, DOI: 10.5517/ccssg55

(35) Roy, A.S.; Weyhermuller, T.; Ghosh, P. CCDC 646793: Experimental Crystal Structure Determination, **2008**, DOI: 10.5517/ccpq19q

(36) Jardim, G. A. M.; da Silva Júnior, E. N.; Bower, J. F. Overcoming naphthoquinone deactivation: rhodium-catalyzed C-5 selective C–H iodination as a gateway to functionalized derivatives. *Chem. Sci.* **2016,** *7*, 3780-3784.

(37) Frasco, D. A.; Lilly, C. P.; Boyle, P. D.; Ison, E. A. Cp^*Ir^{III}-Catalyzed Oxidative Coupling of Benzoic Acids with Alkynes. *ACS Catal.* **2013,** *3*, 2421-2429.

(38) Shannon, R. D. Revised effective ionic radii and systematic studies of interatomic distances in halides and chalcogenides. *Acta Cryst. A* **1976**, *32*, 751-767.

(39) D. D. Perrin, *Ionisation Constants of Inorganic Acids and Bases in Aqueous Solution*, Pergamon Press, New York, **1982**.

(40) (a) D'Souza, F.; Zandler, M. E.; Deviprasad, G. R.; Kutner, W. Acid-Base Properties of Fulleropyrrolidines: Experimental and Theoretical Investigations. *J. Phys. Chem. A* **2000,** *104*, 6887-6893. (b) D'Souza, F.; Chitta, R.; Gadde, S.; Zandler, M. E.; Sandanayaka, A. S. D.; Araki, Y.; Ito, O. Supramolecular porphyrin-fullerene via 'two-point' binding strategy: axial-coordination and cation-crown ether complexation. *Chem Commun.* **2005**, *10*, 1279-1281.

(41) (a) Lionetti, D.; Day, V. W.; Lassalle-Kaiser, B.; Blakemore, J. D. Multiple binding modes of an unconjugated bis(pyridine) ligand stabilize low-valent [Cp*Rh] complexes. *Chem. Commun.* **2018,** *54*, 1694-1697. (b) Lionetti, D.; Day, V. W.; Blakemore, J. D. Structural and chemical properties of half-sandwich rhodium complexes supported by the bis(2-pyridyl)methane ligand. *Dalton Trans.* **2019,** *48*, 12396-12406.

(42) Robinson, J. R.; Gordon, Z.; Booth, C. H.; Carroll, P. J.; Walsh, P. J.; Schelter, E. J., Tuning Reactivity and Electronic Properties through Ligand Reorganization within a Cerium Heterobimetallic Framework. *J. Am. Chem. Soc.* **2013**, *135*, 19016-19024.

(43) (a) Hu, Y.; Li, L.; Shaw, A. P.; Norton, J. R.; Sattler, W.; Rong, Y. Synthesis, Electrochemistry, and Reactivity of New Iridium(III) and Rhodium(III) Hydrides. *Organometallics* **2012,** *31*, 5058-5064. (b) Hull, J. F.; Balcells, D.; Blakemore, J. D.; Incarvito, C. D.; Eisenstein, O.; Brudvig, G. W.; Crabtree, R. H. Highly Active and Robust Cp* Iridium Complexes for Catalytic Water Oxidation. *J. Am. Chem. Soc.* **2009,** *131*, 8730-8731. (c) Davies, D. L.; Al-Duaij, O.; Fawcett, J.; Giardiello, M.; Hilton, S. T.; Russell, D. R. Room-temperature cyclometallation of amines, imines and oxazolines with $[MCl_2Cp^*]_2$ (M = Rh, Ir) and $[RuCl_2(p\text{-cymene})]_2$. *Dalton Trans.* **2003**, *21*, 4132-4138. (d) Scheeren, C.; Maasarani, F.; Hijazi, A.; Djukic, J.-P.; Pfeffer, M.; Zarić, S. D.; Le Goff, X.-F.; Ricard, L. Stereoselective “Electrophilic” Cyclometalation of Planar-

Prochiral (η6-Arene)tricarbonylchromium Complexes with Asymmetric Metal Centers: pseudo-T-4 $[Cp^*RhCl_2]_2$ and $[Cp^*IrCl_2]_2$. *Organometallics* **2007,** *26*, 3336-3345. (e) Hull, J. F.; Balcells, D.; Blakemore, J. D.; Incarvito, C. D.; Eisenstein, O.; Brudvig, G. W.; Crabtree, R. H. Highly Active and Robust Cp* Iridium Complexes for Catalytic Water Oxidation. *J. Am. Chem. Soc.* **2009**, *131*, 8730-8731.

(44) Boyer, P. M.; Roy, C. P.; Bielski, J. M.; Merola, J. S. Pentamethylcyclopentadienylrhodium bis-carboxylates: monohapto carboxylate coordination, dihapto carboxylate coordination, and water coordination to Cp∗Rh. *Inorg. Chim. Acta* **1996,** *245*, 7-15.

(45) Fulmer, G. R.; Miller, A. J. M.; Sherden, N. H.; Gottlieb, H. E.; Nudelman, A.; Stoltz, B. M.; Bercaw, J. E.; Goldberg, K. I. NMR Chemical Shifts of Trace Impurities: Common Laboratory Solvents, Organics, and Gases in Deuterated Solvents Relevant to the Organometallic Chemist. *Organometallics* **2010**, *29*, 2176-2179.

(46) Harris, R.K.; Becker, E.D.; Cabral de Menezes, S.M.; Goodfellow, R.; Granger, P. NMR nomenclature. Nuclear spin properties and conventions for chemical shifts (IUPAC Recommendations 2001)**.** *Pure Appl. Chem.* **2001**, *73*, 1795-1818.

(47) Harris, R.K.; Becker, E.D.; Cabral de Menezes, S.M.; Granger, P.; Hoffman, R.E.; Zilm, K.W. Further conventions for NMR shielding and chemical shifts (IUPAC Recommendations 2008)**.** *Pure Appl. Chem.* **2008**, *80*, 59-84.

(48) Takamura, T.; Harada, T.; Furuta, T.; Ikariya, T.; Kuwata, S. Half-Sandwich Iridium Complexes Bearing a Diprotic Glyoxime Ligand: Structural Diversity Induced by Reversible Deprotonation. *Chem. Asian J.* **2020,** *15*, 72-78.

(49) Kölle, U.; Raabe, E.; Krüger, C.; Rotzinger, F. P. Pentamethylcyclopentadienyl-übergangsmetallkomplexe, XI Metallorganische Monoglyoximato-Komplexe von Co und Rh. *Chem. Ber.* **1987**, *120*, 979-985.

Chapter 9

Summary and Future Outlook: The Bright Horizon for Lewis Acid-Promoted Tuning of *d*- and *f*-block Chemistry

9.1 Summary and Future Outlook

The results described in Chapters 2 through 8 of this dissertation show that incorporation of Lewis acidic metal ions into heterobimetallic complexes is an effective strategy for modulating the properties and reactivity of the redox-active metals at their cores. The systems developed here were inspired by Nature's beautiful and exquisitely tuned enzymes but show functions beyond those found in Nature. For example, we showed that olefin polymerization catalysis and hydrogenation catalysis can be modulated by Lewis acids, and perhaps most importantly, that Lewis acids can be deployed for optimization of uranyl redox cycling, a process which is of relevance to development of next-generation nuclear fuel processing technologies.

In Chapter 2, we discussed the interrogation of Lewis acid effects in a series of macrocyclic Ni complexes, especially ones that incorporate highly Lewis acidic trivalent ions. We employed a novel divergent approach for selective preparation of a variety of bimetallic complexes within a ditopic macrocyclic ligand platform.; in our approach, nickel was readily coordinated to a Schiff-base cavity in a first synthetic step, and then a range of redox-inactive cations (M = Na^{+}, Ca^{2+}, Nd^{3+}, and Y^{3+}) were subsequently installed in a pendant crown ether-like site. This modular strategy allowed us to access complexes with the highly Lewis-acidic trivalent cations Nd^{3+} and Y^{3+}, a class of compounds that were previously inaccessible. Careful selection of reaction conditions allowed for generation of stable heterobimetallic species by treatment with stoichiometric amounts of redox-inactive metal salts. Studies of the effects of redox-inactive metals on the electronic properties of these well-defined bimetallic species in acetonitrile revealed substantial influences on both electronic and structural properties. However, exposure to dimethylformamide, a strongly

coordinating ligand, drove loss of Nd^{3+} and Y^{3+} from the pendant crown-ether site, suggesting solvent effects must be carefully considered in future applications involving use of highly Lewis acidic metals.

Our study of Lewis acid effects in complexes of the transition metal nickel encouraged us forward and paved a way to studying analogous effects in complexes of *f*-block elements, particularly uranium. We were motivated to pursue this study since heterobimetallic chemistry of the actinide (and lanthanide) elements is a frontier area ripe for exploration and discovery. Uranium typically exists in the form of water-soluble uranyl dication (UO_2^{2+}) in aqueous environments, and capture and activation of this species remains a challenging problem; simultaneously, few rational approaches are available for modulating the reactivity of this species. To develop a fundamental understanding of parameters that govern U–O bond activation in UO_2^{2+}, we synthesized and characterized a series of heterobimetallic complexes containing UO_2^{2+} as described in Chapter 4. In these complexes, UO_2^{2+} is coordinated to a Schiff-base cavity and redox-inactive ions are contained in a pendant 18-crown-6-like site. We studied Lewis acid effects on UO_2^{2+} redox chemistry by installing a range of mono-, di-, and tri-valent Lewis acids (M^{n+}) in close proximity to the uranium center. Crystallographic and spectroscopic studies confirmed assembly of homologous $U^{VI}(\mu\text{-}O_{Ar})_2M^{n+}$ cores (M = K^+, Na^+, Ca^{2+}, Nd^{3+}, and Y^{3+}). Notably, this family of compounds represents the first example of a structurally characterized series of macrocyclic heterobimetallic UO_2^{2+} complexes. In this work, we systematically tuned the redox properties of uranium using Lewis acid effects for the purpose of gaining fundamental insights into chemistries related to nuclear fuel reprocessing. Our electrochemical findings demonstrate that the U^{VI}/U^{V} reduction potential in these complexes is modulated over a span

of 600 mV, depending linearly on the Lewis acidity of the redox-inactive metal incorporated with a sensitivity of 61±9 mV/pK_a unit. Furthermore, we observed that the rate of electron transfer decreases with increasing Lewis acidity, suggesting significant reorganization is involved in electron transfer when stronger Lewis acids are utilized. Taken together, these findings suggest that interactions with Lewis acids can be effectively leveraged for rational tuning of the electronic and thermochemical properties of the 5*f* elements, reminiscent of strategies more commonly employed with 3*d* transition metals. Furthermore, our work reveals that the scope of tuning possible with actinides by redox-inactive Lewis acids is essentially just as broad as the scope of tuning possible with transition metals, opening up heterobimetallic chemistry as a plausible strategy for the development of next-generation approaches to uranium handling and redox chemistry.

In Chapters 2 and 3, we showed that the incorporation of Lewis acids into heterobimetallic complexes is an attractive strategy for modulating the thermochemical properties of redox-active nickel and uranium compounds. In both the nickel and uranium complexes, pendant crown-ether-like sites were used to bind Lewis acidic metal ions of interest, an approach which overcomes the need for ions to associate directly with the modestly basic nickel centers or uranyl oxygen atoms present in the parent complexes. However, the role of the structure of the secondary metal ion binding sites in affecting Lewis acid/base chemistry of the type explored here is not yet well understood, offering the opportunity in our system to better understand how the coordination environment around the Lewis acid itself might impact or modulate the chemistry. In Chapter 4, we discussed our newest findings regarding tailored macrocyclic ligands that present either an 18-crown-6- or a 15-crown-5-like site and thus provide the platforms needed to control coordination of the

Lewis acid. We mapped the influences of secondary metal ions incorporated into these different receptor sites and the two ligand structures on uranyl redox cycling for the two resulting closely related modular families of heterobimetallic [U(μ-O_{Ar})$_2$$M^{n+}$] complexes, where M is Cs^+, Rb^+, K^+, Na^+, Li^+, or Ca^{2+}. Both families of complexes displayed chemically reversible behaviors which enable determination of thermodynamic reduction potentials, heterogeneous electron transfer rate constants, and reorganization energy values associated with the U^{VI}/U^V redox manifold. Optimized, rapid reduction was found to occur only when tight supramolecular binding of the secondary metals was balanced with Lewis acidity, leading to characteristic "volcano" plots that result from the interplay of these opposing factors. The trends in the data presented in Chapter 4 offer a mechanistic foundation for optimization of uranium redox cycling and design rules for supramolecular structures that promote efficient electron transfer. In this context, the newer heterobimetallic complexes featuring the 15-crown-5-like binding sites represent an improved second-generation family of heterobimetallic uranyl complexes in comparison to those described in Chapter 3.

To more fully understand the activation of UO_2^{2+} ion, however, a thermochemical understanding of the U–O bond properties in our compounds will eventually be needed. We have pursued the electrochemical data described in this dissertation to move toward this important target, in that reduction potentials are one key determinant of bond strengths in any $[M{=}O]^{n+}/[M{-}OH]^{n+}/[M{-}OH_2]^{n+}$ system involving both electron and proton transfers. In the end, the free energies of the various species involved in the activation of U–O bonds will determine the outcomes of chemical reactivity. In this reactivity, addition of one proton (H^+) and one electron (e^-) to the U^{VI}=O unit would transform it into a U^V–OH species, which could be further be reduced to U^{IV}. Reductions weaken the strength of the U–O bonds, as

shown in prior work, although the reactivity with protons mentioned here, so far, remains out of reach. However, toward the goal of cleanly forming UO–H bonds for U–O activation, electron transfer (ET) and proton transfer (PT) can be envisioned to either happen in a stepwise sequence or concerted fashion wherein transfer of both e^- and H^+ take place simultaneously. Tackling these steps separately can help disentangle the individual contributions to the thermochemistry of the O–H bond formation, a bellweather for the activation of the U–O bond through transformation of [U=O] into [U–OH]. The bond dissociation free energy of a given O–E (E = model electrophile) bond is governed by both the reduction potential of the uranium center and the effective pK_a of the electrophile involved, in a generalized conception not reliant on Brønsted acidity. Our strategy of tuning the reduction potential of the $U^{VI/V}$ couple to more positive values offers a strategy for modifying the strength of the O–E bond and, conversely, the U–O bond. Our macrocyclic ligand was designed to allow binding of different Lewis acids for tuning of the UO_2^{2+} reduction potential in the positive direction, along with enabling facile activation and functionalization of U–O bonds in future work. It is our hope that such work may be fruitful, and enable studies of strategies to optimize U–O bond activation.

In both Parts I and II of this dissertation, Lewis acid effects promoted by redox-inactive metal ions were discussed for systems investigated under non-aqueous conditions. Parametrizing the behavior of these ions in such non-aqueous conditions has been challenging in the past due to the lack of direct measures of the Lewis acidity of metal ions in polar organic solvents. In Chapter 5, we reported the use of triphenylphosphine oxide (TPPO) as a ^{31}P nuclear magnetic resonance (NMR) probe to quantify the Lewis acidity of a library of metal triflate salts using the Gutmann-Beckett method. Plots of the pK_a values

of the corresponding metal-aqua species, $[\mathbf{M}(H_2O)_m]^{n+}$, measured in H_2O vs. the ^{31}P NMR shifts of TPPO in the presence of these metals in deuterated acetonitrile (d_3-MeCN) and deuterated dichloromethane (CD_2Cl_2) displayed tightly co-linear relationships, suggesting similar behavior for these ions in water, d_3-MeCN, and CD_2Cl_2. This collinearity reinforces the utility of the common approach of using the aqueous pK_a values as a descriptor of Lewis acidity, regardless of the solvent used in the immediate experiments, and provides an insight into the usefulness of this descriptor in wide-ranging applications. Titration studies in d_3-MeCN suggested 1:1 binding of TPPO with monovalent ions, greater than 1:1 binding with divalent ions, and formation of multiple species with the highly Lewis acidic trivalent ions. Together, these data suggested that both aqueous pK_a values and other single-measurement descriptors, while useful, provide only a snapshot of the influence of Lewis acidity on multimetallic chemical systems. For example, we observed that the 1:1 mixture of TPPO and strongly Lewis acids trivalent ions lead to NMR spectra with multiple peaks that could suggest speciation with these highly Lewis acidic ions. Thus, future work with more strongly coordinating phosphine oxide probes like triethylphosphine oxide (TEPO) or Lewis acidic salts with counteranions other than triflate (e.g., PF_6^-) could be useful in better understanding the speciation behavior of all these systems, especially those displaying contributions from multiple equilibria and/or speciation.

In Chapters 6, 7, and 8, we extended our work to studies of the effects of Lewis acids on complexes not supported by macrocyclic ligands and their roles in catalysis. In collaboration with Chevron Phillips Chemical, we endeavored in this work to understand the role of trialkylaluminum reagents in phosphinimide-supported titanium catalysts that are active for polymerization of ethylene. In Chapters 6 and 7, we showed that the treatment of a Ti(IV)

precursor, formulated as [(Ind)(*t*Bu$_3$P=N)TiCl$_2$] (Ind = indenyl), with AlR$_3$ (R = Et, *i*Bu, Me) in a range of solvents afforded the emerald green heterobimetallic complex [(Ind)(*t*Bu$_3$P=N)Ti(μ$_2$-Cl)$_2$AlR$_2$] (R = Et, *i*Bu, oe Me) where Ti was found to be in the +3 oxidation state in all cases. In this work, we found that the alkylaluminum reagents were involved as both reagents for incorporation of the AlR$_2$ units as well as reductants for generation of Ti(III). Consequently, these compounds could be formed either chemically or electrochemically, with the electrochemical case involving selective triggering of reactivity by reduction of [(Ind)(*t*Bu$_3$P=N)TiCl$_2$] in THF electrolyte solution containing AlR$_3$. Cyclic voltammetry studies indicated that [(Ind)(*t*Bu$_3$P=N)TiCl$_2$] undergoes one-electron reduction at ca. −2.0 V vs. ferrocenium/ferrocene; in the presence of AlR$_3$, reduction initiates coordination of [AlR$_2$] to the nascent [Ti^{III}] core and form the heterobimetallic species. Single-crystal X-ray diffraction (XRD) analysis and magnetic resonance experiments confirmed the formation of paramagnetic [Ti^{III},Al^{III}] species with each AlR$_3$ reagent.

In Chapter 6, results were described that show both [(Ind)(*t*Bu$_3$P=N)TiCl$_2$] and the heterobimetallic [Ti,Al] complexes derived from this precusor complex are active toward ethylene polymerization in the presence of AlEt$_3$ and a solid superacid. The product polyethylene materials were found to have similar molecular weight distributions in each case when AlEt$_3$ was used, implicating involvement of similar active catalysts in both. Spectroelectrochemical studies were used to demonstrate that reduction of [(Ind)(*t*Bu$_3$P=N)TiCl$_2$] in the presence of AlEt$_3$ led to clean formation of the desired heterobimetallic complex. In Chapter 7, we extended our study by replacing the -R groups on aluminum with methyl and isobutyl variants to compare with the prior work focusing on ethyl substituents. Spectroscopic results and gas chromatography showed that the variant

supported by methyl ligands is significantly less stable than the variant supported by isobutyl groups, and that the variant supported by isobutyl groups is less stable than the parent complex supported by ethyl groups. All the bimetallic complexes are active precatalysts for ethylene polymerization, but the diminished stability of the variants supported by methyl and isobutyl groups are reflected in unique polymerization results in each case. Of note, the isobutyl variant was found to produce polyethylene with a particularly broad molecular weight distribution (MWD), suggesting useful formation of multiple active species during catalysis. Conversely, the methyl-supported variant is a poor catalyst, suggesting detrimental speciation occurs with this system under the polymerization conditions.

Overall, these findings in Chapters 6 and 7 support key roles for AlR_3 in (1) catalyst alkylation, (2) chemical reduction of titanium via one-electron chemistry, and (3) provision of the highly Lewis acidic [AlR_2] fragment that stabilize the Ti^{III} center in the heterobimetallic complexes, as judged by the voltammetric data. Notably, our findings also show that macrocyclic ligands are not strictly necessary for generation of useful heterobimetallic complexes, in line with prior work in the field of heterobimetallic polymerization chemistry. Future work in this area might usefully focus on understanding and controlling speciation of non-macrocyclic heterobimetallic catalysts, especially under more forcing conditions (e.g., elevated temperatures, use of coordination media) that might promote detrimental speciation and/or scission of the desired heterobimetallic complexes.

From the results described in Chapters 2-7, it can be seen that the chemistry driving formation of the heterobimetallic complexes is crucially important. In our work with nickel and uranium, macrocycles were particularly used to engender formation of the desired heterobimetallic species. In the case of the titanium complexes described in Chapters 6 and

7, serendipitous formation of the species occurred, attributable to the intrinsic preference of the two *cis*-geometry chloride ligands to coordinate a second metal (aluminum). Without such preferences or pre-designed ligands, heterobimetallic complexes would not be accessible. Accordingly, only a limited number of ligands have been studied that enable synthesis of isolable families of heterobimetallic complexes in comparison to monometallic analogues. To contribute in this area, in Chapter 8, we developed a new strategy for installation of organometallic half-sandwich [Cp*M] (M = Rh, Ir) fragments (Cp* = η^5-pentamethylcyclopentadienyl) into metallomacrocyclic structures based on the workhorse diimine-dioxime ligand system. Six new heterobimetallic compounds were prepared to explore this synthetic chemistry, which relies on *in situ* protonolysis reactivity with precursor Ni(II) or Co(III) monometallic complexes in the presence of suitable [Cp*M] species. Solid-state X-ray diffraction studies confirmed installation of the [Cp*M] fragments into the metallomacrocyles via effective chelation of the Rh(III) and Ir(III) centers by the nascent dioximato site. Spectroscopic and electrochemical studies revealed only subtle influences of the metals on each other's properties, however, consistent with the rather long M′•••M distances of ca. 3.6–3.7 Å in the modular compounds. A pilot study with the [Co,Rh] complex showed that this complex can catalyze hydrogenation of *p*-trifluoromethylbenzaldehyde to *p*-trifluoromethylbenzyl alcohol more cleanly than a 1:1 mixture of the individual monometallic precursor complexes, suggesting that this family of heterobimetallic complexes could be useful in future studies of multimetallic chemistry, especially in light of the starring role of other [Cp*M] complexes in diverse catalytic systems. However, this ligand system and the chemistry it promotes seem ripe for further

development, especially in light of the clean reactivity accessed through the *in situ* protonolysis route used for synthesis of the complexes.

In this dissertation, we have shown that incorporation of Lewis acids can significantly affect the redox properties of multimetallic systems. The ability of redox-inactive Lewis acidic metal ions to tune the reduction potential(s) of redox-active metals leads to interesting and useful changes in the properties of the metal complexes. Consequently, these tuning effects extend to the realm of chemical reactivity. We have particularly focused here on understanding and optimizing reductive electron transfer as a key reaction of fundamental importance across many fields, including both processing of uranium and transition-metal catalysis. However, the precise mechanistic role of Lewis acids in modifying the outcomes of most chemical transformations is unclear, even in well-studied biological systems. Future work should continue to address this need for mechanistic insight. Our new contributions in the area expand the scope of these important Lewis acid effects and thus open new arenas for scientists and engineers to study reactions in which these Lewis acids are involved.

Appendices for Chapters in Part I

Appendix A

Supplementary Information for Chapter 2

NMR Spectra

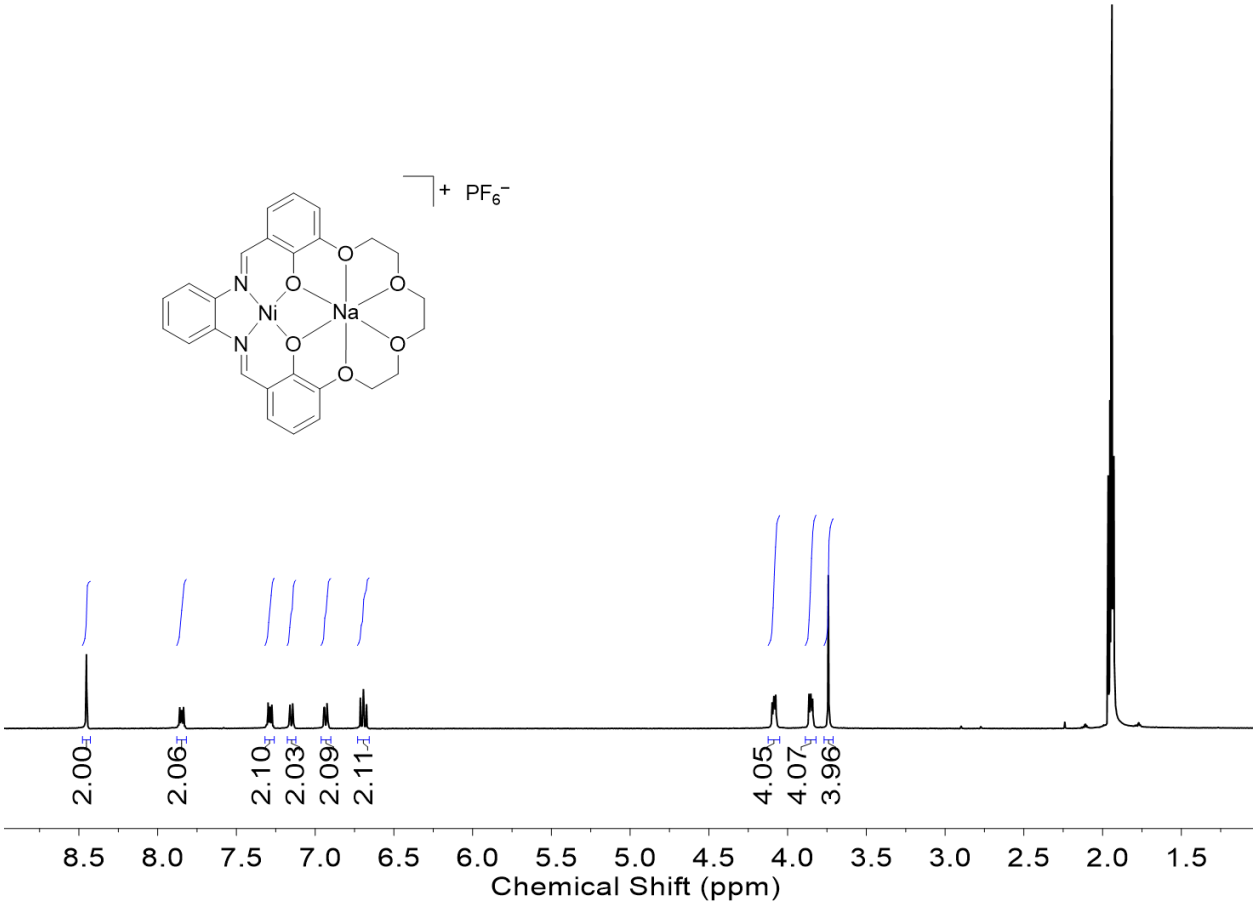

Figure A1. ^{1}H NMR spectrum (400 MHz, CD_3CN) of **L^{6}NiNa**.

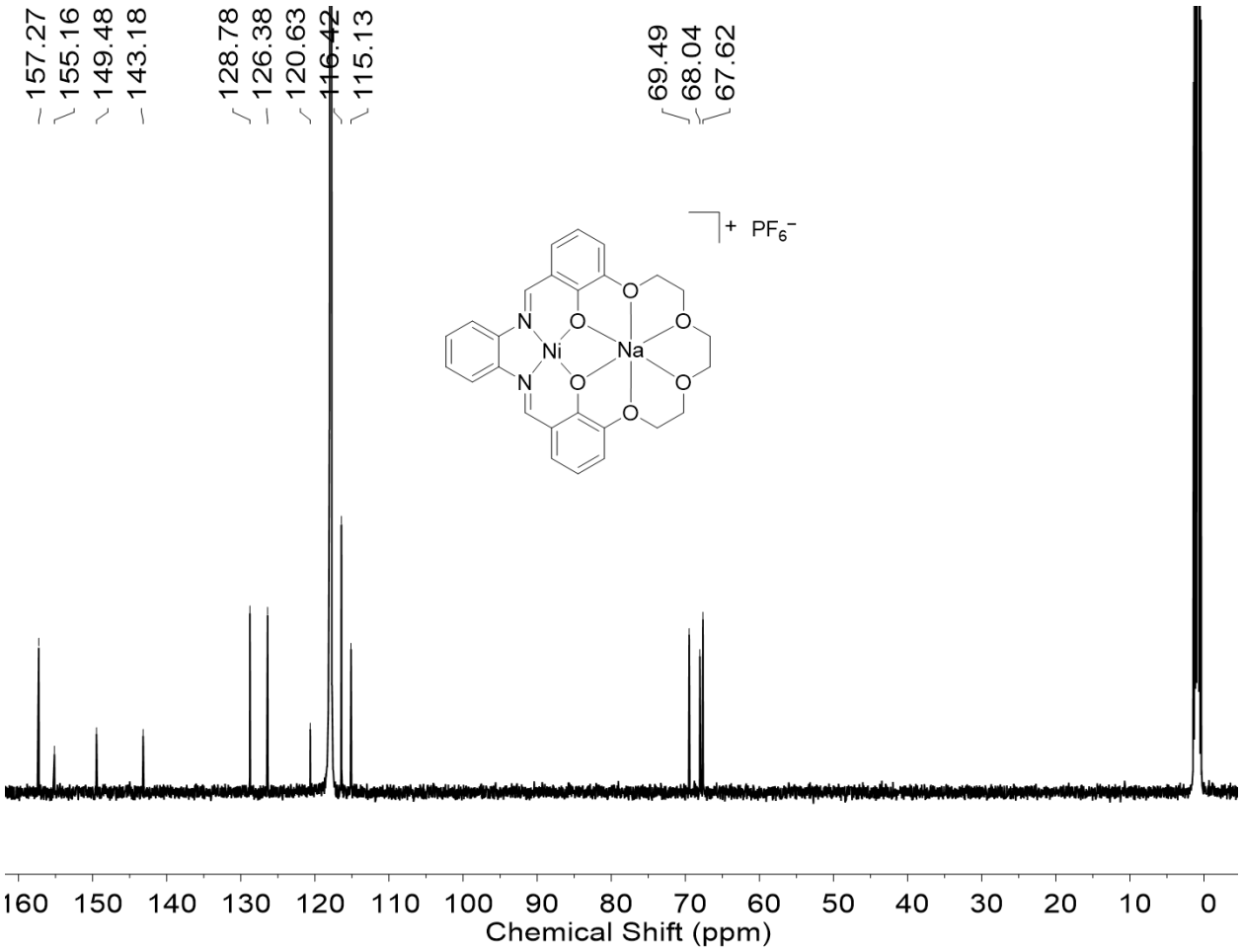

Figure A2. $^{13}C\{^{1}H\}$ NMR spectrum (126 MHz, CD_3CN) of **L^{6}NiNa**.

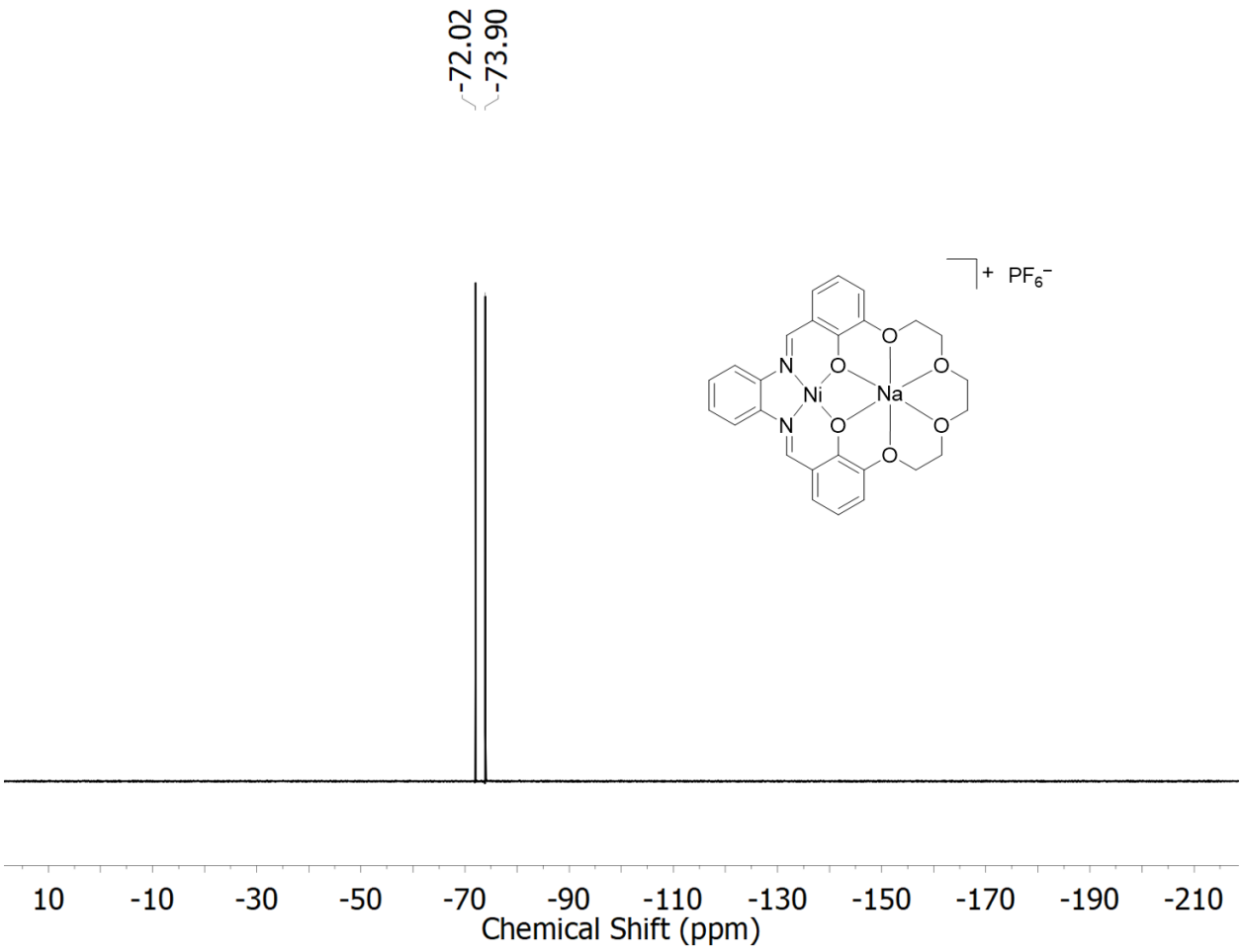

Figure A3. ^{19}F NMR spectrum (376 MHz, CD_3CN) of **L^{6}NiNa**.

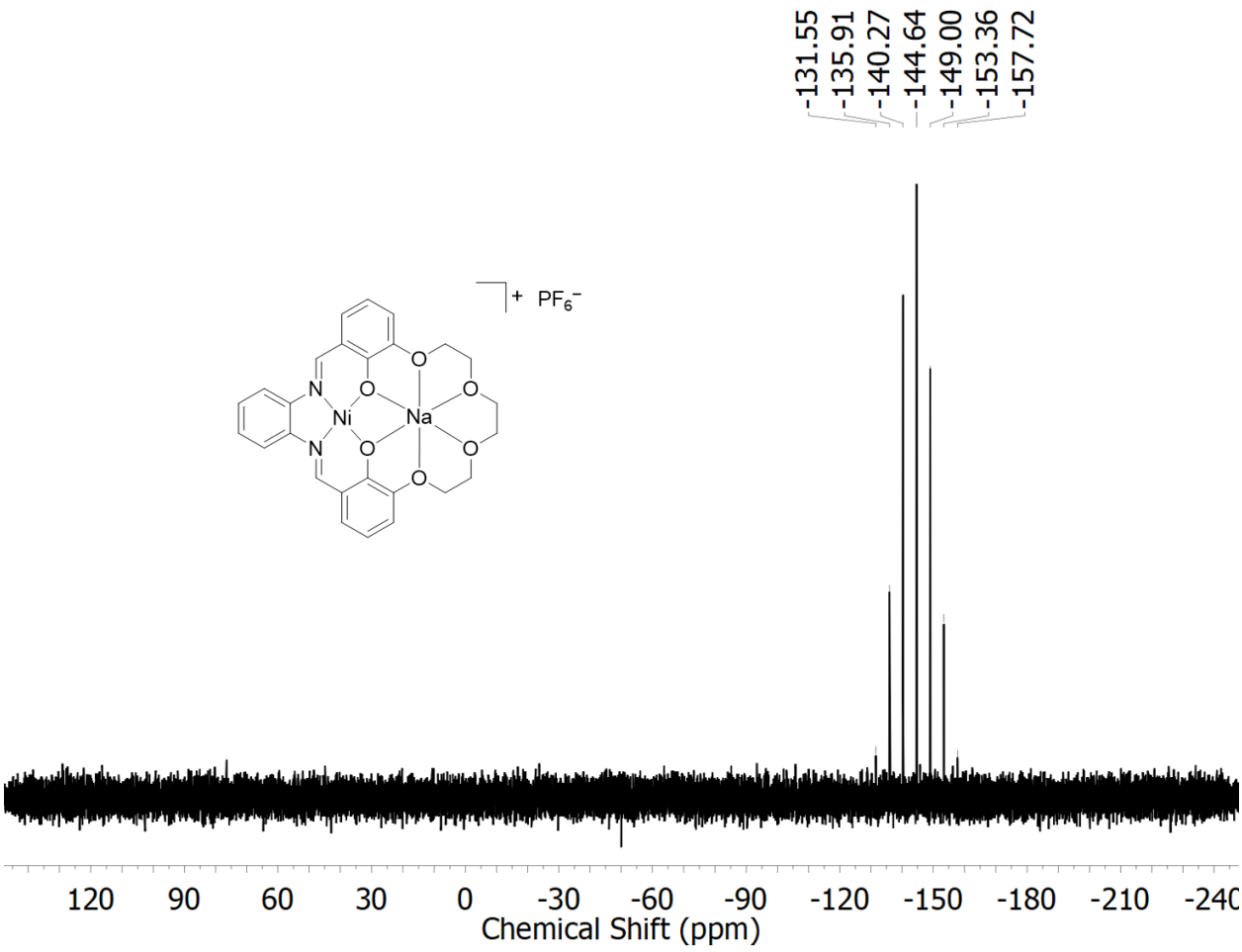

Figure A4. ^{31}P NMR spectrum (162 MHz, CD_3CN) of **L^{6}NiNa**.

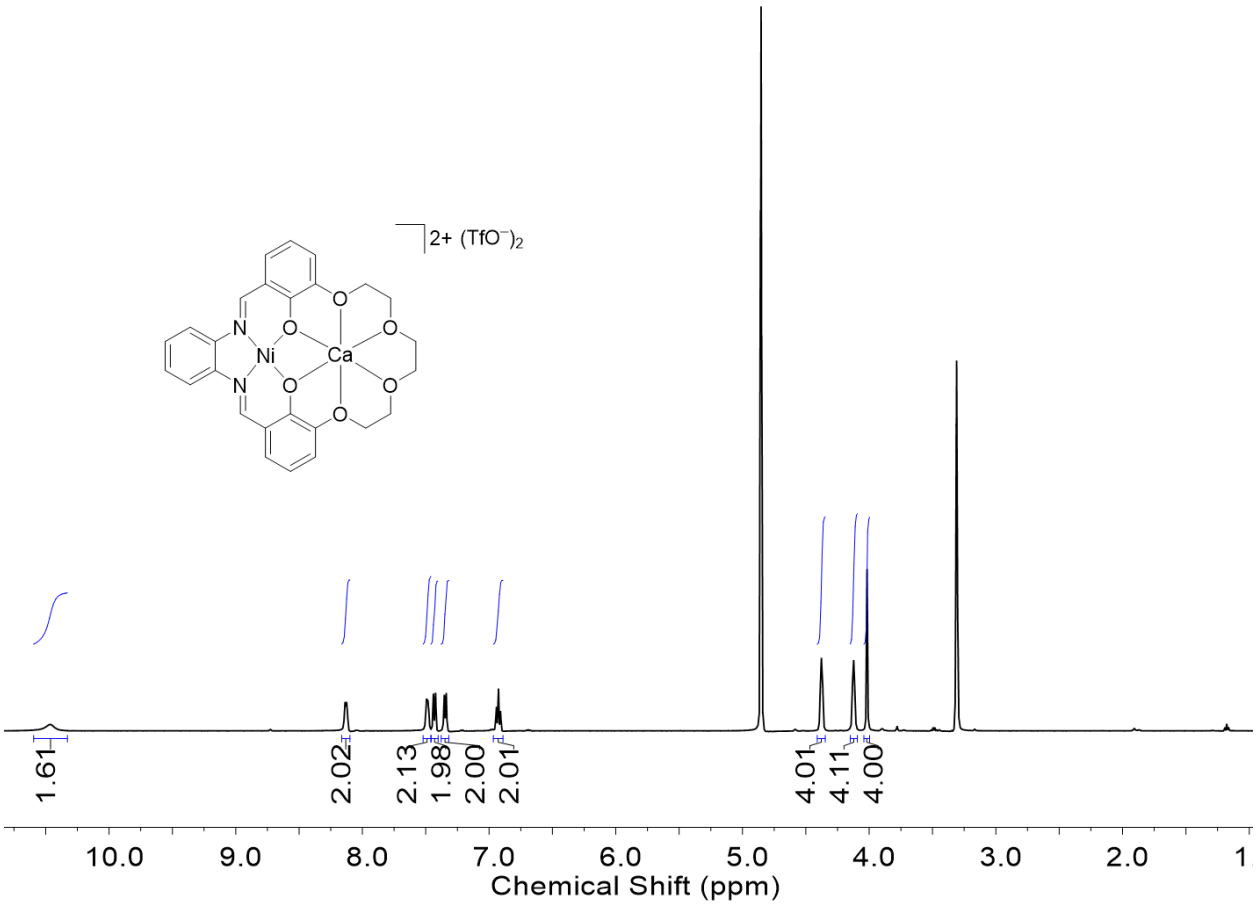

Figure A5. ^{1}H NMR spectrum (500 MHz, CD_3OD) of **L^{6}NiCa**.

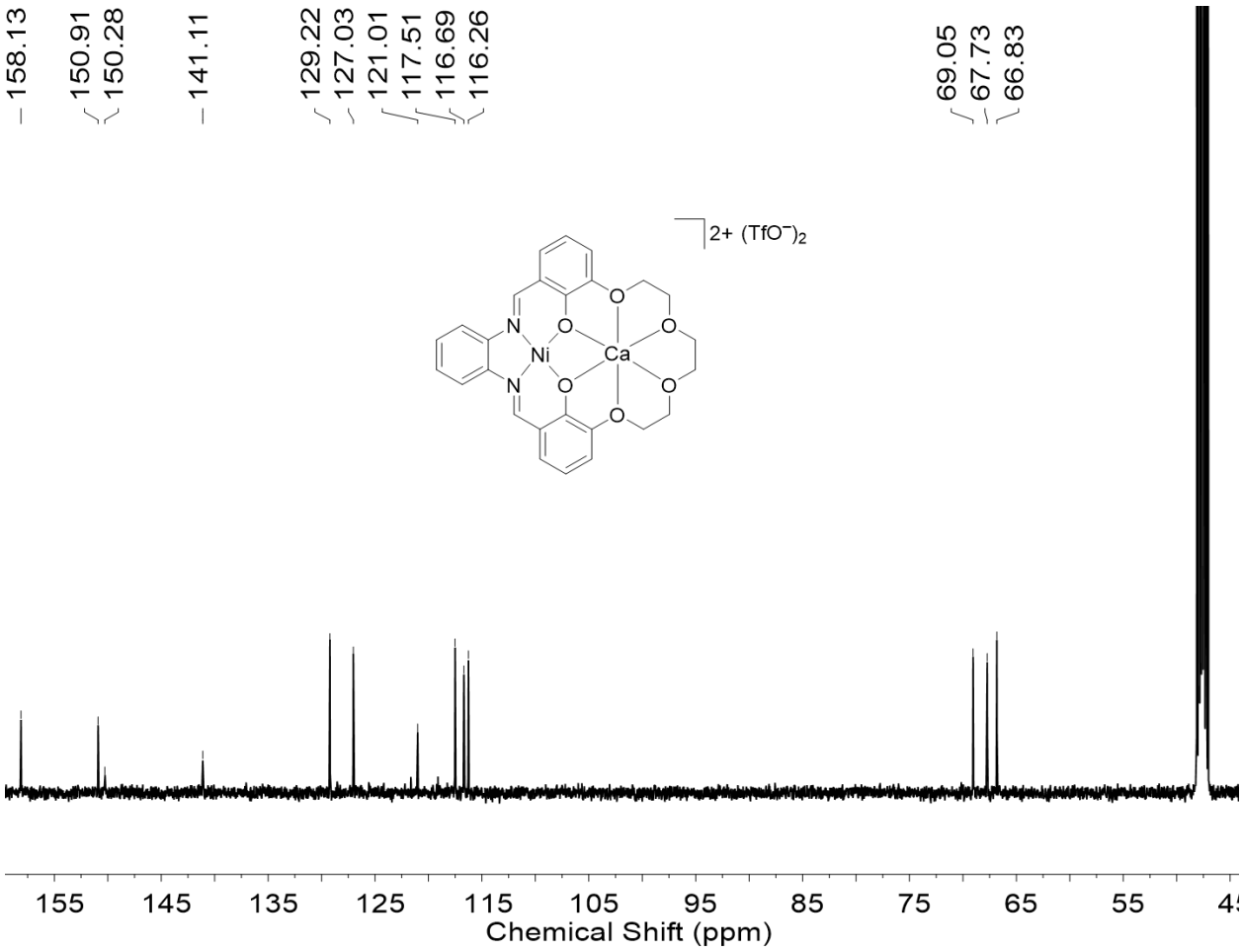

Figure A6. $^{13}C\{^{1}H\}$ NMR spectrum (126 MHz, CD_3OD) of **L^{6}NiCa**.

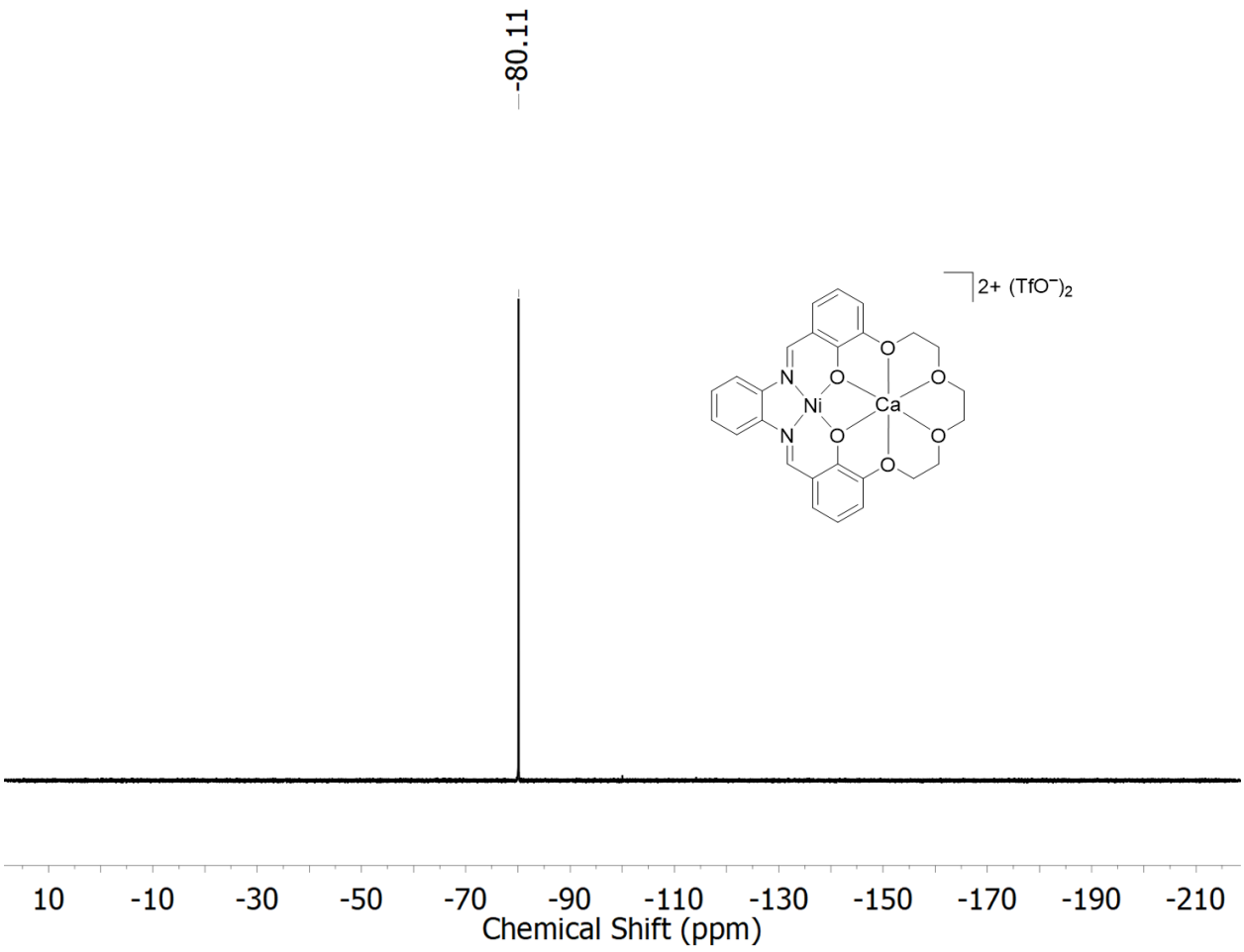

Figure A7. ^{19}F NMR spectrum (376 MHz, CD_3OD) of **L^6NiCa**.

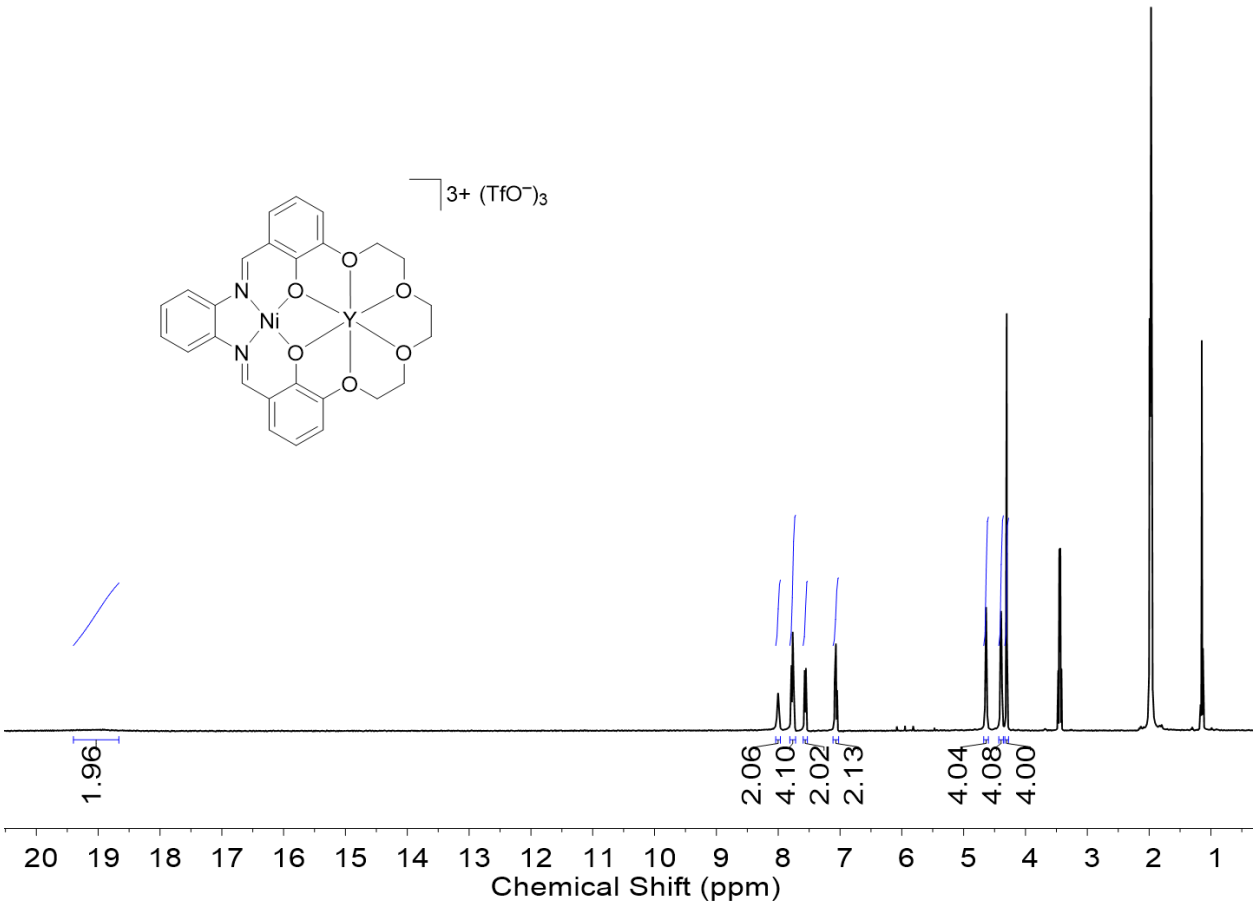

Figure A8. ^{1}H NMR spectrum (400 MHz, CD_3CN) of **L^{6}NiY**.

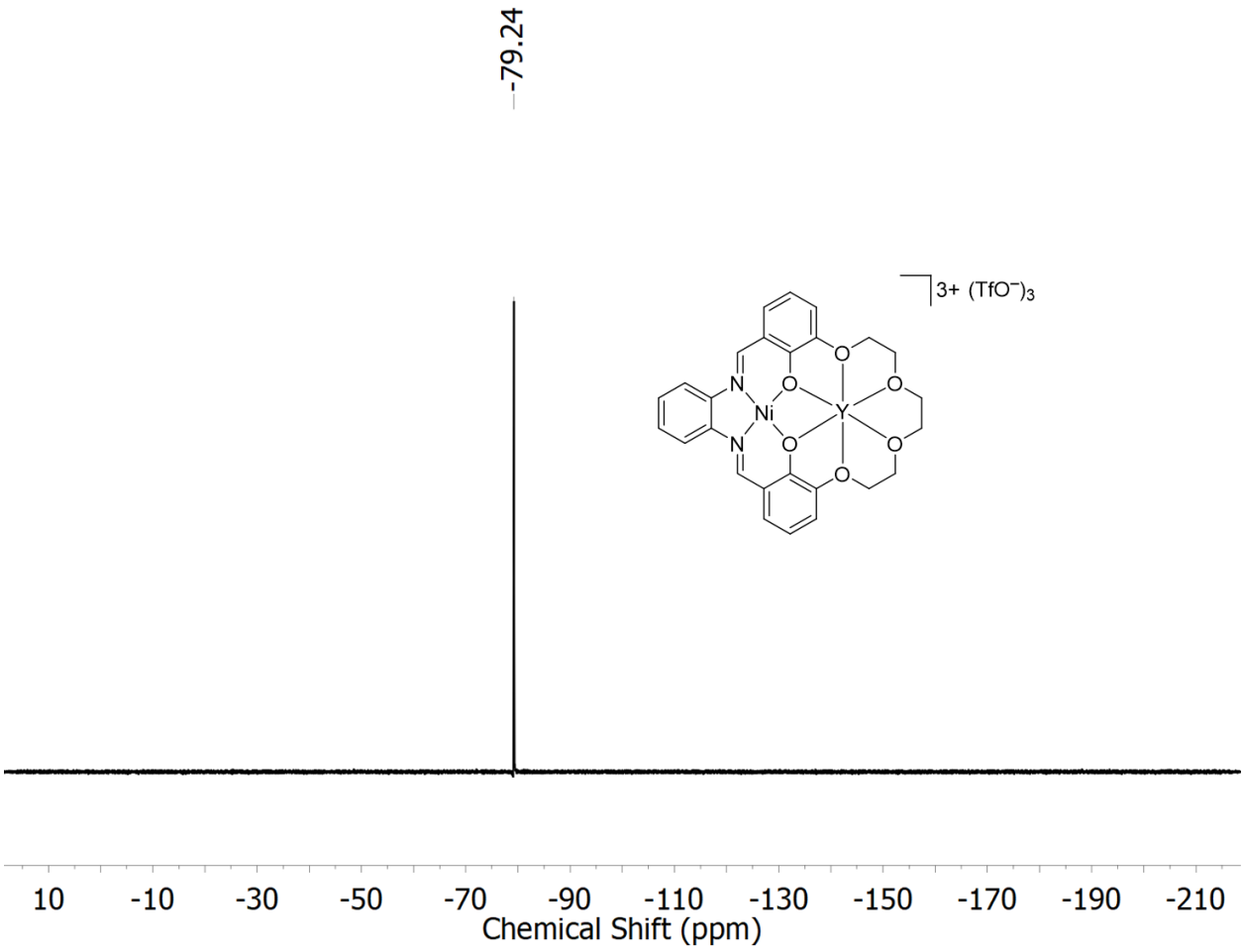

Figure A9. ^{19}F NMR spectrum (376 MHz, CD_3CN) of **L^{6}NiY**.

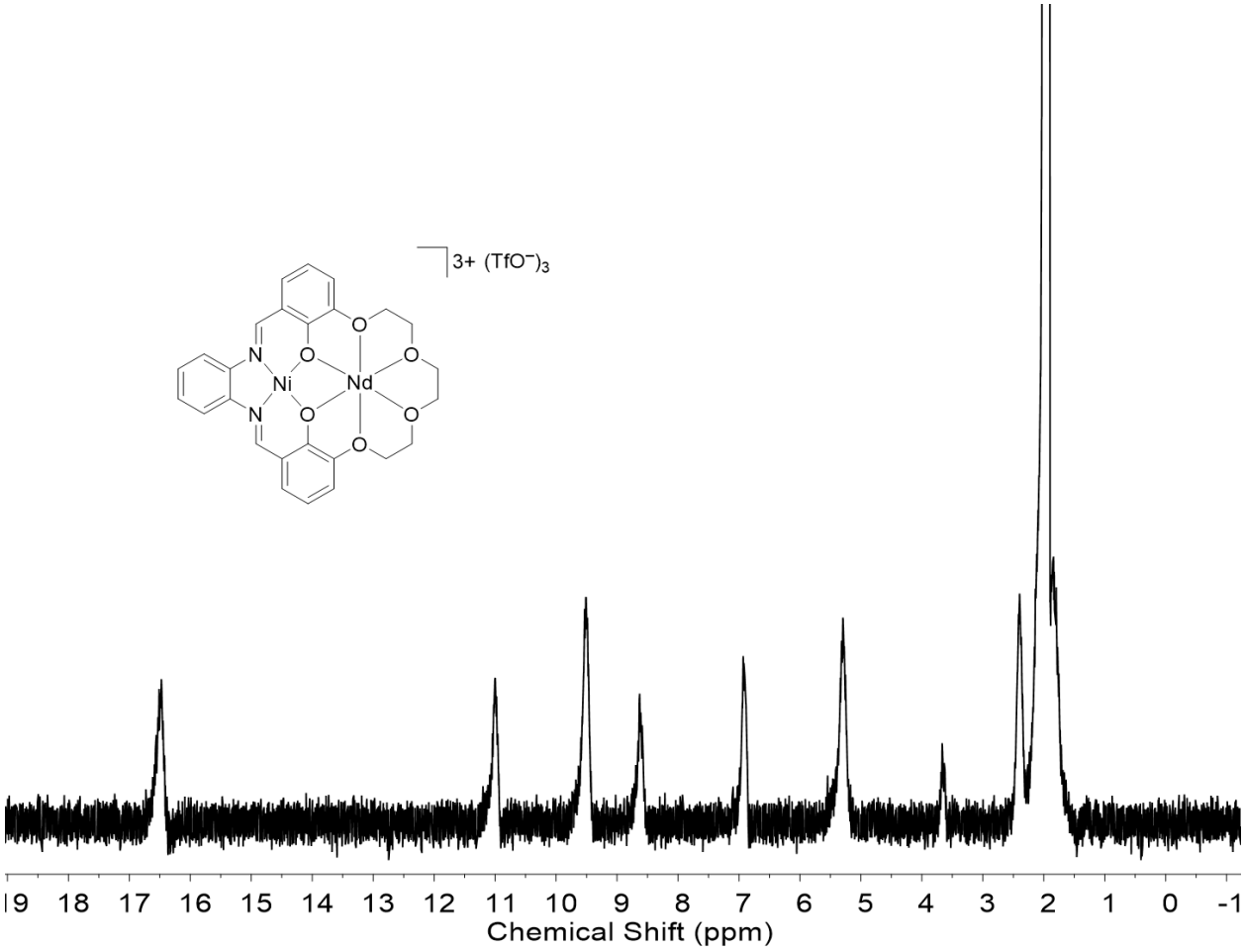

Figure A10. ^{1}H NMR spectrum (400 MHz, CD_3CN) of **L^{6}NiNd**.

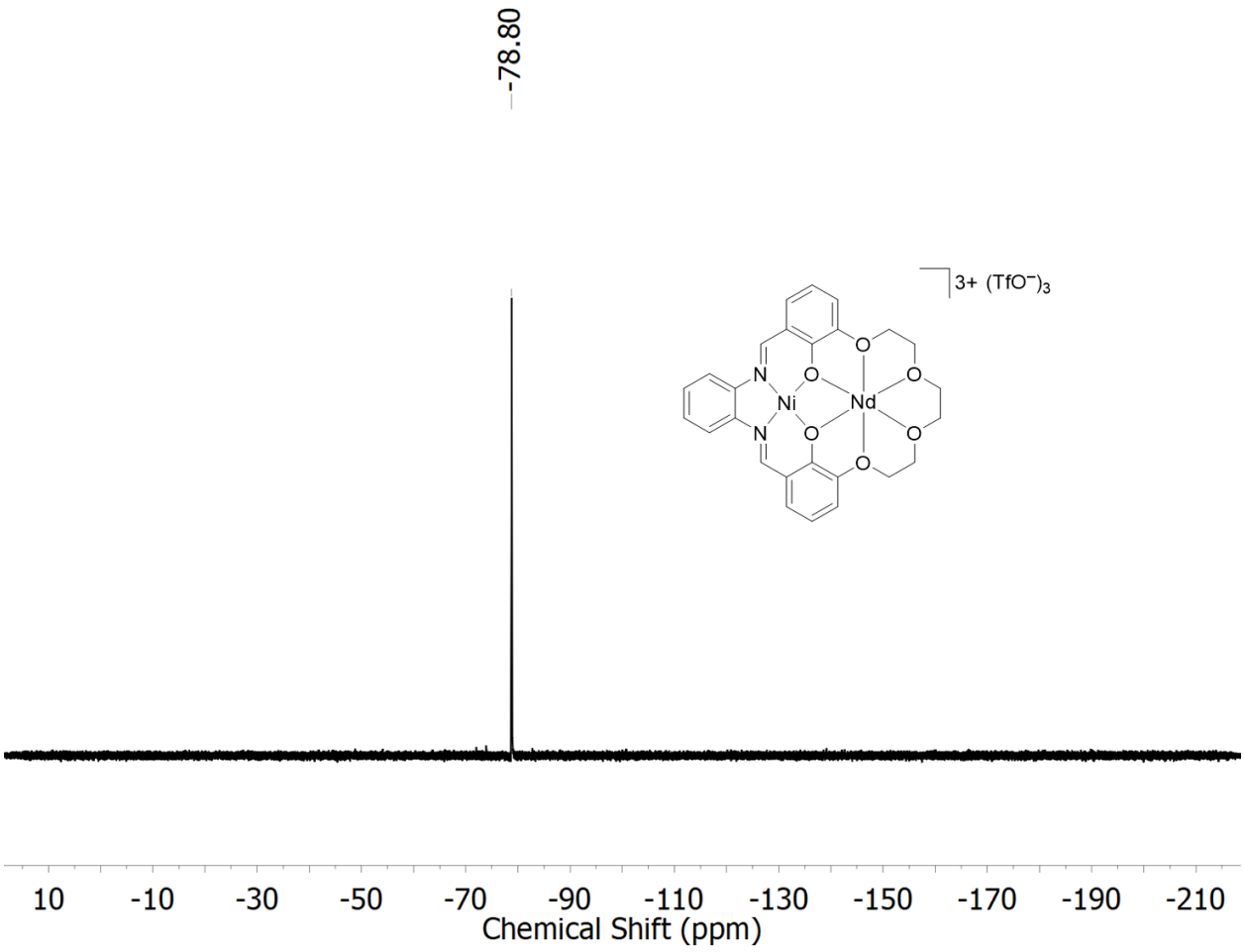

Figure A11. ^{19}F NMR spectrum (376 MHz, CD_3CN) of **L^6NiNd**.

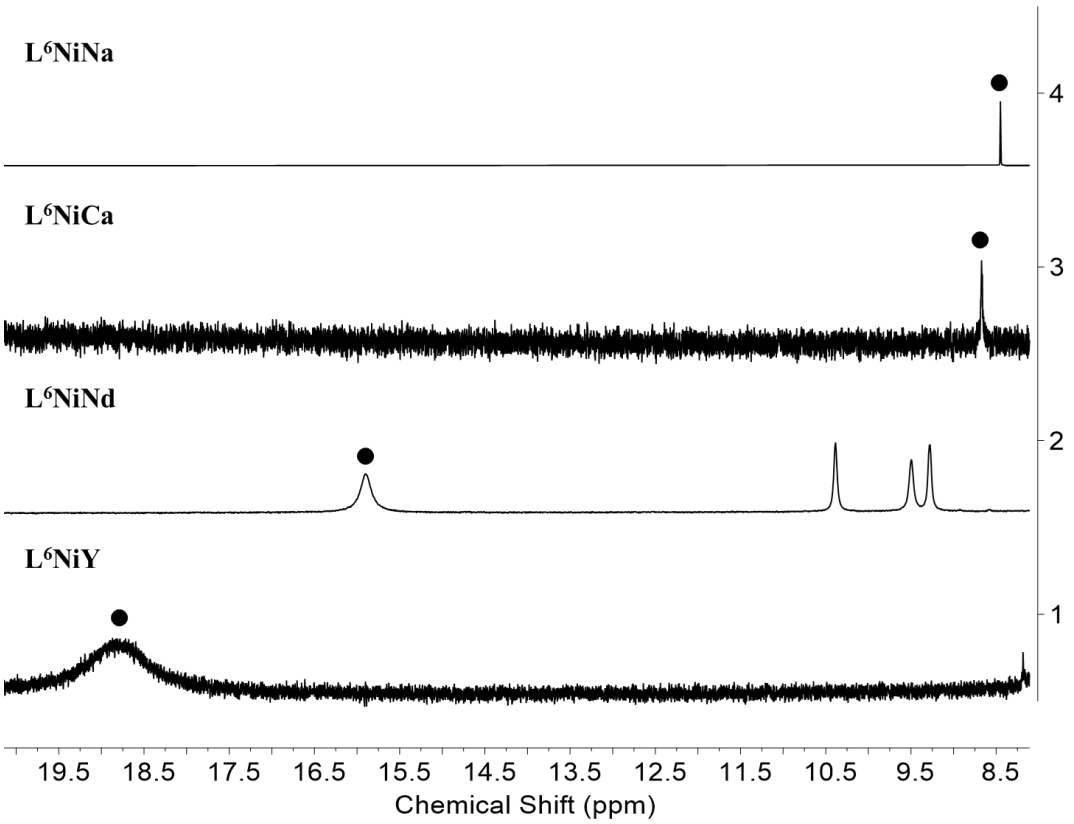

Figure A12. Stacked ^{1}H NMR spectra of **L^{6}NiM** complexes in CD_3CN. The ● indicates the resonance corresponding to the imine protons for each compound.

Electronic Absorption Spectra (EAS)

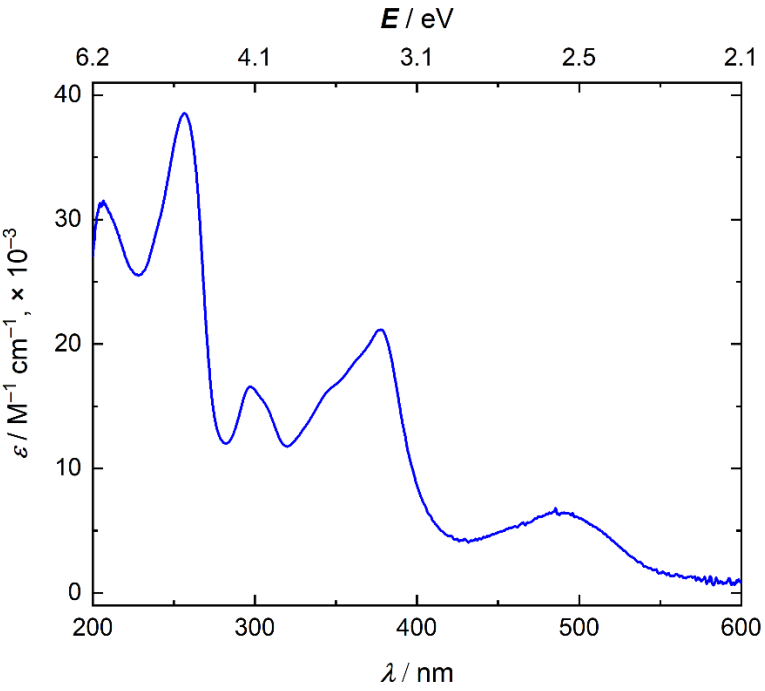

Figure A13. Electronic absorption spectrum of **L^{6}Ni** in MeCN.

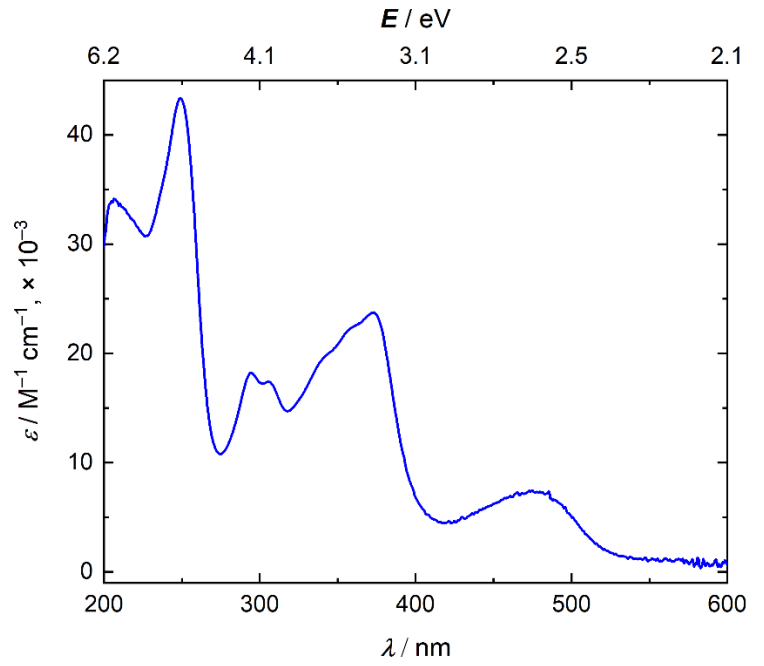

Figure A14. Electronic absorption spectrum of **L^{6}NiNa** in MeCN.

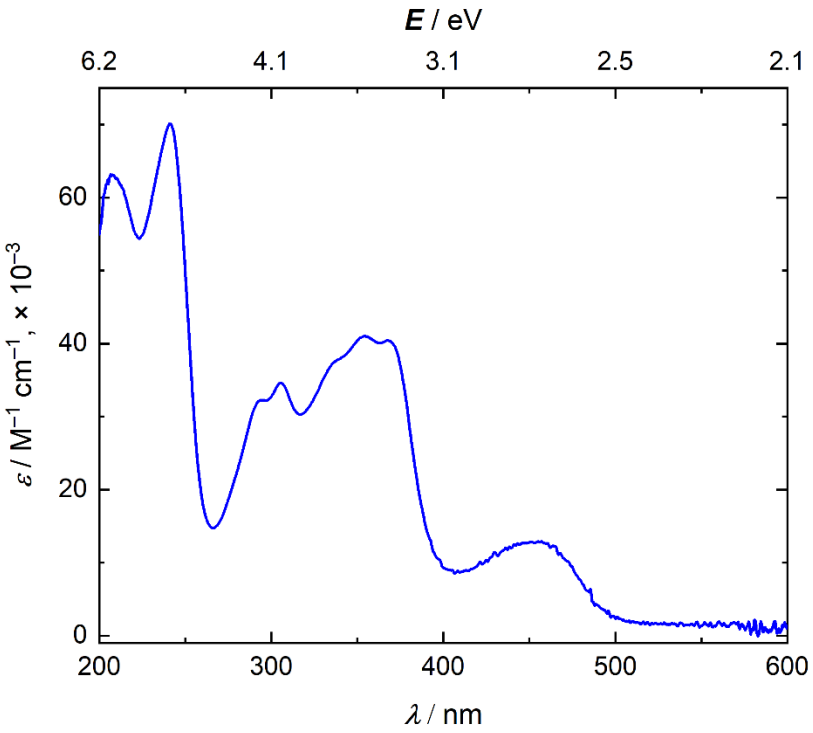

Figure A15. Electronic absorption spectrum of **L^{6}NiCa** in MeCN.

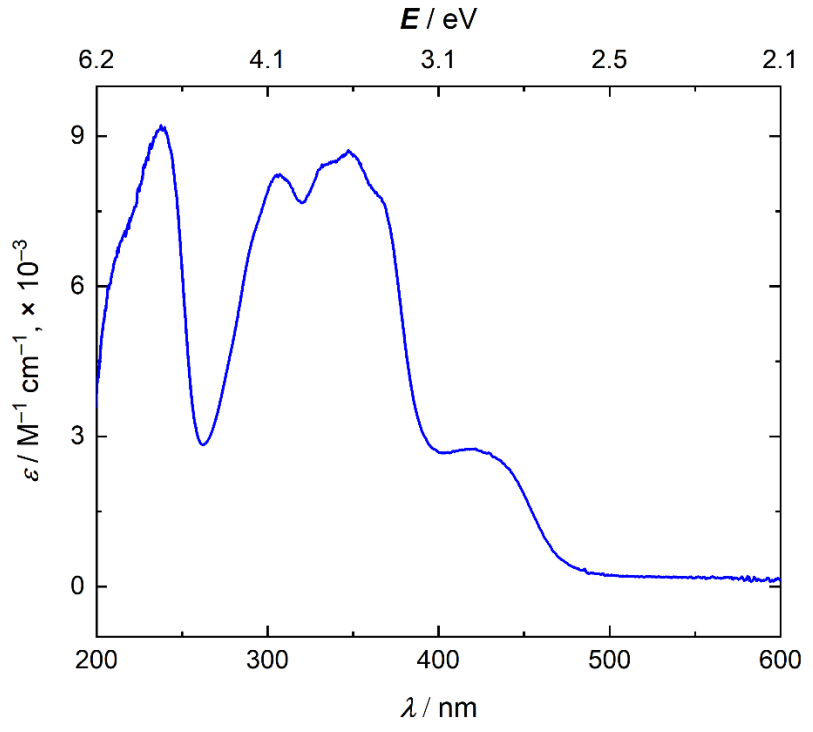

Figure A16. Electronic absorption spectrum of **L^{6}NiNd** in MeCN.

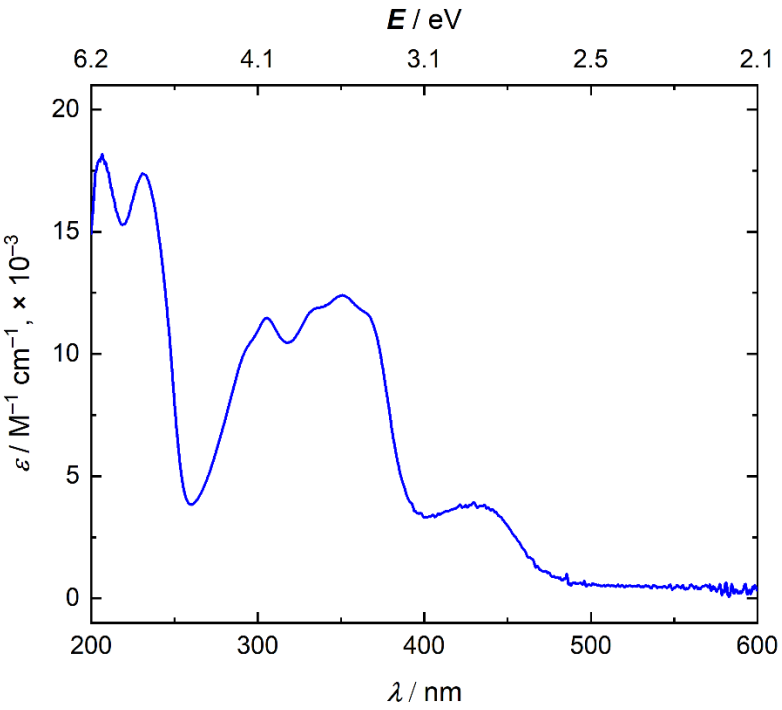

Figure A17. Electronic absorption spectrum of **L^{6}NiY** in MeCN.

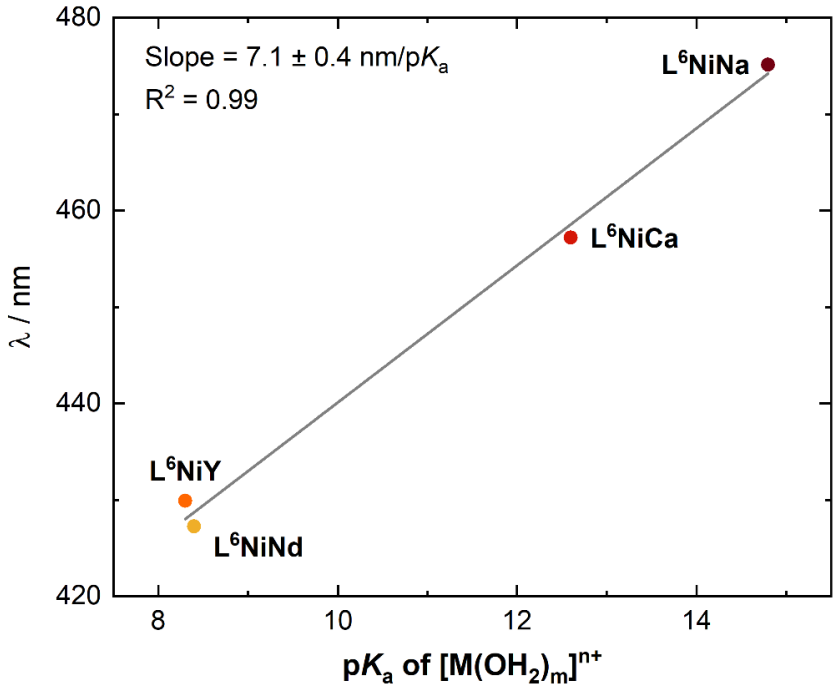

Figure A18. Dependence of the lowest energy absorption band (wavelength) for **L^{6}NiM** complexes on the Lewis acidity (pK_a) of the corresponding **M**-aqua complexes.

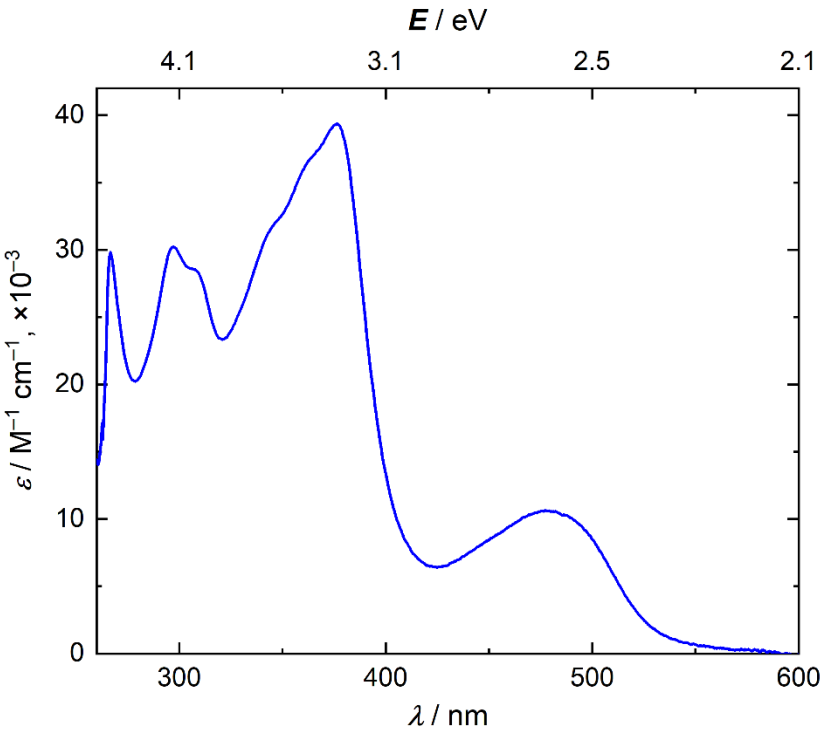

Figure A19. Electronic absorption spectrum of **L^{6}Ni** in DMF.

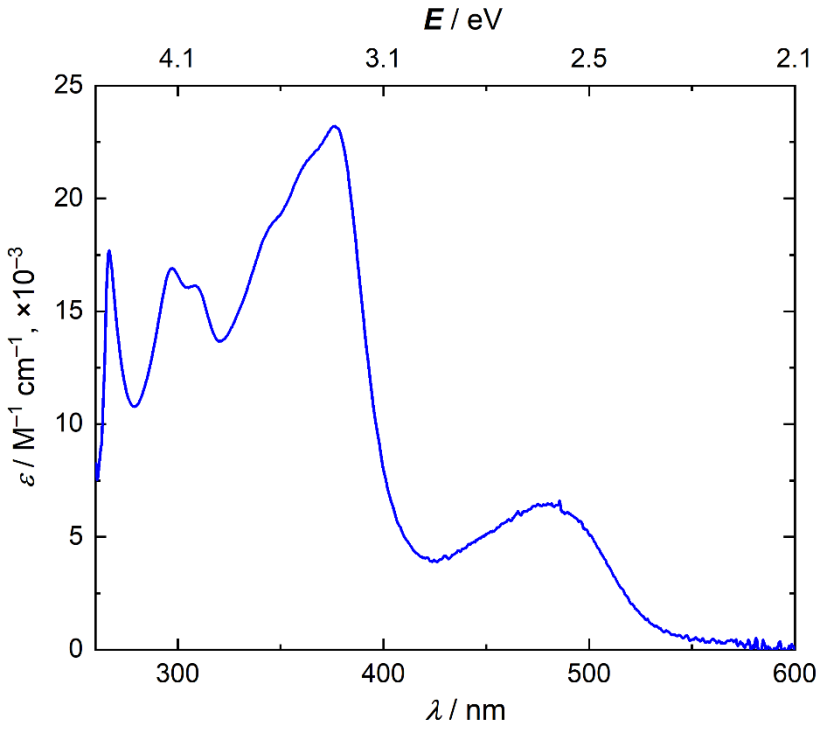

Figure A20. Electronic absorption spectrum of **L^{6}NiNa** in DMF.

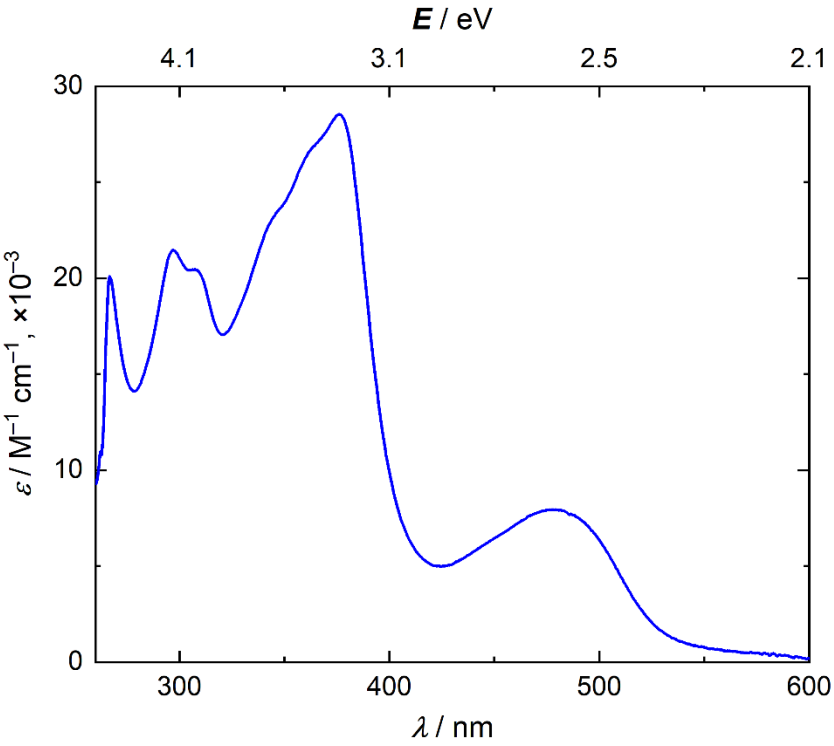

Figure A21. Electronic absorption spectrum of **L^{6}NiCa** in DMF.

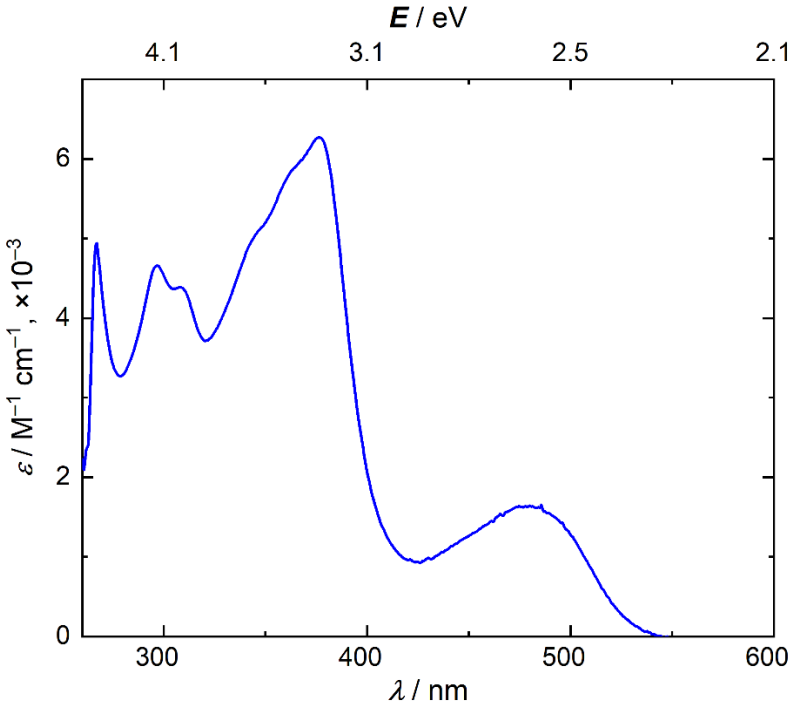

Figure A22. Electronic absorption spectrum of **L^{6}NiNd** in DMF.

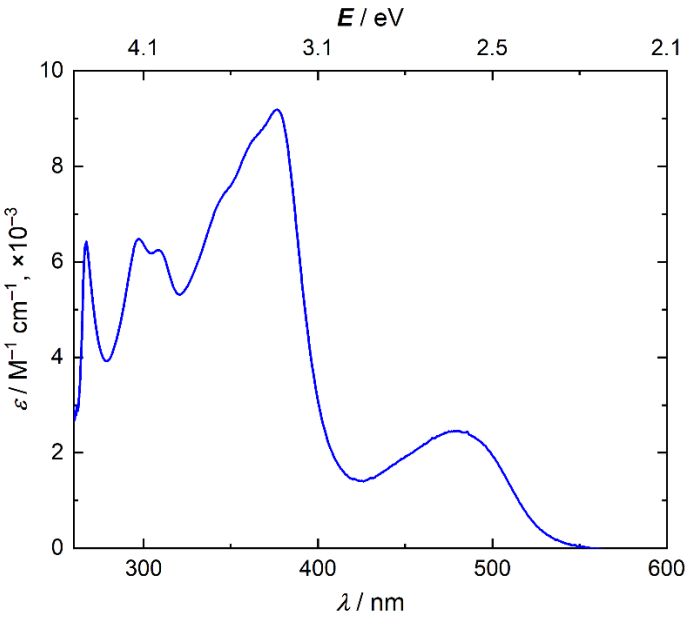

Figure A23. Electronic absorption spectrum of **L^{6}NiY** in DMF.

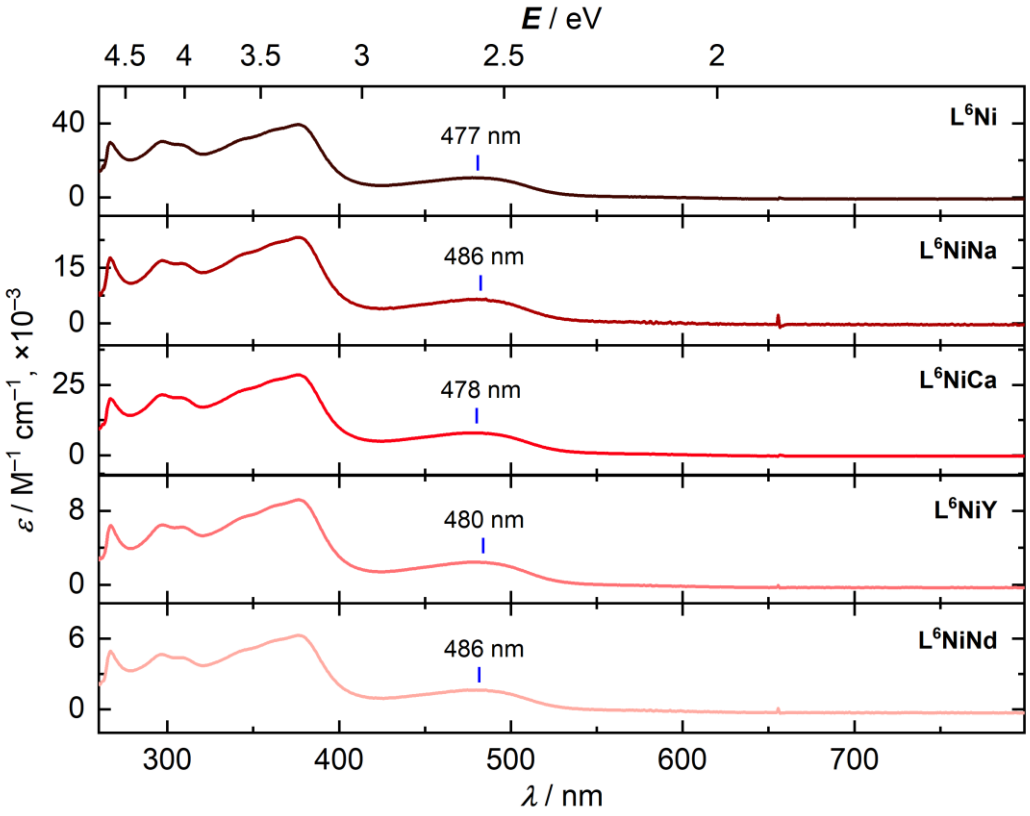

Figure A24. Stacked EA spectra of **L^{6}Ni** and **L^{6}NiM** complexes in DMF.

IR Spectra

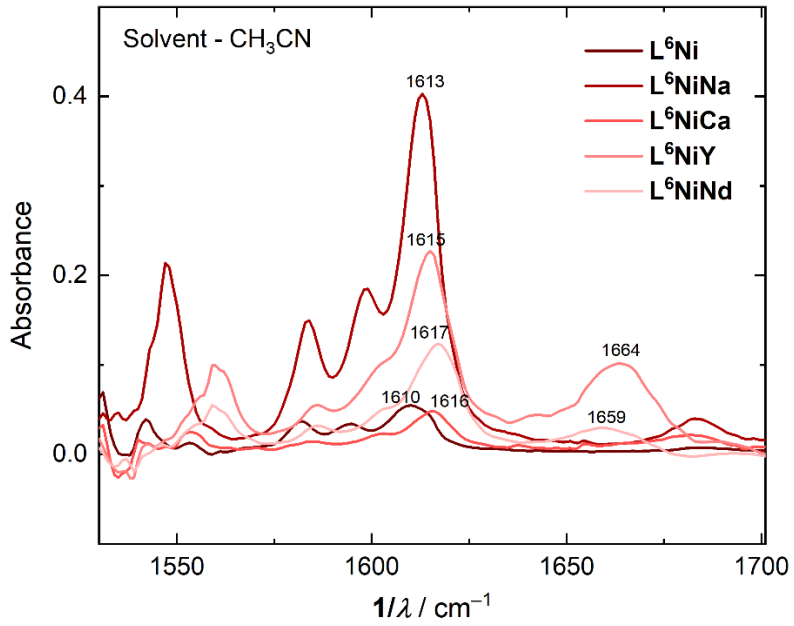

Figure A25. Solution IR spectra of **L^{6}Ni** and **L^{6}NiM** complexes in MeCN.

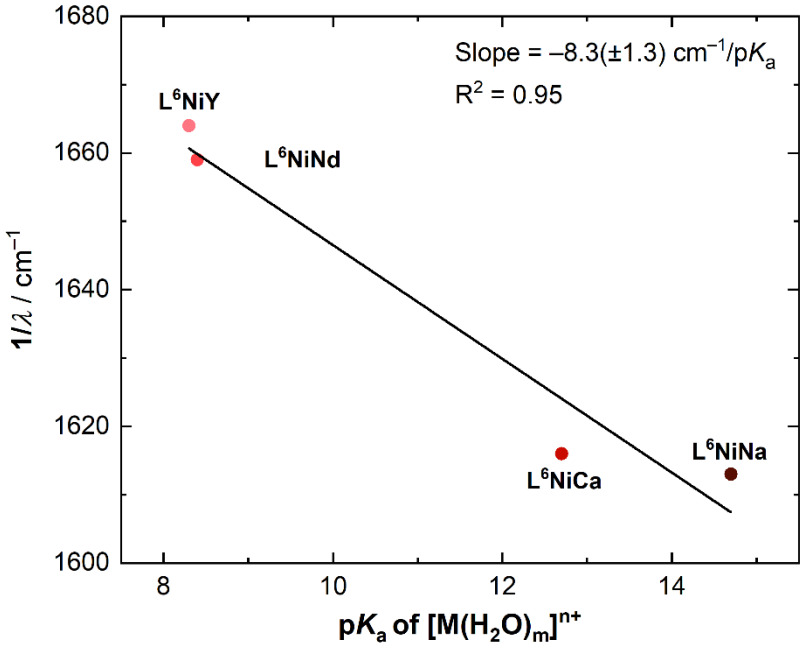

Figure A26. Dependence of C=N stretching frequency of **L^{6}NiM** complexes on the Lewis acidity of **M**-aqua species.

Electrochemistry

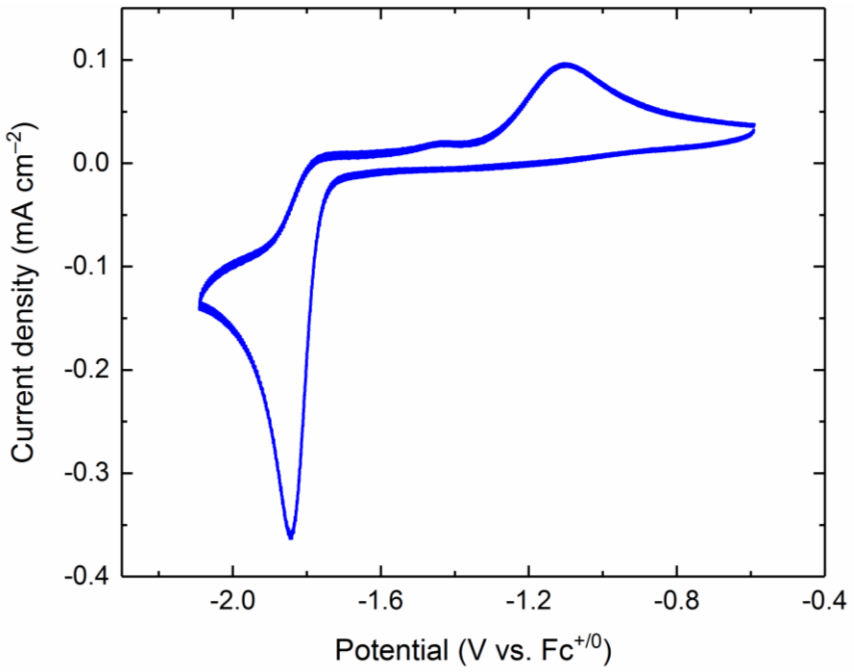

Figure A27. CV data for complex **L^{6}Ni** in MeCN (0.1 M [^{n}Bu$_4$N]$^+$[PF$_6$]$^-$, 100 mV/s).

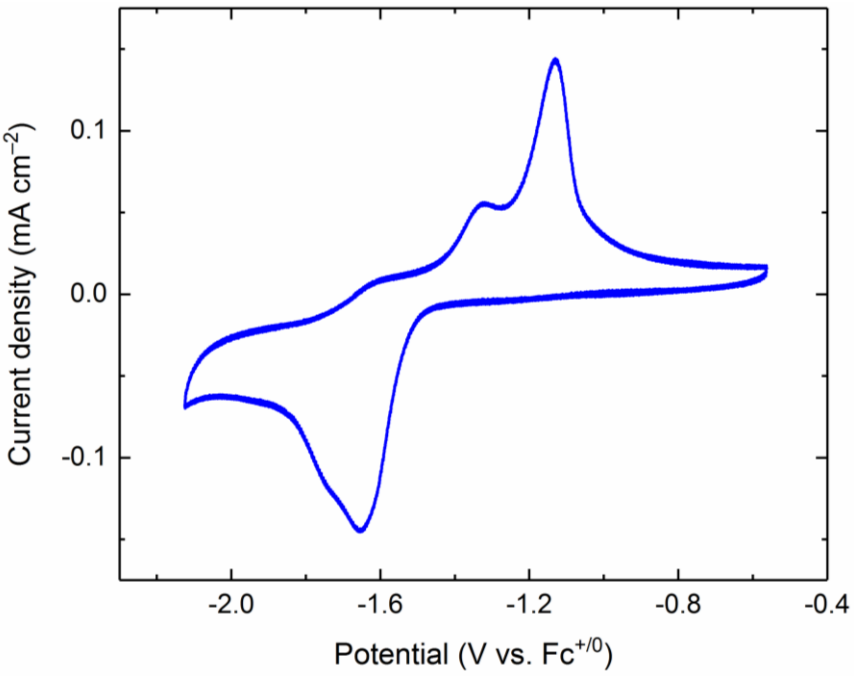

Figure A28. CV data for complex **L^{6}NiNa** in MeCN (0.1 M [^{n}Bu$_4$N]$^+$[PF$_6$]$^-$, 100 mV/s).

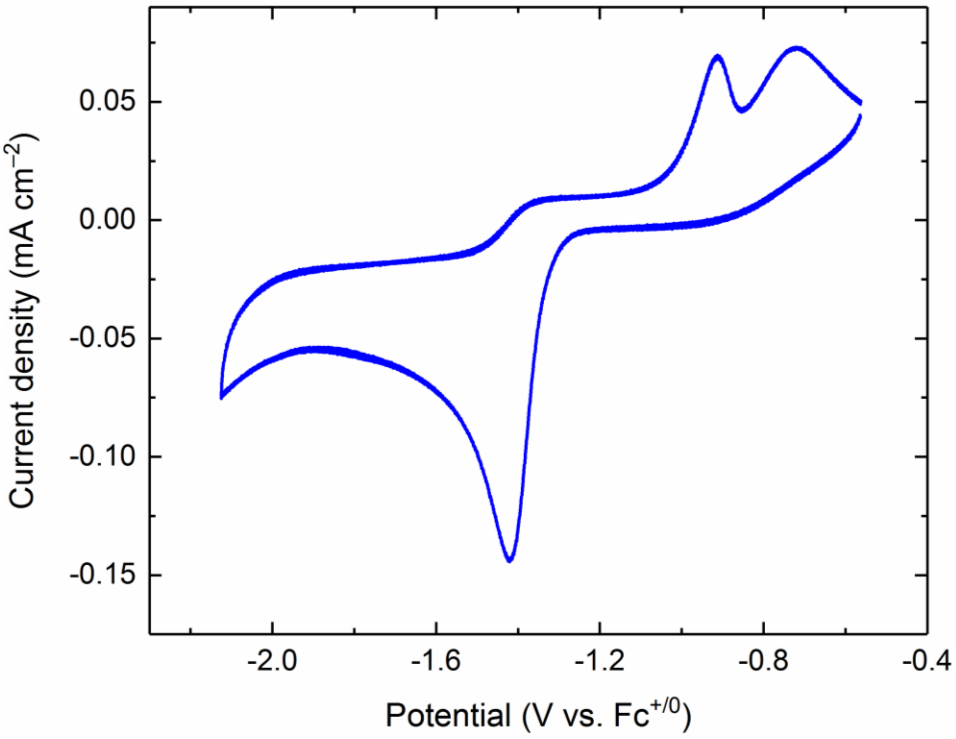

Figure A29. CV data for complex **L^{6}NiCa** in MeCN (0.1 M [^{n}Bu$_4$N]$^{+}$[PF$_6$]$^{-}$, 100 mV/s).

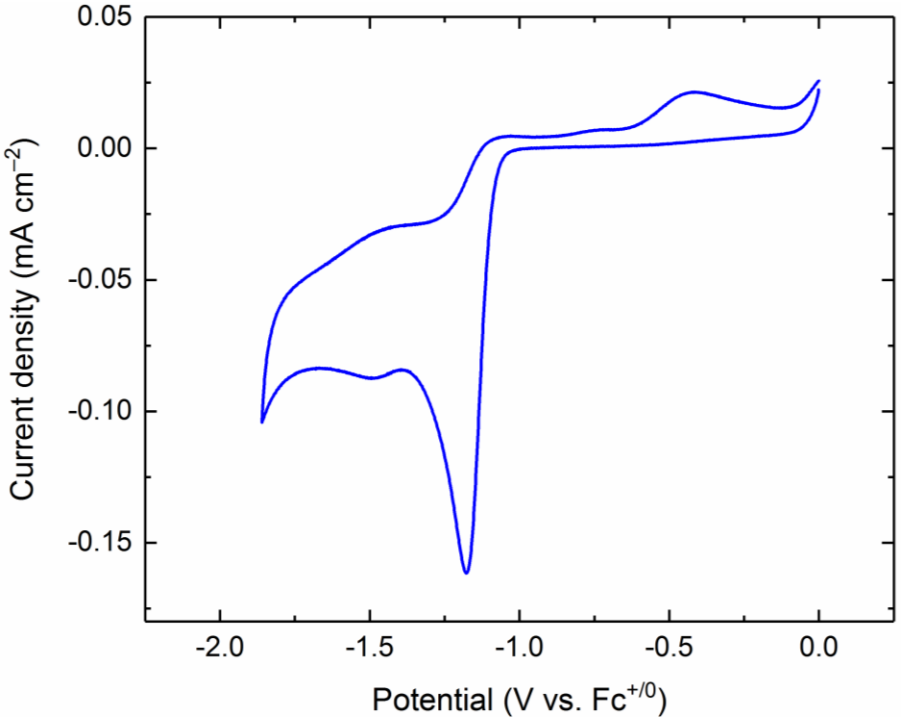

Figure A30. CV data for complex **L^{6}NiNd** in MeCN (0.1 M [^{n}Bu$_4$N]$^{+}$[PF$_6$]$^{-}$100 mV/s).

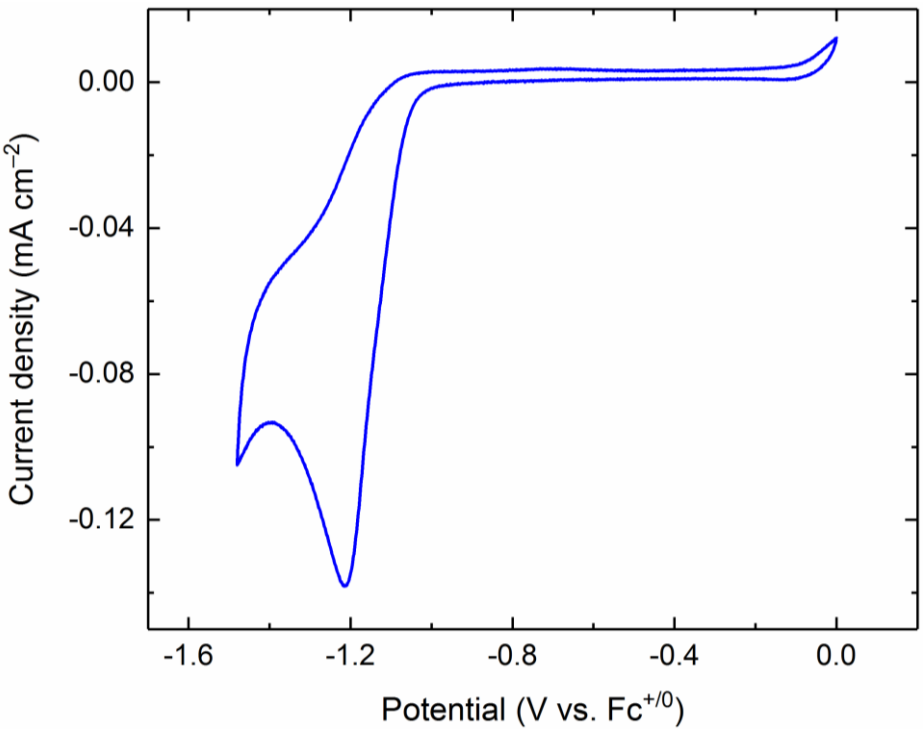

Figure A31. CV data for complex **L^{6}NiY** in MeCN (0.1 M [^{n}Bu$_4$N]$^+$[PF$_6$]$^-$, 100 mV/s).

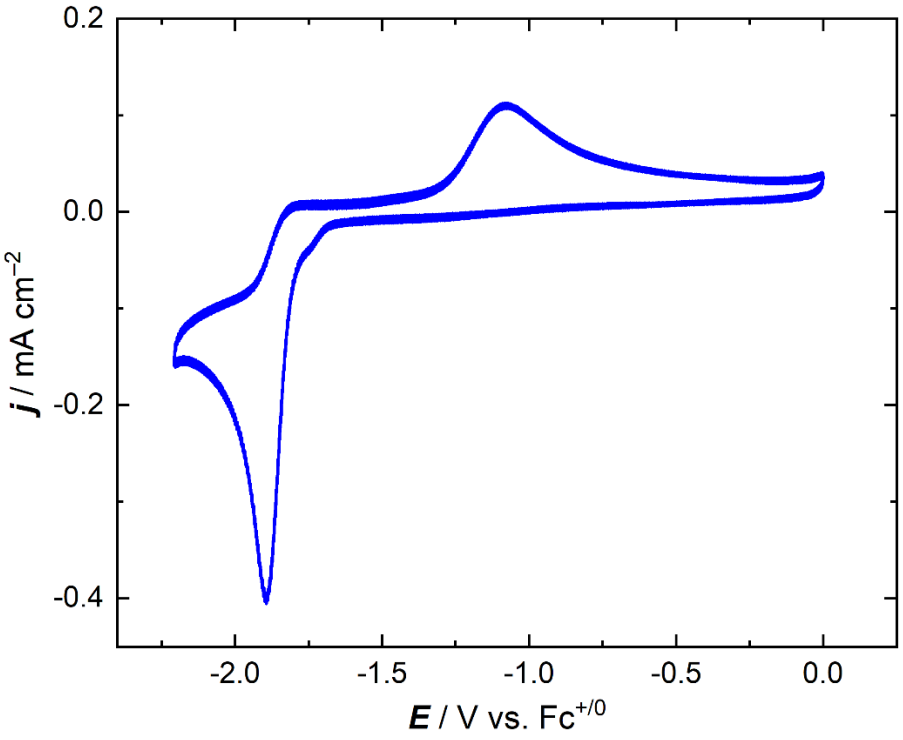

Figure A32. CV data for complex **L^{6}Ni** in DMF (0.1 M [^{n}Bu$_4$N]$^+$[PF$_6$]$^-$, 100 mV/s).

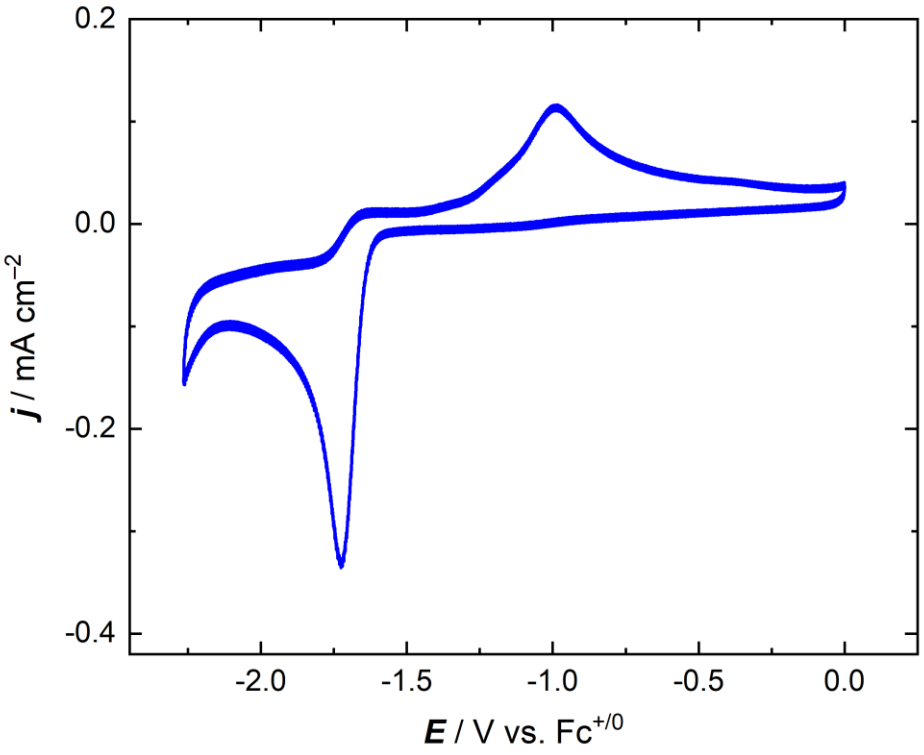

Figure A33. CV data for complex **L^{6}NiNa** in DMF (0.1 M [^{n}Bu$_4$N]$^+$[PF$_6$]$^-$, 100 mV/s).

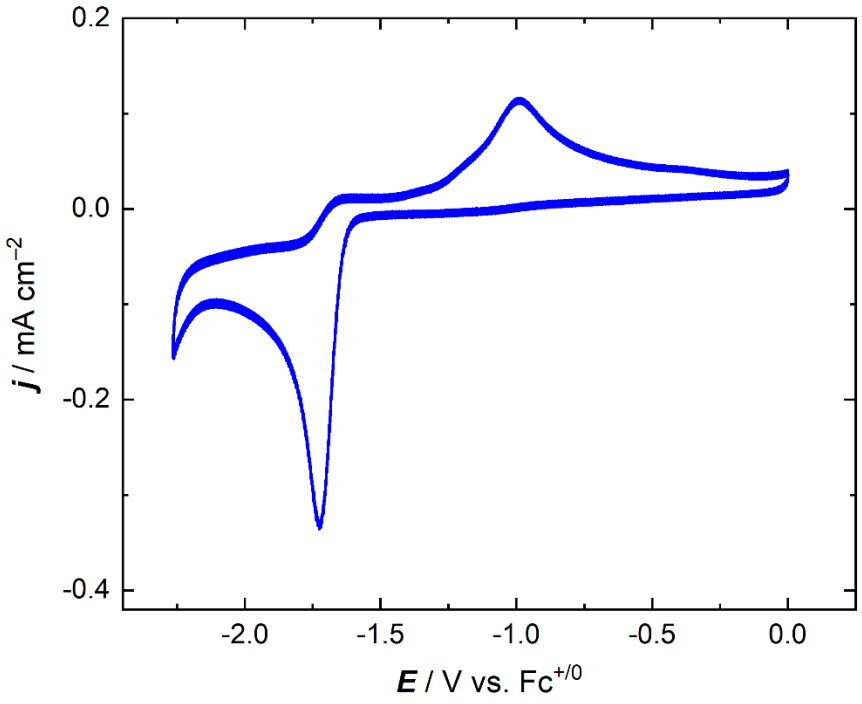

Figure A34. CV data for complex **L^{6}NiCa** in DMF (0.1 M [^{n}Bu$_4$N]$^+$[PF$_6$]$^-$, 100 mV/s).

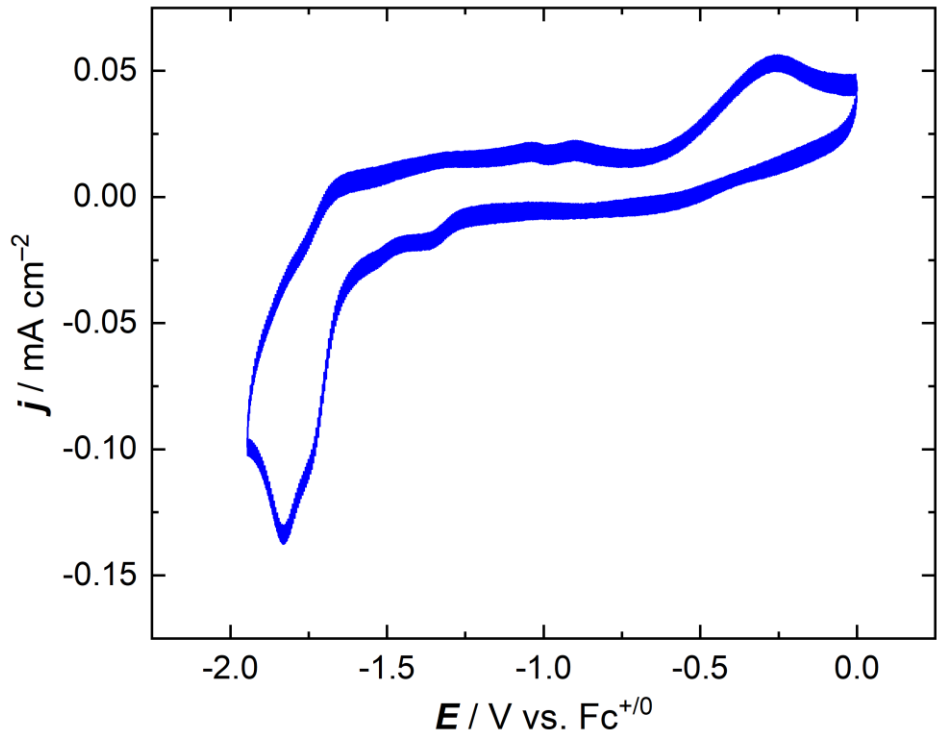

Figure A35. CV data for complex **L^{6}NiNd** in DMF (0.1 M [^{n}Bu$_4$N]$^+$[PF$_6$]$^-$, 100 mV/s).

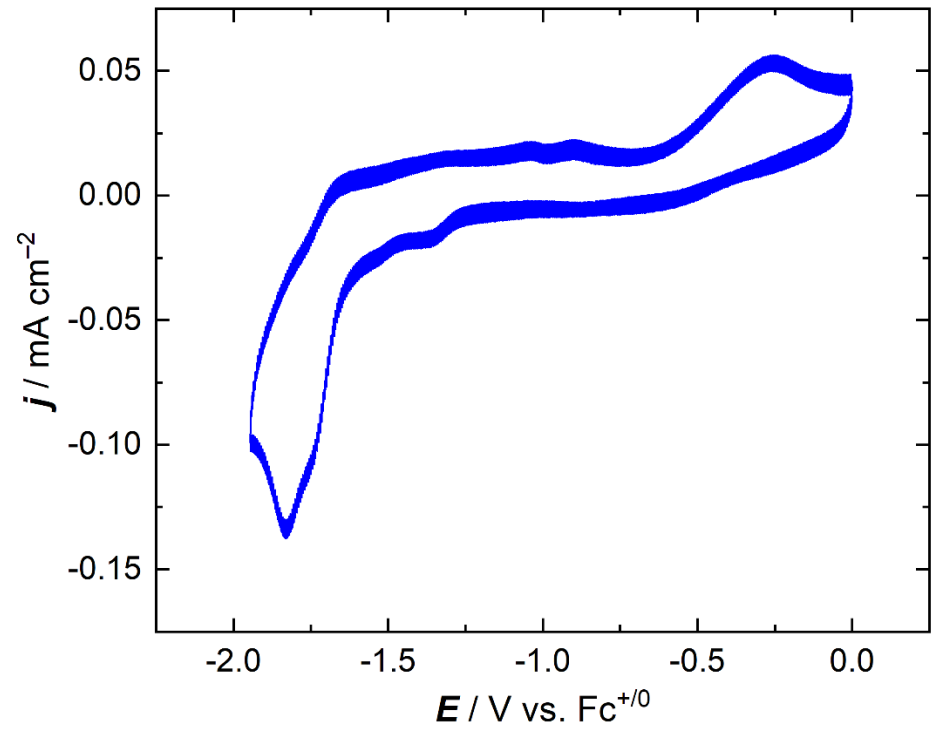

Figure A36. CV data for complex **L^{6}NiY** in DMF (0.1 M [^{n}Bu$_4$N]$^+$[PF$_6$]$^-$, 100 mV/s).

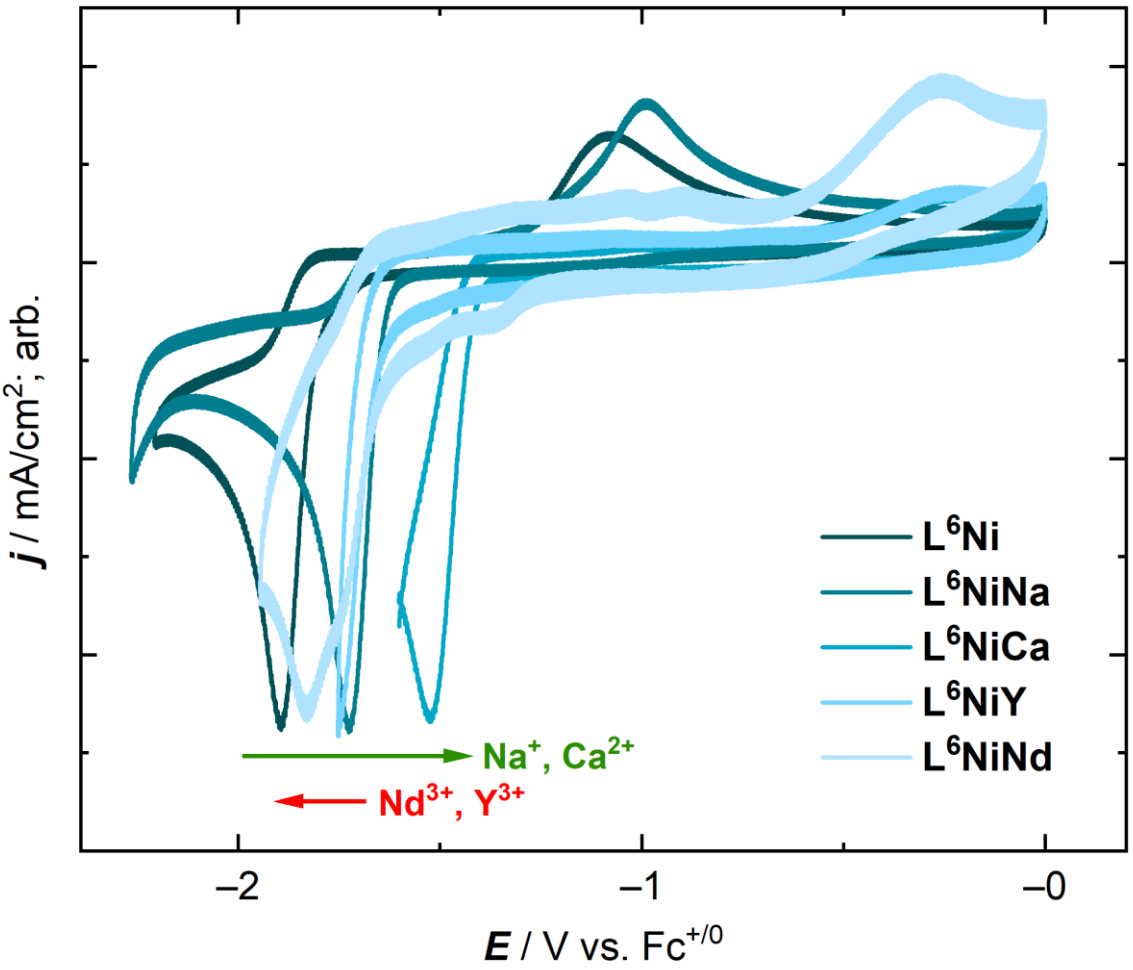

Figure A37. Overlay of CV data for **L^{6}Ni** and **L^{6}NiM** complexes in DMF (0.1 M $[^nBu_4N]^+[PF_6]^-$, 100 mV/s).

Crystallographic Information

Refinement Details

Crystals were mounted on a nylon loop using Paratone oil under a nitrogen stream. Low temperature (200-273 K) X-ray data were obtained with a Bruker MicroStar microfocus rotating anode generator running at 60mA and 45kV (Cu K_α = 1.54178 Å; APEX II detector positioned at 50.0 mm and equipped with Helios multilayer mirror optics). All diffractometer manipulations, including data collection, integration and scaling were carried out using the Bruker APEX II software.[1] Absorption corrections were applied using SADABS.[2] Space groups were determined on the basis of systematic absences and intensity statistics and the structures were solved by direct methods using SIR2004[3] or XS[4] or (incorporated into SHELXTL) and refined by full-matrix least squares on F^2. All non-hydrogen atoms were refined using anisotropic displacement parameters. Hydrogen atoms were placed in idealized positions and refined using a riding model. The structures were refined (weighted least squares refinement on F^2) to convergence using the Olex software package equipped with XL.[5]

The relevant crystallographic and structure refinement data for all five compounds are given in Tables A1 and A2.

Special Refinement Details for L^6Ni.

No special refinement was required. The structure contains two co-crystallized acetonitrile solvent molecules. The high (0.221) R_{int} value (giving a B-level alert during CheckCIF report validation) is due to weak high angle data.

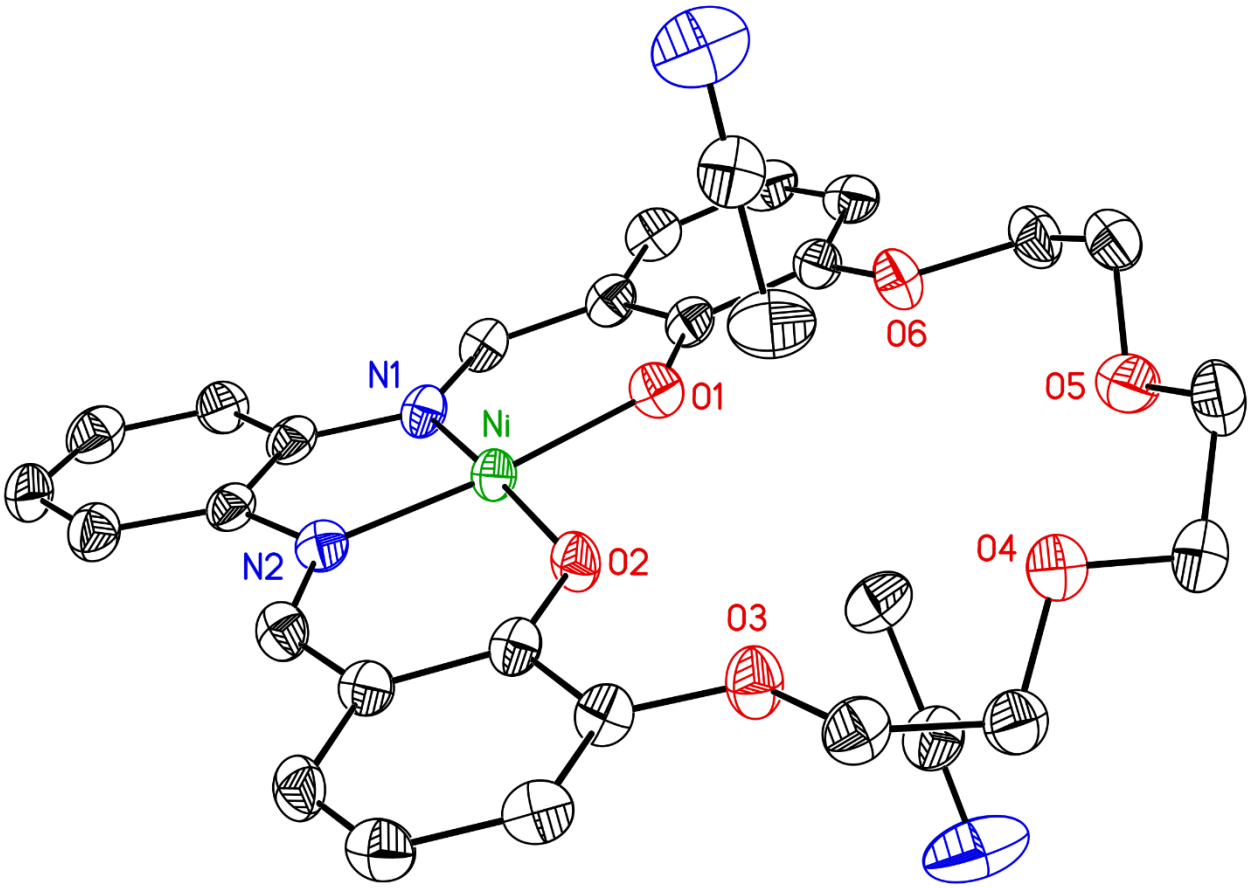

Figure A38. Full solid-state structure of **L^6Ni**. Hydrogen atoms omitted for clarity. Displacement ellipsoids shown at the 50% probability level.

Special Refinement Details for L^6NiNa.

The outer-sphere hexafluorophosphate counteranion was disordered over two orientations and was fully refined anisotropically in two distinct parts with 59:41 occupancy. The structure also contains a coordinated acetonitrile solvent molecule.

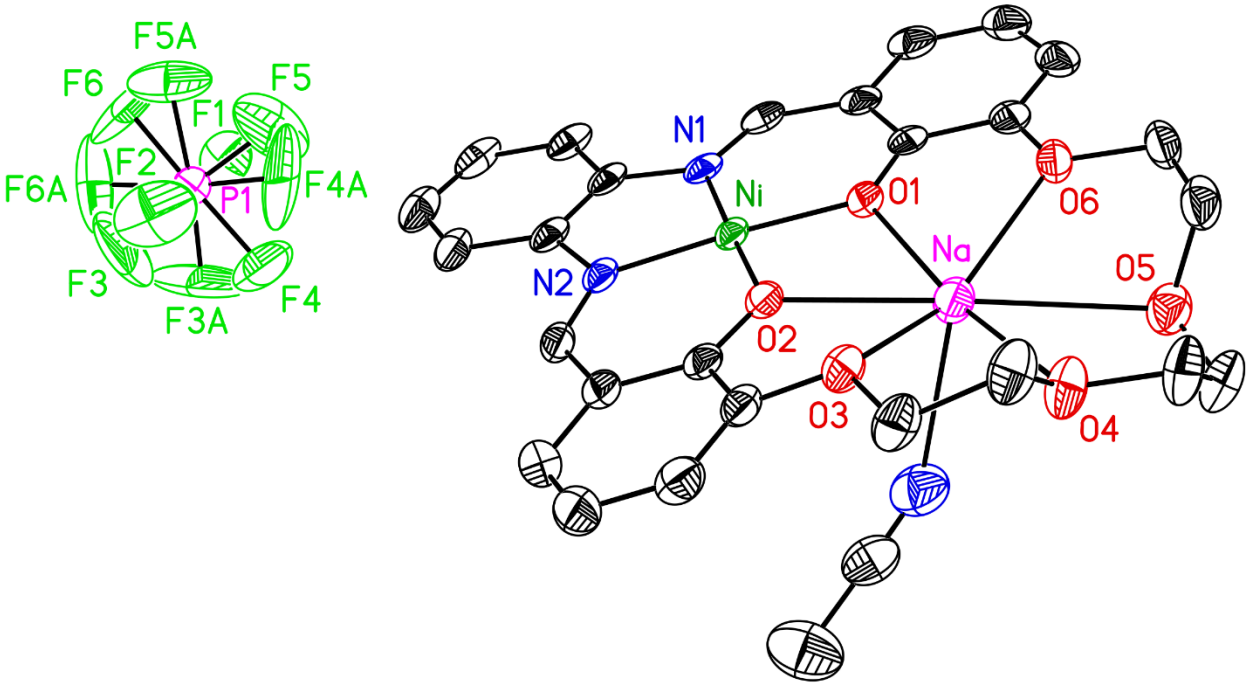

Figure A39. Full solid-state structure of **L^6NiNa**. Hydrogen atoms omitted for clarity. Displacement ellipsoids shown at the 50% probability level. Both orientations of the disordered PF_6^- counteranion are shown.

Special Refinement Details for L^6NiCa.

No special refinement was required.

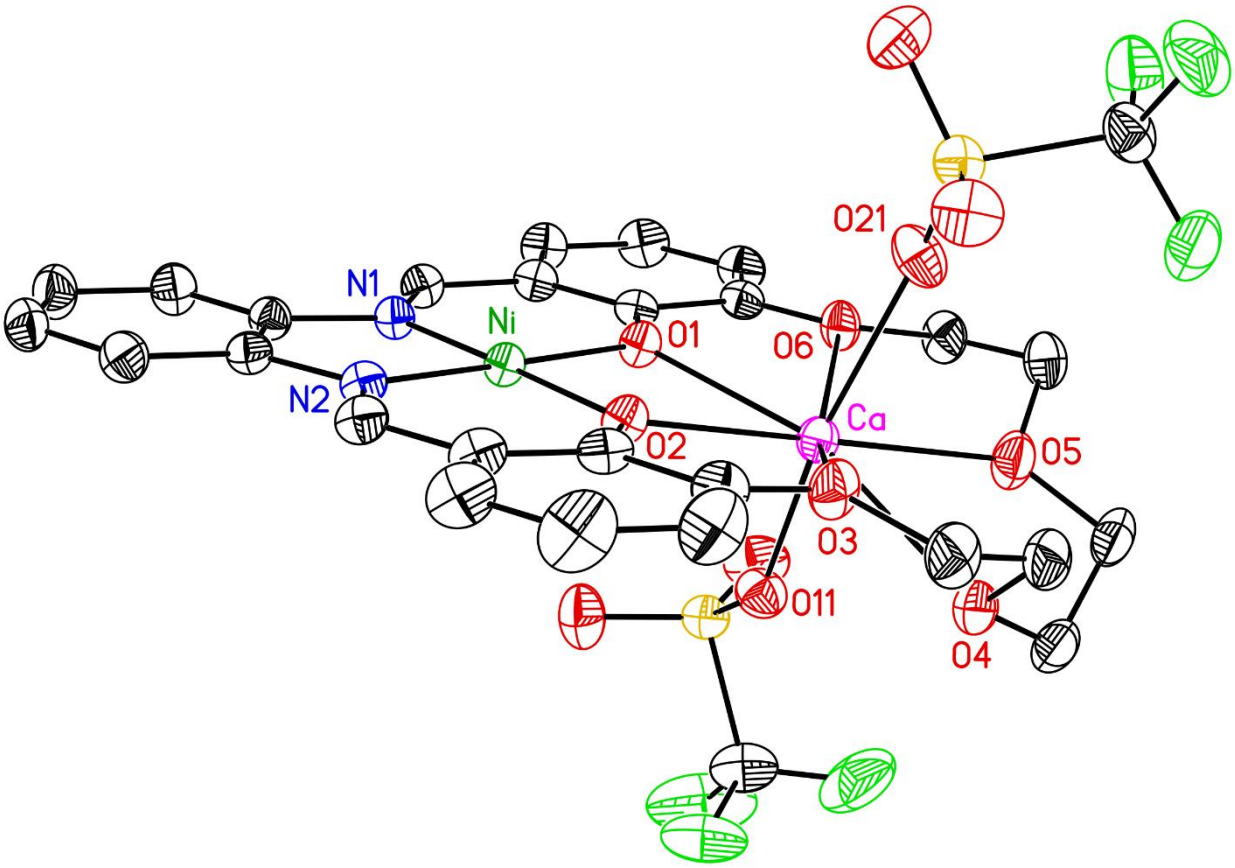

Figure A40. Full solid-state structure of **L^6NiCa**. Hydrogen atoms omitted for clarity. Displacement ellipsoids shown at the 50% probability level.

Special Refinement Details for L^6NiNd.

One of the inner sphere triflate was disordered over three orientations with 78.0:11.5:10.5 occupancy. The two minor occupancy orientations were refined isotropically and the major occupancy orientation was refined anisotropically.

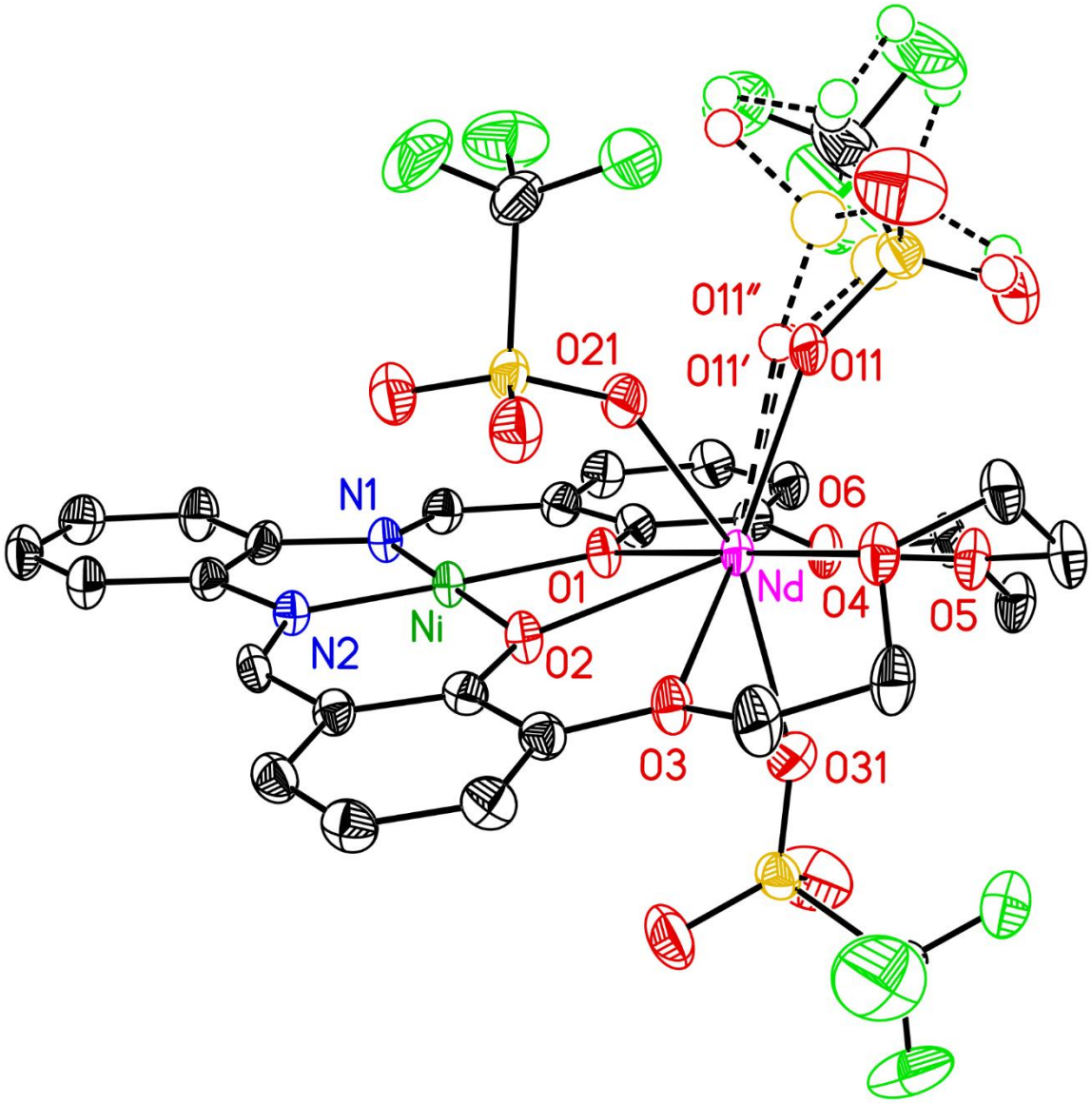

Figure A41. Full solid-state structure of **L^6NiNd**. Hydrogen atoms omitted for clarity. Displacement ellipsoids shown at the 50% probability level.

Special Refinement Details for L^6NiY.

No special refinement was required.

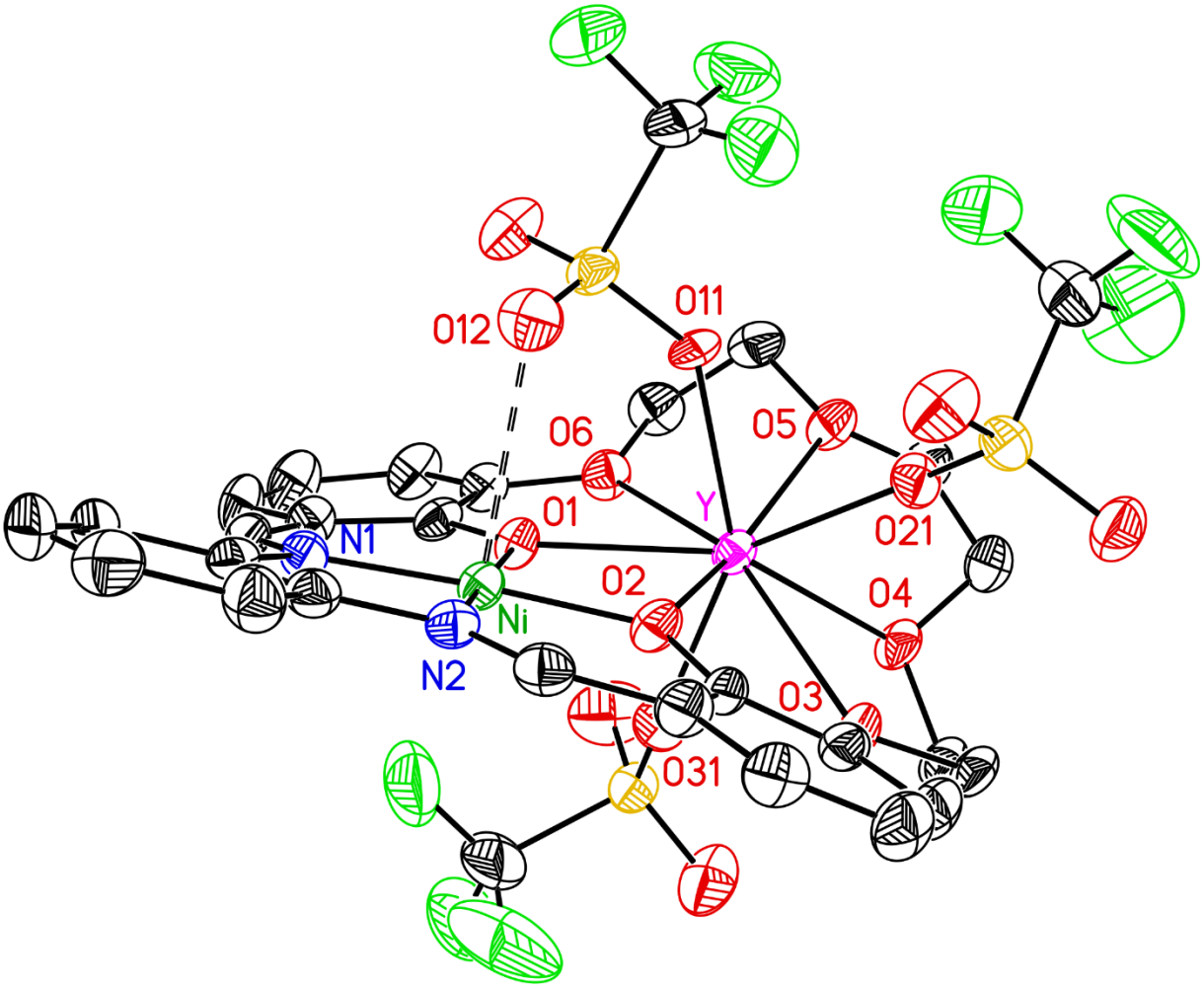

Figure A42. Full solid-state structure of **L^6NiY**. The structure has a weak axial interaction (shown by dashed lines) between Ni and O12, an oxygen atom of a Y-bound triflate group. Hydrogen atoms omitted for clarity. Displacement ellipsoids shown at the 50% probability level.

Table A1. Crystal and refinement Data for **L^6Ni, L^6NiNa,** and **L^6NiCa**

	L^6Ni	L^6NiNa	L^6NiCa
CCDC #	1569883	1569884	1569885
empirical formula	$C_{30}H_{30}N_4NiO_6$	$C_{28}H_{27}F_6N_3NaNiO_6P$	$C_{28}H_{24}CaF_6N_2NiO_{12}S_2$
formula wt	601.29	728.19	857.40
T (K)	296.15	200	200
a, Å	13.0777(9)	28.3375(9)	10.7224(2)
b, Å	15.2615(13)	16.0850(5)	14.0417(2)
c, Å	27.823(2)	13.0204(4)	21.6994(4)
α, deg	90	90	90
β, deg	90	92.3451(14)	99.1530(10)
γ, deg	90	90	90
V, Å^3	5553.0(7)	5929.8(3)	3225.48(10)
Z	8	8	4
crystal system	orthorhombic	monoclinic	monoclinic
space group	Pbca	C2/c	$P2_1/n$
μ_{calcd}, g/cm^3	1.438	1.631	1.766
2θ range, deg	6.354 to 133.422	6.242 to 141	7.528 to 139.758
μ, mm^{-1}	1.440	2.381	4.404
abs corr	Multi-scan	Multi-scan	Multi-scan
GOOF[c]	0.999	1.059	1.041
R1,[a] wR2[b] (I > 2σ(I))	0.0910, 0.2118	0.0533, 0.1328	0.0410, 0.1026

[a] $R1 = \Sigma||F_o|-|F_c|| / \Sigma|F_o|$ [b] $wR2 = [\ \Sigma[w(F_o^2-F_c^2)^2] / \Sigma[w(F_o^2)^2]\ ]^{1/2}$ [c] $GOOF = S = [\ \Sigma[w(F_o^2-F_c^2)^2] / (n-p)\ ]^{1/2}$

Table A2. Crystal and refinement Data **L^6NiNd,** and **L^6NiY**

	L^6NiNd	**L^6NiY**
CCDC #	1569886	1569887
empirical formula	$C_{29}H_{24}F_9N_2NdNiO_{15}S_3$	$C_{29}H_{24}F_9N_2NiO_{15}S_3Y$
formula wt	1110.63	1055.30
T (K)	200	200
a, Å	10.71370(10)	10.1094(4)
b, Å	11.7783(2)	12.8241(6)
c, Å	16.1822(2)	15.5798(7)
α, deg	81.8861(8)	91.796(3)
β, deg	81.1704(7)	101.743(2)
γ, deg	69.0966(8)	105.6776(18)
V, Å^3	1876.74(4)	1895.98(15)
Z	2	2
cryst syst	triclinic	triclinic
space group	P-1	P-1
μ_{calcd}, g/cm^3	1.965	1.849
2θ range, deg	5.55 to 140.604	5.818 to 141.058
μ, mm^{-1}	13.692	5.272
abs corr	Multi-scan	Multi-scan
GOOF^c	1.067	1.163
R1,^{a} wR2^b (I > 2σ(I))	0.0325, 0.0810	0.0658, 0.1783

^{a} $R1 = \Sigma||F_o|-|F_c|| / \Sigma|F_o|$ ^{b} $wR2 = [\ \Sigma[w(F_o^2-F_c^2)^2] / \Sigma[w(F_o^2)^2]\ ]^{1/2}$ ^{c} $GOOF = S = [\ \Sigma[w(F_o^2-F_c^2)^2] / (n-p)\ ]^{1/2}$

References

(1) *APEX2, Version 2 User Manual, M86-E01078*: Bruker Analytical X-ray Systems, Madison, WI, June 2006.

(2) *Sheldrick, G. M., SADABS (version 2008/1)*: Program for Absorption Correction for Data from Area Detector Frames, University of Göttingen, 2008.

(3) Burla, M. C.; Caliandro, R.; Camalli, M.; Carrozzini, B.; Cascarano, G. L.; De Caro, L.; Giacovazzo, C.; Polidori, G.; Siliqi D.; Spagna, R. IL MILIONE: a suite of computer programs for crystal structure solution of proteins. *J. Appl. Cryst.* **2007**, *40*, 609–613.

(4) Sheldrick, G. Crystal structure refinement with SHELXL. *Acta Cryst.* **2015**, *C71*, 3-8

(5) Dolomanov, O. V.; Bourhis, L. J.; Gildea, R. J.; Howard J. A. K.; Puschmann, H. OLEX2: a complete structure solution, refinement and analysis program. *J. Appl. Crystallogr.* **2009**, *42*, 339-341.

Appendix B

Supplementary Information for Chapter 3

NMR Spectra

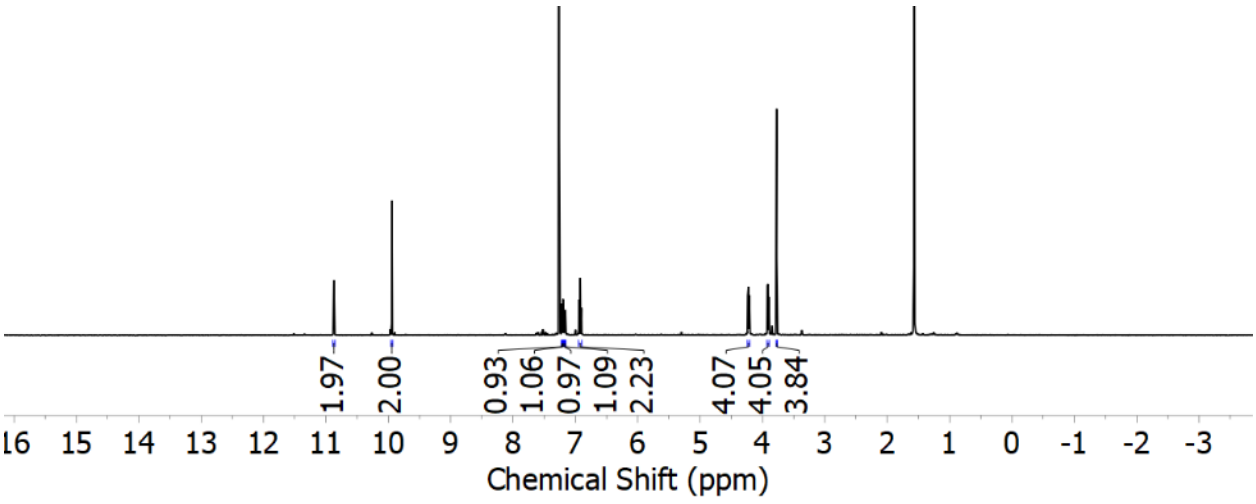

Figure B1. ^{1}H NMR spectrum (400 MHz, CD_3CN) of **3,3'-(3,6-Dioxaoctane-1,8-diyldioxy)bis(2-hydroxybenzaldehyde)**.

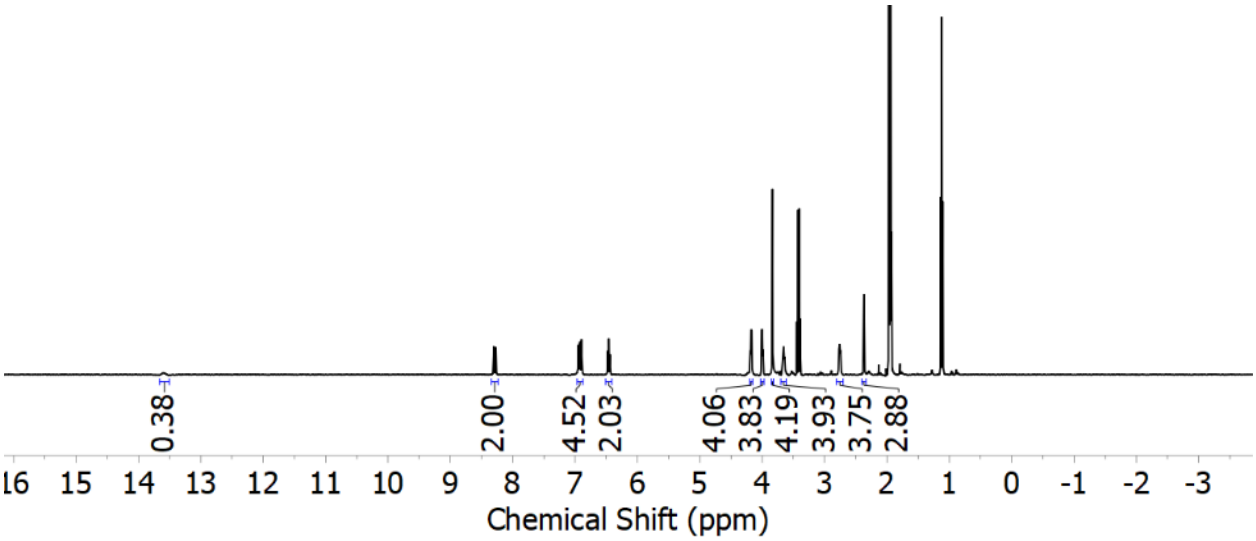

Figure B2. ^{1}H NMR spectrum (400 MHz, CD_3CN) of **L^6H_2Ba**.

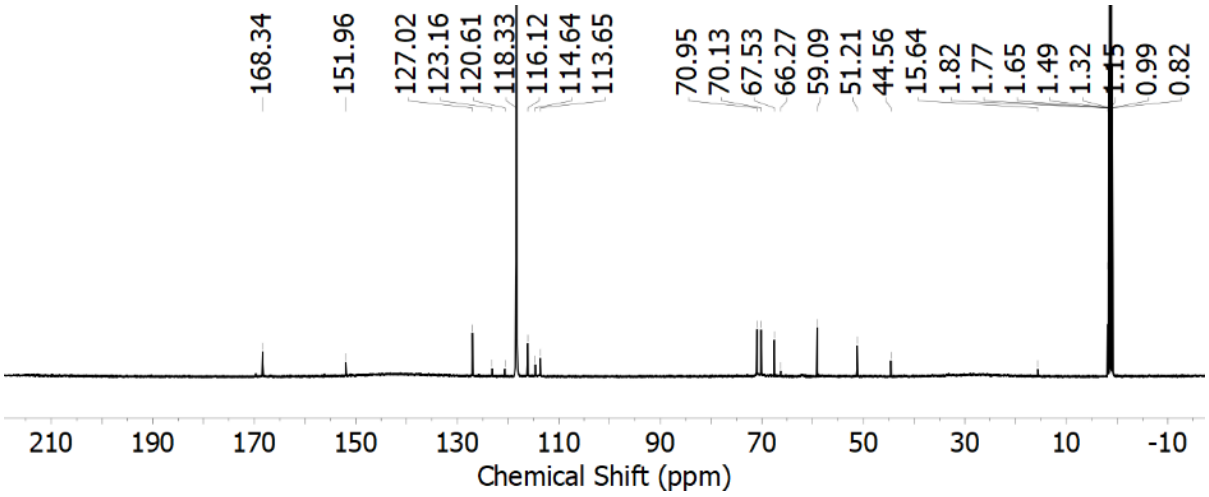

Figure B3. $^{13}C\{^{1}H\}$ NMR spectrum (126 MHz, CD_3CN) of **L^6H_2Ba**.

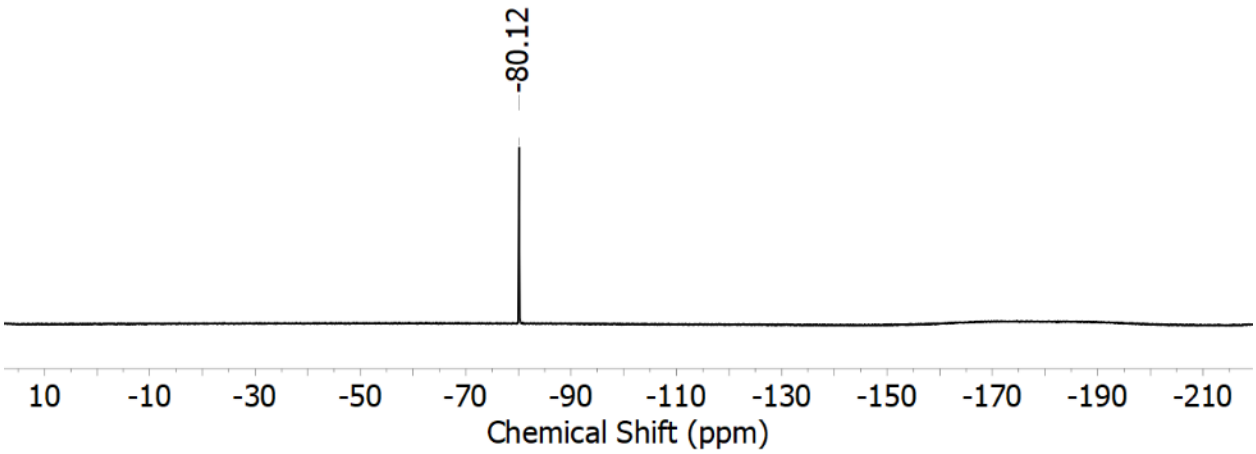

Figure B4. ^{19}F NMR spectrum (376 MHz, CD_3CN) of **L^6H_2Ba**.

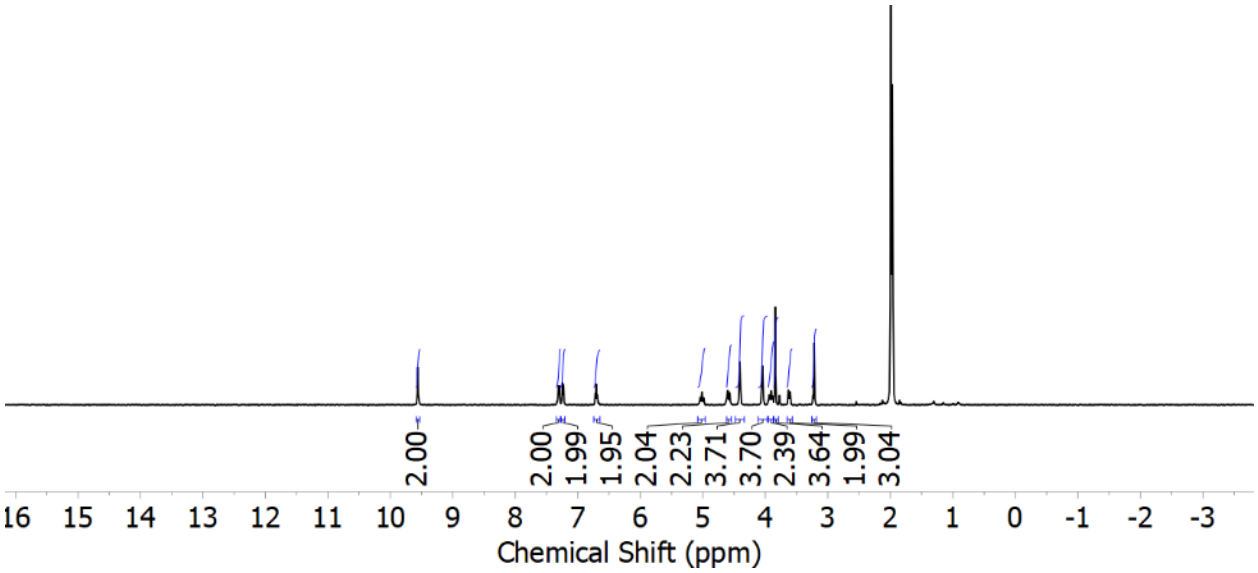

Figure B5. ^{1}H NMR spectrum (500 MHz, CD_3CN) of **L^6UO_2**.

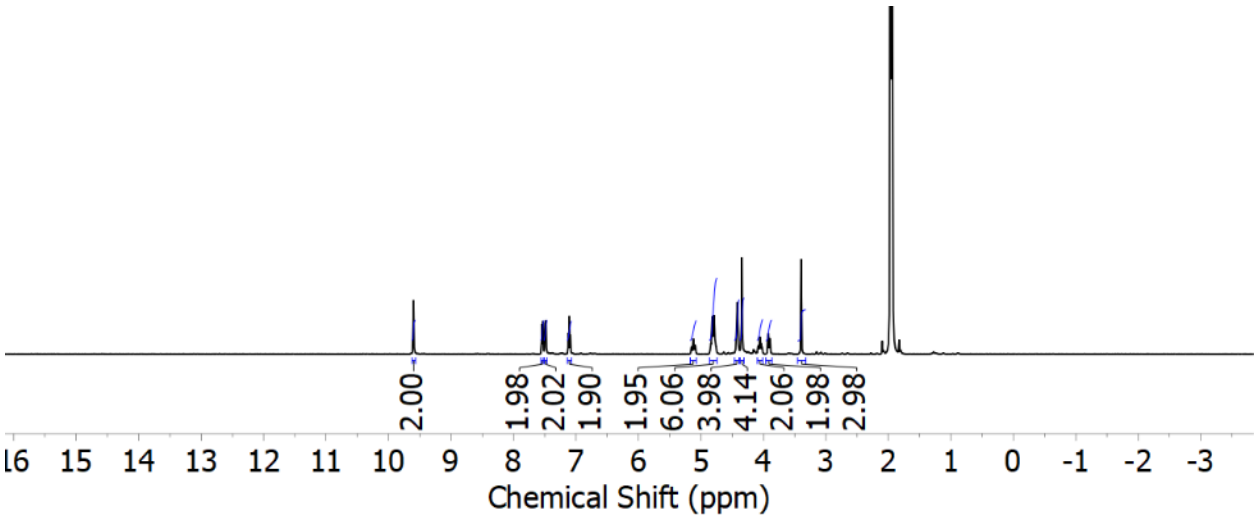

Figure B6. ^{1}H NMR spectrum (500 MHz, CD_3CN) of **L^6UO_2K**.

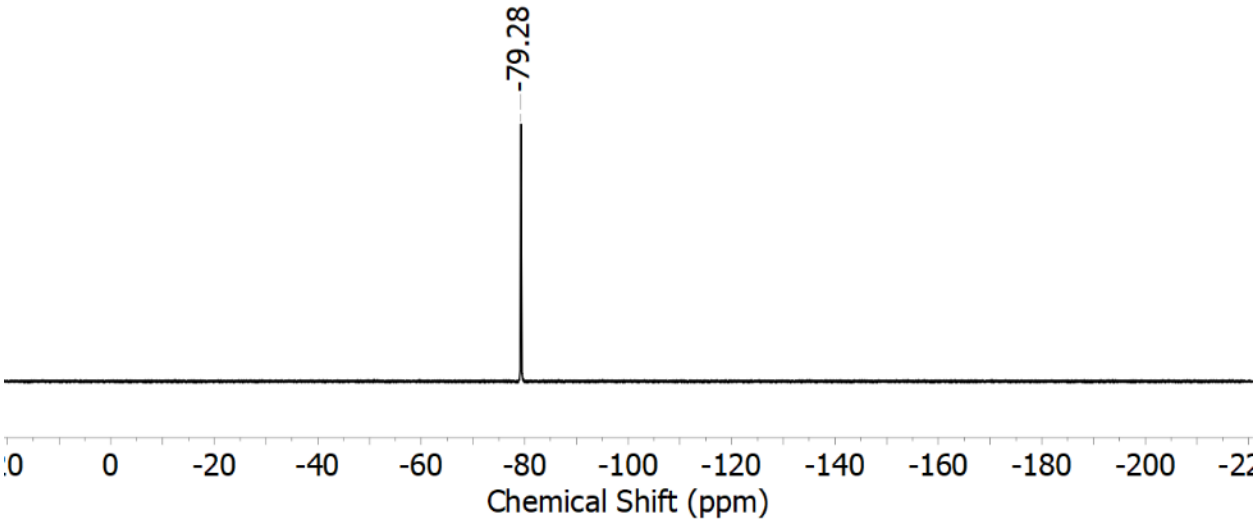

Figure B7. ^{19}F NMR spectrum (376 MHz, CD_3CN) of **L^6UO_2K**.

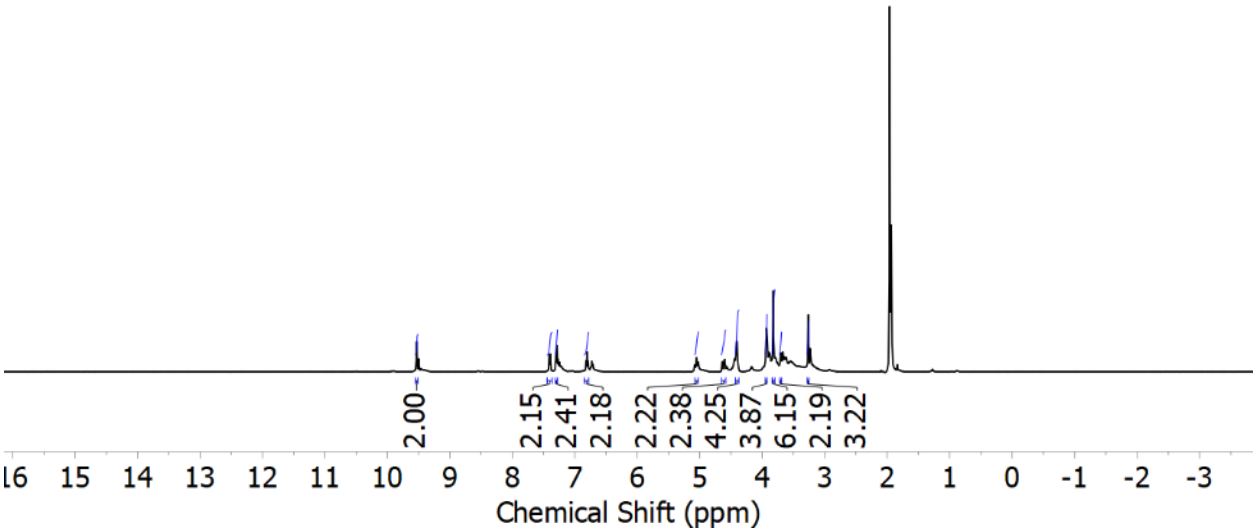

Figure B8. ^{1}H NMR spectrum (500 MHz, CD_3CN) of **L^6UO_2Na**.

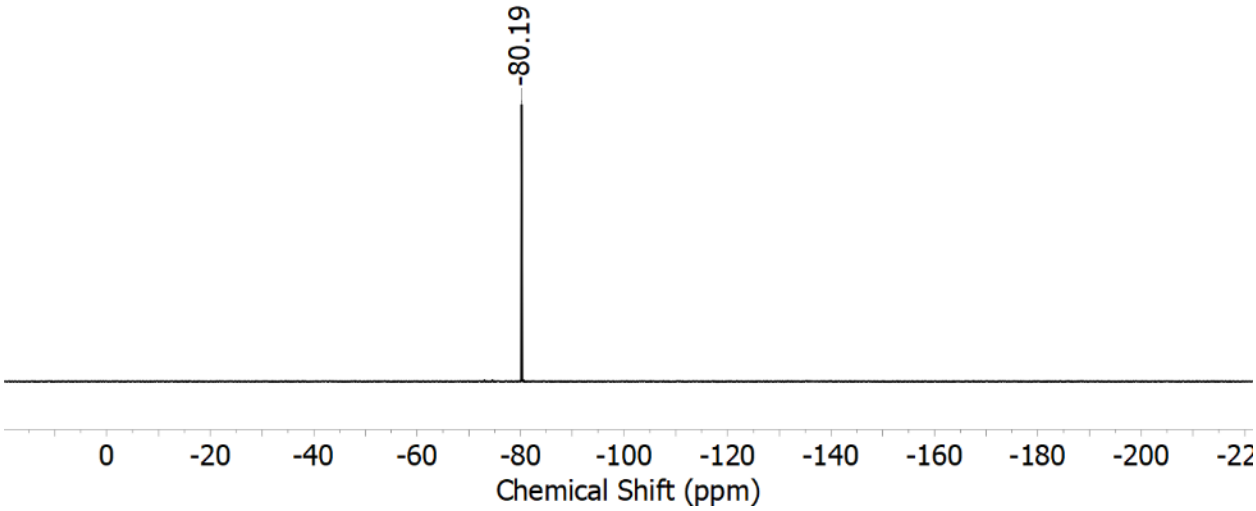

Figure B9. ^{19}F NMR spectrum (376 MHz, CD_3CN) of **L^6UO_2Na**.

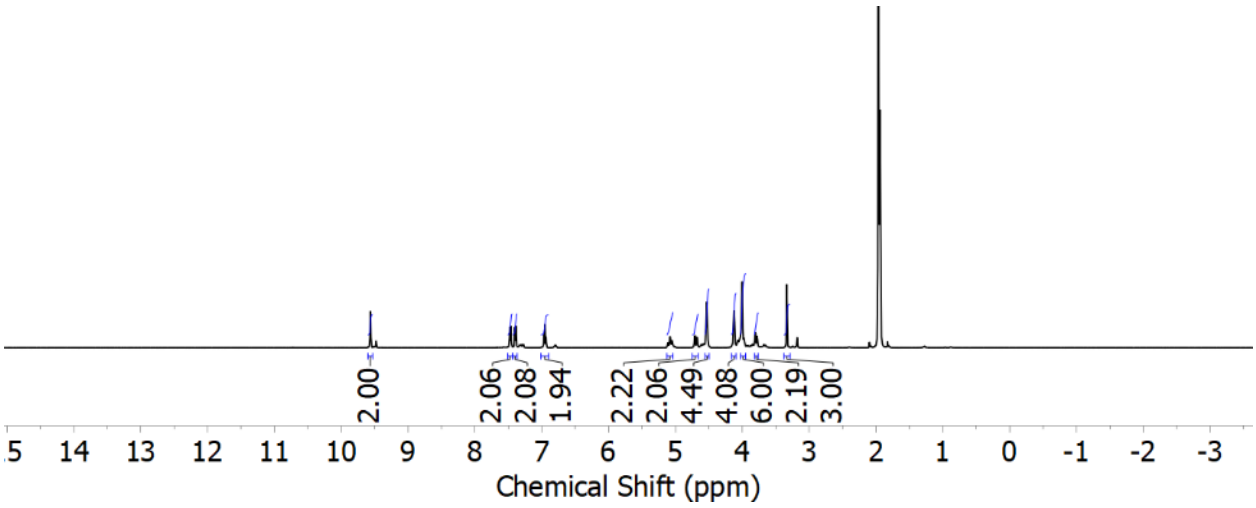

Figure B10. ^{1}H NMR spectrum (500 MHz, CD_3CN) of **L^6UO_2Ca**.

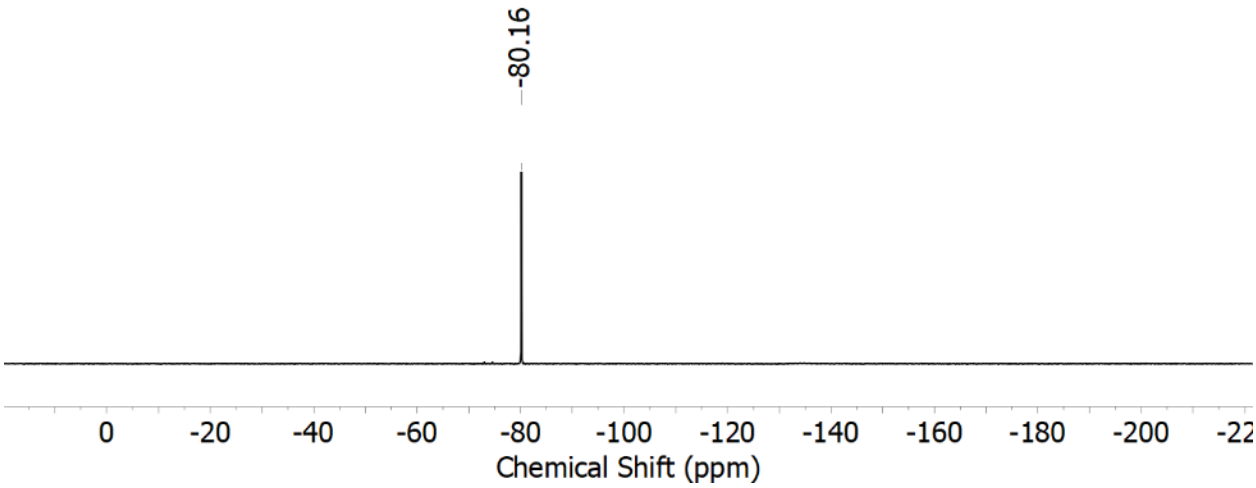

Figure B11. ^{19}F NMR spectrum (376 MHz, CD_3CN) of **L^6UO_2Ca**.

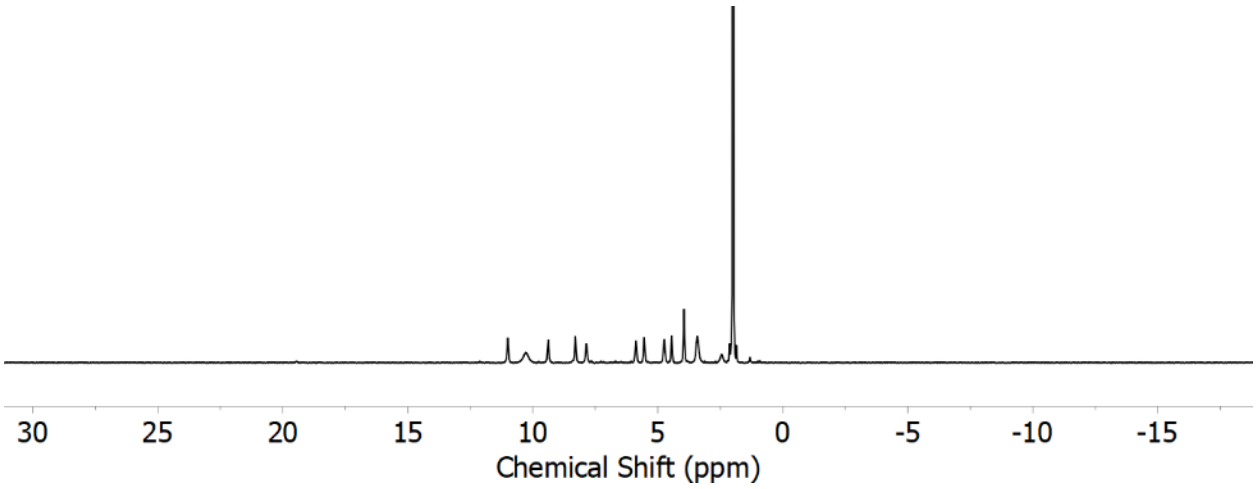

Figure B12. ^{1}H NMR spectrum (500 MHz, CD_3CN) of **L^6UO_2Nd**.

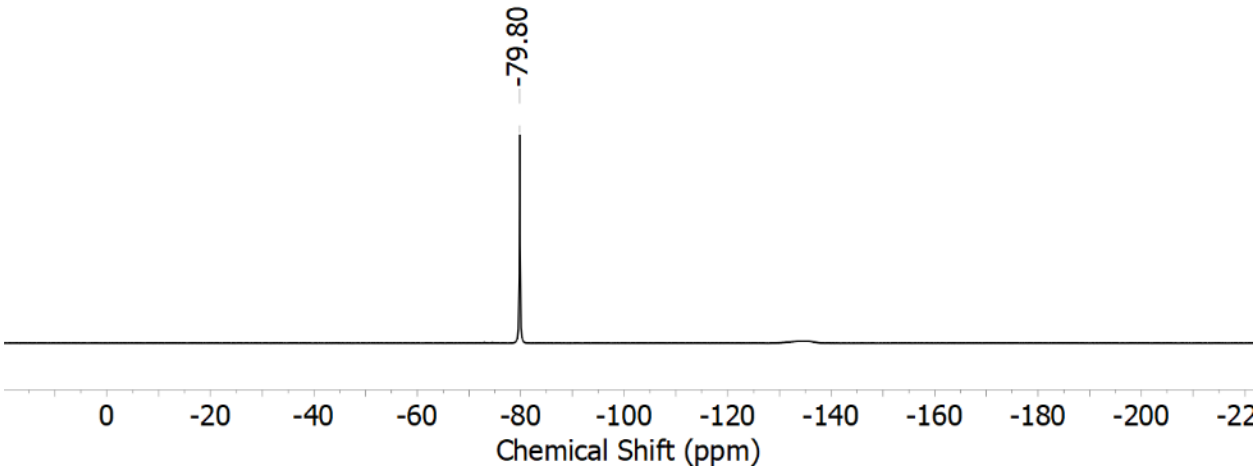

Figure B13. ^{19}F NMR spectrum (376 MHz, CD_3CN) of **L^6UO_2Nd**.

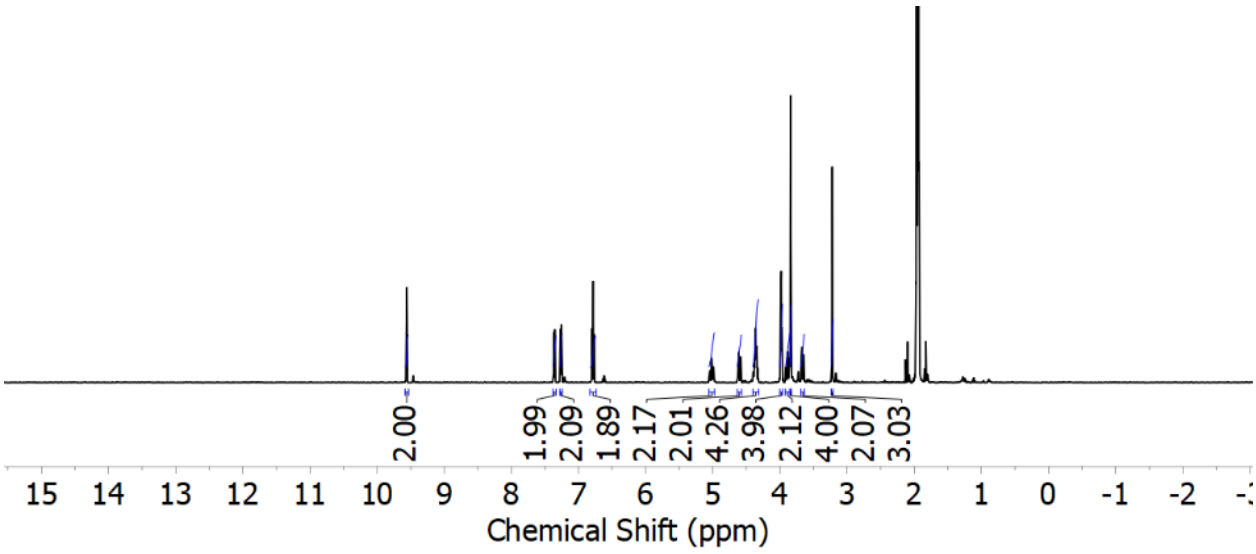

Figure B14. ^{1}H NMR spectrum (400 MHz, CD_3CN) of **L^6UO_2Y**.

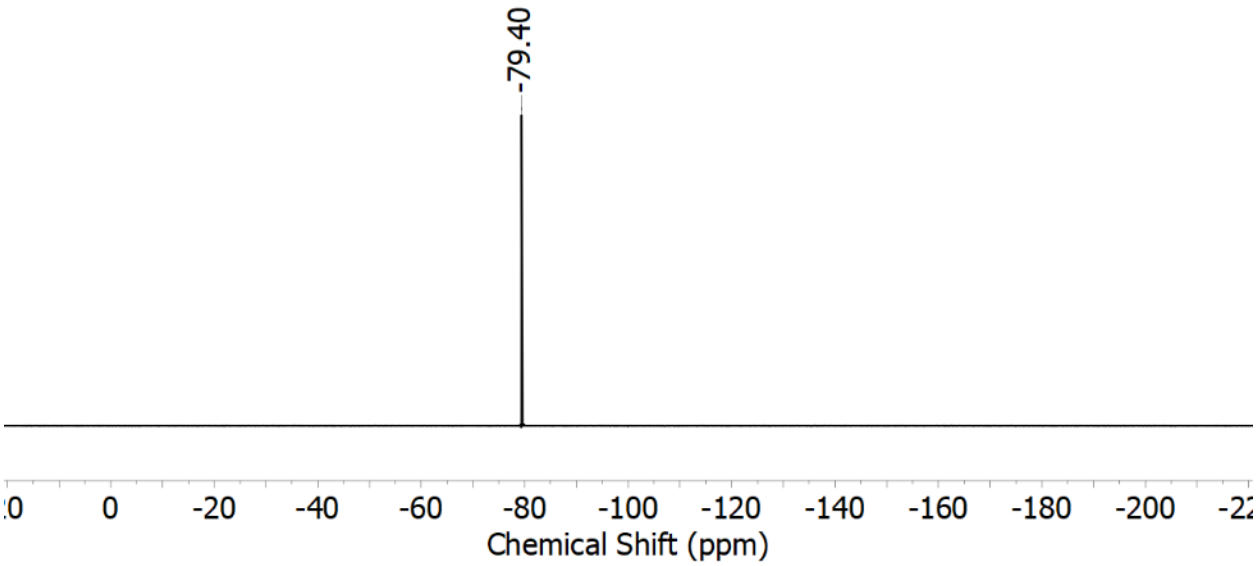

Figure B15. ^{19}F NMR spectrum (376 MHz, CD_3CN) of **L^6UO_2Y**.

Features of the uranyl (UO_2^{2+}) containing complexes

These complexes are only slightly soluble in common solvents such as CH_3CN and THF which precludes collection of conclusive $^{13}C\{^1H\}$ NMR. Furthermore, as observed in crystallographic data (Figures B51 and B58), there are two possible orientations of the trialkyl amine bridge that forms a portion of the pentadentate site for uranyl binding. Upon binding of Lewis acids in the crown ether cavity, distortion and anticipated rigidification of the trialkyl amine bridge gives rise to a uniform set of small satellite peaks (corresponding to ca. 10% population) associated with the minor isomer (Figures B8, B10 and B14). Additionally, we find all the compounds must be handled under dry inert atmosphere likely due to both the high Lewis acidity of the redox-inactive cations as well as the strongly Lewis acidic nature of the UO_2^{2+} (pK_a = 5.8) itself.[1]

Electronic Absorption Spectra

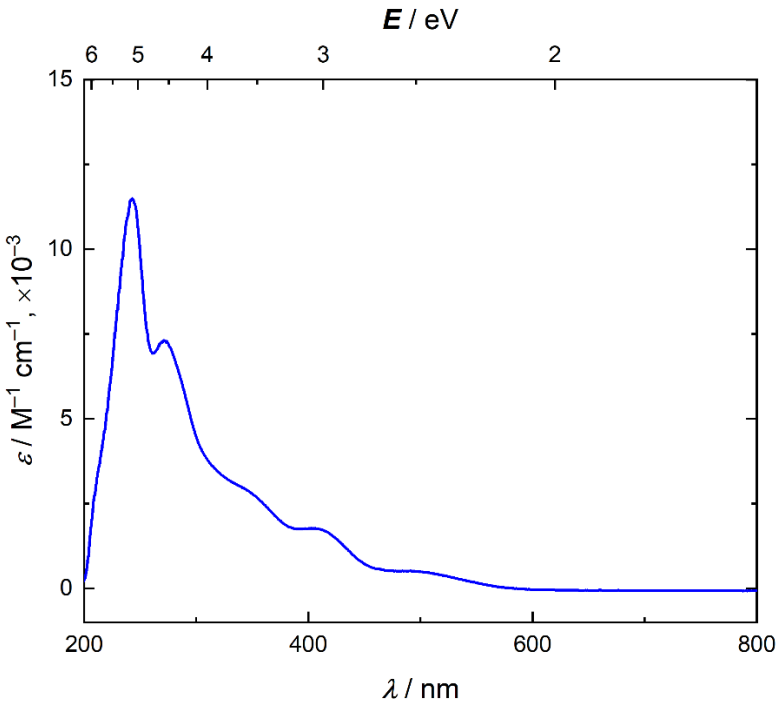

Figure B16. Electronic absorption spectrum of **L^6UO_2** in CH_3CN.

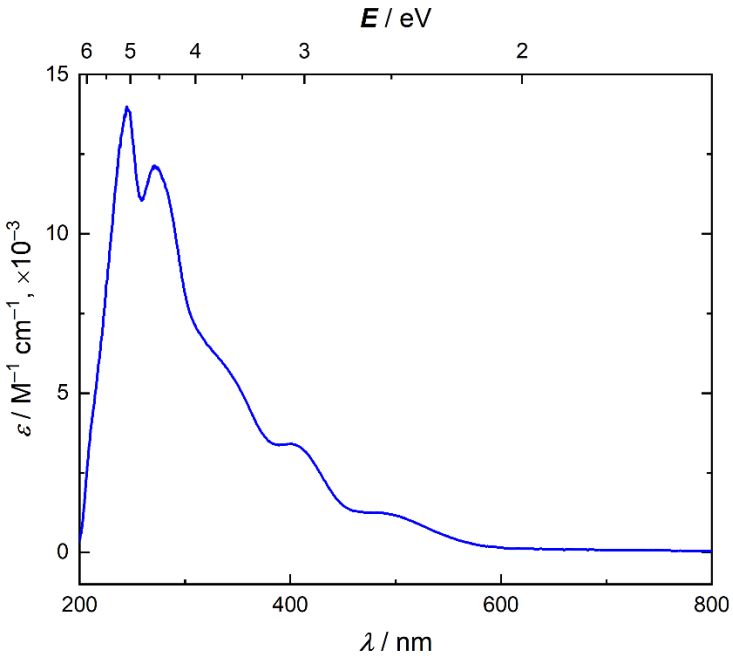

Figure B17. Electronic absorption spectrum of **L^6UO_2K** in CH_3CN.

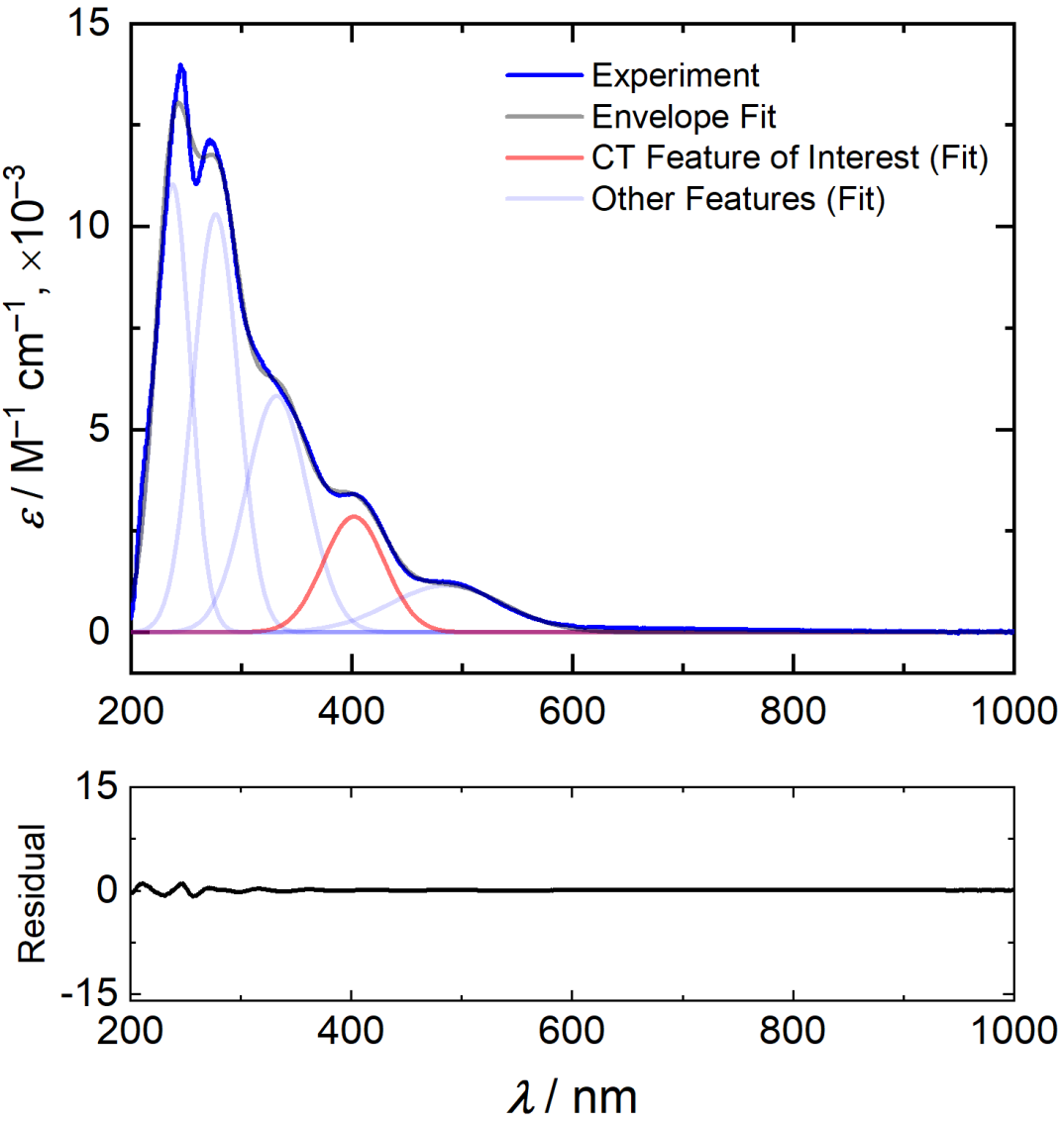

Figure B18. Peak Deconvolution of the Electronic absorption spectrum of **L^6UO_2K** in CH_3CN using Gaussian fit method. The trace in red displays the charge transfer (CT) band of interest which was used to get the λ_{max} value.

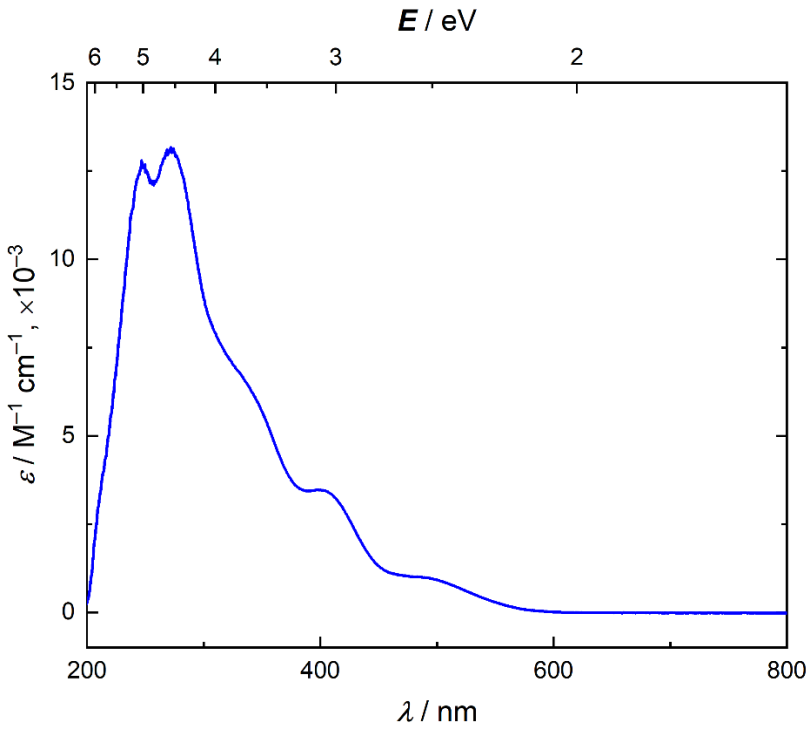

Figure B19. Electronic absorption spectrum of **L^6UO_2Na** in CH_3CN.

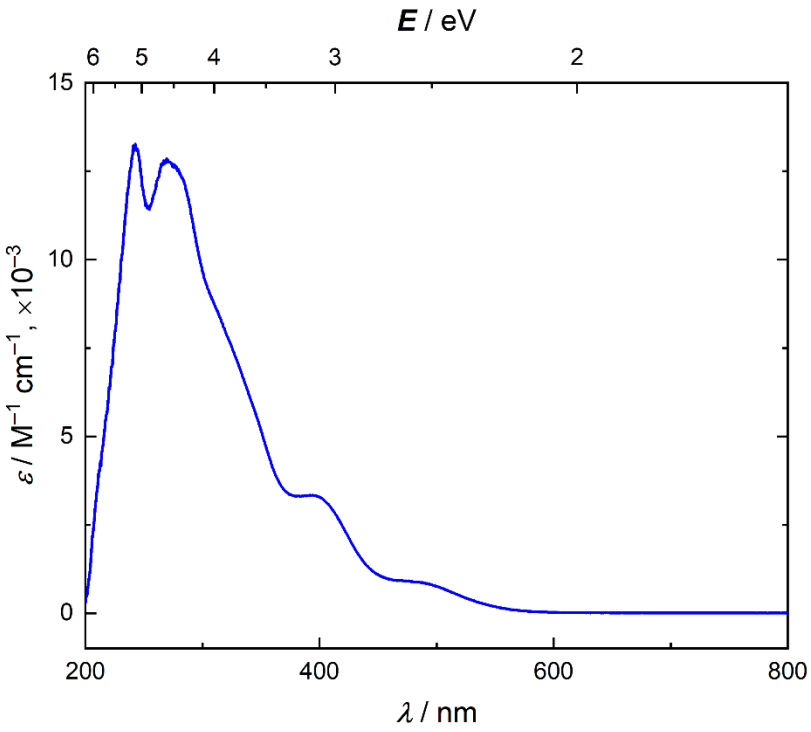

Figure B20. Electronic absorption spectrum of **L^6UO_2Ca** in CH_3CN.

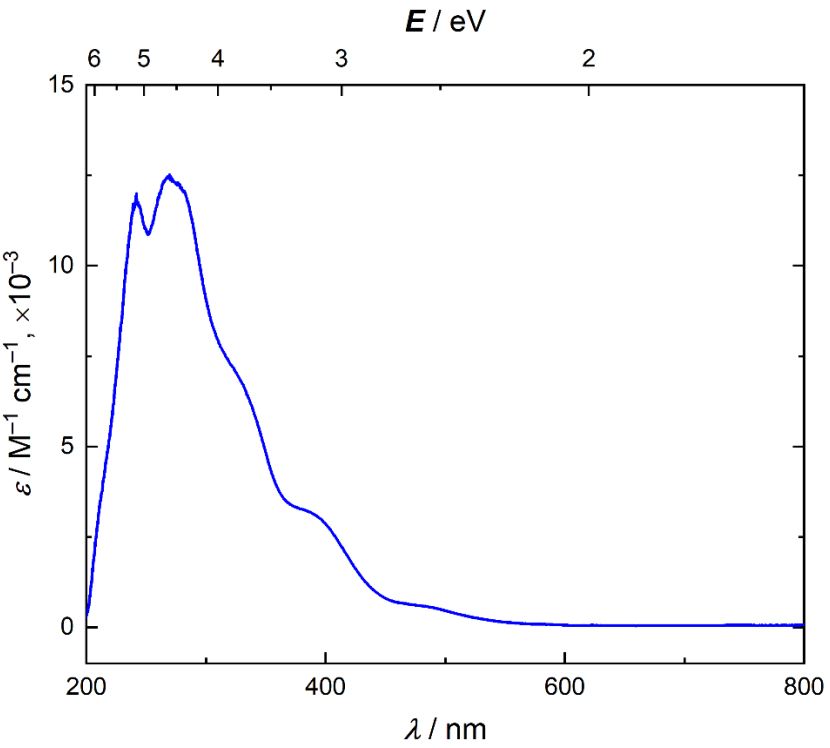

Figure B21. Electronic absorption spectrum of **L^6UO_2Nd** in CH_3CN

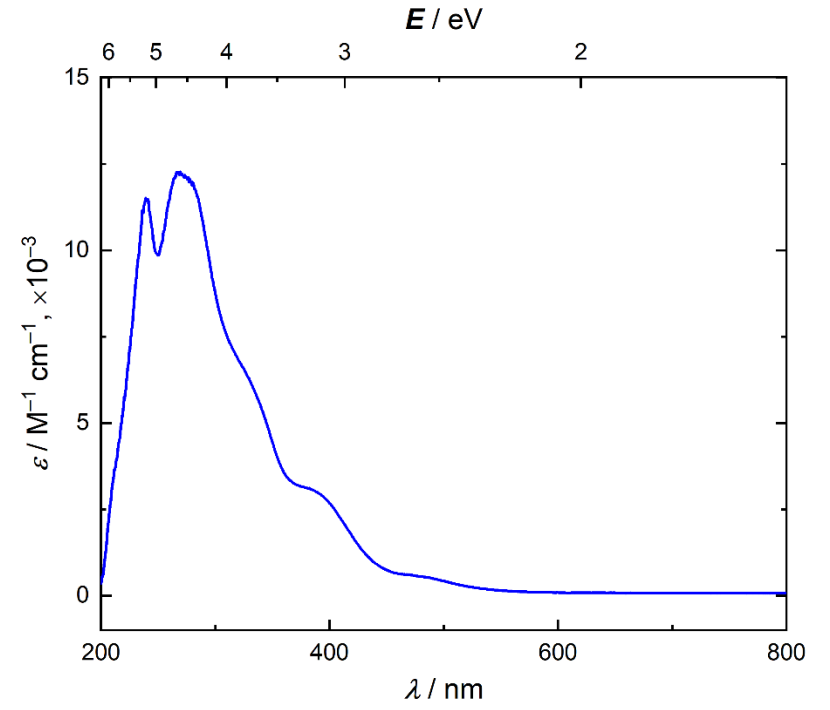

Figure B22. Electronic absorption spectrum of **L^6UO_2Y** in CH_3CN

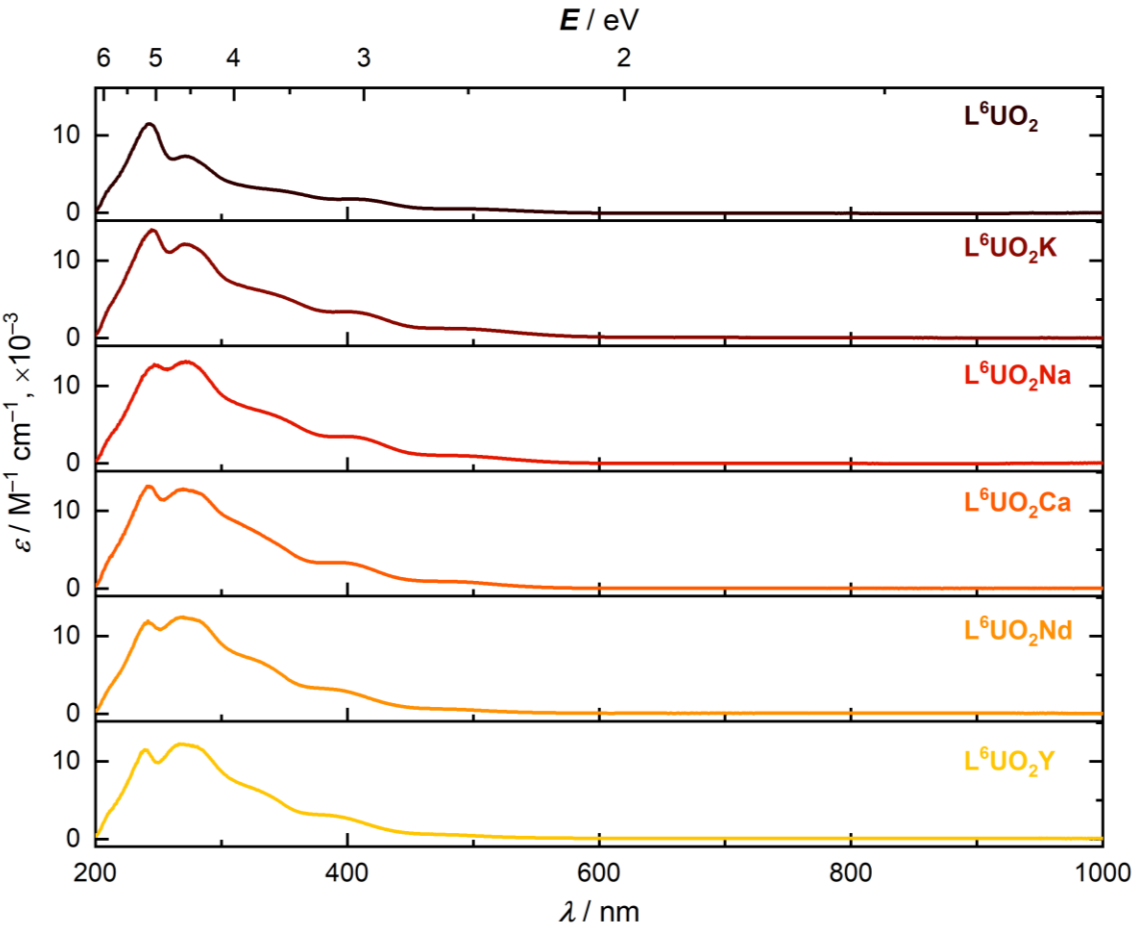

Figure B23. Stacked electronic absorption spectra of the **L^{6}UO$_2$** and **L^{6}UO$_2$M** complexes focusing on π-π* transitions.

Electrochemistry

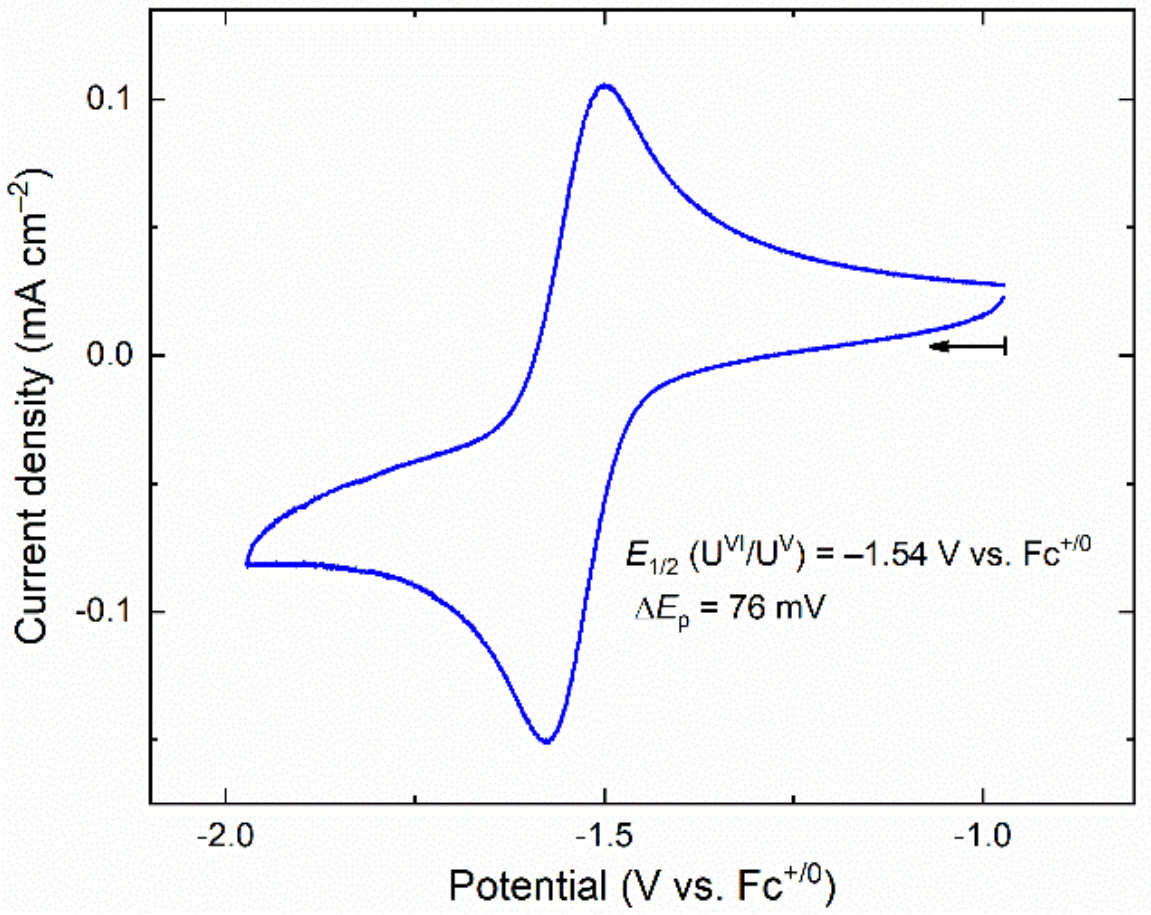

Figure B24. CV data for **L^6UO_2** in CH_3CN (0.1 M $[^nBu_4N]^+[PF_6]^-$, 100 mV/s).

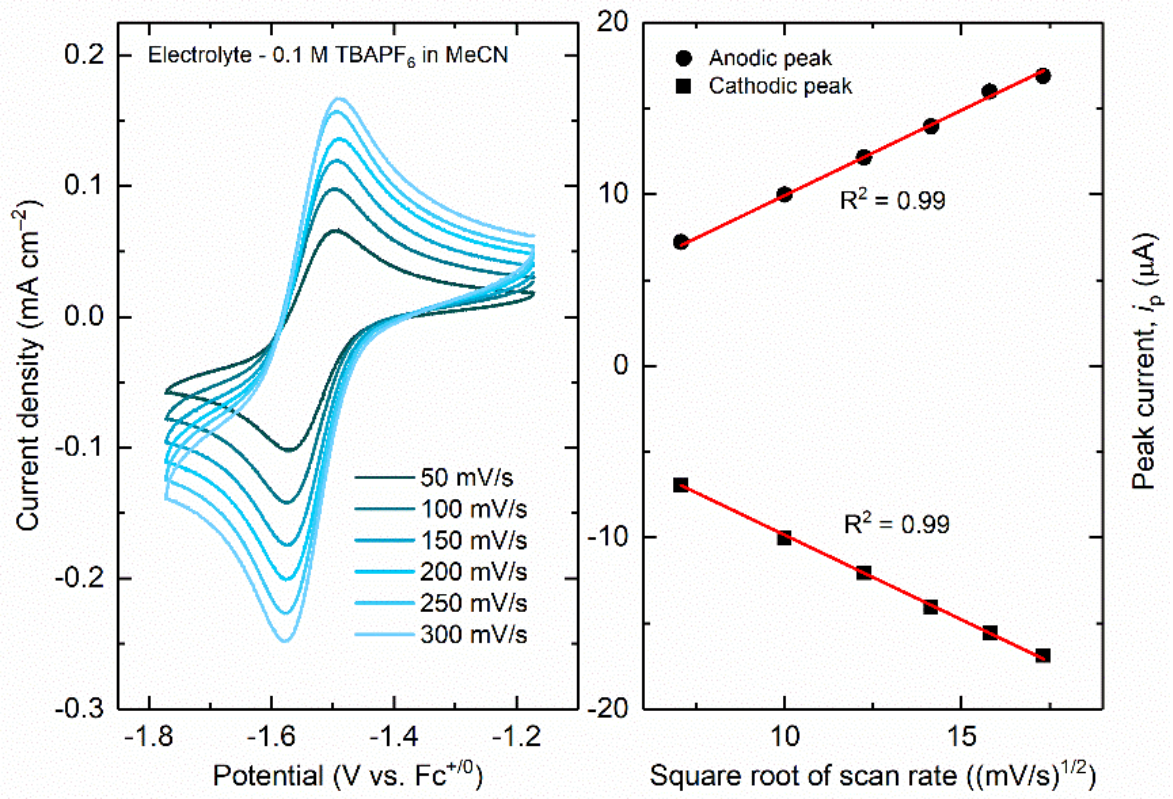

Figure B25. Left panel: scan rate dependence data for $\mathbf{L^6UO_2}$. Right panel: plot of peak current density vs. (scan rate)$^{1/2}$, demonstrating the diffusional nature of the oxidized and reduced species involved in the redox couple in question.

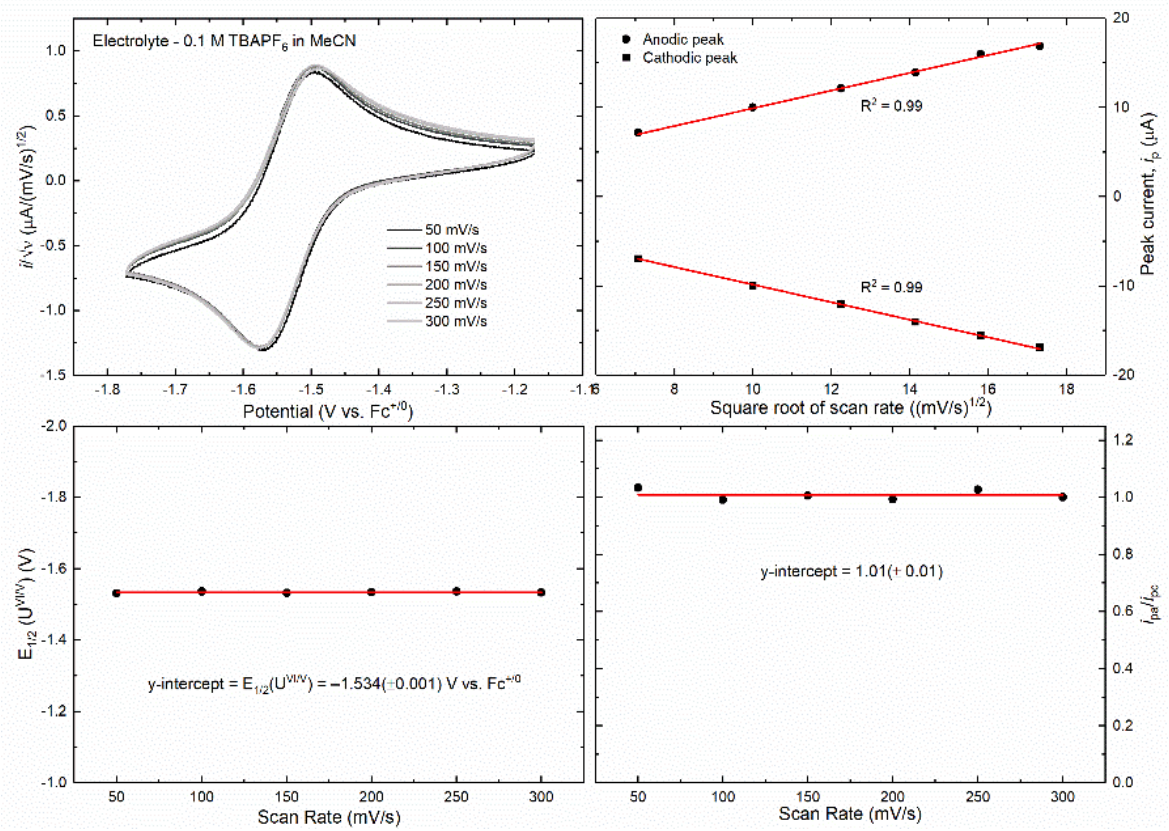

Figure B26. Analysis of electrochemical data confirming chemical reversibility of reduction of $\mathbf{L^6UO_2}$. The chemically reversible nature of electron transfer to this compound is confirmed[2] by the scan rate-independent $E_{1/2}$ value (lower left panel) as well as the scan rate-independent ratio of anodic to cathodic peak currents equal to 1.01(±0.01) (lower right panel). This ratio indicates that electrochemically generated U^V is recollected to regenerate the U^{VI} starting complex with unity efficiency. These data were tabulated from background corrected current-voltage curves derived from a spline-fit procedure available in the literature[3] which approximates the current-time (Cottrell-like) behavior of a diffusional process in cyclic voltammetry.[4] These spline background-corrected data also effectively remove contributions from non-Faradaic currents at higher scan rate with the result that current-voltage curves normalized by the square root of scan rate overlap with high similarity (upper left panel). Consequently, the spline background-corrected anodic and cathodic peak currents tightly obey the expected dependence on the square root of scan rate required by the Randles-Ševčik equation for freely diffusing species (upper right panel).[5,6] This tight agreement includes the expected *y*-intercept value of 0 within the error of the data

(0.35±0.32; –0.26±0.19). As the scan rate range accessible with our working electrodes (A = 0.09 cm^2) is not especially wide, the spline background-corrected data plotted to check agreement with the Randles-Ševčik equation do not differ greatly from their non-background-corrected counterparts (Figure B23).

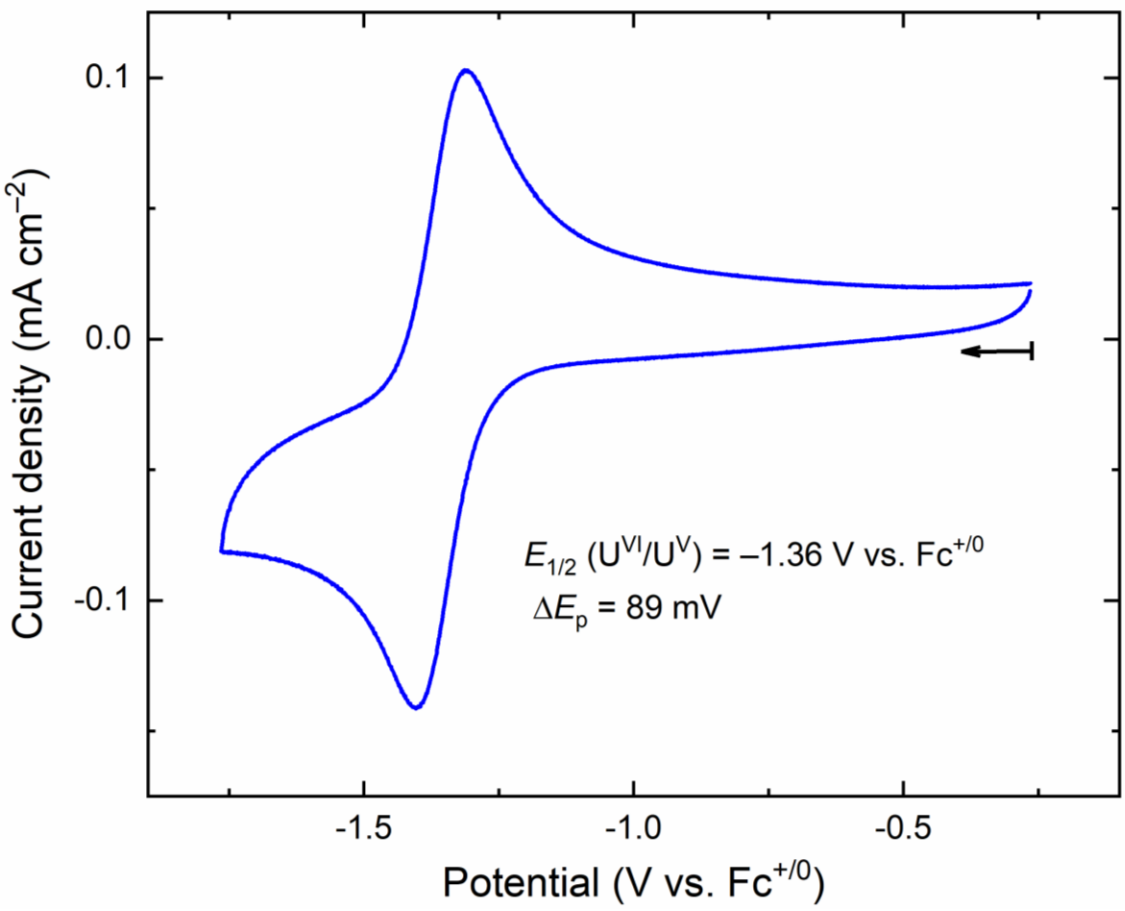

Figure B27. CV data for **L^6UO_2K** in CH_3CN (0.1 M $[^nBu_4N]^+[PF_6]^-$, 100 mV/s).

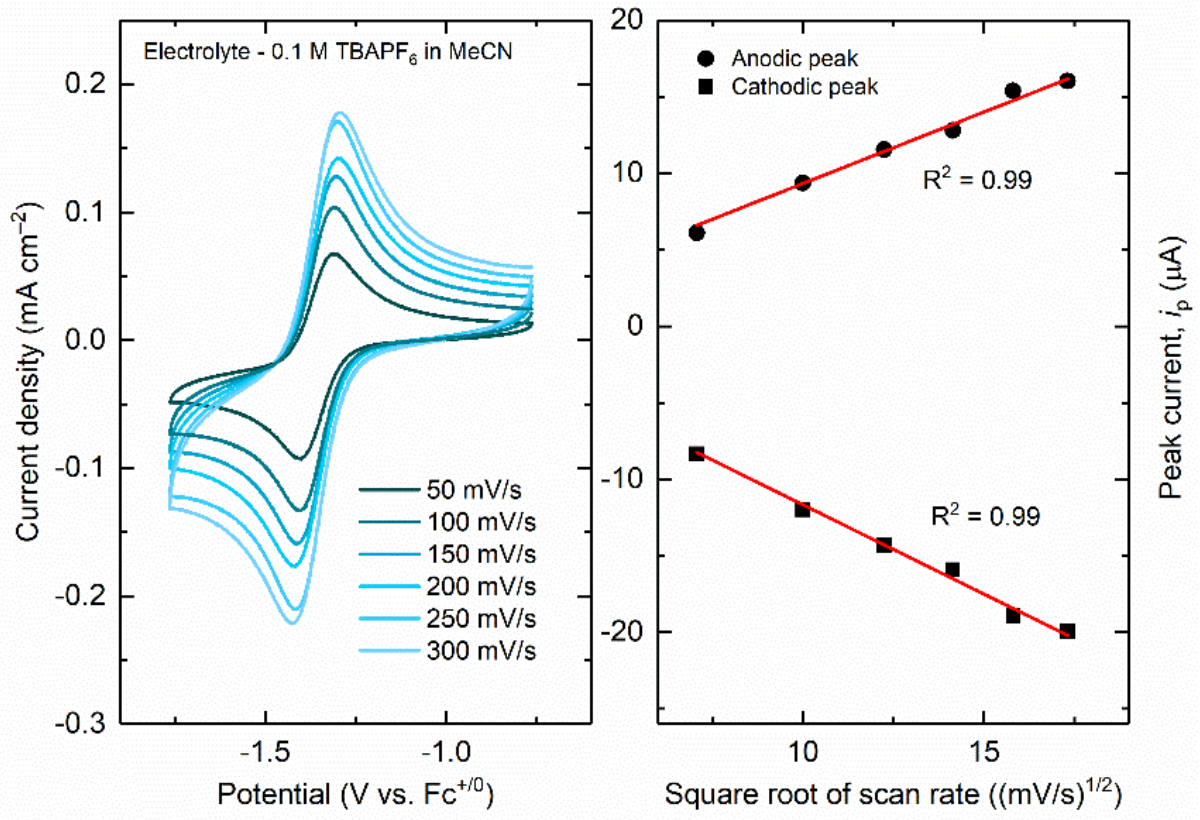

Figure B28. Left panel: scan rate dependence data for **L^{6}UO$_2$K**. Right panel: plot of peak current density vs. (scan rate)$^{1/2}$, demonstrating the diffusional nature of the oxidized and reduced species involved in the redox couple in question.

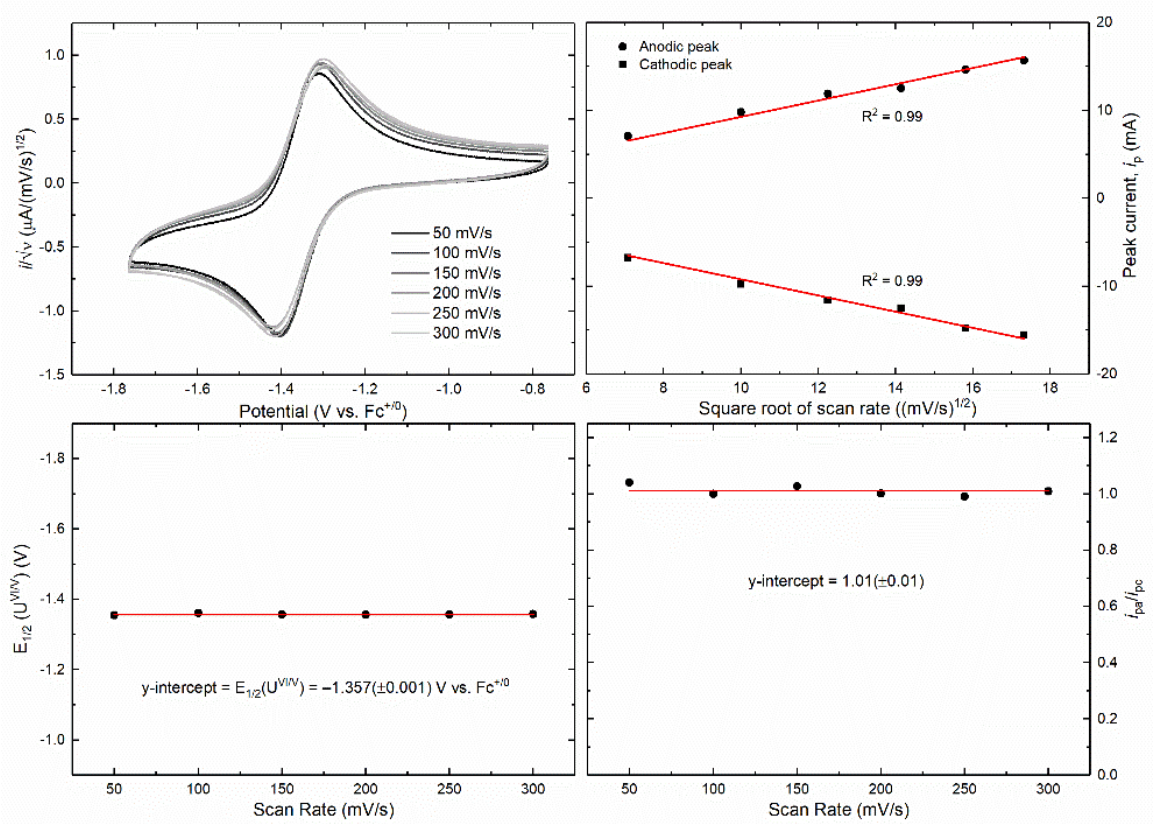

Figure B29. Analysis of electrochemical data confirming chemical reversibility of reduction of **L^{6}UO$_2$K**. The chemically reversible nature of electron transfer to this compound is confirmed[2] by the scan rate-independent $E_{1/2}$ value (lower left panel) as well as the scan rate-independent ratio of anodic to cathodic peak currents equal to 1.01(±0.01) (lower right panel). This ratio indicates that electrochemically generated U^V is recollected to regenerate the U^{VI} starting complex with unity efficiency. These data were tabulated from background corrected current-voltage curves derived from a spline-fit procedure available in the literature[3] which approximates the current-time (Cottrell-like) behavior of a diffusional process in cyclic voltammetry.[4] These spline background-corrected data also effectively remove contributions from non-Faradaic currents at higher scan rate with the result that current-voltage curves normalized by the square root of scan rate overlap with high similarity (upper left panel). Consequently, the spline background-corrected anodic and cathodic peak currents tightly obey the expected dependence on the square root of scan rate required by the Randles-Ševčik equation for freely diffusing species (upper right panel).[5,6] This tight agreement includes the expected *y*-intercept value of 0 within the error of the data

(1.39±0.58; –1.02±0.60). As the scan rate range accessible with our working electrodes (*A* = 0.09 cm^2) is not especially wide, the spline background-corrected data plotted to check agreement with the Randles-Ševčik equation do not differ greatly from their non-background-corrected counterparts (Figure B26).

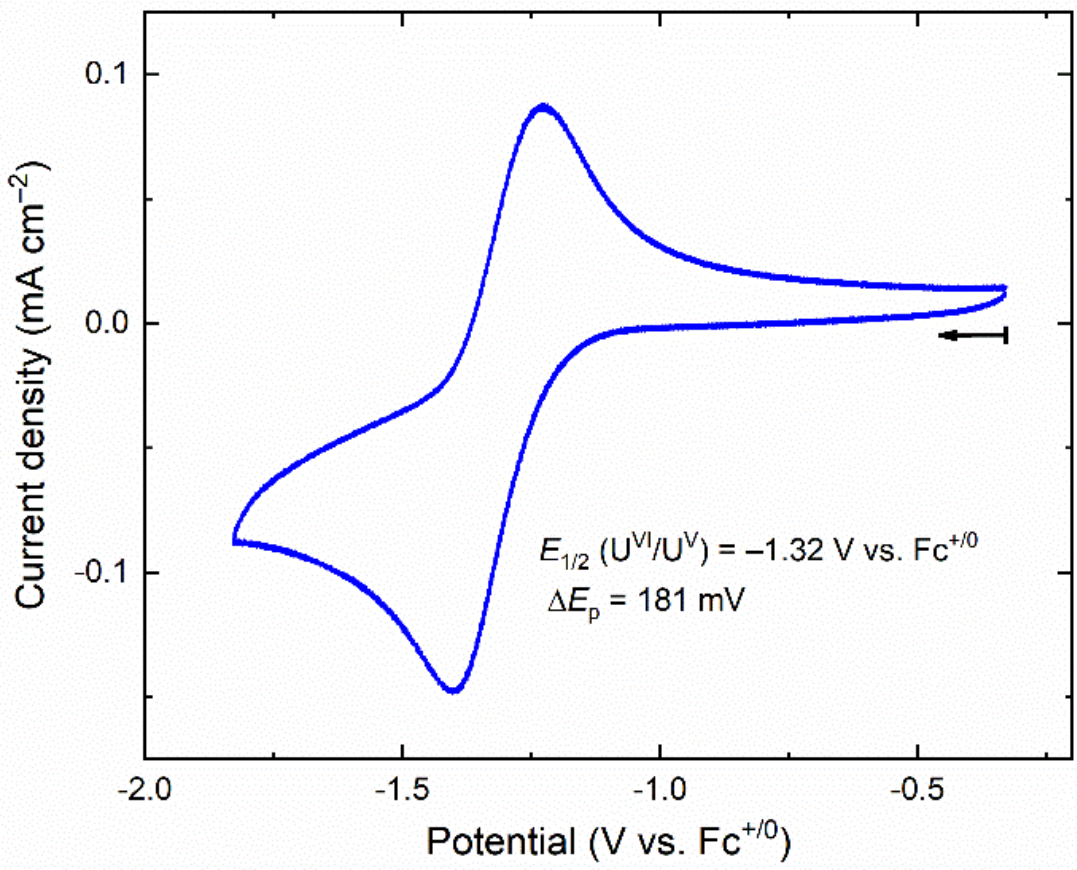

Figure B30. CV data for **L^6UO_2Na** in CH_3CN (0.1 M $[^nBu_4N]^+[PF_6]^-$, 100 mV/s) showing the 'Early' scan.

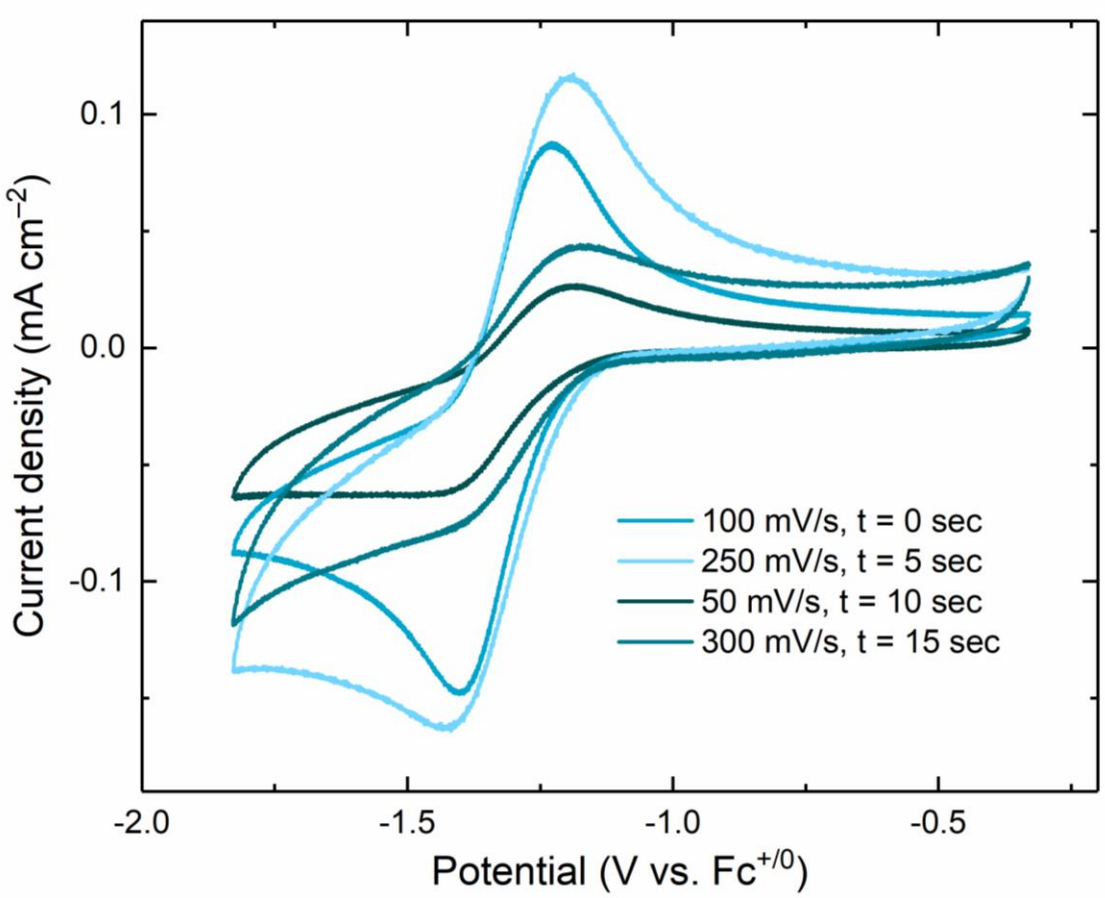

Figure B31. Scan rate dependence data for **L^6UO_2Na** showing its decomposition after multiple scans spread over ca. 30 seconds.

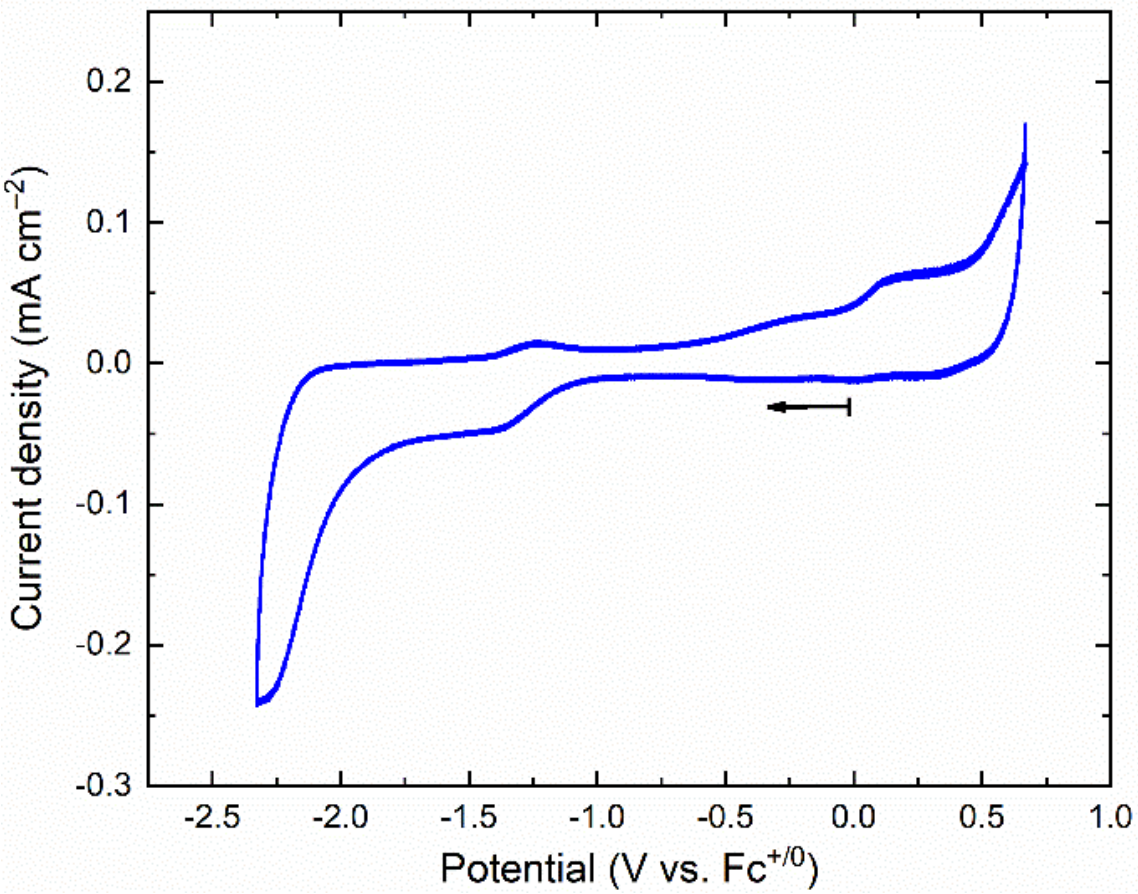

Figure B32. CV data for **L^{6}UO$_2$Na** in CH_3CN (0.1 M $[^{n}Bu_4N]^{+}[PF_6]^{-}$, 100 mV/s) showing the 'Late Scan'. The CV shows decomposition of the complex after multiple scans (ca. 20 scans over 10 minutes).

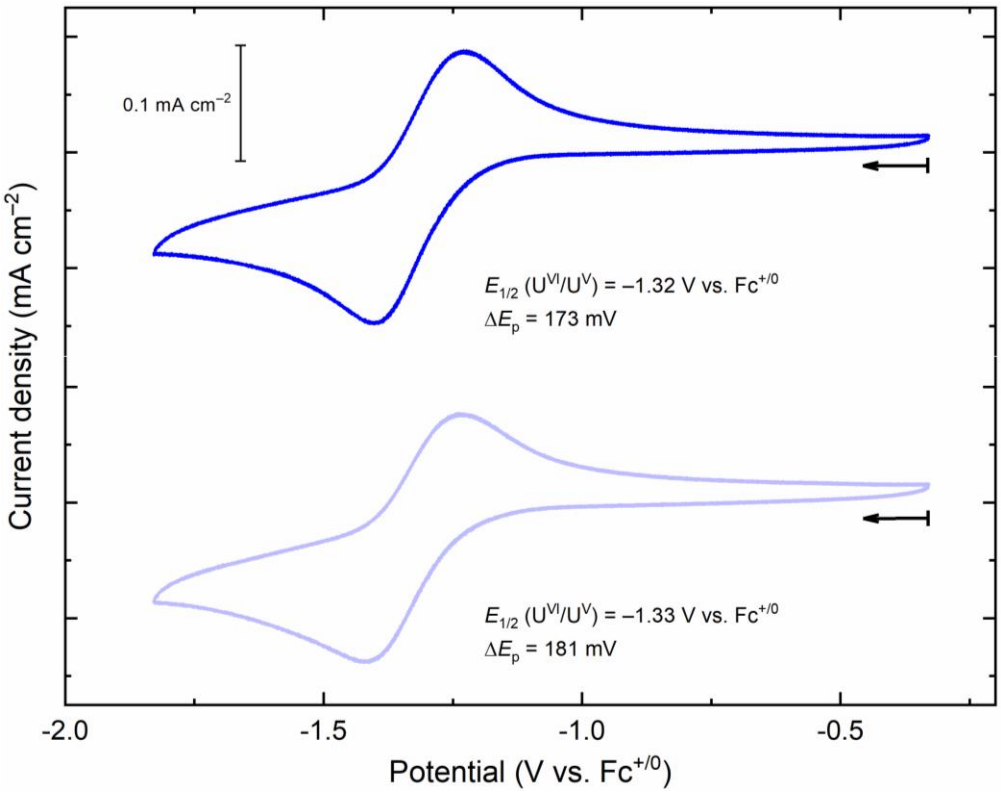

Figure B33. Cyclic voltammetry data for **L^6UO_2Na** in CH_3CN (0.1 M $[^nBu_4N]^+[PF_6]^-$, 100 mV/s) using two different electrodes.

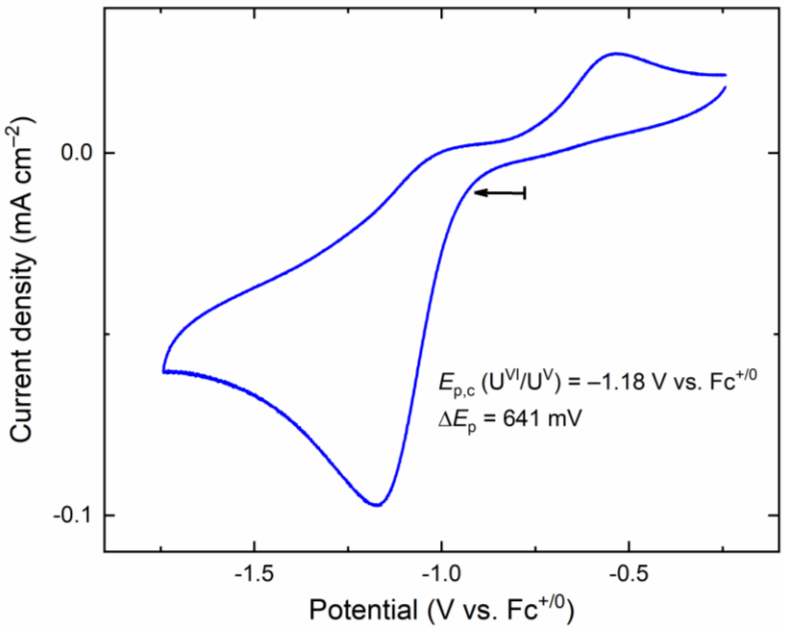

Figure B34. CV data for **L^6UO_2Ca** in CH_3CN (0.1 M $[^nBu_4N]^+[PF_6]^-$, 100 mV/s) with a smaller potential window.

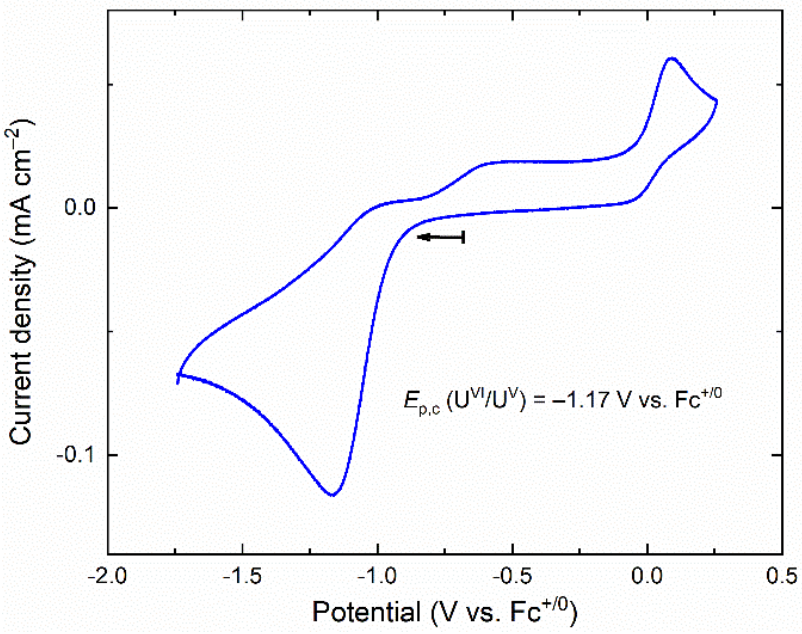

Figure B35. CV data for **L^{6}UO$_2$Ca** in CH_3CN (0.1 M [$^{n}Bu_4N$]$^{+}$[PF_6]$^{-}$, 100 mV/s) with a larger potential window.

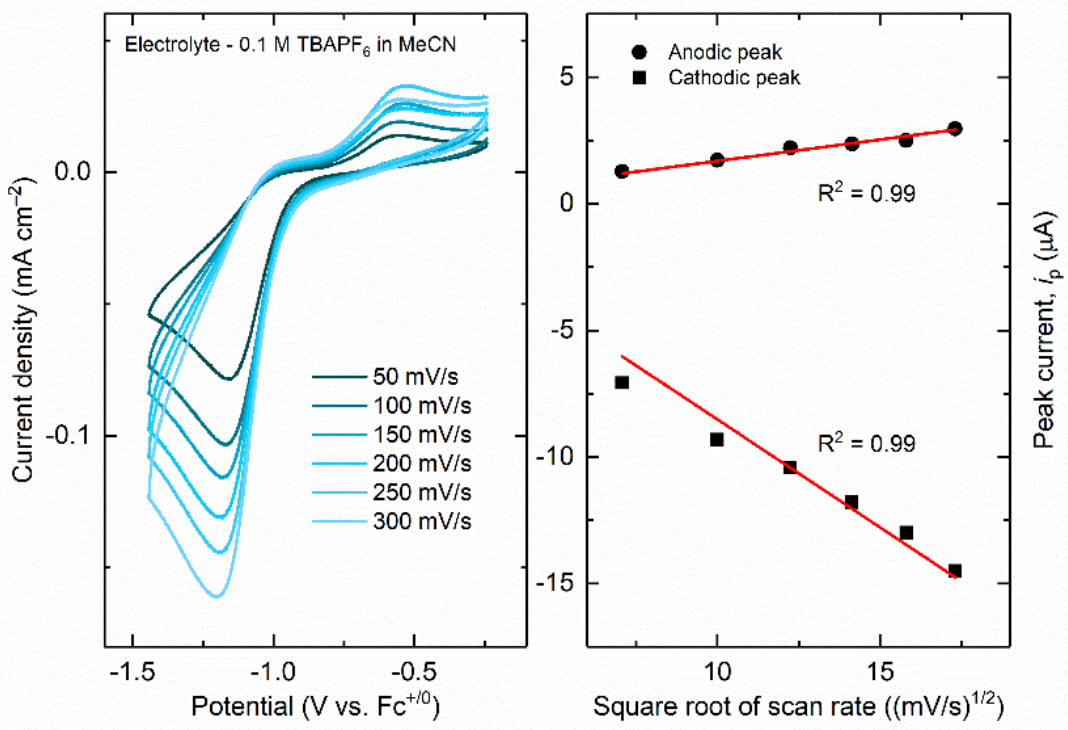

Figure B36. Left panel: scan rate dependence data for **L^{6}UO$_2$Ca**. Right panel: plot of peak current density vs. (scan rate)$^{1/2}$, demonstrating the diffusional nature of the oxidized and reduced species involved in the redox couple in question.

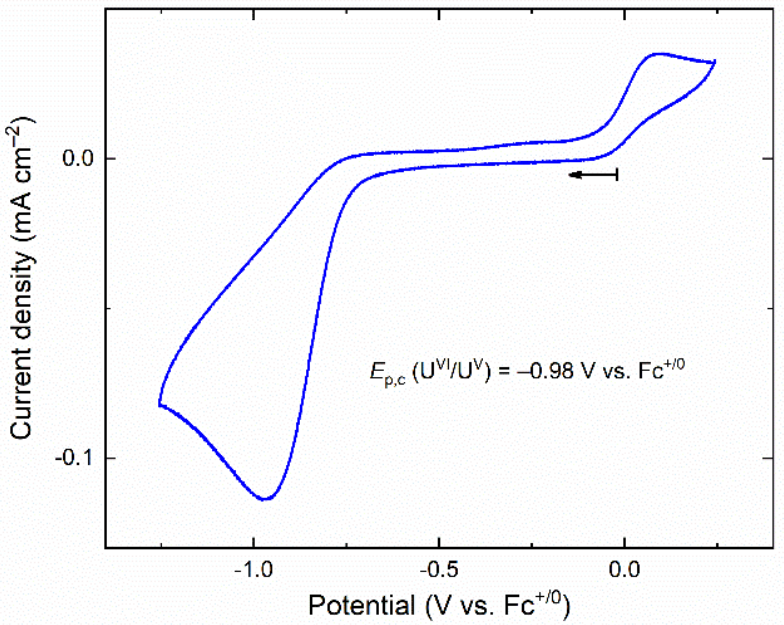

Figure B37. CV data for **L^{6}UO$_2$Nd** in CH_3CN (0.1 M [$^{n}Bu_4N$]$^{+}$[PF_6]$^{-}$, 100 mV/s).

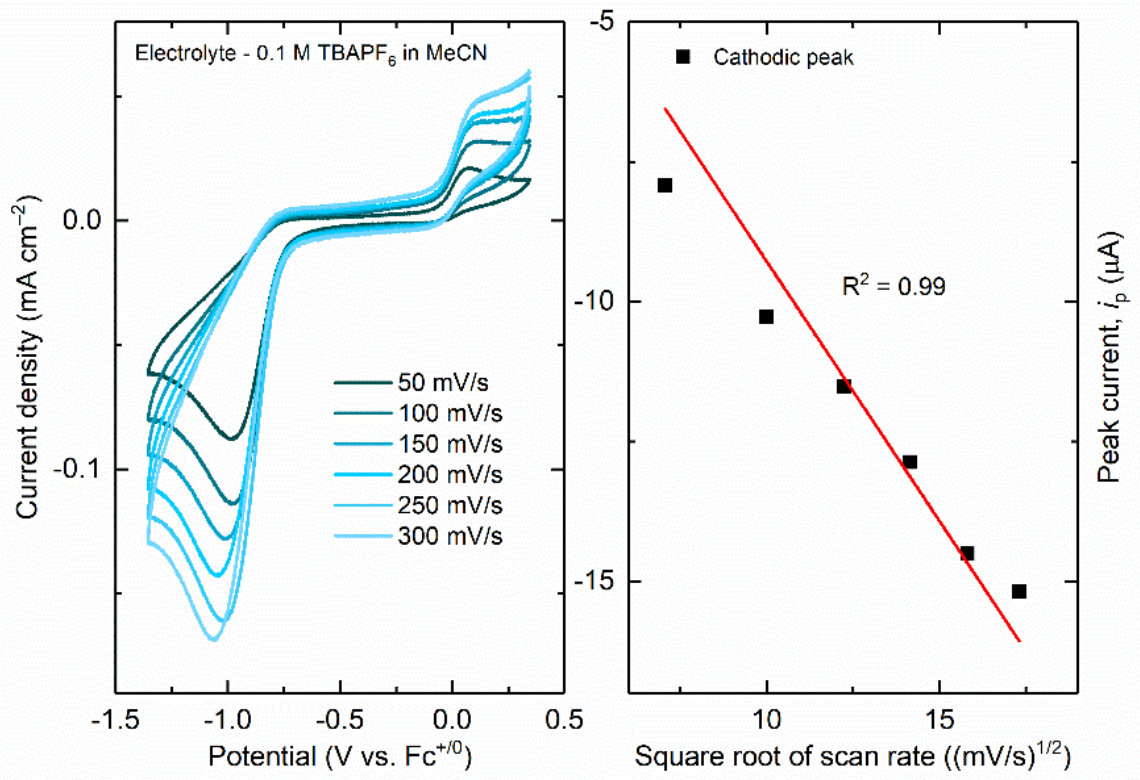

Figure B38. Left panel: scan rate dependence data for **L^{6}UO$_2$Nd**. Right panel: plot of peak current density vs. (scan rate)$^{1/2}$, demonstrating the diffusional nature of the reduced species involved in the redox couple in question.

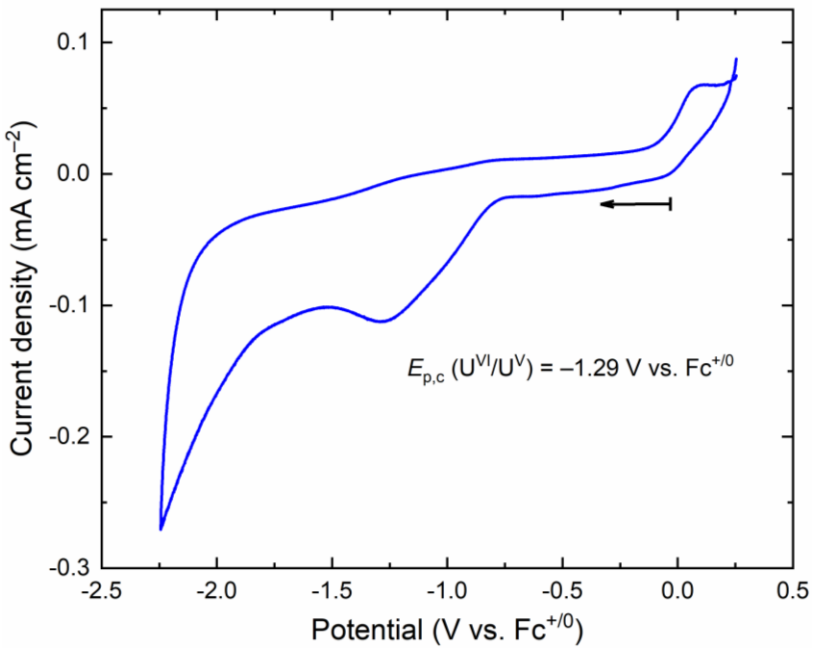

Figure B39. CV data for **L^{6}UO$_2$Y** in CH_3CN (0.1 M $[^{n}Bu_4N]^{+}[PF_6]^{-}$, 100 mV/s).

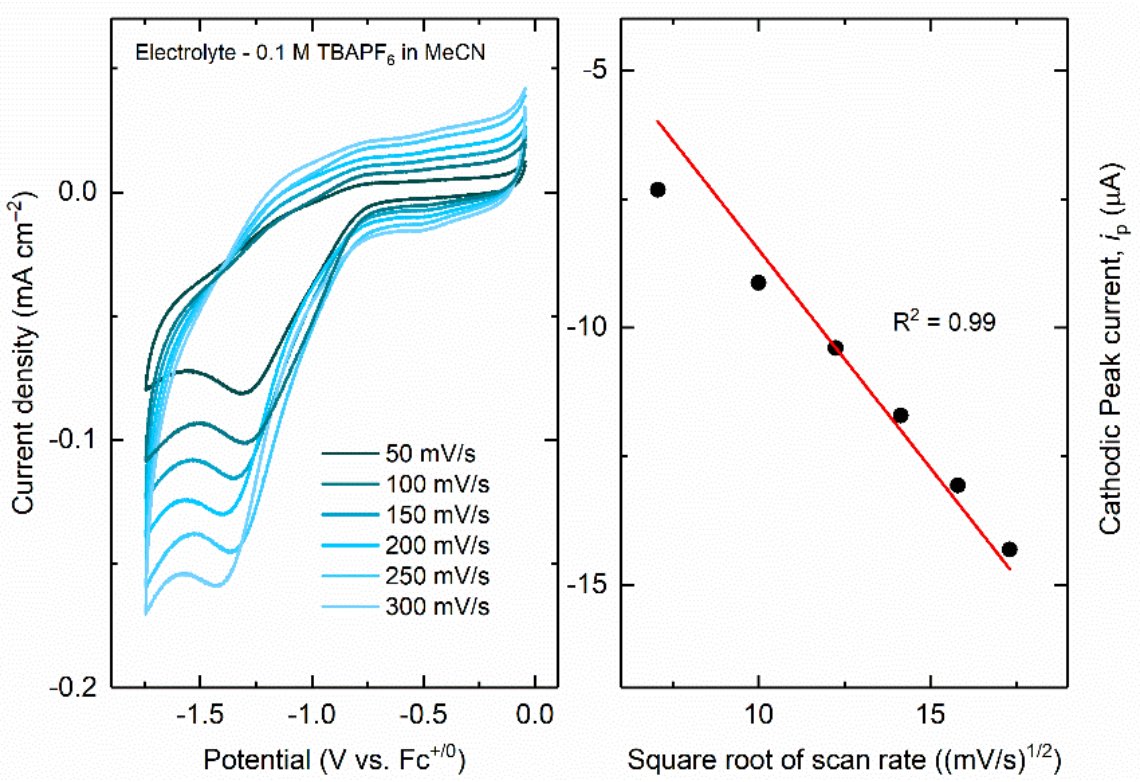

Figure B40. Left panel: scan rate dependence data for **L^{6}UO$_2$Y**. Right panel: plot of peak current density vs. (scan rate)$^{1/2}$, demonstrating the diffusional nature of the reduced species involved in the redox couple in question.

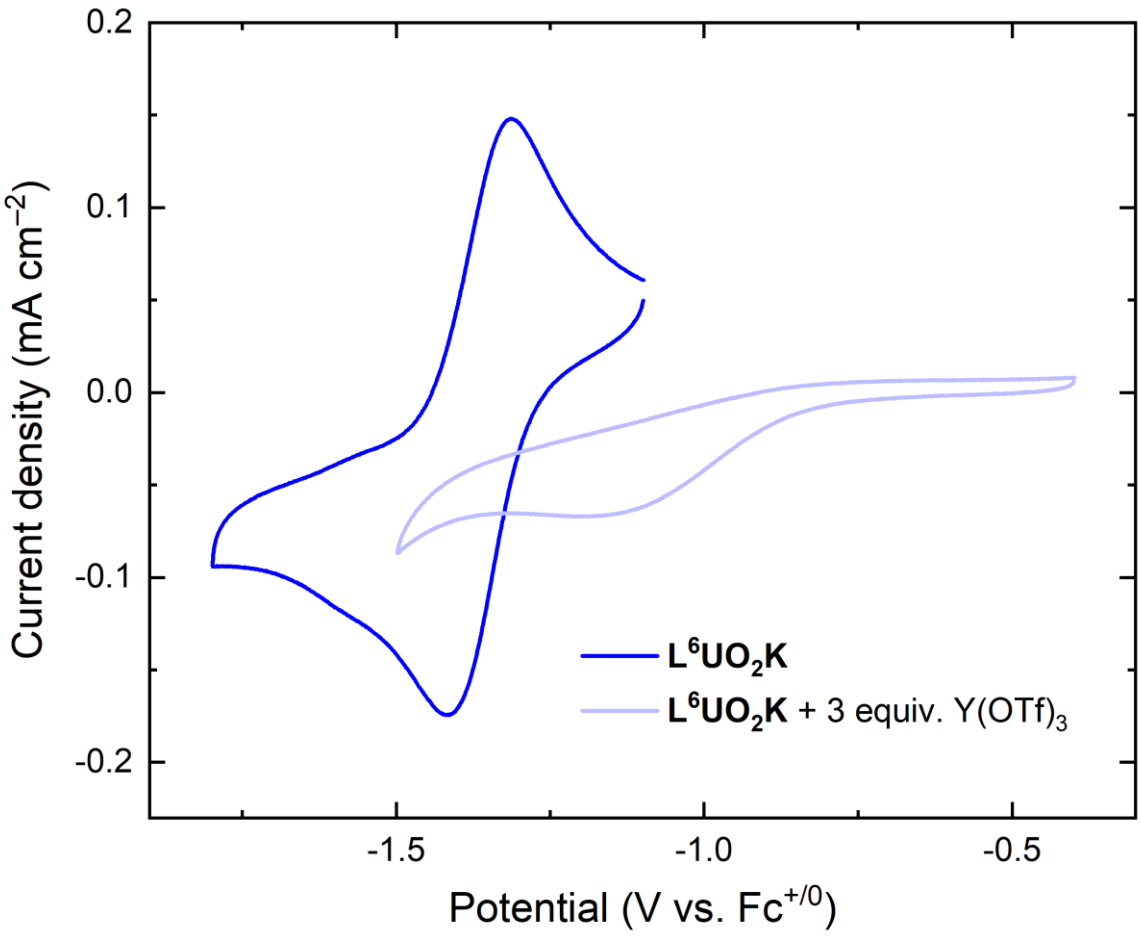

Figure B41. Plot showing variations in the cyclic voltammetry data of **L^{6}UO$_2$K** after addition of 3 equivalents of Y(OTf)$_3$ to the working solution. Conditions: CH_3CN (0.1 M $[^nBu_4N]^+[PF_6]^-$, 100 mV/s).

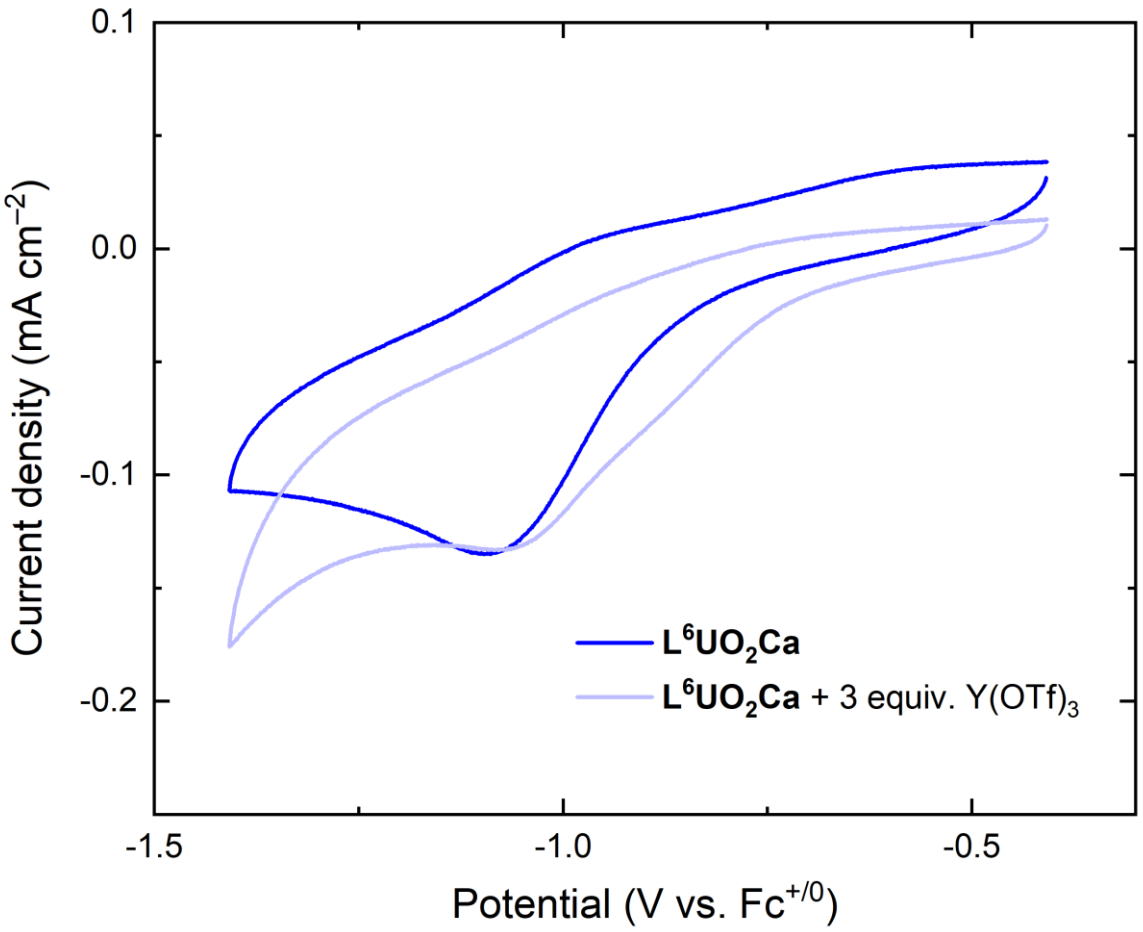

Figure B42. Plot showing small variations in the cyclic voltammetry data of **L^{6}UO$_2$Ca** after addition of 3 equivalents of Y(OTf)$_3$ to the working solution. Conditions: CH_3CN (0.1 M $[^nBu_4N]^+[PF_6]^-$, 100 mV/s).

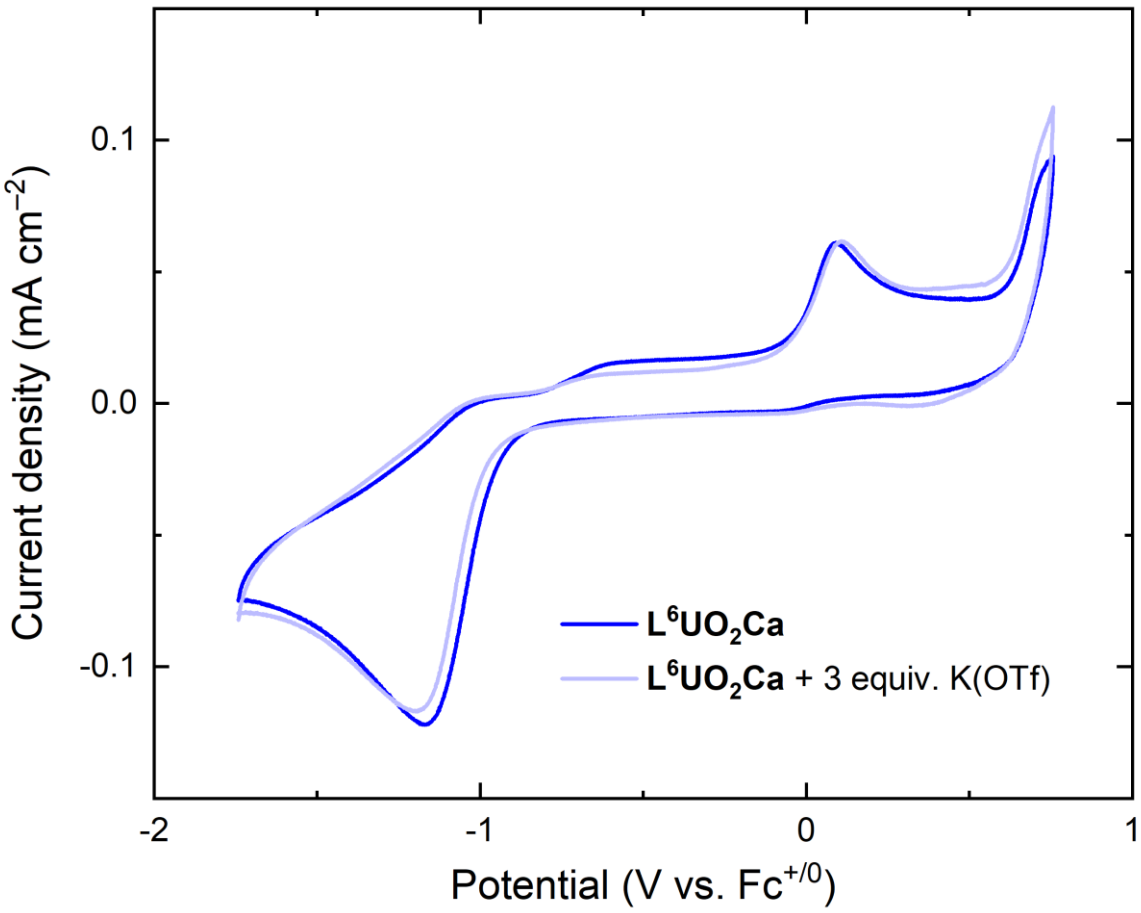

Figure B43. Plot showing negligible change in the cyclic voltammetry data of **L^{6}UO$_2$Ca** after addition of 3 equivalents of K(OTf) to the working solution. Conditions: CH_3CN (0.1 M $[^nBu_4N]^+[PF_6]^-$, 100 mV/s).

Spectroelectrochemistry

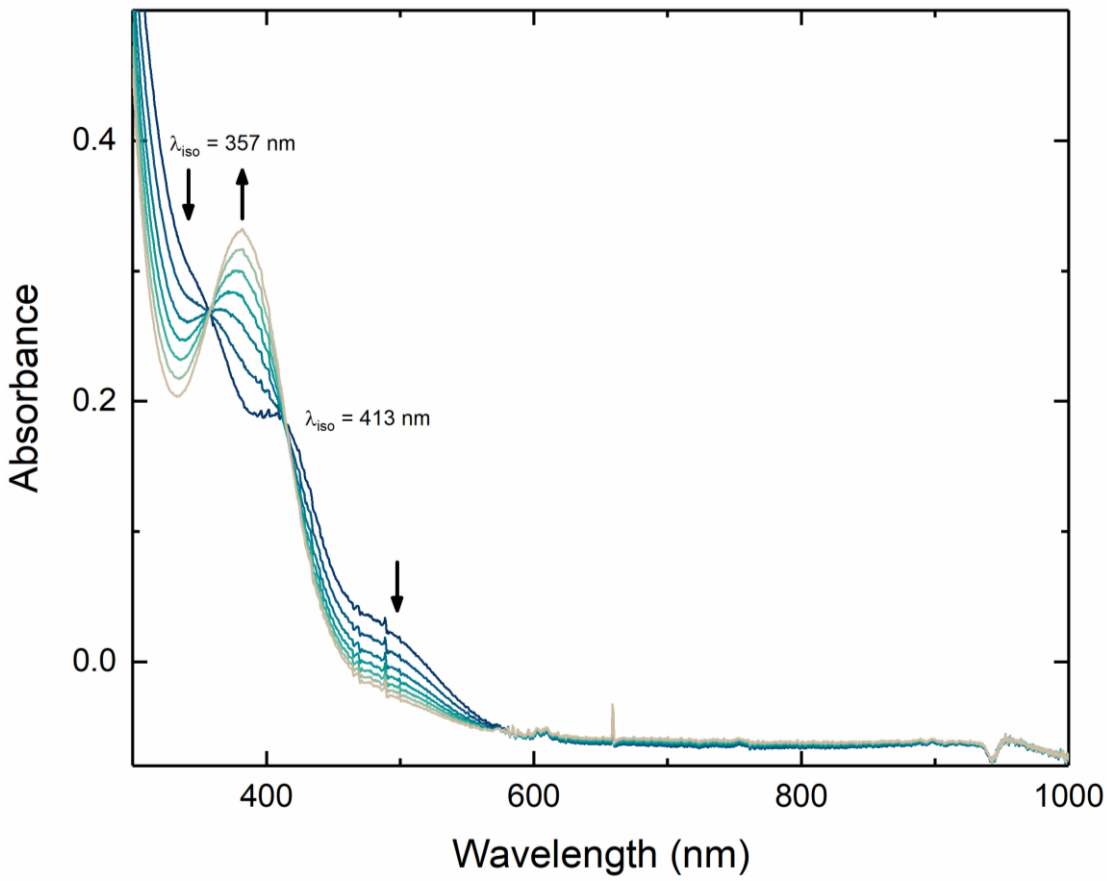

Figure B44. Spectroelectrochemical data for the electrolysis of $\mathbf{L^6U^{VI}O_2}$ over a period of 5 minutes. Step potential for generation of $\mathbf{L^6U^{V}O_2}$ was −1.2 V vs. reference. Electrolyte: 0.1 M $[^nBu_4N]^+[PF_6]^-$ in DMF.

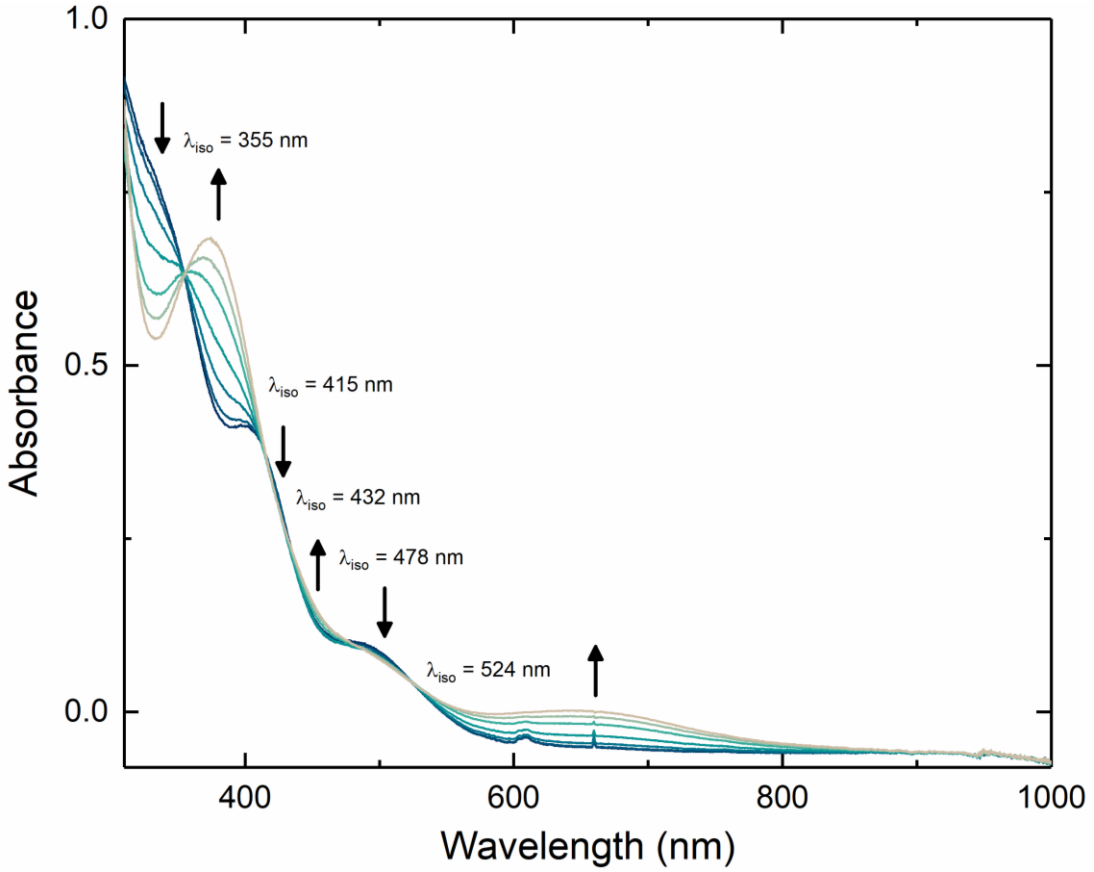

Figure B45. Spectroelectrochemical data for the electrolysis of $\mathbf{L^6U^{VI}O_2K}$ over a period of 6 minutes. Step potential for generation of $\mathbf{L^6U^{V}O_2K}$ was −3.0 V vs. reference. Electrolyte: 0.1 M $[^{n}Bu_4N]^{+}[PF_6]^{-}$ in CH_3CN.

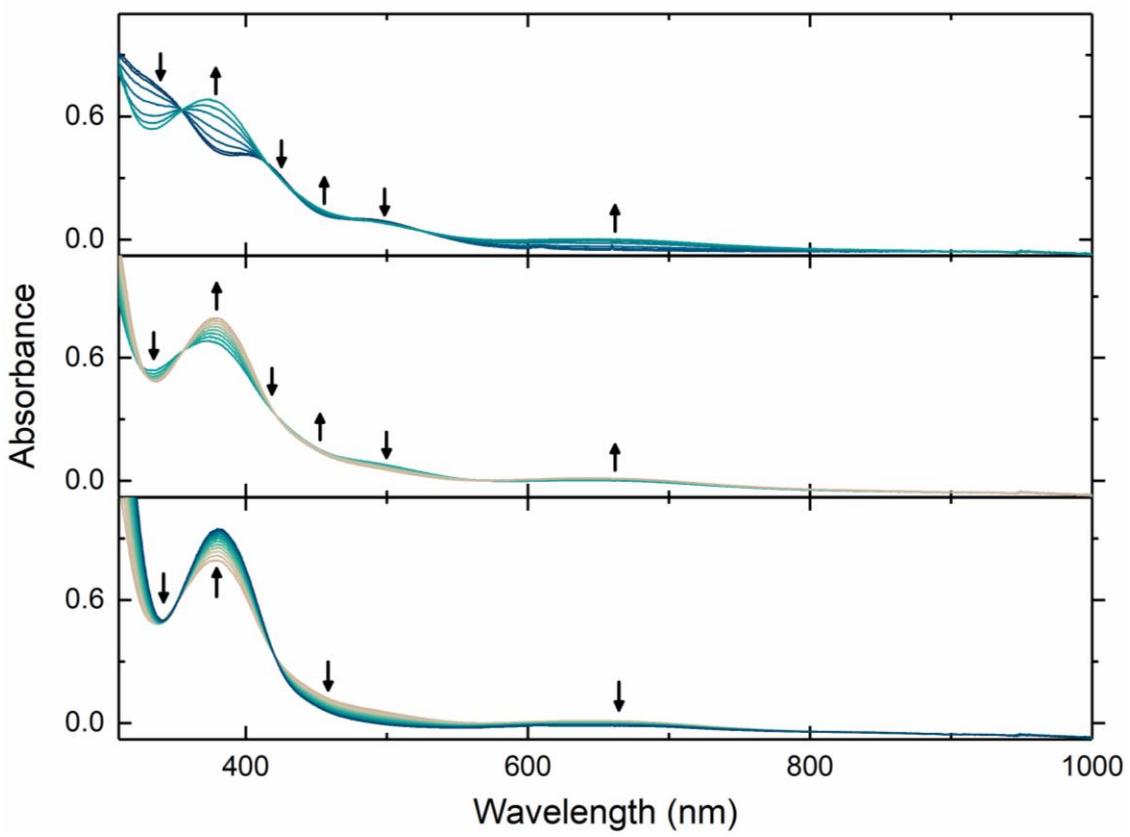

Figure B46. Stacked spectroelectrochemical data (full region) for the electrolysis of $\mathbf{L^6U^{VI}O_2K}$ showing changes over a period of 23 minutes. **Top**: t = 0 min to t = 6 min; **Middle**: t = 6 min to t = 10 min; **Bottom**: t = 6 min to t = 23 min. Step potential for generation of $\mathbf{L^6U^{V}O_2K}$ was −3.0 V vs. reference. Electrolyte: 0.1 M $[^{n}Bu_4N]^{+}[PF_6]^{-}$ in CH_3CN.

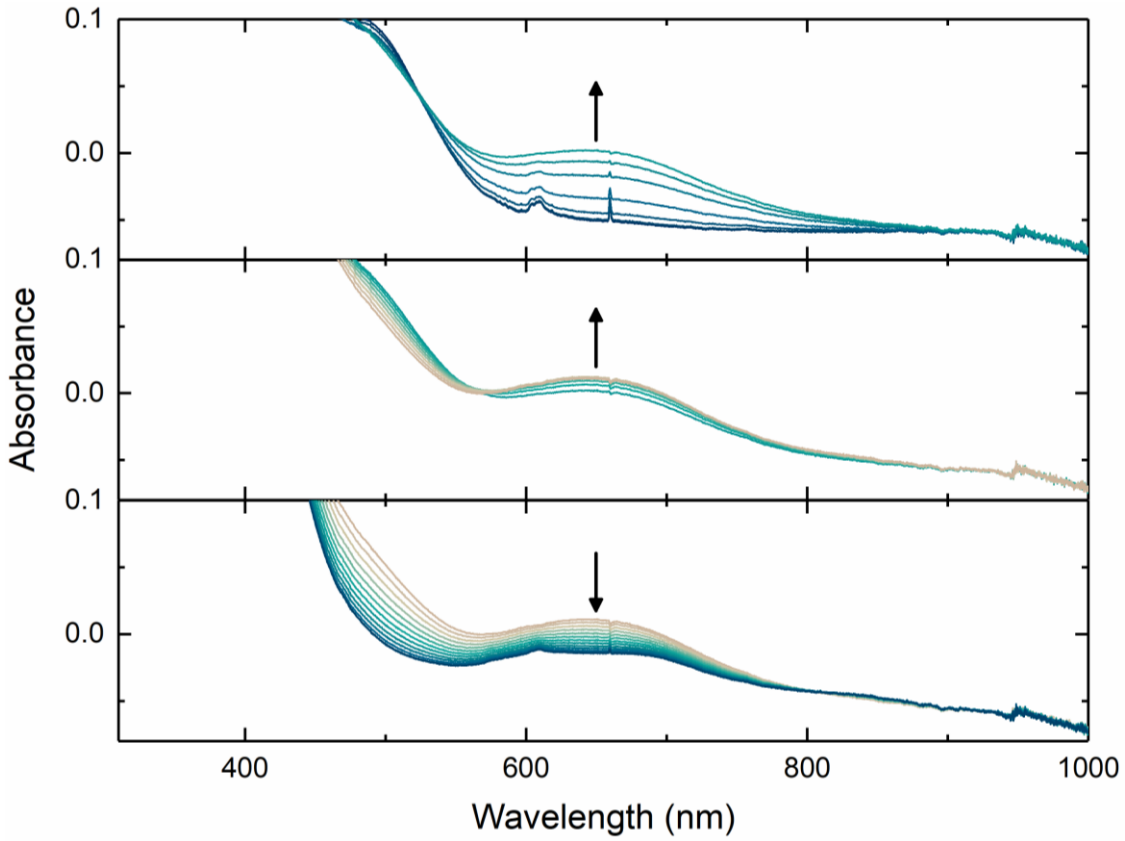

Figure B47. Stacked spectroelectrochemical data (small region) for the electrolysis of **$L^6U^{VI}O_2K$** showing changes over a period of 23 minutes. **Top**: t = 0 min to t = 6 min; **Middle**: t = 6 min to t = 10 min; **Bottom**: t = 6 min to t = 23 min. Step potential for generation of **$L^6U^{V}O_2K$** was −3.0 V vs. reference. Electrolyte: 0.1 M $[^nBu_4N]^+[PF_6]^-$ in CH_3CN.

X-Ray Crystallography

All crystals were mounted in Paratone oil on MiTeGen MicroMounts and complete sets of low temperature (200 K) diffraction data frames were collected using 1˚-wide ω- or φ-scans with a dual CCD detector Bruker Proteum X-ray diffractometer. X-rays were provided by a Bruker MicroStar microfocus rotating anode generator running at 45 mA and 60 kV (Cu K_α = 1.54178 Å). Data for **L^6UO_2Na** and **L^6UO_2Y** were collected with a Bruker APEX II CCD detector positioned at 50.0 mm and equipped with Helios multilayer mirror optics; data for **L^6H_2Ba**, **L^6UO_2**, **L^6UO_2K** and **L^6UO_2Ca** were collected with a Bruker Platinum 135 CCD detector positioned at 80.0 mm and equipped with Helios high-brilliance multilayer mirror optics. All diffractometer manipulations, including data collection, integration and scaling were carried out using the Bruker APEX2 software.[7] Absorption corrections were applied using SADABS.[8] Probable space groups were determined on the basis of systematic absences and the structures were solved by direct methods using SIR2004[9] or XS[10] (incorporated into SHELXTL) and refined to convergence by weighted full-matrix least squares on F^2 using the Olex2 software package equipped with XL.[11]

All non-hydrogen atoms were refined using anisotropic displacement parameters. Hydrogen atoms for all structures except **L^6H_2Ba** were placed at idealized positions and refined using a riding model. Rigid body methyl groups with sp^3-hybridized carbons and C-H bond lengths of 0.98 Å were placed either at idealized "staggered" positions or they were allowed to rotate freely about their O–C, N–C or C–C bonds in least-squares refinement cycles. Hydrogen atoms for **L^6H_2Ba** were located in a difference Fourier map and refined as independent isotropic atoms in least-squares refinement cycles.

The relevant crystallographic and structure refinement data for all six compounds are given in Tables B1, B2 and B3.

The location and refinement of all hydrogen atoms in **L^6H_2Ba** permits the unambiguous identification of two intramolecular N-H•••O hydrogen bonds which provide additional rigidity to one end of the macrocycle. The uranyl group occupies this end of the macrocycle in the other five structures.

The U=O bond lengths in **L^6UO_2**, **L^6UO_2K**, **L^6UO_2Na**, **L^6UO_2Ca** and **L^6UO_2Y** range from 1.771(6) Å to 1.795(4) Å. The linear uranyl group is within 1.4° of being perpendicular to the mean planes for each of the U, O1, O2, N1, N2 and N3 groupings. Each of these 6-atom groupings are nearly coplanar with a narrow range of rms (root-mean-square) deviations from their respective mean planes (the parameter defined in this report as ω_{crown}) ranging from 0.038 to 0.160 Å. Maximum deviations of individual atoms from these 6-atom mean planes range from 0.070 Å to 0.272 Å. Each of the 9-atom (N1, O6, C1, C2, C3, C4, C5, C6 and C7; N2, O3, C14, C15, C16, C17, C18, C19 and C20) groupings are also nearly coplanar with rms deviations from their respective 9-atom mean planes ($\omega_{iminophenoxide}$ values) ranging from 0.010 Å to 0.090 Å. Maximum deviations of individual atoms from the 9-atom mean plane range from 0.022 Å to 0.206 Å. The six macrocyclic oxygen donors of the crown-ether-like moiety are significantly less coplanar with a broader range of rms deviations from their respective 6-atom mean planes (ω_{crown}) ranging from 0.214 Å to 0.642 Å. The metals binding to these oxygens have coordination numbers ranging from seven to ten: Na^+ and K^+, 7; Ca^{2+} and Y^{3+}, 9; and Ba^{2+}, 10. **L^6UO_2K**, **L^6UO_2Na** and **L^6UO_2Ca** all have a single κ^1-coordinated triflate also bound to the second metal. The Ca^{2+} in **L^6UO_2Ca** also has two coordinated methanol ligands. The Y^{3+} in **L^6UO_2Y** has two κ^1-coordinated

triflates and a coordinated acetonitrile while the Ba^{2+} in **L^6H_2Ba** has two κ^2-coordinated triflates.

Although **L^6UO_2K** and **L^6UO_2Na** are isomorphous and the 7-coordinate ionic radius for Na^+ is 0.34 Å less than the 7-coordinate ionic radius for K^+, the average Na–O bond lengths are only 0.02 Å shorter than the average K–O bond lengths. Nonetheless, the M–O bond lengths for this series of compounds generally follow a trend based on the respective ionic radii of M; thus, those for Y^{3+} are the shortest as it has the smallest ionic radius. As a result, the O•••O and O•••N contacts on the Y^{3+} coordination sphere are the shortest for this series and are essentially at, or slightly below, the sum of the respective van der Waals radii.

The O1•••O2 separation (the separation between the phenoxide donor O atoms) changes dramatically through this series with values of 3.64 Å, 3.14 Å, 2.99 Å, 2.97 Å, 2.95 Å and 2.78 Å for **L^6H_2Ba, L^6UO_2**, **L^6UO_2K**, **L^6UO_2Na**, **L^6UO_2Ca** and **L^6UO_2Y,** respectively.

Special Refinement Details for L^6H_2Ba.

No special refinement was required. Both triflate counteranions are bound in a κ^2 fashion to the formally 10-coordinate Ba^{2+}.

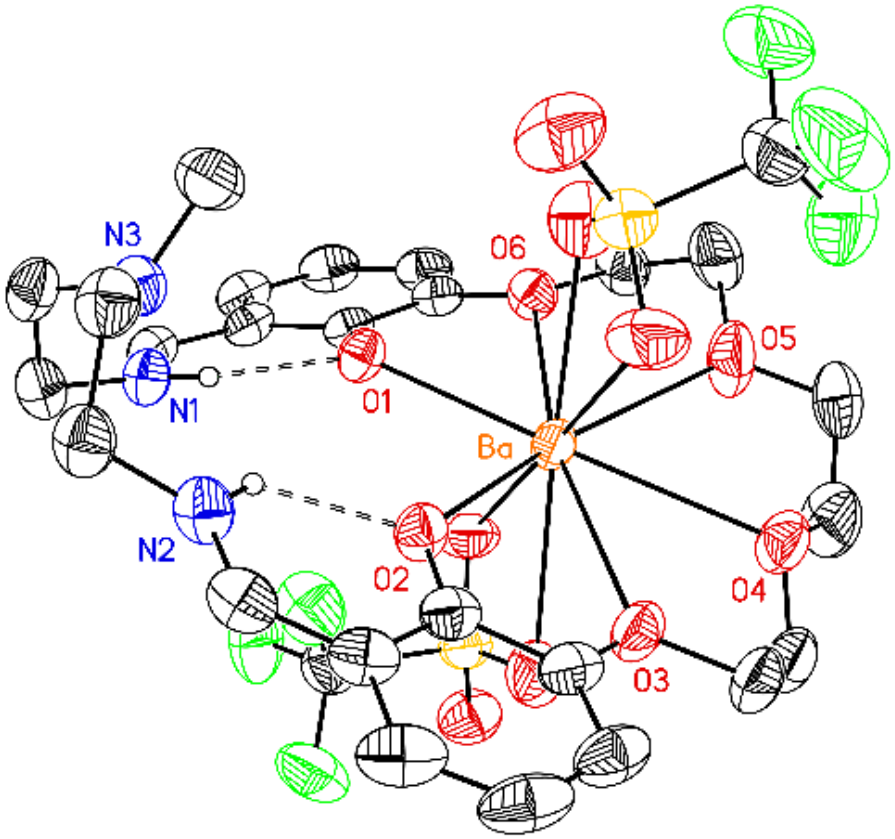

Figure B48. Solid-state structure (from XRD) of **L^6H_2Ba**. H-atoms except those covalently bonded to N1 and N2 and involved in intramolecular N–H•••O H-bonds are omitted for clarity. Displacement ellipsoids are shown at the 50% probability level.

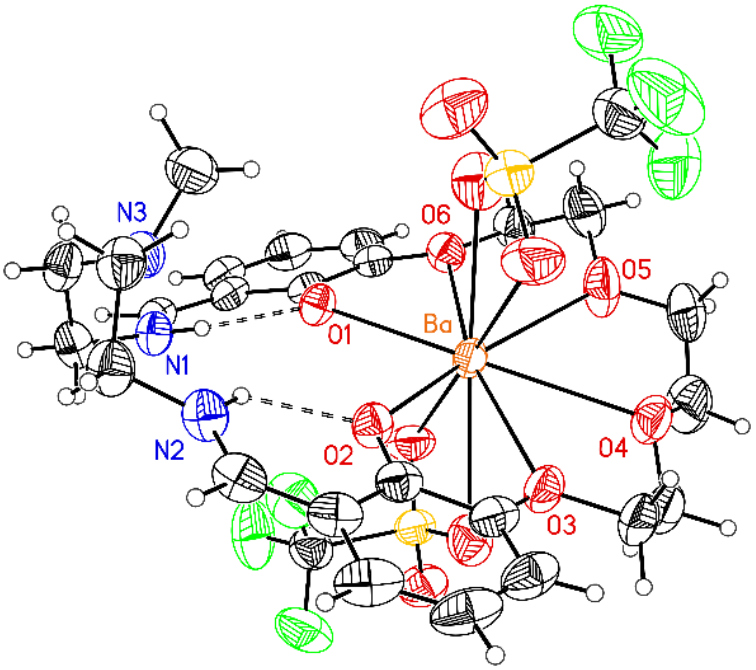

Figure B49. Solid-state structure (from XRD) of **L^6H_2Ba**. Displacement ellipsoids are shown at the 50% probability level.

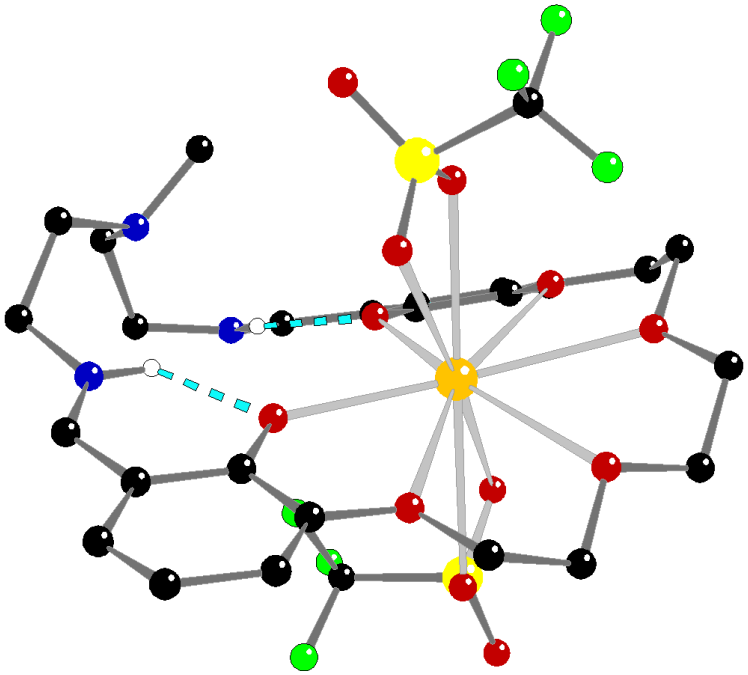

Figure B50. Ball and stick representation of **L^6H_2Ba** showing intramolecular H-bonds.

Special Refinement Details for L^6UO_2.

The atoms bonded to amine nitrogen N3 are 80/20 disordered with two alternate orientations about the U–N3 bond. Atoms for the major (80%) occupancy orientation are labeled with an A and those for the minor (20%) occupancy orientation are labeled without an A in the CIF-format file. Both orientations for this disordered methylamine moiety were restrained to have nearly idealized geometries by using a free variable for the C21–C22, C23–C24, C21A–C22A and C23A–C24A bond lengths. This free variable refined to a final value of 1.518(7) Å. The remaining bond lengths and angles for this disordered group were restrained to be multiples of this free variable that were consistent with sp^3-hybridization.

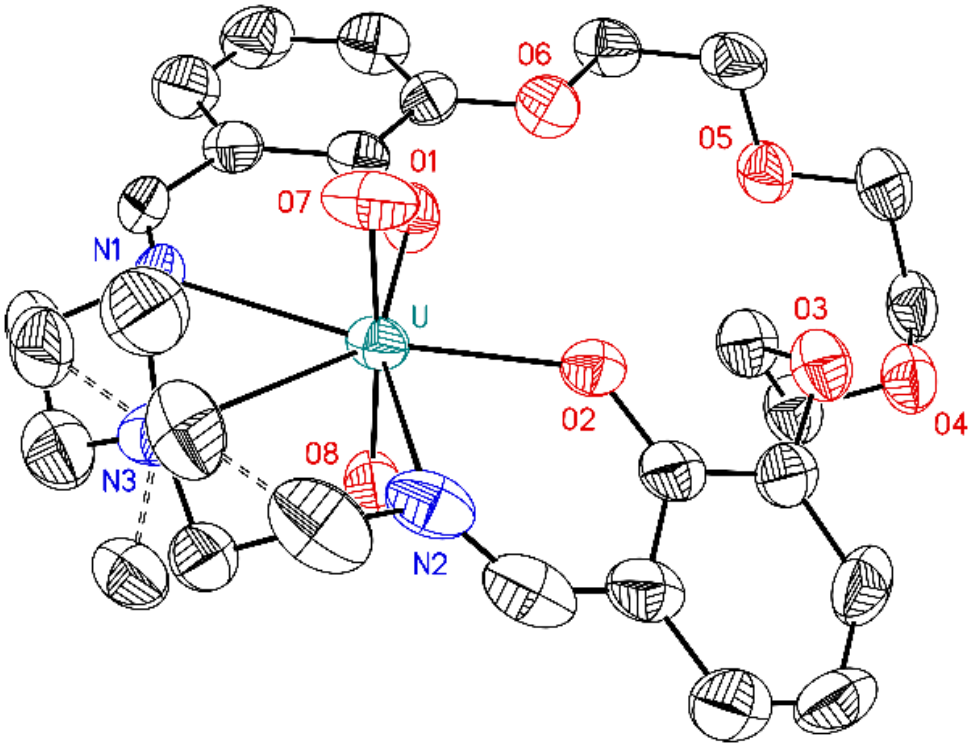

Figure B51. Solid-state structure (from XRD) of L^6UO_2. H-atoms are omitted for clarity. Displacement ellipsoids are shown at the 50% probability level.

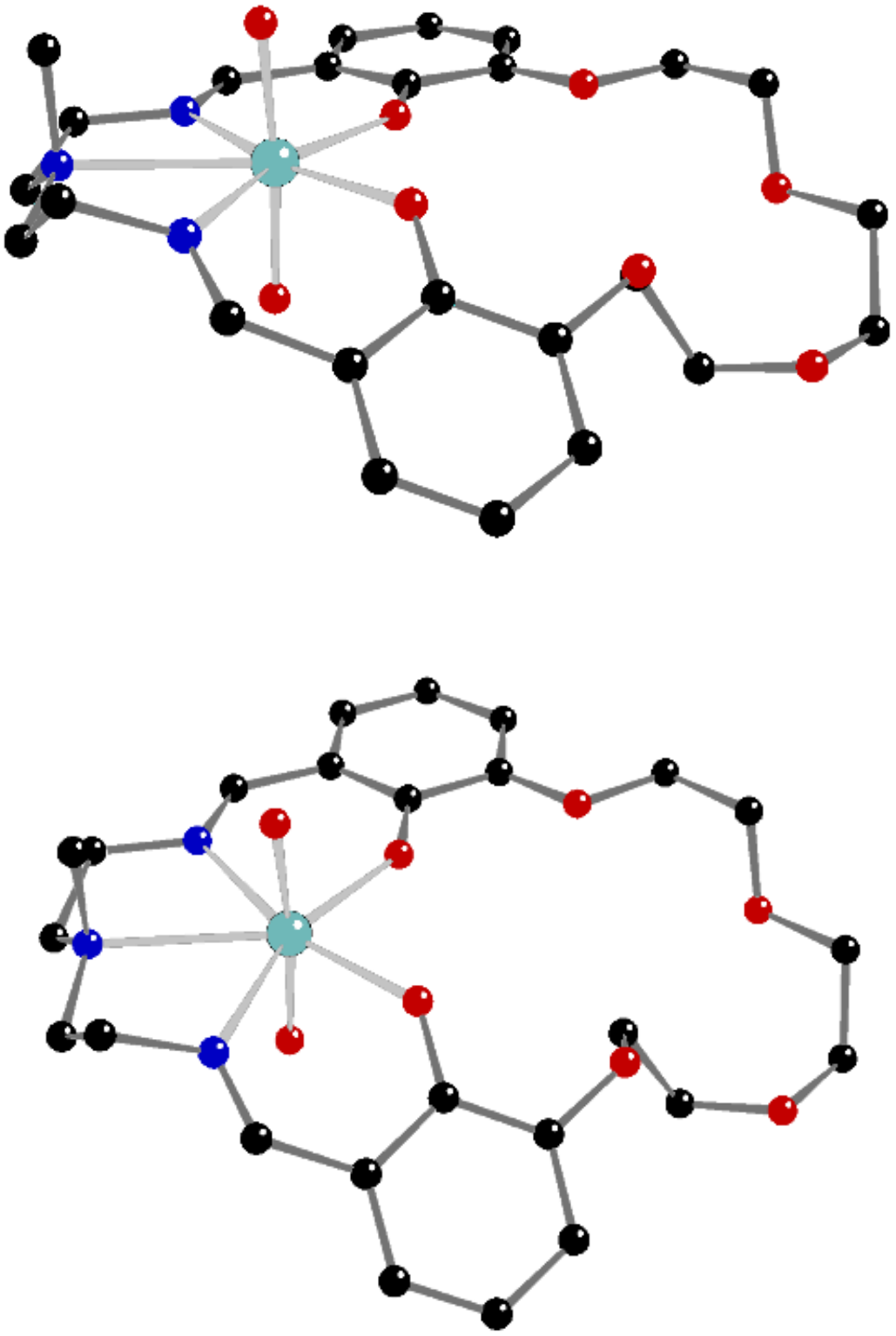

Figure B52. Ball and stick representations of $\mathbf{L^6UO_2}$.

Special Refinement Details for L^6UO_2K.

The triflate counteranion is bound in a κ^1 fashion to the formally 7-coordinate K^+ and is 72/28 disordered with two orientations about the K–O11 bond. Both orientations for this disordered triflate moiety were restrained to have nearly idealized geometries by using a free variable for the S=O bond length. This free variable refined to a final value of 1.410(6) Å. The remaining bond lengths and angles for this disordered group were restrained to be appropriate multiples of this free variable that were consistent with accepted bond lengths and sp^3-hybridization. The C8–C9 link between O5 and O6 is also 71/29 disordered and these linkages were restrained to be consistent with sp^3-hybridization. Mild restraints were applied to the anisotropic thermal parameters of partial-occupancy atoms C26, O12', O13', F12', F13' and C26'.

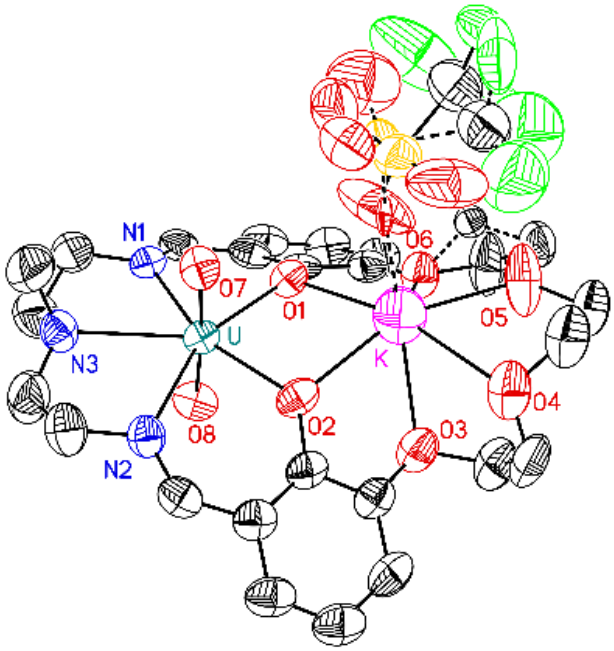

Figure B53. Solid-state structure (from XRD) of $\mathbf{L^6UO_2K}$. H-atoms are omitted for clarity. Displacement ellipsoids are shown at the 50% probability level.

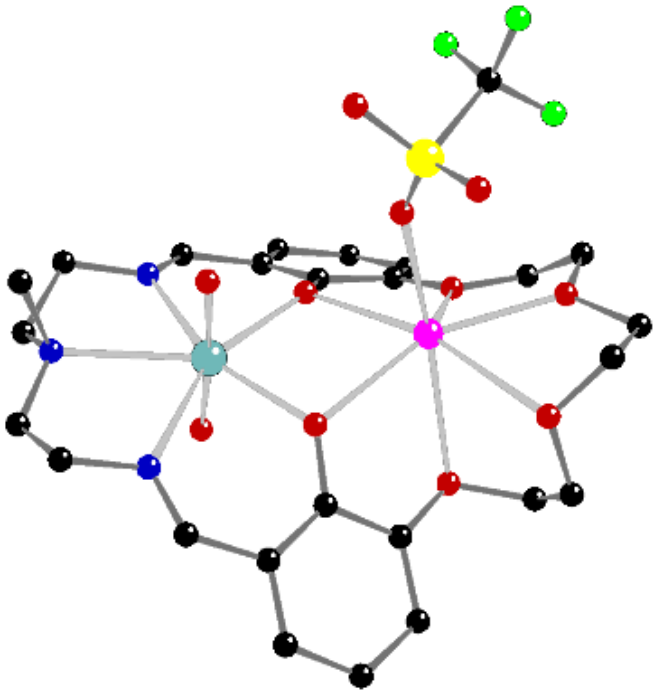

Figure B54. Ball and Stick representation of $\mathbf{L^6UO_2K}$.

Special Refinement Details for L^6UO_2Na.

The triflate counteranion is bound in a κ^1 fashion to the formally 7-coordinate Na^+ and is 67/33 disordered with two orientations about the Na–O11 bond. Both orientations for this disordered triflate moiety were restrained to have nearly idealized geometries by using a free variable for the S=O bond length. This free variable refined to a final value of 1.412(5) Å. The remaining bond lengths and angles for this disordered group were restrained to be appropriate multiples of this free variable that were consistent with accepted bond lengths and sp^3-hybridization. The C8–C9 link between O5 and O6 is also 57/43 disordered and these linkages were restrained to be consistent with sp^3-hybridization. Mild restraints were applied to the anisotropic thermal parameters of partial-occupancy atoms C26, O12', O13', F12', F13' and C26'.

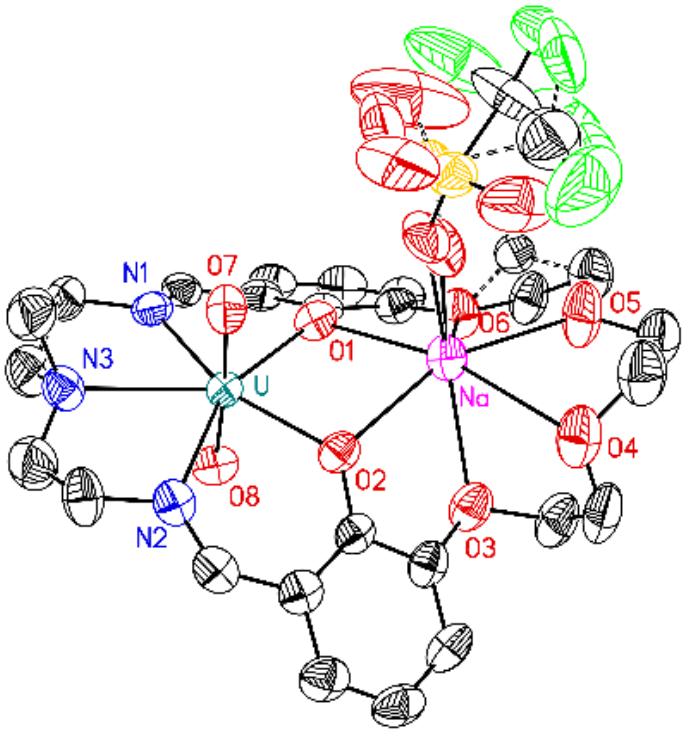

Figure B55. Solid-state structure (from XRD) of **L^6UO_2Na**. H-atoms are omitted for clarity. Displacement ellipsoids are shown at the 50% probability level.

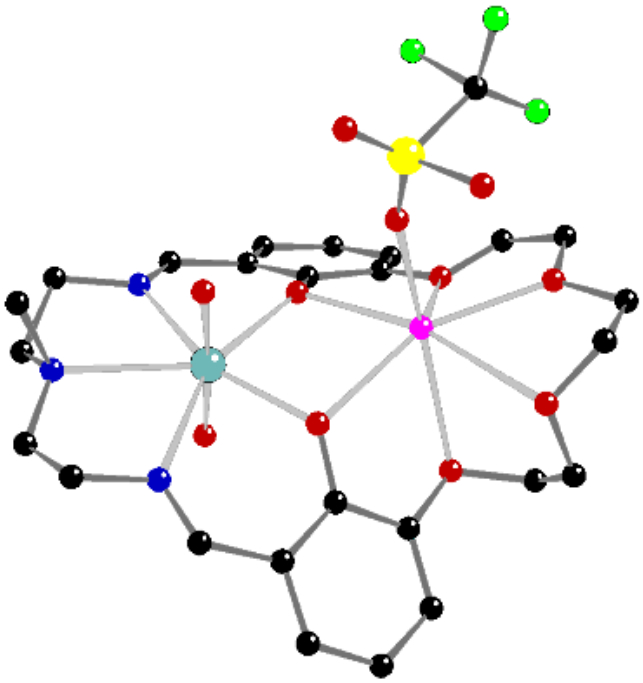

Figure B56. Ball and stick representation of **L^6UO_2Na**.

Special Refinement Details for L^6UO_2Ca.

Interestingly, no crystals of **L^6UO_2Ca** suitable for XRD analysis could be grown by vapor diffusion of diethyl ether into acetonitrile. Thus, acetonitrile was replaced by methanol in the successful solvent system for growing single crystals. The vapor diffusion setup was kept at 5°C under ambient laboratory atmosphere, giving single crystals after several days. We conclude that both slow exchange of one of the triflate counter anions with methanol at Ca^{2+} as well as inclusion of a water molecule (described below) resulted in formation of single crystals suitable for XRD that contain a 50/50 mixture of co-crystallized **$L^6UO_2Ca(MeOH)_2$** and **$L^6UO_2Ca(MeOH)(H_2O)$** where the second coordinated methanol and coordinated water molecule occupy a disordered site in the asymmetric unit that contains a single U and a single Ca.

Two methanol molecules or one methanol molecule and a water molecule plus one of the triflate counteranions are each bound in a κ^1 fashion to the formally 9-coordinate Ca^{2+} in these two co-crystallized species. A third methanol is present as a solvent molecule of crystallization. The atoms bonded to amine nitrogen N3 are 65/35 disordered with two alternate orientations about the U–N3 bond. Atoms for the minor (35%) occupancy orientation are labeled with an A and those for the major (65%) occupancy orientation are labeled without an A in the CIF-format file. Both orientations for this disordered methylamine moiety were restrained to have nearly idealized geometries by using a free variable for the C21–C22, C23–C24, C21A–C22A and C23A–C24A bond lengths. This free variable refined to a final value of 1.525(5) Å. The remaining bond lengths and angles for this disordered group were restrained to be appropriate multiples of this free variable that were consistent with sp^3-hybridization.

The first coordinated methanol in **$L^6UO_2Ca(MeOH)_2$** is ordered and always present as methanol. But the second coordinated methanol is disordered in the average co-crystallized structure that relates the distinct **$L^6UO_2Ca(MeOH)_2$** and **$L^6UO_2Ca(MeOH)(H_2O)$** moieties by a rigorous crystallographic inversion center. The coordination site for the second methanol in the co-crystallized structure is present 50% of the time as methanol and 50% of the time as water. They share a common oxygen (O2S) and H-bonded hydrogen atom (H2SA). This disorder is obviously necessary to form the crystal, and it prevents a short 2.250 Å intermolecular methyl•••methyl contact between pairs of these ligands in contiguous inversion-related molecules if no water were present. The oxygen atom (O2S) is present 100% of the time but the carbon atom (C2S) and its hydrogens are present only 50% of the time. The other 50% of the time this methyl group is replaced by the second idealized hydrogen atom (H2SB) of a water molecule. This was confirmed by electron density in a difference Fourier calculated with C2S and O2S removed from the structural model as well as by refinement of the occupancy factor for C2S that refined to 0.65(1). The common O–H hydrogen atom (H2SA) was located from a difference Fourier and included as an independent isotropic atom in the least-squares refinement cycles. The presence of H2SA for both ligands permits an uninterrupted intermolecular O–H•••O hydrogen-bonding network that stabilizes the crystal and promotes crystallization. The C–O–H groups for the other two methanol moieties were incorporated into the structural model as idealized tetrahedral rigid groups that were free to rotate about their C–O bonds in least-squares refinement cycles.

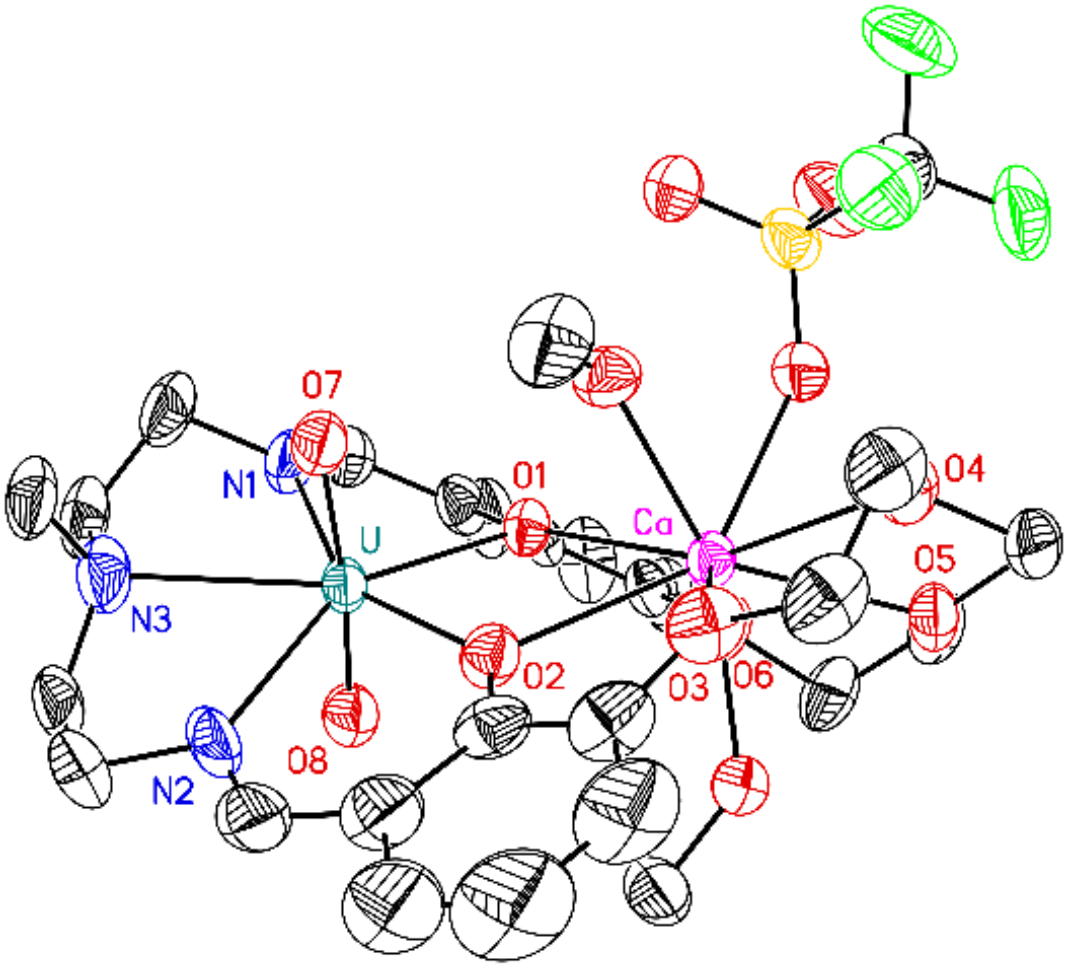

Figure B57. Solid-state structure (from XRD) of **L^6UO_2Ca** showing two methanol molecules coordinated to Ca. H-atoms, disorder in the amine linkage, outer-sphere triflate counteranion, and outer-sphere methanol/water (O2S) are omitted for clarity. Displacement ellipsoids are shown at the 50% probability level.

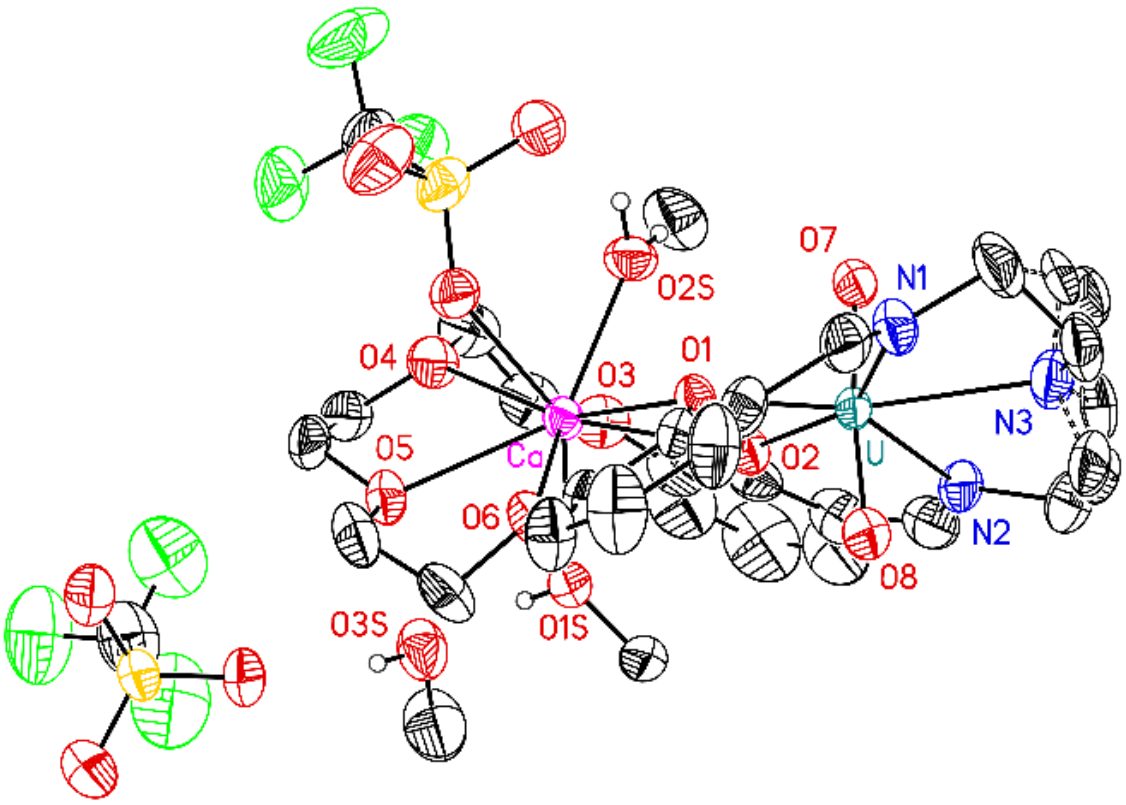

Figure B58. Solid-state structure (from XRD) of **L^6UO_2Ca** showing half-occupancy methanol (O2S and methyl carbon) coordinated to Ca and showing the unique hydrogen from the half-occupancy coordinated water (H2SB). All H-atoms except those associated with the methanol (and water) solvent molecules are omitted for clarity. Displacement ellipsoids are shown at the 50% probability level.

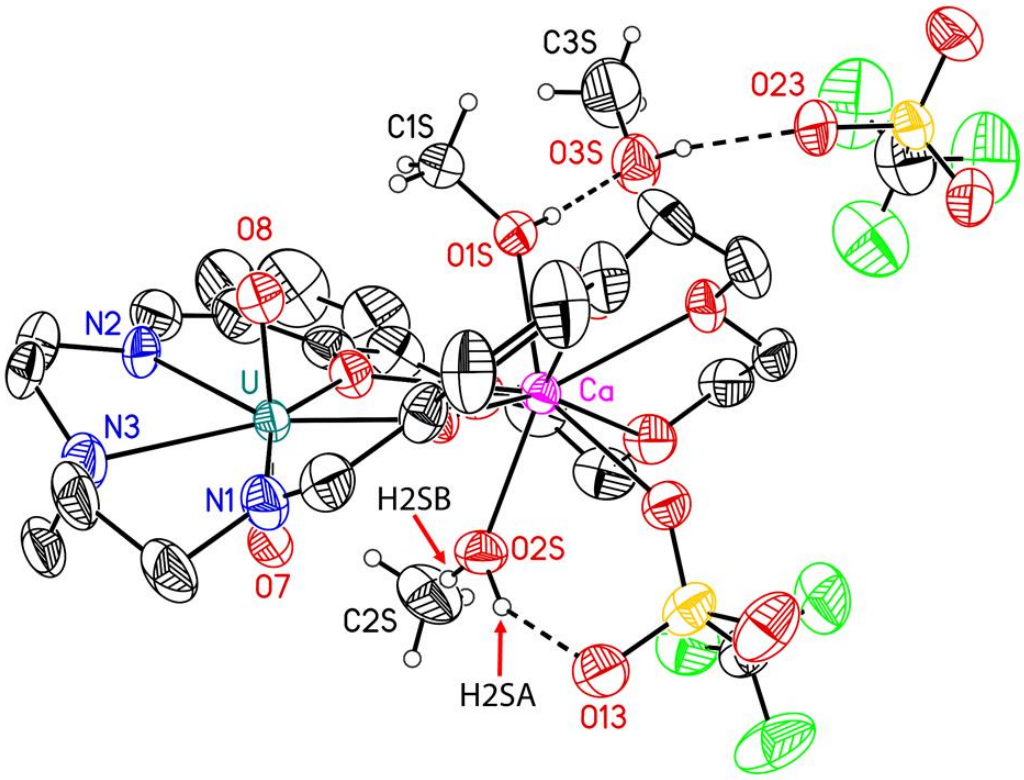

Figure B59. Solid-state structure (from XRD) of **L^6UO_2Ca** showing hydrogen bonds involving the methanol and methanol/water solvent molecules. All H-atoms except those associated with the methanol solvent molecules are omitted for clarity. Displacement ellipsoids are shown at the 50% probability level. Note that the methyl group associated with C2S is present 50% of the time, and the hydrogen (H2SB; associated with a corresponding bound water) near C2S is present 50% of the time. O2S is common between the bound methanol and water. H2SA was located in a difference Fourier and included as an independent isotropic atom in the least-squares refinement.

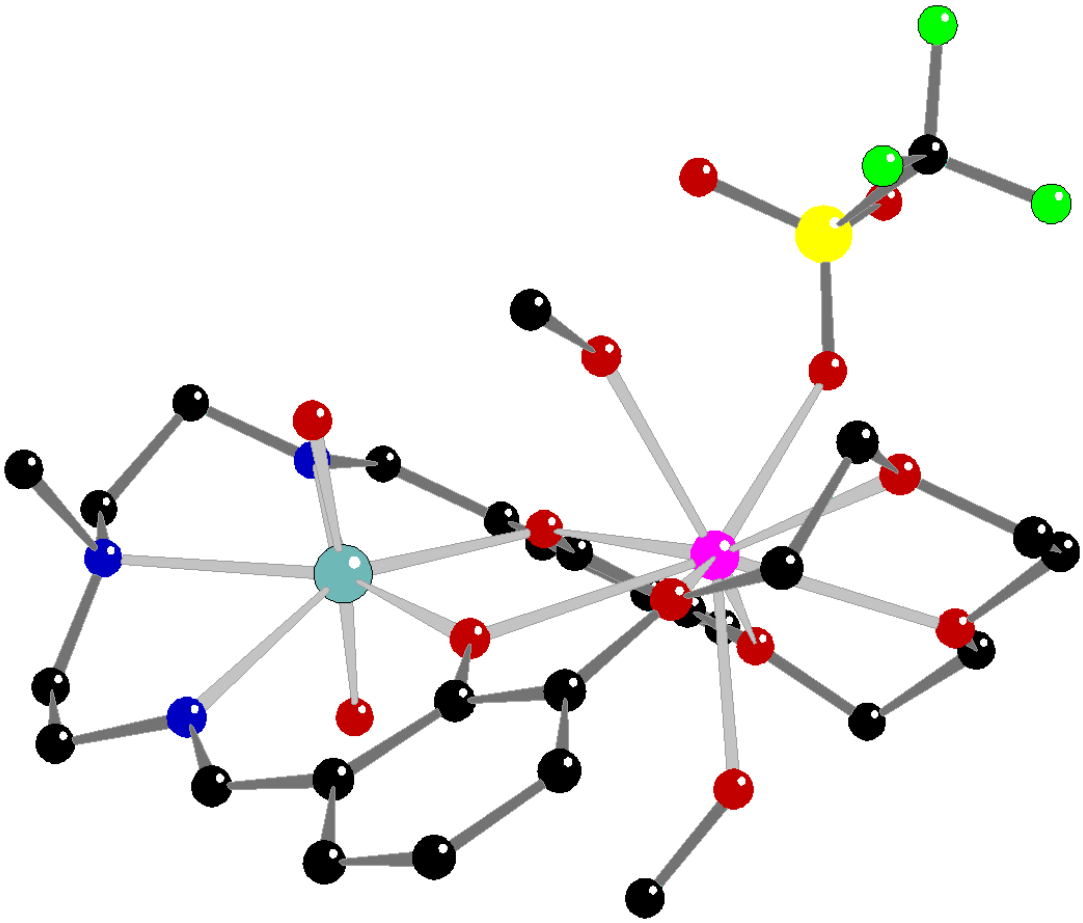

Figure B60. Ball and stick representation of **L^6UO_2Ca**.

Special Refinement Details for L^6UO_2Y.

No special refinement was required. An acetonitrile molecule and two of the triflate counteranions are each bound in a κ^1 fashion to the formally 9-coordinate Y^{3+}.

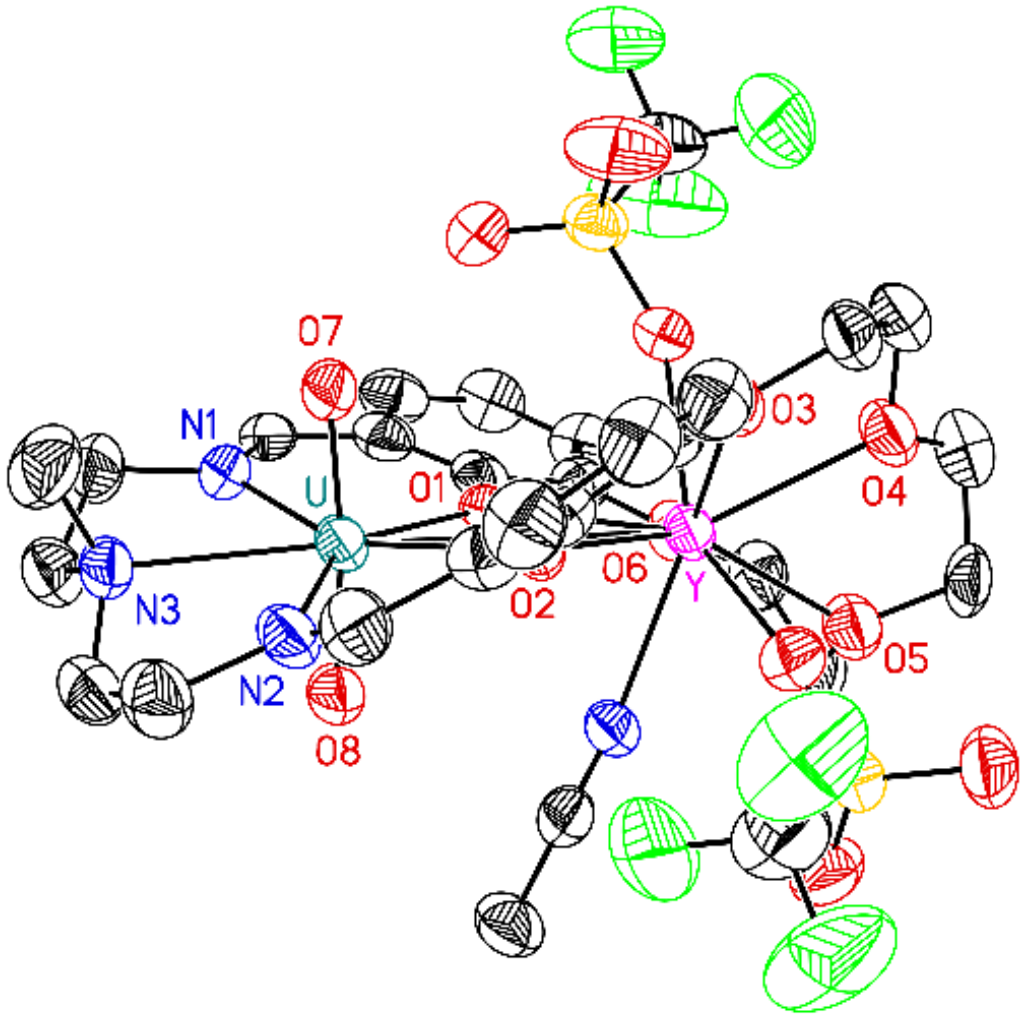

Figure B61. Solid-state structure (from XRD) of **L^6UO_2Y**. H-atoms and outer-sphere triflate counteranion are omitted for clarity. Displacement ellipsoids are shown at the 50% probability level.

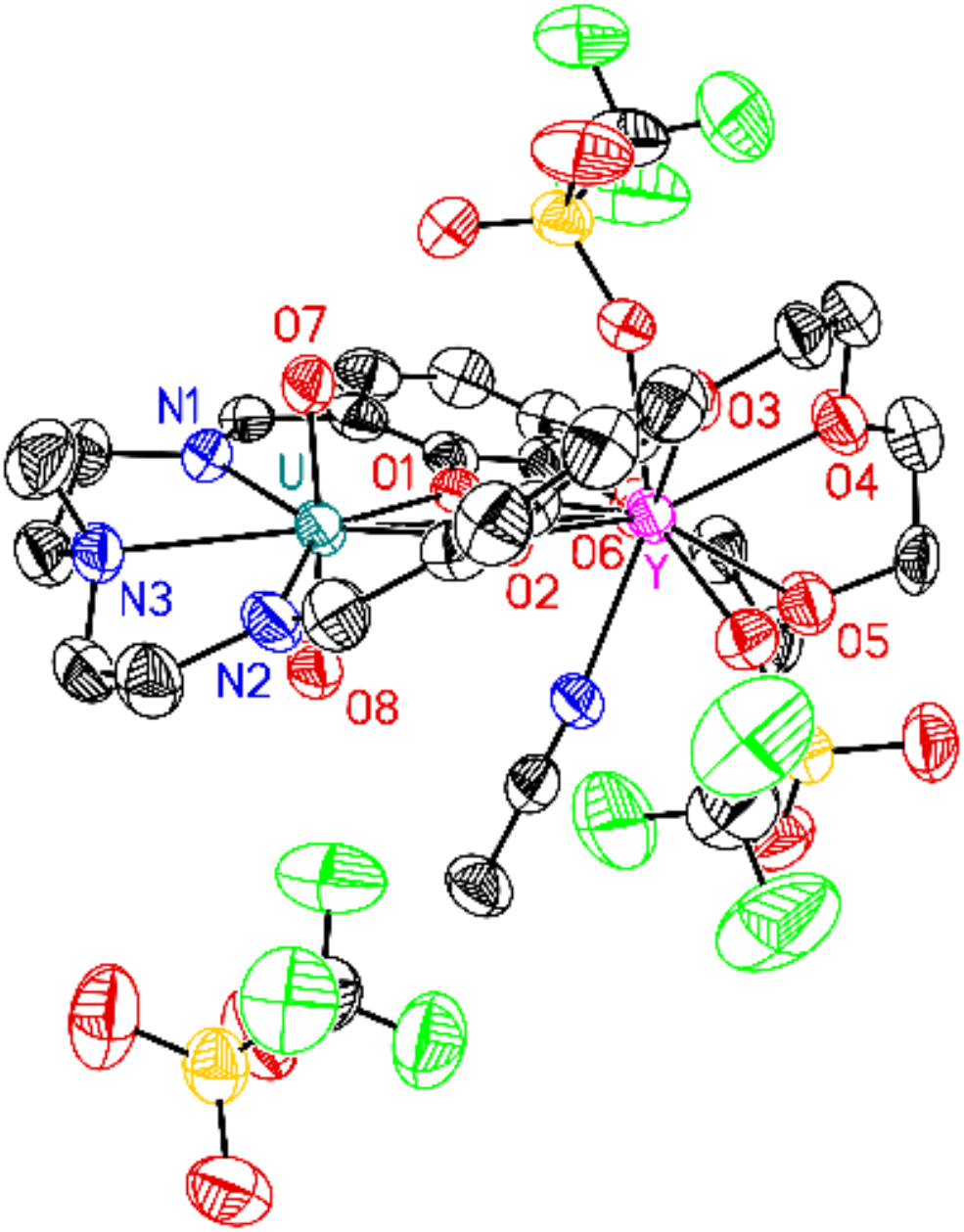

Figure B62. Solid-state structure (from XRD) of **L^6UO_2Y**. H-atoms are omitted for clarity. Displacement ellipsoids are shown at the 50% probability level.

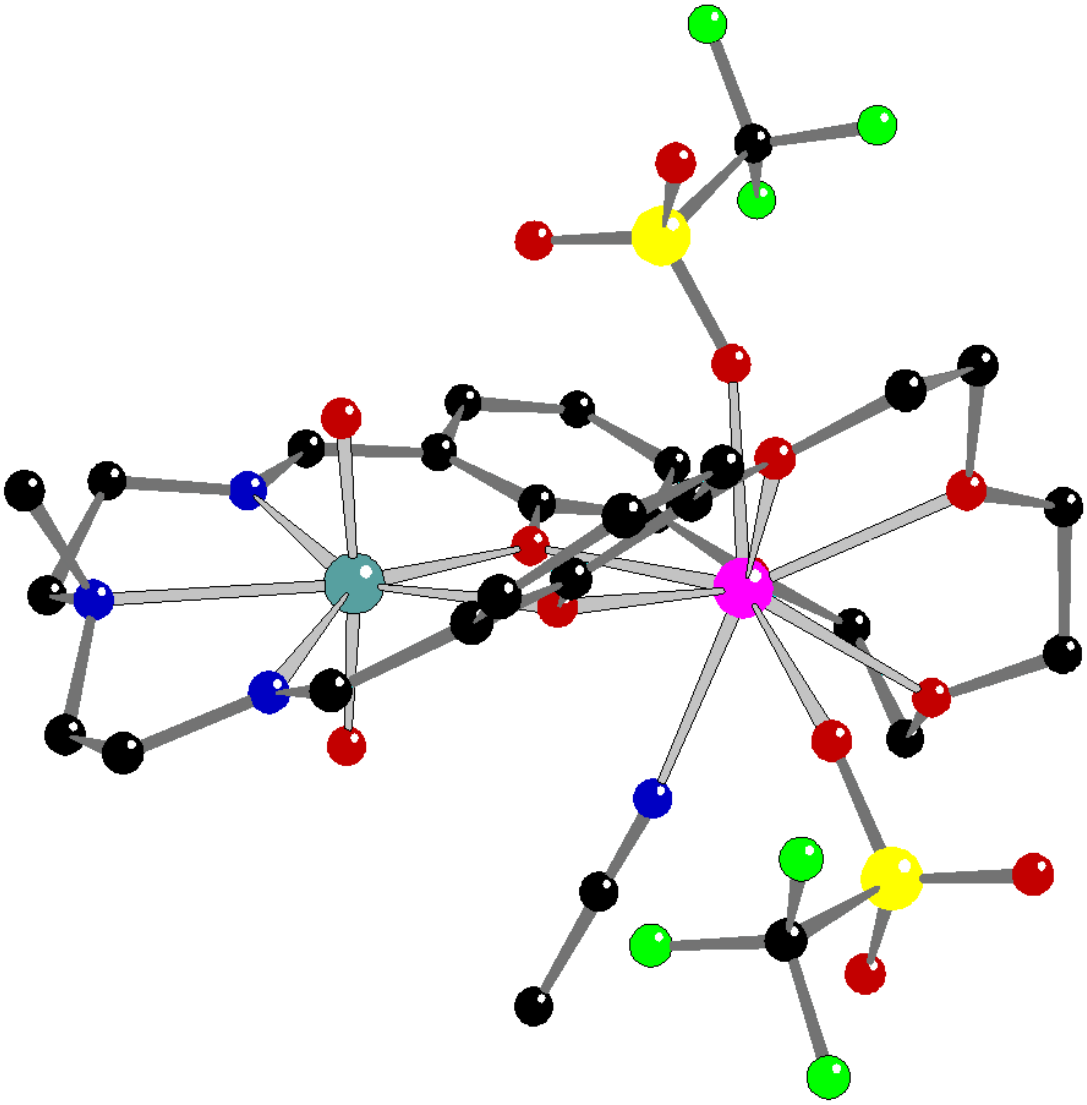

Figure B63. Ball and stick representation of **L^6UO_2Y**.

Table B1. Crystal and Refinement Data for **L^6H_2Ba** and **L^6UO_2.**

	L^6H_2Ba	**L^6UO_2**
CCDC number	1960625	1960626
empirical formula	$C_{27}H_{33}BaF_6N_3O_{12}S_2$	$C_{25}H_{31}N_3O_8U$
formula weight	907.02	739.56
T (K)	200	200
wavelength, Å	1.54178	1.54178
crystal system	orthorhombic	orthorhombic
space group	Pbca (D_{2h}^{15}-No. 61)	$P2_12_12_1$ (D_2^4-No. 19)
***a*, Å**	10.9261(6)	11.8509(3)
***b*, Å**	17.1581(9)	12.0635(4)
***c*, Å**	37.691(2)	17.8749(5)
***α*, deg**	90	90
***β*, deg**	90	90
***γ*, deg**	90	90
Volume, Å^3	7065.9(7)	2555.5(1)
Z	8	4
ρ_{calcd}, g/cm^3	1.705	1.922
F(000)	3632.0	1432.0
crystal dimensions, mm^3	0.135 × 0.13 × 0.03	0.135 × 0.095 × 0.065
2θ range, deg	9.36 to 137.01	8.84 to 136.71
index ranges	$-13 \le h \le 11$, $-20 \le k \le 18$, $-41 \le l \le 44$	$-14 \le h \le 14$, $-14 \le k \le 12$, $-21 \le l \le 16$
reflections collected	39237	21288
independent reflections	6423 [R_{int} = 0.061, R_{sigma} = 0.104]	4586 [R_{int} = 0.052, R_{sigma} = 0.044]
absorption correction	multi-scan	multi-scan
Max./Min. Transmission	0.538/1.000	0.570/1.000
Refinement method	Full-matrix least-squares on F^2	Full-matrix least-squares on F^2
Data/restraints/parameters	6423/0/592	4586/38/364
Goodness-of-fit[c] on F^2	1.032	1.043
R_1,[a] wR_2[b] [I>2σ(I)]	R_1 = 0.037, wR_2 = 0.098	R_1 = 0.030, wR_2 = 0.070
R_1,[a] wR_2[b] (all data)	R_1 = 0.041, wR_2 = 0.101	R_1 = 0.0322, wR_2 = 0.071
Largest diff. peak & hole	0.57 and –0.95 e$^-$/Å^3	1.56 and –1.21 e$^-$/Å^3

[a] $R1 = \Sigma||F_o|-|F_c|| / \Sigma|F_o|$ [b] $wR2 = [\ \Sigma[w(F_o^2-F_c^2)^2] / \Sigma[w(F_o^2)^2]\ ]^{1/2}$ [c] $GOOF = S = [\ \Sigma[w(F_o^2-F_c^2)^2] / (n-p)\ ]^{1/2}$

Table B2. Crystal and Refinement Data for **L^6UO_2K** and **L^6UO_2Na.**

	L^6UO_2K	**L^6UO_2Na**
CCDC number	1960628	1960629
empirical formula	$C_{26}H_{31}F_3KN_3O_{11}SU$	$C_{26}H_{31}F_3NaN_3O_{11}SU$
formula weight	927.73	911.62
T (K)	200	200
wavelength, Å	1.54178	1.54178
crystal system	orthorhombic	orthorhombic
space group	$P2_12_12_1$ (D_2^4-No. 19)	$P2_12_12_1$ (D_2^4-No. 19)
***a*, Å**	12.9299(6)	12.9352(2)
***b*, Å**	13.2222(6)	13.2651(2)
***c*, Å**	18.4887(9)	18.4739(3)
***α*, deg**	90	90
***β*, deg**	90	90
***γ*, deg**	90	90
Volume, Å^3	3160.9(3)	3169.88(9)
Z	4	4
ρ_{calcd}, g/cm^3	1.950	1.910
F(000)	1800.0	1768.0
crystal dimensions, mm^3	0.17 × 0.085 × 0.04	0.13 × 0.04 × 0.02
2θ range, deg	8.22 to 136.85	8.21 to 140.49
index ranges	$-10 \le h \le 15$, $-15 \le k \le 15$, $-22 \le l \le 14$	$-13 \le h \le 15$, $-10 \le k \le 16$, $-20 \le l \le 22$
reflections collected	12833	12908
independent reflections	5277 [R_{int} = 0.039, R_{sigma} = 0.046]	5437 [R_{int} = 0.033, R_{sigma} = 0.039]
absorption correction	numerical	numerical
Max./Min. Transmission	0.054/1.000	0.162/1.000
Refinement method	Full-matrix least-squares on F^2	Full-matrix least-squares on F^2
Data/restraints/parameters	5277/74/496	5437/50/496
Goodness-of-fit[c] on F^2	1.088	1.095
R_1,[a] wR_2[b] [I>2σ(I)]	R_1 = 0.036, wR_2 = 0.095	R_1 = 0.027, wR_2 = 0.064
R_1,[a] wR_2[b] (all data)	R_1 = 0.040, wR_2 = 0.099	R_1 = 0.030, wR_2 = 0.066
Largest diff. peak & hole	1.36/–1.46 e$^-$/Å^3	1.11/–0.58 e$^-$/Å^3

[a] $R1 = \Sigma||F_o|-|F_c|| / \Sigma|F_o|$ [b] $wR2 = [\ \Sigma[w(F_o^2-F_c^2)^2] / \Sigma[w(F_o^2)^2]\ ]^{1/2}$ [c] $GOOF = S = [\ \Sigma[w(F_o^2-F_c^2)^2] / (n-p)\ ]^{1/2}$

Table B3. Crystal and Refinement Data for **L^6UO_2Ca** and **L^6UO_2Y.**

	L^6UO_2Ca	**L^6UO_2Y**
CCDC number	1960630	1960631
empirical formula	$C_{29.5}H_{42}CaF_6N_3O_{17}S_2U$	$C_{30}H_{34}F_9N_4O_{17}S_3UY$
formula weight	1166.89	1316.73
T (K)	200	200
wavelength, Å	1.54178	1.54178
crystal system	triclinic	Triclinic
space group	P-1 (C_i^1-No. 2)	P-1 (C_i^1-No. 2)
***a*, Å**	12.7589(9)	9.1814(6)
***b*, Å**	13.2831(9)	13.6032(8)
***c*, Å**	13.7644(10)	18.8769(12)
***α*, deg**	79.402(3)	102.095(5)
***β*, deg**	64.575(3)	102.738(6)
***γ*, deg**	81.805(3)	103.991(5)
Volume, Å^3	2065.6(3)	2143.6(2)
Z	2	2
ρ_{calcd}, g/cm^3	1.876	2.040
F(000)	1148.0	1276.0
crystal dimensions, mm^3	0.13 × 0.085 × 0.06	0.03 × 0.03 × 0.025
2θ range, deg	6.79 to 136.91	5.00 to 140.87
index ranges	$-15 \le h \le 13$, $-15 \le k \le 15$, $-16 \le l \le 16$	$-11 \le h \le 9$, $-16 \le k \le 16$, $-21 \le l \le 23$
reflections collected	32430	28130
independent reflections	7473 [Rint = 0.059, Rsigma = 0.052]	7605 [Rint = 0.077, Rsigma = 0.068]
absorption correction	multi-scan	multi-scan
Max./Min. Transmission	0.614/1.000	0.704/1.000
Refinement method	Full-matrix least-squares on F^2	Full-matrix least-squares on F^2
Data/restraints/parameters	7473/19/581	7605/0/587
Goodness-of-fit[c] on F^2	1.093	1.067
R_1,[a] wR_2[b] [I>2σ(I)]	R_1 = 0.037, wR_2 = 0.085	R_1 = 0.050, wR_2 = 0.122
R_1,[a] wR_2[b] (all data)	R_1 = 0.040, wR_2 = 0.087	R_1 = 0.067, wR_2 = 0.133
Largest diff. peak & hole	1.52/–1.16 e$^-$/Å^3	2.34/–1.18 e$^-$/Å^3

[a] $R1 = \Sigma||F_o|-|F_c|| / \Sigma|F_o|$ [b] $wR2 = [\ \Sigma[w(F_o^2-F_c^2)^2] / \Sigma[w(F_o^2)^2]\ ]^{1/2}$ [c] $GOOF = S = [\ \Sigma[w(F_o^2-F_c^2)^2] / (n-p)\ ]^{1/2}$

References

(1) Perrin, D. D. *Ionisation Constants of Inorganic Acids and Bases in Aqueous Solution* (Pergamon, 1982).

(2) Nicholson, R. S.; Shain, I. Theory of Stationary Electrode Polarography. Single Scan and Cyclic Methods Applied to Reversible, Irreversible, and Kinetic Systems. *Anal. Chem.* **1964**, *36*, 706-723.

(3) Jakubowska, M. Signal Processing in Electrochemistry. *Electroanalysis* **2011**, *23*, 553-572.

(4) Savéant, J.-M. *Elements of Molecular and Biomolecular Electrochemistry*. Wiley: Hoboken, NJ, 2006.

(5) Randles, J. E. B. A cathode ray polarograph. Part II—The current-voltage curves. *Trans. Faraday Soc.* **1948,** *44*, 327-338.

(6) Ševčik, A. Oscillographic polarography with periodical triangular voltage. *Collect. Czech. Chem. Commun.* **1948**, *13*, 349-377.

(7) *SAINT. Ver. 8.34A.* Bruker Analytical X-ray Systems: Madison, WI, June 2014.

(8) *Sheldrick, G. M., SADABS (version 2008/1)*: Program for Absorption Correction for Data from Area Detector Frames, University of Göttingen, 2008.

(9) Sheldrick, G. SHELXT – Integrated space-group and crystal-structure determination. *Acta Cryst.* **2015**, *A71*, 3-8.

(10) Sheldrick, G. Crystal structure refinement with SHELXL. *Acta Cryst.* **2015**, *C71*, 3-8.

(11) Dolomanov, O. V.; Bourhis, L. J.; Gildea, R. J.; Howard J. A. K.; Puschmann, H. OLEX2: a complete structure solution, refinement and analysis program. *J. Appl. Crystallogr.* **2009**, *42*, 339-341.

Appendix C

Supplementary Information for Chapter 4

NMR Spectra

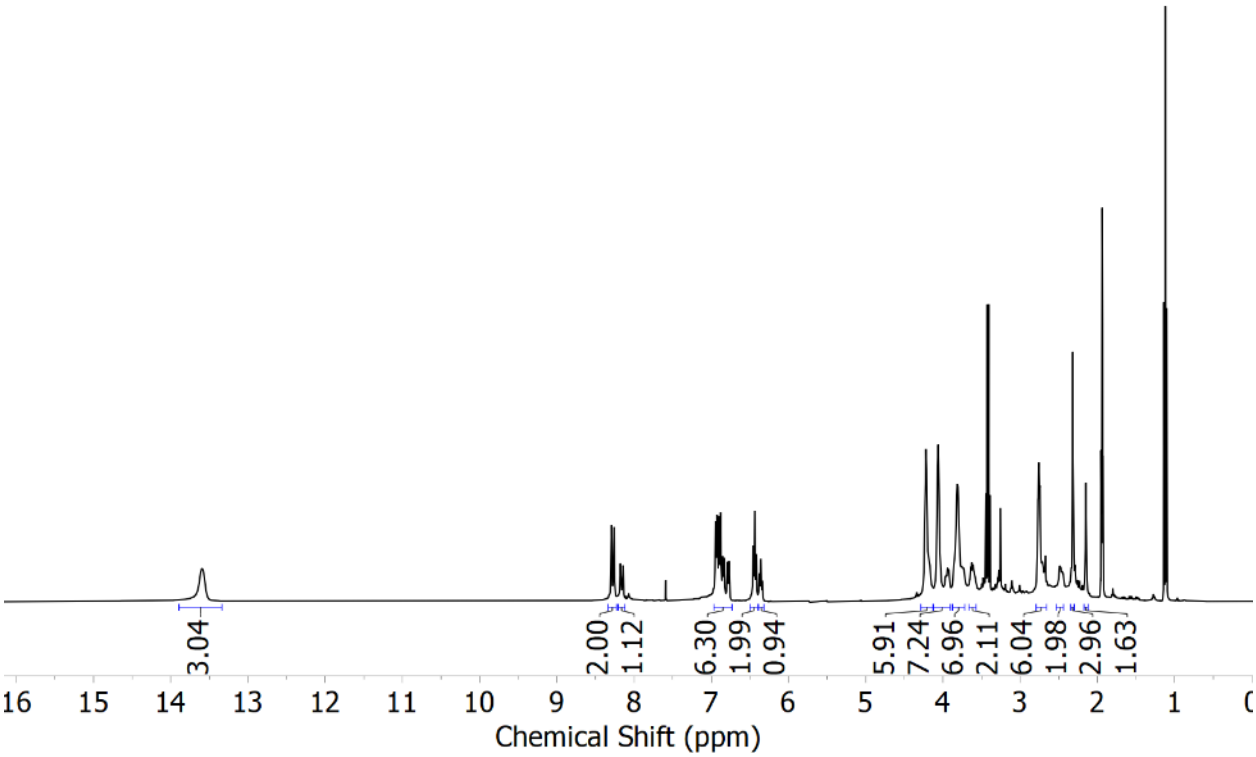

Figure C1. ^{1}H NMR spectrum (400 MHz, CD_3CN) of **BaPenta**.

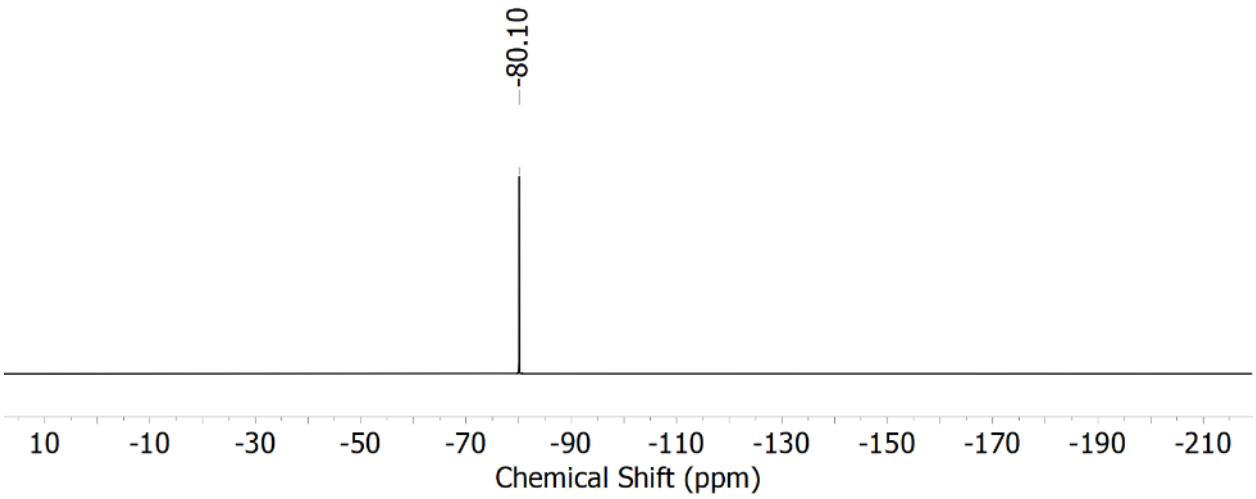

Figure C2. $^{19}F\{^{1}H\}$ NMR spectrum (400 MHz, CD_3CN) of **BaPenta**.

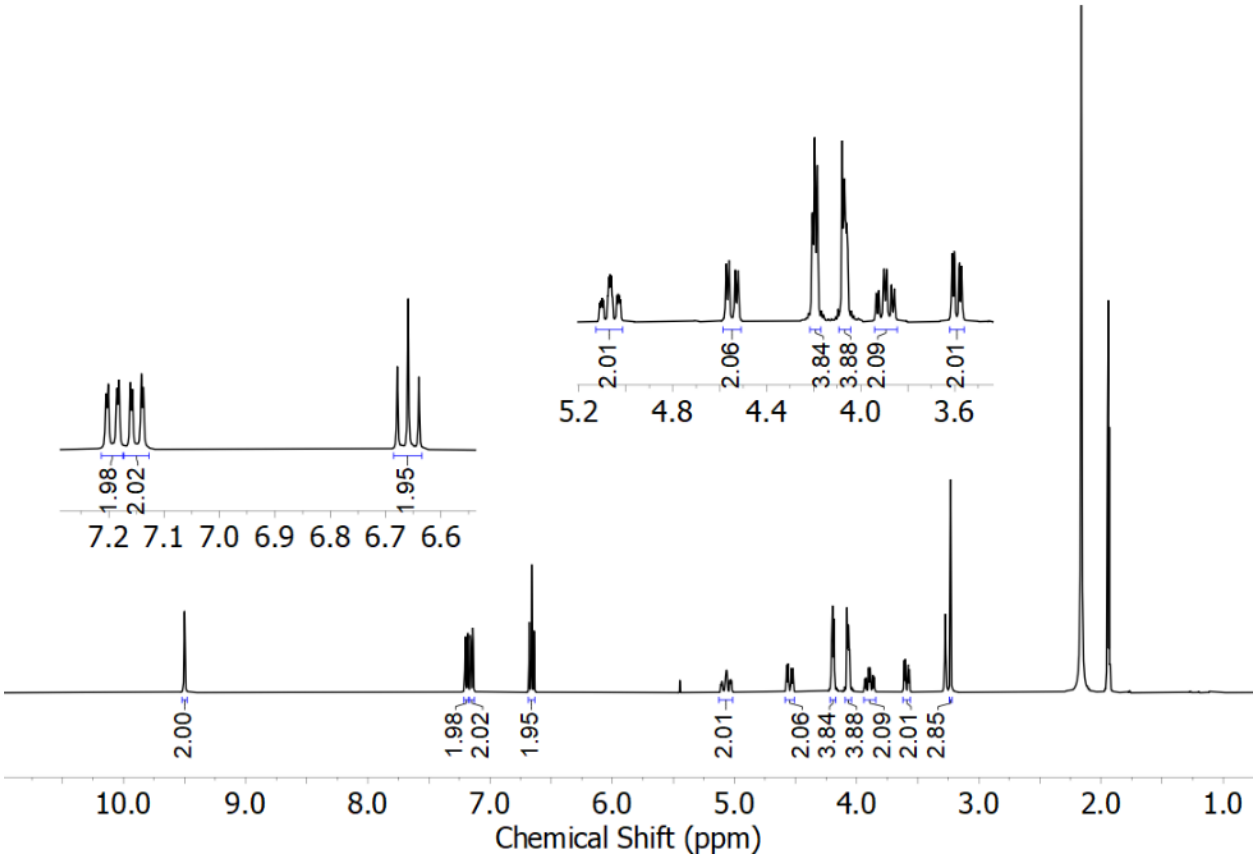

Figure C3. ^{1}H NMR spectrum (400 MHz, CD_3CN) of **L^5UO_2**.

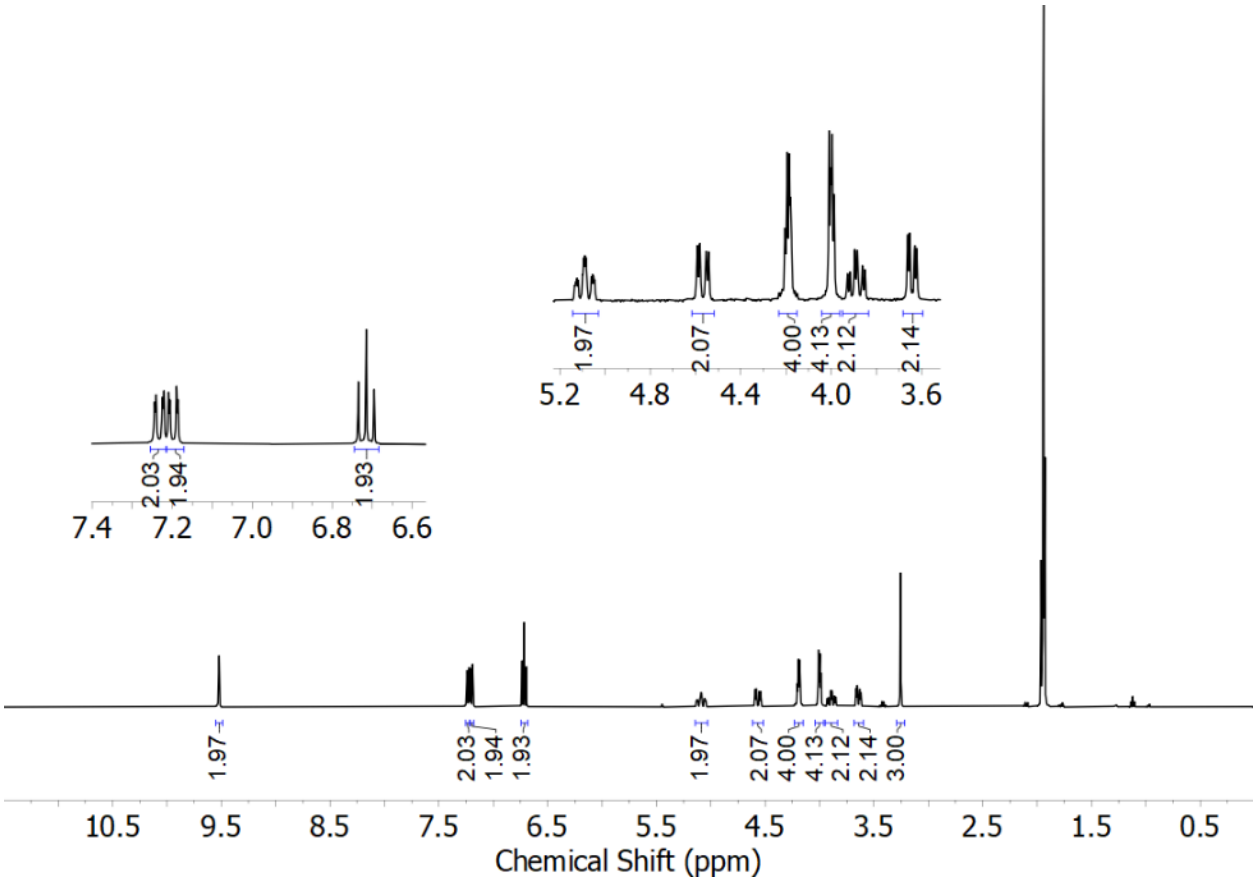

Figure C4. ^{1}H NMR spectrum (400 MHz, CD_3CN) of *in situ* generated **L^5UO_2Cs**.

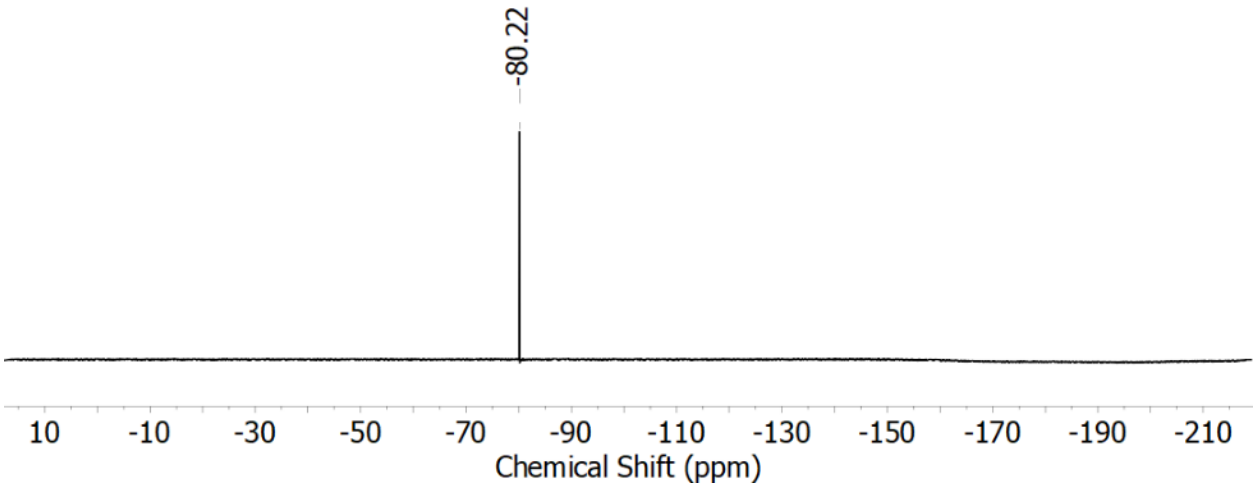

Figure C5. ^{19}F{^{1}H} NMR spectrum (400 MHz, CD_3CN) of *in situ* generated **L^5UO_2Cs**.

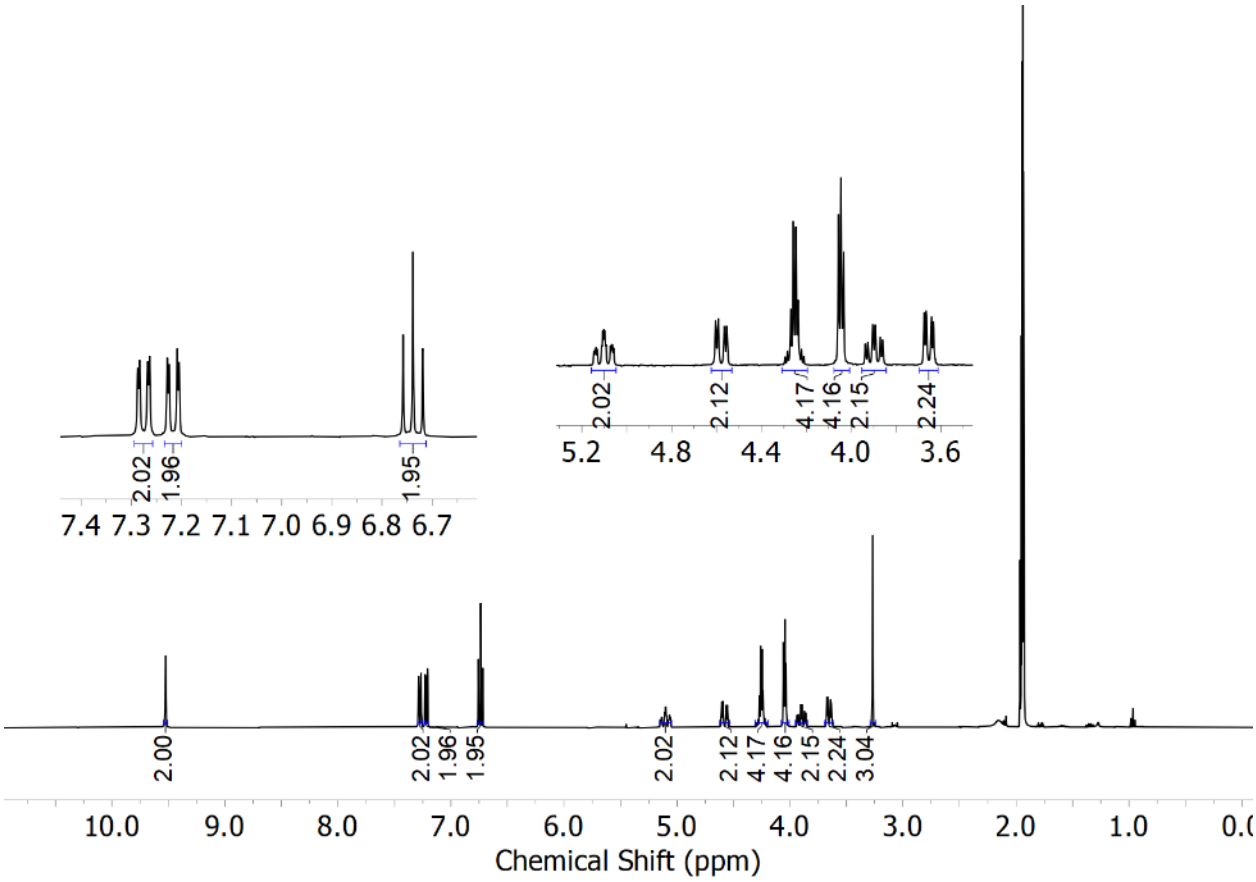

Figure C6. ^{1}H NMR spectrum (400 MHz, CD_3CN) of *in situ* generated **L^5UO_2Rb**.

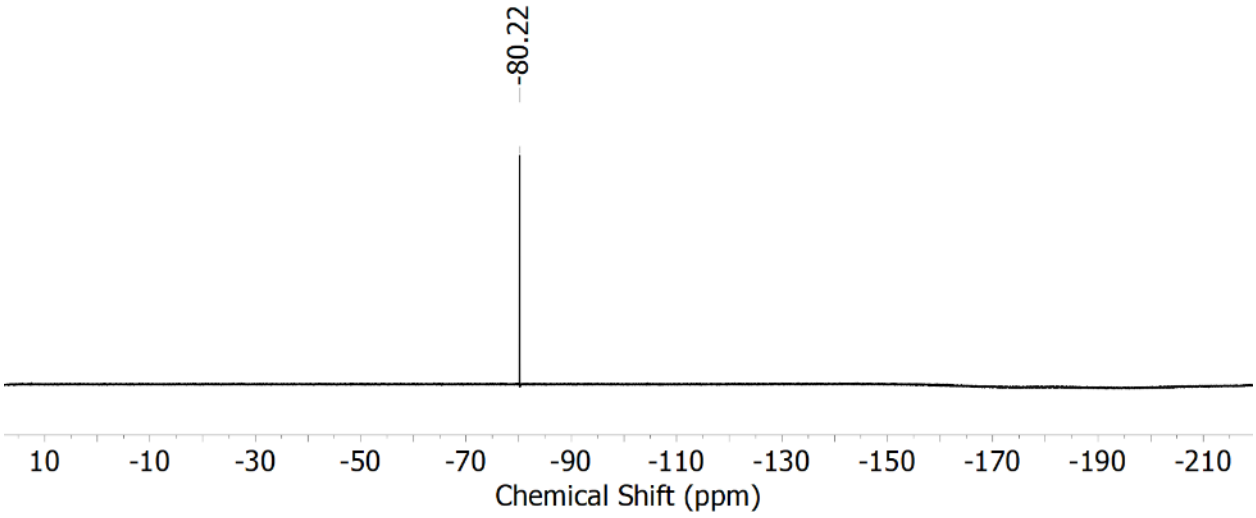

Figure C7. $^{19}F\{^{1}H\}$ NMR spectrum (400 MHz, CD_3CN) of *in situ* generated **L^5UO_2Rb**.

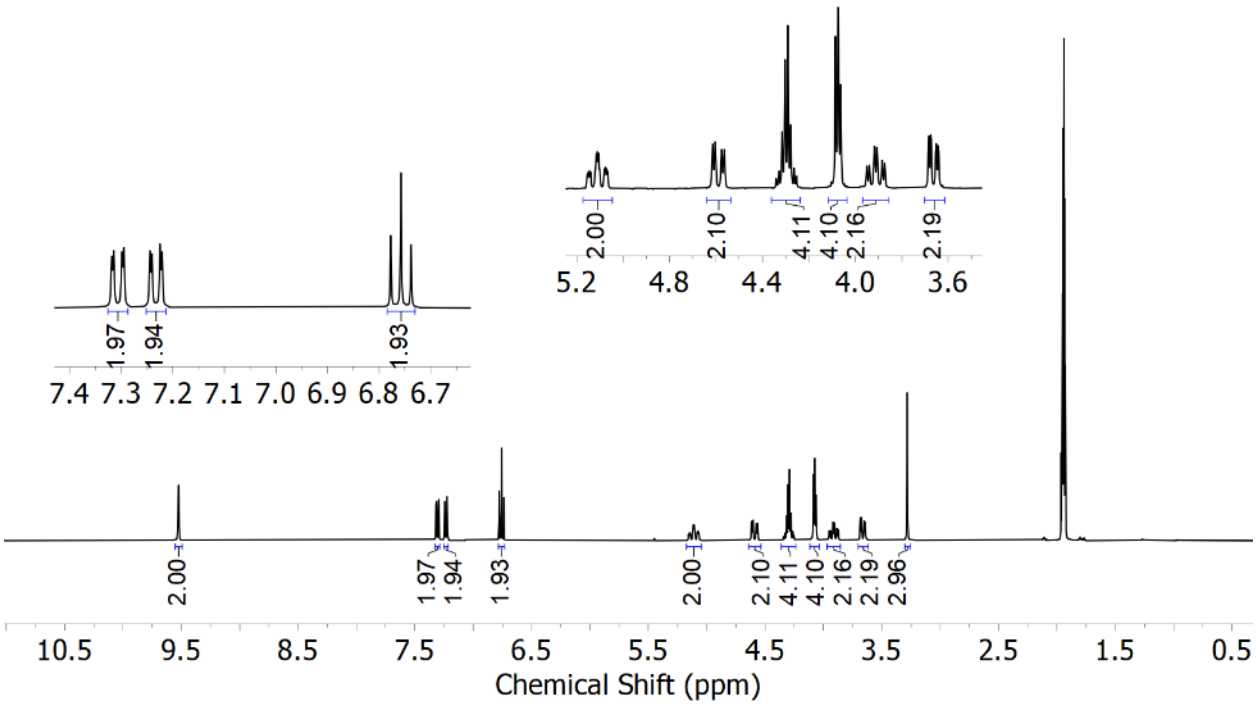

Figure C8. ^{1}H NMR spectrum (400 MHz, CD_3CN) of *in situ* generated **L^5UO_2K**.

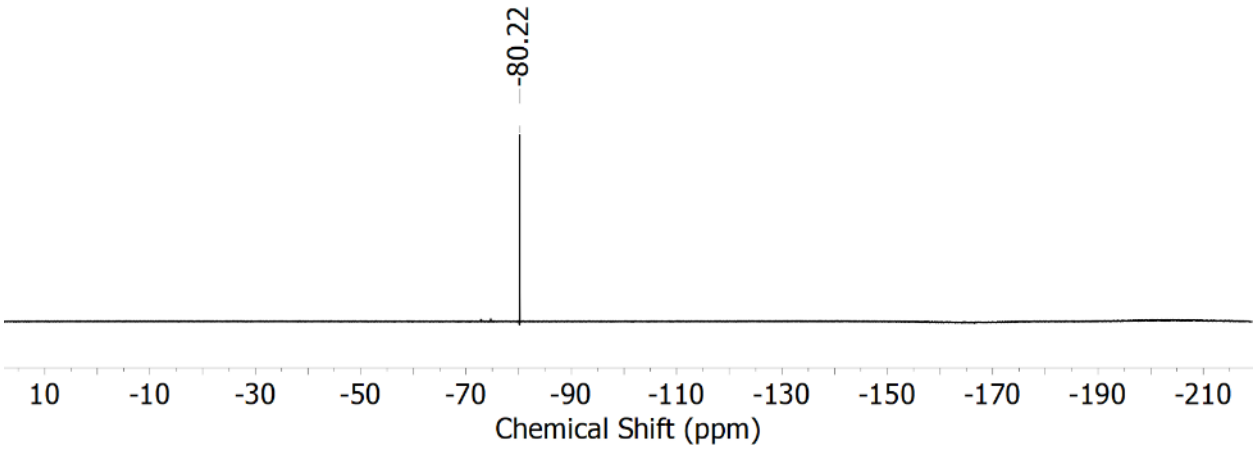

Figure C9. $^{19}F\{^{1}H\}$ NMR spectrum (400 MHz, CD_3CN) of *in situ* generated **L^5UO_2K**.

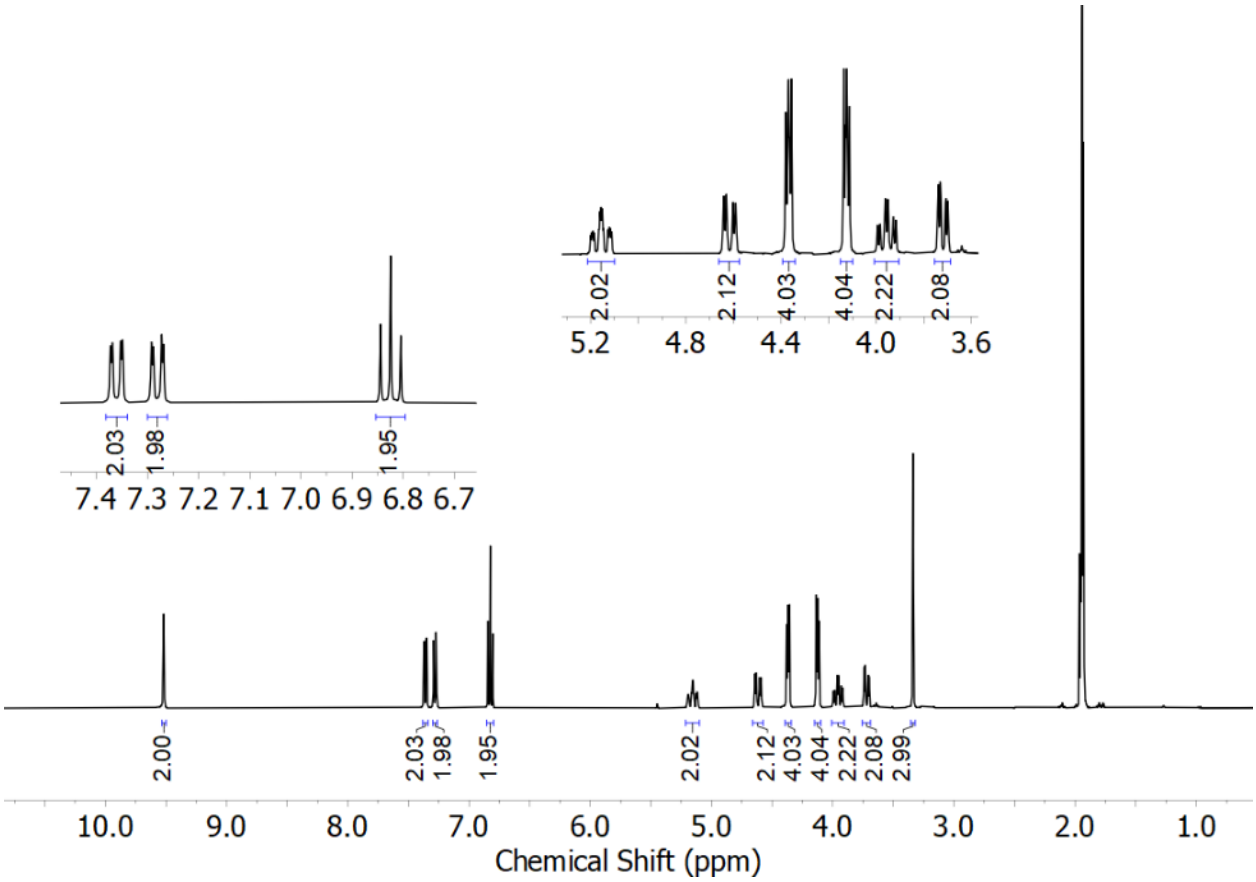

Figure C10. ^{1}H NMR spectrum (400 MHz, CD_3CN) of *in situ* generated **L^5UO_2Na**.

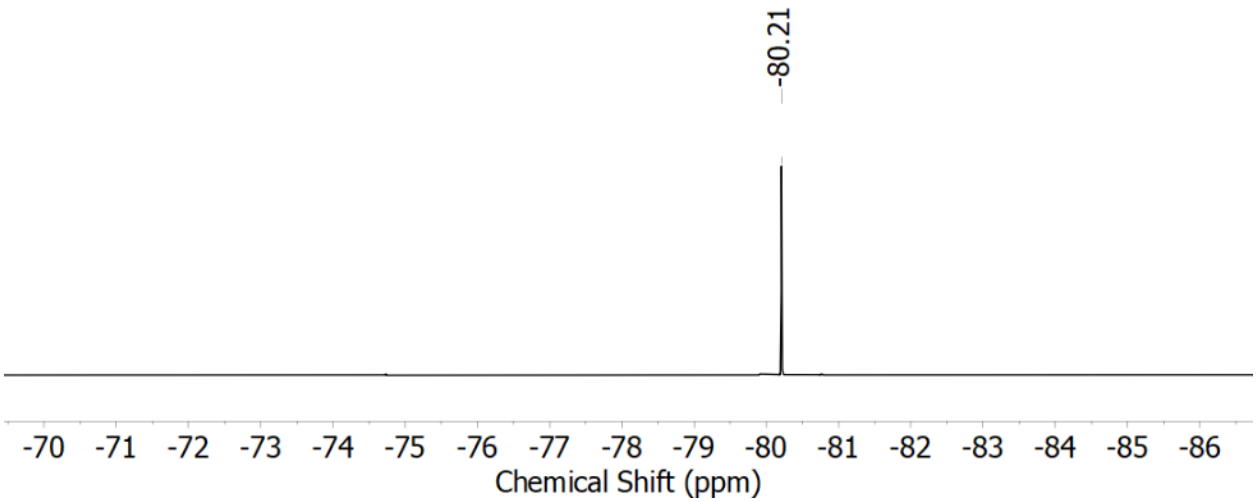

Figure C11. $^{19}F\{^{1}H\}$ NMR spectrum (400 MHz, CD_3CN) of *in situ* generated **L^5UO_2Na**.

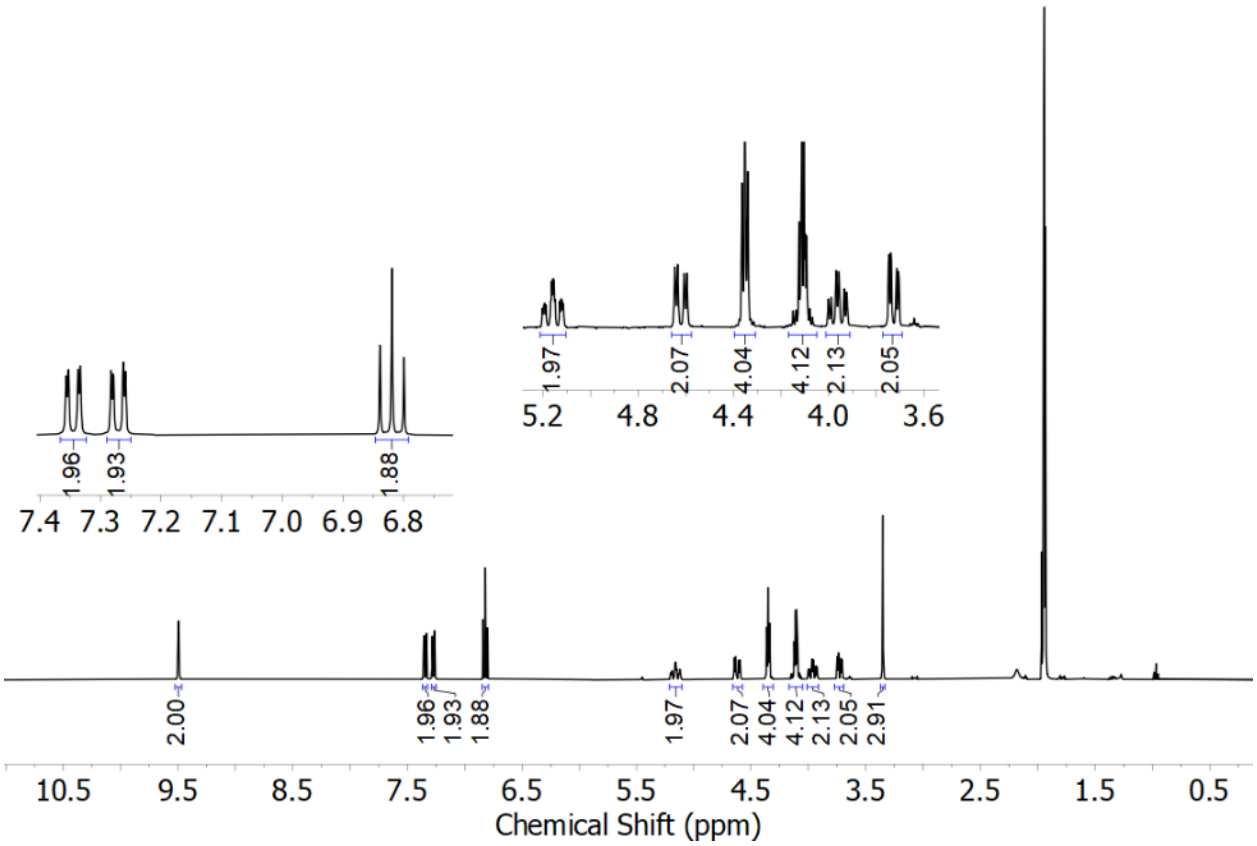

Figure C12. ^{1}H NMR spectrum (400 MHz, CD_3CN) of *in situ* generated **L^{5}UO$_2$Li**.

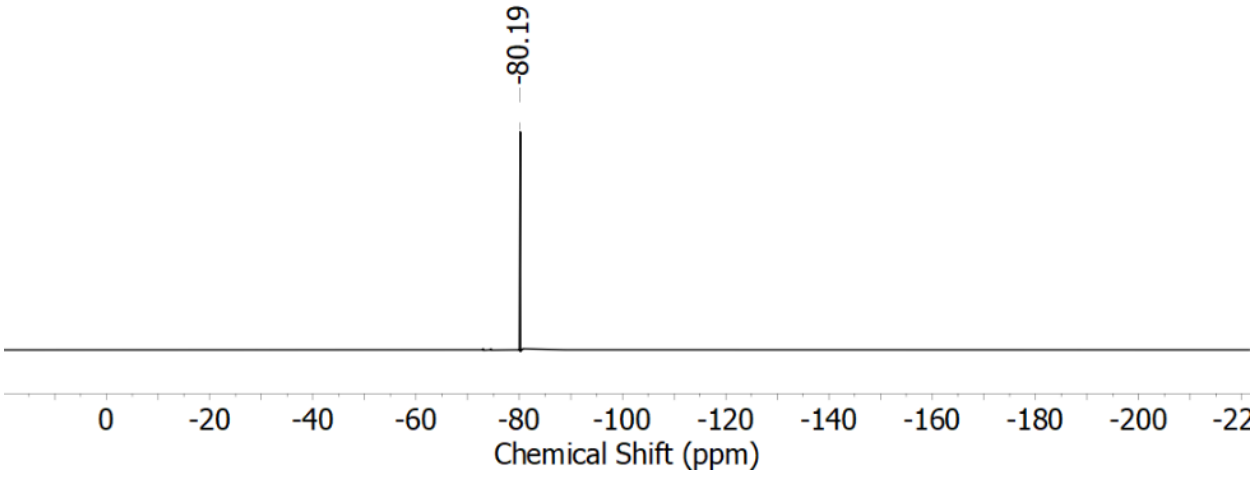

Figure C13. ^{19}F{^{1}H} NMR spectrum (400 MHz, CD_3CN) of *in situ* generated **L^{5}UO$_2$Li**.

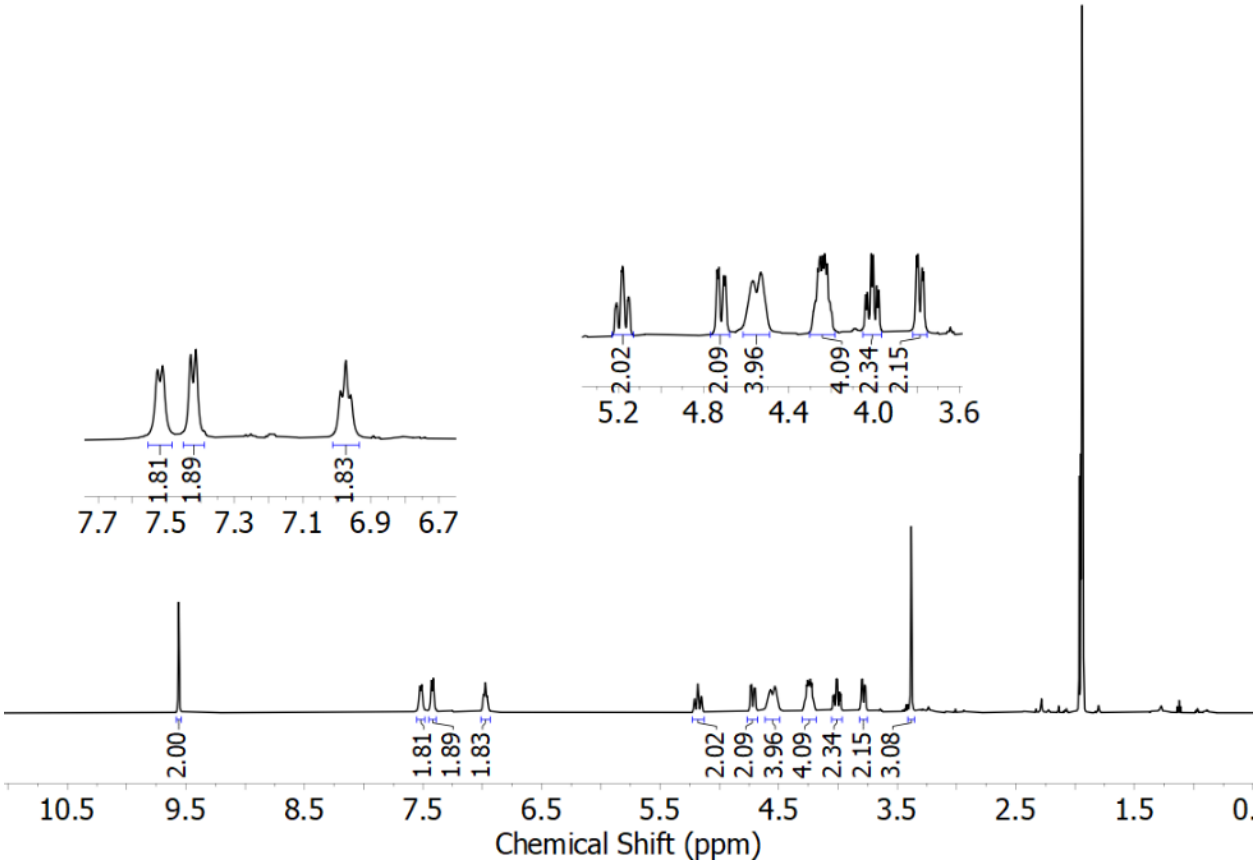

Figure C14. ^{1}H NMR spectrum (500 MHz, CD_3CN) of *in situ* generated **L^5UO_2Ca**.

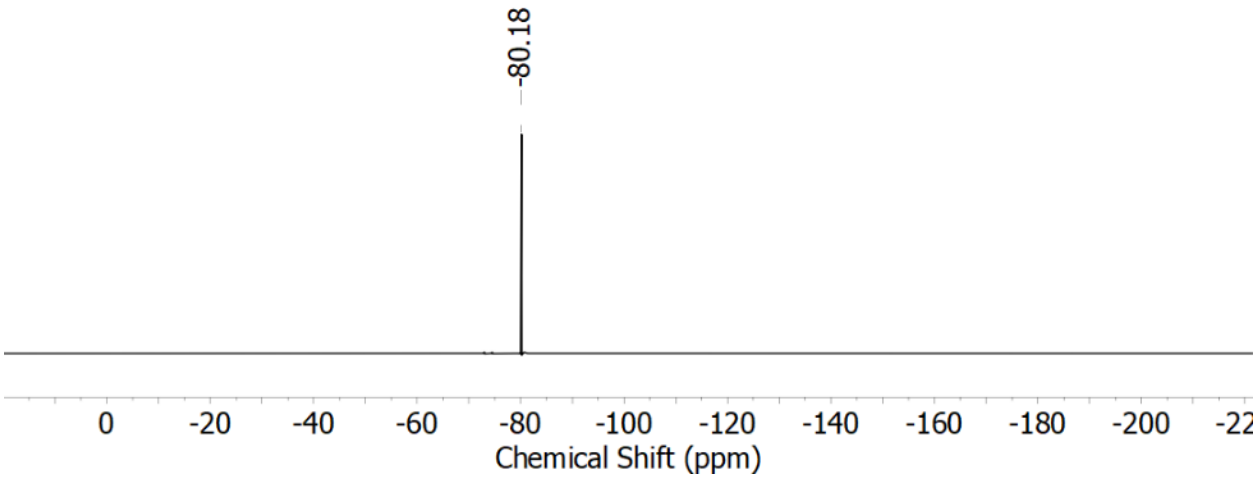

Figure C15. $^{19}F\{^{1}H\}$ NMR spectrum (500 MHz, CD_3CN) of *in situ* generated **L^5UO_2Ca**.

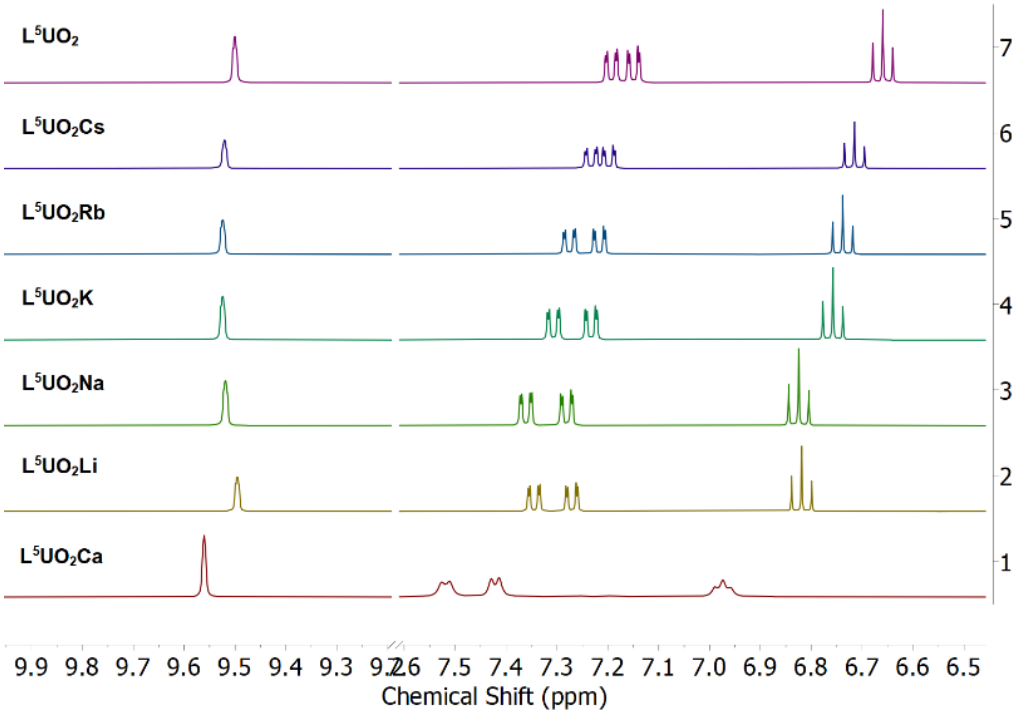

Figure C16. Stacked ^{1}H NMR spectra showing the aromatic and imine region of the **L^{5}UO$_2$** and **L^{5}UO$_2$M** complexes.

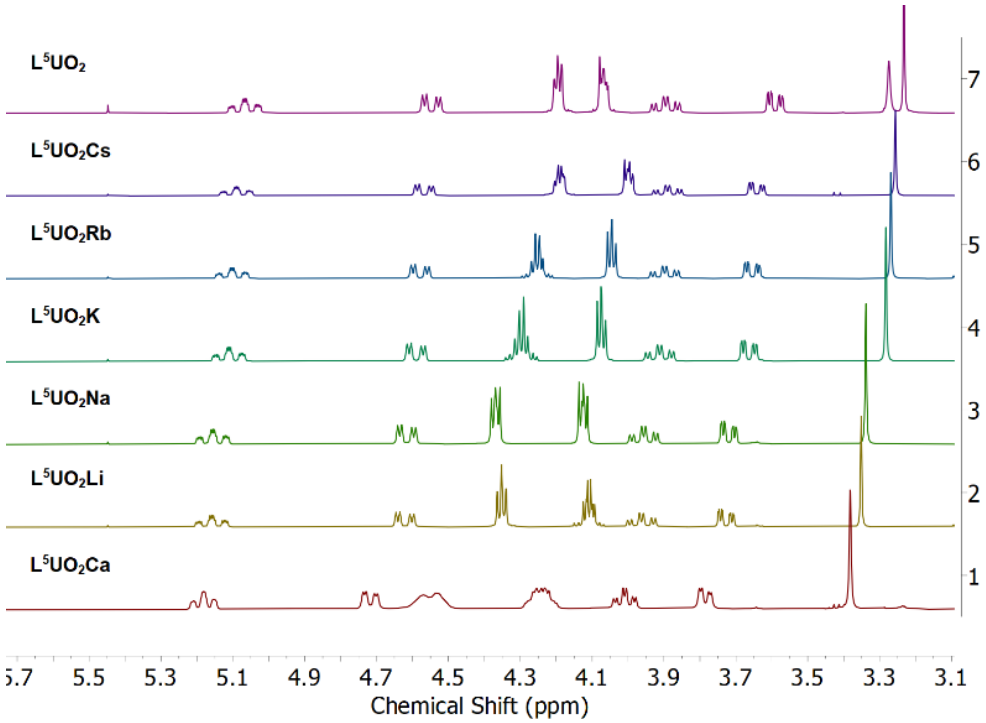

Figure C17. Stacked ^{1}H NMR spectra showing the aliphatic region of the **L^{5}UO$_2$U** and **L^{5}UO$_2$M** complexes.

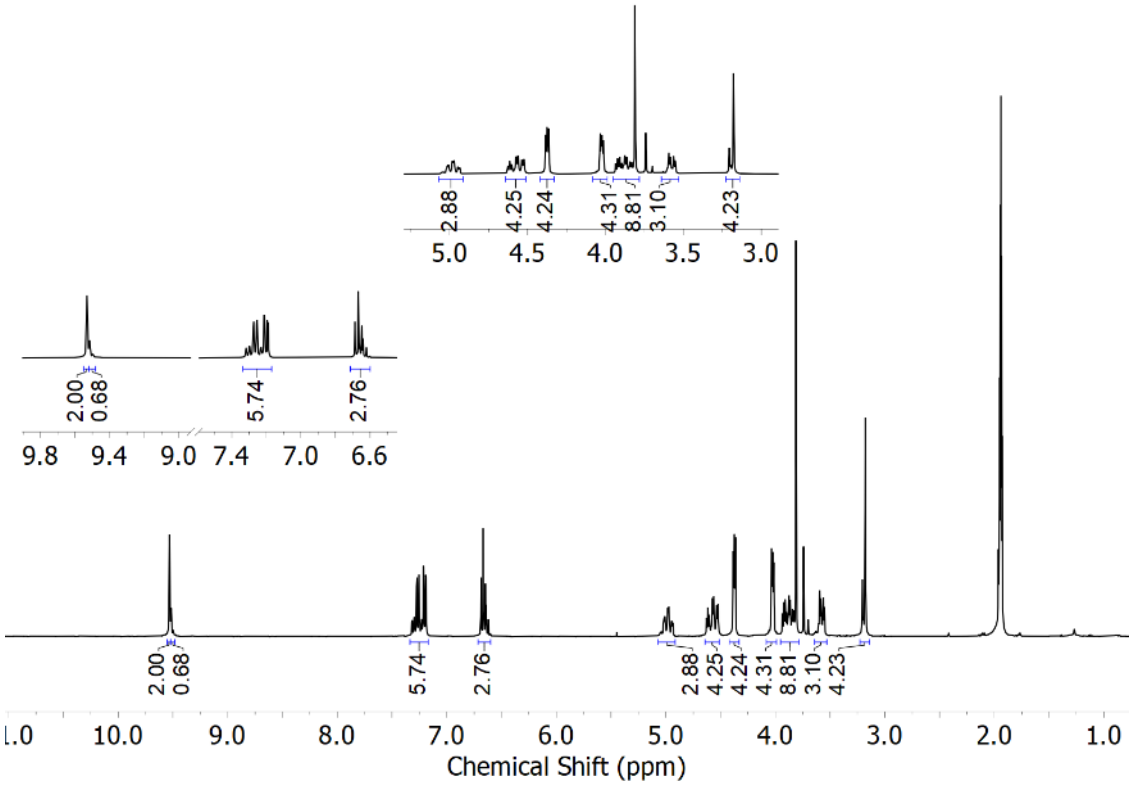

Figure C18. ^{1}H NMR spectrum (400 MHz, CD_3CN) of *in situ* generated $\mathbf{L^6UO_2}$.

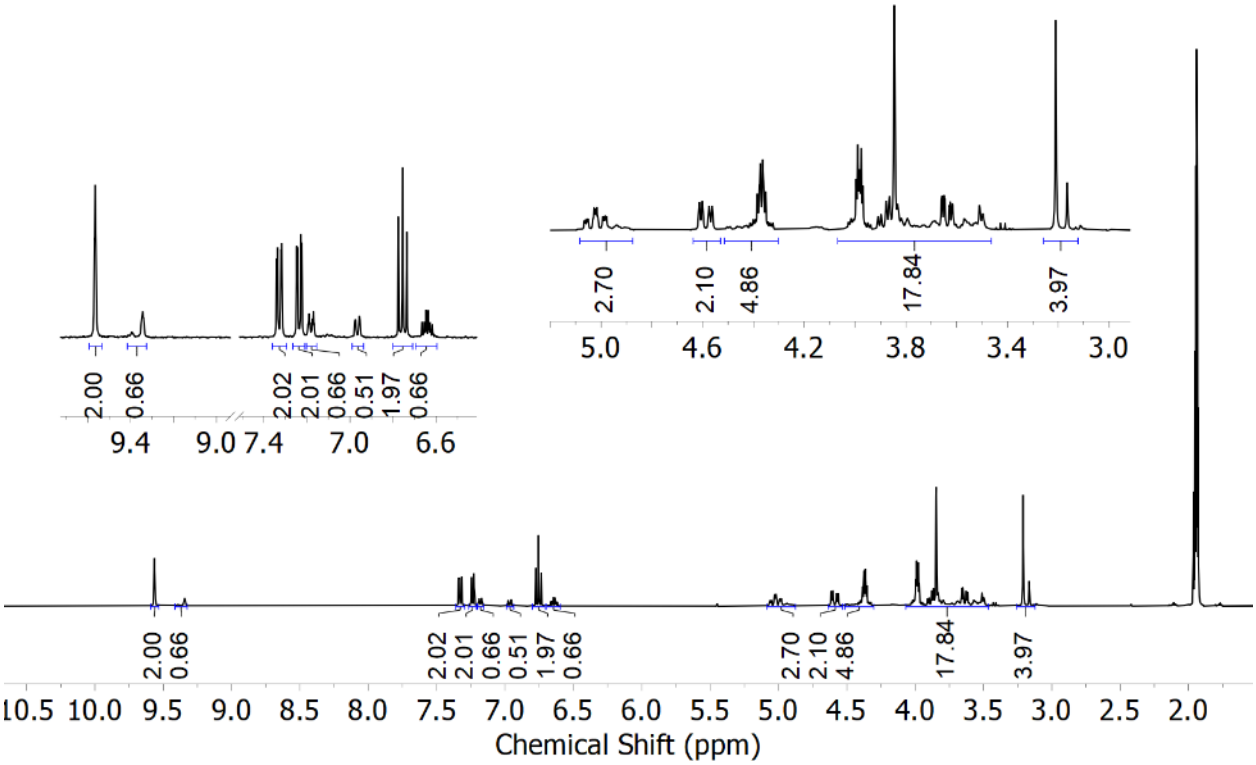

Figure C19. ^{1}H NMR spectrum (400 MHz, CD_3CN) of *in situ* generated $\mathbf{L^6UO_2Cs}$.

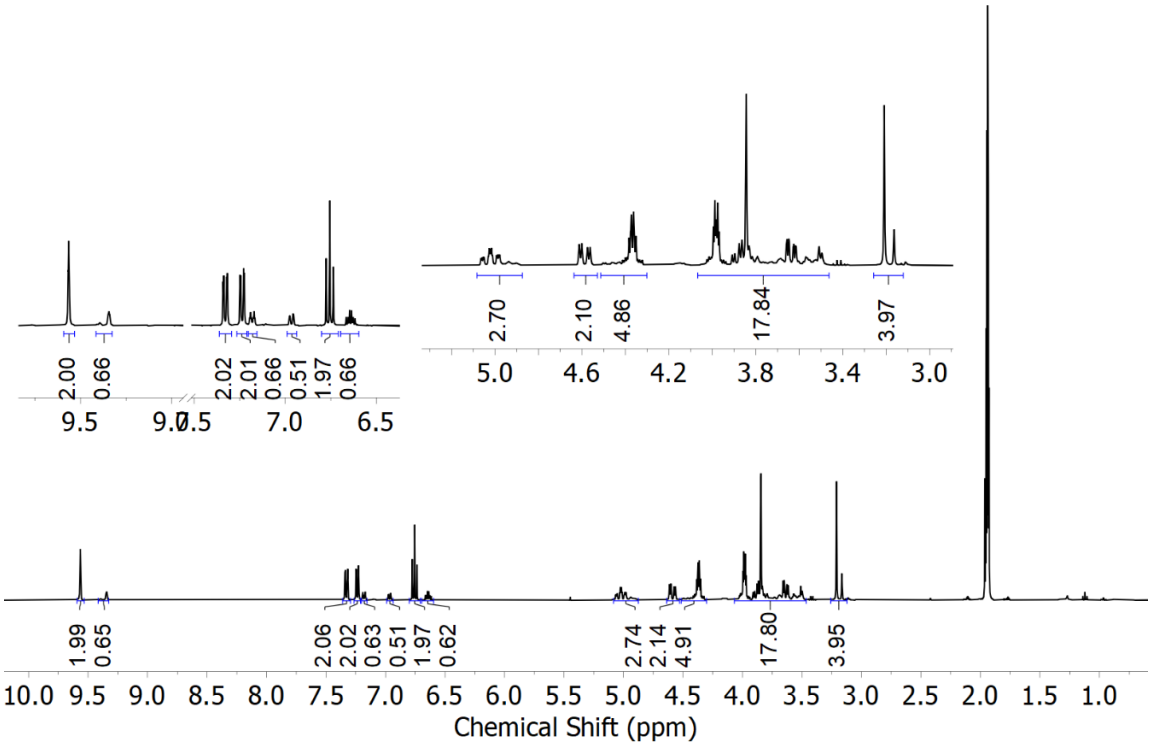

Figure C20. ^{1}H NMR spectrum (400 MHz, CD_3CN) of *in situ* generated **L^{6}UO$_2$Rb**.

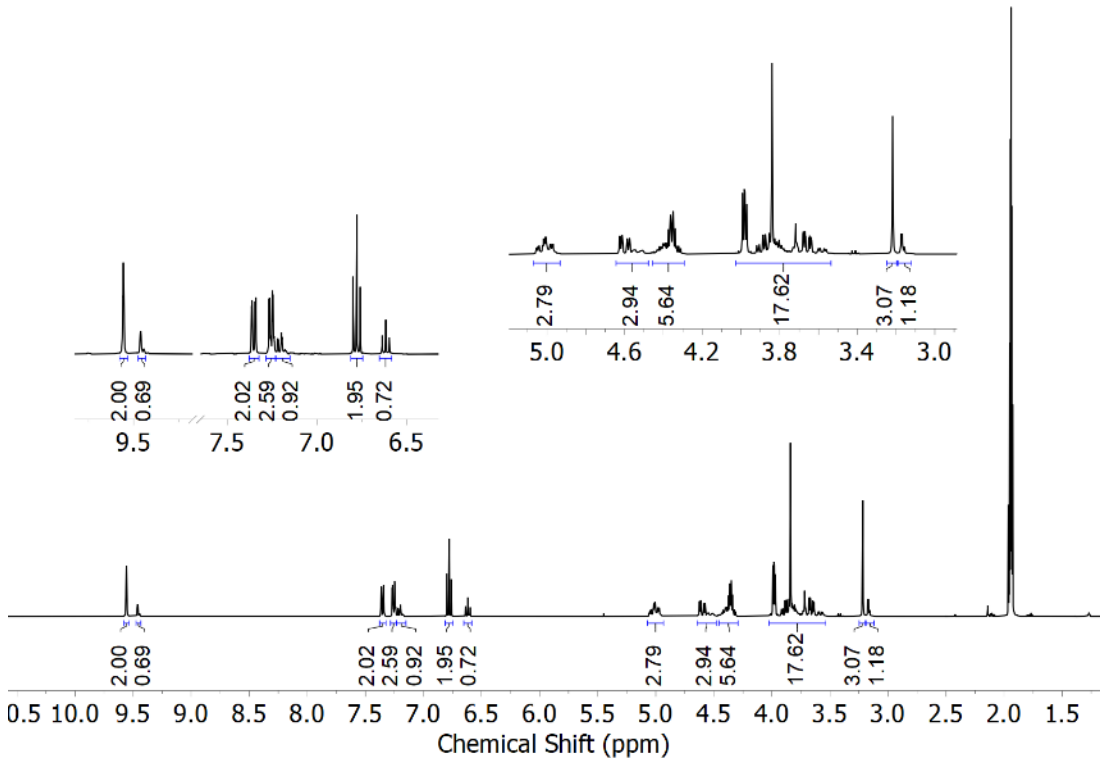

Figure C21. ^{1}H NMR spectrum (400 MHz, CD_3CN) of *in situ* generated **L^{6}UO$_2$K**.

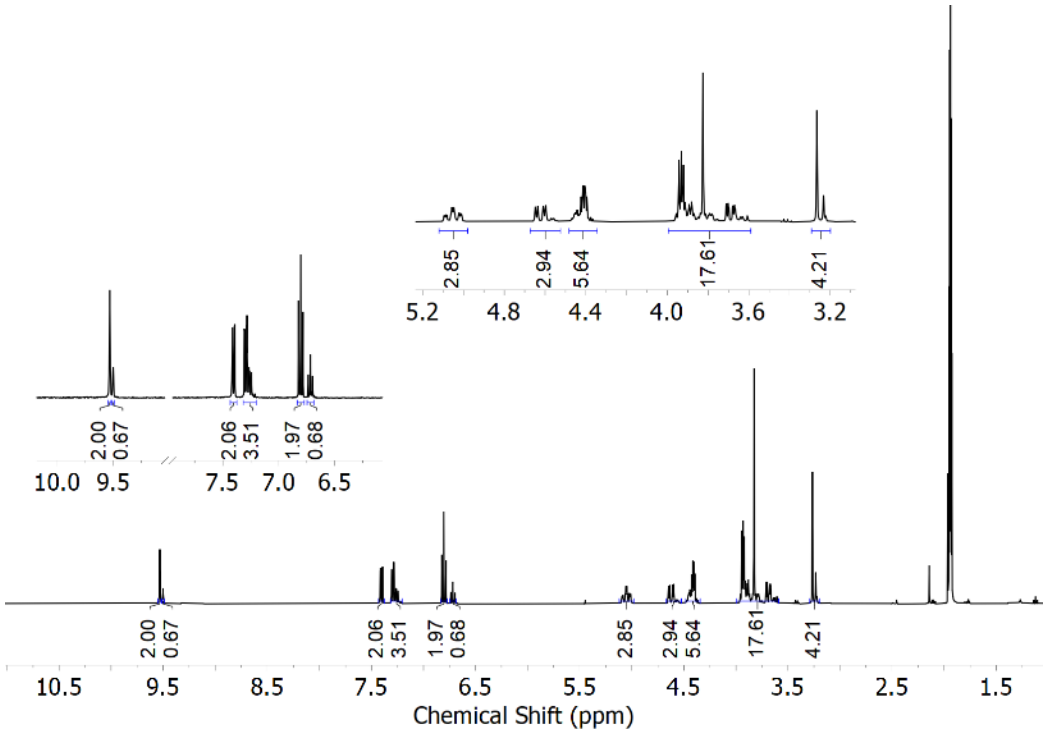

Figure C22. ^{1}H NMR spectrum (400 MHz, CD_3CN) of *in situ* generated **L^{6}UO$_2$Na**.

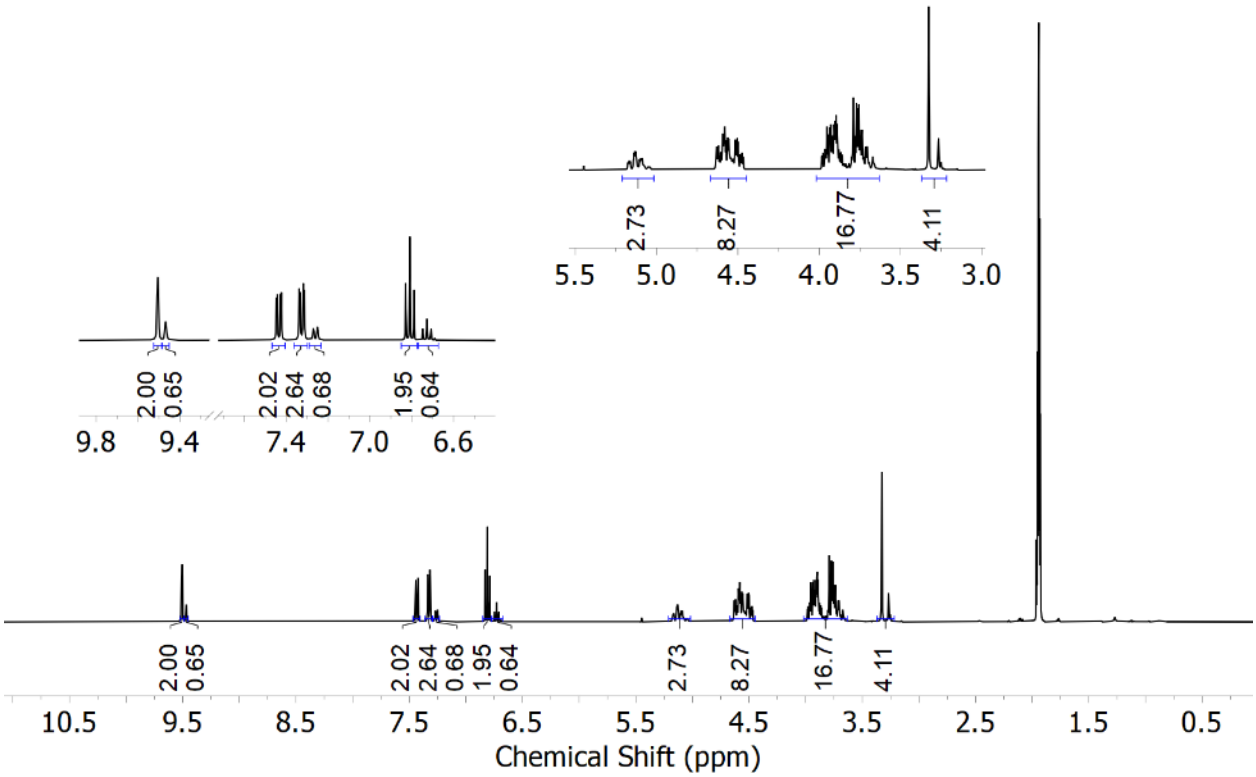

Figure C23. ^{1}H NMR spectrum (400 MHz, CD_3CN) of *in situ* generated **L^{6}UO$_2$Li**.

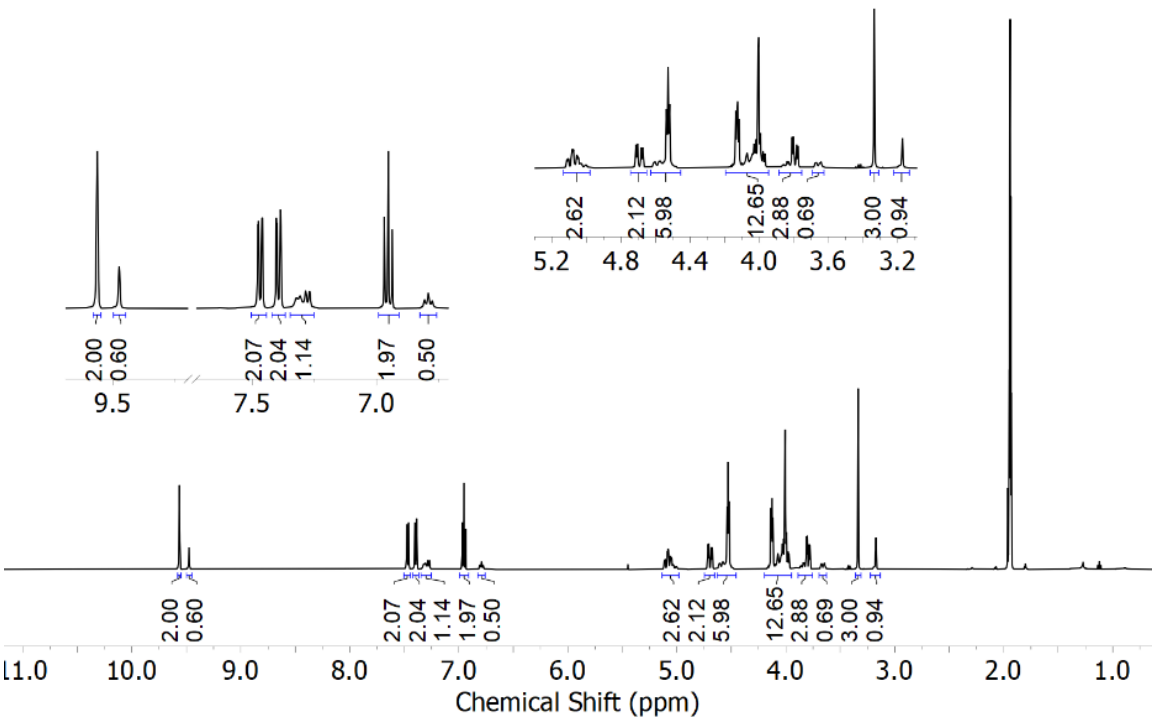

Figure C24. ^{1}H NMR spectrum (500 MHz, CD_3CN) of *in situ* generated **L^{6}UO$_2$Ca**.

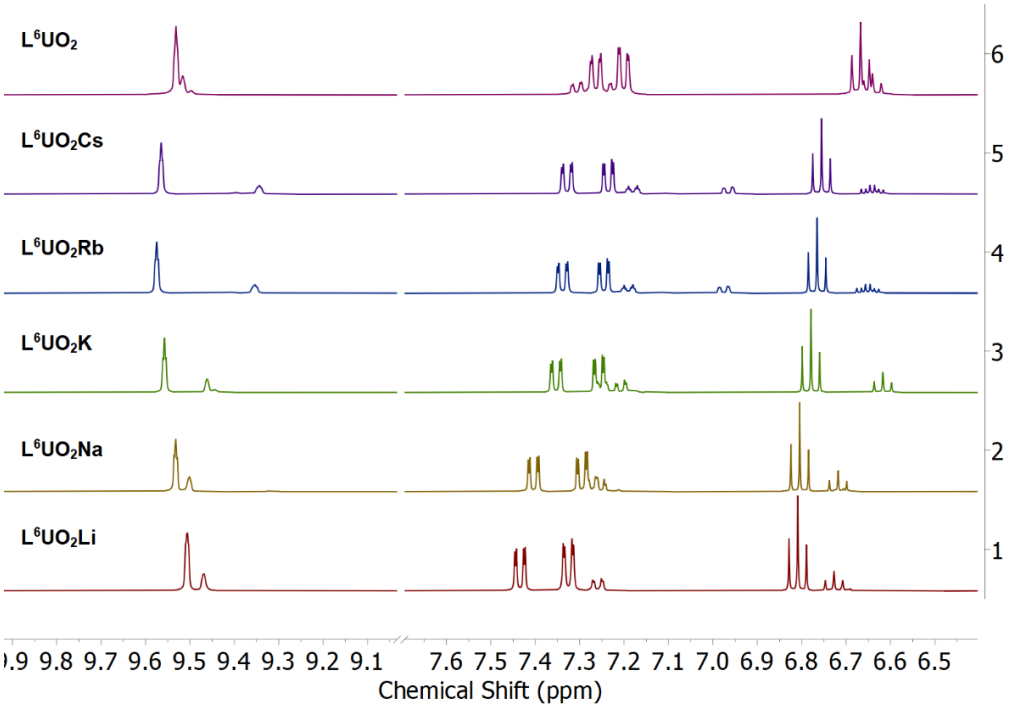

Figure C25. Stacked ^{1}H NMR spectra showing the aromatic and imine region of the **L^{6}UO$_2$** and **L^{6}UO$_2$M** complexes.

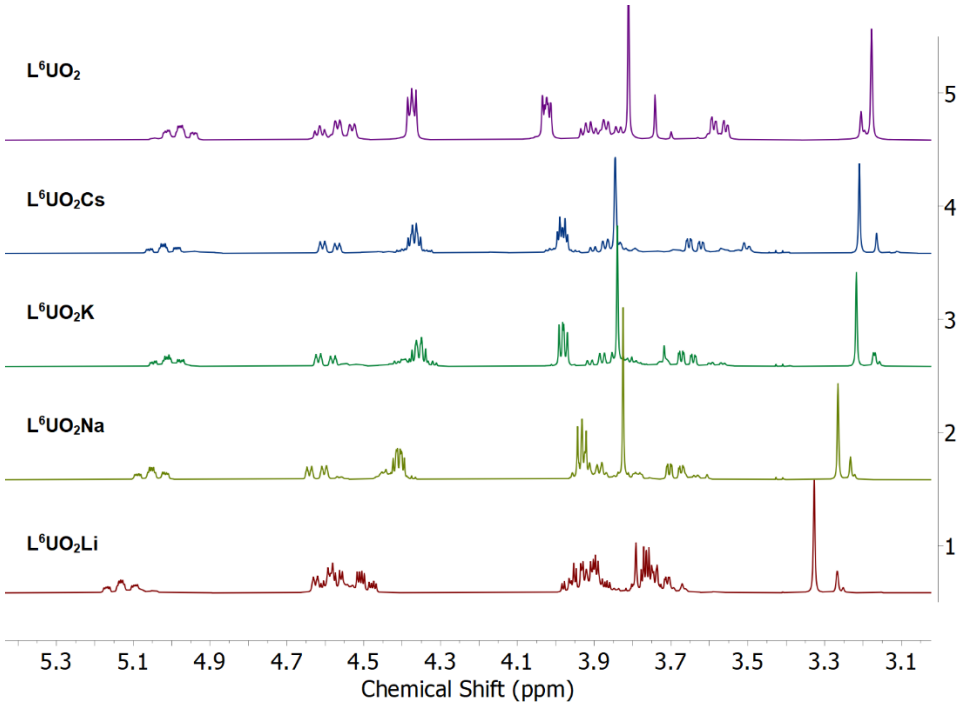

Figure C26. Stacked ^{1}H NMR spectra showing the aromatic and imine region of the **L^{6}UO$_2$** and **L^{6}UO$_2$M** complexes.

Table C1. Comparison of U–O_{oxo} bond length across the series of UO_2^{2+} complexes.

Compound	U–O7	U–O8	U–O_{oxo} (avg., Å)[b]
L^{5}UO$_2$	1.779(4)	1.771(4)	1.775(6)
L^{6}UO$_2$[a]	1.783(8)	1.792(7)	1.788(11)
L^{5}UO$_2$Li	1.778(2)	1.784(2)	1.781(3)
L^{5}UO$_2$Na	1.780(5)	1.780(5)	1.780(7)
L^{6}UO$_2$Na[a]	1.782(5)	1.780(5)	1.781(7)
L^{5}UO$_2$K	1.794(6)	1.788(6)	1.791(8)
L^{6}UO$_2$K[a]	1.773(7)	1.781(7)	1.777(10)

(a) Structural data taken from references 1 (CCDC 1960629) and 2 (CCDC 1960628). (b) Average of the U–O7 and U–O8 bond distances. Errors on the average bond lengths and bond angles were derived by propagation of error from the individual values and estimated standard deviations (e.s.d.'s).

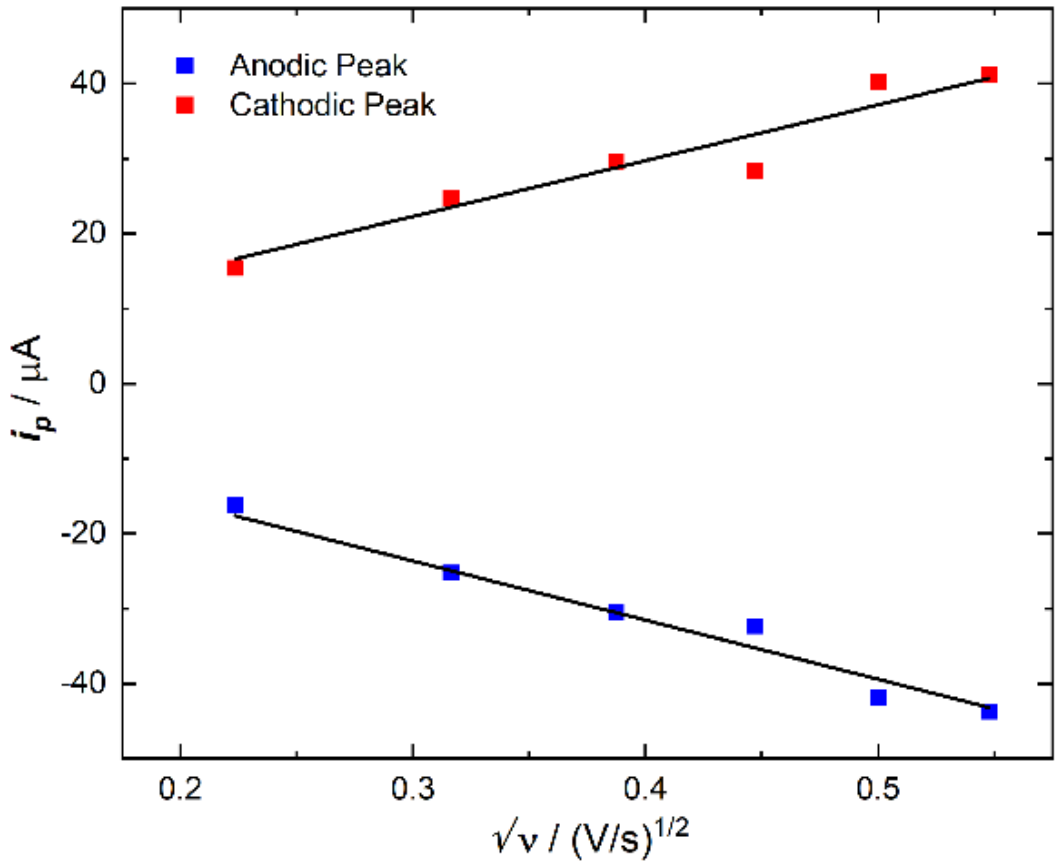

Figure C27. Plot of peak current density vs. (scan rate)$^{1/2}$, demonstrating the diffusional nature of the oxidized species involved in **L^{5}UO$_2$**. Diffusion coefficient of the oxidized species (calculated from the slope of the line represented by blue data points), D_{ox} = 10.6 × 10^{-6} cm^2/s. Diffusion coefficient of the reduced species (calculated from the slope of the line represented by red data points), D_{red} = 9.43 × 10^{-6} cm^2/s.

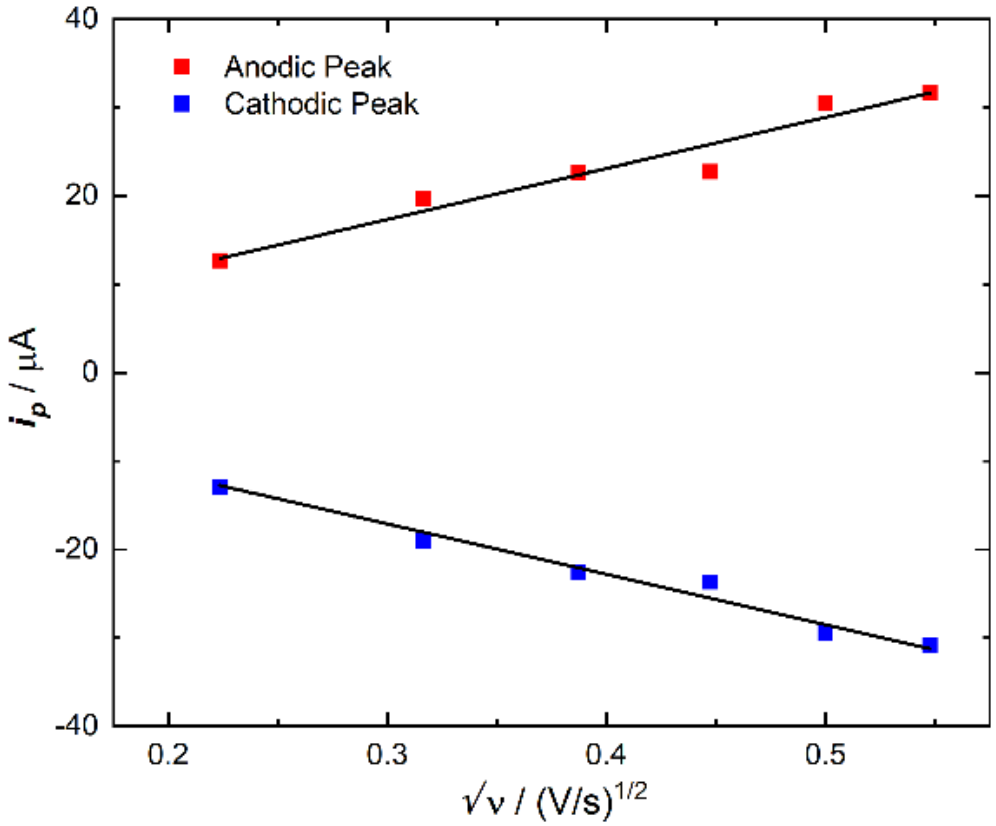

Figure C28. Plot of peak current density vs. (scan rate)$^{1/2}$, demonstrating the diffusional nature of the oxidized species involved in **L^{5}UO$_2$Cs**. Diffusion coefficient of the oxidized species (calculated from the slope of the line represented by blue data points), D_{ox} = 5.55 × 10^{-6} cm^2/s. Diffusion coefficient of the reduced species (calculated from the slope of the line represented by red data points), D_{red} = 5.70 × 10^{-6} cm^2/s.

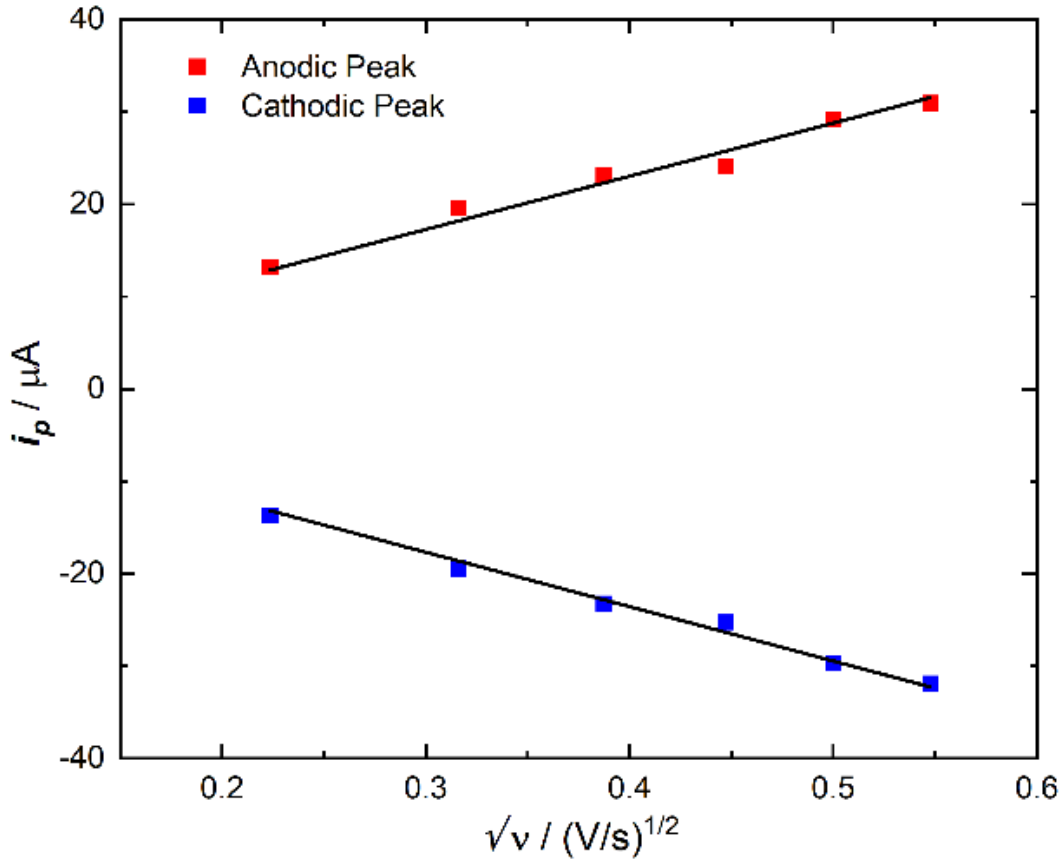

Figure C29. Plot of peak current density vs. (scan rate)$^{1/2}$, demonstrating the diffusional nature of the oxidized species involved in **L^{5}UO$_2$Rb**. Diffusion coefficient of the oxidized species (calculated from the slope of the line represented by blue data points), D_{ox} = 5.92 × 10^{-6} cm^2/s. Diffusion coefficient of the reduced species (calculated from the slope of the line represented by red data points), D_{red} = 5.65 × 10^{-6} cm^2/s.

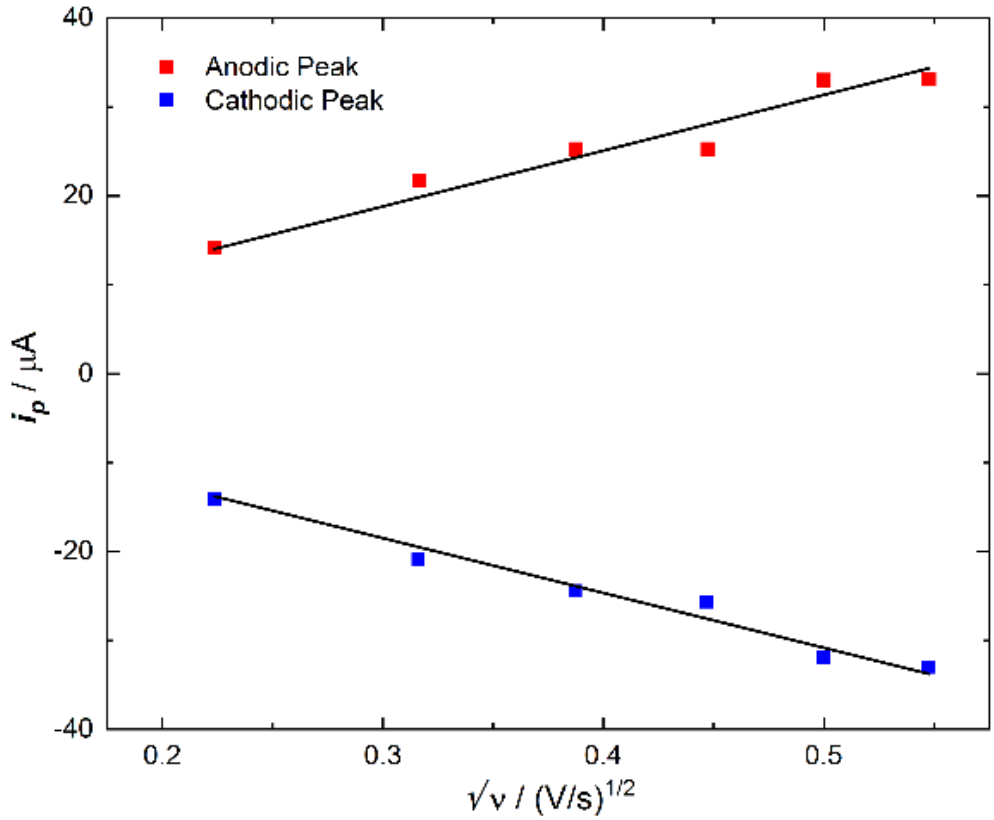

Figure C30. Plot of peak current density vs. (scan rate)$^{1/2}$, demonstrating the diffusional nature of the oxidized species involved in **L^{5}UO$_2$K**. Diffusion coefficient of the oxidized species (calculated from the slope of the line represented by blue data points), D_{ox} = 6.49 × 10^{-6} cm^2/s. Diffusion coefficient of the reduced species (calculated from the slope of the line represented by red data points), D_{red} = 6.71 × 10^{-6} cm^2/s.

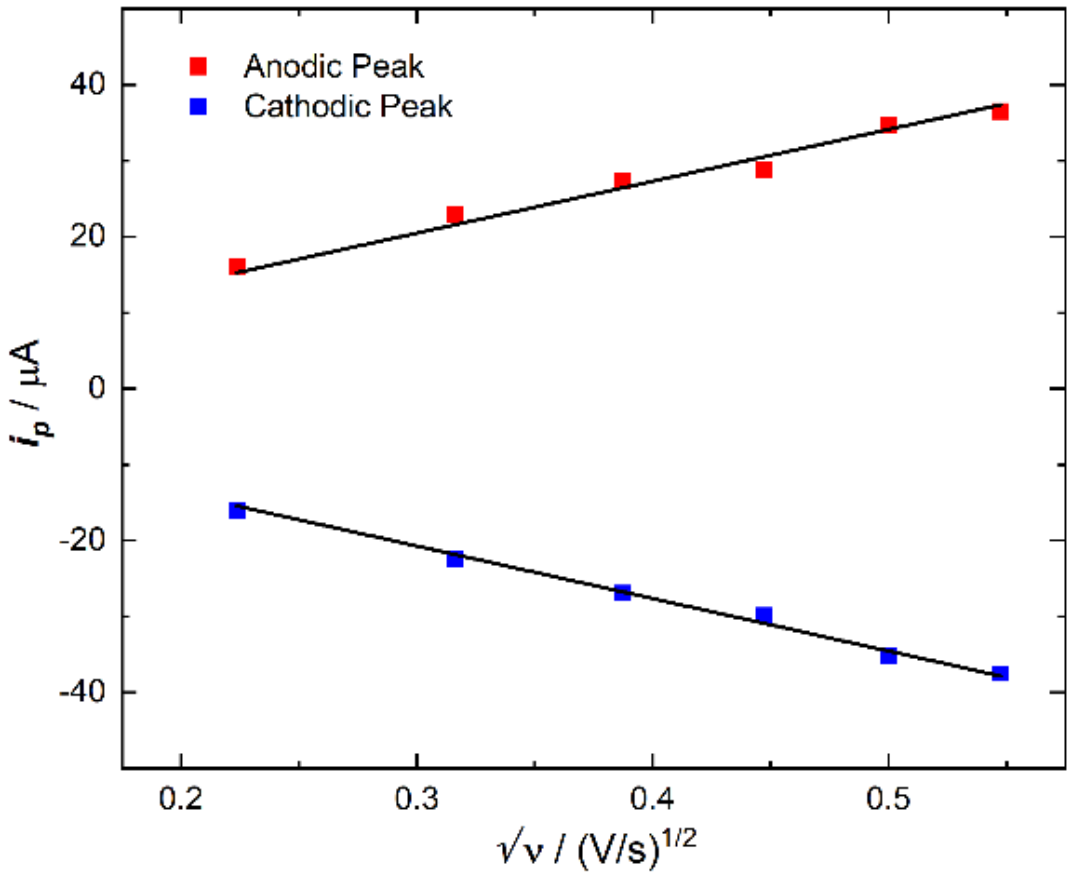

Figure C31. Plot of peak current density vs. (scan rate)$^{1/2}$, demonstrating the diffusional nature of the oxidized species involved in **L^{5}UO$_2$Na**. Diffusion coefficient of the oxidized species (calculated from the slope of the line represented by blue data points), D_{ox} = 8.15 × 10^{-6} cm^2/s. Diffusion coefficient of the reduced species (calculated from the slope of the line represented by red data points), D_{red} = 7.94 × 10^{-6} cm^2/s.

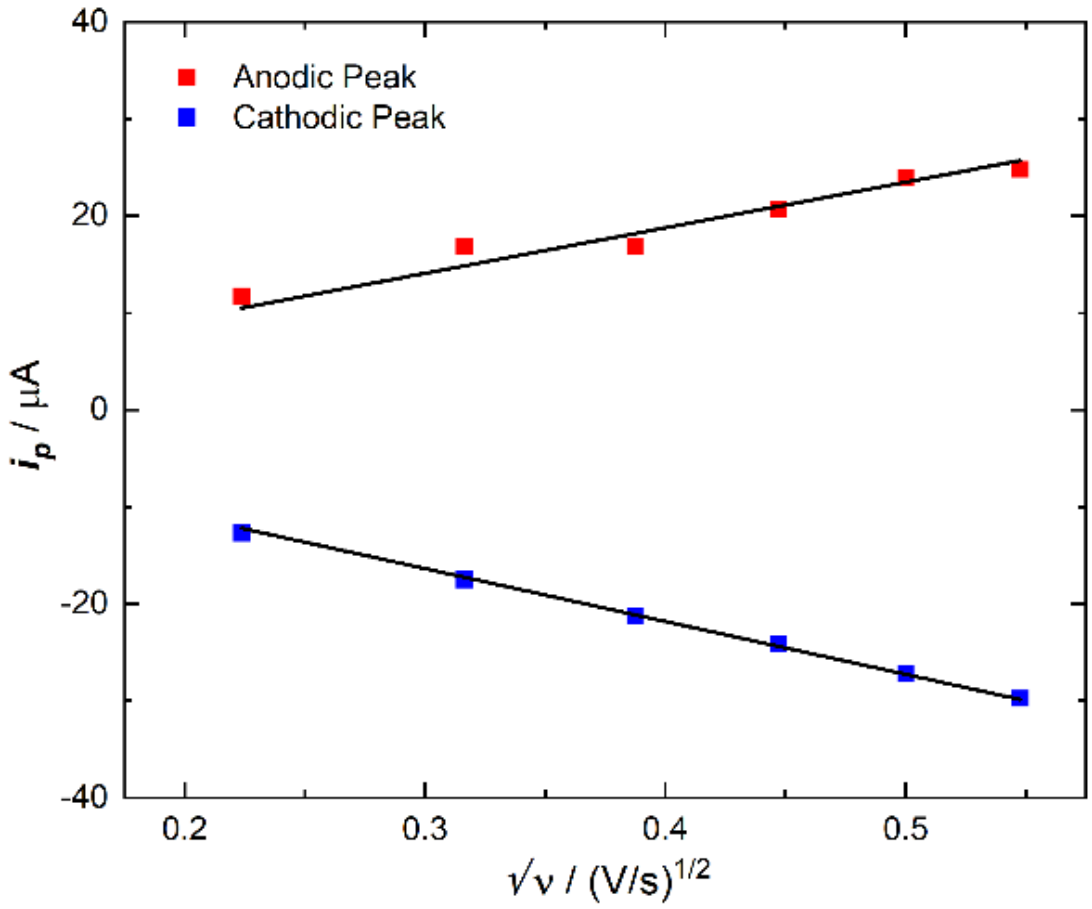

Figure C32. Plot of peak current density vs. (scan rate)$^{1/2}$, demonstrating the diffusional nature of the oxidized species involved in **L^{5}UO$_2$Li**. Diffusion coefficient of the oxidized species (calculated from the slope of the line represented by blue data points), D_{ox} = 5.07 × 10^{-6} cm^2/s. Diffusion coefficient of the reduced species (calculated from the slope of the line represented by red data points), D_{red} = 3.76 × 10^{-6} cm^2/s.

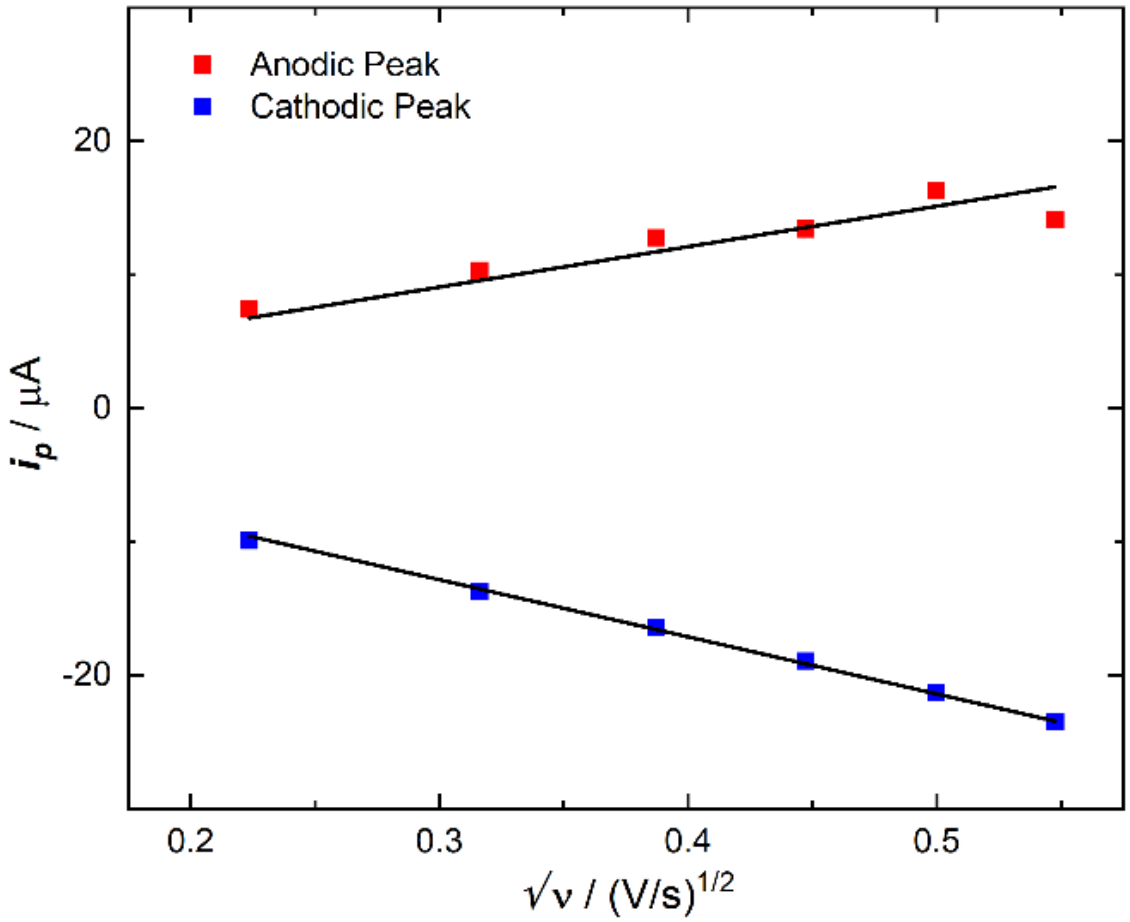

Figure C33. Plot of peak current density vs. (scan rate)$^{1/2}$, demonstrating the diffusional nature of the oxidized species involved in **L^{5}UO$_2$Ca**. Diffusion coefficient of the oxidized species (calculated from the slope of the line represented by blue data points), D_{ox} = 3.12 × 10^{-6} cm^2/s. Diffusion coefficient of the reduced species (calculated from the slope of the line represented by red data points), D_{red} = 1.56 × 10^{-6} cm^2/s.

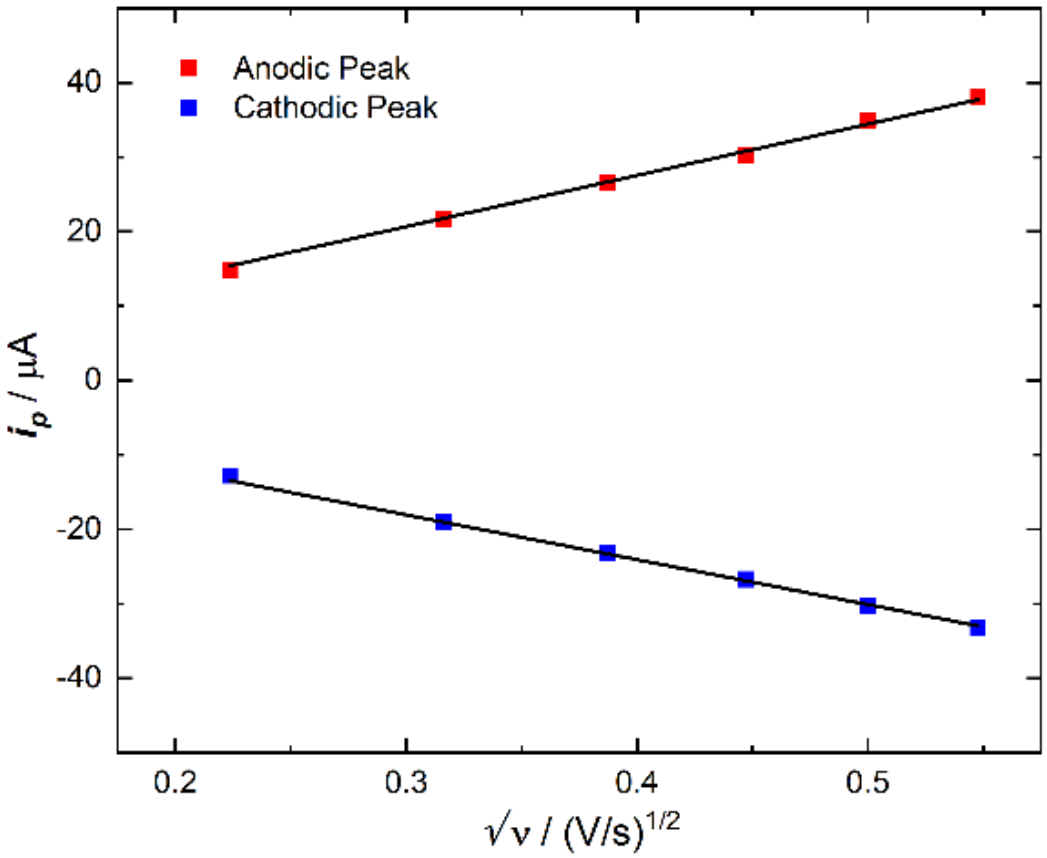

Figure C34. Plot of peak current density vs. (scan rate)$^{1/2}$, demonstrating the diffusional nature of the oxidized species involved in **L^{6}UO$_2$**. Diffusion coefficient of the oxidized species (calculated from the slope of the line represented by blue data points), D_{ox} = 7.86 × 10^{-6} cm^2/s. Diffusion coefficient of the reduced species (calculated from the slope of the line represented by red data points), D_{red} = 7.01 × 10^{-6} cm^2/s.

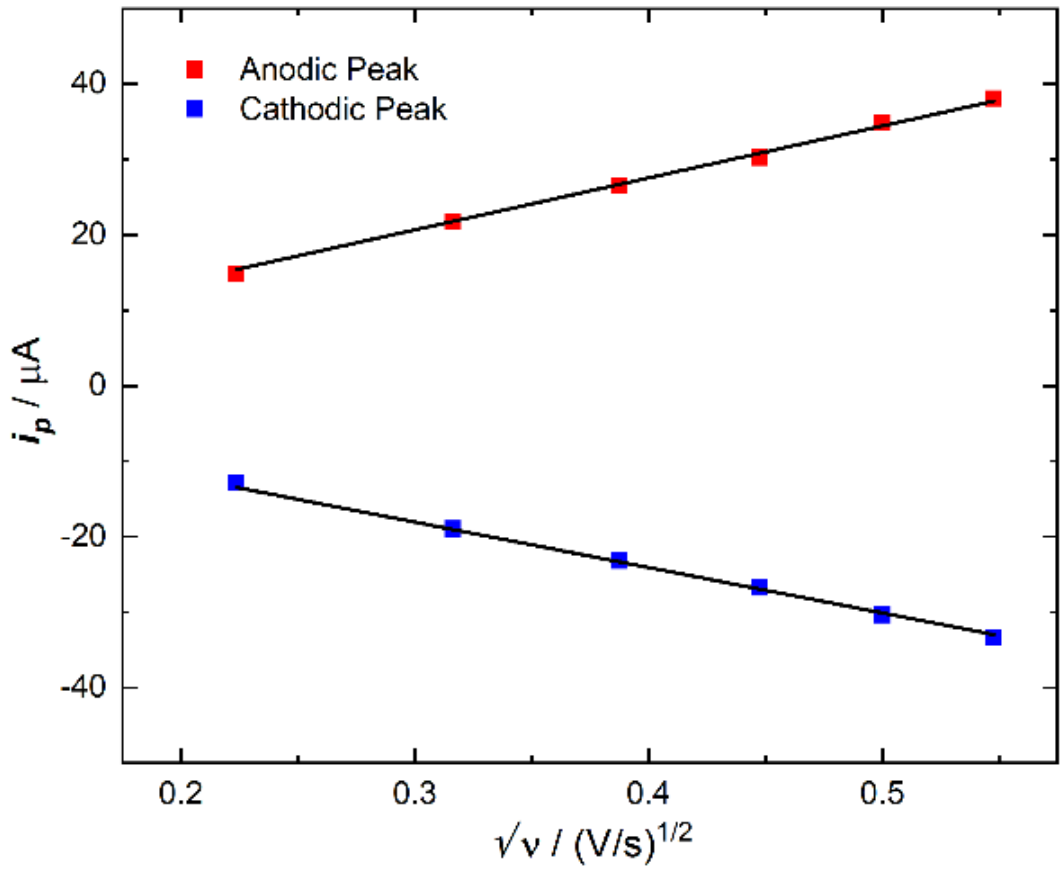

Figure C35. Plot of peak current density vs. (scan rate)$^{1/2}$, demonstrating the diffusional nature of the oxidized species involved in **L^{6}UO$_2$Cs**. Diffusion coefficient of the oxidized species (calculated from the slope of the line represented by blue data points), D_{ox} = 6.18 × 10^{-6} cm^2/s. Diffusion coefficient of the reduced species (calculated from the slope of the line represented by red data points), D_{red} = 8.09 × 10^{-6} cm^2/s.

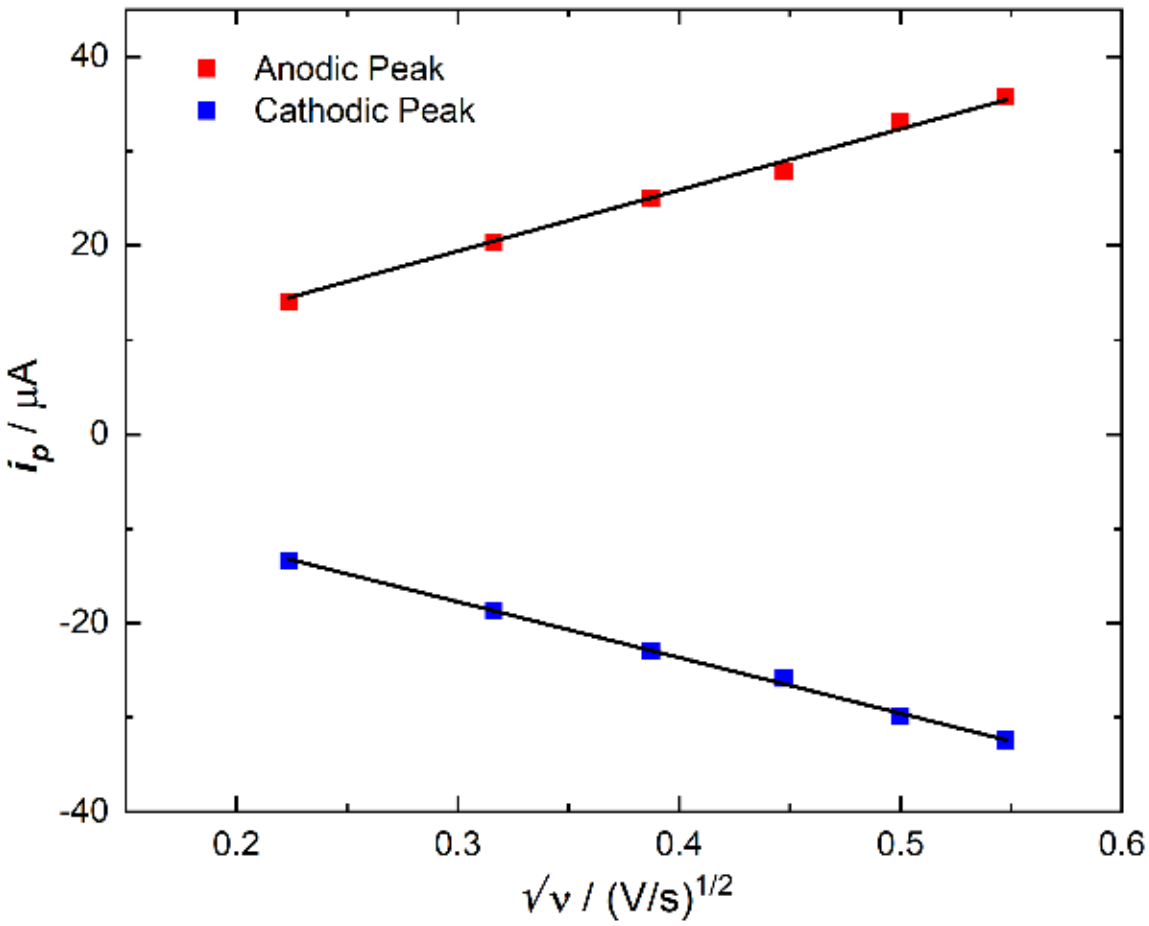

Figure C36. Plot of peak current density vs. (scan rate)$^{1/2}$, demonstrating the diffusional nature of the oxidized species involved in **L^{6}UO$_2$Rb**. Diffusion coefficient of the oxidized species (calculated from the slope of the line represented by blue data points), D_{ox} = 5.96 × 10^{-6} cm^2/s. Diffusion coefficient of the reduced species (calculated from the slope of the line represented by red data points), D_{red} = 7.14 × 10^{-6} cm^2/s.

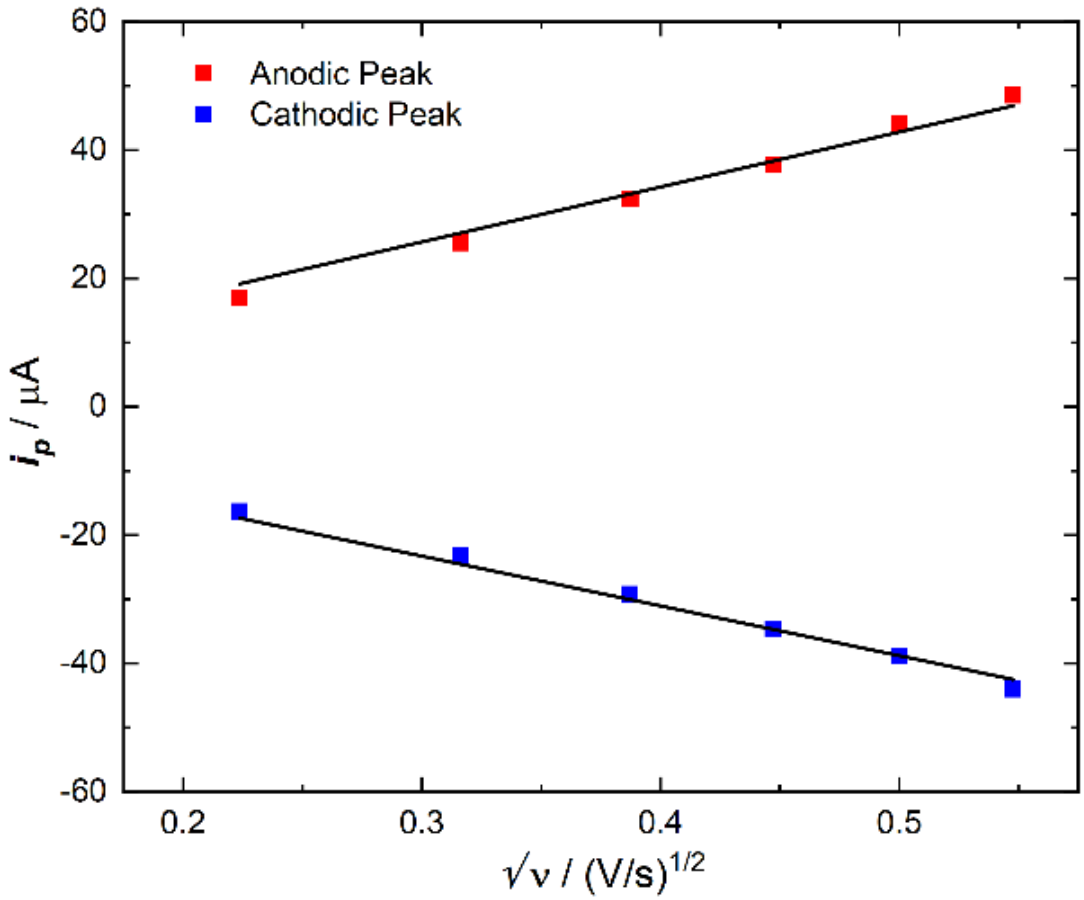

Figure C37. Plot of peak current density vs. (scan rate)$^{1/2}$, demonstrating the diffusional nature of the oxidized species involved in **L^{6}UO$_2$K**. Diffusion coefficient of the oxidized species (calculated from the slope of the line represented by blue data points), D_{ox} = 10.3 × 10^{-6} cm^2/s. Diffusion coefficient of the reduced species (calculated from the slope of the line represented by red data points), D_{red} = 12.5 × 10^{-6} cm^2/s.

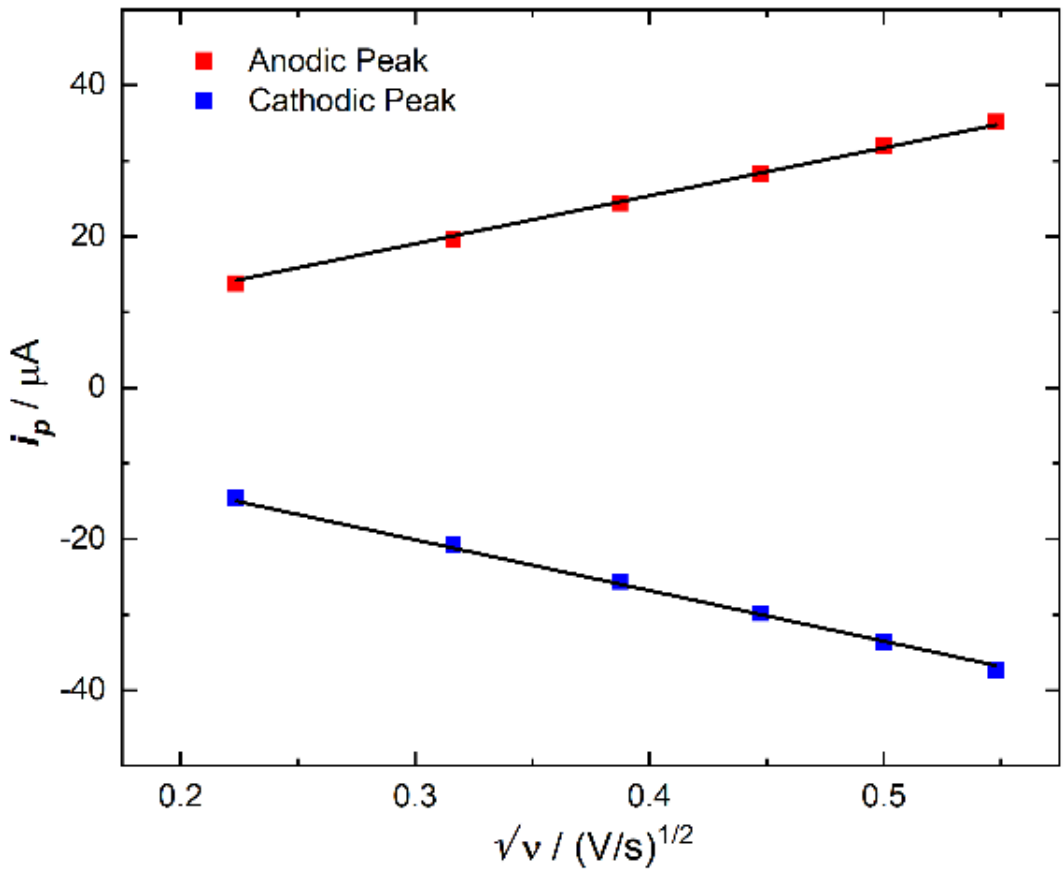

Figure C38. Plot of peak current density vs. (scan rate)$^{1/2}$, demonstrating the diffusional nature of the oxidized species involved in **L^{6}UO$_2$Na**. Diffusion coefficient of the oxidized species (calculated from the slope of the line represented by blue data points), D_{ox} = 7.67 × 10^{-6} cm^2/s. Diffusion coefficient of the reduced species (calculated from the slope of the line represented by red data points), D_{red} = 6.86 × 10^{-6} cm^2/s.

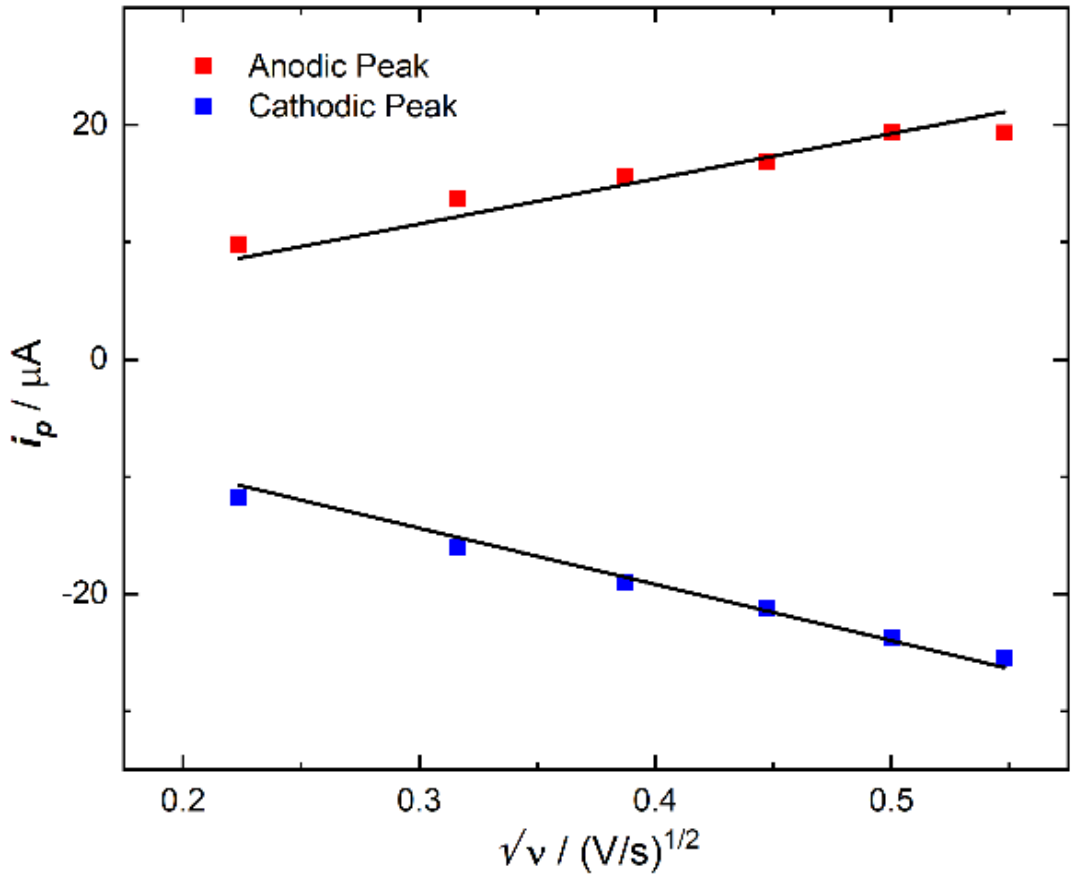

Figure C39. Plot of peak current density vs. (scan rate)$^{1/2}$, demonstrating the diffusional nature of the oxidized species involved in **L^{6}UO$_2$Li**. Diffusion coefficient of the oxidized species (calculated from the slope of the line represented by blue data points), D_{ox} = 3.92 × 10^{-6} cm^2/s. Diffusion coefficient of the reduced species (calculated from the slope of the line represented by red data points), D_{red} = 2.53 × 10^{-6} cm^2/s.

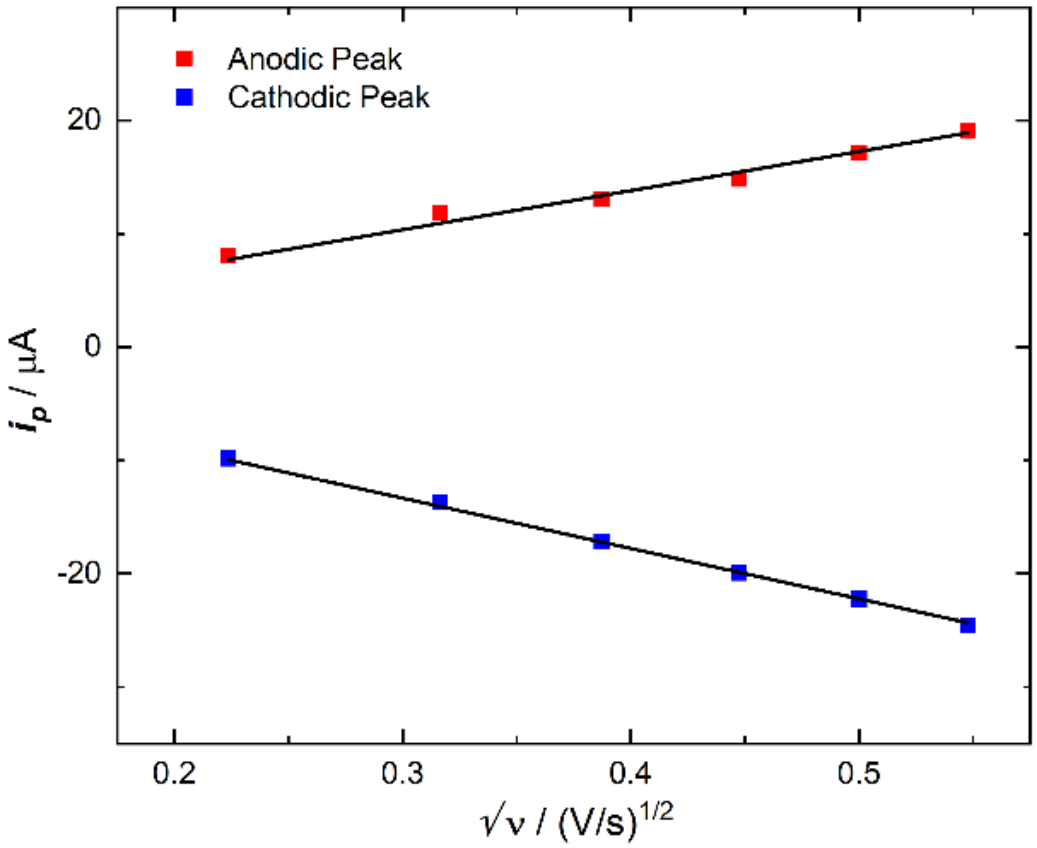

Figure C40. Plot of peak current density vs. (scan rate)$^{1/2}$, demonstrating the diffusional nature of the oxidized species involved in **L^{6}UO$_2$Ca**. Diffusion coefficient of the oxidized species (calculated from the slope of the line represented by blue data points), D_{ox} = 3.36 × 10^{-6} cm^2/s. Diffusion coefficient of the reduced species (calculated from the slope of the line represented by red data points), D_{red} = 2.03 × 10^{-6} cm^2/s.

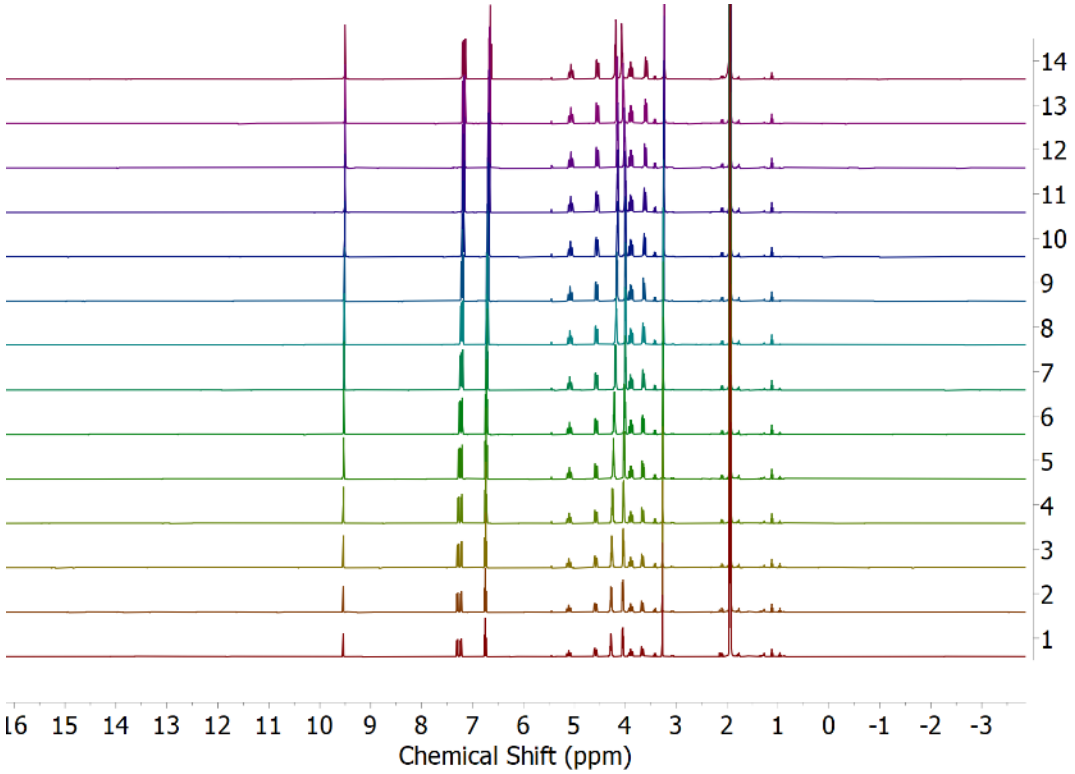

Figure C41. NMR titration experiments with $\mathbf{L^5UO_2}$ with CsOTf showing the full region.

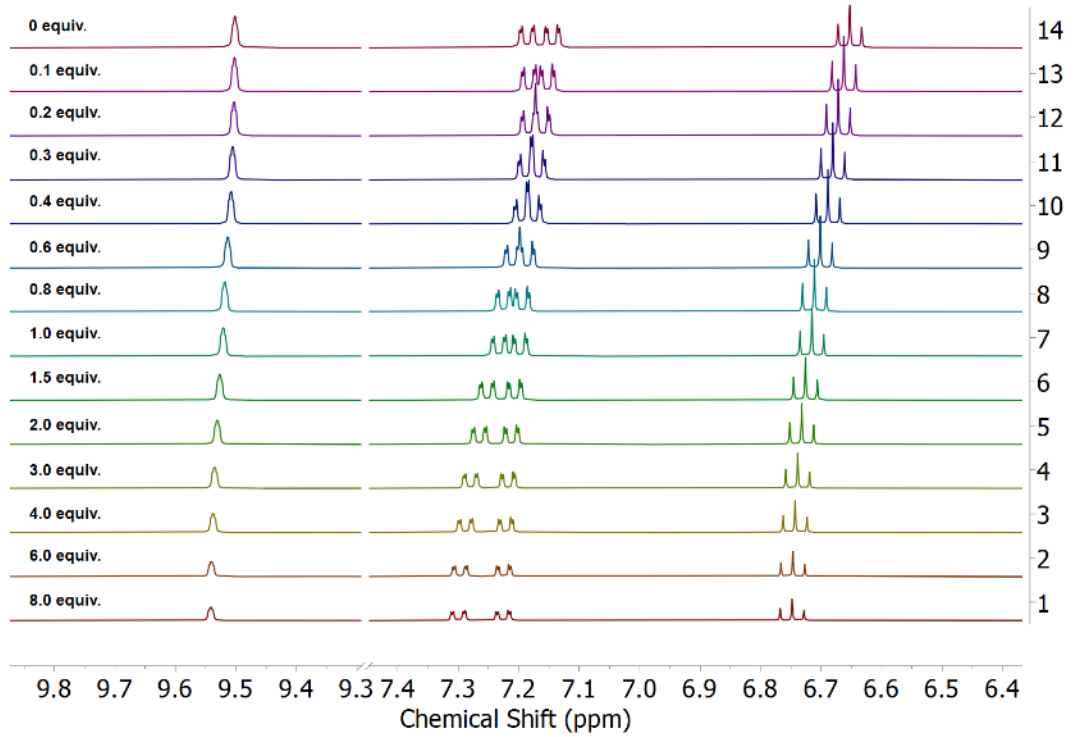

Figure C42. NMR titration experiments with $\mathbf{L^5UO_2}$ with CsOTf showing the imine and aromatic region.

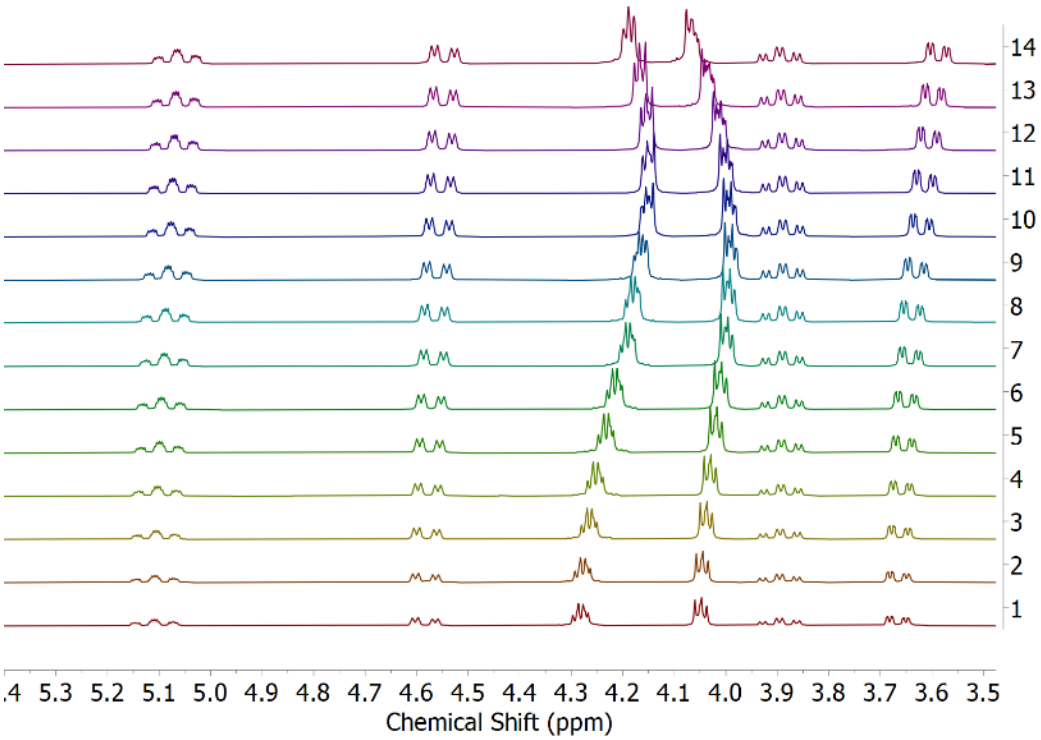

Figure C43. NMR titration experiments with $\mathbf{L^5UO_2}$ with CsOTf showing the aliphatic region.

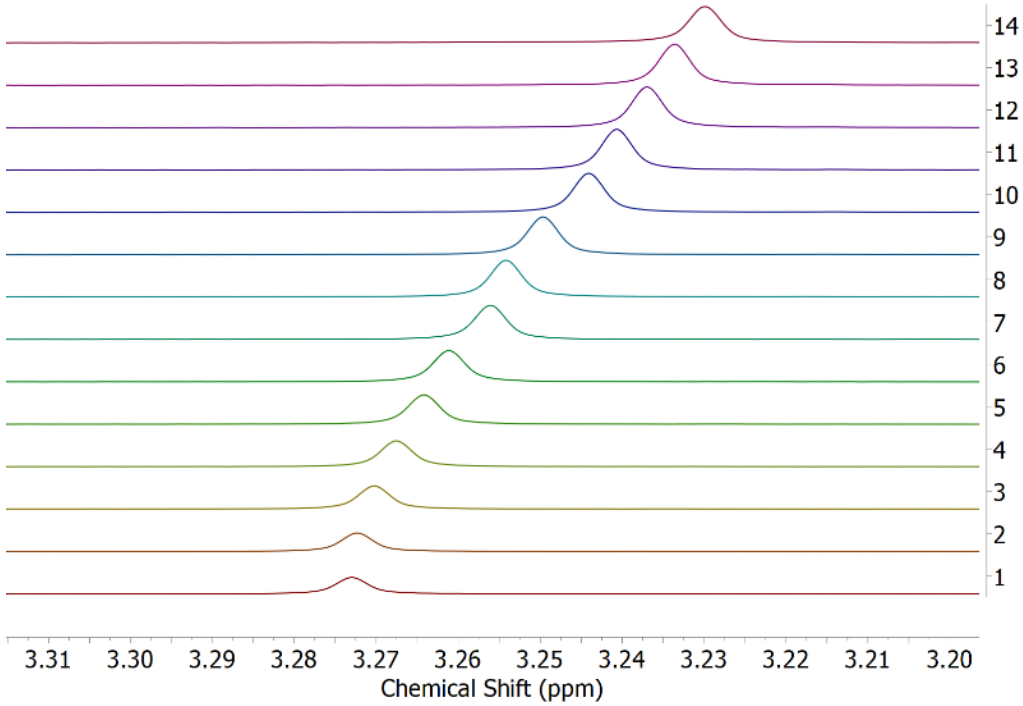

Figure C44. NMR titration experiments with $\mathbf{L^5UO_2}$ with CsOTf showing the peak corresponding to the -N-CH_3 group used to make binding curves.

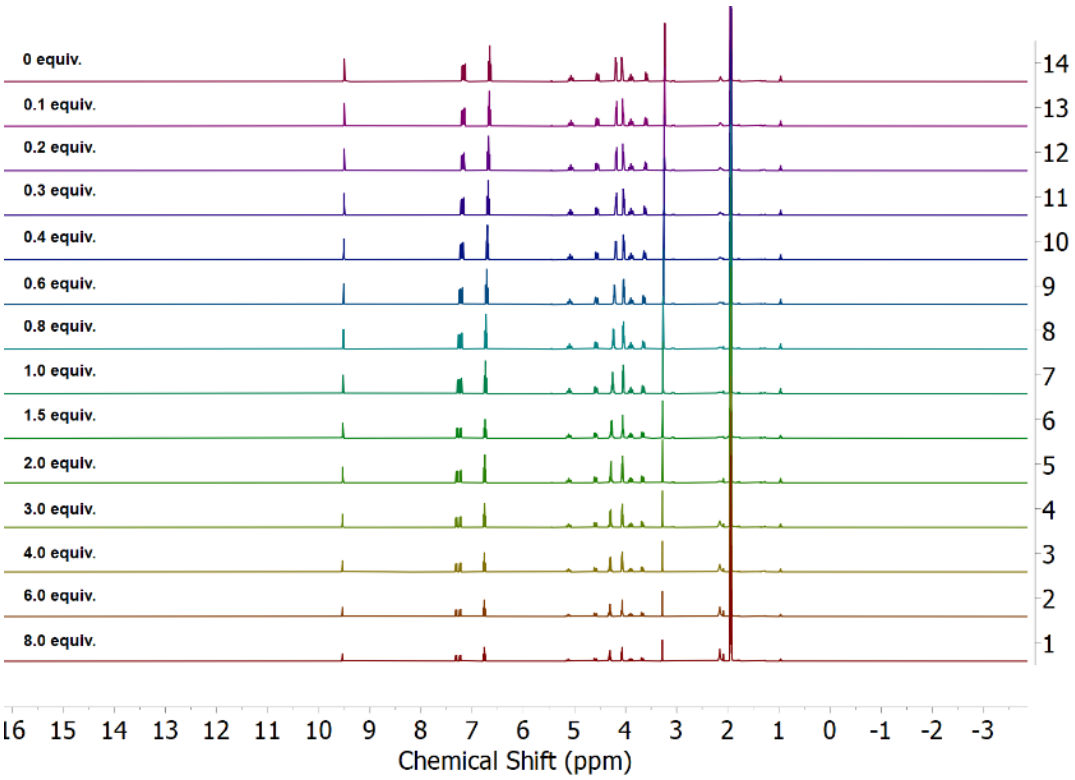

Figure C45. NMR titration experiments with $\mathbf{L^5UO_2}$ with RbOTf showing the full region.

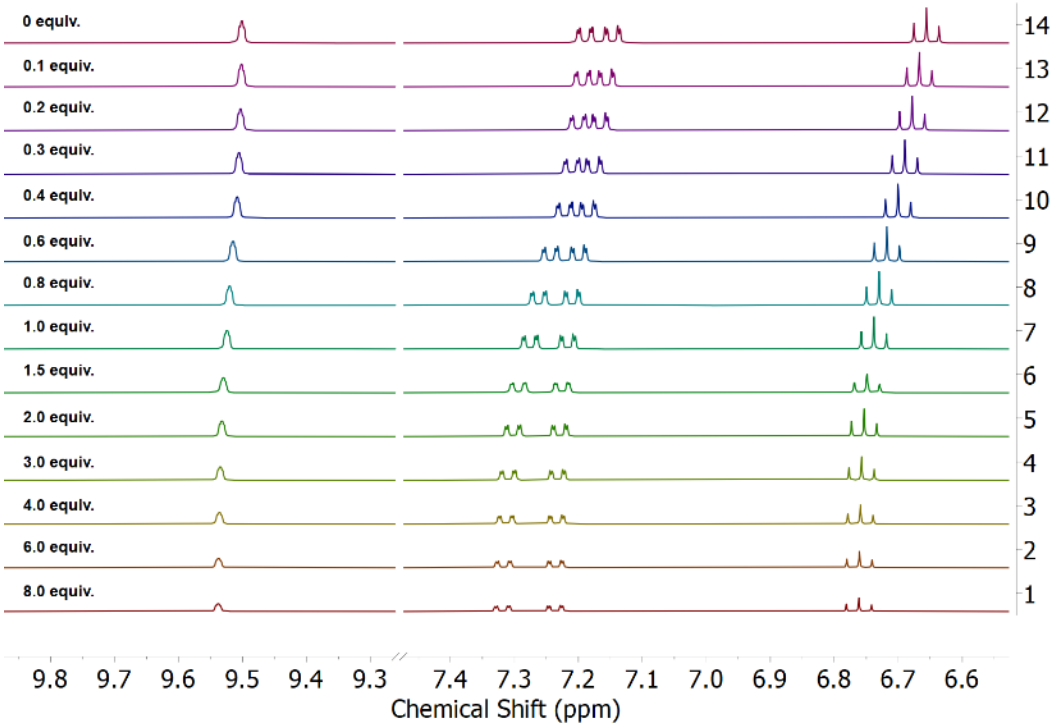

Figure C46. NMR titration experiments with $\mathbf{L^5UO_2}$ with RbOTf showing the imine and aromatic region.

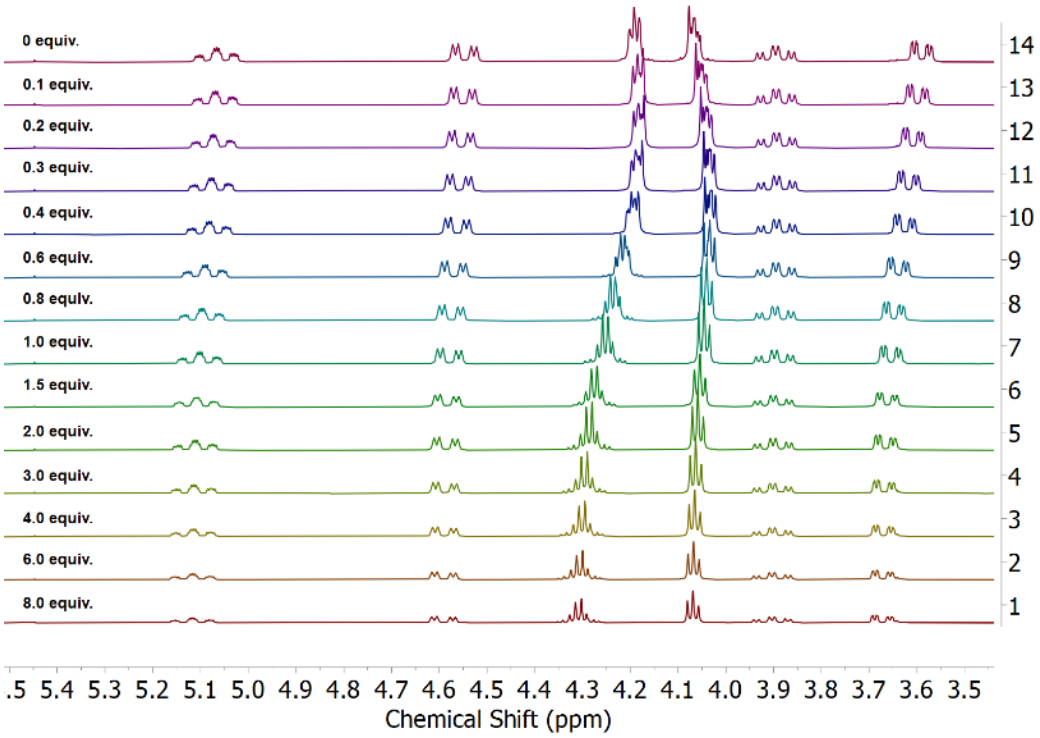

Figure C47. NMR titration experiments with $\mathbf{L^5UO_2}$ with RbOTf showing the aliphatic region.

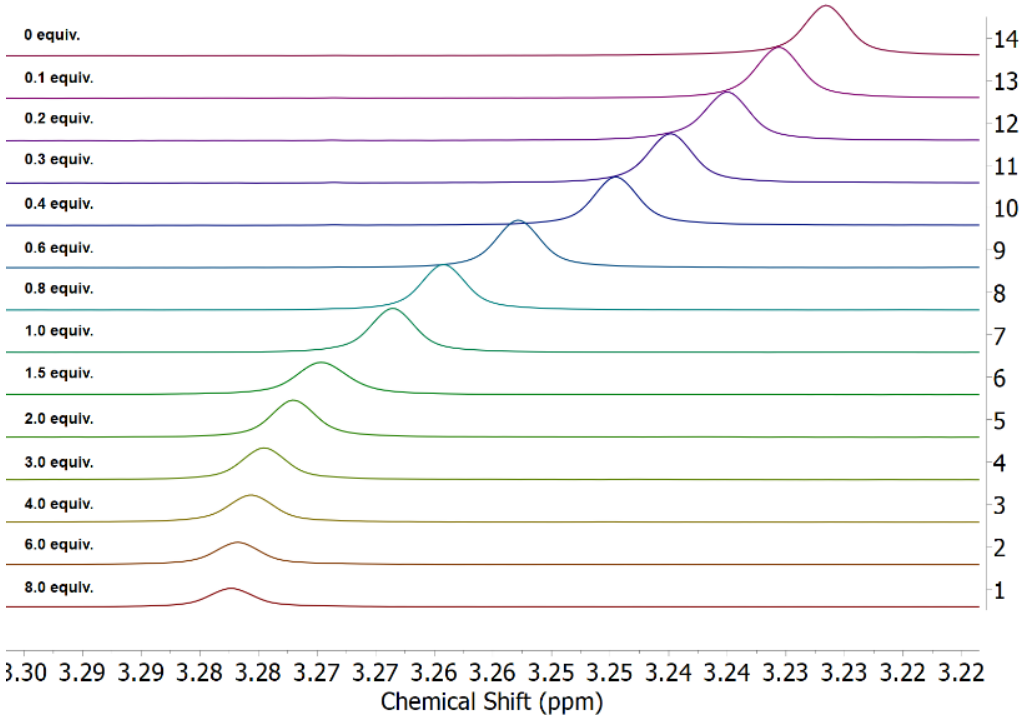

Figure C48. NMR titration experiments with $\mathbf{L^5UO_2}$ with RbOTf showing the peak corresponding to the -N-CH_3 group used to make binding curves.

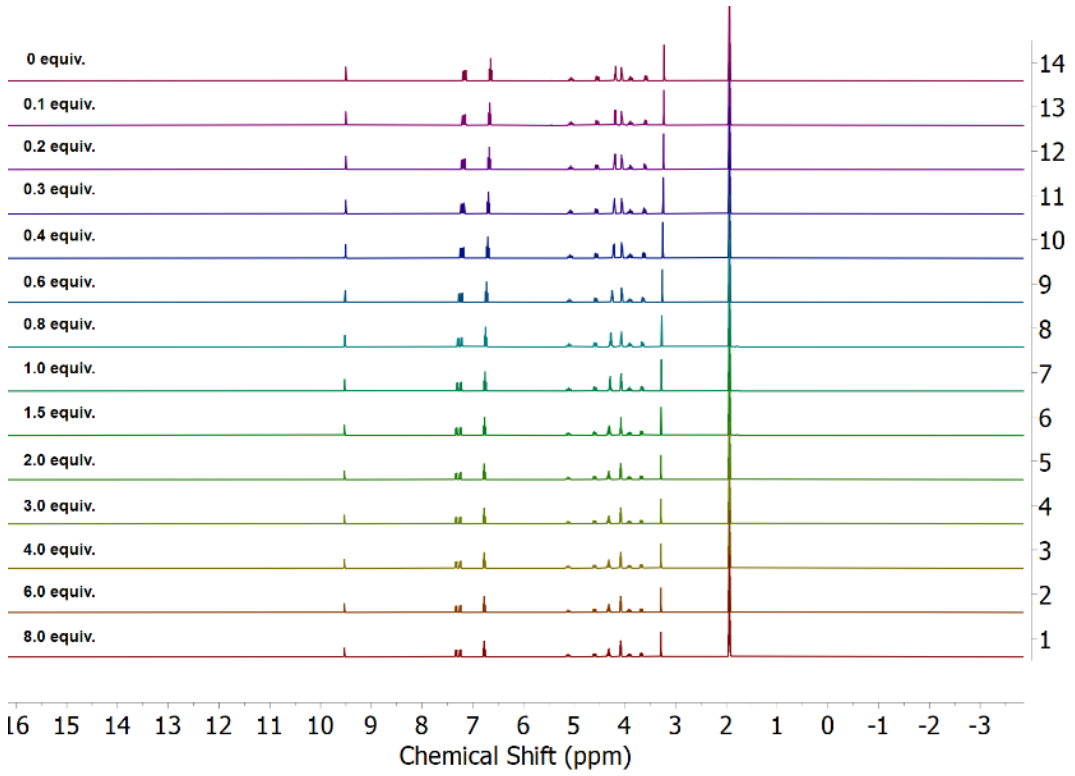

Figure C49. NMR titration experiments with $\mathbf{L^5UO_2}$ with KOTf showing the full region.

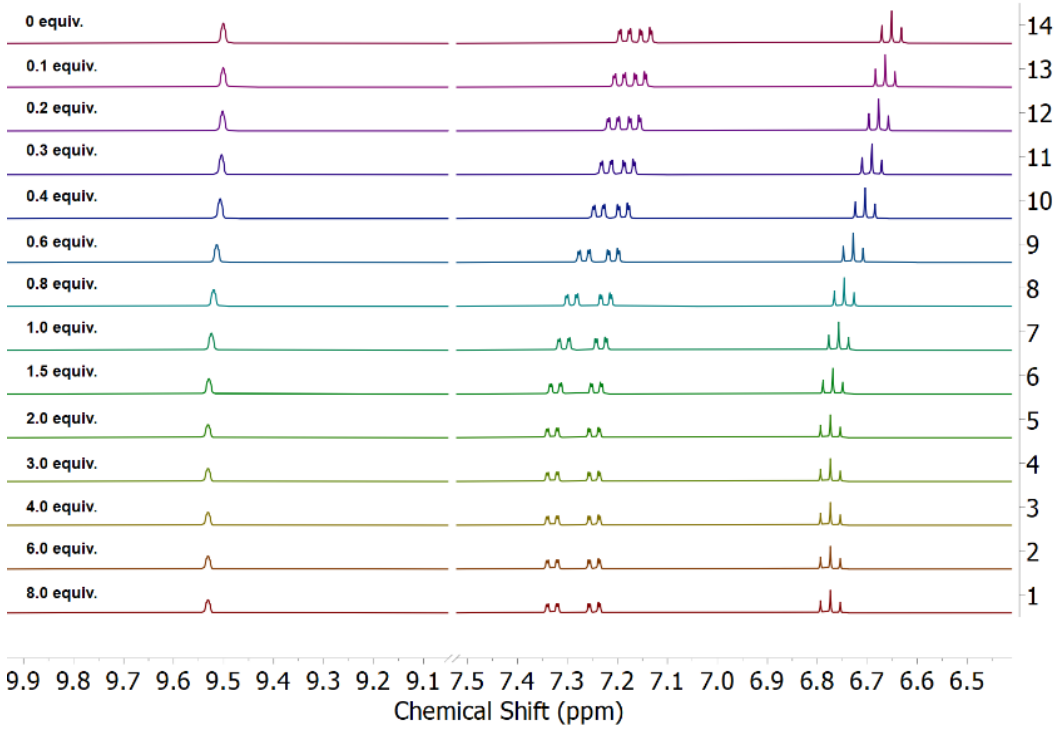

Figure C50. NMR titration experiments with $\mathbf{L^5UO_2}$ with KOTf showing the imine and aromatic region.

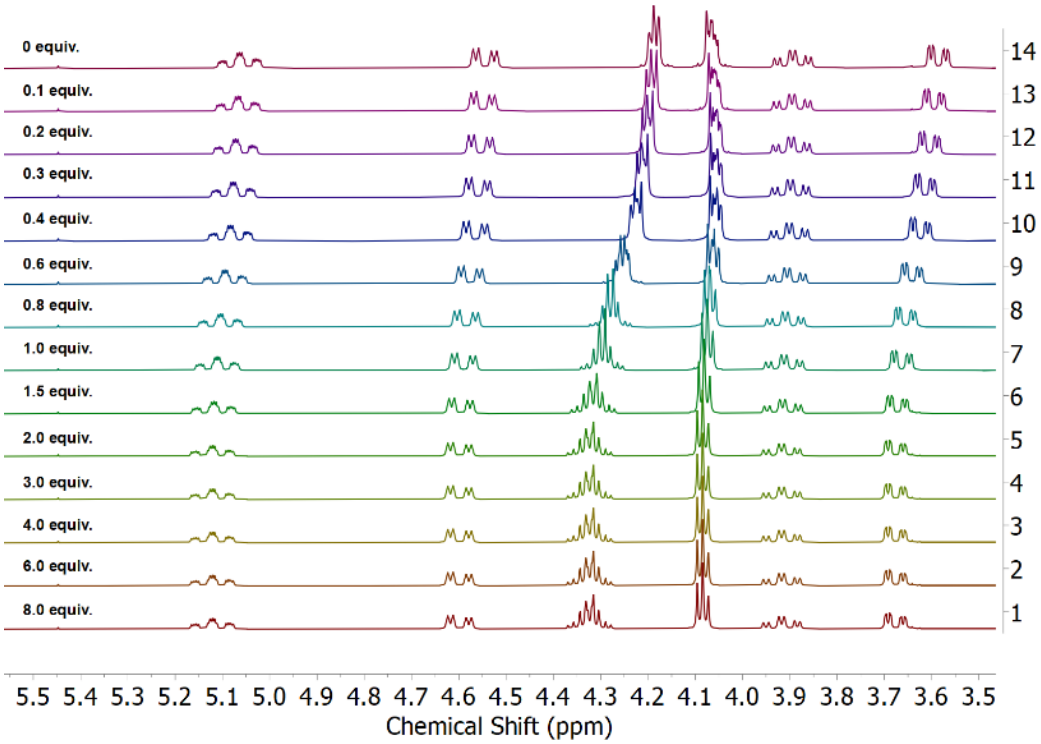

Figure C51. NMR titration experiments with **L^{5}UO$_2$** with KOTf showing the aliphatic region.

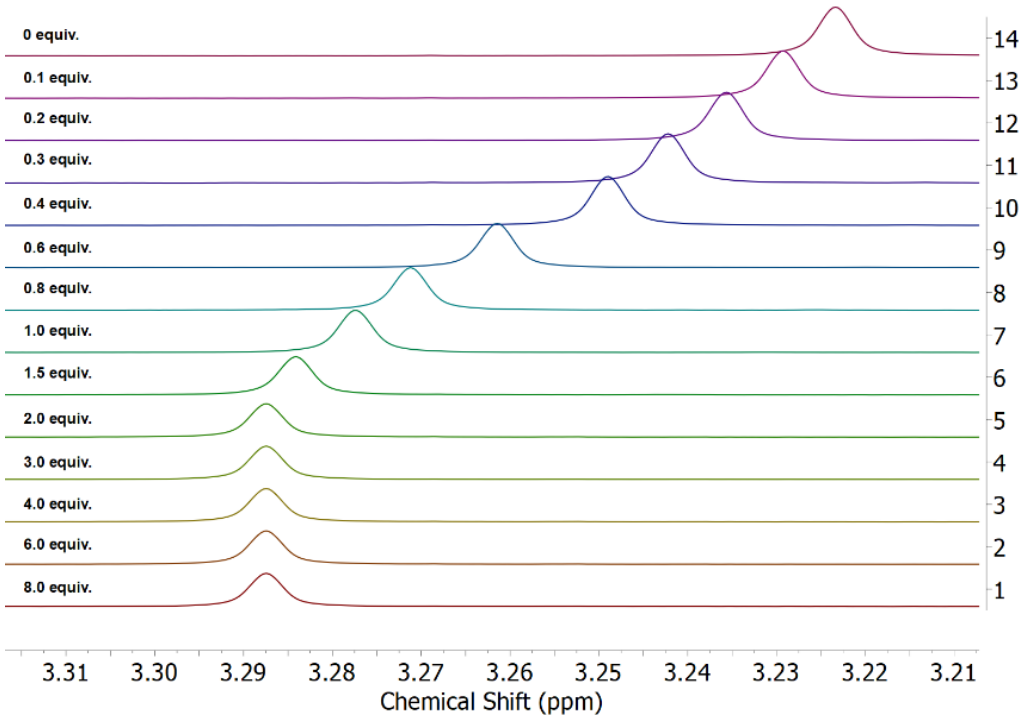

Figure C52. NMR titration experiments with **L^{5}UO$_2$** with KOTf showing the peak corresponding to the -N-C*H*$_3$ group used to make binding curves.

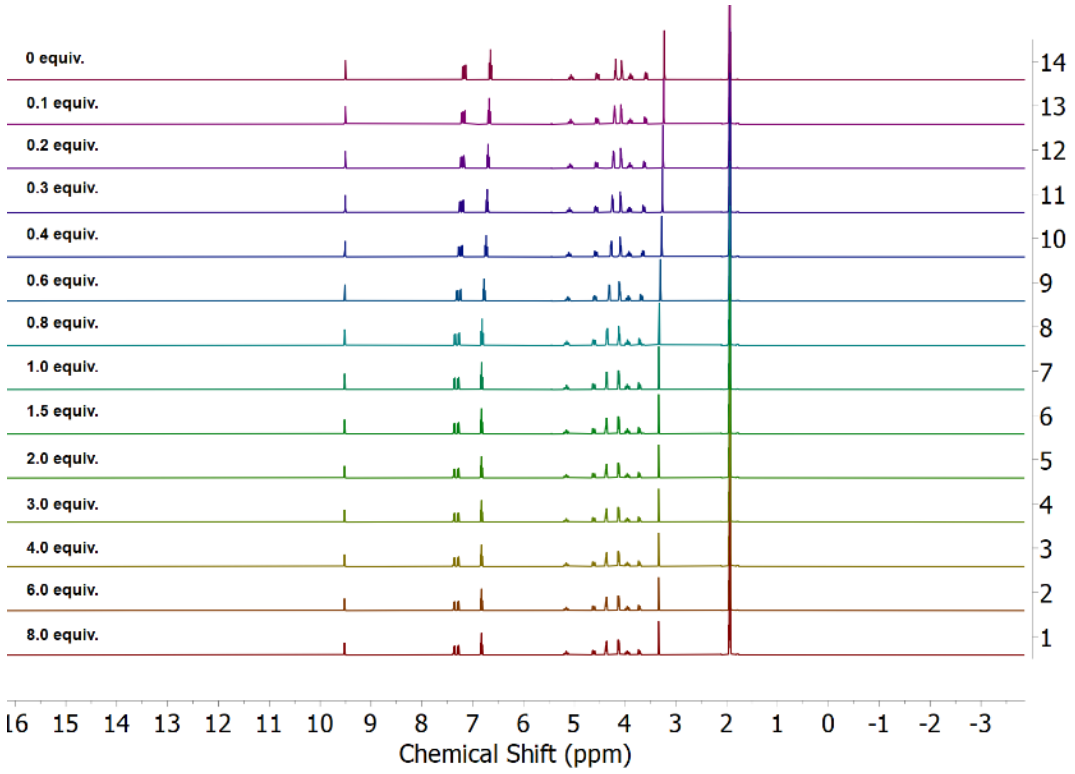

Figure C53. NMR titration experiments with $\mathbf{L^5UO_2}$ with NaOTf showing the full region.

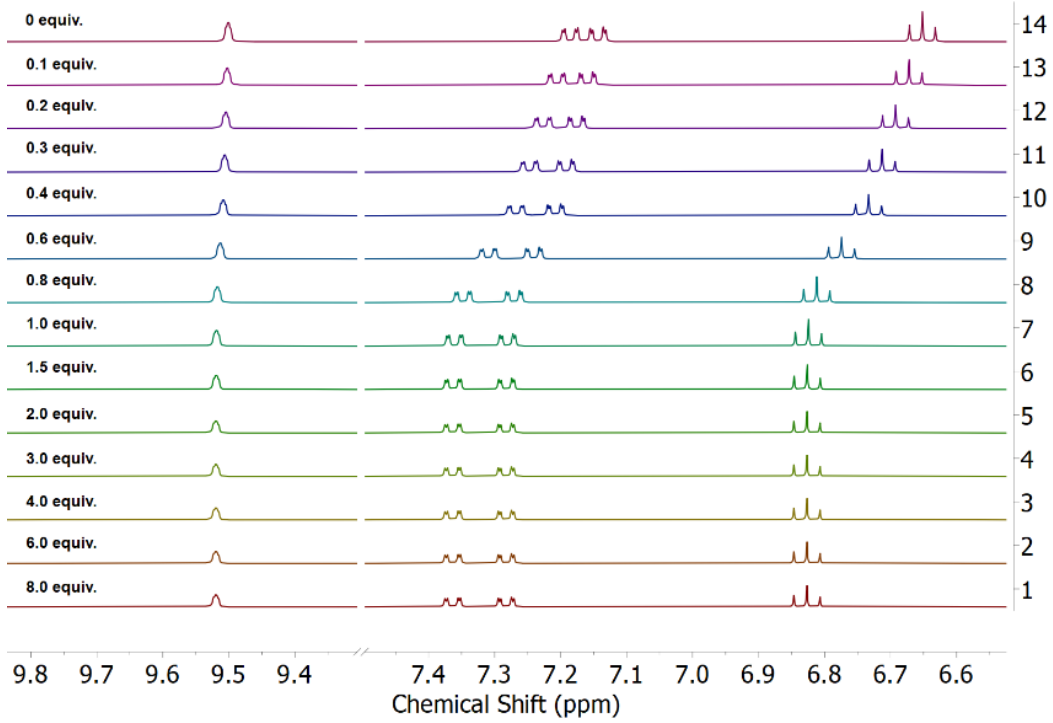

Figure C54. NMR titration experiments with $\mathbf{L^5UO_2}$ with NaOTf showing the imine and aromatic region.

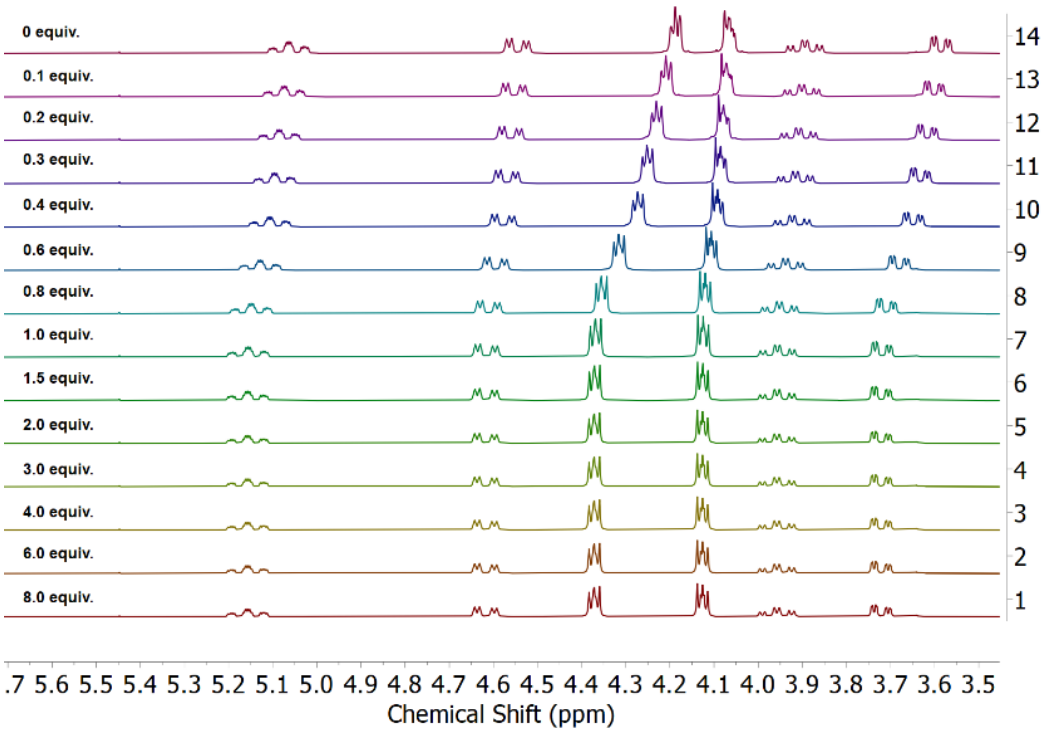

Figure C55. NMR titration experiments with $\mathbf{L^5UO_2}$ with NaOTf showing the aliphatic region.

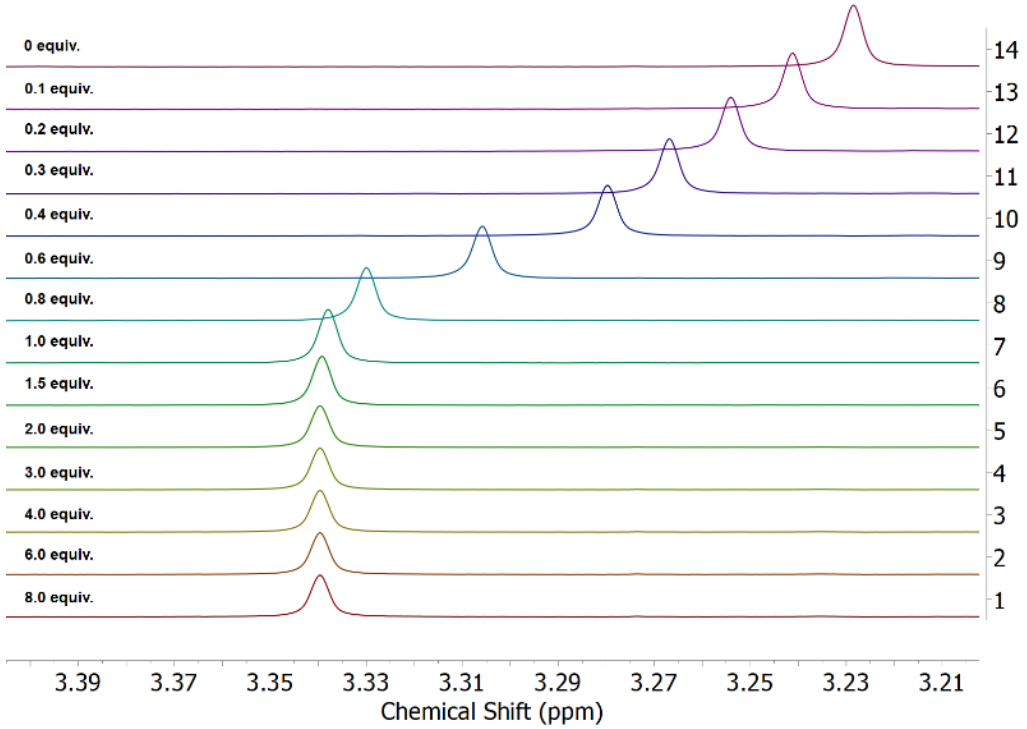

Figure C56. NMR titration experiments with $\mathbf{L^5UO_2}$ with NaOTf showing the peak corresponding to the -N-CH_3 group used to make binding curves.

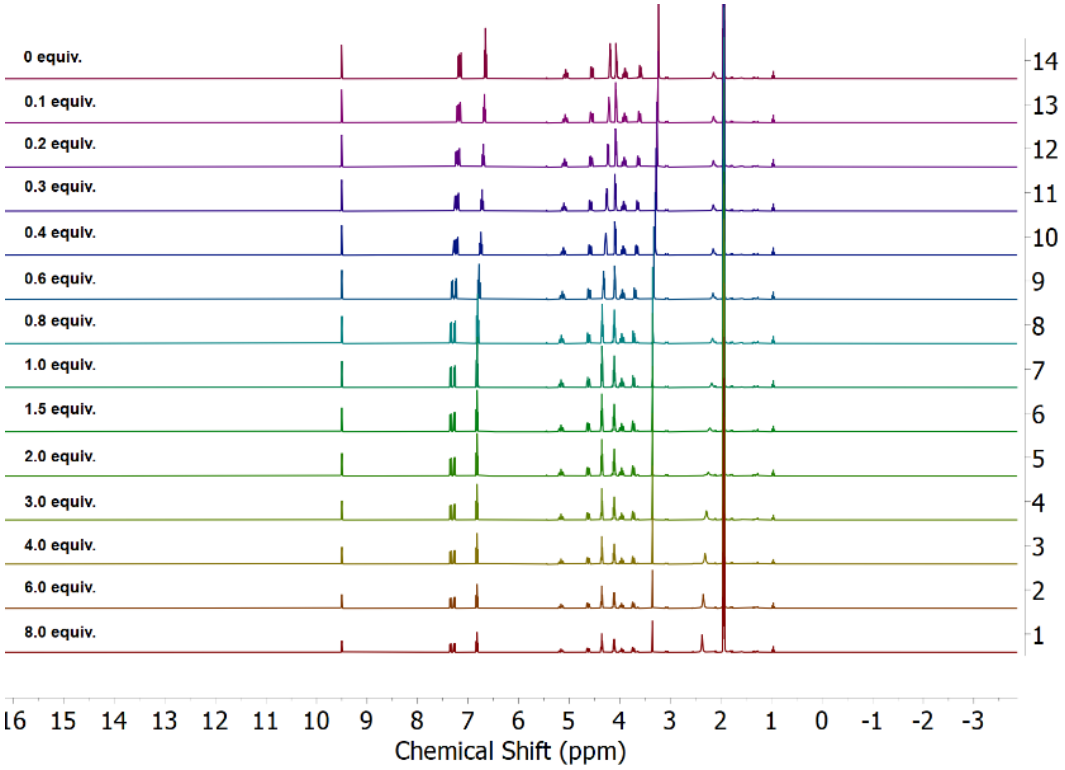

Figure C57. NMR titration experiments with $\mathbf{L^5UO_2}$ with LiOTf showing the full region.

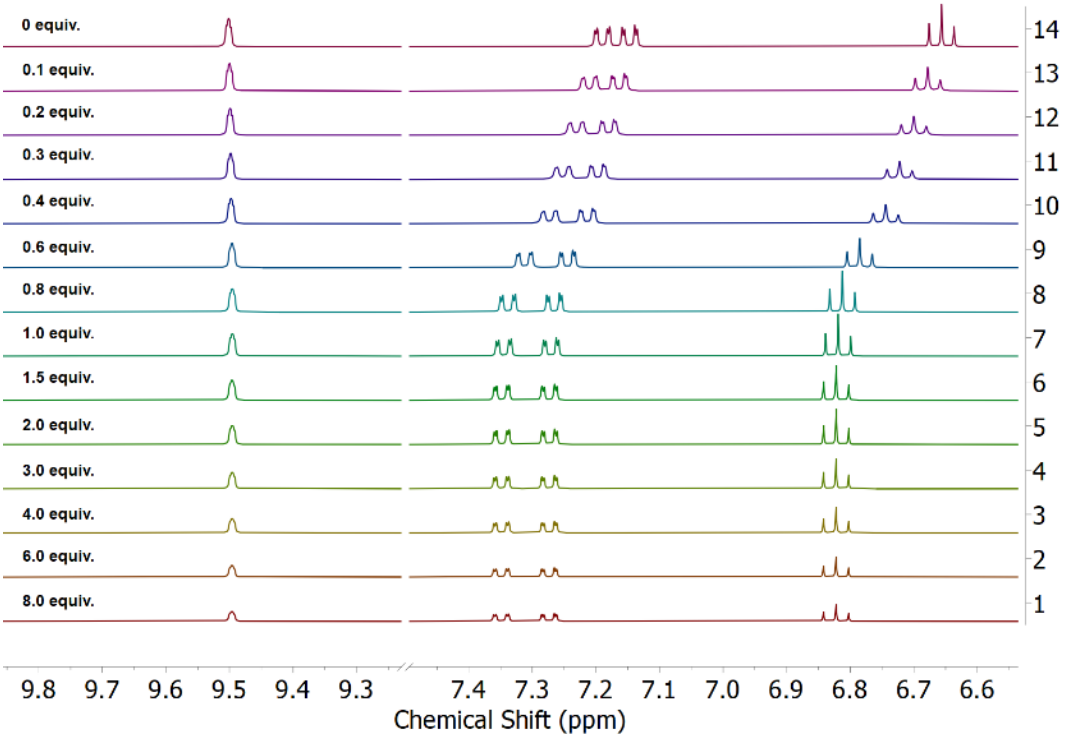

Figure C58. NMR titration experiments with $\mathbf{L^5UO_2}$ with LiOTf showing the imine and aromatic region.

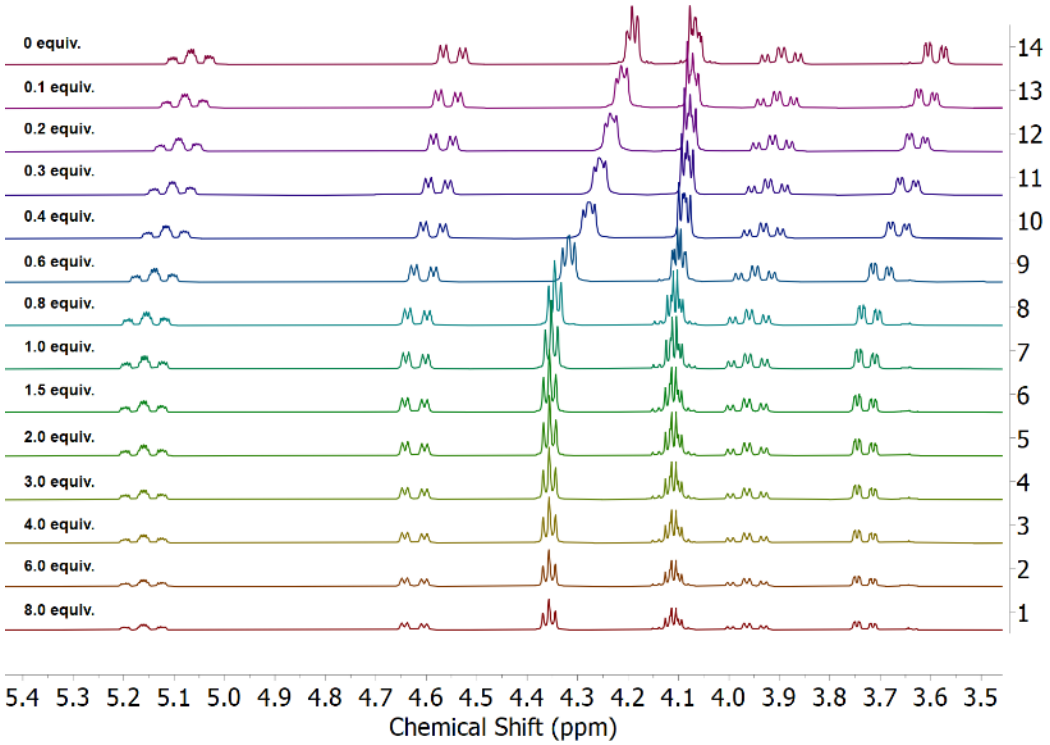

Figure C59. NMR titration experiments with $\mathbf{L^5UO_2}$ with LiOTf showing the aliphatic region.

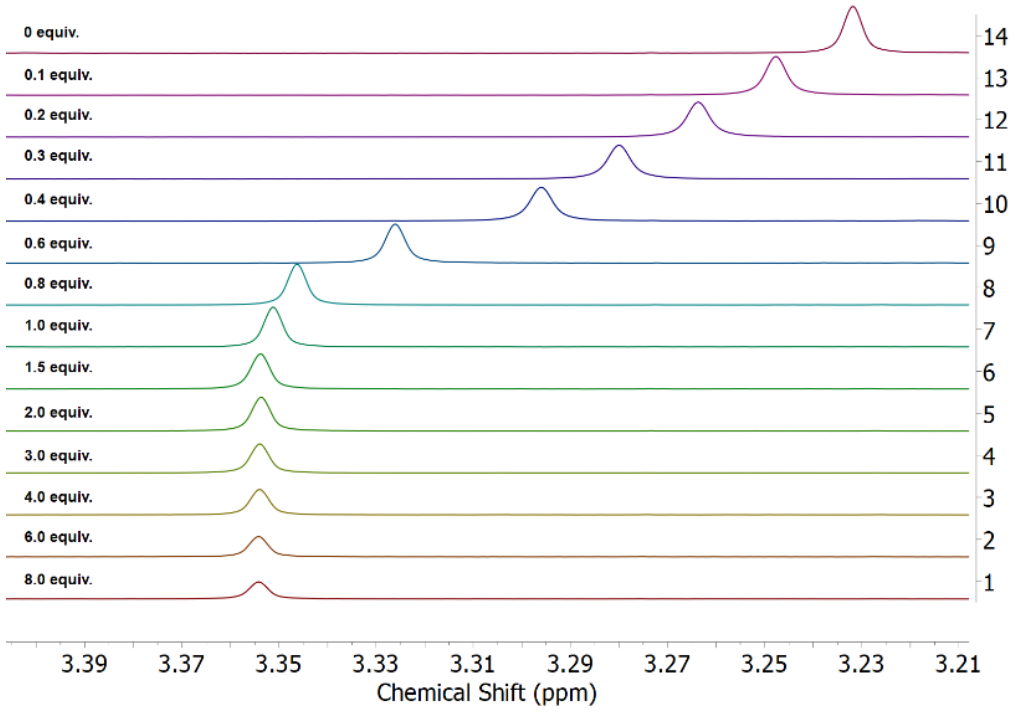

Figure C60. NMR titration experiments with $\mathbf{L^5UO_2}$ with LiOTf showing the peak corresponding to the -N-CH_3 group used to make binding curves.

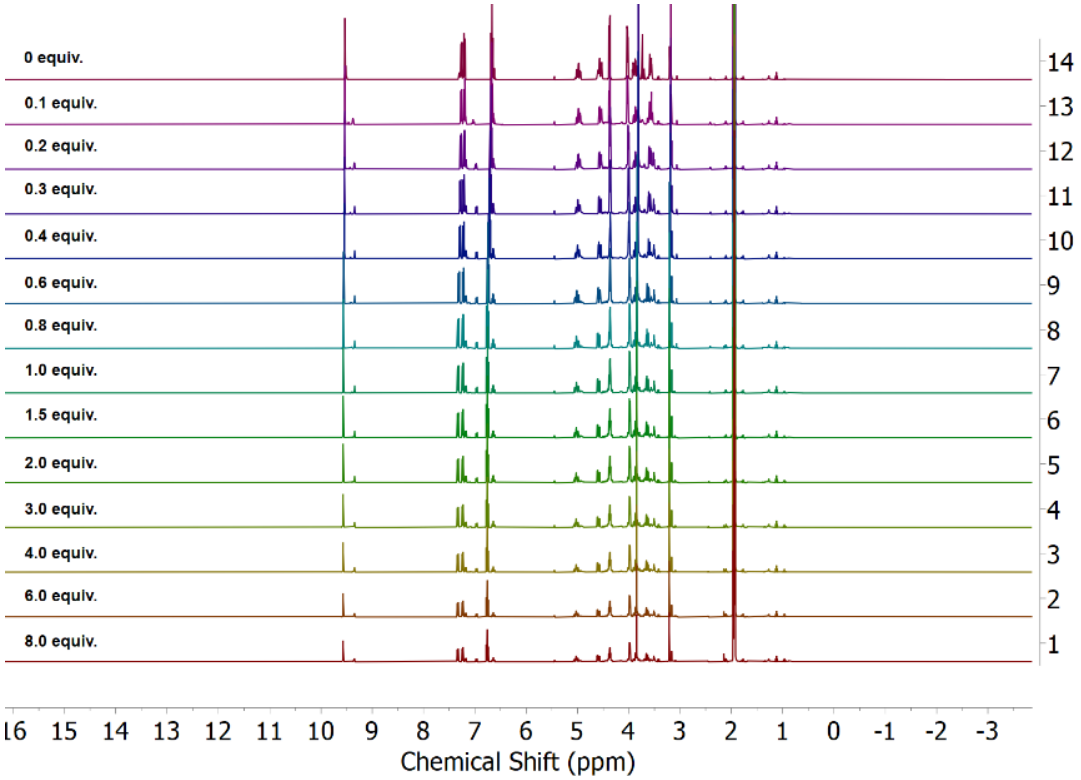

Figure C61. NMR titration experiments with $\mathbf{L^6UO_2}$ with CsOTf showing the full region.

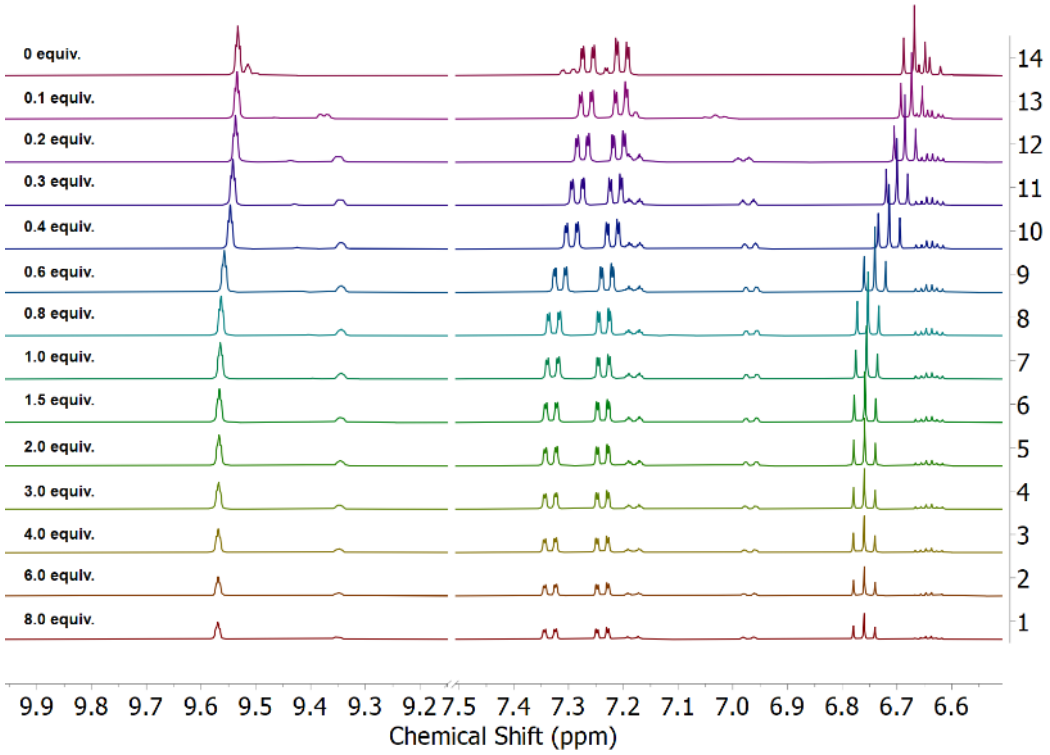

Figure C62. NMR titration experiments with $\mathbf{L^6UO_2}$ with CsOTf showing the imine and aromatic region.

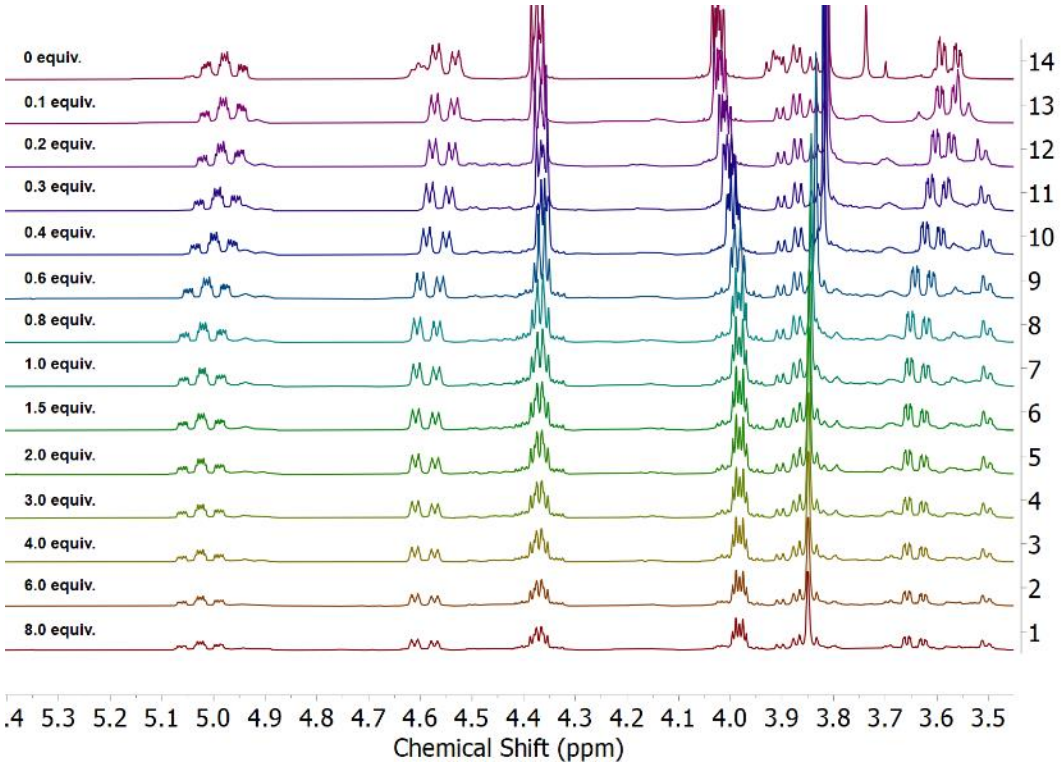

Figure C63. NMR titration experiments with $\mathbf{L^6UO_2}$ with CsOTf showing the aliphatic region.

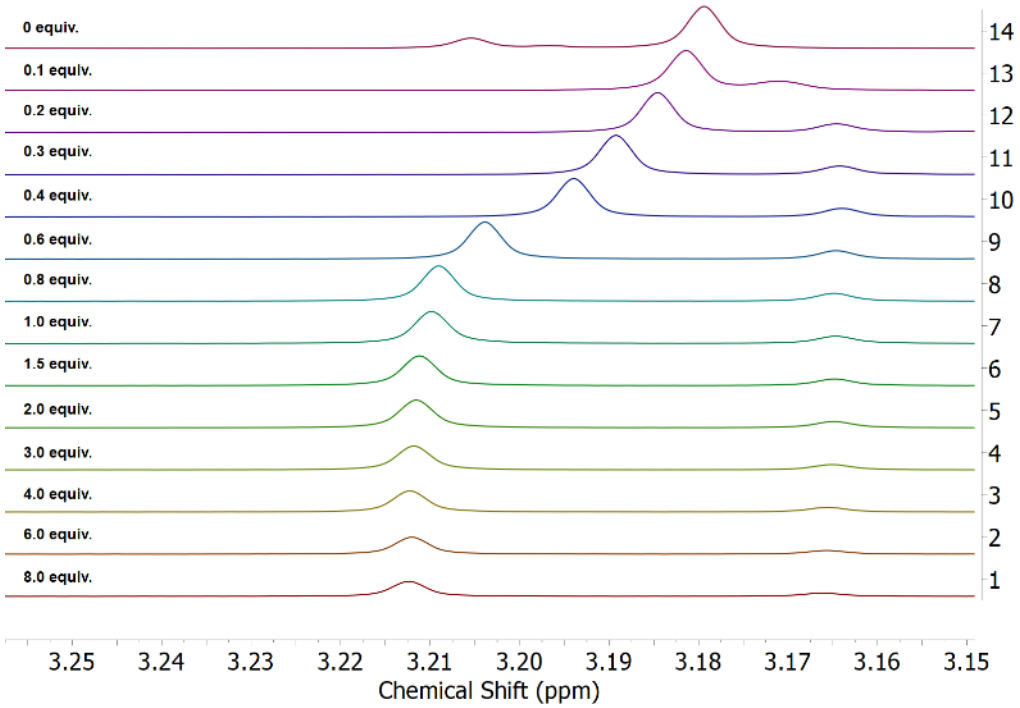

Figure C64. NMR titration experiments with $\mathbf{L^6UO_2}$ with CsOTf showing the peak corresponding to the -N-CH_3 group used to make binding curves.

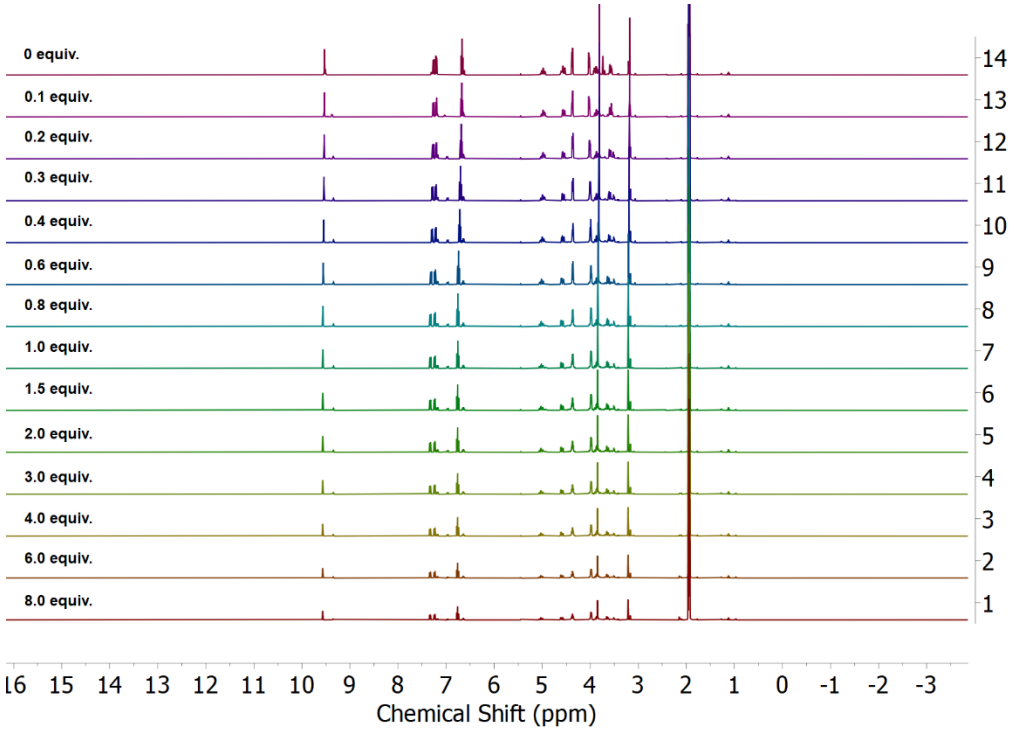

Figure C65. NMR titration experiments with $\mathbf{L^6UO_2}$ with RbOTf showing the full region.

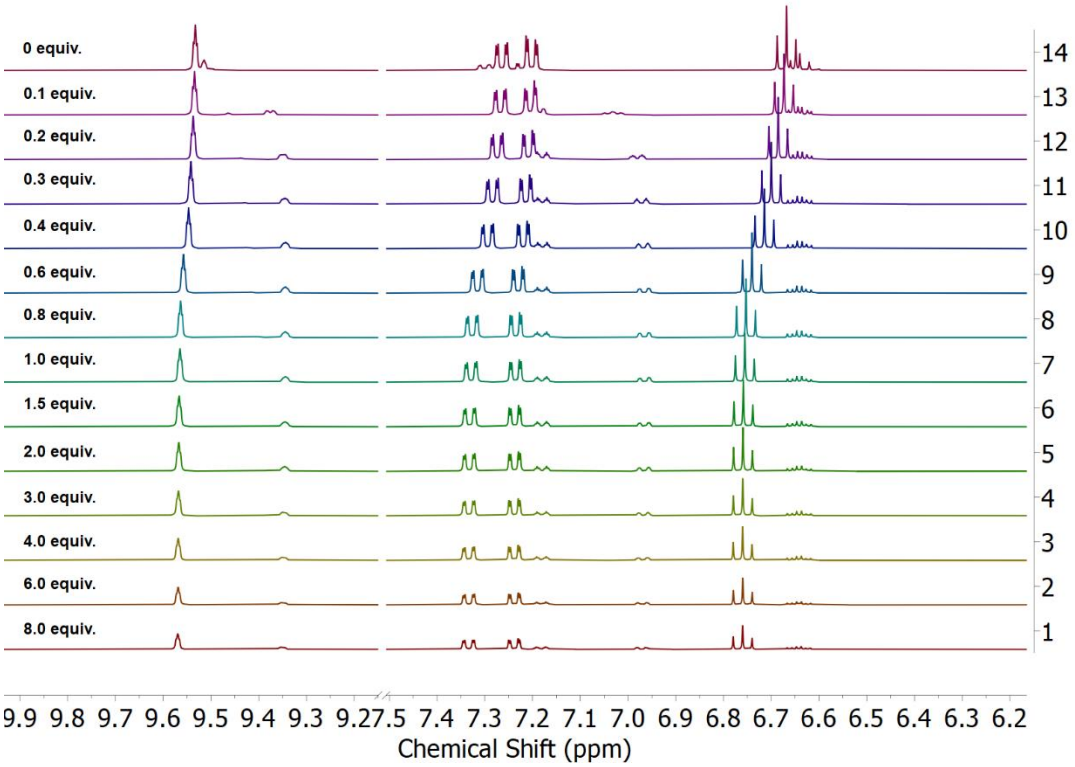

Figure C66. NMR titration experiments with $\mathbf{L^6UO_2}$ with RbOTf showing the imine and aromatic region.

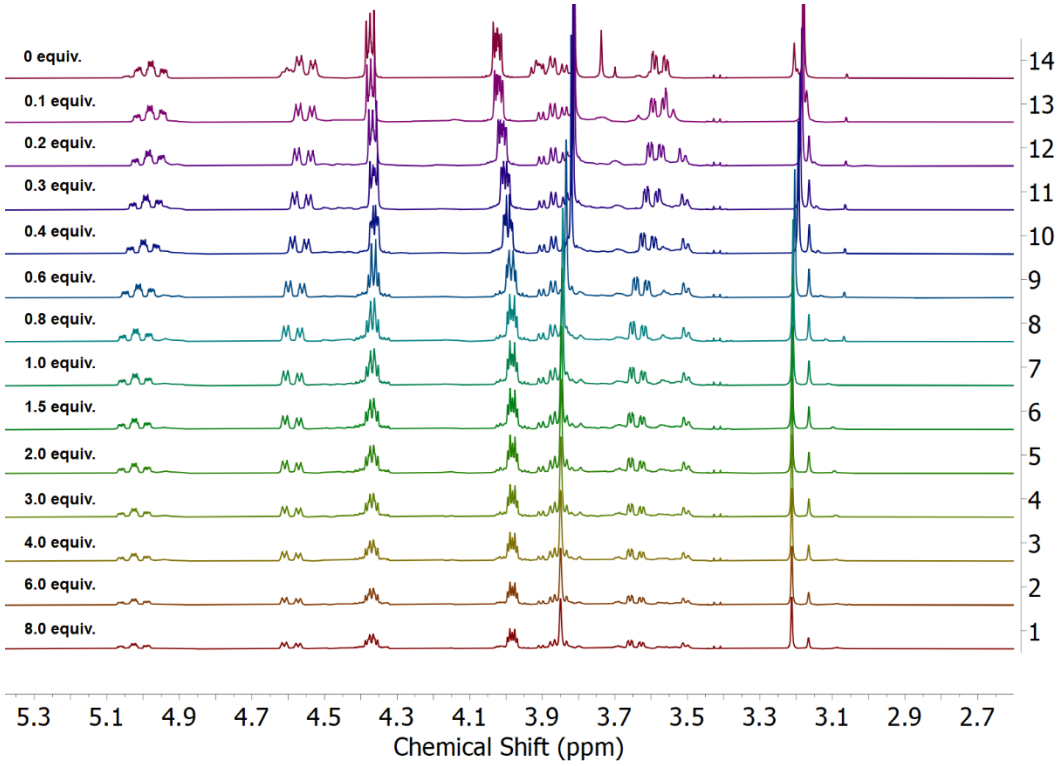

Figure C67. NMR titration experiments with $\mathbf{L^6UO_2}$ with RbOTf showing the aliphatic region.

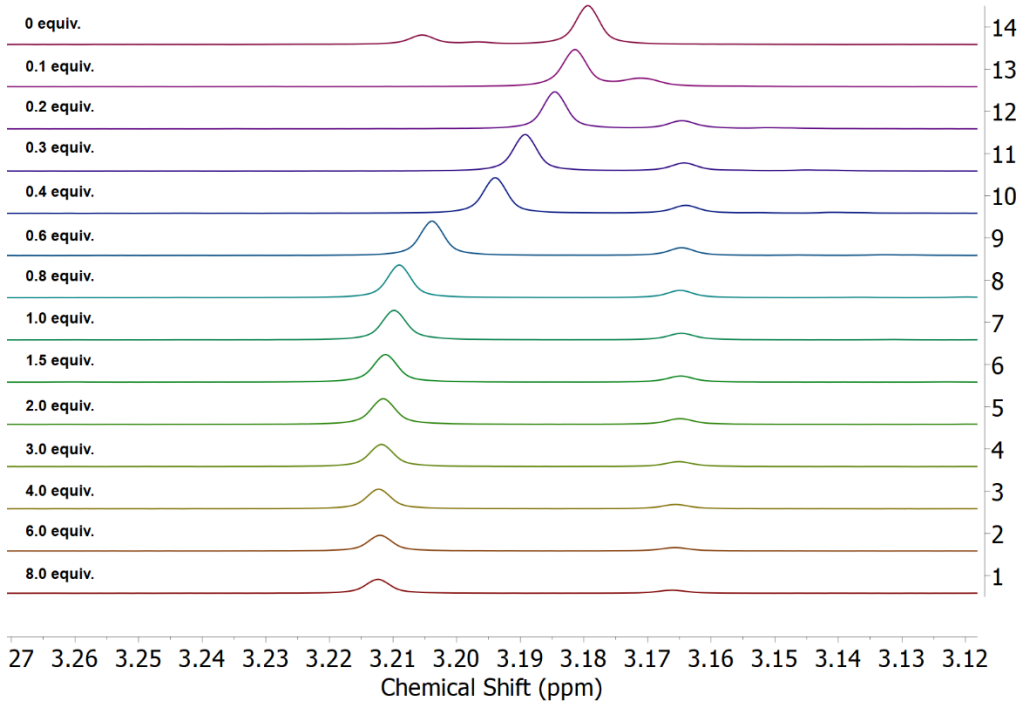

Figure C68. NMR titration experiments with $\mathbf{L^6UO_2}$ with RbOTf showing the peak corresponding to the -N-C*H*$_3$ group used to make binding curves.

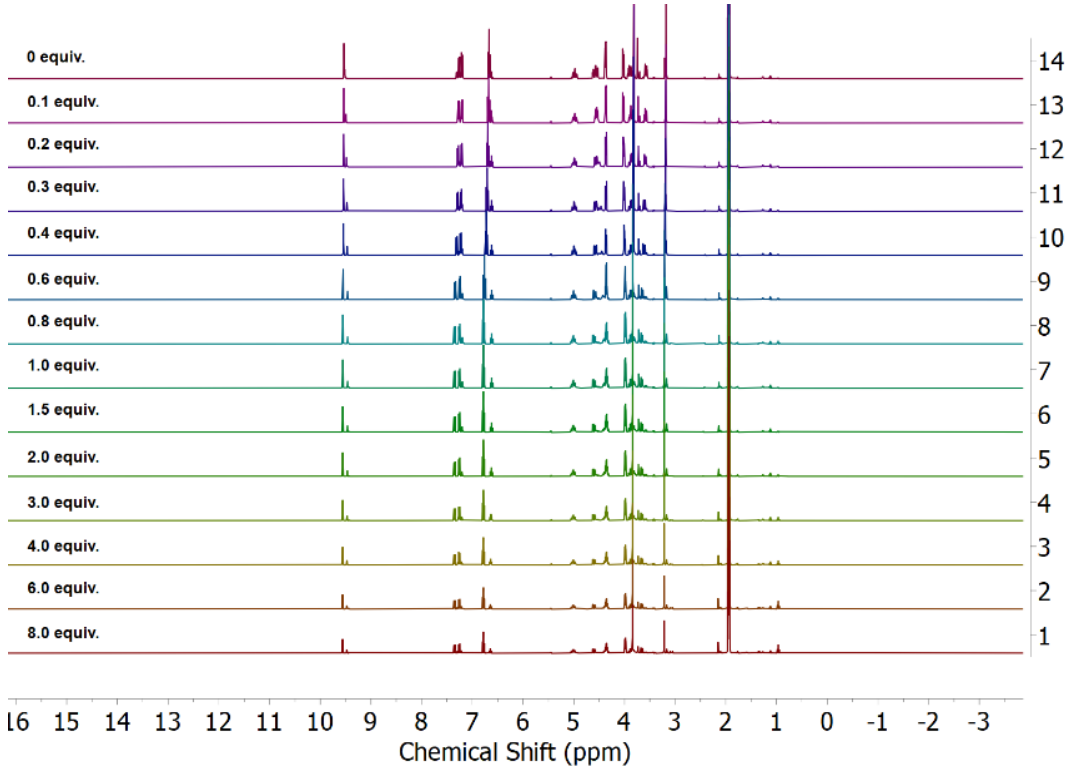

Figure C69. NMR titration experiments with $\mathbf{L^6UO_2}$ with KOTf showing the full region.

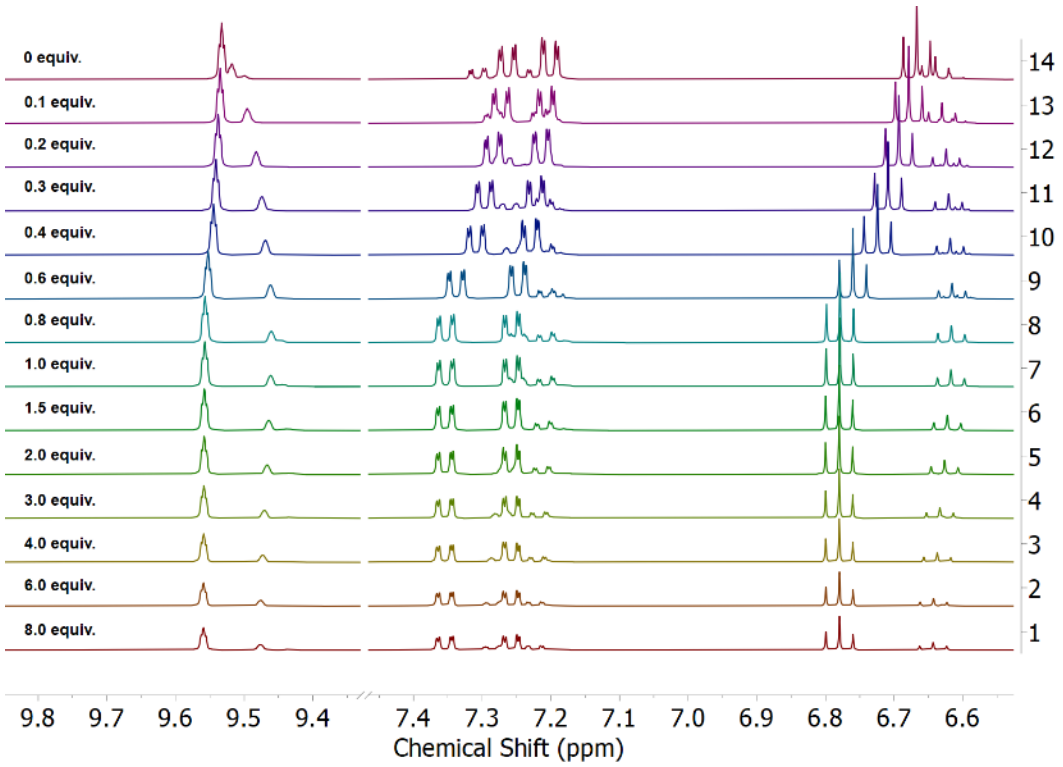

Figure C70. NMR titration experiments with $\mathbf{L^6UO_2}$ with KOTf showing the imine and aromatic region.

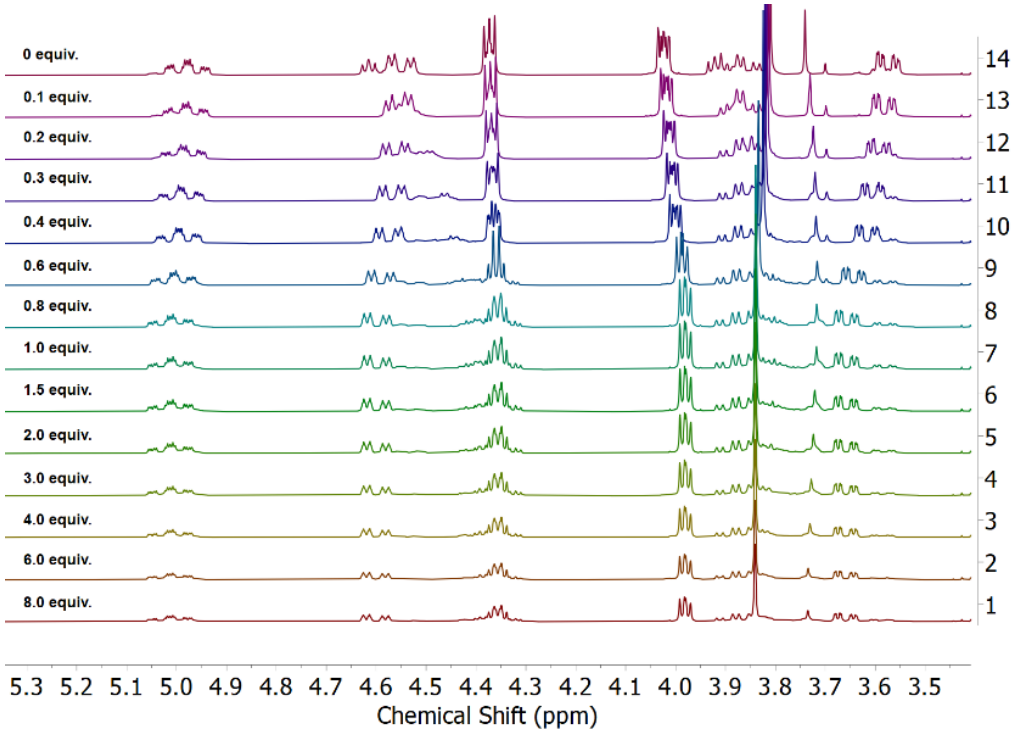

Figure C71. NMR titration experiments with **L^{6}UO$_2$** with KOTf showing the aliphatic region.

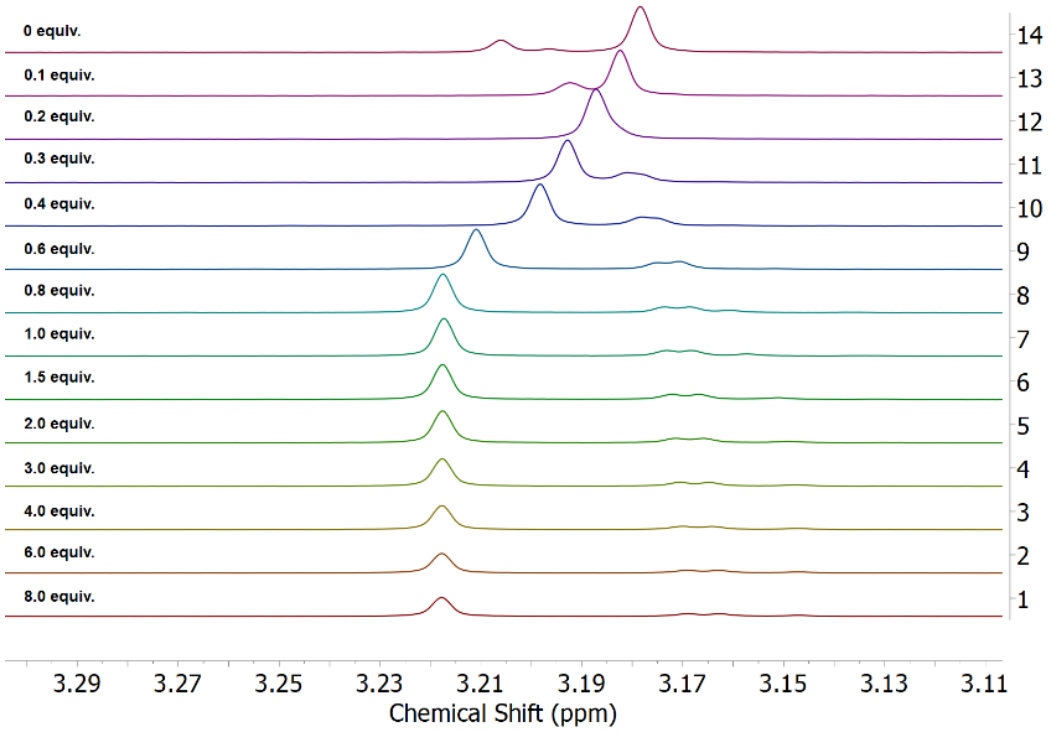

Figure C72. NMR titration experiments with **L^{6}UO$_2$** with KOTf showing the peak corresponding to the -N-C*H*$_3$ group used to make binding curves.

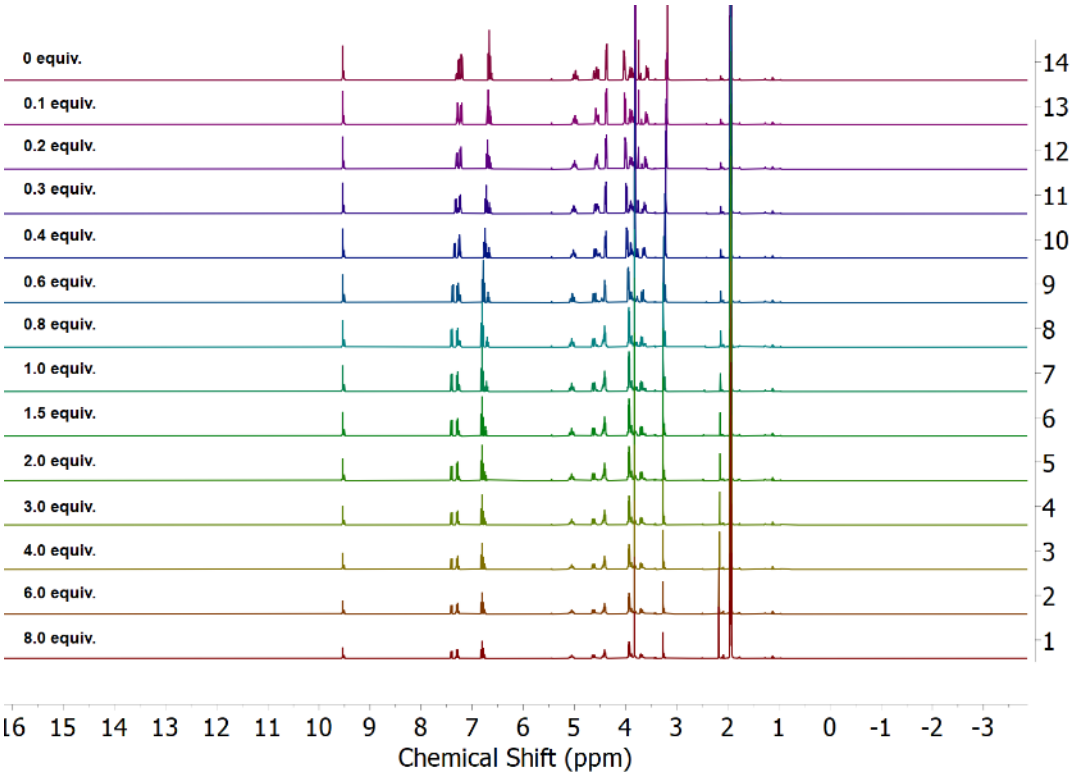

Figure C73. NMR titration experiments with $\mathbf{L^6UO_2}$ with NaOTf showing the full region.

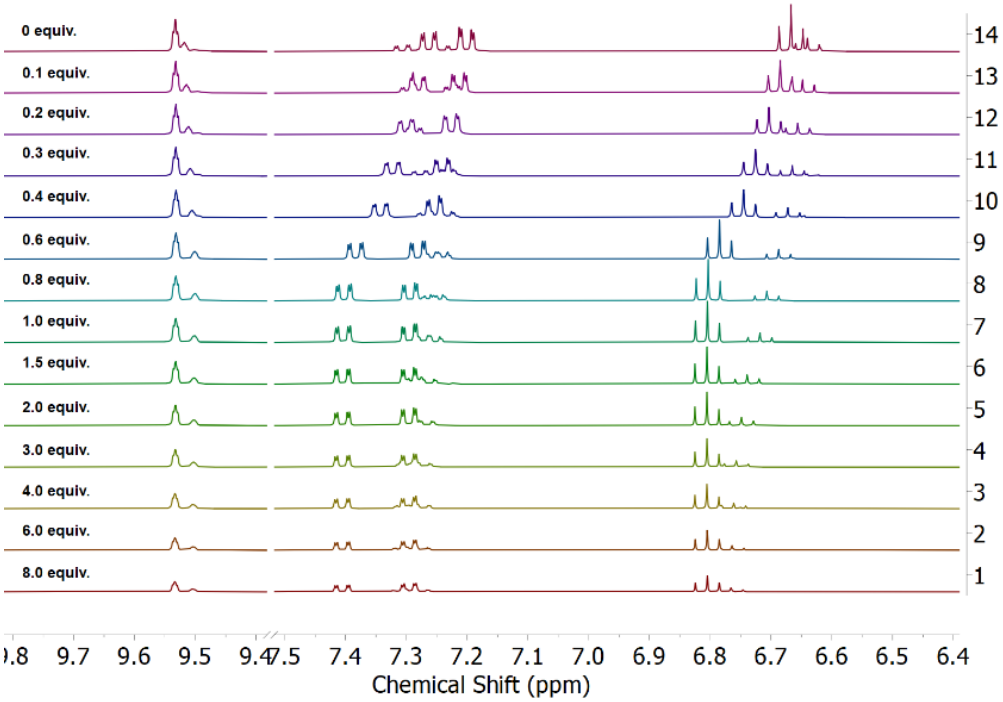

Figure C74. NMR titration experiments with $\mathbf{L^6UO_2}$ with NaOTf showing the imine and aromatic region.

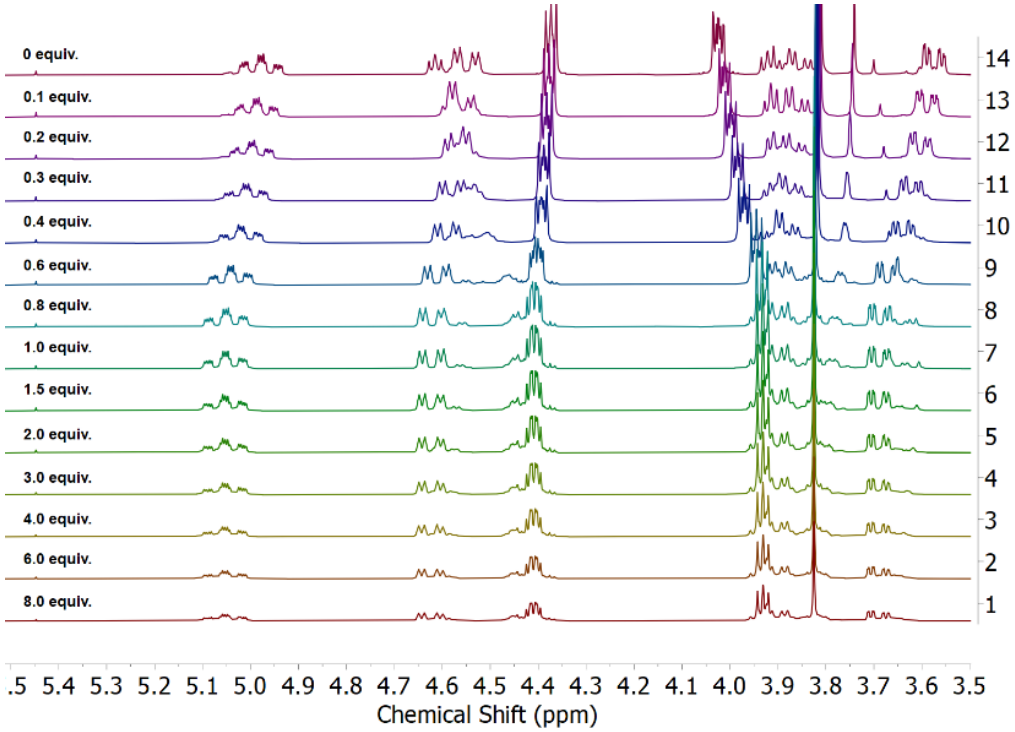

Figure C75. NMR titration experiments with $\mathbf{L^6UO_2}$ with NaOTf showing the aliphatic region.

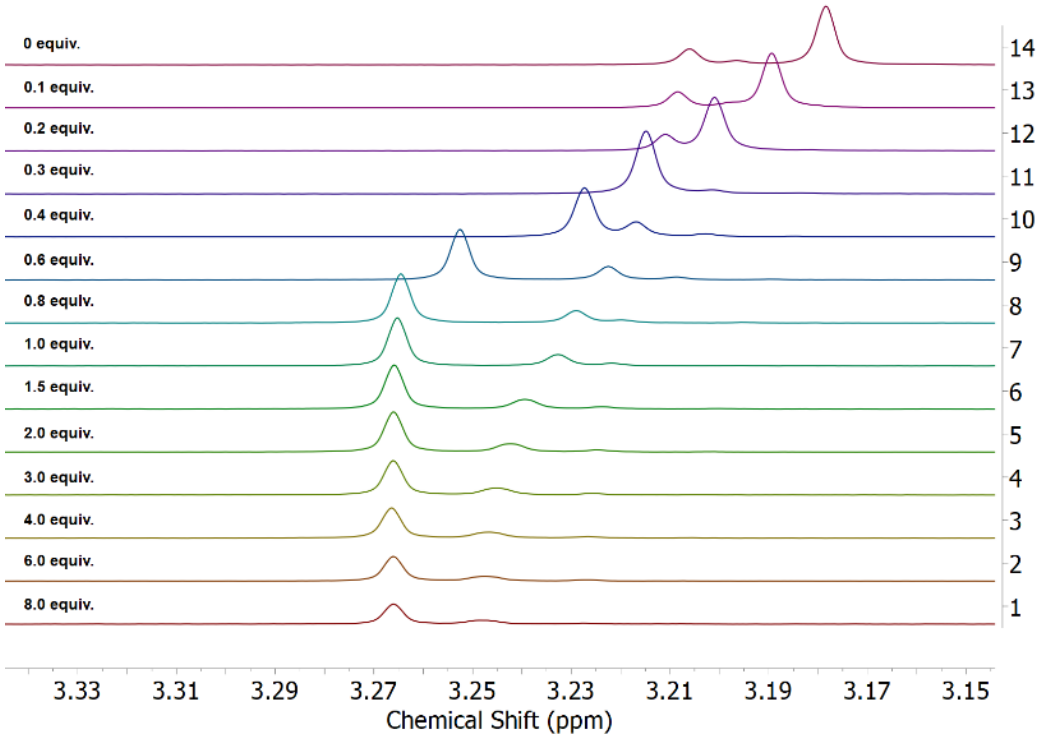

Figure C76. NMR titration experiments with $\mathbf{L^6UO_2}$ with NaOTf showing the peak corresponding to the -N-CH_3 group used to make binding curves.

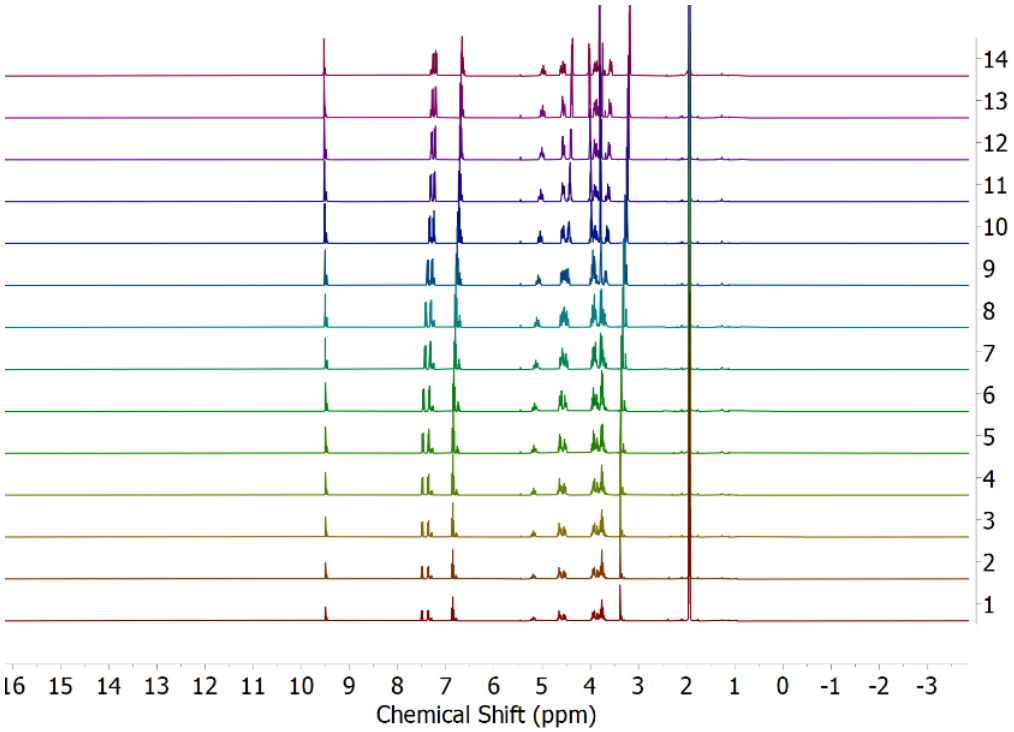

Figure C77. NMR titration experiments with $\mathbf{L^6UO_2}$ with LiOTf showing the full region.

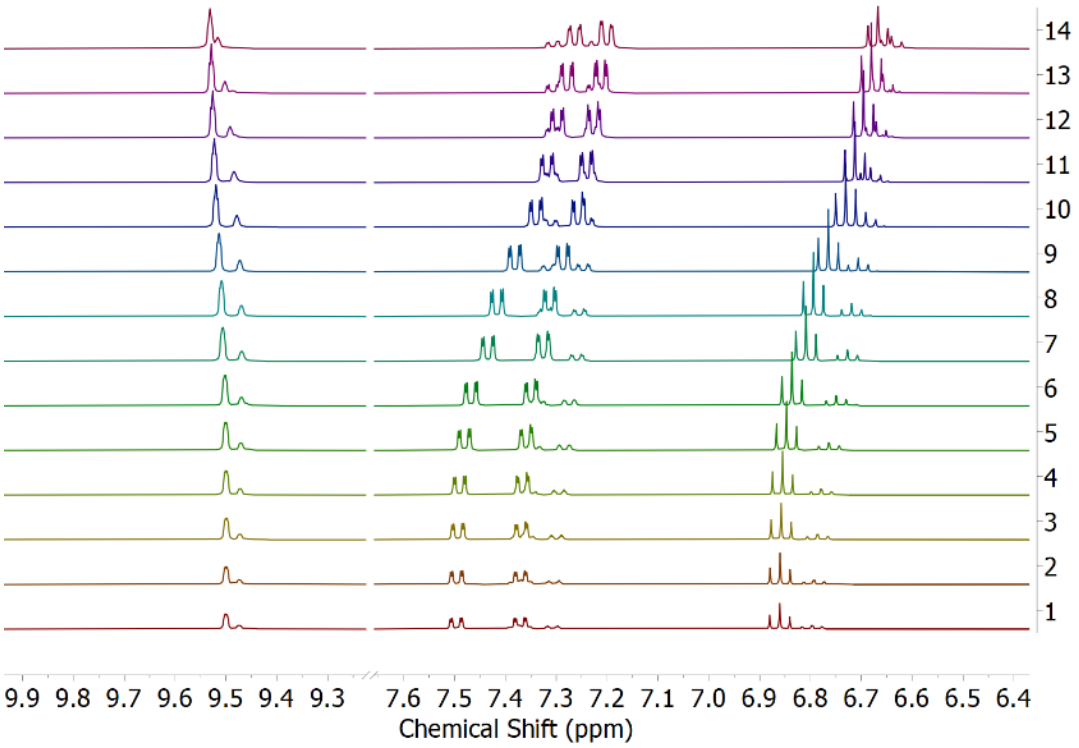

Figure C78. NMR titration experiments with $\mathbf{L^6UO_2}$ with LiOTf showing the imine and aromatic region.

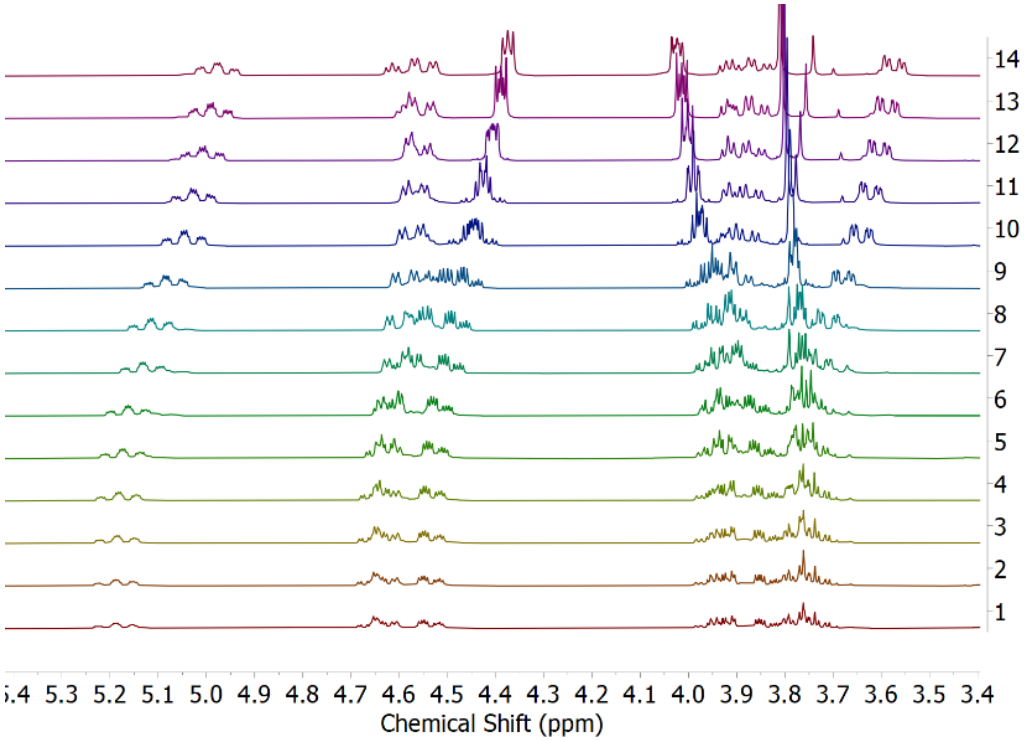

Figure C79. NMR titration experiments with **L^{6}UO$_2$** with LiOTf showing the aliphatic region.

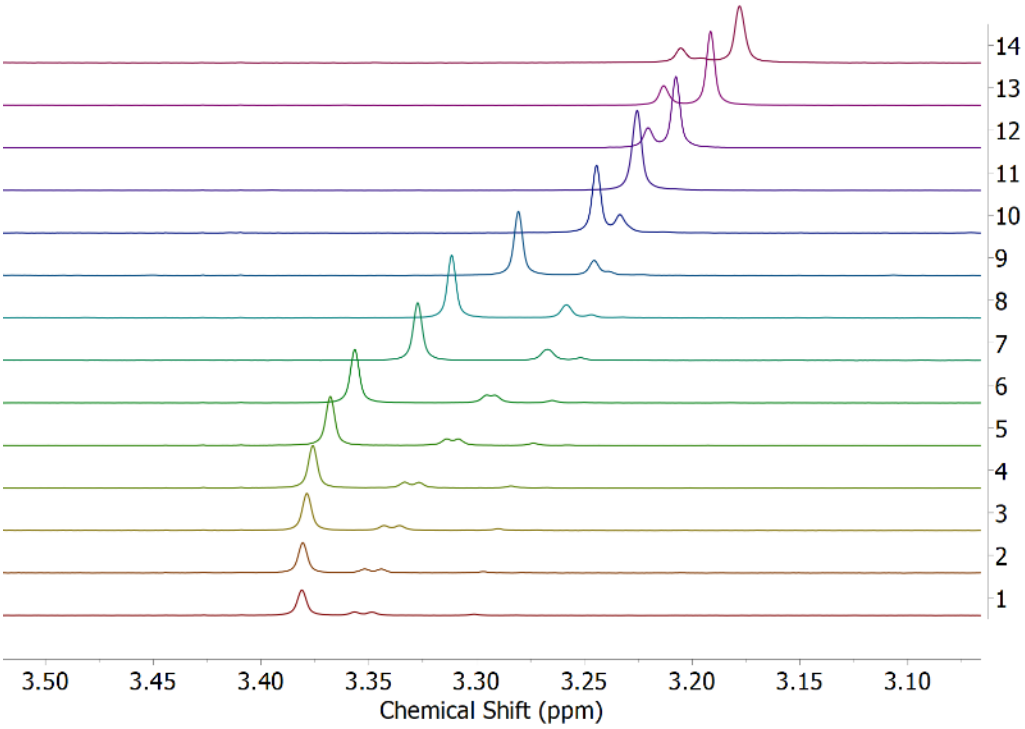

Figure C80. NMR titration experiments with **L^{6}UO$_2$** with LiOTf showing the peak corresponding to the -N-CH_3 group used to make binding curves.

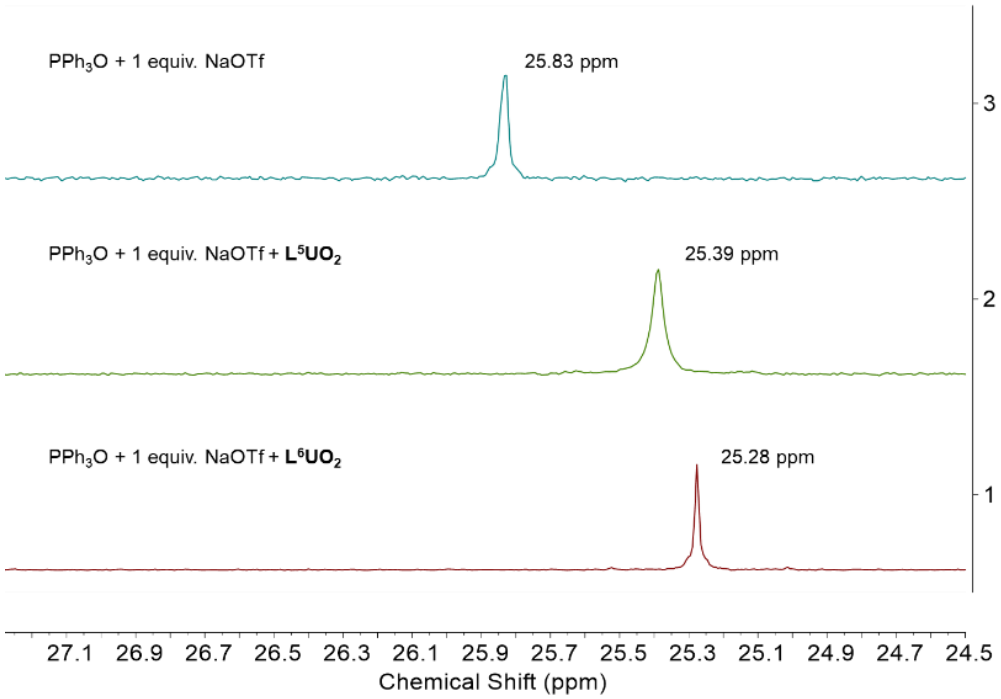

Figure C81. $^{31}P\{^{1}H\}$ NMR for the PPh_3O study with 1 equiv. of $\mathbf{L^5UO_2}$ or $\mathbf{L^6UO_2}$ and NaOTf.

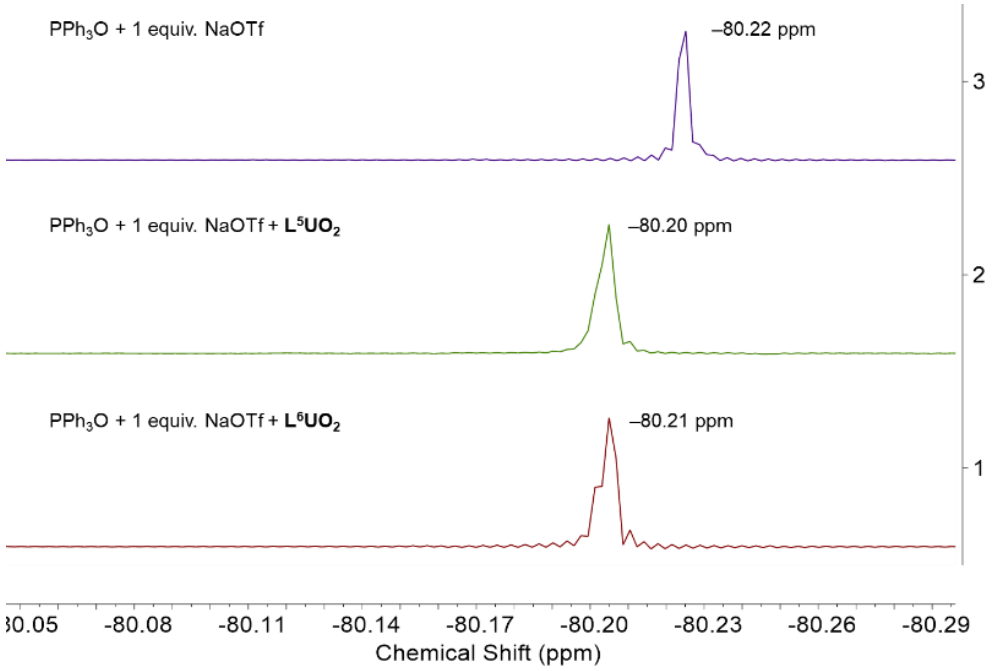

Figure C82. $^{19}F\{^{1}H\}$ NMR for the PPh_3O study with 1 equiv. of $\mathbf{L^5UO_2}$ or $\mathbf{L^6UO_2}$ and NaOTf.

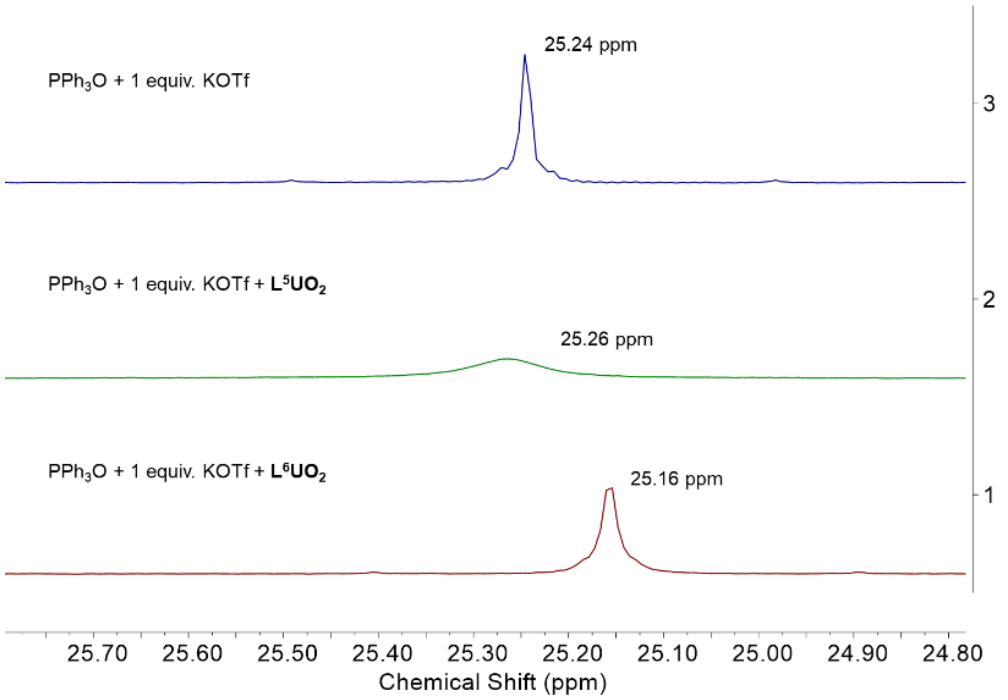

Figure C83. $^{31}P\{^{1}H\}$ NMR for the PPh_3O study with 1 equiv. of $\mathbf{L^5UO_2}$ or $\mathbf{L^6UO_2}$ and KOTf.

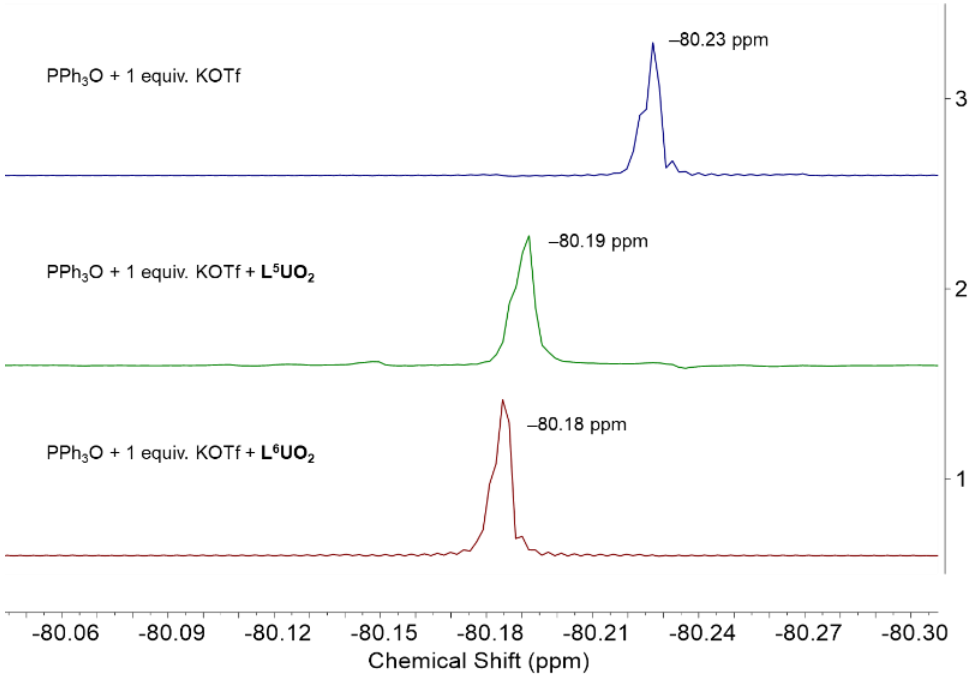

Figure C84. $^{19}F\{^{1}H\}$ NMR for the PPh_3O study with 1 equiv. of $\mathbf{L^5UO_2}$ or $\mathbf{L^6UO_2}$ and KOTf.

Evaluation of the Reorganization Energy λ

We have used the Randles-Ševčik equation to determine the diffusion coefficient *D* (see Figures C24 – C37), of the oxidized species at different scan rates.[3,4]

$$i_{\mathrm{p}} = 0.4463 * \mathrm{nFAC}\sqrt{\left(\frac{\mathrm{nF}\upsilon D}{\mathrm{RT}}\right)}$$

where i_{p} is the maximum peak current in amps, n is the number of electrons transferred, F is Faraday constant in C mol^{-1}, A is electrode area in cm^2, C is concentration in mol/cm^3, υ is scan rate in V/s, R is gas constant in J K^{-1} mol^{-1} and T is temperature (298K).

For determining the charge transfer coefficient α, following equation was used.[5]

$$E_{\mathrm{p}/2} - E_{\mathrm{p}} = 1.857\,\frac{\mathrm{RT}}{\alpha \mathrm{F}}$$

Where E_{p} and $E_{\mathrm{p}/2}$ are peak potential and half-peak potential respectively.

The heterogeneous electron transfer rate, k^0 can be calculated from the equation developed by Nicholson[6] and elaborated by Bard & Faulkner[7].

$$\psi = \frac{\left(\frac{D_{ox}}{D_{red}}\right)^{\alpha/2} k^0}{\sqrt{D_O \pi \upsilon (nF/RT)}}$$

Here, ψ is the dimensionless parameter that can be calculated from known values of the peak-to-peak separations, ΔE_{p} calculated from the CV data, α is the charge transfer coefficient, D_{ox} and D_{red} are the diffusion coefficients of the oxidized and the reduced forms in cm^2/s, n is the number of electrons transferred, F is Faraday constant in C mol^{-1}. R is gas constant in J K^{-1} mol^{-1} and T is temperature (298K).

From the values of D and α calculated at six different scan rates (50 mV/s, 100 mV/s, 150 mV/s, 200 mV/s, 250 mV/s, and 300 mV/s), the free energy of activation $\Delta G^{\ddagger}_{peak}$ for electron transfer was determined by employing the equation derived by Savéant and Costentin.[5]

$$\Delta G^{\ddagger}_{peak} = \frac{\mathrm{RT}}{\mathrm{F}} \ln\left[\left(Z\sqrt{\frac{\mathrm{RT}}{\alpha \mathrm{F} \upsilon D}}\right) - 0.78\right]$$

Here, Z is the collision frequency which could be calculated using the equation,

$$Z = \frac{\sqrt{\mathrm{RT}}}{2\pi \mathrm{M}}$$

where, M is the molar mass of complex involved in the cyclic voltammetry experiment.

Finally, the values of reorganization energies λ for all the complexes were evaluated by utilizing the equation given as follows[8]:

$$\alpha = \sqrt{\frac{\Delta G^{\ddagger}_{\mathrm{peak}}}{\lambda}} \quad \text{or} \quad \lambda = \frac{\Delta G^{\ddagger}_{\mathrm{peak}}}{\alpha^2}$$

The reorganization energies were reported as the average of λ values calculated at four different scan rates. Errors on the λ values are given as $\pm 1\sigma$.

X-Ray Crystallography

Refinement Details

Crystals for all five compounds were mounted on a goniometer head using Paratone oil with MiTeGen MicroMounts and placed in a cold nitrogen stream. Complete sets of low-temperature diffraction data frames were collected for crystals of all nine compounds using 1.0°-wide ω- and/or ϕ-scans. X-rays were provided by a Bruker MicroStar microfocus rotating anode generator running at 45 mA and 60 kV (Cu K_α = 1.54178 Å). Data for **BaPenta** (q55j), **L^5UO_2** (q70k), and **L^5UO_2Na** (q49k) were collected with a Bruker APEX II CCD detector positioned at 50.0 mm and equipped with Helios multilayer mirror optics; data for **L^5UO_2K** (v16f) were collected with a Bruker Platinum 135 CCD detector positioned at 80.0 mm and equipped with Helios high-brilliance multilayer mirror optics. Data for **L^5UO_2Li** (ak_2_133c) were collected with a Bruker APEX II diffractometer.

Data for four compounds (**BaPenta**, **L^5UO_2**, **L^5UO_2K**, and **L^5UO_2Na**) were collected with Cu radiation using a Bruker APEX II detector positioned at 50.0 mm and equipped with Helios multilayer mirror optics; data for the **L^5UO_2Li** were collected with Mo radiation.

Totals of 1756 (**BaPenta**, q55j**)**, 3604 (**L^5UO_2Na**, q49k), 1968 (**L^5UO_2**, q75k), and 2216 (**L^5UO_2K**, v16f), and 1.0°-wide ω- and/or ϕ-scan frames with counting times of 4-6 seconds (q55j, q49k, and q75k) or 5-8 seconds (v16f), were collected on either the Bruker APEX II or the SMART APEX detector. All diffractometer manipulations, including data collection, integration and scaling were carried out using the Bruker APEX2 software package.[9] The data for **BaPenta** was corrected empirically for variable absorption effects with SADABS[10]

using equivalent reflections. A numerical face-indexed absorption correction was used for data sets of all the other eight structures. Probable space groups were determined on the basis of systematic absences and intensity statistics and the structures were solved by direct methods using SIR2004[11] or XS[12] (incorporated into SHELXTL) and refined to convergence by weighted full-matrix least-squares on F_o^2 using the Olex2 software package equipped with XL[13] or with SHELXL that was incorporated into the APEX2 software package.

The final structural model for each compound incorporated anisotropic thermal parameters unless otherwise stated in the special refinement section for each structure; isotropic thermal parameters were used for all included hydrogen atoms**.** Non-methyl hydrogen atoms in each complex were fixed at idealized riding model sp^2- or sp^3-hybridized positions with C–H bond lengths of 0.95 - 0.99 Å. Methyl groups were incorporated into the structural models either as sp^3-hybridized riding model groups with idealized "staggered" geometry and a C-H bond length of 0.98 Å or as idealized riding model rigid rotors (with a C–H bond length of 0.98 Å) that were allowed to rotate freely about their C–C bonds in least-squares refinement cycles. The isotropic thermal parameters of idealized hydrogen atoms in all nine structures were fixed at values 1.2 (non-methyl) or 1.5 (methyl or hydroxyl) times the equivalent isotropic thermal parameter of the carbon or oxygen atom to which they are covalently bonded.

The relevant crystallographic and structure refinement data for all nine compounds are given in Table C2, C3, and C4.

Special Refinement Details for BaPenta.

The outersphere diethyl ether solvent molecule is 64/36 disordered with two orientations.

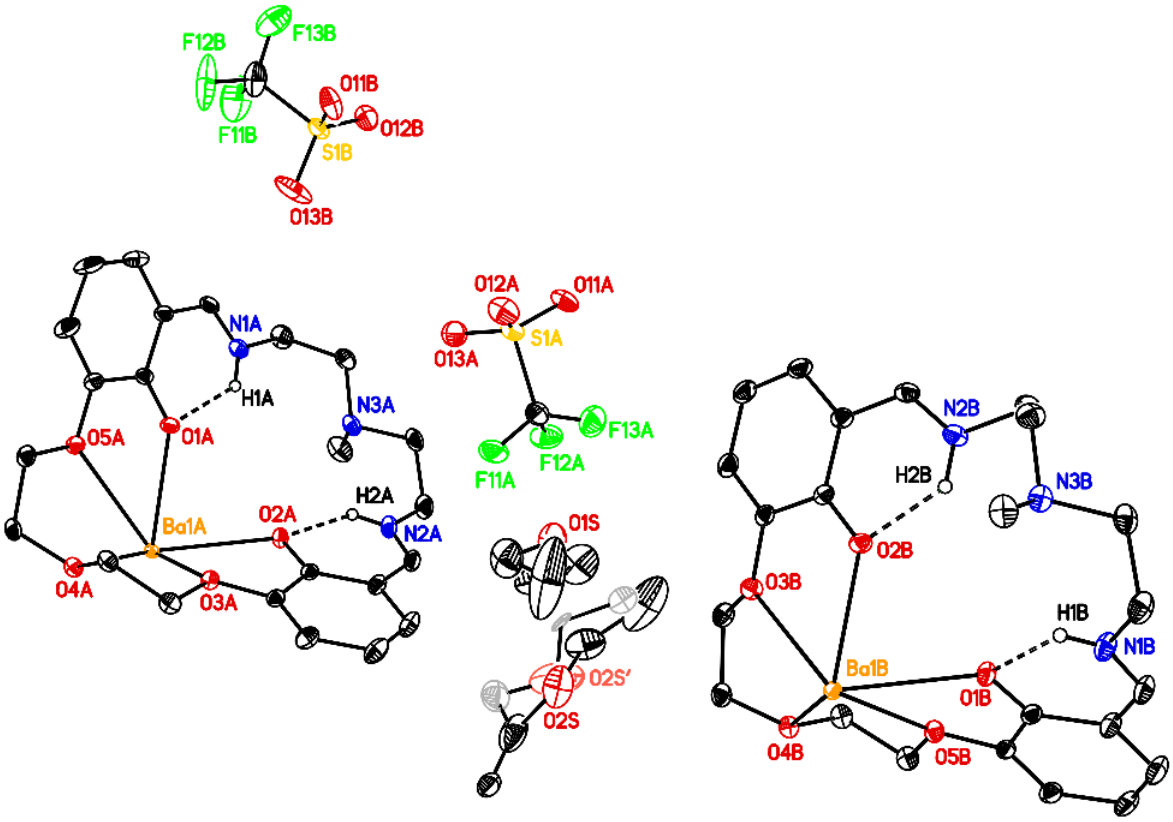

Figure C85. Solid-state structure from XRD of asymmetric unit of **BaPenta** showing 64/36 disorder for the outersphere diethyl ether solvent molecule. Solid bonds are used for the major (64%) orientation of the diethyl ether solvent molecule and dashed bonds for the minor (36%) orientation. H-atoms except those covalently bonded to O1A, O2A, O1B, O2B and involved in intramolecular N–H•••O hydrogen-bonds are omitted for clarity. Displacement ellipsoids are shown at the 20% probability level. Disordered atoms are shown with a lighter shade.

Special Refinement Details for L^5UO_2.

The atoms bonded to amine nitrogen N3 are 79/21 disordered with two alternate orientations about the U–N3 bond.

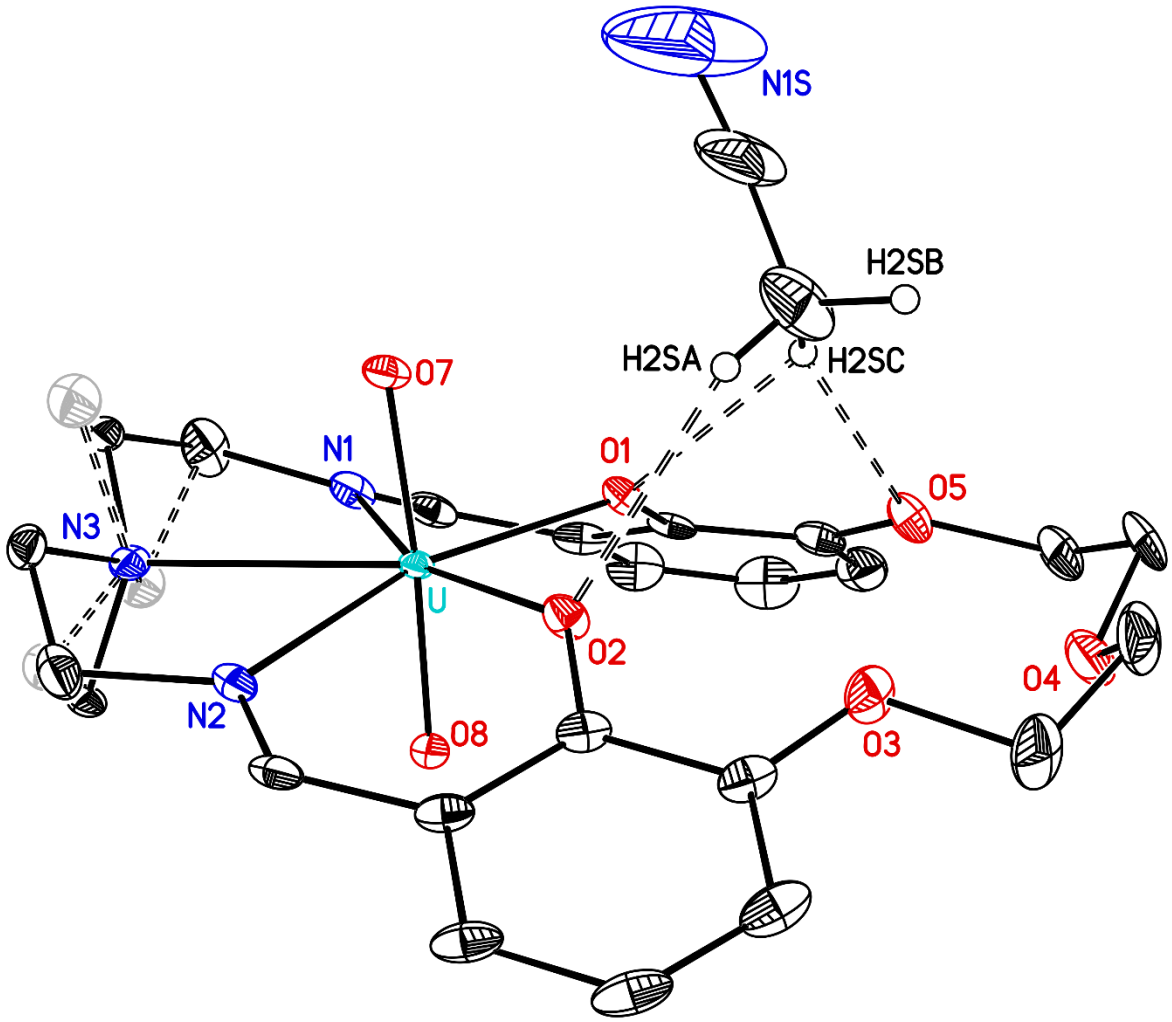

Figure C86. Solid-state structure from XRD of **L^5UO_2** showing 79/21 disorder for the atoms bonded to amine nitrogen N3. Solid bonds are used for the major (79%) orientation about the U–N3 bond and dashed bonds for the minor (21%) orientation. H-atoms except those of covalently bonded to the carbon atom of the outersphere acetonitrile molecule, and involved in intermolecular C–H•••O hydrogen-bonds are omitted for clarity. Displacement ellipsoids are shown at the 20% probability level. Disordered atoms are shown with a lighter shade.

Special Refinement Details for L^5UO_2Li.

The atoms bonded to amine nitrogen N3 are 56/44 disordered with two alternate orientations about the U–N3 bond. The outersphere triflate counteranion is 84/16 disordered with two orientations.

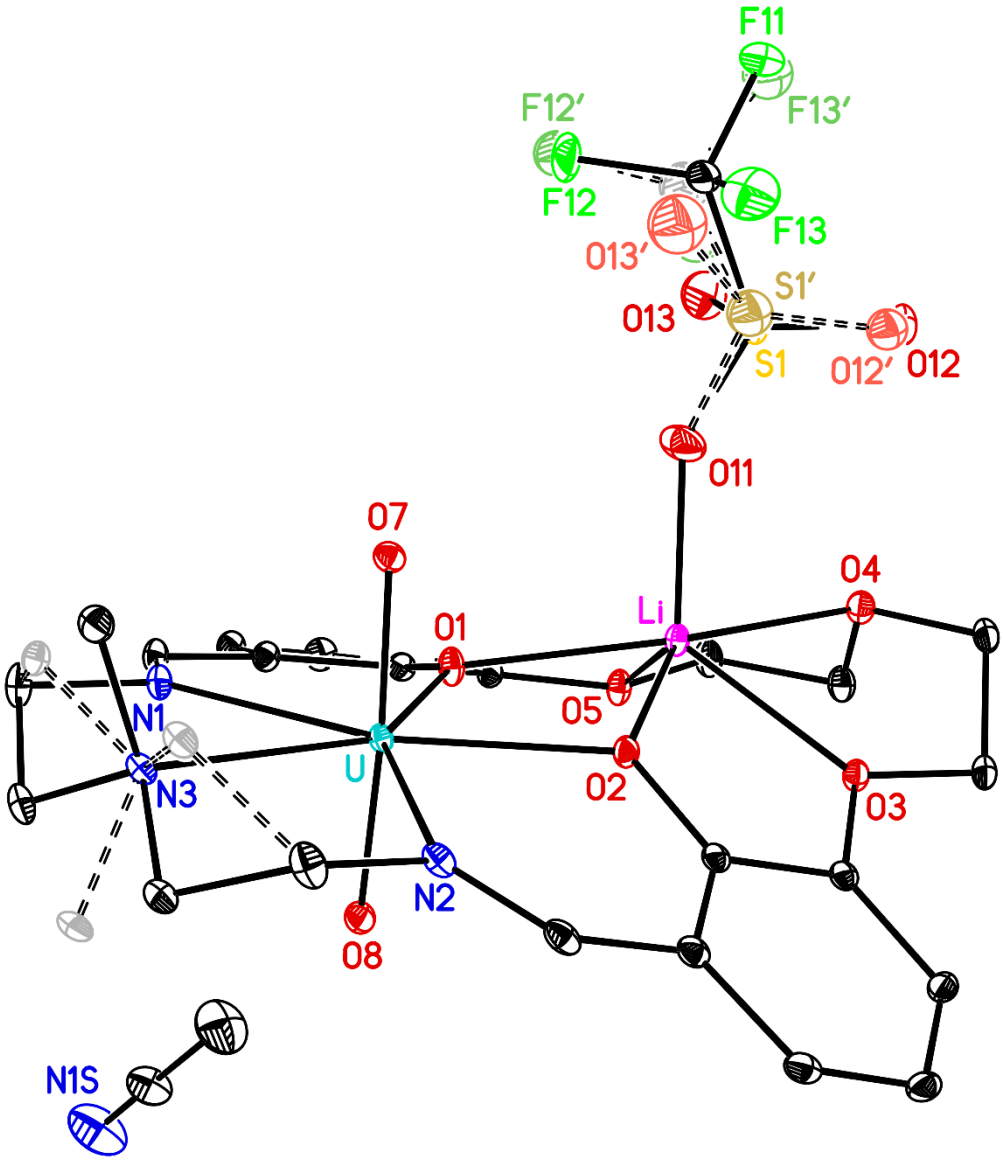

Figure C87. Solid-state structure from XRD of **L^5UO_2Li** showing 56/44 disorder for the atoms bonded to amine nitrogen N3 and 84/16 disorder for the innersphere triflate counteranion. Solid bonds are used for the major orientations and dashed bonds for the minor orientations. H-atoms are omitted for clarity. Displacement ellipsoids are shown at the 20% probability level. Disordered atoms are shown with a lighter shade.

Special Refinement Details for L^5UO_2Na.

The atoms bonded to amine nitrogen N3 are 61/39 disordered with two alternate orientations about the U–N3 bond.

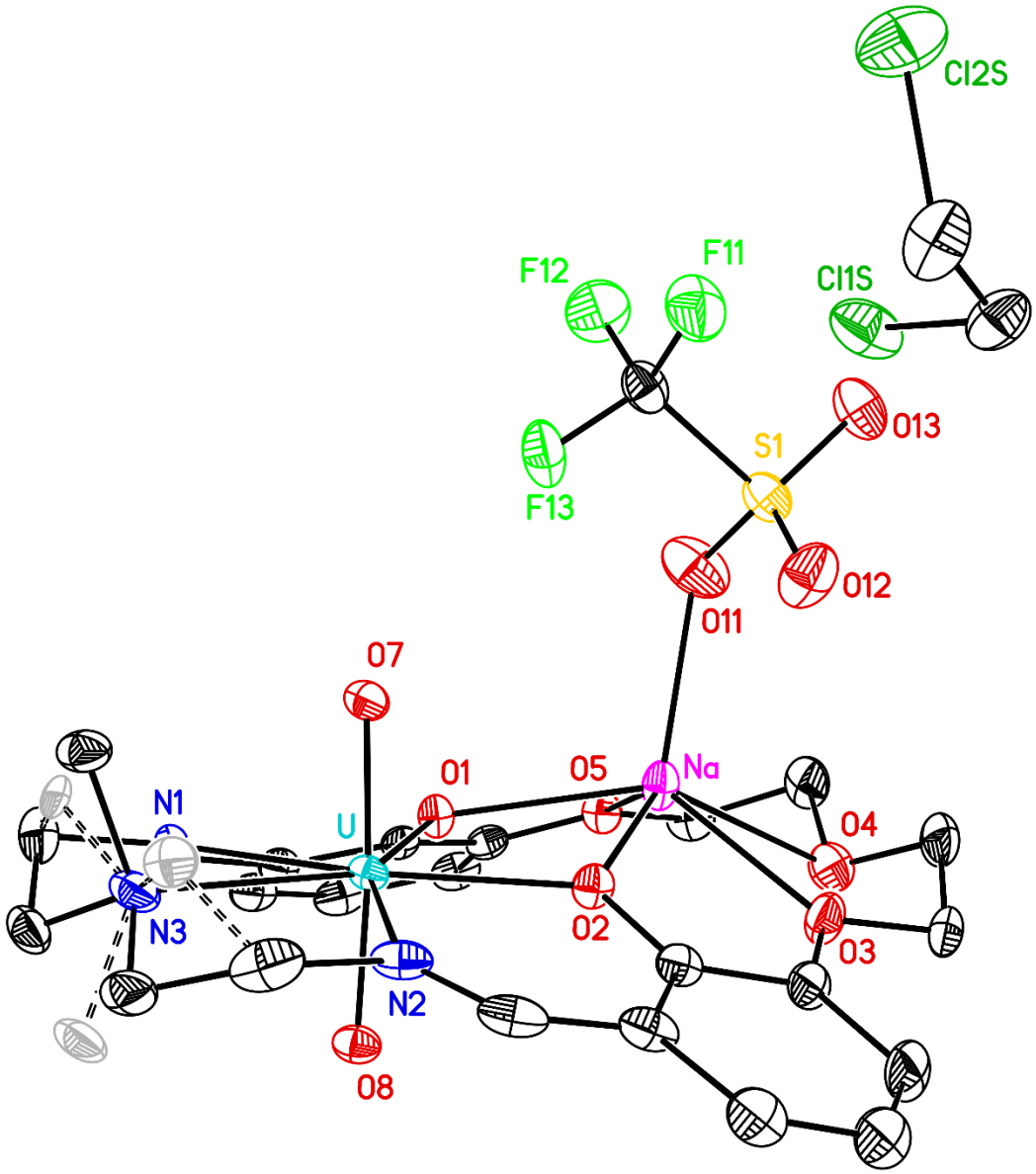

Figure C88. Solid-state structure from XRD of **L^5UO_2Na** showing 61/39 disorder for the atoms bonded to amine nitrogen N3. Solid bonds are used for the major (61%) orientation about the U–N3 bond and dashed bonds for the minor (39%) orientation. H-atoms are omitted for clarity. Displacement ellipsoids are shown at the 20% probability level. Disordered atoms are shown with a lighter shade.

Special Refinement Details for L^5UO_2K.

The atoms bonded to amine nitrogen N3 are 71/29 disordered with two alternate orientations about the U–N3 bond. The outersphere triflate counteranion is 90/10 disordered with two orientations.

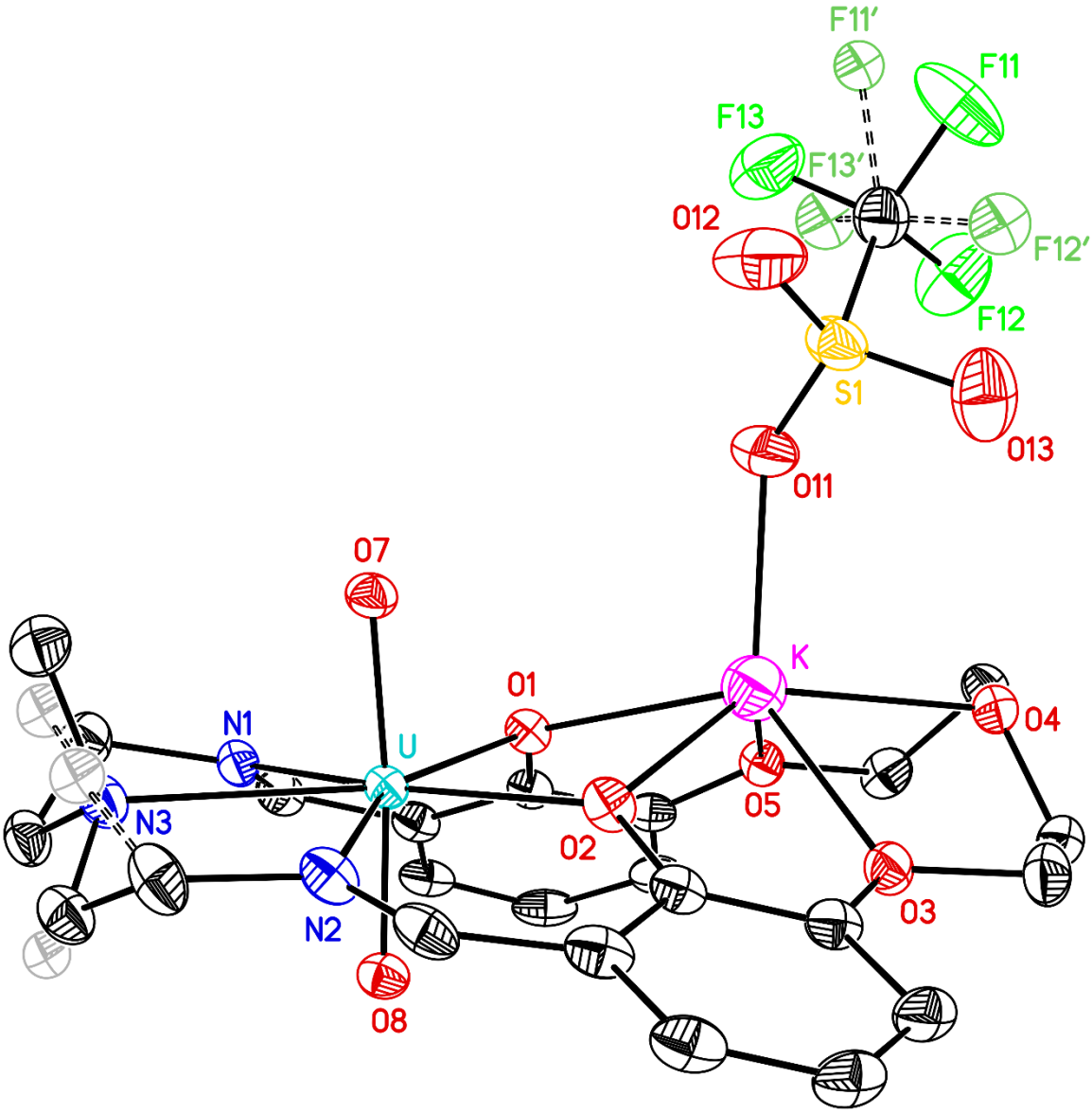

Figure C89. Solid-state structure from XRD of **L^5UO_2K** showing 71/29 disorder for the atoms bonded to amine nitrogen N3 and 90/10 disorder for the innersphere triflate counteranion. Solid bonds are used for the major orientations and dashed bonds for the minor orientations. H-atoms are omitted for clarity. Displacement ellipsoids are shown at the 20% probability level. Disordered atoms are shown with a lighter shade.

Table C2. Crystal and Refinement Data for **BaPenta**.

	BaPenta
Empirical formula	$C_{27.66}H_{37.62}Ba_{0.5}F_3N_3O_9S$
Formula weight	713.87
Temperature	200 K
Wavelength	1.54178 Å
Crystal system	Orthorhombic
Space group	Pccn
a	20.6676(3) Å
b	23.1000(4) Å
c	27.4588(4) Å
α	90°
β	90°
γ	90°
Volume	13109.4(4) $Å^3$
Z	16
Density (calculated)	1.447 g/cm^3
Absorption coefficient	6.070 mm^{-1}
F(000)	5881.0
Crystal size	0.19 × 0.06 × 0.05 mm^3
Theta range	2.869 to 70.352°
Index ranges	$-25 \le h \le 24$, $-27 \le k \le 26$, $-33 \le l \le 23$
Reflections collected	84668
Independent reflections	12312 [R_{int} = 0.039, R_{sigma} = 0.025]
Completeness/θ_{max}	100%/66.00°
Absorption correction	Multi-scan
Max./Min. Transmission	0.753 and 0.396
Refinement method	Full-matrix least-squares on F^2
Data/restraints/parameters	12312/25/865
Goodness-of-fit on F^2	1.144
Final R indices [I>2σ(I)]	R_1 = 0.042, wR_2 = 0.103
R indices (all data)	R_1 = 0.052, wR_2 = 0.110
Largest diff. peak & hole	0.66 and –0.56 $e^-.Å^{-3}$

Table C3. Crystal and Refinement Data for **L^5UO_2** and **L^5UO_2Li**.

	L^5UO_2	**L^5UO_2Li**
Empirical formula	$C_{25}H_{30}N_4O_7U$	$C_{26}H_{30}F_3LiN_4O_{10}SU$
Formula weight	736.56	892.57
Temperature	200 K	120 K
Wavelength	1.54178 Å	0.71073 Å
Crystal system	Monoclinic	Triclinic
Space group	$P2_1/c$	P-1
a	10.3526(3) Å	9.8299(11) Å
b	13.0258(3) Å	12.1237(14) Å
c	19.7606(5) Å	13.9454(16) Å
α	90°	75.861(2)°
β	100.3600(10)°	78.916(2)°
γ	90°	70.940(2)°
Volume	2621.29(12) $Å^3$	1511.7(3) $Å^3$
Z	4	2
Density (calculated)	1.866 g/cm^3	1.961 g/cm^3
Absorption coefficient	17.867 mm^{-1}	5.518 mm^{-1}
F(000)	1424.0	864.0
Crystal size	0.089 × 0.067 × 0.036 mm^3	0.272 × 0.149 × 0.053 mm^3
Theta range	4.085 to 70.183°	2.14 to 27.50°
Index ranges	$-11\leq h\leq 12$, $-15\leq k\leq 15$, $-21\leq l\leq 23$	$-13\leq h\leq 13$,$-16\leq k\leq 16$,$-18\leq l\leq 18$
Reflections collected	16635	35001
Independent reflections	4798 [R_{int} = 0.051, R_{sigma} = 0.049]	7504 [R_{int} = 0.022, R_{sigma} = 0.018]
Completeness/θ_{max}	99.6%/66.00°	100%/25.24°
Absorption correction	Mulit-scan	Numerical face-indexed
Max./Min. Transmission	0.753 and 0.545	0.789 and 0.349
Refinement method	Full-matrix least-squares on F^2	Full-matrix least-squares on F^2
Data/restraints/parameters	4798/0/350	7504/15/475
Goodness-of-fit on F^2	1.093	1.084
Final R indices [I>2σ(I)]	R_1 = 0.036, wR_2 = 0.089	R_1 = 0.016, wR_2 = 0.037
R indices (all data)	R_1 = 0.039, wR_2 = 0.092	R_1 = 0.019, wR_2 = 0.037
Largest diff. peak & hole	1.94 and –2.74 $e^-.Å^{-3}$	1.34 and –0.82 $e.Å^{-3}$

Table C4. Crystal and Refinement Data for **L^5UO_2Na** and **L^5UO_2K**.

	L^5UO_2Na	**L^5UO_2K**
Empirical formula	$C_{26}H_{31}Cl_2F_3N_3NaO_{10}SU$	$C_{24}H_{27}F_3KN_3O_{10}SU$
Formula weight	966.52	883.67
Temperature	200 K	200 K
Wavelength	1.54178 Å	0.71073 Å
Crystal system	Triclinic	Monoclinic
Space group	P-1	$P2_1/c$
a	10.2238(3) Å	12.1206(4) Å
b	12.1909(4) Å	12.9470(4) Å
c	13.9815(5) Å	19.1487(6) Å
α	99.7935(14)°	90°
β	98.0293(15)°	104.1704(11)°
γ	103.3418(13)°	90°
Volume	1641.52(9) $Å^3$	2913.48(16) $Å^3$
Z	2	4
Density (calculated)	1.955 g/cm^3	2.015 g/cm^3
Absorption coefficient	16.814 mm^{-1}	18.342 mm^{-1}
F(000)	936.0	1704.0
Crystal size	0.146 × 0.04 × 0.025 mm^3	0.085 × 0.08 × 0.025 mm^3
Theta range	3.811 to 70.574°	4.163 to 68.334°
Index ranges	$-11\leq h\leq 12$, $-14\leq k\leq 14$, $-14\leq l\leq 16$	$-14\leq h\leq 14$, $-15\leq k\leq 11$, $-20\leq l\leq 22$
Reflections collected	20295	16811
Independent reflections	5758 [R_{int} = 0.050, R_{sigma} = 0.045]	5185 [R_{int} = 0.043, R_{sigma} = 0.043]
Completeness/θ_{max}	96.0%/66.00°	99.0%/66.00°
Absorption correction	Numerical face-indexed	Numerical face-indexed
Max./Min. Transmission	0.987 and 0.098	0.352 and 0.098
Refinement method	Full-matrix least-squares on F^2	Full-matrix least-squares on F^2
Data/restraints/parameters	5758/6/454	5185/0/389
Goodness-of-fit on F^2	1.047	1.080
Final R indices [I>2σ(I)]	R_1 = 0.037, wR_2 = 0.094	R_1 = 0.046, wR_2 = 0.124
R indices (all data)	R_1 = 0.038, wR_2 = 0.096	R_1 = 0.051, wR_2 = 0.128
Largest diff. peak & hole	1.87 and –1.87 $e^-.Å^{-3}$	2.59 and –2.14 $e.Å^{-3}$

References

(1) Kumar, A.; Lionetti, D.; Day, V. W.; Blakemore, J. D. CCDC 1960629: Experimental Crystal Structure Determination, 2020, DOI: 10.5517/ccdc.csd.cc23t638

(2) Kumar, A.; Lionetti, D.; Day, V. W.; Blakemore, J. D. CCDC 1960628: Experimental Crystal Structure Determination, 2020, DOI: 10.5517/ccdc.csd.cc23t627

(3) Randles, J. E. B. *Trans. Faraday Soc.* **1948,** *44*, 327-338.

(4) Ševčik, A. *Collect. Czech. Chem. Commun.* **1948**, *13*, 349-377

(5) Savéant, J. M.; Costentin, C. *Elements of Molecular and Biomolecular Electrochemistry, An Electrochemical Approach to Electron Transfer Chemistry*, Wiley, Hoboken, NJ, **2019**.

(6) Nicholson, R. S. Theory and application of cyclic voltammetry for measurement of electrode reaction kinetics. *Anal. Chem.* **1965,** *37*, 1351-1355.

(7) Bard, A. J.; Faulkner, L. R. *Electrochemical Methods: Fundamentals and Applications*. 2nd ed.; Wiley: Hoboken, NJ, 2001.

(8) Ching, H. V.; Anxolabéhère-Mallart, E.; Colmer, H. E.; Costentin, C.; Dorlet, P.; Jackson, T. A.; Policar, C.; Robert, M. *Chemical Science* **2014,** *5*, 2304-2310.

(9) *SAINT. Ver. 8.34A.* Bruker Analytical X-ray Systems: Madison, WI, June 2014.

(10) *Sheldrick, G. M., SADABS (version 2008/1)*: Program for Absorption Correction for Data from Area Detector Frames, University of Göttingen, 2008.

(11) Sheldrick, G., *Acta Crystallogr., Sect. A: Found. Crystallogr.* **2015**, *71*, 3-8.

(12) Sheldrick, G. *Acta Crystallogr., Sect. C: Cryst. Struct. Commun.* **2015**, *71*, 3-8.

(13) O. V. Dolomanov, L. J. Bourhis, R. J. Gildea, J. A. K. Howard and H. Puschmann, *J. Appl. Crystallogr.*, 2009, **42**, 339-341.

Appendix D

Supplementary Information for Chapter 5

Table D1. Metal-aqua complex pK_a values and shift in the $^{19}F\{^1H\}$ NMR of their triflate salts in d_3-MeCN.

M^{n+}	pK_a of $[M(OH_2)_m]^{n+}$	$\delta^{19}F$ / ppm
Cs^+	-	–80.26
Rb^+	-	–80.26
K^+	-	–80.26
Na^+	14.8	–80.23
Li^+	13.8	–80.30
Ba^{2+}	13.4	–80.14
Sr^{2+}	13.2	–80.16
Ca^{2+}	12.6	–80.19
La^{3+}	9.1	–80.11
Zn^{2+}	9.0	–80.23
Y^{3+}	8.3	–79.98
Lu^{3+}	7.9	–80.14
Sc^{3+}	5.1	–79.64

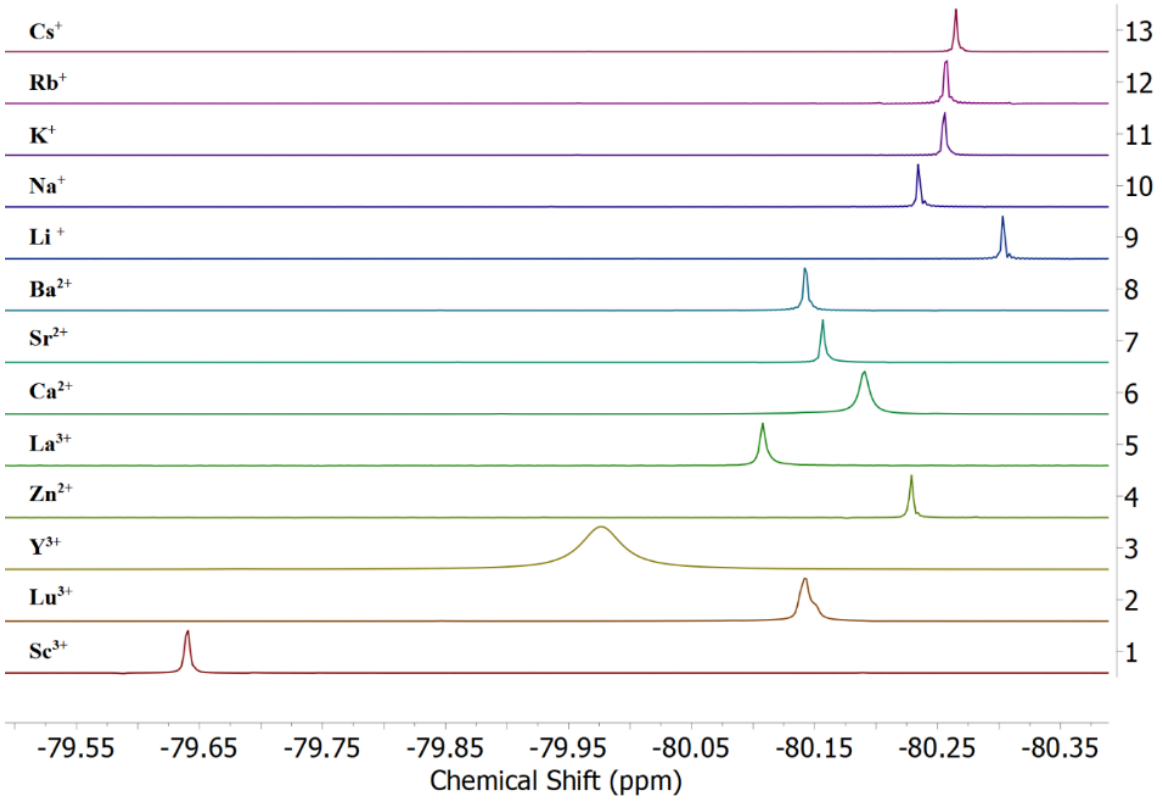

Figure D1. $^{19}F\{^{1}H\}$ NMR spectra (376 MHz, d_3-MeCN) of $M(OTf)_n$.

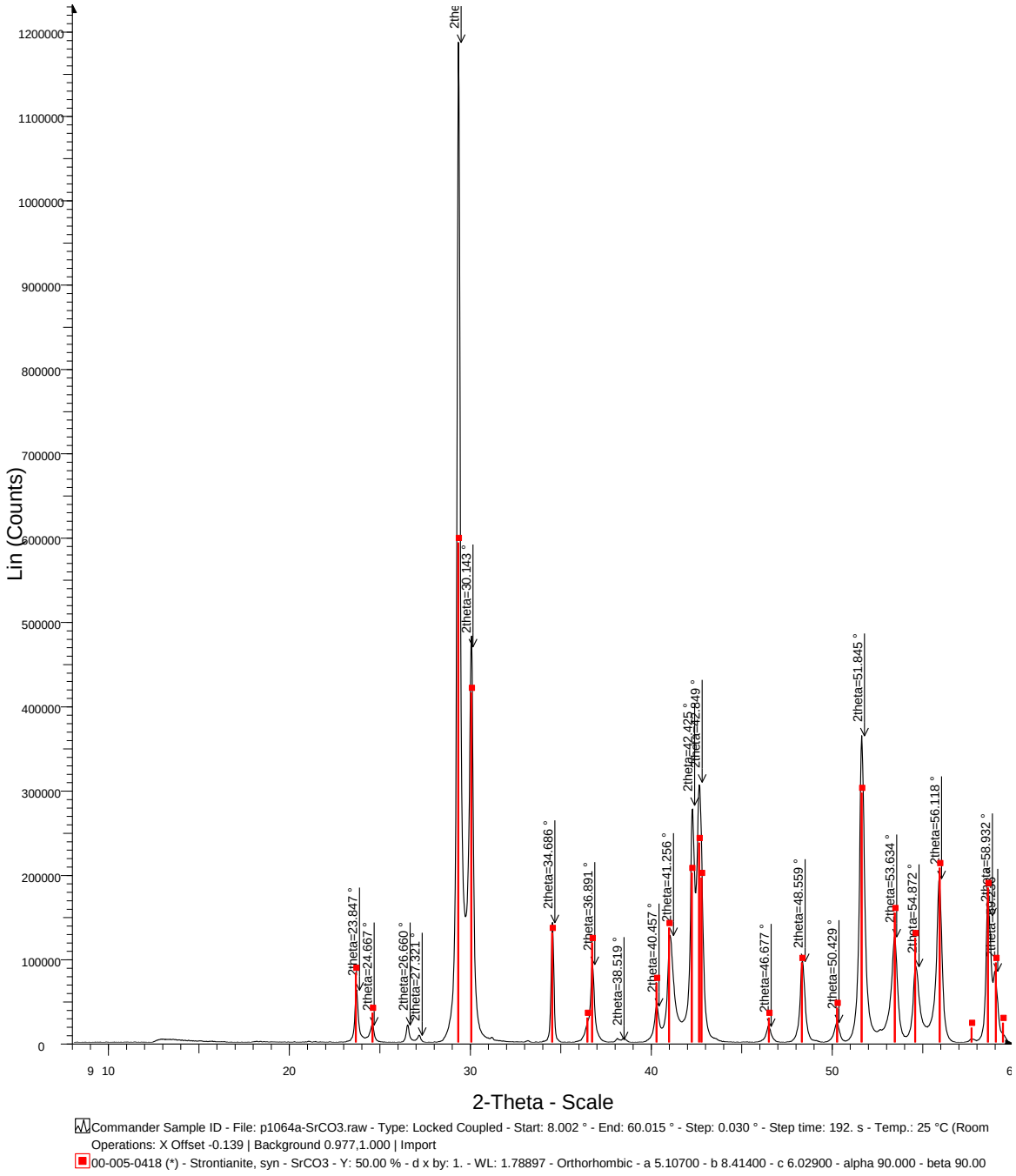

Figure D2. Overlay of powder X-ray diffraction pattern (PXRD) for commercial $SrCO_3$ (black) and $SrCO_3$ (red) from PXRD standards database.

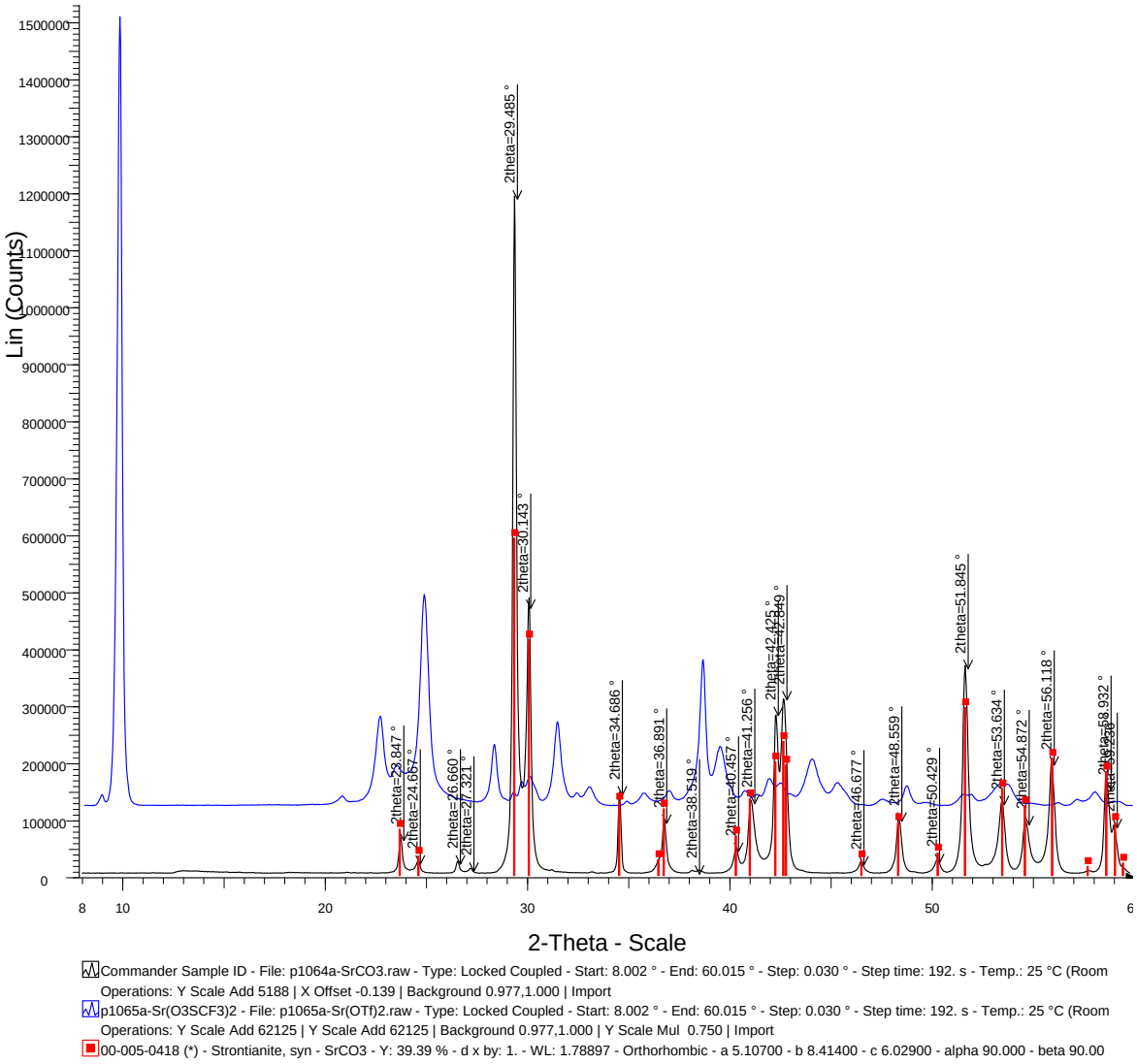

Figure D3. Overlay of powder X-ray diffraction pattern (PXRD) for commercial $SrCO_3$ (black), $SrCO_3$ (red) from PXRD standards database and synthesized $Sr(OTf)_2$ (blue).

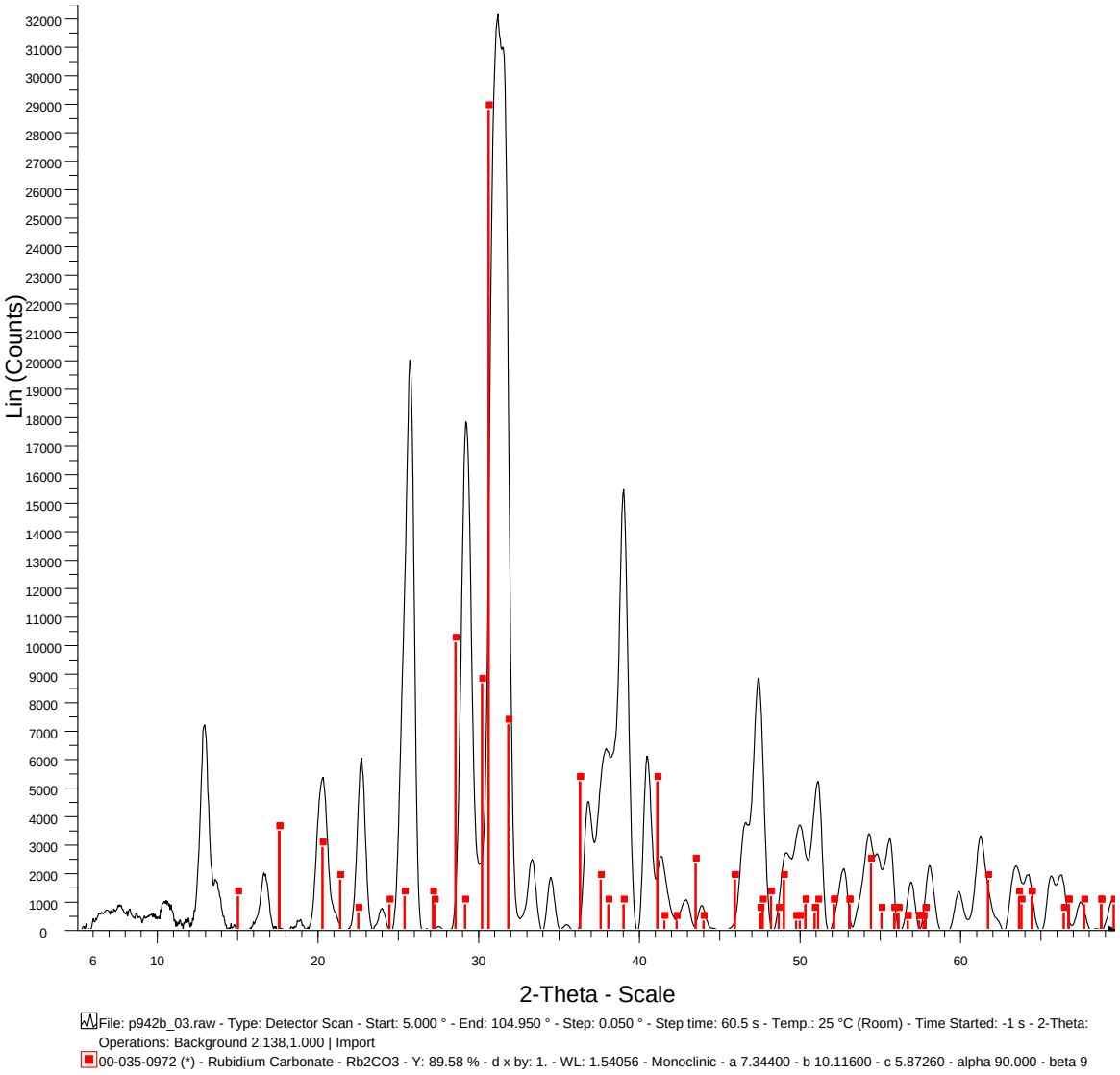

Figure D4. Overlay of powder X-ray diffraction (PXRD) pattern for synthesized Rb_2CO_3 (black) and a different polymorph of Rb_2CO_3 (red) from PXRD standards database.

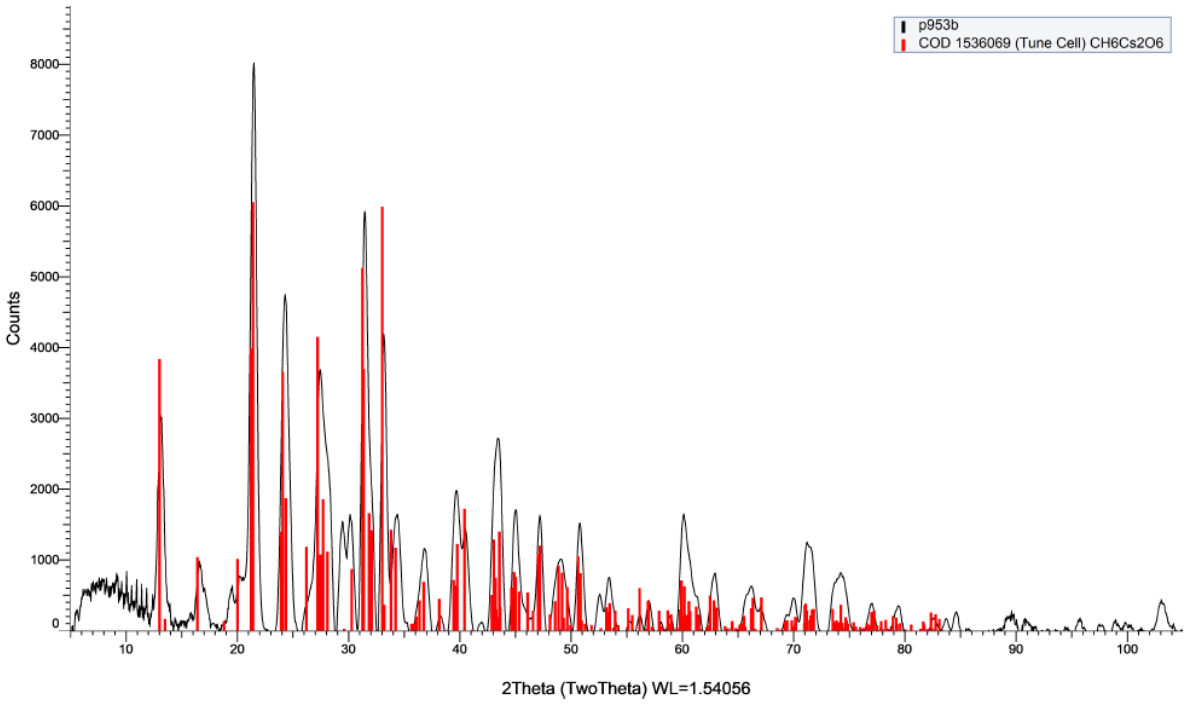

Figure D5. Overlay of powder X-ray diffraction (PXRD) pattern for synthesized CsOTf (black) and CsOTf.3H_2O (red) from PXRD standards database.

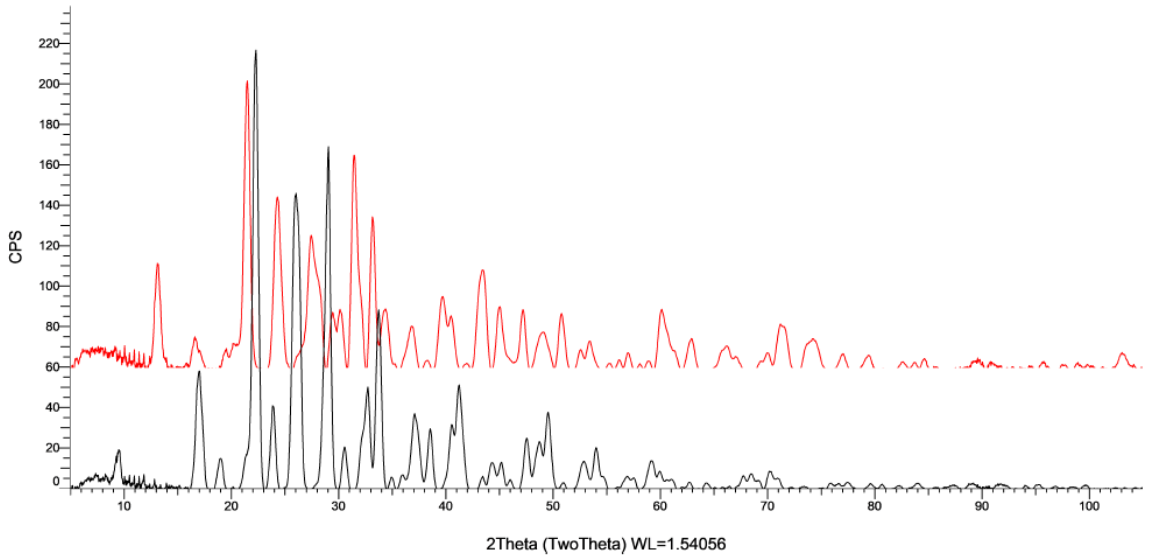

Figure D6. Overlay of powder X-ray diffraction pattern (PXRD) for commercial Cs_2CO_3 (red) and synthesized CsOTf (black).

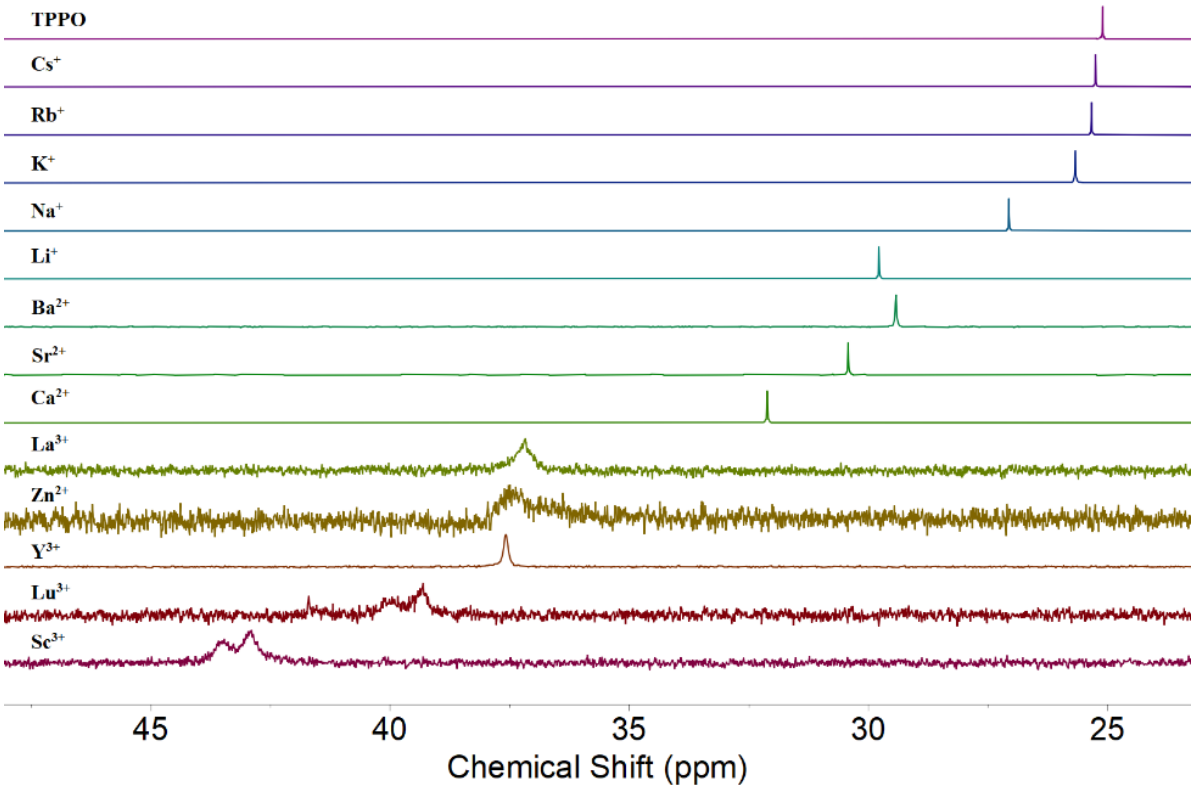

Figure D7. $^{31}P\{^{1}H\}$ NMR spectra (162 MHz, d_3-MeCN) of TPPO in the presence of 1 equiv. $M(OTf)_n$.

Table D2. Metal-aqua complex pK_a values and shift in the $^{31}P\{^1H\}$ NMR of their triflate salts in the presence of 1 equiv. of TPPO in d_3-MeCN.

M^{n+}	pK_a of $[M(OH_2)_m]^{n+}$	$\delta^{31}P$ / ppm	$\Delta\delta^{31}P$ / ppm
TPPO	-	25.10	-
Cs^+	-	25.22	0.12
Rb^+	-	25.30	0.20
K^+	-	25.67	0.57
Na^+	14.8	27.07	1.97
Li^+	13.8	29.78	4.68
Ba^{2+}	13.4	29.43	4.33
Sr^{2+}	13.2	30.42	5.32
Ca^{2+}	12.6	32.12	7.02
La^{3+}	9.1	37.17	12.07
Zn^{2+}	9.0	37.61	12.51
Y^{3+}	8.3	37.58	12.48
Lu^{3+}	7.9	39.83a	14.73
Sc^{3+}	5.1	43.13b	18.03

Note: For spectra with multiple peaks the $\delta^{31}P$ values are weighted-averaged [a]Individual peak $\delta^{31}P$ shifts with their relative integrations in parentheses in case of Lu^{3+}: 41.71 ppm (1.00), 40.02 ppm (5.73) and 39.36 ppm (6.61), [b]in case of Sc^{3+}: 43.47 (1.00) ppm and 42.90 (1.48) ppm.

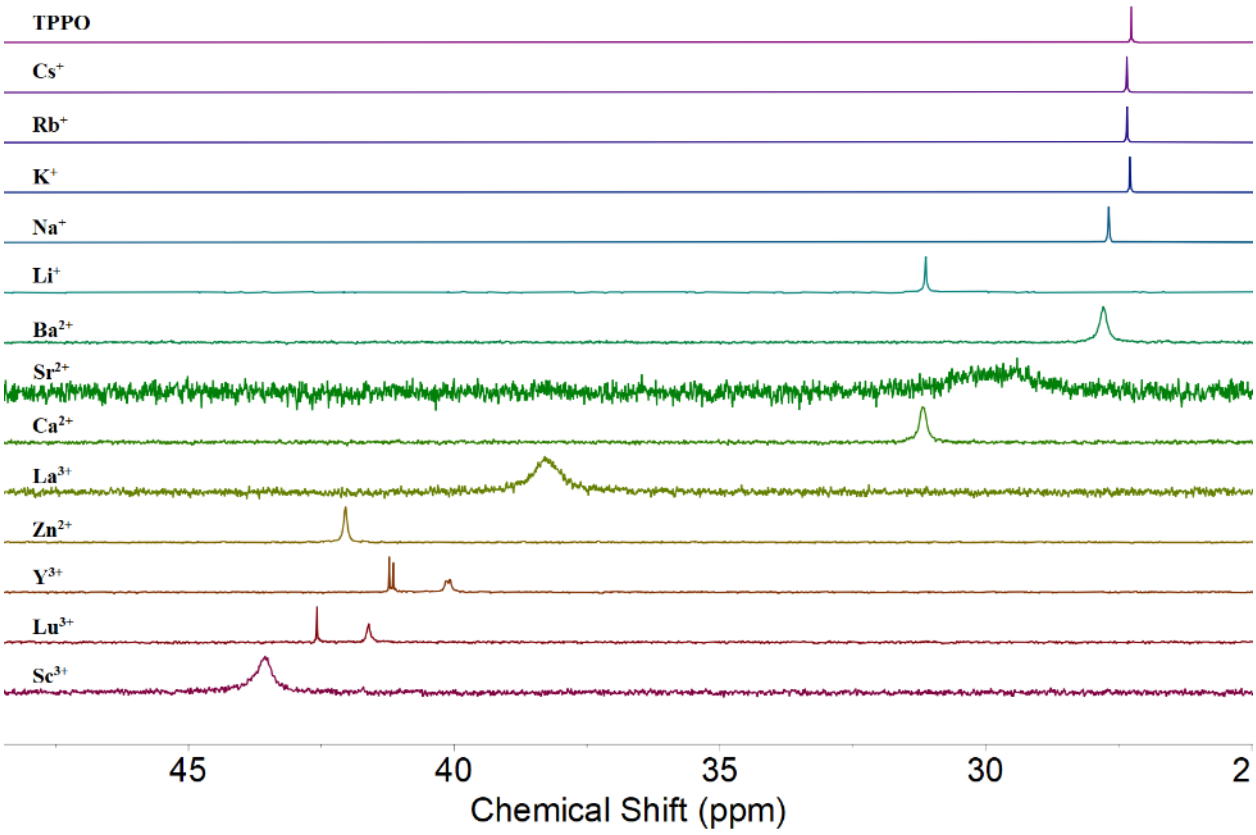

Figure D8. $^{31}P\{^{1}H\}$ NMR spectra (162 MHz, CD_2Cl_2) of TPPO in the presence of 1 equiv. $M(OTf)_n$.

Table D3. Metal-aqua complex pK_a values and shift in the $^{31}P\{^1H\}$ NMR of their triflate salts in the presence of 1 equiv. of TPPO in CD_2Cl_2.

M^{n+}	pK_a of $[M(OH_2)_m]^{n+}$	$\delta^{31}P$ / ppm	$\Delta\delta^{31}P$ / ppm
TPPO	-	27.26	-
Cs^+	-	27.34	-0.078
Rb^+	-	27.33	-0.074
K^+	-	27.24	0.022
Na^+	14.8	27.68	0.42
Li^+	13.8	30.97	3.71
Ba^{2+}	13.4	27.79	0.52
Sr^{2+}	13.2	29.90	2.64
Ca^{2+}	12.6	31.19	3.92
La^{3+}	9.1	38.30	11.03
Zn^{2+}	9.0	42.04	14.79
Y^{3+}	8.3	40.54a	13.28
Lu^{3+}	7.9	41.92b	14.66
Sc^{3+}	5.1	43.58	16.32

Note: For spectrum with multiple peaks the $\delta^{31}P$ values are weighted-averaged [a]Individual peak $\delta^{31}P$ shifts with their relative integrations in parentheses in case of Y^{3+}: 41.22 ppm (1.00), 41.15 ppm (1.07) and 40.12 ppm (3.18), [b]in case of Lu^{3+}: 42.58 ppm (1.00) and 41.61 ppm (2.17).

Table D4. Estimation of pK_a values of selected metal ions in H_2O using their ^{31}P NMR shifts in CD_2Cl_2.

M^{n+}	$\delta_{max}{}^{31}P$ / ppm	$\Delta\delta_{max}{}^{31}P$ / ppm	Estimated pK_a
K^+	27.28	0.02	14.95 ± 1.90
Rb^+	27.19	–0.07	15.00 ± 1.91
Cs^+	27.19	–0.08	15.00 ± 1.91

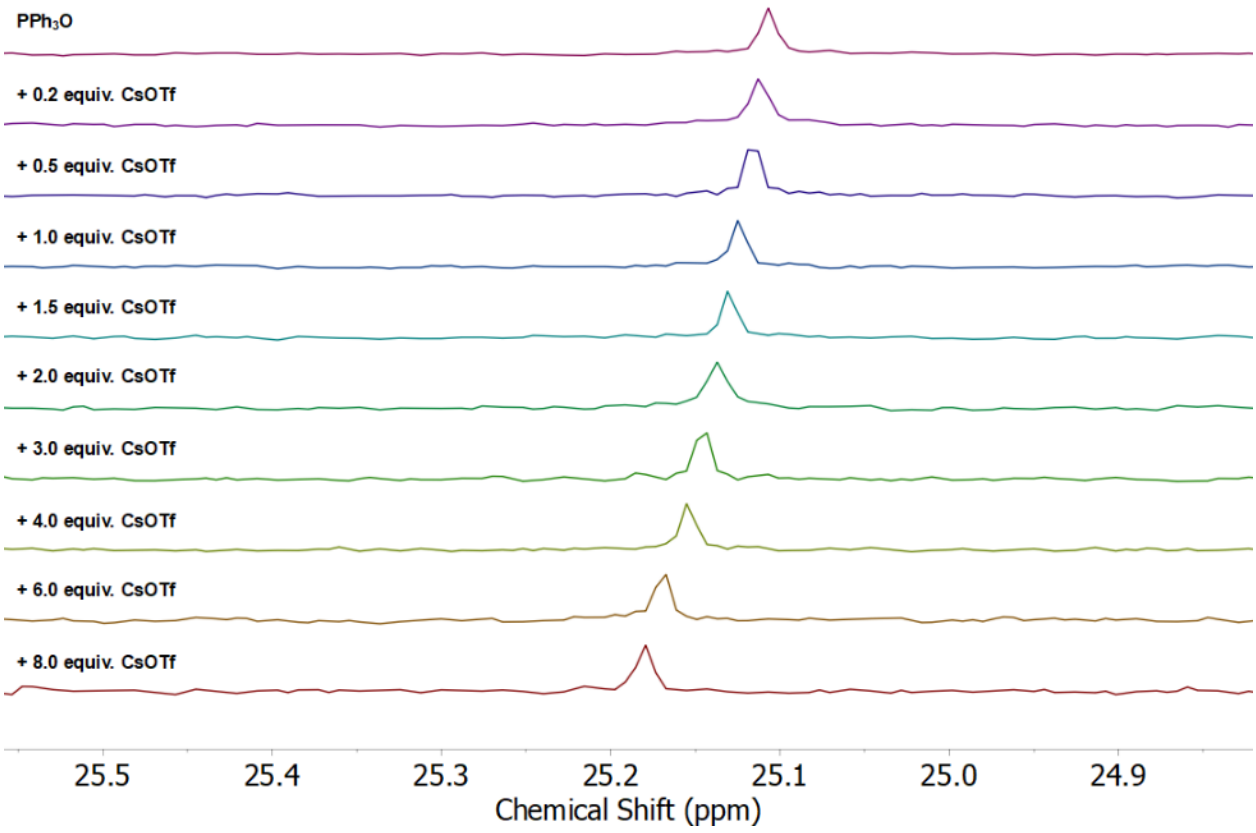

Figure D9. Stacked $^{31}P\{^1H\}$ NMR spectra (162 MHz, d_3-MeCN) for the titration of TPPO with CsOTf.

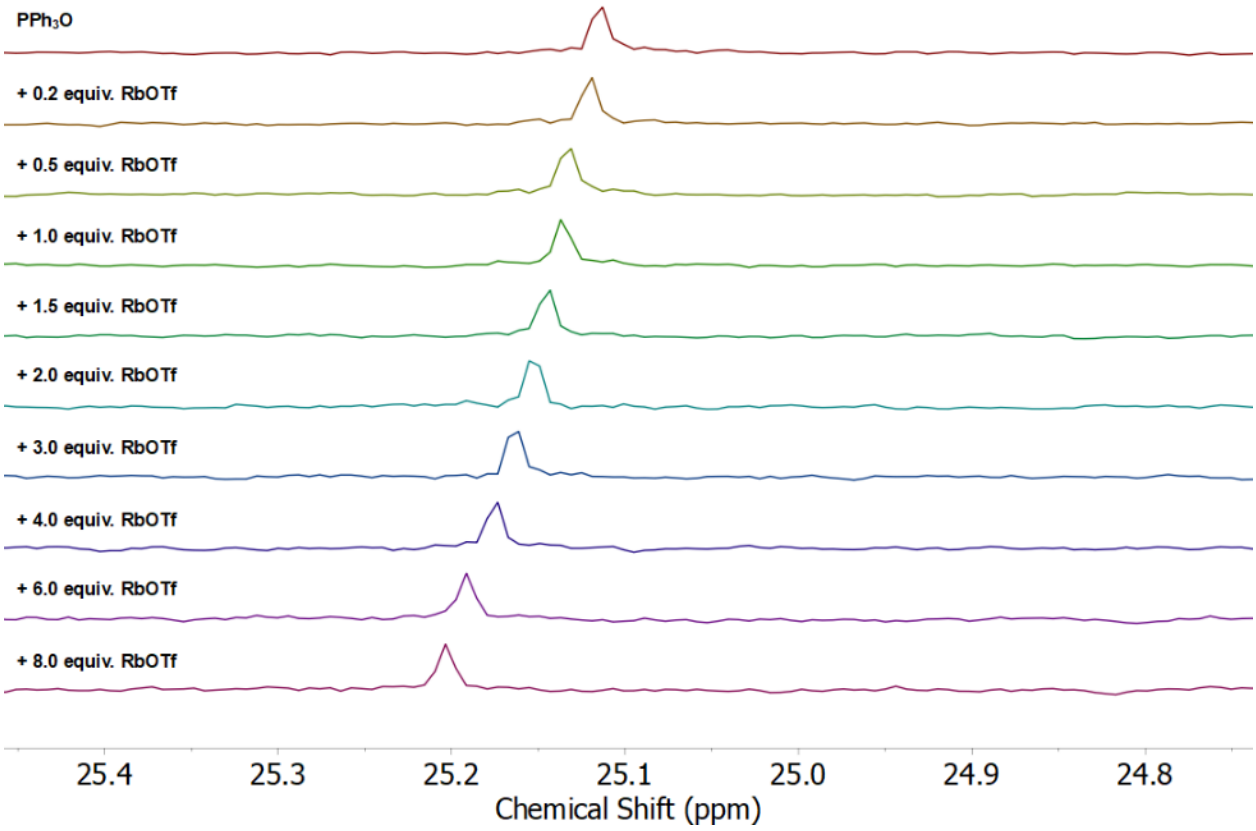

Figure D10. Stacked $^{31}P\{^{1}H\}$ NMR spectra (162 MHz, d_3-MeCN) for the titration of TPPO with RbOTf.

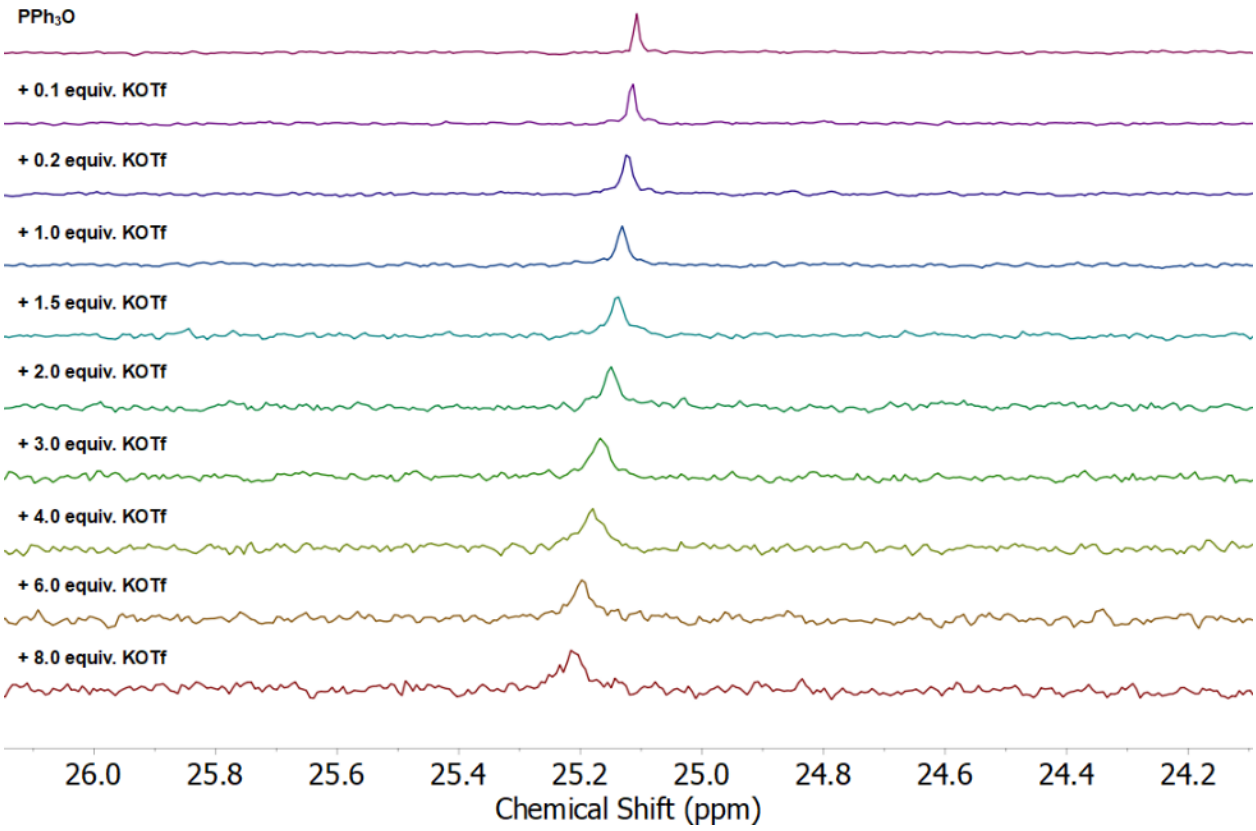

Figure D11. Stacked $^{31}P\{^{1}H\}$ NMR spectra (162 MHz, d_3-MeCN) for the titration of TPPO with KOTf.

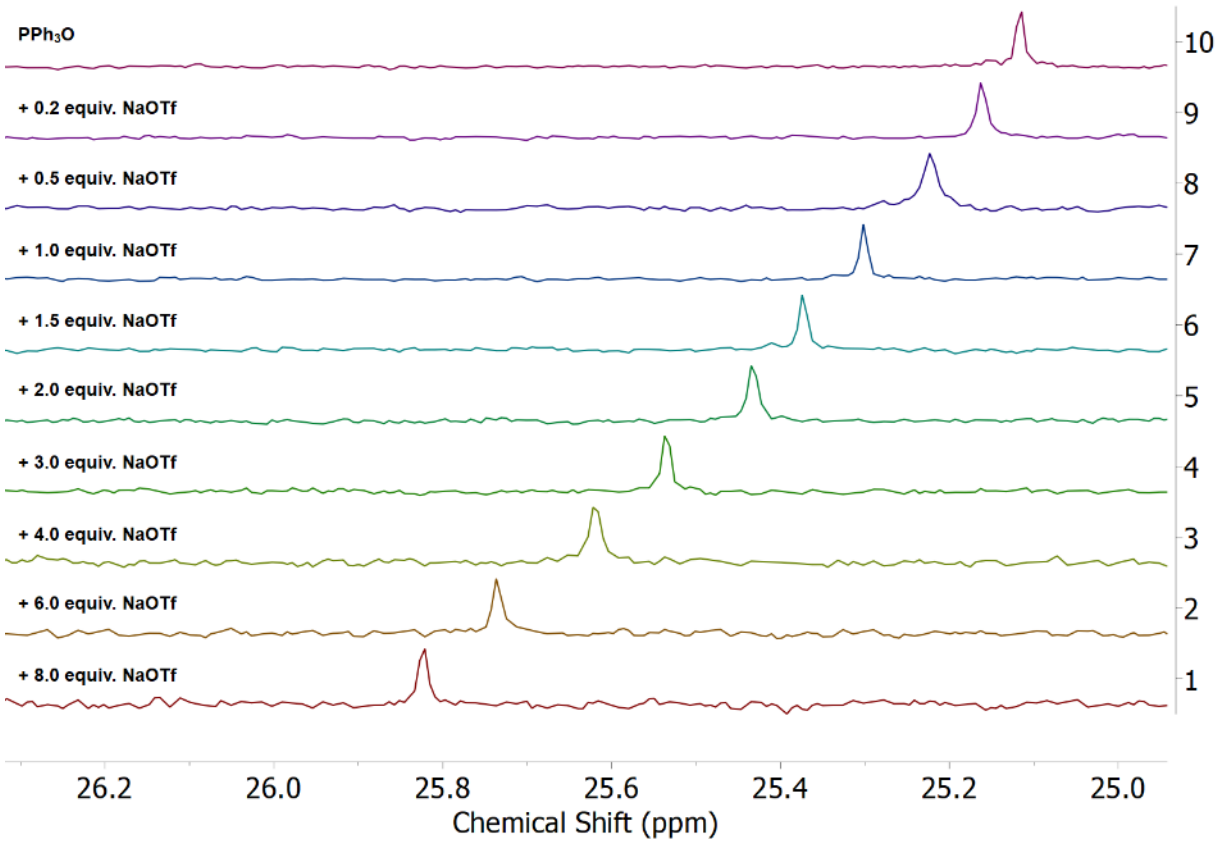

Figure D12. Stacked $^{31}P\{^{1}H\}$ NMR spectra (162 MHz, d_3-MeCN) for the titration of TPPO with NaOTf.

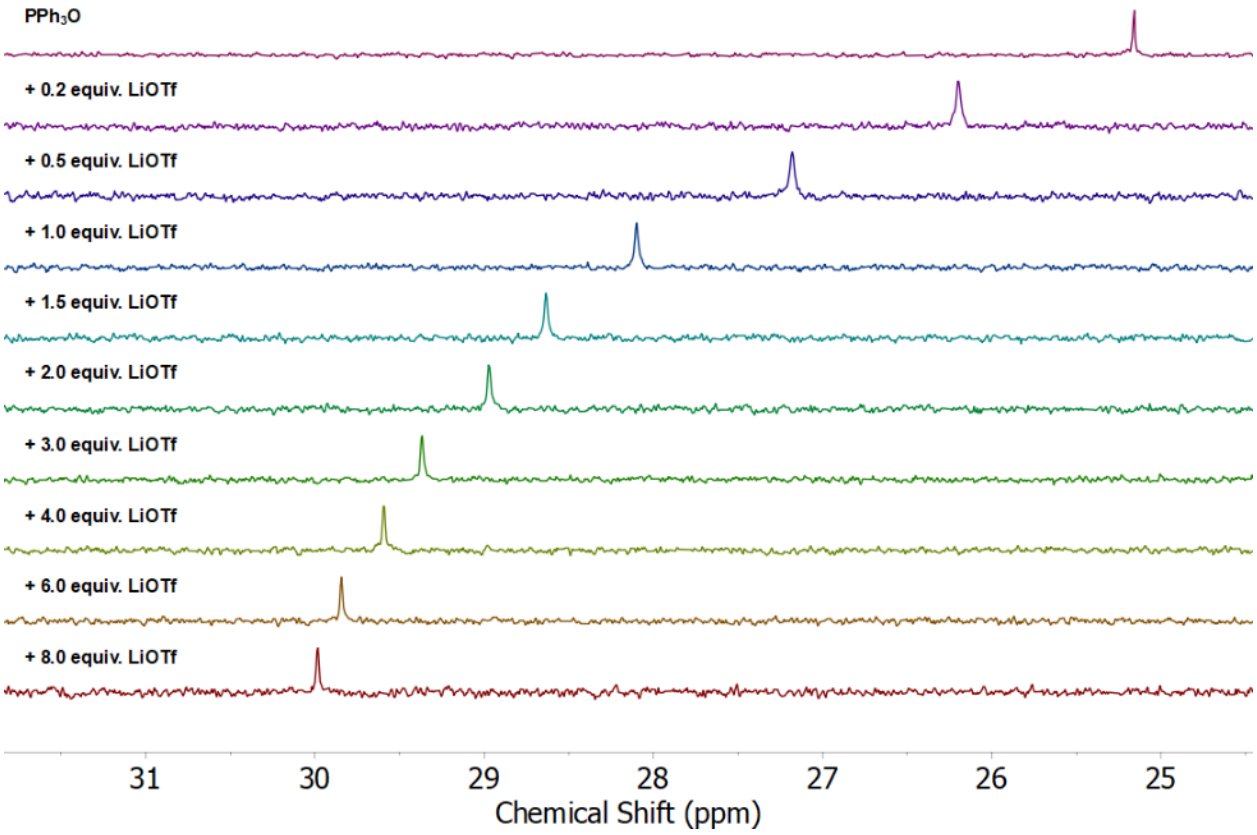

Figure D13. Stacked $^{31}P\{^{1}H\}$ NMR spectra (162 MHz, d_3-MeCN) for the titration of TPPO with LiOTf.

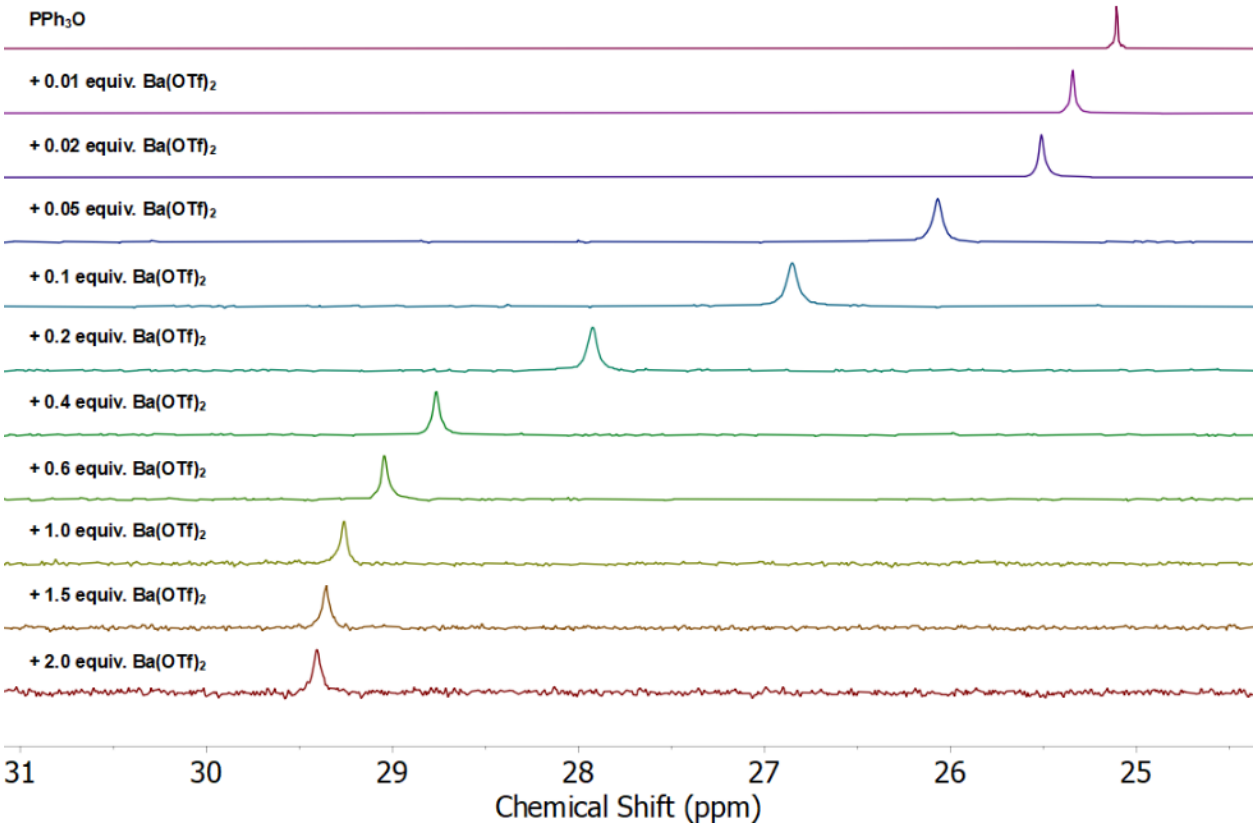

Figure D14. Stacked $^{31}P\{^{1}H\}$ NMR spectra (162 MHz, d_3-MeCN) for the titration of TPPO with $Ba(OTf)_2$.

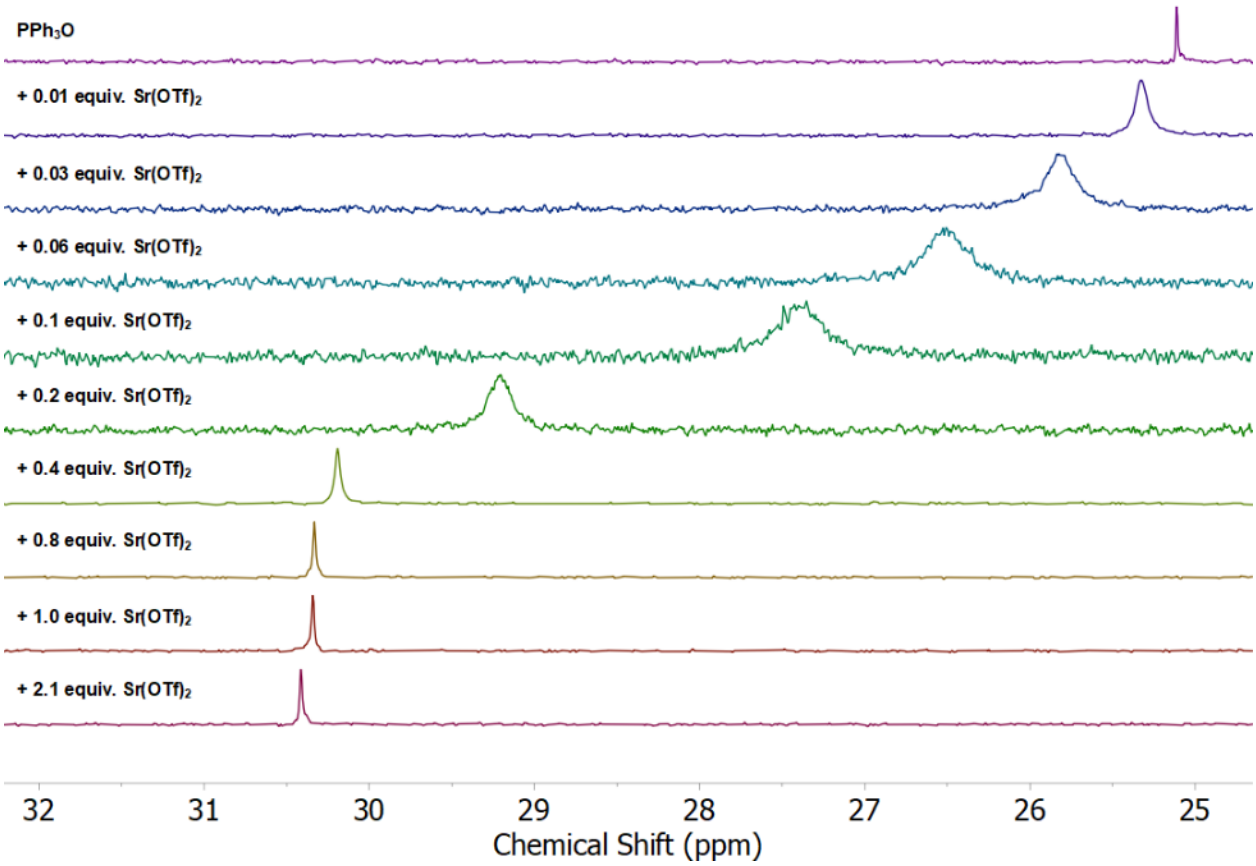

Figure D15. Stacked $^{31}P\{^{1}H\}$ NMR spectra (162 MHz, d_3-MeCN) for the titration of TPPO with $Sr(OTf)_2$.

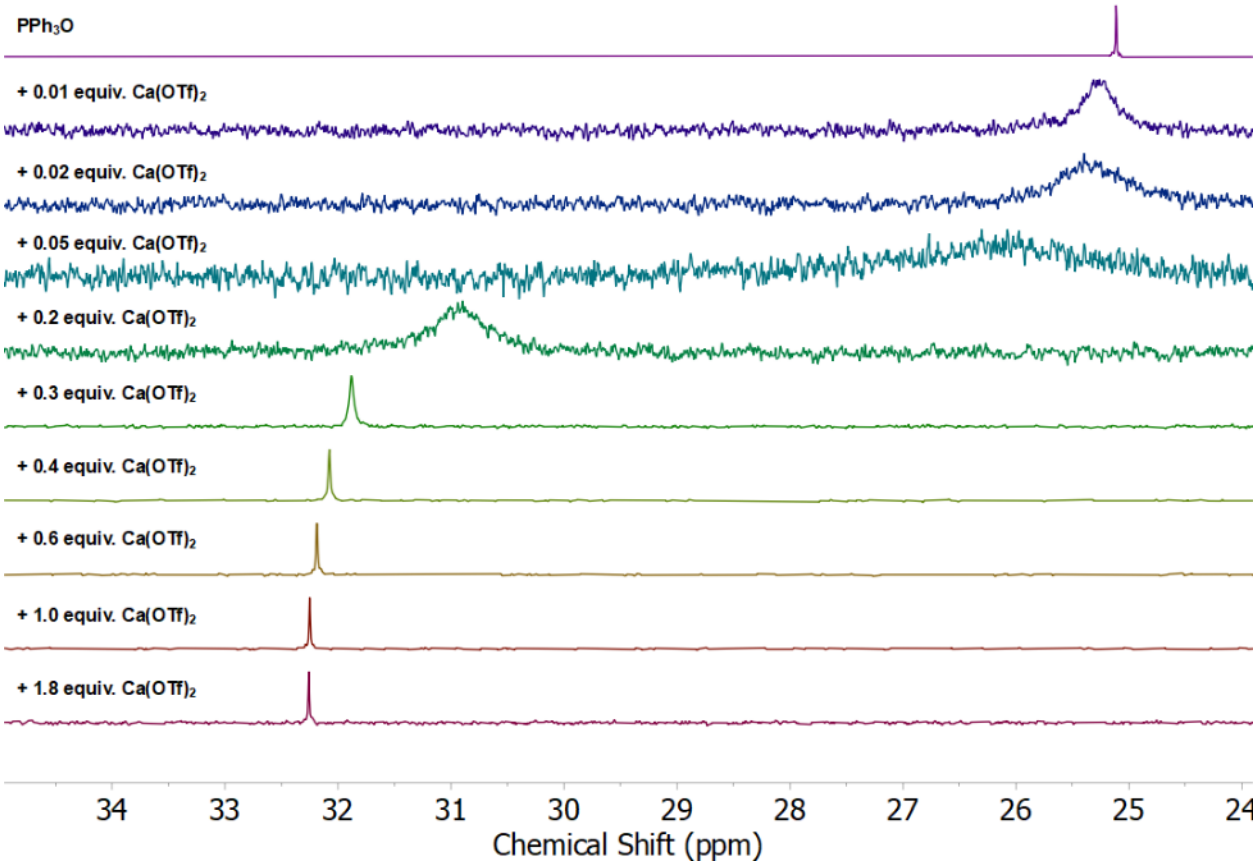

Figure D16. Stacked $^{31}P\{^{1}H\}$ NMR spectra (162 MHz, d_3-MeCN) for the titration of TPPO with $Ca(OTf)_2$.

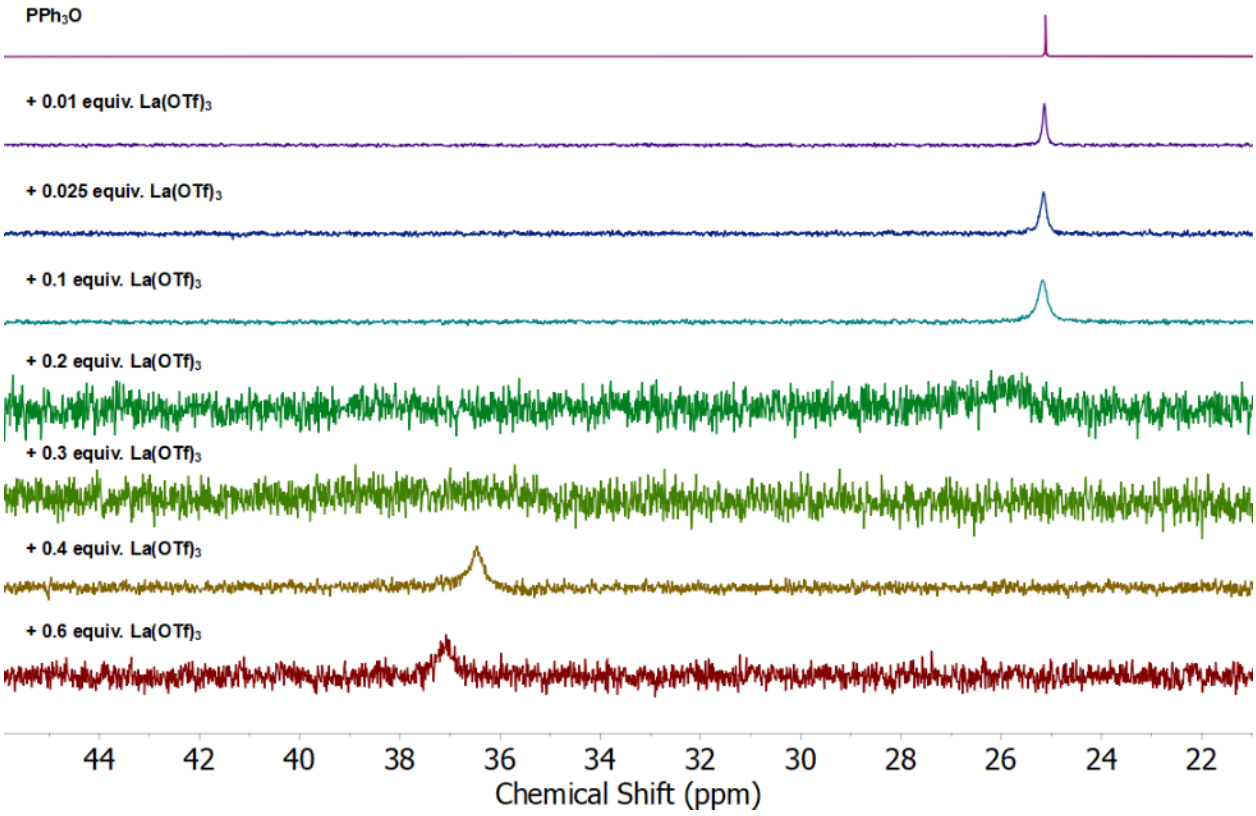

Figure D17. Stacked $^{31}P\{^{1}H\}$ NMR spectra (162 MHz, d_3-MeCN) for the titration of TPPO with $La(OTf)_3$.

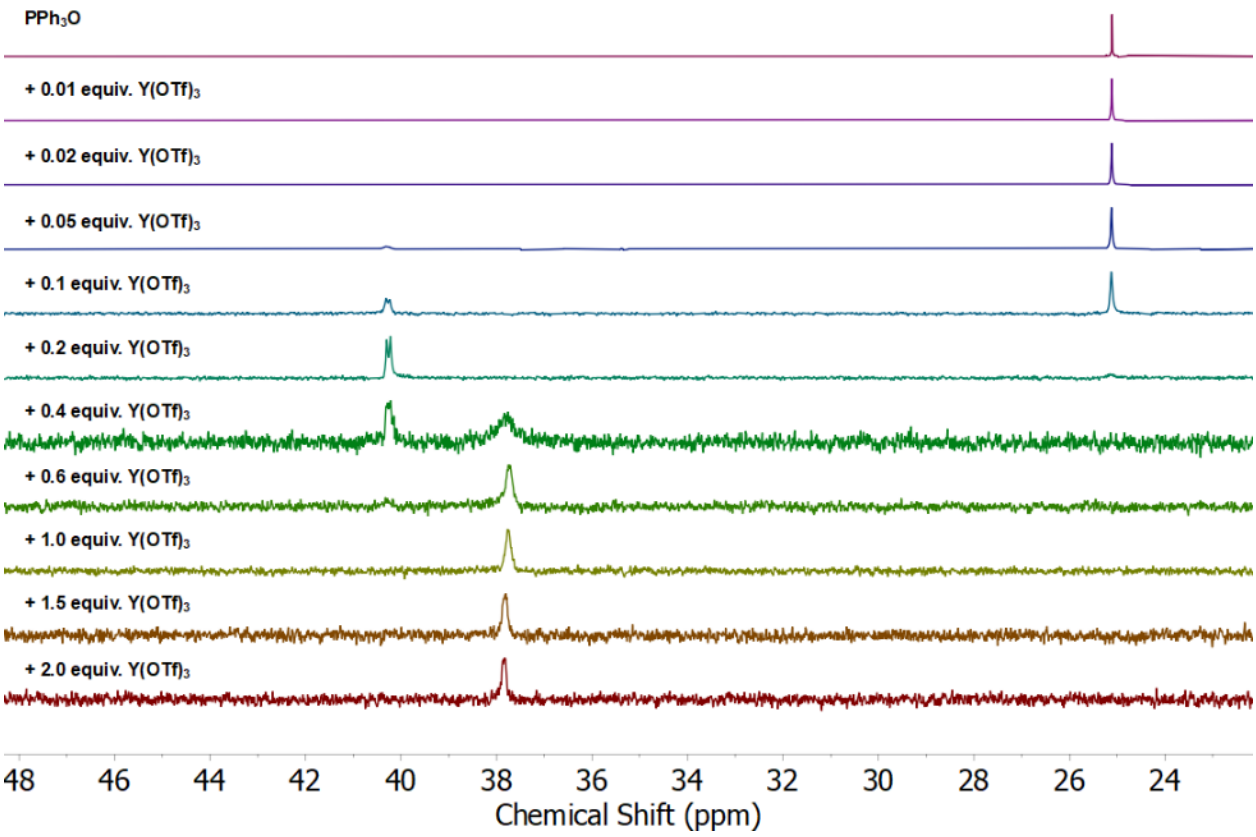

Figure D18. Stacked $^{31}P\{^{1}H\}$ NMR spectra (162 MHz, d_3-MeCN) for the titration of TPPO with $Y(OTf)_3$.

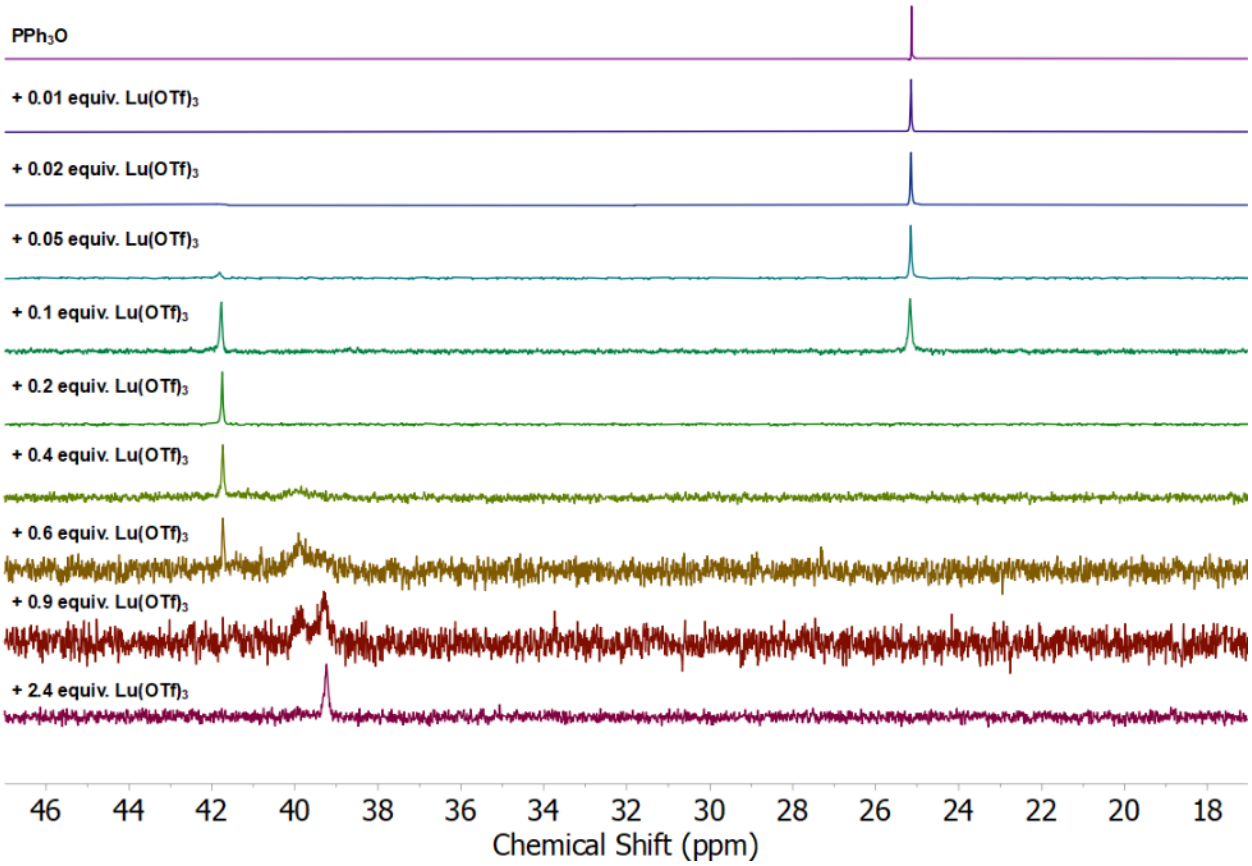

Figure D19. Stacked $^{31}P\{^{1}H\}$ NMR spectra (162 MHz, d_3-MeCN) for the titration of TPPO with $Lu(OTf)_3$.

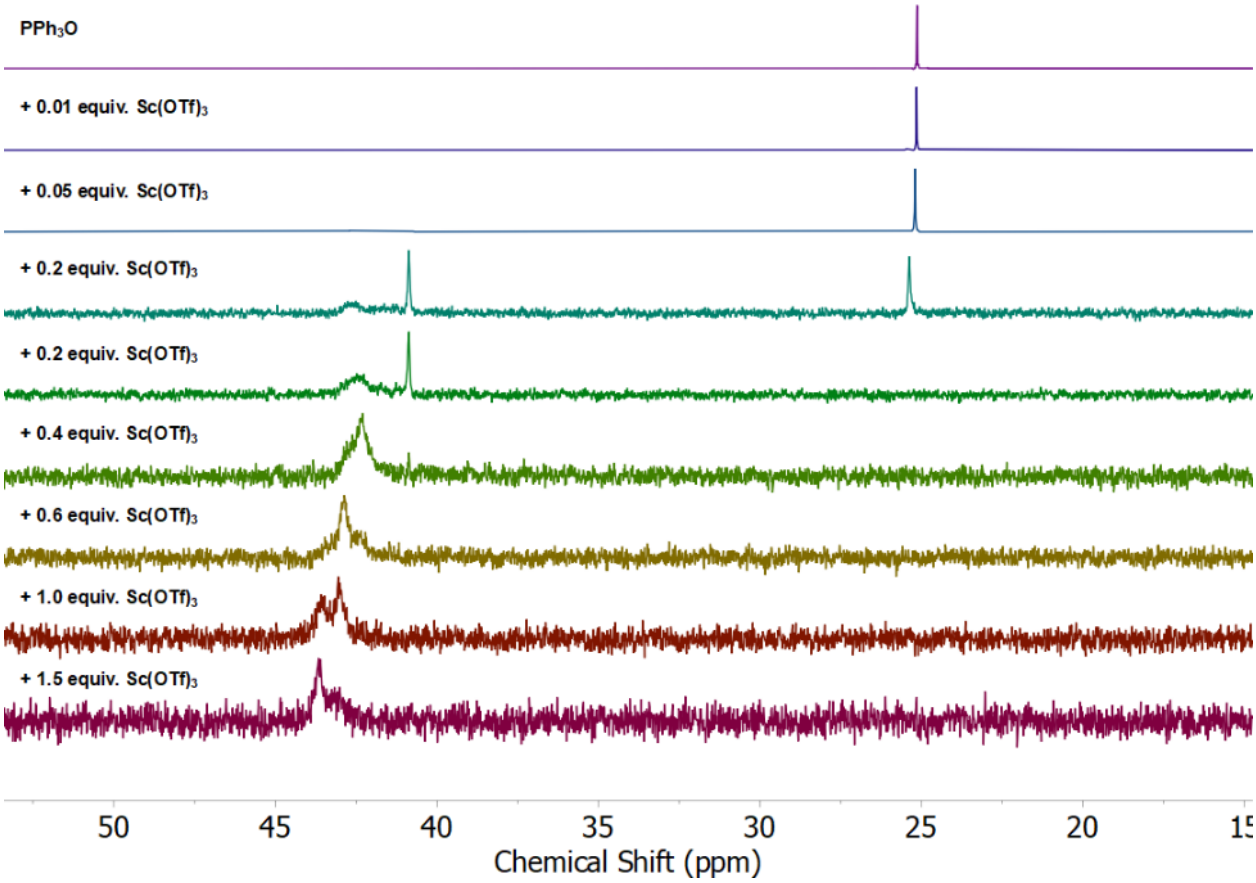

Figure D20. Stacked $^{31}P\{^{1}H\}$ NMR spectra (162 MHz, d_3-MeCN) for the titration of TPPO with $Sc(OTf)_3$.

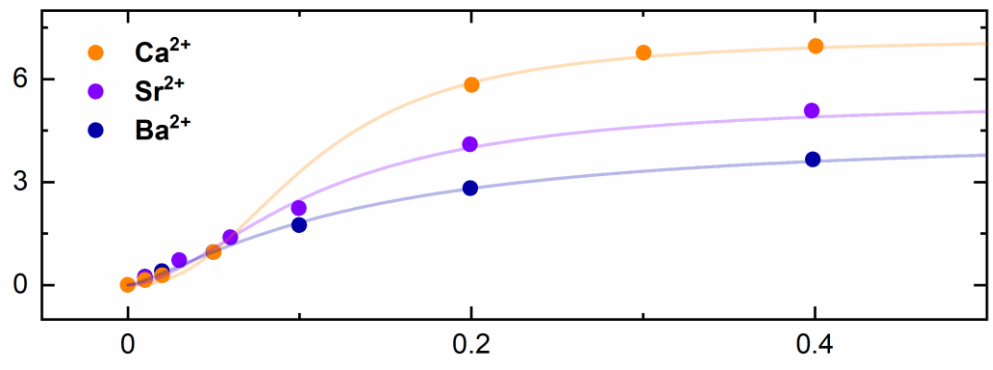

Figure D21. Titration data for divalent ions showing fit to the Hill-Langmuir equation given in the main text. The curvature between 0 to 0.1 equiv. suggests positive cooperativity.

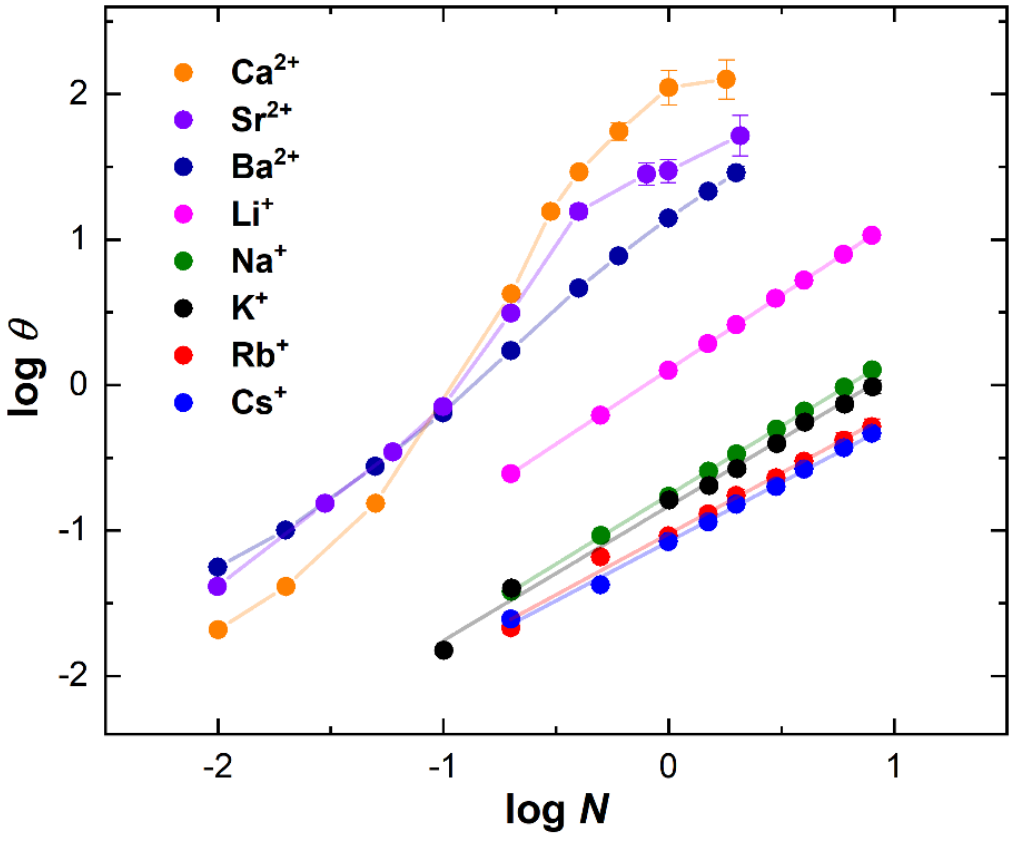

Figure D22. Hill plots for selected metal ions showing fit to the linearized form of Hill-Langmuir equation given in the main text. Here, θ [= $\Delta\delta/(\Delta\delta'_{max} - \Delta\delta)$] represents the normalization of $^{31}P\{^{1}H\}$ NMR shifts for respective ions from its maximum possible shift.

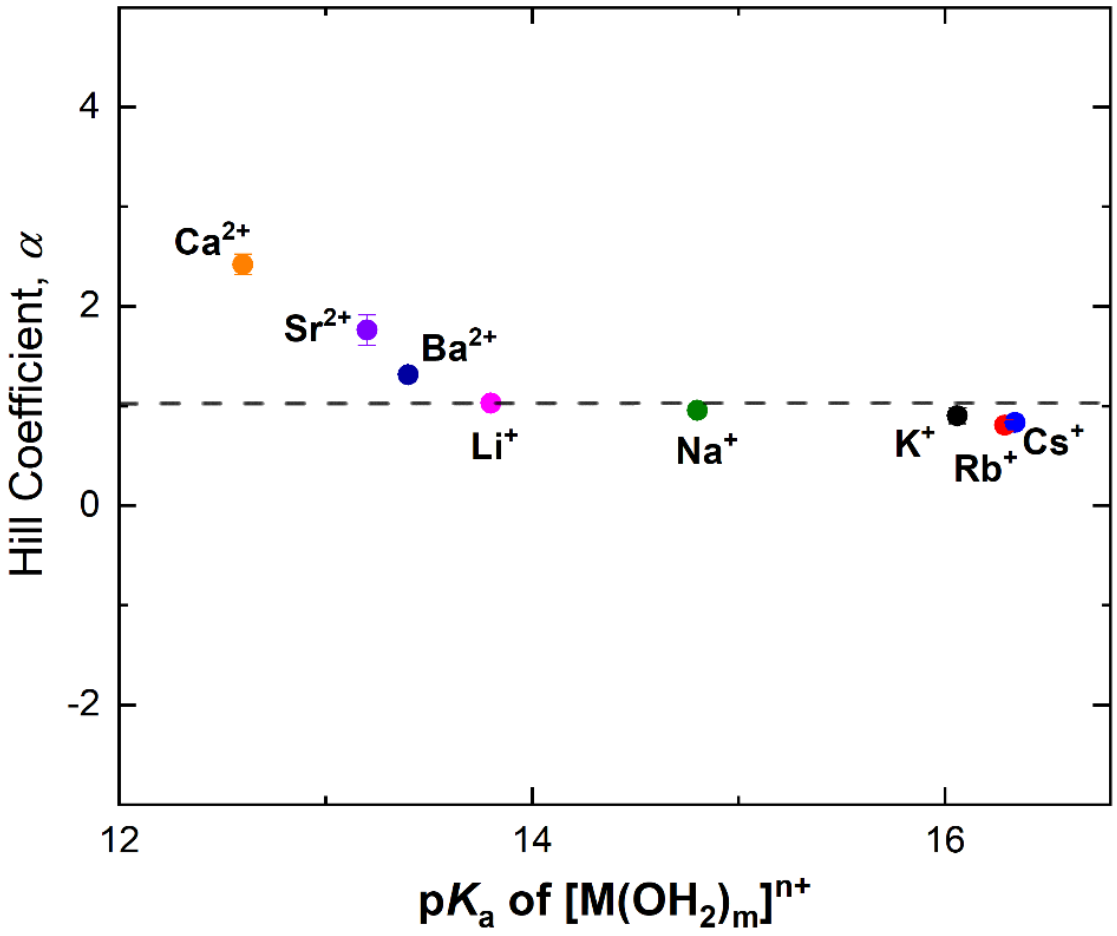

Figure D23. Plot of Hill Coefficient (α) measured in d_3-MeCN vs. pK_a of metal-aqua complexes. The graph suggests no cooperativity (α ≈ 1) in monovalent ions and positive cooperativity (α > 1) in divalent ions, when these ions interact with TPPO in d_3-MeCN.

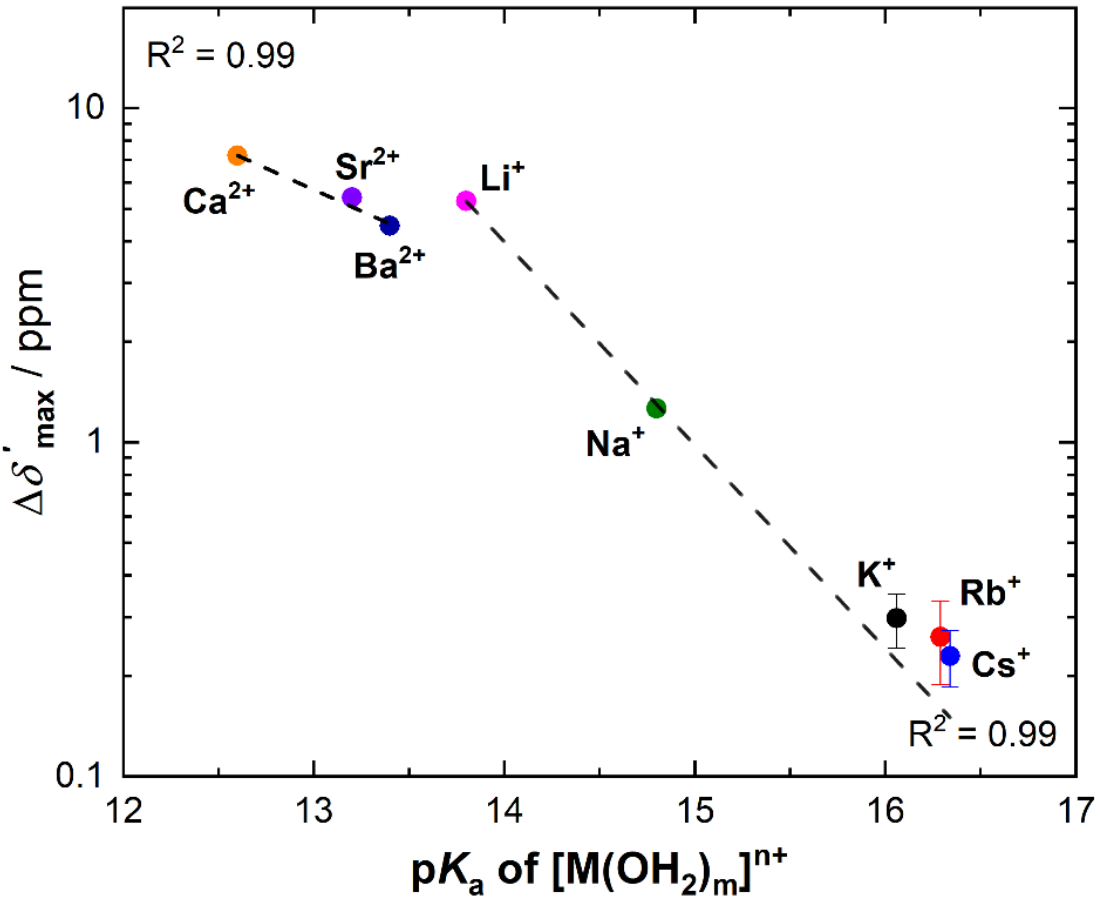

Figure D24. Plot of $\Delta\delta'_{max}$ ^{31}P measured in d_3-MeCN vs. pK_a of metal-aqua complexes.

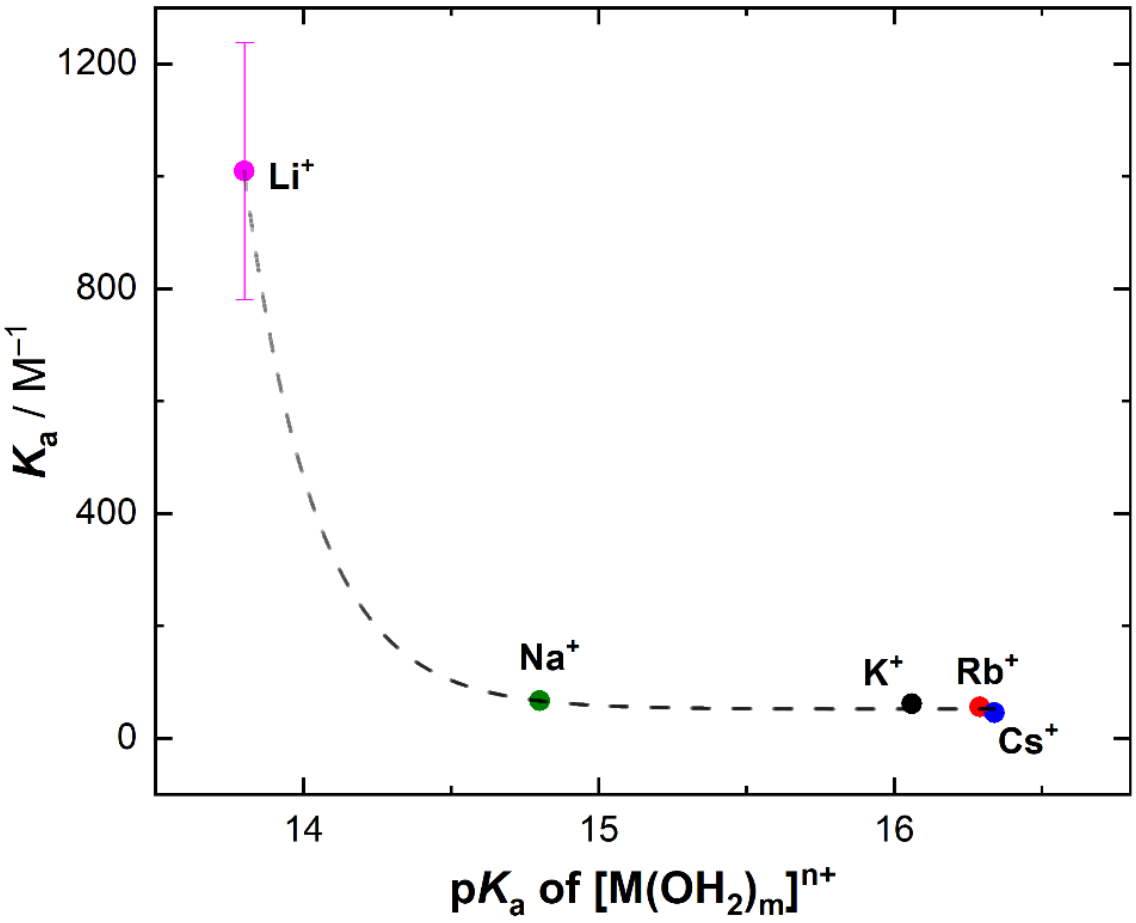

Figure D25. Plot of K_a for monovalent ions measured in d_3-MeCN vs. pK_a of metal-aqua complexes.

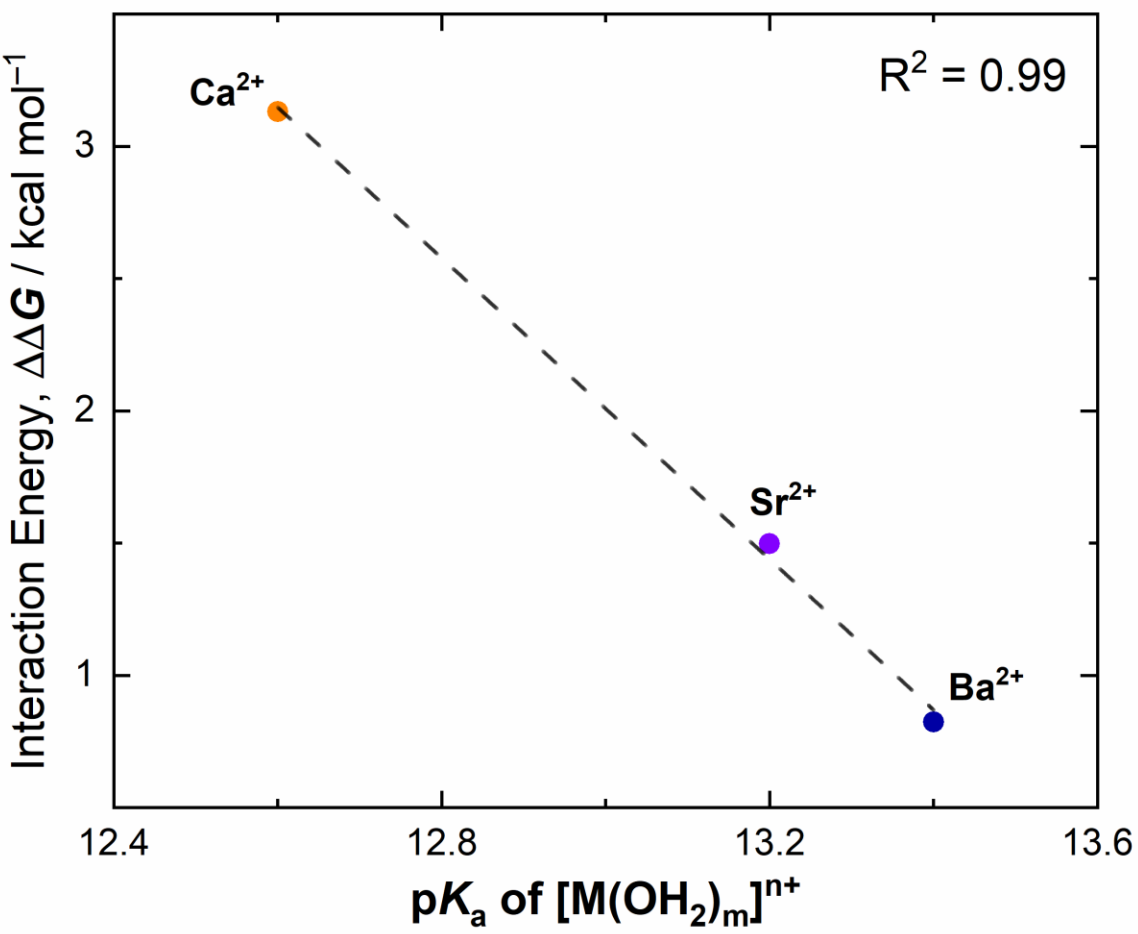

Figure D26. Plot of interaction energy for TPPO binding in d_3-MeCN to divalent metal ions versus the corresponding aqueous metal-aqua pK_a values.

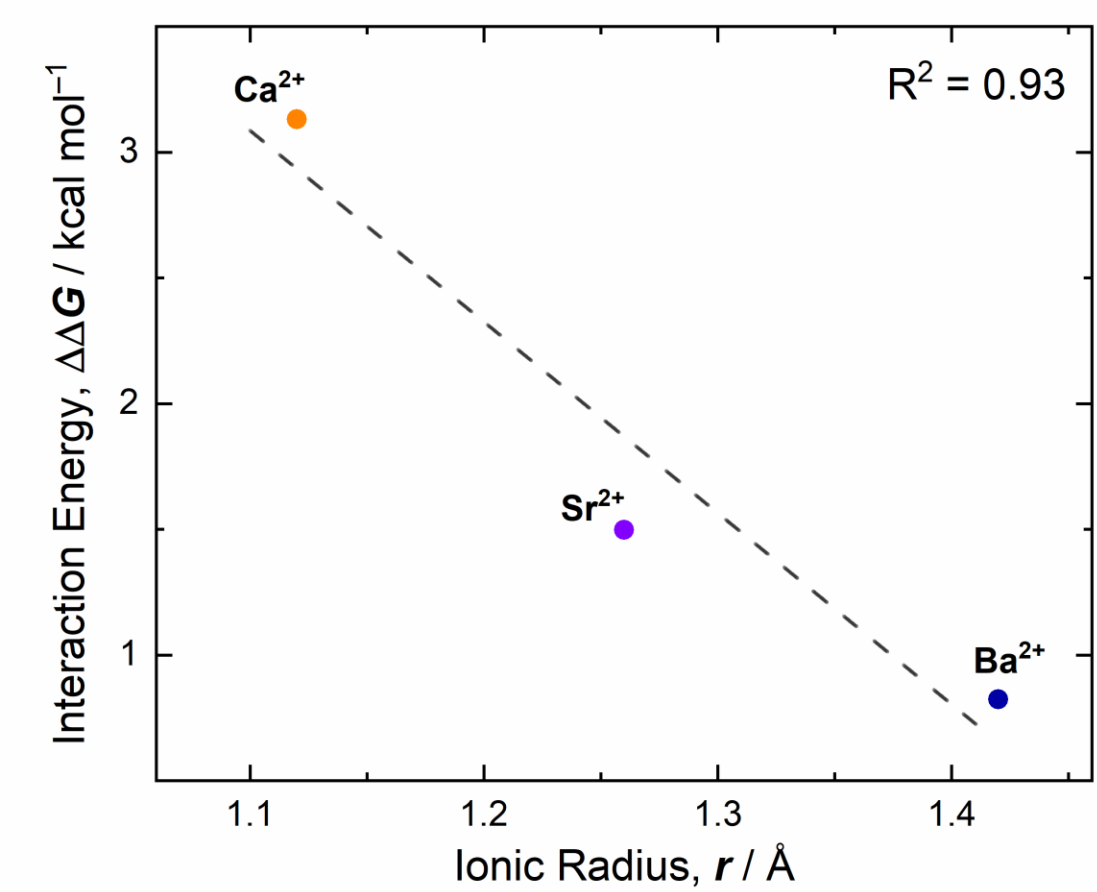

Figure D27. Plot of interaction energy for TPPO binding in d_3-MeCN to divalent metal ions versus the corresponding ionic radii for a coordination number of 8.

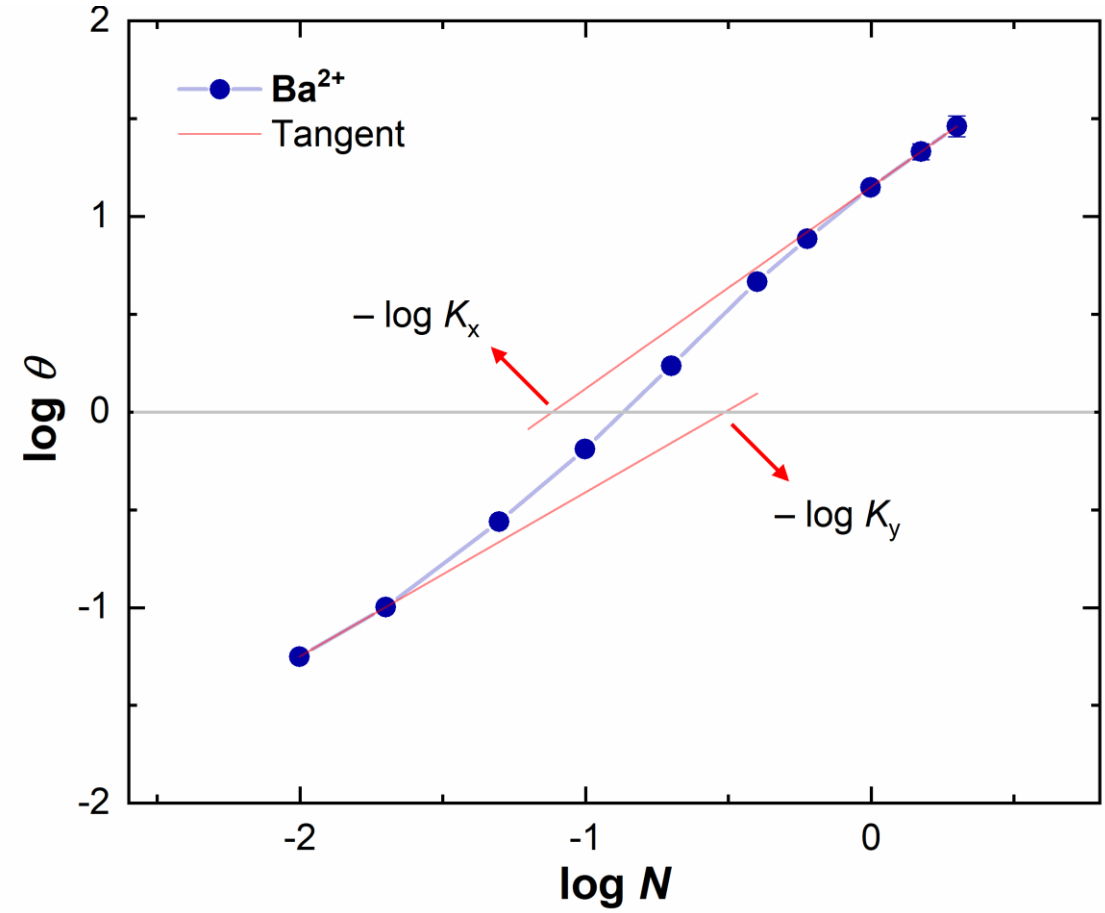

Figure D28. Extrapolation of tangents from the extremes of the data with Ba^{2+} ion for estimation of interaction energy (ΔΔG).

Table D5. Tabulation of K_x, K_y, and ΔΔG values for divalent ions

M^{n+}	pK_a of $[M(OH_2)_m]^{n+}$	r / Å for C.N. = 8	– log K_x	K_x	– log K_y	K_y	ΔΔG = RT ln (K_x/K_y) / kcal mol^{-1}
Ca^{2+}	12.6	1.12	–2.58	383.6	–0.287	1.94	3.13
Sr^{2+}	13.2	1.26	–1.94	88.0	–0.845	7.01	1.50
Ba^{2+}	13.4	1.42	–1.12	13.1	–0.512	3.25	0.82

Table D6. Replicate measurements for estimation of error on the amount of Lewis acid (NaOTf taken as this example case) added to standard solutions for titration experiments.

Time Point	Amount Displayed on the Weighing Balance
12:00 pm	5.5 mg
12:10 pm	5.5 mg
12:13 pm	5.5 mg
12:41 pm	5.5 mg
1:30 pm	5.6 mg
2:45 pm	5.4 mg
3:00 pm	5.6 mg

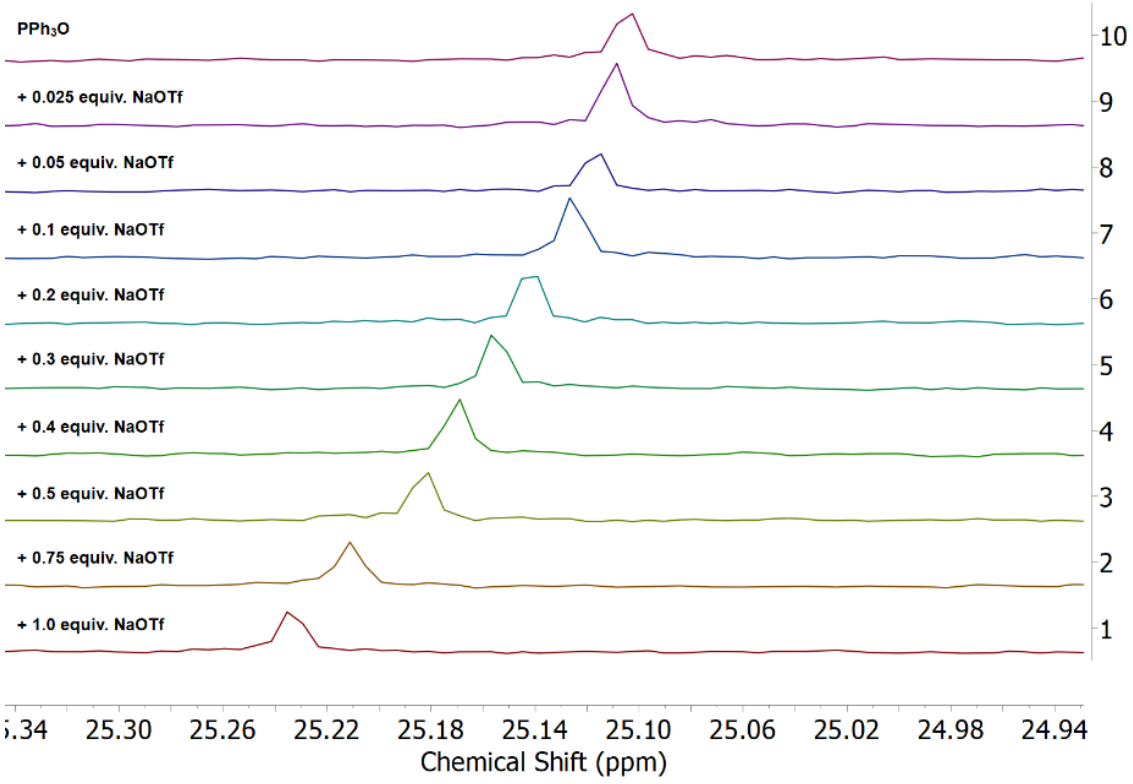

Figure D29. Stacked $^{31}P\{^{1}H\}$ NMR spectra (162 MHz, d_3-MeCN) for the titration of TPPO with NaOTf at relatively low concentrations of NaOTf.

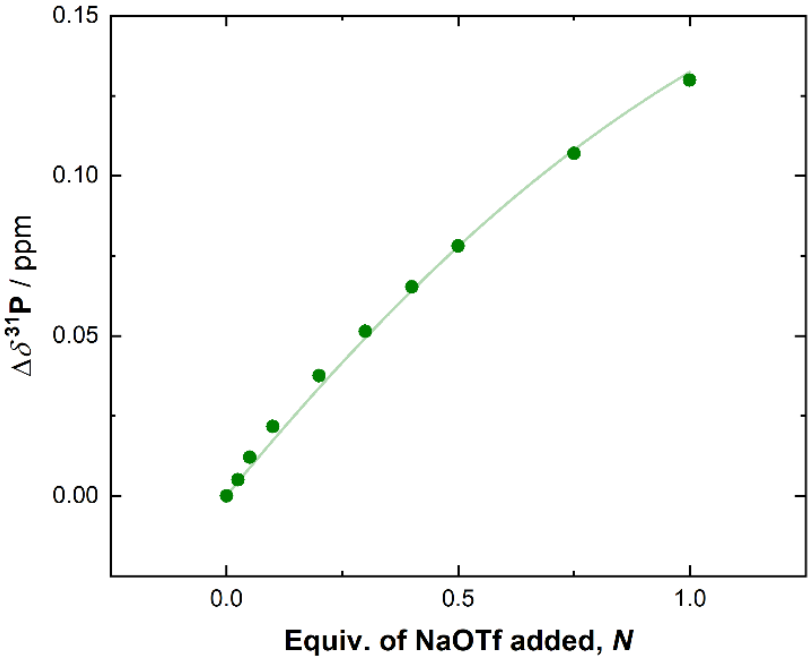

Figure D30. Titration studies showing 1:1 binding of NaOTf and TPPO at relatively low concentrations of NaOTf to focus on substoichiometric quantities. Solvent: d_3-MeCN.

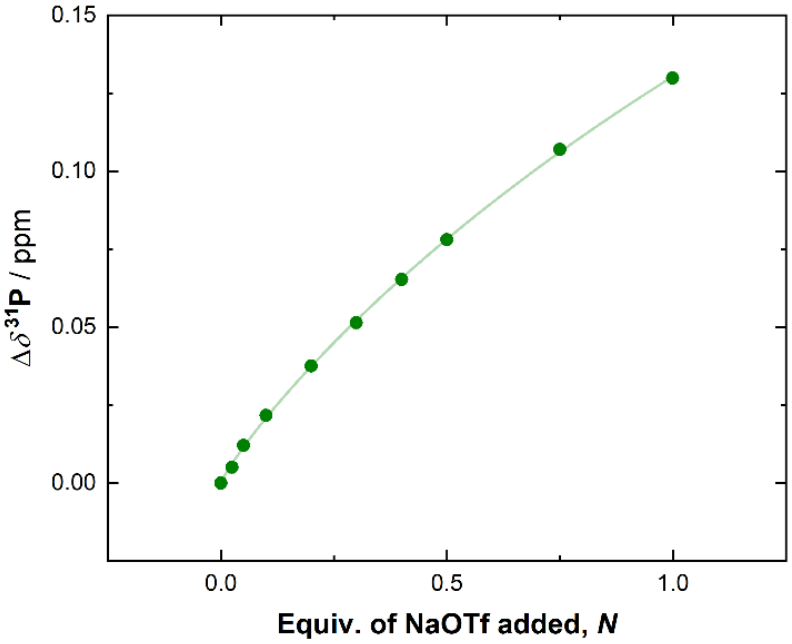

Figure D31. Titration data showing fit to the Hill-Langmuir equation ($\alpha = 0.88 \pm 0.03$; $K_{1/2} = 4.44 \pm 1.60$ equiv. ; $\Delta\delta'_{max}{}^{31}P = 0.62 \pm 0.14$ ppm).

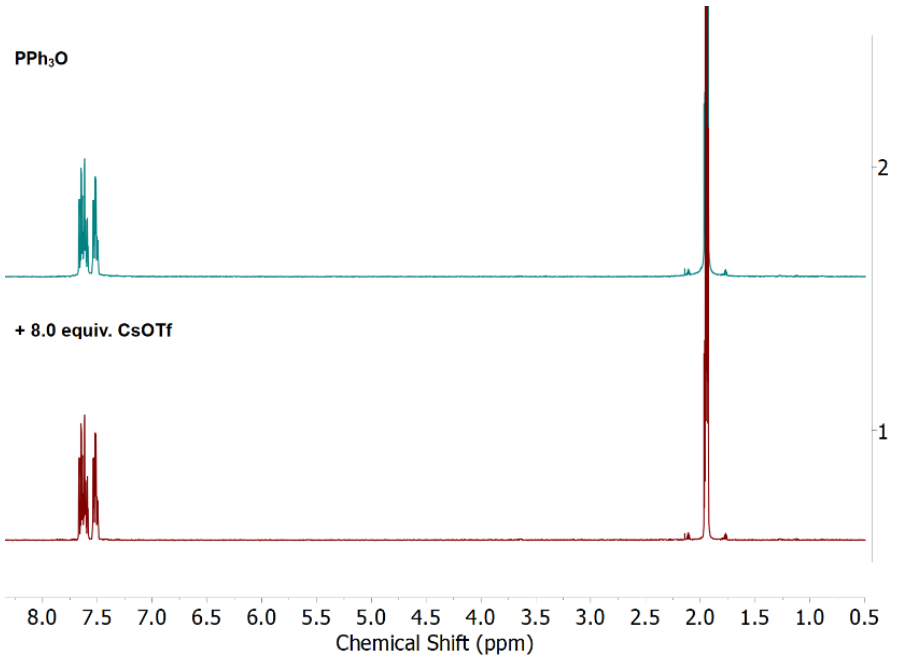

Figure D32. Stacked ^{1}H NMR spectra (400 MHz, d_3-MeCN) for TPPO with added CsOTf.

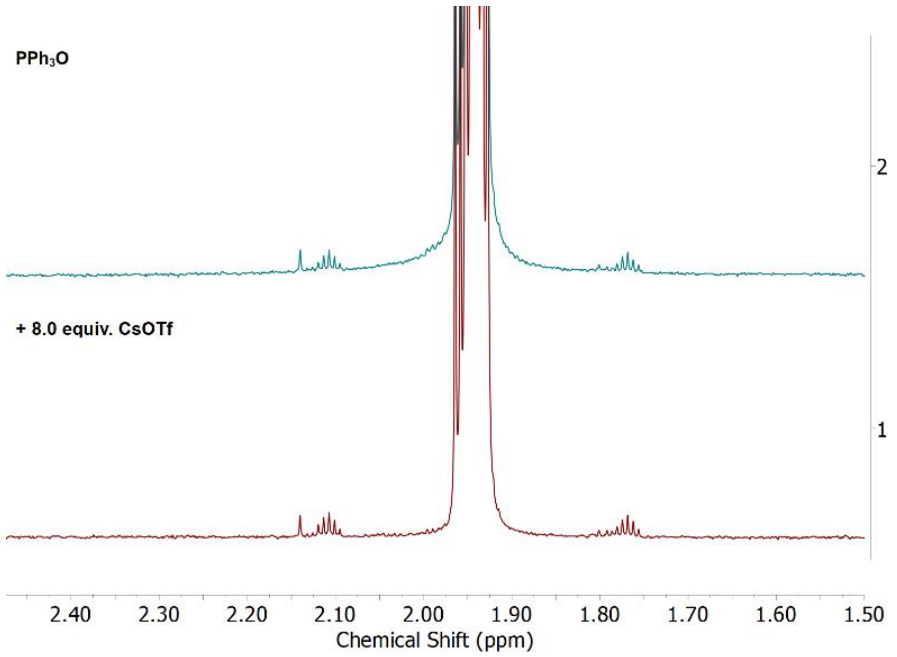

Figure D32. Stacked ^{1}H NMR spectra (400 MHz, d_3-MeCN) from the treatment of TPPO (3.6 mM) with CsOTf showing that the small amount of water present (108 μM; 0.03 eq. per TPPO) does not arise from added CsOTf.

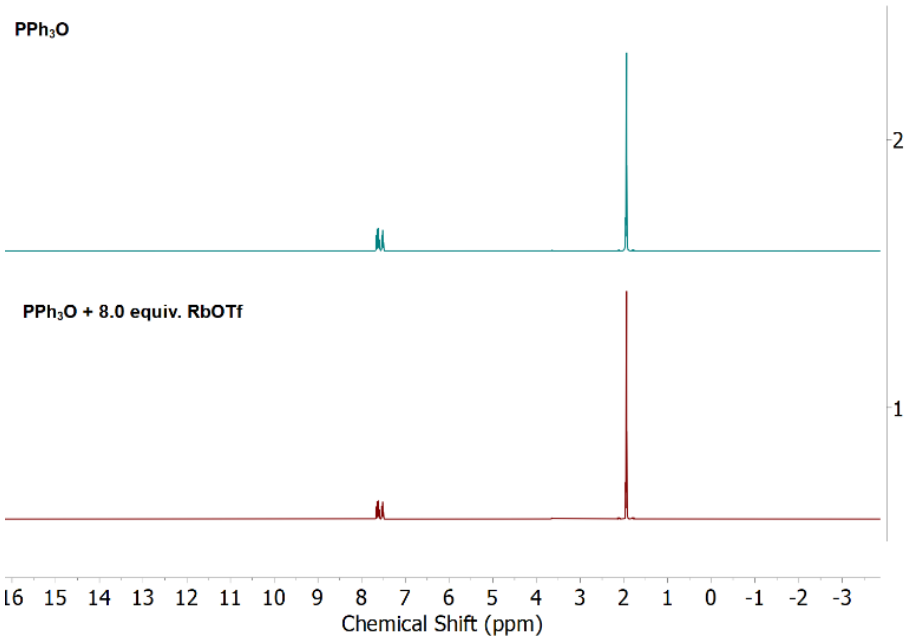

Figure D33. Stacked ^{1}H NMR spectra (400 MHz, d_3-MeCN) for treatment of TPPO with RbOTf.

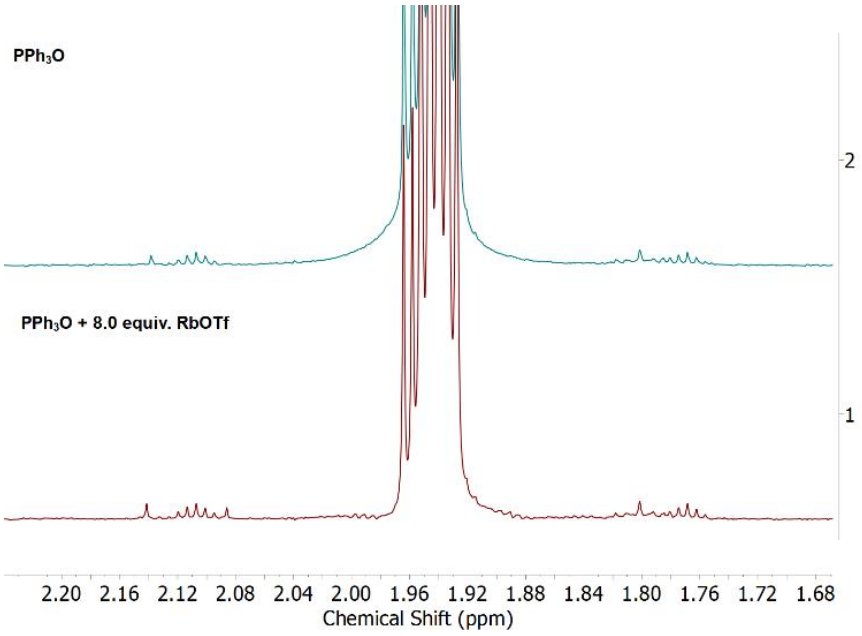

Figure D34. Stacked ^{1}H NMR spectra (400 MHz, d_3-MeCN) from the treatment of TPPO with RbOTf showing essentially no above-background signal for H_2O in the system.

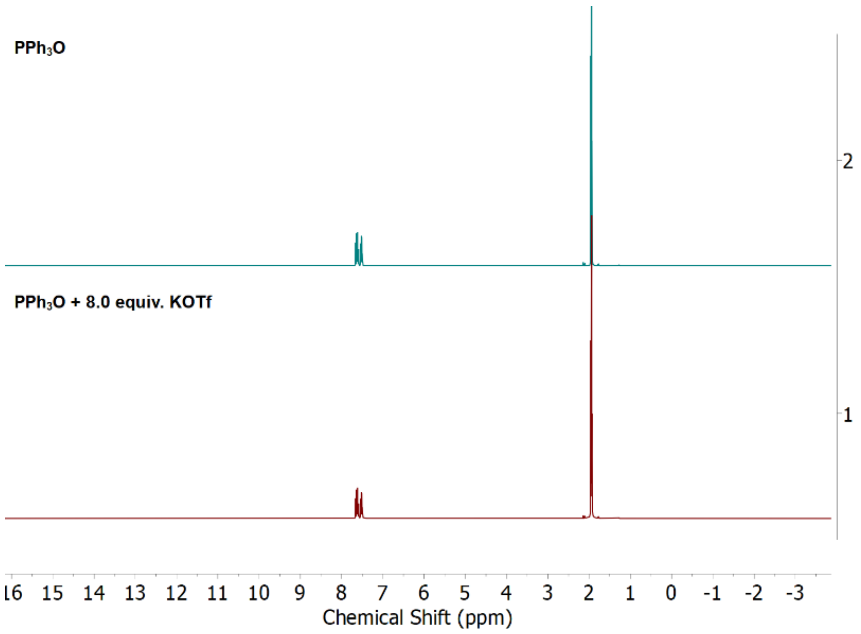

Figure D36. Stacked ^{1}H NMR spectra (400 MHz, d_3-MeCN) for the treatment of TPPO with KOTf.

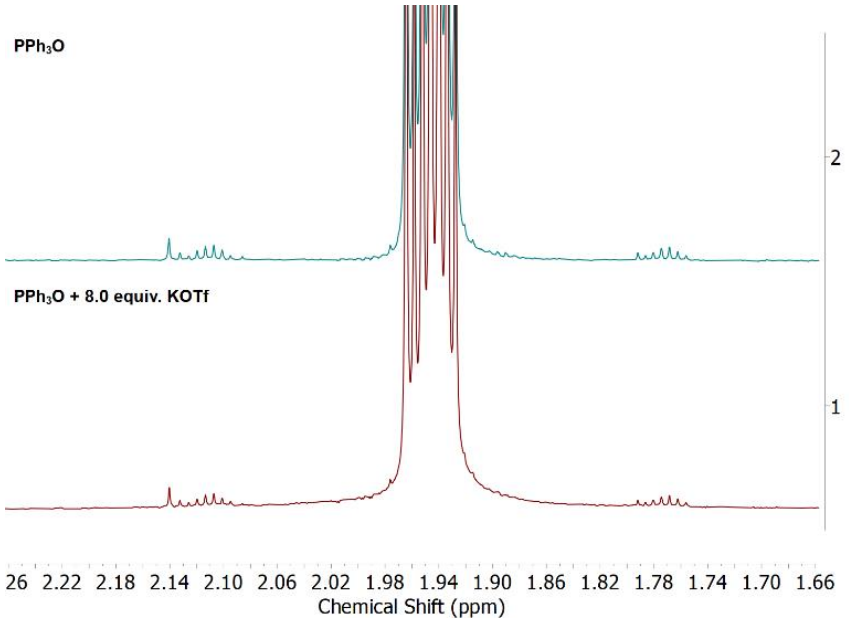

Figure D37. Stacked ^{1}H NMR spectra (400 MHz, d_3-MeCN) from the treatment of TPPO with KOTf showing a small amount of water present (144 μM) that does not arise from the KOTf added.

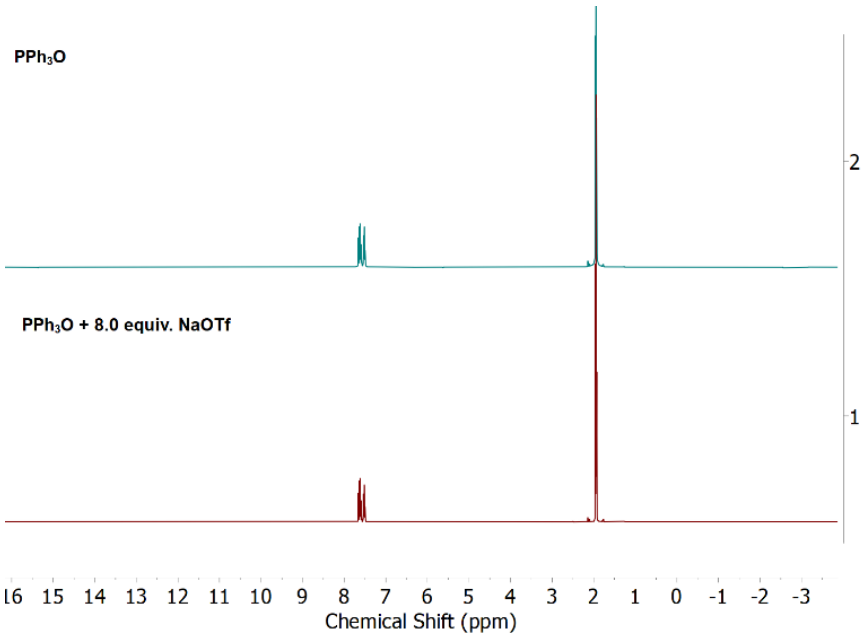

Figure D38. Stacked ^{1}H NMR spectra (400 MHz, d_3-MeCN) for the treatment of TPPO with NaOTf.

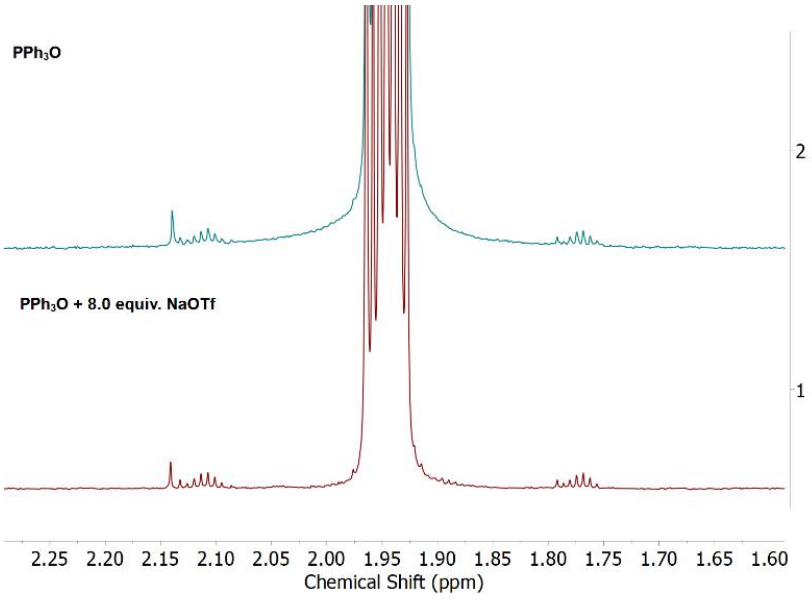

Figure D39. Stacked ^{1}H NMR spectra (400 MHz, d_3-MeCN) from the treatment of TPPO with NaOTf showing that the small amount of water (126 μM) present is not associated with the NaOTf added.

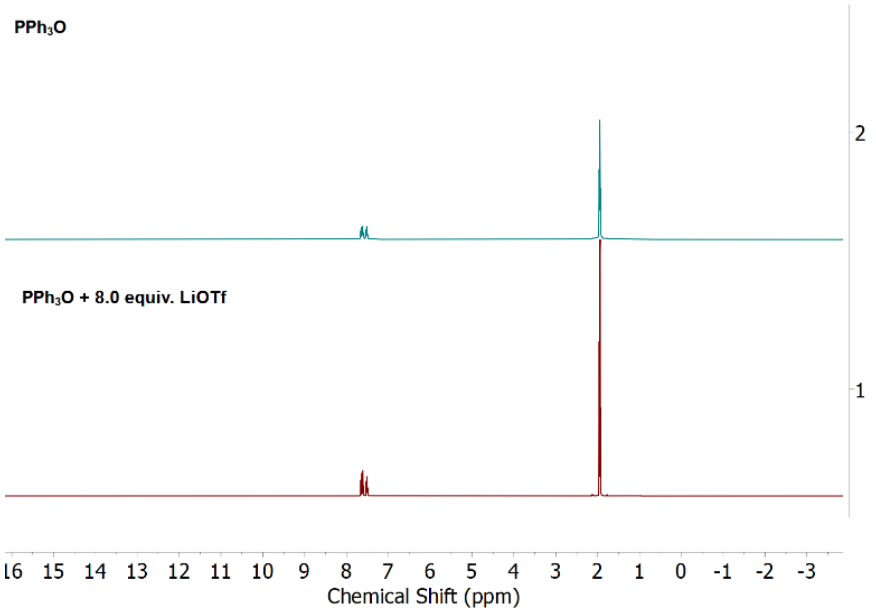

Figure D40. Stacked ^{1}H NMR spectra (400 MHz, d_3-MeCN) for the treatment of TPPO with LiOTf.

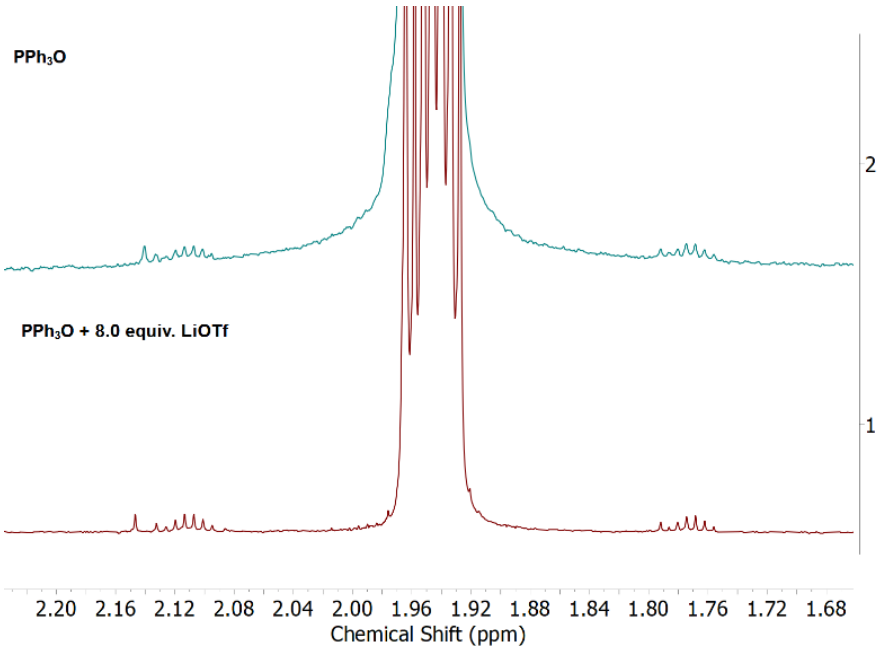

Figure D41. Stacked ^{1}H NMR spectra (400 MHz, d_3-MeCN) for the treatment of TPPO with LiOTf showing essentially no above-background signal for H_2O in the system.

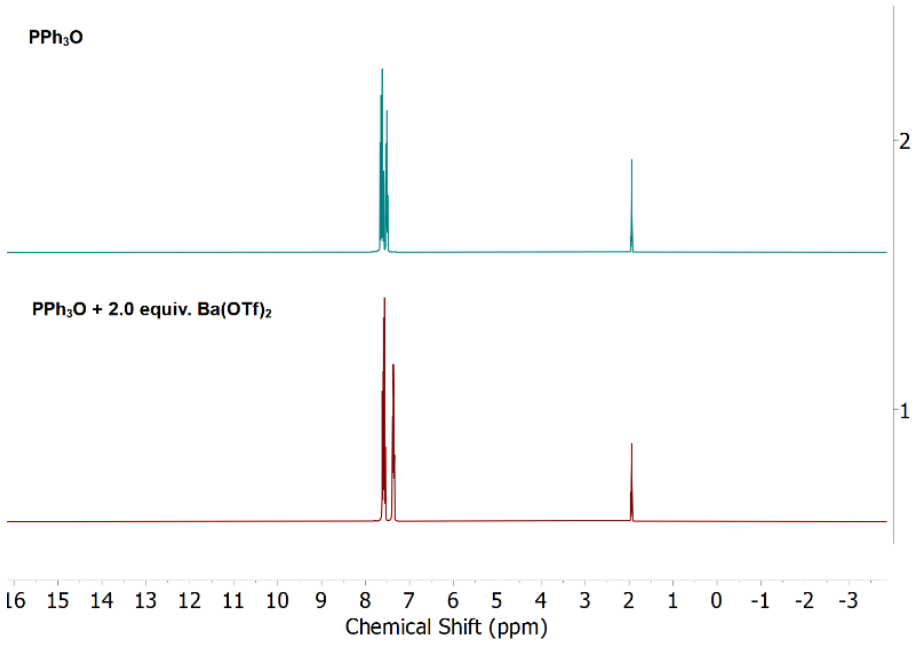

Figure D42. Stacked ^{1}H NMR spectra (400 MHz, d_3-MeCN) for the treatment of TPPO with $Ba(OTf)_2$.

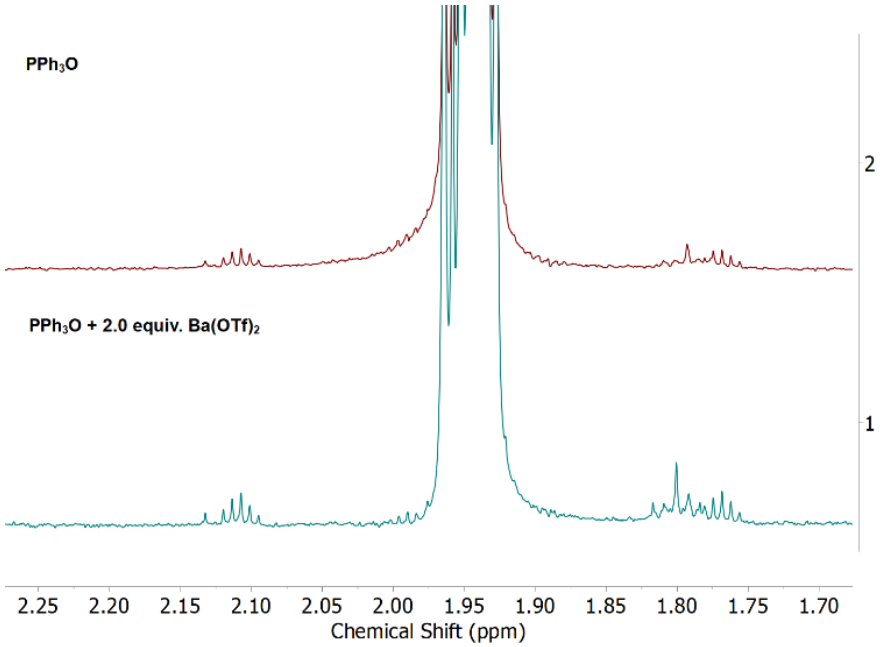

Figure D43. Stacked ^{1}H NMR spectra (400 MHz, d_3-MeCN) for the treatment of TPPO with $Ba(OTf)_2$ showing essentially no above-background signal for H_2O in the system.

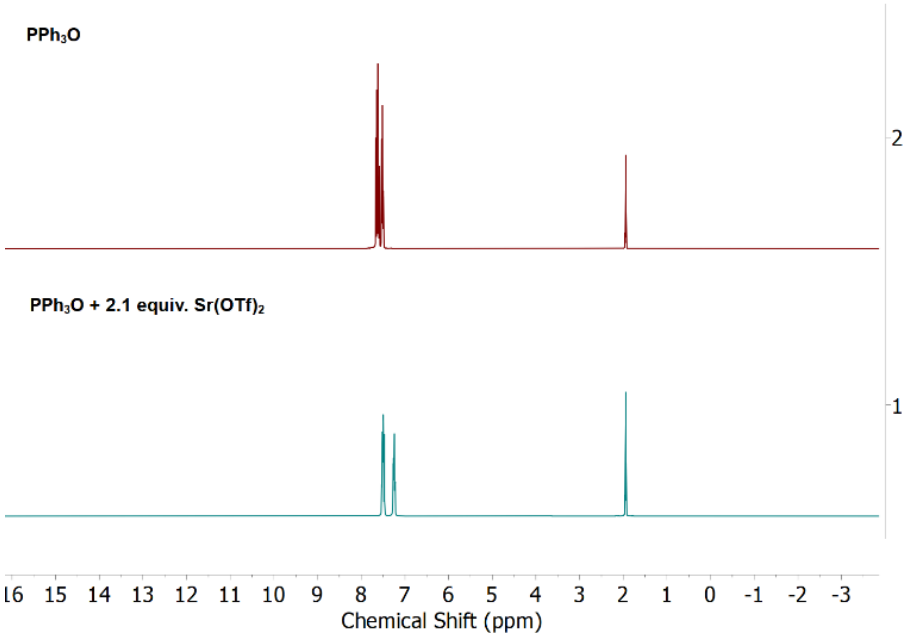

Figure D44. Stacked ^{1}H NMR spectra (400 MHz, d_3-MeCN) for the treatment of TPPO with $Sr(OTf)_2$.

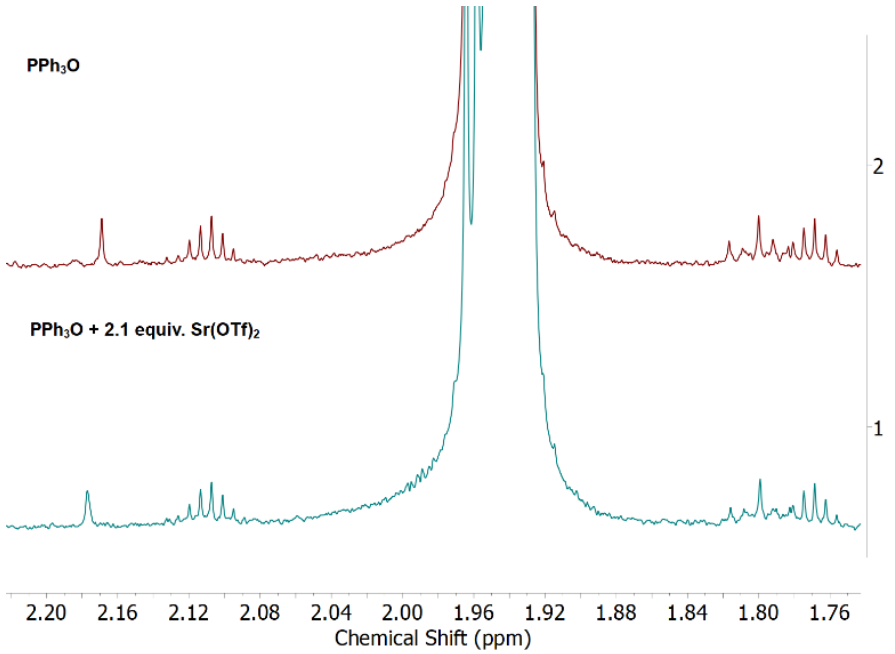

Figure D45. Stacked ^{1}H NMR spectra (400 MHz, d_3-MeCN) for the treatment of TPPO with $Sr(OTf)_2$ showing that a small amount of water is not associated with $Sr(OTf)_2$ added.

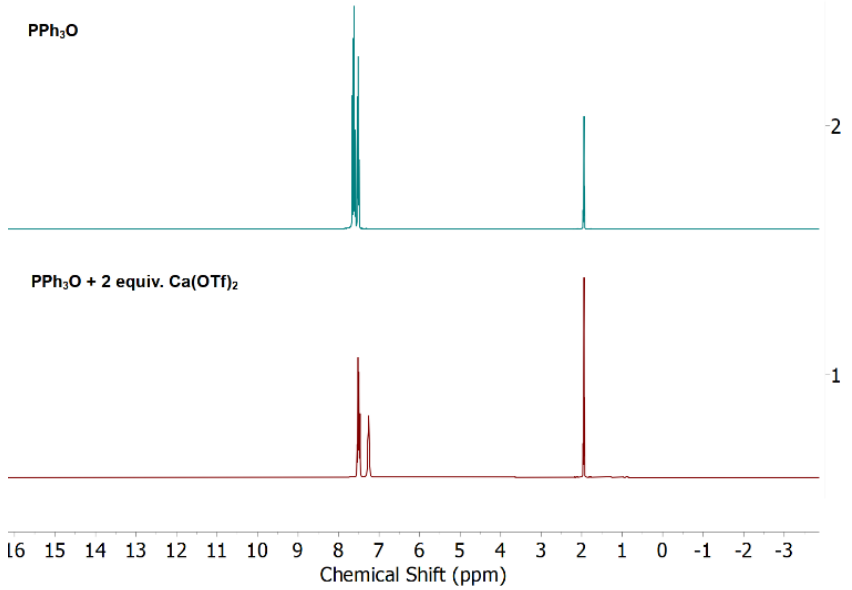

Figure D46. Stacked ^{1}H NMR spectra (400 MHz, d_3-MeCN) for the treatment of TPPO with $Ca(OTf)_2$.

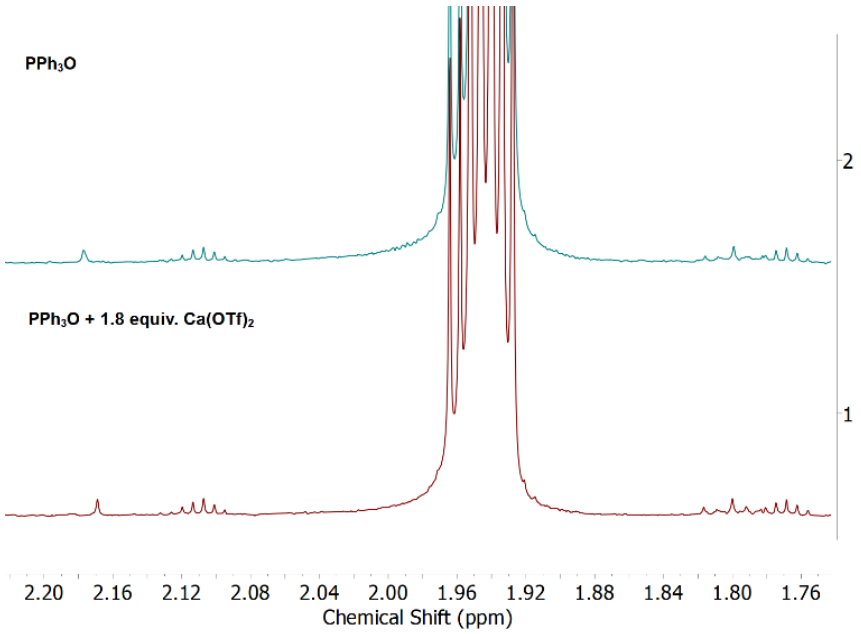

Figure D47. Stacked ^{1}H NMR spectra (400 MHz, d_3-MeCN) for the treatment of TPPO with $Ca(OTf)_2$ showing that a small amount of water present is not associated with the $Ca(OTf)_2$ added.

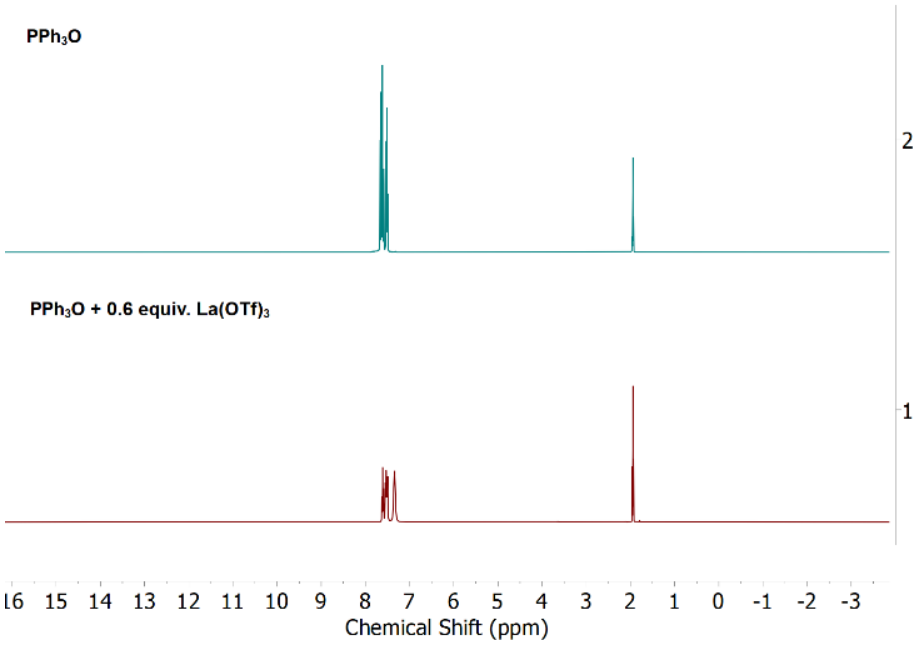

Figure D48. Stacked ^{1}H NMR spectra (400 MHz, d_3-MeCN) for the treatment of TPPO with La(OTf)$_3$.

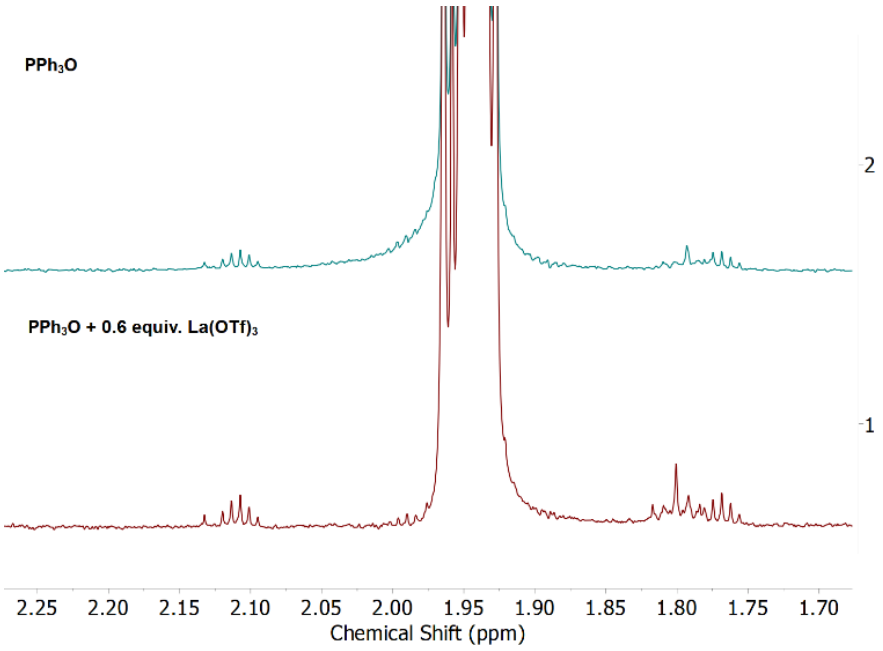

Figure D49. Stacked ^{1}H NMR spectra (400 MHz, d_3-MeCN) for the treatment of TPPO with La(OTf)$_3$ showing the virtual absence of water in the system.

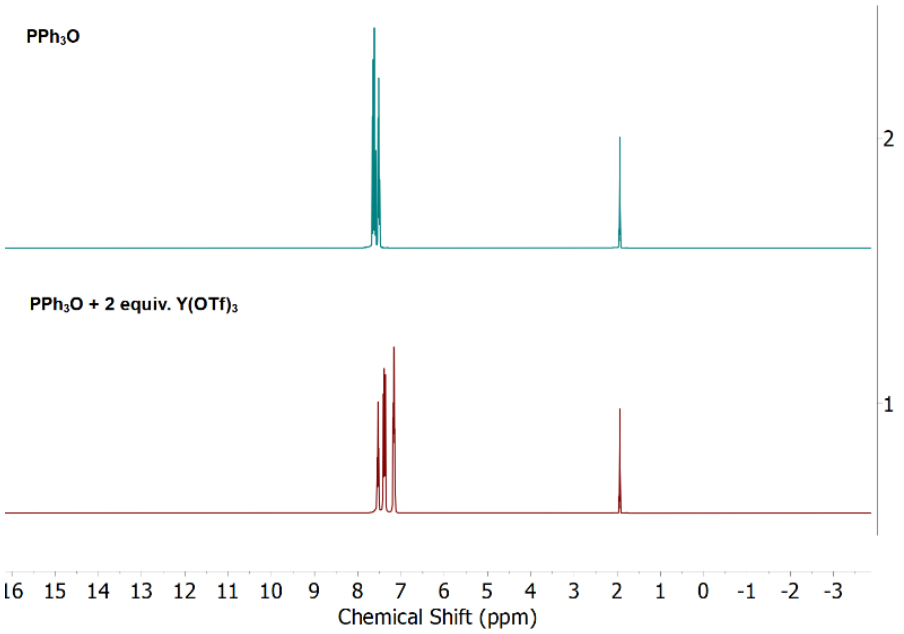

Figure D50. Stacked ^{1}H NMR spectra (400 MHz, d_3-MeCN) for the treatment of TPPO with $Y(OTf)_3$.

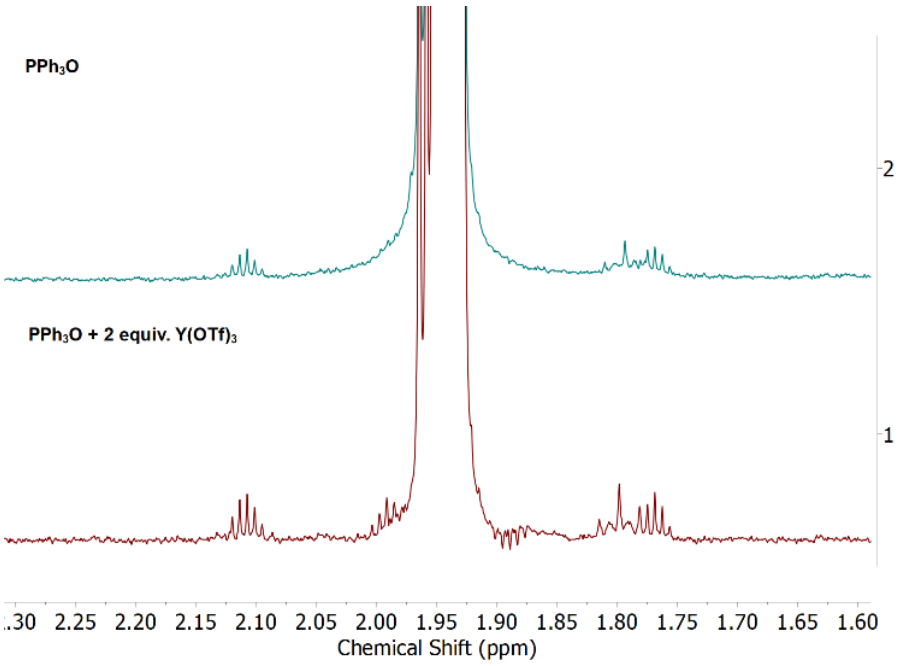

Figure D51. Stacked ^{1}H NMR spectra (400 MHz, d_3-MeCN) for the treatment of TPPO with $Y(OTf)_3$ zoomed in to show the absence of water in the system.

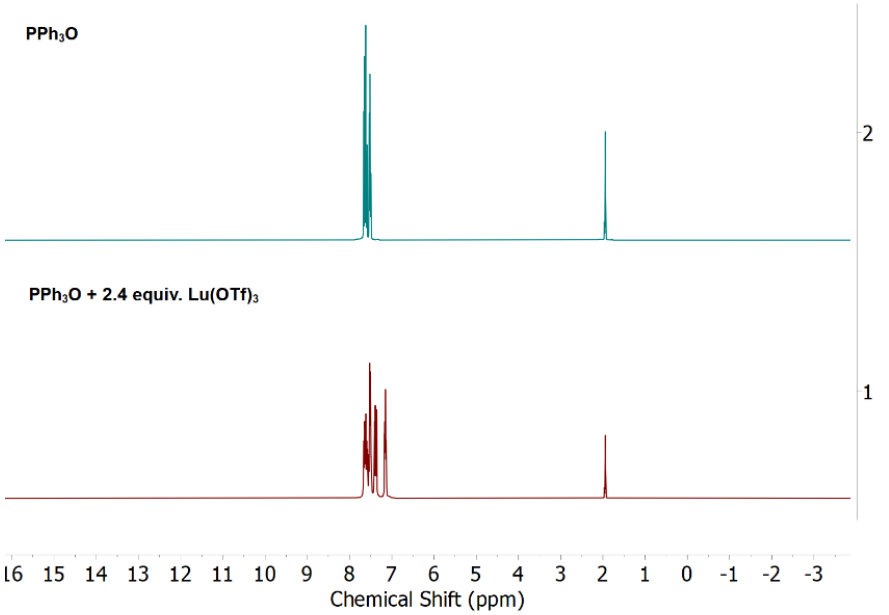

Figure D52. Stacked ^{1}H NMR spectra (400 MHz, d_3-MeCN) for the treatment of TPPO with $Lu(OTf)_3$

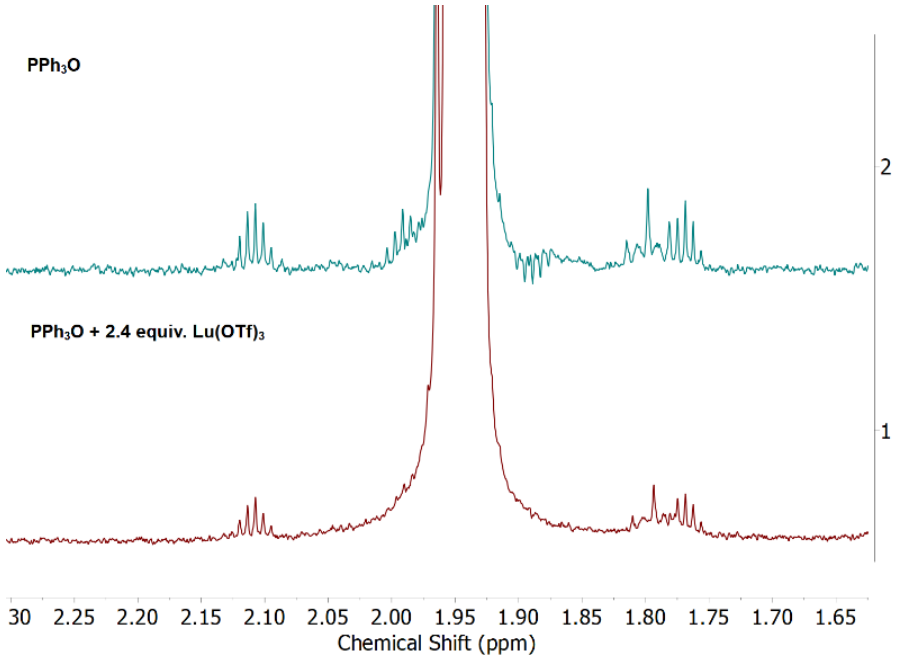

Figure D53. Stacked ^{1}H NMR spectra (400 MHz, d_3-MeCN) for the treatment of TPPO with $Lu(OTf)_3$ showing the virtual absence of water in the system.

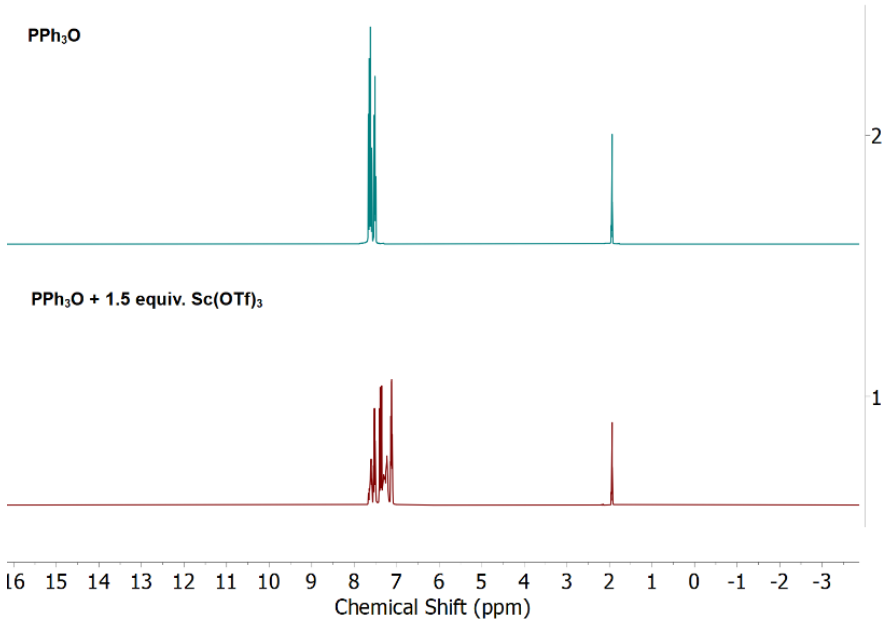

Figure D54. Stacked ^{1}H NMR spectra (400 MHz, d_3-MeCN) for the treatment of TPPO with $Sc(OTf)_3$.

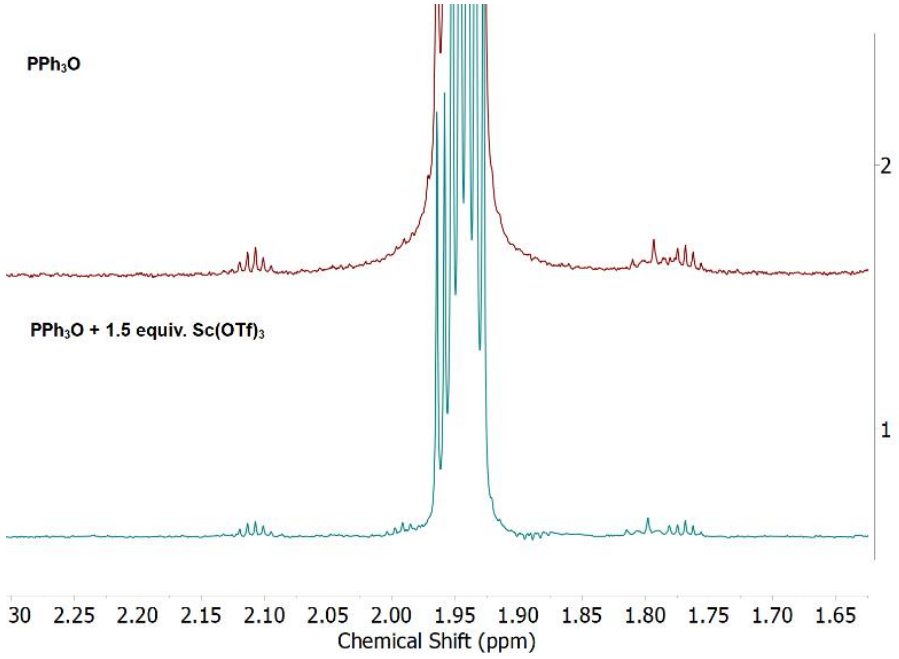

Figure D55. Stacked ^{1}H NMR spectra (400 MHz, d_3-MeCN) for the treatment of TPPO with $Sc(OTf)_3$ showing the virtual absence of water in the system.

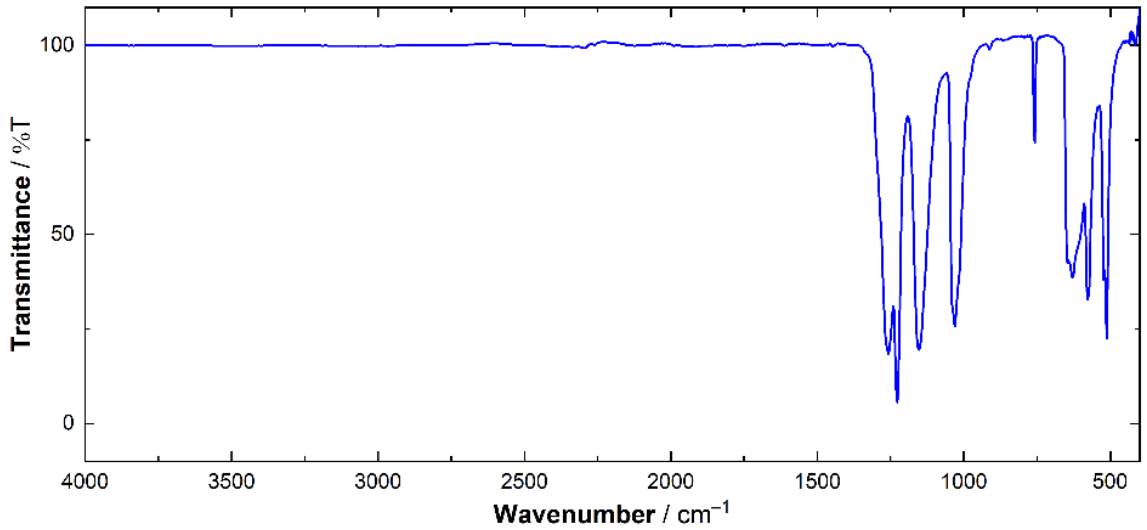

Figure D56. Solid-state IR spectrum of CsOTf.

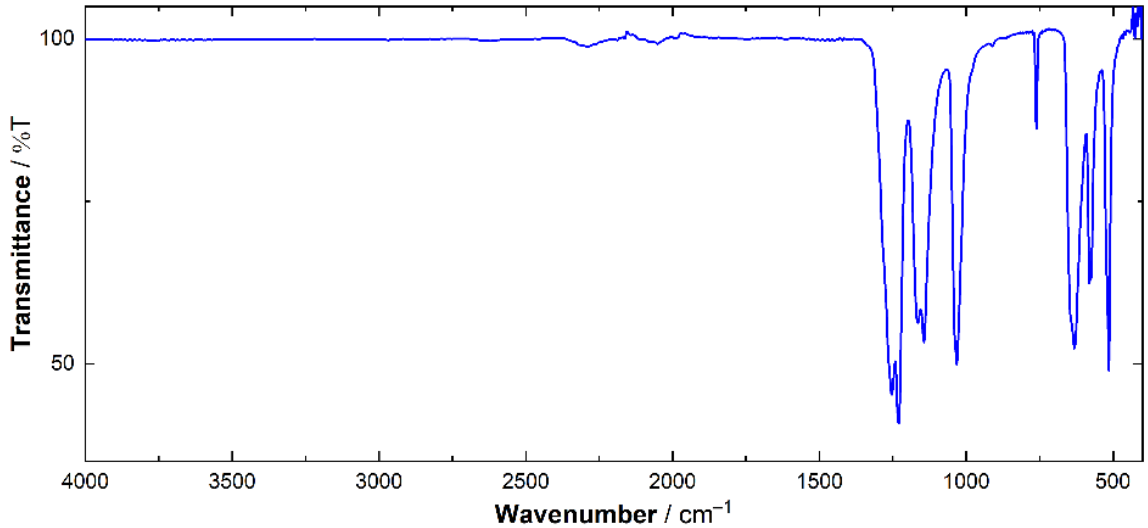

Figure D57. Solid-state IR spectrum of RbOTf.

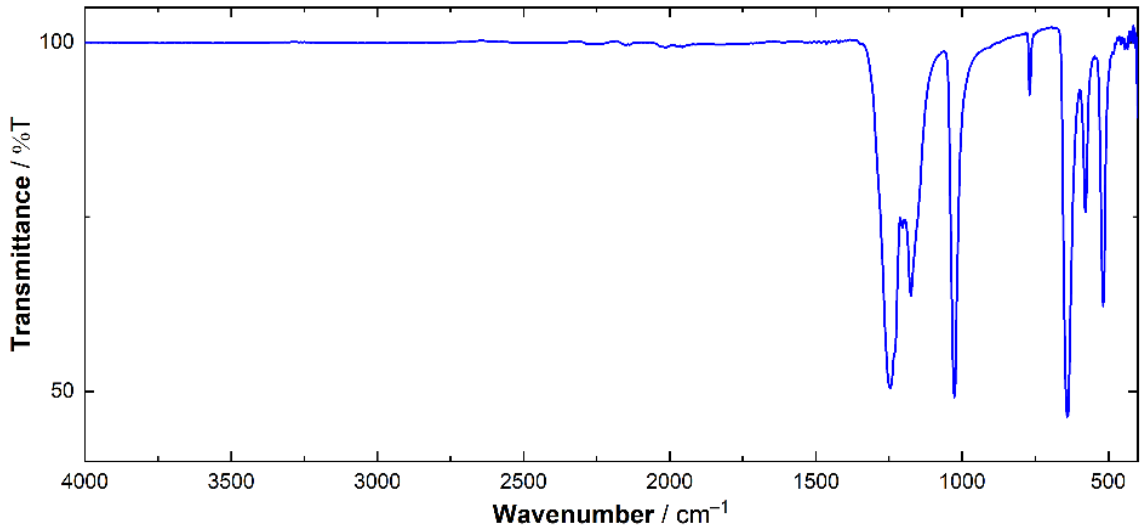

Figure D58. Solid-state IR spectrum of KOTf.

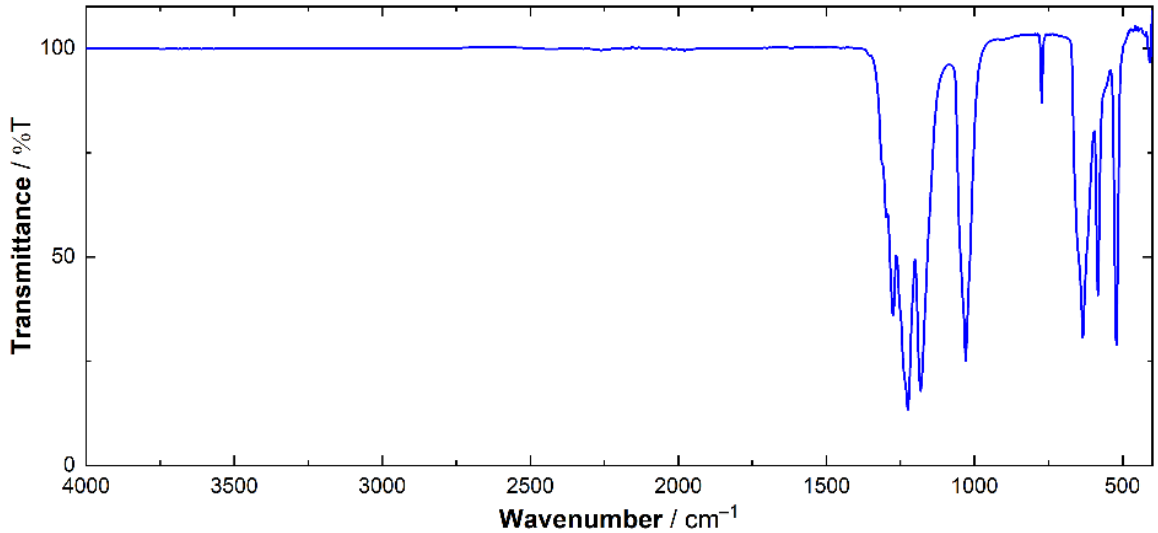

Figure D59. Solid-state IR spectrum of NaOTf.

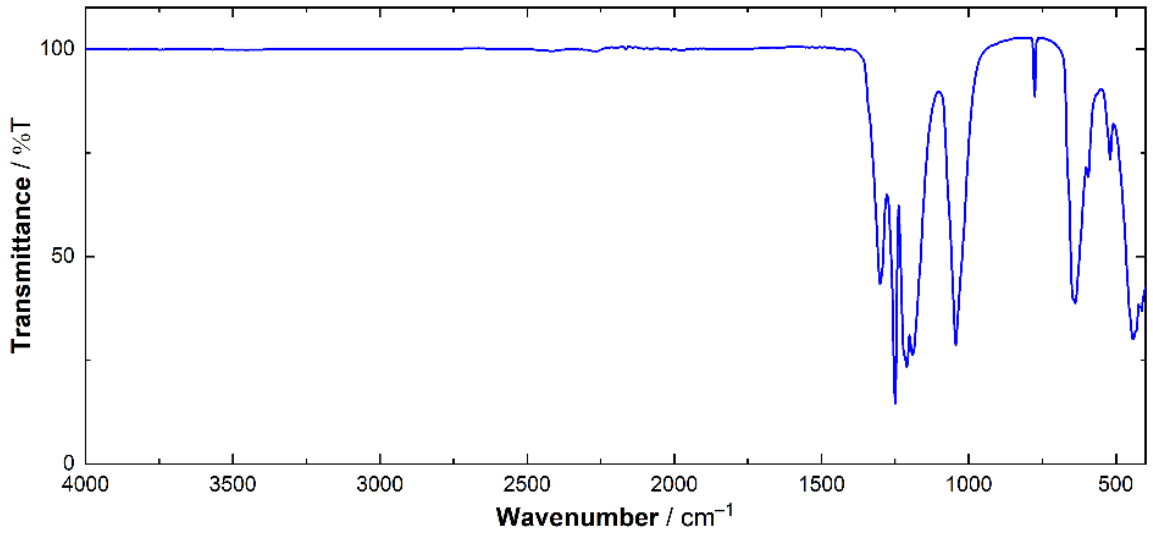

Figure D60. Solid-state IR spectrum of LiOTf.

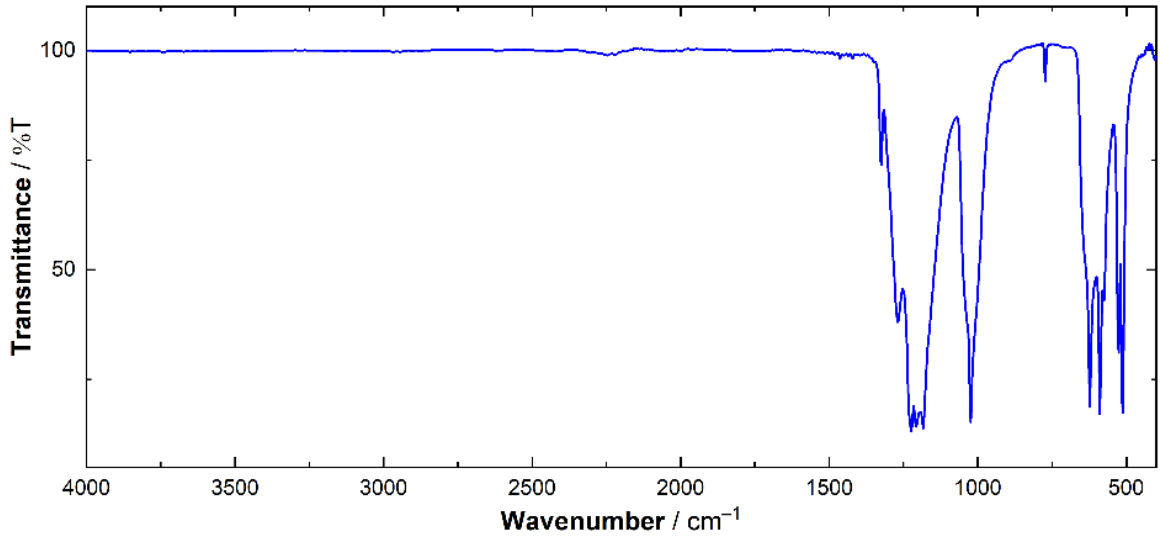

Figure D61. Solid-state IR spectrum of $Ba(OTf)_2$.

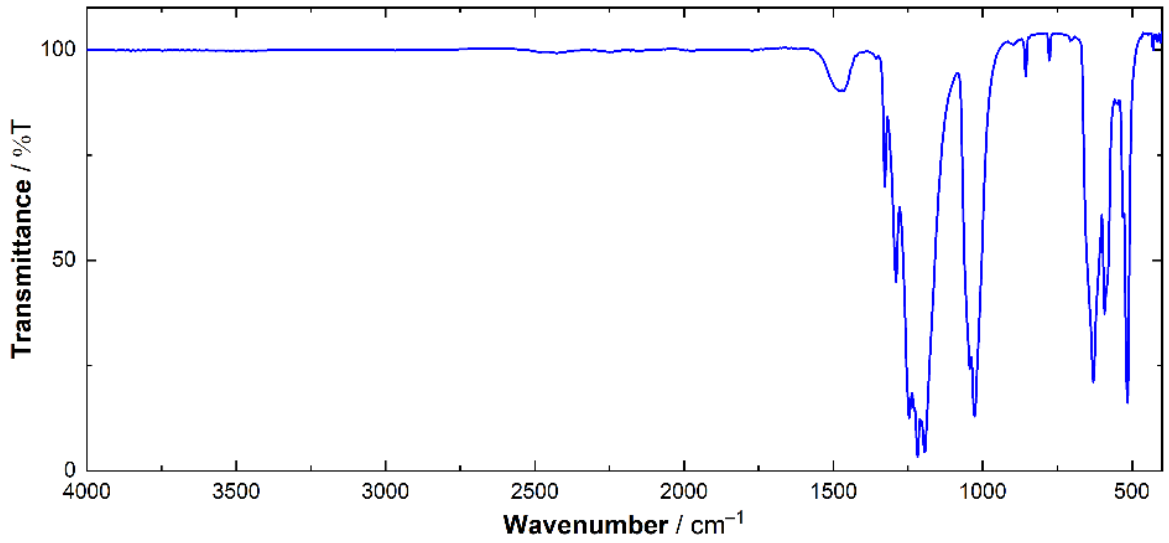

Figure D62. Solid-state IR spectrum of $Sr(OTf)_2$.

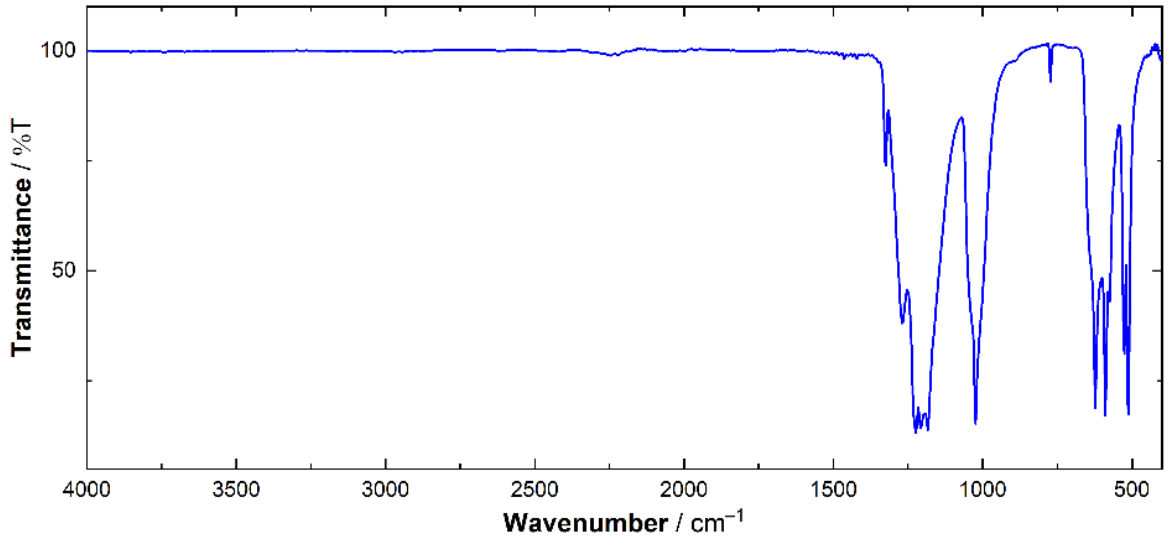

Figure D63. Solid-state IR spectrum of $Ca(OTf)_2$.

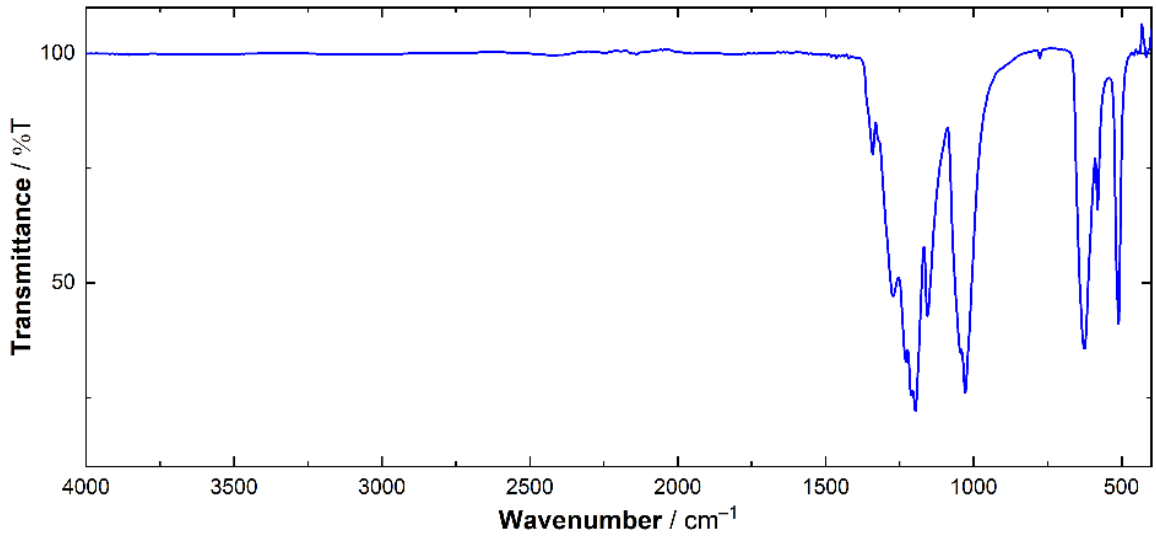

Figure D64. Solid-state IR spectrum of $La(OTf)_3$.

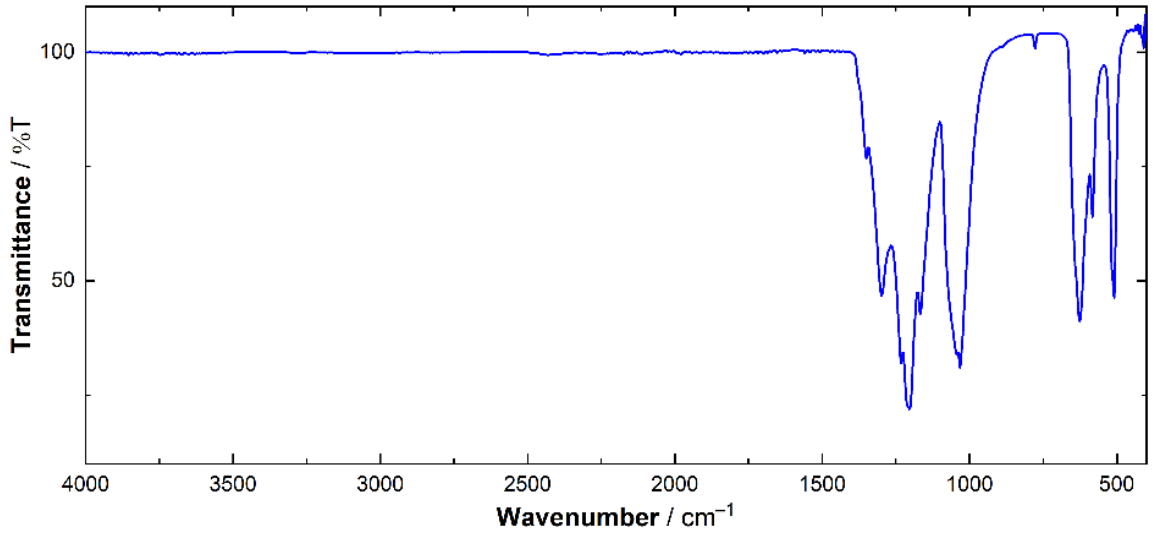

Figure D65. Solid-state IR spectrum of $Y(OTf)_3$.

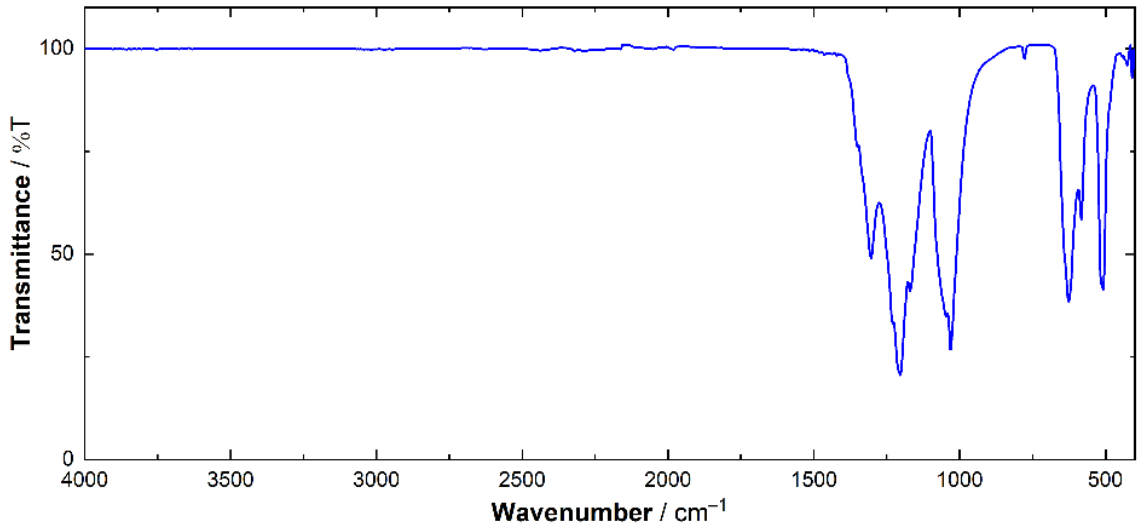

Figure D66. Solid-state IR spectrum of $Lu(OTf)_3$.

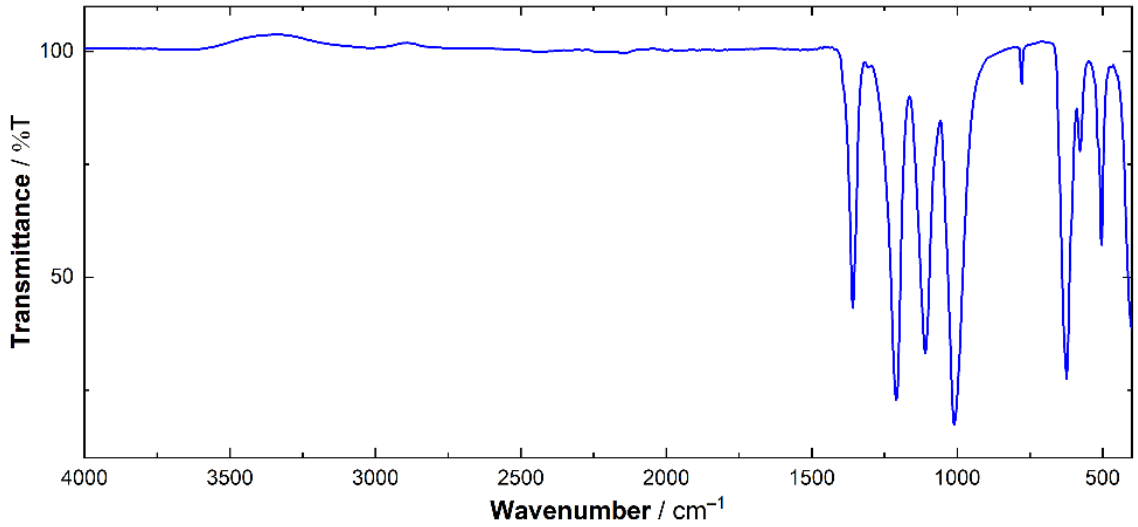

Figure D67. Solid-state IR spectrum of $Sc(OTf)_3$.

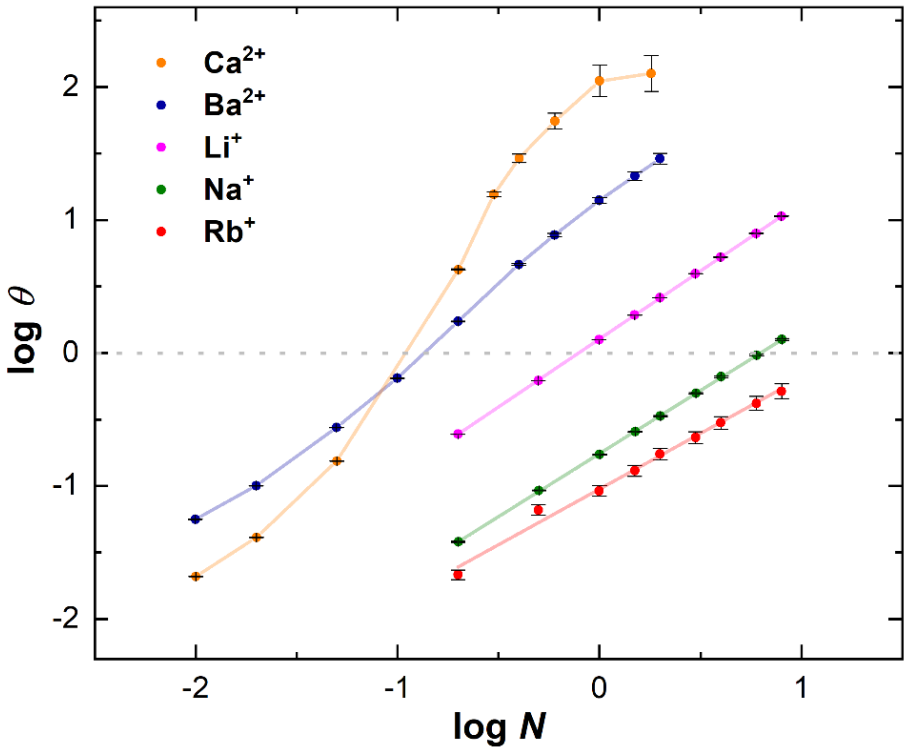

Figure D68. Hill plots for selected metal ions in this study. The y-axis is plotted from the relationship $\theta = [\Delta\delta/(\Delta\delta'_{max} - \Delta\delta)]$ representing normalization of the individual ^{31}P NMR shifts ($\Delta\delta$ values) for respective ions from their maximum shift ($\Delta\delta'_{max}$) determined from the direct nonlinear fit of the data to Equation 2. Errors on θ (shown as the error bars in black with each point) are plotted as ±0.3σ.

Appendices for Chapters in Part II

Appendix E

Supplementary Information for Chapter 6

NMR Spectra

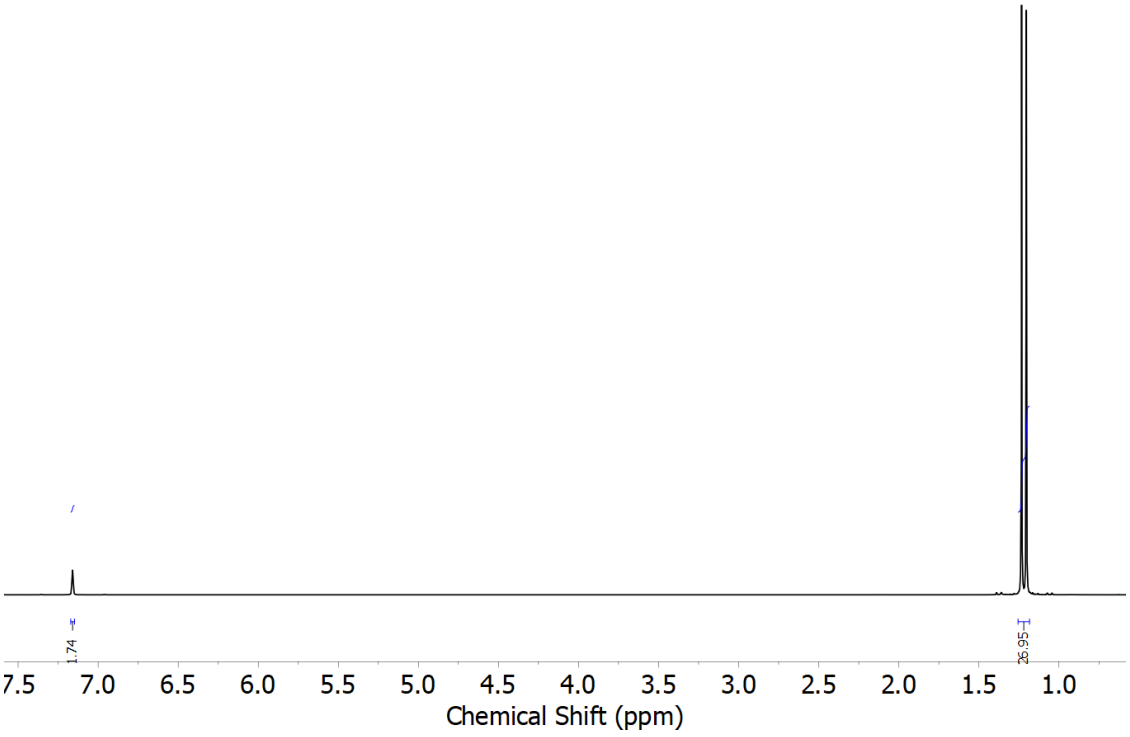

Figure E1. ^{1}H NMR spectrum (400 MHz, C_6D_6) of **Phosphinime**.

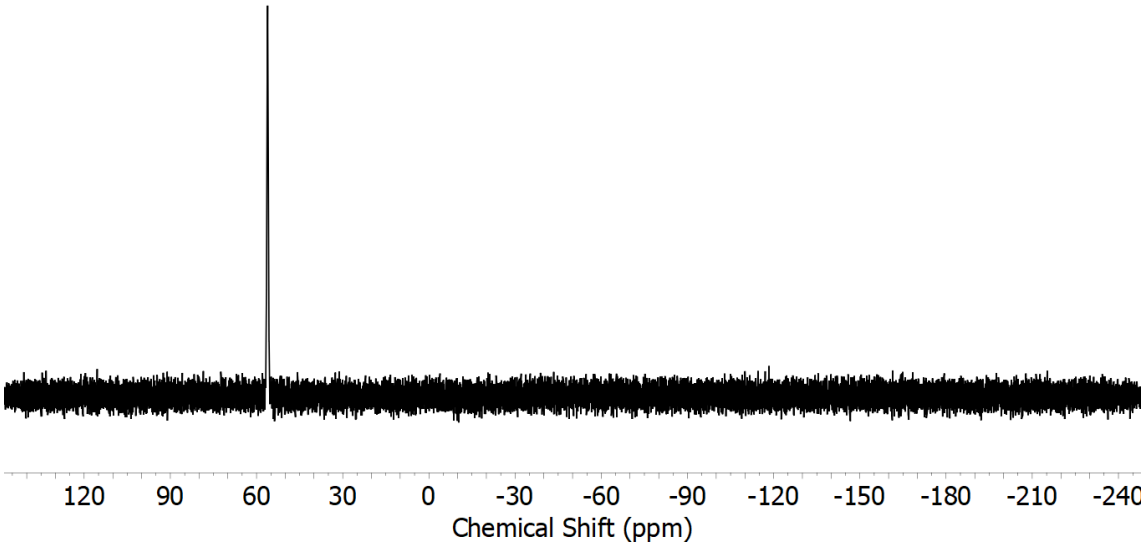

Figure E2. ^{31}P NMR spectrum (162 MHz, C_6D_6) of **Phosphinime**.

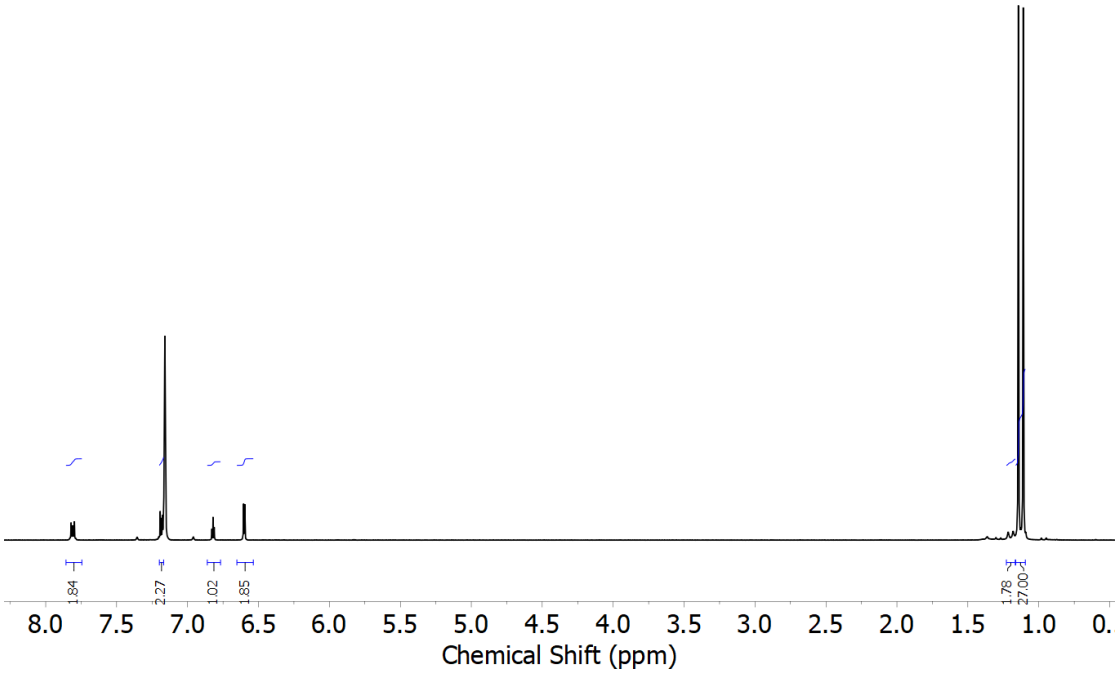

Figure E3. ^{1}H NMR spectrum (400 MHz, C_6D_6) of **1**.

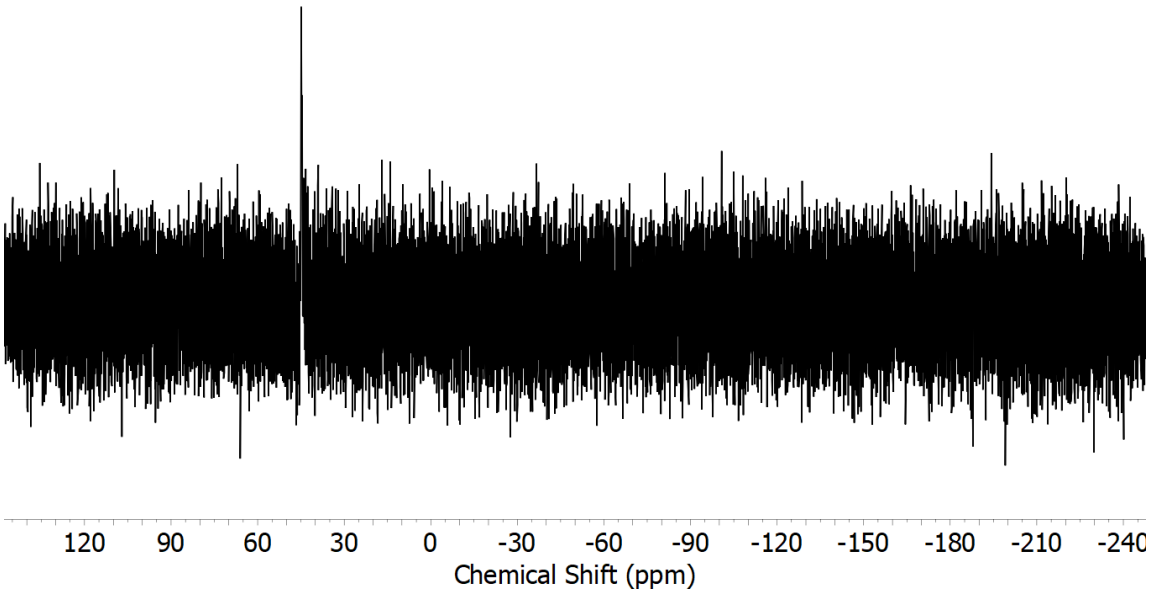

Figure E4. ^{31}P NMR spectrum (162 MHz, C_6D_6) of **1**.

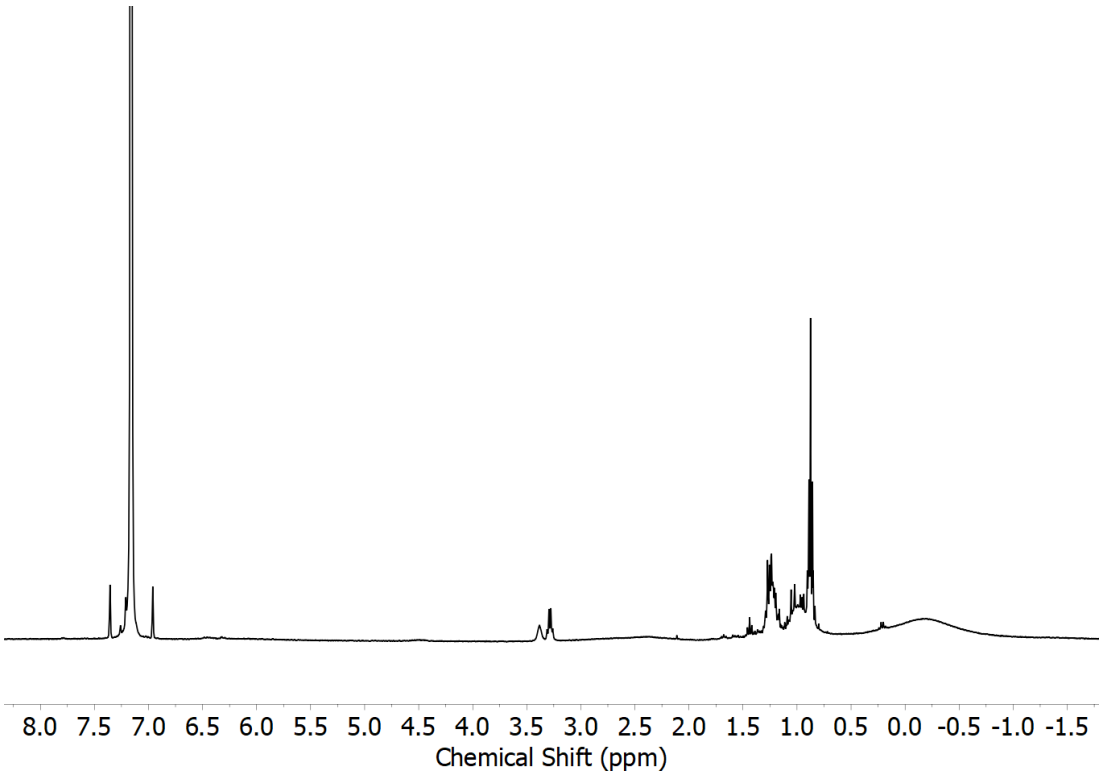

Figure E5. ^{1}H NMR spectrum (400 MHz, C_6D_6) of **2-Et**.

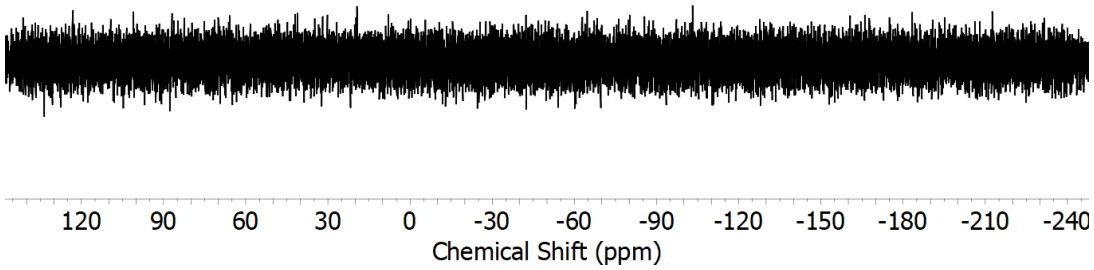

Figure E6. ^{31}P NMR spectrum (162 MHz, C_6D_6) of **2-Et**.

Electronic Absorption Spectra

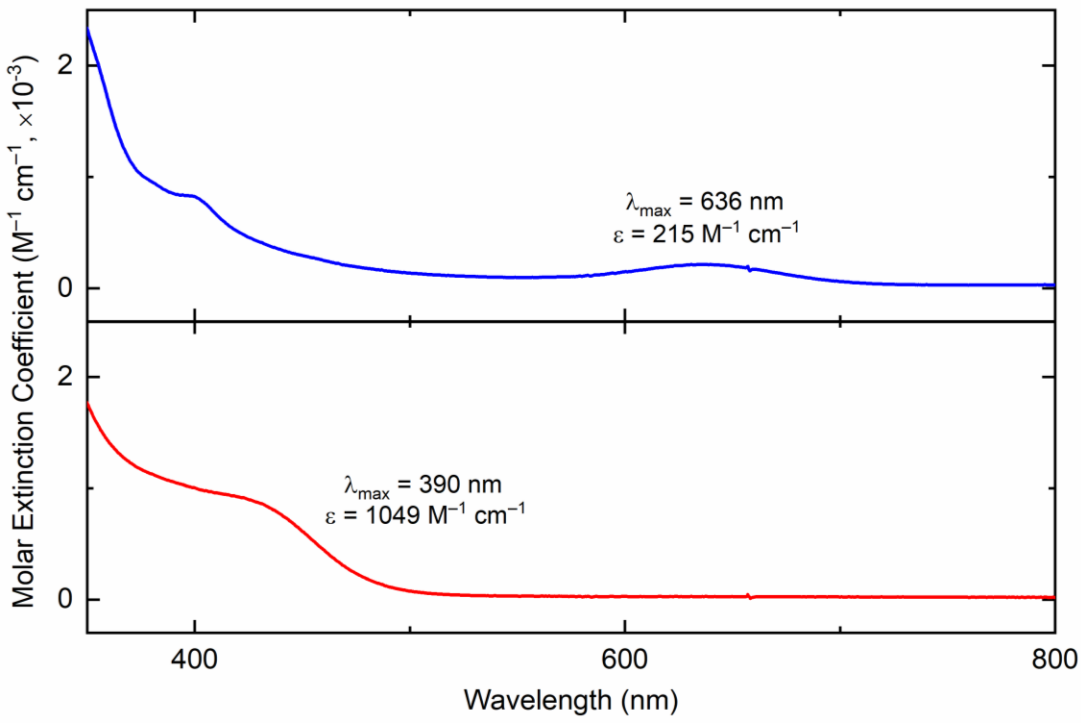

Figure E7. Stacked Electronic absorption spectra of **2-Et** (blue) and **1** (red) in pentane.

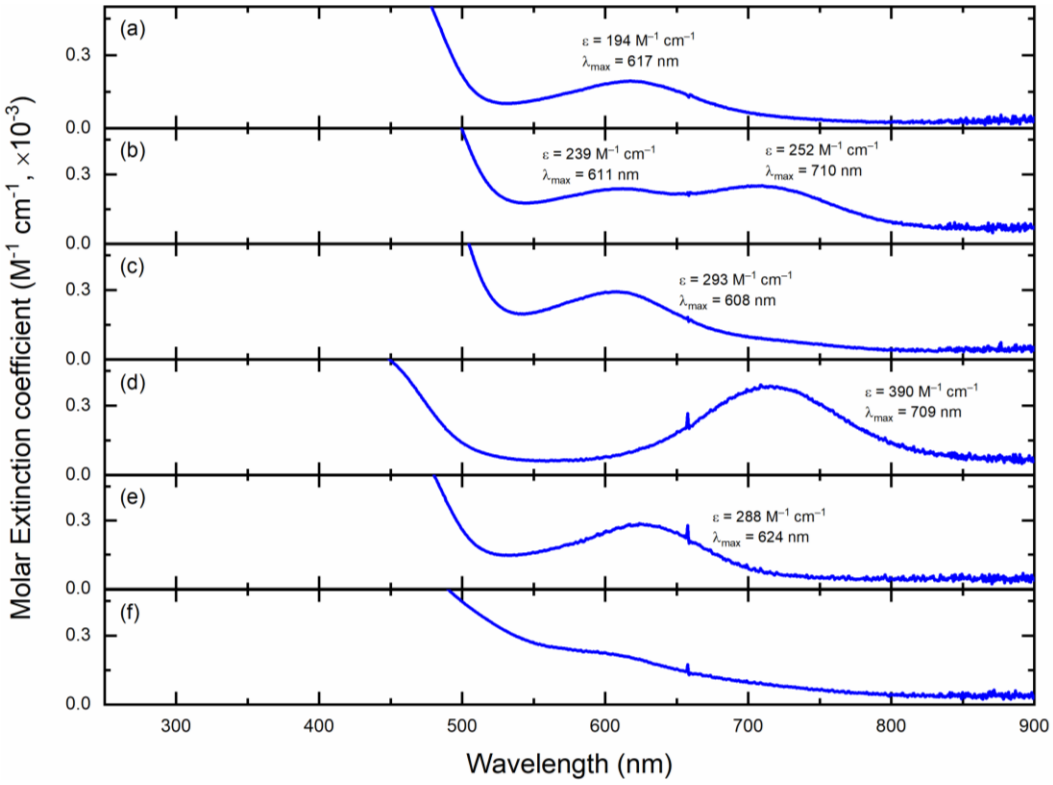

Figure E8. Electronic absorption spectra of **2-Et** in (a) Pentane, (b) Benzene, (c) Toluene, (d) THF, (e) Hexane, (f) MeCN.

Electrochemistry

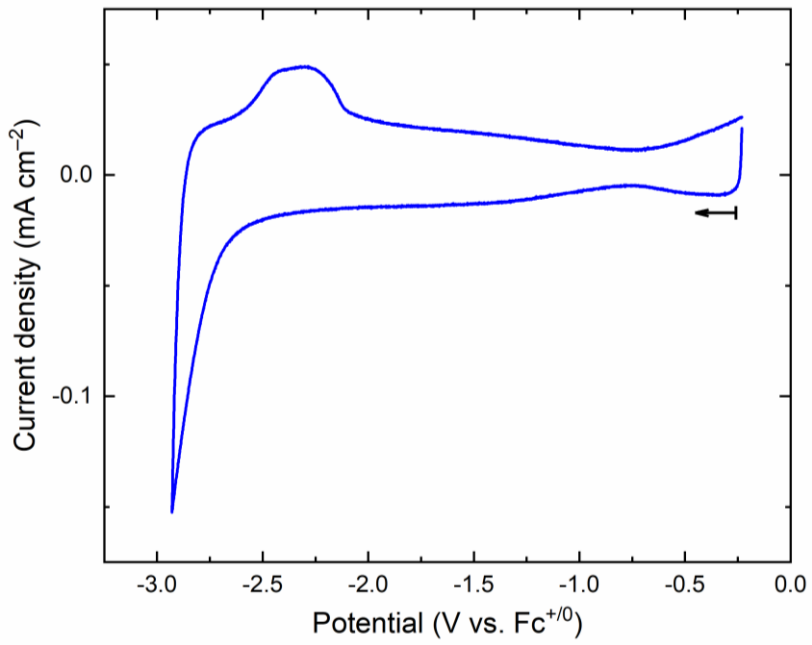

Figure E9. Cyclic voltammetry data for $AlEt_3$ in THF (0.1 M $[^nBu_4N]^+[PF_6]^-$, 100 mV/s).

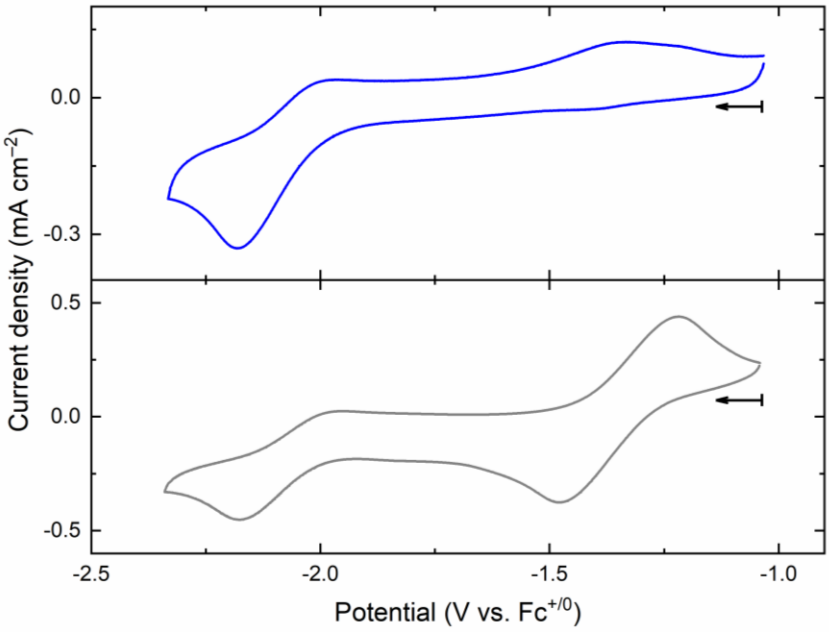

Figure E10. Cyclic voltammetry data for **4** (blue) and **4** in the presence of 1 equiv. of Cobaltocene (grey) in THF (0.1 M $[^nBu_4N]^+[PF_6]^-$, 100 mV/s).

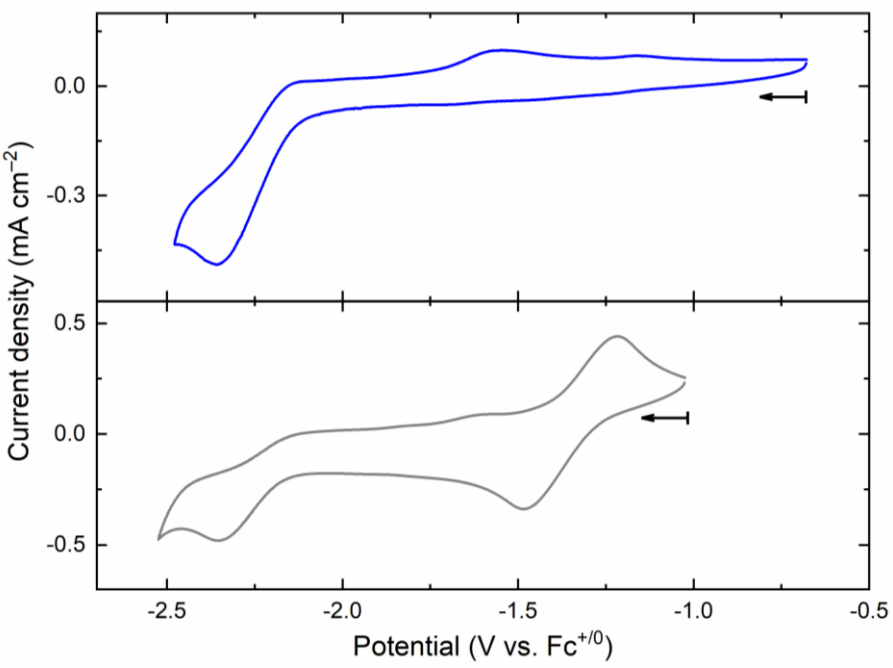

Figure E11. Cyclic voltammetry data for **5** (blue) and **5** in the presence of 1 equiv. of Cobaltocene (grey) in THF (0.1 M $[^{n}Bu_4N]^{+}[PF_6]^{-}$, 100 mV/s).

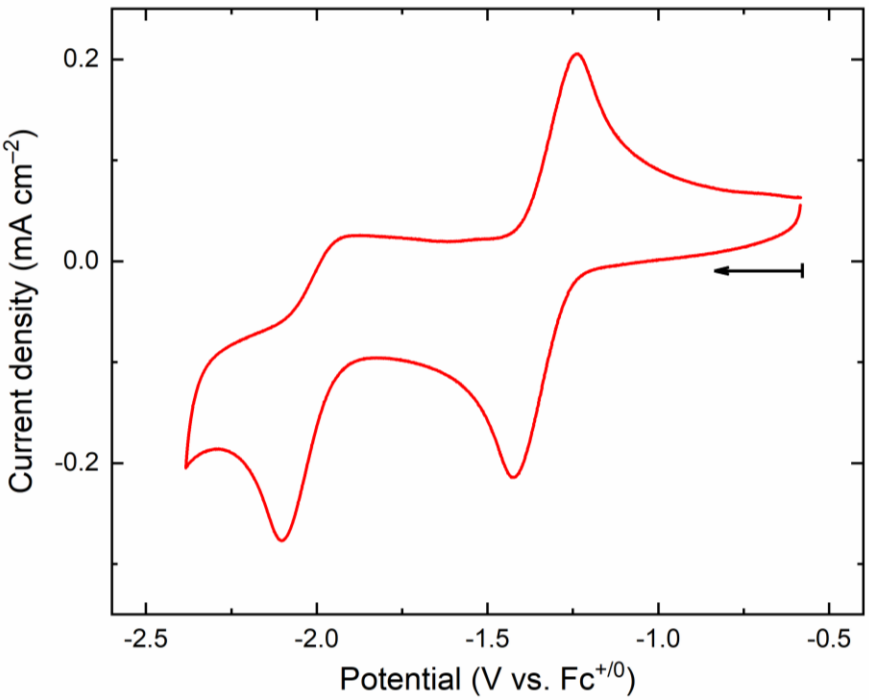

Figure E12. Cyclic voltammetry data for **1** in the presence of 1 equiv. of Cobaltocene in THF (0.1 M $[^{n}Bu_4N]^{+}[PF_6]^{-}$, 100 mV/s).

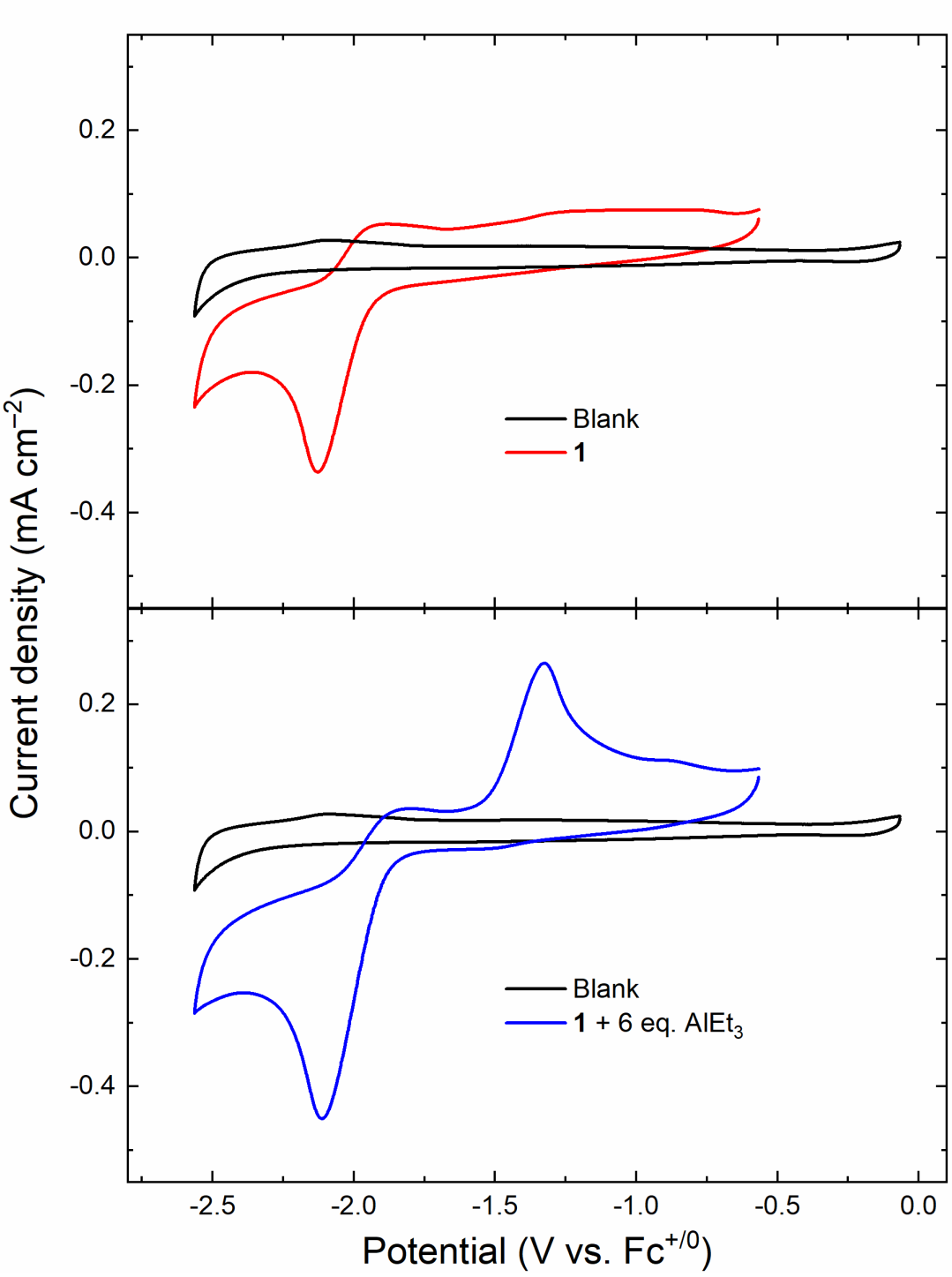

Figure E13. Cyclic Voltammetry Data for **1** (red) and **1** in the presence of $AlEt_3$ (blue) in THF (0.1 M $[^nBu_4N]^+[PF_6]^-$, 100 mV/s).

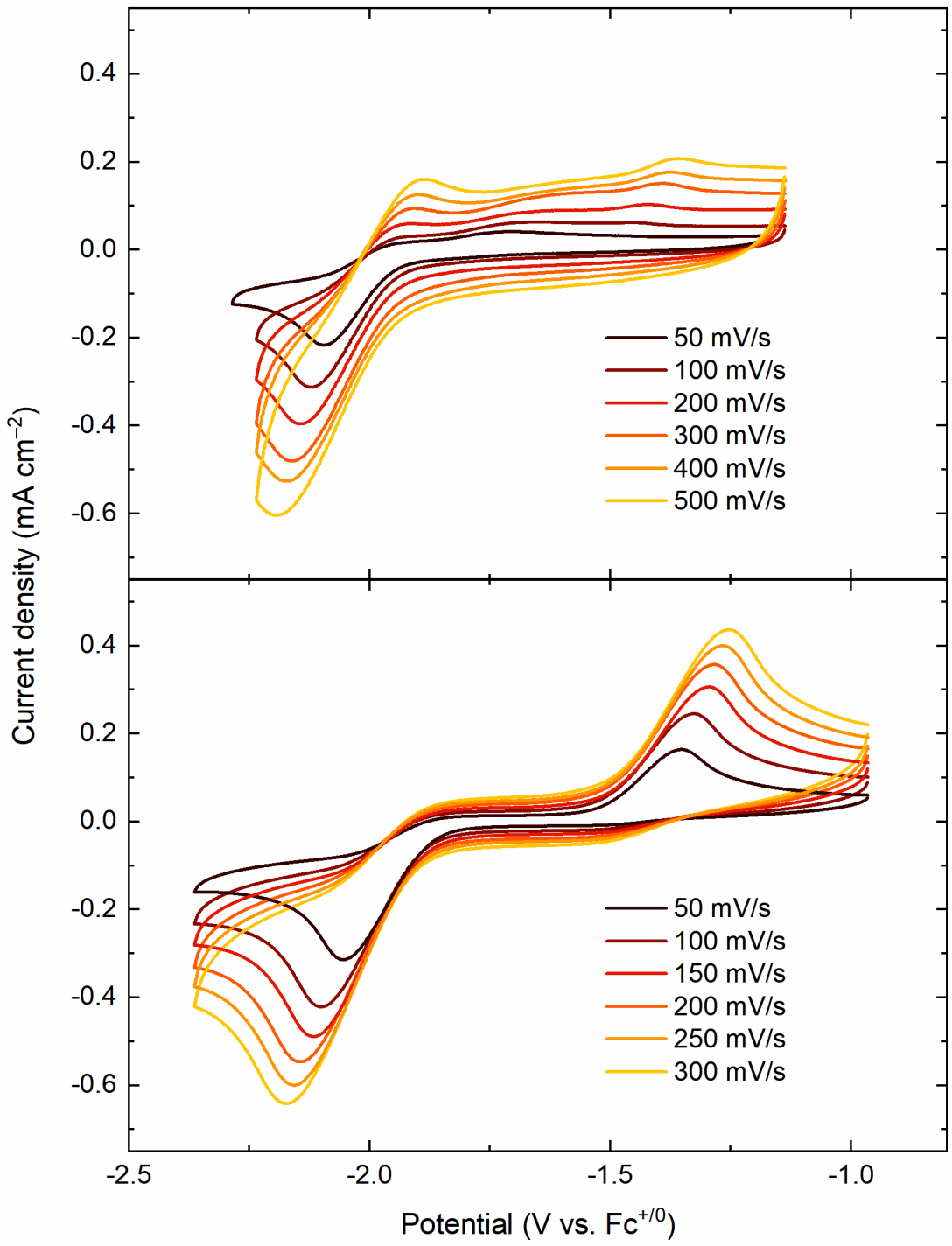

Figure E14. Cyclic voltammetry data for **1** (top) and **1** in the presence of $AlEt_3$ (bottom) in THF at varying scan rates (0.1 M $[^nBu_4N]^+[PF_6]^-$).

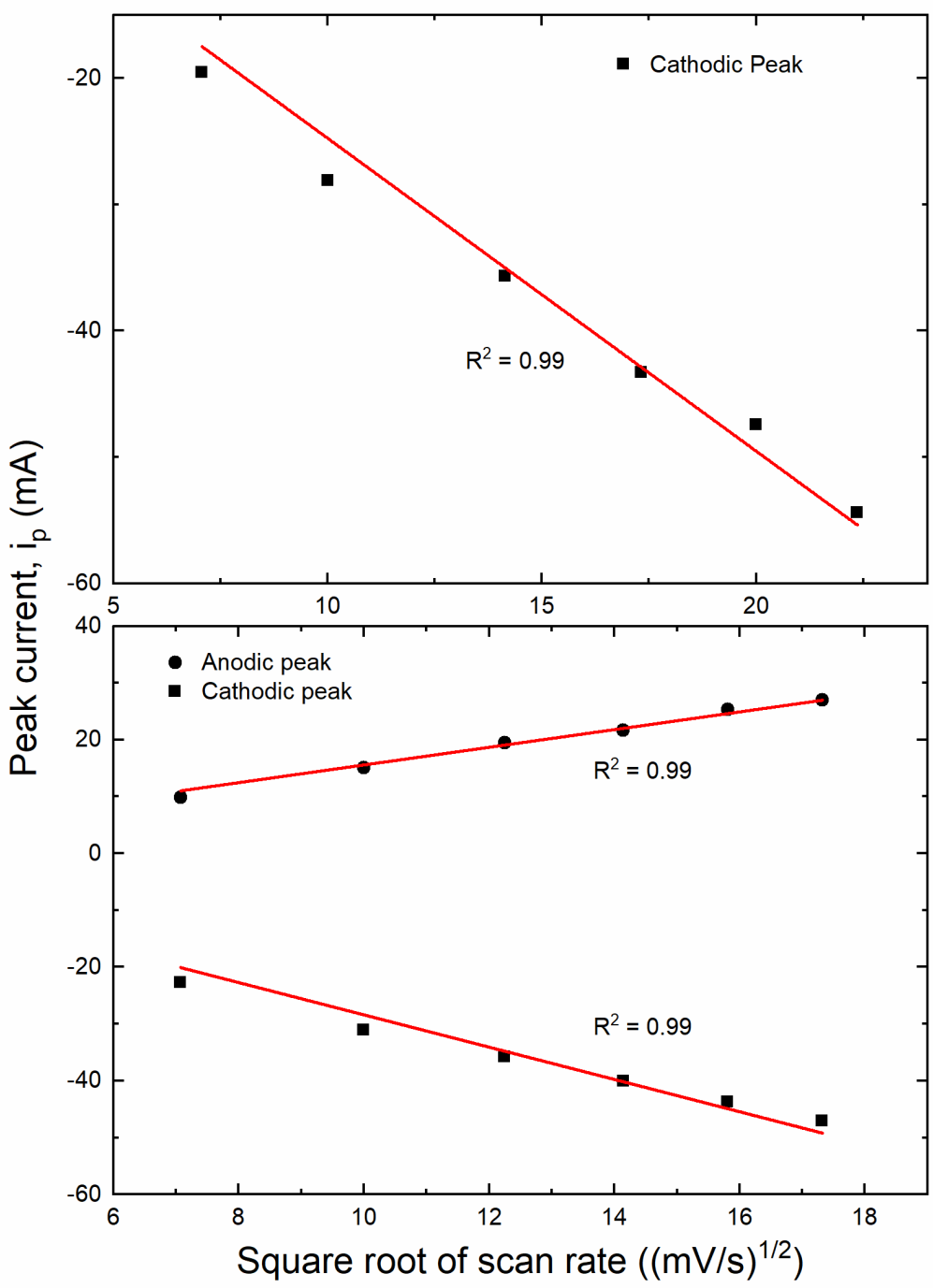

Figure E15. Linear dependence of peak current on square root of scan rate for **1** (top) and **1** in the presence of $AlEt_3$ (bottom).

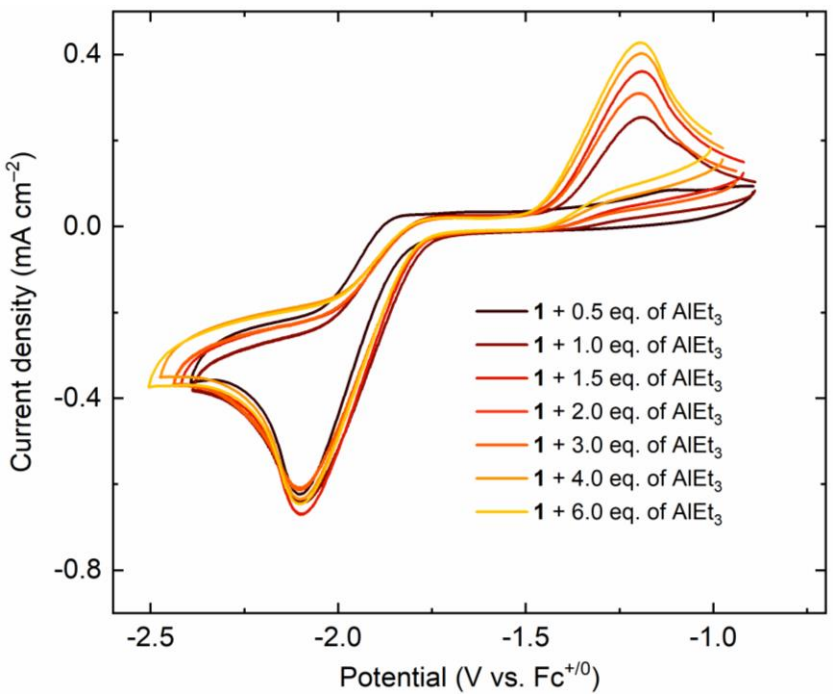

Figure E16. Electrochemical titration of **1** in the presence of increasing amounts of $AlEt_3$ in THF (0.1 M $[^nBu_4N]^+[PF_6]^-$, 100 mV/s).

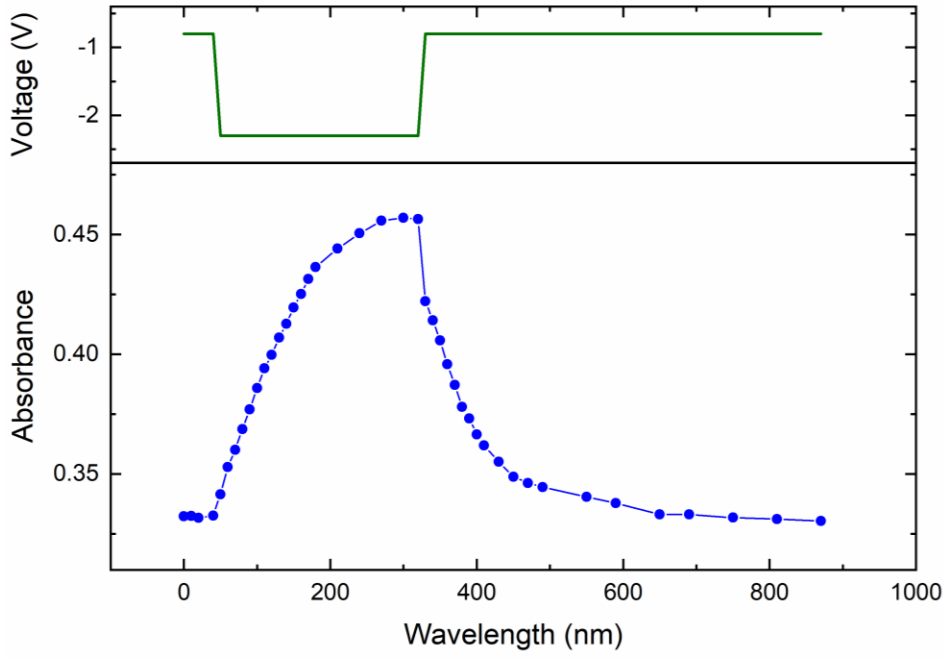

Figure E17. Spectroelectrochemical Data (Absorbance vs. Wavelength) for **1** in the presence of $AlEt_3$ in THF (0.1 M $[^nBu_4N]^+[PF_6]^-$).

Gas Chromatography

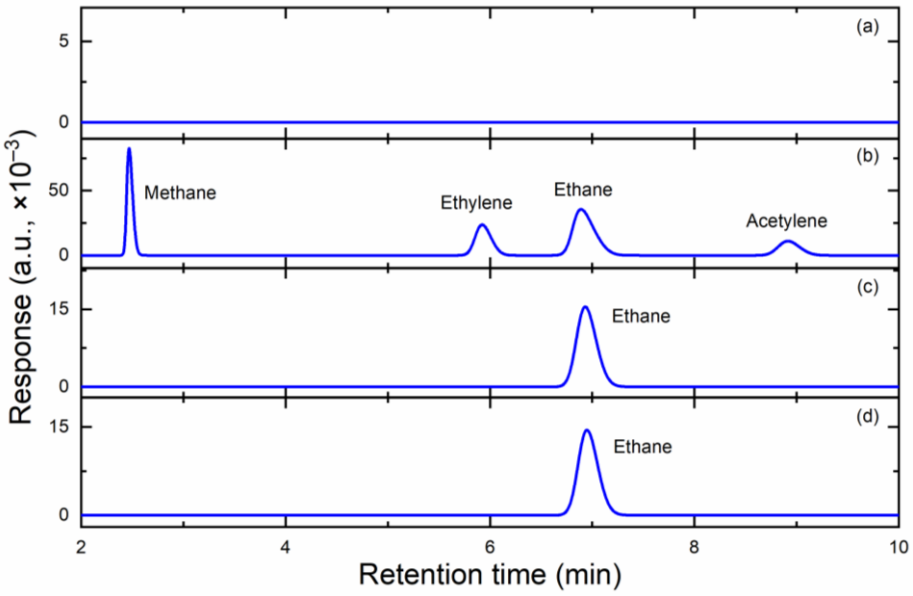

Figure E18. Gas Chromatography of **1** in the presence of $AlEt_3$ during chemical reduction; (a) Blank, (b) Check Gas, (c) **1** with 2 equiv. of $AlEt_3$ in Benzene, (d) **1** with 2 equiv. of $AlEt_3$ in Pentane.

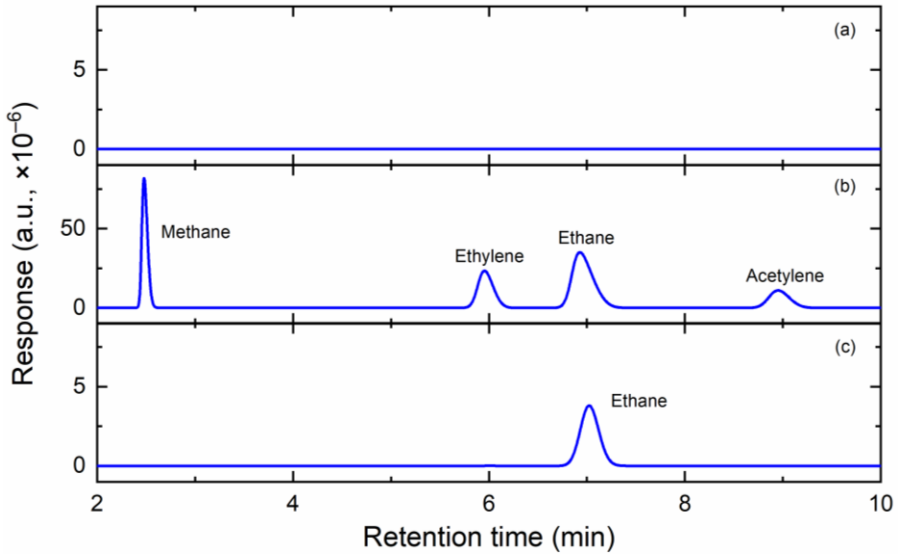

Figure E19. Gas Chromatography of **1** in the presence of $AlEt_3$ during Bulk Electrolysis experiment; (a) Blank, (b) Check Gas, (c) **1** with 2 equiv. of $AlEt_3$. Conditions: Electrolyte: 0.1 M $[nBu_4N]^+[PF_6]^-$ in THF; Electrolysis Potential: –2.4 V; Time: 2 hours.

EPR Spectra

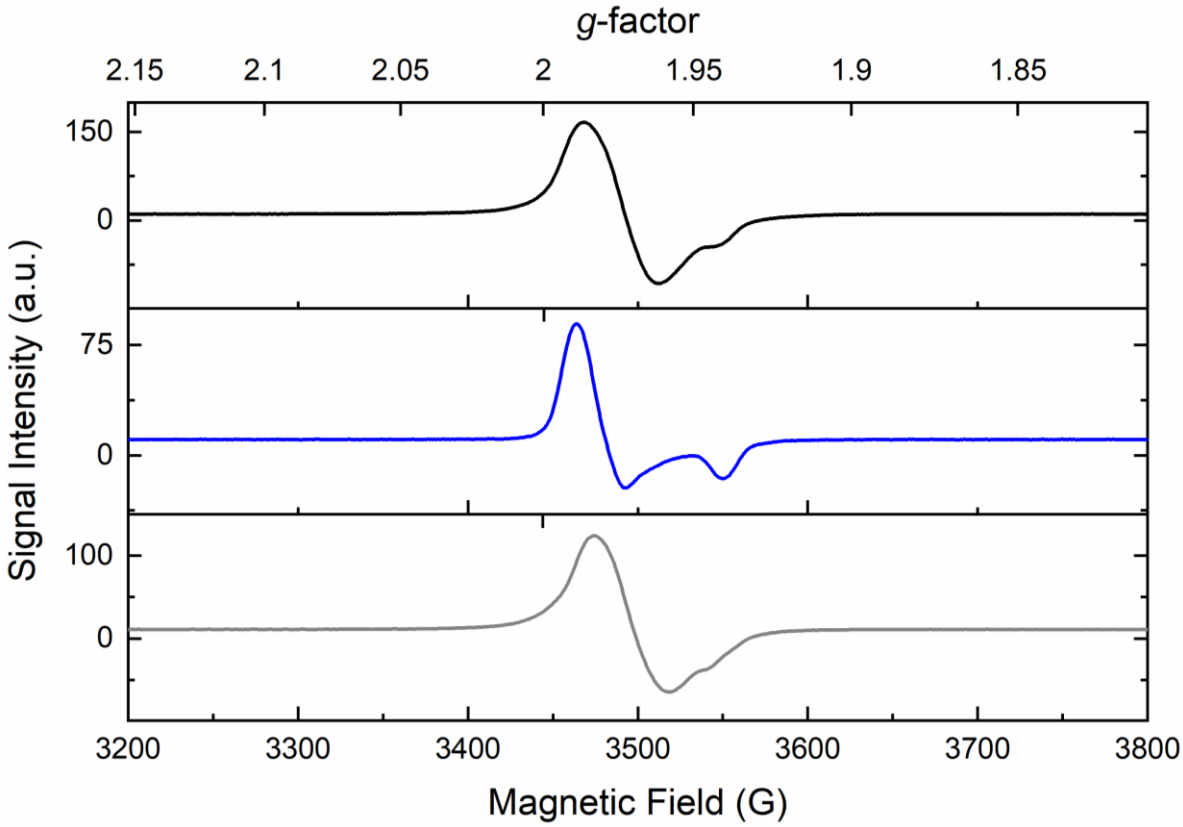

Figure E20. X-band CW EPR spectrum of **2-Et** in hexane (black), toluene (blue) and THF (grey).

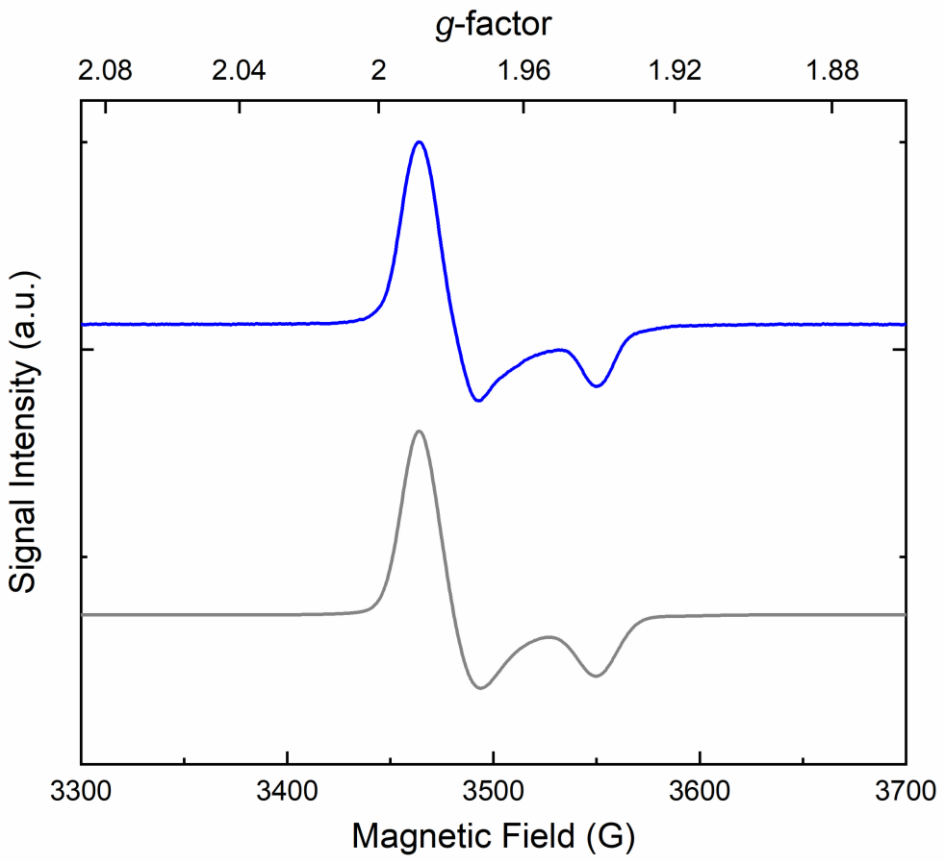

Figure E21. Blue: Electron paramagnetic resonance spectrum of **2-Et** in frozen toluene at 55 K (Frequency: 9.6426 GHz; power: 0.032 mW; time constant: 5 ms; modulation amplitude: 4.0 G). Grey: Easyspin simulation of EPR data (simulation parameters: S = 0.5; g = [1.979 1.989 1.940]; nuclei: Ti; A= [2 34 45]; HStrain = [65 49 60]; lw = 0.41).

Mechanistic Pathway

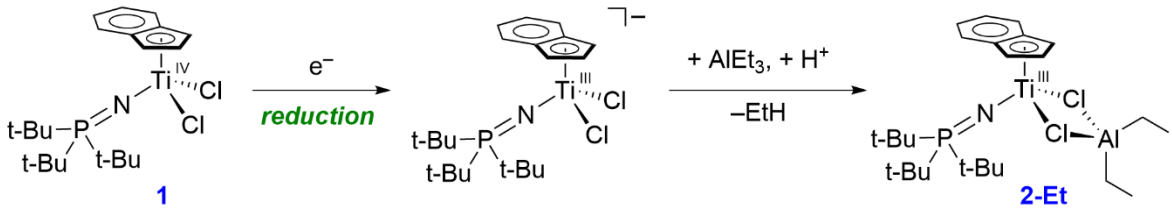

Figure E22. Electrochemical Pathway for the formation of **2-Et** from **1**.

X-Ray Crystallography

The single crystal X-ray diffraction studies were carried out on a Bruker APEX-II ULTA CCD diffractometer equipped with Mo K_α radiation (λ = 0.71073 Å).

[(Ind)(*t*Bu$_3$P=N)TiCl$_2$] (1)

Crystals of the subject compound were used as received (grown from Toluene layered with Hexane –30°C). A 0.220 x 0.220 x 0.180 mm green block crystal was mounted on a Cryoloop with Paratone oil. Data were collected in a nitrogen gas stream at 100(2) K using φ and ω scans. Crystal-to-detector distance was 55 mm and exposure time was 15.0 seconds per frame using a scan width of 0.60°. Data collection was 95.7% complete to 25.00° in θ. A total of 10969 reflections were collected covering the indices, -14<=h<=14, -14<=k<=14, -18<=l<=11. 12455 reflections were found to be symmetry independent, with a R_{int} of 0.0524. Indexing and unit cell refinement indicated a primitive, triclinic lattice. The space group was found to be *P*-1. The data were integrated using the Bruker SAINT Software program[4] and scaled using the SADABS[5] software program. Solution by direct methods (SHELXT)[6] produced a complete phasing model consistent with the proposed structure. All nonhydrogen atoms were refined anisotropically by full-matrix least-squares using Olex software package (SHELXL-2014).[7-8] All carbon bonded hydrogen atoms were placed using a riding model. Their positions were constrained relative to their parent atom using the appropriate HFIX command in SHELXL-2014. Crystallographic data are summarized in Table E1. Note: Twin data, used HKL 5 format for final refinement. RIGU instruction applied.

[(Ind)(*t*Bu$_3$P=N)Ti(μ$_2$-Cl)$_2$AlEt$_2$] (2-Et)

Crystals of the subject compound were used as received (grown from Hexane –30°C). A 0.220 x 0.175 x 0.130 mm irregular piece of green crystal was mounted on a Cryoloop with Paratone oil. Data were collected in a nitrogen gas stream at 100(2) K using φ and ω scans. Crystal-to-detector distance was 45 mm and exposure time was 7 seconds per frame using a scan width of 1.00°. Data collection was 99.9% complete to 25.00° in θ. A total of 31728 reflections were collected covering the indices, -13<=h<=13, -23<=k<=18, -30<=l<=29. 5024 reflections were found to be symmetry independent, with a R_{int} of 0.1027. Indexing and unit cell refinement indicated a primitive, orthorhombic lattice. The space group was found to be *P*bca. The data were integrated using the Bruker SAINT software program[1] and scaled using the SADABS[2] software program. Solution by direct methods (SHELXT)[3] produced a complete phasing model consistent with the proposed structure. All nonhydrogen atoms were refined anisotropically by full-matrix least-squares using Olex software package (SHELXL-2014).[4,5] All carbon bonded hydrogen atoms were placed using a riding model. Their positions were constrained relative to their parent atom using the appropriate HFIX command in SHELXL-2014. Crystallographic data are summarized in Table E1. Note: Minor twin component, best refinement "ignoring" the twin and integrating as a single component.

Table E1. Crystal and Refinement Data for **1** and **2-Et**.

	1	**2-Et**
CCDC number	1900171	1900172
Empirical formula	$C_{21}H_{34}Cl_2NPTi$	$C_{25}H_{44}AlCl_2NPTi$
Formula weight	450.26	535.36
Temperature	100.0	100
Wavelength	0.71073	0.71073
Crystal system	triclinic	orthorhombic
Space group	P-1	Pbca
a	12.360(4) Å	11.3833(16) Å
b	12.453(5) Å	19.759(3) Å
c	15.659(6) Å	25.362(3) Å
a	84.536(6)	90
β	89.935(5)	90
γ	76.277(5)	90
Volume	2330.2(14) $Å^3$	5704.4(14) $Å^3$
Z	4	8
Density (calculated)	1.283 g/cm3	1.247 g/cm3
Absorption coefficient	0.671 mm-1	0.588 mm-1
F(000)	952.0	2280.0
Crystal size	0.22 × 0.22 × 0.18 mm3	0.22 × 0.175 × 0.13 mm3
Theta range	4.068 to 50.12	4.424 to 50
Index ranges	$-14 \le h \le 14$, $-14 \le k \le 14$, $-18 \le l \le 11$	$-13 \le h \le 13$, $-23 \le k \le 18$, $-30 \le l \le 29$
Reflections collected	12455	31728
Independent reflections	10969 [R_{int} = 0.0524, R_{sigma} = 0.1165]	5024 [R_{int} = 0.1027, R_{sigma} = 0.0703]
Absorption correction	Multi-scan	Multi-scan
Refinement method	Full-matrix least-squares on F^2	Full-matrix least-squares on F^2
Data/restraints/parameters	10969/156/488	5024/0/291
Goodness-of-fit on F2	0.996	1.061
Final R indices [I>2σ(I)]	R1 = 0.0595, wR2 = 0.1110	R1 = 0.0673, wR2 = 0.1426
R indices (all data)	R1 = 0.1081, wR2 = 0.1266	R1 = 0.0965, wR2 = 0.1546
Largest diff. peak & hole	0.54 and –0.71 $e^-/Å^3$	0.73 and –0.50 $e^-/Å^3$

Table E2. Comparison of Select Bond Lengths (Å).

Bonds	1	2-Et
Ti-N	1.729(5)	1.797(4)
Ti-Cl	2.288(2), 2.310(2)	2.532(1), 2.521(1)
P=N	1.622(5)	
Ti-C$_{ind}$	2.360(6) – 2.545(7)	2.304(5) – 2.509(4)

Table E3. Comparison of Select Bond Angles (°).

Angles	1	2-Et
P-N-Ti	172.5(3)	175.9(2)
Cl-Ti-Cl	103.6(1)	81.5(1)
Cl-Ti-N	102.0(2), 103.2(2)	102.7(1), 106.0(1)
Cl-Al-Cl	-	93.8(1)
Al-Cl-Ti	-	92.2(1), 92.4(1)

References

(1) *SAINT. Ver. 8.34A.* Bruker Analytical X-ray Systems: Madison, WI, June 2014.

(2) *Sheldrick, G. M., SADABS (version 2008/1)*: Program for Absorption Correction for Data from Area Detector Frames, University of Göttingen, 2008.

(3) Sheldrick, G. SHELXT – Integrated space-group and crystal-structure determination. *Acta Cryst.* **2015**, *A71*, 3-8.

(4) Sheldrick, G. Crystal structure refinement with SHELXL. *Acta Cryst.* **2015**, *C71*, 3-8.

(5) Dolomanov, O. V.; Bourhis, L. J.; Gildea, R. J.; Howard J. A. K.; Puschmann, H. OLEX2: a complete structure solution, refinement and analysis program. *J. Appl. Crystallogr.* **2009**, *42*, 339-341.

Appendix F

Supplementary Information for Chapter 7

NMR Spectra

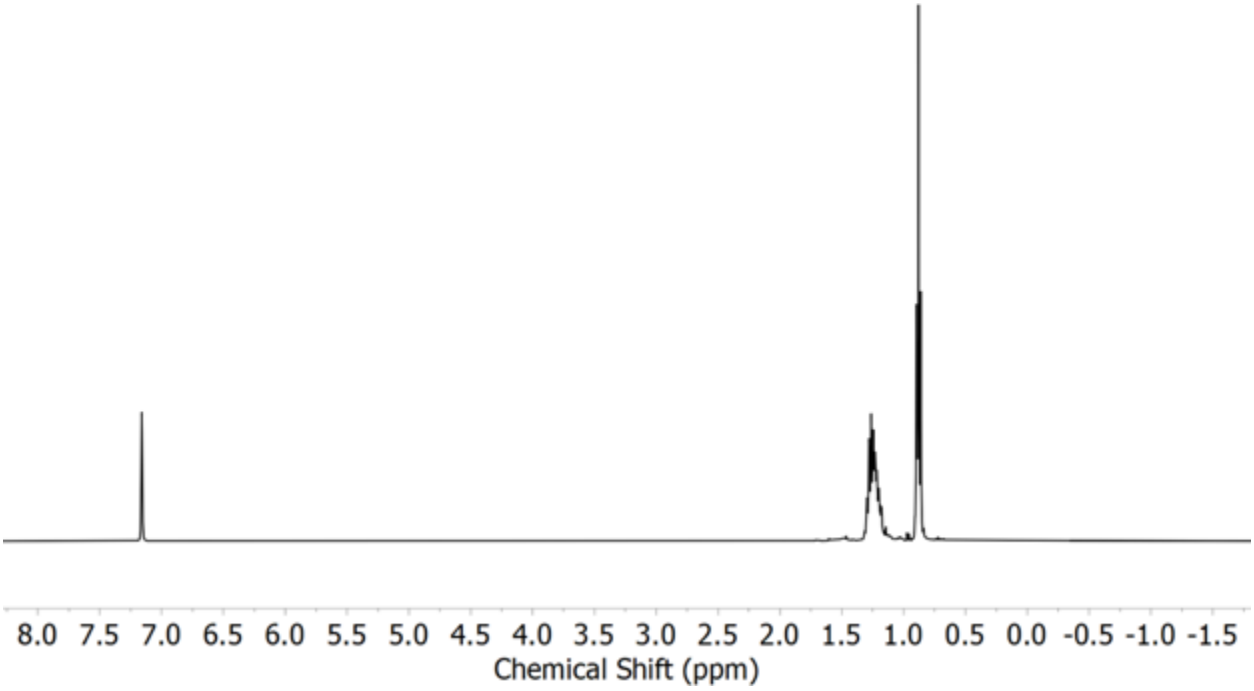

Figure F1. ^{1}H NMR spectrum (400 MHz, C_6D_6) of cleanly isolated **2-*i*Bu**.

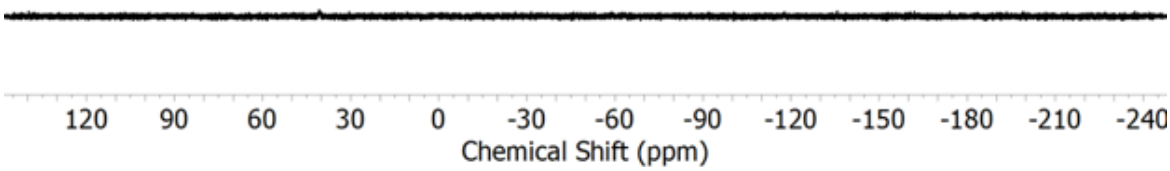

Figure F2. ^{31}P NMR spectrum (162 MHz, C_6D_6) of cleanly isolated **2-*i*Bu**.

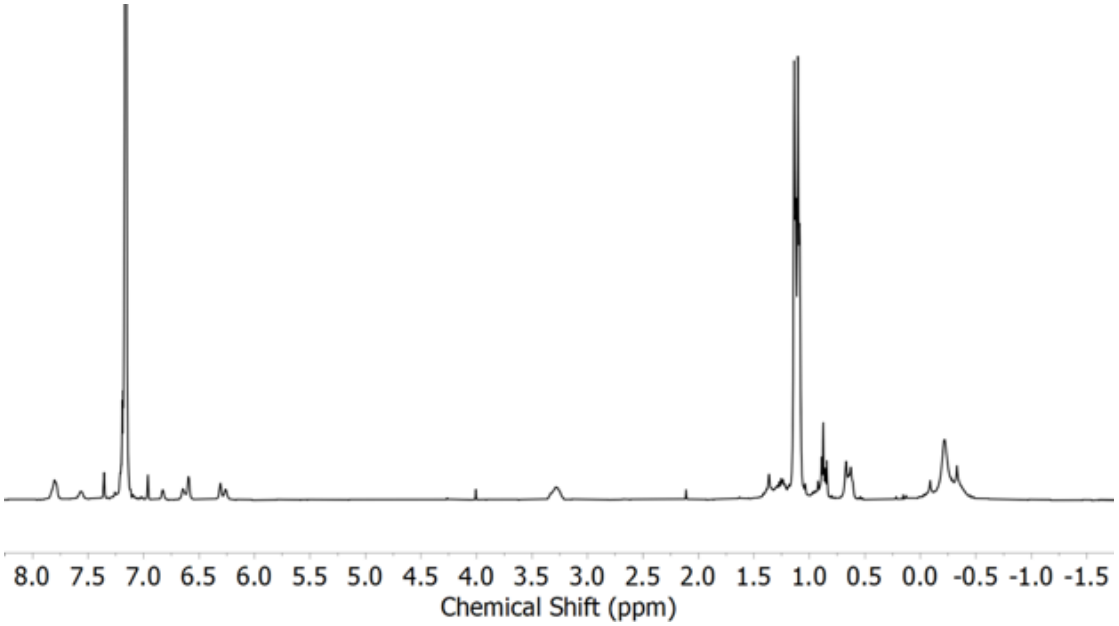

Figure F3. ^{1}H NMR spectrum (400 MHz, C_6D_6) for the isolated residue obtained after stirring a pentane solution of **1** with 5 equivalents of $AlMe_3$ for 30 minutes and evaporating the volatiles.

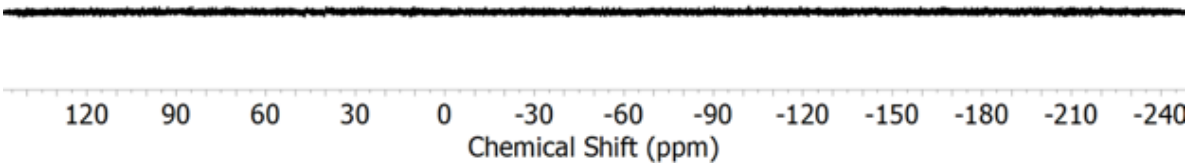

Figure F4. ^{31}P NMR spectrum (162 MHz, C_6D_6) for the isolated residue obtained after stirring a pentane solution of **1** with 5 equivalents of $AlMe_3$ for 30 minutes and evaporating the volatiles.

Electronic Absorption Spectra (EAS)

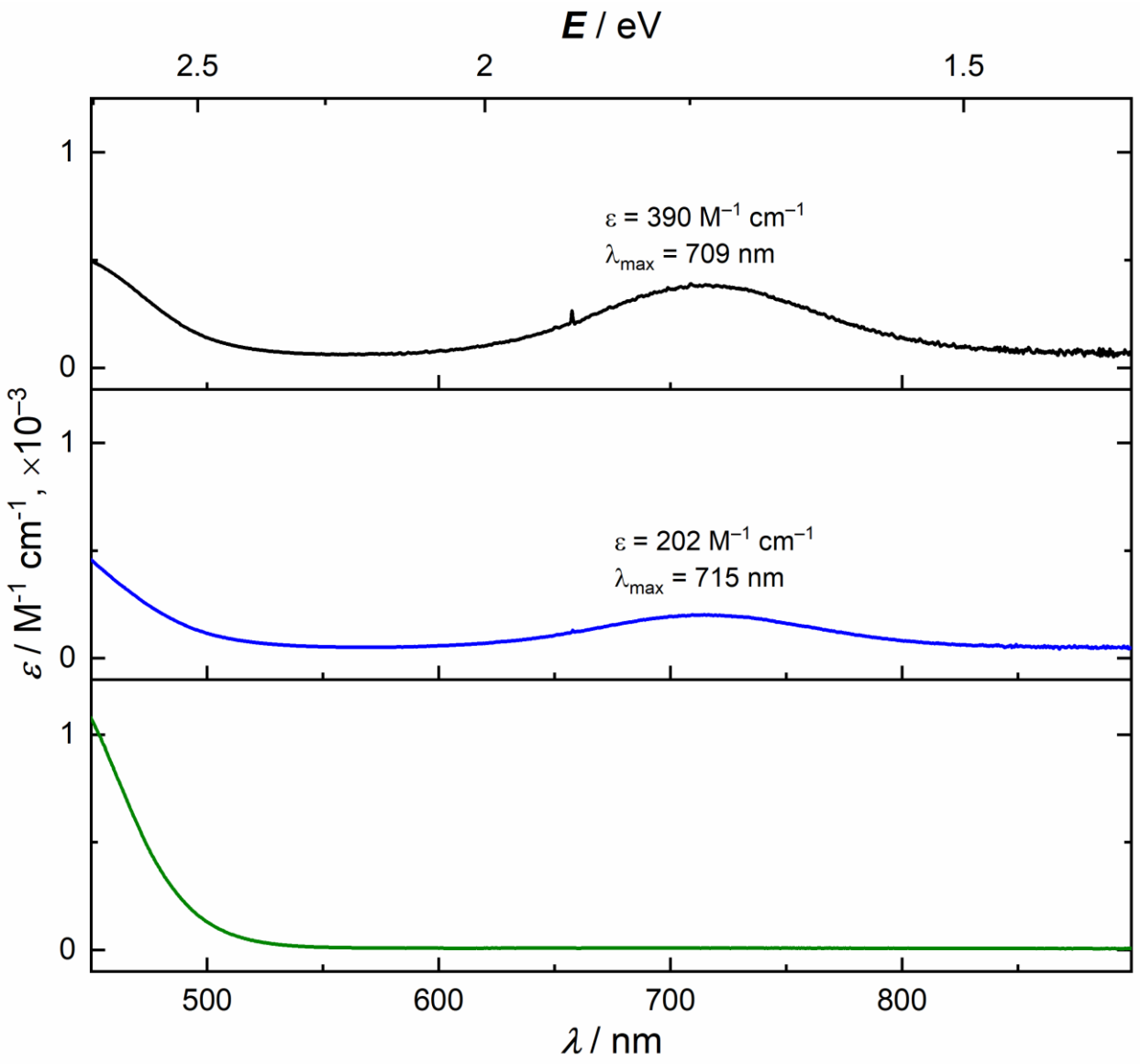

Figure F5. EA spectra of *in situ* generated **2-Et** (upper panel), **2-*i*Bu** (middle panel), and generated **2-Me** (lower panel) in THF. The spectra were recorded after stirring a THF solution of **1** with 5 equivalents of corresponding **AlR_3** (R = Et, *i*Bu, Me) for 30 minutes.

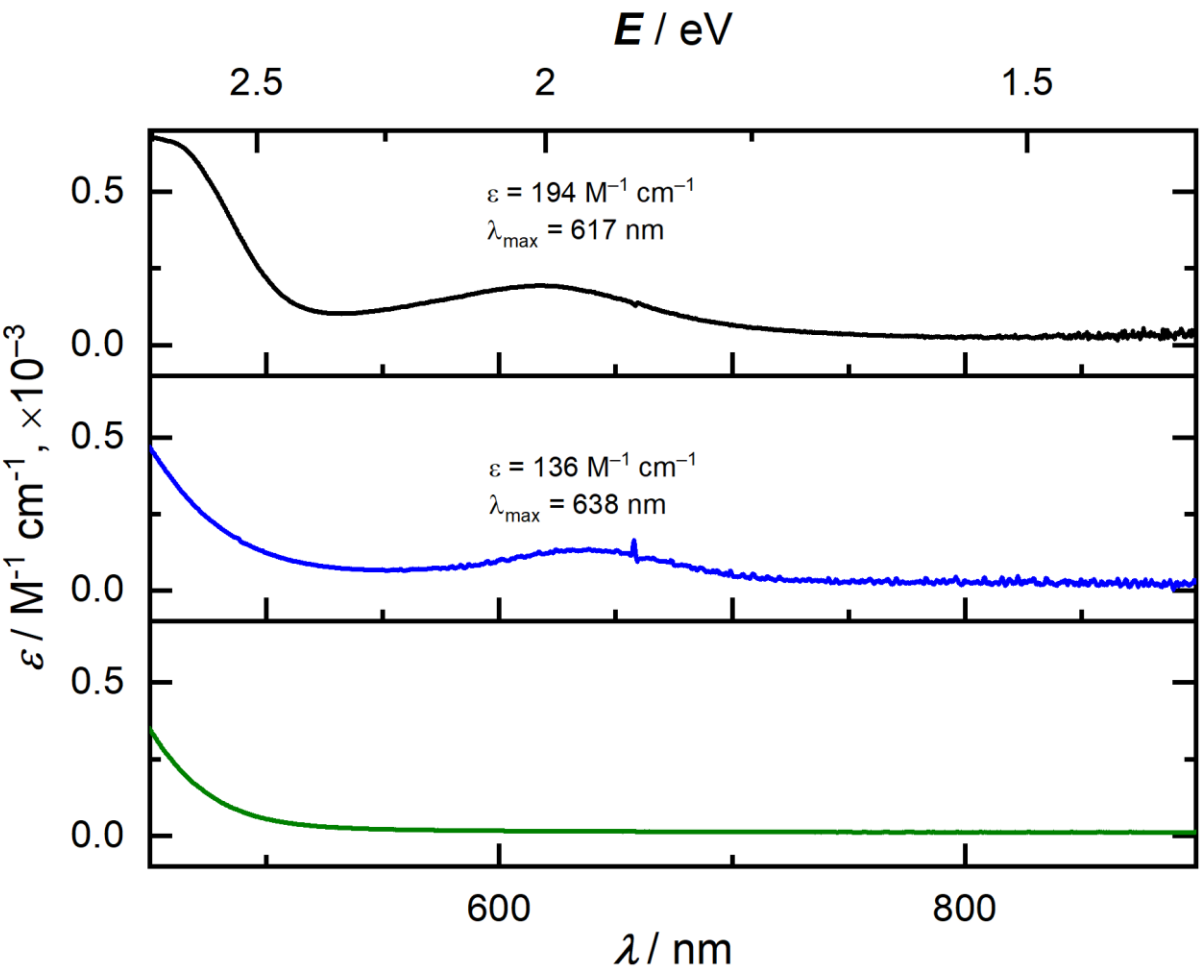

Figure F6. EA spectra of *in situ* generated **2-Et** (upper panel), **2-*i*Bu** (middle panel), and generated **2-Me** (lower panel) in pentane. The spectra were recorded after stirring a pentane solution of **1** with 5 equivalents of corresponding **AlR$_3$** (R = Et, *i*Bu, Me) for 30 minutes.

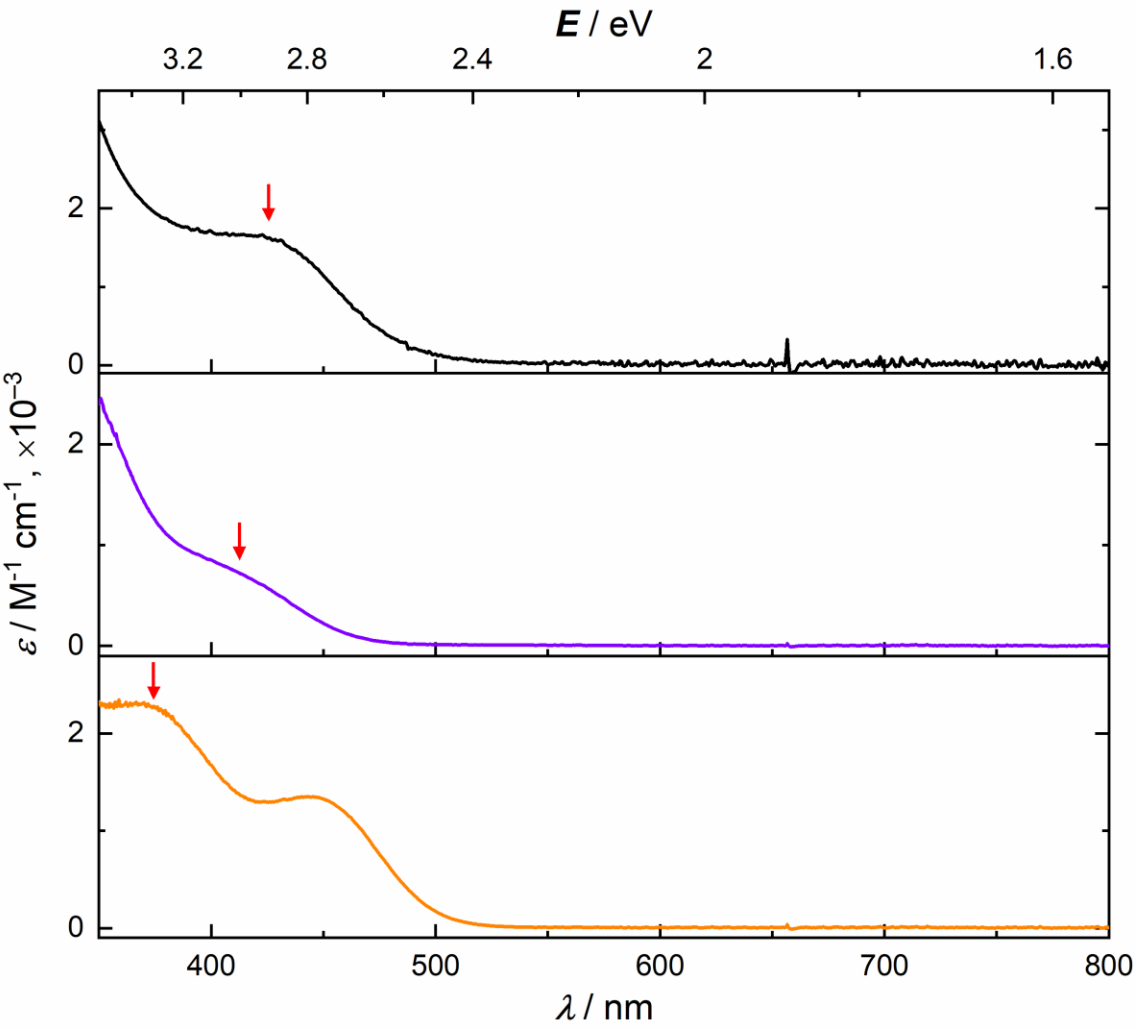

Figure F7. Electronic absorption spectra of **1** ([IndTi], black), **4** ([CpTi], violet), and **5** ([Cp*Ti], orange) in THF. The red arrows indicate the peak of interest that is linearly correlated with $E_{p,c}(Ti^{IV/III})$.

Polymerization

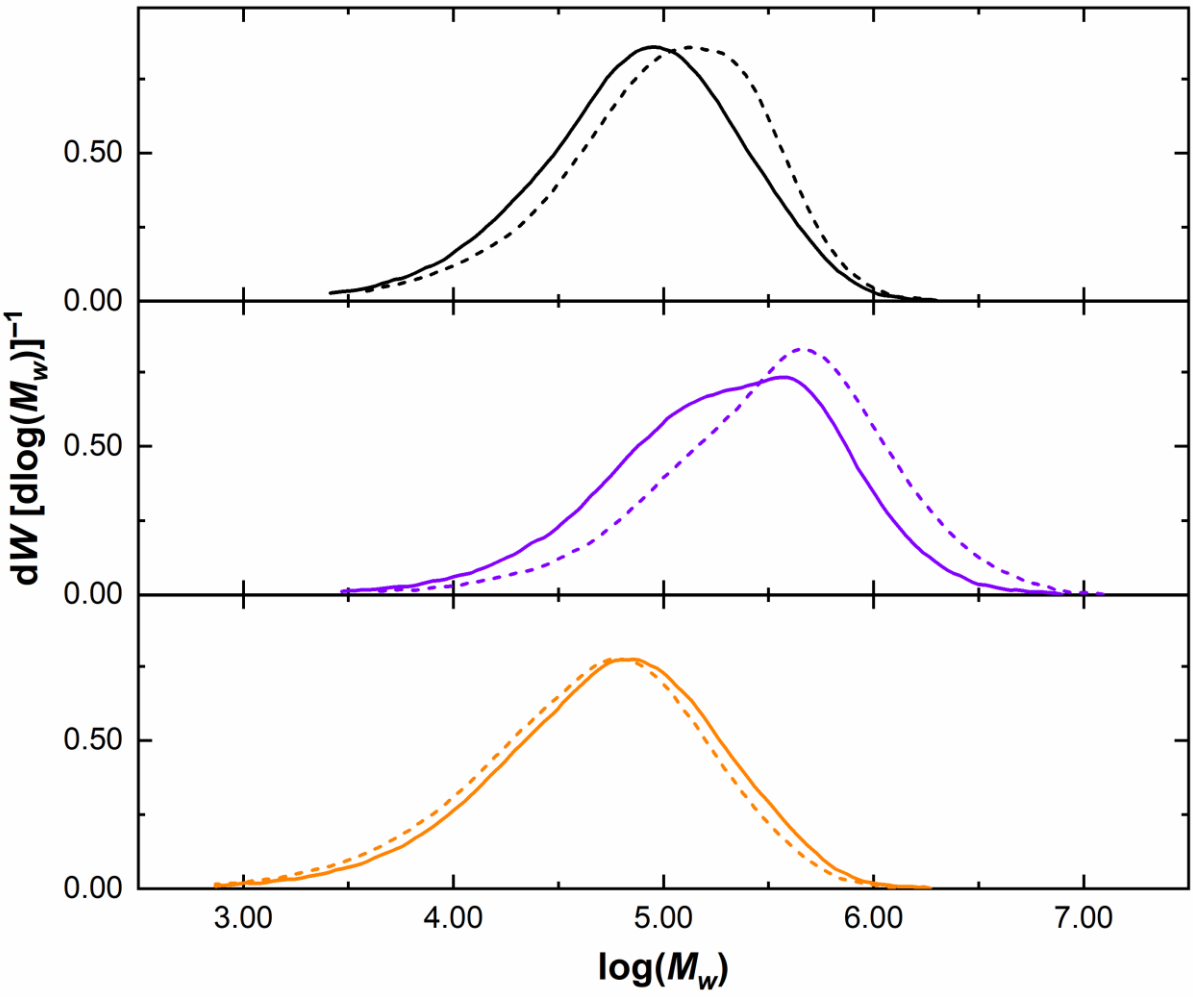

Figure F8. Gel permeation chromatograms for comparison of PE produced under a variety of conditions. Upper panel: PE produced with **1** [IndTi] and $AlEt_3$; not prereduced (black line) and prereduced (dotted black line). Middle panel: PE produced with **4** [CpTi] and $AlEt_3$; not prereduced (violet line) and prereduced (dotted violet line). Lower panel: PE produced with **5** [Cp*Ti] and $AlEt_3$; not prereduced (orange line) and prereduced (dotted orange line).

Electrochemistry

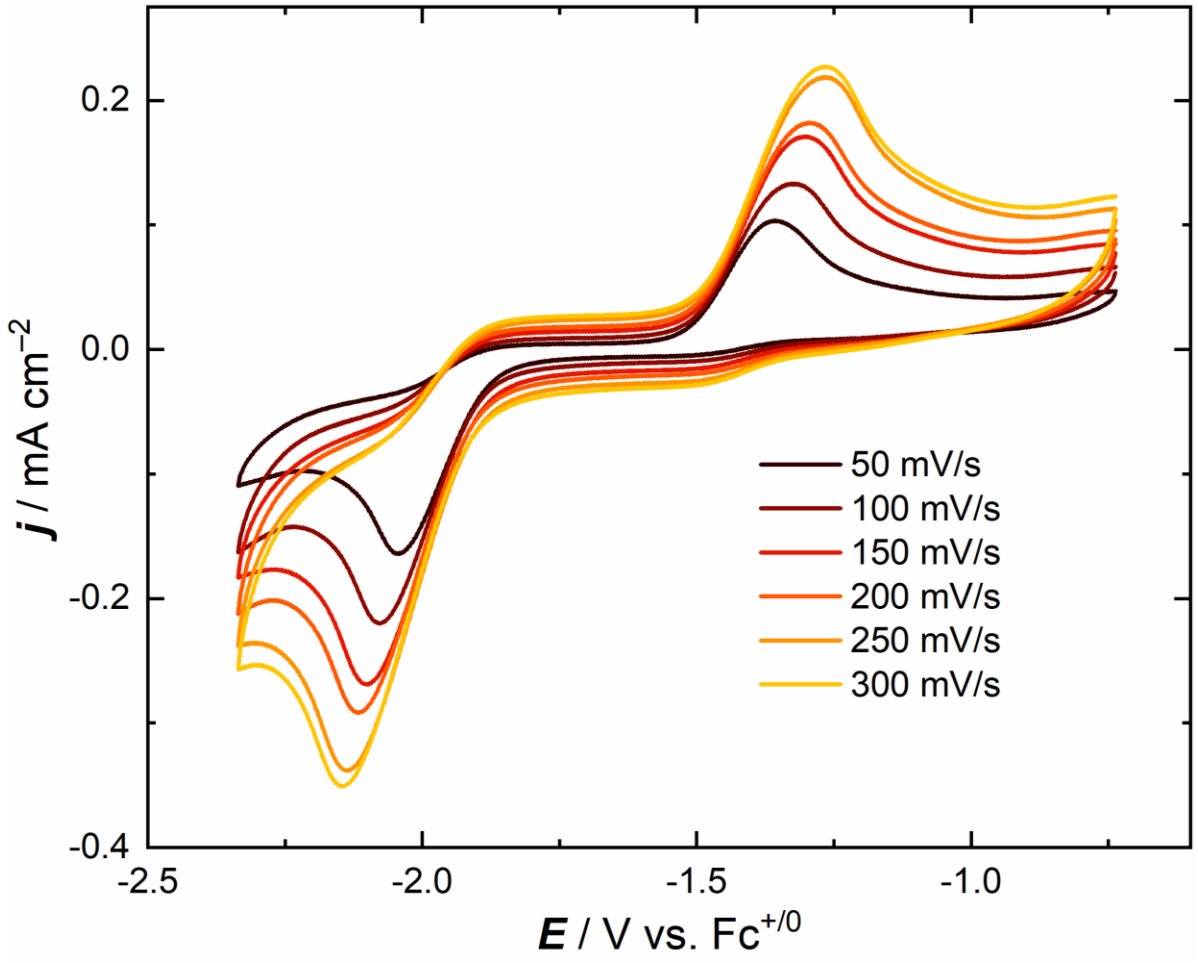

Figure F9. Cyclic voltammetry data for **1** in the presence of Al*i*Bu$_3$ in THF at varying scan rates (0.1 M [^{n}Bu$_4$N]$^+$[PF$_6$]$^-$).

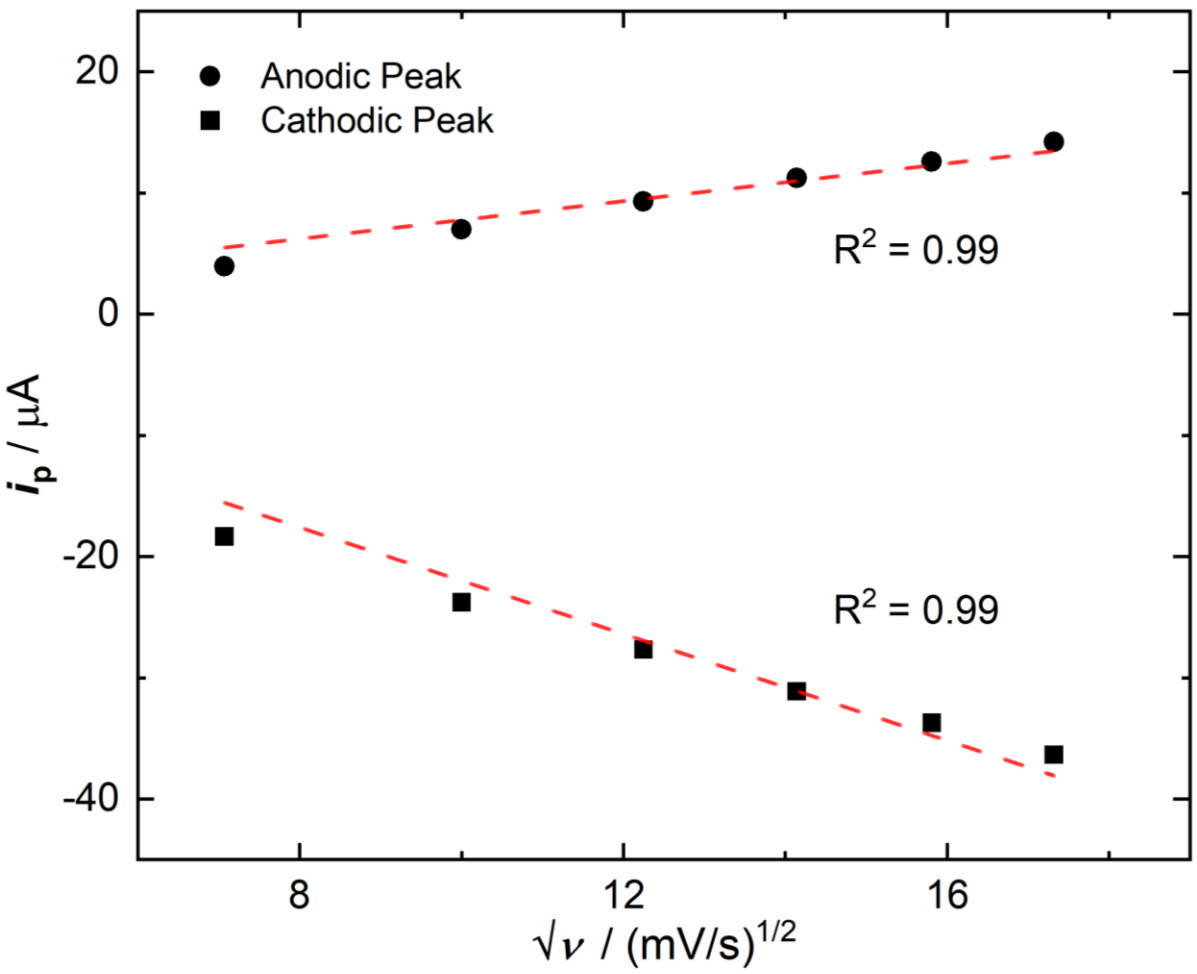

Figure F10. Linear dependence of peak current on the square root of scan rate for **1** in the presence of Al*i*Bu$_3$**.**

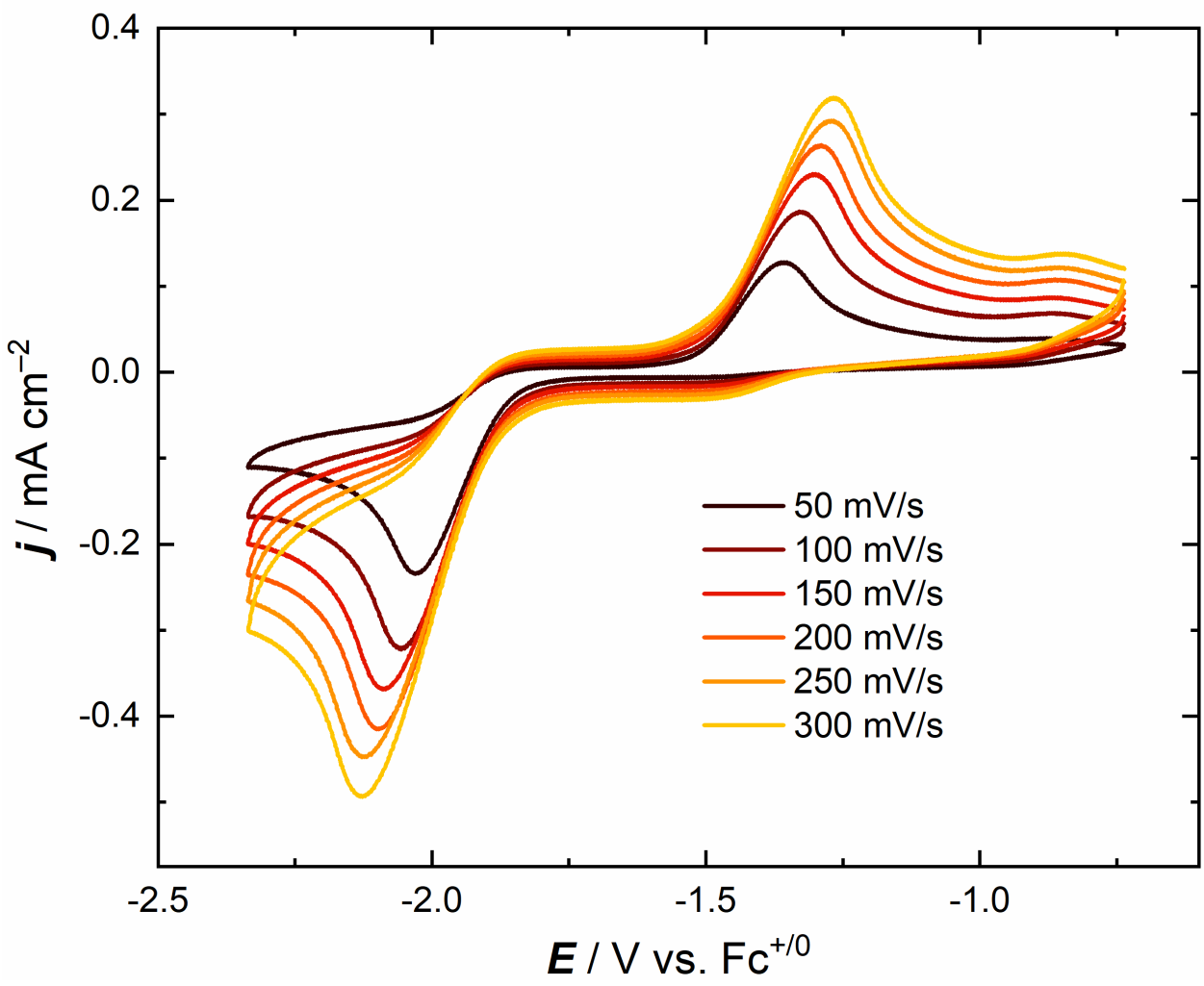

Figure F11. Cyclic voltammetry data for **1** in the presence of $AlMe_3$ in THF at varying scan rates (0.1 M $[^nBu_4N]^+[PF_6]^-$).

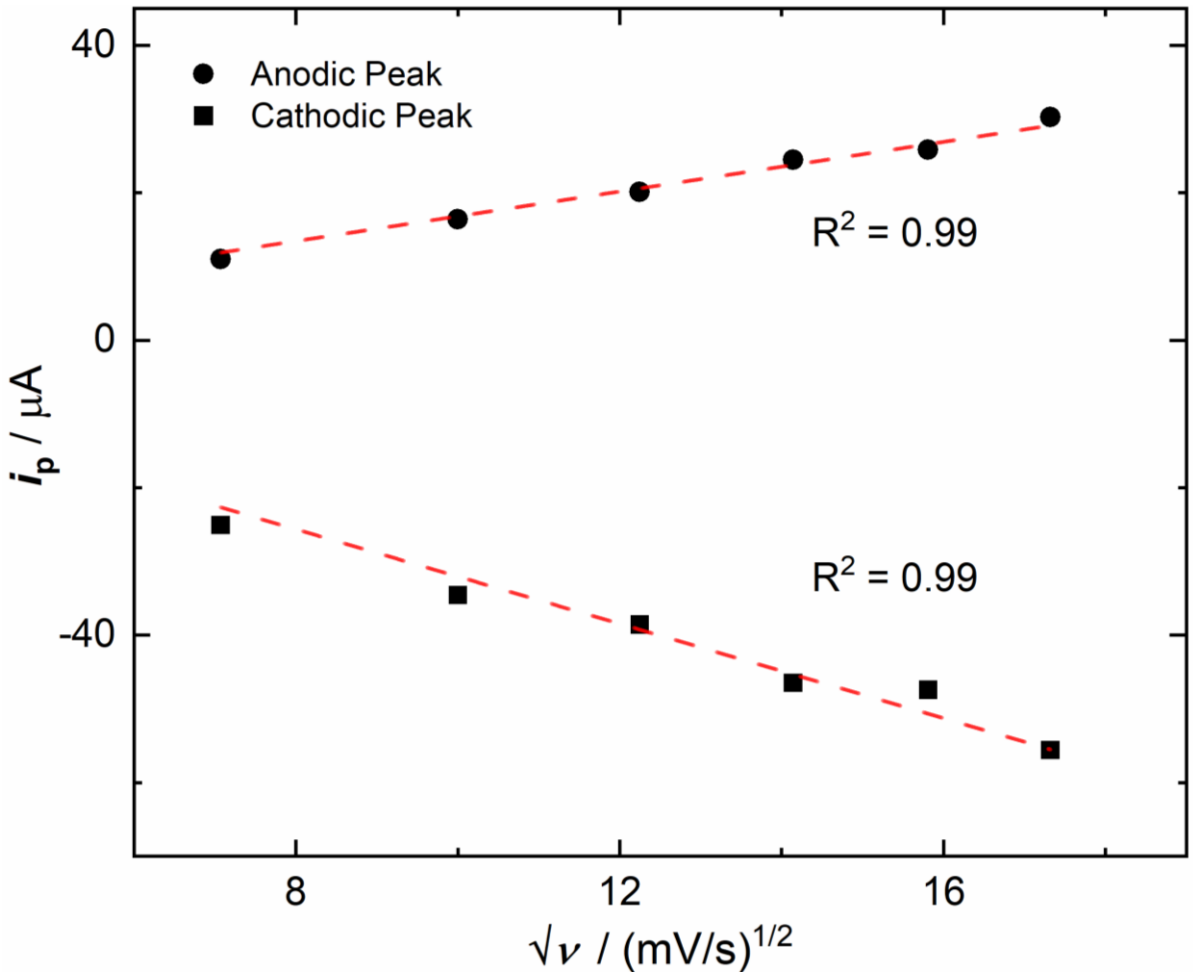

Figure F12. Linear dependence of peak current on the square root of scan rate for **1** in the presence of $AlMe_3$**.**

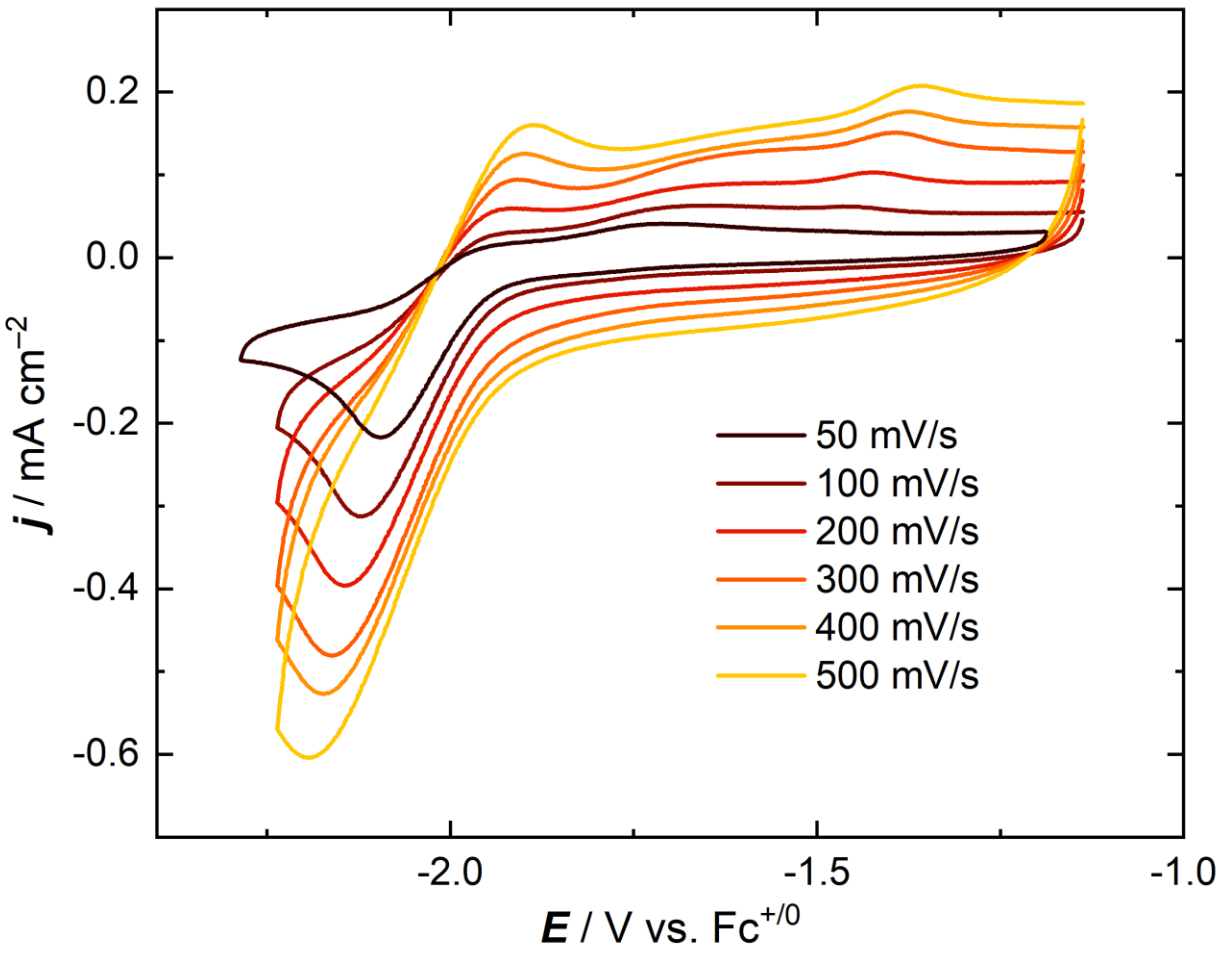

Figure F13. Scan rate dependence data for complex **1** demonstrating a coupled return oxidation after reduction at higher scan rates (>300 mV/s), implicating formation of the transient Ti^{III} species **1′**.

Gas Chromatography

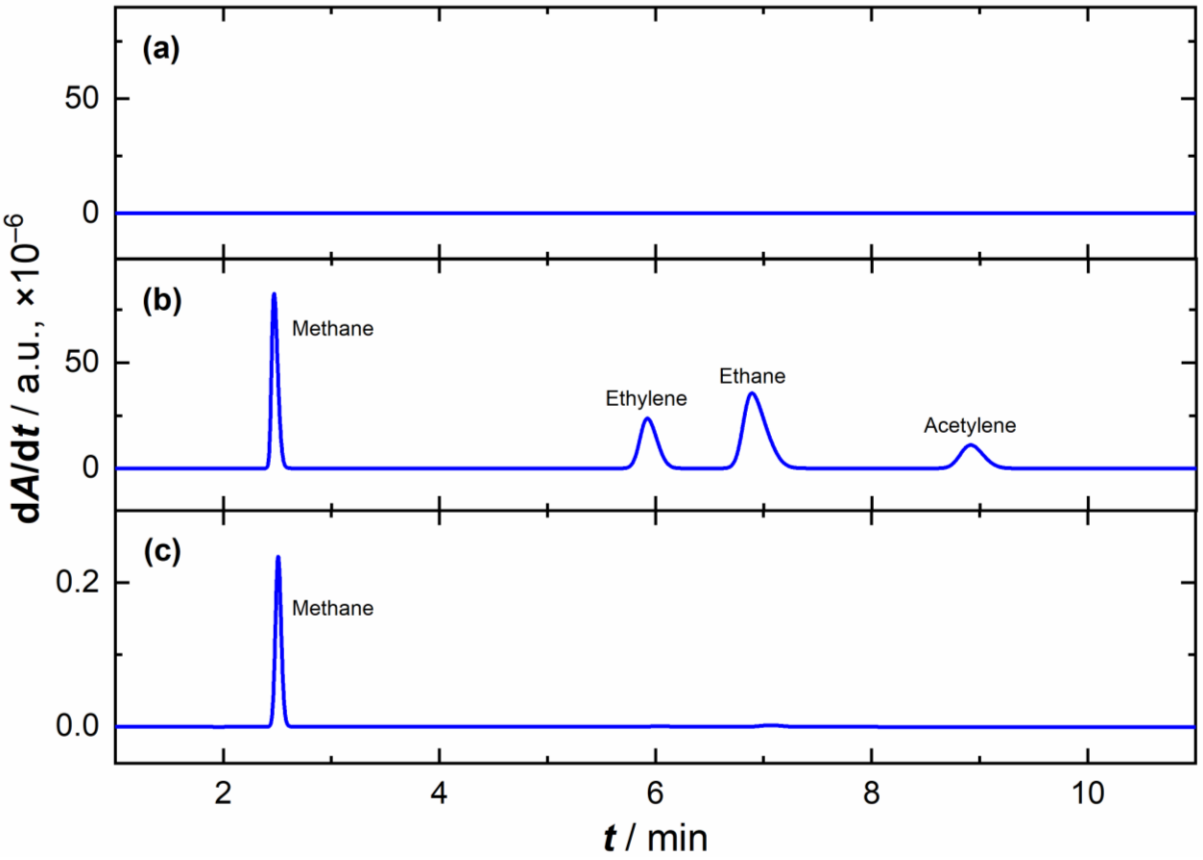

Figure F14. Gas chromatography data for **1** in the presence of Al*i*Bu$_3$ during chemical reduction; (a) Glovebox atmosphere, (b) Check Gas, (c) **1** with 2 equiv. of Al*i*Bu$_3$ in Pentane. The headspace of the reaction mixture was analyzed after 1 hour of stirring.

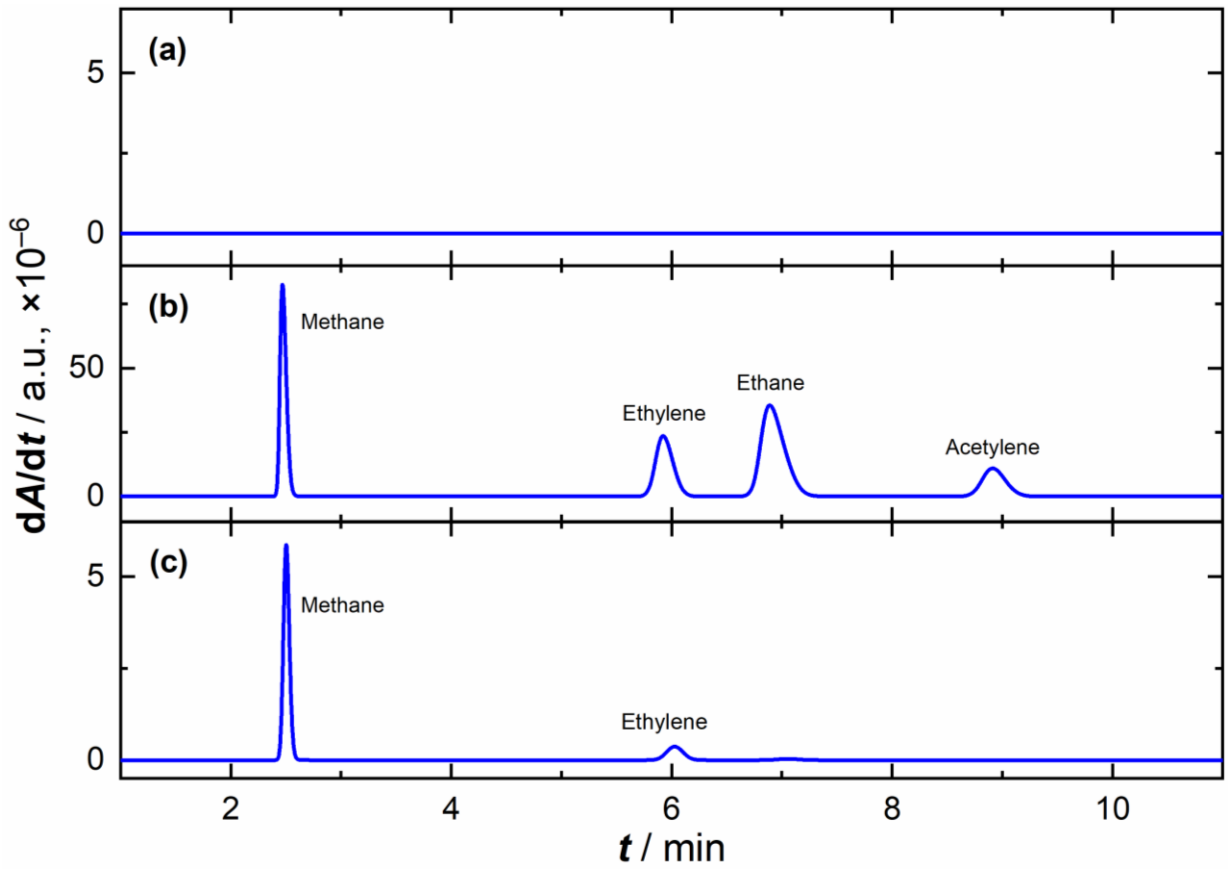

Figure F15. Gas chromatography for **1** in the presence of Al*i*Bu$_3$ during chemical reduction; (a) Glovebox atmosphere, (b) Check Gas, (c) **1** with 2 equiv. of Al*i*Bu$_3$ in Pentane. The headspace of the reaction mixture was analyzed after 24 hours of stirring.

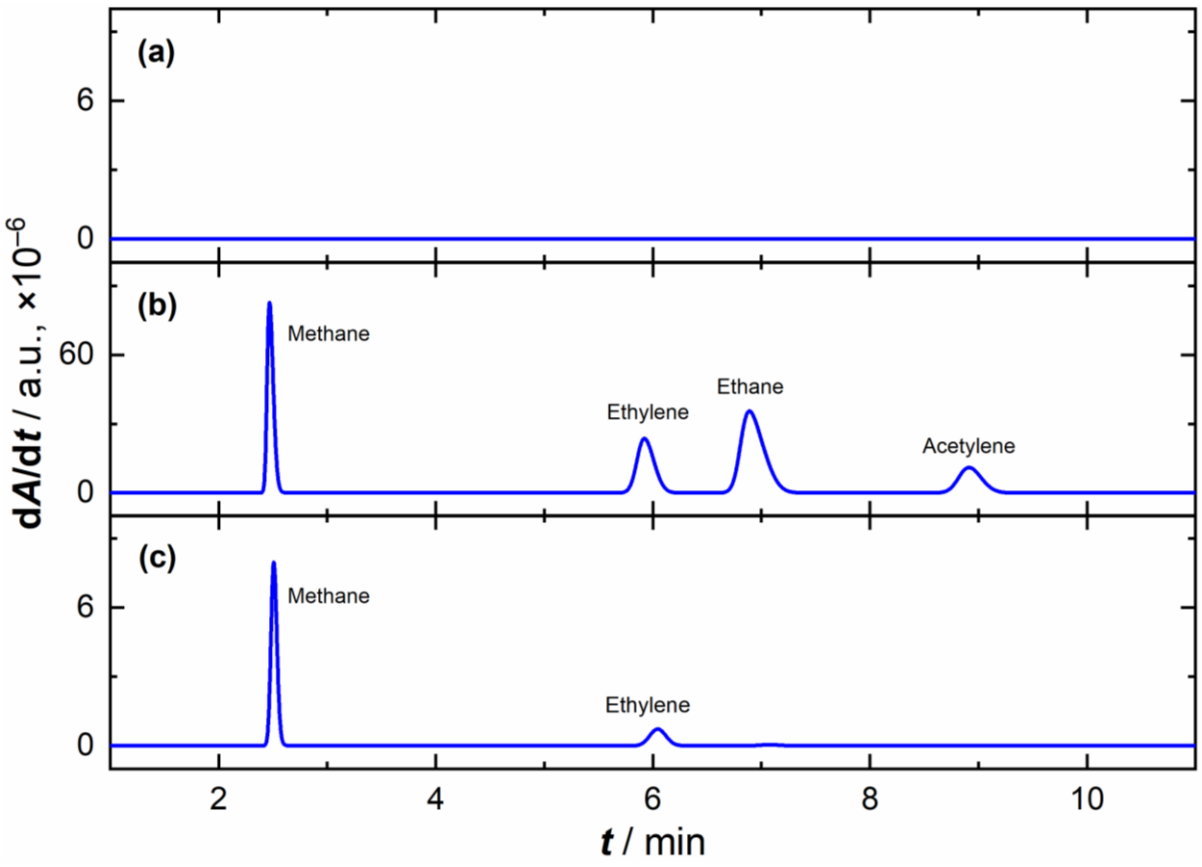

Figure F16. Gas chromatography for **1** in the presence of $AlMe_3$ during chemical reduction; (a) Glovebox atmosphere, (b) Check Gas, (c) **1** with 2 equiv. of $AlMe_3$ in Pentane. The headspace of the reaction mixture was analyzed after 1 hour of stirring.

EPR Spectra

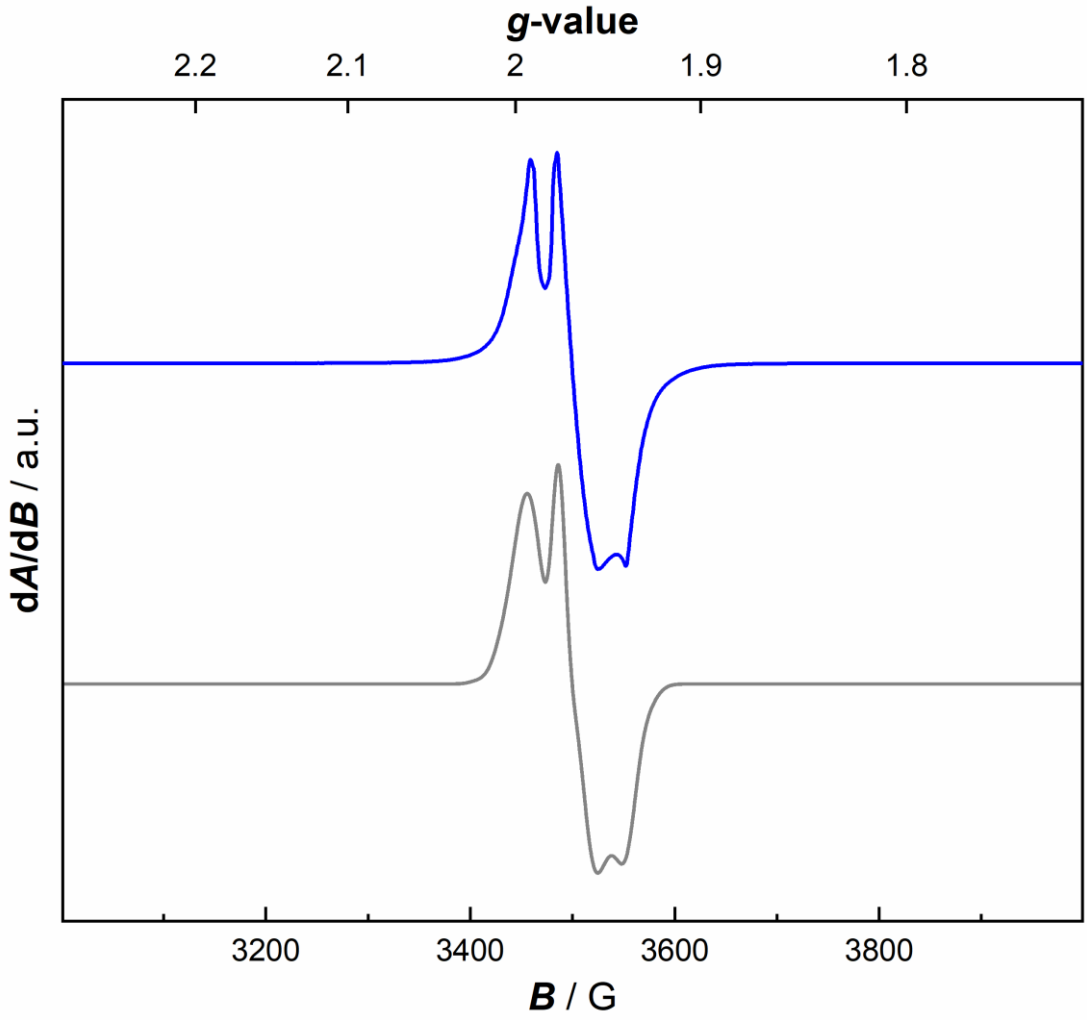

Figure F17. Blue trace: X-band CW EPR spectrum of *in situ* generated **1′** (using layering method by combining 1 equiv. of **1** and 1 equiv. of ketyl radical) in frozen THF at 10 K (Frequency: 9.6408 GHz; power: 2.000 mW; attenuation: 20.0 dB; time constant: 5.12 ms; modulation amplitude: 4.000 G). Grey trace: EasySpin simulation of EPR data; simulation parameters for component **A**: S = 1/2, g = [1.9754 1.9612 1.9404], nucleus: Ti, A = [65 38 2], HStrain = [12 54 63], lw = 1.51, weight = 0.75; simulation parameters for component **B** : S = 1/2, g = [1.9818], nucleus: (C,O), A = [34,99]; HStrain = [84], lw = 3.65, weight = 0.51. The ratio of the two components obtained from the fitting program was 1.5:1.

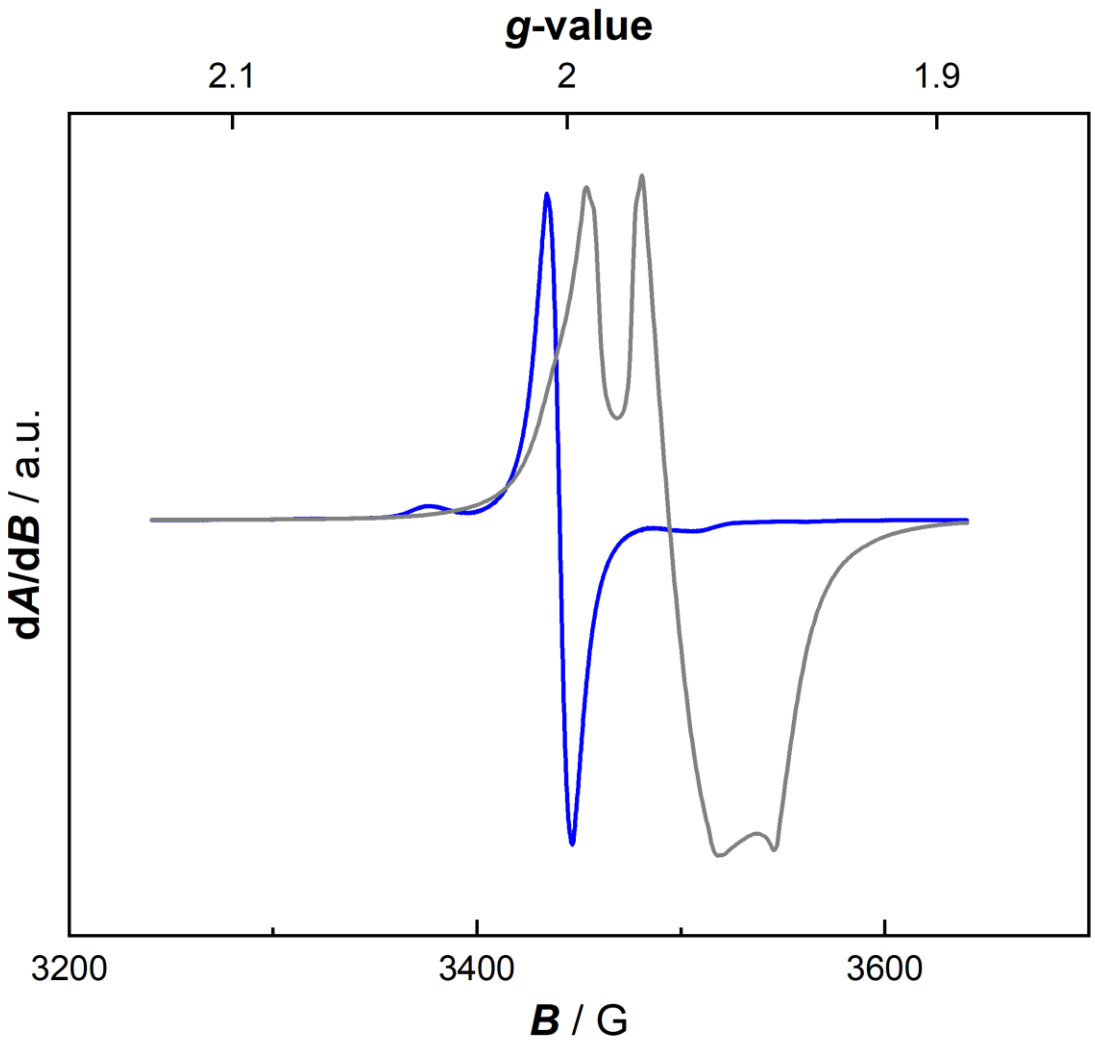

Figure F18. Blue trace: X-band CW EPR Spectrum of ketyl radical in frozen THF at 5 K (Frequency: 9.6411 GHz; power: 7.962 mW; attenuation: 14.0 dB; time constant: 10.24 ms; modulation amplitude: 6.993 G). Grey trace: X-band CW EPR spectrum of the mixture of 1 equiv. of **1** plus 1 equiv. of ketyl radical in frozen THF at 10 K (Frequency: 9.6408 GHz; power: 2.000 mW; attenuation: 20.0 dB; time constant: 5.12 ms; modulation amplitude: 4.000 G).

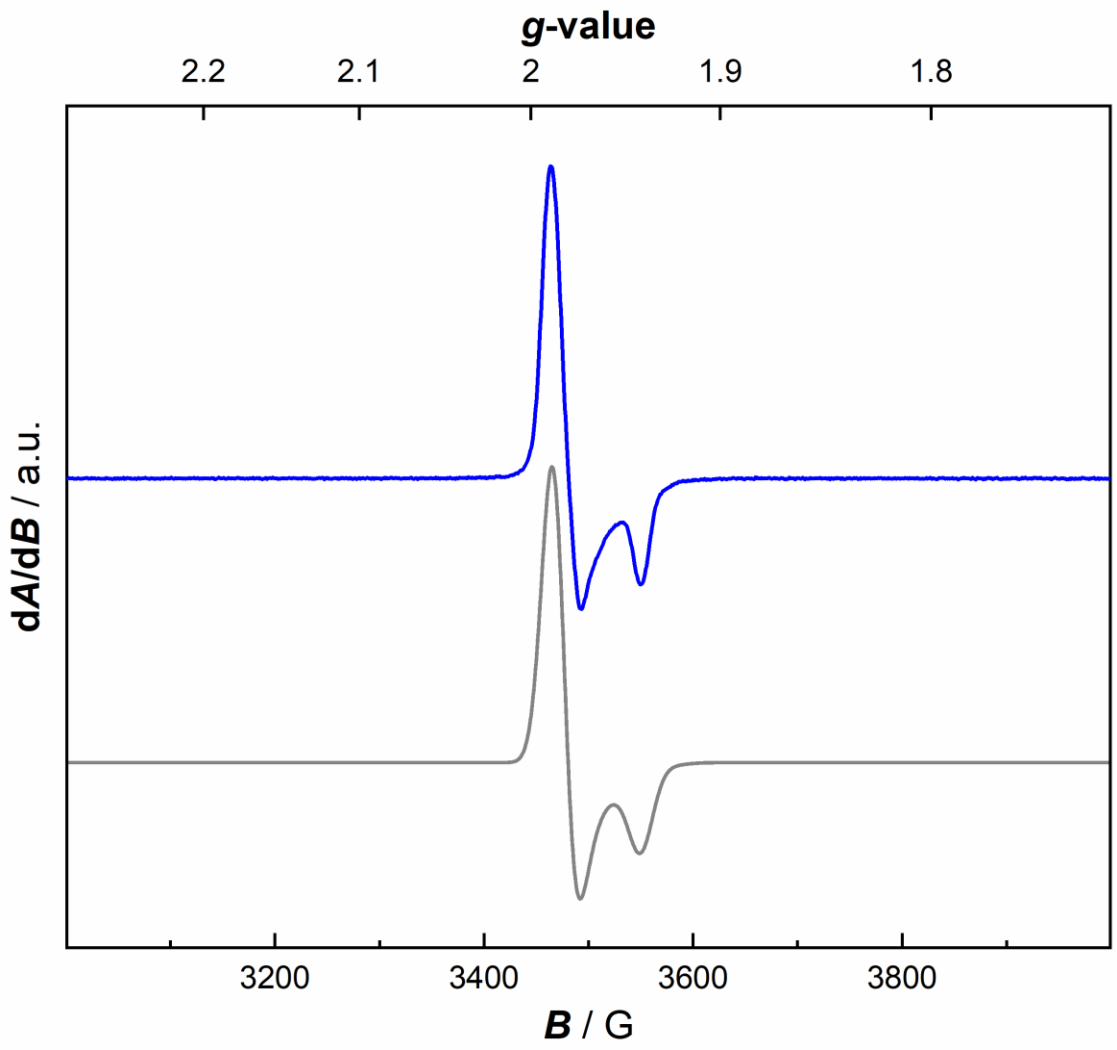

Figure F19. Blue: X-band CW EPR spectrum of cleanly isolated **2-Et** in frozen toluene at 55 K (Frequency: 9.6426 GHz; power: 0.032 mW; attenuation: 38.0 dB; time constant: 5.12 ms; modulation amplitude: 4.000 G). Grey: EasySpin simulation of EPR data; simulation parameters: S = 1/2, g = [1.9843 1.9405], nucleus: Ti, A = [2 34], HStrain = [15 1], lw = 2.69.

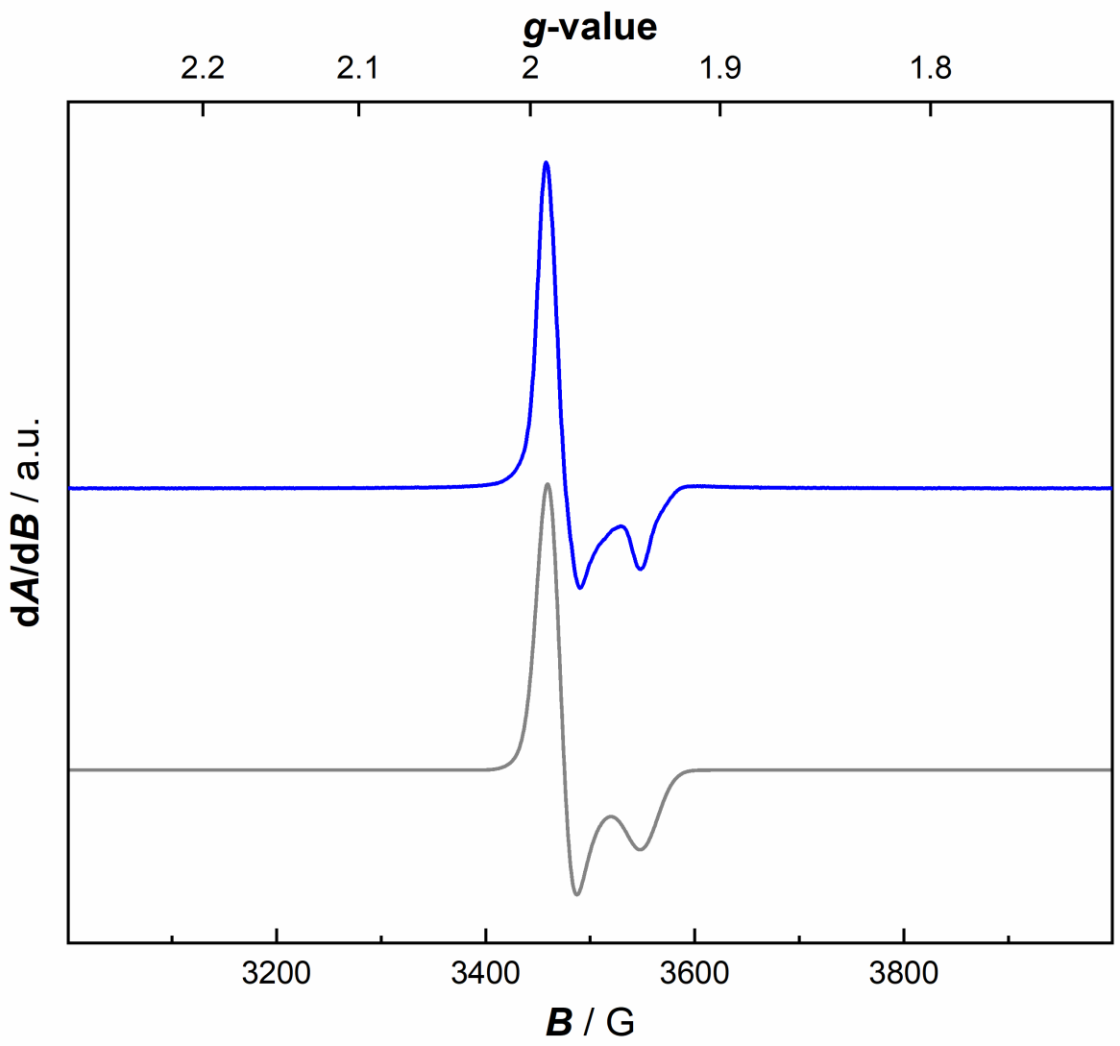

Figure F20. Blue: X-band CW EPR spectrum of cleanly isolated **2-*i*Bu** in frozen toluene at 10 K (Frequency: 9.6369 GHz; power: 0.032 mW; attenuation: 38.0 dB; time constant: 2.56 ms; modulation amplitude: 4.000 G). Grey: EasySpin simulation of EPR data; simulation parameters: S = 1/2, g = [1.9863 1.9392], nucleus: Ti, A = [27 1], HStrain = [39 72], lw = 2.43.

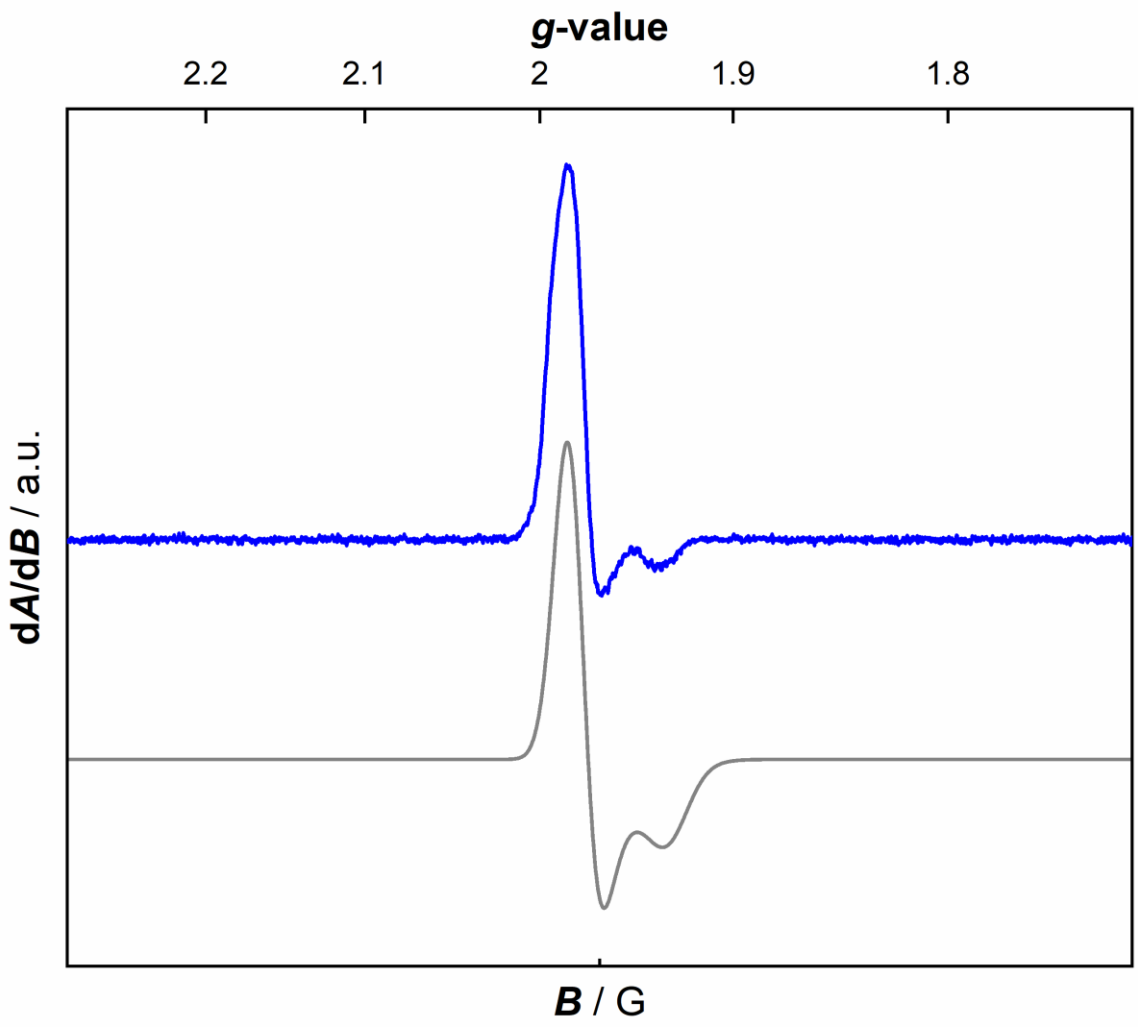

Figure F21. Blue: X-band CW EPR spectrum of *in situ* generated **2-Me** (using layering method by combining 1 equiv. of **1** and 5-6 equiv. of $AlMe_3$) in frozen toluene at 7.2 K (Frequency: 9.6394 GHz; power: 2.000 mW; attenuation: 20.0 dB; time constant: 2.56 ms; modulation amplitude: 4.000 G). Grey: EasySpin simulation of EPR data; simulation parameters: S = 1/2, g = [1.9797 1.9320], nucleus: Ti, A = [3 39], HStrain = [20 80], lw = 3.43.

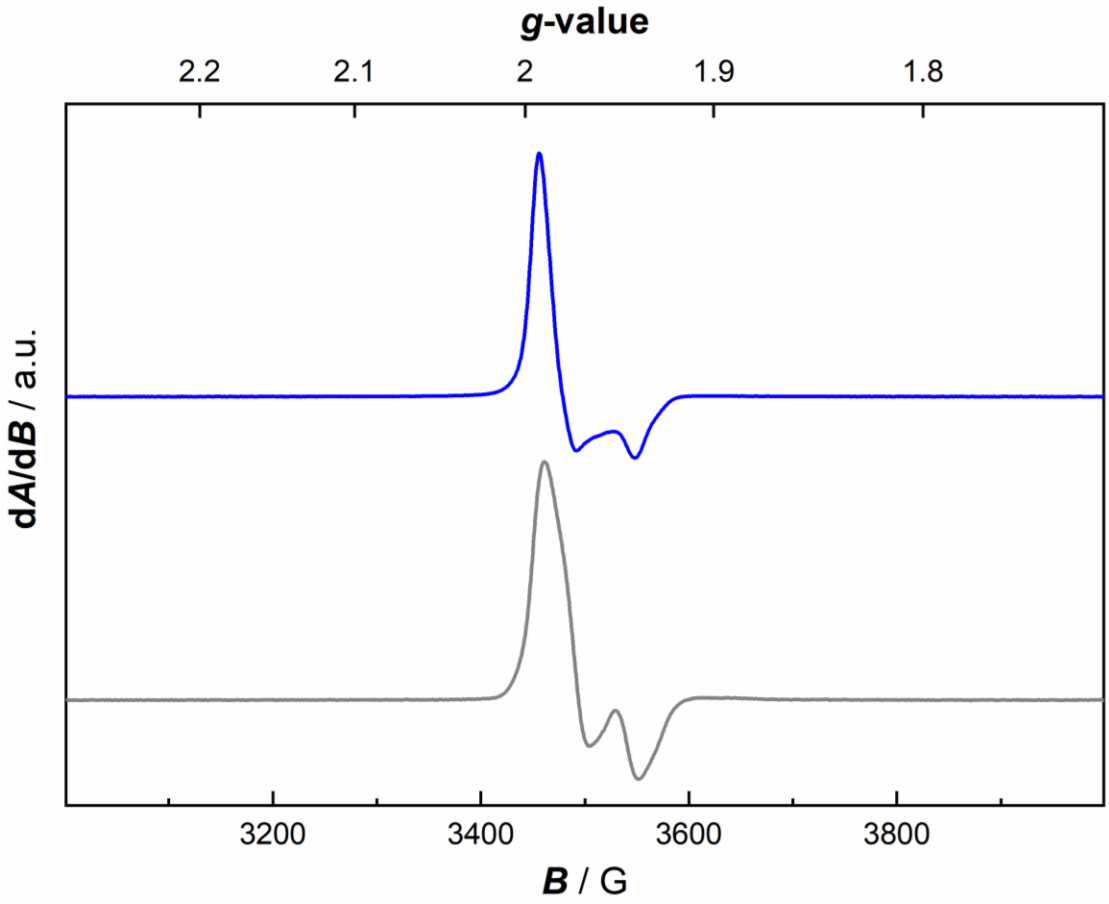

Figure F22. Blue: X-band CW EPR spectrum of *in situ* generated **2-*i*Bu** (mixture obtained after stirring 1 equiv. of **1** with 5-6 equiv. of Al*i*Bu$_3$ for 30 minutes) in frozen toluene at 7.6 K (Frequency: 9.6368 GHz; power: 0.1262 mW; attenuation: 32.0 dB; time constant: 2.56 ms; modulation amplitude: 4.000 G). Grey: X-band CW EPR spectrum of magenta-colored solution (mixture obtained after stirring **1** with 5-6 equiv. of Al*i*Bu$_3$ for 24 hours) in frozen toluene at 10 K under perpendicular mode (Frequency: 9.6423 GHz; power: 0.1262 mW; attenuation: 32.0 dB; time constant: 5.12 ms; modulation amplitude: 4.000 G).

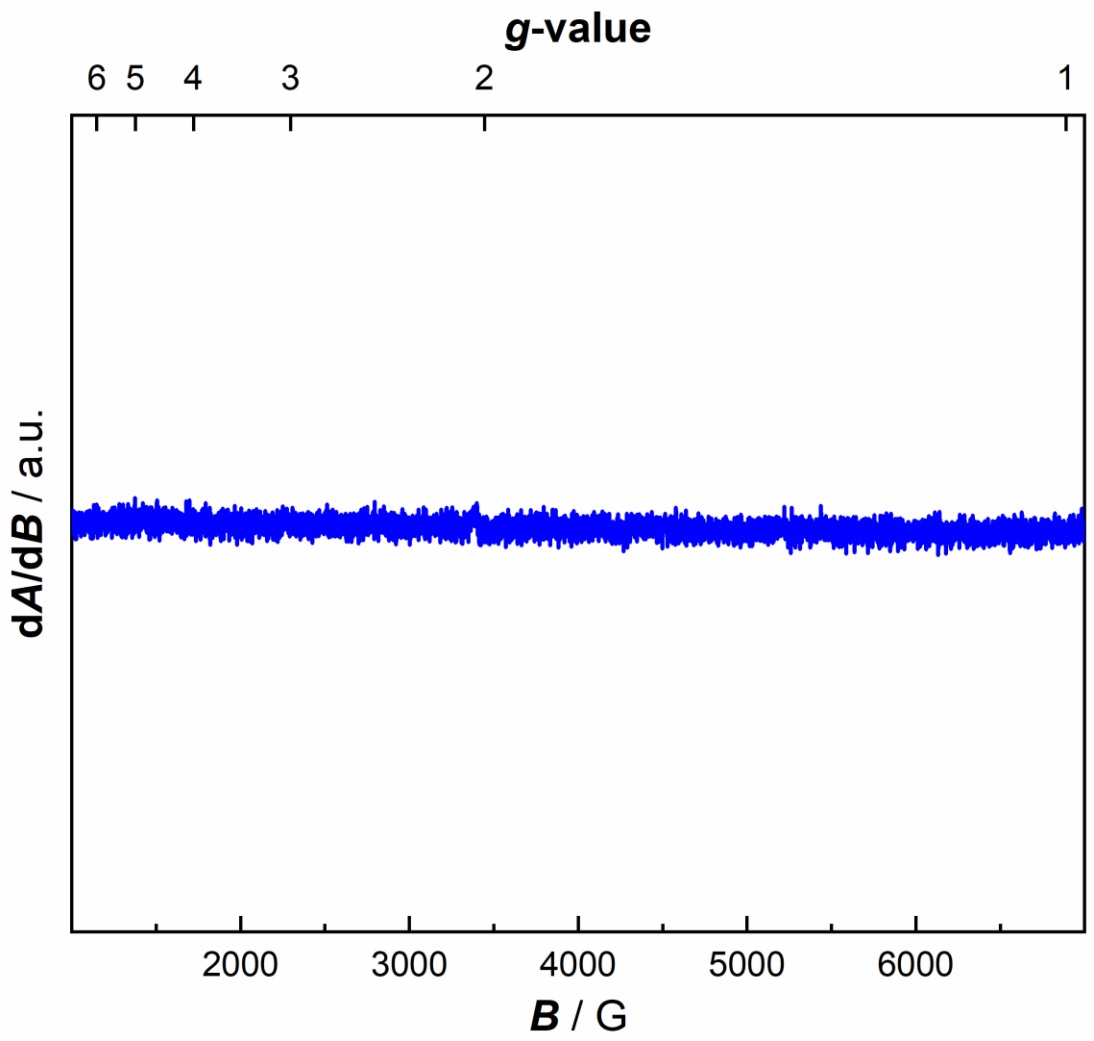

Figure F23. X-band CW EPR spectrum of magenta-colored solution (mixture obtained after stirring 1 equiv. of **1** with 5-6 equiv. of Al*i*Bu$_3$ for 24 hours) in frozen toluene under parallel mode (Frequency: 9.4326 GHz; power: 2.000 mW; attenuation: 20.0 dB; time constant: 10.24 ms; modulation amplitude: 6.000 G).

X-Ray Crystallography

2-*i*Bu (Prepared with Al*i*Bu$_3$)

The single-crystal X-ray diffraction studies were carried out on a Bruker Kappa APEX-II CCD diffractometer equipped with Mo K_α radiation (λ = 0.71073 Å). A 0.357 x 0.286 x 0.241 mm piece of a green block was mounted on a Cryoloop with Paratone oil. Data were collected in a nitrogen gas stream at 125(2) K using φ and ω scans. Crystal-to-detector distance was 50 mm, and the exposure time was 2 seconds per frame using a scan width of 2.0°. Data collection was 100% complete to 25.00° in θ. A total of 64660 reflections were collected covering the indices, –29<=h<=29, –13<=k<=13, –25<=l<=31. 6713 reflections were found to be symmetry independent, with a Rint of 0.0939. Indexing and unit cell refinement indicated a primitive, orthorhombic lattice. The space group was found to be Pbca. The data were integrated using the Bruker SAINT software program[1] and scaled using the SADABS[2] software program. Solution by direct methods (SHELXT)[3] produced a complete phasing model consistent with the proposed structure. All nonhydrogen atoms were refined anisotropically by full-matrix least-squares (SHELXL-2014).[4,5] All hydrogen atoms were placed using a riding model. Their positions were constrained relative to their parent atom using the appropriate HFIX command in SHELXL-2014. Crystallographic data are summarized in Table S1.

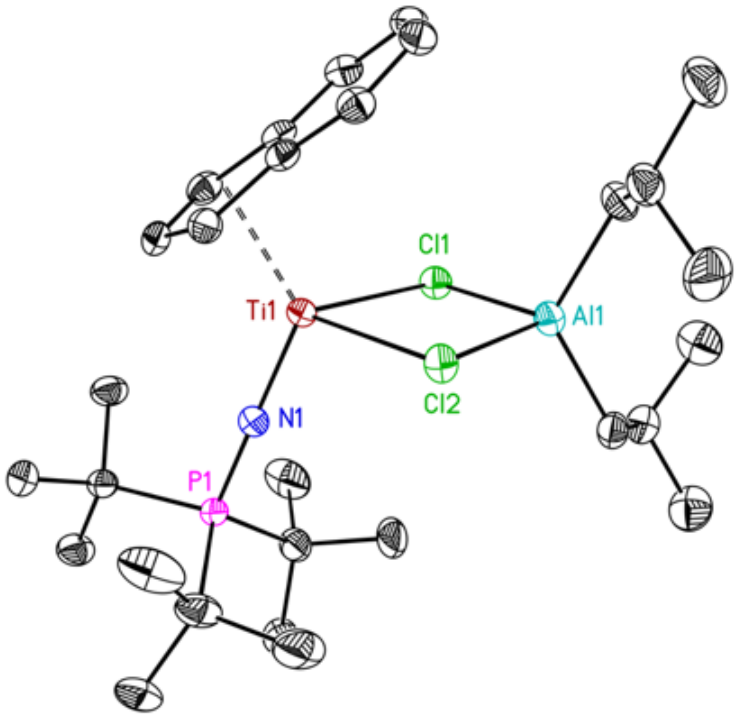

Figure F24. Solid-state structure (from XRD) of **2-*i*Bu** produced from the reaction of **1** with Al*i*Bu$_3$. Displacement ellipsoids are shown at the 50% probability level.

2-*i*Bu (Prepared with Al*i*Bu$_2$H)

The single-crystal X-ray diffraction studies were carried out on a Bruker APEX-II ULTRA CCD diffractometer equipped with Mo K_α radiation (λ = 0.71073 Å). Crystals of the subject compound were used as received (grown from hexane at -30°C). A 0.130 x 0.100 x 0.075 mm green block crystal was mounted on a Cryoloop with Paratone oil. Data were collected in a nitrogen gas stream at 100(2) K using φ and ω scans. Crystal-to-detector distance was 60 mm, and the exposure time was 4.0 seconds per frame using a scan width of 0.80°. Data collection was 100.0% complete to 25.242° in θ. A total of 60471 reflections were collected covering the indices, –30<=h<=20, –13<=k<=13, –31<=l<=27. 6937 reflections were found to be symmetry independent, with a R_{int} of 0.0547. Indexing and unit cell refinement indicated a Primitive, Orthorhombic lattice. The space

group was found to be Pbca. The data were integrated using the Bruker SAINT Software program[3] and scaled using the SADABS[4] software program. Solution by direct methods (SHELXT)[5] produced a complete phasing model consistent with the proposed structure. All nonhydrogen atoms were refined anisotropically by full-matrix least-squares (SHELXL-2014).[6,7] All carbon bonded hydrogen atoms were placed using a riding model. Their positions were constrained relative to their parent atom using the appropriate HFIX command in SHELXL-2014. Crystallographic data are summarized in Table S1.

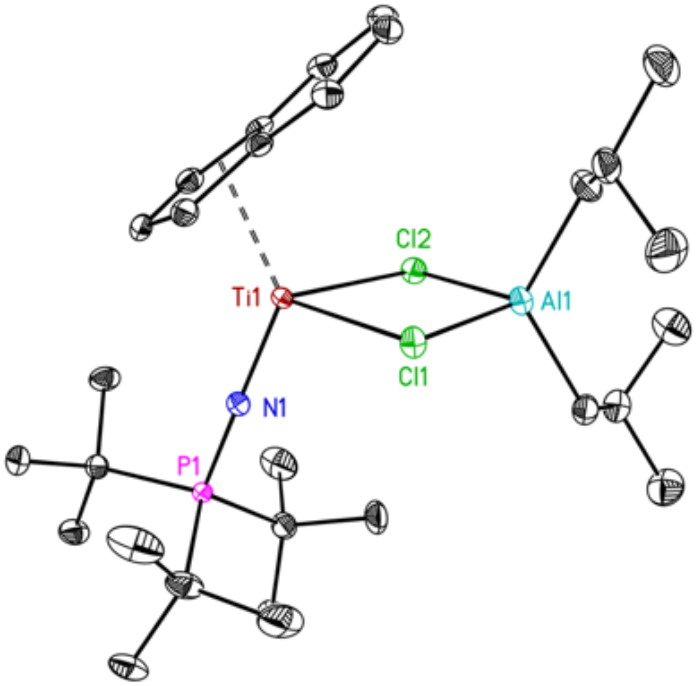

Figure F25. Solid-state structure (from XRD) of **2-*i*Bu** produced from the reaction of **1** with Al*i*Bu$_2$H. Displacement ellipsoids are shown at the 50% probability level.

3

The single-crystal X-ray diffraction studies were carried out on a Bruker Kappa APEX-II CCD diffractometer equipped with Mo K_α radiation (λ = 0.71073 Å). A 0.117 x 0.103 x 0.085 mm piece of an orange block was mounted on a Cryoloop with Paratone oil. Data were collected in a nitrogen

gas stream at 100(2) K using φ and ω scans. Crystal-to-detector distance was 40 mm, and the exposure time was 30 seconds per frame using a scan width of 0.70°. Data collection was 100% complete to 25.00° in *θ*. A total of 53264 reflections were collected covering the indices, –16<=h<=16, –20<=k<=13, –18<=l<=18. 6829 reflections were found to be symmetry independent, with a Rint of 0.0700. Indexing and unit cell refinement indicated a primitive, monoclinic lattice. The space group was found to be P21/c. The data were integrated using the Bruker SAINT software program[3] and scaled using the SADABS[4] software program. Solution by direct methods (SHELXT)[5] produced a complete phasing model consistent with the proposed structure. All nonhydrogen atoms were refined anisotropically by full-matrix least-squares (SHELXL-2014).[6,7] All hydrogen atoms were placed using a riding model. Their positions were constrained relative to their parent atom using the appropriate HFIX command in SHELXL-2014. Crystallographic data are summarized in Table S2.

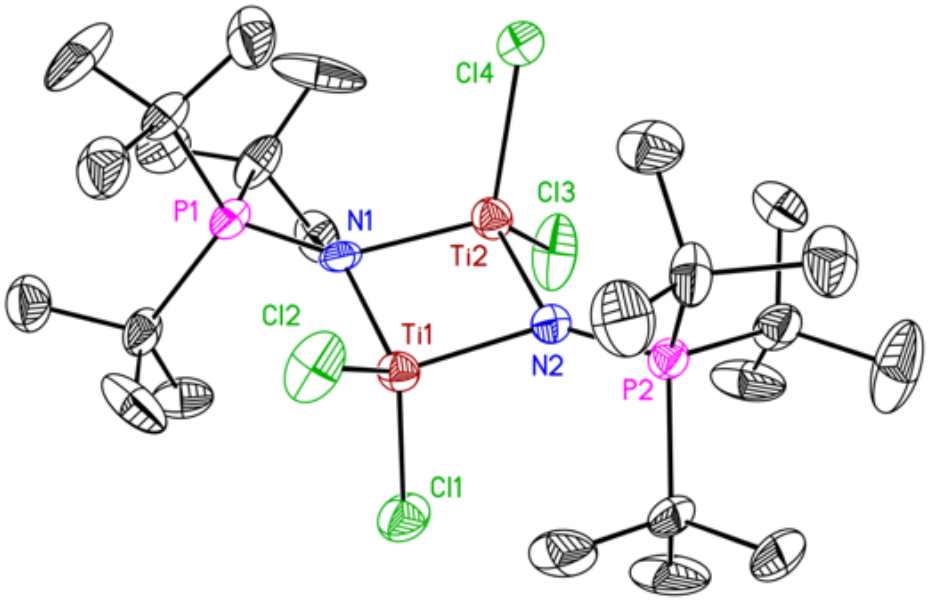

Figure F26. Solid-state structure (from XRD) of **3**. Displacement ellipsoids are shown at the 50% probability level.

Table F1. Crystal and Refinement Data for **2-*i*Bu** (from Al*i*Bu$_3$) and **2-*i*Bu** (from Al*i*Bu$_2$H).

	2-*i*Bu (from Al*i*Bu$_3$)	**2-*i*Bu** (from Al*i*Bu$_2$H)
CCDC deposition number	2010189	2010188
Empirical formula	$C_{29}H_{52}AlCl_2NPTi$	$C_{29}H_{52}AlCl_2NPTi$
Formula weight	591.46	591.46
Temperature	125	100
Wavelength	0.71073	0.71073
Crystal system	orthorhombic	orthorhombic
Space group	Pbca	Pbca
a	23.9159(19)	23.9084(5)
b	10.9314(9)	10.9331(2)
c	25.056(2)	25.0243(6)
α	90	90
β	90	90
γ	90	90
Volume	6550.6(9)	6541.2(2)
Z	8	8
Density (calculated)	1.199	1.201
F(000)	2536.0	2536.0
Crystal size	0.357 × 0.286 × 0.241	0.13 × 0.1 × 0.075
2θ range	3.406 to 52.832	3.256 to 53.462
Index ranges	$-29 \le h \le 29$, $-13 \le k \le 13$, $-26 \le l \le 31$	$-30 \le h \le 20$, $-13 \le k \le 13$, $-31 \le l \le 27$
Reflections collected	64660	60471
Independent reflections	6713 [R_{int} = 0.0939, R_{sigma} = 0.0541]	6937 [R_{int} = 0.0547, R_{sigma} = 0.0324]
Absorption correction	multi-scan	multi-scan
Refinement method	Full-matrix least-squares on F^2	Full-matrix least-squares on F^2
Data/restraints/parameters	6713/0/329	6937/0/329
Goodness-of-fit on F^2	1.013	1.040
Final R indices [I>2σ(I)]	R_1 = 0.0392, wR_2 = 0.0884	R_1 = 0.0312, wR_2 = 0.0712
R indices (all data)	R_1 = 0.0571, wR_2 = 0.0980	R_1 = 0.0428, wR_2 = 0.0770
Largest diff. peak & hole	0.29 and –0.35 $e^-/Å^3$	0.59 and –0.24 $e^-/Å^3$

Table F2. Crystal and Refinement Data for **3**.

	2-*i*Bu (from Al*i*Bu$_3$)
CCDC deposition number	2010190
Empirical formula	$C_{24}H_{54}Cl_4N_2P_2Ti_2$
Formula weight	670.23
Temperature	100
Wavelength	0.71073
Crystal system	monoclinic
Space group	$P2_1/c$
a	13.4629(17)
b	16.393(2)
c	14.889(2)
α	90
β	90.048(6)
γ	90
Volume	3285.9(7)
Z	4
Density (calculated)	1.355
F(000)	1416.0
Crystal size	0.117 × 0.103 × 0.085
2θ range	2.484 to 53.07
Index ranges	$-16 \le h \le 16$, $-20 \le k \le 13$, $-18 \le l \le 18$
Reflections collected	53264
Independent reflections	6829 [R_{int} = 0.0700, R_{sigma} = 0.0481]
Absorption correction	multi-scan
Refinement method	Full-matrix least-squares on F^2
Data/restraints/parameters	6829/0/326
Goodness-of-fit on F^2	1.033
Final R indices [I>2σ(I)]	R_1 = 0.0729, wR_2 = 0.1785
R indices (all data)	R_1 = 0.1007, wR_2 = 0.1995
Largest diff. peak & hole	1.37 and –0.46 $e^-/Å^3$

References

(1) *SAINT. Ver. 8.34A.* Bruker Analytical X-ray Systems: Madison, WI, June 2014.

(2) *Sheldrick, G. M., SADABS (version 2008/1)*: Program for Absorption Correction for Data from Area Detector Frames, University of Göttingen, 2008.

(3) Sheldrick, G. SHELXT – Integrated space-group and crystal-structure determination. *Acta Cryst.* **2015**, *A71*, 3-8.

(4) Sheldrick, G. Crystal structure refinement with SHELXL. *Acta Cryst.* **2015**, *C71*, 3-8.

(5) Dolomanov, O. V.; Bourhis, L. J.; Gildea, R. J.; Howard J. A. K.; Puschmann, H. OLEX2: a complete structure solution, refinement and analysis program. *J. Appl. Crystallogr.* **2009**, *42*, 339-341.

Appendix G

Supplementary Information for Chapter 8

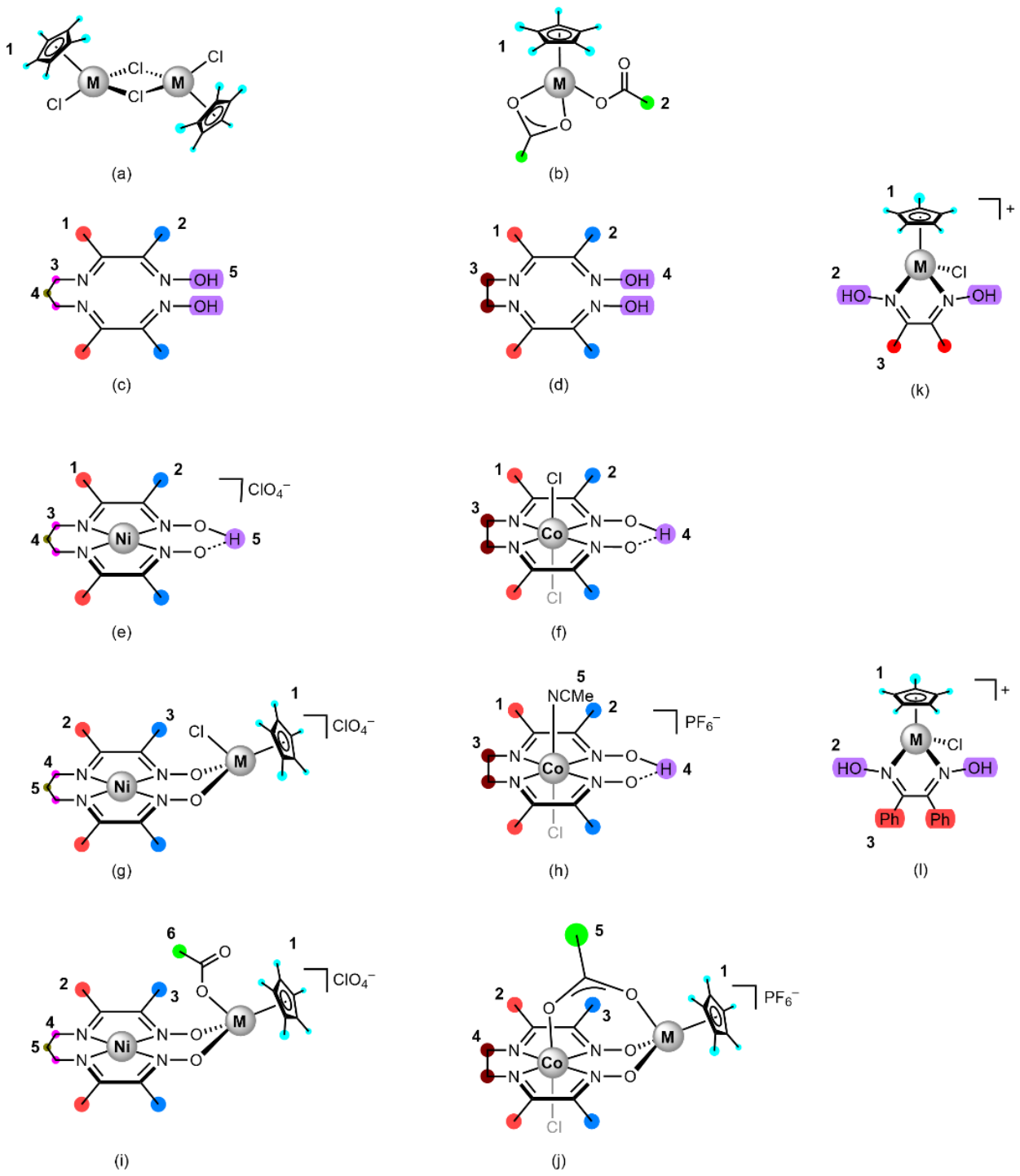

Figure G1. Numbering scheme for assignment of NMR spectra of (a) **[Cp*MCl$_2$]$_2$** (b) **M-OAc** (c) **(DOH)$_2$pn** (d) **(DOH)$_2$en** (e) Ni (f) **Co-Cl$_2$** (g) **Ni,M-Cl** (h) **Co-Cl** (i) **Ni,M-OAc** (j) **Co,M-μ-OAc** (k) **dmgM-Cl** and (l) **dpgM-Cl** complexes where M = Rh or Ir.

NMR Spectra

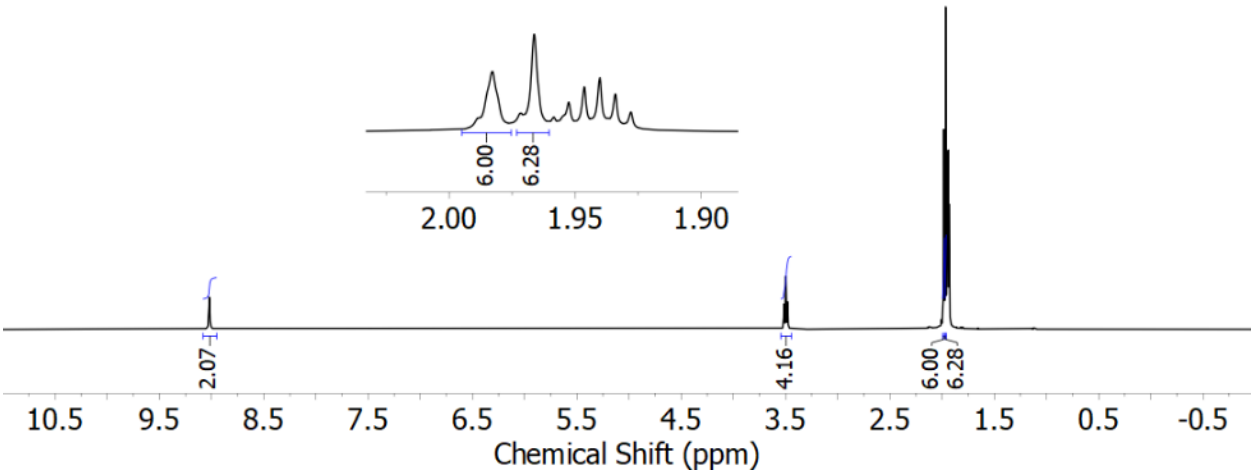

Figure G2. ^{1}H NMR spectrum (400 MHz, CD_3CN) of **(DOH)$_2$pn**.

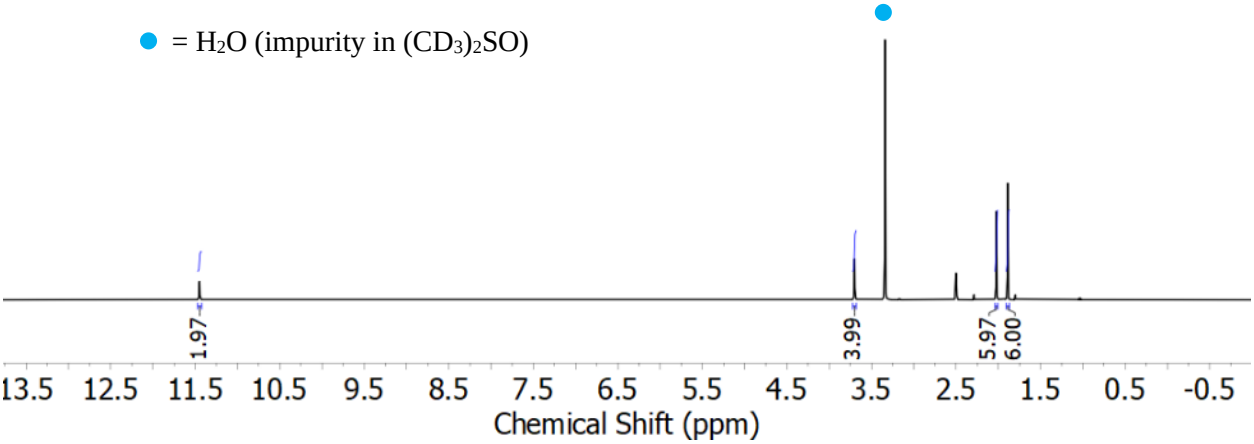

Figure G3. ^{1}H NMR spectrum (400 MHz, $(CD_3)_2SO$) of **(DOH)$_2$en**.

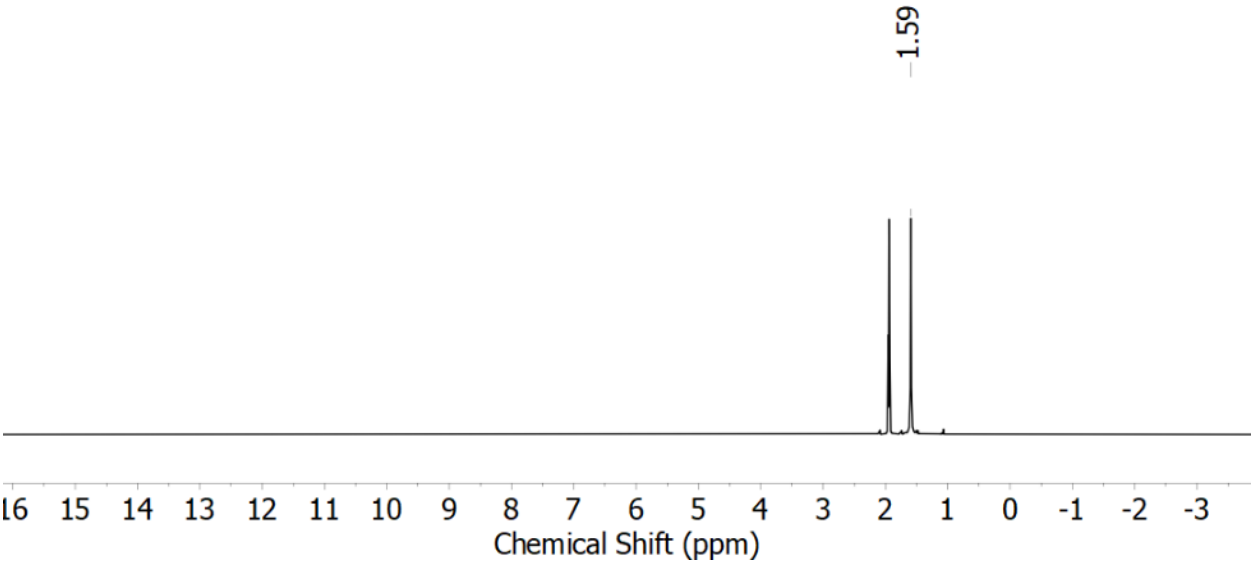

Figure G4. ^{1}H NMR spectrum (400 MHz, CD_3CN) of $[Cp^*RhCl_2]_2$.

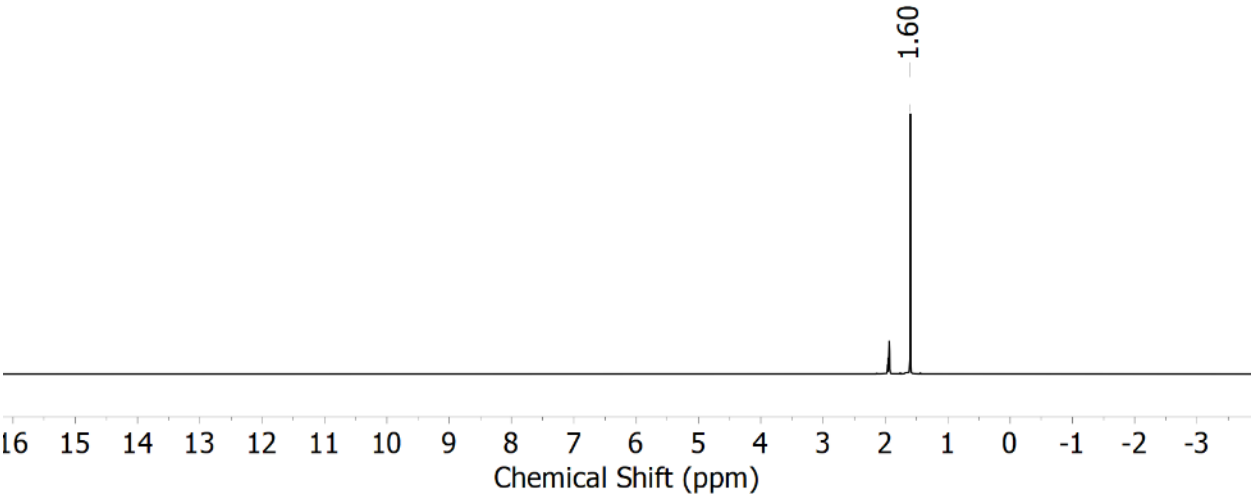

Figure G5. ^{1}H NMR spectrum (400 MHz, CD_3CN) of $[Cp^*IrCl_2]_2$.

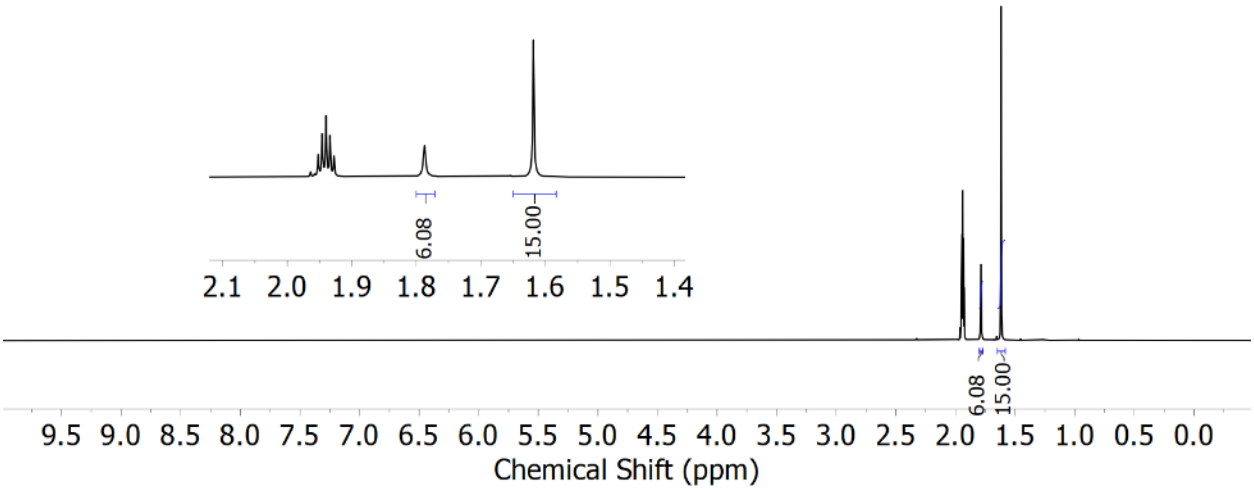

Figure G6. ^{1}H NMR spectrum (400 MHz, CD_3CN) of **Rh-OAc**.

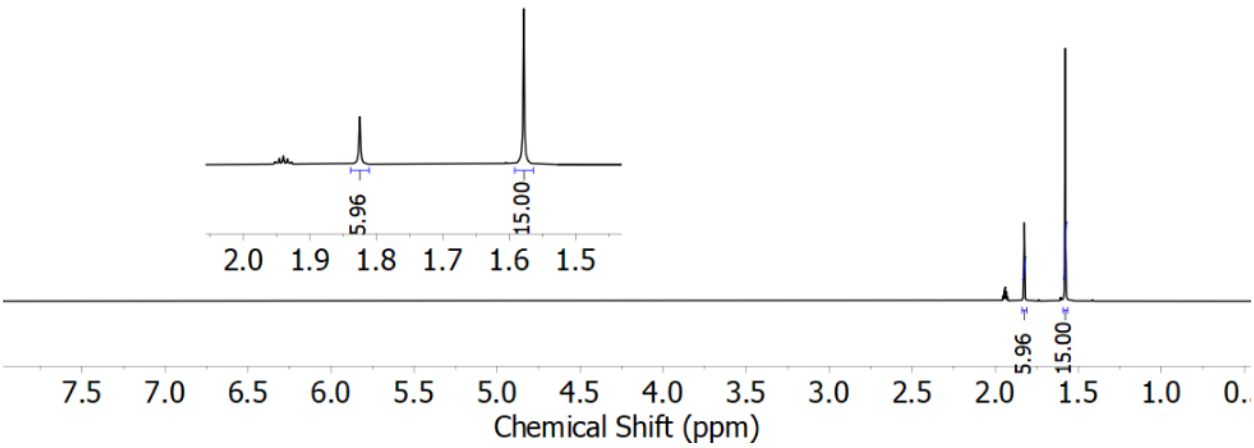

Figure G7. ^{1}H NMR spectrum (400 MHz, CD_3CN) of **Ir-OAc**.

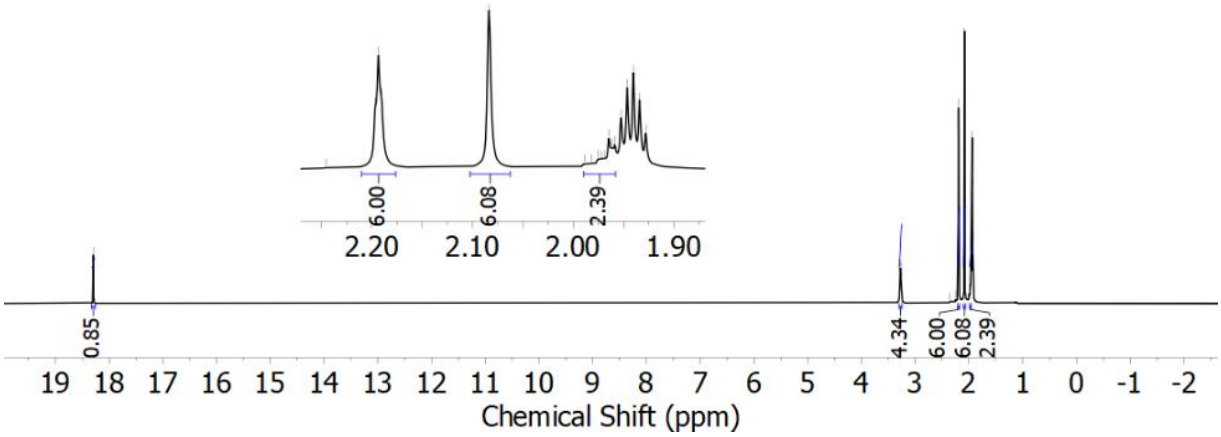

Figure G8. ^{1}H NMR spectrum (400 MHz, CD_3CN) of **Ni**.

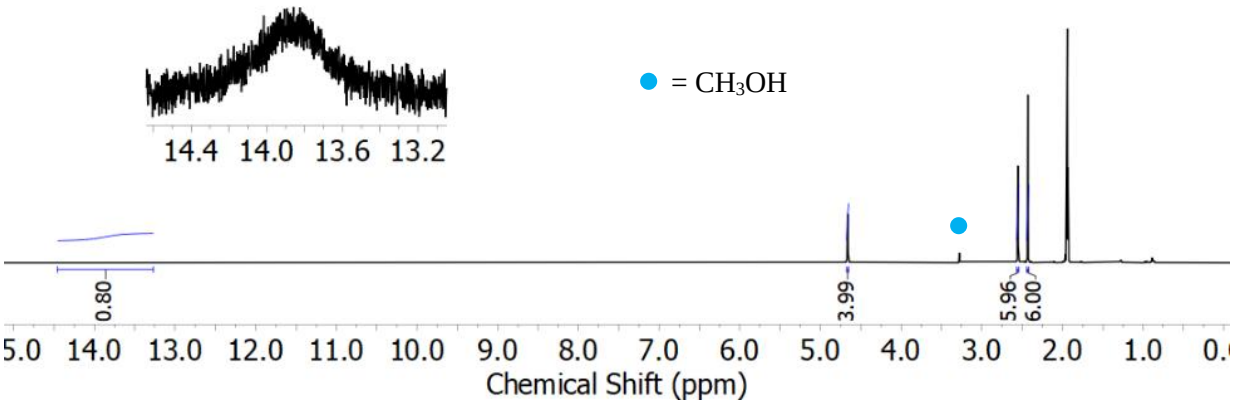

Figure G9. ^{1}H NMR spectrum (400 MHz, CD_3CN) of **Co-Cl$_2$**.

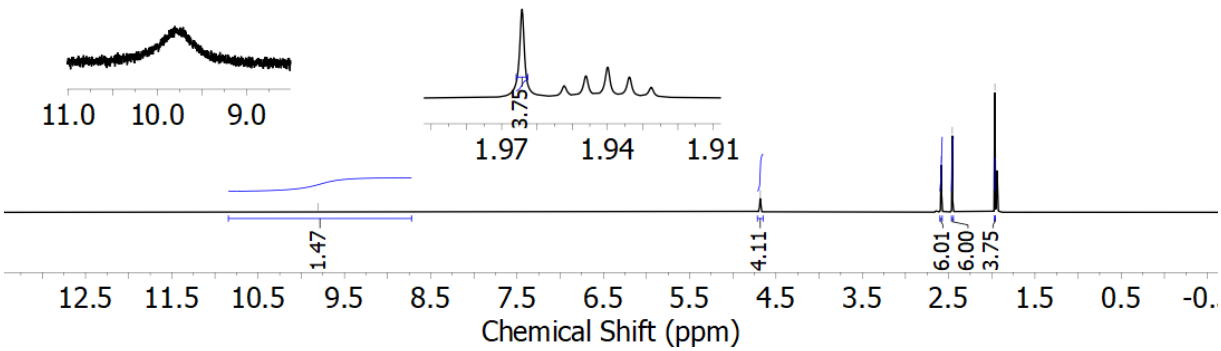

Figure G10. ^{1}H NMR spectrum (400 MHz, CD_3CN) of **Co-Cl**.

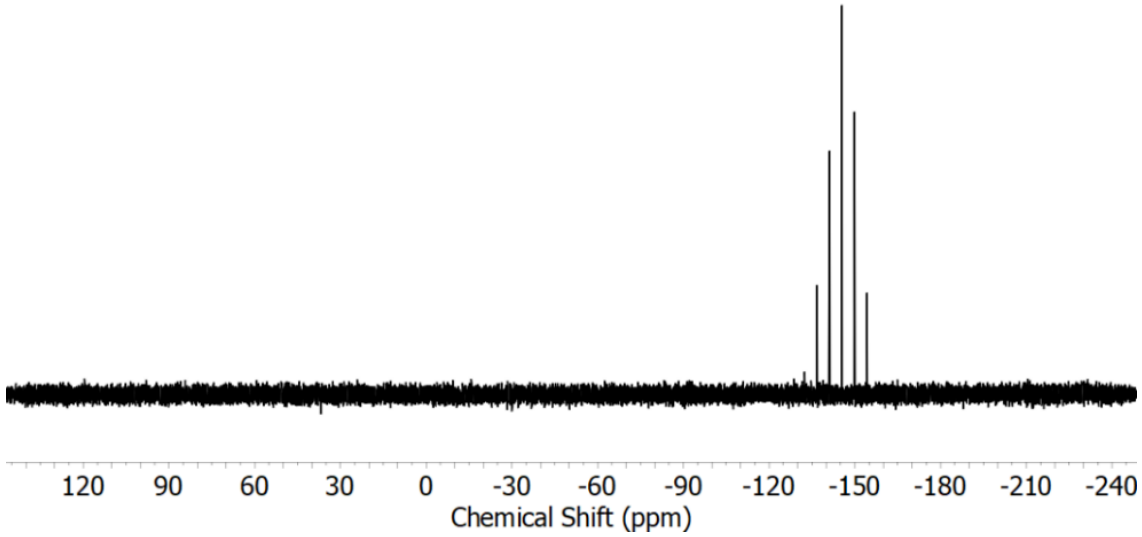

Figure G11. $^{31}P\{^{1}H\}$ NMR spectrum (162 MHz, CD_3CN) of **Co-Cl**.

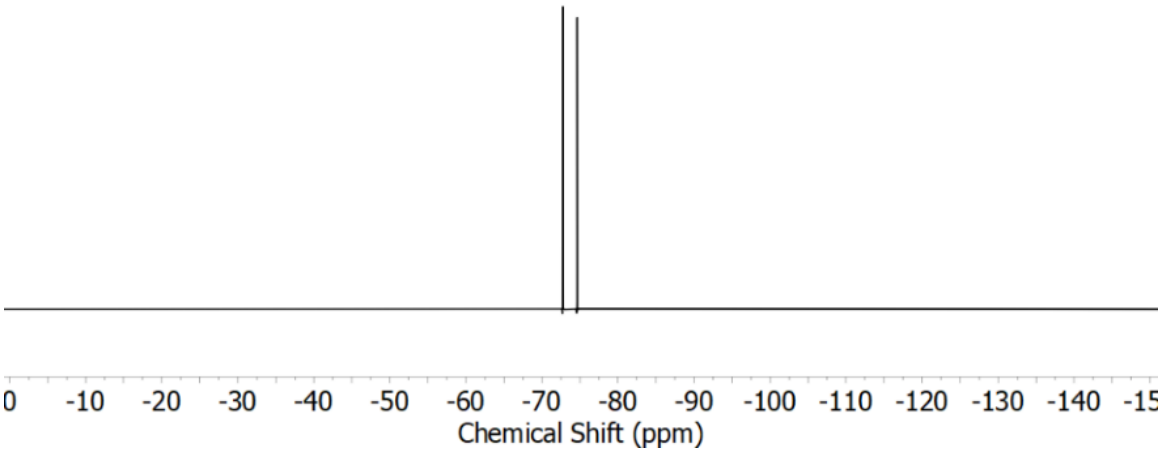

Figure G12. $^{19}F\{^{1}H\}$ NMR spectrum (376 MHz, CD_3CN) of **Co-Cl**.

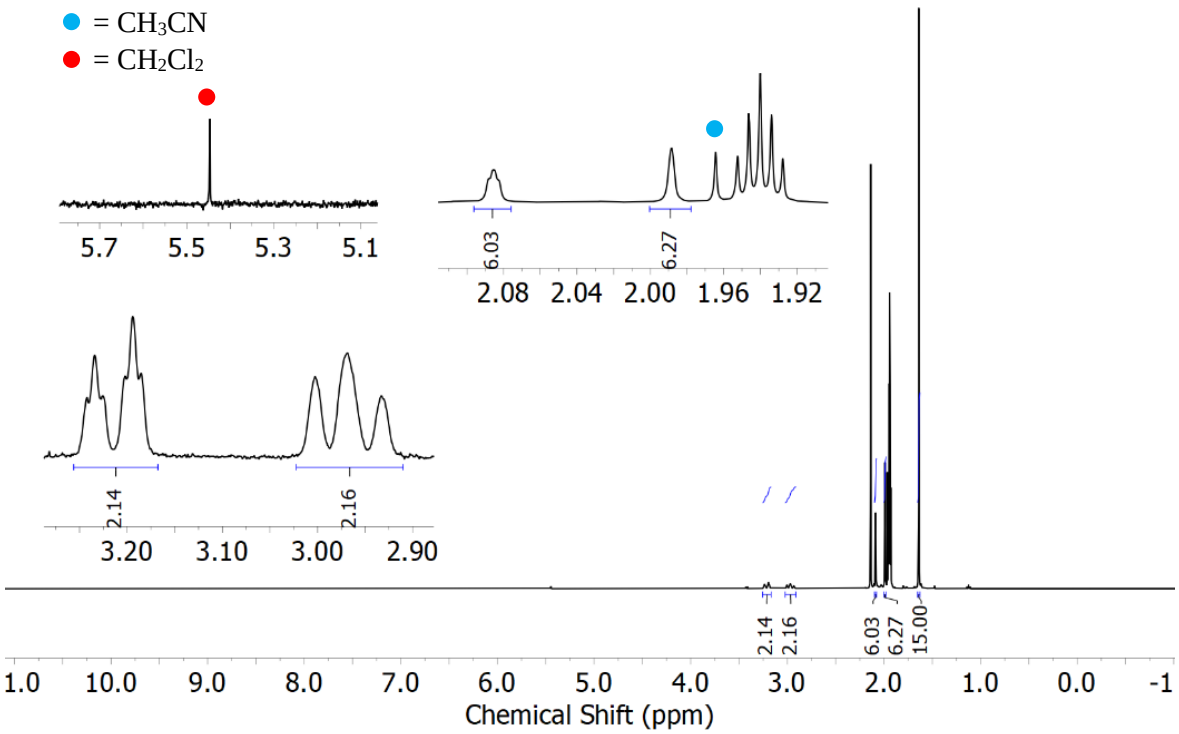

Figure G13. ^{1}H NMR spectrum (400 MHz, CD_2Cl_2) of **Ni,Rh-Cl**.

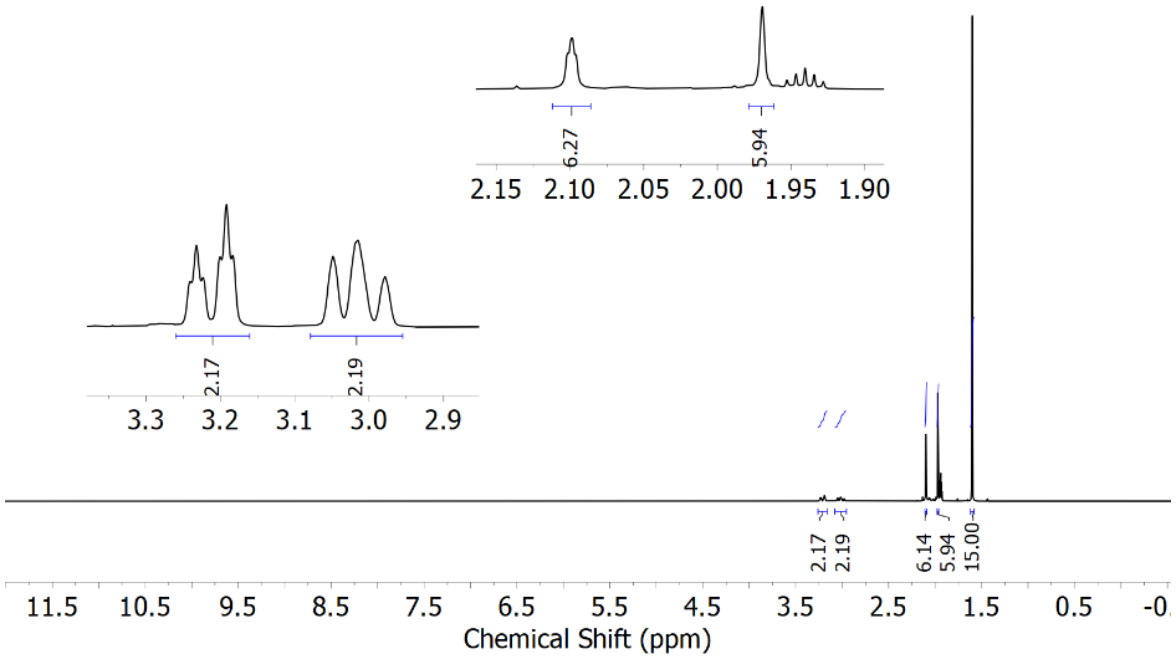

Figure G14. ^{1}H NMR spectrum (400 MHz, CD_2Cl_2) of **Ni,Ir-Cl**.

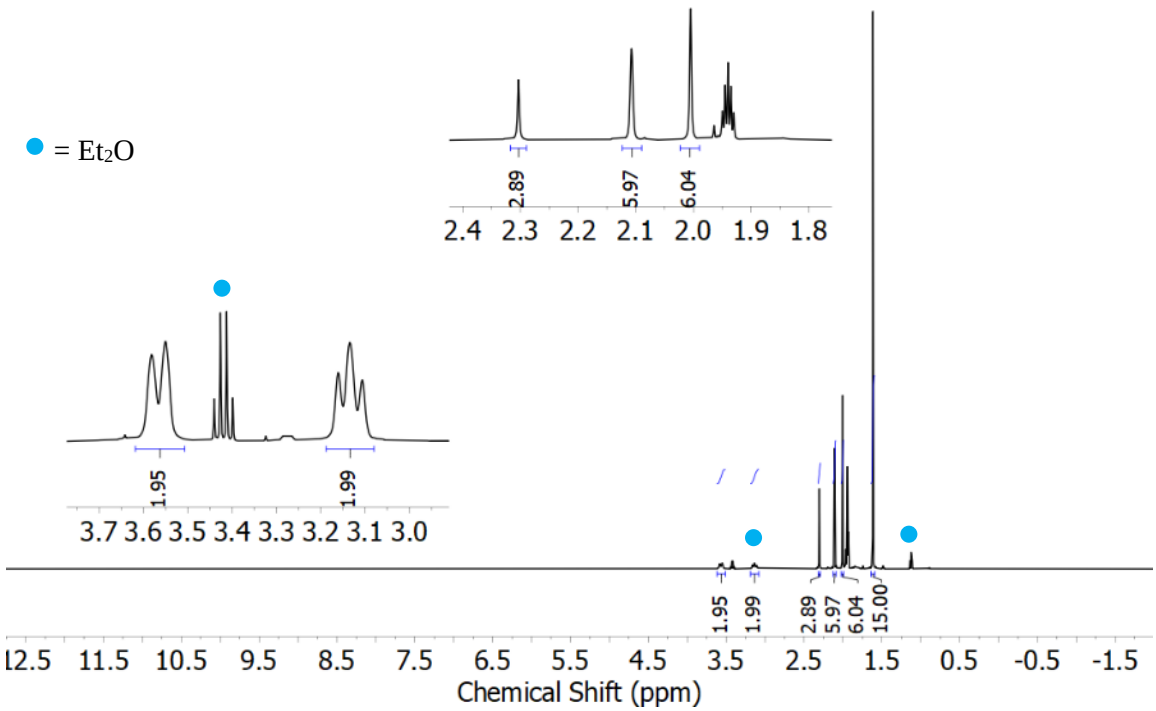

Figure G15. ^{1}H NMR spectrum (400 MHz, CD_3CN) of **Ni,Rh-OAc**.

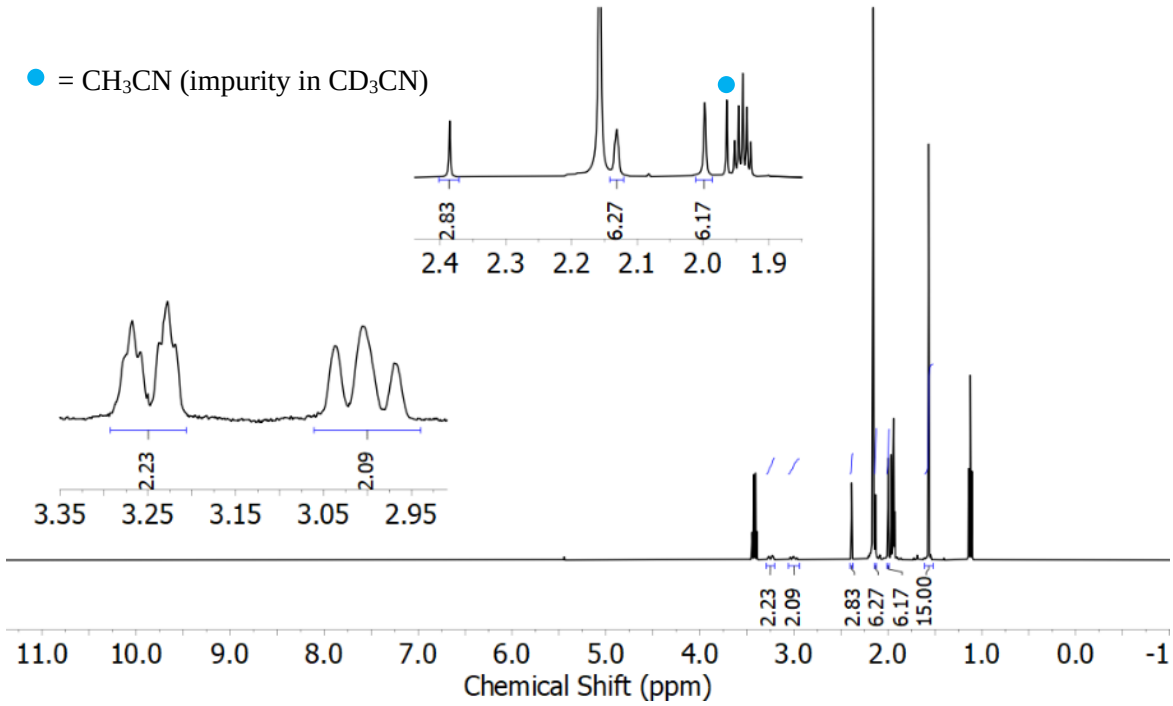

Figure G16. ^{1}H NMR spectrum (400 MHz, CD_3CN) of **Ni,Ir-OAc**.

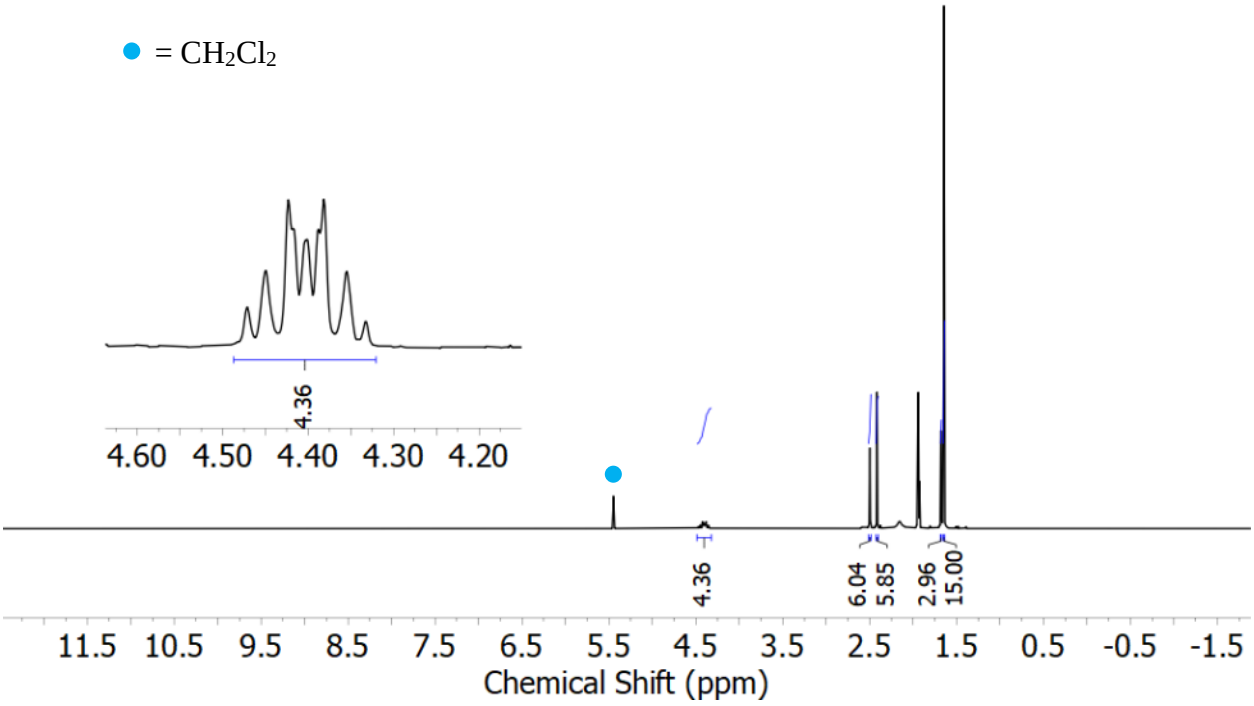

Figure G17. ^{1}H NMR spectrum (400 MHz, CD_3CN) of **Co,Rh-μ-OAc**.

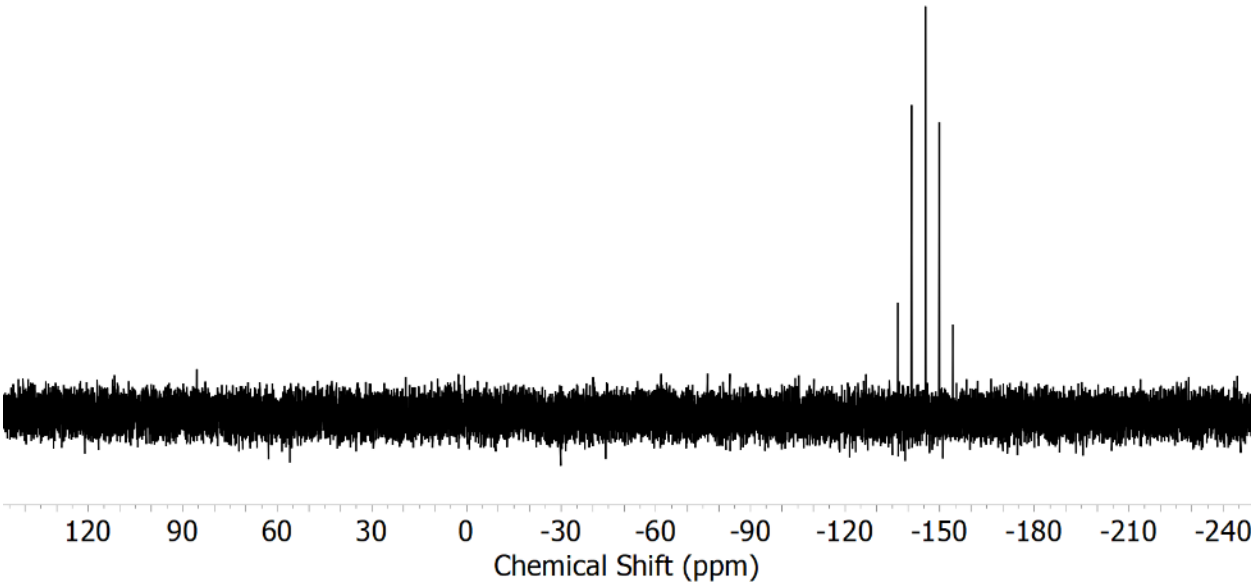

Figure G18. $^{31}P\{^{1}H\}$ NMR spectrum (162 MHz, CD_3CN) of **Co,Rh-μ-OAc**.

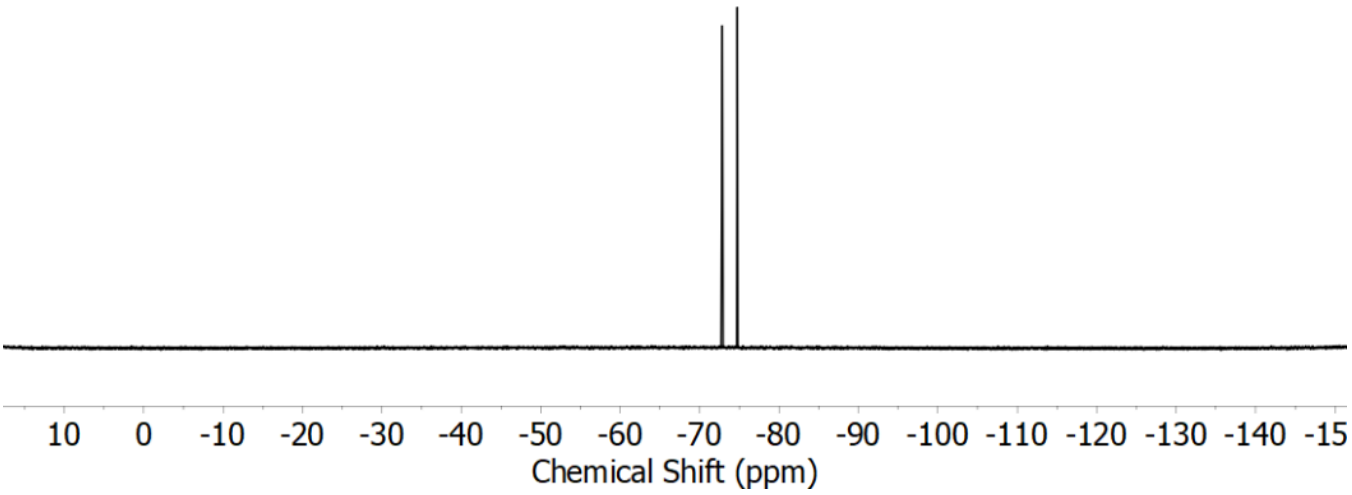

Figure G19. $^{19}F\{^{1}H\}$ NMR spectrum (376 MHz, CD_3CN) of **Co,Rh-μ-OAc**.

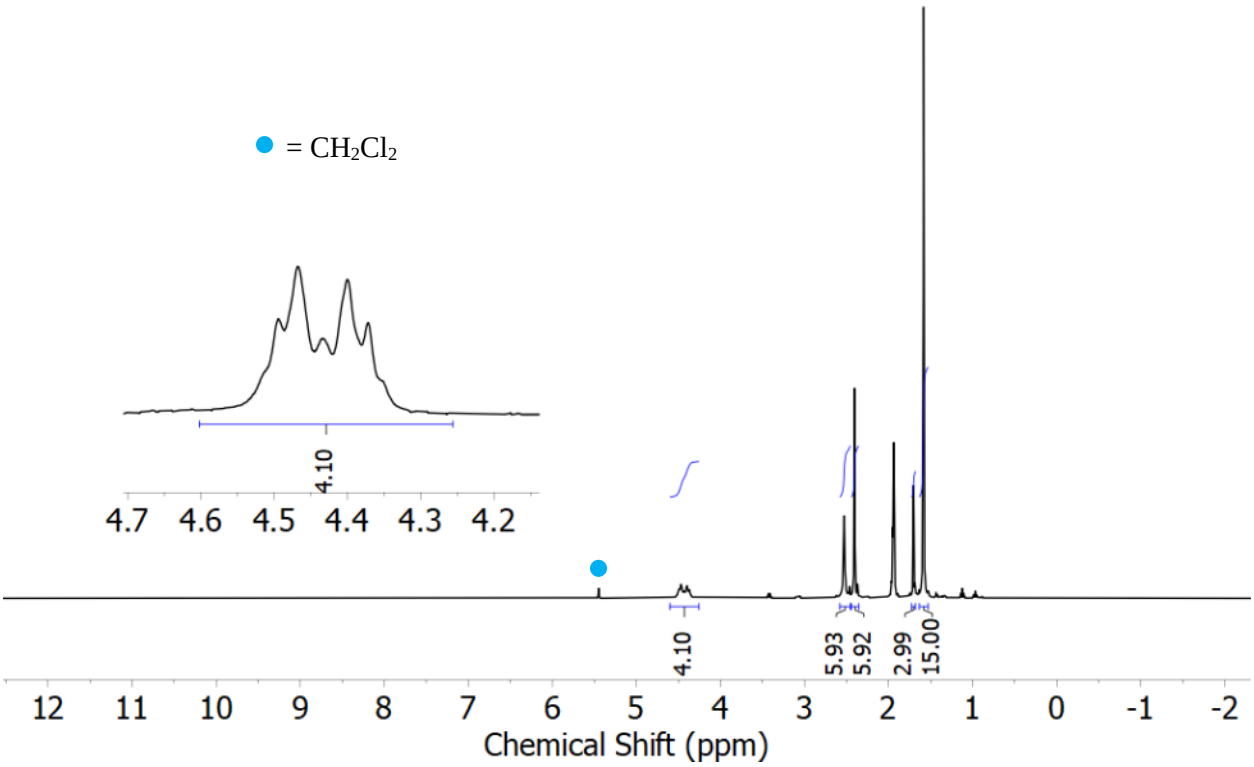

Figure G20. ^{1}H NMR spectrum (400 MHz, CD_3CN) of **Co,Ir-μ-OAc**.

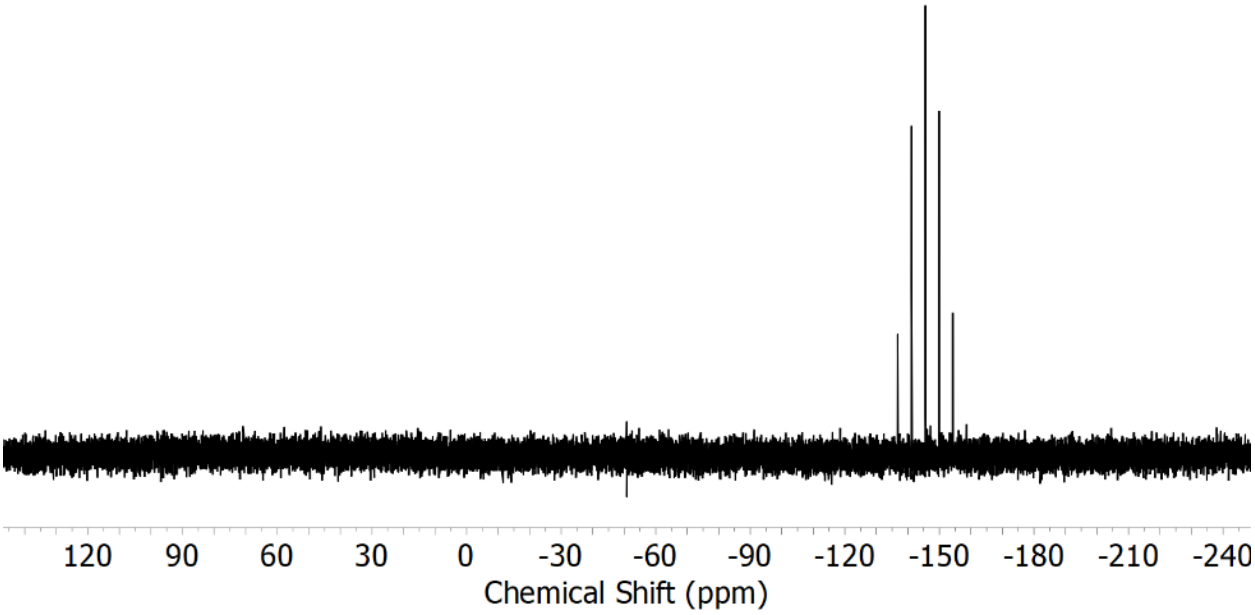

Figure G21. $^{31}P\{^{1}H\}$ NMR spectrum (162 MHz, CD_3CN) of **Co,Ir-μ-OAc**.

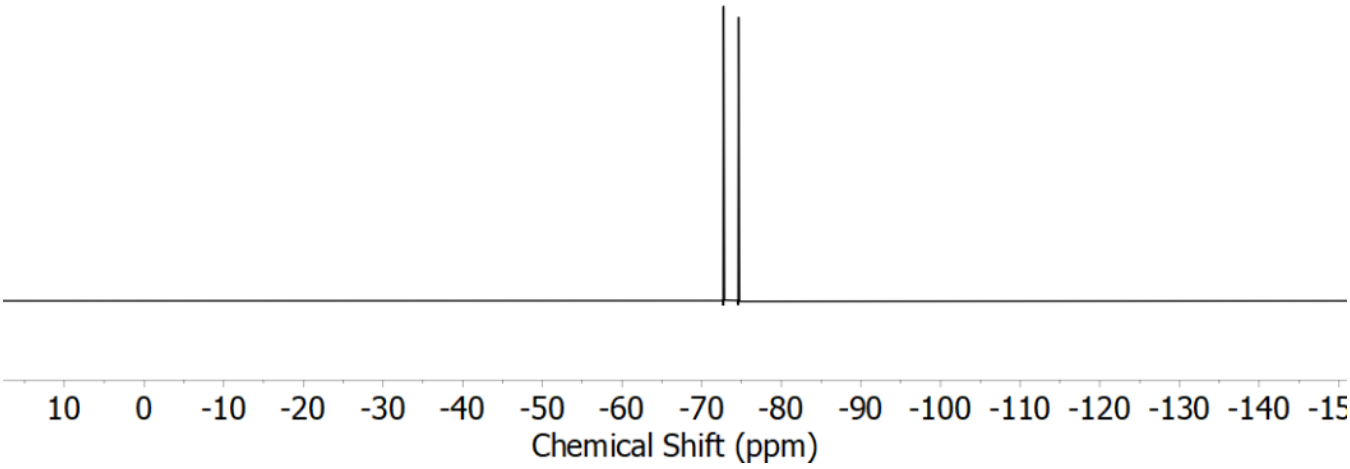

Figure G22. $^{19}F\{^{1}H\}$ NMR spectrum (376 MHz, CD_3CN) of **Co,Ir-μ-OAc**.

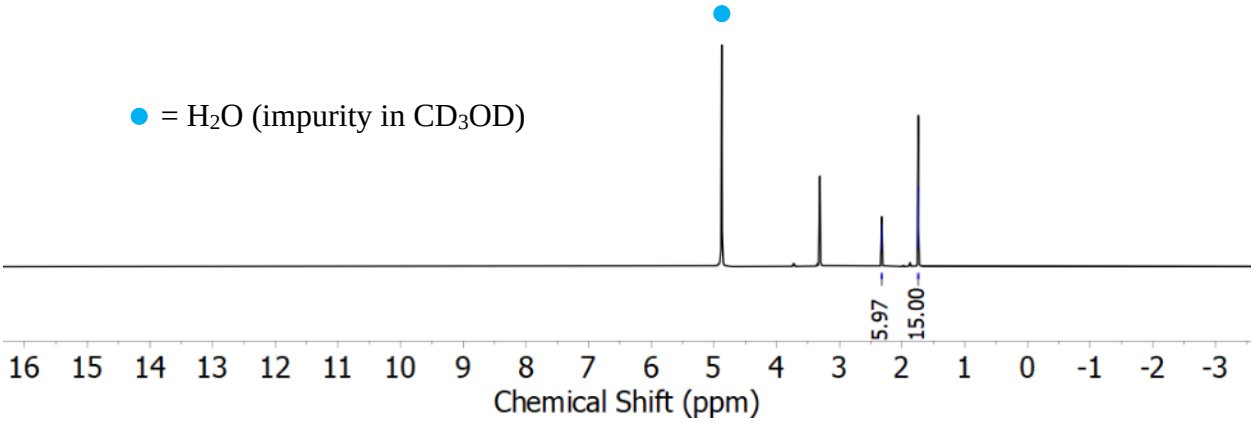

Figure G23. ^{1}H NMR spectrum (400 MHz, CD_3OD) of **dmgIr-Cl**.

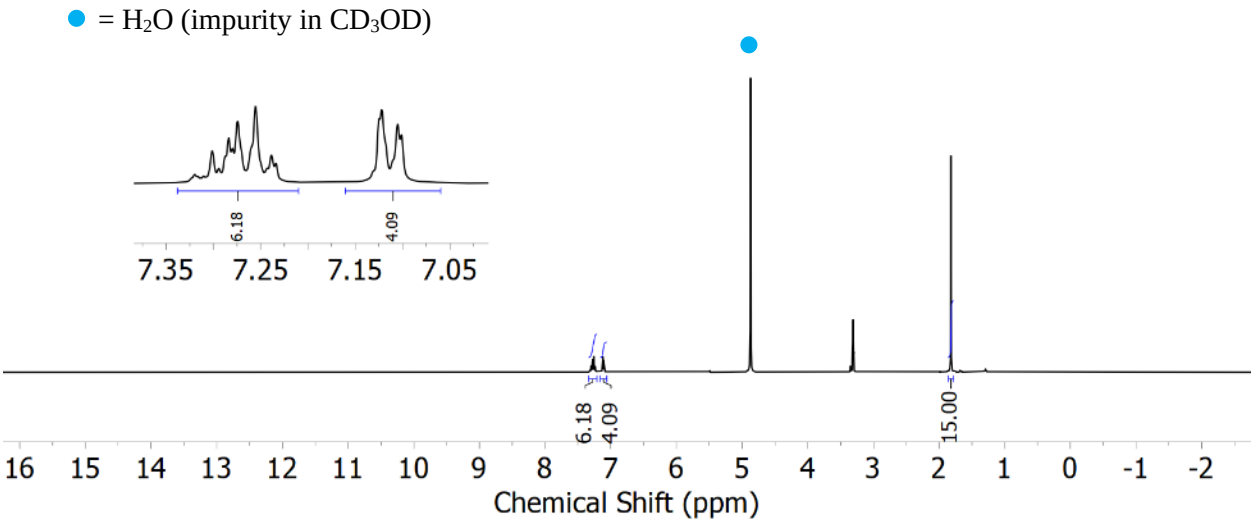

Figure G24. ^{1}H NMR spectrum (400 MHz, CD_3OD) of **dpgRh-Cl**.

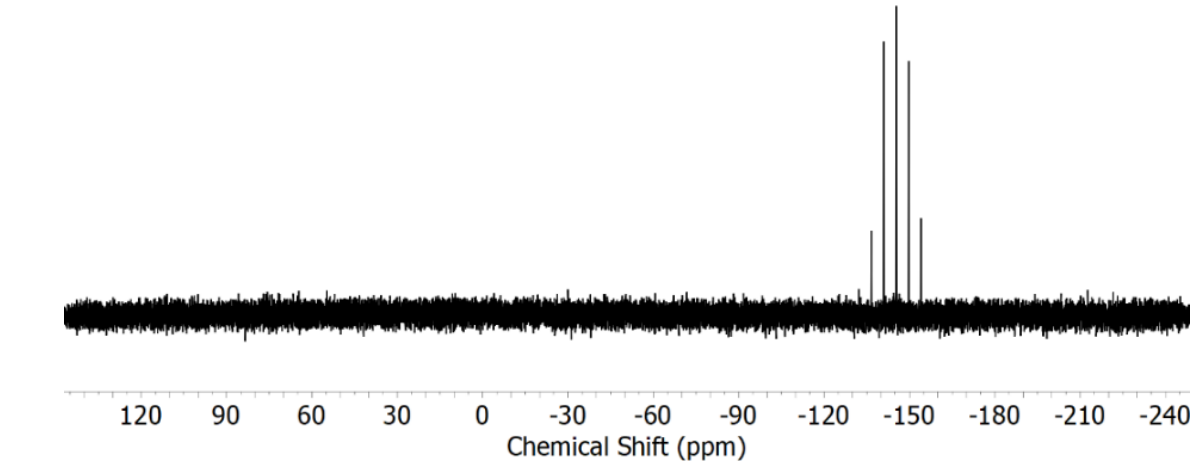

Figure G25. $^{31}P\{^{1}H\}$ NMR spectrum (162 MHz, CD_3OD) of **dpgRh-Cl**.

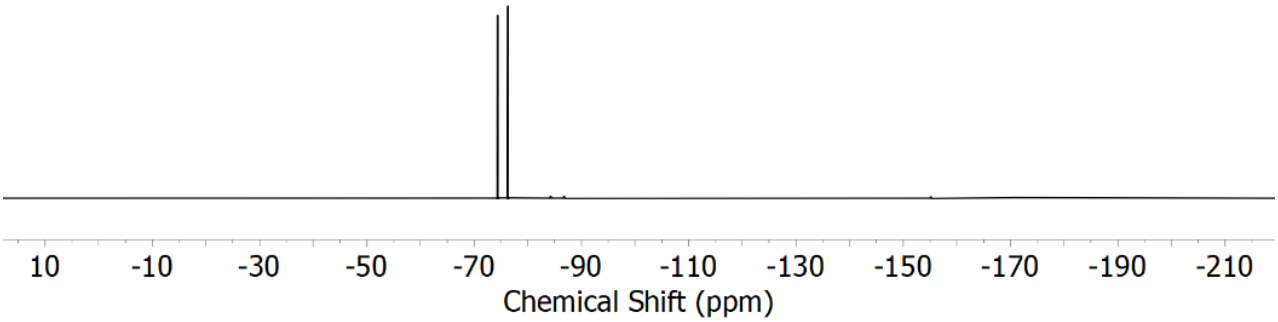

Figure G26. $^{19}F\{^{1}H\}$ NMR spectrum (376 MHz, CD_3OD) of **dpgRh-Cl**.

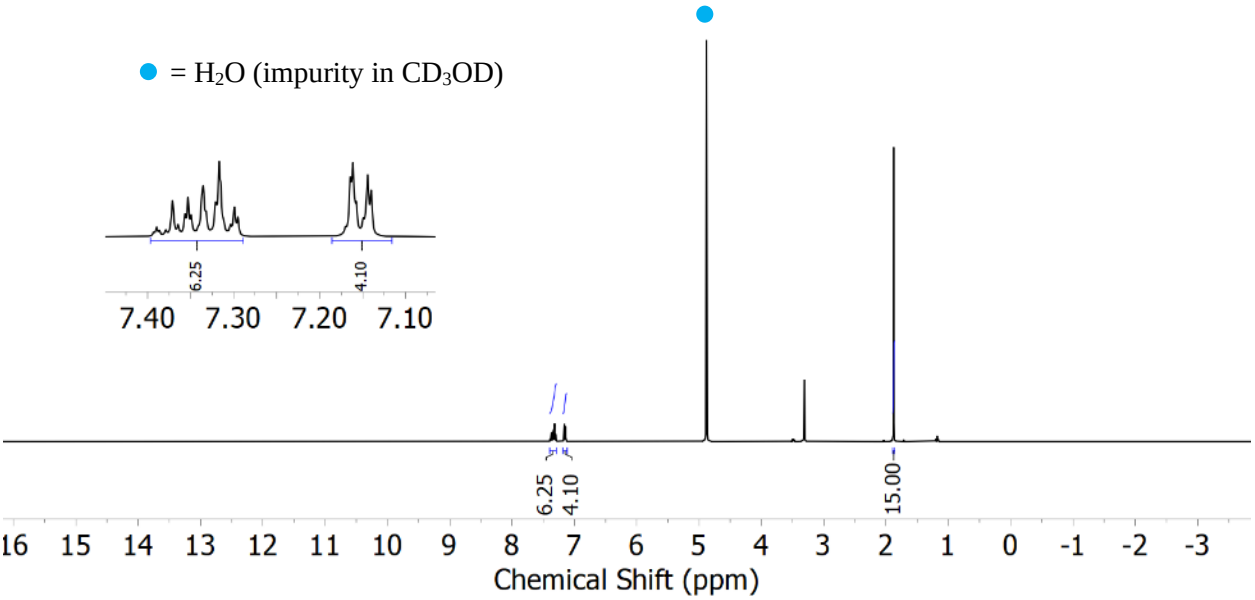

Figure G27. ^{1}H NMR spectrum (400 MHz, CD_3OD) of **dpgIr-Cl**.

Electronic Absorption Spectroscopy (EAS)

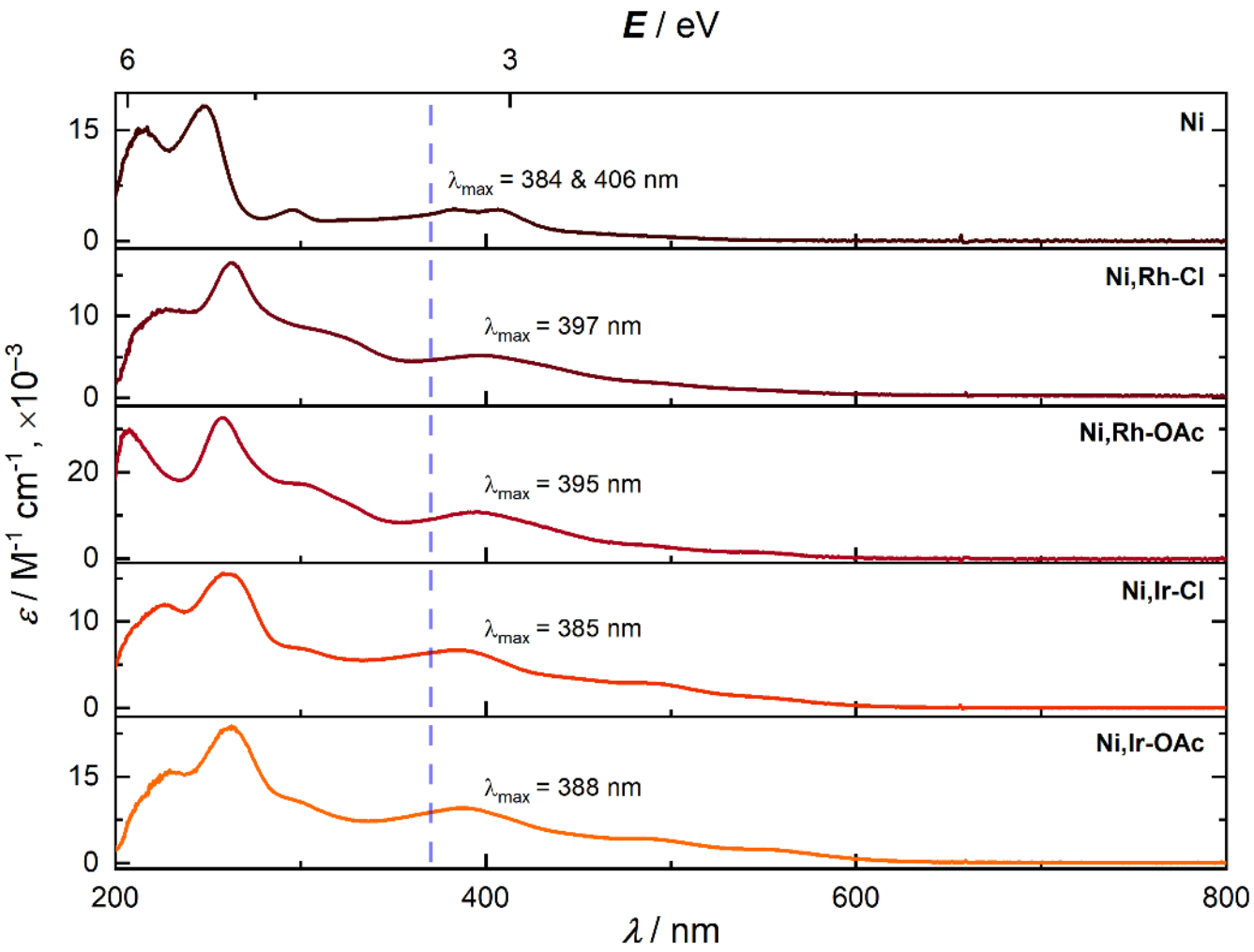

Figure G28. Stacked EA spectra of heterobimetallic complexes of Ni in CH_3CN. Concentration of the analyte in all cases = 0.1 mM.

Electrochemistry

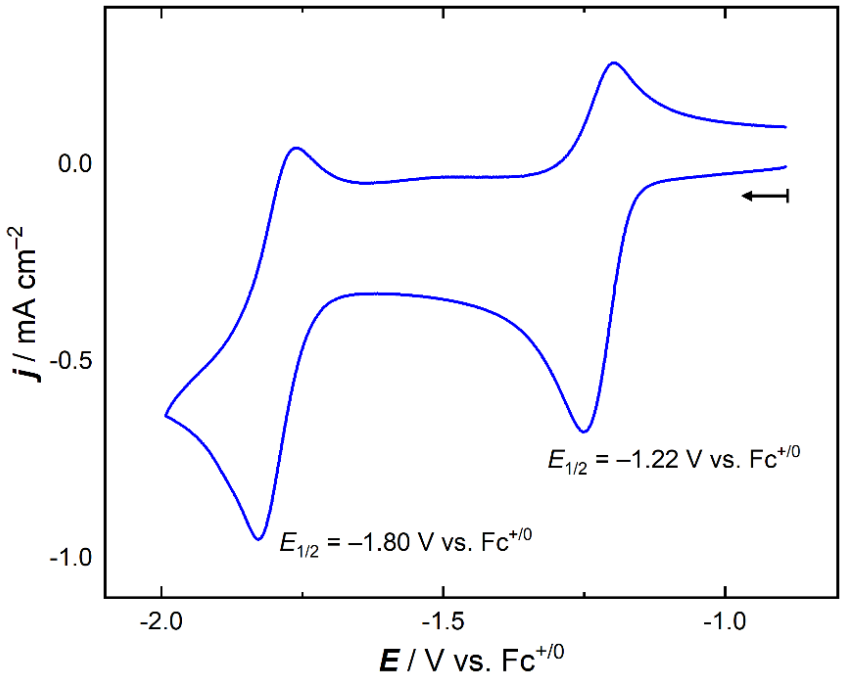

Figure G29. Cyclic voltammetry data for **Ni** in CH_3CN (0.1 M $[^nBu_4N]^+[PF_6]^-$, 100 mV/s).

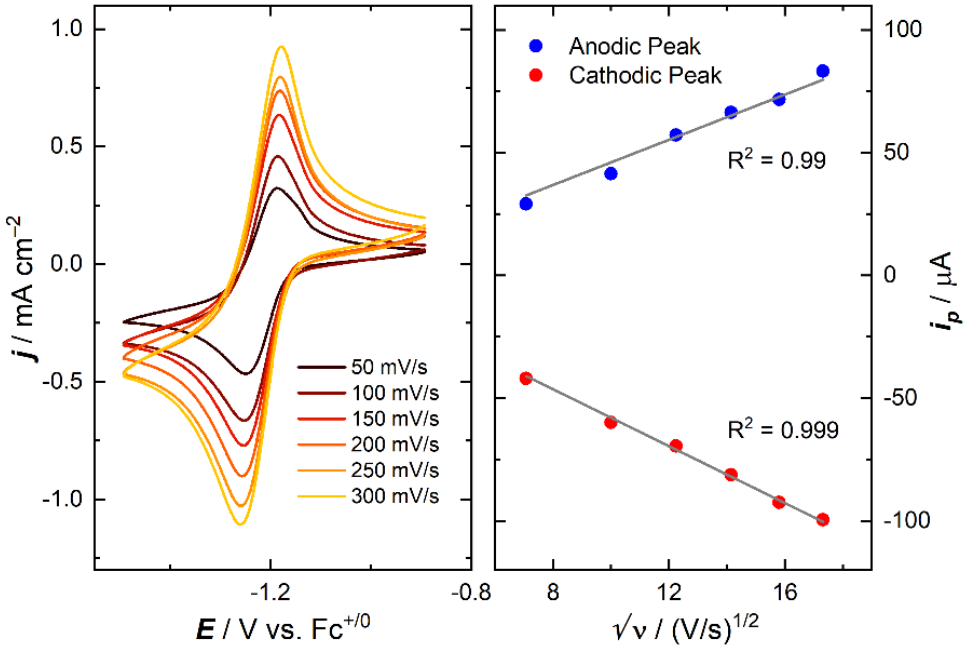

Figure G30. Left panel: scan rate dependence data for feature at $E_{1/2}$ = –1.22 V vs. $Fc^{+/0}$ in the **Ni** complex. Right panel: plot of peak current density vs. $(\text{scan rate})^{1/2}$, demonstrating the diffusional nature of the oxidized and reduced species involved.

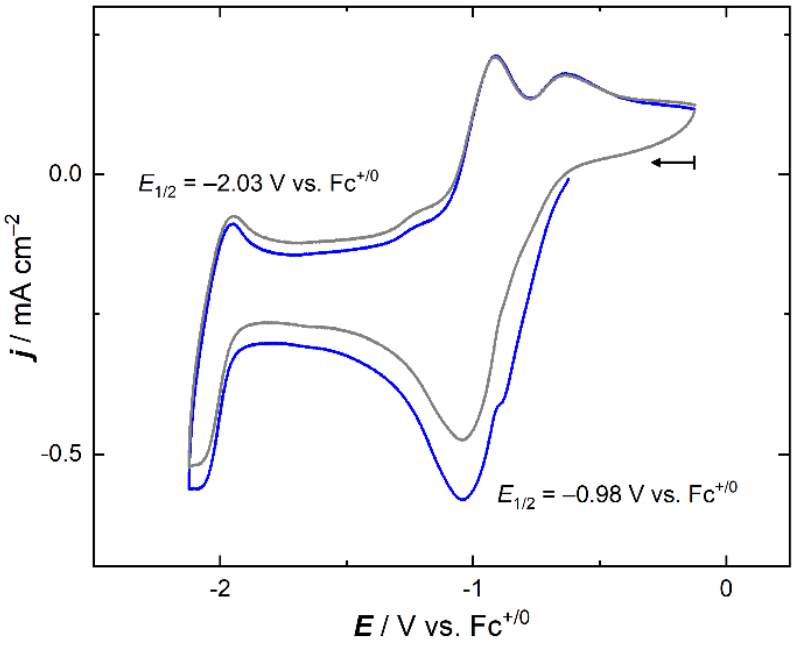

Figure G31. Cyclic voltammetry data for **Co-Cl$_2$** in CH_3CN showing the first (blue) and the second (grey) scan (0.1 M $[^nBu_4N]^+[PF_6]^-$, 100 mV/s).

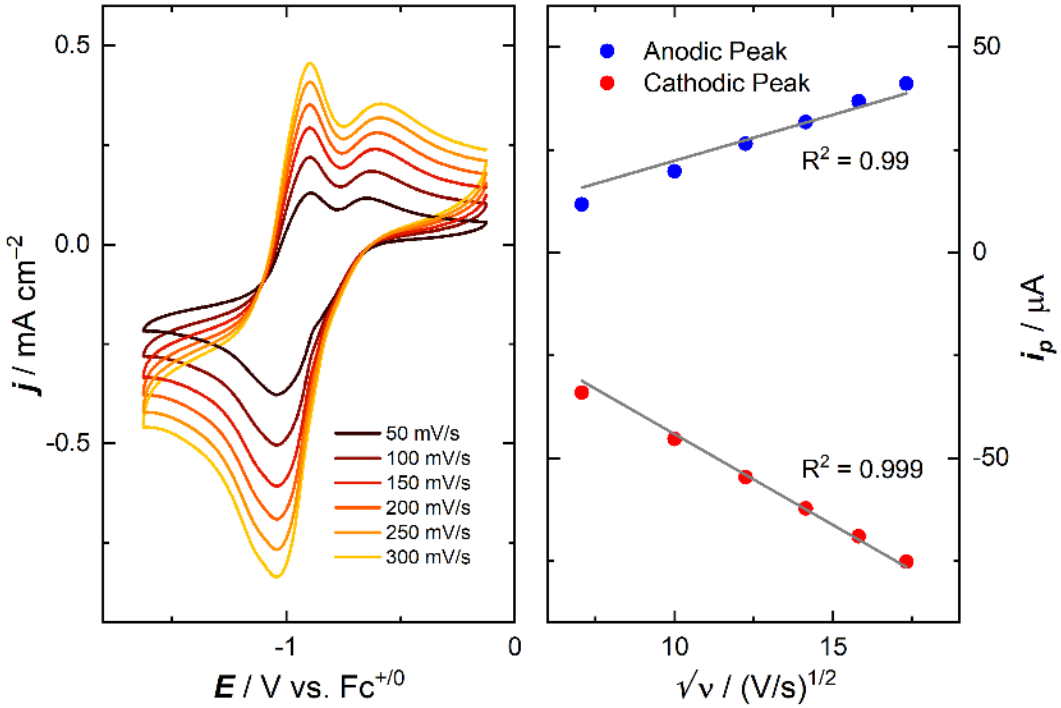

Figure G32. Left panel: scan rate dependence data for feature at $E_{1/2}$ = –0.98 V vs. $Fc^{+/0}$ in the **Co-Cl$_2$** complex. Right panel: plot of peak current density vs. (scan rate)$^{1/2}$, demonstrating the diffusional nature of the oxidized and reduced species involved.

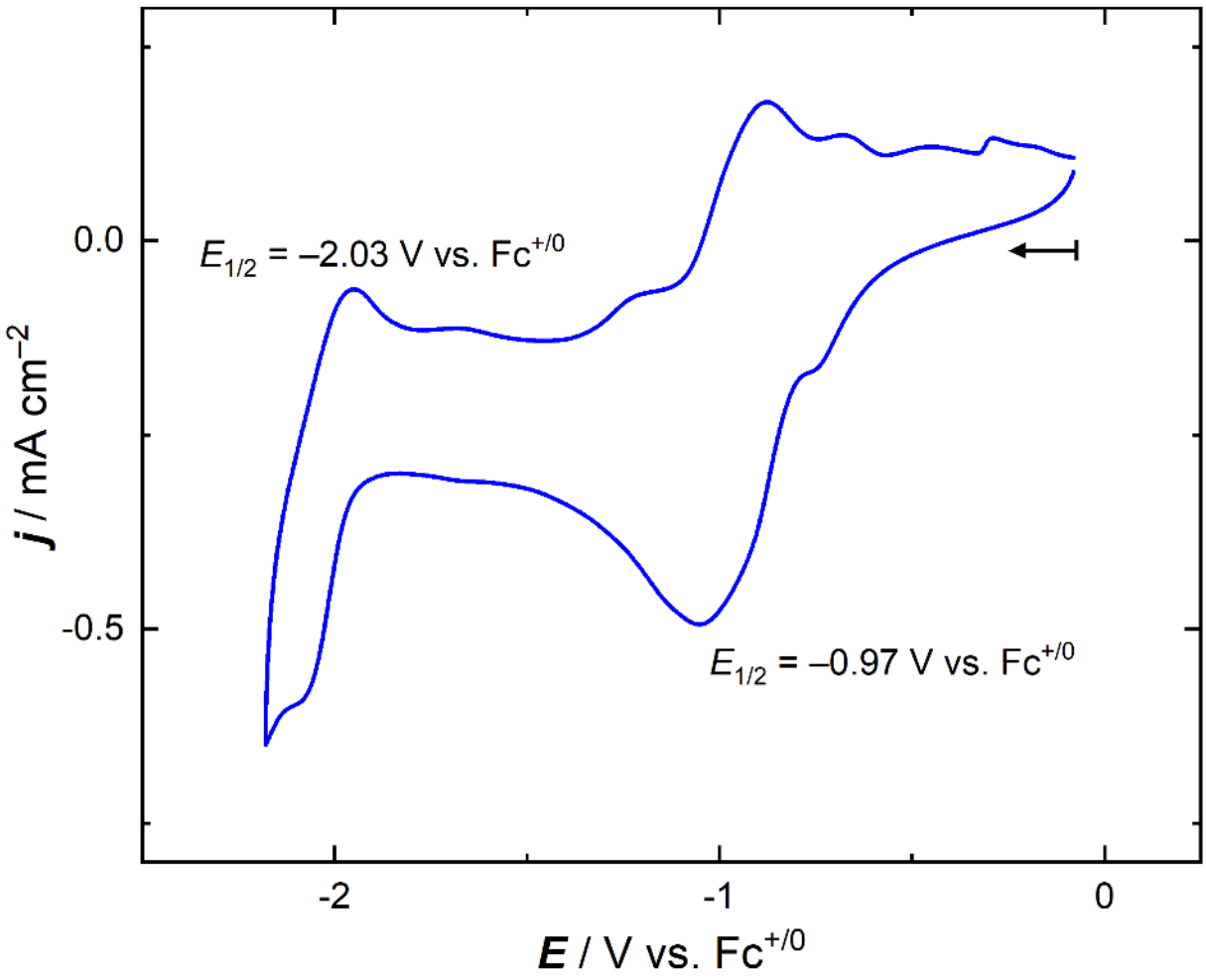

Figure G33. Cyclic voltammetry data for **Co-Cl** in CH_3CN (0.1 M $[^nBu_4N]^+[PF_6]^-$, 100 mV/s).

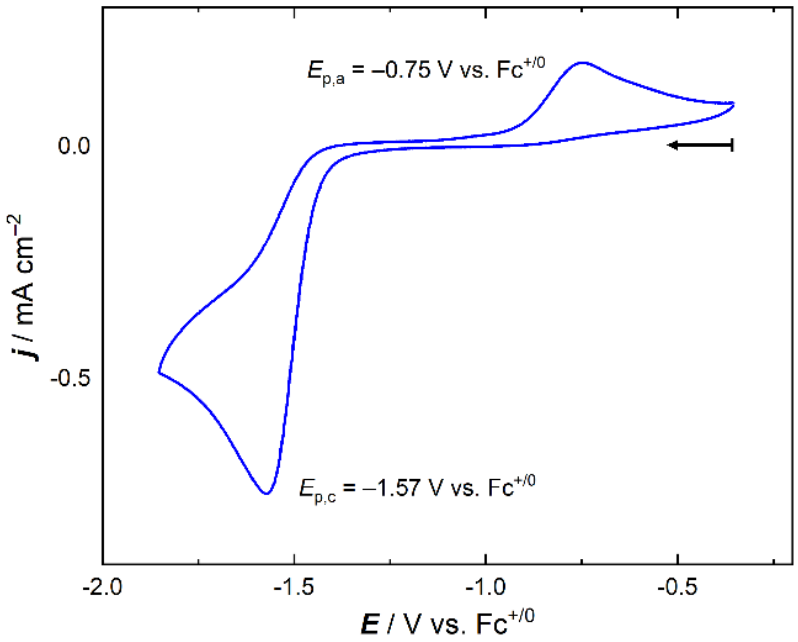

Figure G34. Cyclic voltammetry data for **Rh-OAc** in CH_3CN (0.1 M $[^nBu_4N]^+[PF_6]^-$, 100 mV/s).

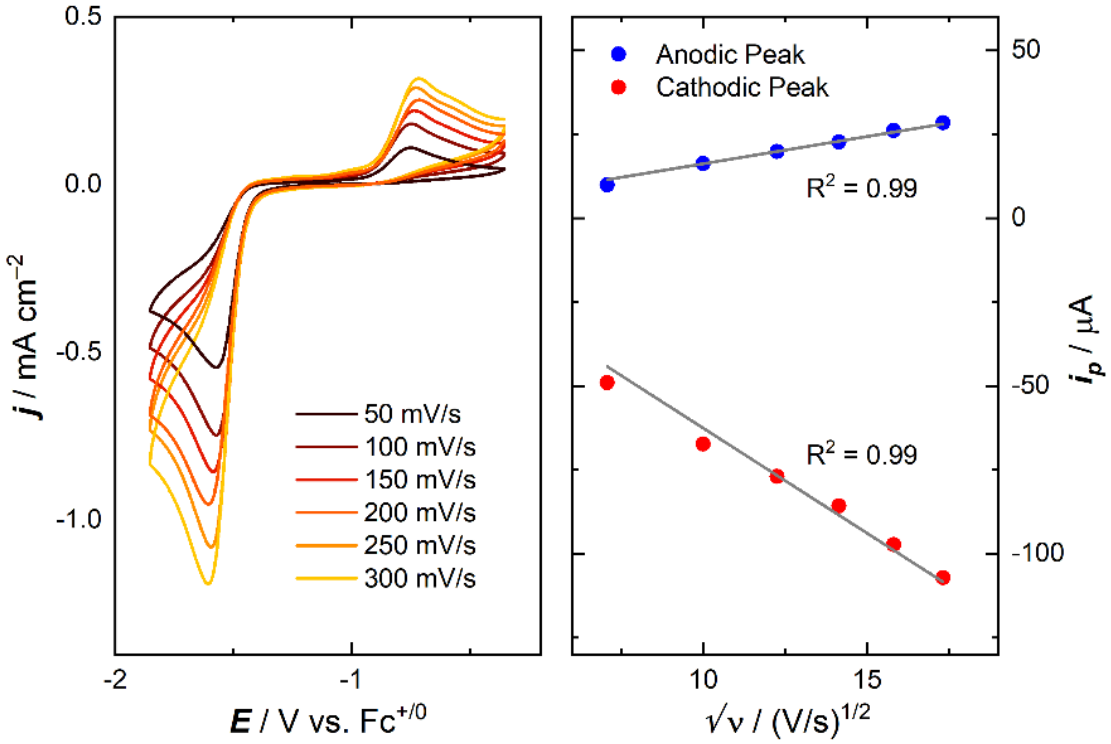

Figure G35. Left panel: scan rate dependence data for **Rh-OAc** complex. Right panel: plot of peak current density vs. (scan rate)$^{1/2}$, demonstrating the diffusional nature of the oxidized and reduced species involved.

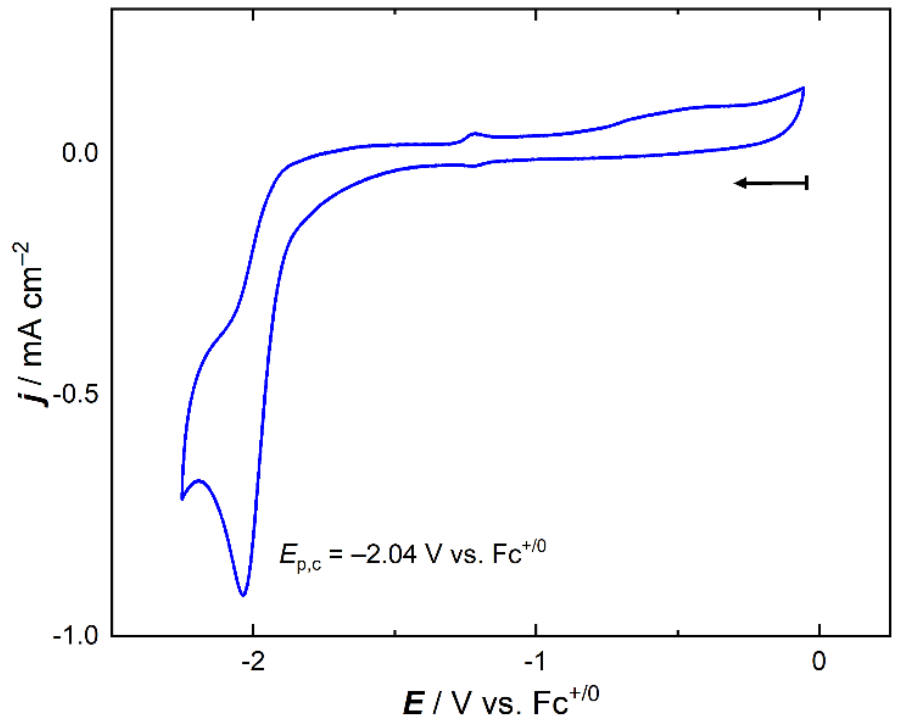

Figure G36. Cyclic voltammetry data for **Ir-OAc** in CH_3CN (0.1 M $[^nBu_4N]^+[PF_6]^-$, 100 mV/s).

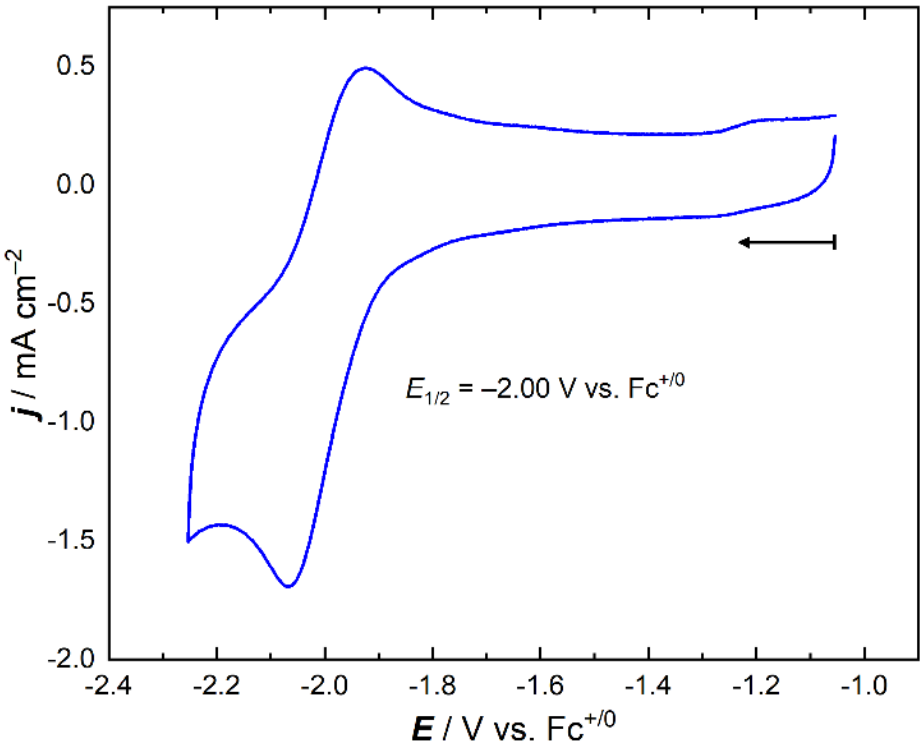

Figure G37. Cyclic voltammetry data for **Ir-OAc** in CH_3CN (0.1 M $[^nBu_4N]^+[PF_6]^-$, 1000 mV/s).

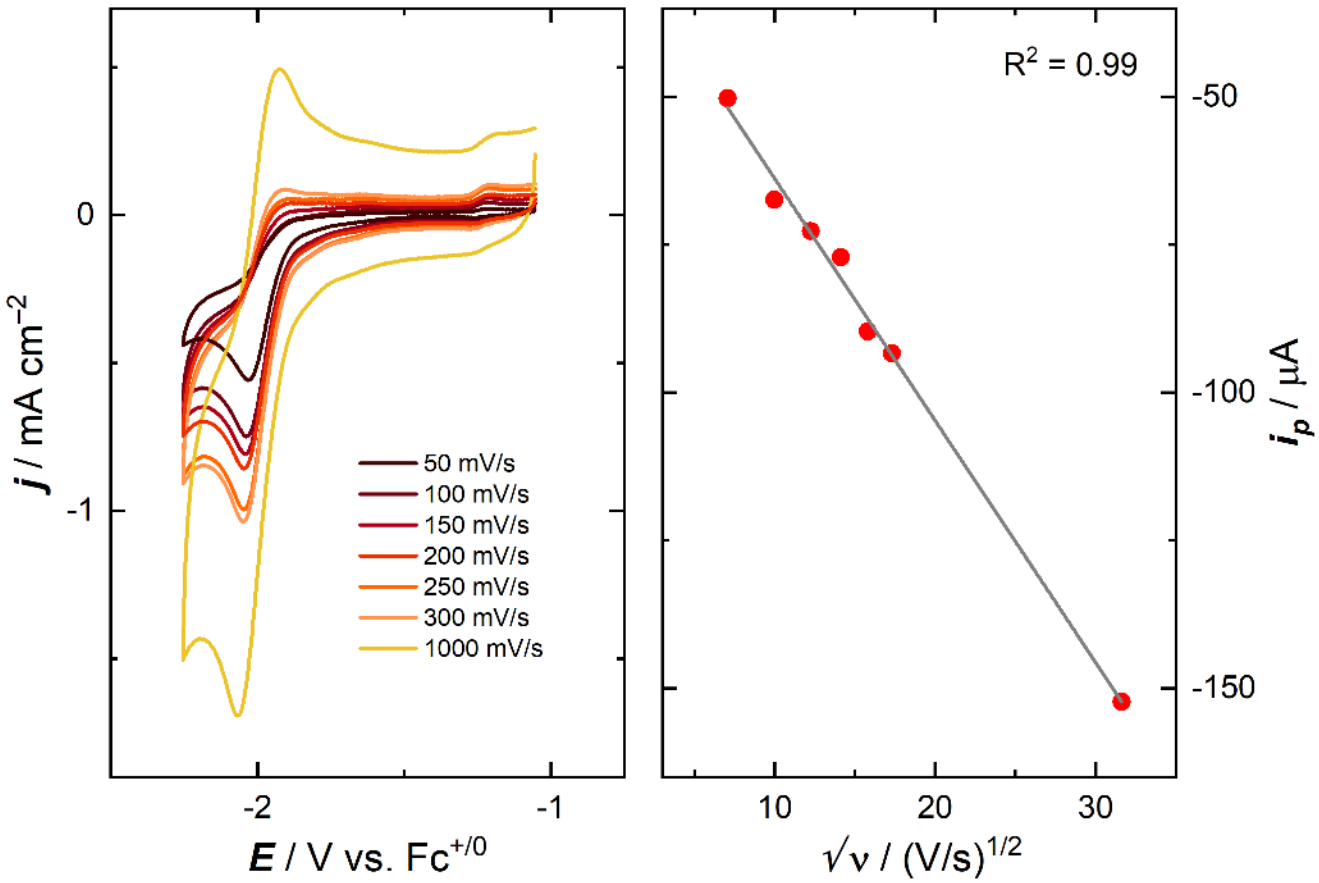

Figure G38. Left panel: scan rate dependence data for **Ir-OAc** complex. Right panel: plot of peak current density vs. (scan rate)$^{1/2}$, demonstrating the diffusional nature of the oxidized species involved.

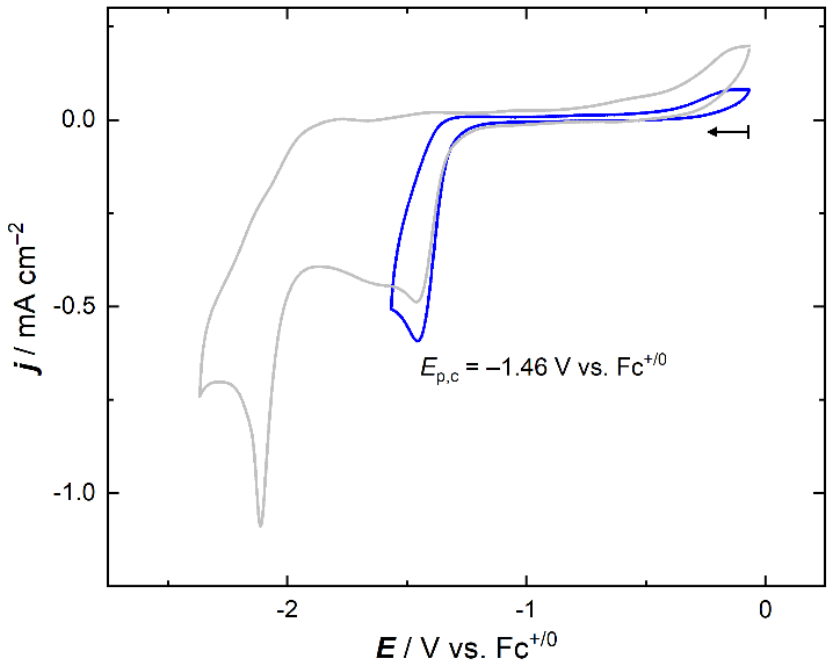

Figure G39. Cyclic voltammetry data for **Ni,Rh-Cl** in CH_3CN showing the feature of interest (blue) and full scan (grey) (0.1 M $[^nBu_4N]^+[PF_6]^-$, 100 mV/s).

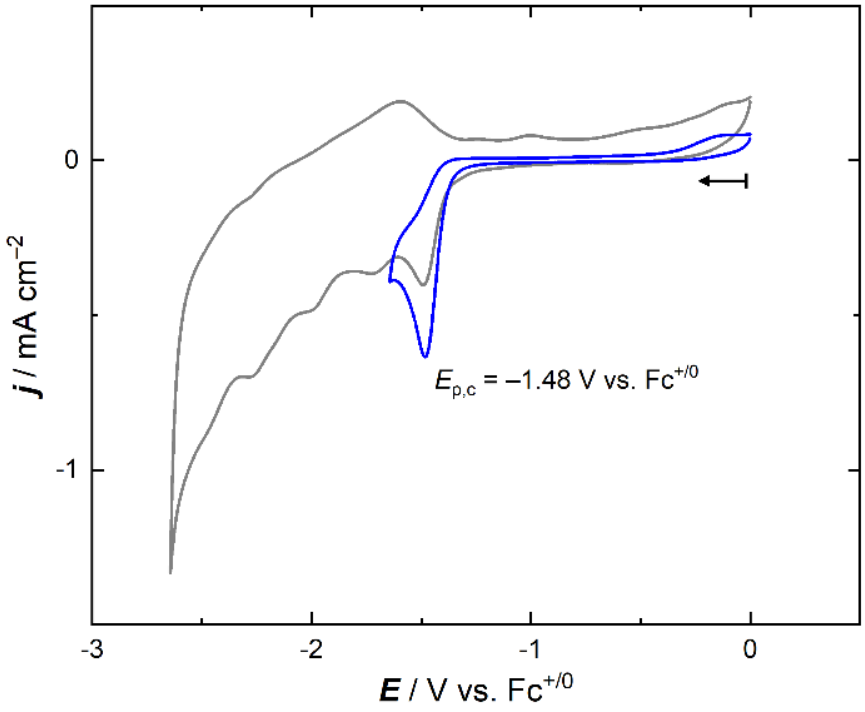

Figure G40. Cyclic voltammetry data for **Ni,Ir-Cl** in CH_3CN showing the feature of interest (blue) and full scan (grey) (0.1 M $[^nBu_4N]^+[PF_6]^-$, 100 mV/s).

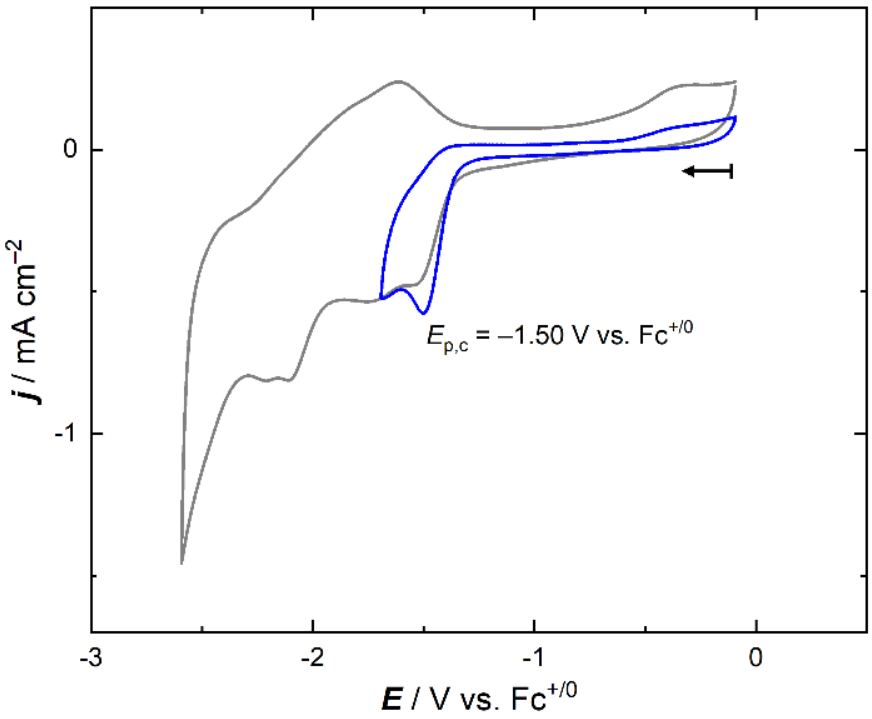

Figure G41. Cyclic voltammetry data for **Ni,Rh-OAc** in CH_3CN showing the feature of interest (blue) and full scan (grey) (0.1 M $[^nBu_4N]^+[PF_6]^-$, 100 mV/s)

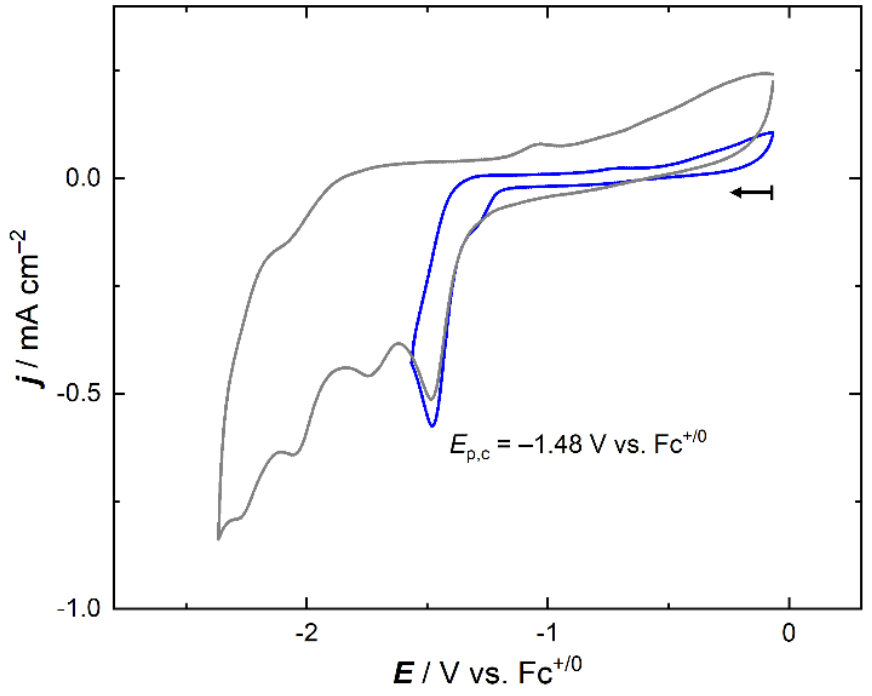

Figure G42. Cyclic voltammetry data for **Ni,Ir-OAc** in CH_3CN showing the feature of interest (blue) and full scan (grey) (0.1 M $[^nBu_4N]^+[PF_6]^-$, 100 mV/s).

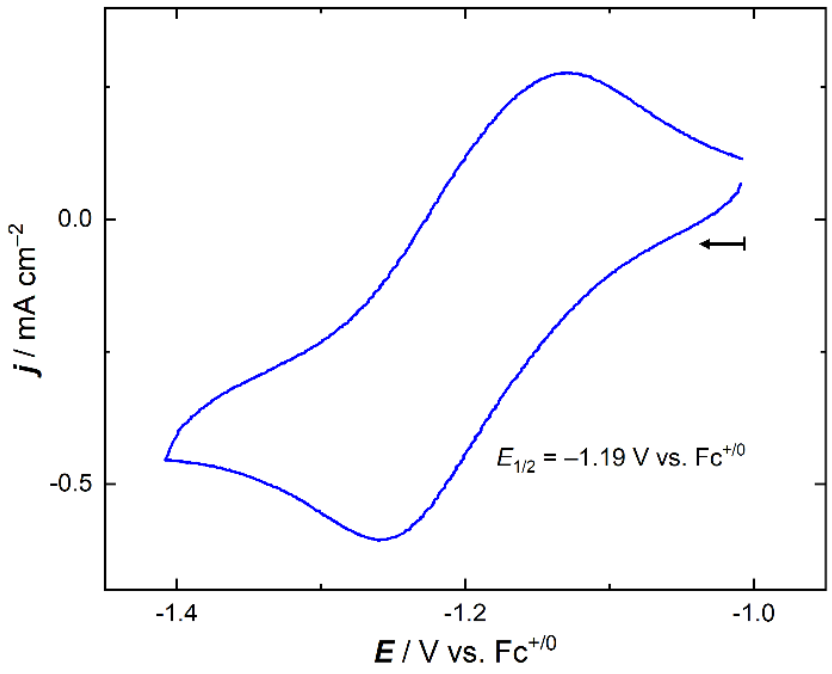

Figure G43. Cyclic voltammetry data for **Co,Rh-μ-OAc** in CH_3CN showing the feature of interest (0.1 M $[^nBu_4N]^+[PF_6]^-$, 100 mV/s).

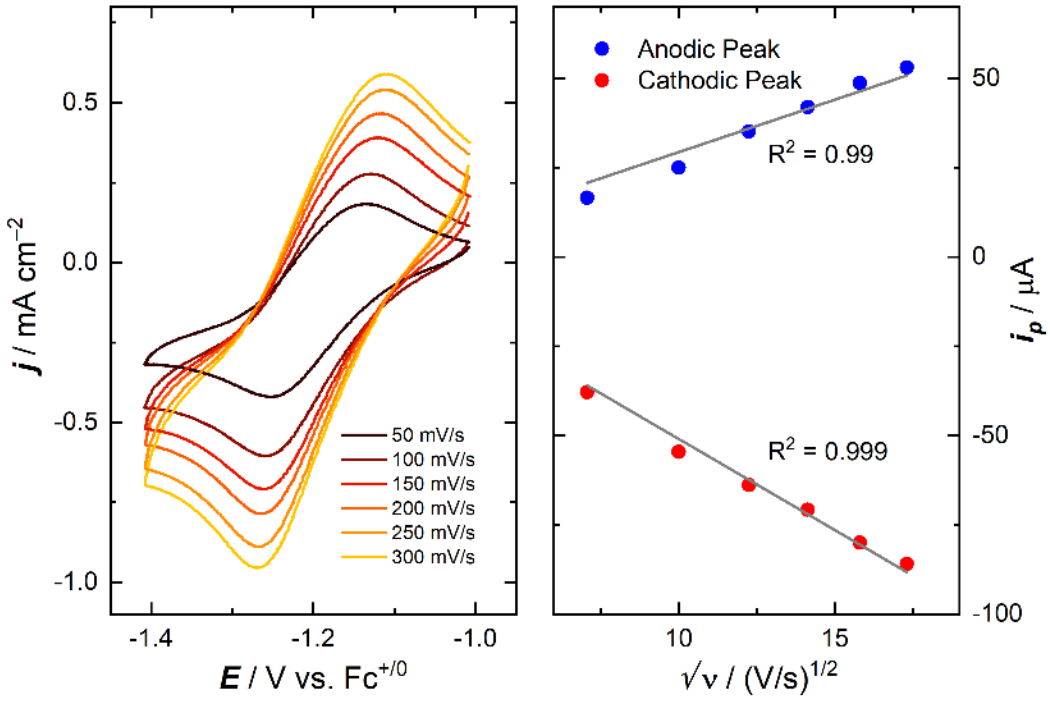

Figure G44. Left panel: scan rate dependence data for **Co,Rh-μ-OAc** complex. Right panel: plot of peak current density vs. (scan rate)$^{1/2}$, demonstrating the diffusional nature of the oxidized and reduced species involved.

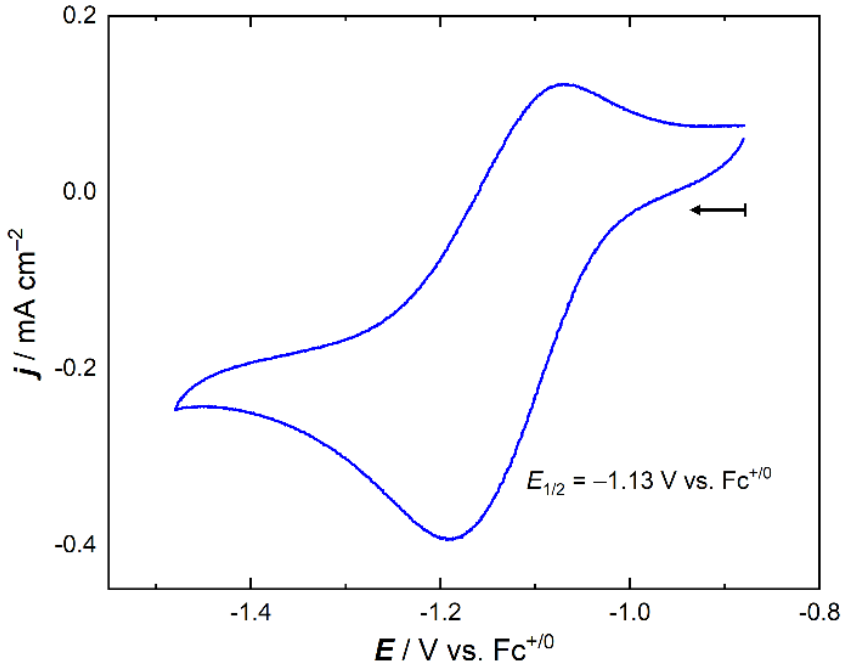

Figure G45. Cyclic voltammetry data for **Co,Ir-μ-OAc** in CH_3CN showing the feature of interest (0.1 M $[^nBu_4N]^+[PF_6]^-$, 100 mV/s).

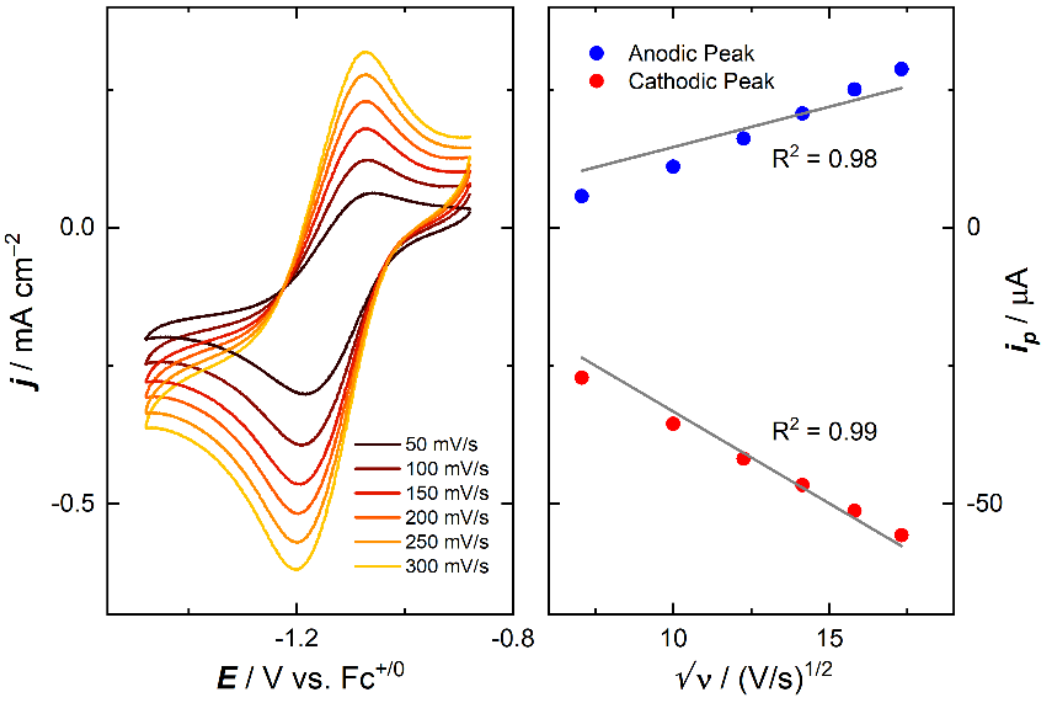

Figure G46. Left panel: scan rate dependence data for **Co,Ir-μ-OAc** complex. Right panel: plot of peak current density vs. (scan rate)$^{1/2}$, demonstrating the diffusional nature of the oxidized and reduced species involved

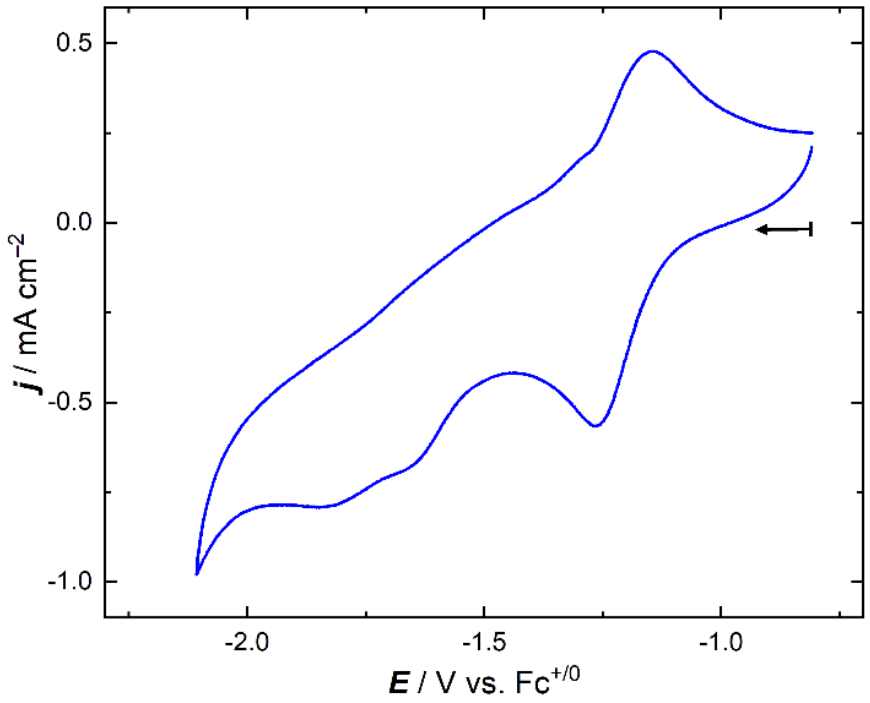

Figure G47. Cyclic voltammetry data for **Co,Rh-μ-OAc** in CH_3CN showing the full scan (0.1 M $[^nBu_4N]^+[PF_6]^-$, 100 mV/s).

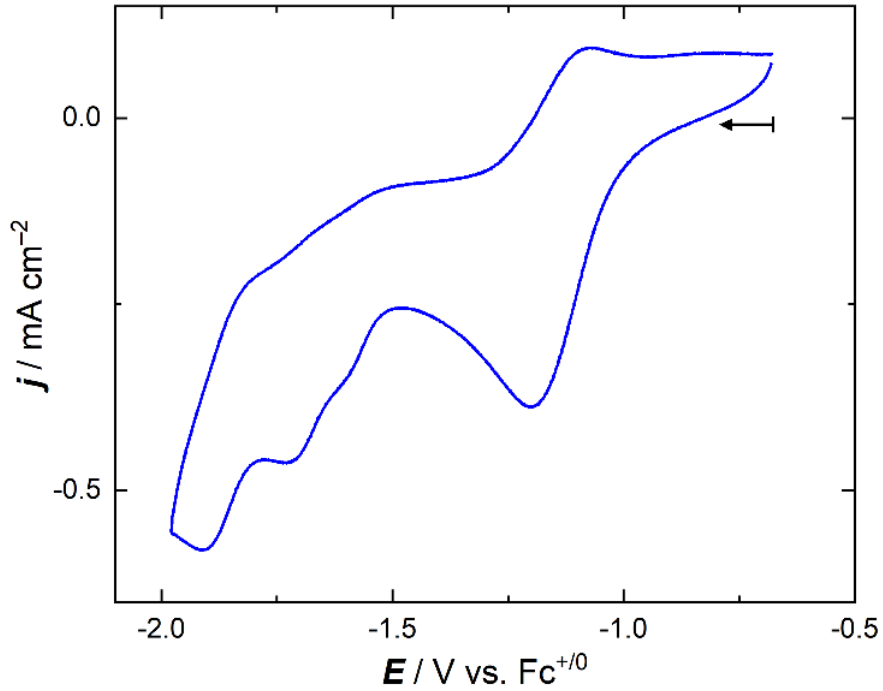

Figure G48. Cyclic voltammetry data for **Co,Ir-μ-OAc** in CH_3CN showing the full scan (0.1 M $[^nBu_4N]^+[PF_6]^-$, 100 mV/s).

Hydrogenation Catalysis

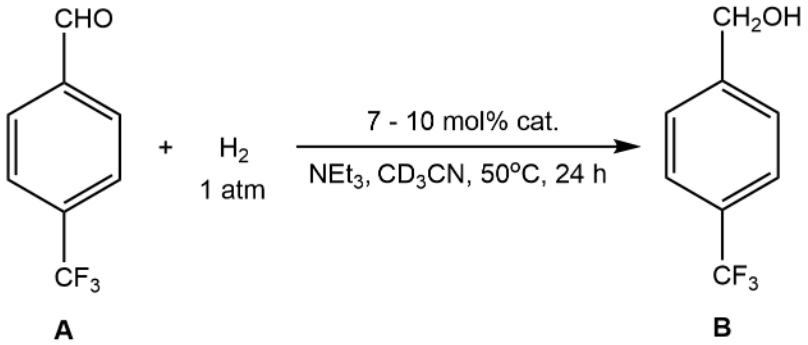

In an inert atmosphere glovebox, a J-young NMR Tube was charged with trifluoromethylbenzaldehyde, **A**. Subsequently, 7 to 10 mol% of the metal complex(es), to be studied for hydrogenation catalysis, was dissolved in 1 mL CD_3CN and added to the NMR tube. A catalytic amount of NEt_3 as a base was also added to the tube. The sealed tube was then transferred to a Schlenk line and degassed using three freeze-pump-thaw cycles. After degassing, the tube was sparged with 1 atmosphere of H_2 gas for few seconds, and the resultant mixture was heated at 50°C for 24 hours. ^{19}F NMR was monitored to check the formation of hydrogenated product trifluoromethylbenzyl alcohol, **B**.

In the absence of any metal complex, no conversion of **A** to **B** was observed. When 10 mol% of **Co-Cl$_2$** was tested for catalysis, again, no conversion was observed. However, usage of 10 mol% **Rh-OAc** (represented by **C**) showed some conversion (13%) of A to B, as judged by ^{19}F NMR. Along with the observance of the peak corresponding to the hydrogenated compound **B** in the ^{19}F NMR, a set of small peaks, indicated by **D**, were also observed, suggesting formation of multiple species or possible decomposition of the catalyst/substrate. The NMR spectrum showed more complex peaks when 10 mol% of a 1:1 mixture of **Co-Cl$_2$** and **Rh-OAc** (reagents used in the synthesis of **Co,Rh-μ-OAc**) was tested for catalysis, however, more conversion (40%) of **A** to **B**

was observed in the ^{19}F NMR. On the other hand, when approximately 7 mol% of the bimetallic complex **Co,Rh-μ-OAc** was tested for catalysis, significant conversion (80%) of **A** to **B** was observed, and no decomposition products could be seen in ^{19}F NMR.

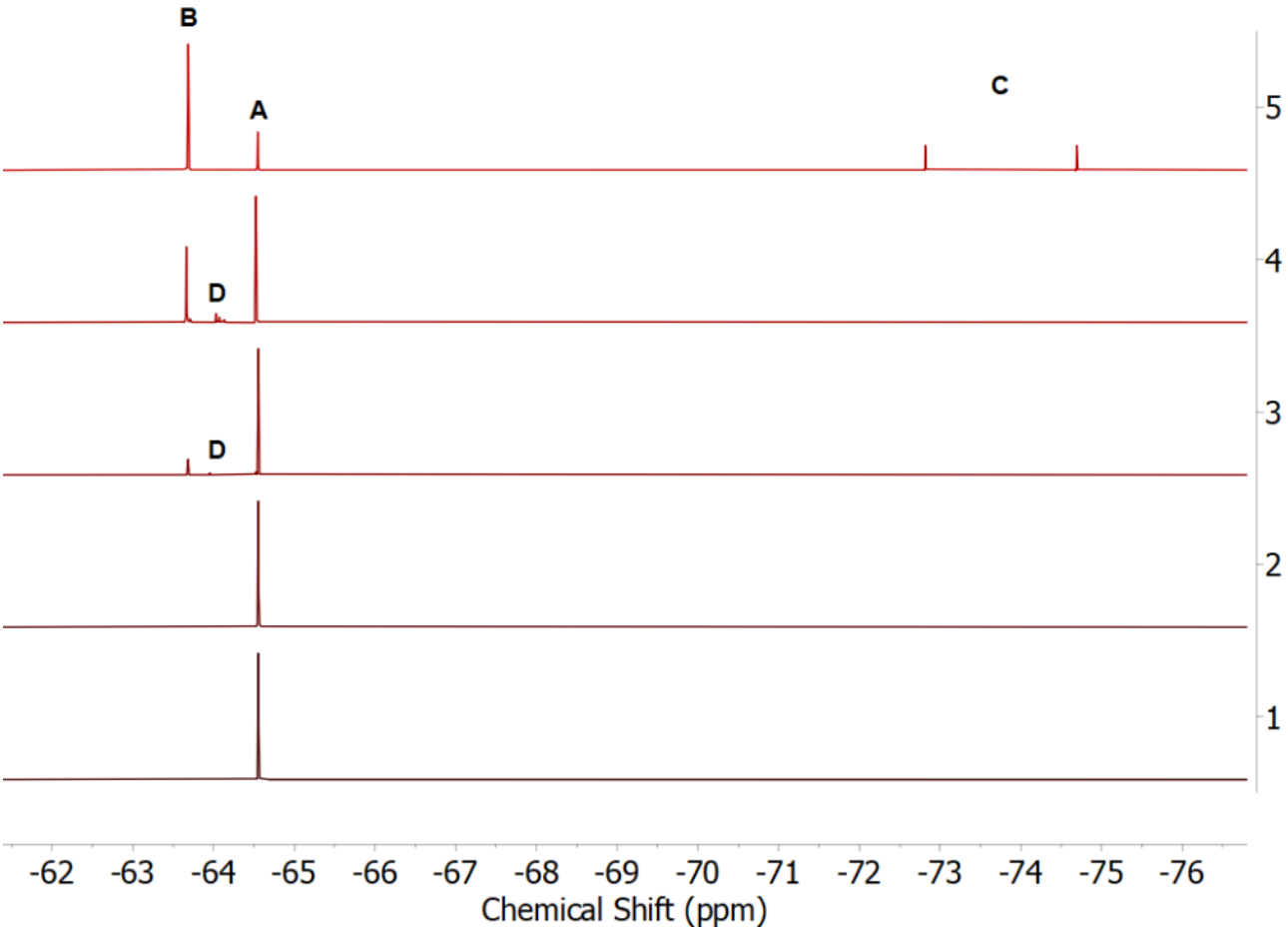

Figure G49. Stacked $^{19}F\{^{1}H\}$ NMR (376 MHz, CD_3CN) spectra showing the effectiveness of hydrogenation of trifluorobenzaldehyde to trifluorobenzyl alcohol. Conditions: (1) No catalyst (2) 10 mol% **Co-Cl$_2$** (3) 10 mol% **Rh-OAc** (4) 10 mol% of a 1:1 mixture of **Co-Cl$_2$** and **Rh-OAc** (5) 7 mol% **Co,Rh-μ-OAc**

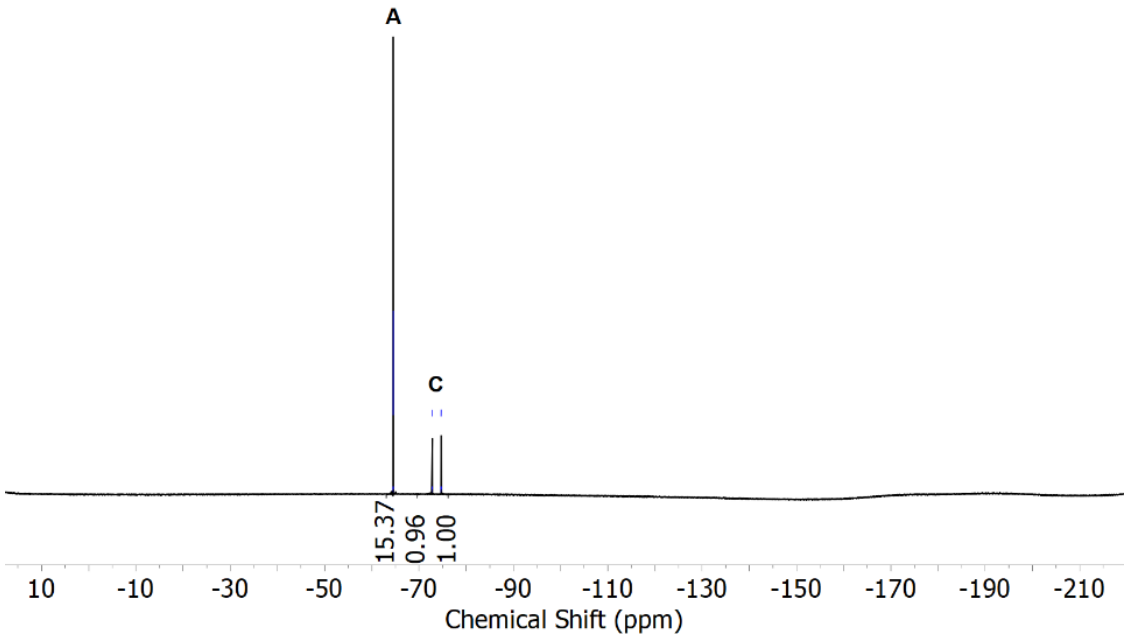

Figure G50. $^{19}F\{^{1}H\}$ NMR (376 MHz, CD_3CN) spectrum recorded before addition of H_2; the spectrum shows 15:1 ratio of trifluorobenzaldehyde to **Co,Rh-μ-OAc** (7 mol% of the catalyst).

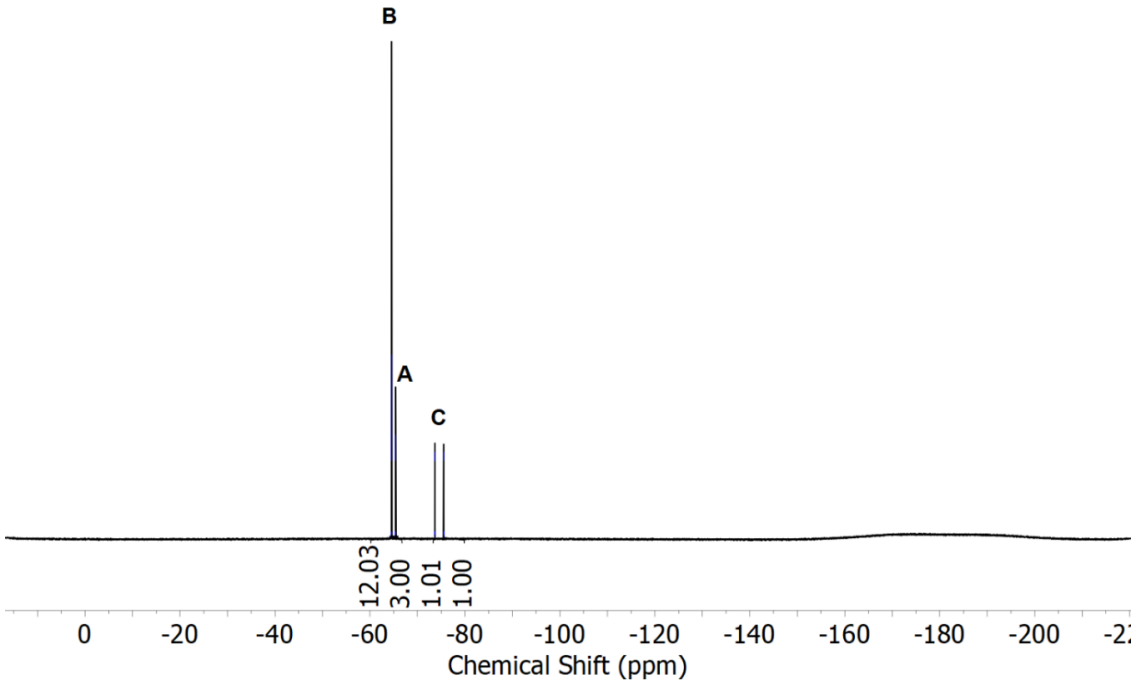

Figure G51. $^{19}F\{^{1}H\}$ NMR (376 MHz, CD_3CN) spectrum showing 1:4 ratio (80% conversion) of trifluorobenzaldehyde to trifluorobenzyl alcohol when hydrogenation experiment was performed in the presence of 7 mol% of **Co,Rh-μ-OAc**.

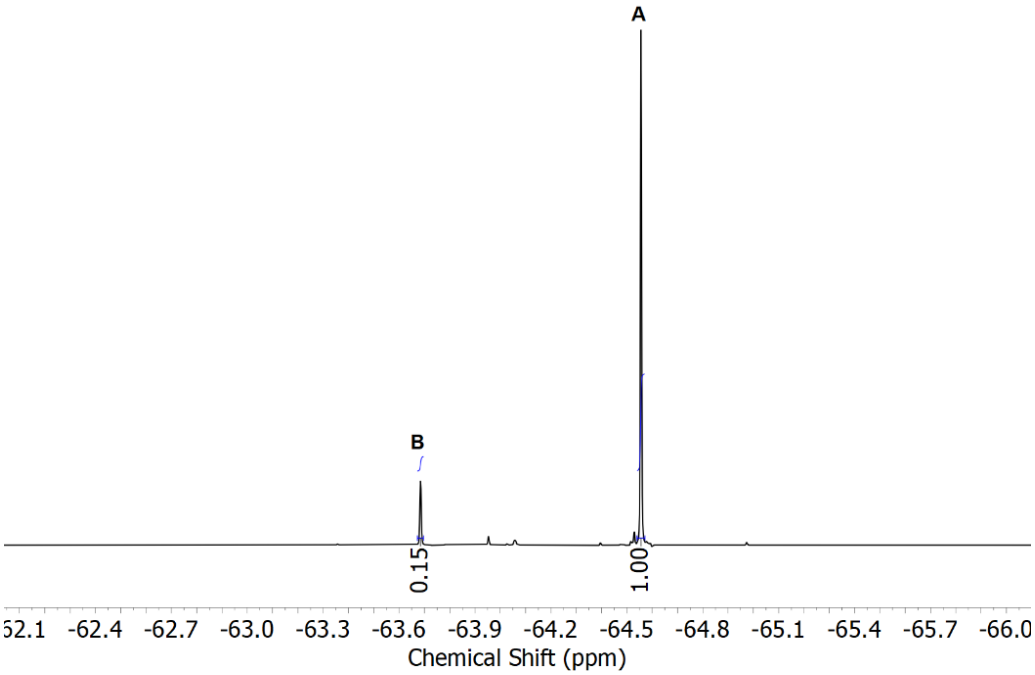

Figure G52. $^{19}F\{^{1}H\}$ NMR (376 MHz, CD_3CN) spectrum showing 1:0.15 ratio (13% conversion) of trifluorobenzaldehyde to trifluorobenzyl alcohol when hydrogenation experiment was performed in the presence of 10 mol% of **Rh-OAc**.

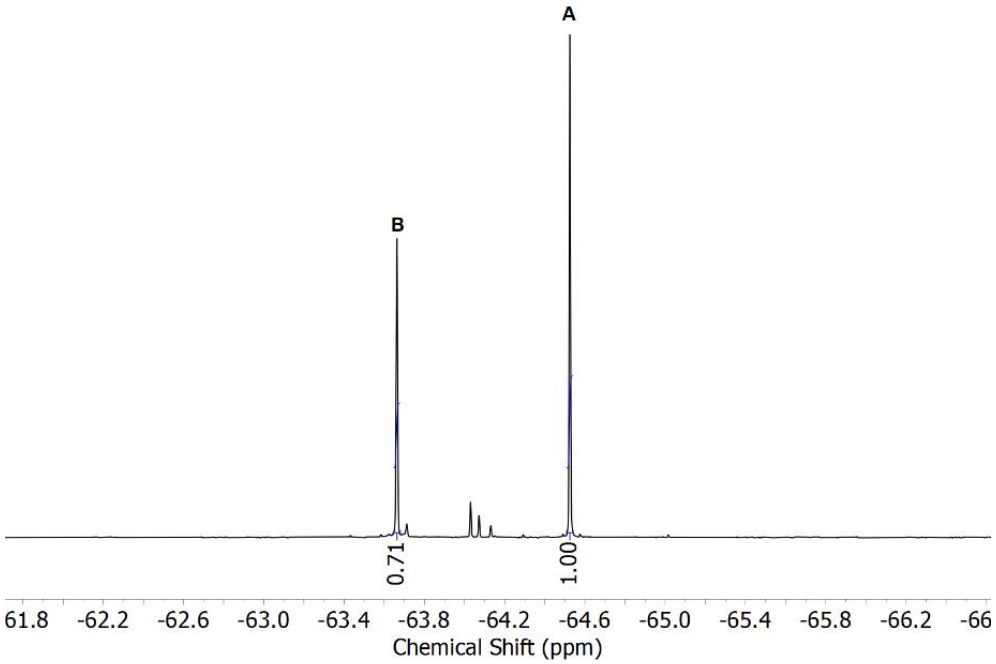

Figure G53. $^{19}F\{^{1}H\}$ NMR (376 MHz, CD_3CN) spectrum showing 1:0.7 ratio (40% conversion) of trifluorobenzaldehyde to trifluorobenzyl alcohol when hydrogenation experiment was performed in the presence of 1:1 mixture of **Co-Cl$_2$** and **Rh-OAc**.

Crystallographic Information

Refinement Details

Crystals for all nine compounds were mounted on a goniometer head using Paratone oil with MiTeGen MicroMounts and placed in a cold nitrogen stream. Complete sets of low-temperature (200 K) diffraction data frames were collected for crystals of all nine compounds using 1.0°-wide ω- and/or ϕ-scans. X-rays were provided either by a Bruker MicroStar microfocus rotating anode generator running at 60 mA and 45kV (Cu K_α = 1.54178 Å) or by a Bruker generator using a fine-focus Mo sealed tube running at 35 mA and 50 kV (Mo K_α = 0.71073 Å). Data for seven compounds (**Ni,Rh-Cl**, **Ni,Rh-OAc**, **Ni,Ir-OAc**, **Co,Rh-μ-OAc**, **Co,Ir-μ-OAc**, **dpgRh-Cl** and **dpgIr-Cl**) were collected with Cu radiation using a Bruker APEX II detector positioned at 50.0 mm and equipped with Helios multilayer mirror optics; data for the other two compounds (**Ni,Ir-Cl** and **dmgIr-Cl**) were collected with Mo radiation using a SMART APEX detector positioned at 50.0 mm and equipped with a MonoCap collimator and graphite monochromator.

Totals of 4444 (**Ni,Rh-Cl)**, 560 **(Ni,Ir-Cl)**, 5238 **(Ni,Rh-OAc)**, 4585 **(Ni,Ir-OAc)**, 3928 **(Co,Rh-μ-OAc)**, 3122 **(Co,Ir-μ-OAc)**, 560 **(dmgIr-Cl)**, 3409 **(dpgRh-Cl)**, and 3928 (**dpgIr-Cl)** 1.0°-wide ω- and/or ϕ-scan frames with counting times of 4-6 seconds (**Ni,Rh-Cl**, **Ni,Rh-OAc**, **Ni,Ir-OAc**, **Co,Rh-μ-OAc**, and **Co,Ir-μ-OAc**), 4-5 seconds **dpgIr-Cl**, 5-8 seconds **dpgRh-Cl**, 5 seconds **dmgIr-Cl** or 10 seconds **Ni,Ir-Cl** were collected on either the Bruker APEX II or the SMART APEX detector. All diffractometer manipulations, including data collection, integration and scaling were carried out using the Bruker APEX2 software package.[1] Eight of the nine data sets were corrected empirically for variable absorption effects with SADABS[2] using equivalent reflections. A numerical face-indexed absorption correction was used for the ninth (**dpgIr-Cl**) data set. Probable space groups were determined on the basis of systematic absences and intensity statistics and the structures were solved by direct methods using SIR2004[3] or XS[4] (incorporated

into SHELXTL) and refined to convergence by weighted full-matrix least-squares on F_o^2 using the Olex2 software package equipped with XL[5] or with SHELXL that was incorporated into the APEX2 software package.

The final structural model for each compound incorporated anisotropic thermal parameters for all but one (water oxygen atom O1W for **dpgIr-Cl**) nonhydrogen atoms; isotropic thermal parameters were used for all included hydrogen atoms and partial-occupancy oxygen atom O1W for **dpgIr-Cl.** Non-methyl hydrogen atoms in each complex were fixed at idealized riding model sp^2- or sp^3-hybridized positions with C–H bond lengths of 0.95 - 0.99 Å. Methyl groups were incorporated into the structural models either as sp^3-hybridized riding model groups with idealized "staggered" geometry and a C-H bond length of 0.98 Å (**dpgRh-Cl**) or as idealized riding model rigid rotors (with a C–H bond length of 0.98 Å) that were allowed to rotate freely about their C–C bonds in least-squares refinement cycles. Oxime hydroxyl groups for all structures except **dpgRh-Cl** were incorporated into the structural models as sp^3-hybridized riding model rigid rotors (with a O–H bond length of 0.84 Å) that were allowed to rotate freely about their N-O bonds in least-squares refinement cycles. Oxime hydroxyl hydrogen atoms for **dpgRh-Cl** were located from a difference Fourier and included in the structural model as independent isotropic atoms whose parameters were allowed to vary in least-squares refinement cycles. The isotropic thermal parameters of idealized hydrogen atoms in all nine structures were fixed at values 1.2 (non-methyl) or 1.5 (methyl or hydroxyl) times the equivalent isotropic thermal parameter of the carbon or oxygen atom to which they are covalently bonded.

Notably, the structures of **Co,Rh-μ-OAc** and **Co,Ir-μ-OAc** are isomorphous. Although the 6-coordinate ionic radius for Rh^{3+} is 0.015 Å smaller than the 6-coordinate ionic radius for Ir^{3+} (from the standard Shannon values[6]), the average $Ir–O_{oxime}$ bond length is 0.004 Å shorter than the

analogous average Rh–O_{oxime} bond length. We ascribe this difference to greater M–L covalency for the Ir vs. Rh system. This is consistent with a slightly shorter O1•••O2 contact between the oxime moieties for **Co,Ir-μ-OAc**.

The relevant crystallographic and structure refinement data for all nine compounds are given in Table G1, G2, G3, G4 and G5.

Special Refinement Details for Ni,Rh-Cl.

No special refinement was required.

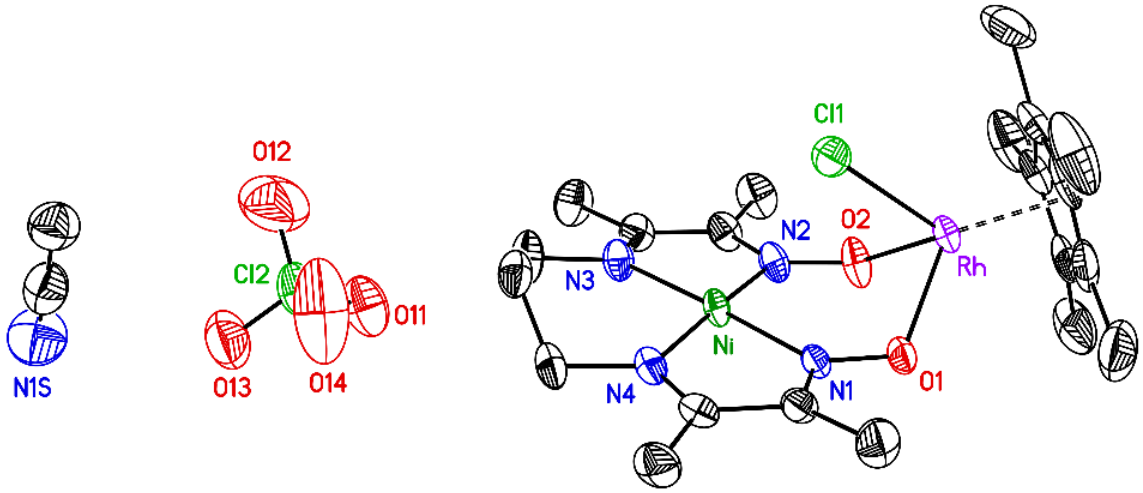

Figure G54. Solid-state structure from XRD of **Ni,Rh-Cl**. H-atoms are omitted for clarity. Displacement ellipsoids are shown at the 50% probability level.

Special Refinement Details for Ni,Ir-Cl.

No special refinement was required.

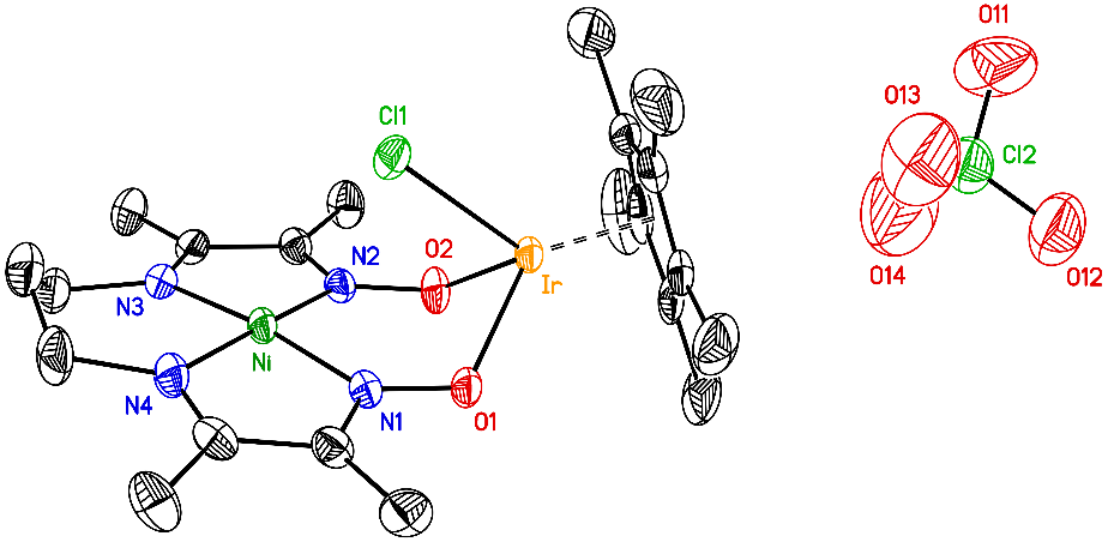

Figure G55. Solid-state structure from XRD of **Ni,Ir-Cl**. H-atoms are omitted for clarity. Displacement ellipsoids are shown at the 50% probability level.

Special Refinement Details for Ni,Rh-OAc.

The outersphere perchlorate counteranion is 56/44 disordered with two orientations.

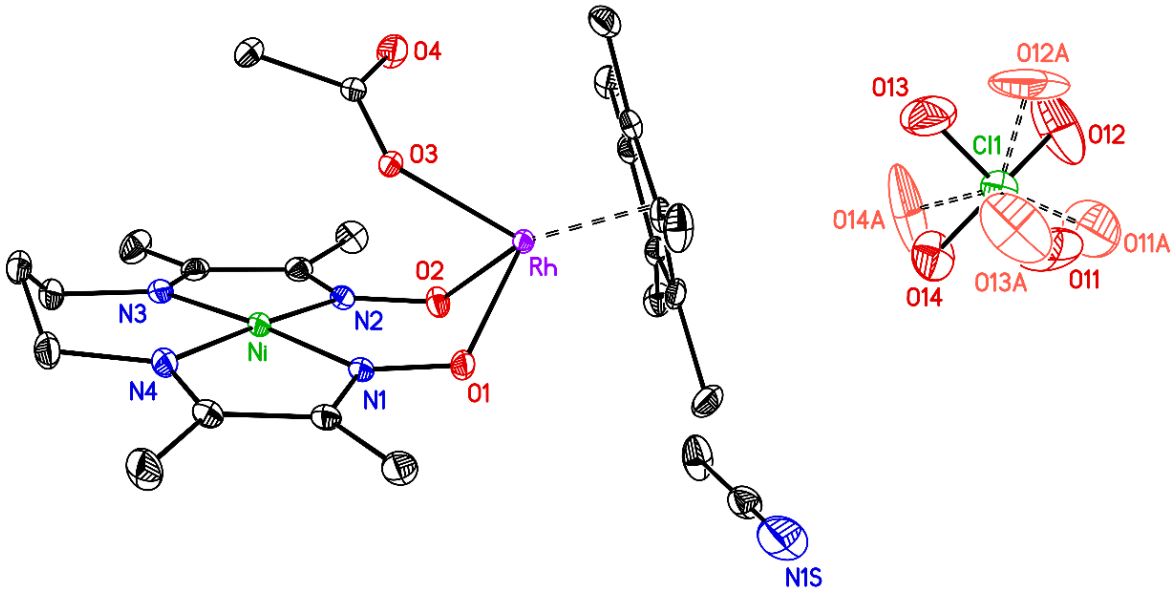

Figure G56. Solid-state structure from XRD of **Ni,Rh-OAc** showing 56/44 disorder for the outersphere perchlorate counteranion. Solid bonds are used for the major (56%) orientation of the perchlorate anion and dashed bonds for the minor (44%) orientation. H-atoms are omitted for clarity. Displacement ellipsoids are shown at the 50% probability level.

Special Refinement Details for Ni,Ir-OAc.

No special refinement was required.

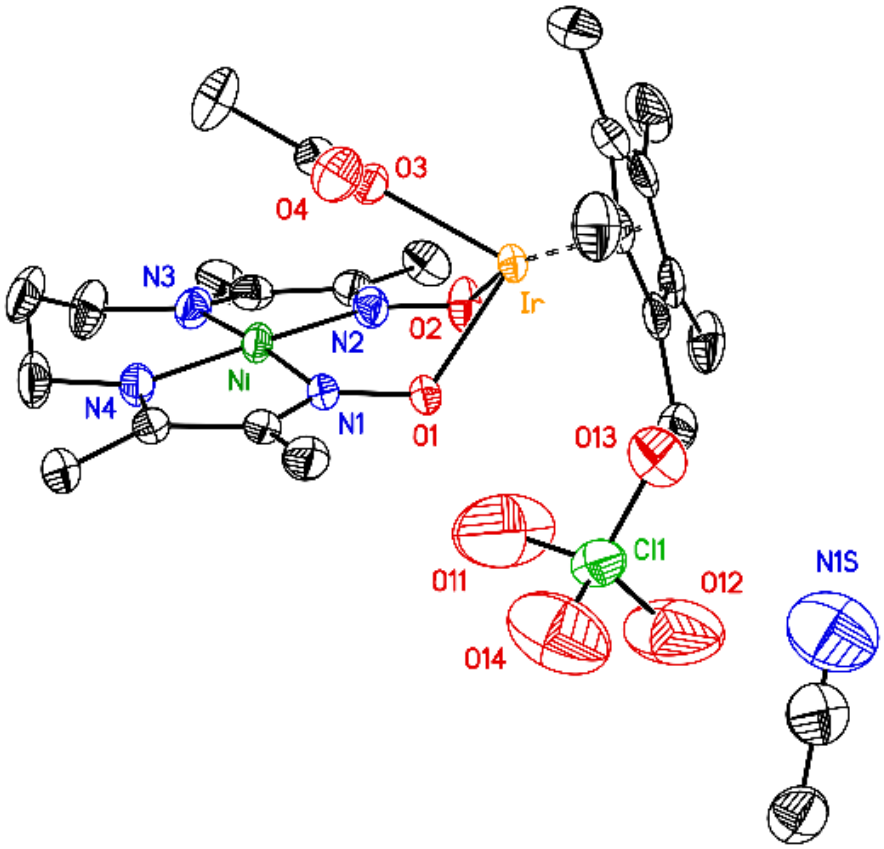

Figure G57. Solid-state structure from XRD of **Ni,Ir-OAc**. H-atoms are omitted for clarity. Displacement ellipsoids are shown at the 50% probability level.

Special Refinement Details for Co,Rh-μ-OAc.

Mild restraints were applied to the anisotropic thermal parameters of atoms C3 and C8.

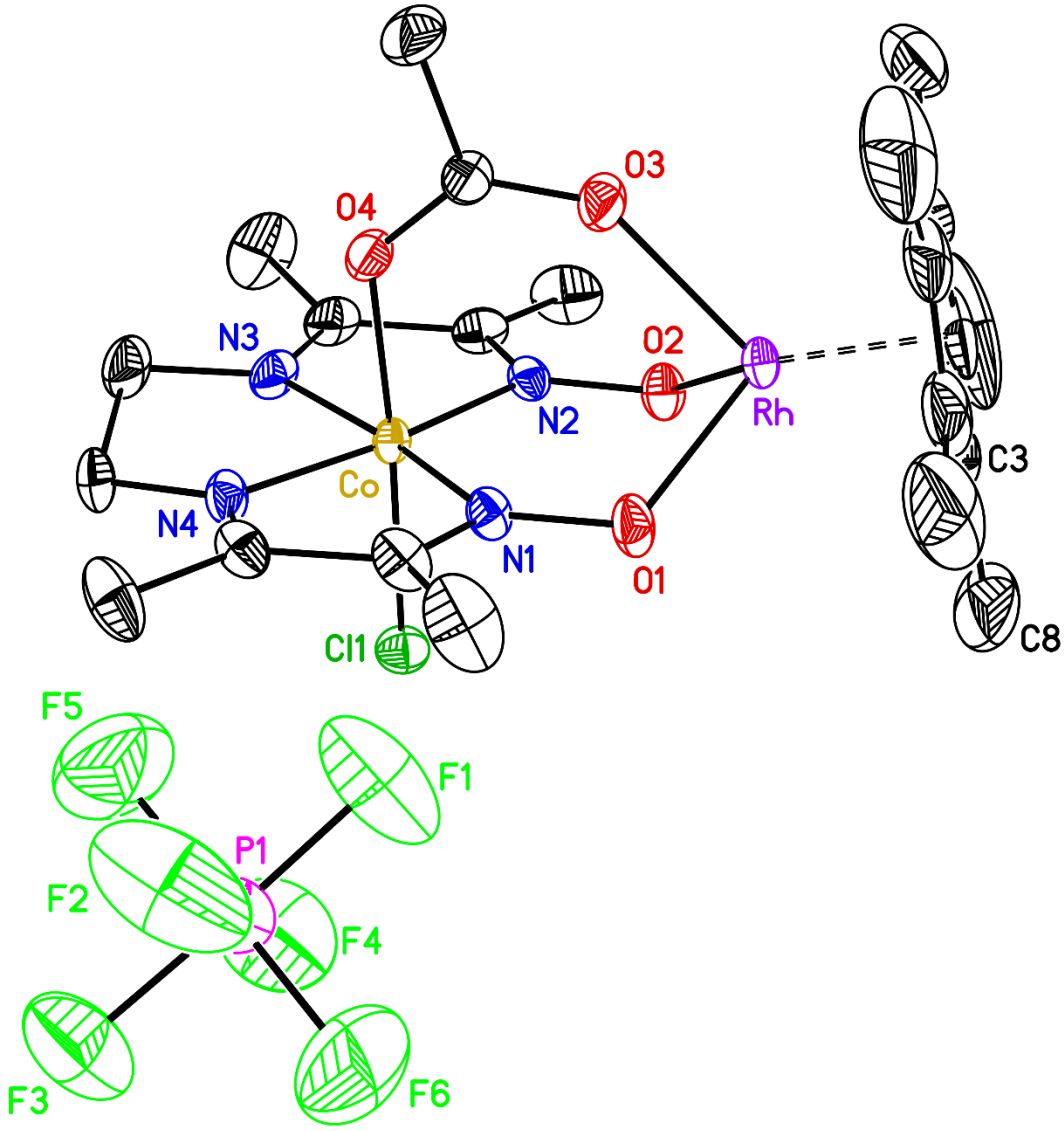

Figure G58. Solid-state structure from XRD of **Co,Rh-μ-OAc** (isomorphous with the Ir analogue). H-atoms are omitted for clarity. Displacement ellipsoids are shown at the 50% probability level.

Special Refinement Details for Co,Ir-μ-OAc.

No special refinement was required.

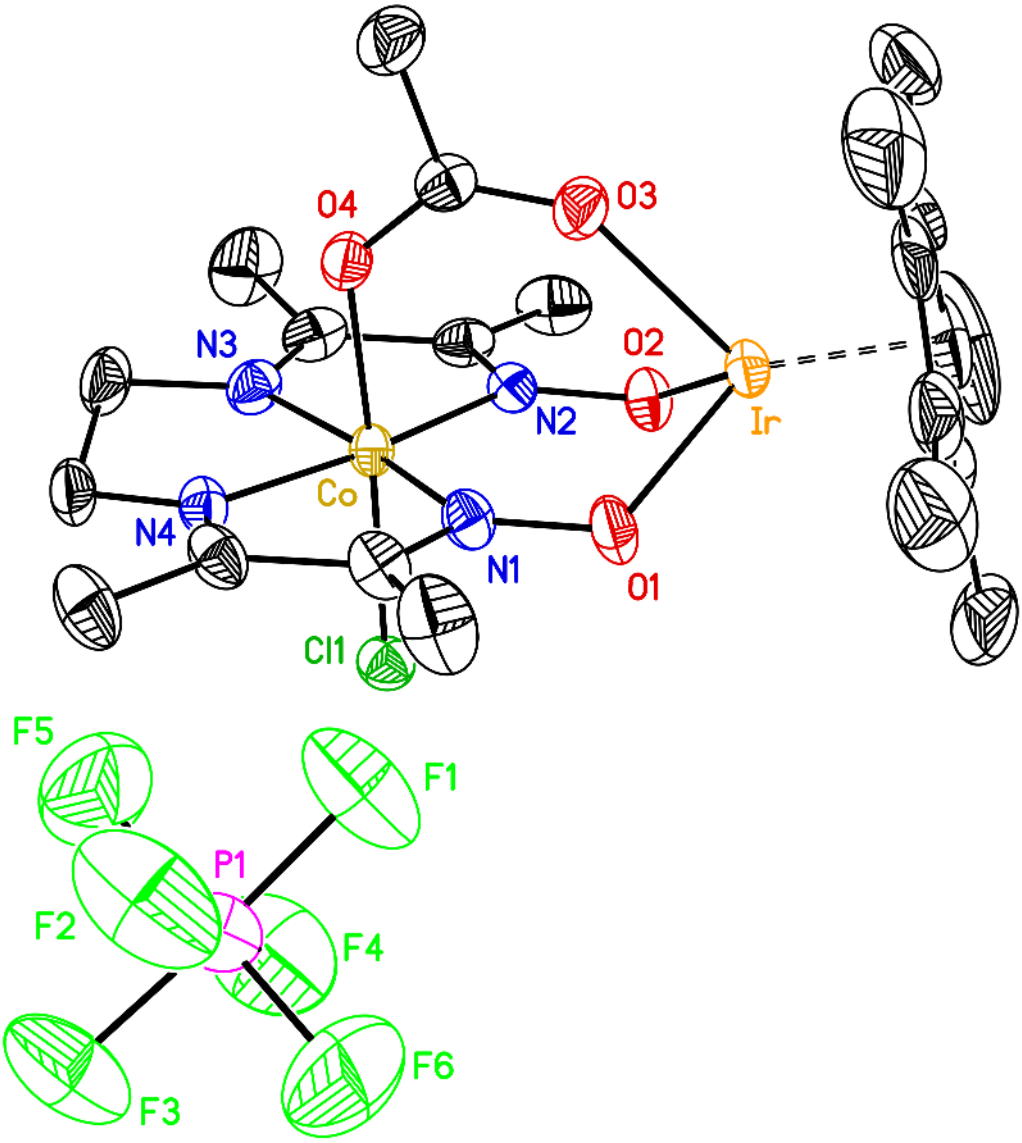

Figure G59. Solid-state structure from XRD of **Co,Ir-μ-OAc** (isomorphous with the Rh analogue). H-atoms are omitted for clarity. Displacement ellipsoids are shown at the 50% probability level.

Special Refinement Details for dmgIr-Cl.

No special refinement was required.

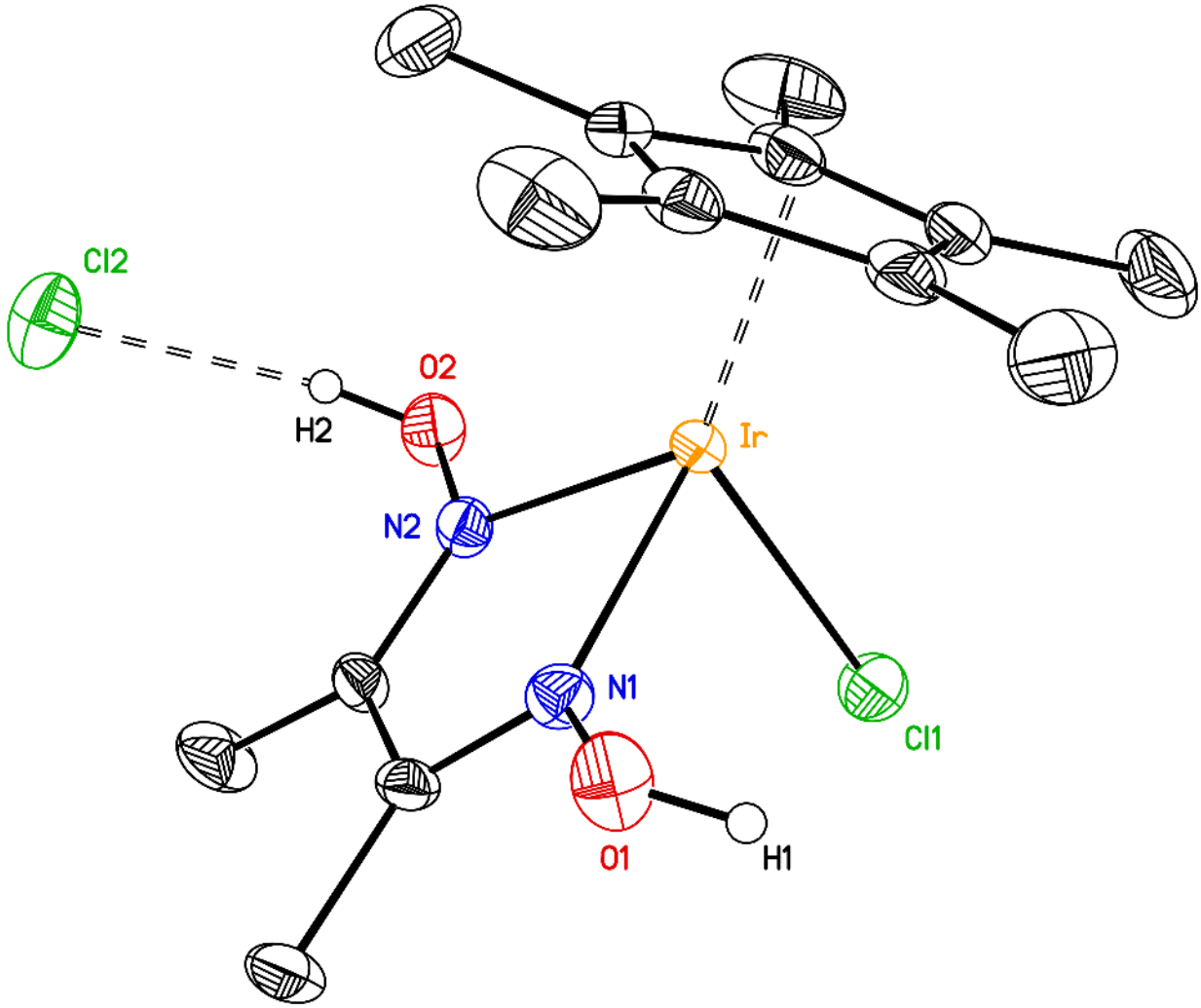

Figure G60. Solid-state structure from XRD of **dmgIr-Cl**. H-atoms except for the ones on oxime oxygen atoms O1 and O2 are omitted for clarity. Hydrogen bonds between the oxime group and the chloride anion are shown with dashed lines. Displacement ellipsoids are shown at the 50% probability level.

Special Refinement Details for dpgRh-Cl.

Methyl groups were fixed at idealized "staggered" positions and the two oxime hydroxyl hydrogen atoms (H1 and H2) were located from a difference Fourier and refined as individual isotropic atoms in least squares cycles.

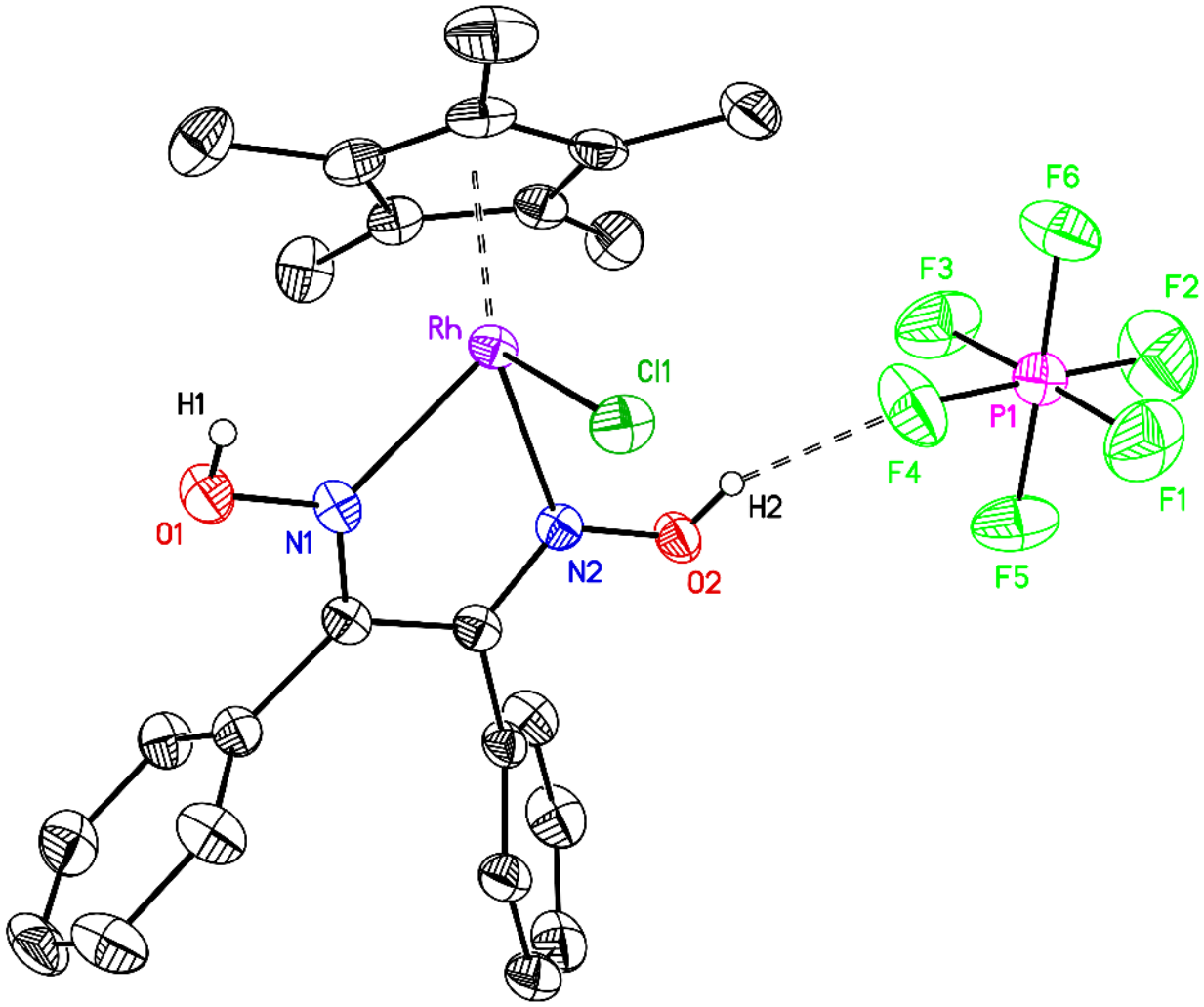

Figure G61. Solid-state structure from XRD of **dpgRh-Cl**. H-atoms, except for the ones on oxime atoms O1 and O2, are omitted for clarity. The hydrogen bond between the oxime group and $[PF_6]^-$ anion is shown with a dashed line. Displacement ellipsoids are shown at the 50% probability level.

Special Refinement Details for dpgIr-Cl.

The second outersphere acetonitrile is 58/42 disordered with two orientations and the anisotropic thermal parameters for the three nonhydrogen atoms of the minor orientation were set to the same values as their counterparts in the major orientation. Water oxygen atom O1W is present only 34% of the time and was included in the refinement as an independent isotropic atom; its hydrogen atoms were not included in the structural model.

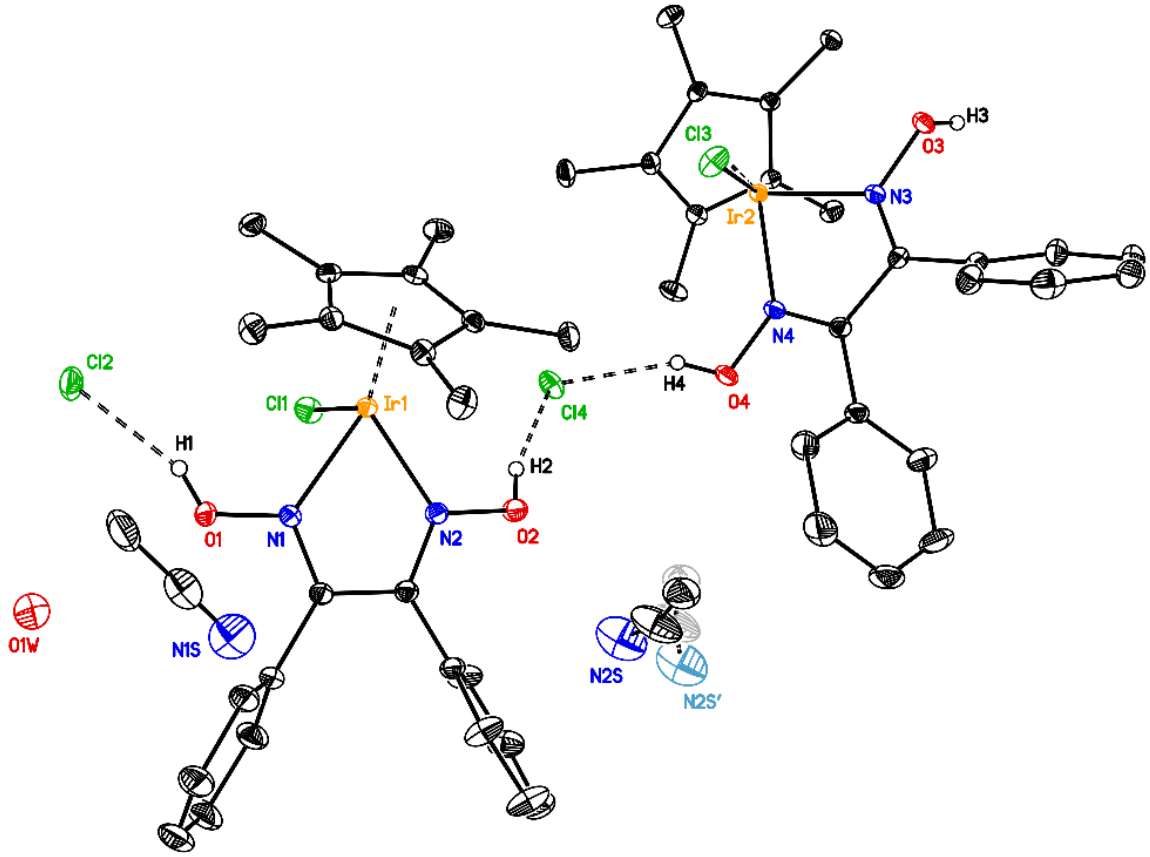

Figure G62. Solid-state structure from XRD of **dpgIr-Cl** showing 58/42 disorder for the second CH_3CN solvent molecule of crystallization. Solid bonds are used for the major (58%) orientation of the CH_3CN and dashed bonds for the minor (42%) orientation. H-atoms, except for the ones on the oxime atoms O1, O2, O3 and O4, are omitted for clarity. Hydrogen bonds between the oxime groups and chloride anions are also shown with dashed lines. Displacement ellipsoids are shown at the 20% probability level.

Table G1. Crystal and Refinement Data for **Ni,Rh-Cl** and **Ni,Ir-Cl**.

	Ni,Rh-Cl (q53g)	**Ni,Ir-Cl (k79k)**
CCDC deposition number	2079401	2079405
Empirical formula	$C_{23}H_{36}Cl_2N_5NiO_6Rh$	$C_{21}H_{33}Cl_2N_4NiO_6Ir$
Formula weight	711.09	759.32
Temperature	200 K	200 K
Wavelength	1.54178 Å	0.71073 Å
Crystal system	Triclinic	Triclinic
Space group	P-1	P-1
a	8.7884(4) Å	8.816(2) Å
b	11.7108(5) Å	11.628 (3) Å
c	15.0396(6) Å	13.486(4) Å
α	69.601(1)°	78.384(3)°
β	87.238(2)°	74.264(3)°
γ	88.203(2)°	89.059(3)°
Volume	1448.9(1) $Å^3$	1302.3(6) $Å^3$
Z	2	2
Density (calculated)	1.630 g/cm^3	1.936 g/cm^3
Absorption coefficient	7.498 mm^{-1}	6.076 mm^{-1}
F(000)	728.0	748.0
Crystal size	0.11 × 0.07 × 0.045 mm^3	0.28 × 0.15 × 0.095 mm^3
Theta range	3.14 to 70.42°	2.14 to 27.50°
Index ranges	$-9\leq h\leq 10$, $-14\leq k\leq 14$, $-18\leq l\leq 16$	$-11\leq h\leq 11$, $-15\leq k\leq 14$, $-17\leq l\leq 17$
Reflections collected	25145	13129
Independent reflections	5159 [R_{int} = 0.056, R_{sigma} = 0.049]	5945 [R_{int} = 0.036, R_{sigma} = 0.048]
Completeness/θ_{max}	96.0%/66.00°	99.9%/25.24°
Absorption correction	Multi-scan	Multi-scan
Max./Min. Transmission	0.753 and 0.427	0.746 and 0.516
Refinement method	Full-matrix least-squares on F^2	Full-matrix least-squares on F^2
Data/restraints/parameters	5161/0/353	5945/0/325
Goodness-of-fit on F^2	1.060	1.034
Final R indices [I>2σ(I)]	R_1 = 0.054, wR_2 = 0.138	R_1 = 0.029, wR_2 = 0.068
R indices (all data)	R_1 = 0.054, wR_2 = 0.140	R_1 = 0.035, wR_2 = 0.070
Largest diff. peak & hole	1.39 and –2.01 $e^-.Å^{-3}$	1.69 and –0.85 $e.Å^{-3}$

Table G2. Crystal and Refinement Data for **Ni,Rh-OAc** and **Ni,Ir-OAc**.

	Ni,Rh-OAc (q67g)	**Ni,Ir-OAc (q54g)**
CCDC deposition number	2079404	2079402
Empirical formula	$C_{25}H_{39}ClN_5NiO_8Rh$	$C_{25}H_{39}ClN_5NiO_8Ir$
Formula weight	734.68	823.97
Temperature	200 K	200 K
Wavelength	1.54178 Å	1.54178 Å
Crystal system	Triclinic	Triclinic
Space group	P-1	P-1
a	9.9107(2) Å	9.9231(2) Å
b	11.6763(2) Å	11.9396(2) Å
c	14.0115(3) Å	14.4187(2) Å
α	73.7861(7)°	72.5977(7)°
β	78.3021(9)°	74.0129(8)°
γ	79.1168(7)°	78.1543(6)°
Volume	1509.45(5) $Å^3$	1552.93(5) $Å^3$
Z	2	2
Density (calculated)	1.616 g/cm^3	1.762 g/cm^3
Absorption coefficient	6.475 mm^{-1}	10.170 mm^{-1}
F(000)	756.0	820.0
Crystal size	0.095 × 0.05 × 0.04 mm^3	0.095 × 0.065 × 0.02 mm^3
Theta range	3.33 to 70.09°	3.3 to 70.31°
Index ranges	$-11\leq h\leq 11$, $-14\leq k\leq 14$, $-15\leq l\leq 17$	$-12\leq h\leq 11$,$-14\leq k\leq 14$,$-17\leq l\leq 17$
Reflections collected	29084	25699
Independent reflections	5372 [R_{int} = 0.026, R_{sigma} = 0.018]	5537 [R_{int} = 0.044, R_{sigma} = 0.035]
Completeness/θ_{max}	96.6%/66.00°	96.7%/66.00°
Absorption correction	Multi-scan	Multi-scan
Max./Min. Transmission	0.753 and 0.568	0.753 and 0.469
Refinement method	Full-matrix least-squares on F^2	Full-matrix least-squares on F^2
Data/restraints/parameters	5372/0/418	5537/0/381
Goodness-of-fit on F^2	1.050	1.048
Final R indices [I>2σ(I)]	R_1 = 0.023, wR_2 = 0.059	R_1 = 0.036, wR_2 = 0.091
R indices (all data)	R_1 = 0.023, wR_2 = 0.059	R_1 = 0.037, wR_2 = 0.092
Largest diff. peak & hole	0.34 and –0.56 $e^-.Å^{-3}$	2.44 and –2.14 $e.Å^{-3}$

Table G3. Crystal and Refinement Data for **Co,Rh-μ-OAc** and **Co,Ir-μ-OAc**.

	Co,Rh-μ-OAc (q79g)	**Co,Ir-μ-OAc (q27h)**
CCDC deposition number	2079406	2079400
Empirical formula	$C_{22}H_{34}ClCoF_6N_4O_4PRh$	$C_{22}H_{34}ClCoF_6N_4O_4PIr$
Formula weight	760.79	850.08
Temperature	200 K	200 K
Wavelength	1.54178 Å	1.54178 Å
Crystal system	Monoclinic	Monoclinic
Space group	$P2_1/c$	$P2_1/c$
a	8.4404(1) Å	8.4262(1) Å
b	12.9229(2) Å	12.9556(2) Å
c	27.3355(5) Å	27.4712(4) Å
α	90°	90°
β	97.5220(10)°	97.8184(7)°
γ	90°	90°
Volume	2955.95(8) $Å^3$	2971.06(7) $Å^3$
Z	4	4
Density (calculated)	1.710 g/cm^3	1.900 g/cm^3
Absorption coefficient	10.923 mm^{-1}	14.919 mm^{-1}
F(000)	1536.0	1664.0
Crystal size	0.17 × 0.11 × 0.07 mm^3	0.045 × 0.04 × 0.015 mm^3
Theta range	3.26 to 70.32°	3.25 to 70.46°
Index ranges	$-10\leq h\leq 10$, $-15\leq k\leq 13$, $-32\leq l\leq 32$	$-10\leq h\leq 10$,$-15\leq k\leq 13$,$-30\leq l\leq 32$
Reflections collected	35679	31276
Independent reflections	5511 [R_{int} = 0.049, R_{sigma} = 0.031]	5544 [R_{int} = 0.054, R_{sigma} = 0.035]
Completeness/θ_{max}	99.8%/66.00°	99.5%/66.00°
Absorption correction	Multi-scan	Multi-scan
Max./Min. Transmission	0.753 and 0.500	0.753 and 0.527
Refinement method	Full-matrix least-squares on F^2	Full-matrix least-squares on F^2
Data/restraints/parameters	5511/12/372	5544/0/372
Goodness-of-fit on F^2	1.164	1.057
Final R indices [I>2σ(I)]	R_1 = 0.039, wR_2 = 0.127	R_1 = 0.029, wR_2 = 0.069
R indices (all data)	R_1 = 0.040, wR_2 = 0.128	R_1 = 0.035, wR_2 = 0.071
Largest diff. peak & hole	0.91 and –0.81 $e^-.Å^{-3}$	0.75 and –0.99 $e.Å^{-3}$

Table G4. Crystal and Refinement Data for **dmgIr-Cl**

	dmgIr-Cl (k73k)
CCDC deposition number	2079407
Empirical formula	$C_{14}H_{23}Cl_2N_2O_2Ir$
Formula weight	514.44
Temperature	200 K
Wavelength	0.71073 Å
Crystal system	Orthorhombic
Space group	$P2_12_12_1$
a	11.069(5) Å
b	11.926(5) Å
c	13.290(6) Å
α	90°
β	90°
γ	90°
Volume	1754.4(14) $Å^3$
Z	4
Density (calculated)	1.948 g/cm^3
Absorption coefficient	7.920 mm^{-1}
F(000)	992.0
Crystal size	0.55 × 0.29 × 0.17 mm^3
Theta range	2.29 to 33.08°
Index ranges	$-16\leq h\leq 16, -18\leq k\leq 17, -20\leq l\leq 20$
Reflections collected	23774
Independent reflections	6448 [R_{int} = 0.054, R_{sigma} = 0.055]
Completeness/θ_{max}	99.9%/25.24°
Absorption correction	Multi-scan
Max./Min. Transmission	0.746 and 0.333
Refinement method	Full-matrix least-squares on F^2
Data/restraints/parameters	6448/0/200
Goodness-of-fit on F^2	0.997
Final R indices [I>2σ(I)]	R_1 = 0.027, wR_2 = 0.054
R indices (all data)	R_1 = 0.032, wR_2 = 0.055
Largest diff. peak & hole	1.07 and –1.90 e.$Å^{-3}$

Table G5. Crystal and Refinement Data for **dpgRh-Cl** and **dpgIr-Cl**.

	dpgRh-Cl (q65g)	**dpgIr-Cl (q58g)**
CCDC deposition number	2079403	2079408
Empirical formula	$C_{24}H_{27}ClF_6N_2O_2PRh$	$C_{26}H_{30}Cl_2N_3O_{2.17}Ir$
Formula weight	658.80	682.33
Temperature	200 K	200 K
Wavelength	1.54178 Å	1.54178 Å
Crystal system	Monoclinic	Monoclinic
Space group	C2/c	$P2_1/c$
a	28.9187(8) Å	21.2353(7) Å
b	8.1156(2) Å	16.5815(5) Å
c	22.5591(6) Å	16.8692(6) Å
α	90°	90°
β	93.588(1)°	109.643(2)°
γ	90°	90°
Volume	5284.1(2) $Å^3$	5594.2(3) $Å^3$
Z	8	8
Density (calculated)	1.656 g/cm^3	1.620 g/cm^3
Absorption coefficient	7.348 mm^{-1}	11.214 mm^{-1}
F(000)	2656.0	2683.0
Crystal size	0.25 × 0.03 × 0.01 mm^3	0.12 × 0.08 × 0.02 mm^3
Theta range	3.93 to 70.32°	4.42 to 70.44°
Index ranges	$-34\leq h\leq 34$, $-9\leq k\leq 9$, $-27\leq l\leq 25$	$-25\leq h\leq 25$, $-19\leq k\leq 17$, $-20\leq l\leq 20$
Reflections collected	31243	61538
Independent reflections	4919 [R_{int} = 0.062, R_{sigma} = 0.046]	10442 [R_{int} = 0.063, R_{sigma} = 0.036]
Completeness/θ_{max}	99.9%/66.00°	99.6%/66.00°
Absorption correction	Multi-scan	Numerical face-indexed
Max./Min. Transmission	0.753 and 0.557	0.783 and 0.406
Refinement method	Full-matrix least-squares on F^2	Full-matrix least-squares on F^2
Data/restraints/parameters	4918/0/342	10442/9/645
Goodness-of-fit on F^2	1.050	1.043
Final R indices [I>2σ(I)]	R_1 = 0.034, wR_2 = 0.085	R_1 = 0.029, wR_2 = 0.071
R indices (all data)	R_1 = 0.040, wR_2 = 0.089	R_1 = 0.033, wR_2 = 0.074
Largest diff. peak & hole	1.09 and –0.42 $e^-.Å^{-3}$	2.43 and –1.13 $e.Å^{-3}$

References

(1) *SAINT. Ver. 8.34A.* Bruker Analytical X-ray Systems: Madison, WI, June 2014.

(2) *Sheldrick, G. M., SADABS (version 2008/1)*: Program for Absorption Correction for Data from Area Detector Frames, University of Göttingen, 2008.

(3) Sheldrick, G. SHELXT – Integrated space-group and crystal-structure determination. *Acta Cryst.* **2015**, *A71*, 3-8.

(4) Sheldrick, G. Crystal structure refinement with SHELXL. *Acta Cryst.* **2015**, *C71*, 3-8.

(5) Dolomanov, O. V.; Bourhis, L. J.; Gildea, R. J.; Howard J. A. K.; Puschmann, H. OLEX2: a complete structure solution, refinement and analysis program. *J. Appl. Crystallogr.* **2009**, *42*, 339-341.

(6) Shannon, R. D. Revised effective ionic radii and systematic studies of interatomic distances in halides and chalcogenides. *Acta Cryst.* **1976**, *A32*, 751-767.